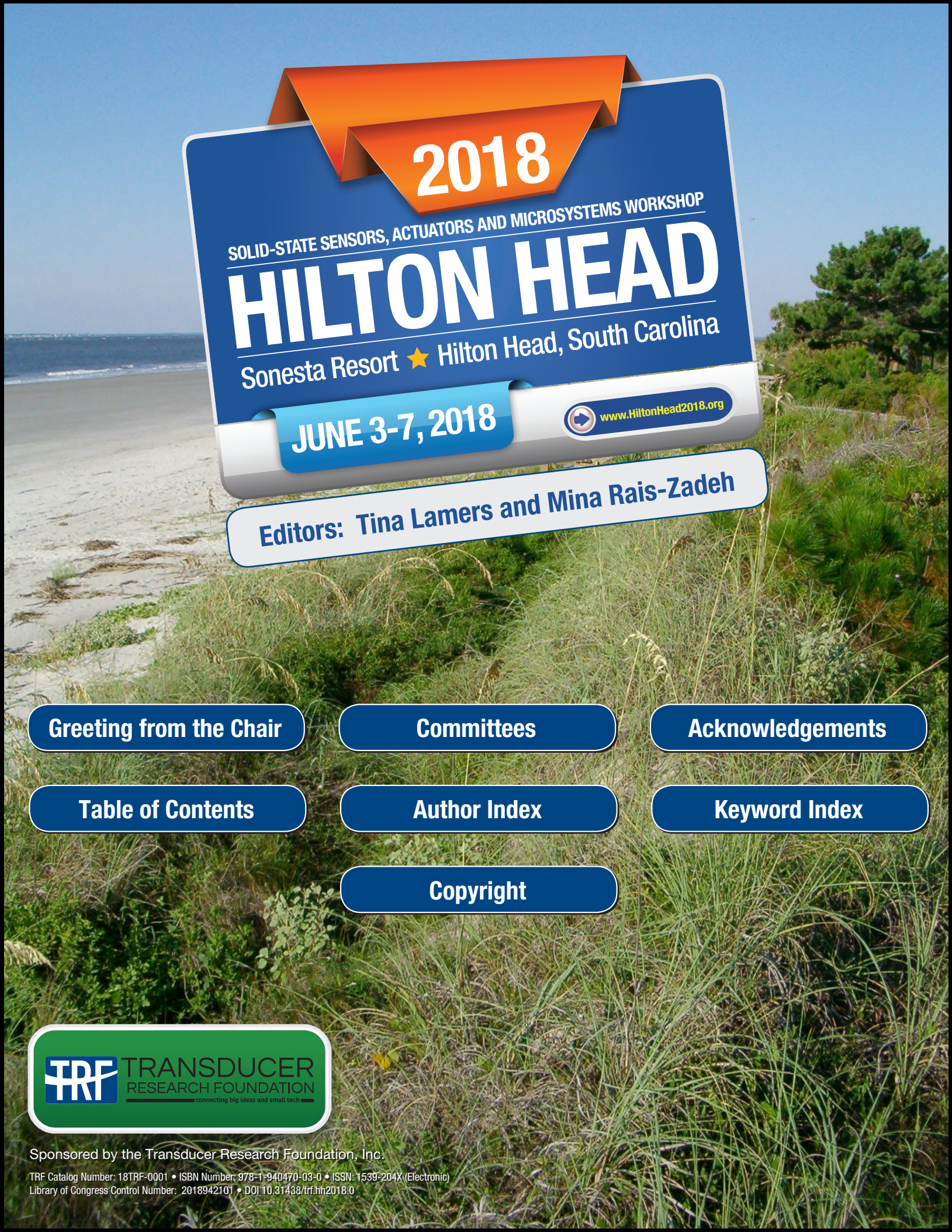

2018

SOLID-STATE SENSORS, ACTUATORS AND MICROSYSTEMS WORKSHOP

HILTON HEAD

Sonesta Resort ★ Hilton Head, South Carolina

JUNE 3-7, 2018

www.HiltonHead2018.org

Editors: Tina Lamers and Mina Rais-Zadeh

TRF TRANSDUCER RESEARCH FOUNDATION
connecting big ideas and small tech

Sponsored by the Transducer Research Foundation, Inc.

TRF Catalog Number: 18TRF-0001 • ISBN Number: 978-1-940470-03-0 • ISSN: 1539-204X (Electronic)
Library of Congress Control Number: 2018942101 • DOI 10.31438/trf.hh2018.0

Greetings from the Chair

I am very excited to welcome you to the 2018 Solid State Sensors, Actuators, and Microsystems Workshop; the eighteenth in the biennial series of regional meetings that alternate with the International Transducers Conference. The goal of the Workshop - since its inception in 1984 - has been to provide a forum for exchange of new ideas and leading-edge research achievements in MEMS and Sensors, in a setting that facilitates community building. I am thrilled you are here to experience this year's excellent program with us.

Mina Rais-Zadeh has assembled an expert program committee in support of the Workshop's goal. Mind-expanding plenary presentations by leading government and academic experts will kick-off each day, followed by oral and poster sessions of contributed papers. The Workshop schedule continues to be organized around single session oral and poster presentations. We have continued the tradition of significant unstructured time for informal discussions and networking. Be sure to use these times for technical brainstorming and collaboration building, as well as career and business development.

All papers were selected on the basis of high-quality content and leading-edge contribution. Those deemed of broader interest to the attendees were designated as oral and those of special interest as poster. The "shotgun" format is used to inform the attendees of the content of the upcoming poster session of the day. Late News Oral and Poster papers selection process occurred in mid-March and bring the latest research to the attendees. During the period formally known as the "Rump Session", we will be asking for your input on the meeting. We have also incorporated a radio play by our own Steve Senturia on a topic pertinent to this audience into this year's program. A tremendous "thank you" goes to Mina Rais-Zadeh and the Technical Program Committee for putting together the technical content of the Workshop, which required studying, debating, ranking, and selecting from 133 submitted high quality abstracts.

Michelle Bourke worked tirelessly to create the commercial support and exhibition contributions of this meeting. A special thanks also goes to the Transducer Research Foundation for their travel grant support for the presenting student authors. The involvement of these individuals, and the financial support of the exhibitors and corporate sponsors are invaluable features of the Hilton Head Workshop, and I am grateful to have had these outstanding people and companies participate.

Sara Stearns and her team at Preferred Meeting Management, Inc., above all, deserve special recognition and thanks for all of their hard work and superb organization in pulling this meeting together and for making it run so smoothly. The work they do "behind the scenes" over the two years of preparation to make this meeting special is exceptional; our community and our meeting are the beneficiaries of their high caliber work.

This meeting belongs to all of you; thank you for your enthusiastic participation. My best wishes for a memorable gathering in Hilton Head Island this June 2018.

Tina Lamers
General Chair

Organizing Committee

General Chair Tina Lamers, *Uber ATG, USA*

Technical Program Chair Mina Rais-Zadeh, *JPL and University of Michigan, USA*

Commercial Development Committee Michelle Bourke, *Lam Research, USA*

Technical Program Committee Members

Farrokh Ayazi
Georgia Institute of Technology, USA

Sarah Bergbreiter
University of Maryland, USA

Emmanunelle Briot
Qorvo, USA

Cullen Buie
Massachusetts Institute of Technology, USA

Jenna Chan
ECS Federal LLC, USA

Karen Cheung
University of British Columbia, CANADA

Amy Duwel
Charles Stark Draper Laboratory, Inc., USA

Sam Emaminejad
University of California, Los Angeles, USA

Jason Gorman
National Institute of Standards & Technology (NIST), USA

Amy Herr
University of California, Berkeley, USA

Hal Jerman
Coherent, USA

Amit Lal
Cornell University, USA

Mary Ann Maher
SoftMEMS, USA

Mehrnaz Motiee
Analog Devices, USA

Raviv Perahia
HRL Laboratories, USA

Steven Tin
Honeywell, USA

Dana Weinstein
Purdue University, USA

Euisik Yoon
University of Michigan, USA

Y.-K. Yoon
University of Florida, USA

Maryam Ziaei
iSono Health, USA

Qiang Zou
Broadcom, USA

Technical Program Committee

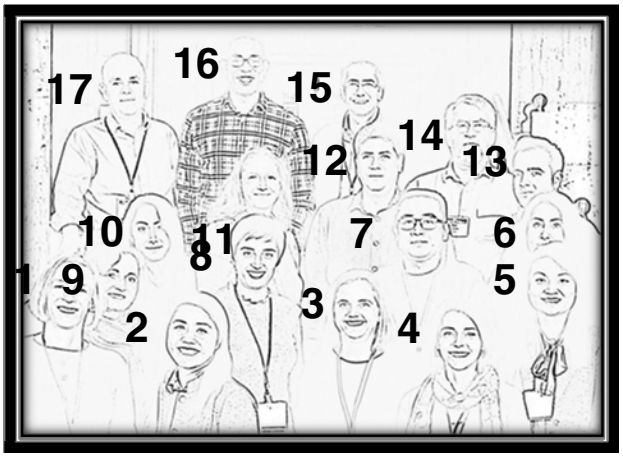

1 – Tina Lamers
2 – Karen Cheung
3 – Sarah Bergbreiter
4 – Dana Weinstein
5 – Jenna Chan
6 – Mehrnaz Motiee
7 – Qiang Zou
8 – Mina Rais-Zadeh
9 – Emmanuelle Briot
10 – Maryam Ziaie
11 – Mary Ann Maher
12 – Raviv Perahia
13 – Sam Emaminejad
14 – Hal Jerman
15 – Farrokh Ayazi
16 – Cullen Buie
17 – Jason Gorman

Not Pictured: Amy Duwel, Amy Herr, Amit Lal, Steven Tin, Euisik Yoon and Y.-K Yoon

Transducer Research Foundation

Officers

President ..... Thomas W. Kenny, Stanford University, USA
Vice-President ..... Antonio J. Ricco, NASA Ames Research Center, USA
and Dublin City University, IRELAND
Treasurer ..... Dave Monk, NXP Semiconductor, USA
Secretary ..... Kimberly Foster, University of California, Santa Barbara, USA

Directors

Mark Allen ..... University of Pennsylvania, USA
Alissa M. Fitzgerald ..... AMFitzgerald, USA
Thomas W. Kenny ..... Stanford University, USA
Tina Lamers ..... Uber ATG, USA
Ellis Meng ..... University of Southern California, USA
Dave Monk ..... NXP Semiconductor, USA
Antonio J. Ricco ..... NASA Ames Research Center, USA
and Dublin City University, IRELAND
Leland "Chip" Spangler ..... Aspen Microsystems, USA
Kimberly Foster ..... University of California, Santa Barbara USA
James Walker ..... KBSO Patent Law, USA

Executive Director ..... Katharine K. Cline

Overseers

Luc Bousse ..... POC Medical Systems, USA
Joe Giachino
G. Benjamin Hocker
Roger Howe ..... Stanford University, USA
Mehran Mehregany ..... Case Western Reserve University, USA
Richard Muller ..... University of California, Berkeley, USA
Kurt Petersen ..... Silicon Valley Band of Angels, USA
Martin A. Schmidt ..... Massachusetts Institute of Technology, USA
Steve Senturia
Ken Wise

Acknowledgements

Special acknowledgement to the Transducer Research Foundation, Inc. for their educational grant funding support of this Workshop.

Exhibitors and Benefactors

We gratefully acknowledge the support of this Workshop from the following companies and institutions as of the printing of May 9, 2018:

Advanced Micro Patterning

BSAC: Berkeley Sensor & Actuator Center

Coventor, Inc.

Grinding & Dicing Services Incorporated

Heidelberg Instruments, Inc.

Institute for Nano-Engineered Systems (NanoES) - University of Washington

IntelliSense

InvenSense, a TDK Group Company

Knowles Corporation

LioniX International

LynceeTec SA

MEMS Journal

memsstar

MEMStaff Inc.

Microsystems & Nanoengineering/Nature Publishing Group

NXP Semiconductors

Okmetic

Polytec, Inc.

Silex Microsystems, Inc.

Solmates B.V.

SPTS Technologies

TechInsights

ULVAC

WIMS^2: Wireless Integrated MicroSystems and
Systems Electrical and Computer Engineering (ECE) at Michigan

Table of Contents

Scroll to the title and select a **Blue** link to open a paper. After viewing the paper, use the bookmarks to the left to return to the beginning of the Table of Contents.

Sunday, June 3

6:00 pm - 9:00 pm **Registration and Welcome Reception**

Monday, June 4

7:00 am **Breakfast**

7:45 am **Welcome**
Tina Lamers, *Uber ATG, USA*
Mina Rais-Zadeh, *University of Michigan, USA*

Plenary Presentation I

Session Chair: M. Rais-Zadeh, *University of Michigan, USA*

Session 1 - Physics of Microfluidics

Session Chair: C. Buie, *Massachusetts Institute of Technology, USA*

10:05 am **Break and Table Top Exhibits**

Session 2 - Optical Microsystems

Session Chair: J. Gorman, *National Institute of Standards & Technology (NIST), USA*

10:30 am **TUNABLE COLOR REFLECTOR WITH ZERO STATIC POWER** 15
M. Jafari[1], L.J. Guo[1], and M. Rais-Zadeh[1,2]
[1]University of Michigan, USA and [2]NASA Jet Propulsion Laboratory (JPL), USA

10:50 am **A RECONFIGURABLE OPTOFLUIDIC DEVICE FOR ADAPTIVE IMAGING AND POSITION ESTIMATION WITH A WIDE FIELD OF VIEW** 19
H. Huang and Y. Zhao
Ohio State University, USA

11:10 am **BIOINSPIRED MULTIFUNCTIONAL NANOSTRUCTURES FOR MICRO-OPTICAL IMPLANTS** 23
V. Narasimhan[1], R.H. Siddique[1], J.O. Lee[1], S. Kumar[1], B. Ndjamen[1], J. Du[2], N. Hong[1], D. Sretavan[2], and H. Choo[1]
[1]California Institute of Technology, USA and
[2]University of California, San Francisco, USA

11:30 am **Preview of Poster Session 1 Presentations**
Session Chairs: E. Briot, *Qorvo, USA* and J. Chan, *ECS Federal, LLC, USA*

12:00 pm **Networking Lunch**

Poster Session 1

Session Chair: D. Weinstein, *Purdue University, USA*

1:30 pm **Contributed and Late News**

4:00 pm **End of Day**

Tuesday, June 5

7:30 am **Breakfast**

8:10 am **Announcements**

Plenary Presentation II

Session Chair: A. Herr, *University of California, Berkeley, USA*

8:15 am **TOWARDS INDUSTRIALISATION OF MICROFLUIDIC SAMPLE-TO-ANSWER SOLUTIONS ENABLING POINT-OF-USE TESTING OF BIOSAMPLES: A DESIGN-FOR-MANUFACTURE LED PLATFORM APPROACH** 26
Jens Ducrée
Dublin City University, Ireland

Session 3 - Wearable Devices

Session Chair: Y.-K. Yoon, *University of Florida, USA*

9:05 am **PRECISION HIGH-BANDWIDTH OUT-OF-PLANE ACCELEROMETER AS CONTACT MICROPHONE FOR BODY-WORN AUSCULTATION DEVICES** 30
P. Gupta, Y. Jeong, J. Choi, M. Faingold, A. Daruwalla, and F. Ayazi
Georgia Institute of Technology, USA

9:25 am **MICROFABRICATED ELECTRODYNAMIC WIRELESS POWER RECEIVER FOR BIO-IMPLANTS AND WEARABLES** 34
N. Garraud, D. Alabi, J.D. Varela, D.P. Arnold, and A. Garraud
University of Florida, USA

9:45 am **A WIRELESSLY CONTROLLED FULLY IMPLANTABLE MICROSYSTEM FOR NANO-LITER RESOLUTION INNER EAR DRUG DELIVERY** 38
F. Forouzandeh[1], A. Alfadhel[1], X. Zhu[2], J.P. Walton[2], D.R. Cormier[1], R.D. Frisina[2], and D.A. Borkholder[1]
[1]Rochester Institute of Technology, USA and [2]University of South Florida, USA

10:05 am **Break and Table Top Exhibits**

Session 4 - Microsystems for Biological Applications

Session Chair: M. Ziaei, *iSono Health, USA*

10:30 am **MULTISCALE LIQUID METAL THIN-FILM PATTERNING BASED ON SOFT LITHOGRAPHY FOR SKIN-MOUNTABLE, SOFT AND 3D-INTEGRATED BIOLOGICAL MICROSYSTEMS** 42

M. Kim, C. Kim, H. Alrowais, P. Getz, and O. Brand

Georgia Institute of Technology, USA

10:50 am **ROBUST AND SCALABLE TISSUE-ENGINEERINED ELECTRONIC NERVE INTERFACES (TEENI)** 46

C.A. Kuliasha, B.S. Spearman, E.W. Atkinson, P. Rustogi, A.S. Furniturewalla, E.A. Nunamaker, K.J. Otto, C.E. Schmidt, and J.W. Judy

University of Florida, USA

11:10 am **One Man's Purpose – A Radio Play**

12:15 pm - 1:45 pm **Networking Lunch**

7:00 pm - 10:00 pm **Tuesday Banquet**

Wednesday, June 6

7:30 am **Breakfast**

8:10 am **Announcements**

Plenary Presentation III

Session Chair: F. Ayazi, *Georgia Institute of Technology, USA*

8:15 am **WIRELESS INTEGRATED MICRO SYSTEMS (WIMS): PAST, PRESENT, FUTURE** 50
Khalil Najafi
University of Michigan, USA

Session 5 - Levitated, Flying & Running Microrobots

Session Chair: S. Bergbreiter, *University of Maryland, USA*

9:05 am **A SIX-LEGGED MEMS SILICON ROBOT USING MULTICHIP ASSEMBLY** 54
D.S. Contreras and K.S.J. Pister
University of California, Berkeley, USA

9:25 am **A 3D-PRINTED 1 MG LEGGED MICROROBOT RUNNING AT 15 BODY LENGTHS PER SECOND** 59
R. St. Pierre[1], W. Gosrich[2], and S. Bergbreiter[1]
[1]University of Maryland, USA and [2]State University of New York, Buffalo, USA

9:45 am **BATCH-FABRICATION OF DIAMAGNETICALLY LEVITATED MICROROBOTS** 63
C. Velez[1], R.E. Pelrine[2], A. Wong-Foy[2], and D.P. Arnold[1]
[1]University of Florida, USA and [2]SRI International, USA

10:05 am **TAKEOFF OF A FLYING MICROROBOT WITH COTS SENSOR PAYLOAD USING ELECTROHYDRODYNAMIC THRUST PRODUCED BY SUB-MILLIMETER CORONA DISCHARGE** 67
D.S. Drew and K.S.J. Pister
University of California, Berkeley, USA

10:25 am **Break and Table Top Exhibits**

Session 6 - Micro-Resonators & Resonator-Based Frequency Combs

Session Chair: A. Duwel, *Charles Stark Draper Laboratory, Inc., USA*

10:50 am **A FERROELECTRIC CAPACITOR (FECAP) BASED UNRELEASED RESONATOR** 71
Y. He[1], B. Bahr[2], and D. Weinstein[1]
[1]Purdue University, USA and [2]Texas Instruments, USA

11:10 am **PIEZOELECTRIC SINGLE CRYSTAL 6H SILICON CARBIDE MICROELECTROMECHANICAL RESONATORS** 75
R. Perahia, L.D. Sorenson, J.L. Bregman, L.X. Huang,
M.S. White, K.S. Holabird, and D.T. Chang
HRL Laboratories, LLC, USA

11:30 am **FREQUENCY COMB GENERATION IN A NONLINEAR RESONATOR THROUGH MODE COUPLING USING A SINGLE TONE DRIVING SIGNAL** 79
D.A. Czaplewski[1], S.W. Shaw[2], O. Shoshani[3], M.I. Dykman[4], and D. Lopez[1]
[1]Argonne National Laboratory, USA, [2]Florida Institute of Technology, USA,
[3]Ben-Gurion University of the Negev, ISRAEL, and [4]Michigan State University, USA

11:50 am **ULTRA-HIGH Q MONOCRYSTALLINE SILICON CARBIDEDISK RESONATORS ANCHORED UPON A PHONONIC CRYSTAL** 83
J. Yang, B. Hamelin, S.-D. Ko, and F. Ayazi
Georgia Institute of Technology, USA

12:10 pm - **Poster Preview of Poster Session 2 Presentations**
Session Chairs: A. Lal, *Cornell University, USA* and M.A. Maher, *SoftMEMS, USA*

12:40 pm - **Networking Lunch**

Poster Session 2

Session Chair: M. Motiee, *Analog Devices, USA*

2:10 pm - 4:40 pm **Contributed and Late News**

Poster Session 3

Session Chair: Q. Zou, *Avago Technologies, USA*

6:30 pm - **Commercial and Open Posters**

8:00 pm - **Awards Ceremony**

8:15 pm 10:00 pm **RUMP Session**

Thursday, June 7

7:30 am **Breakfast**

8:10 am **Announcements**

Plenary Presentation IV

Session Chair: T. Lamers, *Uber ATG, USA*

8:15 am **TOWARDS INTEGRATED OPTICAL GYROS USING BRILLOUIN LASERS** 87
Kerry Vahala, Y.H. Lai, M.G. Suh, J. Li, and K.Y. Yang
California Institute of Technology, USA

Session 7 - Late News Frequency-References, -Combs, and -Shifting Sensors

Session Chair: R. Perahia, *HRL Laboratories, USA*

9:05 am **A NEW LOW POWER MEMS DUAL MODE CLOCK WITH PPB STABILITY OVER TEMPERATURE** 90
L. Comenencia Ortiz[1], H.-K. Kwon[1], J. Rodriguez[1], D.B. Heinz[1], Y. Chen[2], G.D. Vukasin[1], D.D. Shin[1], and T.W. Kenny[1]
[1]Stanford University, USA and [2]Apple, Inc., USA

9:25 am **TOWARDS REAL-TIME MIDDLE ULTRAVIOLET (MUV) LIGHT DETECTION BY BETA GALLIUM OXIDE (-Ga_2O_3) NEMS OSCILLATOR** 92
X.-Q. Zheng[1], J. Lee[1], S. Rafique[1,2], M. Rezaul Karim[2], L. Han[1,2], H. Zhao[2], C.A. Zorman[1], and P.X.-L. Feng[1]
[1]Case Western Reserve University, USA and [2]Ohio State University, USA

9:45 am **SELF-SUSTAINED DUAL-MODE MECHANICAL FREQUENCY COMB SENSORS** 94
M. Park and A. Ansari
Georgia Institute of Technology, USA

10:05 am **Break and Table Top Exhibits**

Session 8 - Late News Advanced Processes for Bio Applications

Session Chair: A. Lal, *Cornell University, USA*

10:30 am **ENTERIC & 3D-PRINTED HYBRID PACKAGE FOR SAMPLING IN DIGESTIVE REGIONS** 96
G.E. Banis, L.A. Beardslee, J.M. Stine, and R. Ghodssi
University of Maryland, USA

Poster Session 1
Contributed and Late News
Monday, June 4 1:30 pm – 4:00 pm

Acoustic Transducers and Delay Lines

Bio-Inspiration and Biomedical Devices and Systems

Characterization, Fabrication and Materials

Chemical, Biomedical, and Gas Sensors

Micro Robots

Microfluidics

Modeling

Physical and Optical Sensors and Actuators

Power Generation and Management

Resonant Devices

Late News

Poster Session 2
Contributed and Late News
Wednesday, June 6 2:10 pm – 4:40 pm

Acoustic Transducers and Delay Lines

Bio-Inspiration and Biomedical Devices and Systems

Characterization, Fabrication and Materials

Chemical, Biomedical, and Gas Sensors

Micro Robots

Microfluidics

Modeling

Physical and Optical Sensors and Actuators

Power Generation and Management

Resonant Devices

Late News

ENABLING THE NEXT GENERATION OF MEMS TECHNOLOGY

W. Chappell[1], R. H. Olsson III [1], and R.G. Polcawich[1,2]
[1]DARPA, Arlington, VA, USA
[2]US Army Research Laboratory, Adelphi, MD, USA

HISTORICAL PERSPECTIVE

As the fourth decade of MEMS research and development begins, a few important questions become of interest namely where are the technology transition opportunities, what lessons can be learned from previous R&D investments, and what are the new areas of research investment. Over the years, DARPA has invested in MEMS technology at the exploration phase of the technology and more recently into application specific areas where MEMS technology was explored as a possible solution. A review of the lessons learned from these investments and how they have and are impacting current DARPA programs will be discussed as a gauge of where the new investment opportunities may push the technology.

The early days of the MEMS investments focused on novel fabrication processes with a focus on novel sensor and actuator modalities. This transitioned into programs with specific device as well as system metrics but still plenty of investment in novel processes. Then, there was a shift toward more system driven performance metrics combined with a reduction in the generic investing in MEMS for the sake of MEMS. To address a growing gap in the fundamental challenges affecting several MEMS technologies, a joint government and industry collaboration was explored through the N/MEMS S&T Fundamentals Program to tackle the most pressing of these fundamental challenges. Currently, we are back to a more system driven program model where we can take advantage of the previous investments and strategically invest in foundational research in targeted areas of interest.

CURRENT INVESTMENTS

Recent and current areas of investment in MEMS technology have been in adaptable RF technologies, GPS denied position navigation and timing, and low power sensors. The initial investments across a broad area of technologies have resulted in highlighted successes that include phase change materials and switches, inertial sensors, low power thermal imaging, and lithium niobate based components for low power RF receivers to name a few. Within the Adaptable RF Technology (ART) program portfolio, several programs were able to leverage earlier investments in resistive phase change materials [1, 2] to realize high performance RF switches [3, 4]. Through continued investment as part of the RF FPGA program, these switches are making their way into commercial production.

With the challenges of maintaining assured and trusted position, navigation, and timing (PNT) of elevated importance across the Department of Defense, DARPA has continued its investments in advanced inertial sensors. The most recent program, Precise Robust Inertial Guidance for Munitions (PRIGM), is a broad attempt looking at novel and foundational technologies as well as maturing previous investments to get miniature navigation grade inertial measurement units (IMUs) into the DoD by early 2020.

PRIGM comprises two focus areas: development of a navigation-grade inertial measurement unit (NGIMU) based on micro-electromechanical systems (MEMS) platforms, and basic research of advanced inertial micro sensor (AIMS) technologies for future gun-hard, high-bandwidth, high-dynamic-range, GPS-free navigation.

The PRIGM:NGIMU focus area will develop a MEMS-based navigation-grade IMU that has a mechanical/electronic interface compatible with drop-in replacement for existing tactical-grade IMUs on legacy DoD platforms. The results from Phase 1 of this effort have shown individual accelerometers exceeding the navigation grade specifications with the individual gyroscope performance close to meeting the targeted navigation grade specifications. The early and continued engagement of the DoD Service Labs has been essential in evaluating the early performance, providing guidance and technical feedback for surviving the harsh munitions environments, and to facilitate rapid transition of NGIMU technology.

PRIGM:AIMS is a basic research program exploring alternative technologies and modalities for inertial sensing, including photonic and MEMS-photonic integration, as well as novel architectures and materials systems. The principal objective of PRIGM:AIMS is to identify promising candidate technologies for further development as high-performance inertial sensors for long-duration missions and deployment in extreme environments. Examples from the current program include investments in MEMS fabricated glass structures [5], a "no proof mass" accelerometer using atomic layer deposited materials as both heaters and thermometers as a thermal bubble inspired accelerometer [6], surface acoustic wave gyroscope [7], and micromachined photonic based gyroscopes [8, 9].

The Signal Processing at RF (SPAR) program aims to mitigate both externally generated and self-generated interfering signals (from transmitters within a shared network or RF systems on a common platform, for example) of known and unknown characteristics. SPAR's engineering challenges center on designing, building and demonstrating RF signal-processing components that can remove in-band interferers from the desired receive signal at the RF front end—that is, before the signals reach the receiver electronics, while maintaining the required low noise figure and high linearity required to operate directly at the antenna. SPAR is pursuing both micromechanical and integrated circuit based approaches to realize miniature correlator and circulator components for in-band interference suppression. Microacoustic correlators [10] being developed under the program have the advantages of high linearity (IIP3 > 30 dBm) and ease of synchronization but have more limited coding flexibility (4 vs. 1000's of codes), bandwidth (25 MHz vs > 100 MHz) and processing gain (12 dB vs 27 dB) when compared to the integrated circuit based efforts. Similar benefits to mechanical approaches, especially high linearity, are seen for the micromechanical based circulator efforts. All told, SPAR aims to enhance radio and radar operation in increasingly congested and contested RF environments through innovation of a new class of low loss RF signal processing components.

Microsystem investments have long been a core component reflecting the DoD's desire to reduce the size, weight and power of sensing, processing, and communications systems. The Near Zero Power RF and Sensor Operations (N-ZERO) program is pursuing a revolutionary leap in the sensing and processing that can be achieved over long durations (i.e. many years) from a miniature battery or without a battery at all. The program is developing the technological foundations for persistent, event-driven sensing capabilities in which sensors can remain dormant, with near-zero power consumption, until awakened by an external trigger or stimulus. To break the paradigm of using active power to sense

978-1-940470-03-0/HH2018/$25©2018TRF
DOI 10.31438/trf.hh2018.1

Solid-State Sensors, Actuators and Microsystems Workshop
Hilton Head Island, South Carolina, June 3-7, 2018

infrequent, high-consequence events, N-ZERO is developing a class of sensors that exploit the energy in the signal signature itself to detect and discriminate the events of interest while rejecting noise and interference. The N-ZERO program has had numerous successes across several technology areas. Focusing on the MEMS related technologies, the successes include the ability to detect, process and classify IR [11], acoustic [12] and inertial [13] spectral signatures while in some cases consuming zero stand-by power. The ability to sense and process information over long durations in a miniature, inexpensive form factor is critical for future internet-of-things (IoT) applications in industrial and infrastructure health monitoring, agriculture and security.

NEXT GENERATION OF MEMS

Before discussing what may be next for MEMS technology, it is worthwhile looking inward at some of the most recent hard lessons that have been learned. One of the key challenges that has arisen with several of the current programs is how to innovate faster within very custom fabrication processes that are sensitive to process stability and reproducibility. Compared to the integrated circuit community, where design innovations can occur twice or three plus times a year, the MEMS designer is generally getting one design cycle per year. Furthermore, the extremely custom processes that are being utilized have risks associated with single equipment, personnel, or facility failures. Additionally, these unique processes generally are not considering the requirements of transitioning from a university or small R&D facility to a more production proven facility and its processing constraints.

Related to this challenge, the questions being pondered now are the following: How can the MEMS community innovate faster with higher levels of integration and tighter control on our fabrication processes? Can the MEMS community leverage the way that the solid state electronics community innovates within the semiconductor and integrated circuit industry? Is there a path to leveraging or accessing the production proven processes currently supplying commercial MEMS devices and components? Can higher levels of device yields, reproducibility, and integration enable novel arrayed device architectures? What is the best model for handling and enabling access to intellectual property and process design kits for the MEMS community? The answer to these questions will begin to shape a path forward to ultimately realize a more flexible, rapidly innovative MEMS community capable of addressing technology gaps with a faster time to market and product insertion.

In addition, there is a continued interest in exploring those foundational technologies that can provide groundbreaking solutions for national security. Whether new material breakthroughs, innovation in material processing and patterning techniques, novel design architectures, or innovative integration strategies, there will be continued interest especially if it pushes the art of the possible and further ensures the leading edge of technology for national security.

WORD COUNT: 1435

REFERENCES

[1] E. K. Chua, L. P. Shi, R. Zhao, K. G. Lim, T. C. Chong, T. E. Schlesinger, and J. A. Bain, “Low Resistance, High Dynamic Range Reconfigurable Phase Change Switch For Radio Frequency Applications, Appl. Phys. Lett., 97, 183506 (2010)

[2] E. K. Chua, R. Zhao L. P. Shi, T. C. Chong, T. E. Schlesinger, and J. A. Bain, “Effect Of Metals And Annealing On Specific Contact Resistivity Of Gete/Metal Contacts,” Appl. Phys. Lett., 101, 012107 (2012)

[3] N. El-Hinnawy, P. Borodulin, B. P. Wagner, M. R. King, E. B. Jones, R. S. Howell, M. J. Lee, and R.M. Young, “Low-Loss Latching Microwave Switch Using Thermally Pulsed Non-Volatile Chalcogenide Phase Change Materials, Appl. Phys. Lett., 105, 013501 (2014).

[4] R. Singh, G. Slovin, M. Xu, T. E. Schlesinger, J. A. Bain, J. Paramesh, "A Reconfigurable Dual-Frequency Narrowband CMOS LNA Using Phase-Change RF Switches", IEEE Trans. Microwave Theory Techniques, 65, 4689, (2017).

[5] B. Shiari, T. Nagourney, S. Singh, J. Y. Cho and K. Najafi, “Simulation-based Approach for Fabrication of Micro-shell Resonators with Controllable Stiffness and Mass Distribution,” IEEE Intern. Symp. Inertial Sensors & Systems, Italy (2018), pp. 145-148.

[6] K. E. Kaplan, M. M. Winterkorn, C. L.M. Everhart, D. D. Shin, G. J. O’Brien, F. B. Prinz, T. W. Kenny, “Active Temperature Compensation of Thermal Accelerometer for Improved Stability,” IEEE Intern. Symp. Inertial Sensors & Systems, Italy (2018), pp. 169-170.

[7] A. Mahmoud, M. Mahmoud, T. Mukherjee, G. Piazza, “Investigating the Impact of Resonant Cavity Design on Surface Acoustic Wave Gyroscope,” IEEE Intern. Symp. Inertial Sensors & Systems, Italy (2018), pp. 57-60.

[8] J. Li, M.-G. Suh, K. Vahala, “Microresonator brillouin gyroscope” Optica, 4, 346 (2017).

[9] T. Huffman, M. Davenport, M. Belt, J. E. Bowers, D.J. Blumenthal, “Ultra-Low Loss Large Area Waveguide Coils for Integrated Optical Gyroscopes,” IEEE Photonics Tech. Lett., 29, 185 (2017).

[10] J. Lovseth et al. “A passive surface acoustic wave correlator for simultaneous transmit and receive radios,” Proc. of the 2018 GOMAC Tech. Conf., March 2018.

[11] Z. Qian, S. Kang, V. Rajaram, C. Cassella, N. E. McGruer, M. Rinaldi., “Zero-power infrared digitizers based on plasmonically enhanced micromechanical photoswitches." Nature Nano, 12, Oct. 2017.

[12] J. Bernstein, M. Bancu, D. Reilly, M. Weinberg, D. Gauthier, R. Elliot, “MEMS resonant acoustic wake-up sensor,” The J. Acoust. Soc. Am., 141, 3721 (2017).

[13] R. W. Reger et al., "Near-zero power accelerometer wakeup system," 2017 IEEE Sensors, Glasgow, 2017, pp. 1-3.

PROBING THE FUNDAMENTAL EVAPORATION LIMIT WITH A NANOPOROUS MEMBRANE DEVICE

Zhengmao Lu[1], Kyle L. Wilke[1], Ikuya Kinefuchi[2], and Evelyn N. Wang[1]
[1] Massachusetts Institute of Technology, Massachusetts, USA
[2] University of Tokyo, Bunkyo, Japan

ABSTRACT

We designed and fabricated an ultrathin nanoporous membrane device to probe the fundamental limit of evaporation which has remained elusive based on theory and experiments for decades. Our device overcomes the experimental challenge in prior works, including the inability to isolate the interfacial heat transfer resistance and monitor the interface temperature accurately and non-invasively, to characterize kinetically limited evaporation. We showed with both experiments and modeling that kinetically limited evaporation, when normalized properly, is solely determined by the pressure ratio between the ambient and the interface. This has great implications for achieving efficient evaporative transport in practical applications.

INTRODUCTION

Evaporation, a commonly found phenomenon in nature, is extensively used in water desalination [1], steam generation [2], and thermal management [3]. Despite decades of studies [4], the fundamental understanding of evaporation remains limited to date. To recognize the full potential of evaporation, it is desirable to have systems that minimize transport resistances associated with thermal conduction [5, 6], liquid supply [7, 8], and vapor removal [5, 9], and maximize interfacial heat transfer, where evaporation can be considered to be kinetically limited. This proved difficult in previous studies [5-14].

Evaporation can be generally driven by the vapor concentration gradient or pressure difference between the interface and the far field. The net molecular flux due to evaporation disturbs the local thermodynamic equilibrium near the interface. This non-equilibrium region, usually a few mean free paths to the interface, is known as the Knudsen layer [15]. Beyond this layer, the disturbance is relaxed by collisions between molecules and the vapor flow regains thermodynamic equilibrium. We define the transport resistance across the Knudsen layer as R_{kinetic}. For air ambient evaporation, the Maxwell-Stefan diffusion outside the Knudsen layer dominates the overall heat transfer [9] ($R_{\text{diffusion}} \gg R_{\text{kinetic}}$), which is non-ideal for characterizing R_{kinetic}. To make R_{kinetic} the dominant transport resistance, or to realize kinetically limited evaporation, in this study, we investigated evaporation in pure vapor, where the flow is pressure driven. Based on continuum gas dynamics [16], the pressure loss associated with the gas expansion resistance beyond the Knudsen layer is minimal ($P_K \approx P_\infty$) for $M_K = u_K/u_s \ll 1$. Here, P_K and u_K are the pressure and bulk velocity of the vapor right outside the Knudsen layer, respectively, P_∞ is the far field pressure, and $u_s = (\gamma R T_0)^{1/2}$, where γ is the adiabatic index, R is the specific gas constant, T_0 is the interface temperature. This means $R_{\text{expansion}} \ll R_{\text{kinetic}}$.

DEVICE DESIGN

The interfacial transport can still be possibly limited by the thermofluidic resistance in the liquid. To address this issue, we designed and fabricated an ultrathin nanoporous membrane device (Figure 1a-d). Figure 1a shows the nanodevice design that allows the liquid to wick into the nanopores in the membrane with capillarity, where it is resistively heated by a gold layer and evaporates. The free-standing membrane, connecting two gold contact pads (Figure 1b) is of thickness $t_m \approx 200$ nm, made of silicon nitride.

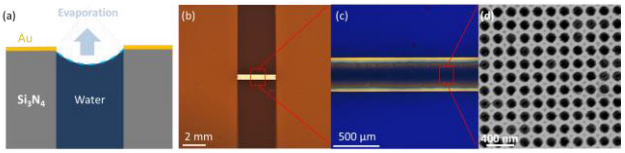

Figure 1: Nanoporous evaporation device. (a) Schematic of evaporation from a nanopore (not to scale). The gold layer is resistively heated to induce evaporation from a pinned meniscus in each nanopore. (b) Image of device with two gold contact pads connected by a free-standing membrane (≈200 nm thick). (c) Magnified view of free-standing membrane where the central part is porous and coated with gold. (d) SEM image of the nanoporous membrane with ≈140 nm diameter pores.

The active part of the membrane, located in the middle, is coated with ≈40 nm gold (Figure 1c). We defined a nanoporous pattern with pore diameter $d_p \approx 140$ nm and porosity ≈ 0.40 (>20,000,000 pores) in this active area using interference lithography [17] (Figure 1d), while the rest of the membrane is kept non-metallic and impermeable. The combination of small d_p and t_m minimizes the thermal resistance ($\sim d_p$) and viscous loss ($\sim t_m$) in the liquid and the large number of pores ensures high signal (evaporation) to noise (heat loss) ratios during the experiment. Note that the gold layer also serves as a resistive temperature detector (RTD) which monitors the interface temperature in close vicinity in a non-invasive manner. The other common issue associated with nanoporous configurations is clogging due to non-evaporative contaminants. In the current design, the ultralow thickness of the membrane automatically mitigates the clogging risk. It creates high concentration gradients along the pore with even a small amount of contaminants at the liquid-vapor interface, which drives the contaminants back to the flushing liquid flow underneath the membrane with diffusion. This may have more implications for membrane-based water purification applications. Overall, with evaporation from this ultrathin nanoporous membrane in a pure vapor ambient, we were able to probe the kinetic limit of steady evaporation, which has otherwise been impossible in previous works.

EXPERIMENTS

To perform characterizations, the device was placed in an environmental chamber to enable controlled vapor temperature and pressure (Figure 2a-b). A custom test fixture interfaced the device to the liquid ports, electrical connections, and facilitates visualization to ensure that liquid did not flood the membrane surface (Figure 2c).

978-1-940470-03-0/HH2018/$25©2018TRF
DOI 10.31438/trf.hh2018.2

Prior to the experiment, the liquid reservoir tank was filled with deionized water (Sigma-Aldrich, Water for HPLC) and then heated to > 100 °C for thermal degassing. The liquid reservoir was subsequently sealed from the ambient. Meanwhile, we calibrated the RTD to an industrial temperature sensor (Omega P-L-A-1/4-6-1/4-T-6) in a convection oven (see Supplementary S3). During experiment, the environmental chamber was first pumped down to <0.5 Pa (confirmed by MKS 925 Micro Pirani™ vacuum transducer) and then backfilled with pure water vapor from the reservoir. The vapor pressure in the far field was regulated by the chamber wall temperature and measured by a capacitance pressure transducer (MKS 740C Baratron® Manometer). With a peristaltic pump (Masterflex UX-77921-77), the inlet flow rate was maintained at 1 mL/min. We applied a four-point method to measure the total Joule heating power and read the interface temperature from the RTD.

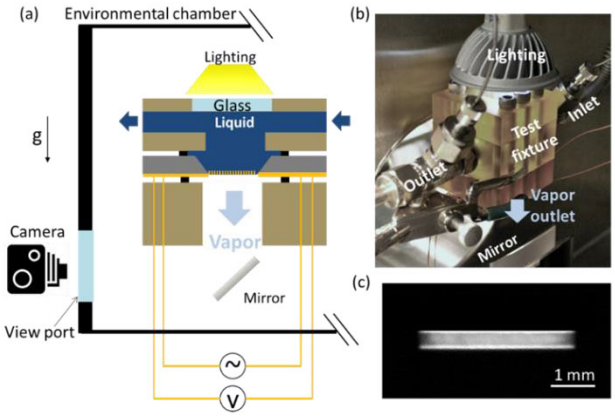

Figure 2: Experimental setup. (a) Schematic showing device placed in a custom test fixture in an environmental chamber which allows for liquid feedthrough, electrical connection, and visualization. (b) Image of experimental setup. (c) Image of the nanoporous membrane device during an experiment.

To characterize the heat loss of the system, we fabricated a control sample with the same structure as the designed device except that the active part was also impermeable. With liquid supplied at 1 mL/min (same as in the evaporation experiment), we measured the heating power Q_{loss} as a function of the temperature rise of the membrane of the control sample ΔT as the sample was cooled down by convection and conduction. Q_{loss} is plotted as a function of ΔT in Figure 3 and the experimental data (red triangles) are fitted to a linear model (black dashed line) $Q_{loss} = C\Delta T$, which give C = 4.7±0.1 mW/K.

We determined the heat loss conductance of the system to be C = 4.7±0.1 mW/K. The interfacial heat flux $\dot{q}''$ during operation was then recorded as

$$\dot{q}'' = \frac{Q - C\Delta T}{A} \qquad (1)$$

where Q is the total Joule heating power, A is the total interface area and $\Delta T = T_0 - T_\infty$, where T_∞ is the temperature of the ambient. The heat loss was generally less than 5% of the total power input in the present study. We characterized evaporation with ambient vapor pressure P_∞ = 2.643 kPa, and the associated saturation temperature is T_∞ = 22.0 °C. Throughout the experiment, the uncertainty in vapor pressure measurement is ±138 Pa and the one in interface temperature measurement is ±0.52 K.

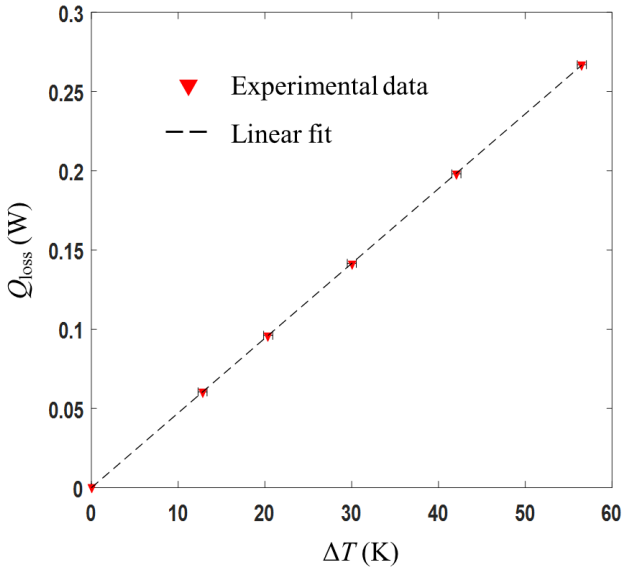

Figure 3 Heat loss characterization using a control sample with impermeable membrane. Q_{loss} is plotted as a function of ΔT and the experimental data (red triangles) are fitted to a linear model (black dashed line) $Q_{loss} = C\Delta T$, which give C = 4.7±0.1 mW/K.

RESULTS AND DISCUSSION

The interfacial heat flux $\dot{q}''$ is shown in Figure 4 as a function of the temperature rise ΔT. The blue asterisks represent the results from evaporation into an air ambient reported in our previous work [9]. The red diamonds, on the other hand, are the experimental data in the present study of evaporation into a vapor ambient for T_∞ = 22.0 °C. Comparing the red diamonds to the green crosses, we note that for similar far field vapor temperatures, the heat transfer coefficient ($h = \dot{q}''/\Delta T$) associated with evaporation into vapor is much higher than that in the air, because the former is kinetically limited and the latter is diffusion limited. The evaporation data from the present work (red diamonds) show a nearly 10× improvement from the evaporation into air case (blue asterisks) for the same interface temperature, which is the highest improvement to date.

To properly interpret this trend, we analyzed the non-equilibrium vapor motions in the Knudsen layer using the Boltzmann transport equation (BTE), as the usual thermodynamic quantities are not necessarily well defined under non-equilibrium.

$$\frac{\partial \xi}{\partial t} = -\mathbf{u}\cdot\nabla_x \xi + \left[\frac{\partial \xi}{\partial t}\right]_{\text{collison}} \qquad (2)$$

where ξ is the mass-based distribution function, t is time, and $\mathbf{u}$ is the molecular velocity. The first term on the right hand side represents the streaming of molecules and the second term is the change of distribution function due to collisions between molecules. The boundary condition at the liquid-vapor interface is characterized by the evaporation coefficient and condensation coefficient (σ_e and σ_c) [18-20]. At equilibrium conditions, $\sigma_e = \sigma_c$, analogous to the Kirchhoff's law in thermal radiation [21]. We carried on this equality in our analysis as the Knudsen layer can be considered in near equilibrium for $M_K \ll 1$. The vapor distribution function at the interface ξ_0 can be written as:

$$\xi_0\,|_{u_z>0} = \left[\sigma_e\rho_0 + (1-\sigma_c)\int_{u_z<0}\xi_0 d\mathbf{u}\right]\frac{\exp\left[-\mathbf{u}^2/2RT_0\right]}{(2\pi RT_0)^{3/2}} \qquad (3)$$

where u_z is its z-component. The distribution function for the vapor flow coming out of Knudsen layer can be expressed a drifted Maxwell-Boltzmann distribution:

$$\xi_K|_{u_z>0} = \rho_K \frac{\exp\left[-(\mathbf{u}-u_K\hat{\mathbf{z}})^2/2RT_K\right]}{(2\pi RT_K)^{3/2}} \quad (4)$$

where T_K is the temperature of the vapor right outside the Knudsen layer. We adopted an evaporation model based on the linearized version of BTE [18, 19] using these boundary conditions with $\sigma_e = \sigma_c = 1$, which predicts the trend well, but generally overestimates the interfacial heat flux, indicating non-idealities at the interface. It is plotted as orange solid line in Figure 4.

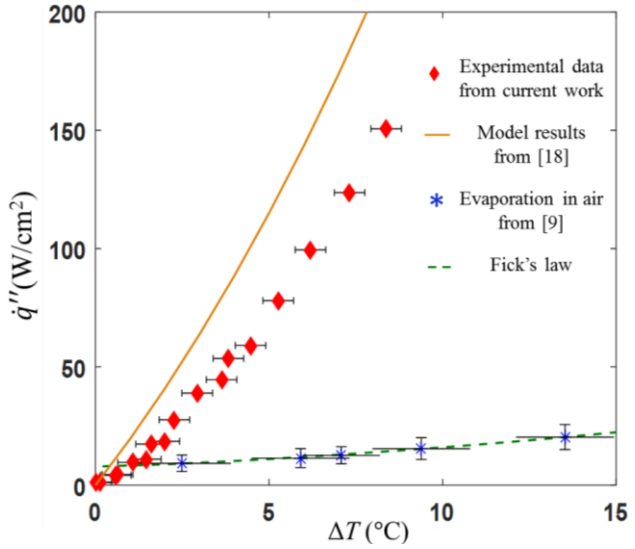

Figure 4: Experimental and modeling results from nanoporous membrane with water as a working fluid. (a) Interfacial heat flux $\dot{q}''_{in}$ as a function of membrane superheat ΔT for T_∞ = 22 °C: red diamonds represent the evaporation data from the present work; the brown solid line is the model results from [9]; and the blue asterisks and the green dashed line are the experimental data and model prediction for evaporation into air from [18], respectively.

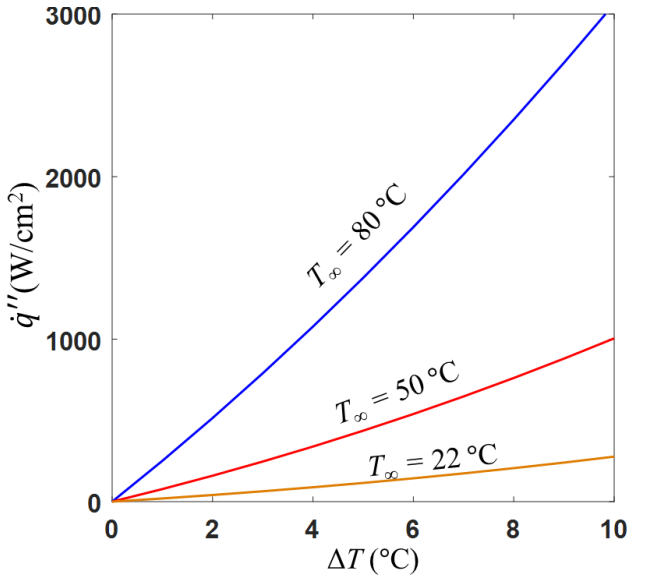

Figure 5: Model prediction of $\dot{q}''$ as a function of ΔT for select T_∞ based on the linearized BTE [18]

Moreover, with the trend predicted by this linearized BTE model, by increasing T_∞ while maintaining the superheats, the interfacial heat transfer can be further enhanced shown in Figure 5. The linearized BTE model in fact gives a general figure of merits for evaporative heat transfer: $\rho_0 u_s \Delta h_{lv}$. As the vapor ambient temperature becomes higher, the vapor density increases sharply and so does this figure of merits. This explains why we expect a higher interface heat transfer coefficient for higher vapor ambient temperatures.

CONCLUSIONS

The ultrathin nanoporous design presented in this study enabled kinetically limited evaporation with non-invasive and accurate interface temperature measurement. With both experiments and modeling, we demonstrated that the kinetic limit of evaporation, enhance the interfacial heat transfer significantly compared to the diffusion-limited evaporation. We generally showed that the interfacial heat transfer coefficient scales with $\rho_0 u_s \Delta h_{lv}$ and increases with higher ambient temperatures. This gives the figure of merits for choosing working fluids and operating conditions to maximize evaporative heat transfer. The current work improves the fundamental understanding of the kinetically limited evaporation and shows the significant promise of utilizing an ultrathin nanoporous design to achieve efficient evaporative heat and mass transfer in thermal management, desalination, and steam generation applications, among others. We gratefully acknowledge funding support from the Air Force Office of Scientific Research with Dr. Ali Sayir as program manager.

REFERENCES

[1] Zhou, L., Tan, Y., Wang, J., Xu, W., Yuan, Y., Cai, W., Zhu, S., and Zhu, J., 2016, "3D self-assembly of aluminium nanoparticles for plasmon-enhanced solar desalination," Nature Photonics, 10(6), p. 393.

[2] Ghasemi, H., Ni, G., Marconnet, A. M., Loomis, J., Yerci, S., Miljkovic, N., and Chen, G., 2014, "Solar steam generation by heat localization," Nature communications, 5, p. ncomms5449.

[3] Lu, Z., Salamon, T. R., Narayanan, S., Bagnall, K. R., Hanks, D. F., Antao, D. S., Barabadi, B., Sircar, J., Simon, M. E., and Wang, E. N., 2016, "Design and modeling of membrane-based evaporative cooling devices for thermal management of high heat fluxes," IEEE Transactions on Components, Packaging and Manufacturing Technology, 6(7), pp. 1056-1065.

[4] Eames, I., Marr, N., and Sabir, H., 1997, "The evaporation coefficient of water: a review," Int. J. Heat Mass Transfer, 40(12), pp. 2963-2973.

[5] Narayanan, S., Fedorov, A. G., and Joshi, Y. K., 2009, "Gas-assisted thin-film evaporation from confined spaces for dissipation of high heat fluxes," Nanoscale and Microscale Thermophysical Engineering, 13(1), pp. 30-53.

[6] Weibel, J. A., Garimella, S. V., and North, M. T., 2010, "Characterization of evaporation and boiling from sintered powder wicks fed by capillary action," Int. J. Heat Mass Transfer, 53(19-20), pp. 4204-4215.

[7] Wilke, K. L., Barabadi, B., Lu, Z., Zhang, T., and Wang, E. N., 2017, "Parametric study of thin film evaporation from nanoporous membranes," Appl. Phys. Lett., 111(17), p. 171603.

[8] Xiao, R., Maroo, S. C., and Wang, E. N., 2013, "Negative pressures in nanoporous membranes for thin film evaporation," Appl. Phys. Lett., 102(12), p. 123103.

[9] Lu, Z., Wilke, K. L., Preston, D. J., Kinefuchi, I., Chang-Davidson, E., and Wang, E. N., 2017, "An Ultrathin Nanoporous Membrane Evaporator," Nano Lett., 17(10), pp. 6217-6220.

[10] Li, Y., Alibakhshi, M. A., Zhao, Y., and Duan, C., 2017,

"Exploring Ultimate Water Capillary Evaporation in Nanoscale Conduits," Nano Lett., 17(8), pp. 4813-4819.
[11] Ćoso, D., Srinivasan, V., Lu, M.-C., Chang, J.-Y., and Majumdar, A., 2012, "Enhanced heat transfer in biporous wicks in the thin liquid film evaporation and boiling regimes," J. Heat Transfer, 134(10), p. 101501.
[12] Adera, S., Antao, D., Raj, R., and Wang, E. N., 2016, "Design of micropillar wicks for thin-film evaporation," Int. J. Heat Mass Transfer, 101, pp. 280-294.
[13] Fang, G., and Ward, C., 1999, "Temperature measured close to the interface of an evaporating liquid," PhRvE, 59(1), p. 417.
[14] Lee, J., Laoui, T., and Karnik, R., 2014, "Nanofluidic transport governed by the liquid/vapour interface," Nature nanotechnology, 9(4), p. 317.
[15] Sone, Y., 2000, "Kinetic theoretical studies of the half-space problem of evaporation and condensation," TTSP, 29(3-5), pp. 227-260.
[16] Kundu, P. K., Cohen, I. M., and Dowling, D., 2008, "Fluid Mechanics 4th," Elsevier, Oxford.
[17] Xie, Q., Hong, M., Tan, H., Chen, G., Shi, L., and Chong, T., 2008, "Fabrication of nanostructures with laser interference lithography," J. Alloys Compd., 449(1-2), pp. 261-264.
[18] Frezzotti, A., 2011, "Boundary conditions at the vapor-liquid interface," PhFl, 23(3), p. 030609.
[19] Sone, Y., Takata, S., and Golse, F., 2001, "Notes on the boundary conditions for fluid-dynamic equations on the interface of a gas and its condensed phase," PhFl, 13(1), pp. 324-334.
[20] Meland, R., Frezzotti, A., Ytrehus, T., and Hafskjold, B., 2004, "Nonequilibrium molecular-dynamics simulation of net evaporation and net condensation, and evaluation of the gas-kinetic boundary condition at the interphase," PhFl, 16(2), pp. 223-243.
[21] Lu, Z., Narayanan, S., and Wang, E. N., 2015, "Modeling of Evaporation from Nanopores with Nonequilibrium and Nonlocal Effects," Langmuir, 31(36), pp. 9817-9824.

CONTACT

*E.N. Wang, tel: +1-617-324-3311; enwang@mit.edu

A MICROFLUIDIC DEVICE FOR MECHANICAL PROFILING OF HYDROGEL MICROPARTICLES

Ye Niu, and Yi Zhao[*]
The Ohio State University, Columbus, Ohio, USA

ABSTRACT

This paper reports a continuous flow microfluidic device capable of measuring the geometric and viscoelastic properties of hydrogel microparticles by flowing them into a tapered microchannel with an interdigitated microelectrode array patterned underneath. The geometric and viscoelastic properties of microbeads/microcapsules are derived from their motion profiles monitored by the microelectrode array. Different from previous studies, the measurement inaccuracy associated with the negligence of the viscous effect is avoided. This work also eliminates the complicated optical systems used in previous microfluidic approaches, which makes it a truly miniaturized system with great potential for real-time characterization, separation, and sorting of particulate species based on their geometric and viscoelastic properties in a non-laboratory setting.

INTRODUCTION

Hydrogel materials are polymeric networks that contain a significant amount of water [1]. They can be easily engineered into either homogeneous microbeads or core/shell microcapsules with functional materials encapsulated in the hydrogel shell. Due to the softness and biocompatibility, hydrogel microparticles are used extensively in cell therapies, drug delivery, tissue, and food engineering [2, 3]. The geometric (size, shell thickness) and mechanical (stiffness, viscosity) properties of hydrogel microparticles are crucial for their efficacy in respective applications. In particular, the viability of encapsulated cells changes with the size of the hydrogel microcapsules. Studies showed that human cancer cells exhibit a high necrosis ratio while being encapsulated in the microcapsules larger than a certain size (around 200 μm) [4-6]. The shell thickness also regulates the cell viability and the drug releasing performance. A thick shell may provide an extended drug releasing profile but may decrease the cell viability [7]. Mechanical properties of hydrogel microparticles are also important. Studies showed that hydrogel microparticles with higher stiffness promote chondrogenesis [8-10], whereas such high stiffness reduces the proliferation rate of stem cells [11]. In cell therapies, the differentiation of the stem cells cultured in the hydrogel microparticles is regulated by the mechanical properties of the hydrogel shells [12].

Since hydrogel microcapsules are often used in batches, fast screening of a large number of microparticles based on their geometric and mechanical properties is required. The size and shell thickness can be measured using optical microscopy. However, the boundary between the aqueous core material and hydrogel shell may be indiscernible due to low image contrast between the two layers [13]. Although fluorescent dyes can be used to enhance the contrast, the dyes may diffuse into the hydrogel shell and cause inaccurate measurements. Continuous flow microfluidics is a high throughput mechanical profiling approach [14]. Similar as in geometric screening, most continuous flow mechanical measurements rely on the use of high-speed optical systems. The measurements thus cannot be performed in a truly miniaturized setting, limiting the applications in non-laboratory settings. Moreover, in above measurements geometrical and mechanical properties often cannot be decoupled from each other, which can lead to significant measurement errors.

In this study, we report a continuous flow approach to simultaneously measure the geometric and viscoelastic properties of hydrogel microparticles without the use of high-speed optical systems. The size and viscoelastic properties of microbeads were decoupled using a viscoelastic model and measured simultaneously. The shell thickness of hydrogel microcapsules can also be determined. This device provides a high throughput profiling approach for characterizing hydrogel microparticles within a miniaturized setting.

MATERIAL AND METHODS

Device Design and Fabrication

The device consists of a glass substrate patterned with an array of interdigitated microelectrodes and a PDMS substrate that has a tapered channel segment with the linearly changed width (**Fig. 1b**). The width at the channel inlet was greater than the size of the microparticles to be measured, and the width at the channel outlet was smaller than the size of the microparticles to be measured. After bonding the glass substrate and the PDMS substrate together, the microelectrode array was arranged underneath the tapered channel segment. Every two neighboring electrodes worked in a pair and were connected to a reference resistor of 100 $k\Omega$ (Sparkfun Electronics, CO) and an AC voltage source (1 V in amplitude and 3000 Hz in frequency). There was a total of 15 electrode pairs (**Fig. 1c**). The electrical voltage changes across the reference resistors

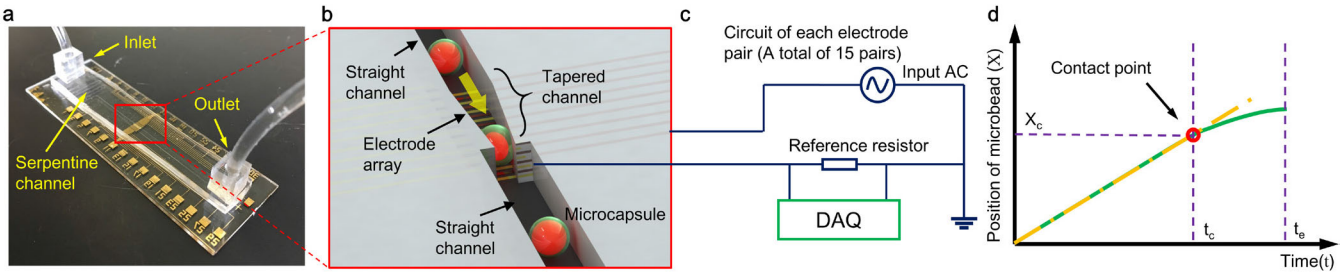

Figure 1. Schematic of this approach. a) *An assembled device;* ***b)*** *Schematic of the tapered channel segment;* ***c)*** *The electrical circuit for each electrode pair; and* ***d)*** *The illustrative motion profile. The green line represents the motion profile. The intersect point between the linear and non-linear portions represents the contacting point with the channel sidewalls.*

978-1-940470-03-0/HH2018/$25©2018TRF
DOI 10.31438/trf.hh2018.3

Solid-State Sensors, Actuators and Microsystems Workshop
Hilton Head Island, South Carolina, June 3-7, 2018

were measured using a data acquisition board (National Instrument, TX) at a sampling rate of 30 *kHz*.

Preparation of Homogeneous Microbeads and Core/shell Microcapsules

All the chemicals were purchased from Sigma-Aldrich (MO) unless otherwise noted. Na-alginate solution was prepared by dissolving Na-alginate powder in deionized (DI) water and stirring at 900 *rpm* under 45 *°C* for 8 hours. $CaCl_2$ and mannitol solutions were prepared by dissolving $CaCl_2$ and mannitol powders in DI water and 1.0% *w/v* cellulose solution separately at the room temperature and stirring thoroughly. Carbon black ink (Yasutomo, Japan) was added to the aqueous core solution (1.0% *w/v* mannitol) with the volumetric ratio of 1:50 to make the core/shell boundary discernible.

Hydrogel microcapsules were prepared using a co-axial electrospray setup [15]. Briefly, 1.0 % *w/v* Na-alginate solution (the outer layer) and 1.0% *w/v* mannitol solution (the inner layer) were pumped through a metallic co-axial syringe needle using two syringe pumps (New Era Pump Systems Inc. NY). The inner diameter of the needle was 0.8 *mm*, and the outer diameter was 1.4 *mm*. A 2.0 % *w/v* $CaCl_2$ bath was placed under the metallic needle. The distance between the metallic needle and the $CaCl_2$ bath was 10 *cm*. The needle was set at +15 *kVDC*, and the $CaCl_2$ bath was set at 0 *kV*. Under such condition, a stable Taylor cone can be formed at the co-axial needle tip. The solutions were sheared off and sprayed towards the $CaCl_2$ bath. After the bi-layered microdroplets entered the $CaCl_2$ bath, the Ca^{2+} ion induced gelation occurred in the outer layer. The inner layer remained in the liquid phase. By changing the flow rates of the two solutions, core/shell microcapsules with different diameters and shell thicknesses were obtained. After electrospray, the microcapsules were washed three times and re-suspended in 1.0% *w/v* mannitol solution. Homogeneous hydrogel microbeads were prepared following a similar procedure, except that a single-axial electrospray process was used [16]. The concentrations of the prepared solid microbeads were 0.5% *w/v*, 1.0% *w/v*, 2.0% *w/v* respectively.

Measurement Principle

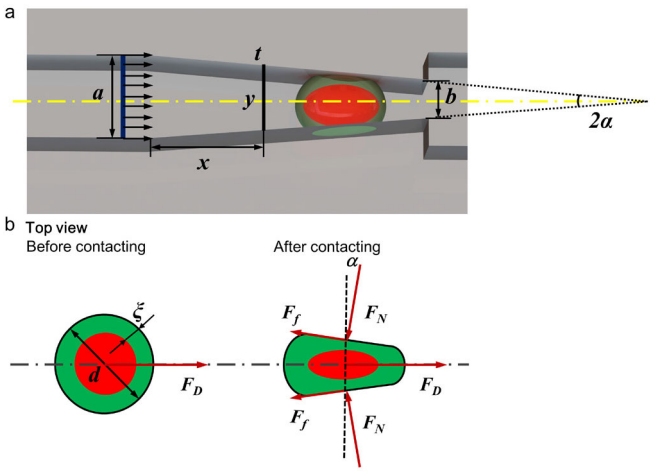

Figure 2. The schematic of the microcapsule deformation when it passes through the tapered channel segment. a) *The schematic view and* ***b)*** *The free-body diagram of a microcapsule after contacting with the sidewalls (top view).*

Once a hydrogel microparticle flows over an electrode pair, the electrical resistance between the two electrodes changes. This is because the microparticle (Ca-alginate) has a different electrical property from the carrying medium (mannitol). The voltage amplitude across the respective reference resistor changes accordingly. The peak of the voltage amplitude change represents the moment when the center of the microparticle overlaps with the center of the subject electrode pair. The position of the microparticle can be derived from the voltage amplitude changes across all the reference resistors. Continuous scanning can obtain the motion profile of the microparticle.

Before the microparticle contacts the sidewalls of the tapered channel, the displacement changes linearly over time. After the contact, the velocity decreases substantially. The motion profile thus deviates from the linear line. The deviation point (t_c, X_c) indicates the contact point and can be used to determine the size (**Fig. 1d**), expressed as $d = Y_c \cos\alpha$, where Y_c is the channel width at X_c. The curved motion profile (from t_c to t_e) represents the microparticle's viscoelastic behavior while it is squeezed through the tapered channel. A quasi-linear viscoelastic (QLV) model can be used to derive the viscoelastic properties of homogenous microbeads as well as the shell thickness of the microcapsules [17, 18].

After the microparticle contacts with the sidewalls, its motion is regulated by:

$$F_D - 2F_f cos\alpha - 2F_N sin\alpha = m\frac{d^2x}{dt^2} \quad (1),$$

wherein F_D denotes the drag force due to the leak flow, the velocity difference between the microparticle and the medium, and the pressure difference between the front and the rear surfaces; F_f denotes the friction force between channel sidewalls and the microparticle, F_N denotes the compressive force due to the contact, m is the mass of the microparticle, α is the half oblique angle of the tapered channel segment and x is the lateral displacement along the flow direction (**Fig. 2a**). Because of the low Reynolds number, the flow is laminar and the drag force F_D can be determined by Stokes' Law. Here, we consider the microparticle as a viscoelastic sphere. Since the half oblique angle (α) of the tapered channel is very small ($< 2.4°$), the loading can be approximated as a uniaxial compression. A QLV model can be established and expressed as:

$$F_N = \sigma(\varepsilon)\left[1 - C\left(1 - e^{-t/\tau}\right)\right] \quad (2).$$

The first term on the right side of the equation represents the instantaneous elastic function. The second term on the right side of the equation is a first-order reduced relaxation function expended using the Prony series, where τ (the time constant) and C (the coefficient of Prony series) denote the constants related to the viscosity of the microbeads. To measure the viscoelastic properties, the first term on the right side of **Eqn. 2** can be approximated using Hertz's theory [19]:

$$\sigma(\varepsilon) = \left[\frac{E\sqrt{d}}{3(1-\nu^2)}(d-y)^{3/2}\right] \quad (3).$$

To measure the shell thickness of microcapsules, the first term on the right side of **Eqn. 2** can be estimated by Reissner's theory [20]:

$$\sigma(\varepsilon) = \left[\frac{4\xi^2 E}{d\sqrt{3(1-\nu^2)}}(d-y)\right] \quad (4),$$

wherein ξ is the shell thickness, E is the instantaneous elastic response of the hydrogel shell, d is the original diameter of microcapsules, and ν is the Poisson's ratio (approximated as 0.5). The friction force has the expression of $F_f = \eta \times F_N$, wherein η is the coefficient of friction (*COF*) between the hydrogel and the sidewall, approximated as 0.06 [21].

By inserting **Eqns. 2**, **3** and **4** into **Eqn. 1**, a second order nonlinear differential equation can be established. The displacement profiles of microparticles can be estimated by solving this equation numerically. The geometric and viscoelastic parameters of microcapsules thus can be determined by fitting the displacement

profiles with the QLV model using the electrically measured data points.

RESULTS AND DISCUSSION

Size Measurement

The sizes of core/shell hydrogel microcapsules and homogeneous hydrogel microbeads determined from electrical voltage measurements were compared with those by the optical measurements. The coefficients of determination between the two measurements are: $R^2 = 0.978$ for core/shell microcapsules and $R^2 > 0.99$ for 1.0% *w/v* and 2.0% *w/v* solid homogeneous microbeads (**Fig. 3a**). For 0.5% *w/v* microbeads, $R^2 = 0.73$. The large deviation is because the 0.5% *w/v* Na-alginate solution has a relatively low viscosity, causing unstable dripping in the electrospray process. This leads to uncontrolled, non-spherical, and asymmetric shaped Ca-alginate microbeads. However, for 1.0% and 2.0% *w/v* microbeads, and microcapsules (made of 1.0% *w/v* alginate), such irregular shapes were not observed (**Fig. 3b**). The results showed the sizes of both homogenous microbeads and core/shell microcapsules can be determined with high accuracy.

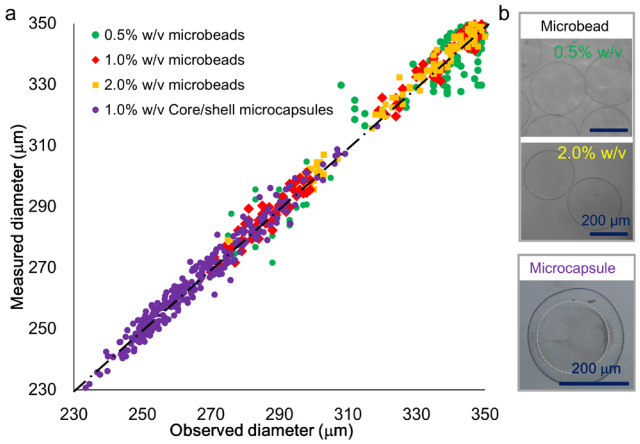

Figure 3. Size determination of homogeneous microbeads and core/shell microcapsules. a) *The comparison of electrically measured sizes versus optically measured sizes.* ***b)*** *The representative micrographs of microbeads and core/shell microcapsules.*

Viscoelastic Measurement of the Solid Microbeads

The mechanical properties were estimated using both a linear elastic model (where the reduced relaxation function on the right of **Eqn. 2** equals to 1) and the QLV model. It is found that although the linear elastic model (denoted by the green line) can match the total transmit time ($t_e - t_c$), a good fit with the trajectory of a microbead (denoted by red dots) cannot be reached (**Fig. 4a**). The QLV model (denoted by the blue line) can reach a much better fit with the experimental data and is expected to yield more accurate results.

The instantaneous elastic response E, the time constant τ, and the coefficient of the Prony series C can be determined by fitting the experimental data with QLV model. The results showed that microbeads with the highest concentration have the highest E, the lowest τ and C, and vice versa (**Fig. 4b-d**). Statistical analysis showed that the viscoelastic parameters vary significantly with the alginate concentration of the microbeads. The C values for 2.0% *w/v* microbeads were very small (0.04±0.01). The reduced relaxation function is approximately 1. The 2.0% *w/v* microbeads can thus be regarded as linear elastic bodies. For 0.5% and 1.0% *w/v* microbeads, the viscous behaviors cannot be neglected. The results also showed that the viscoelastic properties do not show significant difference at different flow rates. This indicates that the geometric and mechanical measurements using the QLV model are independent of input flow rates. This makes it possible to design devices to accommodate the needs for various throughputs.

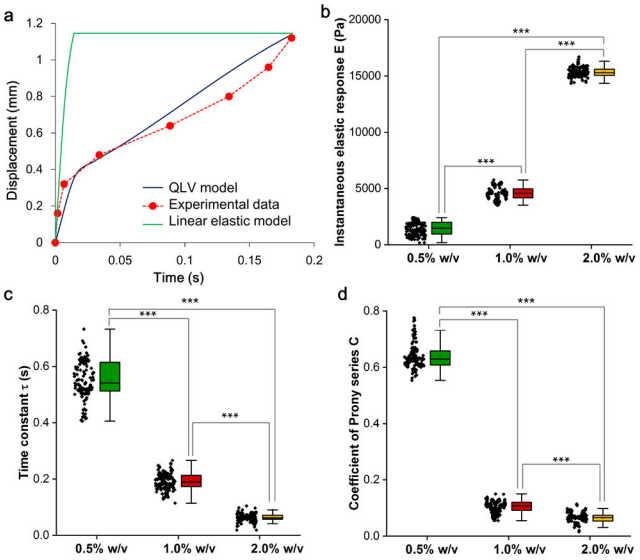

Figure 4. Estimation of the viscoelastic properties of homogeneous microbeads. a) *The comparison of the QLV model and the linear elastic model using a representative trajectory of a 1.0% w/v and 332 μm microbead under 60 ml/h (the circles and the short-dashed line). The fitted curves using the linear elastic model is denoted by the long-dashed line and the QLV model is denoted by the solid line.* ***b-d)*** *The viscoelastic parameters of homogeneous microbeads derived after the data fitting. *** denotes $p < 0.005$.*

Shell Thickness Measurement of the Core/shell microcapsules

Similar as for homogeneous microbeads, the size and the shell thickness of core/shell microcapsules were determined from electrically measured displacement profiles. The comparison between the QLV model and the linear elastic model showed that the I/O ratios estimated by the QLV model agree better with those by the optical measurements ($R^2 = 0.878$ versus $R^2 = 0.649$) (**Fig. 5**). The larger errors associated with the linear elastic model indicated that the viscous behavior of the core/shell microcapsules with a hydrogel shell and an aqueous core is not negligible.

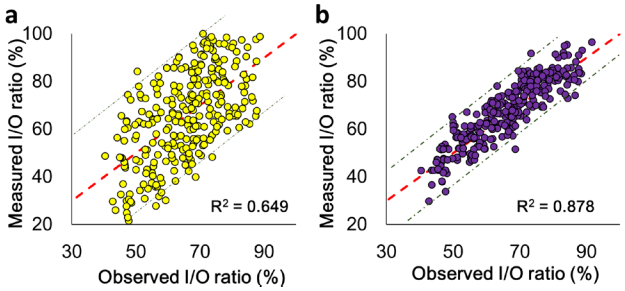

Figure 5. Determination of the shell thickness of core/shell hydrogel microcapsules. *The calculated I/O ratios compared with the observed I/O ratios using* ***a)*** *the linear elastic model and* ***b)*** *the QLV model.*

CONCLUSION

In this work, a continuous-flow device was developed and validated for geometric and viscoelastic profiling of hydrogel microparticles (*i.e.* homogeneous microbeads and core/shell microcapsules). Homogeneous Ca-alginate microbeads with different concentrations (0.5% *w/v*, 1.0% *w/v* and 2.0% *w/v*) were prepared using a single-axial electrospray system. Ca-alginate core/shell microcapsules (1.0% *w/v* Ca-alginate as the shell, 1.0% mannitol as the aqueous core) with different shell thicknesses were prepared using a co-axial electrospray system. The microcapsules and microbeads were pumped through a microfluidic microchannel with a tapered channel segment under a constant flow rate. The displacements of the microparticles were recorded by an array of microelectrodes patterned underneath the microchannel. A viscoelastic model was developed to determine the viscoelastic parameters, shell thickness, and diameter of these microparticles from their displacement profiles. The results showed that viscoelastic parameters and size of homogeneous alginate microbeads, the shell thickness, and the size of core/shell hydrogel microcapsules can be determined simultaneously by fitting their displacement profiles with a viscoelastic model. This work demonstrates a high-throughput (up to 584 microparticles per minute) geometric and viscoelastic profiling method for hydrogel microparticles. Higher throughput is possible by increasing the flow rate, changing the microelectrodes layout, and increasing the sampling rate. It also eliminates external high-speed optical systems and shows potential for high throughput measurements towards subsequent real-time microparticle/microcapsule sorting and separation within a truly miniaturized non-laboratory setting.

REFERENCES

[1] K. Y. Lee and D. J. Mooney, "Alginate: Properties and biomedical applications," *Progress in Polymer Science,* vol. 37, pp. 106-126, Jan 2012.

[2] A. S. Hoffman, "Hydrogels for biomedical applications," *Bioartificial Organs Iii: Tissue Sourcing, Immunoisolation, and Clinical Trials,* vol. 944, pp. 62-73, 2001.

[3] H. M. Shewan and J. R. Stokes, "Review of techniques to manufacture micro-hydrogel particles for the food industry and their applications," *Journal of Food Engineering,* vol. 119, pp. 781-792, Dec 2013.

[4] X. L. Zhang, W. Wang, W. T. Yu, Y. B. Xie, X. H. Zhang, Y. Zhang*, et al.*, "Development of an in vitro multicellular tumor spheroid model using microencapsulation and its application in anticancer drug screening and testing," *Biotechnology Progress,* vol. 21, pp. 1289-1296, Jul-Aug 2005.

[5] S. L. Ham, R. Joshi, G. D. Luker, and H. Tavana, "Engineered breast cancer cell spheroids reproduce biologic properties of solid tumors," *Advanced healthcare materials,* vol. 5, pp. 2788-2798, 2016.

[6] J. L. Horning, S. K. Sahoo, S. Vijayaraghavalu, S. Dimitrijevic, J. K. Vasir, T. K. Jain*, et al.*, "3-D tumor model for in vitro evaluation of anticancer drugs," *Molecular pharmaceutics,* vol. 5, pp. 849-862, 2008.

[7] S. F. Chong, J. H. Lee, A. N. Zelikin, and F. Caruso, "Tuning the Permeability of Polymer Hydrogel Capsules: An Investigation of Cross-Linking Density, Membrane Thickness, and Cross-Linkers," *Langmuir,* vol. 27, pp. 1724-1730, Mar 1 2011.

[8] J. W. Choi, B. H. Choi, S. H. Park, K. S. Pai, T. Z. Li, B. H. Min*, et al.*, "Mechanical Stimulation by Ultrasound Enhances Chondrogenic Differentiation of Mesenchymal Stem Cells in a Fibrin-Hyaluronic Acid Hydrogel," *Artificial Organs,* vol. 37, pp. 648-655, Jul 2013.

[9] X. Li, S. Chen, J. Li, X. Wang, J. Zhang, N. Kawazoe*, et al.*, "3D culture of chondrocytes in gelatin hydrogels with different stiffness," *Polymers,* vol. 8, p. 269, 2016.

[10] V. Moulisová, S. Poveda-Reyes, E. Sanmartín-Masiá, L. Quintanilla-Sierra, M. Salmerón-Sánchez, and G. Gallego Ferrer, "Hybrid Protein–Glycosaminoglycan Hydrogels Promote Chondrogenic Stem Cell Differentiation," *ACS omega,* vol. 2, pp. 7609-7620, 2017.

[11] L. L. Ouyang, R. Yao, S. S. Mao, X. Chen, J. Na, and W. Sun, "Three-dimensional bioprinting of embryonic stem cells directs highly uniform embryoid body formation," *Biofabrication,* vol. 7, Dec 2015.

[12] D. E. Discher, P. Janmey, and Y.-l. Wang, "Tissue cells feel and respond to the stiffness of their substrate," *Science,* vol. 310, pp. 1139-1143, 2005.

[13] C. Siltanen, M. Diakataou, J. Lowen, A. Haque, A. Rahimian, G. Stybayeva*, et al.*, "One step fabrication of hydrogel microcapsules with hollow core for assembly and cultivation of hepatocyte spheroids," *Acta Biomaterialia,* vol. 50, pp. 428-436, Mar 1 2017.

[14] E. M. Darling and D. Di Carlo, "High-throughput assessment of cellular mechanical properties," *Annual review of biomedical engineering,* vol. 17, pp. 35-62, 2015.

[15] S. T. Zhao, P. Agarwal, W. Rao, H. S. Huang, R. L. Zhang, Z. G. Liu*, et al.*, "Coaxial electrospray of liquid core-hydrogel shell microcapsules for encapsulation and miniaturized 3D culture of pluripotent stem cells," *Integrative Biology,* vol. 6, pp. 874-884, Sep 2014.

[16] X. Zhang and Y. Zhao, "Programmable patterning of polymeric microparticles by floating electrodes-assisted electrospray," *Journal of Micromechanics and Microengineering,* vol. 22, p. 047001, 2012.

[17] Y. Niu, X. Zhang, T. Si, Y. Zhang, L. Qi, G. Zhao*, et al.*, "Simultaneous Measurements of Geometric and Viscoelastic Properties of Hydrogel Microbeads Using Continuous-Flow Microfluidics with Embedded Electrodes," *Small,* pp. 1702821-n/a.

[18] C. Haas, T. M. Best, Q. Wang, T. A. Butterfield, and Y. Zhao, "In vivo passive mechanical properties of skeletal muscle improve with massage-like loading following eccentric exercise," *J Biomech,* vol. 45, pp. 2630-6, Oct 11 2012.

[19] S. Tripathy and E. Berger, "Measuring viscoelasticity of soft samples using atomic force microscopy," *Journal of biomechanical engineering,* vol. 131, p. 094507, 2009.

[20] M. Pretzl, M. Neubauer, M. Tekaat, C. Kunert, C. Kuttner, G. Leon*, et al.*, "Formation and Mechanical Characterization of Aminoplast Core/Shell Microcapsules," *Acs Applied Materials & Interfaces,* vol. 4, pp. 2940-2948, Jun 2012.

[21] A. C. Dunn, J. A. Cobb, A. N. Kantzios, S. J. Lee, M. Sarntinoranont, R. Tran-Son-Tay*, et al.*, "Friction coefficient measurement of hydrogel materials on living epithelial cells," *Tribology Letters,* vol. 30, pp. 13-19, Apr 2008.

CONTACT

*Y. Zhao, tel: +1-614-247-7424; zhao.178@osu.edu

DROPLET ACTUATION ON A SURFACE WITH ANISOTROPIC WETTABILITY USING IN-PLANE SYMMETRIC CYCLIC VIBRATION

Lin Qi, Cody Ruck and Yi Zhao[*]
The Ohio State University, OH, USA

ABSTRACT

This paper reports a simple droplet manipulation approach that can displace aqueous droplets over a long distance within the working plane. Repeated gradient wettability patterns were produced on the working surface. The aqueous droplet can be moved along the gradient direction under in-plane symmetric cyclic vibration. Typical droplet manipulations, such as unidirectional movement, droplet mixing and merging, were successfully demonstrated. A bicinchoninic acid (BCA) assay was implemented to illustrate the use of this approach for biochemical detection.

INTRODUCTION

Microfluidic systems that perform biochemical reactions with less sample and reagent consumptions have been widely employed in various fields in the past two decades [1, 2]. Droplet-based microfluidic systems that exhibit reduced biomolecule adsorption with a low risk of cross-contamination [3] comparing to conventional closed-channel continuous-flow microfluidic systems have received extraordinary attentions. In droplet-based microfluidics (also known as digital microfluidics), liquid droplets containing various chemical species can be separated from each other or mixed with other droplets on demand. Each droplet with the volume of a few μL or less may serve as an individual microreactor. High-throughput experimentations with a low sample volume and a small overall device footprint are thus possible [4]. Among numerous droplet-based microfluidic designs, open-channel microfluidics owns several distinct advantages. It is free from the reliance on excessive driving fluids and complicated pumping units. The entire working surface can be utilized through reconfiguring the trajectories of droplet motions. In addition, the leaking issue associated with closed-channel continuous-flow microfluidic systems is no longer a concern.

In open-channel microfluidics, liquid droplets are manipulated on the working surface by various physical means. Electrowetting-on-dielectric (EWOD) is a prevalent approach for droplet manipulation [5], where the droplet motion is induced by creating a wettability difference between the front and the rear edges of the droplet by the electrowetting effect. Typical droplet motions including linear translocation, droplet merging, and mixing were successfully demonstrated. Nonetheless, droplet manipulation by EWOD is limited by possible electrical leakage/breakdown [6]. In particular, a droplet with a high ionic concentration can significantly reduce the breakdown voltage and fail the EWOD chip [5]. In view of this, other non-electrical digital microfluidic stimulation approaches have been developed for droplet manipulation [7-10]. The stimulation can be applied to either the droplets [11] or to the working substrates [7]. Among these methods, mechanical stimulations exhibit a great potential for droplet manipulation due to the relatively simple setup and high process flexibility [11]. In particular, droplets can be moved on a non-wettable surface under asymmetric mechanical vibration [7, 12], or along the gradient of surface wettability under out-of-plane mechanical agitation [13]. Gravitational force and mechanical agitation can also be combined to induce droplet motion [14]. Unfortunately, current mechanical droplet manipulation approaches have several drawbacks. The moving direction of the droplets under asymmetric mechanical vibration highly depends on the droplet size. Simultaneous manipulation of multiple droplets with varied volumes is challenging.

In this study, an alternative mechanical stimulation approach was developed for open-channel digital microfluidics. Repeated patterns with gradient surface wettability were arranged head-to-tail on a superhydrophobic working substrate (**Figure 1**). The wettability gradient in each pattern aligns with the longitudinal axis of the patterns. An aqueous droplet sitting within the pattern thus sees different magnitudes of wettability at its two edges. Upon an in-plane symmetric mechanical vibration along the longitudinal axis of the patterns, the droplet has the tendency to move along the longitudinal axis of the pattern, and start moving once the vibration magnitude exceeds a certain threshold. The inertial motion allows the droplet to reach the next pattern. Continuous vibration can cause a net displacement of the droplet along one direction. Basic droplet motions, including linear translocation, mixing, and merging were successfully demonstrated. In addition, droplet-based on-chip protein concentration measurement was performed. Different from previous mechanical stimulation methods that require complicated motorized stages, the mechanical stimulation was produced by a modified vertex mixer that is widely available in a biochemical laboratory. Besides, the working surface with repeated gradient wettability was generated using a commercial laser engraver. The low-cost fabrication and simple operation of the digital microfluidic system show the potential for various droplet-based on-chip analyses.

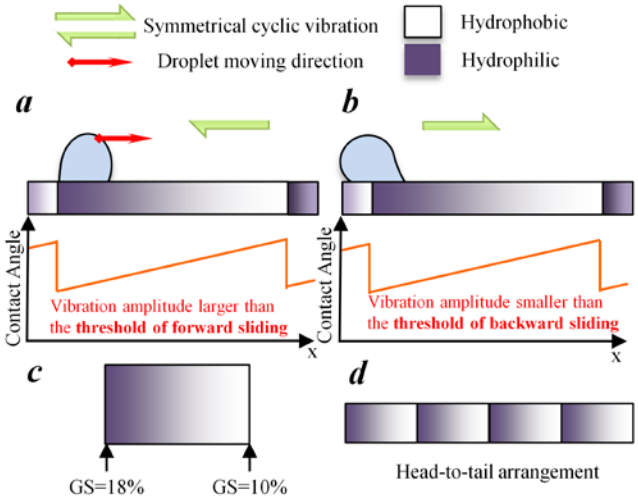

Figure 1: *Schematic of the droplet actuation on a surface with repeated patterns of gradient wettability using in-plane cyclic vibration.*

EXPERIMENTAL SECTION

Device Preparation

Before the laser irradiation, a superhydrophobic substrate was prepared. A PDMS (Sylgard 184, Dow Corning, MI) substrate was fabricated by mixing a base pre-polymer and a curing agent at a

978-1-940470-03-0/HH2018/$25©2018TRF
DOI 10.31438/trf.hh2018.4

Solid-State Sensors, Actuators and Microsystems Workshop
Hilton Head Island, South Carolina, June 3-7, 2018

weight ratio of 10:1. The well-mixed pre-polymer solution was degassed in the vacuum for 30 min. The gas-less solution was then dispensed and spread on a petri dish to achieve a 2 mm thick PDMS layer. The solution was cured on a hotplate at 65°C for 2 hours. A super-hydrophobic surface layer (Rust-Oleum NeverWetTM, IL, USA) was spun on the PDMS substrate at 6000 RPM. The substrate was placed in a ventilation cabinet for 3 hours for solvent evaporation, and then cut into rectangular pieces (70 mm × 30 mm) before use.

The super-hydrophobic coating was modified by laser irradiation (25W, VSL2.30, Universal Laser Systems, AZ) (*Figure 2a*). The operating parameters of the laser have been described in a previous report [15]. Briefly, the laser irradiation was controlled by varying the Gray Scale (GS, 10~18%). Other operating parameters, including the Raster Intensity (RI, -40%), the number of the engraving cycles (n=8), the laser spot size (~127 μm), the lateral traveling speed of the laser head (0.2629m/s), the laser repetition rate (5000Hz), and the spatial resolution (500 PPI (point per inch)) were kept constant throughout the experiments. After the treatment, the PDMS substrate was air blown and visually examined (*Figure 2b*).

Wettability Measurements of Laser Irradiated Patterns

The wettability of the substrate was examined by measuring the static contact angle of a 10 μL water droplet dispensed on the substrate using a contact angle goniometer (*Figure 2c*). The contact angle hysteresis was examined by titling the substrate and examining the minimal angle that can move a 20μL droplet on the surface (*Figure 2d&e*). The titling angle increased from 0° with the increment of 1°. The stage was held still after each increment.

Testing Rig

After laser irradiation, the substrate was mounted on a customized stage, and connected to a commercial vortex mixer. The stage translated the two-dimensional vibration generated by the vortex mixer into a linear sinusoidal wave with the amplitude of ~4mm. The frequency can be adjusted from 1~50 Hz. After a droplet was dispensed on the substrate, the motion of the droplet was recorded using a high-speed camera (Exilim Pro EX-F1, CASIO, Tokyo, Japan).

RESULT AND DISCUSSION

Gradient Wettability

An area of 4 mm×2.5 mm were irradiated by the laser. By changing the GS from 10% at one edge of the area to 18% at the other edge (*Figure 1c*), the degree of decomposition of the super-hydrophobic coating varied spatially, and so did the surface wettability. Such areas were repeatedly patterned on the surface, where the edge subject to the laser irradiation with the GS of 18% in one pattern met the edge subject to the laser irradiation with the GS of 10% of the neighboring pattern. The contact angle measurements showed that a high GS led to a more wetted surface. Within each pattern, the contact angle varied from ~126° (measured at the edge with 18% GS) to ~153° (measured at the edge with 10% GS) (*Figure 2c*). The spatially varied wettability also caused different minimal sliding angles towards opposing directions *(Figure 2f)*. The 20 μL droplet started to move towards the direction of increasing surface wettability at the minimal sliding angle of ~37°, whereas it started to move towards the direction of decreasing surface wettability at the minimal sliding angle of ~53° (*Figure 2d-f*). This indicated that the minimal inertial forces that can displace the droplets along opposing directions were different.

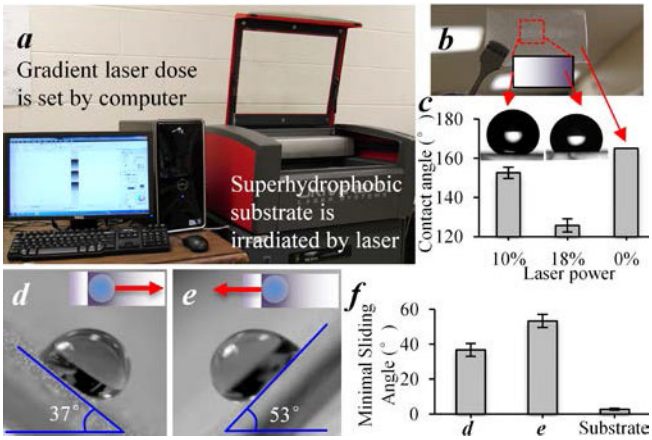

***Figure 2**: The gradient wettability induced by the laser irradiation. (a) Laser engraver used for irradiation. (b) A substrate after laser irradiation. (c) The contact angle of a 10 μL water droplet on the substrates treated with varied laser doses. (d-f) The minimal sliding angles towards the opposing directions.*

Linear Droplet Translocation

A 20 μL droplet was dispensed on the pattern with gradient wettability. The droplet spontaneously migrated to the most wetted edge of the pattern. This is because the gradient of the surface wettability is large enough to overcome the contact angel hysteresis of the droplet. When an in-plane cyclic vibration of 10 Hz was applied, the droplets moved along the longitudinal axis of the pattern towards the less wetted area and came across the edge to the neighboring pattern (*Figure 3a*). In particular, the droplet moved across an edge of the neighboring within each vibration cycle, and travelled over a distance of 40 mm within 1s (Figure 3b). Continuous vibration can move the droplet over a long distance.

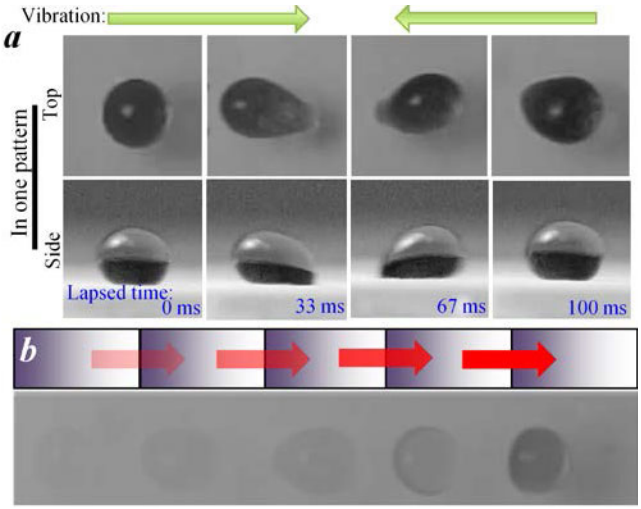

***Figure 3:** Droplet manipulation by cyclic in-plane symmetric vibration. (a) The top and cross-sectional views of a droplet manipulation in one pattern. (b) Long distance droplet movement (~16 mm). 5 time-lapsed photographs were overlapped. The faded droplets represent the positions of a droplet at the different time.*

Droplet Mixing and Merging

Droplet mixing is an essential functions of droplet based microfluidic and is used extensively for biochemical analysis. The mixing of two droplets by the symmetric in-plane vibration was

demonstrated by arranging two groups of patterns towards the opposite directions. As shown in the *Figure 4*, both pattern groups were connected to a square area which had been irradiated by laser with the GS of 25%. The square area was thus more hydrophilic than the hydrophilic edge of the patterns. Two 20μL droplets stained with different colors were dispensed on the distal ends of the two opposite patterns. Once the in-plane vibration of 10Hz was applied, both droplets moved toward the square area at the center due to the gradient wettability. The two droplets met with each other within ~300 ms. The in-plane vibration also helped to quickly mixed the two droplets, which was evidenced by the color of the merged droplet. The color of the merged droplet became homogenous within 2.5 s (25 cycles of vibration). When the two droplets of the same volumes were mixed without vibration, it took more than 25 s before the color of the merged droplet became homogenous.

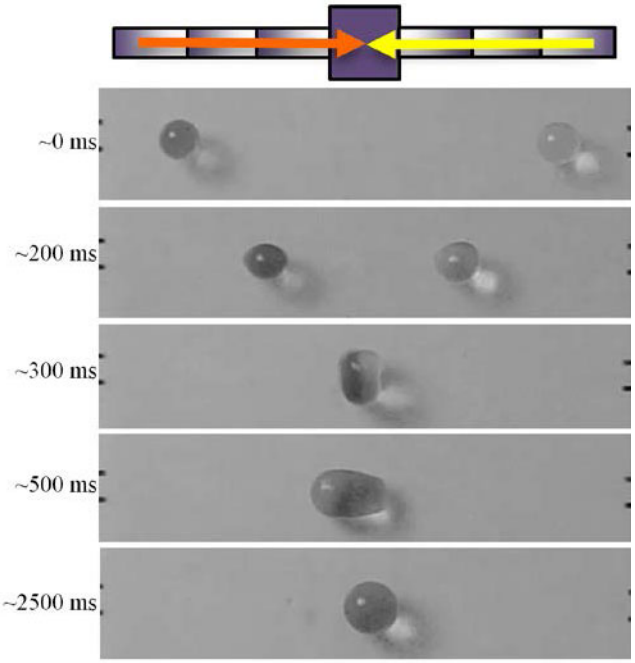

Figure 4: *Droplet mixing by moving two droplets toward each other.*

In above mixing experiment, the two droplets moved towards each other and met at a center place. In droplet based operation, there were also needs to dislocate only one droplet, while keeping the other stationary. This was demonstrated by patterning the areas with gradient wettability with different widths. The areas with three different widths, *i.e.*, 2.5 mm, 3 mm and 3.3 mm, were patterned. The length of the area were the same (4mm). The areas with different widths were connected along the longitudinal direction (*Figure 5*). Three 20μL droplets were dispensed at the locations shown in the figure. The in-plane vibration of 10Hz was applied. At the beginning, only the droplet on the area with the width of 2.5mm was dislocated, while the other two droplets stay stationary. Once the moving droplet met the droplet on the area with the width of 3mm, the merged droplet gained the volume of 40 μL and started to move under the same vibration. Similarly, once the merged droplet with the volume of 40 μL met the droplet on the area with the width of 3.3 mm, the merged droplet gained the volume of 60 μL and started to move further along the longitudinal direction. This study showed that the motion of the droplet not only depends on the wettability of the pattern and the mechanical stimulation, but also on the width of the wettability pattern and the droplet volume.

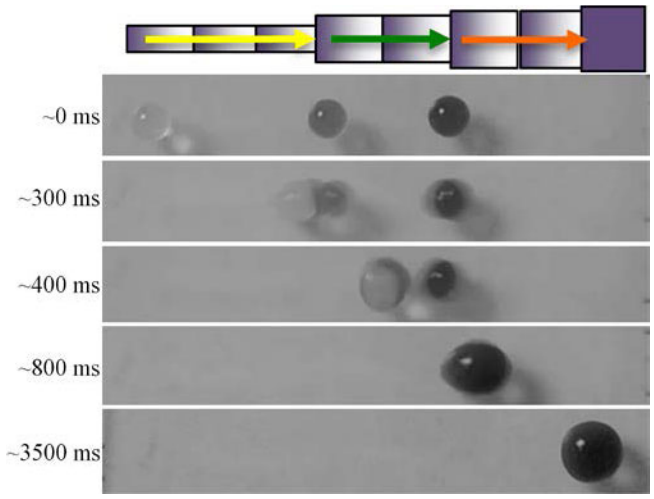

Figure 5: *Sequential merging by selectively manipulating the droplets by placing them on patterns with different widths.*

Measurement of Albumin Concentration

The efficacy of this droplet manipulation approach for biochemical analysis was demonstrated through the measurement of the albumin concentration of a sample solution (*Figure 6a*). Multiple groups of repeated patterns with the gradient wettability were first irradiated using the laser with the GS from 10% to 18%. All the groups were terminated with a hydrophilic square that was treated using the laser with the GS of 25%. The 1000 μg/mL albumin solution was diluted by DI water to obtain the albumin solutions with the concentration from 0.3 to 1000μg/mL. These solutions were used to build a standard curve for albumin concentration quantification. A 10 μL droplet of albumin solution at each concentration was dispensed within a hydrophilic square and dried. The bicinchoninic acid (BCA) working reagent was prepared by mixing the reagent A and the reagent B of Pierce BCA protein assay kit (Thermo Fisher Scientific, MA, USA) with the volume ratio of 50:1.

A 2 μL droplet with an unknown albumin concentration was dispensed on the hydrophilic square of an unoccupied pattern group. A 20 μL BCA working reagent was dispensed to the other end of the pattern group. Similarly, a 20 μL BCA working reagent was dispensed to the distal end of each pattern group that has the immobilized albumin. The in-plane vibration of 10Hz was applied along the longitudinal direction of the pattern. Upon the vibration, all the BCA droplets were transported to the hydrophilic squares within 2 s (*II, Figure 6a*). The substrate was continuously vibrated to allow thorough mixing of the BCA reagents with albumin. The temperature of the substrate was elevated to 37ºC to assist the reaction. The colors of the droplets changed due to the reaction between albumin and BCA (*III, Figure 6a*). The concentration of the unknown albumin droplet was quantified by measuring the absorption of light at the wavelength of 562 nm and compare the absorption of the standard samples with known concentrations. In particular, a linear standard curve with a high regression coefficient > 0.98 was obtained (*Figure 6b*). The concentration of the droplet to be measured was calculated as ~239 μg/mL. This value was close to its actual concentration of ~ 230 μg/mL. The reaction time of the droplet based protein analysis was compared to the BCA assay performed using the standard protocol. The light absorption of the droplet based analysis reached 95% of its maximal within 10 min (*Figure 6c*), which was three times faster than that of the standard BCA assays. The shorter reaction time is

due to the in-plane vibration that continuously accelerated the mixing of reagents and the smaller sample volume.

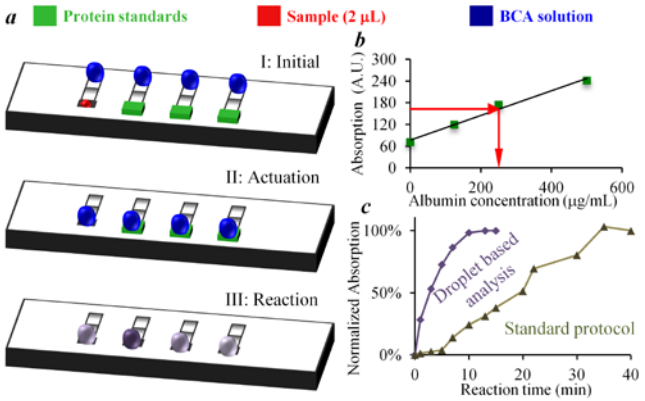

Figure 6: *Droplet-based protein measurement. (a) The schematic of the device. (b) The light absorption at 562 nm of the droplet with unknown albumin concentration and the standard curve. The red arrows indicates the albumin concentration in the unknown sample. (c) The comparison of the droplet based analysis with the measurement using a standard BCA assay protocol.*

CONCLUSION

In this paper, we report an approach of open channel droplet manipulation by arranging repeated patterns of gradient wettability on the working substrate and applying symmetric in-plane vibration. The gradient wettability created by decomposing the super-hydrophobic coating by the laser irradiation with different doses causes different minimal inertial forces that can move the droplet along the opposing directions. As such, the droplets can be dislocated and generate a net displacement along the longitudinal direction of the patterns upon in-plane cyclic vibration. Continuous vibration is able to have the droplet travel over a long distance. Typical droplet manipulations including unidirectional movement, and droplet merging and mixing were implemented. The measurement of protein concentration using this approach was demonstrated, which showed a faster reaction rate than the measurements using the standard BCA assay protocol.

REFERENCES

[1] T. Konry, S. S. Bale, A. Bhushan, K. Shen, E. Seker, B. Polyak, *Et Al.*, "Particles And Microfluidics Merged: Perspectives Of Highly Sensitive Diagnostic Detection," *Mikrochim Acta,* Vol. 176, Pp. 251-269, Feb 2012.

[2] P. S. Dittrich And A. Manz, "Lab-On-A-Chip: Microfluidics In Drug Discovery," *Nature Reviews Drug Discovery,* Vol. 5, Pp. 210-218, Mar 2006.

[3] L. S. Roach, H. Song, And R. F. Ismagilov, "Controlling Nonspecific Protein Adsorption In A Plug-Based Microfluidic System By Controlling Interfacial Chemistry Using Fluorous-Phase Surfactants," *Analytical Chemistry,* Vol. 77, Pp. 785-796, Feb 1 2005.

[4] R. B. Fair, "Digital Microfluidics: Is A True Lab-On-A-Chip Possible?," *Microfluidics And Nanofluidics,* Vol. 3, Pp. 245-281, Jun 2007.

[5] H. H. Shen, L. Y. Chung, And D. J. Yao, "Improving The Dielectric Properties Of An Electrowetting-On-Dielectric Microfluidic Device With A Low-Pressure Chemical Vapor Deposited Si3n4 Dielectric Layer," *Biomicrofluidics,* Vol. 9, Mar 2015.

[6] M. Mibus, C. Jensen, X. Hu, C. Knospe, M. L. Reed, And G. Zangari, "Dielectric Breakdown And Failure Of Anodic Aluminum Oxide Films For Electrowetting Systems," *Journal Of Applied Physics,* Vol. 114, Jul 7 2013.

[7] S. Daniel, M. K. Chaudhury, And P. G. De Gennes, "Vibration-Actuated Drop Motion On Surfaces For Batch Microfluidic Processes," *Langmuir,* Vol. 21, Pp. 4240-4248, Apr 26 2005.

[8] S. Biswas, Y. Pomeau, And M. K. Chaudhury, "New Drop Fluidics Enabled By Magnetic-Field-Mediated Elastocapillary Transduction," *Langmuir,* Vol. 32, Pp. 6860-6870, Jul 12 2016.

[9] S. C. S. Lin, X. L. Mao, And T. J. Huang, "Surface Acoustic Wave (Saw) Acoustophoresis: Now And Beyond," *Lab On A Chip,* Vol. 12, Pp. 2766-2770, 2012.

[10] K. A. Wier, L. C. Gao, And T. J. Mccarthy, "Two-Dimensional Fluidics Based On Differential Lyophobicity And Gravity," *Langmuir,* Vol. 22, Pp. 4914-4916, May 23 2006.

[11] Y. Zhang And N. T. Nguyen, "Magnetic Digital Microfluidics - A Review," *Lab On A Chip,* Vol. 17, Pp. 994-1008, Mar 21 2017.

[12] L. Dong, A. Chaudhury, And M. K. Chaudhury, "Lateral Vibration Of A Water Drop And Its Motion On A Vibrating Surface," *European Physical Journal E,* Vol. 21, pp. 231-242, Nov 2006.

[13] S. Daniel, S. Sircar, J. Gliem, And M. K. Chaudhury, "Ratcheting Motion Of Liquid Drops On Gradient Surfaces," *Langmuir,* Vol. 20, Pp. 4085-4092, May 11 2004.

[14] T. Kong, R. Brien, Z. Njus, U. Kalwa, And S. Pandey, "Motorized Actuation System To Perform Droplet Operations On Printed Plastic Sheets," *Lab On A Chip,* Vol. 16, Pp. 1861-1872, 2016.

[15] L. Qi, C. Ruck, G. Spychalski, B. King, B. Wu, And Y. Zhao, "Writing Wrinkles On Polydimethylsiloxane (Pdms) By Surface Oxidation With A Co2 Laser Engraver," *Acs Applied Materials & Interfaces,* 2018.

CONTACT

*Yi Zhao, zhao.178@osu.edu; Tel: 614-247-7424

TUNABLE COLOR REFLECTOR WITH ZERO STATIC POWER

Mohsen Jafari[1], L. Jay Guo[1], and Mina Rais-Zadeh[1,2]*
[1]Department of Electrical Engineering, University of Michigan, Ann Arbor, Michigan, USA
[2]NASA Jet Propulsion Laboratory (JPL), Pasadena, California, USA

ABSTRACT

This paper introduces a tunable color reflector for use in low power display systems employing a phase change material (PCM) within a sub-wavelength layered structure. Optical index tunability of the PCM in the reflection spectrum permits vivid color tuning for low power applications. The phase change material used to achieve these results was Germanium Telluride (GeTe). Specifically, ultra-thin film GeTe was sandwiched between a bottom metallic mirror and a top Indium Tin Oxide (ITO) layer. A thick phase-shift Silicon Dioxide (SiO_2) was placed under GeTe to enhance the color tunability in the setting of GeTe phase transition, thus improving color change. Low sensitivity to incident light angle and polarization provides the potential for this device to be very useful for portable device applications.

INTRODUCTION

Display systems and color filters are among the most commonly used optical components producing colors, where the core principle is based on emitting or filtering white light [1]. Active displays, which need constant power to produce a color, are well developed and utilized technology and have advanced considerably within the past decades [2]. Light emitting diodes (LED), which can produce an array of vivid colors, have both improved in quality and cost leading to their widespread use in commercial products, replacing the old liquid crystal display (LCD) technologies [3]. State of the art Organic LED (OLED) technology can address cost, power, refresh rate, and durability issues that were experienced with the use of traditional LCDs [4, 5]. Despite such advancements in display technologies, active display systems remain to be the main source of power usage in electronic devices. Passive color displays that only consume power to switch color have almost zero static power and are efficient alternatives as ultra-low power displays, especially for low refresh rate applications [6].

Most of the modern display systems use three or more separate pixel components to produce a pixel of an image such as microelectromechanical (MEMS) based mirrors, color E-ink, OLED, etc. [7]. However, generating all three primary colors in a single (component) pixel has always been the best way to produce vivid images. An example of this is a single mirror interferometric device (SMI), where a moving MEMS mirror is used to tune the pixel color in the visible spectrum [8]. However, having movable objects has proven to be a major limitation of these devices in terms of durability, switching power consumption, and reliability in response to mechanical shocks in portable electronics where lower power is necessary. Structural-based color filters may be used but cannot provide the whole range of tunable colors. Chemical-based color pixels, where an electro-chromic, photo-chromic, or thermo-chromic material is used in a photonic cavity can provide a more versatile reflective display. Their tunability adds another dimension to the passive or active components at IR or microwave frequencies [9]. Furthermore, systems such as optical communication [10], memories [11], energy harvesters [12], as well as countless others, may benefit from tunable components to reduce process variation and improve stability when device parameters change in response to harsh environments or due to aging.

Liquid crystals [13], Germanium (Antimony) Telluride [14, 15], and Vanadium Dioxide (VO_2) [16] are among the most commonly used phase change materials as they exhibit significantly different refractive index values in their different phases. Using this mechanism, high amplitude modulation can be achieved by employing both real and imaginary parts of the refractive index [17]. Here, Germanium Telluride (GeTe) was used in a layered photonics structure to produce a color reflector as shown in Figure 1. High optical loss of GeTe in visible-near infrared (NIR) region must always be considered as a potential limitation for its use in transmission based devices [18]. This complication was avoided by making the GeTe very thin and utilizing a reflection-based device for ultra-low power displays [19]. As a result, two vivid colors (red and blue-purple) were achieved in two different crystallographic phases of GeTe. The devices have been switched more than 100 times with application of electrical pulses trains. Ultra-thin GeTe films used in these devices undergo a smoother, more complete, and more reliable crystallographic phase transition (Figure 2) with considerably decreased loss than what has been observed in devices with thicker films. An additional consideration is that unlike VO_2 [16], both phases of GeTe are stable at room temperature, resulting in zero static power consumption. In other words, the devices consisting of GeTe are more stable during retention time without the need for constant heat pumping into the structure. Thus, if designed properly, GeTe-based devices would offer longer life-time with lower aging issues.

GeTe, even though a thermo-chromic PCM, could be transitioned electrically or optically, which may prove useful for a diverse field of applications with fully optical operation. Reliable, fast, and repeatable phase transitions are demonstrated for multiple devices showing minimum variation in their optical responses. Use of GeTe results in much higher stability due to its high phase changing temperature compared to VO_2 and GeSbTe. Compared to previous designs using a singfinale layer of PCM on a noble metal [19], use of optical cavity between PCM and the bottom reflector increases the modulation index per each nm of PCM. An antireflection thin ITO film on top is used to reduce the non-modulated reflection and enhance the device dynamic color range.

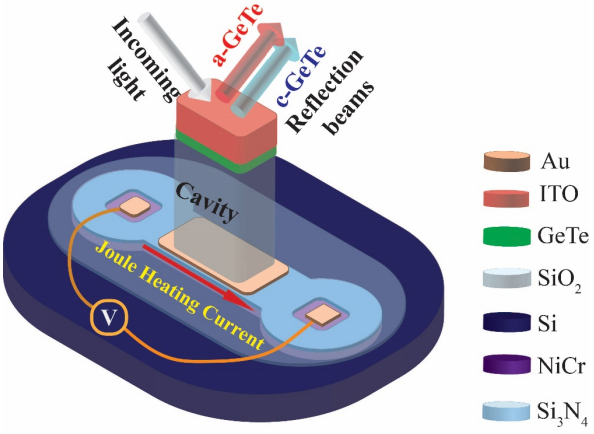

Figure 1. Schematic of the device consisting of a buried NiCr heater connected to gold electrodes to apply current. Stack of TiO_2 (red) and SiO_2(blue) films is shown sitting on top of GeTe film in green.

978-1-940470-03-0/HH2018/$25©2018TRF
DOI 10.31438/trf.hh2018.5

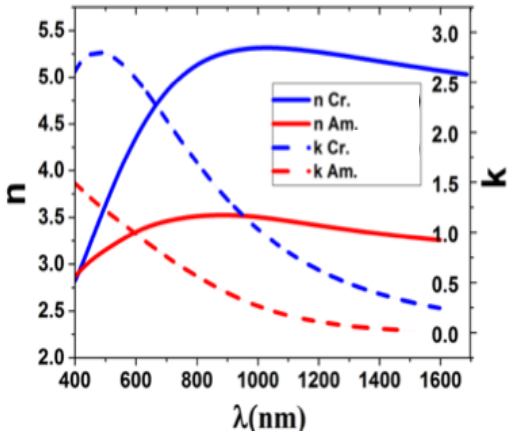

Figure 2. The refractive index of the GeTe in both phases.

The remaining sections of the paper follow this outline: design and characterization of the color filter; fabrication methods and phase transitioning; experimental results; discussion and conclusions.

METHOD OF DESIGN AND FABRICATION

Theory and Design

The device schematic shown in Figure 3(left) consists of a thin GeTe film (20 nm) sitting on top of a SiO_2 phase shift layer. This oxide layer serves as the body of the optical cavity to enhance the light reflection contrast. Under the oxide, a thick gold layer reflects all the light back to oxide. Compared to the thin film resonance-based shutter [18], where there is no optical cavity, addition of this phase shift improves the color contrast of the device in its two different states. This is crucial to achieve low loss high contrast performance with the thinnest possible PCM layer. The buried NiCr is located under the whole stack and used for phase transition through joule heating. To model the total light reflection of this device, one can use the transfer matrix method, where each layer's transfer matrix "M" is defined as:

$$M = \prod_n \begin{bmatrix} e^{\beta_n} & r_n e^{\beta_n} \\ r_n e^{-\beta_n} & e^{-\beta_n} \end{bmatrix}. \quad (1)$$

Here, r_n is the light reflection from n^{th} interface and β_n is the phase accumulation in the n^{th} layer, which are both defined as:

$$r_n = \left(\frac{k_n - k_{n+1}}{k_n + k_{n+1}}\right). \quad (2)$$

$$\beta_n = e^{ik_n t_n}. \quad (3)$$

where k_n is wavevector in layer n and t_n is n^{th} layer thickness. Wavevector (k_n) is $n_n \times \cos(\theta)$ for s-polarization and $n_n/\cos(\theta)$ for p-polarization with θ being the light incidence angle. One can mathematically derive total light reflection from expanding eq (1) as:

$$R = \left|\frac{M_{01}}{M_{00}}\right|^2. \quad (4)$$

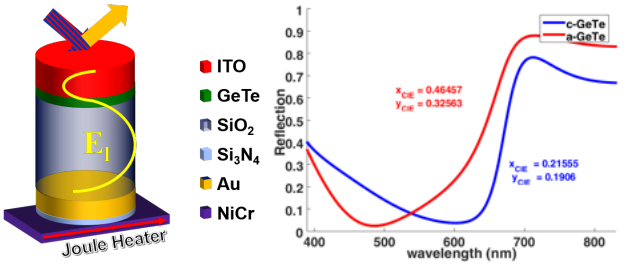

Figure 3. (left) Multi-layer DBR based shutter using ultra-thin PCM layer (20 nm). (right) Light reflection for both phases of the structure (inset: CIE standard coordinates).

Figure 3 demonstrates the device structure consisting of (from top): antireflective ITO coating; GeTe PCM layer; SiO_2 phase shift layer; bottom gold reflector; SiN_3 passivation layer; buried NiCr heater. Placing highly absorptive crystalline GeTe film with thickness t_{GT} in between low loss SiO_2 and ITO films generates a node in the structure for electromagnetic waves. Bottom gold acts as a node in the reflecting waves since the traveling waves have to have similar amplitude which can only satisfy the boundary condition when they are both zero. If the light wavelength is twice the distance between the gold mirror and the lossy crystalline GeTe film, it can reflect back almost perfectly from the stack as shown with reflection peaks at 700 nm. The position of peak is readily derivable as:

$$\frac{\lambda_P}{2} = 2 \times k \times t_{SiO2} \times n_{SiO2} \sim 500 * 1.45 = 725\ nm. \quad (5)$$

Tuning of the peak wavelength within the visible wavelength range follows Equation (5) for SiO_2 changing from 150 nm to 300nm. However, light will acquire minimum loss and phase shift for a round trip between top ITO and bottom gold. Addition of propagation loss through ITO, SiO_2, each of $t_{GT}/2$ crystalline GeTe film, and reflection loss in gold surface results in imperfect reflection at 700 nm. This reflection peak does not move when GeTe transitions to the amorphous state, due to high loss of amorphous GeTe at 700 nm. Moreover, the wide reflection minimum is due to dispersion of refractive indices for gold and GeTe in the visible region. As shown in Figure 2, GeTe refractive index changes when it goes through crystallographic phase transitions between its two stable phases. This phase transition tunes the dispersion of its refractive index, which causes different outcomes for the total light reflection. This is due to tuning in the reflection coefficient in ITO/GeTe and GeTe/SiO_2 interfaces. Materials with different refractive indices, if used instead of ITO and SiO_2, will result in different reflection spectra and thus different colors. To quantitatively show the color change the International Commission on Illumination (CIE-1931) standard is being used. Using density functions defined in this standard, one can transfer the device reflection spectrum to a set of coordinates (x_{CIE},y_{CIE}). Locating such coordinates on a colored map, similar to Figure 4, shows the true reflected color of the device. This device even with an ultra-thin PCM film (~20 nm) tunes the "x_{CIE}" and "y_{CIE}" coordinates by ~53% and 42%, respectively, when GeTe layer is transitioned from amorphous to crystalline state. This change is enough to change the purple reddish color of the device to dark blue (shown in Figure 4).

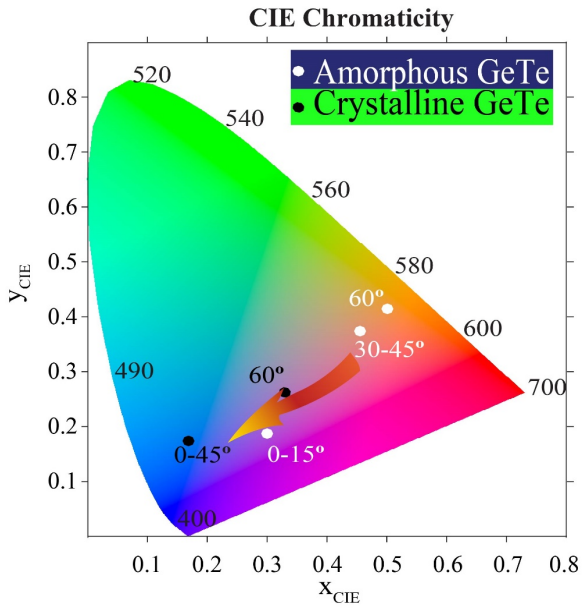

Figure 4. CIE chromaticity graph showing device color in different incidence angles and for crystalline (black dots) and amorphous (white dots) GeTe.

Angle and polarization dependence

Device colors do not change significantly and remain relatively similar at normal incidence even up to 45° oblique incidence. This is demonstrated in Figure 4 for both phases with the inset showing the corresponding colors at each angle.

FABRICATION AND PHASE TRANSITION

Fabrication:

Fabrication starts with cleaned single side polished silicon wafers. The bottom joule-heater is then patterned using conventional optical lithography and the lift-off process. For this purpose, different refractory metals are tested to match input impedance to that of the DC probes used to apply heating pulses. NiCr showed the most reliability with most number of switching cycles for the device. A thin 10 nm Si_3N_4 is deposited on the heater to isolate it electrically from the cavity's bottom reflector which is gold in this case. After passivation, gold mirror is deposited and patterned using the same process used for NiCr heater. The stack is then annealed at 200 ºC to release any residual stress between interfaces. This enhances the yield and reduces the risk of film delamination during next the high temperature Plasma Enhanced Physical Vapor Deposition (PEVCD) step. SiO_2 is then deposited using PECVD as the cavity body using Plasma-Therm 790 PECVD tool (Plasma-Therm Co.) at 200 ºC at a rate of 7.5 A/sec. GeTe films with different thicknesses are then deposited at room temperature in a magnetron deposition system from Kurt J. Lesker® company from a 3 inch $Ge_{50}Te_{50}$ target (Mitsubishi Material Co.) as the top cavity reflector. Disposition rate was maintained at a rate of 0.66 Aº/sec keeping the rate of Ar^+ carrier bombardment with 60 W RF power. This controlled ultra-low rate deposition results in a more uniform film with better adhesion to the bottom SiO_2 layer. Moreover, as-sputtered amorphous GeTe has lower optical loss in visible and NIR wavelengths. SiO_2 films were then deposited. A controlled etching process was developed to dry-etch GeTe film into smaller sizes. This step was followed by ITO sputtering at room temperature using DC reactive sputtering in the same sputtering chamber. A dry-etch was then used to etch through the whole stack and access the bottom heater to apply the joule-heating pulse for GeTe phase transitions.

Phase Transition

Two of the main challenges in the color reflector design process were the design of the heater and the selection of a material with proper resistivity and thermal stability. NiCr, which is a thermally stable material with resistivity of 150×10^{-8} Ωm, was used as the heater adjacent to GeTe. Being isolated from the reflecting gold, the NiCr heater provides the heat required for phase transition of GeTe through joule heating pulses applied to the pads in each side of the device. Pulse energy for crystallization was measured to be 80 nJ with outstanding low current of 40 mA.

EXPERIMENTAL RESULTS

Reflection measurements were performed using a Woollam M-2000 spectroscopic ellipsometer (JA Woollam Co) at different angles ranging from 45º to 75º due to the limitation of the tool setup. Samples were annealed at different temperature ranging from 165 ºC to 180 ºC. The temperature was controlled using an IR-thermometer. The reflection of the device for both "s" and "p" polarizations are shown in Figure 6 at different temperatures at 55º(left) and 65º(right). The GeTe and SiO_2 film thicknesses for these devices were 20 nm and 250 nm respectively. Both polarizations show a wide mode at ~740 nm and a relatively narrower mode at ~380 nm verifying the cavity optical response. The wavelength of these two modes is almost independent of the GeTe phase due to the high loss of both amorphous (a)-GeTe and crystalline (c)-GeTe in the visible wavelengths. The reflection dip for p polarization, on the other hand is tunable depending on the GeTe phase. Shown in this figure, GeTe crystallization causes a blue shift in the p polarized light reflection dip. This blue shift results in better coupling to the mode at 380 nm, i.e. higher light reflection at that wavelength. This along with slight blue shift of the mode at 740 nm due to higher effective refractive index of the cavity yield to a bluer color to reflect from the device. To easily compare the device color tuning during a crystallization event, light reflection at RGB wavelengths are summarized in Table 1 from amorphous phase to fully crystalline films.

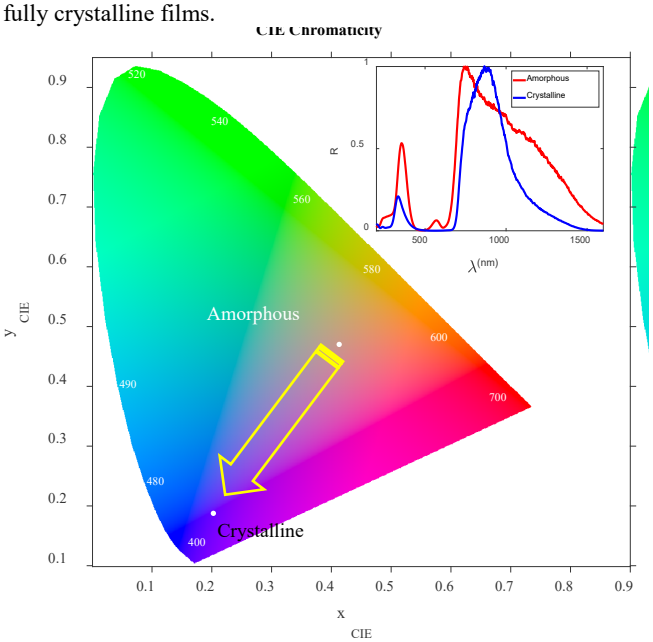

Figure 5. ON and OFF states reflection spectra for non-polarized light using spectroscopic ellipsometer at 45° incident angle. Both states were measured at room temperature in ambient light.

Device reflection is normalized using the sensitivity transfer function of human eyes' cone cells to replicate the true reflected color. The reflection spectrum after normalization is shown in (inset). Such a reflection is then normalized by the CIE standard to find the exact reflected color of the device (Figure 5). Furthermore, the actual color of the device within their pixel areas are shown Figure 7 under ambient white light illumination.

Table 1. Device average reflection change at visible wavelengths under white ambient light

λ_{avg}	Color	$\frac{\overline{R_{partial-cryst}}}{\overline{R_{amorphous}}}$	$\frac{\overline{R_{full-cryst}}}{\overline{R_{amorphous}}}$
470	Blue	0.9688	1.8801
530	Green	1.016	0.405
700	Red	1.02	1.08

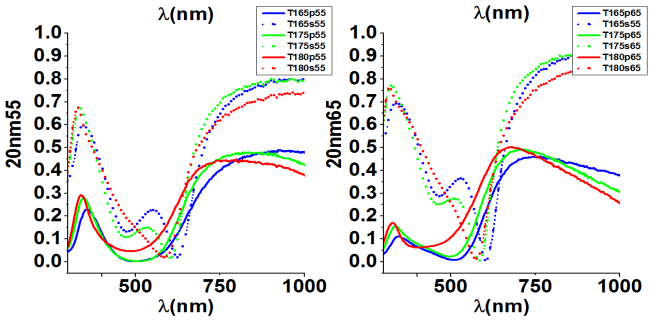

Figure 6. Device reflection at different temperature from 165 ℃ to 180 ℃ for both s and p polarization. The results shown for 55° and 65° incidence angles.

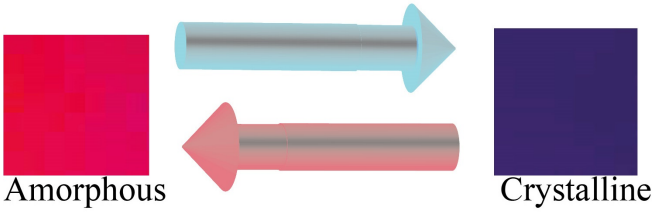

Figure 7. Devices actual colors as they are seen under white ambient light at 45° degree for amorphous (left) and crystalline (right) phases of GeTe.

CONCLUSION

In this paper, a tunable color reflector was introduced using a phase change material (GeTe) sandwiched between a top ITO anti-reflective coating and a bottom gold mirror. Adding a 250 nm thick SiO2 phase shift layer between gold and thin PCM resulted in nodes in the structure and almost perfect reflection. This phase shift layer also helped to increase the color contrast created by GeTe phase transition. Design and modeling details were discussed along with the fabrication method. The device color was change from reddish purple to dark blue by employing a 20 nm film thickness of GeTe PCM. Without losing the generality, the same idea could be expanded to achieve multi-color performance with increasing the numbers of the PCM layers if an effective transition method is used to selectively switch each layer separately.

ACKNOWLEDGEMENT

The authors thank the staff at the Lurie Nanofabrication Facility, University of Michigan, Ann Arbor, MI, USA for providing fabrication facilities. This work is supported by University of Michigan

REFERENCES

[1] Yokogawa, Sozo, Stanley P. Burgos, and Harry A. Atwater. "Plasmonic color filters for CMOS image sensor applications." Nano Letters 12.8 (2012): 4349-4354.

[2] Zeng, Beibei, Yongkang Gao, and Filbert J. Bartoli. "Ultrathin nanostructured metals for highly transmissive plasmonic subtractive color filters." Scientific reports 3 (2013): 2840.

[3] Tan, Zhi-Kuang, et al. "Bright light-emitting diodes based on organometal halide perovskite." Nature nanotechnology 9.9 (2014): 687-692.

[4] Salehi, Amin, et al. "Highly Efficient Organic Light-Emitting Diode Using A Low Refractive Index Electron Transport Layer." Advanced Optical Materials 5.11 (2017).

[5] Page, Zachariah A., et al. "Novel Strategy for Photopatterning Emissive Polymer Brushes for Organic Light Emitting Diode Applications." ACS central science 3.6 (2017): 654-661.

[6] Yan, Jin, et al. "A full-color reflective display using polymer-stabilized blue phase liquid crystal." Applied Physics Letters 102.8 (2013): 081102.

[7] Ma, Ji. "Advanced MEMS-based technologies and displays." Displays 37 (2015): 2-10.

[8] Hong, John, et al. "Continuous color reflective displays using interferometric absorption." Optica 2.7 (2015): 589-597.

[9] Vafapour, Zohreh, et al. "Graphene-based mid-infrared biosensor." JOSA B 34.12 (2017): 2586-2592.

[10] Nafari, Mona, and Josep Miquel Jornet. "Modeling and performance analysis of metallic plasmonic nano-antennas for wireless optical communication in nanonetworks." IEEE Access 5 (2017): 6389-6398.

[11] Ríos, C., Stegmaier, M., Hosseini, P., Wang, D., Scherer, T., Wright, CD., Bhaskaran, H. and Pernice, W.H., "Integrated all-photonic non-volatile multi-level memory." Nature Photonics, 9(11), pp.725-732. (2015)

[12] Nafari, A., and H. A. Sodano. "Surface morphology effects in a vibration based triboelectric energy harvester." Smart Materials and Structures 27.1 (2017): 015029.

[13] Humar, M., et al., "Electrically tunable liquid crystal optical microres- onators," Nature Photonics, 3(10), pp. 595-600. (2009).

[14] Hosseini, P., Wright, CD., and Bhaskaran, H., "An optoelectronic framework enabled by low-dimensional phase-change films". Nature, 511(7508), pp. 206-211. (2014)

[15] Jafari M. and Rais-Zadeh M., "Zero-static-power phase-change optical modulator," Optics letter, pp. 1177-1180. (2016).

[16] Wang H., et al. "Fabrication of vanadium oxide micro-optical switches," Sens. and Act. A, pp. 108-112. (2005).

[17] Jafari, Mohsen, and Mina Rais-Zadeh. "An ultra-high contrast optical modulator with 30 dB isolation at 1.55 μm with 25 THz bandwidth." In Photonic Fiber and Crystal Devices, vol. 10382, p. 1038211. SPIE, 2017.

[18] Jafari, M., and Rais-Zadeh, M. "A 1550 NM phase change electro-optical shutter." Micro Electro Mechanical Systems (MEMS), 2016 IEEE 29th International Conference on. IEEE, 2016.

[19] Jafari, M., Guo, LJ., and Rais-Zadeh, M., "An ultra-fast optical shutter exploiting total light absorption in a phase change material." In Proc. of SPIE Vol, vol. 10100, pp. 101000I-1. (2017).

[20] Jafari, M., Guo, LJ., and Rais-Zadeh, M., " Tunable color reflector with zero static power " In review.

A RECONFIGURABLE OPTOFLUIDIC DEVICE FOR ADAPTIVE IMAGING AND POSITION ESTIMATION WITH A WIDE FIELD OF VIEW

Hanyang Huang, and Yi Zhao[*]
The Ohio State University, Columbus, Ohio, USA

ABSTRACT

Imaging with a wide field-of-view (FOV) is important for versatile applications such as surveillance, robotic vision, and laparoendoscopic imaging. Artificial compound eyes that imitate the insect compound eyes can provide a wide FOV and have a compact size. However, current artificial compound eye devices either require curved photodetectors, have substantial image distortion, or lack self-accommodation capability. In this paper, we present a reconfigurable optofluidic lens that incorporates the architectural merits of the Xenos peckii compound eye and the mammalian eye into one system. The device can provide adaptive imaging and position estimation capability with a wide FOV using a planar image sensor.

INTRODUCTION

Insect compound eye is a unique and sophisticated optical system that excels in its compact design, wide FOV and highly sensitive motion detection capability [1, 2]. Artificial compound eye devices that imitate the wide-angle vision of natural counterparts have shown enormous advantages in various applications including robotic vision, photography, surveillance, medical imaging, motion detection, etc. [3-7]. Several types of artificial compound eye have been developed based on different configurations. One design imitates the compound eye of fruit fly Drosophila [8-10]. A solid microlens array is arranged on a hemispherical surface. Each microlens faces towards a different field angle. This design can offer a FOV as large as 160°×180°. However, a curved image sensor is normally required to accommodate the curved image planes. The fabrication and alignment process are fairly complicated and challenging [11, 12]. Another design imitates the compound eye of Xenos peckii [13-15]. Such device consists of a planar solid microlens array and a planar aperture array. The light beams focused by the microlenses pass through the aperture array and form the images on a planar image sensor. The fabrication and assembly complexities are greatly reduced. The FOV is, however, fairly limited due to the planar arrangement of microlenses. Several additional efforts have also been put in to combine the architectural merits of the above two designs [16, 17]. The microlenses are arranged on a hemispherical surface and an optical replay component is placed in front of the aperture array to steer the light beams on a planar image sensor. Although such design modestly improves the FOV, the maximally obtained FOV is still not sufficient for wide-angle imaging.

These artificial compound eyes also suffer the poor depth perception capabilities, poor image quality and low signal-to-noise ratio (SNR) of their natural counterparts, due to that each small lens only has a small lens aperture [18]. Mammalian eye, another vision system in nature, offers a different configuration. Despite the limited FOV, the relatively large lens aperture increases the light entry and leads to high-resolution images. The lens is deformable under the contraction of ciliary muscles. This changes the focusing power and can bring the objects of interest in focus [19, 20]. The depth perception of different objects positioned at different distances is thus allowed [21, 22].

To achieve wide-angle imaging and position detection using a planar image sensor, we introduce a reconfigurable optofluidic device that incorporates the Xenos peckii compound eye design and the mammalian eye design into one system. A large elastomer membrane is arranged on top of a planar array of apertures and a planar array of small mammalian lenses. The top membrane serves as an array of deformable prisms to enlarge the FOV. A planar image sensor is used for imaging. The device provides an overall FOV as large as 130° with the focusing power of the mammalian small lens varying from 21.4 diopter to 124.9 diopter. The position estimation of the objects in a wide distance range is also demonstrated. The small device can be integrated into portable and miniature systems to expect extensive optical applications.

MATERIAL AND METHOD

Principle and Design

The optofluidic device combines the architectural design of both the Xenos peckii compound eye and mammalian eye. A transparent big membrane atop can be deformed to a dome shape with different radii of curvature. An array (2×2) of small lenses is positioned underneath the big membrane whose focusing powers can be adjusted to focus the objects at different depths. The pinhole mode of the optofluidic device with the image sensor is shown in **Figure 1a**. The optical axis of the small lenses is arranged axial-symmetrically around the center axis of the image sensor that acts as a field stop. When the top membrane remains flat, the initial FOV of the device (FOV_i) is expressed as:

$$FOV_i = 2\delta = 2\arctan\left(\frac{l+w}{v}\right) \quad (1),$$

where δ is half of the FOV_i; l is half width of the image sensor; w is the horizontal distance from the optical center of the small lens to the center axis of the device; and v is the vertical distance from the small lens to the sensor. When the top membrane is deformed, the maximal achievable viewing angle α of the device is expressed as:

$$\alpha = 2\arcsin\left(n * \sin\left[\arcsin\left(\frac{\sin(\delta+\theta)}{n}\right) + \theta\right]\right) \quad (2),$$

where θ is the slope angle of the bottom surface of the top membrane; and n is the refractive index of the fluid. The maximal viewing angle increases with the increasing θ, *i.e.,* the increasing deformation of the top membrane. By combining the initial FOV_i and the FOVs at different top membrane deformations, a large overall FOV can be obtained.

The optofluidic device consists of three glass windows, a cylindrical chamber, a top polydimethylsiloxane (PDMS) membrane with four cylindrical posts bulged atop and microfluidic channels underneath, an iris layer, a bottom microfluidic channel layer, and a bottom PDMS membrane with four small cavities that

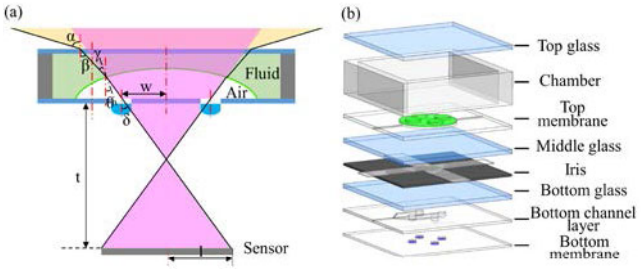

Figure 1: The configuration and optical schematic of the device. *(a) The 2D optical layout. (b) The multi-layer schematic diagram.*

978-1-940470-03-0/HH2018/$25©2018TRF
DOI 10.31438/trf.hh2018.6

are arranged axial-symmetrically around the center of the cylindrical chamber (**Figure 1b**). The iris has two layers. The first layer consists of four films made of polymer dispersed liquid crystal (PDLC). The second layer consists of a black opaque film with four holes that have the same diameter. The locations of the four holes are the same as the four cavities on the bottom membrane. The four films are arranged axial-symmetrically around the center where each one covers the hole on the second opaque layer. When an AC voltage of 110V is applied on the PDLC film, the second layer of the iris changes from opaque to transparent. Switchable imaging among the four individual small lenses can thus be implemented by applying selective electrical activation to the PDLC films. The bottom microfluidic channel and the bottom membrane forms the small lens array. The cylindrical chamber and the cavities of the small lens array are filled with an optical fluid whose refractive index (RI) matches that of PDMS.

Fabrication and Assembly

The cylindrical chamber was fabricated by replicating against a cylindrical acrylic post fabricated using laser engraving. The height of the cylindrical chamber was 7 mm and the diameter was 30 mm. The top membrane, the bottom microfluidic channel layer and the bottom membrane were fabricated by replicating against the respective SU-8 molds that were pre-patterned with complementary features. The edge thickness of the top membrane was 100 μm and the height of the four extruded posts on the top membrane was 600 μm. The distance between the center of each post and the center of the top membrane was 4 mm. The thickness of the bottom microfluidic channel layer was 400 μm. The thickness of the bottom membrane was 400 μm and the diameter of the small lens on the membrane was 2 mm. The distance between the center of each small lens and the center of the membrane is 3.5 mm. All the layers were aligned and assembled under a microscope. The optical fluid was prepared by mixing glycerol with de-ionized water at a weight ratio of 3:2, and was instilled into the cylindrical chamber and the small lens cavities using two syringe pumps.

RESULT AND DISCUSSION

Optomechanical Simulation

In this study, the top membrane serves as a prism to increase the FOV. As such, the bottom surface of the top membrane should be flat. However, the deformed surface of a thin PDMS membrane is often curvilinear, which may cause substantial optical aberration and deteriorate the image quality. To address this, four extruded posts were arranged on the top membrane. Optomechanical simulation was conducted to examine whether this design would help to reduce the curvature of the bottom surface. The top membranes with and without the extruded posts were deformed to the central deflections from 1 mm to 5 mm. The flatness of the membrane was evaluated by calculating the slope angles at the lateral positions from 0.5 mm to 5.5 mm from the edge of the top membrane (**Figure 2a**). The results showed that under the same deflection the slope angle variance of the bottom surface with four extruded posts was significantly smaller than that without the posts. The bottom surface profiles were then imported into OpticStudio to obtain the RMS spot radius of the system at different incident angles (**Figure 2b**). The image plane was placed 11.5 mm away from the small lens. The result showed that when the center deflection of the top membrane reached 5 mm, an overall FOV > 120° can be obtained. The result also showed that the RMS spot radii of the system using the top membrane with the extruded posts were significantly smaller than that without the posts. This indicated that by, the system with the posts can yield better imaging performance.

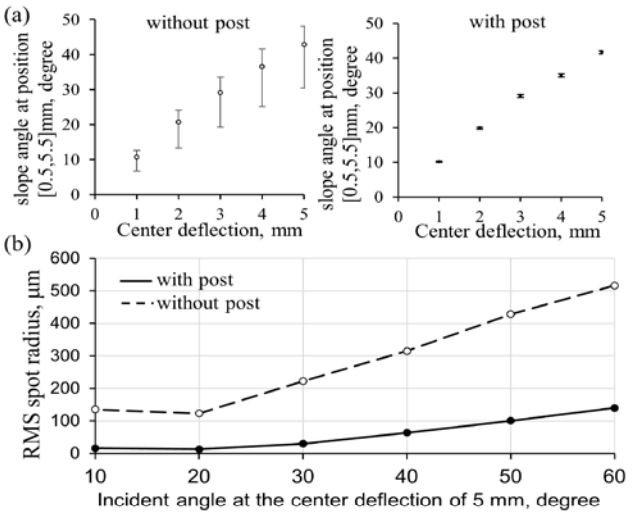

Figure 2: Optomechanical simulation. *(a) The slope angle of the top membrane with and without the extruded posts. (b) The comparison of the RMS spot radii of the devices with and without the extruded posts. The center deflection of the top membrane was 5 mm.*

Optical Power Measurement

The optical power of the small lenses was varied by changing the differential pressure across the corresponding lens membrane. The change of the optical power upon the differential pressure was experimentally measured. The optical power changed from 21.4 diopter at the differential pressure of 80 mbar to 124.9 diopter at the differential pressure of 400 mbar (**Figure 3**). The resolution of the optical power is about 0.25 diopter given the minimal pressure increment of 1 mbar.

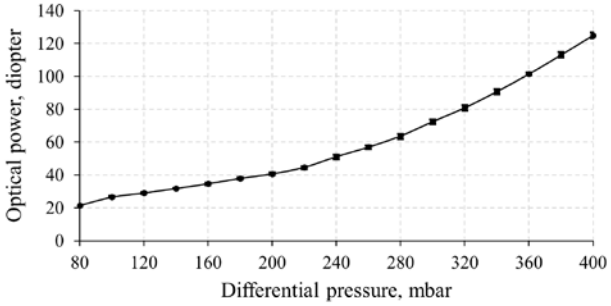

Figure 3: Tunable optical power of single small lens.

FOV Measurement

The FOV of the device was measured by viewing a target object that was placed 60 mm away from the device. A planar 1" CMOS image sensor (CMV4000-3E5, Point Grey) was used for image acquisition. The image sensor was placed 11.5 mm away on the other side of the device. The differential pressure across the top membrane was tuned from 0 to -450 mbar with the decrement of 50 mbar. The overall FOV changed from 82° under the differential pressure of 0 mbar to the maximum of 130° under the differential pressure of -450 mbar (**Figure 4**).

Distortion Characterization

The wide FOV can be obtained by the fisheye lenses. These lenses, however, have severe visual distortions, especially in the peripheral regions. The distorted images cannot be used for measurement purposes. Here, the distortions of the wide-angle images acquired by a fisheye lens and the reported wide-angle lens

were compared. The distortion of the device and the fisheye lens was examined by imaging a dot array target. The array has 26 rows and 15 columns. The distance between the neighboring dots was 14 mm. The target was placed 80 mm away from the device. The image distortion was represented by:

$$\text{Distortion}(\%) = \left|\frac{\text{AD}-\text{PD}}{\text{PD}}\right| \times 100 \qquad (3),$$

where AD is the actual distance between the given dot to the center of the image, and PD is the predicted distance between the corresponding imaginary undistorted dot to the center of the image. The image of the dot array target by our device was formed by stitching individual images captured under the differential pressures across the top membrane of 0 mbar (corresponding to the FOV of 82°), -98 mbar (corresponding to the FOV of 100°), and -296 mbar (corresponding to the FOV of 120°), respectively (**Figure 5a**). The image by the fisheye lens was acquired using the same image sensor (**Figure 5b**). As shown, our device provides a significantly lower distortion than the fisheye lens, especially at the image peripheries. The maximal distortion of the images by the fisheye was 42%, which was significantly higher than the maximal distortion of 16% by our device.

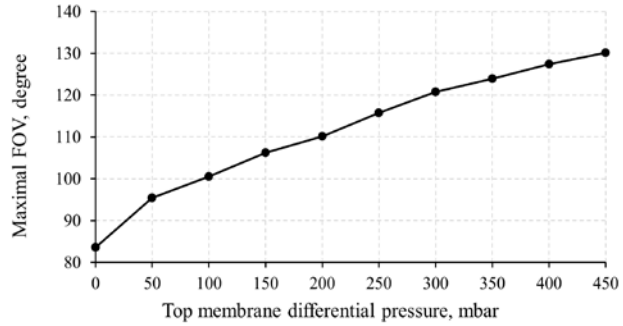

Figure 4: The Overall FOV of the device as a function of the differential pressure across the top membrane.

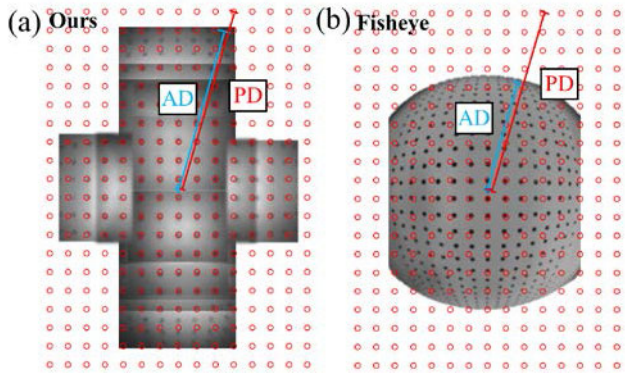

Figure 5: Distortion comparison of the reported device and a fisheye lens. *Image of a dot array by (a) the device and (b) the fisheye lens.*

Wide-angle Imaging

The wide-angle imaging capability was examined by imaging a picture of 'Last Supper' with a length of 340 mm and height of 65 mm. The picture was placed 100 mm away from the device. The image sensor was placed 11.5mm away on the other side of the device. The entire picture was covered within the horizontal FOV of 120°. During the imaging, the top membrane was deformed under the differential pressure across the top membrane of 0 mbar (corresponding to the FOV of 82°), -98 mbar (FOV of 100°), and -296 mbar (FOV of 120°), respectively. Under each FOV, the small lens was continuously tuned to get the different positions of the image in focus. On each image, only the image areas with a relatively high contrast were selected for image stitching. Such areas were adjusted to the same magnification and cropped to the same size. All the cropped neighboring images have 50% overlapped regions. These images were stitched together to form a panorama of the picture (**Figure 6a**). The images taken with a fisheye lens and a single solid lens with the same aperture were also obtained for comparison (**Figure 6b&c**). As seen, the image by the fisheye lens has significantly larger distortions at the peripheries of the image. The image by the solid lens had a significantly smaller FOV.

Figure 6: Wide-angle imaging comparison. *Image of 'Last Supper' by (a) our device, (b) a fisheye lens, and (c) a solid lens. The three lenses had the same aperture.*

Position Estimation

The capability of estimating the spatial positions of the objects was also demonstrated. According to the Snell Law calculation, the coordinates of an object were determined by four variables shown in **Figure 7a**, namely: the prism angle θ, the displacement d, the optical power of the small lens, and the position of the object on the image sensor (point *'A'*). For analysis simplicity, the position of the object on the image sensor was fixed as about 1.88 mm from the edge of the image sensor. The optical power of the small lens was determined by the differential pressure across the small lens membrane. The prism angle θ and the displacement d were both determined by the differential pressure across the top membrane.

Table 1: The Positions of the Nine Objects

(X, Y), mm		
(17, 120)	(28, 120)	(39, 120)
(13, 90)	(21, 90)	(29, 90)
(9, 60)	(14, 60)	(19, 60)

Nine objects were placed in the viewing space in front of the wide-angle lens, with the positions listed in **Table 1**. After bringing the images of the objects to the designed position *'A'*, the coordinates of the objects can be determined from the differential pressures across the top membrane and across the small lens membrane. Given the fact that the small lens had a depth of field and the measurement error in the prism angle membrane was not negligible, the point *'A'* on the image plane corresponded to a small area in the viewing space, as plotted in **Figure 7b**. The areas corresponding to the nine objects were estimated. As shown, all the nine objects fell into the areas estimated from the differential pressures. This indicated that the wide-angle lens can provide the accurate estimation of the object positions.

CONCLUSION

In this paper, we present a reconfigurable optofluidic lens that

combines the architectural design of the Xenos peckii compound eye and the mammalian eye. A tunable FOV as large as 130° was implemented using a planar image sensor. The image distortion of the lens was significantly lower than those of the fisheye lenses. Wide-angle imaging and position estimation were successfully demonstrated.

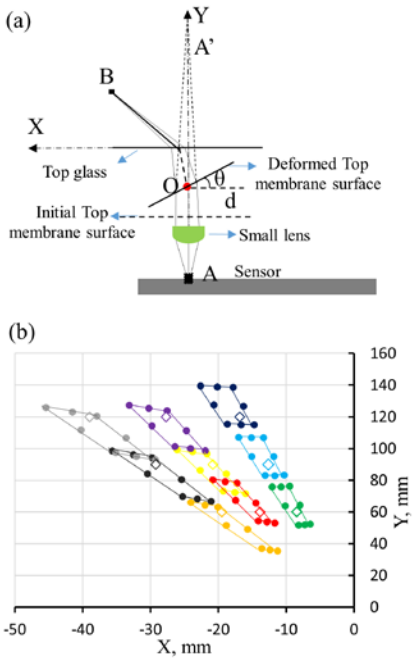

Figure 7: Position estimation. *(a) The optical layout for position calculation; and (b) The position estimation of nine objects placed in the viewing space at different positions. The circles denote the actual position of the objects and the enclosed boxes indicate the estimated position ranges of the objects.*

ACKNOWLEDGEMENT

The authors thank the support from National Science Foundation under the grant number 1509727. The authors also thank the graduate fellowship support from Pelotonia program.

REFERENCES

[1] A. Borst, "Drosophila's View on Insect Vision," *Current Biology,* vol. 19, pp. R36-R47, Jan 13 2009.

[2] A. Borst and J. Plett, "OPTICAL DEVICES Seeing the world through an insect's eyes," *Nature,* vol. 497, pp. 47-48, May 2 2013.

[3] K. H. Jeong, J. Kim, and L. P. Lee, "Biologically inspired artificial compound eyes," *Science,* vol. 312, pp. 557-561, Apr 28 2006.

[4] R. Leitel, A. Brückner, W. Buß, S. Viollet, R. Pericet-Camara, H. Mallot, *et al.*, "Curved artificial compound-eyes for autonomous navigation," in *Micro-Optics 2014*, 2014, p. 91300H.

[5] Y. M. Song, Y. Xie, V. Malyarchuk, J. Xiao, I. Jung, K.-J. Choi, *et al.*, "Digital cameras with designs inspired by the arthropod eye," *Nature,* vol. 497, p. 95, 2013.

[6] R. Szema, J. Rastegar, and L. Lee, "An artificial compound eye for stereoendoscopy," *Journal of medical engineering & technology,* vol. 28, pp. 117-124, 2004.

[7] J. Duparre, F. Wippermann, P. Dannberg, and A. Brauer, "Artificial compound eye zoom camera," *Bioinspiration & Biomimetics,* vol. 3, Dec 2008.

[8] D. Floreano, R. Pericet-Camara, S. Viollet, F. Ruffier, A. Brückner, R. Leitel, *et al.*, "Miniature curved artificial compound eyes," *Proceedings of the National Academy of Sciences,* vol. 110, pp. 9267-9272, 2013.

[9] D. Keum, H. Jung, and K. H. Jeong, "Planar emulation of natural compound eyes," *Small,* vol. 8, pp. 2169-2173, 2012.

[10] P. Qu, F. Chen, H. Liu, Q. Yang, J. Lu, J. Si, *et al.*, "A simple route to fabricate artificial compound eye structures," *Optics express,* vol. 20, pp. 5775-5782, 2012.

[11] I. Jung, J. Xiao, V. Malyarchuk, C. Lu, M. Li, Z. Liu, *et al.*, "Dynamically tunable hemispherical electronic eye camera system with adjustable zoom capability," *Proceedings of the National Academy of Sciences,* vol. 108, pp. 1788-1793, 2011.

[12] H. C. Ko, M. P. Stoykovich, J. Song, V. Malyarchuk, W. M. Choi, C.-J. Yu, *et al.*, "A hemispherical electronic eye camera based on compressible silicon optoelectronics," *Nature,* vol. 454, p. 748, 2008.

[13] E. Buschbeck, B. Ehmer, and R. Hoy, "Chunk versus point sampling: visual imaging in a small insect," *Science,* vol. 286, pp. 1178-1180, 1999.

[14] D. Keum, D. Jeon, M. Kim, and K. Jeong, "Artificial compound eye inspired by imaging principle of Xenos peckii," in *Solid-State Sensors, Actuators and Microsystems (TRANSDUCERS), 2015 Transducers-2015 18th International Conference on*, 2015, pp. 403-406.

[15] W. Pix, J. M. Zanker, and J. Zeil, "The optomotor response and spatial resolution of the visual system in male Xenos vesparum (Strepsiptera)," *Journal of Experimental Biology,* vol. 203, pp. 3397-3409, 2000.

[16] M. Ma, F. Guo, Z. Cao, and K. Wang, "Development of an artificial compound eye system for three-dimensional object detection," *Applied optics,* vol. 53, pp. 1166-1172, 2014.

[17] H. Zhang, L. Li, D. L. McCray, S. Scheiding, N. J. Naples, A. Gebhardt, *et al.*, "Development of a low cost high precision three-layer 3D artificial compound eye," *Optics express,* vol. 21, pp. 22232-22245, 2013.

[18] J. Howard and A. Snyder, "Transduction as a limitation on compound eye function and design," *Proc. R. Soc. Lond. B,* vol. 217, pp. 287-307, 1983.

[19] Y. X. Yu, T. J. Zhang, A. Meadway, X. L. Wang, and Y. H. Zhang, "High-speed adaptive optics for imaging of the living human eye," *Optics Express,* vol. 23, pp. 23035-23052, Sep 7 2015.

[20] K. Wei, H. Huang, Q. Wang, and Y. Zhao, "Focus-tunable liquid lens with an aspherical membrane for improved central and peripheral resolutions at high diopters," *Optics Express,* vol. 24, pp. 3929-3939, 2016.

[21] K. Wei, H. Zeng, and Y. Zhao, "Insect–Human Hybrid Eye (IHHE): an adaptive optofluidic lens combining the structural characteristics of insect and human eyes," *Lab on a Chip,* vol. 14, pp. 3594-3602, 2014.

[22] K. Wei and Y. Zhao, "A Three-Dimensional Deformable Liquid Lens Array for Directional and Wide Angle Laparoscopic Imaging," *26th IEEE International Conference on Micro Electro Mechanical Systems (MEMS 2013),* pp. 133-136, 2013.

CONTACT

*Y. Zhao, tel: +1-614-247-7424; zhao.178@osu.edu

BIOINSPIRED MULTIFUNCTIONAL NANOSTRUCTURES FOR MICRO-OPTICAL IMPLANTS

Vinayak Narasimhan[1], Radwanul H. Siddique[1], Jeong O. Lee[1], Shailabh Kumar[1], Blaise Ndjamen[1], Juan Du[2], Natalie Hong[1], David Sretavan[2], and Hyuck Choo[1]*
[1]California Institute of Technology, Pasadena, California, USA
[2]University of California, San Francisco, USA

ABSTRACT

We have demonstrated, for the first time, the use of multifunctional biophotonic nanostructures on an implantable medical device to improve its optical readout performance and anti-biofouling properties. Inspired by the unique transmissive light-scattering nanostructures found on the transparent wings of the *Chorinea faunus* (*C. faunus*) butterfly, we fabricated multifunctional bioinspired nanostructures (BINS) on a freestanding Si_3N_4-membrane using a polymer phase-separation process and used the nanostructured Si_3N_4-membrane as an opto-mechanical sensing element in a microscale implantable intraocular pressure (IOP) sensor with remote optical readout. In a 1-month *in vivo* study using New Zealand white rabbits, BINS-integration on the resonance-based IOP sensor significantly reduced the angle dependence of the sensor's readout process and led to 10-fold and 3-fold reduction in IOP error compared to traditional tonometry and an IOP sensor without BINS, respectively. Furthermore, the use of BINS effectively suppressed biofouling and inflammation and greatly improved the sensor's biocompatibility by 12 folds.

INTRODUCTION

With increased dependence on medical implants for improving quality of life, research efforts are underway to integrate multiple functionalities in highly-miniaturized implantable packages while delivering reliable *in vivo* performance [1, 2]. Numerous multifunctional nanostructures on insect wings demonstrating omnidirectional antireflection, self-cleaning, anti-fouling and bactericidal properties have been previously studied and replicated [3, 4]. However, their incorporation into implantable biomedical devices remains unexplored.

Here, inspired by the multifunctional properties of the biophotonic nanostructures found on the wings of the *C. faunus* butterfly, we engineer bioinspired nanostructures (BINS) on a freestanding Si_3N_4-membrane. The BINS exhibit isotropic transmissive light-scattering similar to nanostructures in the inner sections of the *C. faunus* wings (indicated by blue arrows in Figure 1a) that could be beneficial to optical sensors' readout processes. Additionally, being improved on the biophysical properties of the *C. faunus* wing nanostructures, the BINS achieves antifouling through structurally-induced hydrophilicity that inhibits the adhesion of proteins, prokaryotes and eukaryotes *in vitro*. Antifouling by preventing adhesion is more advantageous when used with implants as it could minimize cell and tissue damages and avoid inflammation. Finally, we integrate the BINS Si_3N_4-membrane onto a resonance-based implantable IOP sensor and successfully demonstrated a greatly improved range of optical readout angles and biocompatibility in a month-long *in vivo* study.

THEORY

The AFM, SEM, optical, and biological characterizations have revealed that two groups of dome-shaped nanostructures with different periodicity co-exist on the transparent wings of the *C. faunus*: (1) angle-independent anti-reflective nanostructures with periods of 140-180-nm in the postdiscal areas indicated by red arrows in Figure 1a; and (2) angle-independent transmissive light-scattering nanostructures with periods of 200-300 nm in the basal areas indicated by blue arrows in Figure 1a. The difference in structural periodicity between the two groups of nanostructures is shown in Figure 1b. This zone-dependent variation in periodicity influences the extent of light scattering on the wing. Due to its sub-wavelength structural periodicity (< 200 nm), the postdiscal area is scattering-free and anti-reflective. This phenomenon is consistent with other sub-wavelength nanostructures found in nature and can be modelled using the established effective medium theory and the transfer matrix model [3]. On the other hand, the basal area with a periodicity comparable to light wavelengths (> 200 nm) shows forward narrow-angle Mie scattering. In addition, the diffuse (non-scattered and scattered) and specular (non-scattered only) transmittance of the postdiscal areas were almost identical while the basal areas showed 20% reduction in the specular transmittance, indicating noticeable isotropic scattering effects (Figure 1c-d). Furthermore, the nanostructures in the basal areas exhibit a short-range order and consequently an angle-independent transmissive light-scattering property.

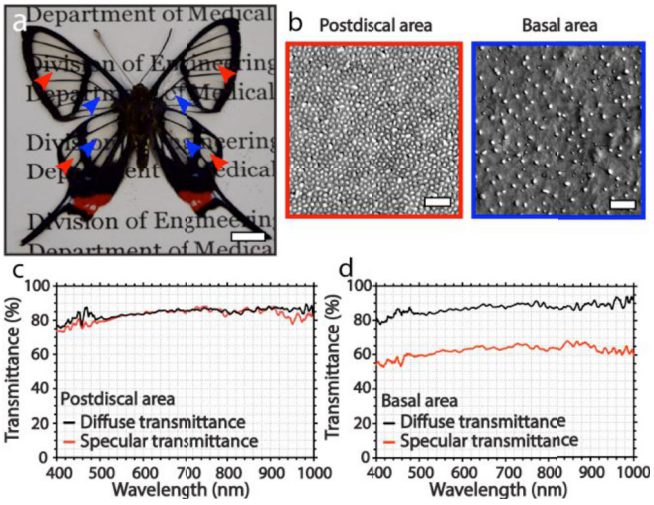

Figure 1: (a) C. faunus butterfly. Postdiscal and basal areas indicated with red and blue arrows, respectively. Scale: 1 cm. (b) SEM images reveal the difference in structural periodicity between the postdiscal and basal areas. Scale: 1 µm. Measured diffuse and specular transmittance of (c) the postdiscal and (d) the basal areas.

RESULTS

Multifunctional BINS Fabrication and Characterization

Modeled after the nanostructures observed in the basal areas of the *C. faunus* wings, we developed short-range ordered BINS on a Si_3N_4-membrane using a highly-scalable polymer-phase-separation process involving poly (methyl methacrylate) (PMMA)

978-1-940470-03-0/HH2018/$25©2018TRF
DOI 10.31438/trf.hh2018.7

and polystyrene (PS) in methyl ethyl ketone (MEK) [5]. The polymer template was then transferred to Si_3N_4-membranes through reactive ion etching (RIE). The periodicity of BINS ranged from 385 to 505 nm and had a height of 150 nm as seen in the SEM and AFM characterizations of the surface in Figure 2a and 2b, respectively. Angle-resolved transmission spectroscopy showed that the BINS-integrated membrane closely replicated the transmissive light-scattering property of the nanostructures found in the basal areas of the *C. faunus* wing, and its light transmission was twice more angle-independent than a flat Si_3N_4-membrane (Figure 2c-d).

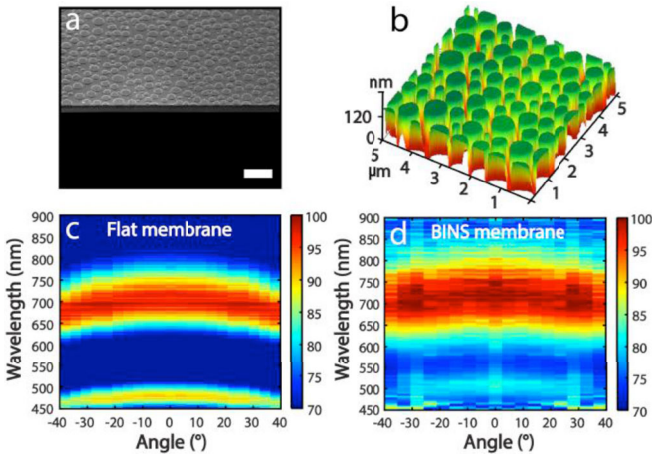

Figure 2: (a) SEM image and (b) AFM image of BINS-integrated Si_3N_4-membrane. (c) Angle-resolved transmission of flat Si_3N_4-membrane showing 30 nm blue-shift at 40° incident angle. (d) BINS-integrated Si_3N_4-membrane showing only 15 nm shift at 40° incident angle.

BINS *In Vitro* Biophysical Properties

The adhesion of representative proteins (albumin and streptavidin), prokaryotes (*E. coli*) and eukaryotes (HeLa cells) on the BINS-integrated Si_3N_4 surface was compared with that on flat Si_3N_4 and control (glass) surfaces in *in vitro* testing. Due to the surface nanostructuring, the BINS-integrated Si_3N_4 surface displays strong hydrophilicity (contact angle: <20°) compared to the flat Si_3N_4 surface which is moderately hydrophilic (contact angle: 35–40°). Due to increased adsorption of proteins, moderately hydrophilic surfaces such as flat Si_3N_4 strongly promote cellular adhesion when compared to strongly hydrophilic surfaces [6]. Additionally, the presence of BINS on the Si_3N_4 surface leads to a reduction in cellular-adhesion points on the surface [7]. As a result, the BINS-integrated Si_3N_4 surface displayed anti-biofouling properties through anti-adhesion against proteins (albumin and streptavidin, ***$P \leq 0.001$), prokaryotes (*E. coli*, **$P \leq 0.01$), and eukaryotes (HeLa cells, ***$P \leq 0.001$) when compared to flat Si_3N_4 and control (glass) surfaces (Figure 3).

BINS-Integrated IOP Sensor *In Vivo* Performance

We used the BINS-integrated Si_3N_4-membrane as a sensing element of a recently developed optical resonance-based IOP sensor (Figure 4a). The resonance of a Fabry-Perot (FP) cavity changes as a function of ambient pressure due to the deflection of the Si_3N_4-membrane (Figure 4b). While the IOP sensor with a flat Si_3N_4-membrane successfully demonstrated *in vivo* IOP monitoring in lab environments [8, 9], but its practical applications were limited by its narrow readout angle inherent to FP-resonators and infrequent but severe biofouling observed after long-term implantation. The BINS integration onto the IOP sensor led to a 2.5-fold improvement in readout angle, or up to 30°, over an IOP sensor without BINS in benchtop testing (Figure 4c). In a one-month *in vivo* study conducted in New Zealand white rabbits (Figure 4d), the BINS-integrated IOP sensor showed a 10-fold and 3-fold reduction in IOP error when compared to conventional rebound tonometry and an IOP sensor without BINS, respectively (Figure 4e).

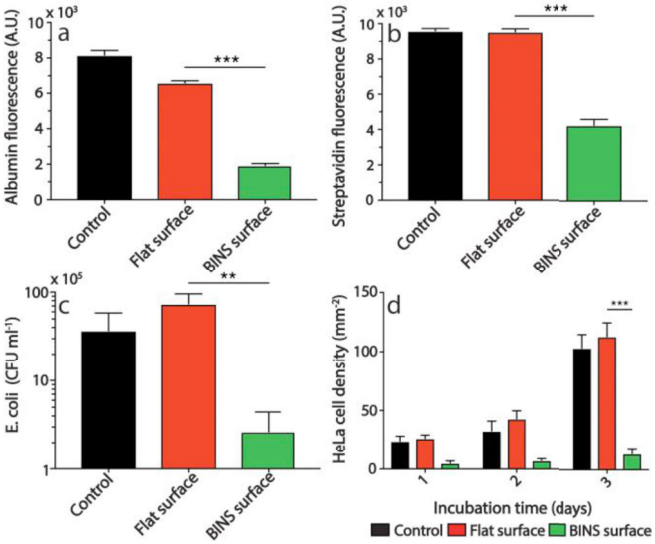

Figure 3: (a) 3-fold reduction of albumin adhesion and (b) 2-fold reduction of streptavidin adhesion on BINS-integrated Si_3N_4 surface over flat Si_3N_4 surface. (c) Significant reduction of E. coli adhesion on BINS-integrated Si_3N_4 surface after 4 hours. (d) 7-fold reduction of HeLa cell adhesion after 72 hours on BINS-integrated Si_3N_4 surface.

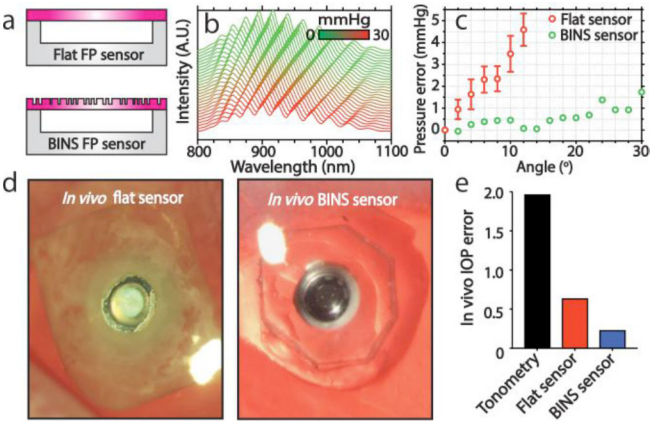

Figure 4: (a) A schematic of a FP-resonator-based IOP sensor with a flat and BINS-integrated opto-mechanical Si_3N_4-membranes that serve as a sensing element. (b) Pressure vs resonance spectra of IOP sensor: a change in the ambient pressure induces a shift in optical resonance of the FP resonator, which is detected remotely using reflected light. (c) Pressure variation of the flat and BINS-integrated IOP sensor as a function of increasing incident angle, measured at 1 atm: The flat sensor shows an IOP error of 4.5 mmHg at 12° while the BINS-integrated sensor shows an IOP error of 1.75 mmHg at 30°, displaying significant improvement in angle independence. (d) Images of the implanted flat and BINS-integrated sensors during the in vivo study: the flat sensor looks

hazy due to tissue build-up. (e) The BINS-integrated sensor displays 10-fold and 3-fold improvement in in vivo IOP-measurement errors compared to traditional tonometry and the flat sensor, respectively.

BINS-Integrated IOP Sensor *In Vivo* Biocompatibility

The IOP sensors with and without BINS integration were harvested from the rabbit eyes after 1 month to evaluate *in vivo* biocompatibility. We used confocal immunofluorescence microscopy to assess the extent of tissue growth over the surface of the two sensors at the time of retrieval. The sensors were stained with DAPI (nucleus marker), Phalloidin (F-actin marker) and MMP-2 (MMP-2 marker). DAPI was used to localize cells in adherent tissue while Phalloidin and MMP-2 were used as indicators for cellular health and inflammation, respectively. Figure 5 shows the images of the two sensors obtained using 3-channel z-stack confocal microscopy. The BINS-integrated IOP sensor (Figure 5a) displayed a 12-fold reduction in surface area covered by adherent tissue when compared to the IOP sensor without BINS (Figure 5b).

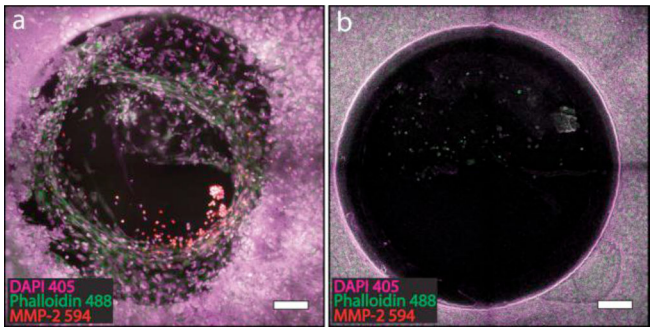

Figure 5: 3-channel z-stack confocal-microscopy images of (a) the IOP sensor without BINS and (b) IOP sensor with BINS, harvested after 1-month in vivo study: DAPI 405 (nucleus, in magenta), Phalloidin 488 (F-actin, in green) and MMP-2 594 (MMP-2, in red) markers were used.

CONCLUSIONS

In this work, inspired by the multifunctional basal nanostructures of the *C. faunus* butterfly wing, we develop BINS on a freestanding Si_3N_4-membrane. The BINS-integrated Si_3N_4-membrane was twice more angle independent than a flat Si_3N_4-membrane. Furthermore, the BINS-integrated Si_3N_4 surface displayed strong hydrophilicity that repelled the adhesion of proteins, prokaryotes and eukaryotes *in vitro*. The BINS-integrated Si_3N_4-membrane was then used as the sensing element on a highly-miniaturized IOP sensor implant. The BINS integration onto the IOP sensor lead to a 2.5-fold improvement in readout angle from 12^o to 30^o on benchtop. In a 1-month in vivo study, the BINS-integrated IOP sensor lowered the *in vivo* IOP error by 10-fold and 3-fold when compared to rebound tonometry and an IOP sensor without BINS, respectively. Finally, the BINS-integrated IOP sensor displayed enhanced *in vivo* biocompatibility through a 12-fold reduction in surface area covered by tissue after a 1-month implantation. With these highly promising results, we envision greater usage for the multifunctional bioinspired nanostructures in medical implant applications.

ACKNOWLEDGEMENTS

The work was funded by the National Institute of Health (NIH) research grant EY024582 to H.C. & D.S., a HMRI Investigator Award, Caltech CI2 program, Powell Foundation Award to H.C., and a Research To Prevent Blindness Innovation Award to D.S. Imaging was performed in the Biological Imaging Facility, with the support of the Caltech Beckman Institute and the Arnold and Mabel Beckman Foundation. We acknowledge support from the Beckman Institute of the California Institute of Technology to the Molecular Materials Research Center.

REFERENCES

[1] Y.-H. Joung, "Development of Implantable Medical Devices: From an Engineering Perspective", International Neurology Journal, 17, 98 (2013).

[2] A. Canales, X. Jia, U. P. Froriep, R. A. Koppes, C. M. Tringides, J. Selvidge, C. Lu, C. Hou, L. Wei, Y. Fink and P. Anikeeva, "Multifunctional Fibers for Simultaneous Optical, Electrical and Chemical Interrogation of Neural Circuits In Vivo", Nature Biotechnology, 32, 1134 (2015).

[3] R. H. Siddique, G. Gomard, and H. Hölscher, "The Role of Random Nanostructures for the Omnidirectional Anti-Reflection Properties of the Glasswing Butterfly", Nature Communications, 6, 6909 (2015).

[4] E. P. Ivanova, J. Hasan, H. K. Webb, V. K. Truong, G. S. Watson, J. A. Watson, V. A. Baulin, S. Pogodin, J. Y. Wang, M. J. Tobin, C. Löbbe, and R. J. Crawford, "Mechanical Rupture of Pseudomonas aeruginosa Cells by Cicada Wings", Small, 8, 2489 (2012).

[5] R. H. Siddique, Y. J. Donie, G. Gomard, S. Yalamanchili, T. Merdzhanova, U. Lemmer, and H. Hölscher, "Bioinspired Phase-Separated Disordered Nanostructures for Thin Photovoltaic Absorbers", Science Advances, 3, e1700232 (2017).

[6] J. H. Lee, S. J. Lee, G. Khang, and H. B. Lee, "The Effect of Fluid Shear Stress on Endothelial Cell Adhesiveness to Polymer Surfaces with Wettability Gradient", Journal of Colloid and Interface Science, 230, 84 (2000).

[7] M. Arnold, E. A. Cavalcanti-Adam, R. Glass, J. Blümmel, W. Eck, M. Kantlehner, H. Kessler, and J. P. Sptaz, "Activation of Integrin Function by Nanopatterned Adhesive Interfaces", Chemphyschem, 5, 383 (2004).

[8] J. O. Lee, H. Park, O. Chen, A. Balakrishna, J. Du, D. W. Sretavan, and H. Choo, "A Microscale Optical Implant for Continuous In Vivo Monitoring of Intraocular Pressure", Microsystems & Nanoengineering, 3, 17057 (2017).

[9] J.O. Lee, V. Narasimhan, J. Du, B. Ndjamen, D. Sretavan, and H. Choo, "Biocompatible Multifunctional Black-Silicon for Implantable Intraocular Sensor", Advanced Healthcare Materials, 6, 1 (2017).

CONTACT

*H. Choo, tel: +1-626-395-8774; hchoo@caltech.edu

TOWARDS INDUSTRIALISATION OF MICROFLUIDIC SAMPLE-TO-ANSWER SOLUTIONS ENABLING POINT-OF-USE TESTING OF BIOSAMPLES: A DESIGN-FOR-MANUFACTURE LED PLATFORM APPROACH

Jens Ducrée
FPC@DCU – Fraunhofer Project Centre for Embedded Bioanalytical Systems at
Dublin City University, Ireland

ABSTRACT

The commercial development of many microfluidics-enabled commercial devices requires rapid, optimization and cost-efficient development of competitively priced, and still very rugged, mostly single-use devices. A key challenge remains the seamless scale-up of manufacture from laborious prototyping techniques based on low-throughput machinery and frequently expensive materials to pilot series and industrializable (polymer) mass replication, (bio-)functionalization and assembly schemes. Furthermore, the time-scales and budgets involved from idea to product are often hard to accept for investors, in particular when considering that many microfluidics-based products will, at least initially, be restricted to comparatively small niche markets or rather tiny fractions of larger markets; hence, economy-of-scale effects are difficult to reach for recovering (sunk) for research and technology development as well as set up of manufacture.

This paper presents a platform approach adopted from many mature industries like automotive or microelectronics for assuring cost-efficient, significantly expedited development of process integrated and automated, microfluidics-enabled solutions at high technology readiness levels (TRLs) with typical application in decentralised "point-of-use" handling and testing of biosamples. Key paradigms supporting this platform approach towards industrialization of microfluidics-enabled solutions are design-for-manufacture (DfM) for seamless scale-up from prototyping to production, quality-by-design (QbD) for robust operation and readiness for scale-up (RfS) towards mass fabrication.

INTRODUCTION

Type of Systems and Industrial Challenge

Since their inception in the 1980s, microfluidic systems have continuously expanded their space of applications as well as underlying liquid handling and manufacturing technologies [1][2][3][4][5][6][7][8][9][10][11]. A huge variety of solutions has been developed, frequently in the context of the life sciences. This paper focusses on process integrated microfluidic systems that are typically used for comprehensive automation of sample preparation and detection, for instance, in the context of sample handling, preconditioning and / or detection at the point of use. Recent business analysis unanimously confirms that such decentralised solutions constitute a significant fraction of the multi-billion-dollar market for microfluidics-enabled products which is forecast to grow by solid, double-digit figures for the near-to-midterm future [13].

The successful commercialization of such microfluidic components are typically characterised by a set of techno-economical requirements that are common in industrial environments: competitive pricing and performance paired with user-friendliness, reliability during storage, shipping and use as well as seamless immersion with established work flows, technical standards and data management. Depending on the application, and particularly in the arena of medical applications, regulatory compliance presents a major roadblock for successful market introduction.

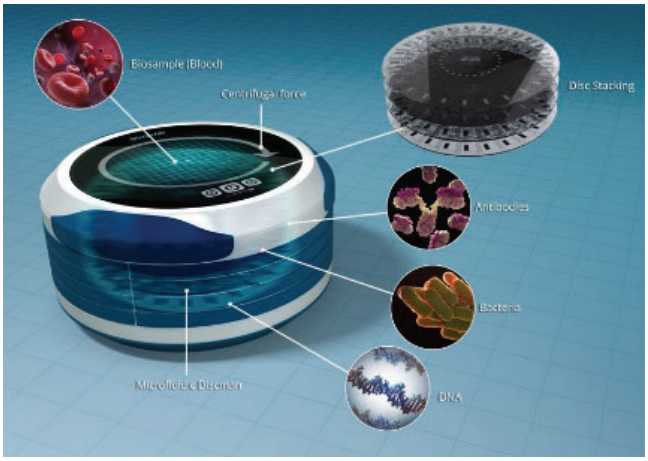

Figure 1: Artist's impression of centrifugal microfluidic "Lab-on-a-Disc" platform; a compact and universal instrument containing a spindle motor and detection units can "play" different disc-shaped polymeric microstructures representing different bioanalytical tests.

Strategies Adopted from Industry and Nature

Over the last two centuries, industrialization has seen a refinement of its strategies how rather complex technical products like automobiles or computers that were initially exclusive to large corporations and exquisite clientele can be introduced into broader consumer markets. A key enabler of this remarkable transition is tapping into economy-of-scale effects which allows distribution of large investments into the development of product and its production technology such as billion-dollar automotive or semiconductor plants and related marketing budgets over a large number of products sold to consumers. A well-proven recipe for this stage of industrialization is mass customisation based on platform-based approaches.

A key aspect of the second industrial revolution about a century ago was the progression from individual hand-crafting of products from start-to-finish by a small cohort of multi-skill experts to streamlining the underlying technical platform and production processes. In addition to eventually treading the path towards cost-efficient, high-quality mass manufacturing, this important step was also instrumental towards establishing complex supply chains for components as well as related fabrication equipment and services.

Henry Ford's conveyor-belt factories were a key element of the second industrial revolution where the semi-finished assembly progressively moves through a series of specialised workstations that can be operated by lower-skilled staff. In the third stage, robotics are increasingly replaced by robotic automation. While individual design of derived products was very restricted at the time, a huge repertoire of products can be derived from the same platform, e.g. for chassis or engines in cars, or consumer electronics.

978-1-940470-03-0/HH2018/$25©2018TRF
DOI 10.31438/trf.hh2018.8

Notably also nature has chosen to strictly adhere to common blue prints; with some variations and extensions of the theme, nucleic acids store genetic information encoding functional proteins and cells constitute the basic building blocks of higher-level organisms. Amongst animals, quadrupeds possess a basic plot featuring a head containing the brain with two eyes and a central nose above a mouth, linked by a neck to a torso with four extremities. There are of course many more examples of "platforms" or blueprints in biology and industry.

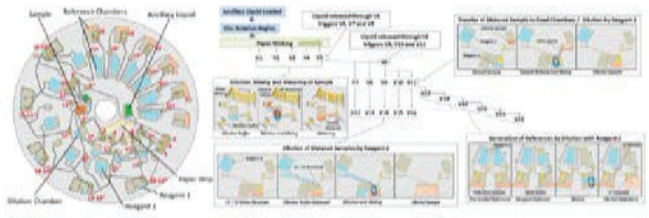

Figure 2: Example for high-level process integration enabled by logical, event-triggered centrifugo-pneumatic flow control on a Lab-on-a-Disc (LoaD) platform. (adopted from [19])

Platform Concept for Industrialization of Microfluidics

Taking such instructive lessons from mature industries and nature into account, we were looking for a common microfluidic platform that can be customized for automating common liquid handling protocols at the backend of a huge variety of bioanalytical methods at the point-of-use. The main types of these laboratory protocols enable general chemistry, immunoassays and nucleic acid testing as well as cell, bacteria and other bioparticle counting / analysis; our internal market research indeed confirmed a wide range of commercially promising applications in the space of biomedical point-of-care / global diagnostics, liquid handling automation for the life sciences, process analytical techniques and cell line development for biopharma as well as decentralised monitoring the environment, infrastructure, industrial processes and agrifood.

Due to their conceptually simple instrumentation based on a commodity spindle motor without (physical) fluidic interfaces to the typically single-use polymer liquid handling device and the availability of a wide repertoire of robust flow control and sample preparation techniques, we chose the centrifugal microfluidic platform.

While such "Lab-on-a-Disc" (LoaD) systems [7][8][9][10][11][12][14][15][16][17] have been one of the earliest (and still existing) instances of commercially available microfluidic "point-of-care" products, some of them even dating back to market entry in the mid-1990s [1][4], its platform capability has been highlighted only more recently [6].

The recently founded FPC@DCU [18] – the Fraunhofer Project Centre for Embedded Bioanalytical Systems at Dublin City University in Ireland - implements wholistic design-for-manufacture (DfM) and quality-by-design (QbD) paradigms to facilitate rapid and cost-efficient development of high-technology-readiness (TRL) solutions for industry.

STREAMLINED PLATFORM APPROACH

Centrifugal Liquid Handling

Testing and handling of biosamples involves a sequence a laboratory unit operations (LUOs) such as sample preparation, reagent addition and mixing / incubation steps. For process automation on microfluidic systems, such protocols are spatio-temporally orchestrated by a sequence of flow control elements such as pumping, valving and routing schemes.

LoaD systems employ the system-innate spindle motor to create a (radial) centrifugal field; due to its strong, square-type scaling, the force field can be modulated over several orders of magnitude by the spin frequency. The rotationally induced artificial gravity conditions also depend on the density of the liquid; this means that handling of (homogeneous) aqueous solutions is quite independent of the given sample and reagents.

Yet, buoyancy effects may be used for stacking layer of (immiscible) media or separating suspended particles possessing specific densities diverging from unity (water). This way often parasitic gas bubbles are suppressed of quickly eliminated from the system. Common batch-wise processing also provides wide independence of flow properties like viscosity which tends to significantly vary in biological samples, thus making the LoaD technology rather robust.

However, the ubiquitous nature of the centrifugal field requires valving schemes to independently control the motion of individual liquid volumes such as sample and multiple reagents that are simultaneously residing on the rotating disc in space and time.

Due to the conceptual difficulty of contact-based interaction from an instrument-based actuation module with a (fast) rotating disc, flow control has often been implemented by variation of the spin rate: high- and low-pass valves open upon transient elevation or reduction of the spin rate, respectively. In the initial state of these typically single-use, normally-closed valves, upstream liquid volumes are held back by counteracting mechanisms such as capillary action, siphoning, sacrificial barriers or opposing pressure differentials, for instance induced by (centrifugal) compression of enclosed gas pockets.

In FPC@DCU, we opted for a new type of centrifugo-pneumatic valving [12][19] based on dissolvable films (DFs) for gating the flow between structures representing LUOs such as metering and mixing that have been developed for performing various tasks in sample preparation.

Platform Approach with Parameterized Elements

Within the platform approach, integrated microfluidic systems are composed from a library containing functional elements for flow control and LUOs for manipulation of liquid samples. These elements are geometrically parametrized, i.e., they can be flexibly adjusted, within a given range, to requirements like volume capacity, shape or their location on the disc.

Design-for-Manufacture for Seamless Scale-Up

The functionality of microfluidic systems is tightly linked to the underlying manufacturing schemes. Issues frequently arise from artefacts intrinsic to the specific fabrication and assembly scheme, and even more when switching manufacturing schemes for the same structure during scale-up from prototyping to small series, e.g., for in-field testing, and mass production.

To mitigate the associated development risks, FPC@DCU implements a design-for-manufacture (DfM) paradigm tackling the issue from two sides; manufacturing tolerances which are likely to impact fluidic functionality are thoroughly qualified and minimized by process optimization. In addition, fluidic elements are designed as forgiving as possible for (unavoidable) statistical deviations in manufacturing processes as well as properties of structural (solid) materials, surfaces and liquids.

Virtual Prototyping for Efficient Development

FPC@DCU's platform approach is supported by fluidic simulation following a strategy that has been termed in other contexts as virtual prototyping or the creation of a digital twin. For the complex, multi-step, multi-phase and multi-branched systems considered here, a full system-level computational fluidic dynamic si-

mulation is often not practical. However, we can make use of the fact that the overwhelming majority of centrifugal microfluidic systems operate in a batch-wise fashion where the individual stages between sample preparation and detection are interspersed by valves and thus hydrodynamically widely decoupled from each other.

This approximate hydrodynamic isolation allows to decompose the network into individual functional units which, in a first step, can be modelled and simulated separately. Transfer functions equivalent to resistors, capacitances, inductances and diodes in electric circuits may be defined, either through analytical formulas or from numerical solutions and their fits. In a lumped-element approach, these separate elements are then linked to create the fluidic networks for automating full assay protocols while massively reducing the numerical complexity and computational requirements for simulation.

On the one hand, such virtual "*in silico*" prototyping and testing of individual elements may reveal fundamental working principles, thus helping to identify critical parameters and the impact of deviations in geometrical structure and liquid (input) volumes. On the other hand, the "lumped-element" modelling also allows to flexibly configure networks enabling new applications from a set of validated, well-understood library elements, thus significantly expediting and de-risking the development of novel, high-technology-readiness-level (TRL) applications.

Quality-by-Design for Robust Functionality

The library of functional fluidic elements is characterized by several (quantitative) figures of merit which, for instance, comprise of the geometry-dependent range and standard deviation for centrifugal burst frequencies, actuation / response times and transferred volumes.

Towards microfluidic system integration needed for multi-step sample preparation, error propagation has a tremendous impact on final results, e.g., on the definition of (preconditioned) sample and reagent volumes to be mixed prior to a final detection step. As a specific feature of centrifugal microfluidic systems, also the overall functionality of liquid handling is impacted by the accuracy of volume definition in the preceding steps. This is because the centrifugally induced field translates, via the mean radial position and extension of the liquid "plug", into the (hydrostatic) pressure governing the transport of the liquid.

Consequently, any volume inaccuracies inflicted in an upstream liquid handling step influence the hydrodynamic behavior of succeeding operations, possibly even leading to malfunction on a system level. Such volume errors might be attributed to the initial loading of the disc by pipetting as well as manufacturing tolerances affecting channel cross sections and thus modulating the radial location and extensions of residual liquid plugs which set the centrifugal force.

FPC@DCU's Quality-by-Design (QbD) strategy pursues a two-pronged approach to increase the robustness of operation. On the one hand, the precision of manufacturing processes is optimized to minimize geometrical deviation in all stages of development from prototyping to mass manufacture (see above). On the other hand, simulation coupled with experimental validation allows to design fluidic elements with maximum tolerance to fluctuations in incoming liquid volumes.

CONCLUSIONS & OUTLOOK

This paper has described a path how to accelerate and de-risk research and technology development of microfluidics-enabled solutions delivering decentralised testing of biosamples engineered for point-of-use applications in the context of the life-sciences. High TRLs will be accomplished by a combination of strategies: a streamlined platform approach based on a library of validated, geometrically parametrized fluidic modules to enable flexible configuration of new networks, design-for-manufacture leveraging quasi seamless scale-up towards mass fabrication, virtual prototyping / digital twin to accelerate functional optimization and quality-by-design to assure error tolerance at the system level.

All these principles are advanced in FPC@DCU and its partner, the Fraunhofer Institute for Production Technology, to offer a viable path towards successful contract development of microfluidics-enabled devices for biomedical point-of-care / global diagnostics, liquid handling automation for the life sciences, process analytical techniques and cell line development for biopharma as well as decentralised monitoring the environment, infrastructure, industrial processes and agrifood.

ACKNOWLEDGEMENTS

This publication has emanated from research conducted with the financial support of Science Foundation Ireland (SFI) and Fraunhofer-Gesellschaft under the SFI Strategic Partnership Programme, Grant Number 16/SPP/3321.

REFERENCES

[1] C. T. Schembri, V. Ostoich, P. J. Lingane, T. L. Burd and S. N. Buhl, Clin. Chem., 38, 1665–70 (1992).

[2] M. J. Madou M J and G. J. Kellogg, Proc. SPIE 3259 80–93 (1998).

[3] M. Madou, J. Zoval, G. Jia, H. Kido, J. Kim and N. Kim, Annu. Rev. Biomed. Eng., 8 601–28 (2006).

[4] M. Gustafsson, D. Hirschberg, C. Palmberg, H. Jörnvall and T. Bergman, Anal. Chem. 76 345–350 (2004).

[5] M. Inganäs, H. Dérand, A. Eckersten, G. Ekstrand, A.-K. Honerud, G. Jesson, G. Thorsén G, T. Söderman and P. Andersson, Clin. Chem., 51 1985–7 (2005).

[6] Jens Ducrée and Roland Zengerle. FlowMap – Microfluidics roadmap for the life sciences. Books on Demand GmbH, Norderstedt, Germany (2004).

[7] J. Ducrée, S. Haeberle, S. Lutz, S. Pausch, F. von Stetten, R. Zengerle, J. Micromech. Microeng., 17, S103–S115 (2007).

[8] D. Mark, S. Haeberle, G. Roth, F. von Stetten and R. Zengerle, Chem. Soc. Rev., 39, 1153–1182 (2010).

[9] O. Strohmeier, M. Keller, F. Schwemmer, S. Zehnle, D. Mark, F. von Stetten, R. Zengerle, N. Paust, Chem. Soc. Rev. 44, 6187–6229 (2015).

[10] M.C.R. Kong, E.D. Salin, Anal. Chem., 84(22): 10038–10043 (2012).

[11] S. Smith *et al*., Micromachines, 7(2), pp. 22 (2016).

[12] R. Gorkin, C.E. Nwankire, J. Gaughran, X. Zhang, G.G. Donohoe, M. Rook, et al., Centrifugo-pneumatic valving utilizing dissolvable films, Lab Chip, 12 2894-902 (2012).

[13] Yole Développement, Status of the Microfluidics Industry (2017).

[14] Beom Seok Lee, Yang Ui Lee, Han-Sang Kim, Tae-Hyeong Kim, Jiwoon Park, Jeong-Gun Lee, Jintae Kim, Hanshin Kim, Wee Gyo Lee, Yoon-Kyoung Cho, Lab Chip 11(1), 70-78 (2011).

[15] Liviu Clime, Daniel Brassard, Matthias Geissler and Teodor Veres, Lab Chip, 15, 2400-2411 (2015).

[16] Brandon L. Thompson, Christopher Birch, Daniel A. Nelson, Jingyi Li, Jacquelyn A. DuVall, Delphine Le Roux, An-Chi Tsuei, Daniel L. Mills, Brian E. Root and James P. Landers, Lab Chip, 16, 4569-4580 (2016).

[17] D. J. Kinahan, S. M. Kearney, N. Dimov, M. T. Glynn, J.

Ducrée, Lab Chip, 14, 2249-58 (2014).
[18] FPC@DCU - Fraunhofer Project Centre for Embedded Bioanalytical Systems at Dublin City University, Ireland, www.dcu.ie/fpc.
[19] David Kinahan, Sinéad Kearney, Olivier Faneuil, Macdara Glynn, and Jens Ducrée. RSC Advances, 5(3):1818–1826 (2015).

CONTACT

* Jens Ducrée, tel: +353-1-700-7658; jens.ducree@dcu.ie

PRECISION HIGH-BANDWIDTH OUT-OF-PLANE ACCELEROMETER AS CONTACT MICROPHONE FOR BODY-WORN AUSCULTATION DEVICES

Pranav Gupta[*], *Yaesuk Jeong, Jaehoo Choi, Mark Faingold, Anosh Daruwalla, and Farrokh Ayazi*
Georgia Institute of Technology, Atlanta, Georgia, USA

ABSTRACT

This paper reports on the implementation and characterization of wafer-level-packaged accelerometer contact microphones having wide bandwidth (f_{res} >10 kHz) and low-noise (<100 μg√Hz) for use as auscultation devices in body-worn sensor arrays. By using wide bandwidth capacitive accelerometers as contact microphones, the encapsulated sensor can detect not only internal sounds from organs but also body motions down to DC frequency levels, significantly reducing sensor size and fabrication cost of wearable technology for health monitoring. The out-of-plane micro-g accelerometers use nano-gap transducers (270 nm) for enhanced signal-to-noise ratio in a high resonant frequency microstructure with small form-factor. Fabricated devices were interfaced with off-the-shelf readout circuits and their performance was compared to commercially available piezoelectric contact microphones. Normal breath sounds in the range of 600-1000Hz along with phonocardiogram (PCG) and ballistocardiogram (BCG) signals are extracted by mounting the device on the chest.

INTRODUCTION

Cardiovascular and cardiopulmonary diseases are considered the leading cause of mortality globally. The interdependency of cardiac and pulmonary health [1] makes continuous monitoring of cardiopulmonary parameters essential for an accurate and timely diagnosis. The use of an auscultation device such as a stethoscope is considered as the first step in clinical evaluation of cardiovascular conditions and a very powerful tool available to physicians.

There is a growing demand for high performance electronic auscultation devices due to their ability to augment traditional clinical equipment for instance, by allowing the physicians to remotely diagnose and track patient health post-treatment. Capturing body motion coupled with the auscultation data can allow physicians to correlate cardiopulmonary sounds to daily activities. Additionally, monitoring the timing of abnormal breath sounds with respect to respiratory cycle is of great interest to doctors for accurate diagnosis [2].

Typical electronic stethoscopes use membrane-type microphones which operate by generating an electrical response to pressure changes in air caused by sound waves. This technique is susceptible to environmental noise and may suffer due to insufficient acoustic energy transfer. The piezoelectric-type stethoscope produces electrical signals due to distortion of a piezo-crystal coupled to the stethoscope diaphragm. Again, due to distortion, this technique does not accurately capture the sound and resultant output may differ from the original tone [3]. Moreover, performance of such microphones is limited by their size [4], and are unable to capture low frequency signals such as respiratory rate and body motion.

A novel approach to tackle these challenges is a capacitive accelerometer contact microphone. A micro-g accelerometer with large bandwidth (f_{res} >10 kHz) and low noise (<100 μg√Hz) out-of-plane sensitivity is essentially a contact microphone. By having a high resonant frequency, the accelerometer can pick up μg-level accelerations produced by acoustically vibrating structures. Such a microphone is not sensitive to air-borne acoustic emissions; only sensitive to vibrations from its contact surface. Its small size allows it to replace bulky stethoscopes with ergonomic wearable auscultation systems that can precisely measure cardiopulmonary sounds, chest wall motion, ballistocardiogram (BCG) signal as well as body motion of the user simultaneously. This opens new gateways in telemedicine and remote health monitoring. Moreover, such an integrated solution significantly reduces fabrication cost of wearable technology, making it more accessible and affordable to the masses.

In this paper, a low noise, wide bandwidth out-of-plane accelerometer with nano-gaps (270nm) capacitive electrodes implemented using HARPSS+ process [5] is fabricated and characterized as a contact microphone. The performance of the accelerometer contact microphone (ACM) is compared with a commercial piezoelectric contact microphone. Further, the paper addresses the use of this contact microphone as a body-worn auscultation device by mounting it on the chest and recording sounds produced in the thoracic cavity. The recorded signals are filtered and processed to extract the heart sound and BCG signal from the recorded data. Similarly, lung sound and chest wall motion are extracted using data processing techniques, demonstrating the possibility of accurately capturing multiple types of acoustic and vibrational data from the body at the same time.

ACCELEROMETER CONTACT MICROPHONE

It is useful to express vibration in terms of acceleration, rather than velocity or displacement, due to availability of a wide range of low-cost accelerometers. To capture high quality audio signal using an accelerometer as a contact microphone, small MEMS accelerometers with wide operational bandwidth and micro-g resolution are needed.

Considering use of an encapsulated accelerometer as a contact microphone, there is an absence of a through-hole to generate any acoustic pressure on the MEMS device. The acoustic vibrations are therefore expressed in units as 'Vibration Acceleration Level (VAL)' rather than 'Sound Pressure Level (SPL)', which is given by equation (1), where a_{ref} corresponds to a reference acceleration, typically 1 μg (9.8 μm/sec^2) [6].

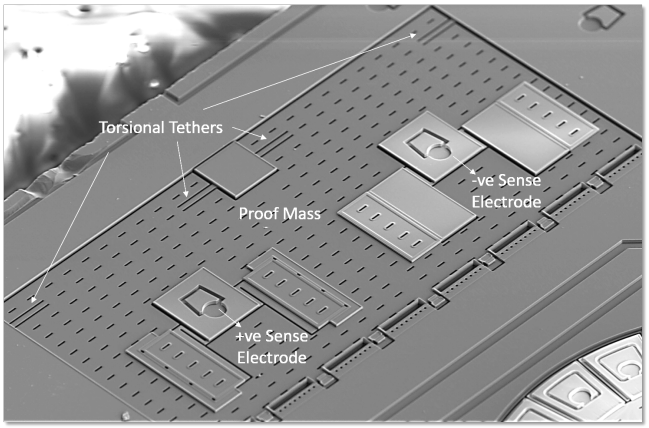

Figure 1: SEM view of the accelerometer contact microphone

978-1-940470-03-0/HH2018/$25©2018TRF
DOI 10.31438/trf.hh2018.9

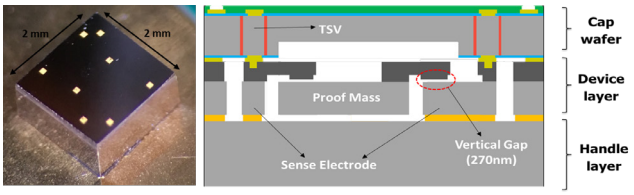

Figure 2: The wafer-level-packaged ACM die (left) and its cross-sectional schematic showing differential capacitive sensing scheme.

$$L_a = 10\log\left[\left(\frac{a}{a_{ref}}\right)^2\right] \quad dB \qquad (1)$$

The sensitivity of a microphone is defined as the ratio of the electrical output of the device to a given standard acoustic input. Typical acoustic microphones use a 1 kHz sinusoidal signal at 94 dB SPL (equivalent to 1 Pa pressure) as the standard pressure input [7] for characterization. Analogous to pressure input, the sensitivity of the contact microphone can be characterized by measuring the electrical response to a standard vibration input of a 1 kHz sinusoidal signal at 120 dB VAL (equivalent to 1 g acceleration).

Design and Fabrication

A torsional cantilever topology [8] is chosen to implement the micro-g accelerometer, wherein the proof mass is supported by torsional tethers at one end. When acceleration is applied in out-of-plane direction, generated torque will rotate the proof-mass, changing the capacitance between sense electrode. To maintain a small form factor, the sense electrodes are placed within the proof mass, and a differential top electrode configuration is employed to suppress common mode noises. The device is fabricated using the HARPSS+ process on an SOI (Silicon-on-Insulator) wafer having 40µm thick device layer with ~270nm capacitive gaps [5, 9] . After the releasing process, completed wafer is then wafer-level packaged using eutectic bonding to a silicon capping wafer with built-in through-silicon-vias (TSV). Fig. 1 shows the SEM of the uncapped ACM device and Fig. 2 shows the wafer level packaged die and the device cross section.

MEASUREMENT RESULTS

Interface Electronics

The microphone is interfaced with MS3110 [10], a commercially available off-the-shelf capacitive readout circuit. A miniature PCB (0.8 inch × 0.8 inch) is designed to accommodate the sensor and interface circuit by utilizing the front and back side of the board to mount the MEMS device and interface IC. The MEMS die is covered using Dow 7920 adhesive to protect the bond wires from accidental damage as shown in Fig. 3.

Device Characterization

To measure sensitivity, the evaluation board is mounted on the shaker table and a sinusoidal 1 g acceleration is applied at 1 kHz frequency. Dynamic Signal Analyzer 35760A is used to precisely measure the scale factor, showing 72.6 mV/g (-22.76 dB relative to 1V/g) as plotted in Fig. 4. The resonant frequency of the device was measured by placing uncapped device into the vacuum chamber and exciting electrostatically using network analyzer E5061B. Fig. 4 shows the measured resonant frequency of 12.5 kHz, confirming high operational bandwidth.

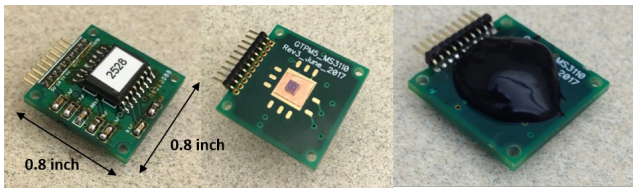

Figure 3: Miniature PCB with MEMS die covered in epoxy.

The Allan deviation (ADEV) plot is extracted by sampling the output at 1 kHz using NI 9220 Data Acquisition (DAQ) card. The measured velocity random walk (VRW) and bias instability (BI) are 85µg/√Hz and 82µg, respectively, as shown in Fig. 4. Due to limited capacitive resolution of the interface circuit, the overall noise of the system is dominated by the electronics. By replacing the MS3110 with a dedicated low-noise ASIC, the overall noise can be lowered to the point where it gets dominated by mechanical noise, which is less than < 20 µg/√Hz. Table 1 provides a summary of the characterization results.

Table 1 Performance Summary

MEMS Device Only	
Sensor dimension	1.6 mm x 0.8 mm
Nano-gap Size	270 nm
F_{res}	12.5 kHz
MEMS Device + Interface IC	
Scale factor	72.6 mV/g (-22.76 dB rel. 1V/g)
VRW	85µg/√Hz
Bias Drift	82µg

ACOUSTIC CHARACTERIZATION

The performance of the ACM is compared with a commercially-available piezoelectric contact microphone (Knowles BU-23173) [11], which is often used as gold standard in acoustic measurements. The form-factor of the MEMS ACM is ~10x smaller than the Knowles BU-23173 microphone.

Audio Reconstruction Test

An audio reconstruction test is performed to validate the functionality of the ACM by mounting alongside the Knowles BU-23173 microphone on a speaker system. A test audio signal is played over the speaker, and the output from the microphones are recorded using NI-9220 DAQ at 8 kHz sampling frequency. Using a

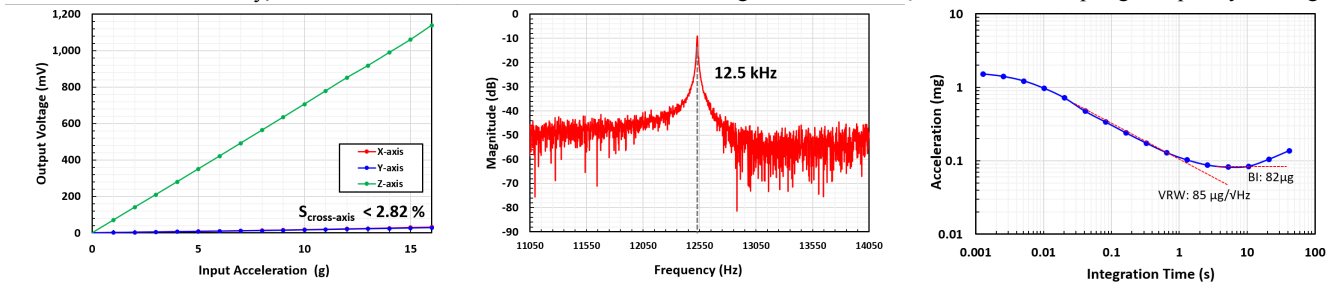

Figure 4: Measured (a) scale-factor, (b) resonant frequency and (c) Allan Deviation for the accelerometer contact microphone

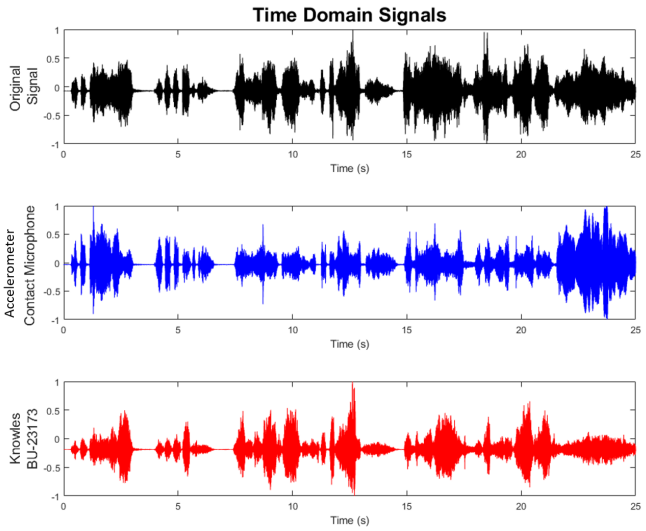

Figure 5: Audio Reconstruction Test showing time domain signals of original and recorded signals

MATLAB program, the captured data is reconstructed into an audio file format for playback. Fig. 5 shows the time domain signals for the original audio clip along with the recorded data. A high degree of similarity is observed between the recorded sounds and original audio clip. High frequency components (>2 kHz) are not picked up by the ACM due to its operation in air. However, on playback, the ACM demonstrates high quality signal specifically at lower frequencies compared to the Knowles microphone which exhibits noticeable distortion. This behavior can be attributed to the ACM's inherent ability to capture high quality signals at low frequencies, including the inaudible range (0-20 Hz), unlike the piezoelectric contact microphones.

BODY-WORN AUSCULTATION DEVICES

Sensor Placement

Several auscultation locations for cardiopulmonary sounds are available in the intercostal spaces (ICS) (i.e. the space between two consecutive ribs) on the chest. Cardiopulmonary sounds, which lie between 20 to 2500 Hz frequency range [12], are recorded by mounting the sensor left of the sternum in the 5th intercostal space, shown in Fig. 6. The PCB is held in place using a chest strap to provide firm contact between the board and skin. Such configuration is essential to pick-up high-fidelity audio signals.

Cardiopulmonary Sound Sensing

The senor board is interfaced with NI-9220 DAQ to collect the data and a MATLAB program is used to filter the recorded signals which can be further stored in audio file format for playback. Unlike piezoelectric microphones, the ACM can measure accelerations

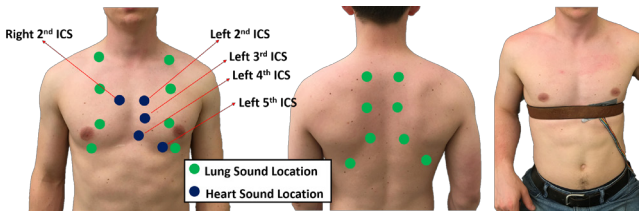

Figure 6: Sensor placement on the body for heart and lung sound acquisition

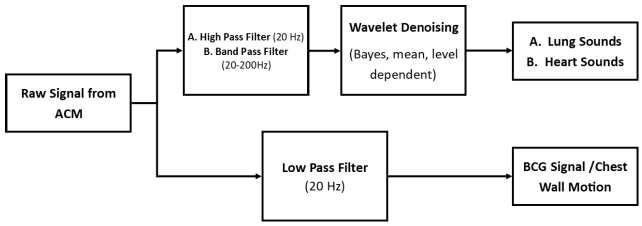

Figure 7: Filtering algorithm for extraction of high frequency sound signal and low frequency motion signal

down to DC level. This attribute is used to obtain additional information such as body motion, heart rate, respiratory rate and even BCG signal. Moreover, using an array of the ACMs can result in high-precision activity detection of the user, thus providing an additional layer of information for correlation of auscultation to daily activities. The higher frequency components (> 20Hz) of the recorded signal correspond to the cardiopulmonary sounds.

The filtering algorithm shown in Fig. 7 is used to separate the low frequency component of chest wall motion and the high frequency component of the sound signal. The filtering is performed using high-order Butterworth filters on the basic criteria of audible (> 20Hz) and inaudible frequencies (< 20Hz). A wavelet denoising technique is used on the high frequency components to reduce noise and extract signal features [13]. The resultant waveforms are shown in Fig. 8, corresponding to extracted cardiopulmonary signals.

There are two major cardiac sounds; S1 and S2, which occur due to closing of the atrioventricular valves (Mitral and Tricuspid) and closing of the semilunar valves (Aortic and Pulmonary), respectively. The period from S1 to S2 is known as Systole, whereas the S2 to S1 period is known as Diastole [14], as shown in Fig. 8. The recorded signal, known as phonocardiogram (PCG), is characterized by a 'lub-dub' sound, and provides a solid foundation for preliminary diagnosis, based on the frequency content and amplitude of the signal, of any cardiac disease.

Another feature captured along with the heart sounds is the ballistocardiogram (BCG) signal, defined as the micro-movements of the body due to shift in center of mass with the pumping of blood at every heartbeat [15]. As this signal lies in the frequency range of 0-20Hz, it is typically captured using a precision micro-g accelerometer. The dual nature of the proposed contact microphone enables the detection of the BCG signal, while measuring cardiac sounds. As shown in Fig. 8, the BCG signal is characterized by the H, I, J, K, L wave, forming a 'W' pattern within the waveform. The importance of capturing this waveform is marked by its unobtrusive nature and ability to detect early onset of several diseases such as acute myocardial disease, asymptotic coronary artery disease and congestive heart failure [16].

Auscultation of the lungs provides vital information regarding their physiology such as obstructions in airway or presence of liquid in the organ. The qualities of breath sounds modify as air passes through the lungs. The pitch and duration of recorded lung sounds differ with respect to location of the senor. The presence of adventitious breath sounds such as crackles or wheezes usually indicate disease [2]. To accurately identify the timing of abnormal breath sounds within a respiratory cycle, the inspiration and expiration can be monitored by tracking the movement of the chest wall. Normal "vesicular" breath sound recorded by our accelerometer contact microphone is shown in Fig. 8.

The ACM demonstrates high-fidelity cardiopulmonary auscultation sensing capability as well as high sensitivity towards motion artifacts. Characteristic features of heart sounds, BCG signal and lung sound are easily detected using the ACM.

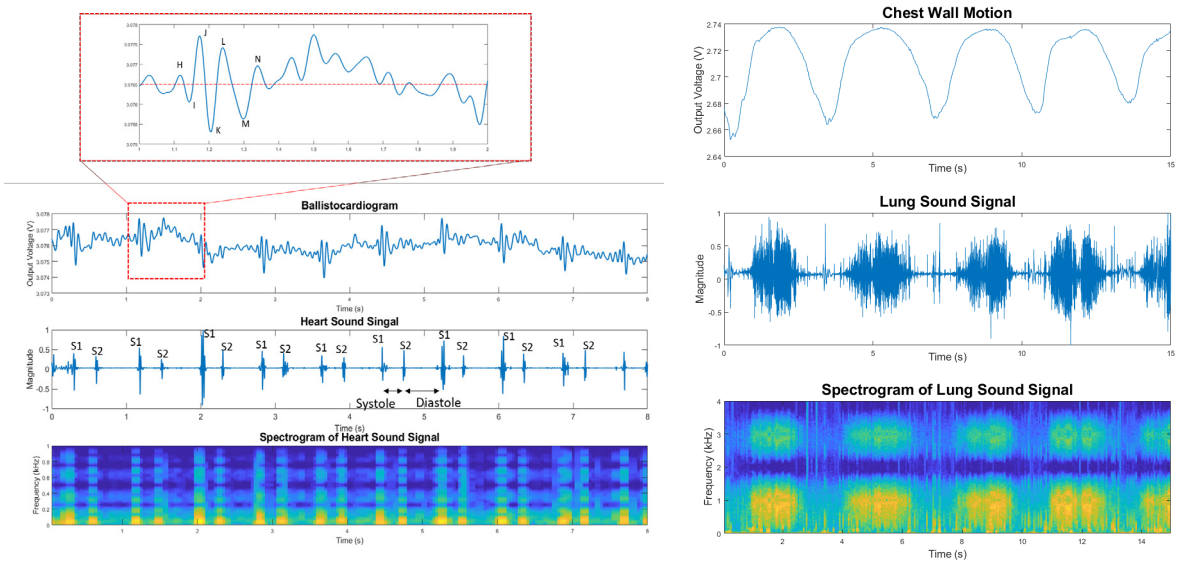

Figure 8: Recorded heart (left) and lung(right) sounds when the subject is sitting idle and breathing heavily respectively. The spectrogram shows the frequency content of the sound signal and its variation with heartbeats and respiratory cycle.

CONCLUSION

The growing demand for remote health monitoring and wearable technologies will necessitate the integration of sensors into smaller form-factor with increased functionality and precision performance. The presented accelerometer contact microphone, whose functionality and feasibility are validated by an audio reconstruction test followed by an on-body auscultation test to capture heart and lung sounds, along with simultaneous recording of BCG signals and chest wall motions, represents as a major step towards this goal. By integrating the functionality of a microphone and an accelerometer in a single MEMS device, the cost of manufacturing wearable devices can be reduced significantly. Using this device, a physician can observe heart and lung sounds remotely with more accuracy and precision than a conventional stethoscope, while having access to low-frequency chest motions and body activities for extracting additional information. Additional degrees of freedom of motion sensing can be added to the same die, e.g. a tri-axial wide-bandwidth micro-g accelerometer can be implemented using the same process platform technology.

ACKNOWLEDGEMENT

This work was supported by a grant from the Georgia Tech Institute for Electronics and Nanotechnology (IEN). The fabrication of the WLP MEMS accelerometers were supported by the DARPA MTO Single-Chip Timing and Inertial Measurement Unit (TIMU) program under contract # N66001-11-C-4176.

REFERENCES

[1] S. Swarup and A. N. Makaryus, "Digital stethoscope: technology update," *Medical Devices (Auckland, N.Z.)*, vol. 11, pp. 29-36,

[2] M. C. Boyars and B. Karnath, "Pulmonary Auscultation," *Hospital Physician*, pp. 22-26, 2002.

[3] S. Leng, R. S. Tan, K. T. C. Chai, C. Wang, D. Ghista, and L. Zhong, "The electronic stethoscope," *BioMedical Engineering OnLine,* vol. 14, p. 66, July 10 2015.

[4] Y. Seo, D. Corona, and N. A. Hall, "On the theoretical maximum achievable signal-to-noise ratio (SNR) of piezoelectric microphones," *Sensors and Actuators A: Physical*, vol. 264, pp. 341-346,

[5] H. Wen, et al., "A high-performance single-chip timing and inertial measurement unit with robust mode-matched gyroscopes," presented at the *31st International Conference on Micro Electro Mechanical Systems*, Belfast, 2018.

[6] J. P. Guyer, Fundamentals of Acoustics, 2013.

[7] Invensense : AN-1112 Microphone Specifications Explained. https://www.invensense.com/wp-content/uploads/2015/02/AN-1112-v1.1.pdf

[8] Y. Jeong, A. Daruwalla, H. Wen, and F. Ayazi, "An out-of-plane "hinge-shaped" nano-gap accelerometer with high sensitivity and wide bandwidth," in *2017 19th International Conference on Solid-State Sensors, Actuators and Microsystems (TRANSDUCERS), 2017,* pp. 2131-2134.

[9] F. Ayazi and K. Najafi, "High aspect-ratio combined poly and single-crystal silicon (HARPSS) MEMS technology," *Journal of Microelectromechanical Systems*, vol. 9, pp. 288-294, 2000.

[10] Irvine Sensors, MS3110 Datasheet.

[11] Knowles, BU-23173 Datasheet, 2007.

[12] S. Reichert, R. Gass, C. Brandt, and E. Andrès, "Analysis of Respiratory Sounds: State of the Art," *Clinical Medicine. Circulatory, Respiratory and Pulmonary Medicine,* vol. 2, pp. 45-58,

[13] S. R. Messer, J. Agzarian, and D. Abbott, "Optimal wavelet denoising for phonocardiograms," *Microelectronics Journal*, vol. 32, pp. 931-941,

[14] Z. Syed, et al. "A Framework for the Analysis of Acoustical Cardiac Signals," *IEEE Transactions on Biomedical Engineering*, vol. 54, pp. 651-662, 2007.

[15] L. Giovangrandi, O. T. Inan, R. M. Wiard, M. Etemadi, and G. T. A. Kovacs, "Ballistocardiography – A Method Worth Revisiting," Conference proceedings : *IEEE Engineering in Medicine and Biology Society. Annual Conference,* vol. 2011, pp. 4279-4282, 2011.

[16] E. Pinheiro, O. Postolache, and P. Girão, "Theory and Developments in an Unobtrusive Cardiovascular System Representation: Ballistocardiography," *The Open Biomedical Engineering Journal*, vol. 4, pp. 201-216

CONTACT

*P. Gupta, tel: +1-404-907-7467; pgupta97@gatech.edu

MICROFABRICATED ELECTRODYNAMIC WIRELESS POWER RECEIVER FOR BIO-IMPLANTS AND WEARABLES

Nicolas Garraud, Daniel Alabi, John D. Varela, David P. Arnold, and Alexandra Garraud*
Interdisciplinary Microsystems Group, University of Florida, USA

ABSTRACT

This paper reports the design, modeling, fabrication, and characterization of a microfabricated receiver as part of an electrodynamic wireless power transmission (EWPT) system. This system differs from inductively coupled wireless power transmission (WPT) by employing low-frequency (<1 kHz) magnetic fields to deliver power over 10's of cm to multiple compact receivers in a cluttered environment. Herein we report the first-ever, chip-scale microfabricated EWPT receiver, which can output 2.5 mW of power under a 744 Hz, 550 μT_{pk} ac magnetic field (equivalent to 20 cm transmission distance). Compared to a previously reported prototype, the microfabricated device is 14.5x smaller (0.55 cm^3 vs. 8 cm^3), and offers a 2.1x increase in power density (4.6 mW/cm^3 vs. 2.2 mW/cm^3).

INTRODUCTION

WPT Challenges

The holy grail objective for wireless power transmission (WPT) is to achieve high efficiency, high power transmission to small power receivers at long distances (Fig. 1). Inductive coupling is well suited for efficient close-range transmission [1], but the efficiency decays quickly with the distance. Magnetic resonant WPT tries to increase distance while maintaining efficiency [2,3], but the system architecture is more complex. Additionally, there are both practical and safety concerns about the RF fields that exist between the transmitter and receiver. Specifically, any object that sits between the transmitter and receiver is subjected to relatively strong RF magnetic fields with frequencies typically ranging from 100's of kHz to 10 MHz. At these frequencies, unwanted eddy currents are generated in electrically conductive objects. At minimum, these eddy currents can attenuate or alter the fields used for power transmission. But worse, these eddy currents can cause undesirable or even unsafe heating in the intervening objects.

Therefore, there is a technology gap for mid-range (~10–100 cm) transmission to compact receivers, as is needed for Internet of Things (IoT) devices, wearables or bio-implants. Electrodynamic WPT (EWPT) has been proposed as a possible solution [4-7], wherein the magnetic fields from a transmitter (generally much lower frequencies than inductive or magnetic resonance methods) are used to excite the mechanical motion of a permanent magnet in the receiver. This mechanical motion is converted into electricity by one or more electromechanical transduction schemes.

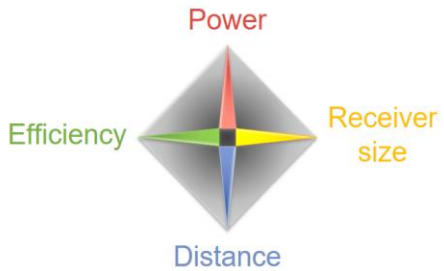

Figure 1: Four competing design objectives for wireless power transmission (WPT).

EWPT Principle

The EWPT method presented here utilizes a receiver with a mechanically resonating permanent magnet embedded in a receiver coil, as shown in Fig. 2. The ac magnetic field generated by the transmitter couples via a torque with the receiver magnet, which torsionally oscillates. While oscillating around its axis, the magnet changes the magnetic flux in the receiver coil and generates an ac voltage by induction. The receiver coil can be connected to suitable power electronics to obtain a regulated dc voltage to charge a battery or directly supply a system.

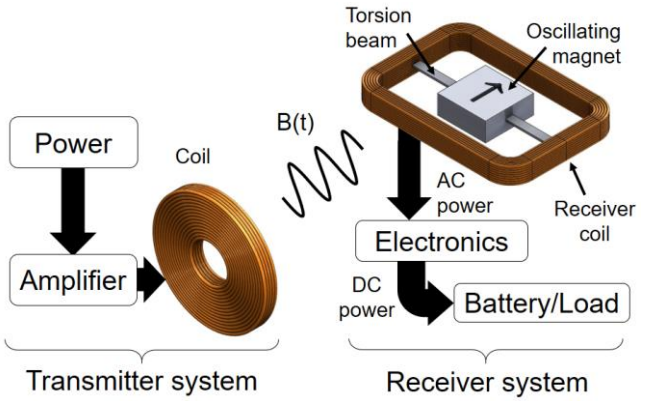

Figure 2: System architecture of electrodynamic wireless power transfer (EWPT). The mechanically resonating magnet is sensitive to time-varying magnetic field from the transmitter and generates power in the receiver coil in which it is embedded.

The uniqueness of the EWPT method is that it operates at low frequency (10-1000 Hz) while maintaining a valuable power density. Considering the voltage V induced on the receiver coil, which is proportional to the time-rate-change of the flux $d\Phi/dt$, the reduction in voltage due to the lower operational frequency is counterbalanced by the much larger magnetic flux (and consequently flux change) produced by the mechanically moving permanent magnet. Furthermore, the lower frequency EWPT approach can safely operate with higher magnetic field strengths, since the admissible magnetic field strength for safe exposure of human is higher at lower frequency [8-9]. Most importantly, the low frequency of operation mitigates the field attenuation and parasitic heating effects that occur with RF fields. This makes EWPT suitable for transmitting power to multiple receivers in an environment crowded and cluttered with metallic objects such as a home, office, or automobile environment, or for powering safely deep biomedical-implants or wearables through human body.

Our research group has previously designed, built, and characterize various macroscale receivers to demonstrate the EWPT method [4-8]. In this paper, we present a significantly miniaturized receiver that utilizes micromachined silicon suspensions. Compared to previously utilized metal and polymer suspensions, the lower loss of the silicon suspension has the potential to increase the resonant amplitude of the receiver making it more responsive to lower magnetic fields, and therefore extending the power transmission distance.

978-1-940470-03-0/HH2018/$25©2018TRF
DOI 10.31438/trf.hh2018.10

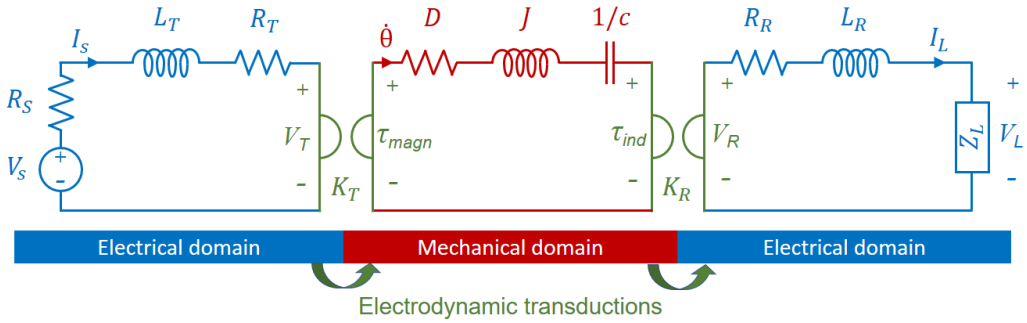

Figure 3: Equivalent electrical circuit of an EWPT system and energy domain flow.

DESIGN OF MECHANICAL SUSPENSION

The EWPT system can be represented by an equivalent electrical circuit shown in Fig. 3. The energy from the source is flowing from the electrical domain through the transmitter coil, to the mechanical domain via the spring-mass-damper, and then back to the electrical domain through the receiver coil and the load. The two transductions between the electrical and the mechanical domains are achieved through electrodynamic coupling.

The chosen architecture, depicted on Fig. 4, integrates two suspensions attached to a frame on which two receiver coils are attached (not shown), and supporting a central platform on which two magnets are attached. Special care has been taken on the optimization of the mechanical suspensions. They are designed to be compact, allow only one degree of freedom around an axis of rotation, while setting the resonant frequency of the resonator through their rotational stiffness and allowing a large rotation of the magnet (± 20º). The length of the suspension should be the smallest possible to minimize the receiver volume (i.e. higher power density), and to minimize the wiring far from the magnets where the fields are weaker (i.e. lower coil resistance leads to higher power).

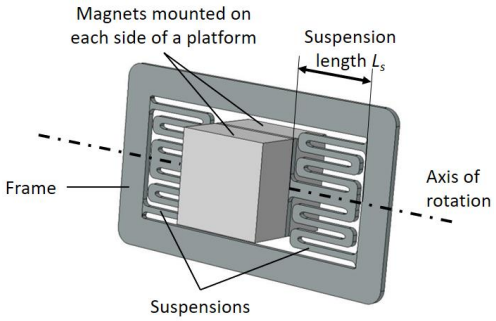

Figure 4: Architecture of the micro-receiver, including the mechanical suspensions to be optimized.

The following prerequisites are chosen and used as inputs of the optimization: the size of the magnet (depending on a limited set of commercially available magnets), the resonant frequency, the maximal rotation amplitude of the magnet, and the wafer thickness and mechanical properties (Young's modulus and Poisson's ratio). The optimization should consider several other constraints and design objectives: the mechanical suspensions should be compliant in the desired mode (here one rotation), while rejecting other vibration modes around the frequency of interest; the stress at the maximum rotation amplitude should be lower than the yield stress adjusted by a multiplicative safety coefficient (chosen here as 0.2); the suspension length L_s should be minimal.

Different torsional suspension configurations are considered as in [10] and [11] (Fig. 5): two simple torsional beams, two meander beams with their main axis perpendicular to the axis of rotation, and two meander beams with their main axis parallel to the axis of rotation. In this example, the three oscillators use the same magnet assembly (two 1/8"×1/8"×1/16" magnets) and resonate at the same frequency around 1 kHz. The challenge is to find a trade-off between a compliant enough structure with the right stiffness for the targeted frequency by changing the beam width and length, and the number of meanders when appropriate. The first configuration with simple torsional beams presents long beams to allow the targeted rotation amplitude. The second configuration, in which the meander beams work mainly in flexural mode, is much more compact, L_s being 1.76 times shorter, and the volume 1.5 times smaller. The third configuration, with beams working both in torsional and flexural mode, presents the most compact suspensions, and is consequently selected. Indeed, L_s is 2.36 times shorter and the volume is 1.77 times smaller than the first configuration. In this configuration, the resonant frequency could be widely adjusted by changing the number of meanders: with more meanders, the more compliant structure resonates at lower frequency, and the suspensions are shorter.

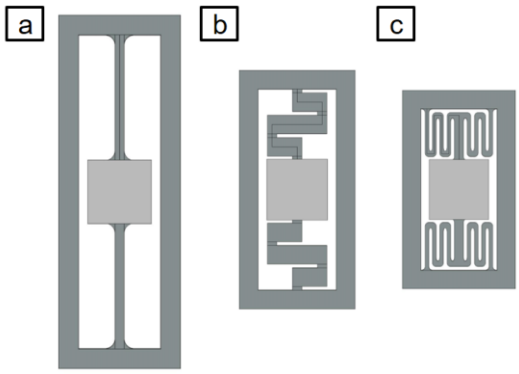

Figure 5: Torsional suspension beam configurations considered in the optimization of the design of the micro-receiver: simple torsional beams (a), meander beams perpendicular (b) and parallel (c) to the axis of rotation.

Once the suspensions are designed, the last element to be optimized is the receiver coil. To maximize the generated power, the winding should as close as possible to the magnet without preventing its rotation. Moreover, the resistivity of the wire material should be the lowest possible, which is achieved with copper wire. The wire gauge does not significantly affect the generated power, meaning that a device with a large number of turns of thin wire will produce about the same amount of power as that using fewer number of turns of a thicker wire. However, it is

preferred to use a small wire diameter (i.e. more turns for a given volume) to obtain a significant enough voltage to ease the voltage regulation electronics.

MICROFABRICATION AND DEVICE ASSEMBLY

The fabrication process and assembly of the receiver are shown in Figs. 6 and 7. The serpentine torsion beams are formed by through-etching via DRIE a 200-µm-thick double-side-polished silicon wafer, using a 6-µm thick photoresist (Fig. 6ab). The 50 structures that fit on a 100 mm wafer are released during the same operation by etching the surrounding of their frames. Next, four Nd-Fe-B 1/8"×1/16"×1/16" magnets are assembled on the silicon platform (two on top and two on bottom). Since their magnetizations all point in the same direction, it is difficult to accurately position the magnet on the platform because they repel each other. The solution is to first demagnetize the magnets with a pulse magnetizer, assemble and glue them on the platform, and then re-magnetize the fully assembled structure with the pulse magnetizer (Fig. 6cdfg). Finally, the two receiver coils (AWG 40, 150 turns each, ~17 Ω each) are wound on a sacrificial foam jig, glued, and then assembled on the silicon frame and connected in series (Fig. 6eh).

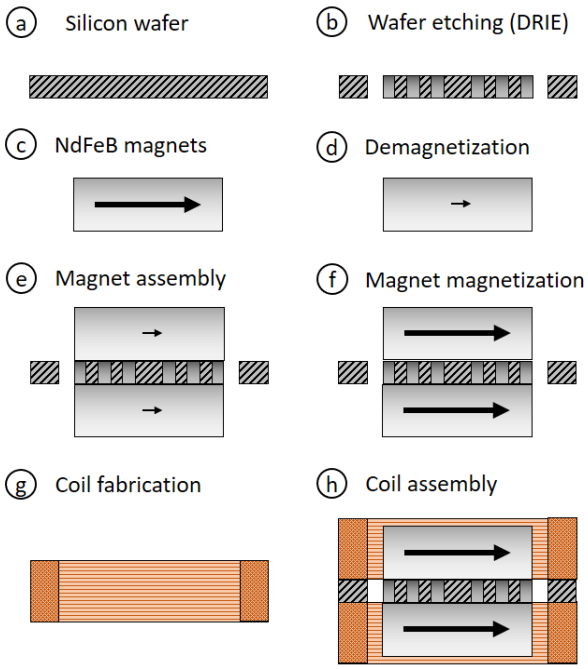

Figure 6: Device microfabrication process: DRIE etch of the suspension (a, b), magnets demagnetization, assembly and re-magnetization (c, d, f, g), and receiver coil fabrication and assembly (e, h).

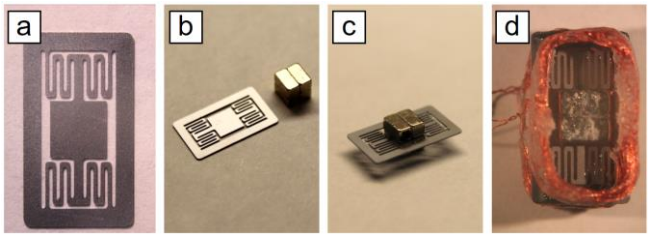

Figure 7: Assembly of the micro-receiver: fabricated suspension (a,b), assembly of the magnets with the suspension (c), and fully assembled micro-receiver (d).

The final device is 10.8×6.1×8.3 mm^3 (0.55 cm^3, 0.75 g), having a size and mass commensurate with common electronic components (Fig. 8ab). This represents a 14.5x volume reduction from the previous handmade macroscale receiver [6] (Fig. 8c).

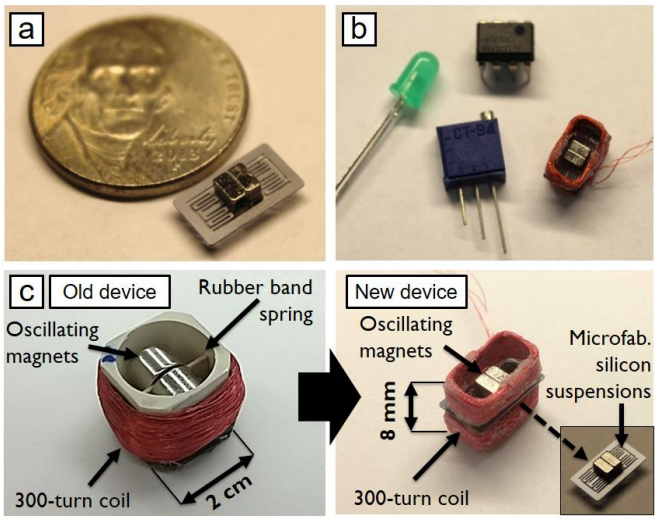

Figure 8: Images of the microfabricated EWPT receiver: size comparison with (a) 5-cent coin and (b) electronic components; and (c) illustration of 14.5x decrease in receiver size compared to previous hand-made receiver.

EXPERIMENTAL RESULTS

The micro-receiver is characterized using a Helmholtz coil pair (28-cm diameter, 15-cm long, 1.2 Ω per coil, 0.74 mT/A). The Helmholtz coils are used in order to apply a purer (more spatially uniform and more controllable) magnetic field and without simultaneously applying a field gradient. Conversely, a typical transmitter coil (like used in [5]) produces both a field and a field gradient at any given distance, which cause a torque and force, respectively, acting on the receiver magnet. For preliminary testing purposes, we wanted to only subject the receiver magnet to a torque and not a force.

Fig. 9 presents the normalized open voltage while varying the excitation frequency from 200 to 780 Hz. The system presents a sharp peak, characteristic of an underdamped 2nd-order system (quality factor estimated to be 50). The maximum output, occurring at the resonant frequency of 744 Hz, is 0.95 V_{rms}/mT in the linear regime.

Fig. 10 shows the actual time-average output power delivered to a resistive load (varied from 0.1 to 2000 Ω) while using a constant amplitude, 300 μT_{pk} ac magnetic field. The power absorbed by the load tends to be low if its resistance is too low (low voltage) or is too high (low current) compared to the receiver coil resistance. The optimal load is about 50 Ω, expectedly close to the receiver coil resistance (34 Ω).

In a last experiment, the field is progressively increased to obtain the highest magnet rotation amplitude and highest power output. At a 550 μT_{pk} field, the maximum transmitted power is found to be 2.55 mW (0.59 V_{rms} output). This magnetic field amplitude corresponds to a field produced at 20 cm by a 15-cm-radius coil supplied by 10 W input power. Above this field, the receiver suspension beams fractured as seen in Fig. 11. The maximum power density of the micro-receiver is 4.6 mW/cm^3,

which is 2.1 times higher than the power density of the last macroscale generation. Indeed, despite a smaller magnet, the small receiver resonates at higher frequency and still induces a larger power density, the generated power being proportional to the square of the frequency.

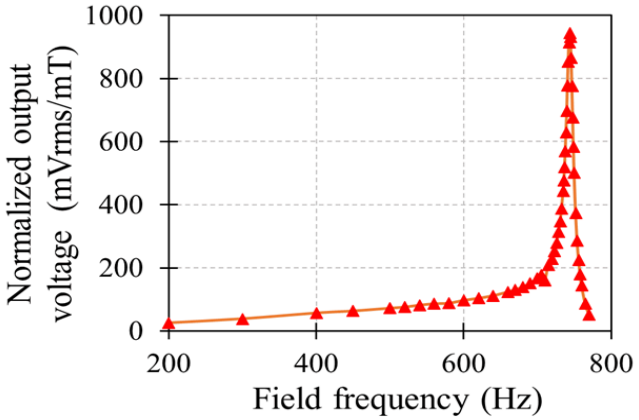

Figure 9: Normalized open-circuit voltage as a function of the frequency of the magnetic field.

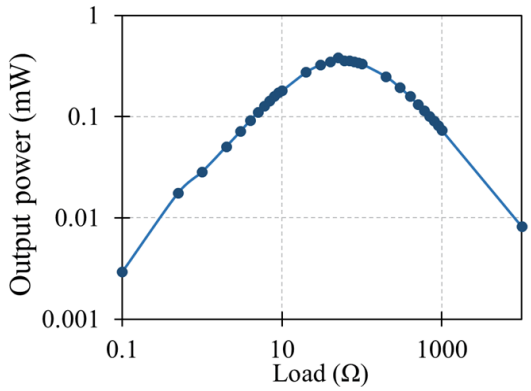

Figure 10: Output power as a function of the resistive load under a 300 μT_{pk} ac magnetic field.

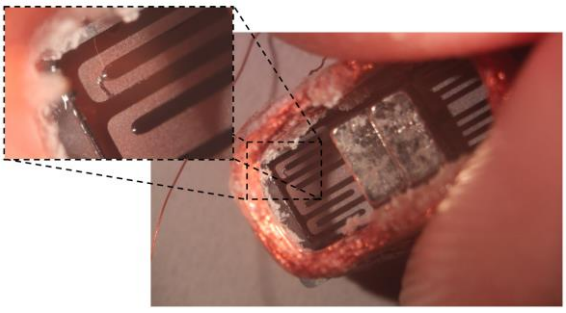

Figure 11: Fractured meander beam after a too high magnetic field amplitude.

CONCLUSION

In this work, we successfully demonstrate for the first time an EWPT system using a chip-sized partially microfabricated receiver. We demonstrate 2.5 mW of power using a 744 Hz magnetic field with an amplitude of 550 μT_{pk}, equivalent to a ~20 cm transmission distance for a typical 10 W transmitter coil. Compared to previous works, the microfabricated device is 14.5x smaller, and offers a 2.1x increase in power density (4.6 mW/cm^3). Future works will focus on further testing the device to improve the output power and developing the AC to DC receiver electronics.

ACKNOWLEDGEMENTS

This work was supported in part by the NSF I/UCRC on Multi-functional Integrated System Technology (MIST) Center (NSF Grant IIP-1439644, IIP-1439680, and IIP-1738752).

REFERENCES

[1] M.P. Kazmierkowski, R.M. Miskiewicz, and A.J. Moradewicz, "Inductive coupled contactless energy transfer systems - a review", 2015 Selected Problems of Electrical Engineering and Electronics (WZEE), Kielce, Poland (2015).

[2] S.D. Barman, A.W. Reza, N. Kumar, M.E. Karim, A.B. Munir, and Abu Bakar, "Wireless powering by magnetic resonant coupling: Recent trends in wireless power transfer system and its applications", Renewable and Sustainable Energy Reviews, 51 (2015), pp. 1525 - 52.

[3] A.M. Jawad, R. Nordin, S.K. Gharghan, H.M. Jawad, and M. Ismail, "Opportunities and Challenges for Near-Field Wireless Power Transfer: A Review", Energies, 10-7 (2017), p. 1022.

[4] V.R. Challa, J.O. Mur-Miranda, and D.P. Arnold, "Wireless power transmission to an electromechanical receiver using low-frequency magnetic fields", Smart Mater. Struct., 21 (2012), p. 115017.

[5] K.M. McEachern, and D.P. Arnold, "Electrodynamic wireless power transmission to a torsional receiver", J. Phys. Conf. Series, 476 (2013), p. 12004.

[6] N. Garraud, D. Alabi, S. Chyczewski, J.D. Varela, D.P. Arnold, and A. Garraud, "Extending the range of wireless power transmission for bio-implants and wearables", PowerMEMS 2017, Kanazawa, Japan (2017).

[7] A. Garraud, and D.P. Arnold, "Advancements in electrodynamic wireless power transmission," Proc. 2016 IEEE Sensors Conf., Orlando, FL, (2016), pp. 82-84.

[8] C95.6 2002 IEEE "Standard for Safety Levels With Respect to Human Exposure to Electromagnetic Fields, 0-3 kHz", (2002).

[9] C95.1 2010 IEEE "Standard for Safety Levels With Respect to Human Exposure to Radio Frequency Electromagnetic Fields, 3 kHz to 300 GHz", (2010).

[10] G. Barillaro, A. Molfese, A. Nannini, and F. Pieri, "Analysis, simulation and relative performances of two kinds of serpentine springs", J. Micromech. Microeng., 15-736 (2005).

[11] Y. Bai, J.T.W. Yeow, and B.C. Wilson, "Design, Fabrication, and Characteristics of a MEMS Micromirror With Sidewall Electrodes", J. Microelectromechanical Systems, 19-3 (2010).

CONTACT

*D.P. Arnold; darnold@ufl.edu

A WIRELESSLY CONTROLLED FULLY IMPLANTABLE MICROSYSTEM FOR NANO-LITER RESOLUTION INNER EAR DRUG DELIVERY

Farzad Forouzandeh[1], Ahmed Alfadhel[1], Xiaoxia Zhu[2], Joseph P. Walton[2], Denis R. Cormier[1], Robert D. Frisina[2], and David A. Borkholder[1]*

[1]Rochester Institute of Technology, Rochester, NY, USA

[2]University of South Florida, Tampa, FL, USA

ABSTRACT

Site-directed and programmable drug delivery systems are important to leverage recent developments in protective and restorative biotherapies. Therapy development in the mouse model system requires advanced nano-liter precision implantable microsystems. Here, an implantable and scalable drug delivery system is presented consisting of a miniaturized, wirelessly controlled phase-change peristaltic micropump and a refillable microreservoir. 3D-printing technology has been used to fabricate the micropump around a microcatheter tubing on the backside of a printed circuit board. *In vitro* characterization results demonstrate nano-liter resolution control over the desired flow rates of 10-100 nL/min in the presence of backpressure 40× larger than experienced in the physiologic system. *In vivo* implantation results show consistency with previously published syringe pump results.

INTRODUCTION

Over 450 million people all around the world suffer from auditory dysfunction, according to World Health Organization [1]. Recent advances in protective and restorative biotherapies have created new opportunities to address auditory and vestibular disorders with site-directed, programmable drug delivery systems. Successful therapy development leveraging the transgenic, knock-in, and knock-out variants of human disease in the mouse model system requires advanced microsystems specifically designed to function with nano-liter precision and with system volumes suitable for implantation.

However, delivering into the inner ear is extremely challenging due to small size, relative inaccessibility, sensitivity to mechanical and chemical stress [2], and the small volume of the cochlear fluid (perilymph), which is approximately 620 nL for mice [3]. Inner ear drug delivery systems need to meet several requirements to address these challenges to be able to provide safe and efficient delivery. Such a system requires precise ultra-low flow rates with a controllable profile while being sufficiently small with a planar form factor to facilitate subcutaneous implantation in animals, and mastoid cavity implantation in humans [4], [5]. Moreover, it must be sufficiently robust to enable long-term, time-sequenced, precise flow rate control with remote activation/deactivation capability.

These requirements limit the application of current microsystem-based drug delivery devices. The state of the art micropump for intracochlear drug delivery provides controlled, automated pumping, but the size is prohibitive for implantation in the mice [4]. The only commercially available micropumps for implanting in mice either provide power-free delivery at fixed flow rates (Alzet®, Durect Co., Cupertine, CA, USA), or controllable and programmable delivery, at a relatively large size (iPRECIO®, Primetech Corporation, Tokyo, Japan). Recently, a miniaturized planar peristaltic micropump for this domain was reported that employed gallium as the phase-change material [6]. However, it was fabricated using micromachining processes and had to overcome traditional microfluidic interconnection challenges [7]. Additionally, unless custom circuits are integrated directly with the microelectromechanical system (MEMS) based micropump, incorporation of control electronics adds significant bulk. Scaling of MEMS-based systems requires modification of the fabrication processes and masks, creating challenges in scalability to human clinical translation.

In this paper, we present a miniaturized, wirelessly controlled and fully implantable phase-change peristaltic micropump to provide programmable and accurate drug delivery for inner ear applications. Employing 3D-printing technology, the micropump is built on the backside of a printed circuit board (PCB) around a microcatheter tubing (OD= 250 µm, ID= 125 µm) to integrate the mechanical and control electronic components while providing a leak-free biocompatible flow path without complex microfluidic interconnects. A refillable and collapsible 50 µL microreservoir is integrated with the micropump while maintaining a form factor optimized for subcutaneous implantation in mice (Figure 1). We present the micropump architecture, control electronics details, and heat transfer analysis for phase-change peristalsis, along with *in vitro* and *in vivo* results, with an emphasis on the functionality of the micropump at ultra-low flow rates.

MICROPUMP ARCHITECTURE

Using a sub-millimeter microcatheter tubing as the fluid-carrying component limits the options for pumping approaches, particularly those that require in-line rectifying valves which add unacceptable bulk for this size-constrained application. Here we employ peristalsis with the microcatheter tubing sequentially compressed in three locations to induce directional flow. Different actuation methods have been used for peristaltic micropumps in the literature such as piezoelectric, pneumatic, thermopneumatic [8], and phase-change [6].

In this study, a phase-change actuation method has been used due to its low driving voltage, small size, and high actuation force enabling effective pumping against backpressure. The actuation material is encapsulated in the body of the micropump surrounded by stiff structures except for one side that is exposed to the deformable microcatheter tubing. Peristalsis takes place by sequential melting / solidification of the phase-change material driving cyclic expansion / shrinking and compression of the tubing to directionally push the pumped fluid from inlet to outlet.

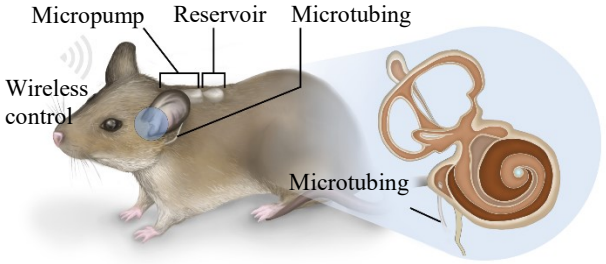

Figure 1: The overall drug delivery system for inner ear application includes a micropump and an integrated refillable microreservoir, designed for subcutaneous implantation. The system can be programmed and wirelessly controlled via an Android device.

978-1-940470-03-0/HH2018/$25©2018TRF
DOI 10.31438/trf.hh2018.11

Different phase-change materials have been used in the literature such as gallium [6], and paraffin wax [9]. Paraffin wax was used for this micropump for its stable phase-change behavior, high actuation pressure, and flexible melting point based on the molecular weight.

The micropump was built directly on the backside of PCB employing 3D-printing technology. Three chambers were fabricated in a linear pattern adjacent to the microcatheter tubing separated by 1.2 mm. Paraffin wax was precisely deposited in the chambers. Three pairs of resistive heaters and thermistors were placed in the chambers for precise control of the temperature. A peristaltic sequence was applied to the micropump, with timing control ensuring two closed chambers at each moment in time.

MICROPUMP CONTROL ELECTRONICS

On the front side of the PCB, the control electronics were fabricated for actuation and control. The micropump electronics use off-the-shelf components and have been designed for ultra-low-power operation. The system is powered by a lithium polymer battery and includes a single cell lithium ion battery charger (BQ25100, Texas Instruments), which was chosen for its low battery leakage current (75 nA) and small footprint. The TPS62743 (Texas Instruments) is a step down buck converter that provides sufficient current output (maximum 300mA) while pumping, high conversion efficiency, and low quiescent current (360nA) when the system is in shutdown mode. Each pump chamber consists of a 40-ohm resistive element for heating, and a thermistor (NCP03WF104F05RL, Murata). Each resistive element uses a discrete NMOS for microprocessor control of the chamber. A 1.8V system power rail minimizes power consumption of the wireless microcontroller.

The wireless microcontroller (MCU) includes a Bluetooth Low Energy transceiver (BLE 4.2), a 32-bit ARM Cortex-M3 processor with a clock speed of up to 48 MHz, and an ultra-low-power sensor controller (CC2640, Texas Instruments). This system provides an ultra-low shutdown current of 100nA, which is important since the system will spend the majority of time in deep sleep mode when the pump is not actively delivering drugs. The system real-time clock utilizes a 32kHz oscillator (SiT1532, SiTime) based on silicon

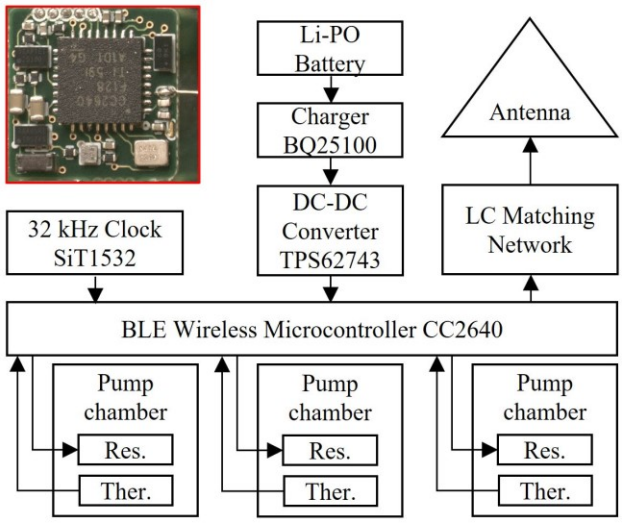

Figure 2: Block diagram of the pump control electronics. Res. and Ther. stand for resistive heater and thermistor, respectively. Inset: An image of the fabricated electronics on top side of the PCB. The electronics assembly is used for actuation, closed-loop feedback to control the temperature in each chamber, and wireless control.

MEMS technology, which has the smallest footprint and lowest power for a commercially available oscillator. A wire antenna with a length of 10 mm keeps the overall device footprint as small as possible. The control electronics are configured and operated using a custom Android application via Bluetooth Low Energy. Figure 2 shows the block diagram of the electronics along with an image of the front side of PCB.

MICROPUMP HEAT TRANSFER ANALYSIS

A phase-change peristaltic micropump with three adjacent actuation chambers requires proper transfer of heat in and out of the medium, affecting actuation frequency and flow rate. COMSOL® simulations were carried out to optimize the heat transfer function of the micropump. The 3D geometry details were designed in SolidWorks® and imported into COMSOL. The material properties were obtained from the COMSOL library or datasheet of the components. Free convection in water was considered for the surface boundary condition, to simulate the *in situ* application of the device. Heat generation was applied to the middle surface of the resistors in the chambers by applying a sequential user-defined function, while the temperature was controlled according to the temperature of the resistor using a user-defined function for closed-loop control.

To achieve the maximum target flow rate of 100 nL/min, high actuation frequencies were required necessitating a 10 °C differential between the wax melting point and the environmental temperature. Simulation results revealed a reduction of the thickness of the Copper in the PCB from 36 µm (1 oz.) to 18 µm (0.5 oz.) enabled the actuation frequency to increase by 14% due to reduced thermal mass and heat transfer away from the chamber. The addition of a copper pad in the bottom of each chamber improved the homogeneity of the temperature distribution in the chambers by 33%.

Using the model with optimized material and geometry, the results of a steady state simulation while chambers 1 and 3 are on, and chamber 2 is off, shows that the chambers are well-insulated. In particular, while two side chambers are set at the melting point the middle chamber stays ~9 °C colder than the melting point as shown in Figure 3A. To estimate the temperature rise of both the micropump exterior surface and the pumped fluid, transient analysis was performed. The surface temperature of the micropump remained 2 °C below the ambient temperature.

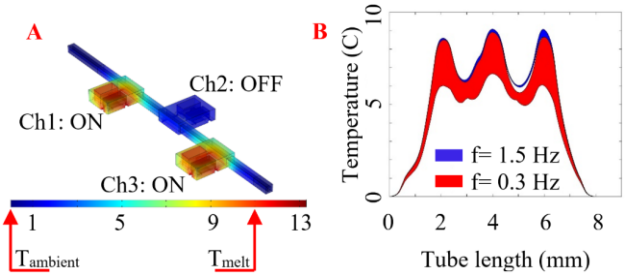

Figure 3: 3D heat transfer analyses were performed on the micropump. A) The design provides effective thermal insulation of the chambers. B) The temperature distribution in the length of the tubing in the last 5 seconds of the simulation of the pump working at 0.33 Hz and 1.5 Hz for 30 seconds. The results show that the drug temperature never exceeds more than 9˚C higher than the ambient temperature and it cools down to ambient temperature before leaving the actuation region of the micropump. The temperatures are normalized to the ambient temperature in all figures.

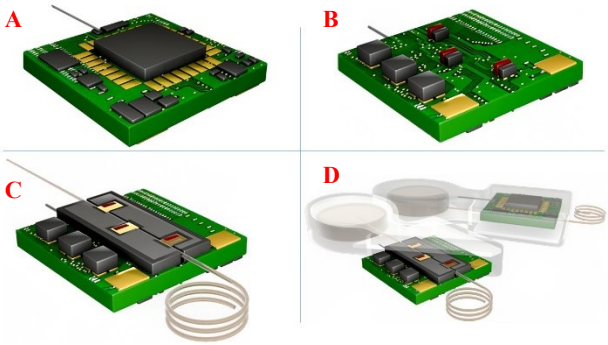

Figure 4: A new low-cost fabrication methodology is presented leveraging 3D printing of micropump features on the backside of a PCB. A) The electronic components for actuation, temperature control, and wireless communication are assembled on the front side of the PCB. B) The micro-heaters and thermistors are assembled on the backside of the PCB, forming a template for three linear chambers and a microcatheter tubing. C) A commercially available catheter microtubing (250µm OD, 125µm ID) is placed within a printed template. A precise volume of Nonadecane with a melting point of 31.8 ˚C is placed in each chamber in contact with the microtubing and integrated micro-heater and thermistor. D) The chambers are covered with a rigid resin. A microreservoir is integrated to the micropump and the entire system is encapsulated with PDMS and parylene-C for biocompatibility.

The pumped fluid temperature increased to 9 °C above the ambient within the micropump, but returned to ambient temperature before leaving the pump platform.

MICROSYSTEM FABRICATION PROCESS

A new fabrication process (Figure 4) was developed using 3D-printing technology, enabling direct write printing of the mechanical structure of the micropump on the backside of a PCB, while on the other side control electronics were populated employing standard PCB assembly technology. Three pairs of thermistors and resistors were fabricated on the backside of the board, forming a template for three linear chambers and a microcatheter tubing. The structure of the micropump was 3D-printed using an inkjet printer (Roland VersaUV LEF-12, Tokyo, Japan) and the microcatheter tubing was fixed and sealed in the designated site using cyanoacrylate resin. A precise volume (240 nL) of Nonadecane (Sigma-Aldrich, USA) was placed in the chambers and the chambers were covered with the resin.

The micropump was bonded to a 3D-printed biocompatible substrate (MED610, Stratasys, MN, USA). A refillable biocompatible PDMS-based microreservoir was fabricated using

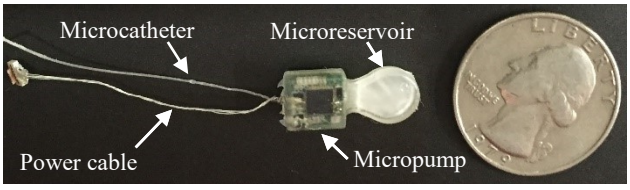

Figure 5: The completed drug delivery microsystem. The system achieves first in class miniaturization for this application for subcutaneous implantation. It is readily scalable by selection of microtubing size, 3D-printed chambers, and actuation frequencies.

PDMS molding method into a 3D-printed (MakerBot, NY, USA) acrylonitrile-butadiene-styrene (ABS) mold. After curing at 60˚C for 4 hours, the PDMS replica was peeled-off and bonded to the substrate using uncured PDMS adhesive layer. The structure was then cured at 40 ˚C for 12 hours. For biocompatibility, the entire system was encapsulated with a ~2µm-thick parylene-C (Specialty Coating Systems, Indianapolis, Indiana) using a custom-built parylene deposition tool (Figure 5).

IN VITRO CHARACTERIZATION

The micropump was first characterized *in vitro*; flow rate measurements were taken at different actuation frequencies and back pressures. The actuation set temperature of the chambers was calibrated based on actuation frequency. The micropump was placed in a petri-dish full of water to simulate the *in situ* conditions. The microcatheter was filled with dyed deionized water, and flow rates were measured considering the fluid front displacement using a ruler at the outlet.

Flow rates were measured for actuation frequencies from 0.0167 to 0.2 Hz at eight different frequencies to cover the entire range of reported drug delivery infusion flow rates of 10-100 nL/min [10]–[13]. Flow rates were measured at two back pressures of 0 and 20 kPa (40× larger than the physiological back pressure).

The results (Figure 6) show that the micropump can provide almost linear results ($R^2 = 0.98$) through the 10-100 nL/min range. Moreover, results show that applying 20 kPa back pressure does not significantly affect the flow rates.

IN VIVO EXPERIMENT

To evaluate the *in vivo* functionality of the micropump, it was tested using an inner ear drug delivery paradigm in the mouse model system, and the results were compared to our previous publication [12]. Salicylate has been shown to cause inhibition of outer hair cells electromotility which can result in a reversible elevation of distortion product otoacoustic emissions (DPOAE) thresholds. Therefore, it was delivered to the round window membrane (RWM) with an assessment of auditory function using DPOAE method. Three micropumps were tested in eight mice with the microcatheter tubing implanted at the RWM niche. The micropumps were held in a water bath to simulate heat transfer associated with implantation. The details of the surgery were presented in our previous work [12]. In the previous publication the salicylate was delivered to RWM using a syringe pump at a flow rate of 50 nL/min for 20 minutes (1000 nL total), and then the pump was deactivated for 40 minutes.

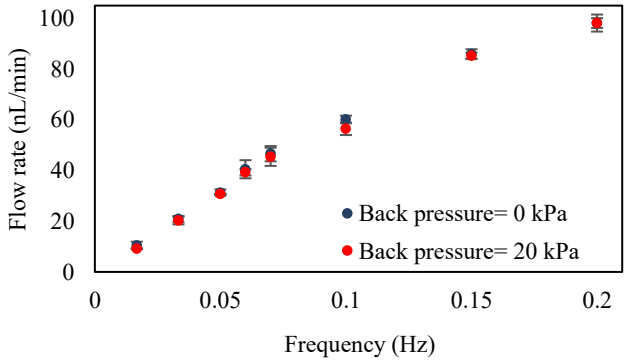

Figure 6: In vitro test results illustrate precise control over the drug delivery flow rate in the desired range (10-100 nL/min) in the presence of 20 kPa backpressure, which is approximately forty-fold higher than mouse intracochlear back pressures.

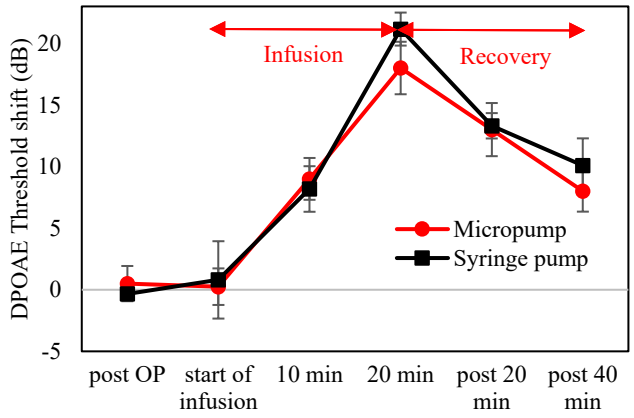

Figure 7: Micropump delivery real-time shifts in DPOAE thresholds as a function of infusion time were consistent with our previously published results [12] which used a syringe pump for delivery of salicylate at the same flow rate. Error bars are standard error of the mean (SEM).

The DPOAE threshold was measured for the entire 60 minutes of the experiment to find the DPOAE shifts during 20 minutes infusion and 40 minutes recovery. The same procedure was repeated for the micropumps.

Figure 7 shows the average in the DPOAE shifts of the 3 micropumps tested in 8 mice, compared to the syringe pump during infusion and recovery. Results show a promising consistency between the two experiments, demonstrating the accuracy and reliability of the micropump.

CONCLUSION AND FUTURE WORKS

In this paper progress on a microsystem for ultra-low flow rate drug delivery for inner ear applications was presented. 3D-printing technology has been employed to fabricate the micropump around a microcatheter tubing on the backside of a PCB, to integrate with the electronics assembled on the front side. The *in vitro* characterization results show precise control over the required ultra-low flow rate of 10-100 nL/min in presence of up to 20 kPa back pressure. In addition, the *in vivo* results show a promising match with a previous experiment using syringe pump. Moreover, the micropump was integrated with a 50 µL microreservoir, keeping the planar form factor for subcutaneous implantation. This microsystem architecture leveraging 3D printing technology and direct peristaltic actuation of the catheter tubing is readily scalable for future human translation.

Future work will focus on the optimization and characterization of the microreservoir and subcutaneous implantation of the microsystem. In addition, a thermal flow meter for feedback control of the flow rate of the micropump will be developed.

ACKNOWLEDGEMENT

This work was supported by the National Institute On Deafness and Other Communication Disorders of the National Institutes of Health, under Award # R01 DC014568.

REFERENCES

[1] http://www.who.int/mediacentre/factsheets/fs300/en/.
[2] E. E. L. Pararas, D. A. Borkholder, and J. T. Borenstein, "Microsystems technologies for drug delivery to the inner ear," Adv. Drug Deliv. Rev., vol. 64, no. 14, (2012), pp. 1650–1660.
[3] M. Thorne, A. N. Salt, J. E. DeMott, M. M. Henson, O. W. Henson, and S. L. Gewalt, "Cochlear Fluid Space Dimensions for Six Species Derived From Reconstructions of Three-Dimensional Magnetic Resonance Images," Laryngoscope, vol. 109, no. 10, (1999), pp. 1661–1668.
[4] V. Tandon, W. S. Kang, T. A. Robbins, A. J. Spencer, E. S. Kim, M. J. McKenna, S. G. Kujawa, J. Fiering, E. E. L. Pararas, M. J. Mescher, W. F. Sewell, and J. T. Borenstein, "Microfabricated reciprocating micropump for intracochlear drug delivery with integrated drug/fluid storage and electronically controlled dosing," Lab Chip, vol. 16, no. 5, (2016), pp. 829–846.
[5] D. G. Johnson, "Integration Technologies For Implantable Microsystems by," 2013.
[6] D. G. Johnson and D. A. Borkholder, "Towards an implantable, low flow micropump that uses no power in the blocked-flow state," Micromachines, vol. 7, no. 6, (2016), p 99.
[7] D. G. Johnson, R. D. Frisina, and D. A. Borkholder, "In-Plane Biocompatible Microfluidic Interconnects for Implantable Microsystems," IEEE Trans. Biomed. Eng., vol. 58, no. 4, (2011), pp. 943–948.
[8] B. D. Iverson and S. V. Garimella, "Recent advances in microscale pumping technologies: A review and evaluation," Microfluid. Nanofluidics, vol. 5, no. 2, (2008), pp. 145–174.
[9] R. Bodén, M. Lehto, U. Simu, G. Thornell, K. Hjort, and J. Å. Schweitz, "A polymeric paraffin actuated high-pressure micropump," Sensors Actuators, A Phys., vol. 127, no. 1, (2006), pp. 88–93.
[10] D. A. Borkholder, X. Zhu, B. T. Hyatt, A. S. Archilla, W. J. Livingston, and R. D. Frisina, "Murine intracochlear drug delivery: Reducing concentration gradients within the cochlea," Hear. Res., vol. 268, no. 1–2, (2010), pp. 2–11.
[11] D. A. Borkholder, "State-of-the-art mechanisms of intracochlear drug delivery," Curr. Opin. Otolaryngol. Head Neck Surg., vol. 16, no. 5, (2008), pp. 472–477.
[12] D. A. Borkholder, X. Zhu, and R. D. Frisina, "Round window membrane intracochlear drug delivery enhanced by induced advection," J. Control. Release, vol. 174, no. 1, (2014), pp. 171–176.
[13] Z. Chen, A. Mikulec, M. McKenna, … W. S.-J. of neuroscience, and U. 2006, "A method for intracochlear drug delivery in the mouse," Elsevier, vol. 150, no. 1, (2006), pp. 67–73.

CONTACT

*D.A. Borkholder, tel: +1-585-475-6067;
David.Borkholder@rit.edu

MULTISCALE LIQUID METAL THIN-FILM PATTERNING BASED ON SOFT LITHOGRAPHY FOR SKIN-MOUNTABLE, SOFT AND 3D-INTEGRATED BIOLOGICAL MICROSYSTEMS

Min-gu Kim, Choongsoon Kim, Hommood Alrowais, Patrick Getz, and Oliver Brand
School of Electrical and Computer Engineering, Georgia Institute of Technology, GA, USA
Institute for Electronics and Nanotechnology, Georgia Institute of Technology, GA, USA

ABSTRACT

This paper presents multiscale liquid metal (eutectic gallium-indium alloy, EGaIn) thin-film patterning by utilizing an additive stamping approach for large-scale (mm-cm) soft electronics and a subtractive reverse stamping approach for micro-scale (μm-mm) soft electronics. By combining these complementary patterning techniques, fabricated soft electronic components can be vertically integrated to form high-density and multifunctional soft microsystems. To highlight the fabrication and integration capabilities, a skin-mountable, soft and 3D-integrated biological microsystem, comprising a soft sensing layer and a soft circuit layer, is demonstrated for non-invasive and real-time heart rate and blood oxygen monitoring.

INTRODUCTION

Progress in soft materials and associated manufacturing technologies has enabled wearable and skin-mountable electronics for various sensing applications [1-3]. In this regard, the use of intrinsically soft conductors, such as gallium-based liquid metal (eutectic gallium-indium alloy, EGaIn), is promising because of its non-toxicity and favorable mechanical and electrical ($\sigma = 3.4 \times 10^6$ S/m) properties [4, 5]. The low melting temperature (MP < 15 °C) and negligible vapor pressure of EGaIn enable room-temperature and ambient pressure material processing [6]. Moreover, thanks to the formation of a thin oxide layer ($t \approx$ 1-3 nm) on the EGaIn surface under atmospheric oxygen level, EGaIn structures maintain their mechanical shape, allowing 2D/3D EGaIn patterns on soft elastomeric substrates, such as poly(dimethylsiloxane) (PDMS) [7].

The moldable characteristics of EGaIn have enabled a range of patterning methods based on lithography-assisted printing [8, 9], fluid injection [10, 11], as well as additive [12, 13] and subtractive [14, 15] direct-write processes. Lithography-assisted stencil printing yields simple and high-throughput EGaIn patterning on elastomeric substrates [8]. However, limitations of this approach are the relatively low resolution, resulting rough EGaIn surfaces, and excessive EGaIn loss during the stencil lift-off process. Subtractive direct patterning techniques enable an inexpensive and facile approach to pattern fine EGaIn lines, but the serial process makes EGaIn removal slow in the case of patterning small EGaIn features on large substrates [15]. 2D/3D direct writing techniques allow to deposit EGaIn patterns in desired locations only, but the resolution is limited because of the size limitation of the injection nozzles [12, 13]. Microfluidic injection and vacuum filling approaches provide better resolution, but the used microchannels require relatively large thicknesses to reduce pressure drops [10]. Using a microtransfer deposition process, the smallest EGaIn features so far with width (w) > 2 μm were demonstrated, but this technology suffered from EGaIn residues formed outside of the channel areas during the molding process [16]. Therefore, creating smooth and uniform EGaIn thin films in combination with high resolution and size scalability remains challenging for high-density and multifunctional soft microsystems [17, 18].

Soft lithography [19, 20] with wetting/non-wetting surface modifications in combination with 3D integration can potentially solve current EGaIn patterning challenges, by providing i) smooth and uniform EGaIn thin-film deposition, ii) multiscale patterning, and iii) high-density and functional integration. Recently, we demonstrated high resolution, uniform, and residue-free EGaIn thin-line patterning ranging from single micrometer to millimeter scales by utilizing a chemical surface modification and residue transfer process in a reverse stamping approach for soft microelectronic devices [21, 22]. Building on our previous work [21-25], this paper presents multiscale EGaIn thin-film patterning by utilizing an additive stamping process for large-scale (mm - cm) soft electronics and the subtractive reverse stamping process for micro-scale (μm - mm) soft electronics, as shown in Figure 1 (a). By combining these complementary patterning techniques, soft electronic components built with different patterning processes can be integrated to form high-density and multifunctional soft microsystems.

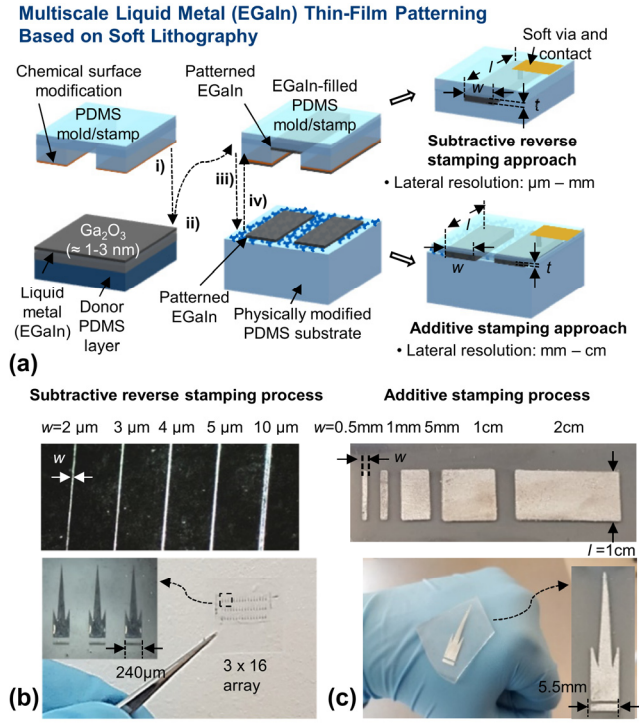

Figure 1: (a) Illustration of complementary multiscale liquid metal (eutectic gallium-indium alloy, EGaIn) thin-film patterning techniques with (b) micro-scale and high-density EGaIn lines and Georgia Tech logos embedded in chemical-surface-modified PDMS molds fabricated using a subtractive reverse stamping process and (c) centimeter-scale and large-area EGaIn patterns and Georgia Tech logo on physical-surface-modified PDMS substrates fabricated using an additive stamping process.

978-1-940470-03-0/HH2018/$25©2018TRF
DOI 10.31438/trf.hh2018.12

DESIGN AND FABRICATION

Multiscale Liquid Metal Thin-Film Patterning: Subtractive Reverse Stamping and Additive Stamping Processes

Figure 1 (a) illustrates the two complementary multiscale EGaIn thin-film patterning techniques based on soft lithography: (1) a subtractive reverse stamping process relying on chemical surface modification for micro-scale and high-density EGaIn patterns embedded in PDMS microchannels and (2) an additive stamping process for centimeter-scale and large-area EGaIn patterns relying on a physical-surface-modified PDMS substrate. Thereby, physical and chemical surface modifications provide proper wetting and non-wetting surfaces, which enable fine, uniform, and residue-free EGaIn thin films. The chemical surface modification using toluene increases the hydrophobicity of PDMS surfaces, which minimizes EGaIn residue formation and allows them to be readily transferred to a sacrificial PDMS layer. Using the reverse stamping process, molded EGaIn in pre-defined PDMS microchannels showed high-resolution, residue-free, and uniform lines (Figure 1 (b)). On the other hand, the physical surface modification creates a paper-textured PDMS surface, increasing the surface area and ultimately enhancing wettability to form uniform and smooth EGaIn thin films using the additive stamping process (Figure 1 (c)).

In both cases, the fabrication process starts with the selective chemical surface modification of either a PDMS mold or PDMS stamp (optional process) (Figure 1 (a)-i)). The PDMS mold/stamp is then pressed onto a donor PDMS substrate coated with EGaIn and separated from it (Figure 1 (a)-ii)). During the molding process, EGaIn adheres to all surfaces of the PDMS mold/stamp, including concave channels and protruding surface areas. In the next step, the PDMS mold/stamp wet with EGaIn can be reverse stamped to remove EGaIn residues on the protruding surfaces or additive stamped to deposit EGaIn films on the physical-surface-modified PDMS substrate (Figure 1 (a)-iii) and -iv)).

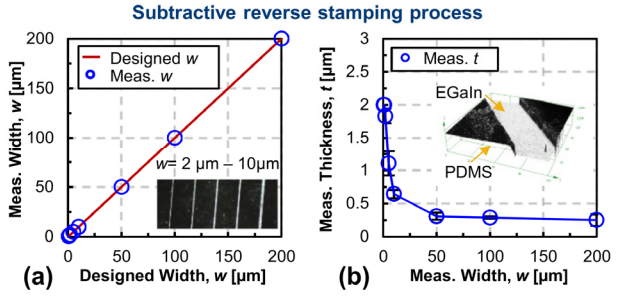

Figure 2: Subtractive reverse stamping process: (a) measured EGaIn width as a function of the designed PDMS mold width and (b) resulting EGaIn thickness as a function of the patterned EGaIn width.

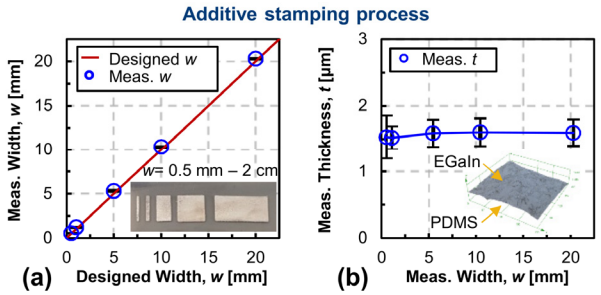

Figure 3: Additive stamping process: (a) measured EGaIn width as a function of the designed stamp width and (b) resulting film thickness as a function of the patterned EGaIn width.

As demonstrated in our previous research [21, 22], the subtractive reverse stamping process yields fine, uniform, and thin EGaIn lines inside of the PDMS channels without residues on the surrounding protruding surfaces, achieving a lateral line width resolution as small as $w = 2$ μm at film thicknesses of $t \approx 1.8$ μm, as shown in Figure 2. The subtractive approach showed size scalability from 2 μm to 1-2 mm in line width. However, for channel widths >2 mm, EGaIn is not effectively transferred to the inside of the PDMS channels because of the sagging deformation of wide channels during the pressure-based molding process. Therefore, the pattern dimensions using the subtractive reverse stamping approach are limited to the single μm to a couple of mm scale.

In contrast, the additive stamping approach provides large-area EGaIn thin-film patterning (Figure 3). In this process, a PDMS stamp wet with EGaIn is stamped onto a paper-textured PDMS substrate. Thereby, the paper texture, which comprises randomly distributed micro cellulose fiber structures, is transferred to a PDMS surface using a conventional PDMS casting method [26]. The resulting paper-textured PDMS exhibits a surface microstructure, which allows it to better wet with EGaIn compared to a normal, smooth PDMS surface (Figure 4). As a result, continuous EGaIn films can be transferred to paper-textured PDMS with multiple stamping steps. The smallest stamped EGaIn feature size was w = 500 μm / $t \approx 1.5$ μm, as shown in Figure 3. While this additive stamping process shows relatively poor lateral resolution, it is very suitable for large-area patterning and thin-film deposition and thus can complement the high-resolution, subtractive reverse stamping process described above.

To evaluate the impact of the physical surface modification, Figure 4 (a)-(b) compare EGaIn wetting properties on a smooth PDMS surface and a paper-textured PDMS surface; clearly, uniform EGaIn films can be patterned on the paper-textured PDMS substrate, while non-uniform EGaIn droplets form on the smooth PDMS substrate. The additive stamping process decreases the surface roughness (R_a) with increasing number of stamping steps (n), which indicates that the stamped EGaIn film is getting smoother and uniformly molded ($t \approx 1.45$ μm at $n = 5$) on the physical-surface-modified PDMS substrate (Figure 4 (c)-(d)).

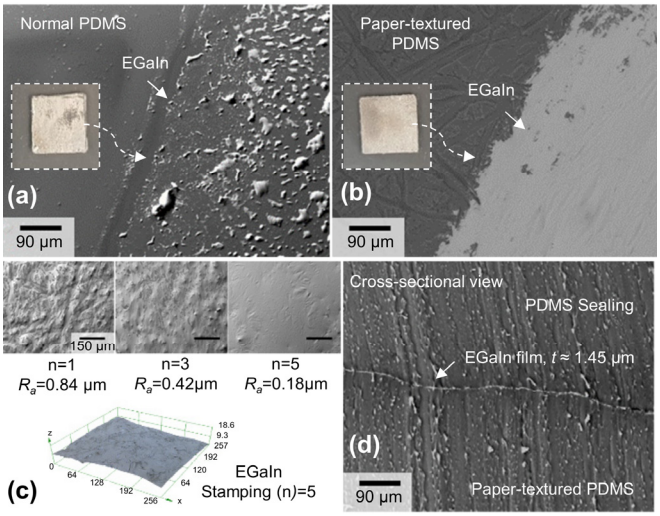

Figure 4: Patterned EGaIn films on (a) a normal, smooth PDMS surface and (b) a paper-textured PDMS surface; (c) surface characteristics of EGaIn thin films as a function of the number of stamping steps (n); (d) cross-sectional view of patterned EGaIn film on paper-textured PDMS after sealing with an additional PDMS layer.

Electrical and Mechanical Characteristics of Fabricated Soft Electronic Devices Using Additive Stamping Process

Using the additive stamping process, soft passive components and circuits were designed and fabricated. Figure 5 (a) shows fabricated soft passive components, such as a resistor (R_{meas} = 16.3 Ω), a planar spiral inductor (L_{meas} = 43.7 nH), and an interdigitated capacitor (C_{meas} = 1.48 pF), all having 1 mm line width and 1 mm line spacing, attached to a non-planar object. One of the main requirements for soft microsystems is to maintain their electronic functionality during mechanical deformation. Thus, we experimentally investigated the electrical functionality by applying bending and stretching forces. Figure 5 (b) shows a simple circuit comprising a 5 × 5 array of light emitting diodes (LEDs). The commercial surface-mount LEDs were manually attached to EGaIn contacts along the patterned EGaIn lines using a tweezer and a stereo microscope for alignment and subsequently sealed using an additional PDMS casting step. Applying a constant current to the soft circuit, the LED array was subjected to bending (bending radius, r = 10 mm) and stretching (strain, $\varepsilon \leq 50\%$) deformation. The soft circuit withstood these bending deformations and strain up to 50% while maintaining its electrical functionality, which also confirmed that the EGaIn thin film was uniformly patterned without voids.

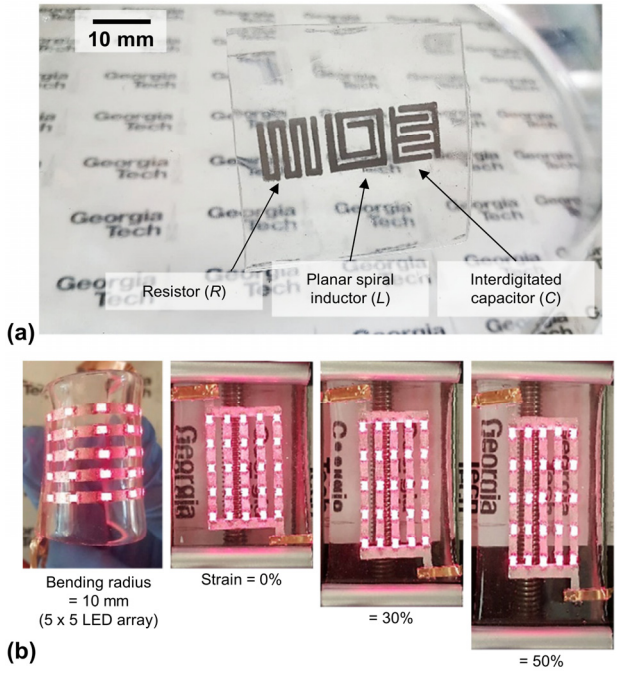

Figure 5: (a) Fabricated soft passive components using the additive stamping process and (b) soft circuit with embedded LEDs (5 × 5 array) operated under bending (bending radius = 10 mm) and stretching (strain ≤ 50%) deformation.

SOFT BIOLOGICAL MICROSYSTEMS

To highlight the multiscale EGaIn patterning capabilities, a fingertip-mountable, soft and 3D-integrated biological sensing platform, comprising a soft sensing layer with an integrated pulse oximeter and a soft interfacing circuit layer, is demonstrated for non-invasive and real-time heart rate and blood oxygen monitoring (Figure 6 (a)). The soft sensor layer is fabricated using the subtractive reverse stamping technique for micro-scale EGaIn patterning to connect an integrated pulse oximeter (MAX30100, Maxim Integrated Products Inc.), while the additive stamping technique is utilized to fabricate the soft printed circuit board (sPCB) for the interfacing circuit (Figure 6 (b)-(d)). The soft sensor and circuit layers are then vertically interconnected through EGaIn soft vias to form a 3D-integrated soft system. Figure 7 shows the measured photoplethysmogram (PPG) waveforms of the infrared (IR) LED and the red LED, as well as the extracted heart rate (HR) and saturation of peripheral oxygen (SpO_2) measured using the PDMS/EGaIn-based soft sensing system (HR = 79 ± 3.6 bpm and SpO_2 = 97%). The results are compared to results obtained using a PCB-based rigid sensing system (MIKROE-2000, Mikro Elektronika Ltd., HR = 79.1 ± 3.1 bpm and SpO_2 = 97%), demonstrating identical sensing performance of the soft microsystem.

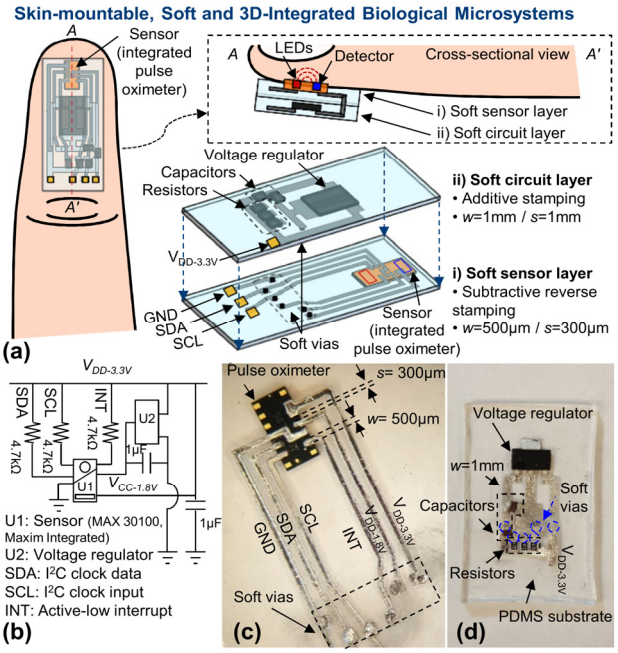

Figure 6: (a) Soft and 3D-integrated biological microsystem using a pulse oximeter mounted on a fingertip for heart rate and blood oxygen monitoring; (b) circuit diagram; fabrication and electric component integration of (c) soft sensor layer patterned using subtractive reverse stamping process and (d) soft circuit layer patterned using additive stamping process.

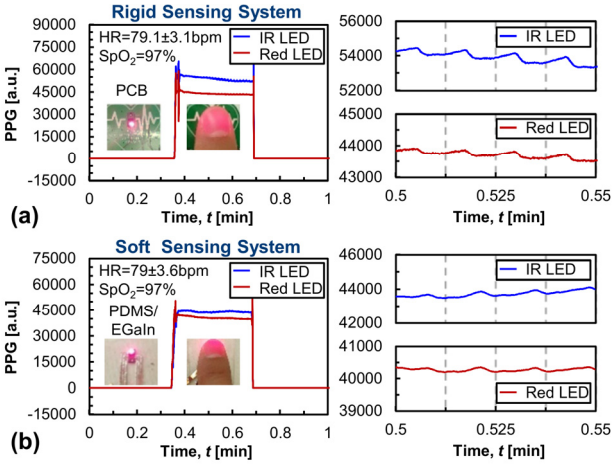

Figure 7: Measured photoplethysmogram (PPG) waveforms of infrared (IR) LED and red LED using (a) PCB-based rigid sensing system (heart rate (HR) = 79.1 ± 3.1 bpm and saturation of peripheral oxygen (SpO_2) = 97%) and (b) PDMS/EGaIn-based soft sensing system (HR = 79 ± 3.6 bpm and SpO_2 = 97%).

CONCLUSION

This paper reports multiscale EGaIn thin-film patterning based on soft lithography by utilizing a subtractive reverse stamping approach for micro-scale and high-density patterns and an additive stamping approach for centimeter-scale, large-area patterns. By combining these complementary patterning techniques, fabricated soft electronic components can be vertically integrated to form high-density and multifunctional soft microsystems for physical, chemical, and biological sensing applications.

ACKNOWLEDGEMENT

This work was performed in part at the Georgia Tech Institute for Electronics and Nanotechnology (IEN), a member of the National Nanotechnology Coordinated Infrastructure, which is supported by the National Science Foundation (Grant ECCS-1542174).

REFERENCES

[1] A. Thomas, "Functional materials: From hard to soft porous frameworks," Angewandte Chemie International Edition, 49, 8328 (2010).

[2] R. L. Truby and J. A. Lewis, "Printing soft matter in three dimensions," Nature, 540, 371 (2016).

[3] A. Chortos and Z. Bao, "Skin-inspired electronic devices," Materials Today, 17, 321 (2014).

[4] M. D. Dickey, "Stretchable and soft electronics using liquid metals," Advanced Materials, 29, 1606425 (2017).

[5] N. Kazem, T. Hellebrekers, and C. Majidi, "Soft multifunctional composites and emulsions with liquid metals," Advanced Materials, 29, 1605985 (2017).

[6] M. D. Dickey, R. C. Chiechi, R. J. Larsen, E. A. Weiss, D. A. Weitz, and G. M. Whitesides, "Eutectic gallium-indium (egain): A liquid metal alloy for the formation of stable structures in microchannels at room temperature," Advanced Functional Materials, 18, 1097 (2008).

[7] M. D. Dickey, "Emerging applications of liquid metals featuring surface oxides," ACS Applied Materials & Interfaces, 6, 18369 (2014).

[8] S. H. Jeong, A. Hagman, K. Hjort, M. Jobs, J. Sundqvist, and Z. Wu, "Liquid alloy printing of microfluidic stretchable electronics," Lab on a Chip, 12, 4657 (2012).

[9] N. Lazarus, S. S. Bedair, and I. M. Kierzewski, "Ultrafine pitch stencil printing of liquid metal alloys," ACS Applied Materials & Interfaces, 9, 1178 (2017).

[10] P. Yong-Lae, C. Bor-Rong, and R. J. Wood, "Design and fabrication of soft artificial skin using embedded microchannels and liquid conductors," IEEE Sensors Journal, 12, 2711 (2012).

[11] Y. Lin, O. Gordon, M. R. Khan, N. Vasquez, J. Genzer, and M. D. Dickey, "Vacuum filling of complex microchannels with liquid metal," Lab on a Chip, 17, 3043 (2017).

[12] J. W. Boley, E. L. White, G. T. C. Chiu, and R. K. Kramer, "Direct writing of gallium-indium alloy for stretchable electronics," Advanced Functional Materials, 24, 3501 (2014).

[13] C. Ladd, J. H. So, J. Muth, and M. D. Dickey, "3d printing of free standing liquid metal microstructures," Advanced Materials, 25, 5081 (2013).

[14] M. R. Khan, C. B. Eaker, E. F. Bowden, and M. D. Dickey, "Giant and switchable surface activity of liquid metal via surface oxidation," Proceedings of the National Academy of Sciences of the United States of America, 111, 14047 (2014).

[15] T. Lu, E. J. Markvicka, Y. Jin, and C. Majidi, "Soft-matter printed circuit board with uv laser micropatterning," ACS Applied Materials & Interfaces, 9, 22055 (2017).

[16] B. A. Gozen, A. Tabatabai, O. B. Ozdoganlar, and C. Majidi, "High-density soft-matter electronics with micron-scale line width," Advanced Materials, 26, 5211 (2014).

[17] I. D. Joshipura, H. R. Ayers, C. Majidi, and M. D. Dickey, "Methods to pattern liquid metals," Journal of Materials Chemistry C, 3, 3834 (2015).

[18] M. A. H. Khondoker and D. Sameoto, "Fabrication methods and applications of microstructured gallium based liquid metal alloys," Smart Materials and Structures, 25, 093001 (2016).

[19] J. A. Rogers and R. G. Nuzzo, "Recent progress in soft lithography," Materials Today, 8, 50 (2005).

[20] D. Qin, Y. Xia, and G. M. Whitesides, "Soft lithography for micro- and nanoscale patterning," Nature Protocols, 5, 491 (2010).

[21] M.-g. Kim, H. Alrowais, S. Pavlidis, and O. Brand, "Size-scalable and high-density liquid-metal-based soft electronic passive components and circuits using soft lithography," Advanced Functional Materials, 27, 1604466 (2017).

[22] M.-g. Kim, H. Alrowais, S. Pavlidis, and Oliver Brand*, "Scalable liquid metal thin line patterning for passive electronic components using soft lithography," in *The 16th Solid-State Sensors, Actuators and Microsystems Workshop*, Hilton Head, USA, 2016, pp. 62-63.

[23] M.-g. Kim, H. Alrowais, C. Kim, P. Yeon, M. Ghovanloo, and O. Brand, "All-soft, battery-free, and wireless chemical sensing platform based on liquid metal for liquid- and gas-phase voc detection," Lab on a Chip, 17, 2323 (2017).

[24] M.-g. Kim, H. Alrowais, and O. Brand, "3d-integrated and multifunctional all-soft physical microsystems based on liquid metal for electronic skin applications," Advanced Electronic Materials, 4, 1700434 (2018).

[25] M.-g. Kim, H. Alrowais, and O. Brand, "All-soft physical and chemical microsystems based on liquid metal for wearable electronics applications," in *The 30th international conference on Micro Electro Mechanical Systems*, Las Vegas, USA, 2017, pp. 1162-1165.

[26] G. Li, M. Parmar, and D. W. Lee, "An oxidized liquid metal-based microfluidic platform for tunable electronic device applications," Lab on a Chip, 15, 766 (2015).

CONTACT

M. Kim, tel: +1-404-317-4892; mgk@gatech.edu
O. Brand, tel:+1-404-894-9425; oliver.brand@ece.gatech.edu

ROBUST AND SCALABLE TISSUE-ENGINEERINED ELECTRONIC NERVE INTERFACES (TEENI)

Cary A. Kuliasha[1,2], *Benjamin S. Spearman*[1,3], *Eric W. Atkinson*[1,4], *Paritosh Rustogi*[1,2], *Abbas S. Furniturewalla*[1,2], *Elizabeth A. Nunamaker*[1,4], *Kevin J. Otto*[1,3], *Christine E. Schmidt*[1,3], *and Jack W. Judy*[1,2,3]

[1]Nanoscience Institute for Medical and Engineering Technology (NIMET), [2]Electrical and Computer Engineering, [3]Biomedical Engineering, and [4]Neuroscience Departments, [4]Animal Care Services, University of Florida, Gainesville, Florida, USA

ABSTRACT

Peripheral nerves are excellent targets for neural interfaces designed to help amputees control prosthetic limbs. However, existing nerve interfaces have designs that significantly limit system performance. To overcome these limitations, we have combined micromachined neural interfaces with tissue-engineered hydrogel-based scaffolds. These tissue-engineered electronic nerve interfaces (TEENI) enable highly scalable nerve interfaces that provide significant interface-design freedom. The use of a high-temperature reactive-accelerated-aging (RAA) soak test sped the identification of a microfabrication processes that can yield robust nerve interfaces. Electrophysiological experiments demonstrate the high-SNR recording performance of chronically implanted TEENI devices.

BACKGROUND

Neurotechnologies that interface portions of the nervous system with implanted electronics have been used to address a wide variety of significant neurological diseases and disabilities. Leading commercialized examples include devices that restore at least a portion of lost sensory function (e.g., cochlear implants to treat deafness, retinal prosthetics to treat forms of blindness, etc.) and devices to recover at least a portion of lost motor function (e.g., deep-brain-stimulation to treat the movement disorders such as Parkinson's disease, peripheral nerve stimulation to reanimate paralyzed limbs, etc.). More recent examples include the use of implantable neurotechnology to stimulate the spinal cord to block pain and to simulate branches of the vagus and other visceral nerves to modulate inflammation and a wide range of autonomic functions. Today, emerging and novel uses of neurotechnology include the treatment of psychiatric conditions (e.g., depression, OCD, PTSD, etc.) and neurologic conditions (e.g., addictions, tinnitus, Tourette's, etc.).

An active field of research is the use of neurotechnology to interface portions of the nervous system with external electronic systems, such as prosthetic limbs for amputees, exoskeletons and other mobility platforms for paralyzed (lower-limb) patients, and computers (e.g., communication, web browsing, etc.) for quadriplegics and other locked-in patients (e.g., ALS, high spinal cord injury, etc.) that are incapable of all (or nearly all) movement. Since these demanding applications benefit from a larger number of channels of independent information, it is not surprising that they have employed the greatest number of electrodes to date (i.e., 100's to 1000's) [1].

Although the primary neuroanatomical target for research on neural interfaces intended to support the control of prosthetic limbs has been the motor-control regions of the brain (e.g., primary motor cortex and dorsal premotor cortex), there are drawbacks to this approach. A key drawback is the fact that interfacing with it at high signal bandwidth (e.g., action potentials from individual cells or local fields potentials from small brain regions) requires invasive brain surgery. This may be acceptable, and indeed the only real option, for locked-in patients, but it is unlikely to be acceptable for amputees. Challenging consequences of using the brain as the target for a motor-control interface include the fact that the representation of the motor system is spread over a large area of the cortex (i.e., many cm^2 for humans) and that the motor-control information is encoded at a higher level of abstraction than the rest of the nervous system. Addressing these challenges can require larger scale systems of greater complexity and likely lower reliability.

INTRODUCTION

For amputees, the peripheral nerve is a much more attractive target than the brain for several reasons: (1) the surgical procedure has less risk and can be more easily revised if needed, (2) instead of skipping all of the neuroanatomy between the amputation and the somatosensory cortex (i.e., spinal cord, brain stem, various brain regions) the neural sensory and motor information is processed by it, (3) as a result the neural sensory-feedback and motor-control information is encoded at a lower level of abstraction in a nerve (e.g., higher firing rates are proportional to greater muscle contractile force and magnitude of sensory percept), and (4) neural information is constrained to geometrically smaller regions (i.e., the cross sections of one or a few mm-scale nerves).

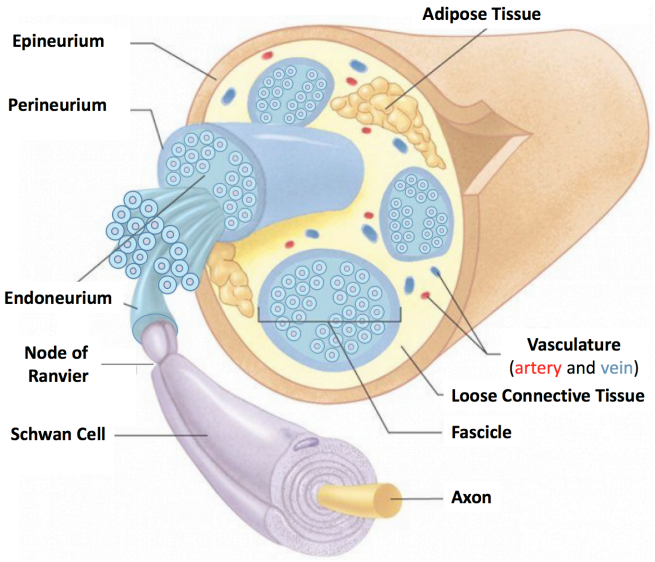

Figure 1. Illustration of the anatomy of a typical peripheral nerve.

Although nerves are not always round, the drawing in Figure 1 highlights key components of the nerve: (a) individual axons that either convey sensory-feedback information up the nerve to the brain from sensory structures or convey motor-control down the nerve to muscles; (b) bundles of axons linked by endoneurium are often grouped into fascicles that are defined by perineurium; (c)

978-1-940470-03-0/HH2018/$25©2018TRF
DOI 10.31438/trf.hh2018.13

vasculature to support the functional viability of the nerve; and (d) epineurium around the outside of the nerve to hold it together. Another critical neuroanatomical feature is that all individual sensory and motor axons associated with movement are myelinated (i.e., they are wrapped by a linear sequence of Schwann cells along its length) to support faster signal transmission. The gaps between adjacent insulating Schwann cells along the fibers, known as the Nodes of Ranvier, are where the dynamic transmembrane currents associated with nerve activity are highly localized. Due to the geometric constraints imposed by the nodes on electrical access to the axon, the nodes represent the strongest signal sources for recording neural activity and also the most sensitive targets for stimulating nerve activity. It is for these reasons that the nodes are the primary targets for neural interfaces designed for peripheral nerves. It should be noted that axon diameter varies significantly (e.g., from 1 to 20 µm) depending on their function and that some axons in a nerve are not myelinated at all and thus conduct signals slowly (e.g., pain fibers).

Although the distribution of the nodes is fairly predictable and regular along an individual myelinated axon (i.e., approximately 100 times the diameter of the axons, thus typically ~1 mm), there is no correlation of node alignment between neighboring fibers. The result is that the nodes, which are the primary targets of electrophysiological nerve interfaces, are arranged in a roughly repeating 3-D "cloud" inside nerves. Unfortunately, nerve interfaces used to date have 1-D or 2-D designs that do not provide for high channel counts of independent sensory and motor-control information. Since nerve cuffs only have a few large electrodes located outside the circumference of the epineurium, they can only capture compound action potentials (i.e., the combined and overlapping signals from 1000's of axons) and typically have a low signal-to-noise ratio (SNR). Although the polymer-based micromachined longitudinal intrafascicular electrodes (LIFE) or transverse intrafascicular multichannel electrodes (TIME) can record from fewer and even individual axons in a nerve, their 1-D design results in significant undersampling. The silicon-based micromachined Utah slant electrode array (USEA), which consists of rows of probes with increasing length, may appear to interrogate every fiber in a nerve, but upon closer inspection it only samples the 3-D cloud of nodes in a 2-D fashion, thus again undersampling it. Regenerative approaches (e.g., sieve electrode array) also sample nerve activity with a 2-D array of electrodes. What's needed is a nerve-interface approach that comprehensively interrogates nerves with 3-D design and can capture the activity of many individual axons with good SNR.

DESIGN

To achieve a 3-D nerve interface, one must find a way to create a 3-D arrangement of electrodes inside a nerve. Ideally this interface would be engineered to minimize foreign-body tissue responses that can limit performance and operational lifetime. One way to do this is by making the interface out of extremely compliant materials and geometric designs to avoid a mechanical stiffness mismatch with nerve tissue (< 100 MPa), which is hypothesized to trigger an exaggerated foreign-body response to the electrodes that can negatively affect their functional longevity [2]. However, such a mechanically compliant design can be extremely challenging to implant in a dense arrangement.

Our novel multidisciplinary solution is to create mechanically compliant, 3-D scalable, and high-performance nerve interfaces through the combination of microfabricated neural-electronic interfaces and key tissue-engineering methods (e.g., multi-component nerve scaffolds engineered to facilitate the successful regeneration of cut nerves across gaps larger than 10 mm) [3]. Specifically, we have developed a hybrid tissue-engineered electronic nerve interface (TEENI), which consists of multi-electrode polyimide-metal-based "threads" embedded into a biodegradable hydrogel composite scaffold that is wrapped in a thin bioresorbable layer of small-intestinal submucosa (SIS) and sutured to the ends of a transected nerve (Figure 2). The multi-electrode TEENI threads are supported by a triple-component hydrogel scaffold, which has mechanical properties designed to hold the TEENI threads in place while also reducing foreign-body response. The hydrogel is also designed to degrade gradually during nerve regeneration and to ultimately be replaced by regrown and maturing axons and vasculature [4].

Since the microfabricated electrode array does not need to be forcibly implanted by itself, it does not need to be made from even temporarily stiff materials nor with a straight buckle-resistant design. Also, since the SIS-wrapped scaffold is handled by the surgeons instead of the TEENI threads themselves, the thickness of the polymer-metal threads could be made much thinner than the 10 µm typically required. Although the TEENI shown in Figure 2 has only a 2-D arrangement of electrodes across 4 "threads", it is possible to stack multiple "thread sets" to achieve a 3-D arrangement of electrodes (see upper right inset image). The TEENI approach has enough design flexibility to accommodate nerves of various sizes and cross-sectional geometries and potentially enough scalability to comprehensively engage with the 3-D distribution of nodes in a nerve.

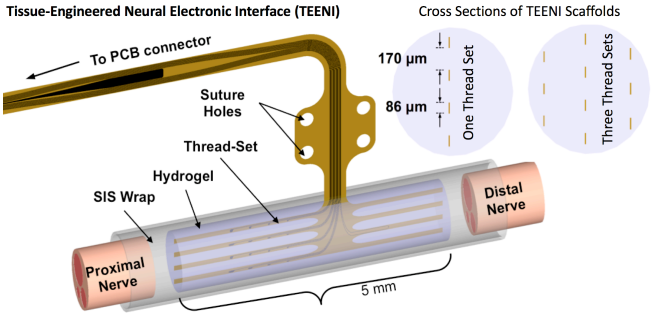

Figure 2: Illustration of a 16-channel TEENI device attached to the ends of a transected nerve. Insets shows 1-mm-diameter cross-sectional views of the construct with a single thread set (4) and a multiple thread-set (3-4-3) arrangement.

FABRICATION

The microfabrication process used to produce the TEENI polymer-metal electrode arrays begins with blank 100-mm diameter silicon wafer. After cleaning in piranha, which forms a thin native oxide layer, the wafers are treated with HMDS and a 5-µm-thick layer of BPDA-PDA polyimide (PI) precursor (U-Varnish S, *UBE Ind.*) is formed by spin coating. After the PI is cured (max temp = 350 ˚C) in a N_2 atmosphere, its surface is activated in a reactive-ion-etching (RIE) O_2 plasma immediately before a 250-nm-thick layer of stoichiometric (1:1 Si:C) a-SiC:H is deposited via PECVD (Unaxis 790, *Plasma-Therm, LLC*) at 300 ˚C and 200 W with 5% SiH_4/He, CH_4, and He gasses (Fig 3a). Using a 3-µm-thick layer of negative photoresist (nLOF 2035, *MicroChemicals GmbH*) as a lift-off mask, a stack of thin metal layers (Ti: 50 nm, Pt: 100 nm, Au: 100 nm, Pt: 100 nm, Ti: 50 nm) are deposited by sputtering (CMS-18 multi-source, *Kurt K. Lesker Company*) (Fig. 3b). After soaking in NMP at 70 ˚C and some sonication, the excess metal is lifted off. A second 250-nm-thick layer of a-SiC:H film is deposited as before (Fig. 3c). Both layers of a-SiC:H are patterned by an SF_6 RIE/ICP dry etch (Unaxis SLR,

Plasma-Therm, LLC.) a thin positive photoresist (AZ1512, *MicroChemicals GmbH*) as the etch mask (Fig. 3d). After the residual surface organics are removed by an O_2 plasma etch, and an aminopropyl triethoxysilane adhesion agent (VM-652, *HD Microsystems*) is applied, a second 5-µm-thick layer of polyimide precursor is formed by spin coating (Fig. 3e). The Pt electrode sites and connector pads are revealed by an RIE/ICP dry etch in O_2 and SF_6 plasmas using a 10-µm-thick layer of positive photoresist (AZ9260, *MicroChemicals GmbH*) as an etch mask (Fig. 3f). To form the shape of the TEENI device, both layers of PI are etched in a single O_2 plasma etch using a 25-µm-thick layer of positive photoresist (AZ9260, *MicroChemicals GmbH*) as an etch mask (Fig. 3g). Finally, the TEENI devices are carefully removed from the carrier wafer using tweezers (Fig. 3h).

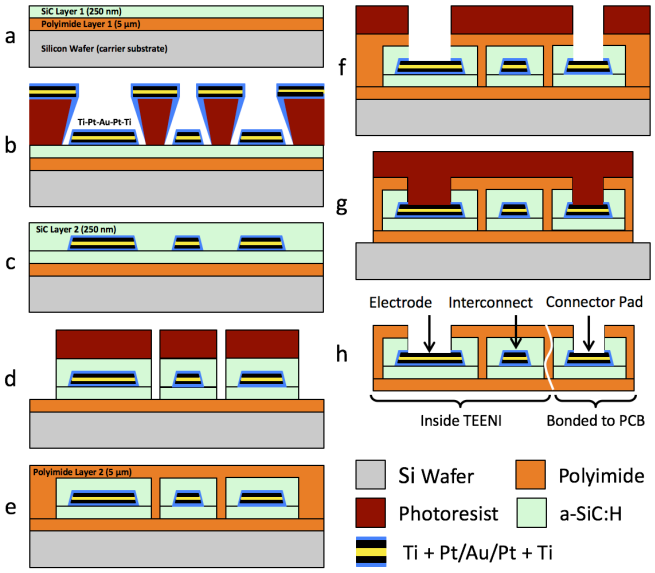

Figure 3: Cross sections of the TEENI microfabrication process.

CHARACERIZATION

To rapidly assess the robustness of implanted electronic devices, it is common to perform soak tests at elevated temperatures. Given the exponential dependence of thermally driven processes on temperatures (i.e., the Arrhenius relationship), raising the temperature from ~37 ˚C (body temperature) to 87 ˚C results in an acceleration factor of ~32X [5]. However, for soak tests to be predictive, the failure modes should be preserved at higher temperatures. For implanted devices, some failures are driven by the aggressive chemical environment (e.g., reactive oxygen species) generated by activated immune cells. However, since the oxygen concentration of saline drops significantly at higher temperatures, it is common for implants to do well with short hot saline-only soak tests and yet fail when implanted for an equivalent time period. A better method is to use a reactive-accelerated-aging (RAA) soak test that employs hydrogen peroxide as a source of reactive oxygen species to simulate the chemistry of the solution surrounding chronic implants [5].

Since delamination of insulating dielectric layers from the conductive metal layers within neural interfaces has been shown to be a significant failure mode, we used RAA soak tests to rapidly assess different combinations of thin films to promote good adhesion between the polyimide and platinum layers in the TEENI [6]. Specifically, we used 10 to 20 mM of H_2O_2 in phosphate buffered saline at 85-87 ˚C and tested for 3 days, which is equivalent to a 3.2-month implantation (ASTM F1980). The results shown in Figure 4 illustrate the significant reduction in impedance (at 1 KHz) observed for different sized electrodes on TEENI made with different combinations of polyimide and various thin adhesion-promoting films. As expected, TEENI made without using an adhesion layer (i.e., for PI-Pt-PI, PI-Pt-Au-Pt-PI) did not maintain electronic integrity (i.e., impedance dropped by 50 to 95%). Although the addition of titanium as an adhesion layer sometimes resulted in improved outcomes (i.e., impedance dropped by 20 to 30%), the combination of silicon carbide and titanium yielded extremely robust results (i.e., impedance changed by < ± 5%). Figure 5 shows that this robustness exists over the entire frequency band of interest for neural interfaces. Subsequent experiments performed for 7 days confirmed the excellent robustness of the PI-SiC-Ti-Pt-Au-Pt-Ti-SiC-PI material stack inside the TEENI devices. To our knowledge, no other peripheral nerve interface has been soak tested as harshly and survived with excellent functionality.

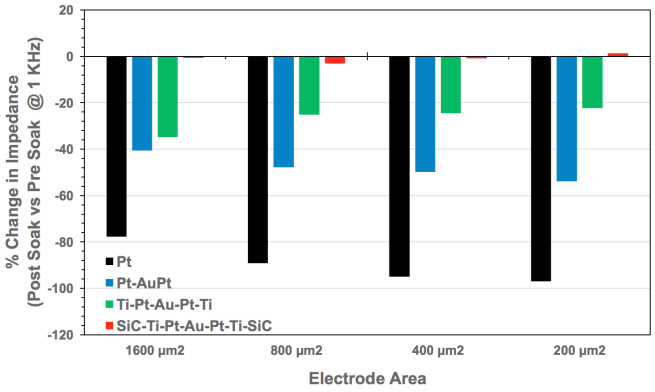

Figure 4. Percent change (reduction) in post-soak impedance (1 KHz) relative to pre-soak values for different sized electrodes.

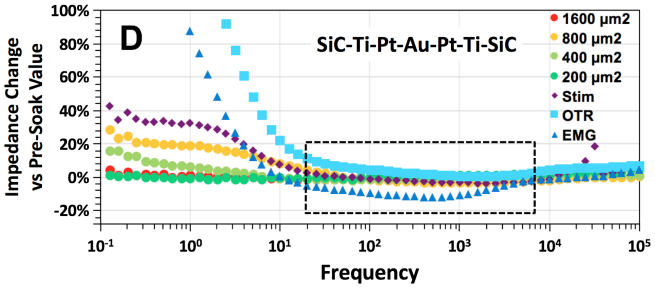

Figure 5. Change in impedance after a reactive-accelerated-aging (RAA) soak test performed at 87 °C with 20 mM H_2O_2 for 7 days (estimated to be equivalent to a 7-months implant). When using SiC and Ti to promote adhesion between the polyimide and the Pt layers, we observed little change in impedance over the frequencies of interest for recording neural signals.

EXPERIMENTAL RESULTS

After the TEENI devices were microfabricated, they were attached to a small circuit board that soldered to a long bundle of fine wires that are soldered on the other end to an external circuit board with a high-channel-count connector convenient for impedance assessment and electrophysiological measurements. Since the small circuit board attached to the TEENI was to be implanted, it was potted in silicone. The implant was then sterilized and the distal TEENI component was integrated into a biodegradable hydrogel composite scaffold that was wrapped in a bioresorbable small intestinal submucosa (SIS) and sutured to the ends of a transected nerve. In our work we used 250 gm Lewis

Rats (LEW/Crl) from Charles River Laboratories (Kingston, NY) and formed a 5-mm-long sciatic nerve gaps that were filled by the TEENI device.

Although we were initially surprised to observe strong single-unit recordings (Figure 6) at the distal electrodes after only 4 days, given that the nerve regeneration rate is ~ 1 mm/day the results are not that unexpected. Recordings with good SNR were observed for 6 weeks (Figure 7), at which point recording was no longer possible due to head-cap failure (i.e., the structure securing the external connector to the implanted TEENI to the skull). Explantation of the TEENI device (Figure 8) revealed that they were well integrated into tissue, exhibited extensive vascularization associated with healthy tissue, and had a significant number and distribution of axons through the scaffold and near the TEENI devices.

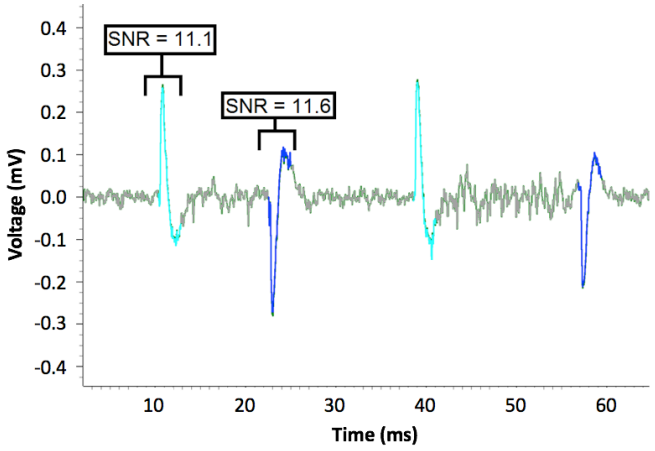

Figure 6. Electrophysiological recording from chronically implanted TEENI device that shows multiple, sortable action potentials from a single electrode.

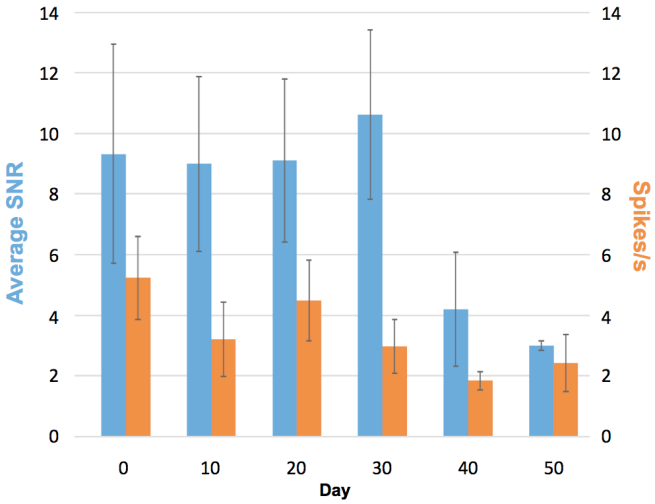

Figure 7: A plot of the signal-to-noise ratio (SNR) of single-unit action potentials and their firing rate versus implant duration.

CONCLUSIONS

By integrating highly compliant micromachined polymer-metal neural interfaces into tissue-engineered scaffolds, it is possible to achieve both a highly scalable and robust nerve interface. Such a nerve-interface design approach is well suited to help amputees control advanced prosthetic limbs with many channels of independent motor-control and sensory-feedback information. Experimental results have shown that single-unit recordings can be obtained from TEENI devices after only 4 days of nerve regeneration and can be maintained for at least several weeks.

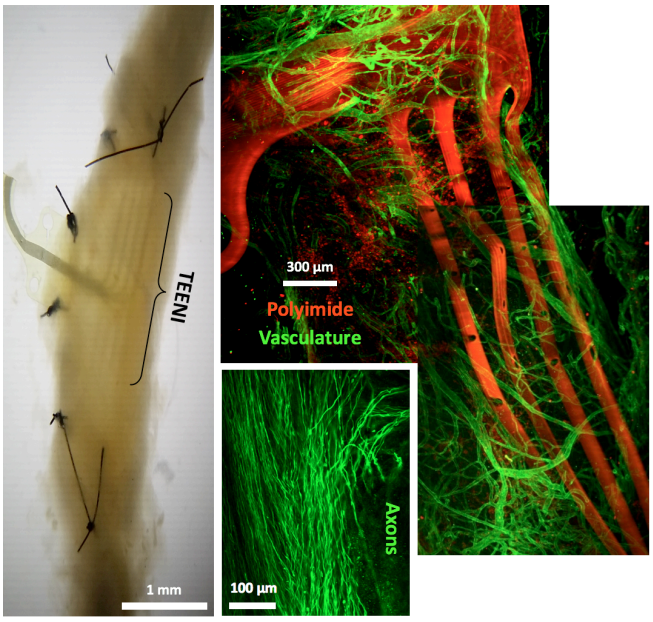

Figure 8: Histological analysis of a TEEN device after a 6-week implantation. (left) Optical microscope image of an explanted nerve that regenerated through a TEENI hybrid scaffold with the microfabricated device visible inside the nerve. (top/right) Lightsheet microscope image of a TEENI device (red) and the vasculature (green) inside a regenerated nerve. (center/bottom) Image of regenerated axons within a TEENI device.

ACKNOWLEDGEMENTS

This work was sponsored by the Defense Advanced Research Projects Agency (DARPA) Biological Technology Office (BTO) Electrical Prescriptions (ElectRx) program under the auspices of Dr. Eric Van Gieson through the DARPA contracts Management Office, Pacific Cooperative Agreement: No. HR0011-15-2-0030. The microfabrication reported here was enabled by the facilities and staff of the University of Florida Research Services Centers.

REFERENCES

[1] J. Collinger, et al., "High-performance neuroprosthetic control by an individual with tetraplegia", *The Lancet*, vol. 381, no. 9866, 2013, pp. 557-564.

[2] R. Biran, et al., "Neuronal cell loss accompanies the brain tissue response to chronically implanted silicon microelectrode arrays", *Exp. Neurol.*, vol. 195, no. 1, pp. 115–126, Sep. 2005.

[2] B.S. Spearman, et al., "Tissue-Engineered Peripheral Nerve Interfaces", Advanced Functional Materials, 2017, vol. 28, no. 12, 2018, p. 1701713.

[4] V. Desai, et al, "Design, fabrication, and characterization of a scalable tissue-engineered-electronic-nerve-interface (TEENI) device", *IEEE Neural Engineering Conference*, pp. 203-206, 2017.

[5] P. Takmakov,…, "Rapid evaluation of the durability of cortical neural implants using accelerated aging with reactive oxygen species", *Journal of Neural Engineering*, vol. 12, no. 2, 2015.

[6] C.A. Kuliasha and J.W. Judy, "*in vitro* Reactive-Accelerated-Aging (RAA) Assessment of Tissue-Engineered Electronic Nerve Interfaces (TEENI)", *IEEE EMBC*, Orlando, FL, 2016.

WIRELESS INTEGRATED MICRO SYSTEMS (WIMS): PAST, PRESENT, FUTURE

Khalil Najafi
Center for Wireless Integrated MicroSensing and Systems (WIMS^2)
University of Michigan, Ann Arbor, Michigan 48109

ABSTRACT

Wireless integrated microsystems (WIMS), also referred to with many names such as IoT/IoE, sensor nodes/motes, or smart nodes, represent portable and stand-alone devices that contain sensors, actuators, signal processing electronics, communication electronics, packaging, and power sources. During the past few years they have become an instrumental part of extending the microelectronics revolution that started many decades ago with the advent of integrated circuits. This paper reviews the past achievements in sensors/actuators, low-power electronics, wireless interfaces, packaging, and provides a perspective on the future trends in both technology and applications for these sensing microsystems and high-performance micro-instruments.

INTRODUCTION

Wireless integrated microsystems (WIMS), also referred to with many names such as IoT/IoE, sensor nodes/motes, or smart nodes, represent portable and stand-alone devices that contain sensors, actuators, signal processing electronics, communication electronics, packaging, and power sources. During the past few years they have become an integral part of many emerging applications and are considered instrumental in achieving the ultimate goal of connecting the world through sensors that can continuously monitor the world around us.

Work on multi-sensor micro-instrumentation systems combining sensors and electronics and wireless interfaces started at Michigan in the early 1990s and led to the demonstration of some of the earliest miniature, low-power, wireless sensor modules [1,2]. The WIMS Center was launched in 2000 at the University of Michigan with funding from the US National Science Foundation to conduct basic research and development of all the critical components of microsystems in areas of sensors/actuators, low-power circuits for signal processing, innovative technologies including RF MEMS for low-power wireless links, new hermetic/vacuum packaging techniques, and active and passive power sources and energy harvesting from the environment [3]. During the past two decades, impressive progress has been made in all these areas. MEMS sensors now provide unprecedented performance at low cost, with performance improvements expected to continue. Extremely low-power circuits for sensor interfaces and signal processing have been demonstrated with nano-watt power levels [4]. New approaches to developing next-generation low-power wireless links based on RF MEMS and low-power micromechanical resonators and circuit techniques have been developed [5-7]. Hermetic and vacuum packaging techniques for MEMS and microsystems have been demonstrated for a number of different microsystems [8]. Low-power sensors from pressure sensors to accelerometers are now available at low-cost and have found many applications. What made this tremendous progress possible, and should we expect this progress to continue? Are there obstacles, and if so what are they? What will be the future trends and applications? This paper will provide a historical perspective of the development of sensors and actuators and their performance trends, fabrication technologies, interface circuits and packaging technologies.

WIRELESS SENSING MICROSYSTEMS

Architecture

Wireless integrated microsystems (WIMS) represent devices that contain sensors, actuators, signal processing electronics, communication electronics, packaging, and power sources, as illustrated in Figure 1 [1,9,10]. Significant progress has been made in each of these areas, and ongoing research promises to produce further significant improvements in each of these areas. It is worth reviewing past and recent progress and discussing future trends in each of these areas.

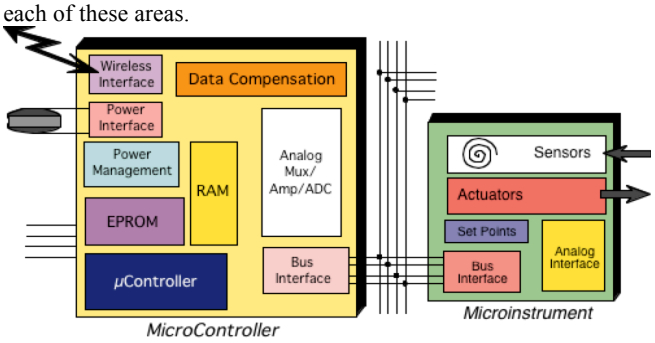

Figure 1: Architecture of a typical sensing microsystem, consisting of front-end sensors/actuators, interface electronics, micro-controller for signal and data processing, a low-power wireless interface, appropriate power source, and packaging suitable for the intended environment (not shown) [1,9,10].

Sensors

Progress in all areas of sensor design, materials, integration, and fabrication technologies has been impressive. MEMS sensors started on the back of silicon-based integrated circuits technologies and have seen the same level of progress in microelectronics.

Performance:

Sensor performance is measured in terms of its resolution (noise) and stability (drift). These and many other performance parameters have seen incredible improvement over time, often much better than those of integrated circuits (IC) as best described by Moore's law. Pressure sensors, inertial sensors, flow sensors, and fluidic components, and many others have improved by more 1.5x per year. An example that the Michigan group has tracked for many years is the performance of inertial sensors [11]. A graph showing performance improvement of MEMS gyroscope was reported in 1998 by the author [11], which illustrated performance improvement of 2x over a period of 10 years up to that time. An updated graph showing an impressive improvement of 1.6x/year over a period of 30 years is shown in Figure 2. The noise in these sensors has improved by a factor of almost 1 million over this period! Although we are approaching the fundamental noise level, further improvements are expected, as our understanding of material properties, device structure and modeling, and circuit readout techniques continue to improve and expand. This continuous improvement is indeed one of the greatest accomplishments of the MEMS and sensor community.

978-1-940470-03-0/HH2018/$25©2018TRF
DOI 10.31438/trf.hh2018.14

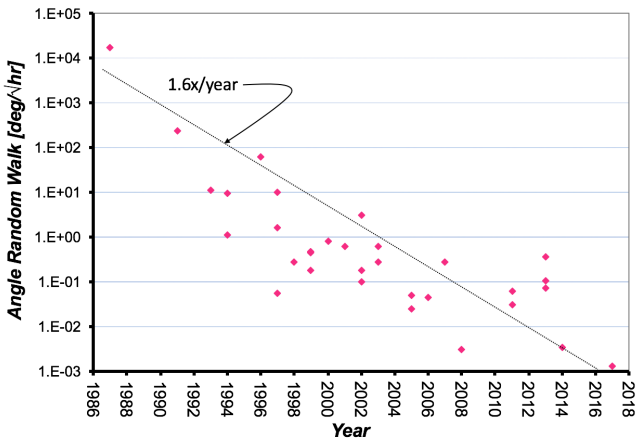

Figure 2: MEMS inertial sensors, such as gyroscopes, have demonstrated at least a factor of 1.6x improvement in their noise over a period of almost 30 years [11].

Materials:

Single-crystal silicon was, and continues to be, the material of choice for MEMS sensors. It is perhaps the best material providing excellent mechanical, thermal, and electronic properties as discussed by Petersen in his seminal paper [12]. Polycrystalline and epi-Si films paved the way for the commercialization of many sensor devices such as accelerometers. Silicon film properties and thickness can now be routinely controlled and reproduced. Other materials such as piezoelectrics (AlN, PZT, ZnO), metals, dielectrics, and polymers are also now routinely utilized in the production of many MEMS components despite early doubts that these materials could be reproducibly utilized in a production environment. Other materials are also finding their way into MEMS devices, including fused-silica [13] and GaN. Although compatibility, ease of deposition, stability, and cost will continue to be issues of concern for these and other new materials, past experience and the need for extending microelectronics beyond the limits of Moore's law clearly indicate that future microsystems will utilize many more materials to realize new functions, improve performance per function, and reduce cost.

Integrate or Not Integrate:

In the early days of MEMS and sensor development, the MEMS community debated whether future commercial sensors needed to monolithically incorporate interface electronics on the sensor chip to further improve performance. Some thought that due to the small sensor signal, and as sensors reduced in size, circuit integration was necessary. Often it was argued that the cost of manufacturing a hybrid system of sensor and circuit chips would be prohibitive. It is clear now that monolithic integration, although preferred, has not been an absolute necessity for either performance or cost. Indeed, this issue has been put to rest for many years with the commercialization of multi-axis inertial sensors, the majority of which are not monolithically integrated. A hybrid system of two separate sensor and circuit chips has been made possible by several factors, including new sensor designs, improved manufacturing techniques, improved readout circuit techniques and technologies, and improved testing and self-calibration approaches.

Heterogeneous integration of silicon ICs with a variety of materials to develop new classes of sensors and microsystems has already started and will certainly continue. These microsystems will advance the state-of-the-art and will help extend microelectronics into many new applications at very low cost and extremely low power.

Three-Dimensional (3D) and Thick Structures:

Early MEMS sensors utilized the entire thickness of a silicon wafer, around 500µm using bulk micromachining [12]. The challenges posed by wet etching techniques limited the range of shapes and dimensions, and led researchers to utilize thin-film polycrystalline silicon on top of a silicon wafer to produce the microstructures needed for a given MEMS function. Polysilicon surface micromachining was indeed a significant advance that liberated the MEMS designer from the limits posed by the crystalline silicon properties and led to the commercialization of the first inertial sensors. However, the limited thickness of polysilicon introduced many other challenges, including limited sensor performance, higher noise, and lower signal. However, these limitations have been largely overcome with the use of SOI and deep RIE etching (DRIE). Figure 3 illustrates the progression of sensor materials used for building truly three-dimensional (3D) silicon MEMS [14]. DRIE silicon etching developed by Laermer and Urban has been an immense capability that had not been imagined until it was introduced in the early 1990 [14]. It has indeed changed the landscape of MEMS, and its impact on MEMS and the IC industry has been impressive. Silicon structures never before imaginable can now been routinely fabricated. This technology has been improved and ultra-deep RIE (UDRIE) is now capable of etching ultra-thick silicon structures with a thickness of 1mm [16]. It is wort noting that by the late 1980s the LIGA process was also introduced and used polymer molds and thick metal electroplating to produce truly 3D and thick MEMS structures [17]. This technology has been widely used to produce many sensor and actuator parts and components.

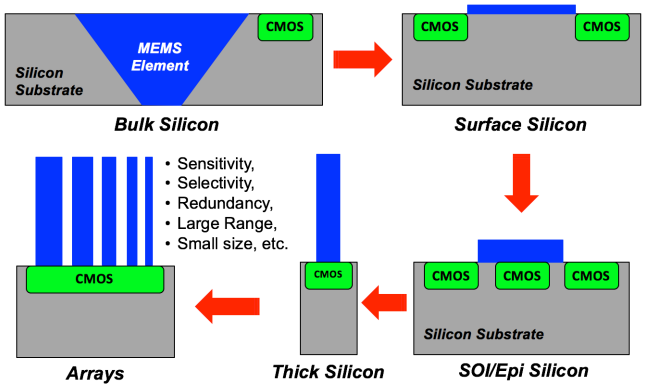

Figure 3: Evolution of silicon MEMs sensors and actuators, from bulk silicon, to thin-film polysilicon, medium thickness SOI silicon, and to very thick DRIE etched bulk silicon [14].

Beyond these wafer-level processes, the MEMS community has also seen impressive growth of a variety of precision mechanical machining techniques, utilizing a variety of approaches such as laser machining, micro electro-discharge machining (µEDM), and ultrasonic machining (USM) [17]. One recent technique used by the author for forming 3D structures from fused-silica is the very old technology of glass blow torching [13]. Extremely high-quality and smooth fused-silica 3D wine-glass resonant structures are fabricated and demonstrated a high quality-factor of almost 10 million [19]. Figure 4 shows the photograph of two fused-silica birdbath resonators with diameters of 2.5 and 5mm, and a thickness in the range of 10-80 µm. Such elegant structures will become more commonplace in the MEMS industry, despite their unconventional materials and fabrication technology.

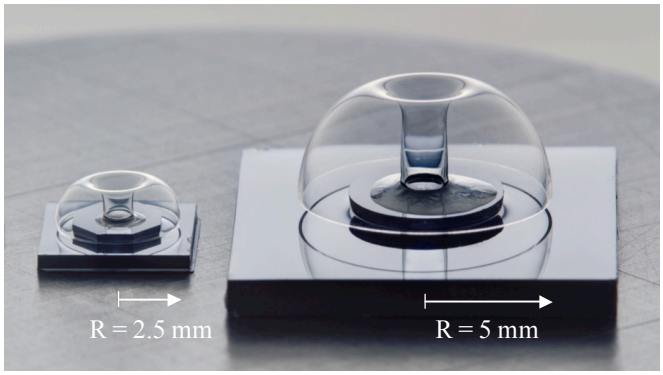

Figure 4: 3D Fused silica micro resonators for use in high-performance gyroscopes fabricated using blow torching [19].

Interface and Signal Processing Electronics

MEMS and microsystems progress would not have been achieved at this level with such speed without the tremendous advancements in integrated electronics. One of the main motivations of developing silicon-based sensors was the potential of interfacing them with electronics. Electronics provide important functions of amplification, filtering, multiplexing, and processing of the acquired data. The IC community has not only realized the predictions provided through Moore's law in terms of density and cost, it has also improved performance. CMOS ICs can achieve low noise, high-speed, and low-power. One of the goals of our program at Michigan from the early days was to demonstrate that future wireless sensor nodes can perform many functions at extremely low power. Millimeter-scale sensor nodes can now provide significant functionality at nano-watt power levels [4,20]. This trend of extremely low-power electronics will continue in the future. There have been several programs aimed at taking advantage of the convergence of extremely high-performance sensors and low-power electronics to develop sensor nodes with near-zero power dissipation, thus enabling continuous sensing and monitoring of specific signals [21].

Wireless Interfaces

RF communication and wireless interfaces have also seen tremendous progress in the past two decades, primarily driven by the mobile phone industry. A variety of protocols from Bluetooth to Zigbe and others have been developed for some sensing applications. For these applications limited range is needed, but power dissipation is critical and needs to be as low as possible. One of the early motivations of RF MEMS was the potential of developing extremely low-power radios by utilizing the high quality mechanical resonance characteristics of micromachined resonators, which are superior to their electronic counterparts by orders of magnitude. The fxQ product for MEMS resonators has continued to improve [5], and nowadays MEMS resonators are used in commercial applications, primarily as timing units, and increasingly in other communication functions [22]. The high Q is a clear advantage for reducing power dissipation. Several different versions of RF MEMS devices have been utilized in the zero-power sensor devices reported by several groups [21]. Extremely low-power radios have been developed for sensor nodes. Nanowatt transceivers with reasonable range have been demonstrated by several groups, including Wentzloff's at Michigan [23]. Figure 6 shows the tradeoff between power and sensitivity. Radios with nano-watt power dissipation and reasonable sensitivity have been demonstrated and are made practical through circuit techniques, IC technologies, use of MEMS timing units, and improved antenna designs.

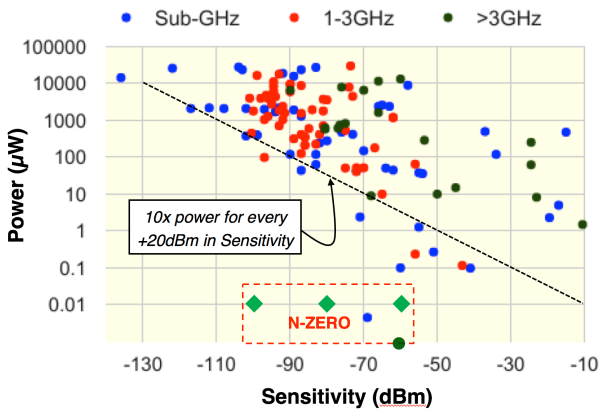

Figure 5: Power dissipation and sensitivity of wireless links [23].

Packaging

Packaging and assembly techniques for MEMS and microsystems have been developed for some applications and being developed for others. There are several key technological challenges in packaging of microsystems. These can be categorized under three general topics of: transducer encapsulation (protection), connection, and assembly as illustrated in Figure 6. MEMS require direct interaction with their surrounding environment. As a result, the device cannot be physically isolated from the surrounding environment and selective access needs to be provided to the sensing/actuating part of the MEMS device. This creates a significant problem for the package. As a result, a lot of effort has been expended on developing the proper protection/encapsulation medium for MEMS. Two general approaches have been taken: the first depends on a package in the form of a shell or capsule that can be bonded to the device substrate as shown in Figure 6; and the second relies on using a thin film material that protects the regions that need protection, while providing access to those that need to interact with the external environment. In either case, the package has to satisfy certain requirements, such as hermeticity, vacuum encapsulation for some applications, ability to provide interconnections to the rest of the system, and ability to protect against harsh environment conditions such as shock, vibration and temperature. Great progress has been made in wafer-level packaging, in sealed feedthroughs and interconnections, and in selective encapsulation. Two challenging areas of stable vacuum packaging and protection against harsh environmental conditions remain. A stable vacuum environment is needed for many devices such as inertial sensors and although a variety of techniques have been demonstrated in research, more work is needed for low-cost vacuum packaging of commercial devices.

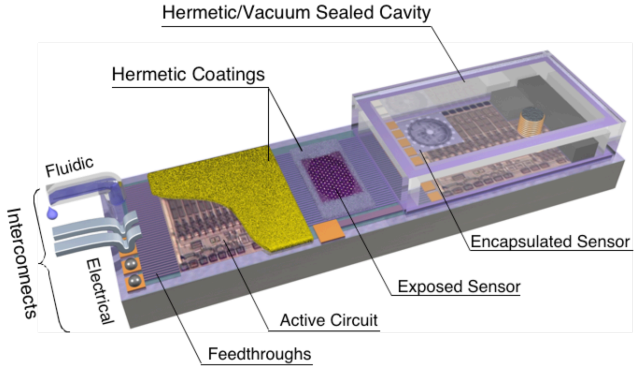

Figure 6: Packaging needs of MEMS/microsystems [8].

FUTURE TRENDS AND CONCLUSIONS

Wireless integrated microsystems (WIMS) have become pervasive in many applications, and will continue to transform many applications ranging from healthcare to environmental monitoring and homeland security. They will help extend connectivity between personal communication devices and the internet to connectivity between us and the environmental directly. MEMS sensors provide excellent performance, and undoubtedly sensors and micro-instruments with better performance will be developed and incorporated into more personal electronic devices from cell phones to wearables to home monitoring systems. The improved performance and enhanced functionality will be made possible through ongoing research on improved understanding of and controlling material properties, heterogeneous integration of sensing with electronics, utilization of integrated and distributed arrays of sensors, and improved design and modeling. Arrays of sensors, integrated on one substrate or distributed over a large area, will be utilized to expand functionality, performance, and stability. Sensing nodes will expand beyond just data gathering and signal processing to information processing and decision making by using machine learning techniques. These techniques can be utilized to generate very accurate information through the use of thousands or millions of medium performance sensors (now routinely available in cell phones and wearables) distributed over a large area. Precision, portable, and low-cost micro-instruments for monitoring chemical, biological, radiological, and physical parameters with performance paralleling bench-top instruments will certainly become available and cost-effective. These chip-scale micro-instruments (CSI) will make enable more applications and will further change the way we interact with our own bodies, the environment around us, and the tools and systems we use to augment many human functions. Past history has taught us that prediction of the future is unreliable. What is certain is that if there is a "pain", researchers and innovators will find an affordable technological remedy. This has been true for MEMS and microsystems. When two decades ago many said that MEMS could not be manufactured and deliver the needed performance, today we have commercial sensors that perform much better than anticipated, and available at much lower cost than predicted. *Smart minds always find smart and simple solutions!*

REFERENCES

[1] A. J. Mason, N. Yazdi, A. V. Chavan, K. Najafi, and K. D. Wise, "A Generic Multi-Element Microsystem for Portable Wireless Applications," (Invited), *Proc. IEEE*, 86, pp. 1733-1746, August 1998

[2] K. D. Wise, "Integrated Sensors: Interfacing Electronics to a Non-Electronic World," *Sensors & Actuators*, *3*, pp. 229-237, July 1982

[3] K. D. Wise, "Realizing the Promise of Wireless MEMS: A Revolution in Information Gathering," *Small Times*, *7*, pp. 18-19, November 2007

[4] Y. Lee, D. Blaauw and D. Sylvester, "Ultralow Power Circuit Design for Wireless Sensor Nodes for Structural Health Monitoring," *IEEE Proceedings*, vol. 104, no. 8, pp. 1529-1546, Aug. 2016

[5] C.T.C. Nguyen, "MEMS technology for timing and frequency control," *IEEE Transactions on Ultrasonics, Ferroelectrics, and Frequency Control*, vol. 54, no. 2, pp. 251-270, Feb 2007

[6] T. Jang *et al*., "Circuit and System Designs of Ultra-Low Power Sensor Nodes with Illustration in a Miniaturized GNSS Logger for Position Tracking: Part II—Data Communication, Energy Harvesting, Power Management, and Digital Circuits," in *IEEE Transactions on Circuits and Systems I: Regular Papers*, vol. 64, no. 9, pp. 2250-2262, Sept. 2017

[7] Roberts N.E., Wentzloff D.D. (2015) Ultra-Low Power Wake-Up Radios. In: Mercier P., Chandrakasan A. (eds) Ultra-Low-Power Short-Range Radios. Integrated Circuits and Systems. Springer, Cham

[8] K. Najafi, "Micropackaging Technologies for Integrated Microsystems: Applications to MEMS and MOEMS," *Proc. SPIE 4979, Micromachining and Microfabrication Process Technology VIII*, (15 January 2003)

[9] D. F. Lemmerhirt and K. D. Wise, "Chip-Scale Integration of Data-Gathering Microsystems," *IEEE Proceedings*, Special Issue on Systems on a Chip, pp. 1138-1159, June 2006

[10] K. D. Wise, "Integrated Sensors, MEMS, and Microsystems: Reflections on a Fantastic Voyage," (Invited), *Sensors and Actuators*, A, pp. 39-50, May 2007

[11] N. Yazdi, F. Ayazi and K. Najafi, "Micromachined inertial sensors," *IEEE Proceedings*, vol. 86, no. 8, pp. 1640-1659, August 1998

[12] K. E. Petersen, "Silicon as a mechanical material," *IEEE Proceedings*, vol. 70, no. 5, pp. 420-457, May 1982

[13] J. Y. Cho, J. K. Woo, J. Yan, R. L. Peterson and K. Najafi, "Fused-Silica Micro Birdbath Resonator Gyroscope (μ-BRG)," *Journal of Microelectromechanical Systems*, vol. 23, no. 1, pp. 66-77, Feb. 2014

[14] K. Najafi, "Biomimetic hair sensors: Utilizing the third dimension," *2012 IEEE Sensors*, Taipei, 2012, pp. 1-4

[15] F. Laermer and A. Urban, "Milestones in deep reactive ion etching," *The 13th International Conference on Solid-State Sensors, Actuators and Microsystems, 2005. Digest of Technical Papers*, pp. 1118-1121 Vol. 2, 2005

[16] Y. Tang, A. Sandoughsaz and K. Najafi, "Ultra high aspect-ratio and thick deep silicon etching (UDRIE)," *2017 IEEE 30th International Conference on Micro Electro Mechanical Systems (MEMS)*, Las Vegas, NV, pp. 700-703, 2017

[17] E.W. Becker, W. Ehrfeld, P. Hagmann, A. Maner, D. Münchmeyer, "Fabrication of microstructures with high aspect ratios and great structural heights by synchrotron radiation lithography, galvanoforming, and plastic moulding (LIGA process)," *Microelectronic Eng.*, pp. 35-56, 1986

[18] Takahata, K., & Gianchandani, Y. B., "Batch mode micro-electro-discharge machining," *IEEE Journal of Micro electro mechanical Systems,* 11(2), 102-110, 2002

[19] T. Nagourney, J. Y. Cho, B. Shiari, A. Darvishian and K. Najafi, "259 Second ring-down time and 4.45 million quality factor in 5.5 kHz fused silica birdbath shell resonator," *IEEE Int. Conf. on Solid-State Sensors, Actuators and Microsystems (TRANSDUCERS)*, Kaohsiung, pp. 790-793, 2017

[20] Y. Chen *et al*., "Energy-Autonomous Wireless Communication for Millimeter-Scale Internet-of-Things Sensor Nodes," *IEEE Journal on Selected Areas in Communications*, vol. 34, no. 12, pp. 3962-3977, Dec. 2016

[21] R. H. Olsson, R. B. Bogoslovov and C. Gordon, "Event driven persistent sensing: Overcoming the energy and lifetime limitations in unattended wireless sensors," *IEEE SENSORS*, Orlando, FL, pp. 1-3, 2016

[22] E. Ng *et al*., "The long path from MEMS resonators to timing products," *2015 28th IEEE Int. Conf. on Micro Electro Mechanical Systems (MEMS)*, pp. 1-2, Estoril, Portugal 2015

[23] F. Asgarian, K. Najafi, unpublished and adapted based on David D. Wentzloff, "Low Power Radio Survey," [Online]. www.eecs.umich.edu/wics/low_power_radio_survey.html

CONTACT

*Khalil Najafi, tel: +1-734-763-6650; najafi@umich.edu

A SIX-LEGGED MEMS SILICON ROBOT USING MULTICHIP ASSEMBLY

Daniel S. Contreras, and Kristofer S. J. Pister
Berkeley Sensor and Actuator Center, Berkeley, California, USA

ABSTRACT

A silicon-based six-legged robot was designed, fabricated, and tested. The robot is based on legs using electrostatic inchworm actuators with force densities of 1.8mN/mm^2 at 100V, a 62% improvement over similar designs previously demonstrated when normalized to V^2. These motors manipulate planar silicon linkages, fabricated alongside the motors in a two-mask silicon-on-insulator (SOI) process. Three of these legs are arranged to actuate off the edge of their fabricated chip. Using pillars with matching through-holes, two of these leg chips are assembled with a central base for mechanical support and electrical routing, totaling 12 motors, 6 linkages, and 12 degrees-of-freedom on the robot. The 3D MEMS assembly process successfully routes 24 separate signals to wires for external control. The robot weighs 200mg and measures 9.6mm wide, 7mm tall, and 13mm long. The robot has walked forward under tethered operation.

INTRODUCTION

Many actuation schemes have been developed for millimeter to centimeter scale terrestrial robots, such as external electric and magnetic fields [1], [2], thermal actuators [3], piezoelectric actuators [4], [5], and electrostatic actuators [6], [7]. Comparing these platforms, robots controlled by external field are dependent on a field source and have limited autonomy. Thermal actuator robots are costly in terms of power draw and have low actuator bandwidth leading to slower operation. Piezoelectric actuator based robots are comparable to electrostatic actuators in terms of power draw and force output, but can have complicated fabrication processes and limited range of travel.

Electrostatic actuators were chosen for this robot due to their low power draw, high force output, long travel and simple fabrication. A single-legged silicon-based robot was previously demonstrated in [8]. This robot relied on electrostatic gap closing actuator (GCA) array based angled-arm inchworm motors based on work in [9]. These motors demonstrated force densities of 0.5mN/mm^2 and have been shown to reach unloaded shuttle speeds of over 30mm/s [10]. The motors manipulated a silicon linkage that actuated off the edge of the chip and had a swept area of approximately 0.5mm x 0.5mm. The robot could walk while connected using long wires to a control and power source.

The robot presented in this work takes a similar version of this leg and uses it as a unit cell for a six-legged robot. Figure 1 shows the robot standing upright. This robot is composed of three separate chips; two leg chips and a top hub chip. Using hand assembly, the robot is constructed from these discrete pieces. It is externally wired to a control and power source through pads on the hub chip, which route the actuator signals from the leg chips.

ROBOT DESIGN

Planar Design Methodology

The design for these robots focuses on using entirely planar mechanisms to develop mobility mechanisms. This takes advantage of the fact that MEMS technology is ideal for fabricating planar mechanisms. It also has the advantage of lending itself to easier fabrication design than previous robots that use complex multi-mask processes to develop out-of-plane joints or depositing piezoelectric materials on complicated topographies. The obvious limitation is that the mechanisms designed in this process can have at most two degrees of freedom.

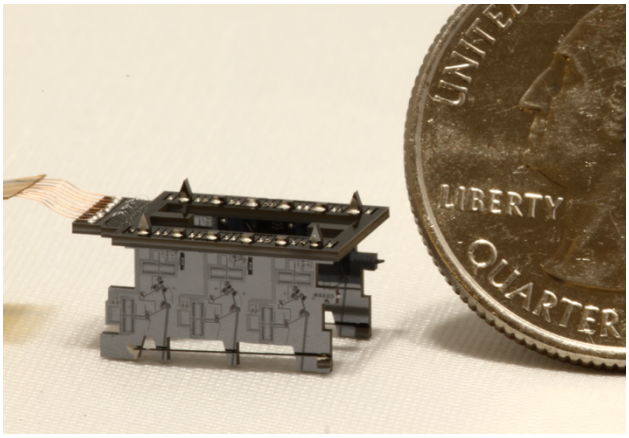

Figure 1: An assembled robot standing upright next to a US quarter

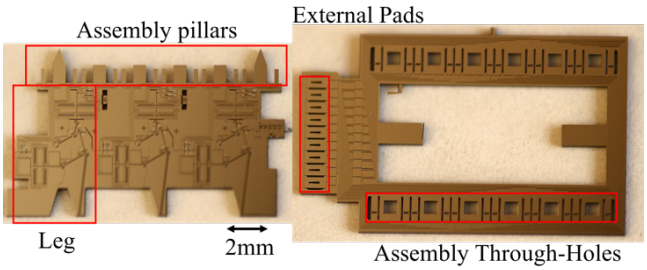

Figure 2: The leg chip, highlighting the leg unit cell and the pillars (left) The hub chip highlighting the assembly through-holes and the pads for external wiring (right)

In order to overcome the planar limitation and actuate on the ground, the robots are designed to extend their legs off the edge of the chip substrate. The entire chip is then flipped on its side to allow for ground actuation. In this way, complex processing is forgone in favor of post-fabrication assembly.

Leg Chip

The leg chip is shown in Figure 2. The leg chips have two main components, the legs and the assembly/routing pillars.

The leg linkage design is similar to the design shown in [8]. The stride length was modified to allow for a longer horizontal sweep when the leg is on the ground. The current stride length is 1mm, twice what was demonstrated before. The linkage also uses newly designed rotary springs. These springs were designed to maintain a constant rotational stiffness through the angular travel of the joint.

Two motors are attached to the leg linkage; one for vertical axis actuation and the other for horizontal axis actuation. The placement of the vertical axis motor was designed to be in-line with the end of the leg linkage for a 1:1 mechanical advantage. This is done in order to maximize the force output as the robot lifts itself. The horizontal axis motor was placed with a 4:1 mechanical advantage, dropping the motor's force output in favor of speed during the robot's horizontal stride. Each leg has 2 degrees-of-freedom, granting the

978-1-940470-03-0/HH2018/$25©2018TRF
DOI 10.31438/trf.hh2018.15

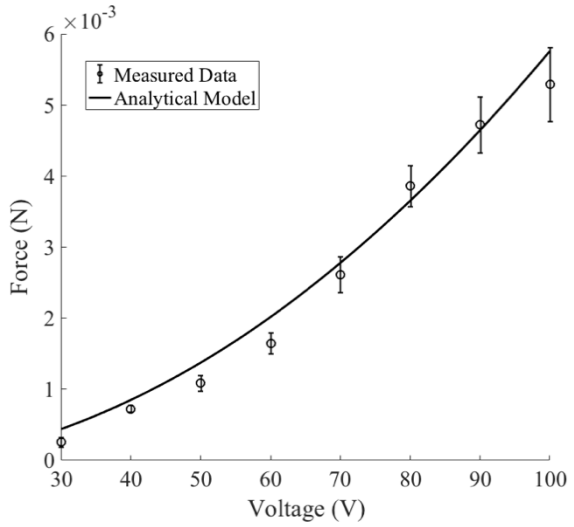

Figure 3: The raw force output of an electrostatic inchworm motor used on the leg chip. At 100V the motor has a force output of approximately 5mN

robot 12 degrees-of-freedom when fully assembled.

The raw force output of the motor is shown in Figure 3. In order to increase the force density of the motor to lift the mass of the robot, the motors were designed using a drawn 1µm feature size between the pawls and the shuttle of the motor. The force was measured using a spring gauge attached to the shuttle. The spring gauge was calibrated using an array of comb drive resonators. The total layout area of the motor measures 2.7mm^2. This leads to a higher force density of approximately 1.85mN/mm^2 while actuating at 100V. Normalizing to V^2, this is a 62% improvement over the previous maximum force density of 1.38mN/mm^2 at 110V [9].

The assembly pillars are shown at the top of the leg chip. The motor signals are routed through wirebonds and silicon to terminate at the pillars. Each motor requires two signals and ground, meaning a single leg requires four signals and a ground. Each leg chip routes 12 signals and ground to the pillars. The ground for each motor is routed to a separate pillar, leaving 18 pillars in total.

The pillars for the high voltage motor signals have the substrate etched from behind them, leaving them as device layer only. The substrate is left behind the ground pillars, since the ground signal is also routed to the substrate. This way they can also be used as durable assembly guides, to protect the fragile device layer pillars.

Hub Chip

The hub chip is also show in Figure 2. The hub chip is meant to fit on top of two adjacent leg chips using a pillar/through-hole assembly technique adapted from work shown in [11].

The purpose of the hub chip is two-fold. First, the hub chip is meant to hold the leg chips upright, such that they can actuate on the ground. Second, the hub chip routes electrical signals from the legs on the leg chip to pads that interface externally with long wire tethers. The robot routes the signals from the legs to demonstrate a dual tripod gait on the robot.

The designed gait and walk cycle of the legs is shown in Figure 4. This gait is hardwired into the routing of the hub chip. For the robot, three legs are actuated in tandem while the remaining set of three legs are actuated out of phase. This gait was chosen because it is statically stable. At any given time, three points around the robot's center of mass are always in contact with the ground.

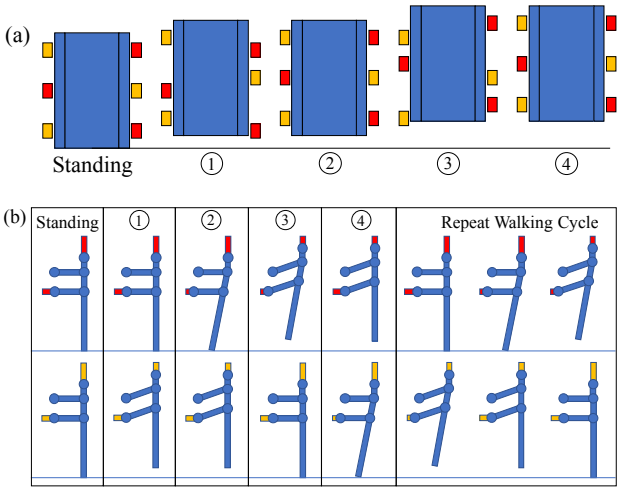

Figure 4: (a) The tripod gait of the robot is shown here. The red squares represent one set of three legs that are actuated in tandem while the orange squares represent the other tripod actuated out of phase with respect to the first set (b) A diagram showing the actuation of the legs. The position of the motors is represented by the colored blocks. The color of the motors and the numbering above the legs matches the colors and numbering in the 5a to correspond to the state of the leg during the robot's state of motion

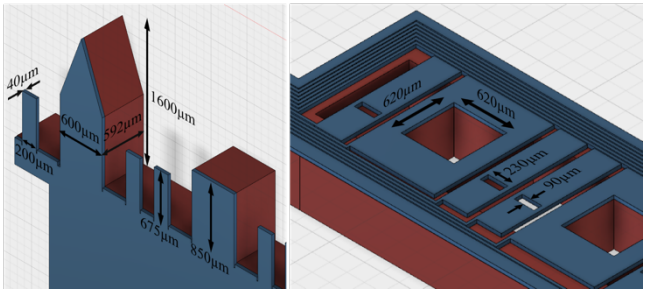

Figure 5: CAD model of chips, detailing dimensions of the pillars (left) and the holes on the hub chip (right)

Pillar Design and Tolerance

Figure 5 details the design and dimensions of the pillars and the holes. There are three types of pillars used in this design; routing pillars for routing the high voltage signals made up of only device layer silicon, square block pillars made of device layer silicon and substrate silicon for mechanical rigidity and to protect the routing pillars, and triangular alignment pillars to align the holes and to gently guide the hub chip into place on the leg chips.

The alignment and block pillars share the same hole size. The hole on the hub chip is designed to have 10µm of tolerance on a given side around the pillars, factoring in the uncertainty in the thickness of the substrate. For the routing pillars, the tolerance is set to 15µm on a given side and 25µm in the dimension of the wafer thickness to account for uncertainty in the substrate thickness. With this larger tolerance, the alignment and block pillars protect the routing pillars as the hub chip falls into place.

FABRICATION AND ASSEMBLY

Processing

All the parts of the robot are fabricated in a two-mask silicon-on-insulator (SOI) process. The SOI wafers have a 40µm device

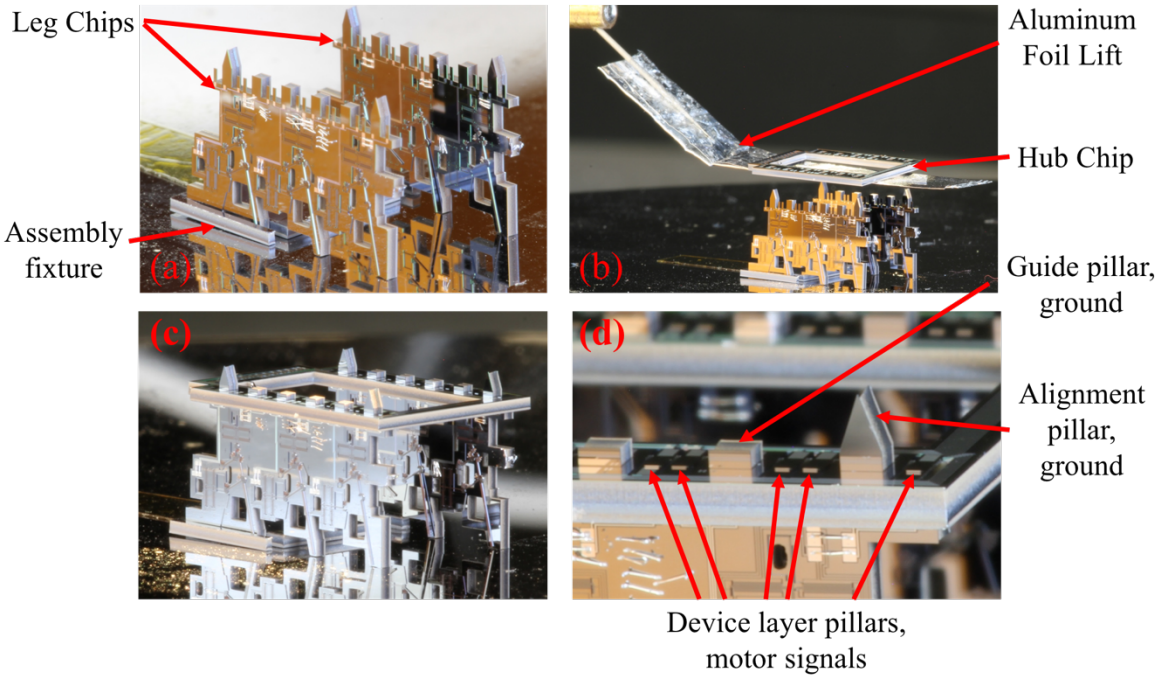

Figure 6: The assembly of the robot (a) The leg chips are held upright in the assembly fixture and are placed underneath a microscope at a probe station (b) The hub chip is placed onto an aluminum foil lift that is glued to a probe tip on a micromanipulator. The holes in the hub chip are aligned to the pillars on the leg chips through the microscope (c) The hub chip is dropped into place and the aluminum lift is removed (d) The pillars are visible through the holes of the hub chip. After the structures are placed correctly, silver epoxy is used to join the pillars and the base around the holes on the hub chip. The assembly is then cured on a hotplate

layer, 2µm buried oxide, and a 550µm substrate. The robot legs, hub chip, and assembly base are patterned into the layer of device layer silicon. The wafer is temporarily bonded to a handle wafer and an etch is performed through the backside of the wafer to reduce the mass of the robot and singulate each of the individual pieces. The pieces are etched in a vapor-phase anhydrous HF etch to release moving parts from the substrate. Once the pieces are released, the chips are wirebonded to route motor signals to the pillars on the leg chips and to route signals to the pads for external connection on the hub chip. The wirebonds are visible in Figure 7 (b) and (c).

Assembly

The assembly process is shown in Figure 6. In addition to the robot chips, additional structures for the purpose of assembly are also fabricated. This includes an assembly base, used to hold the leg chips upright during assembly and a bracket piece to place over the legs to keep ensure they do not come out of plane during actuation. The base is shown in Figure 6 and the leg bracket is shown in Figure 9. The leg chips are manually placed into the assembly base such that they stand upright. This structure is placed at a probe station where a microscope can be used for alignment.

A lift made from folded aluminum foil is glued onto a probe tip which is inserted into a micromanipulator for precision in alignment. The hub chip is manually placed on the lift and positioned above the leg chips. Alignment is performed through the microscope. The holes in the hub chip are positioned such that they line up with the pillars on the leg chips. Once the positioning is correct the hub chip is dropped with the micromanipulator to sit on the leg chips.

The assembly is permanently affixed using silver epoxy to join the pillars to the base of the holes. The epoxy also electrically routes the motor signals between legs that make up each of the tripods and to the hub chip pads. The silver epoxy joints on the pillars are shown in Figure 8.

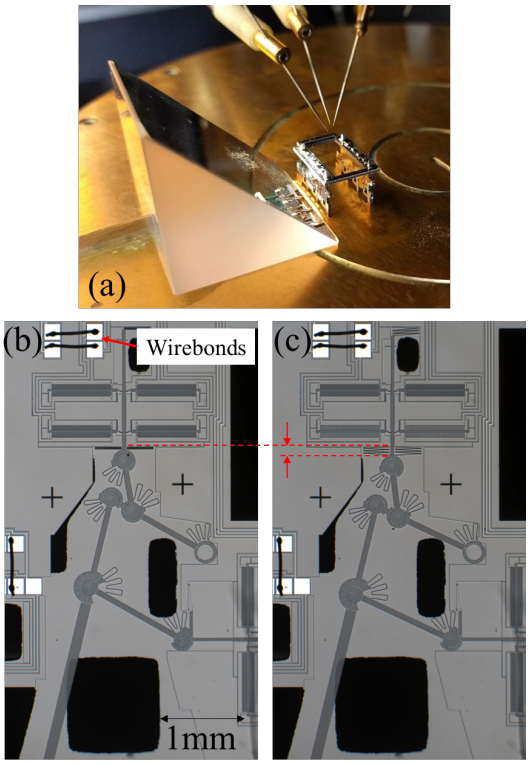

Figure 7: (a) Signals are delivered to the hub chip via probes (b) The unactuated leg seen through the microscope objective off of a 45-degree mirror (c) The leg actuating. The red lines indicate the displacement

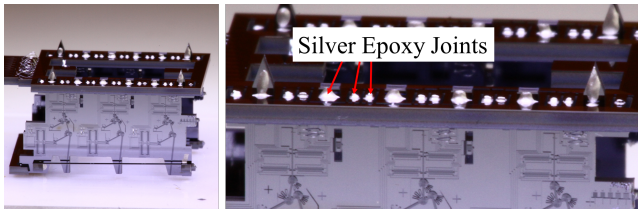

Figure 8: Silver epoxy joints connecting the hub chip to the leg chips

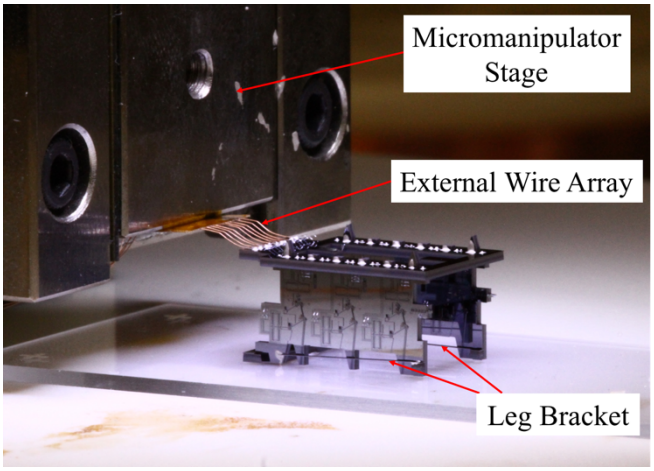

Figure 9: Wiring the robot using a micromanipulator stage

Signal Verification

Once the robot is assembled and the epoxy is cured, it is placed under the probe station to test the connections. A leg actuating through signals to the hub chip is shown in Figure 7. Probes are placed on the hub chip pads to drive each of the motors. A 45-degree mirror is used to inspect the actuation. The silver epoxy on the pillars successfully routes the signals to the correct GCA's through visual inspection of the pull-in voltage.

Wiring

The hub chip has an array of pads extending off the rear of the chip. External wires are connected to these pads. Figure 9 shows the process of wiring-up a robot. An array of 30cm long 60µm thick copper wires are aligned in an array to line up with the pitch of the pads. The ends of the wires are dipped in silver epoxy. The array is held by a micromanipulator and positioned above the pads through a microscope. The wires are than dropped into position on the pads. Once the tips of the wires make contact with the pads, the assembly is cured on a hotplate to cure the epoxy and affix the wires. The other ends of the wires are soldered to a header pin which is inserted into the robot control circuit. After curing, the now wired-up robot can be detached from the micromanipulator.

WALKING

Once the robot is assembled and wired it is placed on a flat surface to walk. Figure 10 shows an assembled robot taking steps. The robot takes two full steps in the sequence shown. This robot had three functioning legs and was able to walk forward using two of the legs which were joined in the dual-tripod actuation scheme. The actuation voltage was 100V

The velocity of the horizontal stride of each step was measured. The first step was 7.5mm/s and the second step was 1mm/s. The motors were actuated at 100Hz, which translates to a horizontal speed of approximately 1mm/s. The first step was faster than

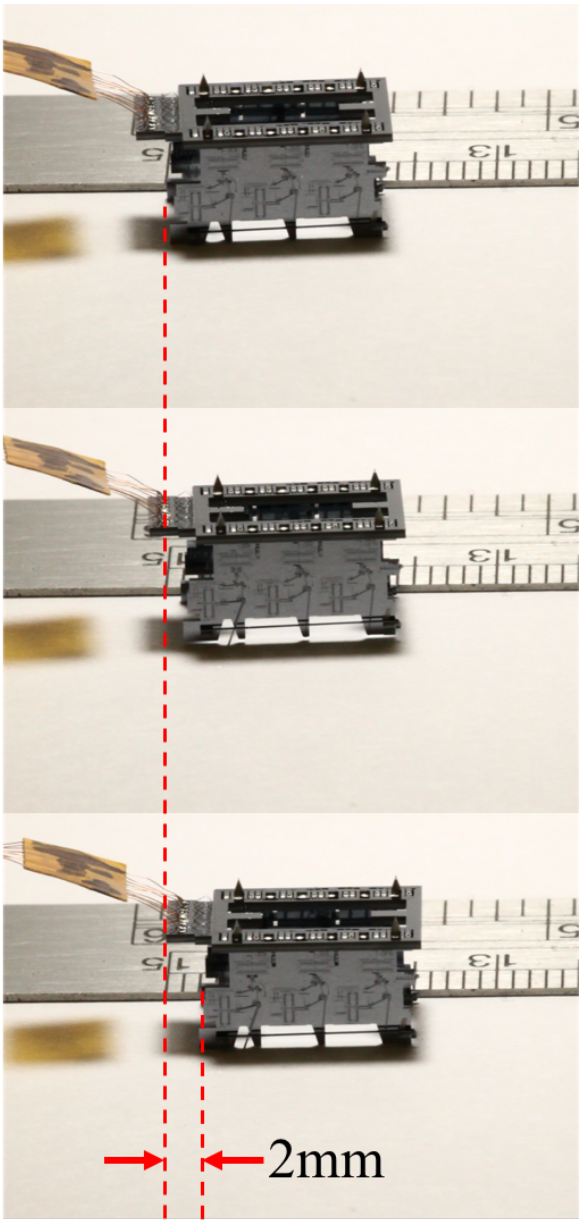

Figure 10: The robot taking steps. In this sequence, the robot takes two steps. Each step moves the robot forward by 1mm. The robot was ultimately limited by tension in the wires and running against the ruler

expected. This could be attributed to the weight of the body carrying the robot forward under the influence of gravity. The robot is designed to drop its mass as it takes its step.

The total capacitive load of a single actuator is estimated to be 26pF when the gaps are fully closed. Operating at 100Hz at 100V this leads to a power draw of 78µW for a single tripod.

In addition to walking forward as designed, the robot also demonstrated repeatable unintentional locomotion schemes. When the leg bracket was not put in place the legs of the robot would splay out of plane upon contact with the ground, and would move the robot to the side, like a crab. The legs would return to their initial position without breaking.

With top motor speeds of 34mm/s demonstrated in [10] and a 4:1 mechanical advantage, the robot could potentially demonstrate

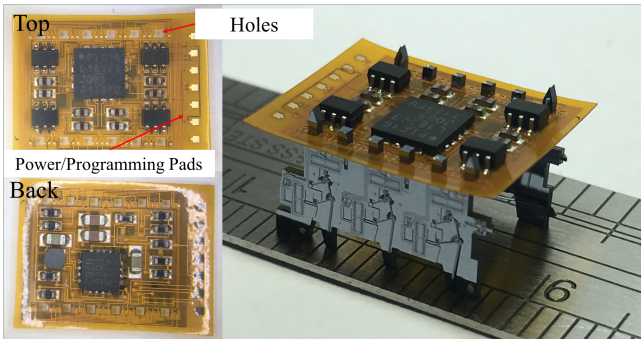

Figure 11: The flexible circuit board. The board has holes that are meant to interface with the pillars on the leg chips in the same way as the hub chip. The top and back of the board are shown. The top has the microcontroller and high voltage transistors while the back of the board has the boost-converter circuit. On the right, a populated board is shown mounted onto the larger pillars of a set of leg chips

top speeds of over 13.6cm/s.

FLEXIBLE CIRCUIT BOARD BACKPACK

In addition to the robot design made entirely of silicon, we have also done work on creating a robot controller and motor driver on a lightweight flexible circuit board substrate, hereby referred to as the robot backpack. The purpose of the robot backpack is to use the most lightweight commercial-off-the-shelf (COTS) and create an on-board controller that is within the robot's payload.

The circuit board is shown in Figure 11. The circuit's mass is approximately 170mg. The backpack operates entirely on a 3.7V source. It uses an LT3482 boost DC/DC converter to generate a 90V signal from the 3.7V source. The high voltage signal is used as the high voltage rail for a network of high voltage transistors through pull-up resistors. These transistors are switched by a PIC16(L)F183XX microcontroller, which was chosen due to mass considerations. The board is meant to generate the high voltage signals for a dual tripod gait. With this board, the number of external connections drops from nine to two after the microcontroller has been programmed. The board has successfully generated an 88V signal that can drive the inchworm motors.

The robot flex backpack has the same array of holes that are on the hub chip. The backpack is meant to interface to the leg chips in the exact same way that the hub chip interfaces to the leg chips. The flexible circuit board was patterned with a 2µm feature size in order to reduce the total size of the board.

CONCLUSION

We have demonstrated successful actuation and steps taken of a six-legged silicon robot made of multiple chips, actuated through long tethers. The robot is able to move forward using only three of its six legs. The multichip assembly process provides reliable routing for the 3D MEMS structure, from the top hub chip to the side leg chips.

Current issues to address with the robot focus on yield and reliability of operation after assembly. Stiction frequently occurs during assembly and while the devices are in operation. This has been attributed to how sensitive the legs are to electrostatic forces and charging causing the legs to snap down and stick to the substrate. Preliminary experiments with self-assembled monolayers, such as FOTS, have shown promising results for preventing in operation stiction. Reduction of the substrate area can also be beneficial for stiction as well as reducing the robot's total mass.

REFERENCES

[1] D. Vogtmann, R. S. Pierre, and S. Bergbreiter, "A 25 mg magnetically actuated microrobot walking at > 5 body lengths/sec," in *Micro Electro Mechanical Systems (MEMS), 2017 IEEE 30th International Conference on*, Las Vegas, Nevada, USA, 2017, pp. 179–182.

[2] B. R. Donald, C. G. Levey, C. D. McGray, I. Paprotny, and D. Rus, "An untethered, electrostatic, globally controllable MEMS micro-robot," *J. Microelectromechanical Syst.*, vol. 15, no. 1, pp. 1–15, 2006.

[3] K. Saito, K. Iwata, Y. Ishihara, K. Sugita, M. Takato, and F. Uchikoba, "Miniaturized Rotary Actuators Using Shape Memory Alloy for Insect-Type MEMS Microrobot," *Micromachines*, vol. 7, no. 4, p. 58, Mar. 2016.

[4] A. T. Baisch, O. Ozcan, B. Goldberg, D. Ithier, and R. J. Wood, "High speed locomotion for a quadrupedal microrobot," *Int. J. Robot. Res.*, vol. 33, no. 8, pp. 1063–1082, 2014.

[5] J. Choi *et al.*, "Thin-film piezoelectric and high-aspect ratio polymer leg mechanisms for millimeter-scale robotics," *Int. J. Intell. Robot. Appl.*, vol. 1, no. 2, pp. 180–194, Jun. 2017.

[6] S. Hollar, A. Flynn, C. Bellew, and K. S. J. Pister, "Solar powered 10 mg silicon robot," in *Micro Electro Mechanical Systems (MEMS), 2003 IEEE 16th International Conference on*, Kyoto, Japan, 2003, pp. 706–711.

[7] M. Qi, Y. Zhu, Z. Liu, X. Zhang, X. Yan, and L. Lin, "A fast-moving electrostatic crawling insect," in *Micro Electro Mechanical Systems (MEMS), 2017 IEEE 30th International Conference on*, Las Vegas, Nevada, USA, 2017, pp. 761–764.

[8] D. S. Contreras, D. S. Drew, and K. S. Pister, "First steps of a millimeter-scale walking silicon robot," in *Solid-State Sensors, Actuators and Microsystems (TRANSDUCERS), 2017 19th International Conference on*, 2017, pp. 910–913.

[9] I. Penskiy and S. Bergbreiter, "Optimized electrostatic inchworm motors using a flexible driving arm," *J. Micromechanics Microengineering*, vol. 23, no. 1, p. 015018, Jan. 2013.

[10] D. S. Contreras and K. S. Pister, "Dynamics of electrostatic inchworm motors for silicon microrobots," in *Manipulation, Automation and Robotics at Small Scales (MARSS), 2017 International Conference on*, 2017, pp. 1–6.

[11] G. Xue, M. Toda, and T. Ono, "Comb-Drive XYZ-microstage With Large Displacements Based on Chip-Level Microassembly," *J. Microelectromechanical Syst.*, vol. 25, no. 6, pp. 989–998, Dec. 2016.

CONTACT

*D.S. Contreras, dscontreras@berkeley.edu

A 3D-PRINTED 1 MG LEGGED MICROROBOT RUNNING AT 15 BODY LENGTHS PER SECOND

Ryan St. Pierre[1], Walker Gosrich[2], and Sarah Bergbreiter[1]*
[1] Department of Mechanical Engineering and the Institute for Systems Research, University of Maryland, College Park, Maryland, USA
[2]Department of Mechanical and Aerospace Engineering, The State University of New York at Buffalo, Buffalo, New York, USA

ABSTRACT

This work presents an experimental platform for studying the locomotion of small-scale (<100 mg) legged microrobots. Robot chassis were fabricated with microscale 3D printing and embedded permanent magnets provide actuation. The design integrates a full rotational friction bearing in the hip joint, capable of actuation up to 150 Hz with no visible signs of wear after rotating at 100 Hz for over 1,000,000 cycles. The robot presented in this work weighs 1 mg and is observed running at speeds up to 37.3 mm/s (14.9 body lengths per second) providing initial insights on the dynamics of legged locomotion at ant-scales.

INTRODUCTION

Empirical biological scaling laws show an increase in relative velocity (body length per second) with decreasing body mass [1]. However, as robots are scaled down, their relative speeds pale in comparison to biological counterparts. An understanding of the dynamics of legged locomotion at insect scales is needed to inform design and control of microrobots. Large-scale robots, such as RHex (7 kg) [2], provide a platform for understanding both the morphology and control of legged locomotion. The large size of RHex enables versatility and flexibility within the platform, allowing design components, such as legs, to be changed easily. By incorporating microscale 3D printing with magnetic actuation, this work provides a versatile platform to study legged locomotion of robots with a mass over 1,000,000 times smaller than RHex. The final robot tested in this work is shown in Figure 1.

Making ant-scale microrobotics, specifically robots less than 100 mg in body mass, is an impressive feat in itself. One of the more successful microrobots, an 80 mg thermally actuated microrobot, presented in [3] used thermal actuation to raise and lower legs. However, the stride length and stride frequency of this robot was limited, showing top speeds up to 6 mm/s (0.8 body lengths per second). The 10 mg solar powered microrobot presented in [4] incorporated actuation, control, and power to achieve a robot capable of autonomous movement, although not appreciable forward propulsion. More recently, the walking robot (18 mg) presented in [5] incorporated electrostatic actuators to generate foot paths in vertical and horizontal directions and demonstrated speeds up to 0.7mm/s (0.15 body lengths per second).

These same microrobots can serve as physical models for understanding milligram-scale legged locomotion. Legged robots with lead zirconate titanate (PZT) were developed to investigate the dynamics of contact interactions in microrobotic legs [6], with more recent, similarly structured, legged microrobots weighing 4.4 g and 379 mg demonstrating walking at 0.06 body lengths per second and 0.1 body lengths per second, respectively [7]. The 25 mg robot fabricated in [8] incorporated compliant materials to create a microrobot with passively articulated legs. By taking advantage of the passive degrees of freedom and incorporating magnetic actuation this robot achieved top speeds of 5 body lengths per second.

Similar to the experimental platform presented in [9], this work takes advantage of 3D printing to create a chassis for a legged robot. By incorporating permanent magnets as a form of wireless actuation the mechanical aspects of legged locomotion can be studied. Additionally, magnetic actuation provides insights into the torque requirements as well as the mechanical power required to achieve motion.

Figure 1: Fabricated 1 mg, 2.5 mm x 1.6 mm x 0.7 mm quadrupedal microrobot pictured with a desiccated bullet ant head (Paraponera clavata).

ROBOT DESIGN AND FABRICATION

The robot design is similar to RHex [2] and the quadrupedal robots presented in [9]. Each leg of the robot is shaped like a "C", providing a rolling contact with the ground. A friction bearing at each hip enables a full rotary motion of the leg from the torque on an embedded permanent magnet.

The microrobots were fabricated using direct laser writing for 3D printing at the microscale. The process is described in Figure 2. A sacrificial layer of 20% dextran (Dextran 70 Sigma-Aldrich) was spin-coated on to an ITO-coated glass slide (Nanoscribe) at 1,500 rpm for 1 minute (Figure 2A). The microrobot structure is patterned using dip-in laser lithography (DiLL) with a Nanoscribe Photonic Professional GT using the 25X objective (Carl Zeiss Microscopy) and a negative tone photoresist (IP-S Nanoscribe). After printing, the microrobots were developed in propylene glycol monomethyl ether acetate (PGMEA) for 2 hours. The slide was removed from the PGMEA bath and rinsed with isopropyl alcohol (IPA) to wash away the PGMEA and excess photoresist. The microrobots were released from the sacrificial layer by dissolving the dextran with deionized (DI) water. The microrobots were then

978-1-940470-03-0/HH2018/$25©2018TRF
DOI 10.31438/trf.hh2018.16

placed in a bath of IPA and sonicated overnight in a heated bath (3510 MTH Branson) to remove any excess photoresist in the rotary joints of the robot. Once fully cleaned, 250 µm cube magnets (C0005-10, SuperMagnetMan) were manually placed in the hip joints and secured with cyanoacrylate (Loctite 401). The final fabricated robot is shown in Figure 1. The orientation of the dipoles of the embedded magnets mechanically programs the gait for the microrobot. In this work, the dipoles were aligned in the same direction, creating a pronking (4-legged hopping) gait.

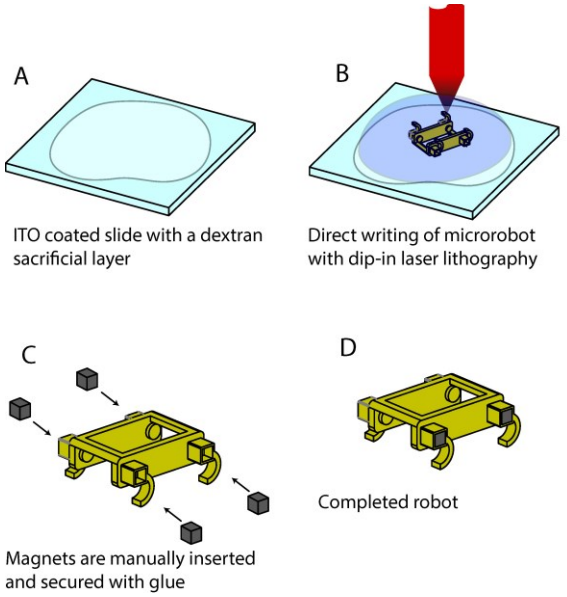

Figure 2: Fabrication process for direct laser writing and embedded permanent magnets for actuation.

EXPERIMENTAL SETUP

Robots were actuated in a custom-made two-axis Helmholtz coil system, used to generate a two-dimensional rotating magnetic field, providing a torque on the embedded magnets and actuating the legs. A schematic of the interaction is shown in Figure 3. The coil brackets are 3D printed (UPrint Plus SE Stratasys) and wrapped with 22 gauge enameled magnet wire. The vertical coil pair has a nominal diameter of 120 mm and 60 turns of wrapping, while the horizontal pair has a nominal diameter of 160 mm and 50 turns of wrapping. To create a rotating magnetic field, each channel of a 2-channel arbitrary function generator (AFG3022C Tektronix) was connected to a current amplifier (TS200-0A Accel Instruments). The output of each channel of the function generator is set to balance the coils, creating a symmetric rotating field with a magnitude of 0.78 mT. The dipole of the 250 µm cube magnets was estimated from the volume and material of the magnets as 17.8 A-mm^2. Using the point-dipole model in [10], the maximum applied torque is calculated as

$$\tau_{max} = \mu_0 h\, m_r. \qquad (1)$$

Where μ_0 is the is the magnetic permeability, $\mu_0 = 4\pi \times 10^{-7}$ N/A^2 (in vacuum), h is the magnetic field from the coil, and m_r is the magnetic dipole of the embedded permanent magnets. The maximum applied torque was calculated as 13.8 µN-mm.

To track the motion of the robot, the robot was filmed in the sagittal plane with a high-speed camera (Fastcam UX100) at 1,000 fps equipped with a macro lens (Zeiss Makro-Planar T* 2/100mm ZF.2 Macro Lens). The field of view of the macro lens was approximately 19 mm wide, accommodating 7.5 body lengths of travel. The motion of the robot was tracked using markerless tracking software (TEMA Image Systems).

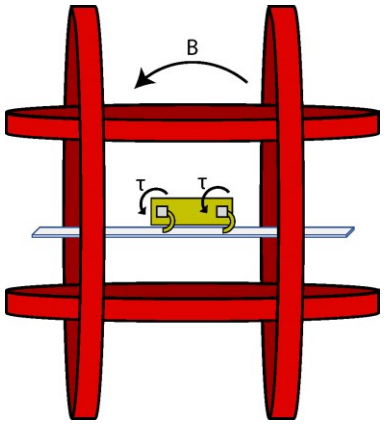

Figure 3: The microrobot is actuated in a rotating magnetic field (B), resulting in a torque applied to each of the embedded magnets in the hip joints. The vertical and horizontal components of the magnetic field are generated from each coil pair.

CHARACTERIZATION OF 3D PRINTED ROTATIONAL BEARINGS

Fully rotational microdevices are limited in their performance by surface forces, such as friction, while solid-solid interfaces in rotating parts often suffer from wear, further decreasing performance. To minimize the effect of friction in rotary devices, contact needs to be limited by either micro-ball bearings [11], hydro-dynamic bearings [12], air bearings created through magnetic or electrostatic suspension [13,14], or a liquid film [15,16]. While most of these strategies require complex manufacturing processes with tight tolerances, the bearings used in this work were printed monolithically, requiring only a single fabrication step. A solid model and photograph of the bearing is shown in Figure 5.

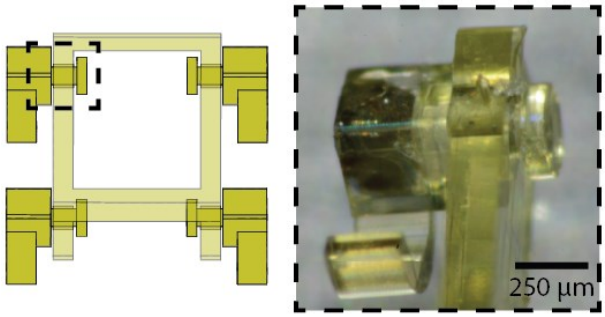

Figure 4: (left) CAD illustration showing the embedded legs within the (transparent) body to create a monolithic bearing. (Right) Photograph of printed component.

Startup torque

The startup torque is the minimum torque applied for the leg to start moving and overcome static friction within the joint. The startup torque was found by positioning the leg both downward and upward, to compensate for any gravitational effects, and energizing the horizontal coil pair to apply a maximal torque to the leg. The coils are powered by a 420 W power supply (Sorensen XPF60-20 DPF) slowly increasing the voltage until the leg moves and the corresponding current is recorded. The applied voltage and

current to the coil is 1.63±0.02 V and 0.55±0.00 A, resulting in a field of 0.31 mT, and a calculated start up torque of 5.47 µN-mm.

Actuation response

The robot was suspended without ground contact and actuated from 10 Hz to 180 Hz in 10 Hz increments. High-speed video of the leg rotating was recorded at 2,500 fps (Fastcam UX100) and processed in markerless tracking software (TEMA Image Systems) to determine the average rotational speed. Figure 5 shows the average rotational speed of the leg as a function of the driving frequency of the coil system. The leg rotation matches the actuation frequency up to 150 Hz. At higher frequencies, the rotation of the leg is no longer in sync with the rotating field. Higher rotation frequencies can be achieved with a stronger magnetic field or by reducing the friction in the joint, though neither is explored here. A lumped parameter approximation of the viscous damping can be estimated from [11],

$$\omega_{S-O} = \frac{\tau}{c} \quad (2)$$

where ω_{S-O} is the step-out frequency when the magnets are no longer in sync, τ is the maximum applied torque, calculated from eq. 1, and c is the viscous damping. The viscous damping in the system was calculated as 13.7 µN-µm-s/rad.

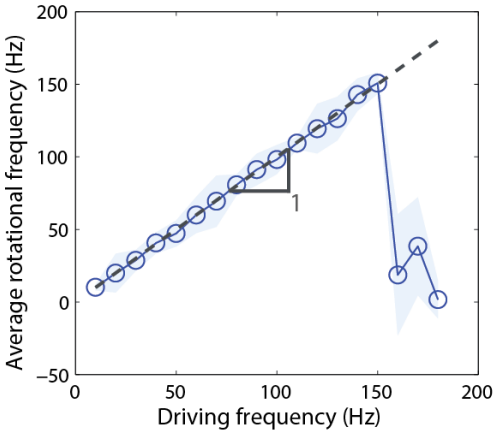

Figure 5: The average rotational frequency of a leg of the microrobot not in contact with the ground vs rotating magnetic field frequency. The solid line represents the average and the shaded area represents the standard deviation over more than five rotations. The dashed line visualizes when the rotational frequency of the leg is equal to the driving frequency.

Wear

The leg was actuated at 100 Hz for three hours, corresponding to over 1,000,000 cycles. A high-speed video taken at 2,500 fps was recorded at 30-minute intervals, corresponding to 180,000 cycle intervals. The data was processed in TEMA to determine the average rotational speed of the mechanism at each video capture. Figure 6 plots the average rotational speed at each 30-minute interval with the shaded area corresponding to one standard deviation. Overall, the average performance does not decrease over 1,000,000 cycles. However, the relatively large, approximately 15 Hz, standard deviations are a combination of both tracking error and frictional properties in the joint, though no visible signs of wear were observed.

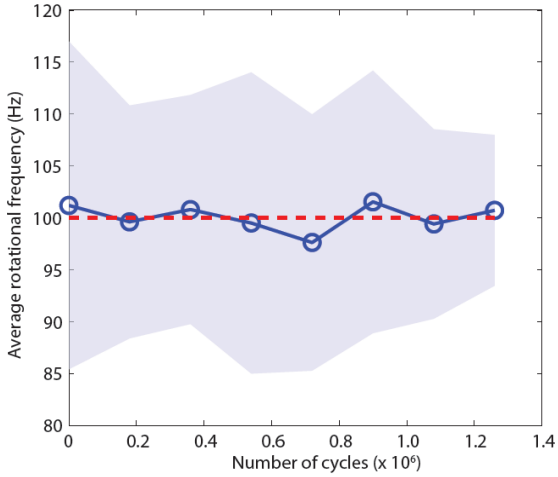

Figure 6: The average rotational frequency (solid line) and standard deviation (shaded area) over ten rotations of the leg actuated at 100 Hz (dashed red line) captured at 30 minute intervals (180,000 cycle intervals).

LOCOMOTION RESULTS

The average horizontal velocity of the robot is shown in Figure 7. The solid line corresponds to the average value, while the shaded area represents one standard deviation over 3 trials for one robot. The maximum observed velocity of 37.3 mm/s (14.9 body lengths per second) occurs at an actuation frequency 35 Hz. Video stills of the robot running at 23.8 mm/s (9.52 body lengths per second) are shown in Figure 8.

The average velocity is approximately linear from 5 Hz to 30 Hz, suggesting that this portion of locomotion is governed largely by the kinematics of the robot design; as frequency increases, horizontal velocity increases proportionally. The slope of this linear fit corresponds to the stride length and is calculated as 0.88 mm, or 0.35 body lengths. In this kinematic dominated regime, changing the effective length of the legs in the robot would provide a longer stride length, and ultimately faster locomotion.

As stride frequency is increased beyond 35 Hz, the velocity performance begins to drop, and becomes more inconsistent with larger variation between trials. In this regime, the robot locomotion is more dynamic, as opposed to kinematic; however, the body dynamics are unfavorable for high-speed running. The robot body was perpetually pitched downward, and the robot propels itself forward with the back legs, rather than performing the pronking gait. During this downward pitched posture, the front of the robot body maintains contact with the ground, reducing the speed of the robot.

At this size scale, surface forces often dominate inertial forces. The Reynolds number (*Re*) describes a ratio of surface forces to inertial forces and is calculated by

$$Re = \frac{\rho v D}{\mu}, \quad (3)$$

where v is the velocity of the robot, D is the characteristic length, in this case, body length, and µ is the dynamic viscosity of air ($1.18\text{x}10^{-5}$ kg m^{-1} s^{-1}), and ρ is the density of air (1.23 kg m^{-3}). At the top speed, the Reynolds number is 9.71, signifying that the robot is operating under laminar conditions. Using Stoke's law, an estimate of the drag force is calculated by

$$F_D = \frac{1}{2}\rho v^2 A\, C_D, \quad (4)$$

where A is the cross-sectional area of the robot (0.98 mm^2), and C_D is the drag coefficient (C_D = 2.1 for a rectangular box). The drag force is equal to 1.77 nN (0.02% of the body weight) on the robot running at top speeds. Viscous forces from drag are not dominating the locomotion of the robot, suggesting that inertial forces still play a role in locomotion at the milligram-scale.

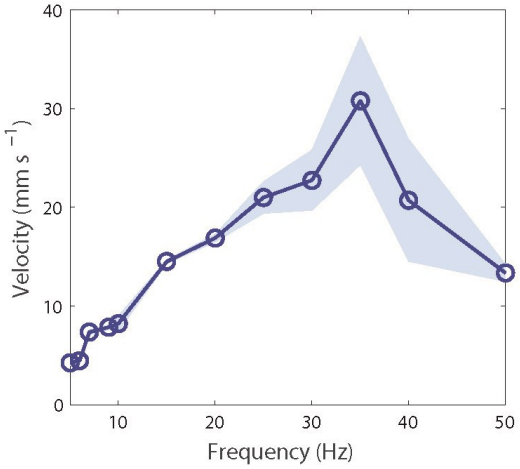

Figure 7: Robot speed vs rotating magnetic field frequency. Solid line represents the average over three trials and the shaded area represents the standard deviation.

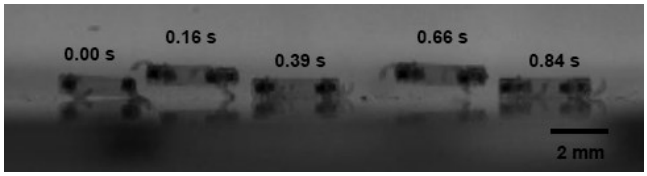

Figure 8: Overlaid frames captured from video of the microrobot walking at approximately 9.5 body lengths per second.

CONCLUSIONS

This work shows one of the smallest legged robot, capable of achieving biologically relevant speeds, up to 15 body lengths per second. This microrobot also provides a platform for studying locomotion at the milligram scale by incorporating microscale 3D printing with magnetic actuation. The monolithically printed chassis creates friction bearings used in the microrobot to provide full rotary actuation, up to 150 Hz, in this experimental setup, with no signs of visible wear or decreased performance after over 1,000,000 cycles of actuation.

This work provides an experimental platform to understand the dynamics of locomotion at the milligram-scale. Integrating magnetic actuation provides a sense of the required power and torque needed to achieve movement. Using the calculated maximum torque, the mechanical power of locomotion ($P = \tau\ \omega\ n_{legs}$) of the robot running at 35 Hz is 12.1 µW. Initial insights into the mechanical aspects of legged locomotion show that inertial forces still contribute to locomotion even at the milligram-scale.

ACKNOWLEDGEMENTS

This work was supported by NSF PECASE Award ECCS1055675.

REFERENCES

[1] S. Rubin, M. H.-Y. Young, J. C. Wright, D. L. Whitaker, and A. N. Ahn, "Exceptional running and turning performance in a mite," *Journal of Experimental Biology*, vol. 219, no. 5, pp. 676–685, 2016.

[2] U. Saranli, M. Buehler, and D. E. Koditschek, "Rhex: A simple and highly mobile hexapod robot," *International Journal of Robotics Research*, vol. 20, no. 7, pp. 616–631, 2001.

[3] T. Ebefors, J. U. Mattsson, E. Kälvesten, and G. Stemme, "A walking silicon micro-robot," in *Proceedings of the International Conference on Solid State Sensors and Actuators*, pp. 1202–1205, 1999.

[4] S. Hollar, A. Flynn, C. Bellew, and K. Pister, \Solar powered 10 mg silicon robot," in International Conference on Micro Electro Mechanical Systems, pp. 706-711, 2003.

[5] D. S. Contreras, D. S. Drew, and K. S. Pister, "First steps of a millimeter-scale walking silicon robot," in *Proceedings of the International Conference on Solid State Sensors and Actuators*, pp. 910–913, IEEE, 2017.

[6] J. H. Ryou and K. R. Oldham, "Dynamic characterization of contact interactions of micro-robotic leg structures," *Smart Materials and Structures*, vol. 23, no. 5, p. 055014, 2014.

[7] J. Qu, C. B. Teeple, and K. Oldham, "Modeling legged micro-robot loco- motion based on contact dynamics and vibration in multiple modes and axes," *Journal of Vibration and Acoustics*, 2017.

[8] D. Vogtmann, R. St. Pierre, and S. Bergbreiter, "A 25 mg magnetically actuated microrobot walking at¿ 5 body lengths/sec," in *Proceedings of the International Conference on Micro Electro Mechanical Systems*, pp. 179– 182, IEEE, 2017.

[9] R. St. Pierre and S. Bergbreiter, "Gait Exploration of Sub-2 g Robots Using Magnetic Actuation," *IEEE Robotics and Automation Letters*, vol. 2, pp. 34–40, Jan. 2017.

[10] A. W. Mahoney and J. J. Abbott, "Generating Rotating Magnetic Fields With a Single Permanent Magnet for Propulsion of Untethered Magnetic Devices in a Lumen," *IEEE Transactions on Robotics*, vol. 30, pp. 411–420, 2014.

[11] N. Ghalichechian, A. Modafe, M. I. Beyaz, and R. Ghodssi, "Design, fabrication, and characterization of a rotary micromotor supported on microball bearings," *Journal of Microelectromechanical Systems*, vol. 17, no. 3, pp. 632–642, 2008.

[12] L. G. Fréchette, S. A. Jacobson, K. S. Breuer, F. F. Ehrich, R. Ghodssi, R. Khanna, C. W. Wong, X. Zhang, M. A. Schmidt, and A. H. Epstein, "High-speed microfabricated silicon turbomachinery and fluid film bearings," *Journal of Microelectromechanical Systems*, vol. 14, no. 1, pp. 141– 152, 2005.

[13] S. Kumar, D. Cho, and W. N. Carr, "Experimental study of electric suspension for microbearings," *Journal of Microelectromechanical Systems*, vol. 1, no. 1, pp. 23–30, 1992.

[14] X.-S. Wu, W.-Y. Chen, X.-L. Zhao, and W.-P. Zhang, "Micromotor with electromagnetically levitated rotor using separated coils," *Electronics Letters*, vol. 40, no. 16, pp. 996–997, 2004.

[15] A. Takei, N. Binh-Khiem, E. Iwase, K. Matsumoto, and I. Shimoyama, "Liquid motor driven by electrowetting," in *Proceedings of the International Conference on Micro Electro Mechanical Systems*, pp. 42–45, 2008.

[16] M. L. Chan, B. Yoxall, H. Park, Z. Kang, I. Izyumin, J. Chou, M. M. Megens, M. C. Wu, B. E. Boser, and D. A. Horsley, "Design and characterization of MEMS micromotor supported on low friction liquid bearing," *Sensors and Actuators A: Physical*, vol. 177, pp. 1–9, 2012.

CONTACT

*R. St. Pierre; rstpierr@umd.edu

BATCH-FABRICATION OF DIAMAGNETICALLY LEVITATED MICROROBOTS

Camilo Velez [1], Ronald E. Pelrine[2], Annjoe Wong-Foy [2], and David P. Arnold [1]*
[1] Department of Electrical & Computer Engineering, University of Florida, USA
[2] Advanced Technology and Systems Division SRI International, Menlo Park, USA

ABSTRACT

This paper reports the batch fabrication of magnetically patterned bases for millimeter-scale, diamagnetically levitated microrobots. A selective-magnetization process is used to imprint checkerboard magnetic pole patterns in a single NdFeB substrate. Further machining of the substrate produces nine microrobots per batch (limited by the surface area of the magnetic substrate). This process represents a leap forward compared to the current fabrication approach, which relies on hand-assembly and gluing arrays of discrete magnets. The diamagnetic repelling forces of bases with two thickness (400 µm and 280 µm) are directly measured (227 µN and 64 µN), showing that the thicker base produced higher force. Furthermore, the microrobots are capable of assisted levitation (external magnetic field bias) and operation in sliding mode (lateral movement) using microfactory drive platform.

INTRODUCTION

Robotics is a driving force for a new industrial revolution, comprising a $26 B [1] worldwide market with the goal for the next 15 years to develop the manufacturing industry (12% of U.S. GDP) by combining advances in micro/nano scale [2]. While there are enumerable macroscale robot systems, there is a huge technology gap for robotic systems that can manipulate/control micron-sized (~10^{-6} m) objects with nanometer resolution. Since the first mention of small scale machines (called today microrobots) in 1959 by Richard Feynman [3], [4], numerous fields of applications for micro/milli robotic systems have emerged such as minimal invasive medicine [5], bioengineering [6], and microassembly [7]–[9]. Inspired by Feynman, some visionaries such as A.M. Flynn [10] and W. Trimmer [11], foresaw creating complex machines with sizes and abilities of insects. Most of researchers working in the field of microrobotics recognize their inspiration in the founding works of R.S. Fearing [12], F. Arai and T. Fukuda [13], that in the International conference on Intelligent robots and systems (ICIRS) on 1995, set the fundamentals of micromanipulation and adhesive forces at microscale.

To address the challenge of microassembly in non-aqueous environments, SRI International has developed a microfactory platform for computer-controlled magnetic manipulation of swarms of microrobots [14] [15]. A typical microrobot comprises a magnet base made of a 3x3 array of poled permanent magnets in a checkerboard pattern and a stick-like end-effector. The microrobots are distributed over a diamagnetic material (pyrolytic graphite) and levitate above this surface via repulsive forces between the magnetic base and the diamagnetic material, as shown in Figure 1. The robots are driven across the substrate using a grid of current-carrying wires positioned beneath the diamagnetic layer, providing lateral positioning capability in the xy-plane, as well as some control of the levitation height in the z-direction.

Heretofore, these millimeter-scale microrobots are assembled and glued together by hand. The contribution of this paper is the first published report of a scalable fabrication technique for mass-manufacturing the magnetic microrobot bases to be operated on the microfactory platform built by SRI. The process yields a mechanically monolithic magnetic base that is magnetically poled into the desired magnetic pattern, as opposed to assembling discrete magnets. In addition to improving fabrication throughput, the process could also be used to fabricate even smaller magnetic microrobots, which are not currently possible with hand assembly.

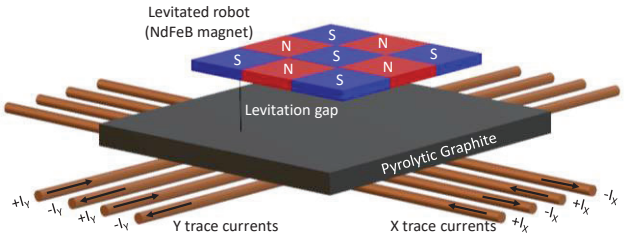

Figure 1: Schematic of diamagnetic levitated robot over a microfactory platform. Colors on robot indicate vertical magnetization polarity to form "checkerboard" pattern. Adapted from [14].

EXPERIMENTAL METHODS

The proposed batch fabrication of levitated microrobotic bases begins with an NdFeB grade N42 substrate (10,000 µm x 10,000 µm x 400 µm) sourced from BJA magnetics. The fabrication could be summarized in three main steps: 1) Polishing the NdFeB substrate, 2) batch-magnetizing the substrate to imprint a complex magnetic pole pattern using a technique called selective-magnetization, and finally, 3) singulating the substrate to create individual magnetic bases. The detailed process steps are:

- Lapping one side of a commercial 10 mm x 10 mm x 0.4 mm NdFeB magnetic substrate, to obtain a designated thickness.
- Polishing the lapped side to obtain mirror finish.
- Fully magnetizing the substrate to create north poles (7 T).
- Selectively reversing areas of the substrate using a magnetization mask to create south poles (1 T).
- Dicing the substrate into 9 microrobot bases using dicing saw.
- Manually cleaning, separating, and packaging the bases.

A total of nine magnetic bases (3 mm x 3 mm) can be fabricated in the selected substrate. Robot distribution over a substrate is presented in Figure 2. Two batches of magnetic bases were fully produced. A ~280 µm and a ~400 µm thick batches, with nine bases each.

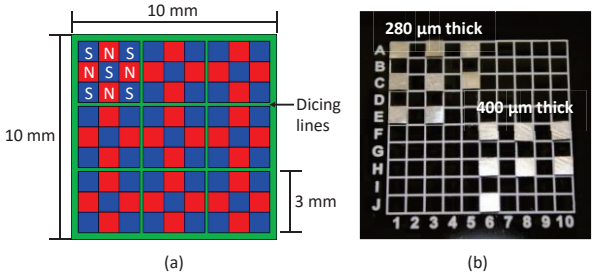

Figure 2: Magnetic base fabrication for microrobots using selective magnetization. (a) Designed and (b) fabricated (singulated and polished) microrobots with two thickness.

978-1-940470-03-0/HH2018/$25©2018TRF
DOI 10.31438/trf.hh2018.17

Microrobot machining

The first important step to guaranty good levitation of the micro-robots is the polishing of the magnetic layer before magnetization. Polishing is mainly necessary on the side facing the diamagnetic board. Because the levitation is of only tens of microns, any particle or surface roughness will be critical and will reduce the motion of the robots. A manual polishing process using progressively smaller grid polish pads was implemented. Sand papers and different lubricants used were used in a sequence: P220/dry, P500/dry, P100/water, P1200/oil, P1200/water. With this process, the magnetic layer with original thickness of 400 µm was lapped to 280 µm. After lapping, a polishing pad of 3 µm grid and water was used, followed by a polishing pad with 0.06 µm of silica slurry. A mirror finish was obtained.

For singulated the robots a hubbed resin-bond diamond dicing blade was used. 2.250" X .750" X .007" Thick, 325 mesh with 40-60 µm grit size (reference CA-007-325-030-H from Dicing Technologies). The parameters used to set up the dicing were: blade thickness of 178 µm, blade exposure of 762 µm, rotation speed of 15 -18 kRPM, feed rate of 0.1 mm/s. Magnetic substrates were successfully diced in 9 squares of 3 mm x 3 mm each. The use of a dicing saw proved to generate repetitive and reliable dimensions with very tight tolerances (dicing lines ~214 µm wide kerf and 422 µm deep).

Low aspect ratio magnetization mask

The most important aspect of the levitated microrobot fabrication is imprinting the magnetic pattern using selective-magnetization [16][17]. Because of the importance of the magnetization mask, this should be accomplished after defining geometry parameters, magnetization mask material and reversal field to be applied during the selective magnetization process (it varies with the mask and substrate material). The mask fabrication is a critical step towards obtaining multiple magnetic bases from a single magnetic substrate (batch-fabrication). Two different masks constructions were evaluated: Low and high aspect ratio.

The aspect ratio of the mask is designated as the thickness divided by the feature length. A square pattern mask was selected to comply with the specifications of the microfactory base. All resulting robots should have the same magnetic pattern. Resulting magnetic square poles at individual bases should have 1 mm side.

To guaranty full magnetization through the substrate thickness, it was important to design and fabricate a double side magnetization mask. The complete mask was designed as sandwich of two identical patterned masks, made of carbon steel (AISI 1018 mild/low carbon steel - ASTM A108). All mask features are 1 mm depth (feature in the mask will have an aspect ratio of 1). In the middle, a zinc spacer was designed to align the magnetic substrate. Figure 3a shows and explosion schematic of the mask. The three parts of the mask and the magnetic layer will hold together using three wood alignment pins. The mask pieces were machined using a Sherline 2000 CNC and 1/64"-two flutes end mills. Figure 3b shows the final machined mask disassembled.

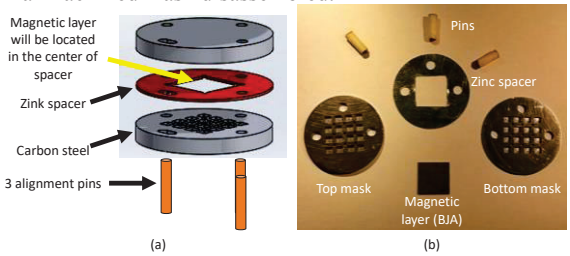

Figure 3: Low aspect ratio magnetization masks. (a) Schematic and (b) disassembled representation of the magnetization mask.

High aspect ratio magnetization mask

A set of finite element simulations modeled the selective-magnetization process using 2D/3D quasi-static magnetic fields in COMSOL multiphysics. Simulation results yielded that the higher the aspect ratio of the mask the better magnetic field quality will be generated during the reversal magnetization. An example of the simulations conducted could be seen in Figure 4.

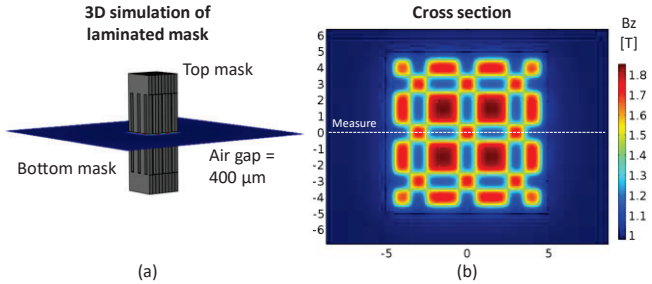

Figure 4: High aspect ratio magnetization mask. Fabrication progress from individual layers.

With this premise of higher aspect ratios in mind, it is necessary to fabricate different magnetization masks, but this raises a fabrication problem. The high complexity of machine carbon steel with high aspect ratios using dimensions smaller than 1 mm. Commercial end-mills smaller than 1/64" are limited to 1 mm length. Therefore, a laminated design was proposed to obtain high aspect ratios: By using a CNC or laser cut to machine individual layers out of 1 mm thick carbon steel sheets (two different designs of layers, one with 6 x 1 mm^3 poles and other with 3 x 1 mm^3 poles to create the checkerboard). This process will generate perfect square shape angles in the features and the most important, controllable aspect rations higher than 10. After three layers are machined, they will be glued together in rows (6/3/6 pole layer) and three rows will be glued with a 300 µm spacer between them, as shown in Figure 5. This fabrication concept was originally tested using laser cur over stainless steel (easier to machine) and then implemented in carbon steel using CNC.

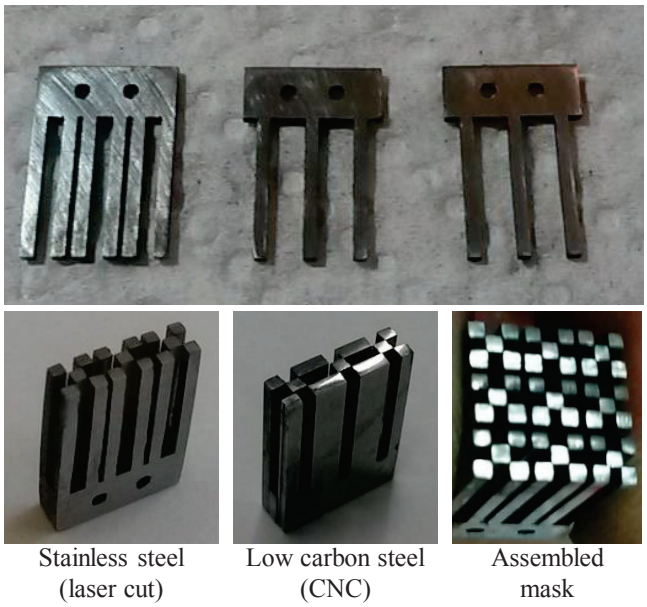

Figure 5: High aspect ratio magnetization mask. Fabrication progress from individual layers.

MICROROBOTS CHARACTERIZATION

Using fabrication methods described above and selective magnetization process to create magnetic bases (at 1 T reversal field), the following results are presented: Figure 6 shows resulting microrobots and the magnetization of the BJA magnetic layer using the low aspect ratio machined double mask. Magnetization images were obtained using magneto optical (MO) sensor of 38 mT saturation field in the "Minimo" magnetic camera (Matesy). These pictures show the entire substrate (10 mm x 10 mm x 0.4 mm) before and after being singulated.

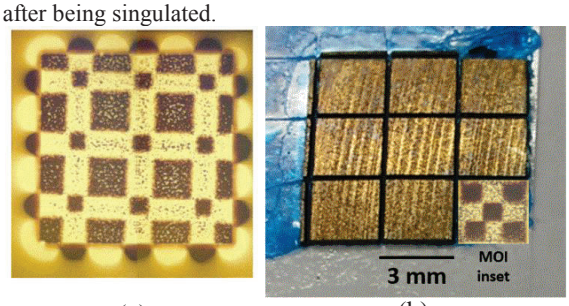

(a) (b)

Figure 6: Magnetic base fabrication for microrobots using selective magnetization. (a) Magneto optic image of the 10 mm x 10 mm magnetic base. (b) Singulation of 9 robots (3 mm x 3 mm) per substrate. MOI superposition in the bottom right robot.

Magnetic characterization

A first attempt to quantify the stray magnetic field and confirm magnetic images, was made using an in-house scanning hall probe. This is a rastering technique that displaces the scanning hall sensor over the magnet area. Scanning hall probe confirms that selective magnetization of 280 µm thick substrates generates patterns with only ~39% of the magnetic field strength of the manually assembled patterns.

Figure 7 depicts the results of the images obtained using magneto optical imaging/field-measurement system [18], comparing manually assembled and selectively magnetized micro-robots. The advantage of this technique is that the intensity of the magnetic field can be quantified and data acquisition is faster than scanning hall probe. By quantifying the stray magnetic field from the magneto optical image, a comparison between three different masks (low and high aspect ratio stainless and low carbon steel) is presented in Figure 8. These measurements show the B field peaks, obtained from the selectively magnetized samples (~50 mT maximum) are about 50% weaker than the manually assembled robot (~100 mT maximum).

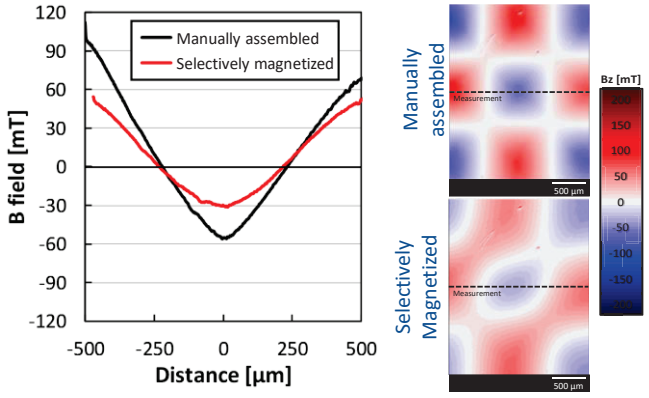

Figure 7: Magneto optical measurements. Assembled and selectively-magnetized levitated micro-robot's comparison. Measurements at 600 µm above the surface.

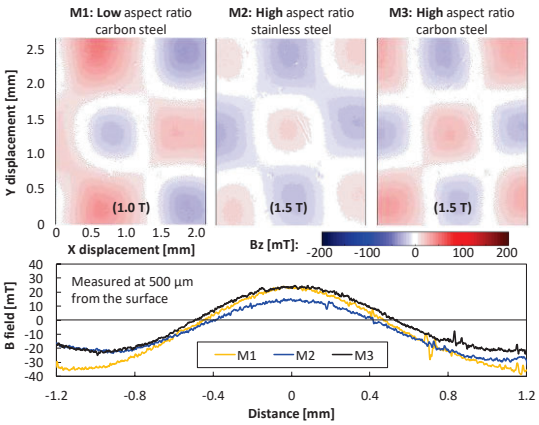

Figure 8: Magneto optical image of a selectively magnetized samples using each of the machined masks. Measured at 500 µm from magnet surface.

Magnetic forces

The final goal of the micro-robots is the diamagnetic levitation of their own masses plus a payload. In this order of ideas, we studied the diamagnetic force generated for three samples: a manually assembled robot, a selectively magnetized 400 µm thick robot and a 280 µm thick robot.

We used a combination of a microbalance (Explorer 2, Ohaus) and a polished pyrolytic graphite as a sensing mechanism, as a variation of experiment conducted by [19]. Each sample was attached to a glass and plastic sample holder facing the graphite and connected the holder using a stiff brass beam with a 3D micro positioner (built in-house with Newport DC servo controllers). By cautiously lowering the magnet on top of the graphite, the repelling diamagnetic levitation force will push the graphite away and this force is measured by the balance. Figure 9 illustrates the experiment and results.

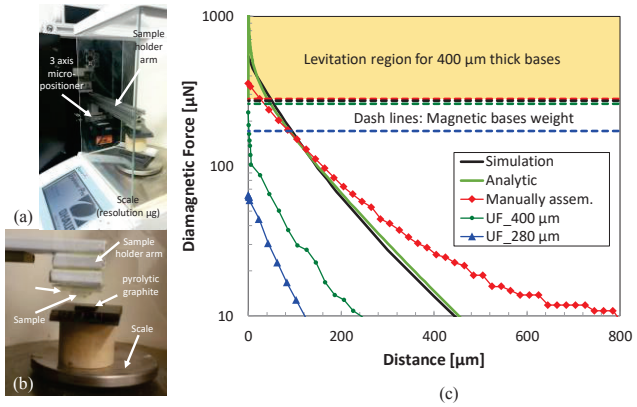

Figure 9: Diamagnetic force measurement using a microbalance. (a) General assembly, (b) close-up of sample holder, and (c) force analytical solution, simulation and measurement results.

Figure 9c compares measurements of the magnetic force with COMSOL simulations and charge model calculations [20]. A factor of 0.35 and 2.8 (simulation and analytic model) are used arbitrarily to compensate variations on material properties for the specific samples. Differences in the slope of the manually assembled base compared with models are attributed to instrumentation error.

It is clear from Figure 9c that the force produced by the manually assembled base is higher than its own weight (red curve). On the other hand, the force produced by 400 µm thick selectively magnetized bases is slightly smaller than their own weights, and

therefore it won't levitate. Similar behavior occurs with the 280 µm thick bases, but the produced force is considerably lower. Enhancing the magnetic field produced by the selective magnetization will increase the diamagnetic force and overcome the weight of the magnet making the micro-robot levitate.

Levitation and sliding

Although the selectively magnetized fields and the diamagnetic forces are weaker than the manually assembled counterparts, experiments conducted using SRI microfactory (Figure 10) verify that this technique can in fact fabricate microrobots to perform assisted levitation (diamagnetic levitation biased by an additional external magnetic field) and assisted magnetic sliding (using the microfactory platform to displace bases, achieved by controlled electric currents and diamagnetic layer).

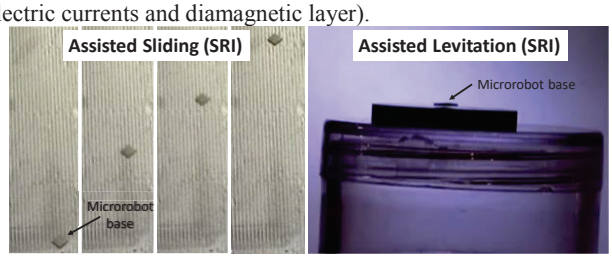

Figure 10: Characterization of batch fabricated robots at SRI. Left: assisted sliding and right: assisted levitation.

CONCLUSIONS

A batch fabrication of monolithic magnetic bases for microrobots was successfully obtained. Selective magnetization was used to imprint alternated magnetic pole patterns in a machinable NdFeB substrate, producing 9 microrobots per batch. Two types of magnetization mask were explored (low and high magnetization) showing similar results among them. The diamagnetic repelling force of bases with two thickness (400 µm and 280 µm) was measured, showing that the thicker base produced higher force. Even though the fabricated bases don't self-levitate, they were capable of assisted levitation (external magnetic field bias) and operation in sliding mode (lateral movement using microfactory platform).

ACKNOWLEDGEMENT

The authors gratefully acknowledge funding support for this work from the Air Force Research Laboratory (AFRL) and the Defense Advanced Research Project Agency (DARPA) under AFRL Contract #FA8650-15-C-7547. The authors thank William Patterson (UF) and Allen Hsu (SRI) for their contribution, as well as the staff of the Herbert Wertheim College of Engineering's Research Service Centers (RSC) at UF, for their assistance in the microfabrication and material characterization.

The views, opinions and/or findings expressed are those of the author and should not be interpreted as representing the official views or policies of the Department of Defense or the U.S. Government.

REFERENCES

[1] J. Wilson, "Robotics: Technologies and global markets," 2016.

[2] Robotics_Technology_Consortium, "A Roadmap for US Robotics, From Internet to Robotics," 2016.

[3] R. Feynman, "Infinitesimal Machinery," *J. Microelectromechanical Syst.*, vol. 2, no. 1, pp. 4–14, 1993.

[4] R. P. Feynman, "There's (still) plenty of room at the bottom," *Applied Thermal Engineering*, vol. 61, no. 2, pp. 22–36, 1960.

[5] B. J. Nelson, I. K. Kaliakatsos, and J. J. Abbott, "Microrobots for Minimally Invasive Medicine," *Annu. Rev. Biomed. Eng.*, vol. 12, no. 1, pp. 55–85, 2010.

[6] M. Sitti, H. Ceylan, W. Hu, J. Giltinan, M. Turan, S. Yim, and E. Diller, "Biomedical Applications of Untethered Mobile Milli/Microrobots," *Proc. IEEE*, vol. 103, no. 2, pp. 205–224, 2015.

[7] M. Probst, K. Vollmers, B. E. Kratochvil, and B. J. Nelson, "Design of an Advanced Microassembly System for the Automated Assembly of Bio-Microrobots," *Proc. 5th Int. Work. MicroFactories, IWMF 2006*, pp. 1–6, 2006.

[8] R. D. D. Souza, S. Sharma, A. Jacob, and A. Al Hashimi, "Microrobotics : Trends And Technologies," *Am. J. Eng. Res.*, vol. 5, no. 5, pp. 32–39, 2016.

[9] J. Agnus, N. Chaillet, C. Clévy, S. Dembélé, M. Gauthier, Y. Haddab, G. Laurent, P. Lutz, N. Piat, K. Rabenorosoa, M. Rakotondrabe, and B. Tamadazte, "Robotic microassembly and micromanipulation at FEMTO-ST," *J. Micro-Bio Robot.*, vol. 8, no. 2, pp. 91–106, 2013.

[10] A. M. Flynn, "Gnat Robots (And How They Will Change Robotics)," Doctoral disertation. 1987.

[11] W. S. N. Trimmer, "Microrobots and micromechanical systems," *Sensors and Actuators*, vol. 19, no. 3, pp. 267–287, 1989.

[12] R. S. Fearing, "Survey of sticking effects for micro parts handling," *Proc. 1995 IEEE/RSJ Int. Conf. Intell. Robot. Syst. Hum. Robot Interact. Coop. Robot.*, vol. 2, pp. 212–217, 1995.

[13] F. Arai, D. Ando, T. Fukuda, Y. Nonoda, and T. Oota, "Micro manipulation based on micro physics-strategy based on\nattractive force reduction and stress measurement," *Proc. 1995 IEEE/RSJ Int. Conf. Intell. Robot. Syst. Hum. Robot Interact. Coop. Robot.*, vol. 2, pp. 236–241, 1995.

[14] R. Pelrine, A. Hsu, A. Wong-Foy, B. McCoy, and C. Cowan, "Optimal control of diamagnetically levitated milli robots using automated search patterns," in *2016 International Conference on Manipulation, Automation and Robotics at Small Scales (MARSS)*, 2016, pp. 1–6.

[15] R. Pelrine, A. Wong-Foy, B. McCoy, D. Holeman, R. Mahoney, G. Myers, J. Herson, and T. Low, "Diamagnetically levitated robots: An approach to massively parallel robotic systems with unusual motion properties," *Proc. - IEEE Int. Conf. Robot. Autom.*, pp. 739–744, 2012.

[16] O. D. Oniku, P. V. Ryiz, A. Garraud, and D. P. Arnold, "Imprinting of fine-scale magnetic patterns in electroplated hard magnetic films using magnetic foil masks," *J. Appl. Phys.*, vol. 115, no. 17, pp. 38–41, 2014.

[17] C. Velez, W. C. Patterson, and D. P. Arnold, "Simulation and experimental validation of a selective magnetization process for batch-patterning magnetic layers," *J. Phys. Conf. Ser.*, vol. 660, pp. 3–7, 2015.

[18] W. C. Patterson, N. Garraud, E. E. Shorman, and D. P. Arnold, "A magneto-optical microscope for quantitative measurement of magnetic microstructures," *Rev. Sci. Instrum.*, vol. 86, no. 9, pp. 1–10, 2015.

[19] D. Laumann and S. Heusler, "Determining magnetic susceptibilities of everyday materials using an electronic balance," *Am. J. Phys.*, vol. 85, no. 5, pp. 327–332, 2017.

[20] H. Allag, J. P. Yonnet, and M. E. H. Latreche, "3D analytical calculation of forces between linear halbach-type permanent-magnet arrays," *2009 8th Int. Symp. Adv. Electromechanical Motion Syst. Electr. Drives Jt. Symp. Electromotion 2009*, no. July, pp. 1–3, 2009.

CONTACT

*Camilo Velez, tel: +1-352-575-7581; camilovelez@ufl.edu

TAKEOFF OF A FLYING MICROROBOT WITH COTS SENSOR PAYLOAD USING ELECTROHYDRODYNAMIC THRUST PRODUCED BY SUB-MILLIMETER CORONA DISCHARGE

Daniel S. Drew and Kristofer S. J. Pister
Berkeley Sensor and Actuator Center, UC Berkeley, USA

ABSTRACT

This paper demonstrates the first flying microrobot using electrohydrodynamic thrusters, or ionocraft, to successfully take off while carrying an onboard commercial sensor package. The 13.6mg, 1.8cm by 1.8cm ionocraft is shown to take off while carrying a 40mg Flex PCB with 9-axis IMU and associated passives while tethered to a power supply. A new emitter electrode design has decreased corona onset voltage by over 30% and takeoff voltage by over 20% from previous efforts. Thrust density scaling with increasing numbers of emitter wires, continued geometric scaling for decreased operating voltage, device lifetime improvement via thin film deposition, and new assembly techniques are all explored.

INTRODUCTION AND RELATED WORK

Pico air vehicles, flying microrobots with mass under 100mg and characteristic length under 5cm, are being developed by a large number of research groups [1]. The majority of efforts focus on biomimetic flapping wing designs, typically using either piezoelectric or electromagnetic actuators. This work is unique in that it uses a microfabricated corona discharge based electrohydrodynamic actuator (Fig. 1) to produce thrust almost silently and with no moving parts, creating the highest thrust-to-weight ratio pico air vehicle capable of takeoff (Fig. 2) to date [2].

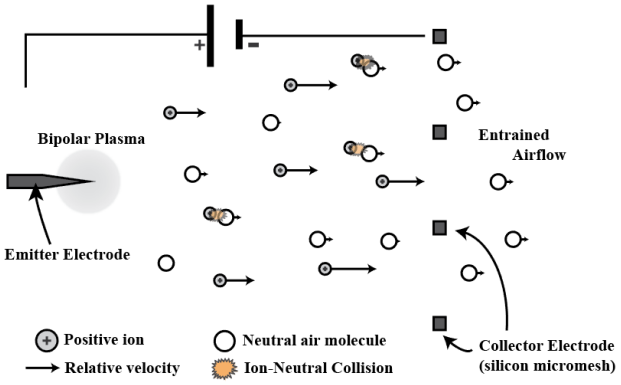

Figure 1: Thrust is produced when ions, drifting in the applied electric field, collide with neutral air molecules and impart momentum. Bipolar ions are generated in the corona plasma region localized at the sharp tip of the emitter electrode, but only positive ions (mainly N_2^+) will drift towards the collector grid.

A one-dimensional model for electrohydrodynamic thrust, based on the electrostatic force on a volume of ions, leads to an expression for force in terms of ion drift current, I, distance the ions travel d, and the ion mobility, μ, which is about $2cm^2/Vs$ for N_2^+ ions in air [3]:

$$F = \beta I d/\mu \qquad (1)$$

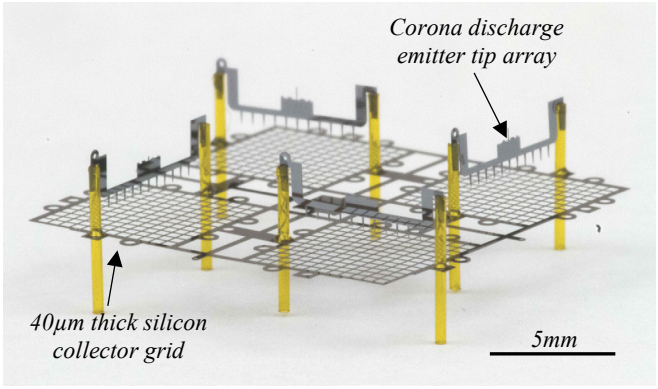

Figure 2: Photograph of the assembled ionocraft. With four individual addressable thrusters, it is about 1.8cm by 1.8cm and masses 13.6mg. It is comprised of 13 individual components connected by a combination of mechanical slots and UV-curable epoxy. The design includes various tabs for handling and connection to power tethers.

The dimensionless term β represents deviation from the ideal force caused by losses in the system due to factors like aerodynamic drag, bipolar plasma radius to drift distance ratio, and undesired ion path directions (e.g. horizontal velocity components "lost" as vertical thrust in collisions) [4].

Ions are generated using corona discharge, an atmospheric-pressure, low-temperature DC plasma mechanism. In this process, an applied voltage between two asymmetric electrodes (e.g. a wire "emitter" and a plate "collector") yields a locally enhanced electric field around one of the two; if the potential is high enough, electrons will gain enough energy to initiate Townsend avalanche breakdown in the neutral air around the electrode, producing a bipolar plasma. Corona discharge is the most common mechanism of ion production for EHD force, with implementations using electrode gaps ranging from the 10s of centimeters [5] to the sub-millimeter [6].

Although models for corona discharge in all but a few simple geometries are largely empirically derived, resultant ion current versus applied voltage generally follows the relationship:

$$I = CV(V - V_0) \qquad (2)$$

Where C is an empirical parameter that is a strong function of electrode geometry and V_0 is the corona onset voltage. The combination of these two governing equations yields an expression for EHD force that depends on two empirical factors, C and β, that can be extracted from experimental data:

$$F = \beta CV(V - V_0)\, d/\mu \qquad (3)$$

Designs for EHD thrusters can be assessed by attempting to maximize C and β while minimizing V_0. Designs can further be

978-1-940470-03-0/HH2018/$25©2018TRF
DOI 10.31438/trf.hh2018.18

assessed quantitatively by thrust-to-weight ratio and holistically by ease of fabrication and assembly.

The use of EHD thrust for a centimeter-scale robot capable of vertical takeoff has already been demonstrated; this work focuses on the steps being taken towards improving device performance, increasing assembly throughput and success rate, and incorporating useful payloads in an effort to move closer to controlled flight.

EXPERIMENTAL METHODS

Silicon electrodes with lithographically defined asperities ("tips") are fabricated in plane, fully released, and then rotated and assembled out of plane. Emitter wires with varying interelectrode gaps and asperity tip angles were fabricated. The fabrication process previously reported at MARSS 2017 [2] is adapted to a single mask SOI process in this work to increase device yield and decrease number of fabrication steps. An improved assembly method (Fig. 3) differs from prior work in that it: allows the electrodes to be designed for mechanical robustness (to survive assembly); separates the power tether connection point from the collector grid by a lithographically defined amount to prevent surface breakdown along the dielectric post; and allows the inter-electrode gap to be controlled semi-lithographically.

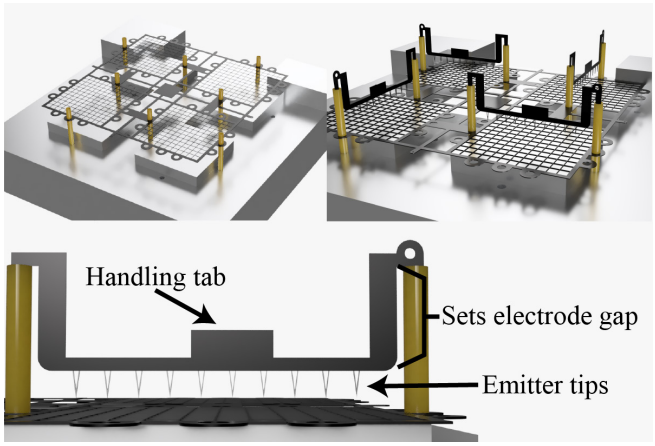

Figure 3: 3D model renders of the assembly process. Pre-cut silica tubes are inserted into slots in a CNC-milled aluminum jig. The ionocraft frame is slid down the guiding posts. The emitter wires are rotated out of plane and tapered guides are inserted into the silica tubes. The inter-electrode distance is now determined by a combination of lithography, slot depth, and tube length.

A Flex PCB board (Fig. 7 inset) has been fabricated containing a commercial 9-axis IMU, the InvenSense MPU-9250, as well as three associated passives and bonding pads. The board's 5mm by 5.5mm footprint allows it to be placed in a designated central region of the robot airframe without interfering with the surrounding thrusters. The total board mass of about 40mg is within the expected payload capacity reported in prior work.

To measure output force, devices are mounted on a threaded nylon post fixed directly to a Phidgets 100g Micro load cell. For full quad-thruster ionocrafts there is a dedicated region in the center of the airframe for mounting; single thrusters are mounted using one of the unused silica tube slots along the grid frame. Multiple instruments are controlled via GPIB for synchronized force-current-voltage sweeps.

RESULTS AND DISCUSSION

The presented data is from a range of fabricated devices; unless otherwise noted, collected data is from the first trial using each device to reduce the effect of lifetime performance degradation. Although presented data is first passed through a low pass filter in the Phidgets data hub and then averaged over 3 seconds of collection for each measurement, there was still significant noise (SD=35μN, n=11) in the strain sensor compared to the values found in this work.

Electrode Geometry

In a widely-used set of empirically derived equations for corona onset voltage formulated by Peek [8] for various electrode geometries, it is found that $V_0 \propto \ln(d)$. Decreasing the electrode gap from 500μm to 250μm (Fig. 4) was shown to decrease the onset voltage, as found by the 0-intercept of the curve fit to Eq.2, by approximately 400V, a larger change than predicted by this trend. Although related work already shows deviation from Peek's equations in sub-millimeter corona discharges [9], this greater deviation at even smaller gaps bears further investigation. The empirical factor C, a metric for change in ion current as a function of input voltage, was shown to increase by about 230%; because current must double to produce the same output force at half the drift distance (Eq. 1), this would ideally correspond to a smaller required operating voltage swing for the same force production range.

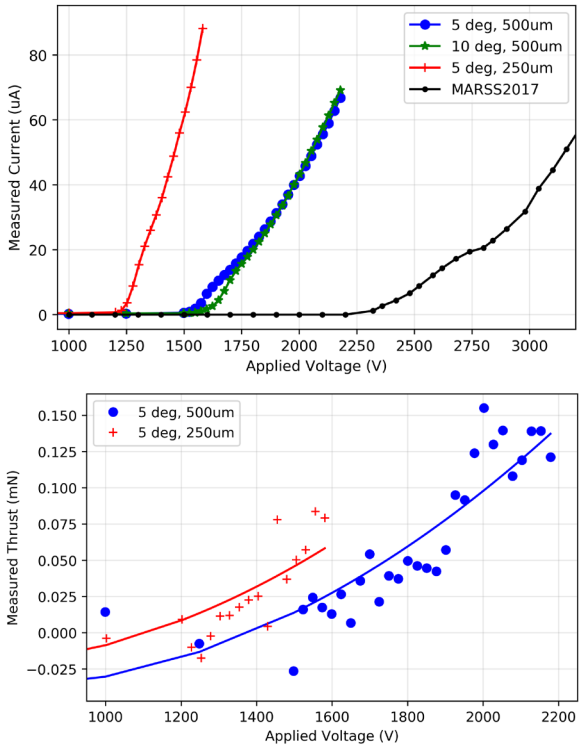

Figure 4: Current and force versus voltage curves for thrusters with different electrode gaps or different drawn emitter tip angles. The current-voltage data from MARSS2017 [2] is a 20μm by 40μm cross section silicon "wire" with no lithographically defined asperities at an electrode gap of 1mm. The 250μm electrode gap device uses a collector grid with 250μm spacing. The plotted lines in the force-voltage plot are 2-degree polynomial fit lines (Eq. 3).

The 250μm gap device has an extracted β via linear fit of current-force data of 0.33, 44% lower than the extracted value of 0.59 for the 500μm gap, 5-degree device. Although the absolute value of this factor may be incorrect due to variation in ion mobility from the assumed 2cm^2/Vs, the trend is expected from prior work

[4] and likely largely due to the effect of aerodynamic drag on the smaller spacing of the 250µm collector grid. Further, device failure (i.e. arcing) occurred before the same maximum force could be produced by the smaller electrode gap, indicating that emitter tip radius, r, should be decreased in an effort to increase the d/r ratio critical for corona discharge.

The onset voltage was not found to change significantly (about 50V) between 5-degree and 10-degree drawn emitter tip angle wires. This could indicate some limit in dimensional scaling following DRIE and current lithography methods, as asperity drawn angle was shown to have a strong effect on onset voltage in prior work [4].

Thrust Density

Adding more emitter wires per collector grid should have the effect of increasing both C and thrust-to-weight ratio at the cost of additional assembly time. Experiments show that corona discharge current scales approximately linearly with number of emitter wires (Fig. 5) at a wire spacing of 3mm for the 2-wire case and 1.5mm for the 3-wire case. Going from one emitter wire per collector grid to three increases C by about 250%, while β decreases from 0.59 to 0.53. The fact that current did not scale linearly may be attributable to assembly or device degradation nonuniformity, and the decrease in beta is within the measurement error for the strain sensor used in this work.

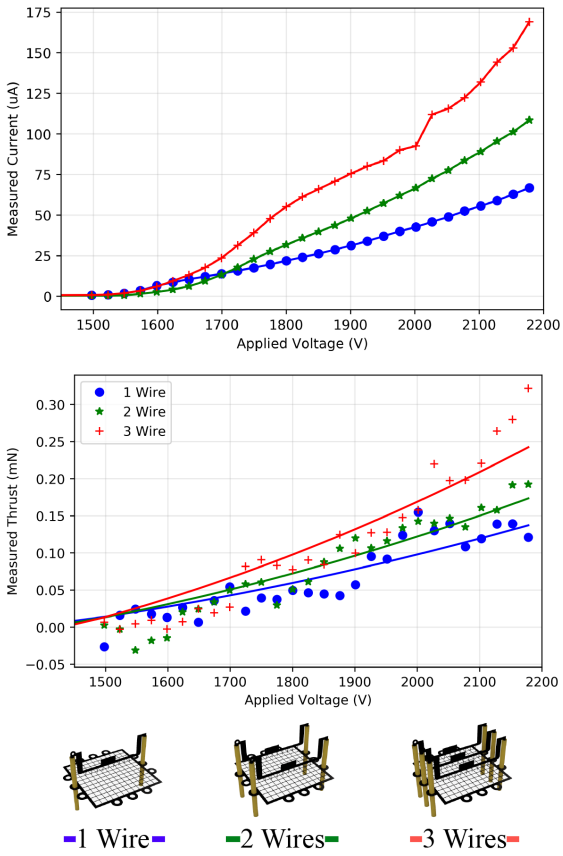

Figure 5: Current-voltage and force-voltage curves produced by varying the number of emitter wires in a thruster. Tests are for 5-degree emitter tips, an electrode gap of 500µm, and a collector grid spacing of 500µm. The plotted lines in the force-voltage plot are 2-degree polynomial fit lines.

The mass of an additional emitter wire and two silica posts is only 1.5mg while the maximum thrust is increased by approximately 100µN (10mg) per set, showing a large potential boost to thrust-to-weight ratio. Prior work in FEA simulation indicates that the space charge region developed from a single emitter wire's corona discharge spans a horizontal radius approximately equal to the electrode gap distance. This indicates that wire neighbor spacing can be decreased from 1.5mm to 1mm and the maximum number of emitter wires per collector grid could double to 6 without significant neighbor interactions; although this would certainly continue to provide an aerial thrust density and thrust-to-weight ratio benefit, assembly complexity would be prohibitive with the current design.

Device Lifetime

Performance of a corona discharge based EHD thruster can be expected to degrade over time, largely as a result of interactions of the bipolar plasma region with the emitter electrode. Initial experiments saw logarithmic decay (R^2=0.98 fit) of discharge current over time with a constant applied voltage (Fig. 6). Scanning electron micrographs showed large amount of physical damage to the emitter wires, localized to the tips themselves, with a damage radius of around 60µm. With the hypothesis that this damage is a result of energetic ion ablation in the bipolar plasma (a plasma radius of 50µm is often assumed in literature), the tips were sputtered with a 100nm titanium nitride layer, turned over, and sputtered with another 100nm layer. Subsequent testing showed no degradation of performance in the same time period. It is expected that the new failure mode will be through oxidation of the tips enhanced by the energetic oxygen in the bipolar plasma; TiN has been experimentally shown to grow 10nm thick oxide films after 1000 seconds in a 200ºC O_2 plasma asher [9].

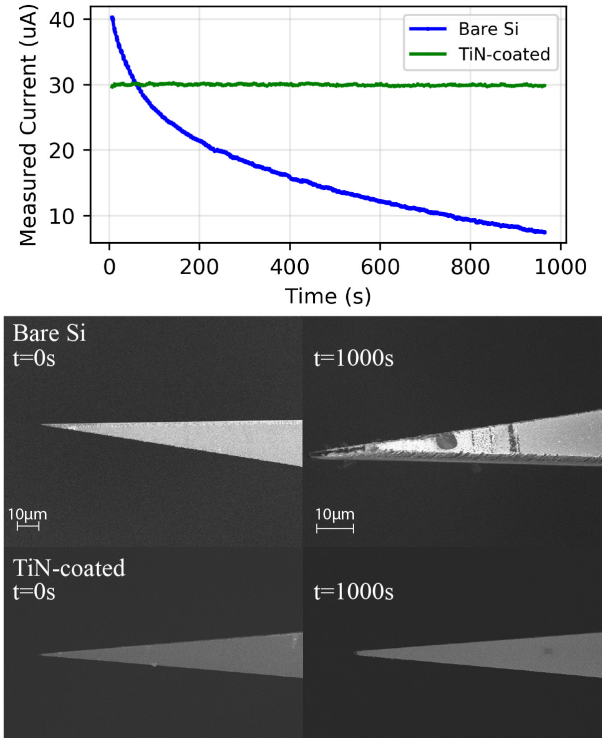

Figure 6: Device lifetime quantified by measured ion current versus time at a constant operating voltage. Bare silicon emitter wires saw immediate performance degradation during testing, while wires coated by about 100nm of sputtered TiN had stable performance up to the measured 1000s of operation. Devices are 10-degree tips at a 500µm gap with 1800V applied.

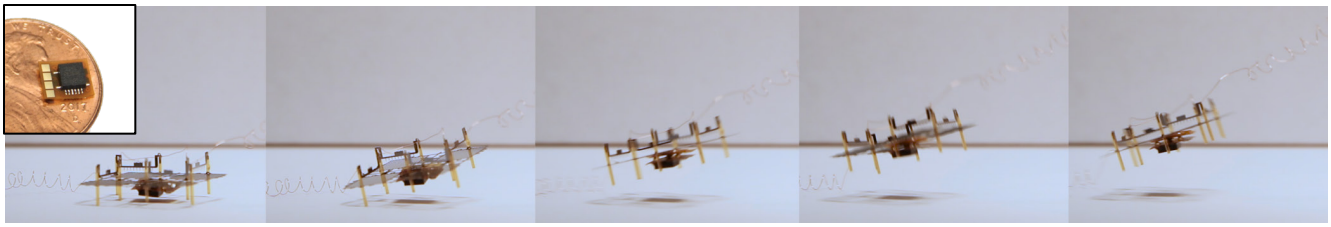

Figure 7: An ionocraft with assembled 40mg Flex PCB IMU board attached to the airframe center pad. At about 2100V, the ionocraft is able to take off from the table; the power and ground wires prevent the ionocraft from going any higher. There is only one high voltage line attached here, with connections between the emitter wires done on the ionocraft itself. The IMU board is not wired or active during takeoff. Inset: Flex PCB IMU board on a U.S. penny. The board is about 5mm by 5.5mm and masses 40mg.

Takeoff with Sensor Payload

Current flying microrobots are typically payload constrained; either they fail to lift the weight of their own actuators and airframe, or must seek to develop novel sensing schemes and platforms to optimize for mass. The relatively high thrust-to-weight ratio (about 4.5 in this work) of the ionocraft means that it may be possible to use standard commercial sensors, simplifying development and implementation. To prove the feasibility of future controlled flight using a commercial sensing package we developed a 40mg FlexPCB with 9-axis IMU, attached it to a designated central region in the ionocraft airframe with UV-curable epoxy, and made the robot take off (Fig. 7). This single-emitter design had an unladen takeoff voltage of about 2000V (2100V with IMU); this number should decrease by using multiple emitter wires per thruster, but with the assembly jig used in this work it was difficult to reliably assembly such a version.

CONCLUSIONS AND FUTURE WORK

Although we have validated the use of multiple emitter wires as a way to increase device performance, with the current design each new emitter wire requires both its own pair of silica posts (with associated epoxy) and electrical connection to its neighbors, decreasing benefit to thrust-to-weight ratio. Future work will explore new methods, for example designing mechanical interlocks into the components themselves, to overcome these challenges.

Future efforts will focus on further decreasing operating voltage and bringing aerial thrust density closer to theoretical limits. Work using FEA simulation will investigate the potential for taking advantage of space charge region interaction between neighboring wires to increase flow efficiency (e.g. through induced jet flow). We also see potential for decreasing aerodynamic drag on the collector grid without influencing corona discharge behavior by using non-uniform geometries (e.g. a grid spacing that varies based on proximity to emitter tip).

Efficiency is a key concern when developing millimeter-scale robots, where resource constraints are projected to dominate potential function. Thrust efficiency in terms of N/W for an EHD thruster scales $\propto 1/E_{drift}$. As electrode gap continues to decrease in an effort to decrease operating voltage, the effect of decreasing electrode d/r ratio on minimum drift field strength, and therefore efficiency, becomes more pronounced. The devices in this work have efficiencies that range from 2mN/W to 1mN/W over their operating range, unacceptably low for a truly autonomous flying robot with any useful mission time. It may be necessary to increase emitter tip sharpness beyond what is possible with standard lithographic techniques, for example with thermal oxide sharpening, in order to operate ionocraft in higher efficiency regimes by trading off output force.

The significant performance degradation of the bare silicon emitter wires shown in Fig. 6 implies that the IV and FV curves presented in this work are strongly (negatively) affected during their approximately 90 second measurement period. Although assuming uniform degradation for all measured emitter wires allows us to draw conclusions about the same general trends, absolute values (e.g. C, β) will be subject to change in future work even for emitter tips with nominally identical radii.

In summary, a steady continued development of the quad-thruster ionocraft has put controlled, tethered flight within reach. Work will continue on decreasing operating voltage while increasing thrust density in order to feasibly include a high voltage boost conversion circuit, similar to [10], and microprocessor onboard.

REFERENCES

[1] R. J. Wood, B. Finio, M. Karpelson, K. Ma, N. O. Pérez-Arancibia, P. S. Sreetharan, H. Tanaka, and J. P. Whitney, "Progress on 'pico'air vehicles," *Int. J. Rob. Res.*, vol. 31, no. 11, pp. 1292–1302, 2012.

[2] D. S. Drew and K. S. J. Pister, "First takeoff of a flying microrobot with no moving parts," in *Manipulation, Automation and Robotics at Small Scales (MARSS), 2017 International Conference on*, 2017, pp. 1–5.

[3] L. Pekker and M. Young, "Model of ideal electrohydrodynamic thruster," *J. Propuls. Power*, vol. 27, no. 4, pp. 786–792, 2011.

[4] D. S. Drew and K. S. J. Pister, "Geometric optimization of microfabricated silicon electrodes for corona discharge-based electrohydrodynamic thrusters," *Micromachines*, vol. 8, no. 5, p. 141, 2017.

[5] K. Masuyama and S. R. H. Barrett, "On the performance of electrohydrodynamic propulsion," *Proc. R. Soc. A Math. Phys. Eng. Sci.*, vol. 469, no. 2154, pp. 20120623–20120623, 2013.

[6] A. O. Ong, A. R. Abramson, and N. C. Tien, "Electrohydrodynamic microfabricated ionic wind pumps for thermal management applications," *J. Heat Transfer*, vol. 136, no. 6, p. 61703, 2014.

[7] R. Tirumala, Y. Li, D. A. Pohlman, and D. B. Go, "Corona discharges in sub-millimeter electrode gaps," *J. Electrostat.*, vol. 69, no. 1, pp. 36–42, 2011.

[8] F. W. Peek, Dielectric phenomena in high voltage engineering. New York: McGraw-Hill, 1915.

[9] H. G. Tompkins and J. A. Sellers, "Oxidation of TiN in an oxygen plasma asher," *J. Vac. Sci. Technol. A Vacuum, Surfaces, Film.*, vol. 12, no. 4, pp. 2446–2450, 1994.

[10] M. Karpelson, G.-Y. Wei, and R. J. Wood, "Milligram-scale high-voltage power electronics for piezoelectric microrobots," in *Robotics and Automation, 2009. ICRA'09. IEEE International Conference on*, 2009, pp. 2217–2224.

CONTACT

D. S. Drew; ddrew73@berkeley.edu

A FERROELECTRIC CAPACITOR (FECAP) BASED UNRELEASED RESONATOR

Yanbo He[1], Bichoy Bahr[2] and Dana Weinstein[1]
[1]Purdue University, West Lafayette, IN, USA
[2]Kilby Labs, Texas Instruments, Dallas, TX, USA

ABSTRACT

We present the first $Pb(Zr,Ti)O_3$ (PZT)-transduced unreleased RF MEMS resonator embedded seamlessly in CMOS. The unreleased resonators were realized by using Texas Instruments' Ferroelectric RAM (FeRAM) 130nm technology [1]. A new method of acoustic waveguiding within the CMOS stack was used to confine the resonance mode and an array of ferroelectric capacitors (FeCAPs) inherent to the technology was used as driving and sensing transducers. A resonance frequency of 722 MHz is observed with quality factor Q of 656 and electromechanical coupling coefficient k_{eff}^2 of 0.35%. This corresponds to $f{\cdot}Q$ of $4.7{\times}10^{11}$, comparable to state-of-the-art PZT resonators [2]. These high Q, small footprint resonators offer a CMOS-integrated RF building block with no post-processing or costly packaging.

INTRODUCTION

Over the past decades, the boom in development of RF communications has enabled a range of applications including high bandwidth 5G radio, wearable radars, mm-wave imaging, and beyond. The demanding performance of these systems alongside requirements for miniaturization, lower power consumption, and lower cost have pushed the limits on what conventional technology can currently achieve [3]. With high-Q and small footprint, CMOS-MEMS resonators can provide ideal RF building blocks for filters, low phase noise clocks, and sensors.

The authors have previously demonstrated high-*Q*, unreleased resonators termed Resonant Body Transistors (RBTs) [4] standard CMOS technology at frequencies ranging from 3 GHz [5] to 32 GHz [6]. These resonators leverage the MOS capacitors inherent to the process for electrostatic actuation to drive acoustic resonance in a solid-state acoustic 'cavity' defined using the CMOS layers. While the *f*.Q products of these devices are record breaking, their insertion loss (IL) is limited by the fundamental limits of electrostatic transduction, which provides limited driving force. This is particularly evident in the case of planar CMOS technology (e.g. 32nm SOI), where the electromechanical transconductance for the 3 GHz resonators is on the order of 100nS. The correspondingly high IL of such a device makes oscillator and filter design very challenging. While FinFET technology has proven an effective way to maximize output signal in spite of electrostatic drive [6], ferroelectric memory-based CMOS technologies offer higher transducer coupling to minimize IL by leveraging piezoelectric materials introduced in the back-end-of-line (BEOL) process. Higher coupling k^2 also translates to larger bandwidth filters and higher frequency tolerance to fabrication variations.

In this work, we focus on piezoelectric resonators designed in Texas Instruments' Ferroelectric RAM (FeRAM) process. TI E035 technology contains ferroelectric PZT capacitors integrated within the metal layers of the CMOS stack, utilizing the hysteresis characteristics for memory devices (Fig. 1) [1].

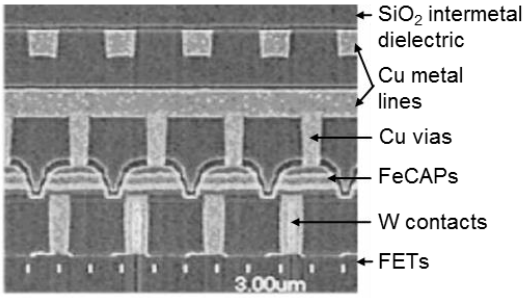

Figure 1: Cross sectional SEM of TI E035 ferroelectric RAM (FeRAM) CMOS technology [1], showing ferroelectric PZT-based capacitors (FeCAPs) within the metal stack.

These devices are the first implementation of ferroelectric capacitor (FeCAP) based unreleased resonators.

This work differs from previously reported devices [4-6] in 3 important ways: (1) The RBTs rely on electrostatic transduction using MOSCAPs with fundamentally lower k_{eff}^2 than the PZT-based resonators in this work. (2) RBTs use transistor sensing to detect the resonance, while the FeCAP resonator is entirely passive. (3) The FeCAP resonator only requires the first metal layer for vertical acoustic confinement, as opposed to a Phononic Crystal composed of all metal layers above the resonance cavity.

SIMULATION AND DESIGN

The side view schematic of the resonator is plotted in Fig. 2, showing an array of trapezoidal FeCAPs each spanning 1.75um in length, connected to Copper strips by Tungsten vias. The resonator consists of 10 driving transducers and 10 sensing transducers alternating with 2um periodicity to form the resonant cavity. To achieve high-Q resonators, it is essential to laterally confine the energy into the resonance cavities while maximizing stress in the vertical direction at the PZT layer within the FeCAP. This is achieved using acoustic waveguiding [4] within the CMOS stack.

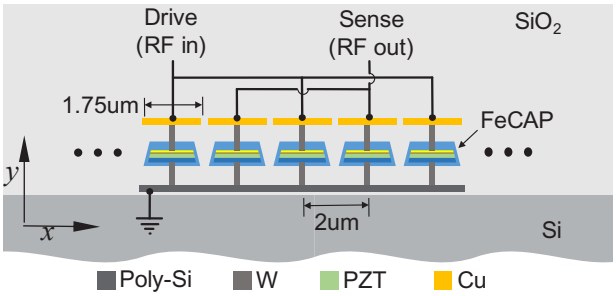

Figure 2: Cross section schematic of FeCAP based resonator (not to scale). A set of 10 drive and 10 sense transducers alternate with 2um periodicity to form an acoustic waveguide in the CMOS BEOL. The resonance cavity is confined laterally with additional dummy FeCAP unit cells on either side of the transducer array.

978-1-940470-03-0/HH2018/$25©2018TRF
DOI 10.31438/trf.hh2018.19

To achieve acoustic waveguiding in CMOS, one must first determine the dispersion relations of the stack assuming lateral (x-direction) translational symmetry. In other words, assuming a repeating structure, we want to find modes that are confined to propagate only in the plane of the wafer. In this case, the periodic structure is the single FeCAP with a 1.75um long Cu strip above it in the BEOL. This unit cell is $a = 2\mu m$ in length. The boundaries are defined as Floquet periodic boundary conditions with $k_x\pi/a$ periodicity. This gives the width of a single period as π/a. This corresponded to the lateral width of the first irreducible Brillouin zone in the reciprocal lattice. The simulation was performed in COMSOL Multiphysics. By searching the eigenmodes along the first irreducible Brillouin zone, the dispersion relations can be mapped as shown in Fig. 3(a).

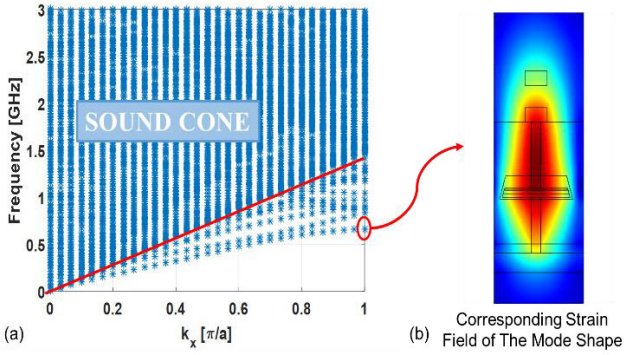

Figure 3: (a) Dispersion relation showing the vertically confined mode. Modes in the sound cone are free to propagate into the bulk Si substrate and cannot be confined. (b) Corresponding localized mode shape of the unit cell FeCAP.

Each point in the dispersion relation (Fig. 3(a)) corresponds to an eigenmode of the periodic FeCAP structure. This dispersion relation can be divided into two regions separated by a sound-line (red) represented by $\omega = c \cdot k$, where c is the shear acoustic velocity in the Si substrate. Above the sound-line is a region where all the modes are free to propagate, referred to as the sound cone. Below the sound line exist several discrete modes with sufficiently low acoustic velocity that they are prohibited from propagation in the bulk and are therefore confined in the BEOL region of the CMOS chip.

It was previously shown [4] that driving near $k_x=\pi/a$ is beneficial for reducing scattering to the sound cone, enabling larger quality factor. Fig. 3(b) shows a vertically confined mode at 700MHz where the strain is well contained in the FeCAP, W via as well as the Cu metal. In practice, the periodic transduction across 20 FeCAPs reinforces the targeted mode with $k_x=\pi/a$ wavenumber. Meanwhile, to laterally confine the waveguided mode, additional dummy FeCAP unit cells are placed on either side of the array. These elements are spaced with the same period as the FeCAP transducers in the resonant cavity.

EXPERIMENTAL RESULTS AND ANALYSIS

The aforementioned devices were fabricated using Texas Instruments' ferroelectric RAM (FeRAM) 130nm technology. Fig. 4 shows a cross-sectional SEM of the device, revealing the periodic FeCAP unit cells above the bulk Si substrate and surrounded by SiO_2 in the BEOL.

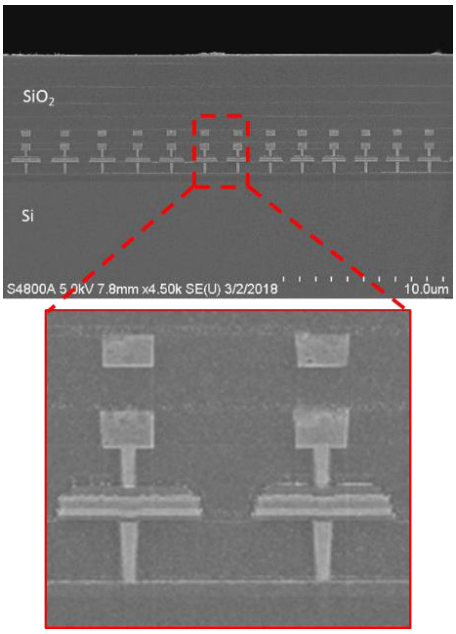

Figure 4: SEM of the waveguided CMOS resonator, showing periodic transducers (alternating drive and sense). Zoom in highlights details of the FeCAPs, with a thin layer of PZT sandwiched between mutli-layered electrodes [1].

The ferroelectric properties of the FeCAP were first characterized to investigate PZT film quality. It should be noted that the film is optimized by the foundry for FE properties for memory and not specifically for piezoelectric coupling. Shown in Fig. 5 is the measured hysteresis of PZT FeCAP polarization.

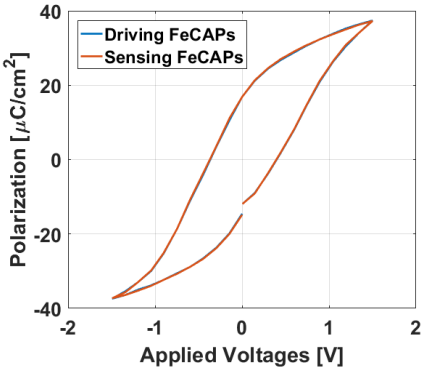

Figure 5: Measured hysteresis of ferroelectric PZT FeCAP polarization. For efficient piezoelectric transduction, a polarization voltage V_P between -1.5V and 1.5V is applied across the device.

The operational polarization voltage V_P is between -1.5 V and 1.5 V. For a total FeCAP area of 98um^2, the maximum polarization obtained is 38uC/cm^2. With this in mind, the 2-port RF measurements were then performed in ambient temperature and pressure using a Keysight PNA N5225A. Two Keithley 2400s were connected to the PNA to set the DC bias. The experimental setup was shown in Fig. 6.

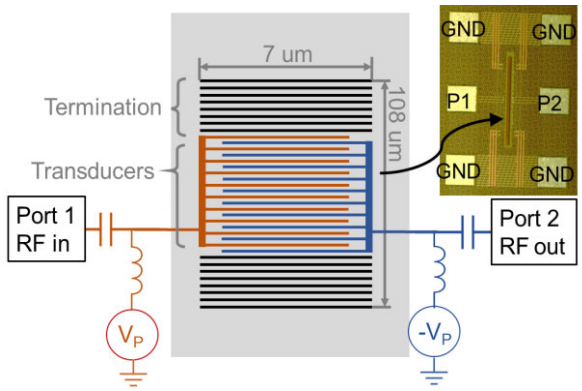

Figure 6: Experimental setup showing top view schematic of resonator. Drive (red) and sense (blue) transducers alternate within the resonator to for the cavity. The acoustic mode is confined laterally using an array of electrically floating FeCAPs (black). Device footprint measures 108 x 7 um.

Driving transducers were connected to Port 1 of the PNA and were biased at 1.5 V whereas the sensing transducers connected to Port 2 and were biased at -1.5 V. The resonators were biased in this way to enforce the excitation of the desired mode at the Brillouin zone edge ($k=\pi/a$). The RF power was set as -15dBm with an IF bandwidth (IFBW) of 500Hz with 30-point sweep averaging.

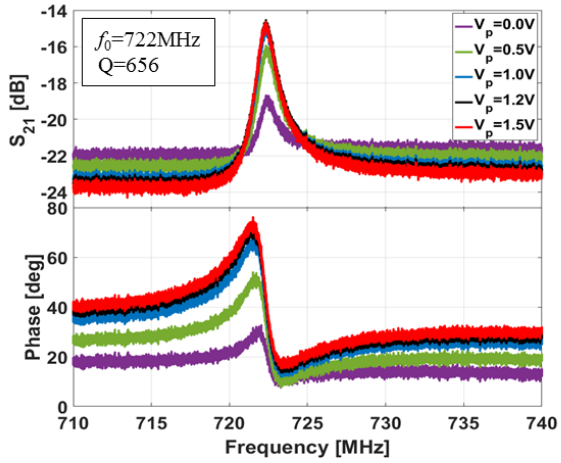

Figure 7 Measured frequency response of FeCAP. Device S21 has been de-embedded from pad/routing parasitics using on-chip Open and Short structures.

Fig. 7 has shown the measured frequency response of the proposed FeCAP resonator. A resonance was observed at 722 MHz. With the increase of polarization voltages, the amplitude of S_{21} increases correspondingly. Table 1 outlines the key specification as a function of V_P.

As shown in Table 1, Q increases with respect to the increasing V_P reaching 656 at the maximum polarization voltage of 1.5 V. This corresponds to an $f{\cdot}Q$ of 4.74×10^{11}. FeCAP transducer capacitance C_0 and electromechanical coupling coefficient k_{eff}^2 were fitted in Advanced Design System (ADS) to a Modified Butterworth-Van-Dyke model. As demonstrated in Table 1, with the increase of polarization voltage, the corresponding C_0 decreases from 21.36pF to 14.06pF. The obtained k_{eff}^2 is 0.35% is lower than typical PZT due to film optimization for ferroelectric hysteresis (memory function) rather than piezoelectric coupling. The maximum Figure of Merit (FOM) k^2Q is 2.3. The demonstrated devices achieve comparable $f{\cdot}Q$ relative to state-of-the-art PZT resonators in a monolithic CMOS platform.

V_P (V)	Q	C_0 (pF)	k_{eff}^2	$f{\cdot}Q$ ($\times10^{11}$)	$k^2{\cdot}Q$
0.0	122	21.36	0.35%	0.88	0.43
0.5	451	17.81		3.26	1.58
1.0	557	14.82		4.02	1.95
1.2	602	13.86		4.35	2.12
1.5	656	14.06		4.74	2.30

Table 1. Key performance of the FeCAP resonator with respect to the increasing driving voltages, with performance improving up to the maximum technology voltage V_P=1.5V.

Temperature stability measurement were also performed on on the FeCAP resonators. Frequency response was obtained between room temperature and 90°C. The extracted Temperature Coefficient of Frequency (TCF) was -58.1±4.6 ppm/°C. This temperature sensitivity matches well to predicted values based on the Temperature Coefficient of Young's Modulus ($TCE = \Delta E/\Delta T$) of the constituent materials in the CMOS BEOL. Both PZT and SiO_2 have positive TCE while W via has negative TCE. In the meantime, most of the strain energy of the resonance mode is localized in the W via (as shown in Fig. 3(b)). Future design may consider BEOL metal geometry for passive temperature compensation.

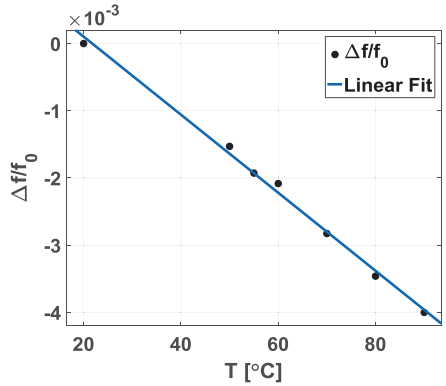

Figure 8: Measured temperature dependence of resonance frequency. A Temperature Coefficient of Frequency TCF=Δf/f0/ΔT of -58 ppm/K is extracted, owing primarily to energy localization in the W vias.

Resonator phase noise, we are using the residue phase noise method [11] with schematic shown in Fig. 9.

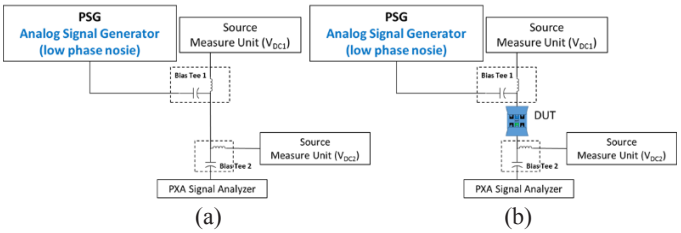

Figure 9: Schematic of the residue phase noise measurement.

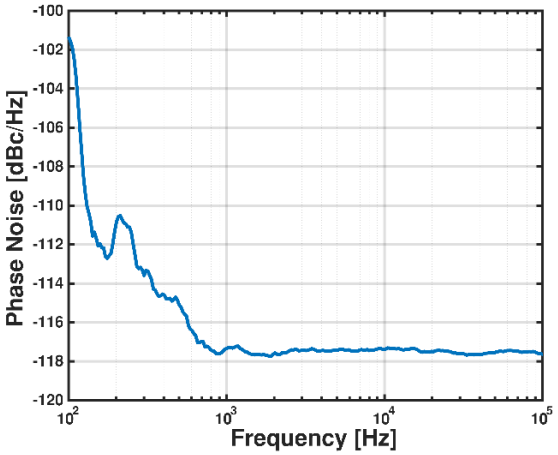

Figure 10: Measured phase noise of the 722 MHz FeCAP resonator, exhibiting -118 dBc/Hz at 1kHz offset from carrier.

The phase noise was measured without the device under test (DUT) (Fig. 9(a)) and with DUT (Fig. 9(b)). The RF signal generator was set in a low phase noise mode. The phase noise of the resonator is then obtained by deembedding the measurement noise from the resonator by:

$$10^{\frac{\mathcal{L}_{component}}{10}} = 10^{\frac{\mathcal{L}_{with\ DUT}}{10}} - 10^{\frac{\mathcal{L}_{without\ DUT}}{10}}.$$

The resulting phase noise of the 722 MHz FeCAP resonator is plotted in Fig. 10. A broadband noise floor of -118 dBc/Hz is measured at 1 kHz offset.

CONCLUSION

This work presents the first demonstration of a PZT-transduced RF MEMS resonator embedded seamlessly in CMOS, leveraging Texas Instrument's FeRAM 130nm technology. The proposed resonator exhibits resonance frequency of 722MHz and Q of 656, alongside an electromechanical coupling coefficient k_{eff}^2 of 0.35%. This corresponds to comparable $f{\cdot}Q$ of 4.7×10^{11} in comparison to state-of-the-art PZT resonators. Table 2 provides a comparison to other IC-integrated and piezoelectric resonators, including previously reported Resonant Body Transistors in GaN MMIC technology. As evident from the table, this work shows higher k_{eff}^2 than the GaN MMIC-integrated resonators primarily due to limits of the material [7-8]. However, this work achieved comparable $f{\cdot}$Q products with most of previous PZT resonators [2], [10], but with the added benefit of direct CMOS integration.

ACKNOWLEDGEMENT

The authors thank Texas Instruments for in-depth design and layout discussions and SEMs, as well as for fabrication of the devices presented here. This work was funded by the DARPA MTO UPSIDE program.

Reference	Type of device	IC	C_0	k_{eff}^2	f(GHz)	Q	$f{\cdot}$Q ($\times10^{11}$)	$k^2{\cdot}$Q
[7]	GaN Lamb mode RBT	MMIC integrated	17 fF	0.17%	1.011	5509	55.70	9.37
[8]	GaN thickness mode RBT	MMIC integrated	1.59 pF	0.08%	4.230	250	10.58	0.20
[2]	PZT FBAR	Not compatible	-	52.7%	3.724	114	4.245	60.08
[9]	PZT contour mode resonator	Not compatible	1.55 pF	0.05%	0.011	6575	0.704	3.29
[10]	AlN contour mode resonator	CMOS compatible	1.25 pF	0.54%	0.223	4300	9.589	23.22
This Work	FeRAM CMOS resonators	CMOS integrated	14.06 pF	0.35%	0.722	656	4.736	2.30

Table 2. Comparison of the key performance of the FeCAP resonators with previously reported IC-compatible and PZT devices.

REFERENCE

[1] K. Udayakumaret, et. al. "Manufacturable High-Density 8 Mbit One Transistor–One Capacitor Embedded Ferroelectric Random Access Memory." Japanese Journal of Applied Physics 47.4S (2008): 2710.

[2] B. Harmeet, and G. Piazza, eds. Piezoelectric MEMS Resonators. Springer, 2017 (Chapter 2).

[3] B. Bhar. Monolithically integrated MEMS resonators and oscillators in standard IC technology. Diss. Massachusetts Institute of Technology, 2016.

[4] D. Weinstein, and S. Bhave. "The resonant body transistor." Nano letters 10.4 (2010): 1234-1237.

[5] B. Bahr, D. Weinstein, "Vertical Acoustic Confinement for High-Q Fully-Differential CMOS-RBTs," Hilton Head 2016.

[6] B. Bahr, Y. He, et al., "32GHz Resonant-Fin Transistors in 14nm FinFET Technology" to be presented at ISSCC 2018.

[7] L. Popa and D. Weinstein. "L-band Lamb mode resonators in gallium nitride MMIC technology." Frequency Control Symposium (FCS), 2014 IEEE International. IEEE, 2014.

[8] A. Ansari, and M. Rais-Zadeh. "A thickness-mode AlGaN/GaN resonant body high electron mobility transistor." IEEE Transactions on Electron Devices 61.4 (2014): 1006-1013.

[9] J. Pulskamp, et al. "Ferroelectric PZT MEMS HF/VHF resonators/filters." Frequency Control Symposium (IFCS), 2016 IEEE International. IEEE, 2016.

[10] G. Piazza, J. S. Philip, and P. Albert. "Piezoelectric aluminum nitride vibrating contour-mode MEMS resonators." Journal of Microelectromechanical systems 15.6 (2006): 1406-1418.

[11] J. Breitbarth, and K. Joe. "Additive (residual) phase noise measurement of amplifiers, frequency dividers and frequency multipliers." Microwave Journal 51.6 (2008): 66.

*Y. He, he355@purdue.edu

PIEZOELECTRIC SINGLE CRYSTAL 6H SILICON CARBIDE MICROELECTROMECHANICAL RESONATORS

Raviv Perahia, Logan D. Sorenson, Jeremy L. Bregman, Lian X. Huang, Makena S. White, Kevin S. Holabird, and David T. Chang*
HRL Laboratories, LLC, Malibu, California, USA

ABSTRACT

Piezoelectrically driven and sensed single-crystalline 6H silicon carbide (SiC) microelectromechanical resonators were designed and fabricated on a novel 100 mm silicon carbide on insulator (SiCOI) process. The prototype resonators have frequencies in the UHF range (464 MHz) with quality factors (Qs) as high as 7,400 for an f*Q product of 3.4×10^{12}. Measurements at temperatures up to +200°C and RF drive levels of up to 30 Vac demonstrate that these resonators are robust for high temperature and high power applications.

INTRODUCTION

In this paper we demonstrate electrically-driven single-crystalline 6H silicon carbide (SiC) microelectromechanical (MEMS) resonators. In contrast to current state-of-the-art SiC resonators, the resonator presented herein is driven electrically by its own piezoelectric properties, not by an additional piezoelectric layer [1-2] or by alternate means [3]. SiC has been recognized as a potential leading MEMS material due to its high bandgap, high thermal conductivity, and ultra-low mechanical loss [4-6]. Yet the difficulty of fabricating silicon-on-insulator (SOI) like structures has held back the proliferation of SiC MEMS technology. In this paper we experimentally demonstrate a resonator fabricated from a SiC-on-insulator (SiCOI) substrate using standard 100 mm wafer bonding, thinning, and etching techniques with significant advantages over smart-cut technologies [3]. The resonator technology presented enables high voltage (> 30 Vac) reference oscillators to generate frequency sources at ultra-high frequencies (300 MHz to 3 GHz), a potential game changer for wireless communication.

6H SILICON CARBIDE RESONATOR DESIGN AND EXPERIMENTAL REALIZATION

A schematic cross section of the piezoelectric resonator is shown in Figure 1. Similar to a SOI process, the 6H SiC layer is bonded to a Si substrate with an intermediate sacrificial silicon dioxide dielectric layer to form the SiCOI wafer. RF electric field is exerted in the thickness-direction (Z) by a set of electrodes formed on top of the SiC layer with alternating polarity. A ground electrode is formed on the bottom of the SiC layer and accessed with metallized vias. Finally, the sacrificial oxide is removed via either vapor HF etching or liquid HF etching followed by critical point drying.

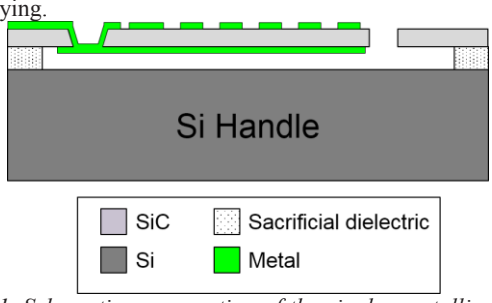

Figure 1. Schematic cross section of the single-crystalline 6H SiC piezoelectric MEMS resonator fabricated on a SiC-on-insulator (SiCOI) wafer.

Figure 2(a) shows a photograph of a typical custom bonded 100 mm SiCOI wafer after thinning of the SiC layer to final target thickness. Only two voids were observed after bonding. Since the SiC to oxide bond is very strong and uniform across wafer, the voids remained the same size after annealing, and the SiC layer only delaminated at the void regions after grind and polish, as shown in the two dark regions in the photograph. Figure 2(b) maps the resulting SiC layer thickness after grind and polish. A median SiC thickness of 3.5 µm was achieved. A thin SiC layer is desirable to exploit the intrinsic piezoelectric properties of 6H SiC, since a greater electric field strength can be imparted across the thickness of the resonator for the same RF drive voltage.

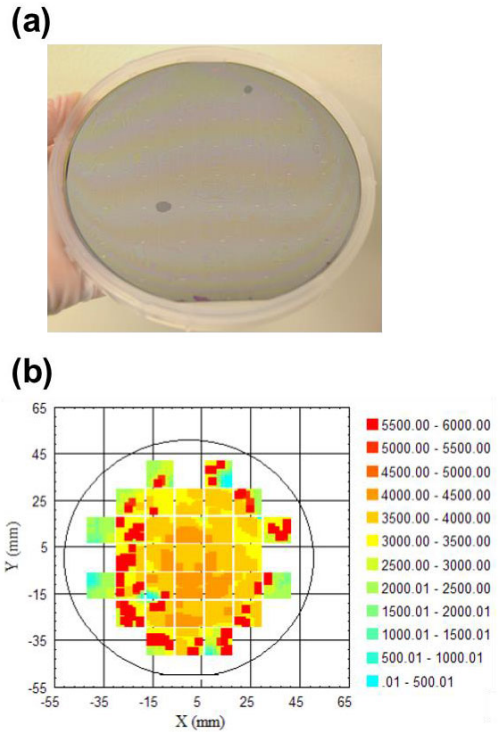

Figure 2. (a) 100 mm SiCOI wafer after grind and polish down to target median thickness of 3.5 µm, (b) wafer map of SiC layer thickness.

Finite element method (FEM) simulation of the expected mode profile of the designed resonator structure is shown in Figure 3. Since the 6H SiC in this work has its crystalline c-axis oriented parallel to the thickness of the device, a high-order in-plane extensional mode is excited via the lateral field piezoelectric coefficient e_{31}. Figure 3(a) shows the total displacement field, while Figure 3(b) and 3(c) show the along length (Y) and along thickness (Z) displacements, respectively. The Z displacement pattern is needed for comparison with laser doppler vibrometer (LDV) measurements presented later. From these figures, it is seen that the alternating electric field polarity induces an alternating polarity extensional strain region centered at each electrode finger. While the Y displacement pattern shows a clean vibration mode, it

978-1-940470-03-0/HH2018/$25©2018TRF
DOI 10.31438/trf.hh2018.20

was found that asymmetries in the thickness direction induced from having a solid blanket metal on the backside of the SiC layer caused the Z displacement to have additional perturbations of the mode pattern in addition to the expected alternating polarity from the in-plane extensional mode. However, the perturbing motion is much smaller than the desired Y displacement pattern and can be ignored for practical purposes. Figure 3(d) plots the result of a coupled piezoelectric frequency domain analysis of the resonator when an RF drive voltage is applied to one of the interleaved electrode plates and the piezoelectrically-generated charge is collected on the other electrode plate. For this particular resonator design, a simulated resonance frequency of 463.7 MHz is obtained, which matches with experimental results from electrical and optical testing (464.5 and 464.2 MHz, respectively).

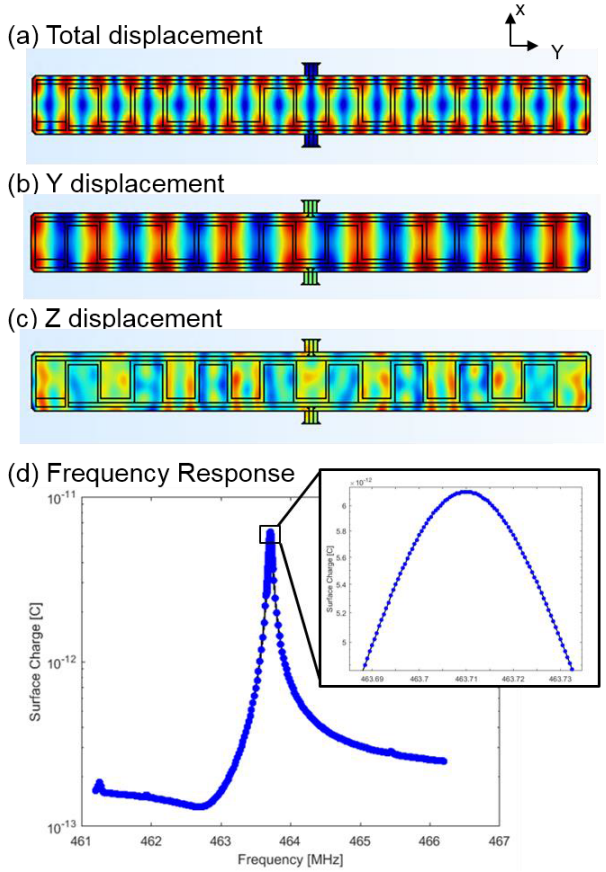

Figure 3. Simulated resonator mode shape at resonance for 2.7 µm SiC thickness (a) total displacement, (b) Y displacement (along length of resonator, L), (c) Z displacement (out-of-plane displacement), (d) simulated resonance response from frequency sweep.

Figure 4 shows several scanning electron microscope (SEM) images of typical fabricated SiC resonators. An overview of the entire device including the ground-signal-ground (GSG) RF pads is captured in Figure 4(a). To facilitate testing of several different resonator geometries without repositioning probes, a common GSG spacing was chosen and 50 Ω coplanar stripline waveguides were designed to bring the RF signal into the device. The resonator plate is etched from a single layer of 6H SiC and has length L and width W as indicated by the yellow arrows in the SEM image in Figure 4(b). The final freestanding SiC resonator is defined by etching of narrow trenches around the resonator except at the tether regions, as shown in the dark black "U" shaped areas in the SEM image, followed by removal of the sacrificial layer. The expected frequency of this device is given by

$$f \approx N/(2L) * v_{\text{acoustic}}, \qquad (1)$$

where L is the resonator plate length, N is the number of interleaved electrodes, and $v_{acoustic}$ is the speed of sound. For our prototype devices, we have selected $N = 17$ to maximize both the strain generated by the voltage applied to the piezoelectric transducers as well as the motional current collected on the output side of the device. The centerline-to-centerline electrode spacing is denoted as the electrode pitch in Figure 4(c), and is determined by

$$P_{\text{electrode}} \approx L / N. \qquad (2)$$

For the resonator shown in Figure 4(b,c), $P_{electrode}$ = 12.35 µm, L = 211 µm, and W = 22 µm. The SiC thickness was 2.7 µm for this device. Also visible are the four via holes which pass the ground planes through to the bottom surface of the SiC layer, after which they are routed across the tethers connecting the resonator body to the surrounding SiC frame. In a similar manner, the RF signal lines bridge the tethers on the top surface of the SiC.

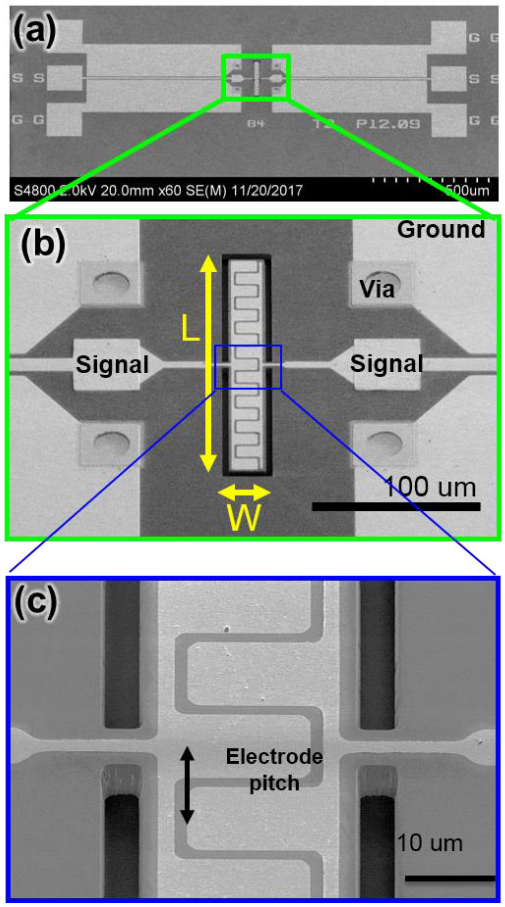

Figure 4. (a) Scanning Electron Microscope (SEM) micrograph of fabricated 6H single-crystalline SiC resonator with input and output RF ports, (b) zoom-in view of SEM micrograph of a full resonator, (c) close-in SEM micrograph of resonator central region and tethers.

ELECTRICAL CHARACTERIZATION OF PIEZOELECTRIC 6H SIC RESONATORS

A set of resonators with varying lengths and two different thicknesses were systematically measured using a vector network analyzer. Figure 5(a) presents a plan view schematic of a 1 cm by 1

cm die containing 30 resonators and 8 de-embedding structures. The 30 resonators are divided into 3 designs, resulting in 10 resonators of each design which occupy two rows of the die. The resonator pitches within a design are varied from 10.53 µm to 12.87 µm in steps of 0.26 µm, resulting in frequency steps between 8 and 13 MHz. Figure 5(b) is a photograph of a corresponding fabricated SiC resonator die. Figure 6 shows the electrical testing setup on a wafer probe station. GSG probes are positioned on the device pads with the aid of the microscope and connected to the vector network analyzer via coaxial cables. An impedance standard substrate is used to bring the calibration plane to the probe tips prior to measurement.

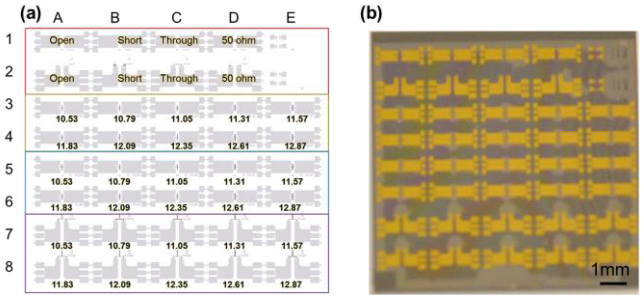

Figure 5. (a) Schematic plan view of a 1 cm by 1 cm resonator die with 30 resonator design variations and 8 de-embedding structures. Electrode pitch (µm) and measured frequency (MHz) is given for each design; (b) Top view photograph of a released die.

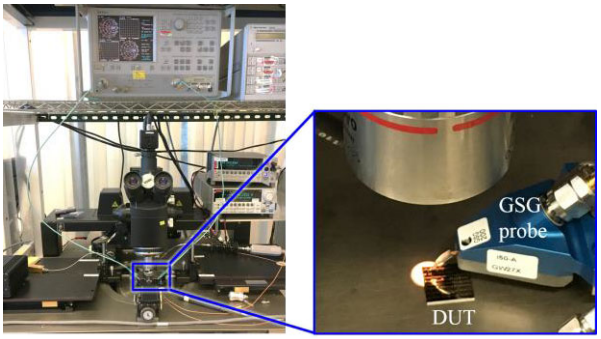

Figure 6. Wafer probe station equipped with vector network analyzer (VNA), microscope, sample stage, and GSG probes. The die under test (DUT) is placed on the sample stage and the GSG probes are positioned under the microscope for each device.

A typical measurement using this setup is shown in Figure 7(a) for the resonator of Figure 4(b,c). The resonance frequency of this particular device is 464.5 MHz, indicated by the sharp peak in the transmission (S21) at that frequency and the corresponding dip in the reflection (S11). The electrical transmission response demonstrates the characteristic anti-resonance indicative of capacitive feedthrough in piezoelectric devices. Measurements of the resonance frequencies as function of resonator pitch are shown in Figure 7(b). Also plotted are finite element method (FEM) predicted frequencies, exhibiting excellent correspondence. As expected from the frequency law above (Eq. 1), an increase in the electrode pitch of the device causes a decrease in the frequency (this is because L increases with electrode pitch for a fixed number of electrodes N). The red and green experimental trend lines (linear fit) are seen to be good agreement with the FEM predicted frequencies, indicating that the resonances observed correspond with the expected vibration modes. This is strong evidence that the observed resonances are the designed piezoelectrically-transduced vibration modes.

OPTICAL CHARACTERIZATION OF PIEZOELECTRIC 6H SIC RESONATORS

Figure 8 shows the experimental configuration of the resonator die and several 2D Laser Doppler Vibrometer (LDV) scans of the same 6H SiC resonator from Figure 4(b,c). To facilitate the LDV measurement, which could not be done on the wafer probe station due to the requirement of a scanning XY stage, the resonator die was mounted and wirebonded in a ceramic leadless chip carrier (LCC) as shown. A socketed breakout board was used to bring in the RF drive signal.

Since the LDV measures motion perpendicular to the wafer, only the Z component of the resonator displacement pattern can be measured. The Z component of displacement is induced through Poisson's ratio in the extensional mode, thus providing a good measure of the extensional strain pattern of the resonator. Clearly visible in Figure 8 are the 17 regions of alternating strain polarity corresponding with the alternating polarity voltage applied to the top electrodes (compare with the Z displacement pattern of Figure 3). Also shown in the figure is the acoustic radiation leaking into the substrate through the support tethers. An AC voltage amplitude of 30 V was used in this experiment, which resulted in a max Z displacement of approximately 50 nm. This demonstrates the potential of MEMS SiC resonators to generate high voltage in ultra-high frequency applications when operated in oscillator configurations.

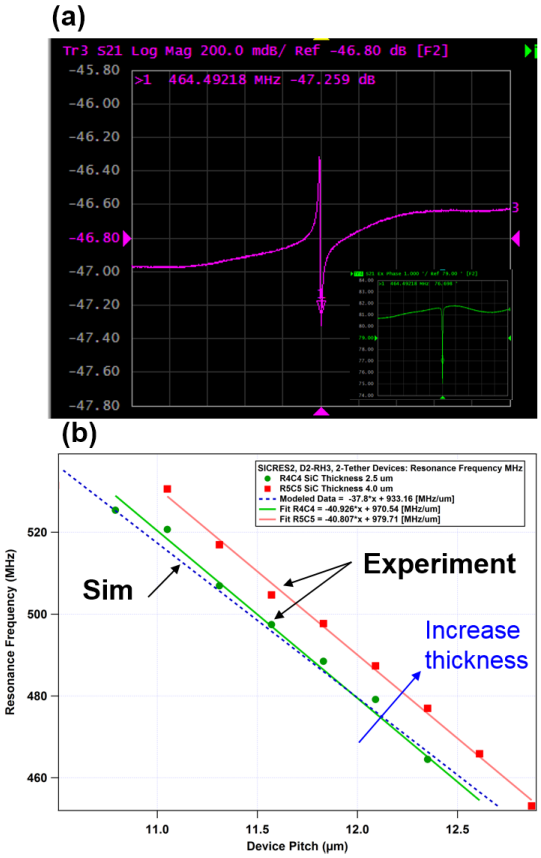

Figure 7. Experimental test results with vector network analyzer: (a) frequency sweep of one resonator design, (b) simulation and experimental data for frequency trend as a function of electrode pitch and device thickness. Frequency decreases when electrode pitch increases, and frequency decreases when electrode thickness decreases.

As shown in Figure 9, the resonance frequency for the 17th order longitudinal extensional mode was found from the LDV to be 464.2 MHz and the measured quality factor (Q) was 7,400 in air, resulting in an f*Q product of 3.4×10^{12}. This is a very high frequency-quality factor product approaching that of crystalline quartz. With further improvements to the resonator design to eliminate anchor loss from the tethers (see Figure 8 inset), we expect that an f*Q product of 6×10^{14} can be achieved [6], surpassing that of quartz and making these resonators the highest performing resonators to date in terms of phase noise and oscillator stability.

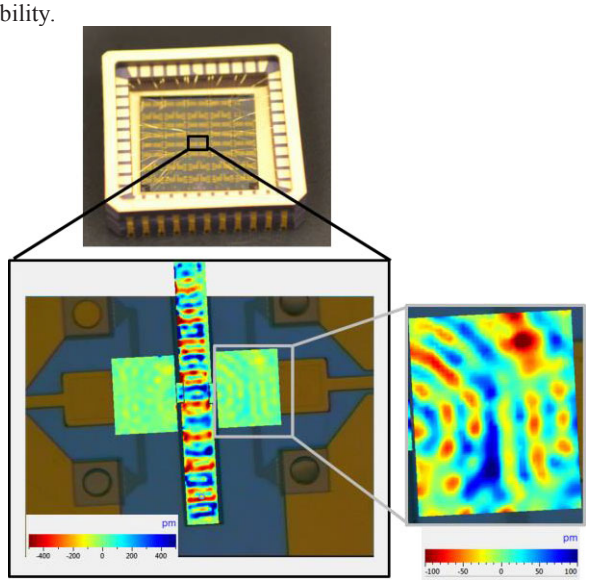

Figure 8. Laser Doppler Vibrometer (LDV) measurement of the Z component of the 6H SiC resonator extensional mode displacement pattern. (Inset) Circular radiation pattern emanating from tether.

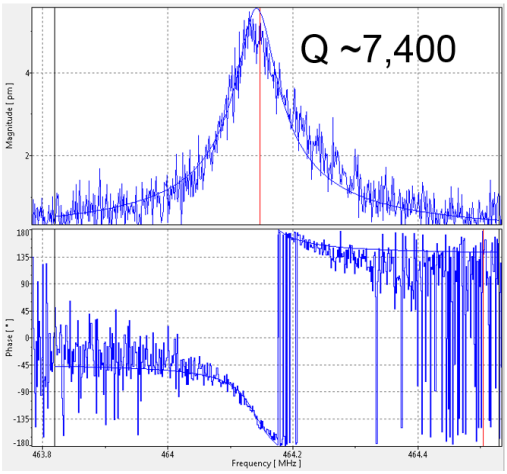

Figure 9. LDV measurement of quality factor (Q) of 7,400 in air at a frequency of 464.2 MHz.

TEMPERATURE CHARACTERIZATION OF PIEZOELECTRIC 6H SIC RESONATORS

Single-crystalline SiC is expected to be a temperature robust MEMS material. To this end, we have measured the device from Figure 2 across temperature on a wafer probe station. The device was tested from +25°C to +200°C and back to +25°C in steps of 10°C with soak time of 10 min per temperature (limited by the wafer probe station maximum temperature). The results of this measurement are plotted in Figure 10. The frequency retrace of the 6H SiC resonator is excellent, exhibiting little hysteresis to within the temperature control ability of the wafer probe station. A linear fit to these results produces a temperature coefficient of frequency (TCf) of -18 ppm/°C for the 6H SiC device.

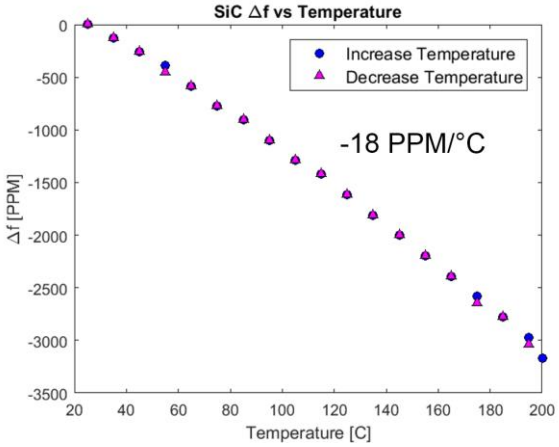

Figure 10. Measurements of the resonance frequency change in PPM of the resonator of Figure 4(b,c) from +25°C to +200°C and back to +25°C.

DISCUSSION AND CONCLUSIONS

The presented 6H SiC resonators were found to be robust to drive voltages up to 30 V_{ac} as well as temperatures at least +200°C, limited by the probe station. A moderate TCf of -18 ppm/°C was obtained for the particular resonator configuration. The piezoelectric response was measurable on a network analyzer up to 200°C, providing evidence that the piezoelectric effect can be maintained in SiC up to even higher temperatures. The relatively weak piezoelectric coupling coefficient of SiC makes it amenable to thin layer thicknesses, wherein the electric field strength can be more concentrated for the same applied drive voltage.

REFERENCES

[1] "Two-Port Piezoelectric Silicon Carbide MEMS Cantilever Resonator", B. Svilčić, E. Mastropaolo, R. Cheung, Informacije Midem, Vol. 43, No. 1 (2013), 22–26.

[2] "Piezoelectric Aluminum Nitride Vibrating Contour-Mode MEMS Resonators," G. Piazza, P. J. Stephanou and A. P. Pisano, Journal of Microelectromechanical Systems, vol. 15, no. 6, (2006), 1406-1418.

[3] "6H-SiC microdisk torsional resonators in a "smart-cut" technology", R. Yang, Z.Wang, J.Lee, K. Ladhane, D.J. Yong, P. X.-L. Feng, Applied Physics Letters 104, 091906 (2014);

[4] "Silicon carbide MEMS for harsh environments", M. Mehregany, C. A. Zorman, N. Rajan, and C. H. Wu, Proc. IEEE 86, 1594 (1998).

[5] "Limits of quality factor in bulk-mode micromechanical resonators", Chandorkar, S. A. et al., Proc. IEEE Int. Conf. MEMS, 74–77 (2008).

[6] "Effect of phonon interaction on limiting fQ product of microelectromechanical resonators", R. Tabrizian, M. Rais-Zadeh, and F. Ayazi, International Solid-State Sensors, Actuators and Microsystems Conference, 2009. (TRANSDUCERS 2009).

CONTACT

*R. Perahia, tel: +1-310-317-5000; rperahia@hrl.com

FREQUENCY COMB GENERATION IN A NONLINEAR RESONATOR THROUGH MODE COUPLING USING A SINGLE TONE DRIVING SIGNAL

David A. Czaplewski[1], Steven W. Shaw[2], Oriel Shoshani[3], Mark I. Dykman[4], and Daniel Lopez[1]
[1]Argonne National Laboratory, Argonne, IL, USA
[2]Florida Institute of Technology, Melbourne, FL, USA
[3]Ben-Gurion University of the Negev, Beersheba, ISR
[4]Michigan State University, East Lansing, MI, USA

ABSTRACT

In this paper, we demonstrate bursting behavior in a nonlinear microelectromechanical (MEMS) resonator that creates a frequency comb in the corresponding spectral response. The bursting behavior occurs for a single driving tone applied to the resonator. The bursting behavior arises from the non-linear analog of "level anti-crossing" in a 1:3 internal resonance that can efficiently transfer energy between two modes of a resonator at low excitation amplitudes. The internal resonance creates a region in parameter space where stable oscillations do not exist, resulting in a forbidden zone of operation.

INTRODUCTION

Mode coupling generates many interesting and novel behaviors in mechanical [1], optical [2], quantum information [3], and biological [4] systems. When the frequencies of two modes are integer multiples of each other, an internal resonance can be achieved, resulting in efficient inter-modal energy transfer. Resonant mode coupling in closed loop applications has led to novel system behaviors including increased frequency stabilization [5] and the appearance of coherence energy transfer between modes, where the amplitude of the oscillations does not decay for a given period of time after the system drive has been turned off [6].

In this paper, we study resonant mode coupling in a non-linear microelectromechanical (MEMS) resonator using an open loop configuration with a single drive frequency. Open loop driving allows us to explore the dynamic response of the system at and near internal resonance at different levels of the drive. We identified two new dynamic behaviors: a bursting type behavior, where the response of the resonator changes drastically on a timescale 5 orders of magnitude greater than the period of a single oscillation, and a "forbidden zone", where the resonator does not exhibit stable operations due to the continual exchange of energy between modes. The bursting behavior results from a bifurcation in the response caused by the internal resonance. We demonstrate control over the bursting period and associated spectrum with a single parameter, the detuning of the drive frequency from the internal resonance frequency.

EXPERIMENT AND RESULTS

We study the non-linear dynamic of a MEMS resonator fabricated from an SOI wafer using the SOIMUMPS process from MEMSCAP. The resonator consists of three clamped-clamped single crystal silicon beams connected in the center to two comb drives (Fig. 1a). The resonator is actuated electrostatically through the output of a Zurich UHFLI lock-in amplifier through one comb drive while the movement is sensed via the displacement current generated in the opposing comb drive that is converted into a voltage through a transimpedance amplifier (FEMTO DHPCA-200) and recorded using the lock-in amplifier.

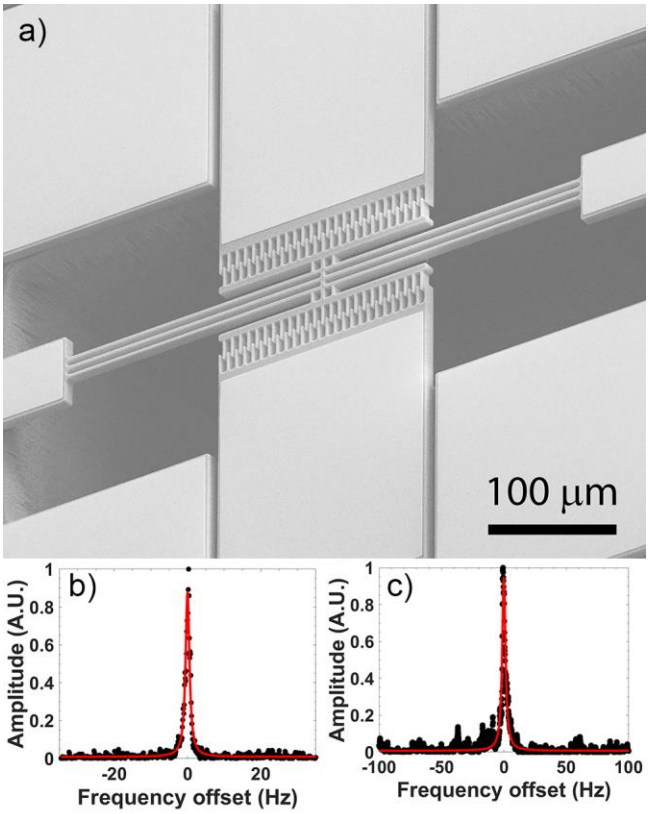

Figure 1 *(a) Scanning electron micrograph of the MEMS resonator showing three single crystal silicon beams connected at their center. The device is actuated using one of the comb drive actuators while the motion is sensed through the generation of a motional current by the other comb. (b) Graph of the amplitude response of the flexural mode as a function of drive frequency offset from the peak response. (c) Graph of the amplitude response of the torsional mode as a function of drive frequency offset from the peak response.*

The frequency response of the MEMS is recorded for various drive voltages. Using the lock-in, the drive amplitude is fixed and the frequency of the drive signal is increased from below the linear resonance frequency of the flexural mode to well above it. The response of the resonator to an applied voltage of 100 μV can be seen in Fig. 1b and corresponds to the fundamental in-plane flexural mode [5]. The response is fit to a Lorentz function and the frequency is measured to be 64580 Hz and the spectral linewidth of the resonator at half power is 0.6 Hz. Similarly, the response of

978-1-940470-03-0/HH2018/$25©2018TRF
DOI 10.31438/trf.hh2018.21

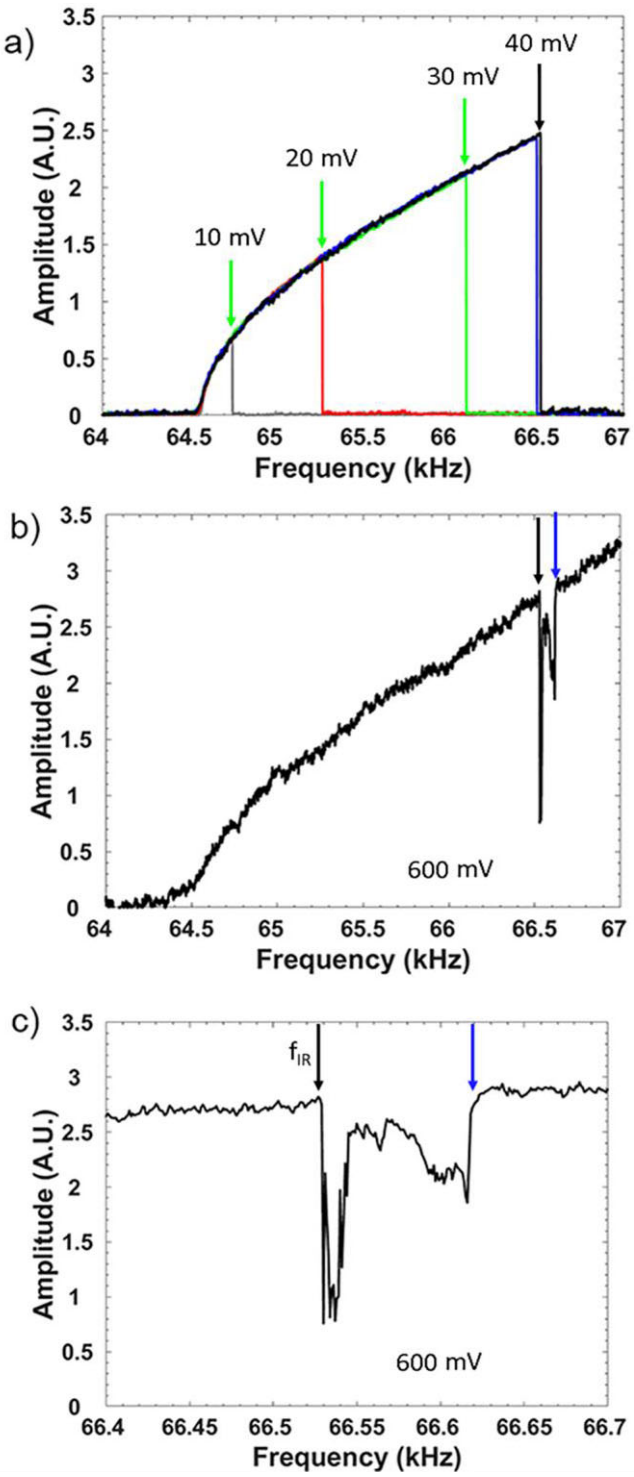

Figure 2 *Amplitude of the first harmonic of the response, i.e., the flexural mode, of the resonator plotted versus the drive frequency. a) As the drive amplitude is increased, the frequency at which the resonator falls to the lower response branch increases until reaching the internal resonance frequency, at which the transitions to the lower branch accumulate. b) For large enough drive amplitudes, the response does not fall to the lower branch, but becomes modulated until resuming normal Duffing behavior. c) Magnified response near internal resonance showing deviation from Duffing behavior that leads to lower average amplitude, but does not transition to the lower branch.*

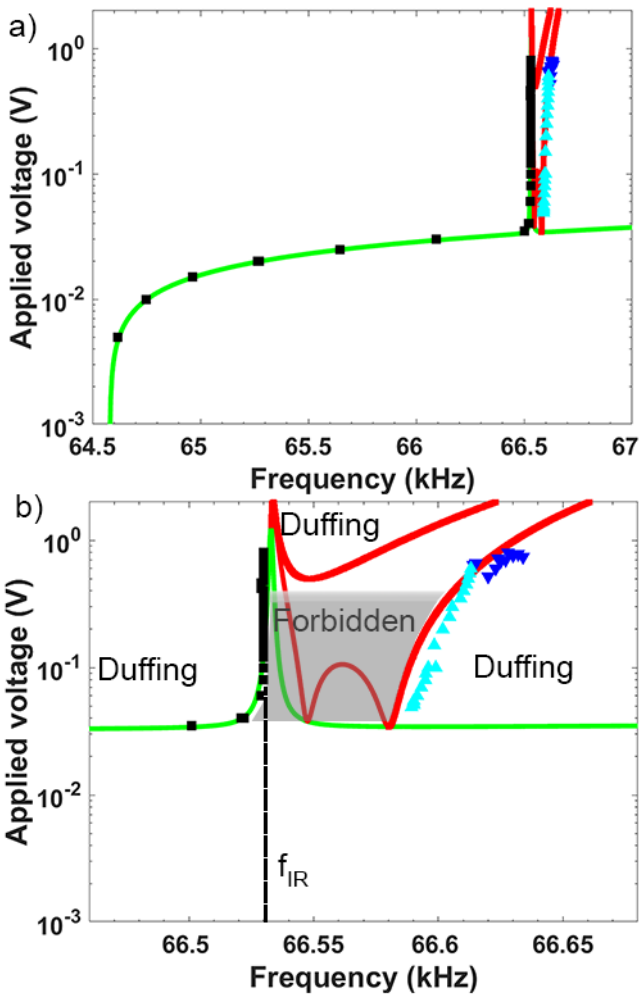

Figure 3 *Bifurcation conditions for which the resonator response changes from Duffing behavior shown in the applied drive voltage versus the drive frequency plane. The squares and triangles are the experimental data while the solid lines are predictions from a model [7, 8].*

a high frequency mode, corresponding to an out-of-plane torsional oscillation [5], is measured (Fig. 1c) at an applied voltage of 500 mV and the frequency found to be 199599 Hz with a spectral line width of 1.6 Hz. The drive amplitude required to actuate the torsional mode is significantly higher than that of the flexural mode due to the inefficient coupling of the drive signal to the torsional degree of freedom using comb drive actuators [5].

As the frequency is swept around the flexural mode resonance at increasingly larger drive voltages, the response of the resonator deviates from Lorentzian and begins to exhibit asymmetries, indicative of a hardening Duffing response [5]. With further increase in drive amplitude, the response curve becomes bistable at larger frequencies, where the resonator response will ultimately fall from the upper branch of the stable response curve to the lower branch. As seen in Fig 2a, the frequency at which this occurs (Fig. 2a green arrows) continues to increase with driving amplitude, until it saturates when it reaches a value around 1/3 of the resonance frequency of the torsional mode, as indicated by a black arrow in Fig. 2a. This behavior is indicative of an internal resonance, where the frequency of one mode corresponds with an integer multiple of the frequency of another mode. As the drive

amplitude is increased, the frequency at which the response falls to the lower branch remains constant at the beginning of internal resonance. However, for even larger drive amplitudes, the response of the resonator can pass through the internal resonance frequency without falling to the lower branch (Fig. 2b black arrow) and finally resume expected Duffing behavior (Fig. 2b blue arrow) after a finite frequency interval. Fig. 2c shows that for this finite frequency interval, the time averaged amplitude is below the expected response from the Duffing model. As the drive amplitude is increased, the range of frequencies over which this reduced mean amplitude behavior occurs, increases. Instead of showing multiple response plots of the data in Fig. 2, it is convenient to plot the frequencies where the resonator response bifurcates, or changes significantly, as a function of the drive amplitude. This mapping from the behavior depicted in Fig. 2 to a bifurcation diagram is shown in Fig. 3. The black squares in Fig. 3a represent the frequencies at which the saddle node bifurcation (Duffing bifurcation) is observed. When the drive amplitude is insufficient to achieve the internal resonance frequency (Fig. 2a green arrows), the resonator response changes from the upper branch to the lower branch at the saddle node bifurcations resulting from the Duffing response as indicated by the vertical lines. For larger drive amplitudes, the resonator response deviates from Duffing behavior and shows a reduced mean behavior starting at the onset of internal resonance (Fig. 2c black arrow) and resumes Duffing behavior again (Fig. 2c blue arrow) at higher frequencies, marked by dark blue triangles in Fig. 3a. The creation of the bifurcation diagram in Fig 3a via frequency sweeps at varying drive levels identifies the locations of many of the system bifurcations. In order to further characterize the bifurcation diagram and determine the resonator response on the right hand side, the resonator was first driven with large enough amplitude to achieve frequencies greater than the internal resonance condition and resume normal Duffing behavior. The drive amplitude was then reduced and the drive frequency decreased toward the internal resonance. When the resonator approaches internal resonance, it transitions to the lower branch as shown in Fig. 3a as light blue triangles. Using this method, the hysteretic frequency response of the resonator is characterized for all frequencies around the internal resonance.

The graph in Fig. 3b shows a zoomed-in region of the parameter space shown in Fig. 3a. The resonator response shows Duffing behavior for much of the operating space, as indicated by the labels "Duffing." When the resonator is driven to those regions of operation, the internal resonance condition is not evident, only the Duffing behavior is measured. However, for the region of internal resonance and low drive levels, the resonator does not have stable oscillations. There is a region of parameter space that is "forbidden", where the resonator transitions to the lower branch of operation and no stable oscillation can be maintained. For driving amplitudes larger than the forbidden region (shaded area in Fig. 3b), the mean amplitude of the resonator is smaller than the expected Duffing response, as shown in Fig. 2c.

A novel dynamic behavior is observed for large driving amplitudes above the forbidden zone. Fig. 4a shows the response of the resonator as a function of time when driven by a single frequency drive. It can be seen from the graph (Fig. 4a blue line) that the response of the first harmonic does not have a constant amplitude: it shows bursting behavior, i.e. it oscillates with a non-sinusoidal pattern which repeats in time with a period several orders of magnitude longer than the relaxation time of either mode. Simultaneous measurement of the third harmonic of the response shows similar periodic behavior.

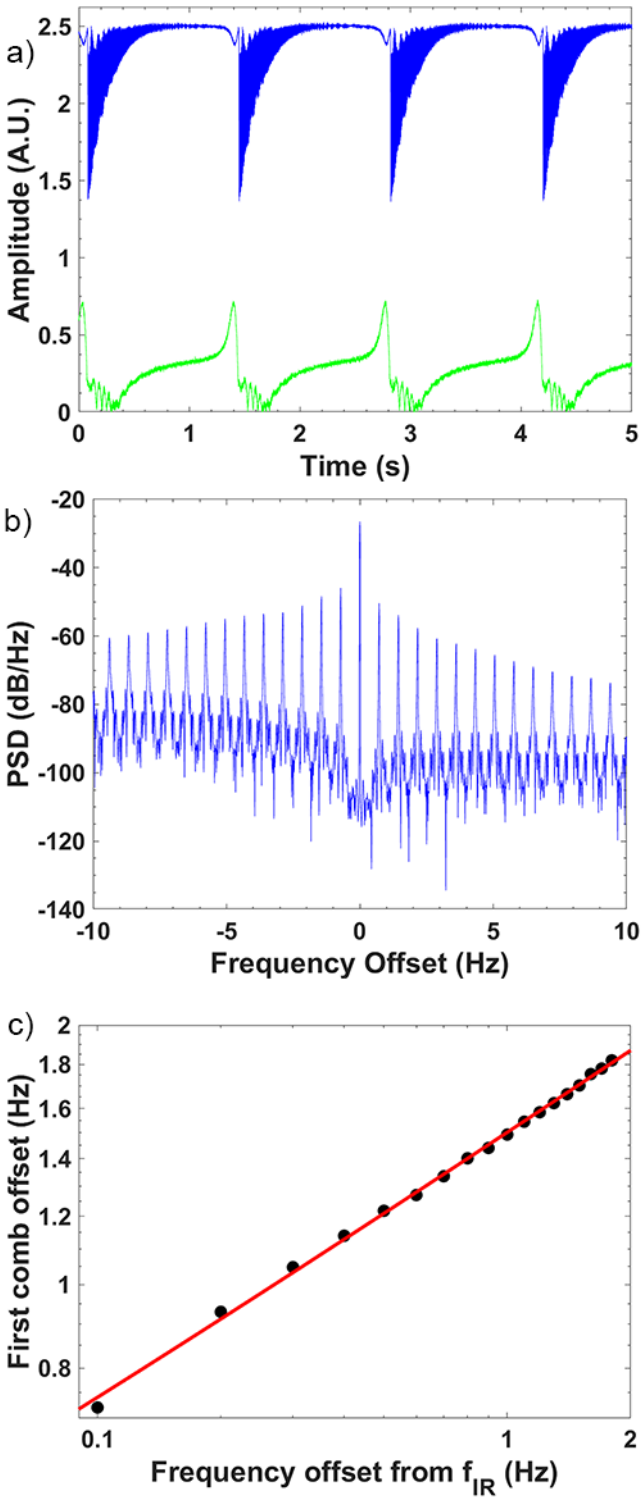

Figure 4 *a) Amplitude of the first harmonic (blue) and third harmonic (green) components of the response of the resonator to a harmonic drive inside the internal resonance region. b) Fast Fourier Transform of the first harmonic of the response in (a) showing the generation of a frequency comb with consistent spacing between the combs. c) Position of the first comb in the FFT as a function of offset frequency from the internal resonance showing cubic scaling (red line).*

At internal resonance, the modes typically associated with the first harmonic (flexural) and third harmonic (torsional) undergo a hybridization [9] and no longer can be described by purely flexural or purely torsional motion in the degrees of freedom. An FFT analysis of the first harmonic component of the response can be seen in Fig. 4b. The bursting nature of the response creates a frequency comb in the spectrum with equally spaced combs in spite of the fact that the resonator is driven with a single frequency drive. As the drive frequency is increased across the internal resonance, the period of the bursting (Fig. 4a) decreases and the spacing of the combs increases. A similar result is obtained from the third harmonic. A graph of the comb spacing versus offset frequency from the internal resonance can be seen in Fig. 4c. A fit of the data to the log-log plot has a slope of 1/3, indicating a cubic relationship between the comb spacing and the driving frequency. The measured response is repeatable with respect to the drive frequency. Also, the response does not show any hysteresis with regards to the frequency; the period of motion and subsequent frequency comb spacing is completely determined by the frequency offset from the onset of internal resonance.

CONCLUSIONS

In this paper, we demonstrate a non-linear MEMS resonator whose primary flexural mode can be detuned through large amplitude driving to achieve mode coupling with the primary torsional mode at an internal resonance. We build a bifurcation diagram of the response of the resonator in the plane of the drive parameters. Near the internal resonance, our measurements demonstrate a region of phase space where the resonator does not show stable oscillations, creating a "forbidden zone" where stable operation is not possible. For single frequency driving signals with amplitudes greater than the forbidden zone, the resonator dynamics is characterized by bursting behavior resulting in the generation of a frequency comb. We speculate that the bifurcation causing the bursting behavior demonstrated here is similar to the mechanism for spiking in neuron models, making this resonator structure a possible candidate to study the mechanical analog of interacting neurons [10].

ACKNOWLEDGEMENTS

The authors thank Scott Strachan for help with the bifurcation diagram. This work was performed, in part, at the Center for Nanoscale Materials, a U.S. Department of Energy Office of Science User Facility, and supported by the U.S. Department of Energy, Office of Science, under Contract No. DE-AC02-06CH11357. OS acknowledges partial support from Ben-Gurion University of the Negev. SWS acknowledges support for this work from the US National Science Foundation under grants CMMI-1662619 and CMMI-1561829.

REFERENCES

[1] R. DeAlba, F. Massel, I. Storch, T. Abhilash, A. Hui, P. McEuen, H. Craighead, and J. Parpia, Nature Nanotechnology **11**, 741 (2016).
[2] A. Sharin, N. Flowers-Jacobs, S. Hoch, A. Kashkanova, C. Deutsch, J. Reichel, and J. Harris, Physical Review Letters **112**, 013602 (2014).
[3] E. Veragen, S. Deleglise, S. Weis, A. Schliesser, and T. J. Kippenberg, Nature **482**, 63 (2012).
[4] G. Buzsaki and A. Draguhn, Science **304**, 1926 (2004).
[5] D. Anonio, D. Zanette, and D. Lopez, Nature Comm. **3** 806 (1012).
[6] C. Chen, et al., Nat. Comm. **8** 15523 (2017).
[7] O. Shshani, S. W. Shaw, and M. I. Dykman, Scientific Reports **7** 18091 (2017).
[8] Scott Strachan, Ph.D. dissertation, Department of Mechanical Engineering, Michigan State University (2017).
[9] J. Guttinger, A. Noury, P. Weber, A. M. Eriksson, C. Lagoin, J. Moser, C. Eichler, A. Wallraff, A. Isacsson, and A. Bachtold, Nature Nano. **12**, 631 (2017).
[10] P. De Maesschalck and M. Wechselberger, J. of Math. Neuroscience **5** 16 (2015).

CONTACT

*D.A. Czaplewski, tel: +1-630-252-3258; dczaplewski-at-anl.gov

ULTRA-HIGH Q MONOCRYSTALLINE SILICON CARBIDE DISK RESONATORS ANCHORED UPON A PHONONIC CRYSTAL

Jeremy Yang, Benoit Hamelin, Seung-Deok Ko, and Farrokh Ayazi
Georgia Institute of Technology, Atlanta, Georgia, USA

ABSTRACT

This work introduces a 3D design incorporating a phononic crystal to decouple a centrally-supported silicon carbide bulk acoustic wave disk resonator from its Si handle layer. By overcoming thermoelastic and anchor losses in bulk acoustic wave resonators, this scheme allows for probing the phonon-phonon dissipation limits i.e. Akhiezer loss. Using a custom silicon carbide on insulator platform, SiC disk resonators anchored upon phononic crystal were fabricated and optically measured. SiC disk resonators exhibit Q-factors near 4M with a record $f \cdot Q$ product of 1.85×10^{13} Hz for the radial breathing mode operating at 5 MHz, limited by thermoelastic losses. This is the highest $f \cdot Q$ measured in monocrystalline silicon carbide resonators, an important step toward the batch fabrication of inertial-grade SiC BAW gyroscopes.

INTRODUCTION

The pursuit of ultra-high quality factors (Q) in micro and nano resonators is of great interest and importance, benefiting a wide range of applications. Bulk acoustic wave (BAW) disk resonator gyroscopes offer a host of benefits including shock and vibration resilience, high bandwidth and high Q in moderate vacuum environment, thanks to their relatively high operating frequencies (MHz). With sufficiently high Q, inertial grade MEMS gyroscopes in small planar form factor are realizable[1], meeting or potentially surpassing the state of the art. The resonator design needs to surmount energy dissipation mechanisms such as thermoelastic dissipation (TED) and anchor loss (ANC) to reach the Akhiezer limit (AKE) of dissipation. As shown in this paper, with a disk resonator centrally-anchored upon a handle layer composed of a phononic crystal structure (Fig.1), one can largely circumvent anchor losses, scaling a significant barrier toward inertial grade SiC BAW gyroscopes. Batch fabrication of monocrystalline disk resonators is enabled by custom-made silicon carbide on insulator substrates (SiCOI) [2].

DISSIPATION IN SIC BAW RESONATORS

An ideal resonator is lossless with an infinite Q. Naturally, various physical phenomena exist to siphon energy from the device, limiting its ultimate performance defined by fundamental AKE phonon-phonon interactions. When the phonon distribution is perturbed from its equilibrium distribution by an acoustic wave, normal and Umklapp scattering with thermal phonons act to bring the distribution back to equilibrium[2]. Strongly temperature and material dependent, dissipation is minimal as lattice thermal vibrations are small; conversely, more lattice vibrations at high temperature offer more scattering opportunities. With a large stiffness and low average Grüneisen parameter, silicon carbide is an ideal candidate for ultra-high Q sensors as it possesses an $f \cdot Q_{AKE}$ of 6.4×10^{14} Hz, over 30× higher than silicon's[3]. However, other dissipation mechanisms must be addressed before hitting Akhiezer limits. Due to the BAW disk resonator's relatively high operating frequency, in vacuum, disks typically suffer from TED and anchor losses.

Thermoelastic dissipation occurs in any material that experiences thermal expansion. Three TED operating regimes exist: isothermal, adiabatic, or maximally dissipative (Debye)[4]. In elliptical bulk acoustic wave disk resonators at the MEMS scale, the resonant mechanical frequency is highly disparate from the principal thermal mode frequencies, pushing the device into the deep adiabatic regime, minimizing TED to elevate Q_{TED} to 14M for the breathing mode (Fig.2) in FEM simulation.

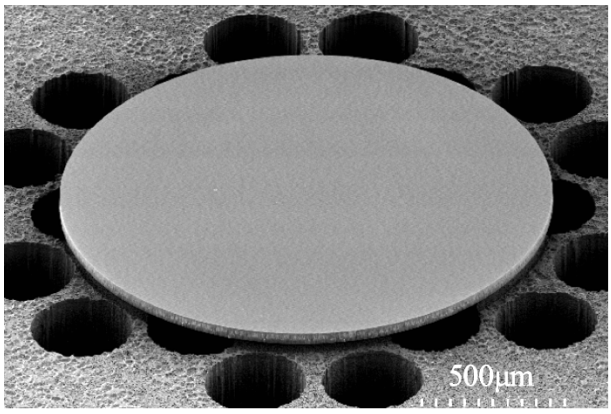

Figure 1: SEM of BAW SiC disk resonator (100µm thick, 1540µm diameter) anchored upon a phononic crystal of three unit cells. The radial mode resonates at 5 MHz.

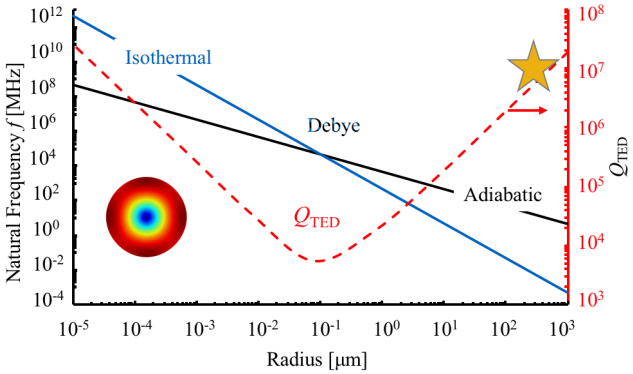

Figure 2: Bulk elliptical modes, the breathing mode in particular (star), of a 1540µm disk operate adiabatically where $f_{mechanical}$ (black)>>$f_{thermal}$ (blue). Minimum Q_{TED} (red) occurs at the Debye frequency. The breathing mode and m=3 modes possess Q_{TED} of 14M and 50M, respectively.

Anchor loss remains as one of the most conspicuous sources of loss, adding unpredictability to the limits of quality factor. In centrally-anchored disk resonators, the suppression of anchor loss is particularly difficult due to large elastic strain energy density in the vicinity of the pedestal. While shrinking the size of the pedestal support monotonically mitigates anchor losses, clearly it cannot be made excessively small to ensure resilience against shock and vibration. Similarly, elongation of the pedestal offers a measure of isolation, again compromising structural integrity. Substrate-decoupling elements may be incorporated into the device layer[5][6]; however, this comes at the expense of increased TED due to additional strain at the sites of the occlusions. Therefore, it's imperative to implement a 3D design in which the substrate-

978-1-940470-03-0/HH2018/$25©2018TRF
DOI 10.31438/trf.hh2018.22

decoupling elements lie in the handle layer beneath the disk, leaving the disk unencumbered by TED while eliminating anchor losses.

PHONONIC CRYSTAL DECOUPLING

A phononic crystal (PnC) is a structure composed of stacked acoustically mismatched layers (superlattice) or a tessellation of periodic inclusions in an elastic medium. Analogous to a photonic crystal for electromagnetic radiation, the mismatch of acoustic impedance between the layers or inclusions reflects waves, introducing wave interference which creates the band gap of the PnC[7]. Two critical parameters determine the behavior and characteristics of the band gap[8]: the center frequency and band gap width. The center frequency is defined principally by the characteristic unit cell length *a*, typically on the order of the propagating wave's wavelength. The width of the band gap is heavily affected by the acoustic impedance discrepancy between the propagating medium and the inclusions. Filling factor (the ratio of the area of the inclusions to the area of the unit cell) is the primary parameter influencing the width of the gap. A structure's bandgap behavior can be described by its $f \cdot a$ product [Hz·m], as wavelength and frequency are inversely proportional. With increasing filling factor, the bandgap widens. Our design implements a honeycomb lattice, previously shown to offer the widest bandgap at the lowest filling factor (Fig.3), conferring exemplary decoupling while maintaining device robustness. FEM eigenmode simulations based on Bloch-Floquet wave theory were performed across the first Brillouin zone of the honeycomb lattice, with the eigenmodes subsequently mapped onto k-space yielding the bandgap[9].

The PnC design addresses the in-plane components of the energy lost to the substrate. However, without proper vertical out-of-plane decoupling, anchor loss remains a significant issue. To enable vertical confinement, it is critical to match the thickness of the silicon handle layer to the quarter wavelength of the acoustic wave[10], determined by its frequency and the speed of wave propagation in silicon (Fig.4). By suspending the device in air to maximize acoustic impedance mismatch, the quarter wavelength roughly creates a standing wave with node and antinode at the surfaces of the handle layer, confining energy and elevating Q_{ANC}.

In perfectly matched layer (PML) simulation, the tandem of quarter wavelength matching and the PnC offer excellent substrate decoupling. Critically, placing more PnC unit cells in the decoupling layer offers greater opportunity for propagating waves to reflect and interfere, improving energy confinement. With a sufficient number of unit cells placed around the anchor of the disk, the disk can be made substrate "deaf," leaving the device limited exclusively by intrinsic dissipation mechanisms i.e. TED and AKE (Fig.5).

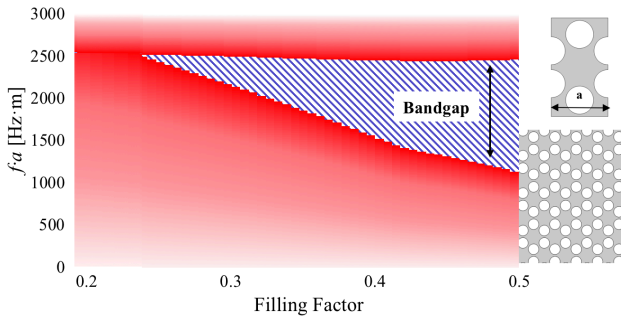

Figure 3: The honeycomb lattice (right) offers the widest bandgap at the smallest filling factor. The unit cell, when placed in a rectangular lattice, creates a honeycomb tessellation (bottom right).

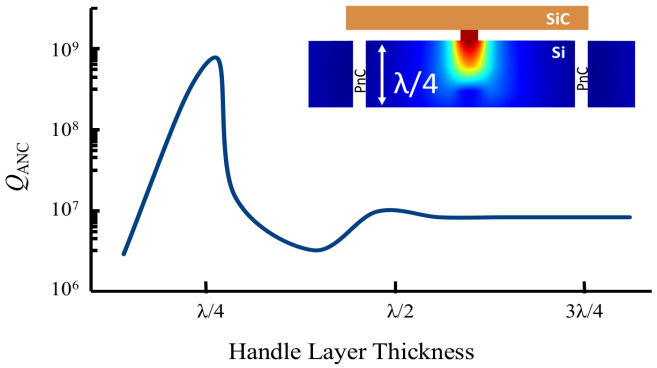

Figure 4: Handle layer thickness affects Q_{ANC}. At λ/4, wave interference creates a standing wave with a node at the suspended end of the device. In concert with a PnC, anchor loss can be made negligible.

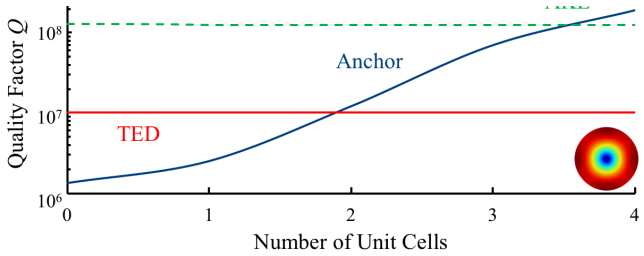

Figure 5: As more unit cells are added, Q_{Anchor} (blue) surpasses Q_{TED} (red) and finally $Q_{Akhiezer}$ (dashed green). In a 1540μm diameter disk, radial mode at 5MHz is TED limited.

DEVICE DESIGN AND FABRICATION

SiCOI substrates with 100μm SiC device layer on a 500μm Si handle layer separated by a thermally grown silicon oxide interlayer were custom-made in a process described in [11]. Complicating substrate choice, silicon carbide has an abundance of polytypes with cubic, hexagonal and rhombohedral symmetries. Among commercially available polytypes, atomically smooth monocrystalline 4H-SiC (hexagonally symmetric) wafers from Cree® exhibit the greatest isotropicity, making it better suited to demonstrate ultra-high *Q* gyroscopic modes in center-supported disk resonators. Notably, the m=3 bulk elliptical gyroscopic modes are fully degenerate in 4H-SiC, critical to mode-matched gyroscopic operation to take full advantage of *Q*.

After deposition of Ti/Cu seed layer, the electroplated nickel mask is formed to define the disk resonators; the λ/4 requirement prescribes the disk diameter to place the mode of interest at 5 MHz. Nickel is used as a hard mask for the subsequent SiC DRIE step, because of its high selectivity over SiC, near 100:1, dwarfing that of SiO_2 (~1:1). The disks are etched in an STS AOE chamber using a mixture of sulfur hexafluoride (SF_6) and Argon (Ar) with a large DC bias voltage. Carbon atoms in the SiC react with SF_6, forming an inherent passivation layer (C_xF_y), enabling anisotropic etching. Proper optimization allows for scallop-less trenches with superb anisotropy (~20:1), albeit at greatly reduced etch rates (~10x slower than in Si). Further, without cycling between etching and passivation steps, control of the trench profile requires fastidious optimization. The remaining nickel mask and any deposition on the sidewall are removed by wet etch. One concern rests in the fact that there is no etch stop, contrary to SOI processing where the BOX layer shows high selectivity over silicon. Conversely, silicon oxide shows no selectivity over silicon carbide, therefore proper timing is

required for a consummate etch.

The PnC geometry is then defined via backside alignment to the SiC layer and etched by a standard Bosch process. This backside 500µm through-etch produces large amounts of Teflon which can exacerbate anchor losses if not properly cleaned. Using a material with higher acoustic velocity for the handle layer would relax this constraint. Finally, the sacrificial buried oxide layer is laterally etched with HF through the PnC structures doubling as release holes, self-aligning the pedestal with a size controlled by release time. The process yields a breathing mode disk resonator (1540µm) supported by a SiO_2 pedestal 100µm (6% of disk size) in diameter (Fig. 6). It is anchored upon a phononic crystal composed of three unit cells, engineered with a unit cell length of 405µm to decouple the 5MHz radial mode. The pedestal is 2µm tall, separating the disk from the silicon handle layer below.

MEASUREMENT AND RESULTS

The fabricated disks are then mounted upon ultrasonic lithium niobate shear mode piezostages, adhered with Crystalbond. The setup is placed in a vacuum chamber and pumped down to sub-mTorr. S21 frequency response measurements were taken with a laser Doppler vibrometer in conjunction with a network analyzer. Three devices of varying diameter were tested, each aiming to position the radial, m=3, and m=4 modes at 5 MHz (1.56mm, 1.7mm, 2.21mm respectively). Notably, the 1.56mm disk displayed a breathing mode Q of 3.7 M at 5 MHz (Fig. 7); to date, this is the highest $f \cdot Q$ product (1.85×10^{13} Hz) measured in SiC resonators. Simulated with Q_{ANC}=350M and a limiting Q_{TED}=14M at 5 MHz, the Q discrepancy arises due to sidewall defects (discussed later). In contrast, a similar disk (5mm diameter) anchored upon an unmodified silicon substrate (without PnC) with smaller anchor diameter (3% of the device diameter) demonstrated a Q of ~1M at 1.7 MHz. Despite its larger size (less TED) and diminished pedestal area, the lack of any substrate decoupling bounds its Q to smaller values.

Vibrational modes inside the bandgap show noticeably higher Q's relative to modes exterior to the gap (Fig. 8), though the radial mode outperforms the others. While the radial mode frequency was accurately simulated, other bulk elliptical mode frequencies systematically diverged from simulation, up to 6%. Nevertheless, measured frequency splits (Δf) are low for measured degenerate elliptical modes (Fig. 9), showing 4H-SiC's suitability for mode-matched gyroscopic operation.

DISCUSSION

The resonance modes, while substrate-decoupled, deviate slightly from TED simulation, which is the predicted limiting mechanism. Upon examination, the disk showed fabrication non-idealities such as horizontal and vertical striation. Previous work has shown defects and asperities in shell resonators significantly contribute to TED[12]. While shells with surface roughness show Qs below 100,000[13], attributable to a high surface area to volume ratio, the effect of surface defects on disks is less explored.

SEMs of the sidewall of the disks show striations on the micron scale. Q_{TED} monotonically decreases with increasing size, flattening to Qs in the millions. Horizontal striations appear when etching is disrupted and restarted, more easily obviated. Vertical striations however, could arise from a fusion of different sources: non-uniformities in the nickel mask that propagate during DRIE, in combination with charging in the passivation layer that segregates and directs plasma species imperfectly, result in a striated sidewall. In simulation, striations are modeled as a hemi-cylindrical defect on the sidewall of the disk, introducing additional strain coupling to thermal fields (Fig 10). Current fabricated SiC disk resonators show

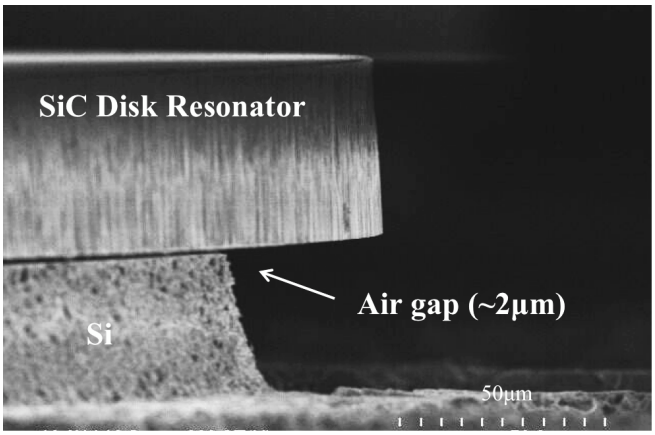

Figure 6: The device rests upon the silicon handle layer with 2µm gap determined by the thickness of the BOX layer. The lack of an etch stop manifests itself as over-etch into the silicon handle layer.

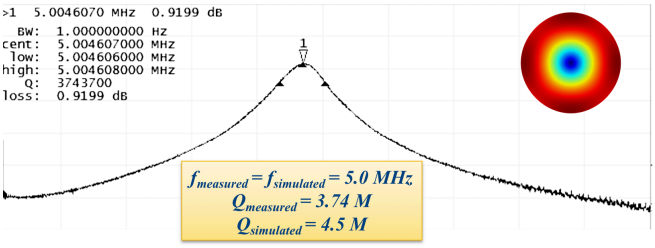

Figure 7: Radial mode frequency response of a 1540µm diameter disk with $f \cdot Q$ product of 1.85×10^{13} Hz. Measured Q and f corroborate simulation well. $Q_{simulated}$ incorporates fabrication defects.

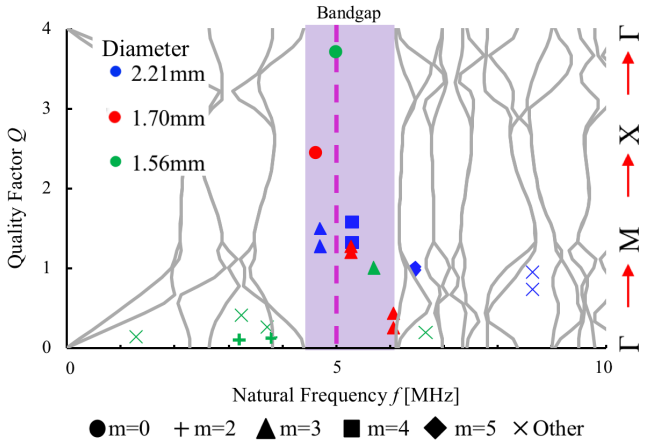

Figure 8: Simulated dispersion curves (gray) depict frequencies of allowed propagation across the first Brillouin zone. Measured Q's of bulk modes across devices of varying size inside and outside the bandgap (purple). The breathing mode (m=0) exhibits Q of 3.7M (green circle), perfectly coinciding with $\lambda/4$ frequency at 5MHz (dashed pink). Modes operating away from the $\lambda/4$ frequency (m=3 modes at 5.3 MHz) suffer in performance.

defects ranging from 1-3µm in lateral dimension (Fig. 11). TED simulations incorporating these defects yield a Q_{TED} of 4.5 M for the radial mode at 5MHz (Fig. 7), confirming measurement as a TED limited mode.

Further discrepancies in Q—particularly for the m=3 modes—can be attributed to anchor losses due to fabrication and material non-idealities affecting the handle layer thickness, the disk frequency, and the PnC itself. Measured and simulated frequencies

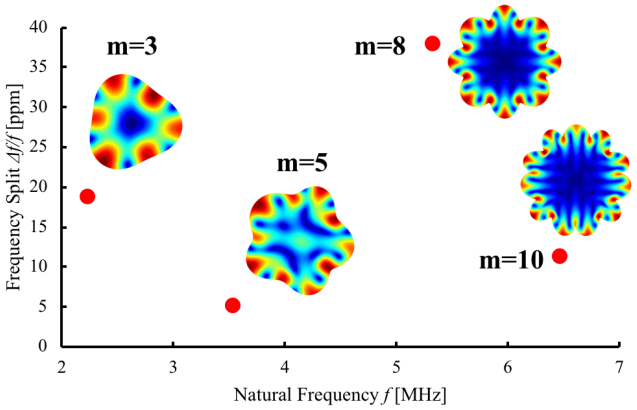

Figure 9: Measured frequency split Δf/f of several bulk elliptical modes below 40 ppm. M=3 modes exhibit 18ppm frequency split.

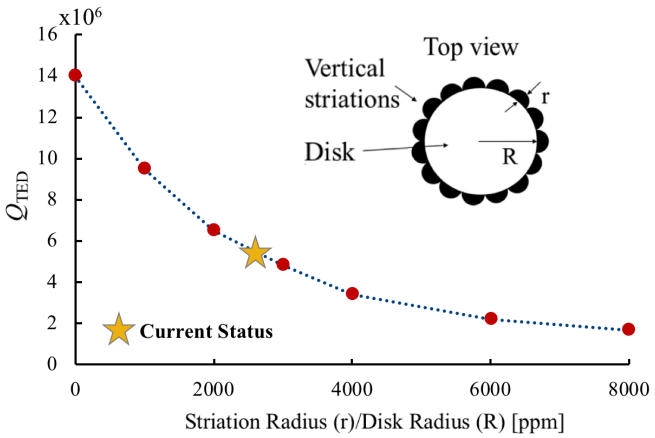

Figure 10: With increasing striation radius/disk radius ratio, simulation shows a precipitous reduction in Q_{TED} of the radial mode.

differ by up to 6%; e.g. the m=3 degenerate modes were measured to be at 5.3 MHz rather than 5MHz as simulated (Fig. 8). Due to strong λ/4 dependence, operating at 5MHz (c=λ·*f*) is critical; in this case, resonance at 5.3 MHz rather than 5MHz reduces Q_{ANC} by a factor of 3 (100M -> 35M). Additionally, the dimensions of the tethers between occlusions in the PnC should be tightly controlled to avoid spurious modes in the handle layer near 5 MHz. As opposed to other bulk elliptical modes, the radial mode showed the greatest consistency with simulation in terms of frequency and *Q*. Potential sources of this disagreement such as residual stresses during fabrication or material properties will be explored.

CONCLUSION

Centrally-supported BAW disk resonators with nano-scale sidewall roughness fabricated on SiCOI offer a pathway to extremely high *Q*'s. Monocrystalline SiC BAW resonators offer low intrinsic material dissipation. Consequently, implementing a 3D substrate-decoupled handle layer—leaving the disk itself unblemished—unlocks the possibility of fabricating disk resonators with *Q's* tethered to intrinsic quantum limits in excess of 100M.

In this work, surface TED limits the radial breathing mode to a *Q* of 4M at 5MHz. We are investigating several paths to improve *Q* including H_2/Ar annealing, roughness-optimized DRIE and SiCOI handle layer materials with lower sound velocity to allow more unit cells and thinner handle layer. Further, material and design anisotropy effects on frequency and *Q* mismatches between gyroscopic modes will be scrutinized.

Harnessing these degenerate modes of SiC disk resonators for use in capacitively actuated gyroscopes presents its own unique challenges, along with remarkable rewards. This work represents a significant step forward in the pursuit of ultra-high *Q* with a view toward achieving inertial grade BAW gyroscopes with superior vibration resilience in a small form factor.

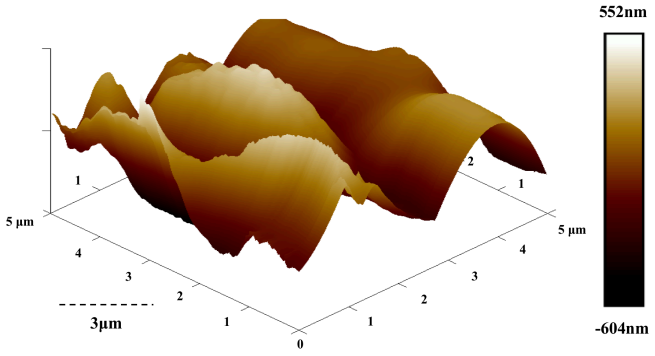

Figure 11: Atomic force micrograph of the sidewall of the disk showing striation and roughness on the micron scale.

ACKNOWLEDGEMENT

This work is supported by the Defense Advanced Research Projects Agency Microsystems Technology Office, Advanced Inertial Micro Sensors (AIMS) program and U.S. Navy (SPAWAR) under grant #N66001-16-1-4027. The authors wish to thank the cleanroom staff at Georgia Tech IEN for their assistance.

REFERENCES

[1] F. Ayazi, "Multi-DOF inertial MEMS: From gaming to dead reckoning," in *2011 16th International Solid-State Sensors, Actuators and Microsystems Conference*, 2011, pp. 2805–2808.

[2] F. Ayazi, L. Sorenson, and R. Tabrizian, "Energy dissipation in micromechanical resonators," presented at the Micro- and Nanotechnology Sensors, Systems, and Applications III, 2011, vol. 8031, p. 803119.

[3] S. Ghaffari *et al.*, "Quantum Limit of Quality Factor in Silicon Micro and Nano Mechanical Resonators," *Sci. Rep.*, vol. 3, p. srep03244, Nov. 2013.

[4] R. Lifshitz and M. L. Roukes, "Thermoelastic damping in micro- and nanomechanical systems," *Phys. Rev. B*, vol. 61, no. 8, pp. 5600–5609, Feb. 2000.

[5] D. E. Serrano *et al.*, "Substrate-decoupled, bulk-acoustic wave gyroscopes: Design and evaluation of next-generation environmentally robust devices," *Microsyst. Nanoeng.*, vol. 2, p. micronano201615, Apr. 2016.

[6] R. Mirjalili, H. Wen, D. E. Serrano, and F. Ayazi, "Substrate-decoupled silicon disk resonators having degenerate gyroscopic modes with Q in excess of 1-million," in *18th Conference on Solid-State Sensors, Actuators and Microsystems*, 2015, pp. 15–18.

[7] M. Maldovan, "Sound and heat revolutions in phononics," *Nature*, vol. 503, no. 7475, pp. 209–217, Nov. 2013.

[8] A. Khelif and A. Adibi, Eds., *Phononic Crystals*. New York, NY: Springer New York, 2016.

[9] Y. Tsaturyan, *et al.*, "Ultracoherent nanomechanical resonators via soft clamping and dissipation dilution," *Nat. Nanotechnol.*, vol. 12, no. 8, p. nnano.2017.101, Jun. 2017.

[10] F. D. Bannon, J. R. Clark, and C. T. C. Nguyen, "High-Q HF microelectromechanical filters," *IEEE J. Solid-State Circuits*, vol. 35, no. 4, pp. 512–526, Apr. 2000.

[11] S.-D. Ko, B. Hamelin, J. Yang, and F. Ayazi, "High-Q Monocrystalline Silicon Carbide Disk Resonators Fabricated Using DRIE of Thick SiC-On-Insulator Substrates," in *The 31st IEEE International Conference on Micro Electro Mechanical Systems (MEMS 2018)*, 2018.

[12] L. Sorenson, P. Shao, and F. Ayazi, "Bulk and Surface Thermoelastic Dissipation in Micro-Hemispherical Shell Resonators," *J. Microelectromechanical Syst.*, vol. 24, no. 2, pp. 486–502, 2015.

[13] B. Hamelin, V. Tavassoli, and F. Ayazi, "Microscale pierced shallow shell resonators: A test vehicle to study surface loss," in *2017 IEEE 30th International Conference on Micro Electro Mechanical Systems (MEMS)*, 2017, pp. 1134–1137.

TOWARDS INTEGRATED OPTICAL GYROS USING BRILLOUIN LASERS

K. Vahala, Y. H. Lai, M. G. Suh, J. Li, K. Y. Yang
Watson Laboratory of Applied Physics, California Institute of Technology
Pasadena, California USA

ABSTRACT

Ultra-low-loss micro-scale optical resonators have advanced to a point where Q factors of nearly 1 billion (monolithic devices [1,2]) and 100 billion (discrete devices [3]) are possible. These resonators have many applications including use for high-coherence compact lasers. Counter-propagating laser waves in these resonators can potentially enable the transfer of ring laser gyroscope technology to a semiconductor chip-based platform. Here, a monolithic optical gyroscope is described that uses counter-propagating Brillouin lasers to measure rotation through a Sagnac-induced frequency shift. Demonstration of rotation measurement below the Earth rotation rate is presented. Prospects for improving the device performance are described.

INTRODUCTION

Optical gyroscopes (ring-laser gyroscopes [4] and fiber-optic gyroscopes [5]) provide high-performance rotation sensors. However, MEMS-based rotation sensors, on account of their compact semiconductor-chip-based form factor and low cost, dominate consumer applications [6]. Nonetheless, the advent of monolithic optical resonators [7] has generated interest in chip-based analogs to the ring laser or fiber-optic gyroscope. Being lightweight with no moving parts, such micro-optical gyros [8] would be highly insensitive to shock and vibration. Moreover, their reliance on the Sagnac effect could potentially allow them to out-perform MEMS devices. To date, however, the performance of micro-optical devices has severely lagged behind MEMS devices on account of difficult-to-achieve requirements for low-loss chip-based waveguides and high Q-factor optical resonators. Recent reports of micro-optical gyroscopes suggest that this landscape is beginning to change.

Both crystalline-based and silica-based optical rotation measurements have recently been demonstrated with performance that greatly exceeds prior micro-optical-gyro efforts [9, 10]. These devices use advanced ultra-high-Q (UHQ) optical resonators [1-3]. In the resonators, light propagates in a circular, 'whispering-gallery' optical path. For example, a recent monolithic UHQ silica-on-silicon ridge resonator is described in figure 1 [2]. Figure 1A shows a scanning electron micrograph of the resonator. At the far right is a silicon nitride waveguide (false color red) that couples light into the resonator near a region circumscribed with a dashed box in the image. As illustrated, light couples into a counter-clockwise path shown by the yellow arrow. In a gyro measurement, Sagnac-induced changes in the resonant frequencies of clockwise and counter-clockwise optical modes are measured to detect rotation. The silicon nitride waveguide in the image can also function as an optical bus to convey the light to other devices on the chip for processing. In figure 1B a concept rendering of a dual optical gyroscope is presented that would use two of the ridge resonator devices for redundant measurement. Other photonic components and electronics are shown on the chip. These can include III-V detectors and lasers that are die-attached at the wafer scale [11,12].

In this presentation, Brillouin laser physics is first reviewed and then Brillouin gyro measurements are described. Finally, ways to improve the gyro performance are discussed.

BRILLOUIN LASER GYROSCOPES

Stimulated Brillouin scattering (SBS) has been intensely studied in silica optical fiber [13]. It results from the interaction of an optical pump wave with microwave-rate phonons. The application of this process for rotation sensing was also demonstrated using optical fibers in the 1990s [14].

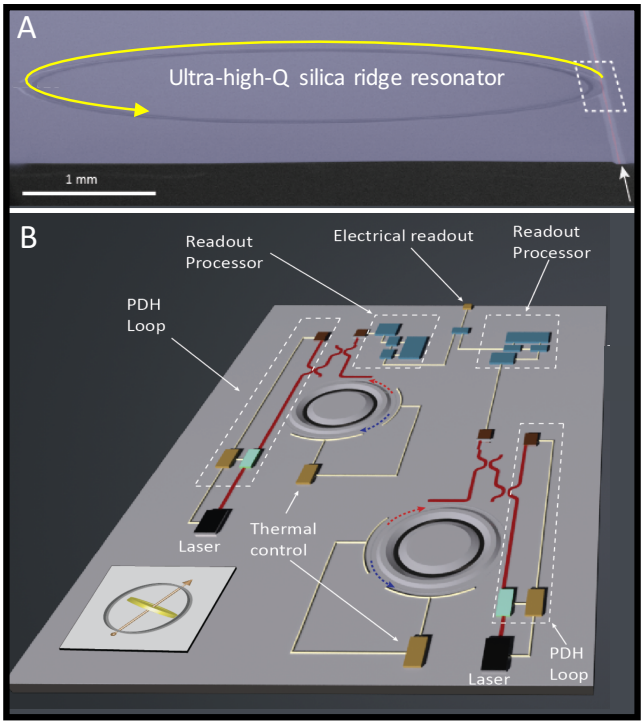

*Figure 1: **A.** SEM image of an ultra-high-Q ridge resonator with a silicon nitride waveguide (false red color). White arrow shows the direction of light coupling and yellow arrow shows circulation within the resonator. Dashed white box is the waveguide-resonator coupling region. This material originally appeared in ref. [2]. **B**. Concept rendering of a dual-gyro chip. Component color coding as follows: silicon nitride waveguides (red lines), electrical traces (silver lines), laser sources (black), detectors (brown), modulators (turquoise), loop-control electronics (gold), and readout processing electronics (blue).*

To initiate Brillouin laser action, a resonator mode is optically pumped as shown in the figure 2A (blue pump line). The ultra-high-Q of the resonator leads to a strong build-up of the circulating intensity. 10s of MW/cm^2 of circulating intensity is possible with only 1 mW of coupled optical pump power. This high-intensity field couples to phonons in the silica glass and, subject to a phase matching condition, will scatter off the phonons into other optical modes. In the whispering-gallery resonator, the scattering will efficiently couple the clockwise pump in figure 2A into a counter-clockwise "Stokes" resonant mode provided that the frequency of the Stokes mode is spectrally shifted relative to the pumping

978-1-940470-03-0/HH2018/$25©2018TRF
DOI 10.31438/trf.hh2018.23

frequency by the Brillouin shift frequency ($\Omega_{Brillouin}$ in figure 2A). For pump wavelengths in the telecom C-band (1.55 microns) this frequency shift is approximately 10.8 GHz [13]. Moreover, in the high-Q resonator environment, the Brillouin coupling causes optical amplification of the Stokes wave. Upon sufficient optical pumping, this amplification overcomes the resonator loss and the Stokes wave will achieve laser threshold. Continued pumping above threshold causes a dramatic line narrowing of the Stokes laser field. In silica devices, this line narrowing achieves sub-Hertz fundamental linewidths [15]. Curiously, the Stokes laser wave can ultimately function as a pumping wave for a second Stokes wave, thereby setting up cascaded laser action in the resonator [15]. A measurement of the optical cascade process out to 9th order is shown in figure 2B [15]. As shown in figure 2A each Stokes wave is shifted to lower frequencies and also switches the direction of propagation relative to its pumping wave. This natural switching of propagation direction sets up an ideal situation for measurement of rotations. Specifically, adjacent Stokes laser lines will experience opposing Sagnac-induced frequency shifts. To measure rotations, a neighboring pair of laser fields is photo-detected and the beat frequency is measured.

The sensitivity of this method of rotation measurement depends upon the fundamental linewidth of the beat note, which, as noted above, is sub-Hertz [15]. Additionally, because the counter-propagating Brillouin lasers are co-lasing within the same cavity, the technical noise contributions to their respective linewidths are largely common-mode-noise. As a result, heterodyne detection of the Brillouin laser waves produces a sub-Hertz beat frequency [16].

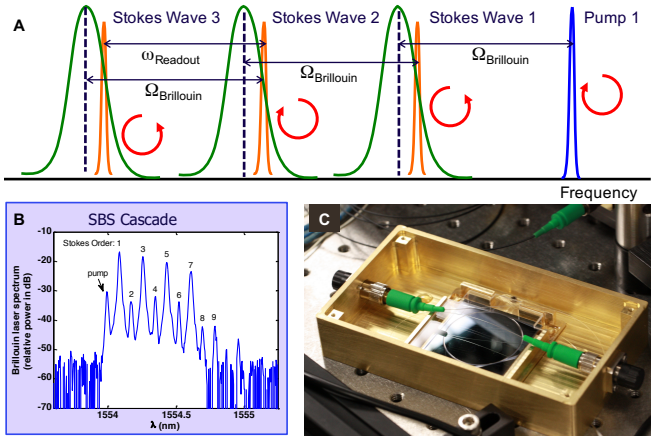

*Figure 2: **A.** Principle of operation of gyroscope based on counter-propagating Brillouin laser oscillation. Stokes laser waves are shown in orange. Neighboring Stokes waves propagate in opposite directions and therefore experience opposing Sagnac frequency shifts.* $\Omega_{Brillouin}$ *is the Brillouin shift frequency. **B.** Measurement of SBS cascaded laser action out to 9th order. The odd orders are prominent in the measurement because the light output was collected in a direction opposite to the pumping direction. **C.** Photograph of a disk resonator gyro packaged in a brass box with fiber connectors.*

ROTATION MEASUREMENT

The current work uses a silicon-chip-based ultra-high-Q disk resonator [1] to generate counter-propagating Brillouin lasers for rotation measurement [9]. A photograph of a resonator packaged into a small box for rotation measurement is shown in figure 2C. Light is coupled into and out from the box by fiber connectors. When the resonator is rotated about an axis perpendicular to the plane of the disk, the counter-propagating Brillouin lasers experience opposing Sagnac frequency shifts. The impact of clockwise and counter-clockwise rotations on SBS 2nd Stokes and SBS 3rd Stokes wave is illustrated in figure 3A and 3B. The measured beat frequency of these two waves (with a constant microwave-rate offset removed) is displayed in figure 3C when the resonator is subjected to a sinusoidal rotation. It is interesting to note that a 90-degree relative phase shift is observable between the rotation angle (blue) and Sagnac frequency shift (red) as is expected since the frequency shift is proportional to an angular rotation rate. Initial work on this device was able to measure rotations rates as low as 22 degrees/hour [9].

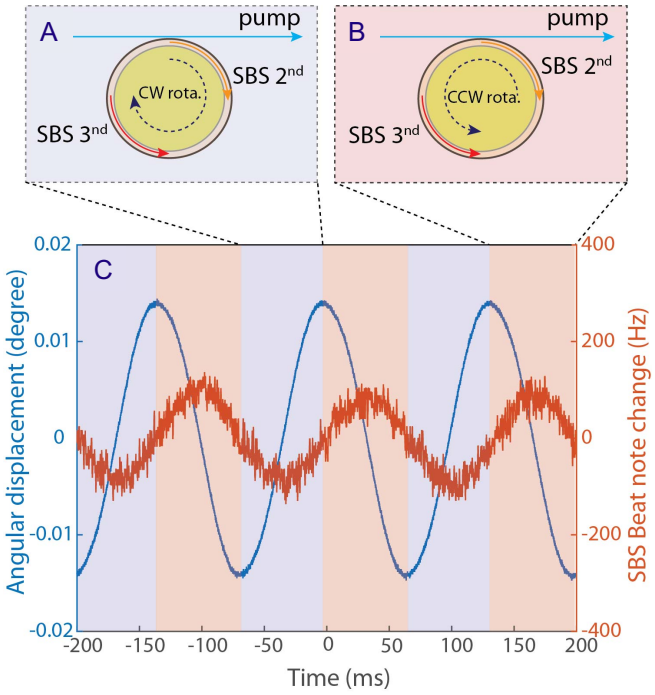

*Figure 3: **A.** Rendering showing counter-propagating 2nd and 3rd Stokes waves in a whispering gallery resonator that is subject to a clockwise rotation. In this arrangement, the 2nd Stokes wave decreases in frequency and the 3rd Stokes wave increases in frequency, thereby causing a net decrease in their beat frequency subject to the Sagnac effect. **B.** Similar to panel A except resonator is now rotated in the counter-clockwise direction so that the beat frequency is increasing. **C**. Sinusoidal rotation measurement. Blue curve is the rotation angle and red is the measured Sagnac frequency shift generated by mixing Stokes 2 and Stokes 3 waves. This material originally appeared in ref. [9].*

Improvements to the system have now boosted the bias stability to around 3.6 degrees/hour (see figure 4). In the newer design, the device is no longer being operated in cascaded fashion, but is using a dual-optical-pumping configuration. Allan deviation measurements of the beat frequency are presented in figure 4 (normalized to an equivalent rotation rate) for two different gyroscope resonator diameters. At short gate times, the system is limited by white frequency noise that is set by the fundamental linewidth of the co-lasing Stokes waves. At longer gate times, there is a drift component that is believed to be associated with thermal drift of the package. The overall improved performance of the larger diameter device is the result of its inherently smaller

fundamental linewidth, its larger Sagnac coefficient, and its larger cavity mode volume which reduces drift. In these measurements there are no active thermal control circuits. Methods underway to address the drift component will be discussed as well as prospects for further reductions in the white frequency noise associated with the Stokes laser action.

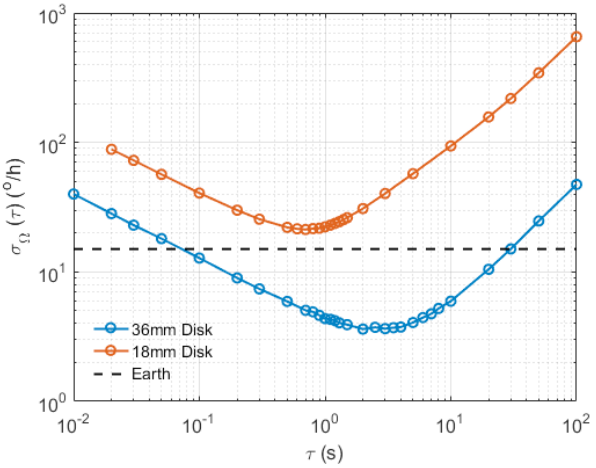

Figure 4: Allan deviation measurement performed on two disk resonator devices having different diameters (see legend).

REFERENCES

[1] Lee, H., Chen, T, Li, J., and Vahala, K, "Chemically etched ultra-high-Q wedge-resonator on a silicon chip," *Nature Photonics*, **6**, 369 (2012).

[2] Yang, K. Y., Oh, D. Y., Lee, S. H., Yang, Q. F., Yi, X., Shen, B., Wang, H., and Vahala, K., "Bridging ultrahigh-Q devices and photonic circuits," *Nature Photonics*, doi:10.1038/s41566-018-0132-5 (2018).

[3] Grudinin, I. S., Ilchenko, V. S., and Maleki, L., "Ultrahigh optical *Q* factors of crystalline resonators in the linear regime," *Phys. Rev. A,* **74**, 063806 (2006).

[4] Chow, W. et al., "The ring laser gyro," *Reviews of ModernPhysics* **57**, 61 (1985).

[5] Lefevre, H. C., "The fiber-optic gyroscope," (Artech house, 2014).

[6] Liu, K. et al., "The development of micro-gyroscope technology," *Journal of Micromechanics and Micro-engineering* **19**, 113001 (2009).

[7] Vahala, K. "Optical Microcavities," *Nature*, **424**, 839 (2003).

[8] Dell'Olio, F., Tatoli, T., Ciminelli, C., and Armenise, M., "Recent advances in miniaturized optical gyroscopes," *Journal of the European Optical Society-Rapid publications* **9** (2014).

[9] Li, J., Suh, M. G., and Vahala, K., "Microresonator Brillouin gyroscope," *Optica* **4**, 346 (2017).

[10] Liang, W., Ilchenko, V. S., Savchenkov, A. A., Dale, E., Eliyahu, D., Matsko, A. B., and Lute, M., "Resonant microphotonic gyroscope," Optica 4, 114 (2017).

[11] Komljenovic, T. et al., "Heterogeneous silicon photonic integrated circuits," *J. Light. Technol.* 34, 20 (2016).

[12] Piels, M., Bauters, J. F., Davenport, M. L., Heck, M. J., and Bowers, J. E., "Low-loss silicon nitride AWG demultiplexer heterogeneously integrated with hybrid III–V/silicon photodetectors," *J. Light. Technol.* **32**, 817 (2014).

[13] E. Ippen and R. Stolen, "Stimulated Brillouin scattering in optical fibers," *Appl. Phys. Lett.* **21**, 539 (1972).

[14] F. Zarinetchi, S. Smith, and S. Ezekiel, "Stimulated Brillouin fiber-optic laser gyroscope*," Optics Letters* **16**, 229 (1991).

[15] Li, J., Lee, H., Chen, T., and Vahala, K., "Characterization of a high coherence, Brillouin microcavity laser on silicon," *Optics Express*, **20**, 20170 (2012).

[16] Li, J., Lee, H., Vahala, K., "Microwave synthesizer using an on-chip Brillouin oscillator," *Nature Communications* **4**, 2097 (2013).

CONTACT

*Kerry Vahala, vahala@caltech.edu

ACKNOWLEDGEMENT

The authors gratefully acknowledge the Defense Advanced Research Projects Agency (DARPA) under the PRIGM:AIMS program (grant no. N66001-16-1-4046) and the Kavli Nanoscience Institute.

A NEW LOW POWER MEMS DUAL MODE CLOCK WITH PPB STABILITY OVER TEMPERATURE

Lizmarie Comenencia Ortiz[1], Hyun-Keun Kwon[1], Janna Rodriguez[1], David B. Heinz[1], Yunhan Chen[2], Gabrielle D. Vukasin[1], Dongsuk D. Shin[1] and Thomas W. Kenny[1]
[1]Stanford University, California, USA
[2]Apple Inc., California, USA

ABSTRACT

In this paper, we demonstrate a novel dual-mode clock with an in-chip device layer micro-oven which operates at 10X reduced power consumption and provides more than 30X improved stability when compared to a recent result with a micro-oven embedded in the cap [2]. The decrease in the thermal time constant and in the micro-oven power dissipation improves compensation for ambient temperature variations and allows for significant improvements in the stability. This device layer micro-oven enables correction for ambient temperature fluctuations and achieves long-term stability over temperature in ppb, which is better than the stability of TCXOs and competes with state-of-the-art OCXOs, while requiring much less power.

BACKGROUND AND DEVICE DESIGN

A combination of passive and active temperature compensation methods can significantly improve the stability of encapsulated MEMS clocks [1-4]. Active compensation has been achieved previously with the use of a micro-oven embedded in the encapsulation lid of the die; while this method is successful in compensating for temperature changes (+/- 0.9ppb/^{o}C), it requires substantial power (approximately 3mW/^{o}C) [2]. The dissipated heat can affect the stability and performance of the device due to temperature gradients and thermal stresses. Previous work has shown that a micro-oven isolated within the device layer of the die can significantly reduce thermal stresses and the power required to ovenize [4, 9].

Here, we extend these efforts by combining the low-power of the device-layer planar suspension with the high-Q and high-linearity of a temperature-compensated Lamé-mode resonator. As shown in Figure 1A, micro-oven structures provide support and thermal isolation for a frame that contacts the dual-mode MEMS resonator at nodes of both vibrational modes.

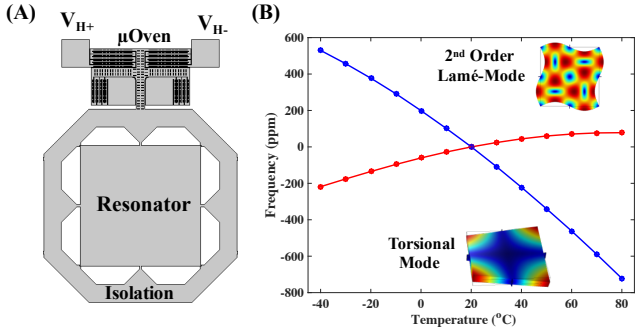

Figure 1: Schematic of dual mode clock: (A) dual Lamé-mode clock, (B) temperature dependence of frequency for each mode using closed loop frequency sweeps.

The devices are fabricated on p-type SOI wafer with a 40µm device layer using commercially-available, high-volume epitaxial thick film encapsulation processes. The temperature dependence of frequency for both modes was determined within a range of -40^{o}C to 80^{o}C, as shown in Figure 1B. Each mode was excited with a Zurich Instruments digital lock-in amplifier and transimpedance amplifiers to amplify the resonators' signal as shown in Figure 2.

Table 1: Summarized clock properties and measurements.

Properties		*Lamé-Mode Clock*
Doping		P-type: 1e20cm^{-3}
Geometry		400µm x 400µm
Mode 1	f_1	20.16MHz
	Q_1	950k
Mode 2	f_2	1.19MHz
	Q_2	770k
µOven Power		0.18mW/^{o}C
Temperature Stability		**< +/- 1.5ppb**

By simultaneously exciting a pair of modes in the same structure, we can continuously determine temperature and provide a frequency reference using a control scheme that is common for quartz OCXOs [5]. The frequency for both modes was tracked with phase lock loops and the frequency difference was regulated by application of voltage across the micro-oven terminals using proportional and integral control.

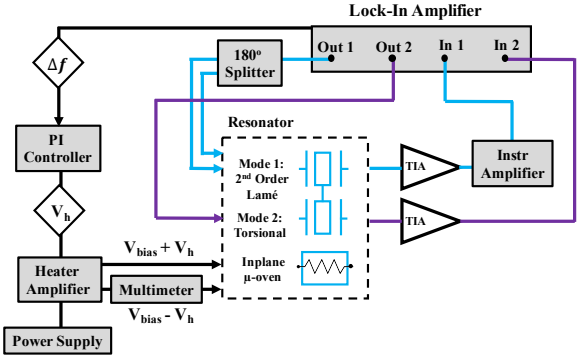

Figure 2: Schematic of experimental set up: a phase locked loop was used to simultaneously track the frequencies of two modes in one resonator. A PI controller was used to control the micro-oven voltage and maintain a constant turnover temperature of 80^{o}C.

RESULTS

This dual-Lamé-mode clock was operated at steady state at -40^{o}C over 12 hours, where 22mW of micro-oven power is required to bring the resonating element to its turnover temperature of 80^{o}C. The Allan Deviation corresponding to this data indicates a minimum of <0.2ppb at 1000s.

A stability of +/-1.4ppb was achieved while ramping temperature from -40^{o}C to 60^{o}C over 10 hours, as shown in Fig. 4. These results exceed the best performance of all previously-published MEMS-based time references. Notably, this is the first MEMS device to demonstrate single-digit ppb stability over time and temperature. Figure 6 shows this new result in the context of prior products and academic demonstrations of MEMS-based and macroscopic time references.

978-1-940470-03-0/HH2018/$25©2018TRF
DOI 10.31438/trf.hh2018.24

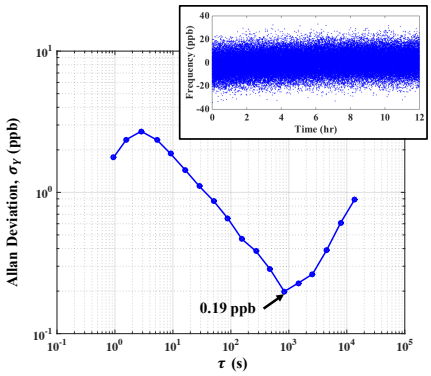

Figure 3: Allan deviation for 2nd order Lamé-mode at an ambient temperature of -40°C with +/-0.3°C temperature fluctuations.

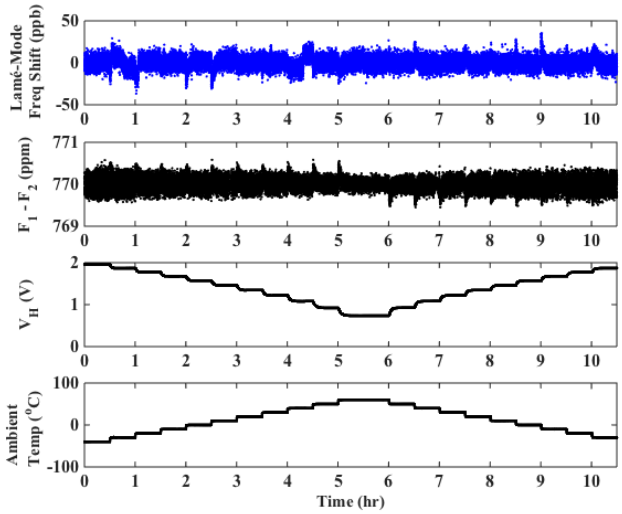

Figure 4: Frequency stability of 2nd order Lamé-mode with changes in ambient temperature. Heater voltage is applied through the micro-oven to maintain the frequency at the turnover temperature.

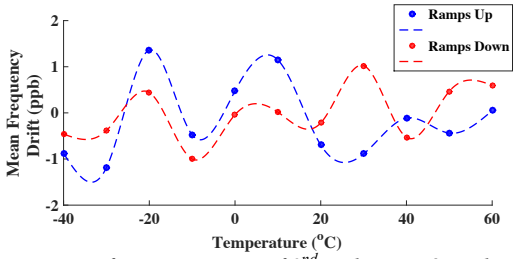

Figure 5: Mean frequency error of 2nd order Lamé-mode at steady state with changes in ambient temperature.

CONCLUSION

In this paper, we demonstrate more than 30X improvement in the stability of a dual Lamé-mode clock and 10X reduction in the power consumption. We show that stiff Lamé-mode bulk resonators are ideal candidates for ultra-precise ovenized clocks since they are less susceptible to thermal expansion nonlinearities. Our results for temperature and long-term stability are the best of any previously-published or commercially produced MEMS-based clock, while also operating with heater power far below any conventional quartz OCXO.

These devices have the potential to revolutionize applications that require ultra-stable references and low power.

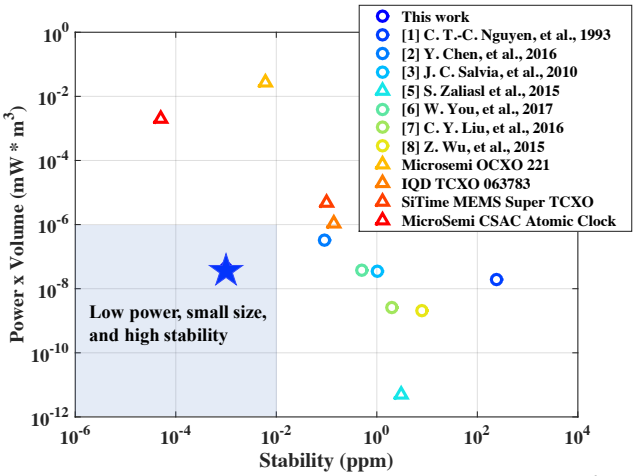

Figure 6: Comparison of clock stability over temperature (-40°C to 80°C) for range of devices shows that the dual Lamé-mode clock (starred) has better stability and power consumption than leading TCXOs and OXCOs used in industrial applications.

[1] C. T.-C. Nguyen, and R. T. Howe, "Microresonator frequency control and stabilization using an integrated micro oven", in Technical Digest of the 1993 Transducers Conference, Yokohama, Japan, 6/7-10/93, IEEE, (1993), pp. 1040-1043.

[2] Y. Chen, E. J. Ng, D. D. Shin, C. H. Ahn, Y. Yang, I.B. Flader, V. A. Hong, and T. W. Kenny, "Ovenized Dual-Mode Clock (ODMC) Based on Highly Doped Single Crystal Silicon Resonators", Technical Digest of the 2016 MEMS Shanghai, China, 6/24-28/16, IEEE and IEEE Robotics and Automation Soc. (2016), pp. 91-94.

[3] J. Salvia, R. Melamud, S. A. Chandorkar, S. F. Lord, and T.W. Kenny, "Real-Time Temperature Compensation of MEMS Oscillators Using an Integrated Micro-Oven and a Phase-Locked Loop," Microelectromechanical Systems,19, 1, (2010).

[4] C. Jha, M. A. Hopcroft, S. A. Chandorkar, J. C. Salvia, M. Agarwal, R. N. Candler, R. Melamud, B. Kim, and T. W. Kenny, "Thermal Isolation of Encapsulated MEMS Resonators," Microelectromechanical Systems, 17, 1, (2008).

[5] S. Zaliasl *et al.*, "A 3 ppm 1.5 × 0.8 mm 2 1.0 µA 32.768 kHz MEMS-Based Oscillator," Solid-State Circuits, 50, 1, (2015).

[6] W. You, B. Pei, K. Sun, L. Zhang, H. Yang, and X. Li, "Oven controlled N++ [1 0 0] length-extensional mode silicon resonator with frequency stability of 1 ppm over industrial temperature range". Micromech. and Microeng., 27, 9, (2017).

[7] C. Y. Liu, M. H. Li, H. G. Ranjith and S. S. Li, "A 1 MHz 4 ppm CMOS-MEMS oscillator with built-in self-test and sub-mW ovenization power," Technical Digest of 2016 Int. Electron Devices Meeting, San Francisco, CA, 12/3-7/16, IEEE, (2016), pp. 26.7.1-26.7.4.

[8] Z. Wu and M. Rais-Zadeh, "A Temperature-Stable Piezoelectric MEMS Oscillator Using a CMOS PLL Circuit for Temperature Sensing and Oven Control," Microelectromechanical Systems, 24, 6, (2015).

[9] L. Comenencia Ortiz, et. al, "Thermal Effects of Ovenized Clocks on Episeal Encapsulated Inertial Measurement Units", Technical Digest 2018 MEMS, Belfast, Ireland, 6/21-25/18, IEEE and IEEE Robotics and Automation, (2018).

CONTACT

*L. Comenencia Ortiz, tel: +1-787-608-9044;
lcomenen@stanford.edu

TOWARD REAL-TIME MIDDLE ULTRAVIOLET (MUV) LIGHT DETECTION BY BETA GALLIUM OXIDE (β-Ga_2O_3) NEMS OSCILLATOR

Xu-Qian Zheng[1], Jaesung Lee[1], Subrina Rafique[1,2], Md Rezaul Karim[2], Lu Han[1,2], Hongping Zhao[2], Christian A. Zorman[1], and Philip X.-L. Feng[1]*

[1]Electrical Engineering, Case School of Engineering, Case Western Reserve University, Cleveland, Ohio, USA

[2]Electrical and Computer Engineering, Ohio State University, Columbus, Ohio, USA

ABSTRACT

We report on the first beta gallium oxide (β-Ga_2O_3) feedback oscillator built by using a β-Ga_2O_3 nanoresonator as the frequency reference for real-time middle ultraviolet (MUV) light detection. We fabricate suspended β-Ga_2O_3 nanodevices through growth of β-Ga_2O_3 nanoflakes using low-pressure chemical vapor deposition (LPCVD), and all-dry transfer of nanoflakes onto microtrenches. Open-loop tests reveal multimode resonances of the β-Ga_2O_3 devices in the ~20 to 50 MHz range. A closed-loop oscillator is then realized by using a combined optical-electrical feedback circuitry, to perform real-time MUV sensing. The oscillator exposed to cyclic MUV irradiation exhibits resonant frequency downshifts, with a responsivity of -3.3 Hz/pW and a power sensitivity of 0.9 nW.

INTRODUCTION

β-Ga_2O_3, a semiconductor with a monoclinic crystal structure (Fig. 1a), is rapidly emerging as a promising candidate for future power electronics, due to its ultrawide bandgap, $E_g \approx 4.5$–4.9 eV, and other excellent electronic properties [1]. In optoelectronics, crystalline β-Ga_2O_3 is suited for making photodetectors in the MUV range (200–300 nm). In addition, owing to its excellent mechanical properties (*e.g.*, measured Young's modulus, $E_Y \approx 250$–300 GPa) [2], β-Ga_2O_3 can be an appealing structural material for building micro/nanoelectromechanical systems (MEMS/NEMS) and new transducers, especially sensors that can capitalize on its ultrawide bandgap embedded in the MEMS/NEMS device platforms. To date, engineering of β-Ga_2O_3 crystal has been mainly focused on electronic devices without any moving component, such as field effect transistors (FETs) [1] and electronic UV photodetectors [3]. Transducers exploiting mechanical properties of β-Ga_2O_3 are yet to be shown and carefully studied. In this digest paper, we describe the construction and measurement of the first self-sustaining β-Ga_2O_3 oscillator by using a β-Ga_2O_3 nanoresonator and a feedback circuitry, for MUV light detection and real-time sensing.

DEVICE FABRICATION

The device fabrication process consists of chemical synthesis and direct transfer of β-Ga_2O_3 nanoflakes for making suspended nanostructures. We perform LPCVD to grow β-Ga_2O_3 nanoflakes on a 3C-SiC-on-Si substrate. Using high purity Ga pellets and O_2 gas precursor in a 950 °C LPCVD chamber for 1.5 hours, the formation of β-Ga_2O_3 nanostructures proceeds, step by step, from β-Ga_2O_3 nanocrystals to nanorods, and then to nanoflakes, without the need of any foreign catalyst (Fig. 1b).

We use an all-dry transfer technique to fabricate suspended β-Ga_2O_3 nanomechanical structures (Fig. 2). We secure and harvest the β-Ga_2O_3 nanoflakes from the growth substrate by using a polydimethylsiloxane (PDMS) stamp. Under an optical microscope, we align a selected β-Ga_2O_3 nanoflake to a predefined microtrench. By pressing down and detaching the PDMS stamp, the nanoflake is transferred onto the microtrench, thus creating a suspended device structure. Both doubly clamped beams/ribbons (Fig. 2d) and circular drumheads (*insets* in Fig. 4b and Fig. 5) have been realized.

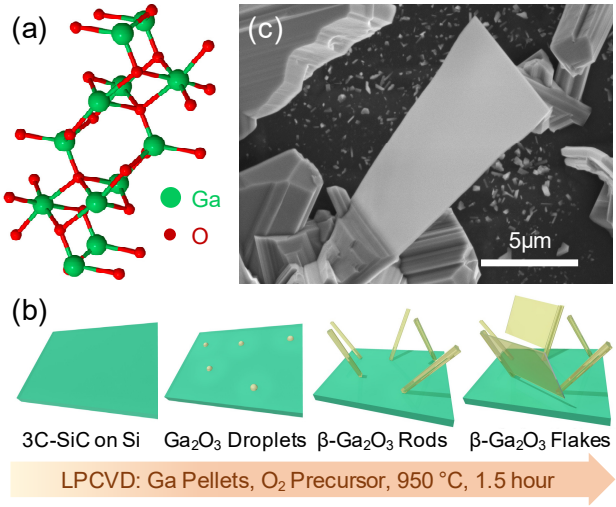

Figure 1: (a) The crystal structure of β-Ga_2O_3. (b) Formation of β-Ga_2O_3 nanoflakes in LPCVD. (c) A scanning electron microscopy (SEM) image of a β-Ga_2O_3 nanoflake on the growth substrate.

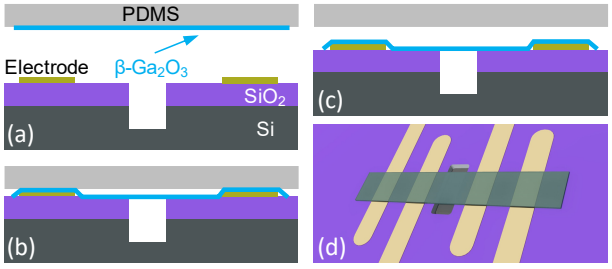

Figure 2: Fabrication of β-Ga_2O_3 nanomechanical structures. (a) Aligning the β-Ga_2O_3 nanoflake to a microtrench. (b) Pressing down the nanoflake. (c) Lifting the stamp, leaving nanoflake on substrate. (d) 3D illustration of the fabricated β-Ga_2O_3 device.

EXPERIMENTAL RESULTS AND DISCUSSIONS

We use a home-built ultrasensitive laser interferometry system [4] to measure both the undriven thermomechanical noise spectra and the photothermally driven resonances of the β-Ga_2O_3 devices in vacuum. We employ a 633nm laser to read out the device motion interferometrically and a 405nm laser to photothermally drive the device. A photodetector (PD) is used to measure the intensity of the device-motion-modulated laser light. A measurement scan captures three thermomechanical resonance modes (here only 633nm laser is used) in the range of 20 to 50 MHz, with quality factors (Qs) in the range of ~320 to ~550, for a doubly clamped, 28nm-thick β-Ga_2O_3 resonator suspended over a 2.2μm-wide microtrench (Fig. 3). Similarly, a 73nm-thick β-Ga_2O_3 nanoflake drumhead on a circular microtrench with a diameter of ~5.2 μm exhibits a measured thermomechanical resonance at ~30 MHz with a $Q \sim 200$ (Fig. 4a). Further, by adding the 405nm laser as the driving source, we measure an open-loop, photothermally driven resonance of the same device, also at ~30 MHz with a $Q \sim 150$ (Fig. 4b).

978-1-940470-03-0/HH2018/$25©2018TRF
DOI 10.31438/trf.hh2018.25

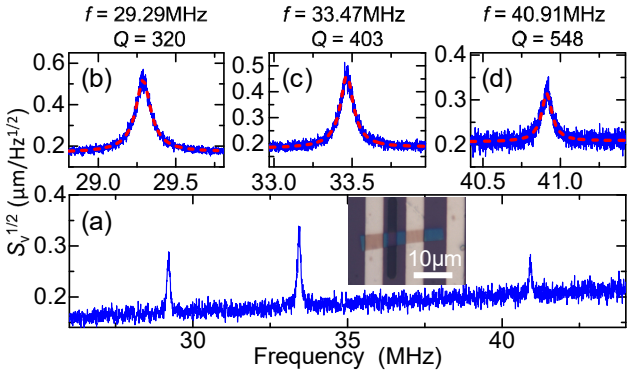

Figure 3: Undriven thermomechanical resonances of a doubly clamped β-Ga_2O_3 device. (a) Wide resonance spectrum. Inset: device optical image. (b)-(d) Zoomed-in spectra of the 3 modes.

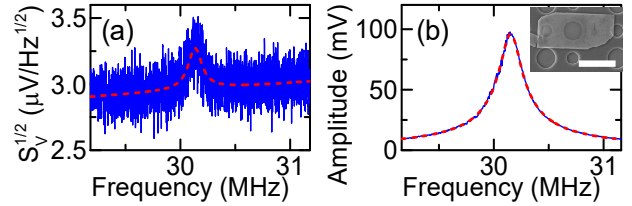

Figure 4: (a) Thermomechanical noise spectrum of a circular drumhead β-Ga_2O_3 resonator. (b) Photothermally driven response of the resonator. Inset: device SEM image. Scale bar is 10 μm.

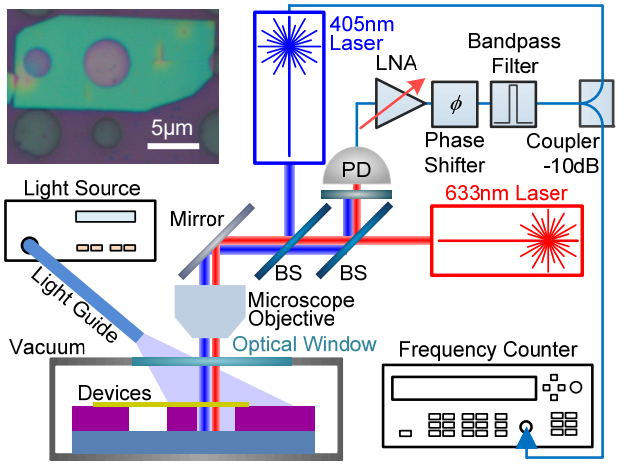

Figure 5: Scheme for demonstrating real-time MUV detection via a self-sustaining β-Ga_2O_3 oscillator. Inset: device optical image.

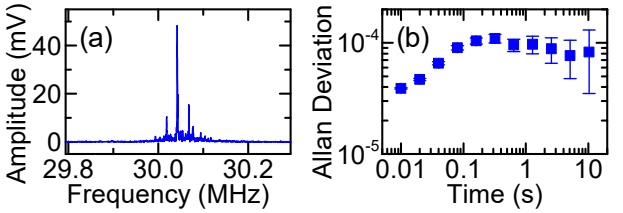

Figure 6: Performance of the β-Ga_2O_3 feedback oscillator. (a) The closed-loop oscillation spectrum. (b) Measured Allan deviation.

Further, we build a closed-loop oscillator by adding a feedback circuit to the β-Ga_2O_3 resonator (Fig. 5). The amplitude and phase of the signal from the PD are adjusted by an amplifier and a phase shifter, respectively, to satisfy the Barkhausen criterion for feedback oscillators. The modified signal is then fed back to the device using the amplitude-modulated 405nm laser. A self-sustaining β-Ga_2O_3 oscillator is therefore achieved without external ac source. The Q of the ~30MHz resonance is boosted from ~200 to an effective Q_{eff} >15,000 (Fig. 6a), with a >70-fold enhancement. We also measure the frequency stability of the oscillator (Fig. 6b), which yields Allan deviation of $\sigma(\tau) \sim 10^{-4}$ for $\tau = 0.1$–10 s.

To demonstrate MUV sensing with the β-Ga_2O_3 oscillator, we employ a light source to illuminate the ~30MHz device with wavelengths of 200 to 600 nm (Fig. 5). We introduce periodic light irradiation to the device with power intensity adjusted to be 1W/cm^2, corresponding to an incident power of ~49 nW on the circular device. The results of real-time tracking of the oscillator frequency show clear frequency downshifts (~0.13 MHz) upon cyclic illumination (Fig. 7), yielding an average responsivity of -3.3 Hz/pW. Given the frequency stability (Allan deviation of ~10^{-4}), the oscillator exhibits a light power sensitivity of 0.9 nW.

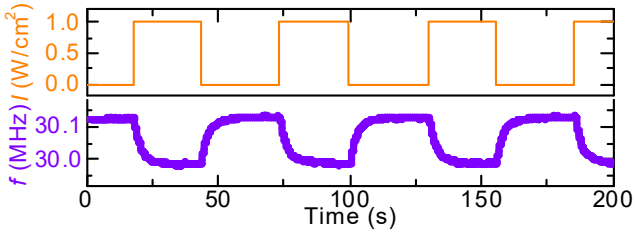

Figure 7: Responses of β-Ga_2O_3 oscillator to photon irradiation.

In analysis, β-Ga_2O_3 crystal absorbs photons with wavelengths <280 nm (because of the ultrawide bandgap) and generates heat. The resulting temperature elevation expands the β-Ga_2O_3 device, softens the resonator, and causes resonance frequency downshift. The SiO_2 (with bandgap ~9 eV) layer beneath β-Ga_2O_3 has minimal photothermal effect and acts as an isolator of mechanical deformation and a heat barrier between the β-Ga_2O_3 nanoflake and the Si substrate. The photothermal effect in the β-Ga_2O_3 crystal is the main contributor to the observed resonance frequency downshift of the oscillator upon MUV irradiation.

CONCLUSION

In summary, the demonstration of MUV light detection by the β-Ga_2O_3 nanostructure-enabled self-sustaining oscillator opens new possibilities of using resonant β-Ga_2O_3 MEMS/NEMS transducers for solar-blind UV (<280 nm) detection and real-time sensing.

ACKNOWLEDGEMENTS

We thank the US Department of Energy (DOE, EERE Grant DE-EE0006719), the National Science Foundation (Grants CMMI-1246715, DMR-1755479), and the Great Lakes Energy Institute (ThinkEnergy Fellowship, X.-Q. Zheng) for financial support.

REFERENCES

[1] W. S. Hwang, *et al.*, "High-voltage field effect transistors with wide-bandgap β-Ga_2O_3 nanomembranes", *Appl. Phys. Lett.*, vol. 104, 203111 (2014).

[2] X.-Q. Zheng, *et al.*, "Ultrawide band gap β-Ga_2O_3 nanomechanical resonators with spatially visualized multimode motion", *ACS Appl. Mater. Interfaces*, vol. 9, 43090-43097 (2017).

[3] W.-Y. Kong, *et al.*, "Graphene-β-Ga_2O_3 heterojunction for highly sensitive deep UV photodetector application", *Adv. Mater.*, vol. 28, 10725-10731 (2016).

[4] X.-Q. Zheng, *et al.*, "Hexagonal boron nitride nanomechanical resonators with spatially visualized motion", *Microsystems & Nanoengineering*, vol. 3, 17038 (2017).

CONTACT

*Philip X.-L. Feng, Tel: +1-216-368-5508; philip.feng@case.edu

SELF-SUSTAINED DUAL-MODE MECHANICAL FREQUENCY COMB SENSORS

Mingyo Park and Azadeh Ansari
School of Electrical and Computer Engineering, Georgia Institute of Technology, Atlanta, GA, 30308

INTRODUCTION

Resonant frequency-shift detection has proven to be a highly-accurate method to detect perturbations in the environment with *Q*-fold passive signal amplification. The challenges associated with such scheme, are (1) sustaining oscillation by utilizing an energy restoring element that compensates for the losses in the mechanical resonator with minimal contribution to the overall noise, and (2) decoupling the frequency shift due to undesired environmental drifts from the frequency shift due to the sensed stimulus.

This work reports on a novel sensing scheme which addresses the two aforementioned challenges by utilizing integrated, self-sustained, high-*Q*, resonant-based frequency comb sensors that track the frequency spacing between the spectral lines as the "beat frequency" in order to increase the sensor sensitivity and cancel out the environmental drift effects on the sensor responsivity.

SENSING MECHANISM

Micromechanical resonators, in the most general definition, are passive components, which have to be integrated with an energy restoring element, *e.g.* electronic amplifiers, to sustain oscillation in a feedback-loop system. MEMS-circuits interface is particularly challenging as the size of the sensor shrinks. Scaling of the resonator is desirable to increase the sensor sensitivity to absorbed mass, justifying the constant efforts observed in shrinking of the size of the M/NEMS sensors. However this in turn yields larger motional impedances, rendering interface with electronic devices challenging. To address this challenge, instead of using electronic amplifiers as the energy restoring element, we utilize a single-tone pump with a frequency equal to the sum of the frequencies of two acoustic modes within the same resonator. This technique offers several advantages over the traditional MEMS-CMOS oscillator counterparts: (1) It obviates the need for electronic circuitry that suffer from shot noise [1], the associated challenges with MEMS-CMOS integration and thus improves the overall noise performance and (2) it offers a smaller footprint that takes advantage of piezoelectric-induced mode coupling between two (or more) resonance modes within the same acoustic cavity and a single-tone pump.

The latter challenge arises from the interfering effects of environmental changes on frequency detection. Various methods have been sought so far including utilizing multiple resonators with different sensitivities, or more efficiently, a dual-mode oscillator using two different resonance modes of the same oscillator, which yields two equations with two unknowns allowing for separation of the different effects [2]. Moreover, multi-mode frequency shift monitoring has been proposed for more accurate readout, as well as for inertial mass spectroscopy [3].

Implementation of dual-mode oscillators is challenging, due to complicated electronics to design two different loops to excite two resonance modes simultaneously. This work reports on a novel sensing technique based on efficient simultaneous excitation of two resonance modes using a single-tone pump. We recently experimentally demonstrated the generation and tuning of phononic frequency combs in a fully-integrated standalone piezoelectric platform [4]. In this work, we report on feasibility of application of such frequency combs for high-precision sensing that tracks the "frequency spacing" between the phase-coherent spectral lines; as the analogue of "beat frequency" in dual-mode oscillators, to increase the frequency shift sensitivity within the same resonant device. The pump frequency which is detuned from (f_{m1} +f_{m2}), where f_{m1} and f_{m2} are the two mechanical modes, induces an idler and signal mode at frequencies close to f_{m1} and f_{m2}.
Frequency mixing between the idler (signal) mode and f_{m1} (f_{m2}) creates Δf_1 (Δf_2) that are proportional to the detuning of the pump from f_{m1}+f_{m2} [5]. Such scheme can significantly reduce the electronics required for multipliers and mixers used in dual-mode oscillators to track "beat frequency".
It must be noted that any two mechanical modes can be chosen to generate the frequency comb based on non-degenerate parametric pumping. The threshold power for comb generation can be reduced by designing high *Q*-resonant modes with high coupling rates. Furthermore, by utilizing two modes with different sensitivities, one can decrease the beat frequency through their linear combination. Figure 1 shows the proposed sensing scheme, the two modes undergo different frequency shifts as the stiffness of the membrane is modulated by DC voltage (from -0.1 V to 0.1V with 0.1 V steps). The shift in the mechanical modes cause a shift in the detuned frequency and thus a change in the frequency spacing.

Another advantage of the proposed technique is the phase-coherence of the spectral lines. It has been shown that the generated side-bands have a defined phase relationship with respect to the pump phase [6]. In practical NEMS resonators, in often cases, the frequency shift detection is in fact not limited by the resonator *Q*, but instead bound to some anomalous temperature-dependent frequency/phase fluctuations [7]. Oscillator circuits traditionally have phase freedom, while their amplitude are limited by a limiting amplifier or a nonlinearities in the system. Using a phase coherent detection mechanism along with two-mode compensation techniques would yield higher phase stability as compared to traditional amplitude-saturated oscillator circuits.

EXPERIMENTAL RESULTS

Figure 2 shows the SEM image of the fabricated AlN-on-Si circular membrane, denoting the measurement setup for frequency comb generation. *Figure 3 (a,b)* show the driven resonance modes of the two acoustic resonance modes at different input power levels, demonstrating the duffing nonlinearity. The governing harmonic oscillator equations that include the two coupled modes are:

$$\ddot{x}_1 + \omega_1^2 x_1 + (^2/_{Q_1})\dot{x}_1 + (\gamma_{12}/m_1)x_1x_2^2 + (\alpha_1/m_1)x_1^3 = (F/m_1)x_2 \cos \omega_p t$$

$$\ddot{x}_2 + \omega_2^2 x_2 + (^2/_{Q_2})\dot{x}_1 + (\gamma_{21}/m_2)x_2x_1^2 + (\alpha_2/m_2)x_2^3 = (F/m_2)x_1 \cos \omega_p t$$

where $x_{1,2}$ are the mode displacements, $Q_{1,2}$ are the *Q* factors, $m_{1,2}$ are the effective masses, $\alpha_{1,2}$ are the duffing nonlinearity coefficients for mode 1 and 2 respectively, and γ_{12} denotes the dispersive coupling between mode 1 and 2. ω_p is the pump frequency and F is the amplitude of the pump.

Figure 4 shows the mechanical frequency comb spectrum, showing a shift in the $f_{spacing}$ when DC voltage shifts the two mechanical modes with different coefficients.

CONCLUSION

This work reports the first demonstration of fully-integrated self-sustained micromechanical frequency combs as highly-sensitive dual-mode sensors that can be optimized to cancel out environmental drifts with enhanced beat frequency, while taking advantage of simplified design and unprecedented footprint of only 30 μm×30 μm.

978-1-940470-03-0/HH2018/$25©2018TRF
DOI 10.31438/trf.hh2018.26

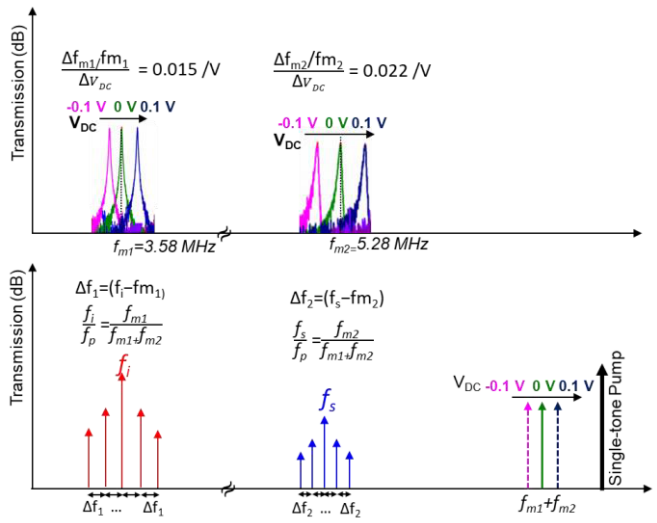

Figure 1: (Top) Resonant frequency shift of the driven modes. The resonant frequency shifts due to a change in the effective mass or stiffness. The DC voltage changes the stiffness of the membrane with different sensitivities at mode 1 and 2. The DC voltage is varied from -0.1 V to 0.1 V in 0.1 V steps and sensitivities of 0.015/V and 0.022 /V are observed for the two resonance modes. (Bottom) Pumping at the blue-side band above a certain threshold (20dBm in this work at 8.78 MHz) causes generation of frequency combs close to the two mechanical modes. As the DC voltage changes the stress, the detuning frequency between the pump and the sum of the two mechanical modes change, thus shifting the frequency spacing between the spectral lines.

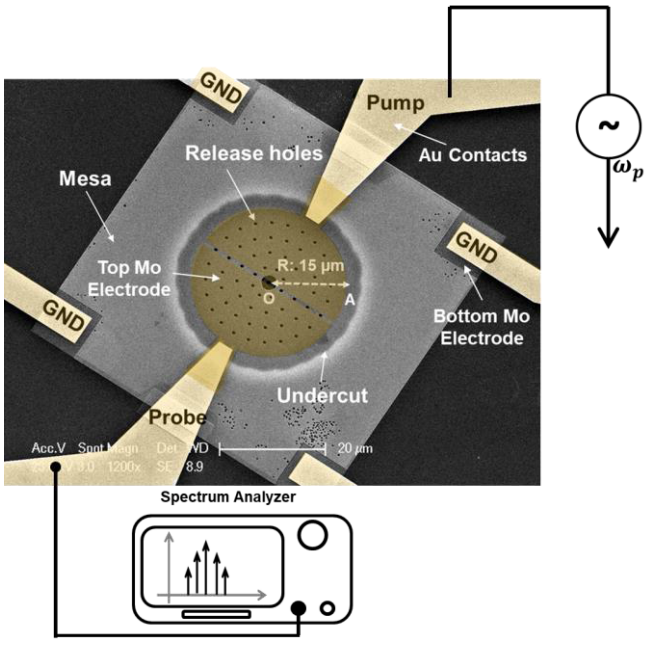

Figure 2. Scanning Electron Micrograph of fabricated AlN-on-Si piezoelectric frequency comb. The radius is 15 µm, and the pump and probe measurement setup are demonstrated.

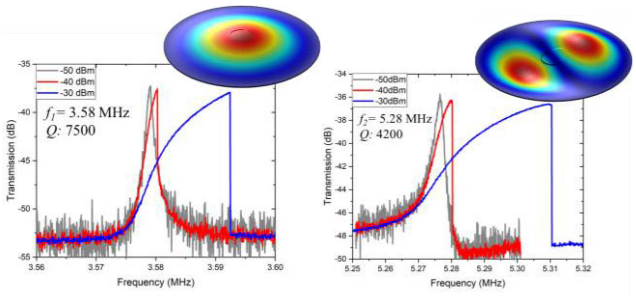

Figure 3: Driven resonance (a) mode 1 and (b) mode 2, along with the displacement mode shape at three different input power levels.

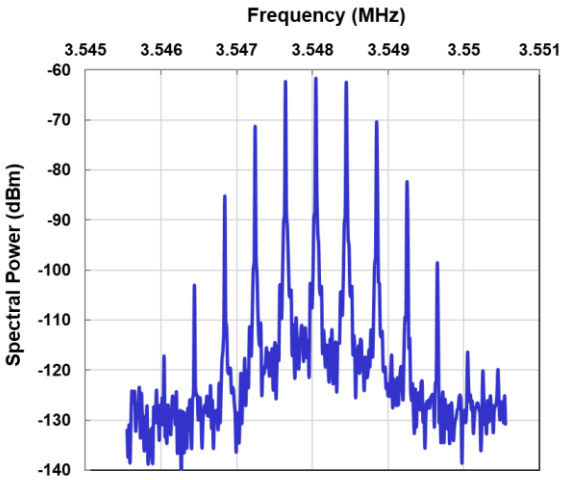

Figure 4: Mechanical resonant-based frequency comb generation, centered at the idler frequency with spacing determined by the detuning of the pump from the sum of mechanical modes.

ACKNOWLEDGEMENTS

The authors would like to thank the Roukes group at Caltech for the help with fabrication and many helpful discussions, in particular Dr. Matheney, Mr. Raj Katti and Mr. Jarvis Li.

REFERENCES

[1] J. Miller, A. Ansari, *et al.*, "Effective Quality factor tuning mechanisms in micromechanical resonators" *Journal of Applied Physics*, (Submitted Feb. 2018, under review).

[2] J. Vig, "Dual-mode Oscillators for Clocks and Sensors," *IEEE Ultrasonic Symposium*, 1999.

[3] M. Hanay *et al.,* "Inertial imaging with nanomechanical systems," *Nat. Nanotechnology*, 2015, DOI: 10.1038.

[4] M. Park and A. Ansari, "Phononic Frequency Combs in Standalone Piezoelectric Resonators" *Accepted for oral presentation, IFCS,* 21-24 May 2018, Olympic Valley, CA.

[5] A Ganesan, C Do, A Seshia, "Excitation of coupled phononic frequency combs via two-mode parametric three-wave mixing," *Physical Review B* 97 (1), 014302.

[6] T. Kippenberg, R. Holzwarth,S. Diddams, "Microresonator-Based Optical Frequency Combs," *Science*, Vol. 332, Issue 6029, pp. 555-559, Apr. 2011.

[7] M. Sansa *et al.*, "Frequency fluctuations in silicon nanoresonators," *Nature Nanotechnology*, 11, pages 552–558 (2016).

[8] P. Del'Haye *et al.*, "Phase steps and resonator detuning measurements in microresonator frequency combs," *Nat. Comm.*, Jan. 2015, DOI: 10.1038/ncomms666.

ENTERIC & 3D-PRINTED HYBRID PACKAGE FOR SAMPLING IN DIGESTIVE REGIONS

G.E. Banis[1,3], L.A. Beardslee[1], J.M. Stine[1,2], and R. Ghodssi[1,2]
[1]Institute for Systems Research, [2]Department of Electrical and Computer Engineering,
[3]Fischell Department of Bioengineering,
University of Maryland, College Park, Maryland 20742 USA

ABSTRACT

We present a packaging concept for an ingestible sensing capsule, which utilizes biodegradable polymers to target the sensors to specific areas of the gut. Interdigitated electrodes (IDE) are inserted into 3D-printed capsules with embedded gratings that are filled with pharmaceutical polymers tuned to dissolve at a specific pH threshold. Sensors, housed within a 3D-printed package accessible only by the gratings, are connected to a microcontroller capable of transmitting data to a smartphone via Bluetooth Low-Energy (BLE). The system is tested with varying amounts and types of enteric coatings over the gratings, used toward optimizing control over timed polymer dissolution. This represents a minimally-invasive strategy toward *in situ* sampling and analysis at pH-targeted locations in the gastrointestinal (GI) tract.

INTRODUCTION

Integrated capsule systems are widely gaining momentum for analysis or drug delivery in GI regions where traditional techniques are expensive, highly invasive, or inadequate [1], [2]. Depending on the region, there are numerous physiological considerations that must be addressed for fluid sampling and sensing with minimal human intervention [3]. Previous passive approaches to GI sampling lack a means of knowing whether a sample has been retrieved in real-time, while active approaches suffer due to cost and complex assembly [4]. In this work, a breadboard level circuit representative of the electronics, ultimately for integration within the device, is used to monitor the removal of polymer material from grids within a 3D printed capsule. The goal is to use the polymers to protect sensors within the capsule, only exposing them when the device has reached the GI region of interest [5]. Different Eudragit polymers are used to target different GI regions, depicted in Figure 1: E PO, S 100, and L 100 dissolve respectively at the stomach, ileum, and duodenum.

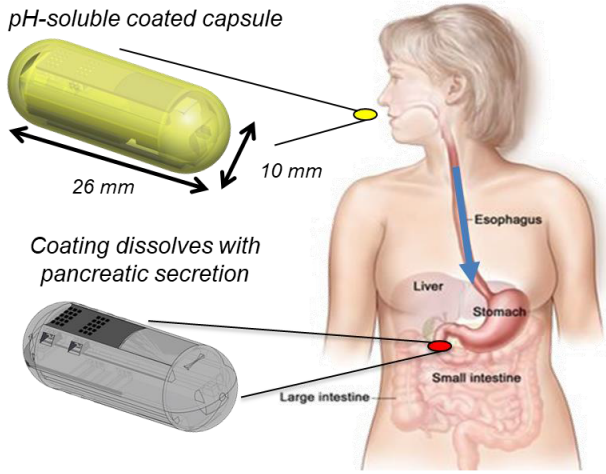

Figure 1: Depiction of system outlook and application (Image credits: NIH). Polymer coatings are intended to dissolve at either the stomach (pH 1.5-3) or the duodenum (pH 7-8.5). At the duodenum, gastric acid-neutralizing bicarbonate is secreted from the pancreas via the sphincter of Oddi.

WORKING PRINCIPLE AND RESULTS

Figure 2 presents a 3D representation of the capsule (left) and a schematic overview of the electronics. Each die, containing four sensors, is inserted into a slot designed in one end of the 3D-printed capsule. Once inserted, the capsule was fastened using built-in threads and sealed with epoxy, then dip-coated into a 30 w/v% solution of each polymer in methanol, each for 1-5 coats with removal for 20 min intervals between each coating. The circuit setup is depicted in Figure 2, characterized in Figure 3a, and transmission protocols are compared in Figure 3b.

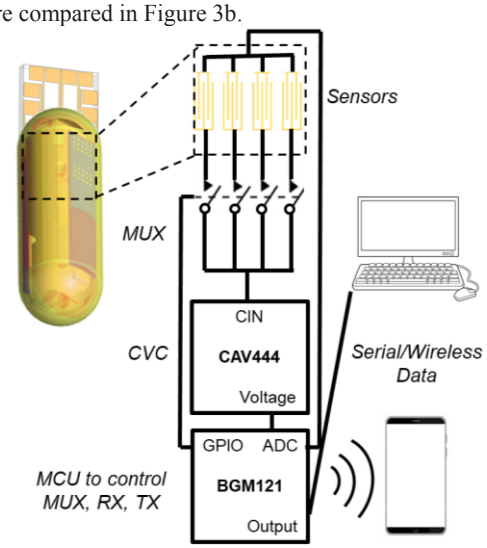

Figure 2: System overview, including the packaging design with the inserted IDEs and the circuit design. The capsule is made from MED610 using a Connex 3 Objet500 (Stratasys). Capacitor electrodes consisting of Cr(20nm)/Au(200nm) IDEs with 75µm width and spacing were fabricated using photolithography and lift-off over a pyrex wafer. Circuit design includes a multiplexer (MUX) integrated circuit (IC), a capacitance-voltage-converter (CVC) IC, a 1.5 MHz step-up DC-DC converter, and a BLE System-in-Package (SIP) microcontroller unit (MCU).

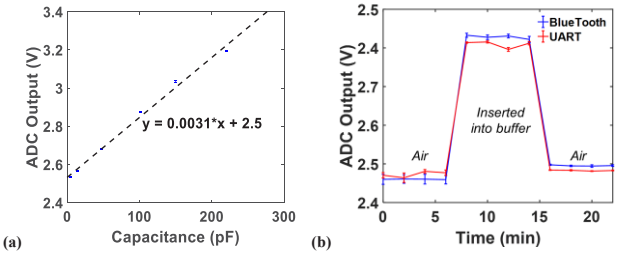

Figure 3: (a) Circuit calibration with standard capacitors across four multiplexed inputs. The resulting system senses capacitive changes in the 0.8-220 pF dynamic range with a sensitivity of $3.2x10^{-3}$ pF/mV and operated using a 3.3 V source. (b) Comparison of data obtained through Bluetooth versus serial (UART) communication, where the capsule (open gratings) was measured in air, inserted into buffer, then removed (n=4).

978-1-940470-03-0/HH2018/$25©2018TRF
DOI 10.31438/trf.hh2018.27

Capsule coating thicknesses for S 100 were analyzed, shown in Figure 4, over gratings and non-grating regions. Gratings resulted in a slower increase (Figure 4d) with each coating due to polymer infill. Capsules were then immersed in 0.1 M acetic acid (pH 3) and progressively adjusted at 30 min intervals to increasing pH levels. Figure 5 presents the sensor output and corresponding change in capacitance over the course of pH adjustments for the S 100 polymers, indicating the expected length of time for chamber filling and sampling dynamics for each coating thickness.

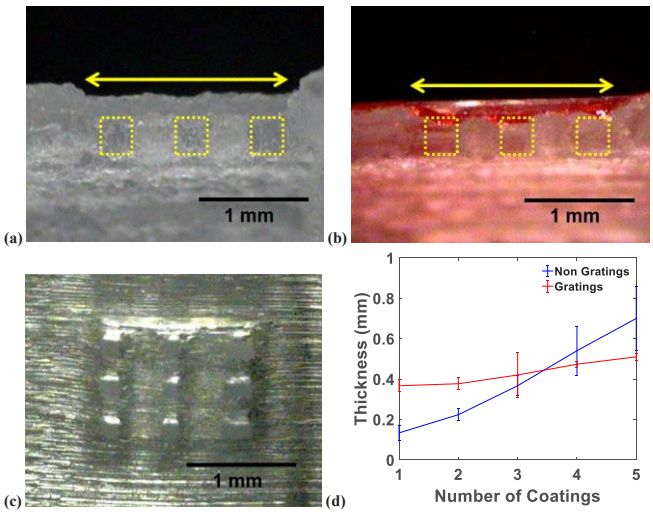

Figure 4: Cross-sectional optical images of the sampling gratings (a) uncoated and (b) with 1 coating of red-dyed polymer, where yellow markers indicate the grating locations. (c) Top-view optical image of uncoated gratings. (d) Characterization of polymer coating thickness vs. number of dipping steps from both non-grating and grating regions over the 3D-printed capsule surface (n=3).

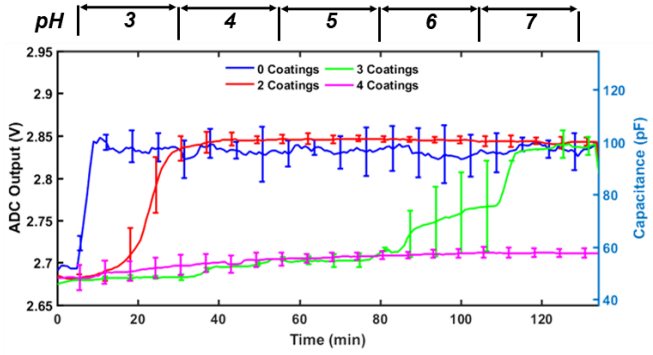

Figure 5: Sensor responses inserted (at 5 min) into capsules with different numbers of S 100 coatings (0, 2, 3, and 4, respectively) with increasing pH using titers of 1 M NaOH (n=4). Chamber filling is characterized by a capacitance change of ~50 pF from the initial capacitance in air. For each formulation, it was determined that 3 coatings was optimal for the w/v% used.

After coating optimization was performed for each polymer, combined coatings were tested to determine ability to tailor sampling for more complex pH sequences. Figure 6 presents representative sequences of L 100 and E PO formulations (a and b, respectively), as well as a combined coating of both polymers. As expected, the capacitance increase did not occur until ~pH 5, indicative that this combined coating strategy can be used to protect the sensing chambers until the characteristic pH-targeted regions are reached.

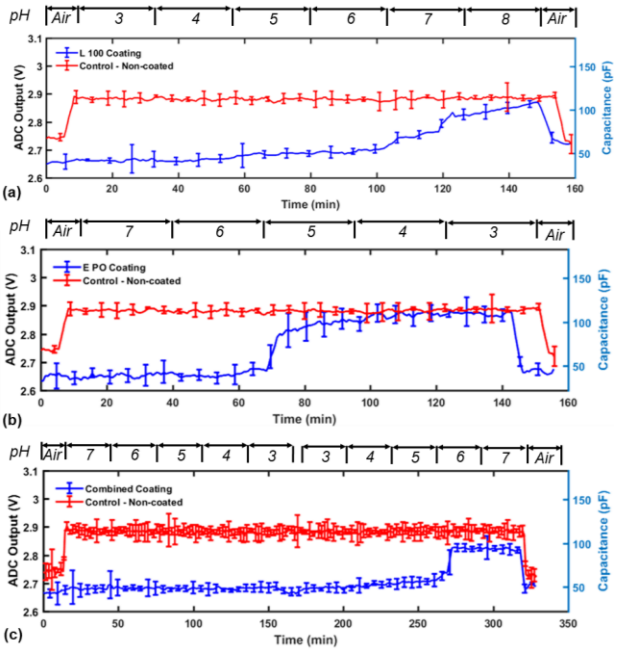

Figure 6: Sensor responses inserted into capsules with different types of coatings (3 dip-coatings each) compared to uncoated controls: (a) L 100, (b) E PO, and (c) combined coatings, where E PO is outer-most and L 100 is between the 3D-printed capsule and the E PO layers (n=4).

CONCLUSION

This work is the first demonstration of a passive pH-dependent packaging strategy for ingestible capsule technology that offers information on the package integrity at any given time, while simultaneously providing a real-time active microelectronics-based system capable of wireless retrieval of sensor data for use in GI sampling and analysis.

ACKNOWLEDGEMENT

This work was supported by the National Science Foundation ECCS Program under Award 1738211. The authors acknowledge the support from the Maryland NanoCenter and its FabLab.

REFERENCES

[1] J. Z. Ou, C. K. Yao, A. Rotbart, J. G. Muir, P. R. Gibson, and K. Kalantar-zadeh, "Human intestinal gas measurement systems: in vitro fermentation and gas capsules," *Trends Biotechnol.*, vol. 33, no. 4, pp. 208–213, Apr. 2015.

[2] S. N. Adler and Y. C. Metzger, "PillCam COLON capsule endoscopy: recent advances and new insights," *Ther. Adv. Gastroenterol.*, vol. 4, no. 4, pp. 265–268, Jul. 2011.

[3] G. Banis, A. L. Beardslee, and R. Ghodssi, "Gelatin-Enabled Microsensor for Pancreatic Trypsin Sensing," *Appl. Sci.*, vol. 8, no. 2, 2018.

[4] "Ingestible Gastrointestinal Sampling Devices: State-of-the-Art and Future Directions," *Crit. Rev. Biomed. Eng.*, vol. 42, no. 1, pp. 1–15, 2014.

[5] G. Banis, L. A. Beardslee, J. S. Stine, and R. Ghodssi, "PH Targeting via Packaging for a Wireless Ingestible Capsule," presented at The 9th International Conference on Microtechnologies in Medicine and Biology, Monterey, CA, Mar-2018.

CONTACT

*R. Ghodssi, tel: +1-301-405-8158; ghodssi@umd.com

ROBUST "RIBBED" NANOPOROUS MEMBRANES FOR IMPLANTABLE BIO-ARTIFICIAL KIDNEYS

B.W. Chui, P. Taheri-Tehrani, N. Wright, J. Ly, and S. Roy
University of California, San Francisco, California, USA

ABSTRACT

We have designed, fabricated, and tested nanoporous membranes with improved robustness and performance for the implantable bio-artificial kidney (iBAK). By superimposing a network of thicker "ribs" onto a thin membrane, we have shown that it is possible to achieve mechanically robust membranes and high filtration rates at the same time.

BACKGROUND

The "implantable bio-artificial kidney" is a national research effort headquartered at UCSF [1] and aimed at eliminating the need for dialysis or kidney transplants for end-stage renal disease (i.e. kidney failure), which affects more than 650,000 patients in the US alone with treatment costs exceeding $35 billion per year.

INTRODUCTION

One critical MEMS component of the iBAK is the filter unit, in which polysilicon membranes with nanoscale slit pores are used to mimic the kidney's filtering function in extracting creatinine, urea, and other harmful substances from blood [1]. The pore width (typically 5-30 nm wide) is set such that "useful" components (e.g. red and white blood cells) remain in the blood while "unwanted" components pass through into the ultrafiltrate due to the difference in pressure between the two sides.

We have previously developed a reliable process for fabricating such membranes with highly uniform and precisely tuned pore sizes [2]. But to match the mass-transfer throughput required for dialysis, another order-of-magnitude improvement is required: for example, by (i) implementing parallelism on the system level (e.g. multiple chips); (ii) increasing pore density at the chip level (advanced lithography or nano-imprint); and (iii) reducing flow-path resistance of the pores (e.g. thinner membranes). This abstract focuses on option (iii): making membranes thinner without sacrificing mechanical integrity.

DETAILED DISCUSSION

While one can imagine thinning a membrane *ad infinitum* to minimize flow-path resistance, eventually it becomes too fragile to withstand typical blood pressures. This is clearly unacceptable in implantable medical devices, where long-term reliability is key.

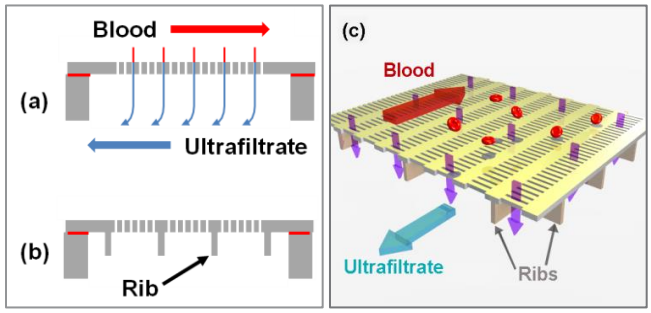

Figure 1: Conceptual diagram of (a) flat, (b) ribbed membrane. Fig.(c) shows 3D rendition of orthogonal backside rib network.

Therefore, we have designed a variable-thickness membrane consisting of a "thin" active porous area reinforced by a scaffolding of "thick" ribs to give it extra rigidity (Fig. 1). Ideally, the reinforcing elements should not take up too much active filter area. Also, the rib protrusions should be on the *back* side (filtrate side) of the chip to avoid disrupting blood flow. This precludes "post-depositing" the rib material on top of an existing membrane.

Given these constraints, in this work we adapted a thin-film plate-stiffening technique [3,4] for use in our membrane process flow as follows: a grid of 1.5 µm-wide grooves (the "rib molds") is etched 2.5-5.0 µm deep into the surface of a silicon substrate (Fig. 2a). A 0.5 µm thermal oxidation followed by a 0.8 µm poly-silicon deposition effectively fills up the grooves (forming the eventual ribs on the *bottom* of the membrane) and re-planarizes the surface. We then revert to the original process flow detailed in [5] (Figs. 2c-2f). The finished device is shown in Fig. 3.

To find a rib configuration that combines robustness with ease of fabrication, we performed finite-element analysis on membrane deflection and maximum stress vs. rib height. We found that membrane strength (maximum principal stress) increased quickly even with modest increases in rib height (Fig. 4). Accordingly, we made nanoporous membranes with 0 µm (flat), 2.5 µm and 5 µm-tall ribs and compared their hydraulic rupture thresholds. Table 1 shows that the ribbed membranes performed 50-85% better than their flat counterparts, well worth the slight loss (13%) in active pore area. Both types of membranes also underwent bio-filtration clearance tests and demonstrated favorable performance (Fig. 5).

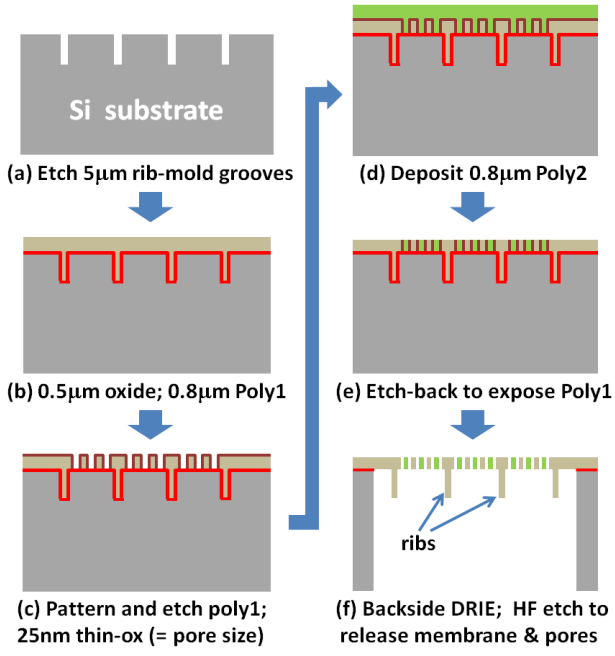

Figure 2: Fabrication process flow for ribbed nanoporous poly-silicon membranes

978-1-940470-03-0/HH2018/$25©2018TRF
DOI 10.31438/trf.hh2018.28

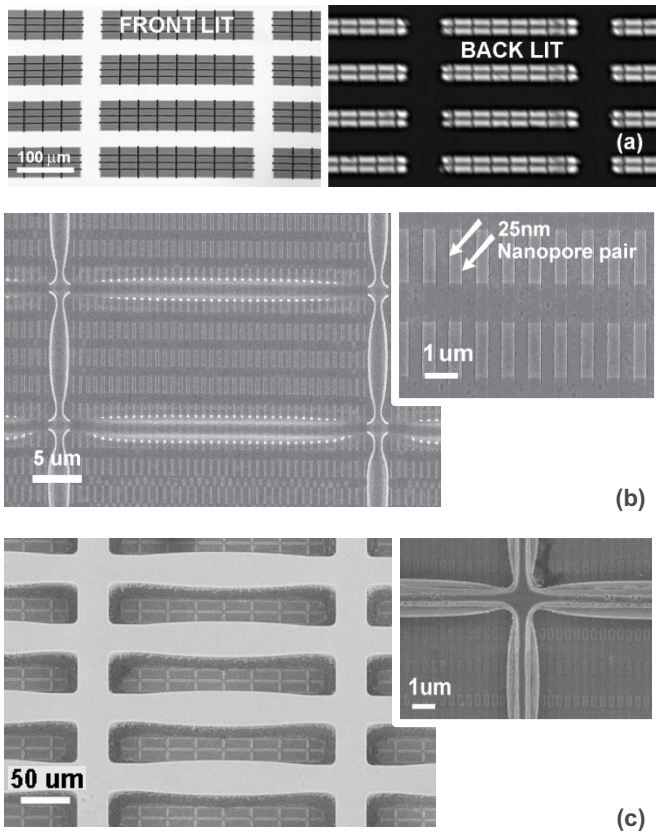

Figure 3: (a) Optical image of ribbed membranes, (b) Top-view scanning electron micrograph (SEM) (inset shows close-up of nanopores), (c) Bottom-view SEM (inset shows details of ribs).

Table 1: Measured hydraulic rupture pressure for various designs

(×1000 mm Hg)	Flat (no ribs)	2.5 µm ribs	5 µm ribs
Sample 1	1.03	2.22	2.69
Sample 2	1.40	2.22	2.74
Sample 3	1.91	--	--
Average	**1.45**	**2.22**	**2.72**

CONCLUSION

We have proven a design and fabrication method that enables significantly thinner nanoporous membranes while preserving device robustness, thereby improving filtration efficiency on our way towards the ultimate goal of a fully implantable bio-artificial kidney─the "silicon kidney."

ACKNOWLEDGEMENTS

We would like to acknowledge the support of the Stanford Nanofabrication Facility, the Berkeley Marvell Nanolab, and NIH Quantum Grant U01EB021214.

REFERENCES

[1] W.H. Fissell and S. Roy. "The Implantable Artificial Kidney," *Semin. Dial.* 2009; 22(6): 665-70.

[2] S. Kim, B. Feinberg, R. Kant, B.W. Chui, K. Goldman, J. Park, W. Moses, C. Blaha, Z. Iqbal, C. Chow, N. Wright, W.H. Fissell, A. Zydney, and S. Roy. "Diffusive Silicon Nanopore Membranes for Hemodialysis Applications," *PLoS One,* 2016; 11(7):e0159526.

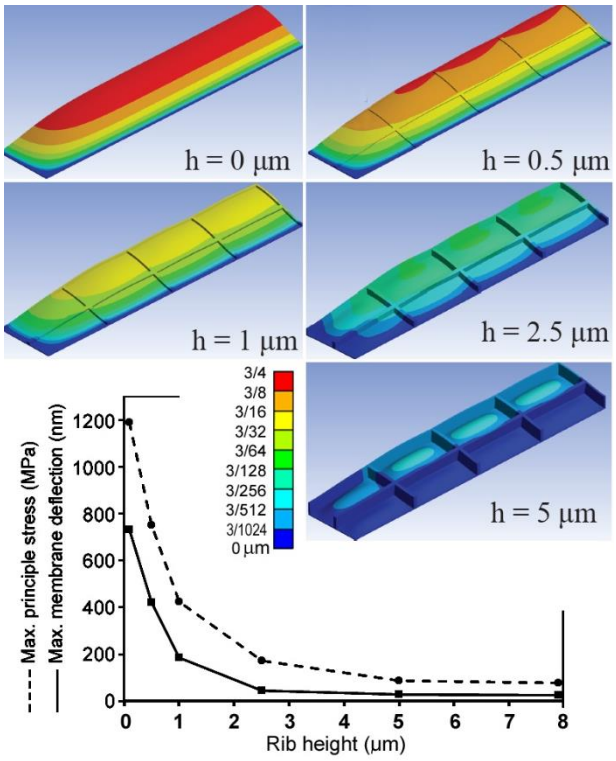

Figure 4: Simulated membrane deflection and peak stress vs. rib height for 300 mm Hg pressure. (A logarithmic color scale is used to resolve the range of all five cases.) It can be seen that membrane deflection (solid line) and peak stress (dotted line) both decrease rapidly with rib height.

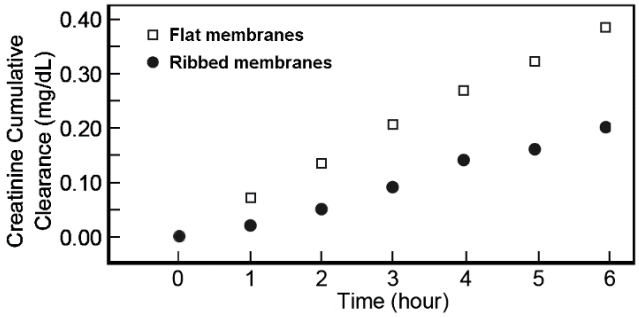

Figure 5: Measured cumulative creatinine clearance for ribbed vs. flat membranes. The lower clearance for the ribbed membranes is partly due to a 13% reduction in active pore area taken up by the ribs.

[3] J. Drake and H. Jerman, "A Micromachined Torsional Mirror for Track Following in Magneto-Optical Disk Drives", Proc. of Hilton Head Solid-state Sensors and Actuators Workshop, 2000.

[4] B. J. Lutzenberger and D. L. Dickensheets, "Fabrication and Modeling of Rib-Stiffened Thin Films," *J. Micromechanics and Microengineering,* 2009; 19 (9).

[5] S. Roy, A. Dubnisheva, A. Eldridge, A.J. Fleischman, K.G. Goldman, H.D. Humes, A.L. Zydney, and W.H. Fissell, "Silicon Nanopore Membrane Technology for an Implantable Artificial Kidney," Proc. of Transducers 2009, Denver, CO, USA, 2009.

AN ULTRASONICALLY POWERED IMPLANTABLE MICRO ELECTROLYTIC ABLATION (IMEA) FOR TUMOR NECROSIS

Anirvan K. Majumdar[1], Sayemul Islam[1], and Albert Kim[1]*
[1]Department of Electrical Engineering, Temple University, Philadelphia, Pennsylvania, USA

ABSTRACT

Electrolytic ablation is a technique that can remove non-resectable tumors from internal organs (such as liver, kidney, pancreas, etc.) with highly localized control to minimize harm to adjoining healthy tissue. Here, we aim to utilize the principle of electrolytic ablation in an implantable platform and power it by an external ultrasonic wave. The implantable micro electrolytic ablation (IMEA) will address challenges of the current existing tethered method such as constraints in electrode size, multiple targets and repeated treatments in case of cancer recurrence. We characterized the prototype of IMEA in an agarose gel containing phenolphthalein to simulate internal body tissue. Color change in phenolphthalein shows that the device responds to external ultrasonic stimulation and shows electrolytic behavior in an area around the electrodes that spreads outward with time. Overall, the IMEA could achieve 0.614±0.01 cm^2 in ablation area (cathode) when ~190 mW/cm^2 ultrasonic intensity was applied for 60min.

INTRODUCTION

Pancreatic ductal adenocarcinoma accounts for about 80% of all malignant pancreatic tumors [1] with an unusually low 5-year survival rate. This is attributed to its rapid growth, aggressive malignancy, and insidious course [2]. These factors are also responsible for the low rates of early detection, which in turn leads to low rates of survival since most of the cases that are finally diagnosed are only done so at late stages [2]. Surgically resectable tumors are observed in only 20% of the diagnosed patients [1]. Chemotherapy and radiotherapy are applied to the remaining nonresectable cases [1]. More recently, ablation technology has become available for locally advanced unresectable non-metastatic tumors [1,2].

Ablation is a minimally invasive technique that uses either thermal or electric energy to cause localized necrosis of tissue. Unfortunately, current ablation technology uses externally inserted electrodes to cause localized cell death within the body. The electrode size becomes a constraint in trying to maximize stiffness (so that it doesn't snap off within the body) and simultaneously minimizing ablation area (to avoid death of neighboring healthy cells). Multiple tumors may require multiple incisions. Moreover, in cases of cancer recurrence, the entire procedure will have to be repeated.

In this paper, we report a novel implantable micro electrolytic ablation device (IMEA) that can be used to perform electrolytic ablation while being powered by an external ultrasound source. It is expected that the IMEA will alleviate some of the issues faced by conventional ablation techniques.

MATERIALS AND METHODS

Figure 1.a shows a schematic view of Implantable Micro Electrolytic Ablation (IMEA). The ultrasonic wave can reach a deeply implanted IMEA device (such as, near the pancreas). The ultrasonic wave is generated from an ultrasonic transducer that is excited by a signal generator via a power amplifier. The ultrasonic wave travels through tissue and reach an implanted IMEA that consists of an ultrasonic receiver, rectifier, and platinum wires (Figure 1.b). The ultrasonic wave is being transformed to electrical power through piezoelectricity, providing sufficient potential for electrolysis. In physiological medium, electrochemical reactions by electrolysis yield changes in pH due to newly generated chemical species (anode: $2H_2O \rightarrow O_2+4H^++4e^-$, cathode: $2H_2O+2e^- \rightarrow H_2+2OH^-$). Therefore, local cytotoxic regions are formed that diffuse around the electrodes [3-5].

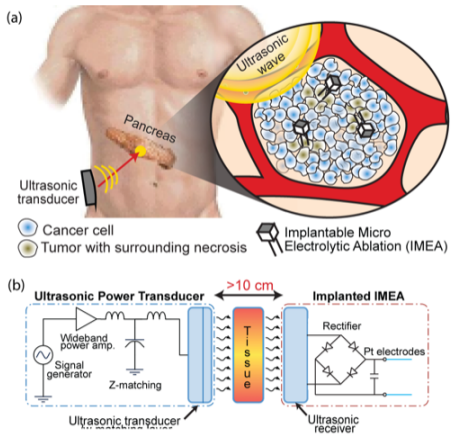

Figure 1: (a) IMEA implanted in a pancreatic tumor for in situ ablation, (b) schematic of ultrasonic system used to power the IMEA

Figure 2 shows the fabrication process. The entire electronics is housed on a flexible PCB made by chemical etching of a copper-clad laminated sheet (Pyralux®, DuPont) on which the routing is drawn (Figure 2.a-b). After the circuit components are soldered (Figure 2.c-d), passivation is done by epoxy, and a custom capsule is 3D printed to fit the device (Figure 2.e). Figure 3 shows a picture of the final prototype of IMEA. Platinum electrodes are approximately 9mm in length for both anode and cathode.

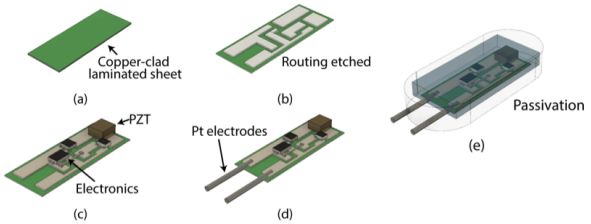

Figure 2: IMEA fabrication process: (a) circuit is drawn on Pyralux, (b) copper etching, (c) electronics integration, (d) platinum electrodes integration, and (e) passivation and packaging

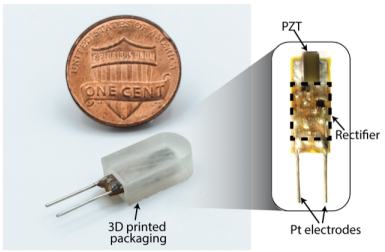

Figure 3: Final prototype of the IMEA showing the device within the packaging as well as without. Electrodes length is approximately 9mm

978-1-940470-03-0/HH2018/$25©2018TRF
DOI 10.31438/trf.hh2018.29

RESULTS AND DISCUSSION

Figure 4 shows the experimental setup. A function generator is used to generate a signal that is amplified by an RF amplifier and converted to ultrasound by a piezoelectric slab (Lead Zirconate Titanate, PZT5H, Piezo Inc.). The ultrasound is transmitted to the IMEA through the agarose. The piezoelectric receiver on the device receives the ultrasonic wave and produces AC power. This is passed through a full-wave rectifier to be converted to DC power. The DC power is finally fed to attached platinum electrodes (cathode and anode) which cause localized pH change by electrolysis.

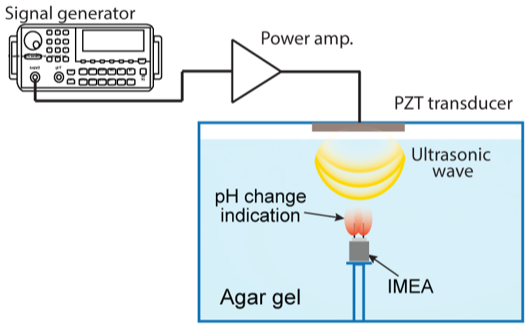

Figure 4: Experimental setup for in vitro characterization of the IMEA operation. The IMEA was placed in agarose gel with pH-sensitive dye while it is powered by an ultrasonic transducer

Phenolphthalein dye-containing agarose gels are prepared to simulate tissue environment. The agarose gel is formed using 0.7wt.% agarose and 0.9wt.% sodium chloride. 1ml of phenolphthalein is added per 100ml of agarose solution. A central crater is chiseled out in the gel to place the device and the electrodes are inserted into the gel leaving the PZT receiver and circuit body in the crater. The crater is filled with deionized water for ultrasonic wave propagation. The ultrasonic transducer (i.e. the PZT slab used to generate the ultrasound) is placed on top of the crater. The signal generator is adjusted to a frequency of 1.15MHz (the resonant frequency of the 2mm-thick PZT). While various input voltage amplitude (50, 75, and 100mVp-p) were applied, corresponding pH changes were analyzed by characterizing the color change of the gel. Note that the ultrasound intensity was calibrated by a fiber optics hydrophone (Precision Acoustic Ltd.). Input voltage of 50, 75 and 100mVp-p input corresponded to maximum acoustic intensity of approximately 46, 119, and 190mW/cm^2, respectively.

As ultrasound is applied to the device, a colored region (theoretical ablation region) is observed around the electrode in response to changing pH. Images are captured at an interval of 5 min over 1hour. The ablation region was measured by image processing using ImageJ. The ablation region around the cathode increases with time until it shows a plateauing (Figure 5). The ablation area around the anode was observed to be smaller than that around the cathode (Figure 6). Ideally, the anode should be inactive, but since the circuit does not have an earth ground, it remains active. Increasing the ultrasonic power decreases the time taken to reach maximum ablation area, though the relationship is not linear.

CONCLUSIONS

We present here an ultrasonically powered implantable micro electrolytic ablation device intended for tumor ablation. *In vitro* results show effective pH change in agar gel that could possibly translate into appropriate *in vivo* tissue necrosis. It is expected that this device alleviates some of the drawbacks of conventional electrolytic ablation by decreasing the number of procedures required in case of cancer recurrences.

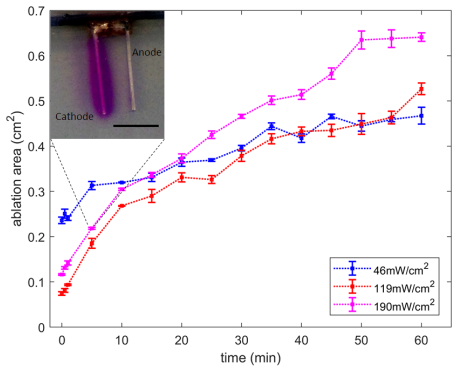

Figure 5: The time-dependent increase in the ablation area of the cathode when supplied with 46mW/cm^2 (blue), 119mW/cm^2 (red) and 190mW/cm^2 (magenta). The insert shows a sample image highlighting the cathode at 5 min time point when the IMEA is supplied with 190mW/cm^2. Insert scale bar represents 5mm.

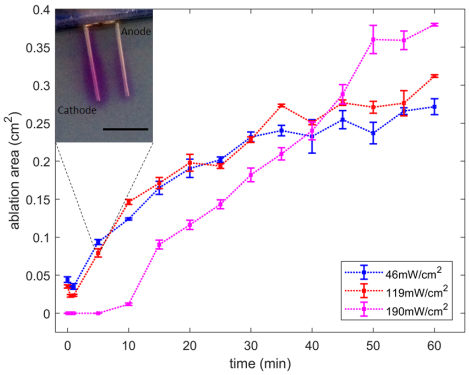

Figure 6: The time-dependent increase in the ablation area of the anode when supplied with 46mW/cm^2 (blue), 119mW/cm^2 (red) and 190mW/cm^2 (magenta). The insert shows a sample image highlighting the anode at 5 min time point when the IMEA is supplied with 119mW/cm^2. Insert scale bar represents 5mm.

REFERENCES

[1] D'Onofrio, M., Ciaravino, V., De Robertis, R., Barbi, E., Salvia, R., Girelli, R., Paiella, S., Gasparini, C., Cardobi, N. and Bassi, C., "Percutaneous ablation of pancreatic cancer", World journal of gastroenterology, 22, 44 (1992), pp. 9661.

[2] Hadjicostas, P., Malakounides, N., Varianos, C., Kitiris, E., Lerni, F. and Symeonides, P., "Radiofrequency ablation in pancreatic cancer", HPB, 8, 1 (2006), pp. 61-64.

[3] Stehling, M.K., Guenther, E., Mikus, P., Klein, N., Rubinsky, L. and Rubinsky, B., "Synergistic combination of electrolysis and electroporation for tissue ablation", PLOS One, 11, 2 (2016), pp. e0148317.

[4] Phillips, M., Krishnan, H., Raju, N. and Rubinsky, B., "Tissue ablation by a synergistic combination of electroporation and electrolysis delivered by a single pulse", Annals of biomedical engineering, 44, 10 (2016), pp. 3144-3154.

[5] Lugnani, F., Macchioro, M. and Rubinsky, B., "Cryoelectrolysis—electrolytic processes in a frozen physiological saline medium", PeerJ, 5 (2017), p. e2810.

ACKNOWLEDGEMENTS

We thank Dr. Iyad Obeid for his support and valuable insights.

CONTACT

*Prof. Albert Kim, albertkim@temple.edu

A RADIO FREQUENCY NON-RECIPROCAL NETWORK BASED ON SWITCHED LOW-LOSS ACOUSTIC DELAY LINES

Ruochen Lu, Tomas Manzaneque, Yansong Yang, Anming Gao, Liuqing Gao and Songbin Gong
University of Illinois at Urbana-Champaign, USA

ABSTRACT

This work demonstrates the first non-reciprocal network based on switched low-loss acoustic delay lines. A 21 dB non-reciprocal contrast between insertion loss (IL=6.6 dB) and isolation (25.4 dB) has been achieved over a fractional bandwidth of 8.8% at a center frequency 155MHz, using a record low switching frequency of 877.22 kHz. The 4-port circulator is built upon a newly reported framework by the authors [1], but using two in-house fabricated low-loss, wide-band lithium niobate ($LiNbO_3$) delay lines with single-phase unidirectional transducers (SPUDT) and commercial available switches. Such a system can potentially lead to future wide-band, low-loss chip-scale nonreciprocal RF systems with unprecedented programmability [1].

INTRODUCTION

Microwave frequency non-reciprocal networks, e.g. circulators and isolators, have been investigated for full-duplexing radios [2]. Non-reciprocity is conventionally achieved by Faraday effect in ferrite materials [3]. Recently, magnet-free non-reciprocal systems based on modulation of reactance or conductance have been demonstrated [4]–[7]. Despite their promising performance, these demonstrations require either a physically large structure for long delays or a high-frequency modulation signals due to the fast phase velocity of electromagnetic waves. Moreover, the bandwidth of non-reciprocity is limited by the modulation frequency and required phase matching condition. To overcome their limitations, we harness shear horizontal acoustic waves in a $LiNbO_3$ thin film to produce long delays (280 ns) with sub-4 dB IL over 1-mm size [8], [9]. Combining with our frequency-independent framework, this work has achieved wideband non-reciprocity employing unprecedentedly low temporal effort (e.g. frequency and modulation depth).

DESIGN AND SIMULATION

The schematic of the 4-port non-reciprocal system [Fig. 1(a)] consists of two delay lines and four single pole single throw switches. The switches are controlled by four control signals [Fig. 1(b)], with a period (4δ) that is four times the delay line's group delay. Control signals on opposite sides of the delay lines are offset by δ. In operation, the signals flowing into Port 1 are time-multiplexed onto the two delay lines and subsequently de-multiplexed to Port 2 by turning on the switches connected to Port 2 δ time after the signals launched from Port 1. The time-reversal symmetry is broken through sequentially timing the switching from one side of the delay lines to the other side. Consequently, signals fed to Port 2 are rejected by Port 1's closed switches and received by Port 3. The assembled circulator performance is simulated [Fig. 5(b)] with the control signal frequency set to 877.2 kHz to match the group delay. An IL of 5.6 dB and an isolation of 30 dB is obtained.

MEASUREMENT AND RESULTS

Experimentally, we implemented two standalone switch boards and one delay line board, and assembled them as the circulator seen in Fig. 1(c). The switch board design schematic and the constructed board are shown in Fig. 2. On the delay line board, a pair of in-house fabricated SPUDT [10]–[12] $LiNbO_3$ acoustic delay lines [Fig. 3(a)-(c)], were wirebonded to LC matching networks [Fig. 3(d)-(e)].

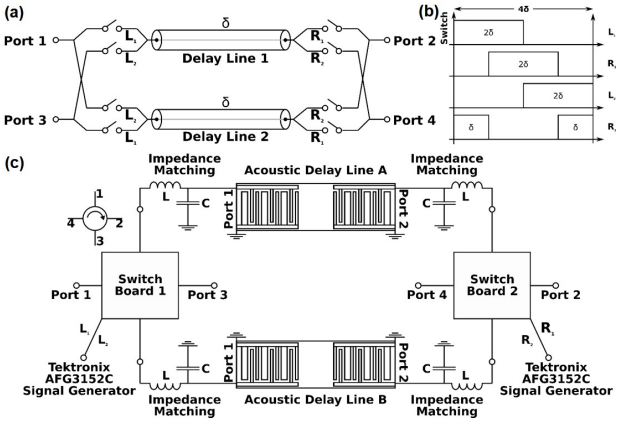

Figure 1: (a) Schematic of 4-port circulator based on switched delay lines. (b) Switch control waveforms applied to the network for producing nonreciprocal response. (c) Block diagram of the constructed 4-port circulator, including switching modules, impedance matching networks, and unidirectional acoustic delay lines.

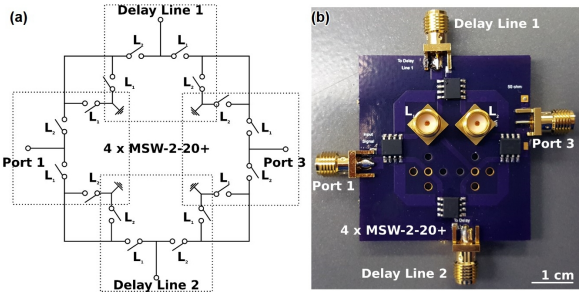

Figure 2: (a) Schematic of the switching module with labeled components and interfaces. (b) Implemented switching module.

Measured and simulated S-parameters and group delays of the delay line board are shown in Fig. 4. 4 dB IL and around 280 ns group delay are measured. As shown in Fig. 6, the measured S-parameters exhibit great performance symmetry between ports, a minimum insertion loss around 6.6 dB, and an isolation larger than 27 dB over a bandwidth of 13.6 MHz (8.7% FBW). Currently, the loss is limited by impedance matching networks and insufficient directionality in the SPUDT design, which will be significantly reduced by further optimization on acoustic delay lines. The spectral contents of different ports are measured when port 1 is excited by a single tone (Fig. 7). The intra-modulated tones are caused by the non-ideal switching and multi-reflection on the delay lines exist in the spectrum, which can be potentially diminished using a differential structure [13] in future work.

CONCLUSION

We presented the first non-reciprocal network based on switched acoustic delay lines. A 4-port circulator is then designed and implemented with two switch modules and the delay line module. The designs and the performance of different modules were

978-1-940470-03-0/HH2018/$25©2018TRF
DOI 10.31438/trf.hh2018.30

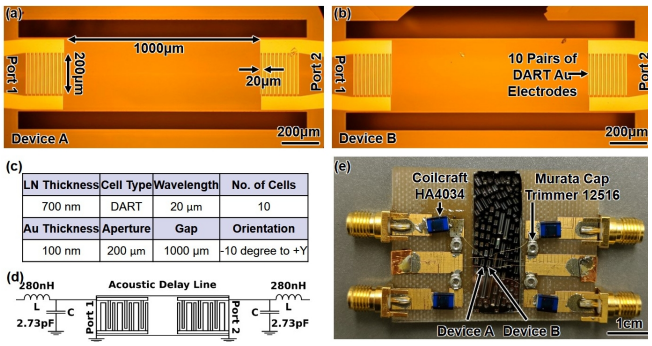

LN Thickness	Cell Type	Wavelength	No. of Cells
700 nm	DART	20 μm	10
Au Thickness	**Aperture**	**Gap**	**Orientation**
100 nm	200 μm	1000 μm	-10 degree to +Y

Figure 3: (a)-(b) Fabricated acoustic delay lines with single-phase unidirectional transducers (SPUDT). A pair of distributed acoustic reflection transducers (DART) are arranged on both end of the suspended $LiNbO_3$ thin film. Design parameters are listed in (c). For lowering the insertion loss of the delay lines, inductor-capacitor (LC) circuits are used to match the impedance to 50 Ω, as seen in (d). (e) delay lines assembled with matching networks on a FR-4 board.

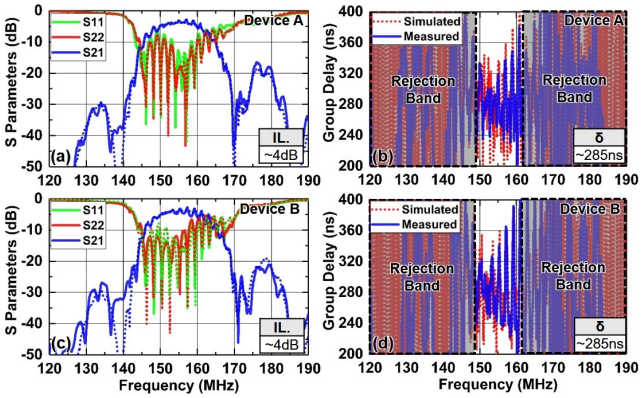

Figure 4: Measured (solid) and simulated (dashed) S-parameters and group delay of the matched (a)-(b) delay line A and (c)-(d) delay line B. An insertion loss around 4 dB and a group delay of 280 ns are measured. In the simulation, acoustic delay lines are represented by their measured S-parameter performance.

individually analyzed, measured, and shown, before the circulator was assembled. The measurement shows a highly symmetric performance across the 4-ports with 18.8 dB non-reciprocal contrast between the IL (6.6 dB) and isolation (25.4 dB) over a FBW of 8.8% at a center frequency 155 MHz, all of which are accomplish with a record low switching frequency of 877.22 kHz. The system also shows 25.9 dB difference between the carrier and the intra-modulated tones. With the employment of faster switches, further optimizations on delay lines and synchronization, such circulators can potentially outperform ferrite-based devices in loss, bandwidth, and isolation while offering a more compact size and reconfigurable operation.

ACKNOWLEDGEMENT

The authors would like to thank DARPA MTO NZERO and SPAR programs for funding support and Dr. Troy Olsson for helpful discussions.

REFERENCES

[1] R. Lu, J. Krol, L. Gao, and S. Gong, "Frequency Independent Framework for Synthesis of Programmable Non-reciprocal Networks," *eprint arXiv:1801.01548*, Jan. 2018.

[2] J. Zhou, T.-H. Chuang, T. Dinc, and H. Krishnaswamy, "Integrated wideband self-interference cancellation in the RF

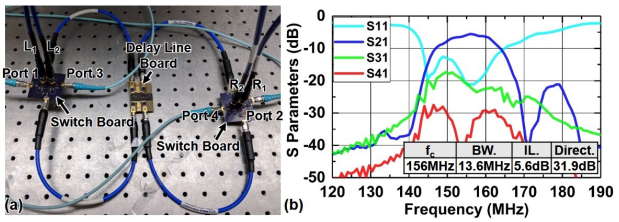

Figure 5: (a) Experiment setup of 4-port circulator, consisting of 2 switch boards and 1 delay line board. Interfaces are labeled on the figure. (b) Simulated S-parameters obtained from Advanced Design System. In the simulation, 2 ns switching time and on-state insertion loss of the switches are considered. ***Control signals are set to be 877.2 kHz*** *(1.14 μs period).*

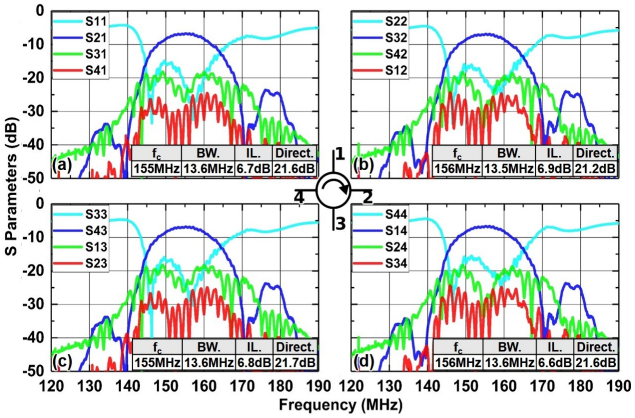

Figure 6: Measured S-parameter performance of the 4-port circulator. Great performance symmetry is shown in the measurement. Minimum insertion loss (IL) around 6.7 dB is measured at different ports. A bandwidth of 13.6 MHz (8.7% fractional bandwidth) is obtained. Directivity larger than 21 dB is obtained between the forward and backward propagation path (e.g. between S_{12} and S_{21}). Return loss is better than 15 dB at each port. Control signals are set to be 877.2 kHz (1.14 μs period).

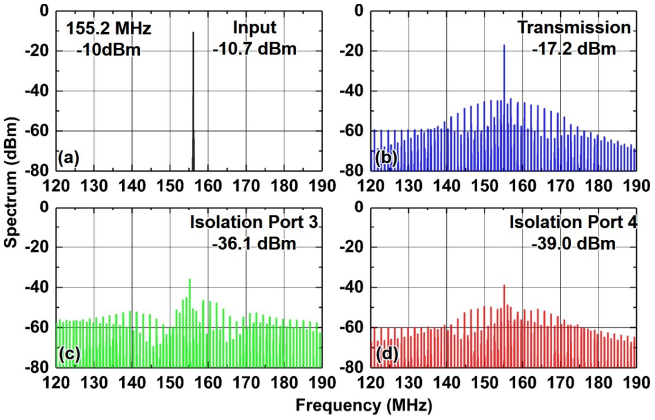

Figure 7: Measured spectral content of (a) input signal, (b) transmitted signal at port 2, showing 6.5 dB insertion loss, (c) transmitted signal at port 3, indicating 25.4 dB isolation at port 3, and (d) transmitted signal at port 4, indicating 28.3 dB isolation at port 4. The intermodulation is caused by the non-ideal switching and multi-reflections in the spectrum.

domain for FDD and full-duplex wireless," *IEEE J. Solid-State Circuits*, vol. 50, no. 12, pp. 3015–3031, 2015.
[3] T. Wada, R. Nakjima, H. Obiya, T. Ogami, M. Koshino, M. Kawashima, and N. Nakjima, "A miniaturized broadband lumped element circulator for reconfigurable front-end system," in *Microwave Symposium (IMS), 2014 IEEE MTT-S International,* 2014, pp. 1–3.
[4] N. A. Estep, D. L. Sounas, and A. Alù, "Magnetless microwave circulators based on spatiotemporally modulated rings of coupled resonators," *IEEE Trans. Microw. Theory Tech.*, vol. 64, no. 2, pp. 502–518, 2016.
[5] N. Reiskarimian and H. Krishnaswamy, "Magnetic-free non-reciprocity based on staggered commutation," *Nat. Commun.*, vol. 7, 2016.
[6] J. Krol and S. Gong, "A non-magnetic gyrator utilizing switched delay lines," in *2017 47th European Microwave Conference (EuMC)*, 2017, pp. 452–455.
[7] M. M. Biedka, R. Zhu, Q. M. Xu, and Y. E. Wang, "Ultra-wide band non-reciprocity through sequentially-switched delay lines," *Sci. Rep.*, vol. 7, p. 40014, 2017.
[8] T. Manzaneque, R. Lu, Y. Yang, and S. Gong, "An SH0 Lithium Niobate dispersive delay line for chirp compression-enabled low power radios," in *Proceedings of the IEEE International Conference on Micro Electro Mechanical Systems (MEMS)*, 2017.
[9] T. Manzaneque, R. Lu, Y. Yang, and S. Gong, "Lithium Niobate MEMS Chirp Compressors for Near Zero Power Wake-Up Radios," *Journal of Microelectromechanical Systems*, pp. 1204–1215, 2017.
[10] J. M. Hodé, J. Desbois, P. Difilie, M. Solal, and P. Ventura, "SPUDT-based filters: Design principles and optimization," in *Ultrasonics Symposium, 1995. Proceedings., 1995 IEEE*, 1995, vol. 1, pp. 39–50.
[11] T. Manzaneque, R. Lu, Y. Yang, and S. Gong, "Low-Loss and Wide-Band Acoustic Delay Lines," *IEEE Trans. Microw. Theory Tech.*, vol. under revi.
[12] T. Manzaneque, R. Lu, Y. Yang, and S. Gong, "Realizing Radio Frequency Acoustic Delays and Transversal Filtering with Sub-2 dB Insertion Loss and 10% Fractional Bandwidth," in *Proceedings of the 2018 Solid-State Sensors, Actuators and Microsystems Workshop (Hilton Head 2018)*, 2018.
[13] A. Kord, D. L. Sounas, and A. Alù, "Differential magnetless circulator using modulated bandstop filters," in *Microwave Symposium (IMS), 2017 IEEE MTT-S International*, 2017, pp. 384–387.

CONTACT

R. Lu, rlu10@illinois.edu

PMUT-BASED HIGH DATA RATE ULTRASONIC WIRELESS COMMUNICATION LINK FOR INTRA-BODY NETWORKS

Bernard Herrera[1], *Emrecan Demirors*[1], *Guofeng Chen*[1], *Raffaele Guida*[1], *Flavius Pop*[1], *Neil Dave*[1], *Cristian Cassella*[1], *Tommaso Melodia*[1], *and Matteo Rinaldi*[1]
[1]Northeastern University, Boston, MA

ABSTRACT

This paper reports on the first demonstration of a high data rate (0.6 Mbit/s) ultrasonic wireless communication link implemented through Aluminum Nitride (AlN) Piezoelectric Micro Machined Ultrasonic Transducers (PMUTs). Real-time video streaming is demonstrated through a phantom mimicking human tissue, thus proving the feasibility of PMUT-based implantable Body Area Networks (BANs). Two 20×20 PMUT arrays were used as transceiver elements and an Orthogonal-Frequency-Division-Multiplexing (OFDM) modulation scheme was implemented resulting in a wideband digital transmission link with a data rate of up to 0.6 Mbit/s at a 5 cm distance between transmitter and receiver. Channel estimation and Bit-Error-Rate (BER) versus Signal-to-Noise-Ratio (SNR) curves were obtained for both the PMUT link and an implementation based on custom-made and miniaturized ultrasonic bulk Lead Zirconate Titanate (PZT) transducers for comparison. The PMUT implementation, characterized by a wider bandwidth than the PZT transducers, showed two orders of magnitude lower BER for the same SNR as compared to its PZT counterpart, while occupying an approximately 100 times smaller volume ($\sim 3\,\text{mm} \times 3\,\text{mm} \times 0.5\,\text{mm}$ PMUT array vs. 9.5 mm diameter, 6 mm thick PZT transducer).

INTRODUCTION

The use of PMUTs in applications such as ultrasound imaging [1], fingerprint scanning [2] and three-dimensional gesture recognition [3] has been widely investigated. Furthermore, several studies focusing on the optimization of specific device performance metrics (such as output pressure or bandwidth) have been reported [4]. However, the application of the PMUT technology for communication purposes remains largely unexplored.

As an example, a high data rate intra-body communication network has potential applications in high resolution wireless endoscopy [5], imaging or biosignal telemetry, continuous ambulatory monitoring of chronic patients, and early disease detection.

The great potential of ultrasonic wireless communication for intra-body networks has been recently demonstrated [6]. Even though a great degree of miniaturization and power consumption optimization was achieved, the implementation is based on Lead Zirconate Titanate (PZT) ultrasonic transducers that remain relatively bulky and are a not fully biocompatible. In fact, the presence of lead in the composition can be toxic for human tissues, particularly in long-term use.

In this article, an ultrasonic transceiver based on miniaturized arrays of AlN PMUTs is demonstrated for the first time, attempting to address these fundamental challenges currently hindering the full deployment of implantable ultrasonic wireless communication devices. AlN is a much more inert material for the intra-body chemistry, which would allow for implants immune to degradation and toxic effects in the long term operation required. Another dramatically enabling feature is that, as the PMUT transducers are built on silicon technology, a single chip implementation of the transducer array and Application-Specific Integrated Circuits (ASICs) can be envisioned, allowing for drastic miniaturization and power consumption reduction.

Therefore, the achievement of a PMUT-based intra-body communication link perfectly fits the development of an implantable, integrated system offering communication, energy harvesting and sensing capabilities [6]. The use of arrays of PMUTs in an ultrasonic transceiver is also attractive because it enables the implementation of functionalities such as focusing and beamforming that are not attainable with the conventional single-element transducers.

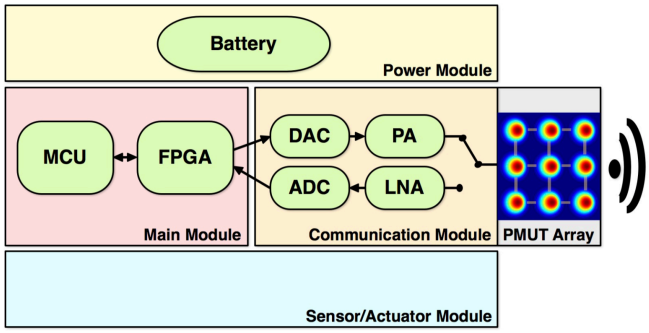

Figure 1: System-wide overview of the application of the PMUT array within an ultrasonic intra-body transceiver.

FABRICATION

The AlN PMUTs were fabricated on a silicon wafer using a 4 masks microfabrication process. A double-side polished, 300 μm silicon wafer was used as a substrate. An 850 nm silicon dioxide layer was then deposited through Plasma Enhanced Chemical Vapor Deposition (PECVD). A 5nm Pt / 95nm Ti bottom electrode was then formed by electron beam evaporation and patterned through a photo lithography and liftoff process. 800nm of the piezoelectric AlN were then reactively sputtered and vias were etched through the layer for access to the bottom electrode by hot phosphoric acid etching. The material stack was completed with a sputtered 5nm Ti / 50nm Au top electrode. Back-side alignment photolithography and Deep Reactive Ion Etching (DRIE) were finally used to etch cavities and release the device membrane (fig. 2).

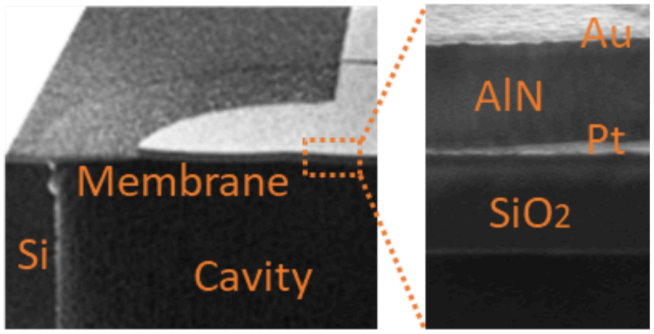

Figure 2: Cross-section SEM images of PMUT element. Left: Overview of the structure: substrate, cavity and membrane. Right: Material stack detail.

978-1-940470-03-0/HH2018/$25©2018TRF
DOI 10.31438/trf.hh2018.31

DEVICE CHARACTERIZATION

A Digital Holographic Microscope (DHM) was used to characterize the membrane displacement as function of the frequency of the input driving signal. The apparatus is based on laser interferometry; the phase difference information between two perpendicular laser paths, one of which reflects on the sample, is directly related to the displacement of the sample. The measurements were taken for both in-air and water immersed operation by calibrating the length of the laser path.

Operation in air yields a very narrow resonant peak and a higher center frequency. On the other hand, a much wider bandwidth was measured when the PMUTs were operated in water (mimicking conditions of intra-body tissue, Fig. 3), indicating a good coupling to the medium.

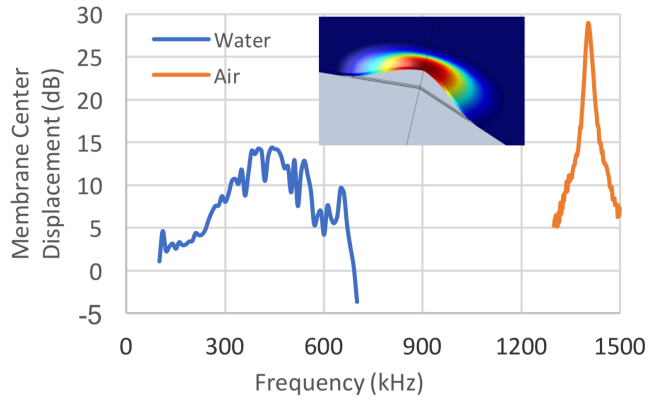

Figure 3: DHM membrane center displacement frequency response measurements of first mode of vibration in air and in water. Inset: Comsol Multiphysics Finite Element Modeling 3D simulation of PMUT membrane displacement.

COMMUNICATION SYSTEM ARCHITECTURE

The frequency response of the PMUT arrays presented a large operating bandwidth that makes them suitable for high data rate ultrasonic intra-body communications. To that end, a generic ultrasonic intra-body communication architecture, showcased in Fig. 1, is interfaced with a PMUT array. The system architecture consists of four modules. The main module includes a processor (e.g., microcontroller (MCU)) and an FPGA that implement the physical layer and data link layer of the communication protocol stack. The communication module manages the digital-to-analog conversion (DAC) and pre-amplification of the transmitted signals, and the amplification and analog-to-digital conversion (ADC) of the received data. The system is energized through the powering module including an energy storage, e.g. a battery, and can have a sensor/actuator module to interact with the human body.

The main module of the system leverages a custom zero-padded OFDM (ZP-OFDM) transmission scheme. OFDM is a digital multi-carrier transmission scheme, which has been used extensively in underwater acoustic (UW-A) communications [7, 8, 9, 10] as it shows robustness against frequency-selective channels with long delay spreads. Given the fact that the human body is composed (up to 65%) of water, intra-body acoustic channels show similar characteristics to UW-A channels. Therefore, OFDM stands out as a favorable transmission scheme for establishing robust high data rate communication links. In the system, to achieve energy efficiency, a zero-padding scheme is chosen over cyclic prefixing (CP), where each OFDM symbol is trailed by padded zeros. Specifically, each transmission packet is formed by N ZP-OFDM symbols preceded by a preamble packet based on a pseudo-random noise (PN) sequence, which is used for packet detection and coarse time synchronization. Each ZP-OFDM symbol has K subcarriers. Each subcarrier is designated as a data, pilot, or null subcarrier. Data subcarriers carry modulated information bits with different gray-coded modulation schemes (i.e. Binary-Phase-Shift-Keying (BPSK) and Quadrature-Phase-Shift-Keying (QPSK)). Pilot subcarriers are allocated to pilot symbols that are leveraged to perform channel estimation and symbol-level (fine) synchronization, while null subcarriers are used for Doppler scale estimation.

EXPERIMENTAL EVALUATION

In this section, practical implementation and performance evaluation of the aforementioned communication system model are reported.

Setup

The experimental setup consists of two ultrasonic nodes featuring the system architecture as explained in the previous section. Particularly, the ultrasonic nodes are implemented adopting USRP N210, a commercially available software-defined radio (SDR) platform based on Field Programmable Gate Arrays (FPGAs) [11, 12]. At the transmitter side, a COTS power amplifier (PA), Mini-Circuits LZY $-$ 22+ with the capability of providing a gain of 43 dB for the operating frequency of 0.1 $-$ 200 MHz, is used to amplify the 2 mW output power of the USRP. At the receiver side, a COTS voltage preamplifier (PreA), Teledyne RESON VP2000, which provides low-noise performance, is leveraged to amplify the received signal before feeding into the USRP.

Both transmitter and receiver chains are connected to 20 $\times$ 20 PMUT arrays (which were wire-bonded to printed circuit boards (PCBs) for electrical connection and for making the structure more mechanically robust) for achieving two-way conversion between electrical and ultrasonic energy. To emulate the intra-body ultrasonic channel characteristics, excepting reflections on hard elements such as bones or organs, a tissue phantom is used where PMUT arrays make contact to its surface on each side as illustrated in the Fig. 6. A coupling gel is used at the interface of the transducers and the phantom to ensure good contact and to minimize the acoustic impedance mismatch due to different materials. A demonstration video showcasing the experimental setup and real-time video steaming experiment is available at [13].

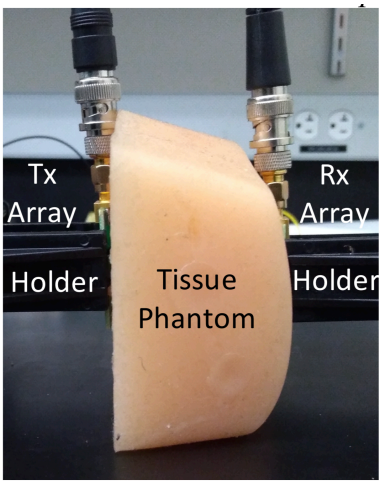

Figure 4: Experimental setup.

Results

In this section, results from two sets of experiments are presented. The experiments are mainly concentrated on comparing the PMUTs with miniaturized ultrasonic bulk Lead Zirconate Titanate (PZT) transducers in terms of bandwidth and data rate capabilities.

In the first set of experiments, a channel estimation for both the PMUT-PMUT link and the PZT-PZT link is performed to characterize the frequency response of the communication link. Fig. 5 shows the obtained curves where the PZT response is centered around the resonant frequency with a much narrower bandwidth compared to the PMUT, which has a larger normalized amplitude over a broader spectrum. This result proves that PMUTs offer more spectrum resources compared PZTs, which could eventually lead to larger data rates.

In the second set of experiments, a ZP-OFDM scheme with a bandwidth of $B = 500$ kHz is realized to quantitatively characterize and compare the data transmission capabilities of both PMUTs and PZTs. Fig. 6 shows the BER performance of PMUTs and PZTs versus SNR for different modulation schemes (i.e. BPSK and QPSK). Both PMUTs and PZTs achieved data rates of 298 kbit/s and 596 kbit/s for BPSK and QPSK, respectively. While data rates are same, for both modulation schemes, PMUTs outperform PZTs in terms of BER performance. Given that the same transmission bandwidth is used in both devices, this result proves the fact that PMUTs offering a more flat frequency response even in the non-resonating region could enable more spectrum resources and accordingly better performance.

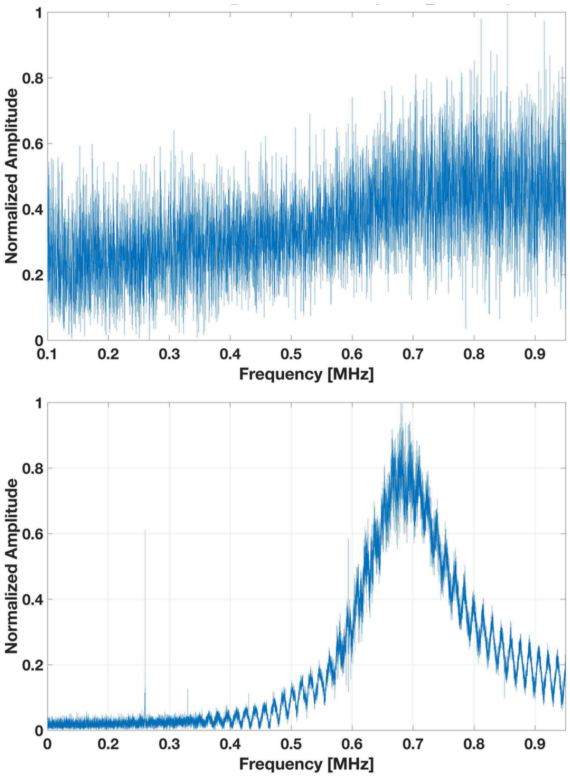

Figure 5: Channel estimation. Top: PMUT link; relatively small normalized amplitude response over frequency. Bottom: PZT transducer; narrow band around center frequency. Normalized amplitude vs frequency (0.1-1MHz).

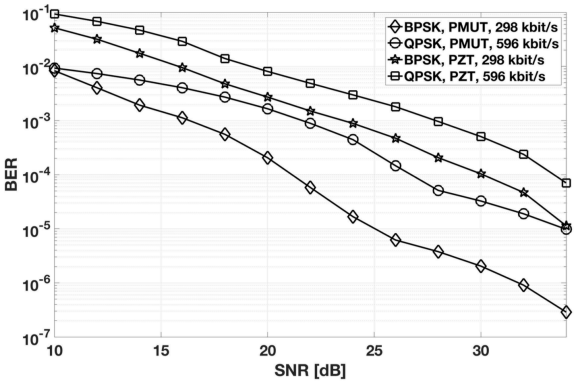

Figure 6: BER vs. SNR curves for Binary Phase shift keying (BPSK) and Quadrature Phase Shift Keying (QPSK) digital modulation schemes. 500 kHz bandwidth. Center frequency: 700 kHz *for PZT and* 600 kHz *for PMUT.*

CONCLUSIONS

The present article demonstrated the feasibility of high data rate ultrasonic communications for intra-body networks by leveraging PMUTs. Specifically, it showcased successful real-time video streaming through a 5 cm thick tissue phantom by using 20×20 PMUT arrays both for transmission and reception.

In addition, this article presented a quantitative comparison between PZTs and PMUTs. Particularly, frequency responses of both the PMUT-PMUT link and the PZT-PZT link were measured and proved that PMUTs can offer more spectrum resources compared to PZTs. Moreover, a ZP-OFDM scheme with a bandwidth of $B = 500$ kHz was tested on both the PMUT and PZT links to quantitatively characterize their data transmission capabilities. It was proved that PMUTs have better BER performance for both BPSK and QPSK modulation schemes compared to PZTs. The maximum achieved data rate with PMUTs was 0.6 Mbit/s with BER of 2×10^{-6}, which can pave the way to realize novel intra-body applications requiring high data rates.

REFERENCES

[1] Y. Lu, A. Heidari, and D. A. Horsley, "A high fill-factor annular array of high frequency piezoelectric micromachined ultrasonic transducers," *Journal of Microelectromechanical Systems*, vol. 24, no. 4, pp. 904–913, 2015.

[2] Y. Lu, H. Tang, S. Fung, Q. Wang, J. M. Tsai, M. Daneman, B. E. Boser, and D. A. Horsley, "Ultrasonic fingerprint sensor using a piezoelectric micromachined ultrasonic transducer array integrated with complementary metal oxide semiconductor electronics," *Applied Physics Letters*, vol. 106, no. 26, p. 263503, 2015.

[3] R. J. Przybyla, H. Y. Tang, A. Guedes, S. E. Shelton, D. A. Horsley, and B. E. Boser, "3d ultrasonic rangefinder on a chip," *IEEE Journal of Solid-State Circuits*, vol. 50, no. 1, pp. 320–334, 2015.

[4] Y. Lu, O. Rozen, H.-Y. Tang, G. L. Smith, S. Fung, B. E. Boser, R. G. Polcawich, and D. A. Horsley, "Broadband piezoelectric micromachined ultrasonic transducers based on dual resonance modes," in *Micro Electro Mechanical Systems (MEMS), 2015 28th IEEE International Conference on*, pp. 146–149, IEEE, 2015.

[5] A. Koulaouzidis, D. K. Iakovidis, A. Karargyris, and E. Rondonotti, "Wireless endoscopy in 2020: Will it still be a capsule?," *World journal of gastroenterology: WJG*, vol. 21, no. 17, p. 5119, 2015.

[6] G. E. Santagati and T. Melodia, "Experimental evaluation of impulsive ultrasonic intra-body communications for implantable biomedical devices," *IEEE Transactions on Mobile Computing*, vol. 16, no. 2, pp. 367–380, 2017.

[7] S. Zhou and Z.-H. Wang, *OFDM for Underwater Acoustic Communications*. John Wiley and Sons, Inc., 2014.

[8] A. Radosevic, R. Ahmed, T. Duman, J. Proakis, and M. Stojanovic, "Adaptive OFDM modulation for underwater acoustic communications: Design considerations and experimental results," *IEEE Journal of Oceanic Engineering*, vol. 39, pp. 357–370, April 2014.

[9] E. Demirors, J. Shi, R. Guida and T. Melodia, "SEANet G2: A Toward a High-Data-Rate Software-Defined Underwater Acoustic Networking Platform," in *Proc. of ACM Intl. Conf. on Underwater Networks & Systems (WUWNet)*, (Shanghai, China), October 2016.

[10] E. Demirors, G. Sklivanitis, G. E. Santagati, T. Melodia, and S. N. Batalama, "A high-rate software-defined underwater acoustic modem with real-time adaptation capabilities," *IEEE Access*, vol. PP, no. 99, pp. 1–1, 2018.

[11] E. Demirors, G. Sklivanitis, T. Melodia, S. N. Batalama, and D. A. Pados, "Software-defined underwater acoustic networks: toward a high-rate real-time reconfigurable modem," *IEEE Communications Magazine*, vol. 53, pp. 64–71, November 2015.

[12] E. Demirors, G. Alba, G. E. Santagati, and T. Melodia, "High Data Rate Ultrasonic Communications for Wireless Intra-Body Networks," in *Proc. of IEEE Symposium on Local and Metropolitan Area Networks (LANMAN)*, (Rome, Italy), June 2016.

[13] E. Demirors, R. Guida, and B. Herrera, "PMUT communications." `http://www.ece.neu.edu/wineslab/pmut_video.php`.

ELECTRIC-FIELD INDUCED INCREASE IN PARACELLULAR VASCULAR PERMEABILITY

Kaushik K. Rangharajan[1], Prashanth Mohanasundaram[1], Jennifer Morris,[1] Ehsan Akbari[1], Griffin B. Spychalski[1], Jonathan W. Song[1,], and Shaurya Prakash[1,*]*
[1]The Ohio State University, Columbus, Ohio, USA

ABSTRACT

We report a state-of-the-art microfluidic model of a branching blood vessel to study the role of simultaneous fluidic and electrical stimuli in regulating endothelial permeability. Previous efforts to modulate endothelial permeability were concentrated on the role of chemical factors and/or local fluidic forces as opposed to electric field inside *in vitro* systems. In this study, we report that addition of electric fields (e-field) over pre-existing flow (1 µl/min) increases the endothelial permeability by ~10 times in comparison to no flow/no e-field control, accompanied by morphological changes to the endothelial cytoskeleton and ultrastructure.

INTRODUCTION

Tissue homeostasis is maintained by transport of oxygen, nutrients, and removal of waste across the body through a network of blood vessels. Endothelial cells (ECs) lining the inside of blood vessels in vascular networks form a semi-permeable barrier, selectively allowing bidirectional transport of small molecules, ions, and fluid transfer between blood and interstitial tissues to regulate angiogenesis, muscle tone, and host-defense reactions – processes essential to outcomes in cancer, wound healing, and cardiovascular pathologies. Loss of endothelial barrier functions, resulting in elevated vessel permeability, is specifically expressed during chronic inflammation, cancer, wound healing, and atherosclerosis [1].

Increased endothelial permeability is also demonstrated in venules and is naturally accompanied by angiogenesis [2]. Angiogenesis is a physiological process characterized by growth of blood vessels from existing vasculature and is critical to wound healing, fetal development, and organ regeneration [3-5]. However, excessive vessel growth is indicative of inflammatory disorders (elevated vessel permeability state), cancer, and eye diseases [6].

From a biophysical standpoint, ECs are continuously exposed to shear stress in a direction tangential to the surface due to blood flow, with a physiological magnitude in the range of 0.7 – 130 dynes/cm^2 [5]. Presence of fluid shear is associated with reduced vessel permeability [7] resulting from actin cytoskeleton re-organization [8]. In contrast, transvascular transport *i.e.*, the flow between two endothelial junction gaps or clefts, is concomitant of elevated vessel permeability [5]. Expansion of vascular networks by angiogenesis was previously shown to be regulated by local fluid mechanics in a shear dependent manner [9, 10]. Notably, microfluidic models that study angiogenesis do not consider branching morphology, and hence the biomechanical effects occurring at vessel bifurcations due to flow stagnation remains uninvestigated.

Similarly, the role of electric stimuli in regulating endothelial paracellular permeability and the resulting changes to cellular and junction morphology remains minimally investigated. Endogenous e-fields exist *in vivo* and arise as a consequence of (**a**) ion and molecule transfer, leading to charge separation from cell to cell *via* gap junctions [11] and (**b**) selective ion transport through ion pumps and channels driving charge segregation [12]. Such endogenous e-fields also exist around vasculature, with a measured zeta potential at the surface of the EC in the 0.1 – 0.4 V range for both the aorta and vena cava [13]. Regulation of endogenous e-fields play a vital role in embryonic growth, where major morphological development events are preceded by specific e-field patterns [14, 15]. Similarly, disruption of epithelial barrier during wound initiation enhances trans-epithelial potential difference, initiating directional migration of cells to facilitate wound healing [16]. Exogenously applied DC e-fields (75 – 100 mV/mm) have shown that human umbilical vein endothelial cell (HUVECs) re-orient, and stimulate VEGF production which are indicative of pre-angiogenic response [17].

The purpose of this paper is to report the morphological alterations to ECs accompanying changes to endothelial permeability when subjected to simultaneous mechanical and electrical stimuli of physiologically relevant magnitude.

METHODS

Microfluidic Cell Culture

SU-8 mold of a branching vessel geometry was embedded on a silicon wafer using optical lithography techniques. Microfluidic channels are 50 µm deep and consist of an inlet vessel 1300 µm wide that bifurcates from a bifurcation point (BP) into two distinct branching vessel (BVA), each with a width of 500 µm (Fig. 1A). The two branching vessels are separated by an extra-cellular matrix (ECM), with targeted aperture windows that facilitate an interface between the ECs and ECM, allowing for transvascular transport from the apical (BP, BVA) side to the Basal (collagen) side [18].

Cured PDMS, present over the silicon mold, was peeled, diced into distinct devices, and bonded *via* plasma bonding to glass. The devices were incubated inside an oven overnight and UV sterilized prior to collagen injection. Type-1 rat tail collagen was prepared and injected into the central collagen channel (Fig. 1A), where the apertures restrict collagen outflow/spill due to capillary forces [18]. The devices were incubated inside an oven at 37°C overnight to complete collagen polymerization.

After polymerization of collagen, the devices were seeded (Fig. 1B) with HUVECs, incubated at 37°C for 24 h to facilitate homogenous endothelial monolayer development (Fig. 1C).

Simultaneous Perfusion and Electric Field Stimulation

Potential difference was applied using gold (Au) electrodes between the inlet ports, and the collagen (ground), outlet ports (ground) to induce a constant DC e-fields of magnitude 70 mV/mm. 3 ml BD-syringes (Fisher Scientific) were mounted on a Harvard apparatus syringe pump and connected to the outlet tubing to perfuse the device at a constant flow rate.

Estimation of Endothelial Permeability

After treating the endothelial monolayer with mechanical and/or electrical stimuli inside the microfluidic devices, changes to endothelial permeability were measured by monitoring extravasation rate of 10 µM FITC (Fluorescein isothiocyanate) conjugated Dextran dye from BP and BVA into the ECM under an elevated pressure head, mirroring physiological hyper-tension effects. Using Matlab, a custom-written code was written to analyze the time-lapse images to extract paracellular permeability

978-1-940470-03-0/HH2018/$25©2018TRF
DOI 10.31438/trf.hh2018.32

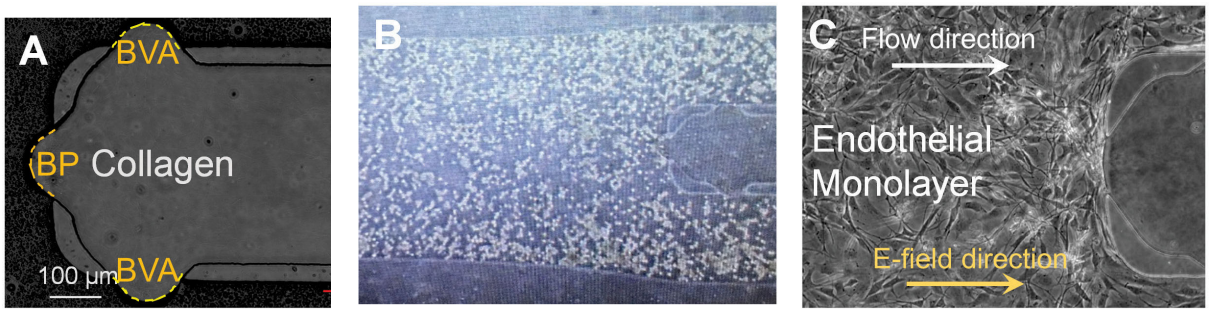

*Figure 1: **(A)** Capillary driven collagen filling inside the microfluidic device, **(B)** Perfusion of endothelial cells inside the device, and **(C)** Formation of endothelial monolayers after 24 h of incubation. White arrows indicate direction of fluid flow, and red arrows indicate direction of electric field.*

[18]. For each case, overall transendothelial transport of 10 kDa FITC-Dextran into the ECM over a period of 1 min was estimated by correlating the enhancement in intensity to enhancement in FITC-dextran concentration. Inside an Eulerian control volume, defined inside the collagen, the rate of enhancement in fluorescent signal was quantified for the tested cases to estimate the transendothelial flowrate and permeability.

Immunofluorescence

Immunofluorescence protocol to stain the endothelial F-actin with Alexa 488-Phalloidin and the nucleus with DAPI for confocal imaging follows from our previous reported protocol [18].

Scanning Electron Microscopy

After experiments, devices were injected thrice with 1X PBS, followed by injection of fixing buffer (2.5% glutaraldehyde in 0.1 M phosphate buffer with 0.1 M sucrose, pH 7.4). The cells were fixed for a duration of 30 mins, following which they were serially dehydrated using ethanol. Briefly, the devices were injected sequentially with 50% (1:1 ethanol: water), 70%, 80%, 90% ethanol, with a total incubation time of 10 mins for each injection. **Note**: After the 90% ethanol injection, no water-based solution should be introduced into the device. Next, three 10 min injections with 100% ethanol were conducted.

After the third ethanol injection, a mixture of HMDS (Hexamethyldisilazane) and ethanol at a volumetric ratio of 1:3, 1:1, and 3:1 were prepared. First, the 1:3 HMDS:ethanol was injected into the device for 15 mins followed by a 15 min injection of the 1:1, and then the 3:1 HMDS:ethanol. Lastly, three 15 min injections with 100% HMDS were conducted, followed which the device was left to air-dry inside a biohood overnight. With a surgical blade, a small incision was made along the periphery of the microfluidic device at the PDMS-glass interface, following which the PDMS was peeled off from the glass, diced into thin sections, sputtered with 15 nm Nickel-Palladium, and mounted for SEM imaging.

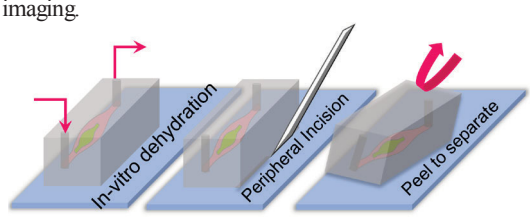

Figure 2: In vitro sample dehydration (increasing dosage from 50% to 100% ethanol, followed by HMDS:ethanol dehydration, 33% - 100% by volume) and detachment methodology of bonded microfluidic device for direct observation of endothelial monolayer via SEM.

RESULTS

Shear Stress and Stagnation Pressure

For a flowrate of 1 µl/min, the shear stress distribution in the branching vessel and at the stagnation point was estimated by multiplying the local shear rate with viscosity of media. The magnitude of shear stress was 0.3 dyn/cm^2 at BVA apertures and negligible at BP (due to flow stagnation). Additionally, the magnitude of stagnation pressure was estimated to be 3.8 dyn/cm^2 at the BP aperture.

Extravasation of Dextran into ECM

After application of simultaneous 1 µl/min flow and 70 mV/mm, the device permeability was estimated next by tracking the intravasation rate of Dextran dye into the collagen. For the same pressure gradient between BVA and collagen, enhanced extravasation of Dextran dye into the ECM compared to the control was observed (without flow or e-field, Fig. 3A), indicative of ~10 fold increase in permeability with application of 70 mV/mm over 1h (Fig. 3B).

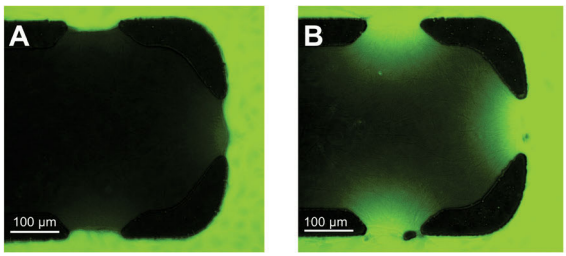

*Figure 3: Intravasation of FITC-tagged Dextran from the Branching vessel and stagnation point into the ECM over a duration of 1 min. **(A)** Compared to the no fluid flow/no electric field control, **(B)** 10 fold enhancement in endothelial permeability was observed under the application of 1 V potential difference with a simultaneous flow of 1 µl/min.*

Cytoskeleton-structure

Changes to endothelial cytoskeleton structure were observed by imaging the F-actin alignment in the presence and absence of e-field. Under the application of 70 mV/mm e-field over a duration of 1 h, the orientation of F-actin filaments was found to align perpendicular to the direction of e-field [17] compared to randomly directed orientation of F-actin filaments in control.

Effective cell-foot print

SEM images revealed a ~3x decrease in effective cell-footprint area (Fig. 4A) with application of 70 mV/mm, compared to the static no flow/no e-field control (Fig. 5A).

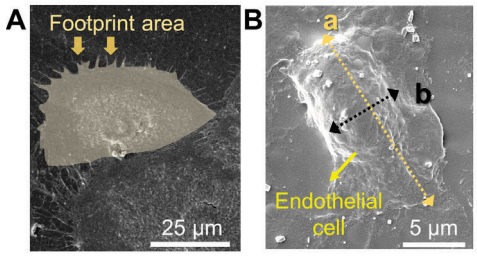

*Figure 4: Representative SEM images of HUVECs of (**A**) control, (**B**) electric field.*

Shape Factor

Quantification of the ratio of short to long axis (*b/a*) of a cell (Fig. 4B) indicated effective circularity increased from 0.46 (control, elliptical) to 0.76 when an e-field of 70 mv/mm was applied (Fig. 5B).

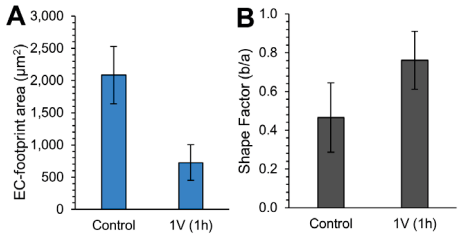

*Figure 5: (**A**) Compared to control (no flow/no e-field), electric stimulation of 70 mV/mm for 1h results in 3x reduction in footprint area. EC footprint area was determined from multiple SEM images. (**B**) Shape factor increases from 0.46 for control (elliptical) to 0.76 (near-spherical) under an e-field of 70 mV/mm (Anova, $F = 18.5$, $p < 0.001$).*

In summary, a novel microfluidic platform to regulate endothelial permeability under simultaneous mechanical and electrical stimuli is reported. Modifications to the endothelial ultrastructure facilitating the changes to permeability were additionally quantified.

ACKNOWLEDGMENTS

This work was supported by The American Heart Association (15SDG25480000), National Institute of Health (NHLBI R01HL141941), and the Center for Emergent Materials, an NSF-MRSEC, grant DMR-1420451, the Center for Exploration of Novel Complex Materials, and the Institute for Materials Research. The authors acknowledge computational support and research license from the Ohio Supercomputer Center (OSC), the OSU Nanotech West cleanroom staff for assistance in fabrication, and the OSU Campus Microscopy and Imaging Facility (CMIF) for assistance with confocal microscopy.

REFERENCES

[1] J.A. Nagy, L. Benjamin, H. Zeng, A.M. Dvorak and H.F. Dvorak, "Vascular permeability, vascular hyperpermeability and angiogenesis", Angiogenesis, 11, 109 (2008).

[2] L. Claesson-Welsh, "Vascular permeability-the essentials", Upsala Journal of Medical Sciences, 120, 135 (2015).

[3] C. Patterson and M.S. Runge, "Therapeutic angiogenesis", Circulation, 99, 2614 (1999).

[4] E.W.K. Young and C.A. Simmons, "Macro- and microscale fluid flow systems for endothelial cell biology", Lab on a Chip, 10, 143 (2010).

[5] W.J. Polacheck, R. Li, S.G.M. Uzel, and R.D. Kamm, "Microfluidic platforms for mechanobiology", Lab on a Chip, 13, 2252 (2013).

[6] J. Folkman "Angiogenesis: an organizing principle for drug discovery?", Nature Reviews Drug Discovery, 6, 273 (2007).

[7] G.M. Price, K.H.K Wong, J.G. Truslow, A.D. Leung, C. Acharya and J. Tien, "Effect of mechanical factors on the function of engineered human blood microvessels in microfluidic collagen gels", Biomaterials, 31, 6182, (2010).

[8] E.A. Osborn, A. Rabodzey, C.F. Dewey and J.H. Hartwig, "Endothelial actin cytoskeleton remodeling during mechanostimulation with fluid shear stress", American Journal of Physiology-Cell Physiology, 290, 444 (2006).

[9] J.W. Song and L.L. Munn, "Fluid forces control endothelial sprouting", Proceedings of the National Academy of Sciences, 108, 15342 (2011).

[10] P.A. Galie, D-H.T. Nguyen, C.K. Choi, D.M. Cohen, P.A. Janmey and C.S. Chen, "Fluid shear stress threshold regulates angiogenic sprouting", Proceedings of the National Academy of Sciences, 111, 7968 (2014).

[11] R.H.W. Funk, "Endogenous electric fields as guiding cue for cell migration", Frontiers in Physiology, 6, 143 (2015).

[12] H. Bai, J.V. Forrester and M. Zhao, "DC electric stimulation upregulates angiogenic factors in endothelial cells through activation of VEGF receptors", Cytokine,110, (2011).

[13] P.N. Sawyer, E. Himmelfar, I. Lustrin and H. Ziskind, "Measurement of streaming potentials of mammalian blood vessels, aorta and vena cava, in Vivo", Biophysical Journalm 6, 641, (1966).

[14] C.D. McCaig, A.M. Rajnicek, B. Song and M. Zhao, "Controlling cell behavior electrically: Current views and future potential", Physiological Reviews, 85,943, (2005).

[15] M. Levin, "Endogenous bioelectrical networks store non-genetic patterning information during development and regeneration", The Journal of Physiology, 592, 2295 (2014).

[16] M. Zhao, "Electrical fields in wound healing—An overriding signal that directs cell migration", Seminars in Cell & Developmental Biology, 20, 674, (2009).

[17] M. Zhao, H. Bai, E. Wang, J.V. Forrester, and C.D. McCaig, "Electrical stimulation directly induces pre-angiogenic responses in vascular endothelial cells by signaling through VEGF receptors." Journal of cell science, 117, 397, (2004).

[18] E. Akbari, G.B. Spychalski, K.K. Rangharajan, S. Prakash and J.W. Song, "Flow dynamics control endothelial permeability in a microfluidic vessel bifurcation model", Lab on a Chip, 18, 1084 (2018).

CONTACT

*J.W. Song; E-mail: song.1069@osu.edu
*S. Prakash; E-mail: prakash.31@osu.edu

MULTIMODAL INTELLIGENT TRANSWELL SYSTEM

P.Ramiah Rajasekaran[1], A. Chapin[2], D.N. Quan[2], S.H. Jang[3], J. Herberholz[4], L. Hu[3], W.E. Bentley[2], and R. Ghodssi,[1,2,3]*
[1]Department of Electrical and Computer Engineering, Institute for Systems Research,
[2]Department of Bioengineering, [3]Department of Materials Science and Engineering,
[4]Department of Psychology in Neuroscience and Cognitive Science
University of Maryland, College Park, Maryland, USA

ABSTRACT

This work is the first demonstration of a 3D printed, modular, multimodal electrochemical-sensor-integrated, transwell system for monitoring tissue culture and molecular signaling, *in vitro*. Integral to the design of this platform is a porous membrane hosting an *in vitro* tissue culture with cell-interfaced electrochemical sensors. Interfacial -electrical cell surface impedance sensing (ECIS) electrodes and -cyclic voltammetric electrodes (CV) are used to monitor epithelial barrier formation and basolateral molecular release respectively. Such interfacial sensor-integrated tissue culture platform enables unprecedented access and provides temporal information that conventional transwells cannot furnish. We use this platform to uncover signaling events occurring along the gut-microbiome-brain-axis (GMBA).

INTRODUCTION

The gut-microbiome-brain-axis (GMBA) is a proposed signal transduction pathway between the gut microbiome and the brain. Human and animal studies have implicated that pathogenic bacteria in the gut play a role in development of both gastrointestinal and neural disorders, such as inflammatory bowel disease and depression, respectively [1]. While most commensal gut bacteria colonize the gut mucosa harmlessly, some commensal and non-commensal microbes degrade the mucosal layer and invade the epithelial barrier to infect deeper tissues [2]. This may negatively affect the brain by altering serotonin signaling of epithelial cells, the signaling method proposed to underlie the GMBA. Specifically, the gut epithelium contains enterochromaffin cells that can sense bacterial metabolites in the lumen (e.g. butyrate) and in turn secrete serotonin on their basolateral side, which stimulates enteric nerves that communicate with the brain [3]. Measuring the changes in serotonin signaling patterns due to different bacterial species may reveal the mechanism of bacterial influence on the brain, but the inaccessibility of the basolateral epithelium makes it difficult to measure this serotonin signaling *in vivo*. Therefore, a new multimodal sensor integrated *in vitro* tissue culture platform is required to provide measurements of basolateral serotonin from these cells and correlate them with measurements of bacterial pathogenicity and epithelial barrier integrity.

Gut-on-a-chip (GOC) platform is one such state-of-the-art *in vitro* platform for studying the dynamics of the gut epithelium in response to various molecular and cellular cues. GOC platforms are designed after conventional transwells. These *in vitro* systems allow for better control over cell environment constituents compared to complex *in vivo* tissues. However, current GOC systems mostly rely on downstream chemical analysis, post mortem histology analysis, and trans-epithelial electrical resistance (TEER) probes to monitor cellular behavior [4]. These systems often require tedious fabrication protocols and provide limited information on molecular mechanisms occurring *in vitro*. Though commercial tissue culture monitoring systems can provide pertinent information, they are expensive, limited in functionality, and lack customization [5].

While *in vitro* cell cultures are invaluable tools for studying biological mechanisms in controlled environments, real-time hierarchical signal transduction is difficult to study with current GOC platforms. Tissue culture sample analysis occurs mostly *ex situ* (e.g. ELISA [6], mass spectrometry [7]), requiring several processing steps, limiting the time resolution of molecular sensing from cells.

Electrochemical methods provide a solution, with the capability for *in situ* electrode integration utilizing simple fabrication protocols for real-time, direct, and label-free detection of molecular and cellular events. MEMS fabrication techniques enable development of customizable electrochemical electrodes on a variety of substrates as bio-interfacial sensors for research and diagnostic use [8].

Here we have propose a transwell-like GOC system incorporating membrane-integrated, cell-interfaced sensors. The housing for the platform is 3D printed and designed to sandwich a porous cell culture membrane with electrochemical sensors fabricated on top and bottom of the membrane. A representative model of the gut epithelium is cultured on ECIS electrodes on the top. The bottom CV electrode electrochemically senses the biomolecule of interest released by the tissue upon stimulation. The system showcased here has the ability to detect, the evolution of tissue growth over the porous membrane via ECIS and, redox molecules diffusing through the membrane via CV, mimicking basolateral cellular secretion. We have developed off the chip carbon nanotube (CNT) modified gold electrode to sense physiologically relevant serotonin concentrations that can be incorporated into the membrane-fabricated electrode design. Ultimately, this platform will be used to investigate the correlation between epithelial barrier degradation by co-cultured pathogenic bacteria, and basolateral serotonin release profiles, enabling the understanding of GMBA signaling.

MATERIALS AND METHODS

Development of a Sensor-integrated Cell Culture Housing

Figure 1 shows a schematic of the 3D printed transwell system with the sensor-integrated porous tissue culture membrane. Unlike off-the-shelf transwells (Corning® Tanswell®) with concentric wells, the proposed modular 3D design consists a top and bottom chamber sandwiching a sensor-integrated tissue culture membrane. The diameter of the electrode fabricated tissue culture membrane is 15 mm, which was chosen to be analogous to the area of a 24 well plate (diameter 15.6 mm). The platform was designed in Autodesk® Inventor™ and 3D printed with Stratasys Objet500 Connex3 3D printer with biocompatible MED610 photopolymer using photopolymer jetting (Polyjet) technology. The electrodes on the membranes were fabricated with e-beam evaporation (20 nm Ti/ 100 nmAu and 500 nm Ag) on track-etched polyester (PETE) membranes (thickness-11μm; porosity-$2x10^7$ pores/cm^2 and pore radius-500 nm, Figure 2a) through laser-cut paper shadow masks. Ag/AgCl reference electrodes were fabricated *in situ* by electrolessly oxidizing Ag to AgCl by exposing it to 50 mM $FeCl_3$ for 45 seconds. Interdigitated fingers of width 500 μm and spacing 500 μm function as ECIS electrodes (face UP). The three-electrode electrochemical system (face DOWN) consists of a working

978-1-940470-03-0/HH2018/$25©2018TRF
DOI 10.31438/trf.hh2018.33

electrode and adjoining reference and counter electrodes was used for CV. The electrodes were extended to fabricate contact pads with an inter-pad spacing of 2.54 mm, so that it can be interfaced with any standard off the shelf contact pins. The sandwiched sensor-fabricated membrane is flexible, compressed, and has a wrinkled architecture that mimics the gut landscape. Sterility of the device is of paramount importance to prevent bacterial or fungal contamination of this *in vitro* platform. All of the individual parts are assembled and the complete device can be sterilized by autoclaving at 121°C for 30 minutes and stored for later use, similar to a traditional transwell.

Cell Culture, TEER and Histology

The cells cultured to model the human gut epithelium *in vitro* were chosen to represent the simplified human gut to the best approximation to stimulate GMBA events. The co-culture consists of three types of cells, (1) Enterocytes (Caco-2), that forms the skeletal framework holding all the other cell types in the model gut. (2) Goblet cells (HT29-MTX) that produce mucus; the foremost protective layer covering the entire gut from mouth to colon. (3) Enterochromaffin cells (ECCs) (RIN14B), the most important cell type responsible for generating serotonin, the cellular metabolite (redox active neurotransmitter) released from the basolateral side involved in signal transduction to the brain. Caco2-, HT29-MTX and RIN14B cell lines were purchased from ATCC®, thawed, passaged and plated on the device in the ratio 4:2:1. The cells were cultured in Dulbecco's Modified Eagle Medium with 10% fetal bovine serum (DMEM + 10% FBS) at 37°C and 10% CO_2 in an incubator. The schematic of the 3D printed platform, membrane interfaced electrode and the tissue culture are shown in Figure 1.

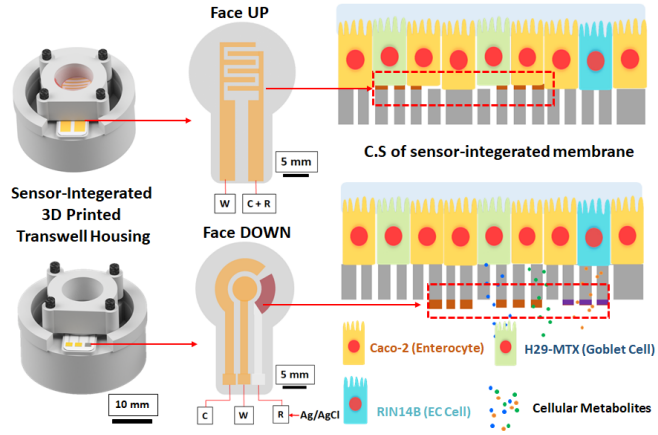

Figure 1: Schematic of the 3D printed device with multimodal electrochemical sensors. Sensors were fabricated on track-etched PETE membranes. Cells were grown directly on impedimetric, sensors (face UP) and opposite face of the potentiometric, sensors (face DOWN). C, R and W represent the counter, reference, and working electrodes respectively. The cross-section on the right shows the position of cells relative to the electrode position.

Cells were cultured over the course of 21 days on the porous membrane (Figure 2a) in the device, growing into a confluent monolayer with high expression of tight junctions. Fluorescent staining shown in Figure 2b demonstrates a classic method to confirm tight junction formation in an epithelial monolayer. In order to fix and stain the cells, the membrane with cells was removed and fixed in 4 % paraformaldehyde for 30 min and washed thrice with phosphate buffered saline (PBS). It was stained with 1mg/ml of DAPI (blue), DNA stain . For staining tight junctions, the membrane was treated with 1% (bovine serum albumin) BSA for 2 hours to block non-specific binding, rinsed and incubated with primary antibody, rabbit anti-rat polyclonal antibody against occludin (1:100). The primary antibodies were incubated overnight at 4 °C. The membrane was washed and incubated with donkey anti-rabbit IgG secondary antibody, and Alexa Fluor 488 conjugate (1:100) to tag tight junctions. This membrane was rinsed and imaged with Zeiss LSM 710 confocal microscope.

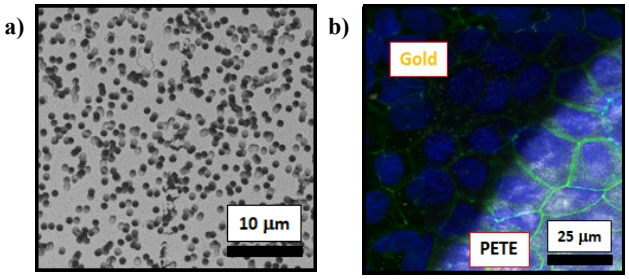

Figure 2: a) SEM of the porous PETE membrane on which the electrodes were fabricated and gut cells were cultured. b) Superimposed bright-field and confocal image of a 21-day co-culture. The Dark area represents the placement of the gold electrode. The co-culture was stained with DAPI (blue) to show the nucleus and an anti-occludin antibody (green) to show the formation of tight junctions.

Impedance monitoring of cell culture growth

Among electrochemical impedance measurements, (ECIS) has evolved to become the preferred tool for label-free and noninvasive sensing of adherent cells. As cells adhere and spread on the electrode surface, the gradual coverage of the electrode surface impedes the flow of electrical current between the electrodes. Subtle responses of cells to chemical, biological or physical stimuli/stressors, affect the cellular monolayer, which can be monitored in real-time with this non-invasive methodology. Impedance values for a confluent monolayer depends upon the given cell type, cell morphology, specific architecture of cell–cell and cell–matrix contacts. When the cells on the electrode change their shape, or if the ECM composition is changed in response to a stimulus, there is a corresponding change in the measured impedance. These physical changes can be interpreted by comparing impedance changes with an equivalent electrical model. Impedance measurements were recorded with a Biologic VSP 300 bipotentiostat by applying a sinusoidal AC voltage with an amplitude of $10mV_{rms}$ and a frequency of 10Hz to 10MHz. The media was changed once every 2 days during the course of the experiment. The obtained data was analyzed by equivalent circuit modeling with inbuilt EC-lab software with Z-fit module (Biologic Inc.).

TEER is complementary and classic method to measure the confluence of cell monolayers. TEER was measured with EVOM2™ Epithelial Voltmeter using chopstick TEER electrodes. TEER was used as a control to validate ECIS measurements of cell growth and coverage of the sensor-integrated membrane. Impedance and TEER measurements were done in sterile conditions in a biosafety cabinet.

Electrochemical sensing of serotonin

The performance of the gold electrochemical electrodes fabricated on PETE membranes was assessed by characterization with CV by detecting 2 mM ferrocene dimethanol (FDM) in 0.1 M phosphate buffered saline (PBS) pH = 7.4. CV was performed by applying a voltage scan from 0 – 350 mV at 300 mV/s and resulting current response was measured. FDM was allowed to diffuse from the top well into the bottom well for CV detection, giving a measurement of both the redox activity and the diffusion rate of small molecules across the membrane mimicking basolateral serotonin release. The Biologic VSP-300 potentiostat was employed for all electrochemical measurements.

Electrochemical detection of serotonin is highly dependent on

electrode materials and the applied cyclic voltammetric (CV) waveform. Therefore, serotonin sensing was optimized on commercial gold disk electrodes before optimizing serotonin sensing on PETE-integrated porous gold electrodes. Working electrodes were created by spray-painting single wall carbon nanotubes (SWCNTs) onto the gold disk surface, following surface polishing with alumina powder. Serotonin solutions were measured by CV at various concentrations (100 nM – 10 M) in DMEM + 10% FBS. CV was performed by measuring current across an applied voltage range of 100 – 450 mV with a scan rate of 50mV/s, using an Ag/AgCl reference electrode and a platinum coil counter electrode. *In vitro* ECCs were also stimulated to produce serotonin in separate cell culture (75 mm^2 surface area) by incubation with 100µM butyrate in 7mL DMEM + 10% FBS for 2-3 h. CV of the resulting supernatant was performed to detect serotonin from ECC cell culture.

RESULTS AND DISCUSSIONS

Membrane-integrated sensor performance

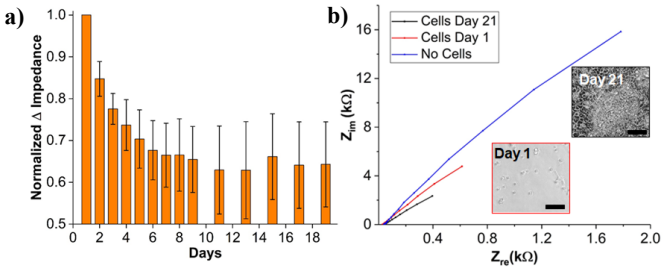

Figure 3: a) The exponential decrease in impedance measured at 10 Hz, representing an increase in double layer capacitance due to increase in the ECM protein (N=3). b) Nyquist plot showing the showing the impedance at 3 stages of cell culture. Inset shows the phase contrast image of the coculture on day 1 and day 21. Scale bar 100 µm.

Impedance values derived from the bode plot show that the normalized change in impedance measured at 10 Hz decreases exponentially and reaches a steady state over the time course of the tissue culture (Figure 3a). This is representative of the initial log phase where the cells grow exponentially, followed by a stationery phase where the cells become confluent and stop multiplying. The observed decrease in impedance corresponds to the increased capacitance from accumulation of ions from cell-associated extra-cellular matrix (ECM) on the surface of the electrode. The corresponding nyquist plots of three cases, (i) No cell (bare electrode), (ii) Day 1 (seeding) and, (iii) Day 21 (confluent monolayer) are shown in Figure 3b. They show a drop in real vs imaginary impedance at low frequency which is dominated by the double layer capacitance of the ECM covered electrode-cell interface. Inset shows the phase contrast image of the coculture on day 1 and day 21.

Figure 4a shows the equivalent circuit model used to fit the data, simulated with Z-fit module from EC-lab. The model is a combination of constant phase element and Waburg impedance that dominates the current at cell-free state and cell-covered state respectively. The direction of current flow in each case is shown by the double-sided arrow. Figure 4b, shows the fitting between the real data (patterns) and the simulated data (solid line) by the model shown in Figure 4a. A close fit and a similar trend between the real and stimulated data shows the validity of equivalent circuit model. It can be seen from the experiment and the model that as the cells reach confluence, the system shift to a charge transfer resistance dominated state, characterized by the emergence of a semicircular profile in the nquist plot. The charge transfer resistance stems from tightly packed monolayer of cells covering the surface of the electrode, resisting any nonspecific charge transfer reactions occurring at the electrode-tissue interface. This state is also characterized by a corresponding high TEER value for day 14 (708 $\Omega.cm^{-2}$), day 16 (1105 $\Omega.cm^{-2}$) and day 18 (1615 $\Omega.cm^{-2}$).

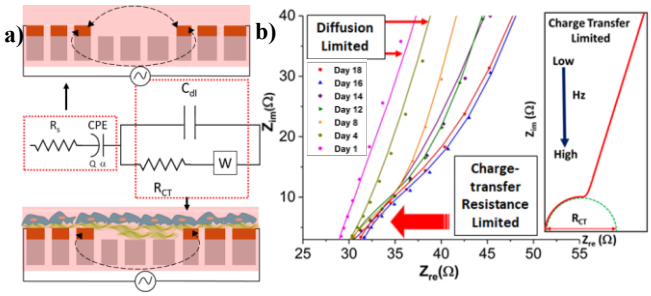

Figure 4: Data Fitting. a) Equivalent circuit model of the bare electrode (top) and cell covered porous electrode (bottom). R_s, R_{CT}, Q, α, CPE, C_{dl} and W are charge transfer resistance, solution resistance, constant phase element (CPE) parameter, CPE exponent, double layer capacitance, and Waburg element respectively. The arrows indicate that CPE dominates the bare electrode case and R_{CT} dominates cell-covered case b) The dot patterns represent the data points obtained in the experiment and the solid lines show the fitting of equivalent circuit to the data. The data also shows the transition of the system from a diffusion limited state to a charge transfer limited state as the cell culture progresses

In-situ electrochemical detection of model metabolite.

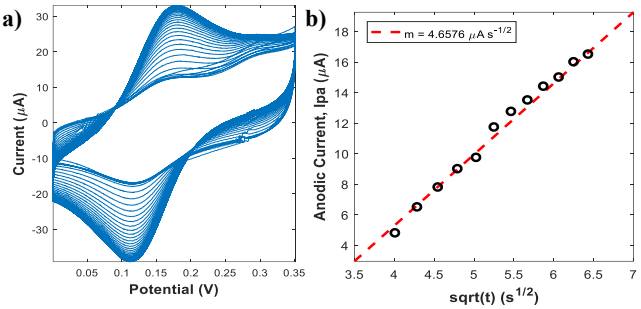

Figure 5: FDM diffusion through PETE membrane, detection by porous gold CV electrodes fabricated on the membrane. a) Cyclic voltammogram detecting diffusion in real time, peak height is proportional to FDM concentration. Scan rate = 300mV/s, 2.3s/cycle. b) Linear fit of peak anodic current vs. $t^{1/2}$ as a measure of diffusion rate: slope = 4.6576µA $s^{-1/2}$.

Figure 5 shows quantifiable detection of FDM at the PETE-integrated gold electrochemical electrodes (without cells). The Nernst equation describes ideal behavior of a redox molecule at the electrode occurs when the anodic and cathodic peak heights are approximately equal, and when the difference between anodic and cathodic potential is ~59 mV for an one electron transfer reaction [9]. These conditions are met for FDM detection (Ipa/Ipc ~ 0.8, Epa-Epc = 56 mV) indicating that the fabricated electrodes are reliable. Figure 5a shows increasing anodic and cathodic peaks over the duration of FDM diffusion, saturating after 60 seconds. The linear relation of anodic peak current and square root of time gives a measure of diffusion rate on the order of 5 µA $s^{-1/2}$ (Figure 5b). These results demonstrate that molecular detection is possible with time resolution in the order of a few seconds, though full diffusion

through the membrane limits time resolution to 1 minute.

Ex-situ electrochemical serotonin detection

Figure 6a shows the ability of CNT-modified gold electrodes to detect serotonin in prepared solutions and samples collected from cells. As shown by the calibration curve of serotonin detection at these electrodes, the linear range of detection spans potential physiological concentrations (100 nM – 10 µM) with a sensitivity of 140 µA/mM. The sensitivity achieved here is higher than both gold and glassy carbon electrodes, owing to the higher surface area and more ideal carbon structure provided by the CNT film. However, the repeatability standard deviation (RSD) of these measurements is in the range 15-40%, indicating relatively poor repeatability over successive trials, especially at lower concentrations. This variation at low concentrations limits the resolution of the technique to 45nA (3σ) and the limit of detection to ~300nM serotonin in cell media. Further experiments detecting cell produced serotonin in cell supernatant (Figure 5b) show that this limit of detection may still be reasonable for our system. In comparison with an electrode-specific calibration curve performed before the detection of cell produced serotonin, the peak shown in Figure 5b corresponds to ~600 nM serotonin. These results provide a proof of concept that CNT-coated gold is an ideal electrode material for serotonin detection in cell media and for serotonin produced directly by cultured cells. The inset on left shows bare gold microdisc electrode (diameter- 1.6 mm) and CNT ink spray painted electrode. The inset on the left shows SEM of the CNT ink covering the gold electrode.

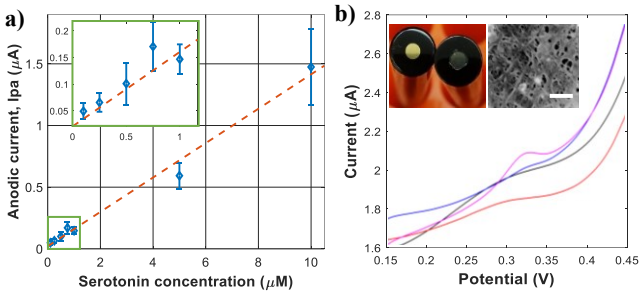

Figure 6: a) Calibration of CV detection of serotonin, showing linear range from 0.1 – 10 µM serotonin in cell media (DMEM + 10% FBS). Inset: Zoom in on 0.1 – 1µM. Error bars denote standard deviation (N=4). R^2 = 0.9866. b) Cyclic voltammogram of serotonin detection from ECC supernatant, after 2h of stimulation with 100µM butyrate (pink) vs. controls (black: DMEM, red: DMEM + 100 µM butyrate, blue: ECC DMEM supernatant with no butyrate). Serotonin peak occurs at E_{pa} = 0.323 V vs. Ag/AgCl. Inset: gold disk electrode vs CNT-ink-coated gold disk electrode (1.6mm radius), and an SEM image of the CNT film (scale bar = 200 nm).

This sensing paradigms supports the integration of both impedance interdigitated electrodes and CNT-gold CV electrodes into the 3D printed cell culture device to directly interface with cells. The serotonin detection methods achieved with commercial electrodes can be directly translated to *in situ* measurements within the cell culture by modifying PETE-fabricated gold electrodes with CNT films. The potential to correlate changes in the epithelial barrier integrity with concentration-specific serotonin detection on the basolateral side may allow research into the direct molecular and cellular influences on GMBA signaling. Further, this modular platform could be redesigned to integrate other types of cell cultures which would benefit from real-time, multimodal, and automatable molecular and cellular sensing.

CONCLUSIONS

This work reports the initial results of the first electrochemical electrode integrated 3D printed cell culture platform, aimed towards detecting signal transduction events within a model of the gut-microbiome-brain axis. Current GOC platforms lack sophisticated on-chip cellular and molecular measurement capabilities that promise to enhance quantification and correlation of biological events. The possibility of performing real-time, direct, automated measurements over the course of a cell culture lifetime is realized by MEMS fabrication of electrodes directly onto bio-interfacing substrates, such as a transwell membrane.

As shown here, gold electrodes can be fabricated onto both sides of a porous membrane with unique and customizable geometries to apply two different sensing modalities. Impedimetric sensing is capable of measuring the quality of cell coverage over the membrane, acting as an online method to compliment standard cell techniques (e.g. TEER, fluorescence microscopy). Electrochemical sensing is capable of measuring redox molecules such as serotonin. By interfacing these electrodes directly underneath the epithelial cell layer, measurement of basolateral serotonin release can be measured, which has not been achieved *in vivo* because of its inaccessibility.

Future measurements using MITS will use impedance to detect changes in epithelial and mucus integrity due to colonization of gut microbiota and simultaneously detect serotonin release from the epithelium. Since these measurements can occur in real-time over the duration of a cell culture lifetime, we can temporally correlate how certain bacteria affect both gut health and serotoninergic nerve stimulation. This type of discovery platform may be used both as a research tool for understanding the bacterial influence on the GMBA and as a diagnostic tool to evaluate patient gut cells and microbiome for signs of altered serotonin signaling. Here, technological advancements may aid in connecting molecular events to incidence of disease in humans.

REFERENCES

[1] M. Carabotti, A. Scirocco, M. A. Maselli, and C. Severi, "The gut-brain axis: Interactions between enteric microbiota, central and enteric nervous systems", Ann. Gastroenterol, 28, 203 (2015).

[2] M. McGuckin, S. Linden, P. Sutton, and T.H. Florin, "Mucin dynamics and enteric pathogens", Nature Review Microbiology, 9, 4 (2011).

[3] J. Zhu, X. Wu, C. Owyang, and Y. Li, "Intestinal serotonin acts as a paracrine substance to mediate vagal signal transmission evoked by luminal factors in the rat", The Journal of Physiology, 530, 3 (2001).

[4]] H. J. Kim, D. Huh, G. Hamilton, and D. E. Ingber, "Human gut-on-a-chip inhabited by microbial flora experiences intestinal peristalsis-like motions and flow,", Lab Chip, 12, 2165 (2012).

[5] xCELLigence RTCA HT Instrument from ACEA Biosciences, Inc. ECIS® ZΘ from Applied Biophysics, Inc.

[6] V. Veregut, M. Florescu, and M. Badea, "Classic and Modern Methods for Detection of Serotonin", Sensing in Electroanalysis, 7 (2012).

[7] J. Arnold, J. Roach, and M. Azcarate-Peril, "Emerging Technologies for Gut Microbiome Research", Trends in Microbiology, 24, 11 (2016).

[8] T. Winkler, S. Lederer, E. Kim, H. Ben-Yoav, D.L. Kelly, G. Payne, and R. Ghodssi, "Molecular processes in an electrochemical clozapine sensor," Biointerphases, 12, 2 (2017).

[9] A. J. Bard, and L. R. Faulkner, "Electrochemical Methods: Fundamentals and Applications", Wiley, New York (2001).

CONTACT

*R. Ghodssi, tel: +1-301-405-8158; ghodssi@umd.com

2D AND 3D DOPING OF SILICON MEMS STRUCTURES USING PHOSPHORUS-DOPED POLYSILICON AS A DOPANT SOURCE

Pascal J. Newby[1], Kazem Zandi[1], Karel Côté[1], Jean-Philippe Richard[1], and Khaled-Amir Belarbi[2]*
[1]MiQro Innovation Collaborative Centre (C2MI), 45 boulevard de l'Aéroport, J2L 1S8, Bromont, Qc, Canada
[2]Teledyne DALSA Semiconductor Inc., 18 boulevard de l'Aéroport, J2L 1S7, Bromont, Qc, Canada

ABSTRACT

We use *in-situ* phosphorus-doped LPCVD (low-pressure chemical vapour deposition) polysilicon as a dopant source for silicon wafers. We used this technique for "3D doping", where poly-Si is deposited over structures patterned in silicon-on-insulator (SOI) wafers, which enables higher doping levels, as diffusion is performed through three surfaces rather than one. This technique can also be used for doping of unpatterned wafers, and we have derived a relation which estimates the doping level achieved with 3D doping using only 4-point probe measurements on blanket wafers. The advantage of this doping method compared to standard methods is that it does not require dedicated equipment and can be carried out using tools commonly available in a MEMS fab.

INTRODUCTION

Besides being used as a mechanical material in MEMS, silicon often also serves as an electrical conductor, so its resistivity must be tuned according to the application. There are many standard methods for *ex-situ* doping of silicon, such as ion implantation, $POCl_3$, or spin-on glass, but these methods all require dedicated and expensive equipment which may not be available in a MEMS fab. As an alternative to these techniques, we propose to use *in-situ* phosphorus-doped polysilicon as a dopant source. Once deposited, the phosphorus can be transferred from the poly-Si to the silicon wafer by annealing, and the advantage of this technique is that it uses equipment readily available in a MEMS fab [1].

Polysilicon has been used before as a dopant source in the 80s and early 90s [2]–[4] for transistor fabrication. In this previous work poly-Si was not *in-situ* doped, but doped after deposition, generally by ion implantation [3], [4], and the focus was on using poly-Si for the fabrication of ultra-shallow junctions in MOSFETs or emitters in bipolar transistors [4]–[6]. Work on the use of poly-Si as a dopant source for MEMS applications has never been published.

We will present the development and optimization of the process, and apply this process to doping of both unpatterned and patterned wafers. The latter process will be referred to as "3D doping". We will also show how doping of unpatterned wafers can be used to predict doping of patterned wafers and discuss the issues encountered during the development of this process.

3D DOPING

In this article we mainly focus on 3D doping of SOI (silicon-on-insulator) wafers. Wafers are patterned and the device layer is etched down to the buried oxide layer, and poly-Si is deposited over the patterned structure. The wafers are then annealed, as illustrated in Figure 1, to transfer dopant atoms to the wafer. The advantage of this technique, compared to 2D doping, is that as doping is performed through three surfaces, much higher doping levels can be reached than with 2D doping for the same thermal budget, and this is especially true for high aspect ratio structures.

EXPERIMENTAL DETAILS

All wafers used were 200 mm in diameter with {100} orientation. The bulk wafers were 725-µm-thick. The SOI wafers had 25-µm-thick device layers and 2-µm-thick buried oxide. Both

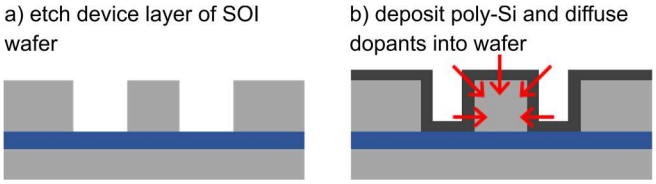

Figure 1: Basic principle of 3D doping.

the bulk wafers and device layer of the SOI wafers had an initial resistivity of 1-10 Ω.cm and were n-type phosphorus-doped.

The SOI wafers were etched by DRIE (deep reactive ion etching) down to the buried oxide layer. The test structures were double beams, each with a width of 7 µm and lengths between 1 and 3 mm, as shown in Fig. 2. Etched dimensions were measured using an optical microscope or SEM (scanning electron microscope).

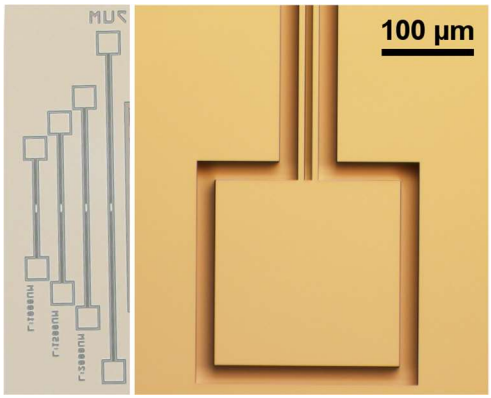

Figure 2: Optical microscope image showing the test structures etched in an SOI wafer by DRIE.

The polysilicon layers were deposited by low-pressure chemical vapour deposition (LPCVD). Doping of the poly-Si was carried out *in-situ* during the deposition so phosphine was used as well as silane. Oxidation of the poly-Si layers was performed by wet thermal oxidation at 1000 or 1100°C. The oxidized poly-Si was etched in 10:1 hydrofluoric acid (HF).

Thickness of the oxide layers was measured by reflectometry using an n&k Olympian. Thickness of the poly-Si layers was measured by reflectometry when they were above an oxide layer (over the buried oxide of a patterned SOI wafer for instance) and by weighing the mass change when they were deposited directly on silicon for the unpatterned wafers. Sheet resistance measurements were performed either with a Prometrix RS55 or with a 4-point probe mounted on a manual prober. Resistance measurements were done with a manual prober using a 4-wire configuration and a Keithley 2400 SMU. Average resistivity of the silicon in the structures is extracted from the resistance measurements.

Both within-wafer non-uniformity (WIWNU) and wafer-to-wafer non-uniformity (WTWNU) were calculated as $(\mathrm{Max} - \mathrm{Min})/(2 * \mathrm{average})$ throughout this paper.

978-1-940470-03-0/HH2018/$25©2018TRF
DOI 10.31438/trf.hh2018.34

RESULTS AND DISCUSSION

Development of the Basic Process Flow

Phosphorus-doped polysilicon is deposited over silicon wafers by LPCVD. Dopants must then be transferred from the poly-Si layer to the wafer, by annealing. It is also desirable to remove the poly-Si after dopant transfer and before further processing, and selectivity between the single-crystal silicon substrate and poly-Si is an obvious challenge in this case. One option for removing poly-Si is a timed etch, either wet or plasma. Instead of this, we have chosen to thermally oxidize the poly-Si and then remove it using HF. This option was chosen as uniformity and repeatability are far better for thermal oxidation than for etching, meaning that poly-Si can be removed while minimizing the effect on the silicon substrate.

The poly-Si film can be oxidized before or after the dopant drive-in anneal, so we compared both options. Two SOI wafers with patterned device layers were used. After depositing the 1-µm-thick poly-Si layer, one wafer was oxidized before the drive-in anneal, and the other was oxidized after annealing. Table 1 summarizes the process steps. When annealing before oxidation, a thin cap-oxide must be created on the poly-Si before annealing to prevent dopant out-gassing [7]. The second oxidation (0.4 µm) was performed as initial electrical measurements after the 2.2 µm oxidation showed that there was still a thin layer of poly-Si left which caused a short-circuit between the test structures and the rest of the wafer.

Table 1: Process steps used to determine optimal order for oxidation and drive-in anneal.

Oxidation *after* drive-in anneal	**Oxidation *before* drive-in anneal**
Photo + DRIE of SOI device layer	
Deposit 1 µm poly-Si	
Thermal cap oxide, 15 nm + 1h anneal 1100ºC	Thermal oxidation 1100ºC, 2.2 µm
Drive-in anneal, 15h 1100ºC	
Thermal oxidation 1100ºC, 2.2 µm	-
Etch oxidized poly-Si in HF	
2nd thermal oxidation, 0.4 µm	
Etch oxidized poly-Si in HF	

After final removal of the oxidized poly-Si, the resistance of the test structures was measured at 13 points across the wafer and the results are given in Table 2. The results show that oxidizing after the drive-in anneal leads to a marginally lower doping level, despite a slightly higher thermal budget. Furthermore, uniformity is better when oxidation is performed before annealing, and there is one less process step, so we chose to use this process.

The oxidation of poly-Si must be well controlled. Indeed, as mentioned above, after the first 2.2 µm thermal oxidation, there was still some remaining unoxidized poly-Si. Conversely, oxidizing for too long will consume silicon from the substrate. Several oxidation runs of poly-Si were carried out with different oxidation times, and our measurements show that poly-Si is oxidized faster than single-crystal <100> silicon, but once oxidized behaves the same as oxidized single-crystal silicon and can be described using the Deal-Grove model [8]. To avoid issues due to incomplete oxidation of the poly-Si, the oxidation time was slightly extended so that about 90 nm of the silicon substrate beneath the poly-Si was consumed.

Table 2: Resistance measurements on SOI wafers, where oxidation was performed either before or after the drive-in anneal.

Process	**Average resistance [mΩ.cm]**	**Range [mΩ.cm]**	**WIWNU [±%]**
Oxidation after anneal	1.19	0.14	6
Oxidation before anneal	1.14	0.08	4

Effect of Polysilicon Thickness

Using the optimized process flow, with oxidation of the poly-Si before the drive-in anneal and the optimized oxidation time, both presented above, the doping process was repeated with a thinner poly-Si layer with a thickness of 0.34 µm to compare with the results obtained for 1-µm layers. Two SOI wafers were used, as well as several unpatterned test wafers. One SOI wafer was cleaved after the poly-Si deposition to observe the poly-Si film using SEM. Figure 3 shows that the film is conformal.

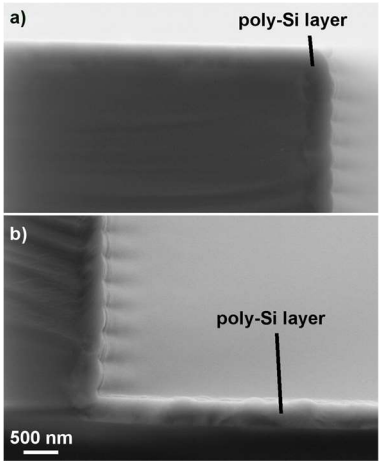

Figure 3: Cross-section SEM images of poly-Si layer deposited over a patterned SOI wafer.

The thickness of the as-deposited and oxidized poly-Si films was measured, as well as its resistivity (see experimental details). The resistance of the test structures on the SOI wafer was measured on 19 dies across the wafer. These results are summarized in Table 3, including data on within-wafer and wafer-to-wafer non-uniformity. In addition, two oxidation runs were performed, and there was a 1.2% difference between the average oxide thicknesses for both runs. For all the steps, wafer-to-wafer and within-wafer uniformity are excellent. The main source of within-wafer non-uniformity is the resistivity of the poly-Si, which is reflected in the WIWNU of the average resistivity of the patterned structures. Compared to the results with a 1-µm poly-Si layer, the 0.34-µm poly-Si layer contains a smaller amount of phosphorus, so as expected the resistivity obtained with the 0.34 µm poly-Si layer is higher.

Table 3: Data for characterization of the main process steps.

Measurement	**Value**	**WIWNU [±%]**	**WTWNU [±%]**
Poly-Si thickness [nm]	337	0.7	1.7
Poly-Si resistivity [mOhm.cm]	1.82	4.8	0.7
Silicon oxide thickness	952	0.3	0.1
Average resistivity of patterned structures [mΩ.cm]	3.9	4.0	-

Using 2D-Doped Wafers to Estimate 3D Doping Level

In order to reduce development costs and time, we have derived a relation which uses only 4-point probe measurements of sheet-resistance performed on 2D-doped unpatterned wafers to estimate the resistivity which would be obtained for 3D doping with the same thermal budget. This saves the photolithography and etch steps, and means the process can be developed using bulk wafers rather than costly SOI wafers.

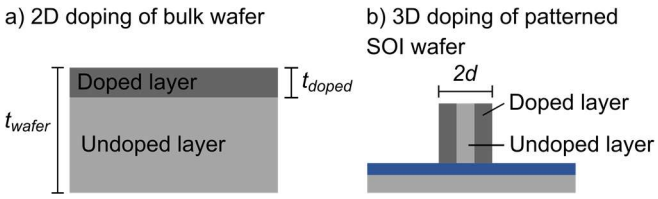

Figure 4: Cross-sections of geometries used to model a) 2D doping of a bulk wafer and b) 3D doping of a patterned SOI wafer.

The first step is to estimate the sheet resistance of the doped layer from the measured sheet resistance of the whole wafer, without knowing the doping depth, as illustrated in Fig. 4a. The measured sheet resistance $R_{s,\,\text{meas 2D}}$ depends on the sheet resistance of the doped layer, $R_{s,\,\text{doped 2D}}$ and the undoped wafer, $R_{s,\,\text{undoped 2D}}$:

$$\frac{1}{R_{s,\,\text{meas 2D}}} = \frac{1}{R_{s,\,\text{doped 2D}}} + \frac{1}{R_{s,\,\text{undoped 2D}}} \qquad (1)$$

The sheet resistance of the undoped part of the wafer is $R_s = \left(t_{\text{wafer}} - t_{\text{doped}}\right)/\rho_0$, where t_{wafer} is the thickness of the wafer and t_{doped} the thickness of the doped layer, and ρ_0 is the initial resistivity of the wafer. The thickness of the doped layer is unknown but on the order of a few microns, so can be neglected compared to the total thickness of the wafer (725 µm), which allows us to express the sheet resistance of the doped layer as a function of known values:

$$\frac{1}{R_{s,\,\text{doped 2D}}} \approx \frac{1}{R_{s,\,\text{meas 2D}}} - \frac{t_{\text{wafer}}}{\rho_0} \qquad (2)$$

We will now use this value to estimate the average resistivity of a 3D doped structure. Our structures have a fairly high aspect ratio, so we will consider only lateral doping. In this case we can represent the doped structure as two doped layers, one on each side of a central undoped layer (see Figure 4b). The sheet resistance of each doped layer is equal to that of the 2D-doped layer calculated in *(2)*, so $R_{s,\,\text{doped 3D}} = R_{s,\,\text{doped 2D}}$. The total sheet resistance of the doped beams, $R_{s,\,\text{beam}}$, is:

$$\frac{1}{R_{s,\,\text{beam}}} = \frac{2d}{\rho_{\text{avg 3D}}} = \frac{2}{R_{s,\,\text{doped 3D}}} + \frac{1}{R_{s,\,\text{undoped 3D}}} \qquad (3)$$

where d is the half-width of the beam and ρ_{avg} the average resistivity of the beam. The thickness of the doped and undoped layers are comparable and the resistivity of the doped layer is orders of magnitude smaller than that of the undoped layer, meaning that $1/R_{s,\,\text{undoped}} \ll 1/R_{s,\,\text{doped}}$. So using the expression for $R_{s,\,\text{doped}}$ calculated in *(2)* the average resistivity of the beam is:

$$\rho_{\text{avg 3D}} = d * R_{s,\,\text{doped 3D}} = \frac{d}{\left(\frac{1}{R_{s,\,\text{meas 2D}}} - \frac{t_{\text{wafer}}}{\rho_0}\right)} \qquad (4)$$

We used *(4)* to estimate 3D resistivities using data from 2D-doped wafers and compared these with resistivities measured on 3D-doped wafers. 2D sheet resistance data for the 0.34 µm poly-Si layer was obtained from two bulk unpatterned wafers which were processed at the same time as the SOI wafer. For the tests presented at the beginning of the results section, with 1 µm of poly-Si, there were no unpatterned wafers, but 4-point probe measurements were taken on unpatterned areas of the SOI wafers. Table 4 shows sheet resistance values and average 3D resistivity estimated from these values. The last column repeats the measured 3D resistivities from previous sections and shows that the agreement between the estimated and measured 3D resistivities is very good. The data for the 1-µm poly-Si was taken from unpatterned areas of SOI wafers with 25-µm-thick device layers, which cannot be considered as infinitely thick compared to the doped layer. This may be a reason why the agreement is not quite as good for 1-µm poly-Si.

Issues

Some minor issues were observed during the development of this process. The first issue is an increase in the roughness of the silicon surface, which appears during the oxidation of the poly-Si layer and remains after removal of the oxidized poly-Si. The roughness was not measured, but is clearly observable under the microscope, as shown in Fig. 5. A possible explanation for this is phosphorus precipitation at the Si/SiO_2 interface during oxidation.

The doping process also led to the formation of dislocations. In Figure 5 we can see lines following the etched edges, which follow the <110> crystal direction. The lines are approximately 18 µm away from the etched edges, which is consistent with a dislocation propagating from the bottom corner of an etched beams along a {111} plane. Like the roughness, the dislocations appeared during the oxidation of the poly-Si and were observed for both the 0.33 and 1-µm poly-Si layers. The most likely explanation is the

Table 4: Sheet resistance measured on unpatterned doped wafers and 3D average resistivity estimated from these values. The last column contains measured 3D resistivities copied from the previous section for ease of comparison.

Wafer	Measured 2D sheet resistance $R_{s,\,\text{meas 2D}}$ [Ohm/sq]	WIWNU $R_{s,\,\text{meas 2D}}$ [±%]	Calculated $R_{s,\,\text{doped 2D}}$ [Ohm/sq]	Estimated average 3D resistivity [mOhm.cm]	Measured average 3D resisitivity [mOhm.cm]
Oxidation after anneal, 1 µm poly-Si	4.69	3.4	4.71	1.41	1.19
Oxidation before anneal, 1 µm poly-Si	4.63	3.2	4.64	1.39	1.14
0.34 µm poly-Si wafer 1	9.37	1.5	12.1	3.93	3.87
0.34 µm poly-Si wafer 2	9.52	1.7	12.4	4.02	

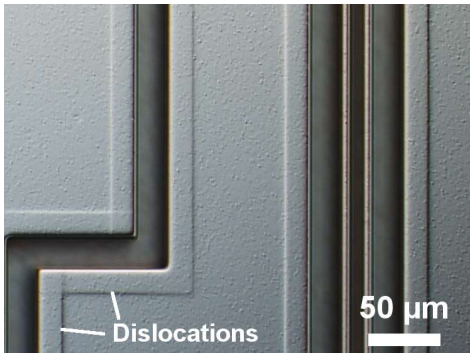

Figure 5: DIC (differential interference contrast) microscope image of a wafer after removing the oxidized poly-Si. The surface roughness and dislocations caused by the doping process are visible.

compressive stress created in the poly-Si layer when it is oxidized. The height of the dislocation was measured by SEM and white-light interferometry and the measured values were between 50 and 90 nm.

The final issue is the presence of a residue of unoxidized poly-Si at the foot of the beams. Fig. 6 shows a cross-section SEM image of a beam after etching of the oxidized poly-Si, and the unoxidized poly-Si is clearly visible at the foot of the beam. It has been shown in the literature that oxidation of silicon is slower around corners due to compressive stress [9]. Whether the three issues presented are a problem or not will depend on each application.

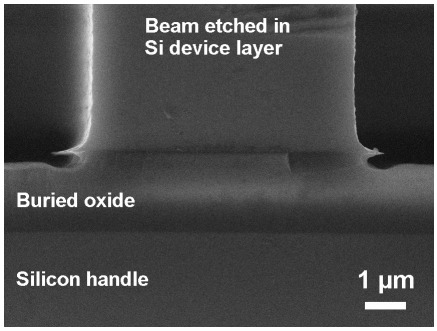

Figure 6: Cross-section SEM image of a beam patterned in the device layer of an SOI wafer after removal of the oxidized poly-Si.

Advantages of Polysilicon Doping

Using polysilicon as a dopant source has several advantages compared to other doping techniques. Standard *ex-situ* doping techniques such as ion implantation, $POCl_3$, and spin-on dopant all require dedicated equipment which may not be available in a typical MEMS fab. Polysilicon doping on the other hand, requires only a poly-Si furnace and an oxidation furnace, which are common tools in a MEMS fab.

Another solution for obtaining doped SOI wafers is simply to purchase wafers with the desired initial doping. However typical within-wafer variation is around ±5% and wafer-to-wafer variation is generally around ±10%, unless the wafers are binned into very small lots, which will increase cost. We do not have wafer-to-wafer data for the final resistivity for poly-Si doping, but it should be commensurate with the wafer-to-wafer variations for the previous steps presented in Table 3, so should be able to achieve better non-uniformities than that of doped SOI wafers.

Furthermore, poly-Si doping enables 3D doping, which can be used to reach lower resistivities for the doped structures, given that three surfaces rather than one are used for introducing dopants. Indeed, 3D doping is not possible with ion implantation, and might be feasible with spin-on dopants, but only for limited step heights.

CONCLUSION

We have developed a technique for doping of silicon wafers using *in-situ* phosphorus-doped LPCVD polysilicon. The poly-Si can be deposited over either unpatterned or patterned wafers, and in the latter case, has the advantage of being able to reach higher doping levels due to the higher surface involved. The poly-Si is thermally oxidized to allow selective removal in HF from the silicon wafers, and we have shown that the process yields better results when oxidation is performed before the drive-in anneal rather than after. Finally, we have established a relation between the sheet resistance of 2D doped wafers and the resistivity of patterned wafers, which can be used to reduce development time and costs.

The main advantage of this technique compared to other doping methods is that it can be performed with equipment available in a typical MEMS fab. Within-wafer and wafer-to-wafer uniformity are excellent, and providing that run-to-run uniformity is as good, this method should be usable in industrial fabrication process-flows.

Future work includes performing more runs to gather data on run-to-run repeatability and varying the thermal budget more to study the effect on final resistivity, as well as resolving the issues with the process which were observed.

ACKNOWLEDGEMENTS

The authors would like to thank the staff of Teledyne Dalsa for their help in the fabrication of the wafers used in this work.

REFERENCES

[1] M. Biebl, G.T. Mulhern, and R.T. Howe, “In Situ Phosphorus-doped Polysilicon For Integrated MEMS,” Proceedings of the International Solid-State Sensors and Actuators Conference - TRANSDUCERS ’95, Stockholm, Sweden, 6/25-29/95, IEEE (1995), pp, 198-201.

[2] W.J.M.J. Josquin, P.R. Boudewijn, and Y. Tamminga, “Effectiveness of polycrystalline silicon diffusion sources,” Appl. Phys. Lett., 43, 960 (1983).

[3] H. Schaber, R. v. Criegern, and I. Weitzel, “Analysis of polycrystalline silicon diffusion sources by secondary ion mass spectrometry,” J. Appl. Phys., 58, 4036 (1985).

[4] K. Park, S. Batra, S. Banerjee, G. Lux, and T.C. Smith, “Analysis of ion-implanted amorphous and polycrystalline silicon films as diffusion sources for ultrashallow junctions,” J. Appl. Phys., 70, 1397 (1991).

[5] T.I. Kamins, “Effect of polysilicon-emitter shape on dopant diffusion in polysilicon-emitter transistors,” IEEE Electron Device Lett., 10, 401 (1989).

[6] G.E. Georgiou, T.T. Sheng, F.A. Baiocchi, J. Kovalchick, W.T. Lynch, and D. Malm, “Shallow junctions by out-diffusion from Arsenic implanted polycrystalline silicon,” J. Appl. Phys., 68, 3714 (1990).

[7] S.P. Murarka, “Phosphorus out-diffusion during high temperature anneal of phosphorus-doped polycrystalline silicon and SiO2,” J. Appl. Phys., 56, 2225 (1984).

[8] B.E. Deal and A.S. Grove, “General relationship for the thermal oxidation of silicon,” J. Appl. Phys., 36, 3770 (1965).

[9] R.B. Marcus and T.T. Sheng, “The Oxidation of Shaped Silicon Surfaces,” J. Electrochem. Soc., 129, 1278 (1982).

CONTACT

*P.J. Newby, Pascal.Newby@c2mi.ca

FABRICATION AND SUB-ASSEMBLY OF ELECTROSTATICALLY ACTUATED SILICON NITRIDE MICROSHUTTER ARRAYS

Lance H. Oh [1], Mary J. Li[2],Kyowon Kim[3], Dan Kelly[3], Alexander Kutyrev[4], Samuel H. Moseley[2], Nick P. Costen[1], and George Manos[2]

[1]SGT Inc., Maryland, USA

[2]NASA/Goddard Space Flight Center, Maryland, USA

[3]ASRC Federal Corp., Maryland, USA

[4]University of Maryland, Maryland, USA

ABSTRACT

We have developed a new microshutter array (MSA) sub-assembly. The MSA and a silicon substrate are flip-bonded together. The MSA has a new back side fabrication process to actuate the microshutters electrostatically, and the new silicon substrate has light shields. The microshutters with a pixel size of 100 x 200 μm^2 are fabricated on silicon with thin silicon nitride membranes. The microshutters rotate 90^o on torsion bars. The selected microshutters are actuated, held, and addressed electrostatically by applying voltages on the electrodes the front and back sides of the microshutters. The substrate has the light shield to block lights around the microshutters. Also, electrical connections are made from the MSA to a controller board via the substrate.

INTRODUCTION

In the Goddard Space Flight Center, we have developed a new MSA sub-assembly. The sub-assembly consists of the MSA and a silicon substrate. The MSA has a new back side fabrication process to actuate the microshutters electrostatically, and the new silicon substrate has light shields.

In the past, a large MSA array size of 175x384 had been developed, fabricated, and installed in the James Webb Space Telescope (JWST) as multi-object aperture selectors [1, 2]. The JWST MSAs were magnetically opened and electrostatically held open. The magnetic operation, however, involved moving magnets thus complicated actuation schemes and increased the payload. Instead, the electrostatic actuation is simple. Thus, the weight of the MSA assembly is far reduced.

The microshutters were made with silicon nitride membranes on silicon with a pixel size of 100 x 200 μm^2 and rotate 90^o on torsion bars. Figure 1 shows a scanning electron microscope (SEM) image of the MSA; on the front side, microshutter blades are suspended on the 2 μm wide torsion bars, the gap around the microshutters is 2 μm wide, aluminum is patterned to create electrodes, and molybdenum nitride is patterned on top of the microshutter blade. Also, the JWST microshutters had the light shields patterned with aluminum overhang around the openings as shown in Figure 2. The purpose of the light shield is to block light passing through the perimeters around the microshutters. The light shield step required 3 lithography steps: a sacrificial layer, partially exposed bumps pattern on the sacrificial layer, and an aluminum pattern over the sacrificial layer. In order to avoid these three lithography steps plus an aluminum deposition, we decided to develop a new silicon substrate with the light shields.

The silicon substrate was first developed and used as a mechanical support for the MSA and an electrical interface between the MSA and the external control electronics on a printed circuit board as shown in Figure 3. For the first time, we present the new MSA indium-flip-chip bonded to the silicon substrate with light shields that block light leak around the openings around the microshutters. The front side of the MSA is flip-chip bonded to the aluminum electrodes on the silicon oxide surface of the silicon substrate. The front electrodes are connected to the substrate electrodes via indium bumps while the back side electrodes are wire bonded to the substrate electrodes.

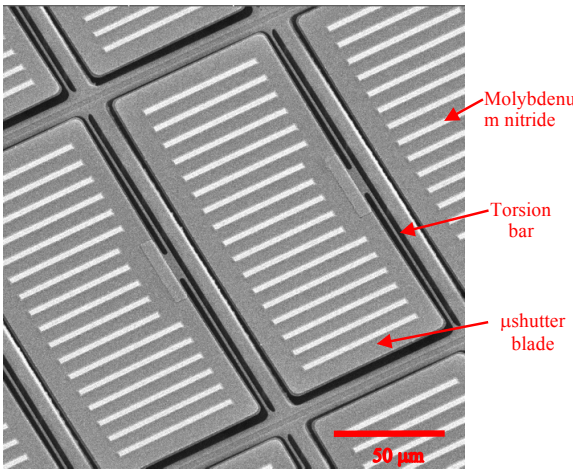

Figure 1: A SEM image of the front side image of the MSA. On the microshutters, the patterned microshutter blade, torsion bar and strips of molybdenum nitride are shown.

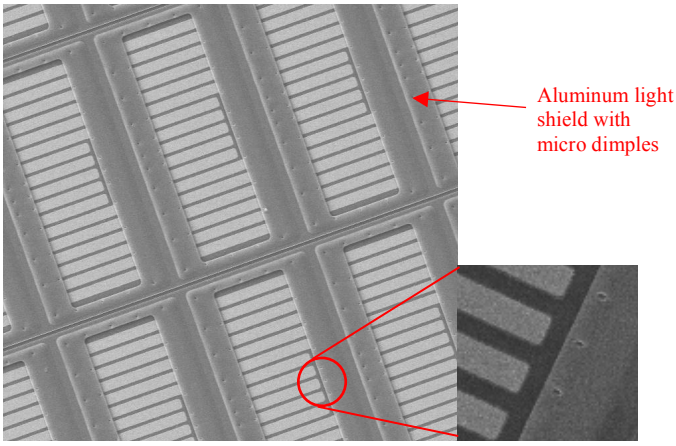

Figure 2: A SEM image of the MSA with aluminum light shields that prevent light passing through the perimeters around the microshutters. There are 1 μm wide and 0.25 μm deep dimples of the light shield bumps to prevent the stiction of the microshutters to the light shields. A close-up photo of the bumps is shown.

978-1-940470-03-0/HH2018/$25©2018TRF
DOI 10.31438/trf.hh2018.35

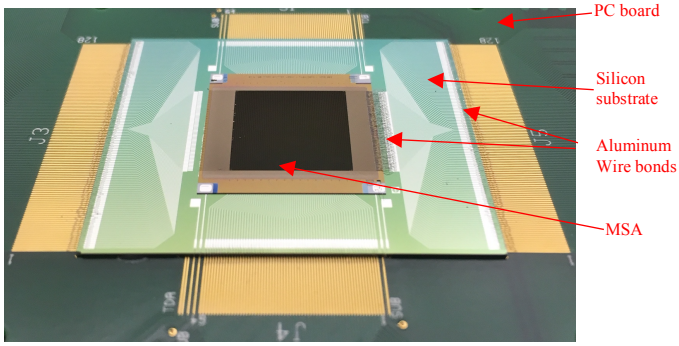

Figure 3: A photo of a sub-assembly of the MSA. The MSA is flip-bonded to a silicon substrate with indium bumps. The front side of the MSA is flip-chip bonded to the substrate electrodes. Thus, the back side of the MSA is shown in the photo. The MSA and the substrate is glued to a PC board with an epoxy. Aluminum wire-bonds are used to connect the back electrodes of the MSA to the substrate and the substrate electrodes to the PC board.

Lastly, in order to open a microshutter electrostatically, we applied a pulsed DC voltage on the front electrode and a DC voltage to the back electrode as shown in Figure 4. The front side electrodes run vertically and separated by 2 μm gap in aluminum while the back side electrodes run horizontally. The back electrodes are individually separated by gaps in aluminum electrodes. Previously in the JWST MSA, we had used e-beam deposited alumina as an electrical insulator for the back electrodes. Even with 1 μm thick e-beam alumina, the resistance and breakdown voltage were still low. Thus, we decided to deposit alumina in an atomic layer deposition (ALD) system. Incorporating the ALD alumina required a development of a new fabrication process on the back side.

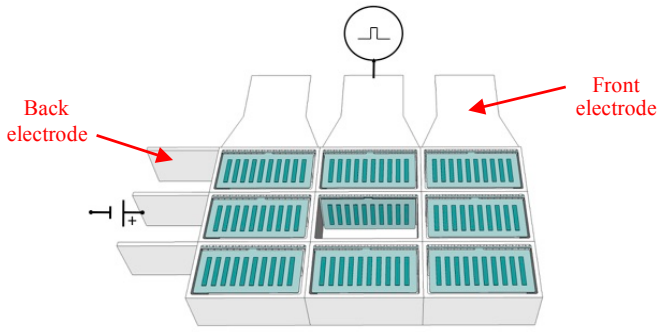

Figure 4: An illustration of how a microshutter is individually actuated: a pulsed DC voltage is applied to the front electrodes (top), and a DC voltage is applied to the back electrodes (left). The front electrodes run vertically while the back electrode runs horizontally.

FABRICATION PROCESS

For the MSA fabrication, first, we thermally grew a thin layer of silicon oxide on a silicon-on-insulator (SOI) wafer; the buried silicon oxide, device, and handle silicon layers were 3000 Å, 100 μm, and 350 μm thick, respectively. This silicon oxide was used as an etch stop during a silicon etch in a deep reactive etching system (DRIE). Then, a layer of low pressure chemical vapor deposition (LPCVD) silicon nitride was deposited; the stress was between 80 – 150 MPa (tensile).

A layer of aluminum was deposited in an e-beam deposition system. Then, the aluminum was etched in an aluminum etchant (FujiFilm E-6) at 45 °C for the front electrodes. The columns of the aluminum electrodes were patterned and separated by 2 μm gap in aluminum. The silicon nitride was etched in a reactive ion etch (RIE) system with tetrafluoromethane (CF_4) to form the microshutters. A layer of molybdenum nitride was deposited in a sputter deposition system to make the microshutters flat. The compressive stress of the film was between 200 – 400 MPa. The film was photo-lithographically patterned in strips and etched in a diluted nitric acid (deionized water: nitric acid = 1:1) at room temperature. Even though the stress of the aluminum was only around 50 MPa (compressive), there was only slight bowing on the microshutters. However, we observed twisting of the microshutters. Thus, the strips of the molybdenum nitride corrected the twisting and made the bilayer flat. Also, the molybdenum nitride was used as bonding pads in one of our packaging steps: the indium flip-chip bonding.

After the front side processing was complete, the wafer was temporarily bonded to a Pyrex wafer using an acetone soluble wax (Crystalbond 509); the Pyrex wafer was used to perform a back-to-front photolithography alignment. In order to prevent the microshutters getting stuck to the silicon frames, the tolerance of the back to front alignment had to be within 1.5 μm. Then, the handle silicon was thinned down to 100 μm in a lapping system and then completely removed in a DRIE system to expose the buried oxide.

On the back side, the buried silicon oxide was first photo-lithographically patterned and dry etched in a RIE system using CF_4. The buried silicon oxide was used to create 6 μm deep and 20 μm wide silicon trenches in the 9 μm wide silicon frame. The silicon frame is first etched in a deep reactive etching system (DRIE) as shown in the step 1 of Figure 5. Then, the photoresist used for the DRIE etch mask was stripped, and the previously patterned silicon oxide was used as a hard mask to etch the silicon trenches 6 μm deep. The trenches were used to separate back electrodes when the subsequent aluminum was deposited at an angle. Figure 6 shows a SEM image of the back side of the MSA and an optical photograph of the separation of the aluminum on bottom of the trench. On the back walls, when the microshutters were held open, we found out that some microshutters were stuck to the smooth walls. Thus, the ribs in the back walls were designed to reduce the microshutter contact surface area and etched to prevent the stiction.

On the back walls, a layer of alumina was deposited conformably using trimethylaluminum (TMA) and oxygen plasma at room temperature in an ALD system to insulate the back side of walls as shown in the step 2 of Figure 5. We needed to keep low temperature because the wafer was still bonded to the Pyrex with the wax, which softens around 70 °C.

On top of the alumina, a layer of aluminum was deposited at an angle in an e-beam deposition system to create the electrodes only on the back walls as shown in the step 3 of Figure 5. On top of the aluminum, a layer of silicon oxide was deposited at a different angle in the same e-beam system as shown in step 4 of Figure 5. The difference in the deposition angles was to cover the aluminum electrode completely with the silicon oxide. The silicon oxide was used as a hard mask for the subsequent dry etch of the alumina in the step 5 of Figure 5. The alumina was only etched behind the microshutter blades with boron trichloride (BCl_3) in an inductively coupled plasma (ICP) RIE system.

The MSA arrays were first release in acetone and rinsed in methanol, and then all the microshutters were freed by removing the thermal silicon oxide in a vapor HF system; the hard mask of the e-beam deposited silicon oxide was also removed in vapor HF. We found out that the vapor HF does not etch either aluminum or molybdenum nitride.

Lastly, in order to further prevent the stiction of the microshutters to either the silicon back walls or the aluminum light shields, we deposited a monolayer of a hydrophobic film: ALD perfluorodecyltrichlorosilane (FDTS). We measured the thickness to be 10 – 20 Å, and the water contact angle to be 108 º on monitor silicon wafers.

For the silicon substrate fabrication, we grew a layer of silicon oxide. Then, we deposited a layer of aluminum in an e-beam system and patterned aluminum with the E-6 aluminum etchant. A layer of molybdenum nitride was deposited in a sputter system and pattered in the diluted nitric acid as shown in the step A in Figure 5. The molybdenum nitride was use as the indium bonding pads. A thick layer of indium (~ 7 μm thick, 10 x 10 μm^2 big) was deposited in a thermal evaporator and lifted off using a thick photoresist (AZ 9245) as a mask as shown in the step B in Figure 5. The thermal silicon oxide was patterned using CF_4 in an RIE system with a thick photoreist, and then silicon is etched through as shown in the step C in Figure 5. Figure 7 shows a SEM photo of the patterned indium and optical photos of the patterned aluminum and silicon on the substrate. The silicon openings are smaller than the perimeters of the microshutters to block the light leak. The front sides of the MSA and the silicon substrate are flip-chip bonded using multiple indium bumps per electrical contact pad by applying 90 N to the entire MSA (6 mN per indium bump) at room temperature. The surface of the silicon sustrate was cleaning with forming gas (N_2/H_2) in a RIE system. When the two layer were pressed by 90 N, the indium bumps were squeezed to 5 μm tall. Thus, we had to make sure that there were no particle bigger than 5 μm tall on the surface. The aluminum electrodes of the both MSA and substrate run vertically, and they were connected by the indium bumps as shown in the step D in Figure 5. Thus, the same voltage was applied to the both, and they repel each other. The back side electrdoes on the MSA are wire bonded using aluminum wires to the aluminum pads on the substrate while the front side is connected with indium pads.

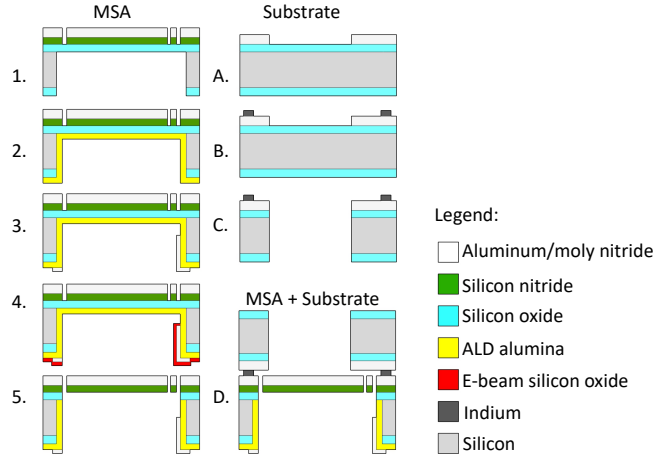

*Figure 5: An illustration of the fabrication process of the MSA and the silicon substrate. 1: For the **MSA**, aluminum, molybdenum nitride, and silicon nitride are patterned on the front side (top). Silicon is etched in a DRIE system from the back side (bottom). 2: ALD aluminum oxide is deposited as an insulator. 3: E-beam aluminum is deposited at an angle for the back side electrodes. 4: E-beam silicon oxide is deposited at an angle. 5: The ALD aluminum oxide is only etched on the bottom in a RIE system, and silicon oxide is removed in vapor HF. A: On the **silicon substrate**, aluminum and molybdenum nitride are deposited and patterned on top of silicon oxide. B: Indium is deposited and lifted off. C: Silicon oxide and silicon are etched. D: Both front sides of the MSA and the substrate are flip-chip bonded.*

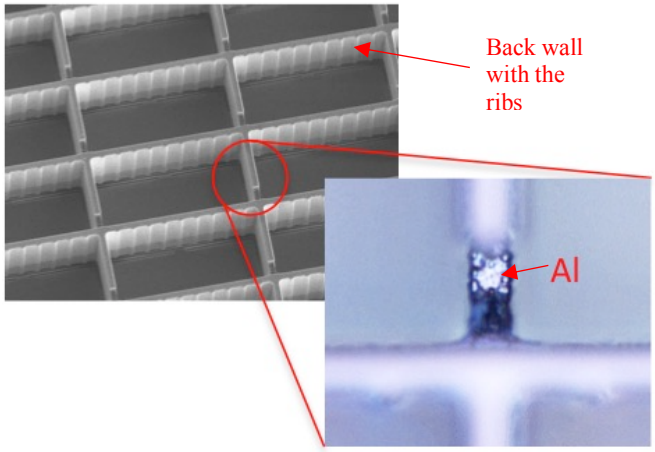

Figure 6: A SEM photo of the back walls with trenches. The close-up photo shows that the aluminum is not continuous on the bottom of the trench. Thus, each back electrode running horizontally is separated.

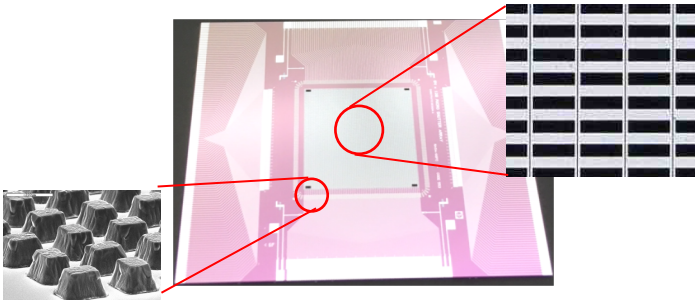

Figure 7: A photo of the silicon substrate with the light shield. The close-up photo (right) with aluminum electrodes are shown. The white columns are the patterned aluminum, and the black is the etched silicon. The close-up photo (left) shows a SEM photo of the indium bumps (7 μm tall and 10 x 10 μm^2 big) on the molybdenum nitride pads.

DISCUSSION

In the new back side fabrication process, we utilized the ALD alumina as the insulation layer between the aluminum back electrodes and silicon walls to replace the e-beam deposited alumina that was used in the previous JWST MSA fabrication. The e-beam deposited alumina was not a reliable insulator for the electrostatic actuation of the microshutters; even though the film was 1 μm thick, the resistance was in 1- 10 MΩ range, and the breakdown voltage was around 40V.

Unlike the e-beam deposited alumina, the ALD alumina was very dense and conformal. Thus, the step coverage over the silicon back walls were much better than that of the e-beam alumina. This explains improved the measured resistance of the ALD alumina on the back side of the silicon walls etched in the DRIE step: the resistance was over 1 GΩ. This also increased the breakdown voltages as shown in Figure 8; the breakdown voltage of 1150 Å and 2340 Å thick of ALD alumina were around 60 and 120 V, respectively while 1 μm thick e-beam alumina was only around 40 V.

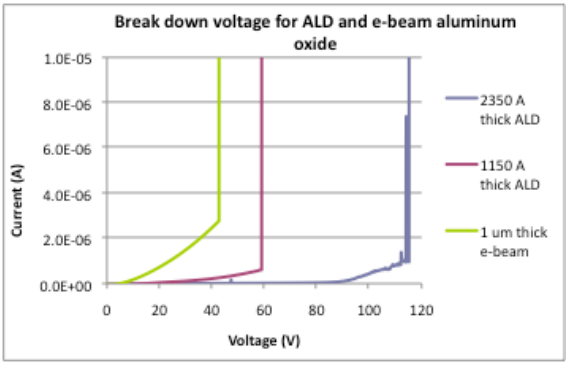

Figure 8: A breakdown voltage comparison by performing I-V curves on 1 μm thick e-beam deposited aluminium oxide, 1150 Å and 2350 Å thick ALD aluminium oxide. The films were deposited on the flat surface of silicon wafers, and 1x1 mm² of 5000 Å thick e-beam aluminium was deposited for this experiment. The breakdown voltage of 1150 Å, 2350 Å thick ALD, and 1 μm thick e-beam alumina are around 60 V, 120 V, and 40 V, respectively.

For the applications in NASA flight missions, we need to keep an operating voltage below 150 V. The JWST MSAs were fabricated on 5000 Å thick silicon nitride. Our finite element analysis model using COMSOL and micro-mechanical force measurements agreed that reducing the silicon nitride from 5000 Å to 2500 Å resulted in the reduction of the stiffness of the silicon nitride by the approximate factor of four [3]. Thus, the microshutters opened with a short DC pulse of 100 V with 200 microsecond duration to the front electrode. When the microshutters opened with the DC pulse, a DC voltage on the back electrode was applied to bring the microshutters to the back electrode and held the microshutters open. The required back electrode voltage was -25 V [4]. During the actuation, the silicon frame on the MSA and silicon substrate are grounded.

The aluminum light shields on the MSA involves 3 lithography steps: a sacrificial photoresist layer, partially exposed light shield bumps (2500 – 5000 Å deep) on the sacrificial photoresist, and an aluminum pattern over the sacrificial photoresist. By moving the light shield structure to the silicon substrate, we could save a lot of fabrication time and improve the fabrication yield.

We also fabricated the silicon substrate without the aluminum electrode running parallel to the front electrodes. However, the microshutters never opened; the microshutters were attracted to the silicon frame on the silicon substrate. Thus, we learned that the light shields needed to have aluminum electrodes the same voltage as the front electrodes of the MSA.

RESULTS

The MSA with the silicon substrate with the light shields was successfully opened and closed. With the actuation scheme discussed above, we were able to open microshutters selectively as shown in Figure 9. Because completing packaging of a PC board and the sub-assembly of the MSA and the substrate with the light shield takes a tremendous effort, these pictures were taken with the MSA without the light shield. The white pixels are where the microshutters were held open while a back illumination was lit; the black background shows that the microshutters stay closed thus block the light.

Figure 9. A photo of the microshutters selectively opened with a back light illumination. These photos were taken with the MSA without the light shields. Thus, there were light leaks around the perimeters of the microshutters.

CONCLUSION

We successfully fabricated the electrostatically actuated microshutter arrays flip-chip bonded to the silicon substrate with the light shields using indium bumps. The array size of the MSA was 64 x 128. The microshutters opened with a 100 V DC pulse and stayed open with -25 V on the back electrode. In order to achieved the electrostatic actuation, we came up with an optimum thickness of silicon nitride. Also, we used the ALD alumina for the insulation on the back electrodes. The use of ALD alumina improved the electrical resistance up to three orders of magnitude and increase the break down voltage. Lastly, the ALD coating of the FDTS film further prevented the stiction of the microshutters to the front and back side.

FUTURE WORK

For the future NASA flight missions, we are currently developing a big array size of 420 x 840 measuring 90 x 90 mm² on 6" wafers. Also, we are redesigning the shapes of the microshutters to optimize the fabrication and the actuation.

So far, all the lithography steps were performed using chromium contact masks in either Suss MA6 or MA8 aligner. Our design rules were limited by how small of a feature we can expose and develop. Also, our fabrication yield was limited to how well we can align in a contact lithography aligner especially the back to front alignment. Currently, we are migrating our alignments and exposures to a Heidelberg direct laser writer. We are expecting to write features smaller than 1 μm and improve the front to front and back to front alignments with less than 1 μm accuracy. Thus, we are expecting to make much bigger arrays with a higher production yield.

REFERENCES

[1] M. J. Li, A. D. Brown, A. S. Kutyrev, S. H. Moseley, and V. Mikula, "JWST Microshutter Array System and Beyond," Proc. SPIE 7594, 2010, 1-9.

[2] M. J. Li, T. Adachi, C. A. Allen, S. R. Babu, S. Bajikar, S., et al., "Microshutter Array System for James Webb Space Telescope," Proc. SPIE 6687, 2007, 1-13.

[3] D. E. Burns, J. S. Jones, and M. J. Li, "Mechanical Behavior of Microelectromechanical Microshutters," Proc. SPIE 9170, 2014.

[4] D. E. Burns, L. H. Oh, M. J. Li, D. P. Kelly, A. S. Kutyrev, and S. H. Moseley, "2-D Electrostatic Actuation of Microshutter Arrays," Journal of Microelectromechanical Systems, Vol: PP, Issue: 99, 2015, 1-7.

CONTACT

*Lance Oh, Lance.H.Oh@nasa.gov

FABRICATION AND CHARACTERIZATION OF 3D PRINTED, 3D MICROELECTRODE ARRAYS WITH SPIN COATED INSULATION AND FUNCTIONAL ELECTROSPUN 3D SCAFFOLDS FOR "DISEASE IN A DISH" AND "ORGAN ON A CHIP" MODELS

Nilab Azim[1, 2], Tariq Ausaf[1, 3], Avra Kundu[1], Lei Zhai[1, 2] and Swaminathan Rajaraman[1, 3, 4, 5]*

[1]NanoScience Technology Center (NSTC), [2]Department of Chemistry, [3]Department of Electrical & Computer Engineering, [4]Department of Material Science & Engineering, University of Central Florida, Orlando, FL 32826, USA

[5]Bridging the Innovation Development Gap (BRIDG), Neo City, FL 34744, USA

ABSTRACT

We demonstrate a new fabrication technology for 3D Microelectrode Arrays (MEAs) to stimulate and record electrophysiological activity from cellular networks *in-vitro*. Electrospun Polyethylene Terephthalate (PET) 3D scaffolds are coupled to the fabricated MEAs which make them fully functional for "disease in a dish" and "organ on a chip" models to promote cell/tissue growth and regeneration. The microfabrication technology involves 3D towers realized by 3D printing and a metallization layer, defined by stencil mask evaporation techniques. Multiple insulation strategies are reported: a drop-casted/spin-coated 3D layer of Polystyrene (PS) and an evaporated layer of SiO_2, both of which are laser micromachined to realize the 3D microelectrodes.

INTRODUCTION

Microelectrode array (MEA) technology is a highly popular and widely used platform for recording and stimulating electrical activity in electrogenic cells such as neurons, cardiomyocytes, pancreatic beta cells etc. for both *in vitro* and *in vivo* applications [1]. In MEA electrophysiology, the quality of the extracellular recording of electrical signals strongly depends on the interfacial contact between the electrogenic cells and the microelectrodes. Additionally, spike activity from a neuron can only be detected up to a distance of <100µm from the planar surface [1]. Thus, the distance between the isopotential source and electrode is typically in the range of 50-100µm, making it essential for the microelectrodes to have high spatial resolution, which is achieved utilizing electrodes that are typically ~30µm in diameter with small inter-electrode distances (200µm). Microfabrication technologies are apt for realizing such designs and thus 3D MEAs have primarily been realized with silicon microassembly or complex glass-based approaches [2]. This however restricts monolithic MEA fabrication technologies to be predominantly two-dimensional (2D) since lithographic techniques on non-planar surfaces is particularly challenging [3], [4]. Absence of 3D functionality in MEAs without complex processes makes them inadequate to capture signals that occur at a certain height when cultures mature to obtain a 3D form. Additionally, the realization of a suitable insulation layer for such 3D electrodes has always remained a challenge due to diverse topographies for conformal deposition of biocompatible materials with a low thermal budget.

Tissue-specialized extracellular matrix (ECM) plays a key role in tissue homeostasis, cell attachment, growth, proliferation, differentiation, morphology, polarization, directional motility, migration and cell spreading [5]. As the tissue environment is essentially three-dimensional (3D), there is an increasing need to extend cell culture matrices, support scaffolds and microelectrodes to 3D as well. While some cells are able to synthesize all required ECM components, others require an external source, particularly when grown in serum-free culture. Therefore the synthetic ECM must mimic the extracellular environment of the host as best as possible [6]. This would reduce the large mismatch between chemical, biomechanical and textural properties of cells and synthetic interfacing devices such as MEAs. As a result, a more stable and functionally predictable interfacial interaction between the cell and its environment, especially ECM, has a profound effect on cell phenotype and fate. Therefore, the chemical, topographical and elastomechanical properties of non-biological substrate surfaces that are supposed to be in intimate contact with cells or tissue needs careful engineering.

Additive manufacturing has recently shown the potential to transform microengineering with its ability to realize true 3D structures monolithically. Such additive manufacturing involves a layer by layer construction of the designed 3D geometry using a 3D printer. Among the various 3D printing technologies, stereolithography (SLA) based 3D printing provides a balance between the print resolution, print time, build volume and cost. SLA 3D printers are inexpensive, benchtop systems typically found in makerspaces, which are providing a growing alternative to clean rooms for realization of nanobiosensors, biomedical micro-electro-mechanical systems (BioMEMS) and micro-total analysis systems (MicroTAS) [7]. We have recently introduced the concept of 'Makerspace Microfabrication' [7] which was used for the realization of biological microdevices such as 2D Microelectrode arrays (MEAs), microneedles (MNs) and Microfluidic channels (MFCs). Specifically, the process described in our prior work was enabled by 3D printing, Ink Casting, Lamination and Micromachining and involved a close synergy between the additive and subtractive micromachining processes. The process described was hierarchical in nature and each subsequent process built upon the functionality provided by the preceding procedure. Due to the highly flexible and adaptive nature of 'Makerspace Microfabrication' new processes offering advanced functionalities can be added to realize other biological microdevices such as 3D MEAs. The realization of an appropriate insulation layer and a synthetic ECM material atop 3D topographies is challenging but can be addressed by adding suitable toolboxes such as benchtop drop-casting/spin-coating, and electrospinning to 'Makerspace Microfabrication'.

In this paper, we report the ***first application of 3D printing toward the microfabrication of 3D MEAs*** that are vital to the understanding of cellular models of excitable cells in a 3D microenvironment *in-vitro* mimicking *in-vivo* like conditions. The metallization of the 3D printed parts has been performed by standard physical vapor deposition techniques through a micromilled stencil mask. Two insulating strategies have been demonstrated for the metallized 3D electrodes. The first employs a drop-casted, spin-on 3D layer of Polystyrene (PS) while the second involves evaporated SiO_2, both of which have subsequently been laser micromachined to realize the recording sites on the 3D printed tower. Non-woven, polyethylene terephthalate nanofiber scaffolds (PET NFS) were

978-1-940470-03-0/HH2018/$25©2018TRF
DOI 10.31438/trf.hh2018.36

prepared by electrospinning technology on the laser micromachined 3D electrodes to mimic the fibrous proteins in native extracellular matrix towards constructing a synthetic 3D scaffold. Full spectrum impedance analysis of the fabricated electrodes confirms microelectrode behavior and Fourier Transform Infrared Spectroscopy (FTIR) analysis confirms the presence of both a drop-casted/spin-on layer and electrospun layer to be PS and PET respectively. SEM imaging has also been performed to demonstrate the geometry of the 3D printed electrode, the conformal deposition of the PS insulating layer and the PET NFS.

MATERIALS AND METHODS

The 3D MEAs were designed in Solidworks (2016 x64 bit edition, Dassault Systems Inc., Waltham, MA, USA). The MEA chip has a size of 49mm x 49mm x 1mm to ensure connectivity with the Multi Channel Systems (Reutlingen, Aspenhaustrasse, Germany) recording amplifiers. Two patches, each containing ten recording sites in the form of 3D towers were designed. The microtowers had a base diameter of 250µm and a height of 400µm. The designed CAD file was directly printed in a 3D SLA printer Form Labs Form 2 (Somerville, MA, USA) with a laser wavelength of 405 nm using a photopolymer clear resin (FLGPCL04, Formlabs, Somerville, MA, USA). The metallization of the 3D MEAs and definition of the traces (200µm wide) are performed by Ti/Au deposition through a micromilled stainless steel stencil mask. For the fabrication of the stainless steel mask a 90-degree T-8 Mill Tool (150µm-250µm diameter; T-Tech, Peachtree Corners, GA, USA) was spun at 55,000 rpm in a T-Tech J5 Quick Circuit Prototyping Systems to cut into a stainless steel sheet (80µm thick; Trinity Brand Industries, Countryside, IL, USA). In order to define the metallization layer, titanium (Ti, 4N5 purity pellets) and gold (Au, 5N purity pellets) [Kurt J. Lesker, Jefferson Hills, Pennsylvania, USA] were deposited by electron-beam (E-beam) evaporation [Thermionics Laboratory Inc., Hayward, California, USA]. The Ti and Au layers were deposited in a vacuum of 3.1 x 10^{-6} Torr to a thickness of 10 nm at a deposition rate of 1.0 nm/s and 100 nm at 1.0 nm/s, respectively. A biocompatible laminate layer (Medco®RTS3851-17 adhesives ~50 µm thick plus poly ethylene terephthalate (PET) ~20 µm thick; Medco Coated Products, Cleveland, OH, USA) is subsequently bonded to the 3D printed chip to insulate the traces thereby enabling realization of 3D tower MEAs with electrodes having a size of the entire 3D printed structure. The biocompatible laminate is additionally micromilled prior to its alignment and attachment to have openings corresponding to the size of the two patches of 3D tower arrays, each containing ten recording sites. A culture well having an inner diameter of 30mm is 3D printed and bonded using a biocompatible adhesive (Epo-tek® 353ND) to realize the final device. Figure 1 (a) depicts an exploded view of the components of the 3D MEAs along with close-up schematic of the ten recording sites in a single patch.

To realize smaller electrodes, an insulation layer is defined atop of the 3D microelectode towers [Figure 2(b)]. In the first strategy, the insulation layer was achieved by a drop-casting/spin-coating technique using polystyrene (PS). The insulation layer via drop-casting/spin-coating was obtained using a polymer solution prepared from 10% (w/v) PS (~280 kDa, Sigma Aldrich, St. Louis, Missouri, USA) dissolved in tetrahydrofuran (THF) (Thermo Fisher Scientific, Waltham, Massachusetts, USA). Approximately 2 mL of 10% PS in THF solution was drop-casted to fully cover the MEA device and allowed to sit at room temperature for the solvent to evaporate to leave behind a thin film layer. The spin-coated insulation layer was defined in the same fashion: 2 mL of 10% PS was drop-casted and immediately spun before the solvent could evaporate. The solution was spun at 500 rpm for 1 minute, followed by drying at room temperature for approximately 10 minutes. In the second strategy, a manually rotated e-beam evaporation of SiO_2 pellets [4N5 purity from Kurt J. Lesker, Jefferson Hills, Pennsylvania, USA] was performed. The deposition rate was 10 nm/s with a thickness of 400 nm. These two strategies were used to define the uniform 3D insulation layer which can subsequently be selectively defined by laser micromachining [Figure 2 (c); electrodes: 30µmx30µm; a 532nm laser beam at an energy level of 1.2 mJ] utilizing QuickLaze 50ST2 (Eolite Lasers, Portland, OR, USA).

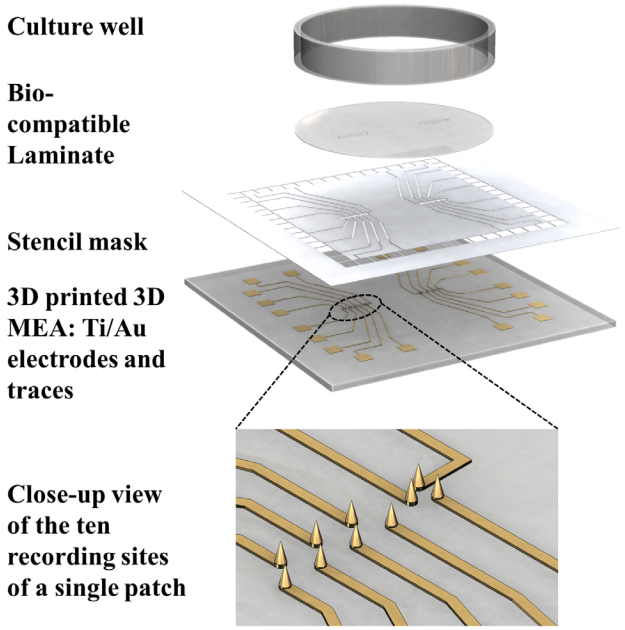

Figure 1: Exploded view of the 3D MEA: 3D microtowers, metallization, laminate insulation and containment culture well with a close-up of the ten recording sites per patch.

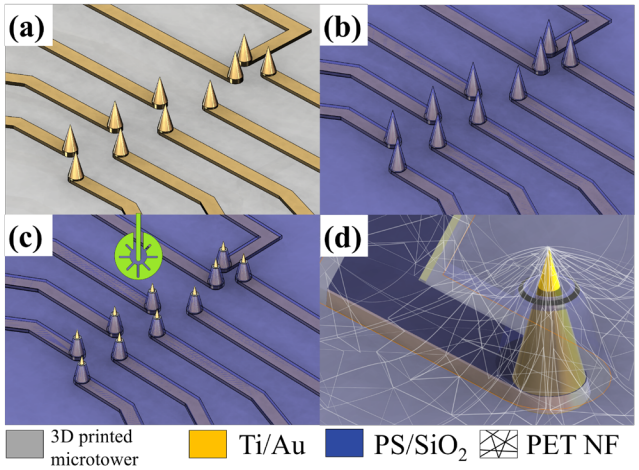

Figure 2: 3D insulation and scaffolding process flow - (a) Metallized 3D towers; (b) PS/SiO_2 insulation atop the metallized 3D towers; (c) Insulation ablation process (Laser symbol in green); (d) PET nanofiber scaffold (NFS) deposited on the insulated, laser ablated, 3D MEA.

The polyethylene terephthalate (PET) nanoscaffold [Figure 2 (d)] can optionally be defined atop either insulation layer using an

electrospinning process. This technique utilizes an electric field to produce a polymer jet from a solution [8], [9]. The polymer jet is formed when the surface tension of the solution is surpassed by the applied electrostatic charge. This jet dries during flight towards the grounded collector and is elongated by electrostatic repulsion with nearby segments of the same jet. By the time the jet reaches the collector, the solvent has evaporated and the jet has solidified into a nanofiber. Critical parameters such as the polymer of interest's molecular weight, concentration of polymer, solution properties, electrical potential between the needle and the collector, flow rate of the solution, the needle gauge and distance between the needle and the collector need to be optimized in order to achieve nanofibers with specific properties. In our work, 3D scaffolds were fabricated from PET nanofibers. The polymer solution was composed of 20% (w/w) PET (Sigma Aldrich, St. Louis, Missouri, USA) dissolved in a mixture of trifluoroacetic acid (TFA) (Thermo Fisher Scientific, Waltham, Massachusetts, USA) and dichloromethane (DCM) (Thermo Fisher Scientific, Waltham, Massachusetts, USA) having a TFA: DCM volume ratio of 70:30. Electrospinning of PET was performed using a working distance of 12 cm, an applied voltage of 10kV and a flow rate of 99 µL/hr. Figures 3 (a) and (b) show schematics of the drop-casting/spin-coating and electrospinning processes respectively.

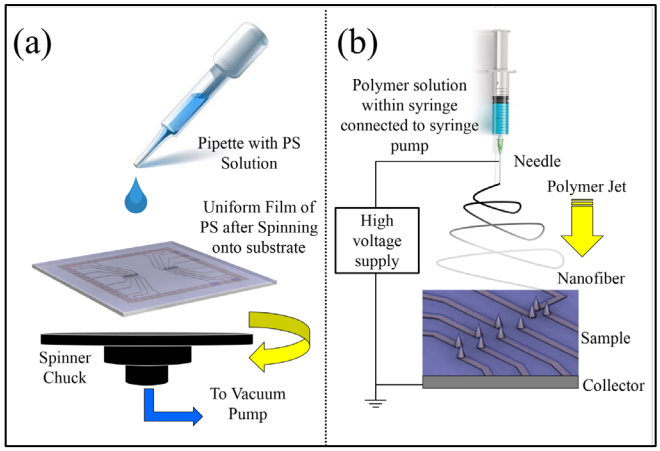

Figure 3: (a) Schematic of the drop-casting and (b) electrospinning techniques, both on 3D microtower arrays.

RESULTS AND DISCUSSIONS

Figure 4 shows the optical micrographs of routed, metallized microtowers with the packaged 3D MEAs depicted in the inset. At this stage the entire 3D printed tower is metallized and the size of the microelectrode corresponds to that of the 3D printed tower (base diameter: 250µm and height: 400µm). The biocompatible transparent lamination layer protects the traces from any culture solution contained in the culture well and as a result from shorting.

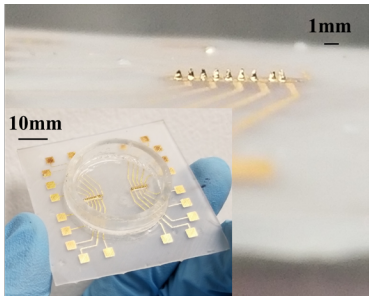

Figure 4: *3D tower MEA: final, packaged device shown in the inset.*

Figure 5 shows the SEM image of the PS insulated, metallized 3D microtower. It is observed that when the PS solution is drop-casted on the 3D printed structure, the PS forms a blanket layer atop the 3D towers as shown in Figure 5 (a) upon drying. A closer look at this image additionally reveals micropores at the base of the towers, formed due to the drop-casted PS solution being thicker around the base of the towers and during the drying of the PS solution, bubbles of the solvent (THF), escape from the PS layer leading to the observed porosity. This issue however is completely resolved when the samples are spin coated after drop casting. The PS layer is uniform and conformal with the 3D printed tower geometry [Figure 5 (b)].

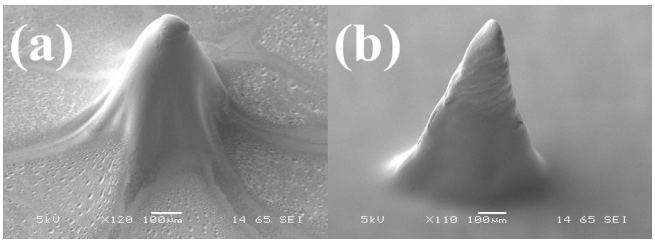

Figure 5: SEM image of 3D tower MEA coated with PS: (a) after drop-casting and (b) drop-casted and spin-coated.

Figure 6 (a) depicts a close-up SEM image of the 3D tower MEA after drop-casting and spin-coating of PS insulation. The recording site in the 3D MEA was defined by laser micromachining and the laser ablated electrode is shown in Figure 6 (b).

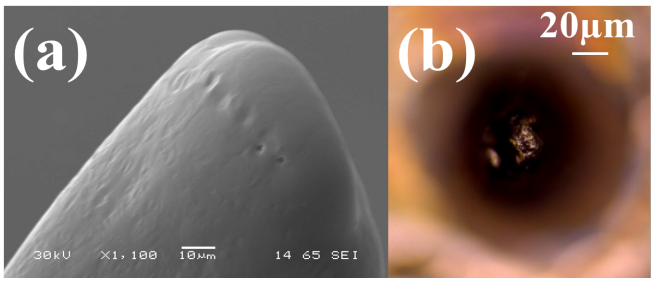

Figure 6: (a) SEM image of 3D tower tip after drop-casting and spin-coating of PS layer and (b) PS ablated 3D tower showing a recording site corresponding to a 30µm x 30µm size.

Figure 7 (a) shows the SEM image of 3D PET nanoscaffold deposited on SiO_2 insulation. It is clearly observed that the nanofibers interlink between the 3D electrodes providing effective scaffolding. Figure 7 (b) shows the close-up of the PET NFS with a fiber width of ~200-500nm.

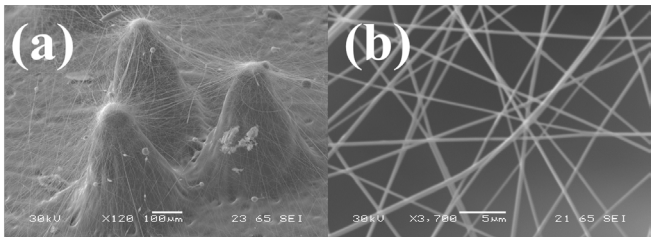

Figure 7: (a) SEM image of 3D PET NFS on SiO_2 insulation and (b) Close-up view of the NFS showing fiber width of ~200-500nm.

Figure 8 shows the FTIR analysis of the electrospun and drop-casted/spin-coated 3D layers with signature peaks of PET and PS respectively. A Spectrum 100 FTIR spectrometer (Perkin Elmer,

Waltham, Massachusetts, USA) was used to obtain the data. Some noteworthy peaks from the PS FTIR are: the 695 cm^{-1} peak from a ring bend indicating that the molecule is monosubstituted and the 748 cm^{-1} peak from C-H wag signifying a C-H bond to a benzene ring, both of which are characteristic peaks of polystyrene. One noteworthy peak for PET was the 726 cm^{-1} peak, which derives from the benzene ring's interaction with polar ester groups. The C-O peaks at 1265 cm^{-1}, 1247 cm^{-1} peak and 1101 cm^{-1} and the very prominent carbonyl peak at 1715 cm^{-1}, confirm the presence of the ester groups from PET. Finally, the peak at 2961 cm^{-1} helps confirm the presence of a methylene group to suggest that the molecule is PET.

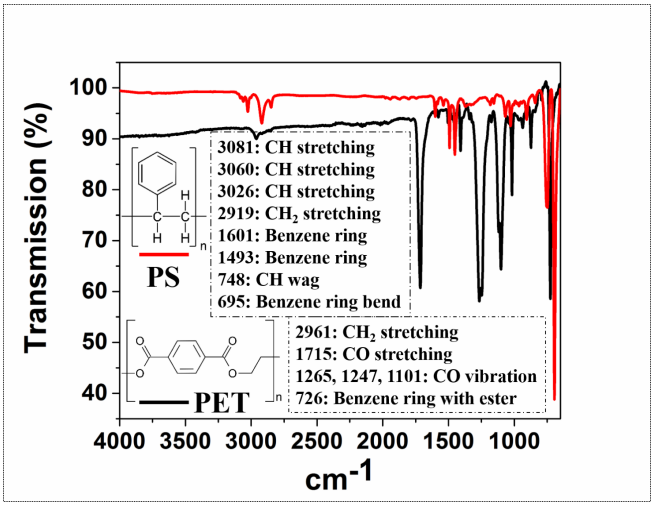

Figure 8: FTIR analysis of the spin coated and electrospun 3D MEA sample showing the distinct signature peaks for various components of both PET and PS respectively.

Impedance measurements of the MEAs were performed with the final device using Bode 100 (Omicron Labs, Houston, TX, USA) with Dulbecco's Phosphate Buffer Solution (Thermo Fisher Scientific, Waltham, MA, USA) as the electrolyte. The impedance scans were carried out from 10 Hz to 1 MHz with a platinum wire (eDAQ, Denistone East, Australia) as the counter electrode. Table 1 depicts the impedance and phase characteristics of the metallized 3D towers, SiO_2 ablated 3D MEA with scaffolding and PS ablated insulation showing comparable properties to others reported values in literature [10], [11].

Table 1: Summary of real part and phase of impedance of the various 3D MEAs developed at electrophysiologically relevant frequencies.

MEA type	Impedance (Ohms)			Phase (degrees)		
	100Hz	*1kHz*	*10kHz*	*100Hz*	*1kHz*	*10kHz*
3D microtower	6.7k	5.3k	4.1k	-50	-15	-10
SiO_2 laser micromachining	80.2k	52.1k	12.2k	-15	-12	-10
PS laser micromachining	47.6k	36.8k	10.3k	-20	-15	-10

CONCLUSIONS

Our fabrication process is capable of rapidly realizing 3D MEAs which are highly versatile and fully functional for *in-vitro* applications. With a union between makerspace microfabrication coupled with standard microfabrication technologies as needed, we have demonstrated the realization of 3D tower MEAs of base dimeter=250µm and height=400µm. The electrodes sizes can be reduced after either evaporating a SiO_2 layer or drop-casting/spin-coating of PS solution, both of which can subsequently be laser micromachined. Additional development of biocompatible 3D scaffolds atop the 3D MEAs provides for a device ready for "disease in a dish" and "organ on a chip" applications of cell/tissue growth, proliferation and long-term cultures *in-vitro*.

REFERENCES

[1] R. Kim, S. Joo, H. Jung, N. Hong, and Y. Nam, "Recent trends in microelectrode array technology for in vitro neural interface platform," *Biomed. Eng. Lett.*, vol. 4, no. 2, pp. 129–141, Jun. 2014.

[2] P. Ruther *et al.*, "The NeuroProbes Project-Multifunctional Probe Arrays for Neural Recording and Stimulation," *Proc. 13th Annu. Conf. IFESS, Sept.21-25, Freiburg, Ger.*, vol. 53, pp. 238–240, 2008.

[3] S. Rajaraman, S.-O. Choi, M. A. McClain, J. D. Ross, M. C. LaPlaca, and M. G. Allen, "Metal-Transfer-Micromolded Three-Dimensional Microelectrode Arrays for in-vitro Brain-Slice Recordings," *J. Microelectromechanical Syst.*, vol. 20, no. 2, pp. 396–409, Apr. 2011.

[4] S. Rajaraman *et al.*, "Microfabrication technologies for a coupled three-dimensional microelectrode, microfluidic array," *J. Micromechanics Microengineering*, vol. 17, no. 1, pp. 163–171, Jan. 2007.

[5] A. Blau, "Cell adhesion promotion strategies for signal transduction enhancement in microelectrode array in vitro electrophysiology: An introductory overview and critical discussion," *Curr. Opin. Colloid Interface Sci.*, vol. 18, no. 5, pp. 481–492, Oct. 2013.

[6] P. Zorlutuna *et al.*, "Microfabricated Biomaterials for Engineering 3D Tissues," *Adv. Mater.*, vol. 24, no. 14, pp. 1782–1804, Apr. 2012.

[7] A. Kundu, T. Ausaf, and S. Rajaraman, "3D Printing, Ink Casting and Micromachined Lamination (3D PICLµM): A Makerspace Approach to the Fabrication of Biological Microdevices," *Micromachines*, vol. 9, no. 2, p. 85, Feb. 2018.

[8] J. Lannutti, D. Reneker, T. Ma, D. Tomasko, and D. Farson, "Electrospinning for tissue engineering scaffolds," *Mater. Sci. Eng. C*, vol. 27, no. 3, pp. 504–509, Apr. 2007.

[9] N. Bhardwaj and S. C. Kundu, "Electrospinning: A fascinating fiber fabrication technique," *Biotechnol. Adv.*, vol. 28, no. 3, pp. 325–347, May 2010.

[10] C. Nick, S. Yadav, R. Joshi, J. J. Schneider, and C. Thielemann, "A three-dimensional microelectrode array composed of vertically aligned ultra-dense carbon nanotube networks," *Appl. Phys. Lett.*, vol. 107, no. 1, p. 13101, Jul. 2015.

[11] G. S. Guvanasen *et al.*, "A Stretchable Microneedle Electrode Array for Stimulating and Measuring Intramuscular Electromyographic Activity," *IEEE Trans. Neural Syst. Rehabil. Eng.*, vol. 25, no. 9, pp. 1440–1452, Sep. 2017.

CONTACT

*Swaminathan Rajaraman; Ph:+1-407-823-4339; Email: Swaminathan.Rajaraman@ucf.edu

FABRICATION OF SUB-MICRON METAL WIRES FOR HIGH-FREQUENCY LITZ WIRE

Kasey J. Russell[1], Aykut Aydin[2], David J. D. Carter[1], Ernest Kim[1], Peter H. Lewis[1], Lu Sun[3], Xian Gong[3], Christina Chang[2], Roy Gordon[2,3], and Amy Duwel[1]*

[1] The Charles Stark Draper Laboratory, Inc., Cambridge MA, USA

[2] Department of Chemistry and Chemical Biology, Harvard University, Cambridge MA, USA

[3] John A. Paulson School of Engineering and Applied Sciences, Harvard University, Cambridge MA, USA

ABSTRACT

At GHz frequencies and above, ohmic losses associated with μm-scale skin depth limit the maximum quality factor, Q, that can be achieved in inductors. We demonstrate fabrication of sub-micron diameter wires over centimeter-scale lengths from a wide variety of materials including copper, gold, and platinum/palladium. By depositing metal and dielectric materials onto a high-strength nanofiber scaffold, we have made conducting wires, insulated conducting wires, and coaxial multilayer structures. Additionally, we have demonstrated the ability to manipulate sub-micron wires into ordered, twisted bundles while maintaining electrical properties.

INTRODUCTION

In radio-frequency and microwave devices, many sophisticated fabrication procedures have been developed to improve the quality factor, Q, of MEMS inductors by reducing coupling to the substrate[1]–[3]. Further improvement in Q is limited by skin effect in the metal and its associated increase in ohmic losses[3]. These ohmic losses could be reduced by using a bundle of thin, hierarchically twisted wires (i.e. litz wire), but it is difficult to achieve the necessary topology using conventional 2D MEMS processing[4], [5]. Traditional litz wire fabrication approaches can achieve the necessary topology but cannot scale to GHz frequencies for two reasons: first, the necessary wire diameter (~1 micron and smaller) is an order of magnitude below the limit of conventional wire drawing, and second, conventional manipulation approaches are not compatible with such fragile wire.

Here we demonstrate methods to overcome both wire fabrication and wire manipulation limitations of conventional approaches. We first demonstrate a method to fabricate sub-micron diameter wires over centimeter-scale lengths. Rather than form fine wire by reducing the diameter of larger wire, as is done in traditional drawing, our approach leverages MEMS fabrication techniques to deposit the desired wire material onto a high-strength nanofiber scaffold. Using this method, we have made conducting wires, insulated conducting wires, and coaxial multilayer structures. We then demonstrate the ability to manipulate sub-micron wires into ordered, twisted bundles while maintaining electrical properties. Using fluid drag, we are able to apply sufficient tension to the wires to enable manipulation and plastic deformation without risk of fracture.

The paper is organized as follows: In the Theory section, we provide a brief overview of the skin effect and its implications. In the Wire Fabrication section, we show preparation of individual centimeter-length nanofiber scaffolds formed via electrospinning from poly(m-phenylene isophthalamide). By varying process parameters, we are able to achieve uniform individual nanofibers of diameters ranging from 300 nm to 600 nm. We then show methods to fixture arrays of nanofibers to enable deposition through a variety of processes including physical vapor deposition, chemical vapor deposition, and atomic layer deposition. Finally, in the Wire Manipulation section, we show how hydrodynamic flow fields can be utilized to tension and maintain absolute position of individual wires, allowing the manipulation of insulated, metal-coated nanofibers into centimeter-long bundles of twisted wires. Further, we demonstrate that the process can be continued hierarchically, forming twisted bundles of twisted bundles (as in conventional litz wire). Finally, we show how these techniques provide a path to nanoscale, GHz frequency litz wire.

THEORY

Skin effect and the related proximity effect have been known since the 1800s. As described by Maxwell's equations, a time-varying current in a conductor induces time-varying magnetic fields, which in turn induce time-varying electric fields and currents that can oppose the flow of current through the conductor. At sufficiently high frequencies, the current through the core of a conductor is suppressed, and power is conducted primarily in an outer layer whose thickness, called the skin depth δ, is given by the equation

$$\delta = (\rho/\pi f \mu)^{1/2}, \quad (1)$$

where ρ and μ are the resistivity and magnetic permeability of the conductor, respectively, and f is the frequency of the time-varying current.

As illustrated in Fig. 1, skin effect greatly reduces the fraction of the wire cross-section that carries current. Finite element model (FEM) simulations (COMSOL) enable quantitative analysis (Fig. 1(a-b)). For a wire with $r >> \delta$, where r is the radius of the wire, a simple estimate can be obtained by assuming the current flows only in an outer layer of thickness δ. This approximation becomes less accurate for small r, but nevertheless provides a way to quickly estimate what wire diameters are appropriate for a given frequency (Fig. 1(c)).

Confining the current to a thin surface layer at higher frequencies leads to higher resistive losses at higher frequencies. The increase in resistance versus frequency can be characterized by the 'resistance ratio' $R_R = R_{AC}/R_{DC}$, where R_{AC} is the high-frequency resistance and R_{DC} is the zero-frequency resistance. At the 5G band near 28 GHz, for example, a 58 AWG copper wire would have R_R near 10 and a typical 1 mil diameter bond wire would have $R_R \sim 20$ (Fig. 1(c)). By comparison, a single copper wire fabricated by our method would have $R_R \sim 1$.

Decreasing wire diameter can reduce R_R, but it obviously increases the absolute resistance of the wire. A solid copper wire of ~1 μm diameter has a resistance per unit length greater than 200 Ω/cm. In a real application, many such wires would be individually insulated and connected electrically in parallel to yield a low-impedance bundle. However, if the wires are simply packed in a bundle, with wires at the periphery remaining at the periphery and wires at the center remaining at the center, then proximity effect would suppress conduction in the wires located in the middle of the bundle. Proximity effect and skin effect are analogous effects that occur in stranded or continuous conductors. To mitigate proximity effect, the wires can be braided or twisted together hierarchically

978-1-940470-03-0/HH2018/$25©2018TRF
DOI 10.31438/trf.hh2018.37

such that wires 'take turns' at the center of the bundle, an arrangement known as 'litz wire'. Typically, the optimal geometry and strand diameter will depend on application, and extensive design guides have been established to aid in analysis[6].

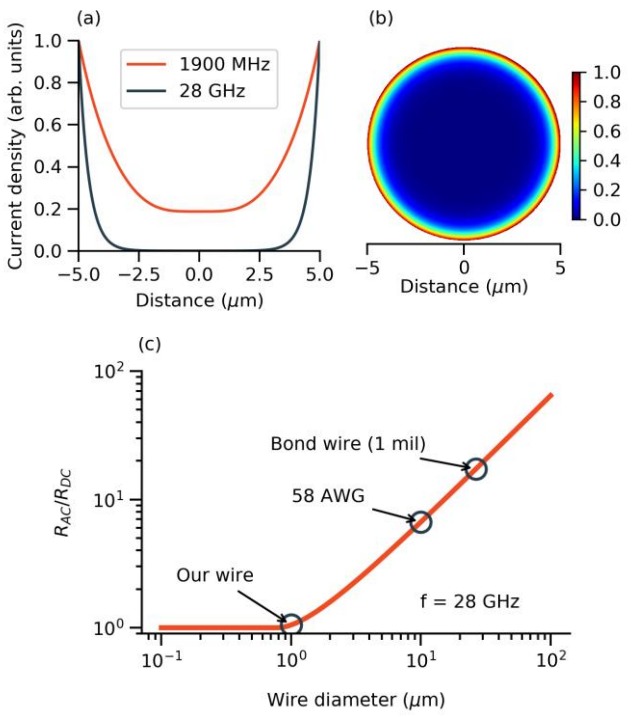

Figure 1:Illustration and ramifications of skin effect. ***(a)****,* ***(b)****, Finite element model simulations of current density in a commercial cylindrical copper wire (58 AWG, ~10 μm diameter).* ***(a)****, Normalized current density as a function of position on a section line through the center of a wire at frequencies of 1900 MHz (a common 4G wireless band) and 28 GHz (the lowest-frequency 5G Upper Microwave Flexible Use service band).* ***(b)****, Normalized current density at 28 GHz.* ***(c)****, Analytical estimate of resistance ratio $R_R = R_{AC}/R_{DC}$ as a function of wire diameter at a frequency of 28 GHz.*

As can be seen in Fig. 1, skin effect leads to significant losses at GHz frequencies, even in the smallest available commercial wire. To enable development of low-loss conductors for future high-frequency technologies, such as communication on the 5G band at 28 GHz, a new technology for litz wire is needed that is compatible with individual strands of diameter near ~1 μm.

WIRE FABRICATION

Our wire fabrication process consists of conformal deposition of metallic and dielectric layers onto a nanofiber scaffold core (Fig. 2). For the nanofiber core, the polymer poly(m-phenylene isophthalamide) (PMIA, trade name Nomex) was selected for its high strength as well as its ability to withstand process temperatures up to 350 °C (Sigma Aldrich). PMIA was dissolved into a solution of $CaCl_2$, loaded into a syringe in a commercial electrospinning apparatus (EC-CLI, IME Technologies), and accelerated toward a rotating spoked-drum collector via a high-voltage bias (typically 6-12 kV). Electrospinning was performed in an environmentally-controlled chamber with a continuous flow of dried air. The morphology of resulting nanofibers varied with humidity, with higher humidity conditions yielding ribbon-like nanofibers and lower humidity (water content below 3 g/m^3) yielding cylindrical nanofibers.

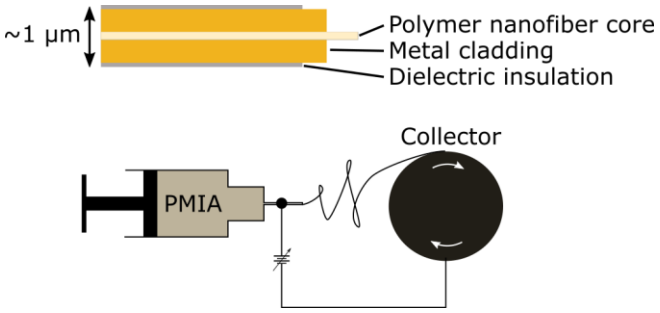

Figure 2: Top: Schematic illustration of target wire geometry for an insulated metal wire of total diameter ~1 μm. Bottom: Schematic illustration of electrospinning single, continuous nanofiber scaffolds onto a rotating spoked-drum collector.

After electrospinning, nanofiber scaffolds are transferred to rectangular fixtures for subsequent deposition of metal and dielectric layers (Fig. 3). Our process is compatible with a variety of conventional deposition processes, and we have successfully deposited layers via physical vapor deposition (PVD, both sputtering and evaporation), chemical vapor deposition (CVD), and atomic layer deposition (ALD).

Conformal deposition techniques such as CVD can in principle deposit nearly perfectly concentric layers, yet the nucleation of CVD-deposited films is very sensitive to chemical compatibility between the substrate and the deposited material. Therefore, we have predominantly fabricated the metal layer via PVD. Because deposition via PVD is inherently directional, we typically deposit material on one 'side' of the fixture, invert the fixture, and then perform a second deposition on the other side. On average, this process produces wires with substantially conformal layers (Fig. 3). Some nanofibers, however, appear to twist on their axis during deposition, resulting in wires whose nanofiber scaffold is off-center. Nevertheless, for frequencies corresponding to skin depths δ comparable to or larger than the wire radius, it is expected that there will be negligible electrical impact from wire cross-section geometry that is not perfectly concentric. The asymmetry is expected to modify mechanical properties such as bending stiffness, but we have not observed any impact on the ability to manipulate and twist wires.

An additional concern particular to our choice of PMIA as nanofiber scaffold material is the presence of large amounts of $CaCl_2$ in the nanofiber after the electrospinning process. The $CaCl_2$ improves dissolution of PMIA and enables formation of uniform, aligned nanofibers via electrospinning. As a drawback, $CaCl_2$ is hygroscopic, absorbing ambient moisture subsequent to the spinning process. This water absorption results in local swelling at $CaCl_2$ crystallites, producing protruding features along the length of the wire. The impact of $CaCl_2$ on the long-term reliability of the wires has not been established. It is likely that the $CaCl_2$ could be removed after electrospinning and before metal deposition by, e.g., immersing the nanofibers in water.

WIRE MANIPULATION

For typical metal wires, conventional manual wire manipulation strategies work well for wire diameters of ~25 μm and larger, where the tensile strength is above 0.1 N, the wire can support many grams of mass, and gravity is the strongest ambient force per unit length on the wire. Wire is typically stored on spools, and

during twisting the wire is pulled off the spools. The rotational motion that results in the twist is generated by moving the spools around each other, while tension is controlled through mechanical means (e.g., by passing the wire under a weighted pulley).

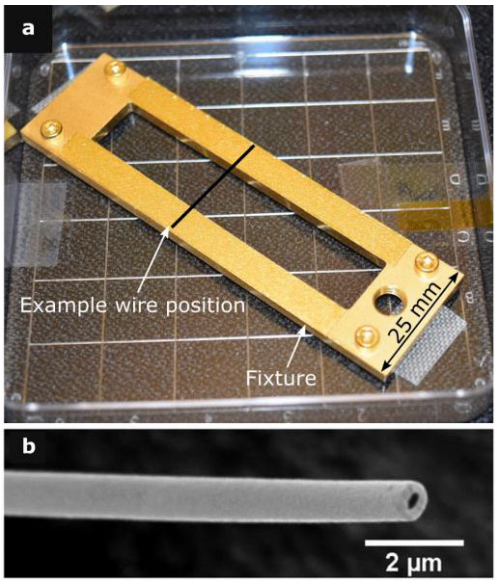

Figure 3: (a), Image of a rectangular fixture containing nine Au-coated nanofibers. Individual wires (not visible at this scale) are oriented as indicated by the black line labeled 'example wire position'. (b), Scanning electron micrograph of a Pt/Pd-coated nanofiber.

In contrast, for wires of diameter ~1 μm, gravity is several orders of magnitude weaker than other ambient forces such as static electricity and fluid drag from air disturbances, and the tensile strength is less than 300 μN. Therefore, despite the macroscopic lengths of such wires, their extremely small diameters require that new techniques be developed for manipulation. Our approach to handling and twisting differs from conventional twisting in several respects (Fig. 4). First, to reduce the influence of uncontrolled ambient forces, twisting and bundling of wires is performed while submerged in fluid. Second, tensile force is generated not mechanically but hydrodynamically by controlling fluid flow along the axes of the wires. This is accomplished by placing each wire inside a separate fluid flow channel (with one end extending out of the channel). Third, our wires are stored and inserted into the twisting apparatus in straight individual sections of ~20 mm length. Fourth, the rotational motion responsible for twisting is generated by an electric motor at the single common attachment of all wires in the bundle. It is worth noting that our approach causes each wire rotate on its axis with the same frequency as the motor, resulting in torsional strain that can lead to torsional buckling and formation of plectonemes if it is not properly mitigated (e.g. via wire tension)[7].

The force required for twisting can be estimated from simple elastostatics of bending a slender rod. For ~1 μm-diameter copper wires, twisting with a pitch of ~50 μm should require μN forces or smaller, depending on the point of application of the force. The force from axial fluid drag can be estimated as Stokes drag via the equation $F \sim 4\pi\mu l u/\ln(l/a)$, where μ is the dynamic viscosity of the fluid, u is the velocity of the fluid relative to the wire, l is the wire length over which the drag force is operating, and a is the wire radius. Using water as a fluid, we are able to twist wires into a pitch of ~50 μm using a fluid velocity of only ~1 m/min, which is

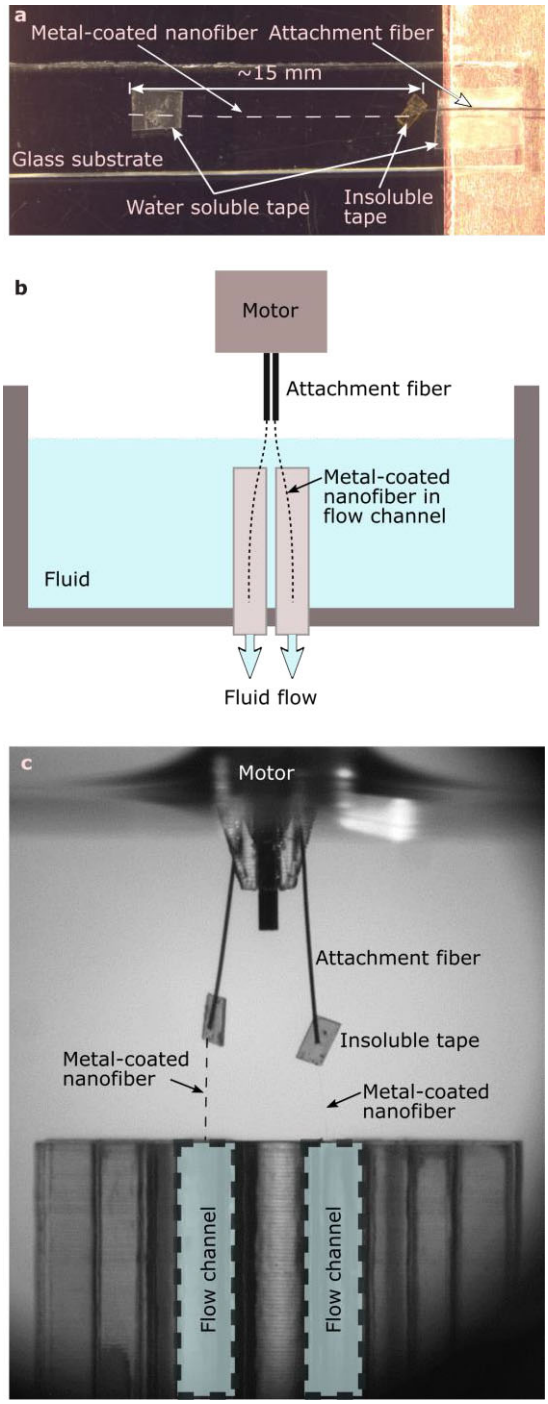

Figure 4. (a), Optical micrograph of a nanofiber (faintly visible; overlaid with dashed line) mounted on glass substrate in preparation for twisting. (b), Schematic diagram of twisting apparatus. (c), Side view image of twisting apparatus during initialization of the system prior to twisting two metal-coated nanofibers. The metal-coated nanofibers (~1 μm diameter) are nearly invisible; dashed line indicates position of the one on the left.

estimated to generate less than 50 nN of force per millimeter of wire. This value is generally consistent with the estimates above given the level of uncertainty around factors such as position of the wire within the flow channel. If needed, larger drag forces can be

generated by increasing flow rate, decreasing cross-sectional area of the channel, or using a fluid with higher viscosity.

Once each wire is isolated in its own fluid flow channel and has one end attached to the spindle of the electric motor, twisting is accomplished by slowly pulling the motor away from the assembly of fluid flow channels (i.e. in the +z direction) while the motor rotates. The pitch of the twist is primarily determined by the ratio of linear velocity to rotational velocity of the motor, provided that the tension applied to the wires is sufficient to provide the necessary bending force for a given bend radius.

While the twisting process itself is relatively straight forward, it can be challenging to achieve the necessary initial conditions of having several individual metal-coated nanofibers, each isolated in its own fluid flow channel, with one end protruding from the channel and attached to the spindle of a motor. One approach we have developed is to first anchor each metal-coated nanofiber to a separate carrier substrate (e.g. 25 mm x 5 mm x 1 mm glass) using water-soluble tape. We then attach one end of each metal-coated nanofiber to one end of a separate macroscopic fiber (e.g., ~100 μm diameter monofilament) using permanent adhesive. The carrier substrates are inserted into an assembly of adjacent flow channels, and the free end of the macroscopic fiber is then attached to the motor. Once the assembly is submerged in water, the water-soluble tape dissolves, achieving the desired initial condition.

Using this wire fabrication twisting procedure, we have successfully twisted a variety of bundles of wires (Fig. 5). The number of individual strands is limited by the number of flow channels in the apparatus, but as in conventional litz wire manufacturing, larger bundles can be assembled by heirarchically twisting bundles of twisted bundles (Fig. 5 c-e). Using this approach, we can therefore fabricate litz wire designed for operation in the GHz regime.

CONCLUSIONS

Resistive loss due to skin effect increases at high frequency, but conventional approaches to mitigating skin effect do not scale to dimensions that allow use at GHz frequencies and higher. By developing a novel bottom-up wire fabrication approach as well as a method to tension and twist micron-scale wire, we enable fabrication of high frequency conductors containing the requisite topology to mitigate skin effect at GHz frequencies.

This work is sponsored by the Air Force Research Laboratory (AFRL) and the Defense Advanced Research Agency (DARPA).

REFERENCES

[1] G. W. Dahlmann and E. M. Yeatman, "High Q microwave inductors on silicon by surface tension self-assembly," *Electron. Lett.*, vol. 36, no. 20, pp. 1707–1708, Sep. 2000.

[2] G. W. Dahlmann, E. M. Yeatman, P. R. Young, I. D. Robertson, and S. Lucyszyn, "MEMS high Q microwave inductors using solder surface tension self-assembly," in *Microwave Symposium Digest, 2001 IEEE MTT-S International*, 2001, vol. 1, pp. 329–332.

[3] C. L. Chua, D. K. Fork, K. Van Schuylenbergh, and J.-P. Lu, "High Q RF coils on silicon integrated circuits," 2003, p. 150.

[4] S. Wang, M. A. de Rooij, W. G. Odendaal, J. D. van Wyk, and D. Boroyevich, "Reduction of high-frequency conduction losses using a planar litz structure," *IEEE Trans. Power Electron.*, vol. 20, no. 2, pp. 261–267, Mar. 2005.

[5] Y. Zhao, M. Nandra, C. Yu, and Y. Tai, "Reduction of AC resistance in MEMS intraocular foil coils using microfabricated planar Litz structure," in *2012 7th IEEE International Conference on Nano/Micro Engineered and Molecular Systems (NEMS)*, 2012, pp. 234–237.

[6] C. R. Sullivan, "Optimal choice for number of strands in a litz-wire transformer winding," *IEEE Trans. Power Electron.*, vol. 14, no. 2, pp. 283–291, Mar. 1999.

[7] B. Lautrup, *Physics of Continuous Matter, Second Edition: Exotic and Everyday Phenomena in the Macroscopic World*. CRC Press, 2011.

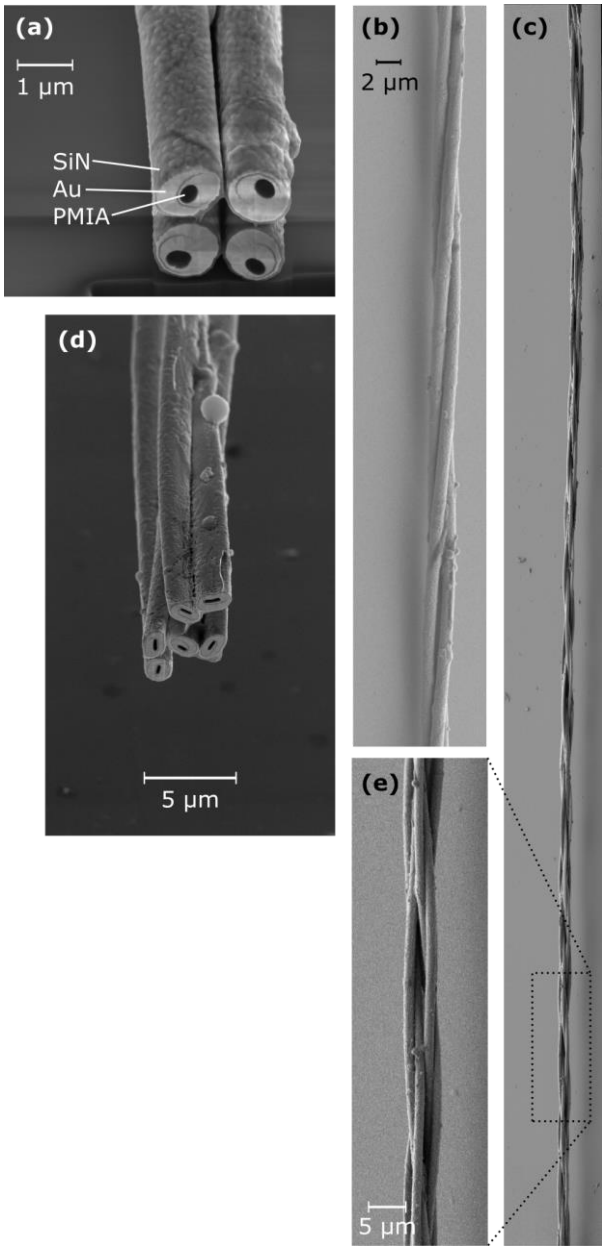

Figure 5. Scanning electron micrographs of fabricated bundles of metal-coated nanofibers. ***(a)****, Cross-section of a bundle of four Au-coated PMIA nanofibers insulated with sputtered SiN.* ***(b)****, Twisted bundle of three Au-coated nanofibers.* ***(c)****, Heirarchically-twisted bundle of three pairs of Au-coated nanofibers (six total wires).* ***(d)****, Cross-section of the bundle in (c). The non-circular geometry was the result of excessive humidity during electrospinning.* ***(e)****, Higher-resolution image of indicated region of the bundle in (c).*

CONTACT

*Kasey J. Russell, krussell@draper.com

FIRST FATIGUE MEASUREMENTS ON THICK EPI-POLYSILICON MEMS IN ULTRA-CLEAN ENVIRONMENT

Anne L. Alter[1], Ian B. Flader[1], Yunhan Chen[2], Lizmarie Comenencia Ortiz[1], Dongsuk D. Shin[1], David B. Heinz[1], and Thomas W. Kenny[1]*
[1]Stanford University, Stanford, California, USA
[2]Apple Inc., Cupertino, California, USA

ABSTRACT

This paper studies, for the first time, fatigue in vacuum encapsulated, oxide-free, thick epi-polysilicon MEMS devices. Thick epi-polysilicon is the device layer material used in more than 1B MEMS inertial sensors produced for consumer electronics and automotive safety system applications every year. The ultra-clean encapsulation process eliminates the sources of environmental effects and prevents formation of surface oxide. In these experiments, we observed fatigue failure in the absence of environmental mechanisms that have typically been linked to fatigue. These results are important due to the ongoing debate among researchers about the mechanisms for fatigue failure in micro-scale silicon MEMS devices.

INTRODUCTION

Background

Fatigue in MEMS resonators is a primary concern when considering the long-term performance and reliability of devices particularly those subject to cyclic loading, such as Coriolis gyroscopes [1]. Gyroscopes and other inertial sensors usually require high amplitude responses, which can lead to stress concentrations within their surfaces. Material failure due to fatigue occurs at stresses much lower than the fracture strength [2], so there is potential to for devices to fail under typical operating conditions.

Even though silicon is a brittle material that does not exhibit dislocation activity at room temperature and thus should not fatigue at room temperature [3], fatigue has been observed in many studies of micrometer-sized silicon. The mechanisms behind micrometer-sized silicon fatigue failure remain controversial due to difficulties in isolating and controlling all the environmental conditions that could contribute to fatigue onset.

Past research has focused on fatigue mechanisms arising from effects taking place in surficial oxides [4][5][6], and is typically studied in environments where the presence of oxygen and relative humidity are factors. The primary fatigue mechanisms that have arisen from this research are 'reaction-layer' fatigue proposed by Muhlstein et al., which requires oxidation of exposed silicon surfaces [5], and the 'subcritical cracking' model proposed by Kahn, in which surface debris, oxide, or other deformities create a wedging effect in the native silicon [6].

Fatigue has been studied in ultra-clean, encapsulated, inert environments, where relative humidity is not a factor for both smooth-walled single crystal silicon (SCS) [7][8] and oxide-coated, rough-walled SCS devices [8]. Results showed no fatigue in SCS up to 7.5GPa, a threshold twice as high as other research efforts were able to achieve. The absence of fatigue was attributed to the ultra-clean encapsulated environment, and hydrogen smoothed surfaces, and aligns with theories that propose that bulk silicon should not fatigue at room temperature. The oxide-coated SCS had a reduced threshold of 2.7GPa, which was attributed to the subcritical cracking model and discussed that introducing oxide to the environment accelerated the fatigue life of these structures by locking in surface structural defects [8].

Polycrystalline silicon (polysilicon), an amorphous form of silicon consisting of random grain boundaries and crystal orientations, has been shown to fatigue at the micrometer scale [4][5][6][9][10][11][12][13]. The polysilicon structures that have been studied are thin-films, typically <10μm, fabricated using LPCVD processes, and are coated in oxide. The structures that have fatigued have occurred in imperfect environmental conditions, although some oxide-coated polysilicon devices have shown fatigue resistance in high vacuum [10].

This work reports the first study of fatigue in vacuum encapsulated, ultra-clean, thick (40μm) epi-polysilicon structures, whose surfaces are free of oxide, and where the inert environment prevents the formation of additional surface oxide. These unique environmental conditions enable the study of intrinsic material fatigue behavior of polysilicon and is the first study of fatigue in thick epi-polysilicon, which is the device layer material used in more than 1B MEMS inertial sensors produced for consumer electronics and automotive safety system applications every year.

EXPERIMENT METHODS

Device Design and Experiment Setup

As shown in Fig. 1, a MEMS device, consisting of a Y-shaped epi-polysilicon proof mass, was biased to a DC voltage and was electrostatically actuated and sensed by a time-varying AC signal applied to the combs on the perimeter. The proof mass was attached to a notched cantilever beam, which is a point of high stress concentration and dictates the ultimate compliance of the structure. The device was driven into resonance, the signal amplified by a trans-impedance amplifier (TIA), and a phase-locked loop (PLL) was used to oscillate the device and track the frequency over time.

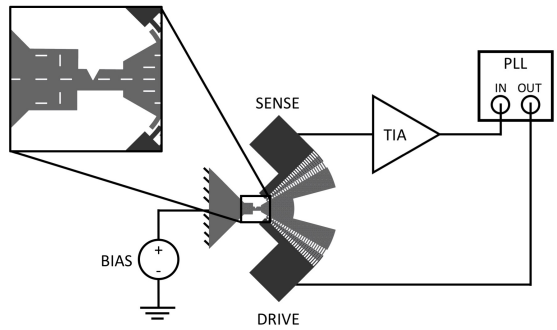

Figure 1: Y-shaped fatigue structure, which is electrostatically driven and sensed, and oscillated in a phase-locked loop. Inset shows notch geometry.

Device Fabrication

The epi-polysilicon fatigue structure was fabricated in an ultra-clean, vacuum-encapsulated package. The fabrication process [14] was derived from a large-gap SCS encapsulation process [15] and a process that incorporated a polysilicon device layer to the large gap process [16]. The device layer, a 40μm thick, N-type polysilicon film, was epitaxially deposited. During the fabrication, all oxide that had been surrounding the device layer was etched with a vapor-

978-1-940470-03-0/HH2018/$25©2018TRF
DOI 10.31438/trf.hh2018.38

phase hydrofluoric acid, releasing the device structure and leaving the device layer surfaces oxide-free. A final high temperature annealing step during device sealing caused the surfaces to roughen due to silicon migration on the randomly oriented epi-polysilicon grain structure [17]. The fabricated device structure and surface roughness are shown in Fig. 2. The surface roughness is <0.3µm which is much smaller than the notch size of just under 7µm deep.

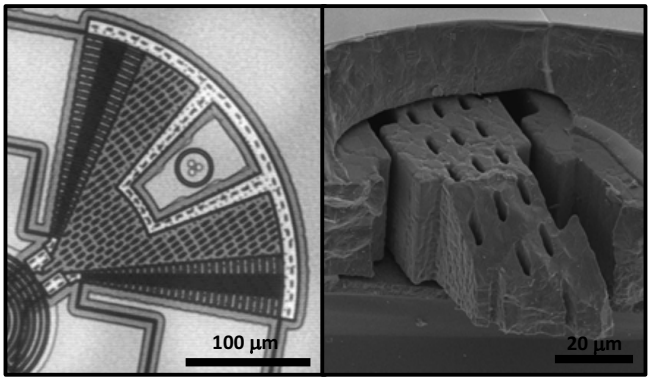

Figure 2: Infrared image of fatigue structure (left); SEM showing surface roughness of epi-polysilicon structure (right).

Experimental Procedure

Devices were biased with a constant 10V DC signal and initially driven with a low amplitude AC signal through the comb drive structures. The initial resonant frequency and phase condition were determined and a PLL was used to lock into the signal and maintain the phase condition over time. The frequency stability, a measure of device compliance and thus notch stability, was measured over 20-hour intervals. After each 20-hour interval, the drive amplitudes were increased (incremented by 50mV), thus increasing the stress at the notch, and the stability measurement was repeated. This process of increasing the AC drive voltage after 20-hour intervals was repeated until device failure.

RESULTS

Fatigue failure was observed in four epi-polysilicon devices and their results are summarized in the following figures. The figures show differing failure drift profiles, along with differing rates of accelerated frequency drift to failure. Imaging results confirm that device failure occurred due to cracking at the notch region, and when plotting results on a S-N curve, we validate that they fit into trend of other similar device fatigue failures.

Frequency Drift Characteristics

As shown in Fig. 3, 'Device 1' showed stability for approximately 161.9 hours. The device was stable at a 650mV drive amplitude for about 1.9 hours before it suddenly began to drift in frequency at a linear accelerated rate. The device drifted approximately 18ppm before failing at approximately 162.5 hours. The calculated stress at failure, based on the output device amplitude, was 2.3GPa.

As shown in Fig. 4, 'Device 2' showed stability for approximately 20 hours. Upon increasing the AC drive voltage to 350mV at 20 hours, the frequency drifted quickly, then slowed but continued to drift for about 1 hour. After approximately 21.8 hours, the frequency drift rapidly accelerated, and the device failed at 21.9 hours. The device frequency drifted by a total of approximately 22ppm. The stress at failure was calculated to be 3.5GPa.

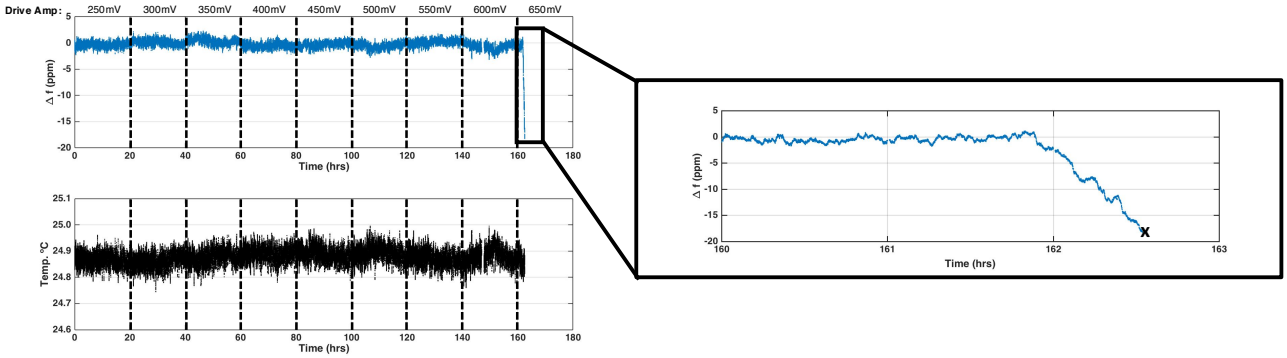

Figure 3: Epi-polysilicon 'Device 1' frequency change and measured temperature over time. Device failure (indicated with an 'x') occurs at 162.5 hours. The drive amplitude was increased at 20-hour intervals as shown at the top of the frequency plot.

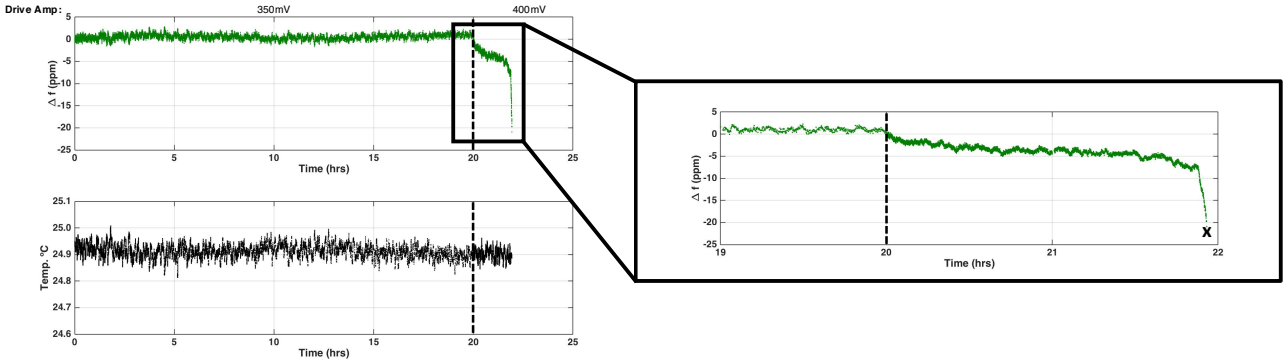

Figure 4: Epi-polysilicon 'Device 2' frequency change and measured temperature over time. Device failure (indicated with an 'x') occurs at 21.9 hours. The drive amplitude was increased at 20-hour intervals as shown at the top of the frequency plot.

Before failure, both devices showed stability of ± 3ppm frequency shift. These small shifts in frequency during stability were directly correlated to slight shifts in temperature. The temperature of both devices was maintained at just below 25°C.

Localized High Resolution Imaging

Since the device layer is fully encapsulated, there is no way of knowing exactly how the devices failed using typical microscopy techniques. So, X-ray imaging, with nanoscale resolution, was performed, as shown in Fig. 5. The images reveal that the two epi-polysilicon devices, 'Device 1' and 'Device 2', did in fact fracture at the notch region. Since the devices failed at the notch region, the decrease in compliance of the structures can be attributed to cracking at the notch region.

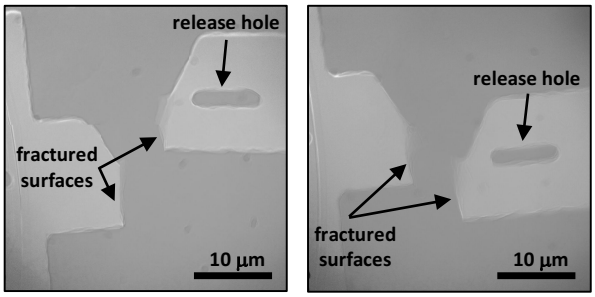

Figure 5: X-ray imaging with nanoscale resolution of fractured notches in epi-polysilicon fatigue 'Device 1' (left) and 'Device 2' (right).

Fig. 5 also reveals some interesting characteristics of device failure. The 'Device 1' crack appears to have initiated directly at the notch tip, while 'Device 2' seems to have propagated just to the left of the notch tip. The images also reveal the rough epi-polysilicon side walls. Release holes, which help ensure that all of the surrounding oxide is etched to release the structure in fabrication are also visible.

Accelerated Drift to Failure

Fig. 6 compares the period just before failure of linear accelerated frequency drift of 'Device 1', 'Device 2', and 2 and two other devices of the same geometry. The results are plotted on a semi-log scale with the inset showing a linear scale to accentuate the linear nature of the drift profiles. 'Device 1' takes noticeably longer time to drift to failure. All devices drift between 6 and 22ppm before failure.

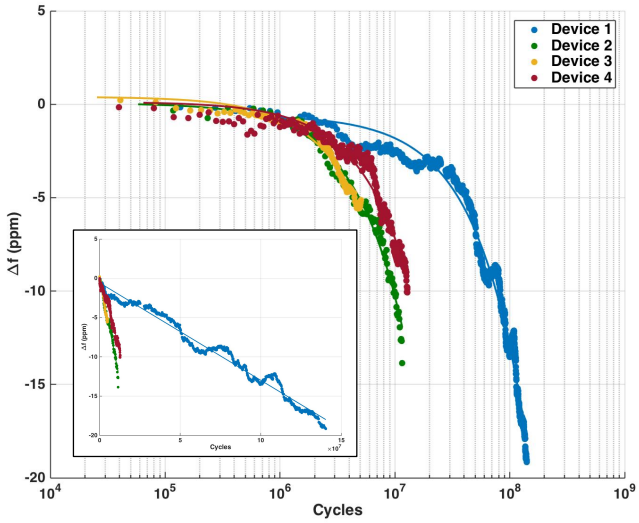

Figure 6: Accelerated drift rate to failure of 4 epi-polysilicon devices. Inset shows same plot on linear scale.

Stress Life Plot

Fig. 7 summarizes the stress-life fatigue behavior of this work compared with other work on MEMS polysilicon and encapsulated oxide-coated SCS structures. Previous fatigue research in MEMS has shown a 'metal-like' stress-life fatigue behavior for polysilicon thin films and 20µm thick films with increased stresses leading to shorter lifespans and vice versa [5][13]. The thick, 40µm, structures in this work seems to fall into this same category of behavior with lower stressed devices having a longer fatigue life than devices exposed to higher stresses. More data points would need to be collected to find a conclusive pattern in the data.

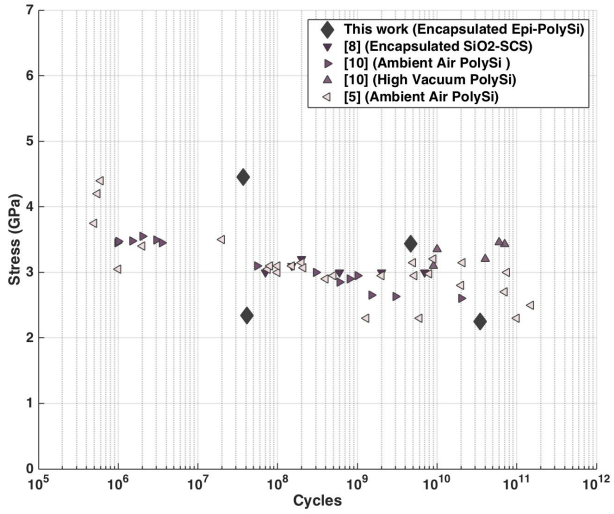

Figure 7: Stress-Life (S-N) plot of this work compared with literature [5][8][10]. This work fits with the trend of lower stress leading to longer fatigue life of the devices and vice versa.

DISCUSSION / CONCLUSIONS

In conclusion, four epi-polysilicon devices operate up to 2GPa without fatigue failure, which is consistent with prior observations in less-pristine environments, clearly indicating that previously-postulated environmental causes for fatigue failure in epi-polysilicon are not important. Furthermore, without the presence of oxygen or native debris, the 'reaction-layer' fatigue model is not consistent with these results.

The most plausible cause for fatigue in these structures aligns most closely with the 'subcritical cracking' model proposed by Kahn et al. due, in this case, to the surface roughness of the structures. During compressive cycles, the rough surfaces at the notch tip wedge to create areas of tension, thus propagating irreversible micro-cracks through the structure [6].

The difference in fatigue drift characteristics between 'Device 1' and 'Device 2' could be attributed to randomness in the orientation of the grain structure. 'Device 1', showed unstable frequency drift to failure and likely reached the critical crack length upon crack initiation. In contrast, 'Device 2' showed behavior that indicated crack initiation, followed quickly by crack arrest, and then crack re-initiation just before failure. 'Device 1' showed behavior consistent with continued material weakening upon reaching critical crack length, while 'Device 2' showed signs

of strengthening during crack arrest, which could be attributed to crack-tip shielding or grain boundary plasticity [18]. Given that all devices do not respond to the drive conditions with the same stress amplitude, due to the randomness in the grain structure, devices may fail by pure weakening or by a combination of weakening and strengthening at the crack tip.

The fatigue failure at the notch tip was validated with X-ray imaging that revealed the devices failed at or close to the notch tip. Furthermore, the results were validated by the stress life behavior of other similar polysilicon devices and encapsulated oxide coated SCS devices.

This first study on thick, 40μm, epi-polysilicon encapsulated structures demonstrates fatigue failure as a potential failure mechanism, and should be taken into consideration in future MEMS design.

ACKNOWLEDGEMENTS

This work was supported by the Defense Advanced Research Projects Agency (DARPA) grant “Precise Robust Inertial Guidance for Munitions (PRIGM)”, managed by Dr. Ron Polcawich, Contract Number # N66001-16-1-4023. This work was performed in part at the Stanford Nanofabrication Facility (SNF), supported by the National Science Foundation under Grand ECS- 9731293. Special thanks to all the staff at SNF for their help during the fabrication process.

REFERENCES

[1] A.D. Romig Jr, M.T. Dugger, and P.J. McWhorter, "Materials Issues in Microelectromechanical Devices: Science, Engineering, Manufacturability and Reliability", Acta Materialia, 51, 19, (2003).

[2] R.W. Hertzberg, *Deformation and Fracture Mechanics of Engineering Materials.* 1989.

[3] K. Sumino, "Deformation Behavior of Silicon", Metallurgical and Materials Transactions A, 30, 6, (1999).

[4] S.M. Allameh, P. Shrotriya, A. Butterwick, S.B. Brown, and W.O. Soboyejo, "Surface Topography Evolution and Fatigue Fracture in Polysilicon MEMS Structures", Journal of Microelectromechanical Systems, 12, 3, (2003).

[5] C.L. Muhlstein, E.A. Stach, and R.O. Ritchie, "A Reaction-Layer Mechanism for the Delayed Failure of Micron-Scale Polycrystalline Silicon Structural Films Subjected to High-Cycle Fatigue Loading", Acta Materialia, 50, 14, (2002).

[6] H. Kahn, R. Ballarini, J.J. Bellante, and A.H. Heuer, "Fatigue Failure in Polysilicon Not Due to Simple Stress Corrosion Cracking", Science, 298, 5596, (2002).

[7] S. Yoneoka, Y.Q. Qu, S. Wang, M.W. Messana, A.B. Graham, J. Salvia, K. Bongsang, R. Melamud, G. Bahl, and T.W. Kenny, "High-Cyclic Fatigue Experiments of Single Crystal Silicon in an Oxygen-Free Environment", IEEE 23rd International Conference on Micro Electro Mechanical Systems (MEMS), Hong Kong, China, 1/24 - 28/10, IEEE, (2010), pp. 224 - 227.

[8] V.A. Hong, S. Yoneoka, M.W. Messana, A.B. Graham, J.C. Salvia, T.T. Branchflower, E.J. Ng, and T.W. Kenny, "Fatigue Experiments on Single Crystal Silicon in an Oxygen-Free Environment", Journal of Microelectromechanical Systems, 24, 2, (2015).

[9] W.W. Van Arsdell, and S.B. Brown, "Subcritical Crack Growth in Silicon MEMS", Journal of microelectromechanical systems, 8, 3, (1999).

[10] D.H. Alsem, R. Timmerman, B.L. Boyce, E.A. Stach, J.T.M. De Hosson, and R.O. Ritchie, "Very High-Cycle Fatigue Failure in Micron-Scale Polycrystalline Silicon Films: Effects of Environment and Surface Oxide Thickness", Journal of Applied Physics, 101, 1, (2007).

[11] D.H. Alsem, C.L. Muhlstein, E.A. Stach, and R.O. Ritchie, "Further Considerations on the High-Cycle Fatigue of Micron-Scale Polycrystalline Silicon", Scripta Materialia, 59, 9, (2008).

[12] J. Bagdahn, and W.N. Sharpe Jr, "Fatigue of Polycrystalline Silicon under Long-Term Cyclic Loading", Sensors and Actuators A: Physical, 103,1-2, (2003).

[13] C.L. Muhlstein, S.B. Brown, and R.O. Ritchie, "High-Cycle Fatigue and Durability of Polycrystalline Silicon Thin Films in Ambient Air." Sensors and Actuators A: Physical, 94, 3, (2001).

[14] I.B. Flader, Y. Chen, C. Ahn, D.D. Shin, A.L. Alter, J. Rodriguez, and T.W. Kenny, "Epitaxial Encapsulation of Fully Differential Electrodes and Large Transduction Gaps for MEMS Resonant Structures", IEEE 31st International Conference on Micro Electro Mechanical Systems (MEMS), Belfast, Ireland, 1/21 - 25/18, IEEE. (2018).

[15] Y. Chen, I.B. Flader, D.D. Shin, C.H. Ahn, and T.W. Kenny, "Robust Method of Fabricating Epitaxially Encapsulated MEMS Devices with Large Gaps", Journal of Microelectromechanical Systems, 26, 6, (2017).

[16] I.B. Flader, Y. Chen, D.D. Gerrard, and T.W. Kenny, "Wafer-Scale Encapsulation of Fully Differential Electrodes for Mutli-Axis Inertial Sensing", International Conference on Solid-State Sensors, Actuators, and Microsystems (Transducers), Kaohsiung, Taiwan, 6/18 - 22/17, IEEE, (2017), pp. 591-594.

[17] Y.B. Gianchandani, M. Shinn, and K. Najafi, "Impact of Long, High Temperature Anneals on Residual Stress in Polysilicon", International Conference on Solid-State Sensors and Actuators (Transducers), Chicago, IL, USA, 6/16 - 19/97, IEEE, (1997), pp. 623-624.

[18] H. Kahn, L. Chen, R. Ballarini, and A.H. Heuer, "Mechanical Fatigue of Polysilicon: Effects of Mean Stress and Stress Amplitude", Acta Materialia, 54, 3, (2006).

CONTACT

*A.L. Alter, tel: +1-651-808-3803; annealtr@stanford.edu

INCREASING THE THICKNESS AND DEPOSITION RATE OF HIGH-PERFORMANCE ELECTROPLATED CoPt PERMANENT MAGNETS

Yuzheng Wang[*]*, Jacob Ewing, and David P. Arnold*
Interdisciplinary Microsystems Group, University of Florida, USA

ABSTRACT

This paper reports the fabrication and magnetic characterization of very thick (50+ µm) and high-performing (coercivity up to 850 kA/m; energy products up to 75 kJ/m^3) electroplated permanent magnets microfabricated on silicon substrates. Intended for MEMS applications, an enhanced fabrication process yields higher areal magnetic energy density (5.6 J/m^2) and faster plating rates (42 µm/hr) compared to previously published work. The magnetic CoPt alloy is co-plated in single electroplating bath and subsequently annealed at 675°C for 30 min to induce a phase transformation to the high-coercivity $L1_0$ CoPt phase. Four main accomplishments are reported: (1) optimization of the underlying seed layer metallurgy to improve film adhesion and prohibit silicon diffusion; (2) development of a warm-bath (50°C), high-current-density (300-2000 mA/cm^2) electroplating process that dramatically increases plating rate while maintaining good magnetic properties; (3) demonstration of a mechanical planarization process yielding smooth surface with no delamination; (4) preliminary study of bath longevity.

INTRODUCTION

There are increasing technological needs for thick, process-integrable micrometer-scale permanent magnets that can provide high magnetic moment and/or large stray magnetic fields for various MEMS and microsystems. Examples include magnetic microactuators, magnetic field sensors, microfluidic devices, wireless power devices, and more (e.g. [1 - 4]).

Larger, thicker magnets are motivated by simple physics. First, the total magnetic moment of a magnet is proportional to its volume. Second, the "reach" of the stray magnetic fields produced by a magnet are also related to its size. At a given distance from the magnet surface, a larger magnet produces a larger magnetic field compared to a smaller magnet. To generate relatively strong fields at distances of tens of micrometers away from the magnet surface, micromagnets are needed with thicknesses of at least tens of micrometers.

Thick film rare-earth sputtered magnets (e.g. Nd-Fe-B, Sm-Co) have been studied for their high remanent magnetization and maximum energy density [5-6]. However, these sputtered magnets are difficult to be patterned into well-controlled shapes and are prone to oxidation, which limits their application in end devices. Alternatively, to provide large and stable bias fields, the $L1_0$ CoPt alloy offers desirable characteristics including strong magnetic properties, good thermal/chemical stability, and capability of fabricating thick films via aqueous electroplating processes (the rare-earth magnets cannot be electroplated from aqueous baths). For deposition, compared to physical or chemical vapor deposition methods, electroplating is more practical to realize multi-micron-thick films and easily scales to large substrates. Our group has previously reported electroplated CoPt magnets (250 µm × 2 mm stripe shapes) with thicknesses of 15 µm electroplated at room temperature and current densities below 200 mA/cm^2, yielding excellent magnetic properties including intrinsic coercivity H_{ci} = ~800 kA/m, squareness > 0.8, and energy product of >150 kJ/m^3 [7]. In this paper, efforts are focused on achieving larger (2 mm diameter round pattern) and thicker (50+ µm) magnet structures with equivalent or better magnetic properties by elevating the bath temperature and also increasing the plating current-density and plating time. Ultimately, dense, thick-film magnets are achieved with 2.5X higher areal magnetic energy density (5.6 J/m^2) and 3X increase in plating rate (42 µm/h) compared to the best previously published work [8-12].

EXPERIMENTAL METHODS

The overall fabrication process of electroplated CoPt thick film magnets includes three main steps. First, multiple thin-film underlayer (seed layers) and a masking layer are deposited on a silicon wafer. Second, 2 mm diameter CoPt films are electroplated using DC currents and an optimized electroplating bath. Third, the deposited CoPt films are annealed to induce strong magnetic properties. Scanning electron microscope (SEM) / energy-dispersive X-ray spectroscopy (EDS) (FEI NOVA 430, column voltage: 18 kV) and vibrating sample magnetometer (VSM) (ADE technologies) characterizations are performed to determine the surface/cross-section morphology, atomic composition and magnetic properties of plated films, respectively.

Underlayers and Masking Layer

N-type silicon wafer with <100> orientation is used as substrate and cleaned by buffered oxide etch (BOE) to remove the native oxide prior to deposition. The optimized seed-layer stack comprises (Fig. 1): 25 nm Cr adhesion, 50 nm titanium nitride (TiN) diffusion barrier, 25 nm Cr adhesion, 500 nm Cu conductive seed, and 500 nm photographically patterned Al_2O_3 (alumina) electroplating mask. All the layers except alumina are deposited by regular sputtering technique (KJL CMS-18 multi-source). The alumina layer is reactive sputtered by introducing oxygen during sputtering with an Al target. The TiN layer is used for preventing silicon atoms from diffusing into CoPt film and forming metal silicides [13]. Considering the high DC current that flows through the cross-section of conductive layer, Cu seed with thickness of 500 nm is chosen. Although photoresist electroplating molds are more commonly used for improved sidewall definition, the polymer-based photoresist suffers from deterioration and delamination in the heated baths. Consequently, a thin patterned alumina layer is used for its good adhesion and thermal stability. The alumina shows no sign of delamination in heated bath (up to 70°C) under high current density (up to 2000 mA/cm^2) for at least 5 h.

Figure 1: Substrate seed layers with lithographically pattered alumina electroplating mask.

CoPt Electroplating Process

The seed layer/masking layers are processed on 100 mm wafers, and the wafer is then singulated for electroplating one magnetic structure at a time using 100 mL of bath. The electroplating bath chemistry is critical to the entire CoPt magnet fabrication process. The electroplating bath contains three

978-1-940470-03-0/HH2018/$25©2018TRF
DOI 10.31438/trf.hh2018.39

components: dinitrodiamine-platinum solution (Sigma Aldrich), cobalt sulfamate salt (Alfa Aesar) and ammonium citrate salt (Sigma Aldrich), which serve as platinum source, cobalt source, and pH buffer, respectively [7]. Since the cobalt sulfamate salt has unknown number of intramolecular combined water (depends on humidity and storage conditions), inductively coupled plasma mass spectrometry (ICP-MS) (Perkin-Elmer Corp.) is used to accurately determine the molecular weight of the cobalt sulfamate hydrate as well as the concentration of the platinum content of the commercial dinitro-diamine platinum solution. The pH of the bath is adjusted to 7 by adding diluted sodium hydroxide (NaOH) into mixed solution. Platinum foil and silicon wafer (with seed layers) are used as anode and cathode, respectively, with anode-to-cathode gap of 2.5 cm and no stirring. Bath temperatures of 50°C and 70°C are explored, as are DC current densities from 300 – 2000 mA/cm^2.

To achieve desired $L1_0$ CoPt crystal phase, an equiatomic CoPt alloy is desired. The film alloy ratio (measured via energy dispersive x-ray spectroscopy, EDS) is controllable by adjusting the concentration of Pt and Co ions in the electroplating bath (measured by ICP-MS) as shown in Fig. 2, and the optimized bath recipe (yielding near equiatomic films) is shown in Table 1.

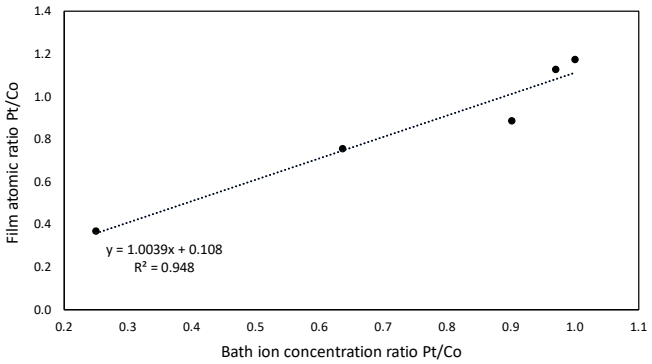

Figure 2: Pt/Co atomic ratio in plated film vs. Pt/Co ion ratio in electroplating bath.

Table 1: Optimized bath composition.

Chemicals	Concentration [M]
Dinitrodiammine-platinum $[Pt(NH_3)_2(NO_2)_2]$	0.05
Cobalt sulfamate $[Co(SO_3NH_2)_2 \bullet xH_2O]$	0.0515
Ammonium citrate $[C_6H_{17}N_3O_7]$	0.1

According to the Arrhenius law, the reduction rate of metal ions increases exponentially with temperature. So, elevated bath temperature from room temperature to 70°C is investigated to increase deposition rate [14].

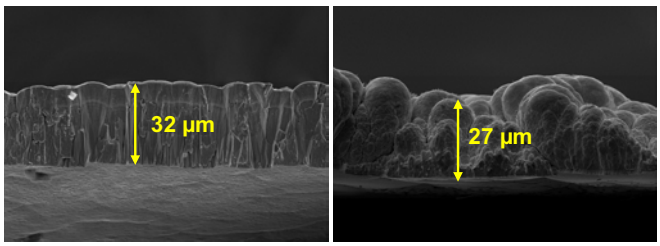

Figure 3: Comparison of film quality between samples plated at 50℃ (left) and 70℃ (right), 1000 mA/cm^2 for 1 h.

High temperatures of 70°C allow layers of ~30 µm to be deposited in only 20 min, and if the time is extended over 45 min, films of 60-80 µm can be obtained. SEM analysis, however, shows that the quality (e.g. coercivity <100 kA/m) and density of the films is compromised at such rapid plating rates. In contrast, a plating bath temperature of 50°C yields much denser films (Fig. 3).

Film Annealing

After film deposition, an annealing step is used to induce a phase transformation of the CoPt alloy from the disordered, low-coercivity A1 phase to the ordered, high coercivity $L1_0$ phase (Fig. 4) [15]. All the plated films are annealed using a tube furnace (Lindberg Blue) with forming gas (96% N_2 + 4% H_2) ambient at 675°C for 30 min with the ramping up rate of 28°C/min.

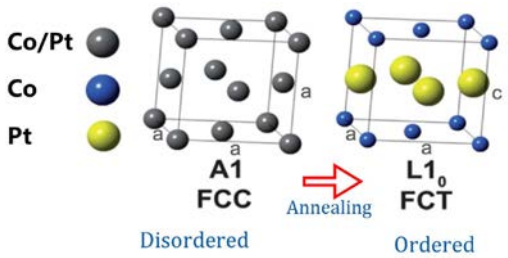

Figure 4: Schematic diagram of CoPt phase transformation from disordered A1 phase (fcc) to the ordered $L1_0$ phase (fct).

EXPERIMENTAL RESULTS

Magnetic Properties vs. Plating Conditions

Using 50°C bath temp., current densities from 300 to 2000 mA/cm^2 are applied for 1 h. Fig. 5 and Fig. 6 shows the plating rate as a function of current density, and the resulting magnetic properties (post annealing). The plating rate increases monotonically with current density ranging from 0.29 µm/min up to 0.71 µm/min, which is important for reaching desired thickness in a reasonable amount of time. The magnetic properties are relatively consistent: coercivity up to 844 kA/m and maximum energy density up to 57 kJ/m^3.

While the highest current densities yielded the fastest plating rate, to maintain such high current density for full-wafer plating with much larger plating area would require a very high-current power supply and may lead to the potential issue of uneven distribution of electric current across the wafer.

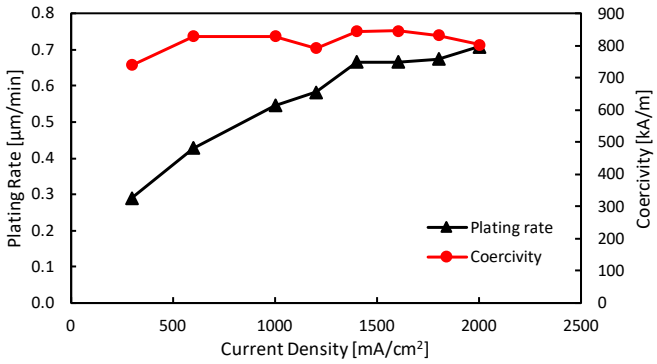

Figure 5: Plating rate and coercivity of electroplated CoPt magnets at various current densities. All the films are plated at 50℃ for 1 h.

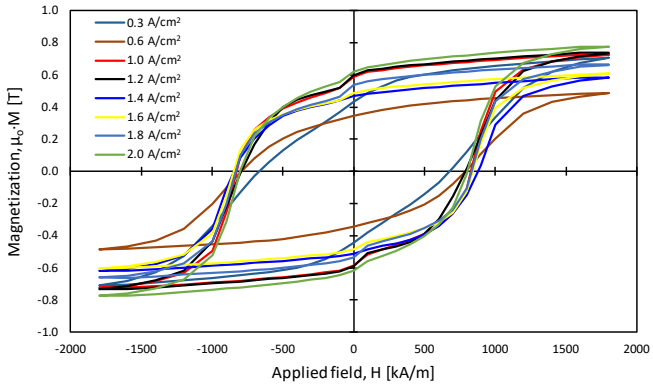

Figure 6: Full hysteresis loops of electroplated CoPt magnets at various current densities. All the films are plated at 50 ℃ for 1 h.

Consequently, current densities of 400-600 mA/cm^2 and temperature of 50°C have proven to be the optimized electroplating conditions. At these conditions, extending the plating time to 5 h allows layer with thickness ranging from 46 to 98 µm to be successfully plated (Fig. 7).

The experimental results show that the magnetic properties are affected by the applied current density to some extent, but not as much as the plating temperature. Best results are obtained at 400 mA/cm^2, yielding a thickness of ~60 µm, coercivity of 820-850 kA/m, a remanence of 0.62 T, saturation magnetization of 0.73 T, squareness of 0.85, and $(BH)_{max}$ of 65-75 kJ/m^3.

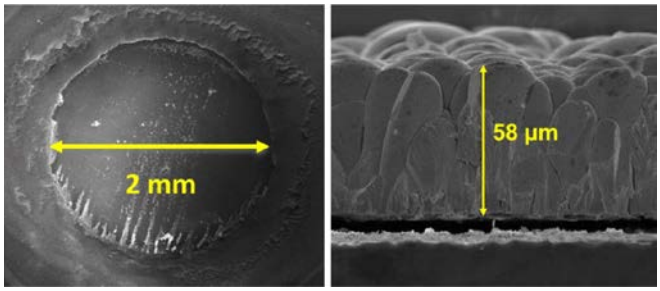

Figure 7: SEM pictures a 2 mm diameter round manually polished CoPt sample (left) and cross-section view of a 58 µm thick unpolished CoPt sample (right) plated at 400 mA/cm^2, 50 ℃ for 3 h. Delamination due to manual cleaving for cross-section view.

Mechanical Polishing

Due to the uneven distribution of current density at the edge of plating area, a super thick "ring" (up to 200 µm) appears around the edge of the sample (Fig. 8). More uniform, cylindrical magnets with smooth surface are typically desired.

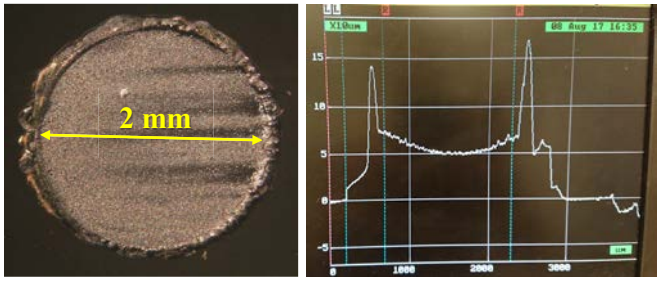

Figure 8: Optical image and profilometer measurement of a 2 mm diameter sample with thick "ring" prior to polishing.

A flatter and smoother surface can be easily achieved by polishing the CoPt magnet on a rotation polishing machine with 0.3 µm alumina polishing pad for only 20 s. No sign of delamination is observed after the polishing step.

Longitudinal Study of Bath Chemistry

Most of the aforementioned results were obtained using relatively "fresh" electroplating baths. However, we have observed deterioration of the magnetic properties after continued use of a given bath. To study this effect more systematically, we initiated a longitudinal study of CoPt bath chemistry Starting with a freshly mixed 100 mL bath, a series of 13 samples are plated without any bath refreshment, each at 50°C and current density of 400 mA/cm^2 for 3 hr. This process typical yields ~20 µm/h plating rates, equivalently ~60 µm thick samples.

Fig. 9 shows the trends in magnetic properties. All samples show relatively consistent coercivity. However, there is more variation in remanence (and saturation). The initial seven samples show relatively high remanence and saturation magnetization. The highest value appears at the 7th sample. After ten samples are plated from the same bath, significant decrease of remanence and saturation magnetization. This change in magnetic properties coincided with the bath color changing from purple to wine red. [Several data points from this set of experiments are missing due to samples that were lost during testing due to machine failure.]

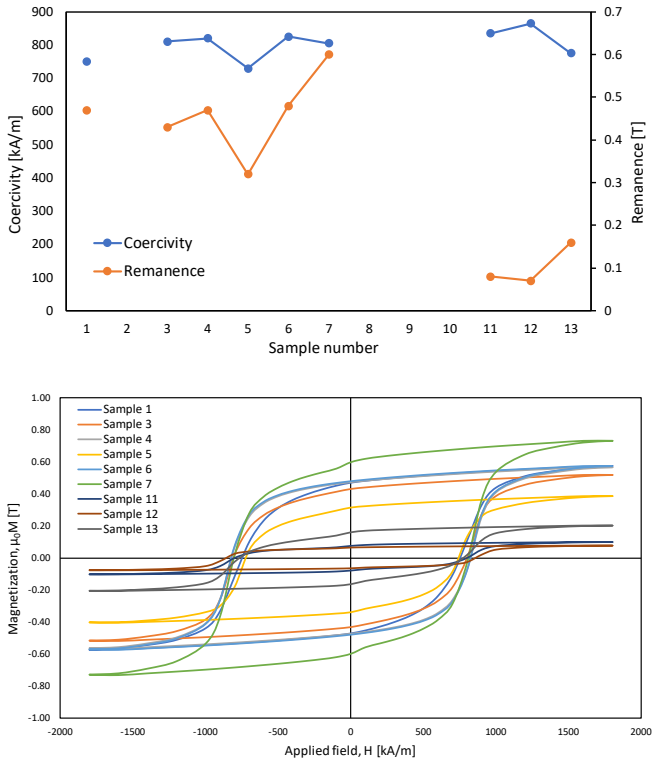

Figure 9: (top) Coercivity, remanence and (bottom) in-plane hysteresis loop comparison of CoPt samples (after annealing) plated from a single bath. All of samples are plated at 400 mA/cm^2, 50 ℃ for 3 h.

The metal ion consumption in the electroplating bath can be roughly calculated. Using the optimized bath recipe (Table 1), 100 mL bath contains 975 mg of Pt and 304 mg of Co. The average mass of single 60 µm thick, 2 mm diameter round equiatomic CoPt magnet is assumed to be 2.86 mg (2.02 mg Pt, 0.84 mg Co) by

averaging the density of Pt and Co. According to this calculation, thirteen 60-µm-thick samples would only correspond to 26 mg of Pt (a reduction of only 2.6%) and 11 mg of Co (a reduction of only 3.6%). Hence, a depletion of metal ions in the bath due is unlikely to be the reason that leads to the decrease of magnetic properties. Further investigation and confirmation by more systematic chemical analysis of the CoPt electroplating bath is still needed.

CONCLUSIONS

A complete fabrication process is demonstrated for yielding high-performance CoPt thick film micro-magnets on Si substrates. Multiple functional layers including Cr adhesion, TiN diffusion barrier, Cu seed and alumina mask layer with optimized thickness are deposited through sputtering and patterned by HF on silicon wafer. Warm electroplating baths and relatively high current densities are shown to increase the plating rate, yielding very thick films while retaining strong magnetic performance. Specifically, CoPt magnets with thicknesses over 50 µm are obtained using optimized electroplating conditions: current densities 400-600 mA/cm^2, bath temperature of 50°C, and plating times of 3-5 h. After post-annealing at 675°C for 30 min, the magnets consistently exhibit coercivities up to 850 kA/m, remanence of 0.62 T, saturation magnetization of 0.73 T, squareness of 0.85 and maximum energy density up to 75 kJ/m^3. Li et al. suggested areal magnetic energy density $t_{film} \times (BH)_{max}$ as a good figure of merit for magnetic films for MEMS [8]. Herein, we demonstrate magnets with more than 2.5X improvement in areal magnetic energy density compared other reported electroplated films on Si substrates (Fig. 10) [7-13].

Longitudinal study of bath chemistry is also conducted, which shows the changing trends of magnetic properties of CoPt samples plated continuously from single electroplating bath. Theoretical calculation indicates that the degraded magnetic performance is not attributed to simple metal ion consumption during electroplating.

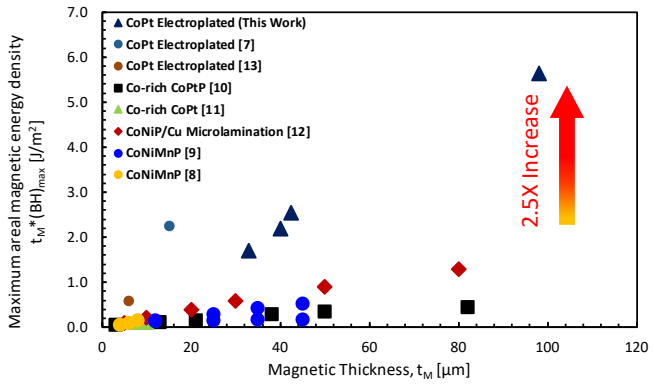

Figure 10: Maximum areal magnetic energy density (figure of merit) vs. film thickness for our results vs. previous work.

ACKNOWLEDGEMENT

This work is sponsored in part by DARPA MTO and the Army Research Office (Grant Number W911NF-17-1-0050). The authors thank the staff of the UF Research Service Centers for their assistance in the microfabrication and material characterization.

REFERENCES

[1] O. Cugat, J. Delamare and G. Reyne, "Magnetic micro-actuators and systems (MAGMAS)," IEEE Trans. On Magnetics, 36, 3607-3612, (2003)

[2] BH. Bahreyni and C. Shafai, "A resonant micromachined magnetic field sensor," IEEE Sensors Journal, 7, 1326-1334, (2007).

[3] Y. Zhang and NT. Nguyen, "Magnetic digital microfluidics - a review," Lab on A Chip, 17, 994-1008, (2017).

[4] D. P. Arnold, "Review of microscale magnetic power generation," IEEE Trans. On Magnetics, 43, 3940-3951, (2007).

[5] T.-S. Chin, "Permanent magnet films for applications in micro electro mechanical systems," J. Magnetism and Magnetic Materials, 209, 75-79, (2000).

[6] D. P. Arnold and N. Wang, "Permanent magnets for MEMS," J. Microelectromech Syst., 18, 1255-1266, (2009).

[7] O. D. Oniku, B. Qi and D. P. Arnold, "Electroplated $L1_0$ CoPt thick-film permanent magnets," J. of Applied Physics, 115, 17, (2014).

[8] Y. Li, J. Kim, M. Kim, A. Armutlulu and M. G. Allen, "Retaining high areal in-plane magnetic energy density over large magnetic thickness: a permanent magnetic microlamination approach based on sequential multilayer electroplating," Solid-State Sensor and Actuator Workshop, Hilton Head Isl., SC, 40-43 (2014).

[9] X.-M. Sun, Q. Yuan, D.-M. Fang and H.-X. Zhang, "Electrodeposition and characterization of CoNiMnP-based permanent magnetic film for MEMS applications," IEEE NEMS, 367-371, (2011).

[10] S. Kulkarni and S. Roy, "Deposition of thick Co-rich CoPtP films with high energy product for magnetic microelectromechanical applications," J. Magnetism and Magnetic Materials, 322, 1592-1596, (2010).

[11] N. Wang and D. P. Arnold, "Thick electroplated Co-rich Co-Pt micromagnet arrays for magnetic MEMS," IEEE Trans. on Magnetics, 44, 3969-3972, (2008).

[12] T. M. Liakopoulos, W. Zhang and C. H. Ahn, "Electroplated thick CoNiMnP permanent magnet arrays for micromachined magnetic device applications," IEEE MEMS, 79-84, (1996).

[13] O. D. Oniku, B. Qi and D. P. Arnold, "Electroplated thick-film cobalt platinum permanent magnets," J. Magnetism and Magnetic Materials, 416, 417-428, (2016).

[14] T. Yanai, R. Hamamura, J. Honda, A. Tomita, H. Yamada, N. Fujita, K. Takashima, M. Nakano and H. Fukunaga, "Electroplated Co–Pt Thick-Film Magnets Prepared in Citric-Acid-Based Plating Baths," IEEE Trans. on Magnetics, 53, 11, (2017).

[15] K. Barmak, "On the relationship of magnetocrystalline anisotropy and stoichiometry in epitaxial $L1_0$ CoPt (001) and FePt (001) thin films," J. of Applied Physics, 98, 033904, (2005).

CONTACT

*Yuzheng Wang, tel: +1-352-222-6995; wangyz0218@ufl.edu

MASKLESS 3D MICROFABRICATION OF DRUG-LADEN CAPSULATED MICROSTRUCTURES

Lin Qi[1], Shuai Yuan[2], Ronald X. Xu[1,2] and Yi Zhao[1]*
[1]The Ohio State University, OH, USA
[2]University of Science and Technology of China, Hefei, China

ABSTRACT

This paper reports the development of 3D capsulated microstructures with the desired geometries for controlled drug releasing. Coaxial electrospray (CES) was used to encapsulate bioactive molecules/drugs in polymeric microcapsules. Microelectrodes were used to collect microcapsules and create particulate 3D microstructures. The shell thickness of the microcapsules and the characteristic dimensions of assembled microstructures were independently controllable, and both can modulate the drug releasing profiles. This approach can extend the releasing period and allow for programmable control of the drug-releasing profile. It thus provides a powerful tool for achieving customized drug releasing in the local regions.

INTRODUCTION

The microsphere-based scaffold is a promising scaffold candidate for promoting functional tissue regeneration [1]. The porosity of the scaffold mimics the native environment of cells, provides structural support and guidance of the regenerating tissue, regulates the interactions between the cells and their surroundings, and allows a good nutrient supply. The microspheres are the carriers of bioactive molecules or drugs, which can allow sustainable drug release at an optimized rate to promote tissue regeneration. Emulsion-solvent extraction is one conventional method to fabricate microspheres [2]. The scaffold materials and bioactive drugs are dissolved in the oil phase and emulsified as micro-droplets in the water phase. Upon the extraction of solvent from the oil phase, the droplets are hardened and solidified. Using this approach, microspheres are obtained at high efficiency and with simple settings. Nonetheless, emulsion-solvent extraction often has poor control over the microsphere size. Customized design of the drug-releasing profile is difficult. To address the broad size distribution, alternative approaches, such as precision particle fabrication and thermally induced phase separation, are developed [3, 4]. However, these approaches have their particular limitations, such as complicated experimental setup and operation complexity, time consuming, and the risk of microsphere coalescence. Besides, bioactive drugs are often heterogeneously distributed in the microspheres, resulting in poor control of the initial drug releasing rate (*e.g.*, initial burst release) and total releasing period [5].

CES is another prevalent approach to generate microspheres [6]. It can encapsulate bioactive molecules or drugs at a high efficiency [7] and have a relatively narrow size distribution as compared to emulsion-solvent extraction. The encapsulation and solvent evaporation often finish within seconds, which minimizes the adverse effect associated with the prolonged exposure of the solvent to bioactive molecules. The bioactive drugs are loaded in the cores of the microcapsules [8]. The initial burst release is thus minimized, and the releasing rate is tunable by controlling the shell thickness of microcapsules. However, there are few reports of functional tissue scaffolds created by CES. This is primarily due to the lack of feasible engineering approaches that can manufacture the microcapsules into desired scaffold shapes to support the tissue growth. So far, most microcapsules prepared by CES are discrete microparticles or particulate aggregates with random shapes. It is challenging to assemble the discrete microcapsules into 3D structures with controllable dimensions. Conventional microsphere assembling/packing methods, such as heat and solvent sintering, may nullify bioactive molecules in the microcapsules or leave cytotoxic residues in the assembled scaffolds, and thus compromise the efficacy of the functional microsphere-based scaffolds for tissue regeneration [1].

In this paper, we introduce a floating electrodes-assisted CES to assemble drug-laden microcapsules in a 3D microstructure during the collecting process. A coaxial flow with the inner drug solution and the outer polymer solution was electrosprayed in a stable cone-jet mode. Microcapsules were selectively deposited on the interdigitated microelectrodes due to the highly non-uniform electrostatic field generated by ground/floating electrodes. Continuous spraying stacked individual microcapsules into 3D capsulated microstructures. By tuning the voltage bias at the needle, the lateral dimension of these microstructures can be changed. The controlled drug releasing rate by such assembled capsulated microstructures was demonstrated. The results showed that both the shell thickness of microcapsules and the characteristic dimensions of the assembled microstructures can modulate the drug release profile. Our approach provides a new solution to control the drug-releasing profiles, validates and extends the potential efficacy of the CES. The study may shed light on the design of smart scaffolds for tissue regeneration.

EXPERIMENTAL SECTION

Materials

Polycaprolactone (PCL, average Mn = 45,000, Sigma-Aldrich, USA) was dissolved in acetone (Sigma-Aldrich) in a concentration of 5 % (w/v) as the outer layer solution. To visualize the core-shell structure, the PCL solution was stained by 0.01% of coumarin 6 (Sigma-Aldrich) in green (EX/EM=549/565nm), whereas the inner layer solution was stained by 0.01% of DiI (AnaSpec, Inc., USA) in red (excitation/emission = 528/617 nm). 70% isopropanol solution (IPA, Sigma–Aldrich) was used to wash and clean the electrodes before 3D patterning process. Deionized (DI) water was prepared by Direct-Q® Water Purification System (Millipore, Inc., USA). Rhodamine B (Sigma-Aldrich) was used as a model drug to demonstrate the release profiles of the resulting 3D patterning (EX/EM=553/627 nm).

3D Coaxial Electrospray Patterning

The enhanced electrospray system consisted of a CES module, a collection module, and a monitor module [9]. To encapsulate drugs in the core of the microcapsules, a coaxial needle (*Figure 1*) with a 17G/22G coaxial needle was used. The tips of the needles were flattened while the edges were rounded. The inner and the outer needles were positioned concentrically with a small vertical displacement (0~0.3 mm). The acetone solution and PCL solution were injected into the inner and outer layers of the needle respectively, using two syringe pumps (NE-1000, New Era Pump Systems, Inc., USA). A positive electrical voltage bias (from 8.5 to 12.5 kV) was applied to the needle (Gamma High Voltage Research, Inc., FL, USA). A negative voltage bias (-10 kV) was applied to the

978-1-940470-03-0/HH2018/$25©2018TRF
DOI 10.31438/trf.hh2018.40

collecting electrodes. The vertical distance between the needle tip and the collecting substrate was kept at 200 mm. The interdigitated microelectrodes were fabricated using standard photolithography [10]. To identify the optimal conditions that can lead to high aspect ratio 3D assembled microstructures, a number of parameters were investigated: the flow rate (1~5 ml/h), the applied positive electric bias (8.5~12.5 kV), the electrode width (25~200μm), the interelectrode spacing (200~1000 μm) and the collecting time (0~50 min). The entire process of electrospray was monitored in real time using a 3 kHz strobe flashlight, a charge-coupled device camera (Allied vision technologies, Inc., MA), a computer and a microscopic lens (Model VT-7DS-2CD, Hangzhou, China).

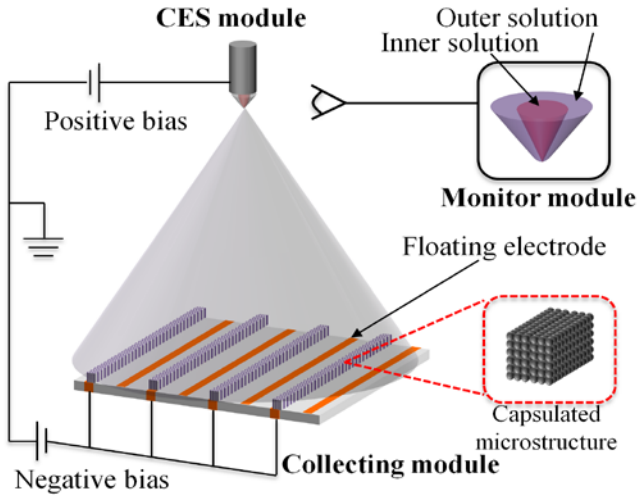

Figure 1: *Schematic of the floating electrode assisted CES process. PCL solution and the acetone solution of the model drug (rhodamine B) were fed through the outer and inner layers of a coaxial needle (17G/22G).*

Morphology Characterization

The morphology of the 3D microstructures was examined using scanning electron microscopy (SEM, A Hitachi S-3000H, Japan). In order to examine the core/shell configuration of the microcapsules, coumarin-6 was added in the outer solution and DiI was added in the inner solution. The microcapsules were examined using fluorescence microscopy (ECLIPSE 80i, Nikon, Japan). The mean size and size distribution of microcapsules were determined from more than 200 particles using a bright field microscope (ECLIPSE LV100D, Nikon, Japan). The images were analyzed using the NIS-Elements AR software (Nikon Instruments Inc., USA).

In Vitro Release Study

The model drug release was determined by placing the assembled 3D microstructure and discrete microcapsules in 2 *ml* phosphate-buffered saline (PBS). These samples were placed within the dialysis bags (Spectra/Por® Biotech Dialysis Membranes, Membranes package: 1M, MWCO 3.5K, W. 10 mm, Diam. 6.4 mm, Vol. 0.32 ml/cm). The dialysis bags were placed at the bottom of 250 ml glass beakers. The beakers were placed on a shaker (ROCKER 35, Labnet International Inc., USA) at 60 rpm in a 37 °C incubator. At the scheduled time intervals, the 3*ml* of the supernatant was collected, and replaced by the same amount of fresh PBS. The concentration of rhodamine B in the supernatant was determined by the light absorbance at 553 nm using a UV-Visible spectrophotometer (50 Bio, Agilent Technologies, USA). To establish the standard releasing rate, pure rhodamine B of the same dose was measured. The experiment was performed in dark. Each experiment was conducted in triplicate.

RESULT AND DISCUSSION

Investigation of CES Instability

The instability of CES was studied by examining the shape of the Taylor cone at the needle tip and resulting core/shell microcapsules. The results showed that the instability of the coaxial flow depends on the total flow rate and the electrostatic field. A high total flow rate or a low voltage bias resulted in the dripping mode of electrospray (I in *Figure 2a*), whereas a low total flow rate or a high voltage bias resulted in the multi-jet mode (III in *Figure 2a*). These modes may cause a broad size distribution and a significant variation of the drug-laden dose. When the total flow rate and the applied voltage bias were in the optimized range (II in *Figure 2a*), the CES system was operated with a stable cone-jet state, where a Taylor cone formed at the tip of the needle, and a liquid jet was ejected from the vertex of the cone. The jet then fissured into droplets with drug-containing cores. The shell dried during the flying process (*Figure 2c*). When the microcapsules approached the collecting substrate, they were attracted towards the electrodes with the negative voltage bias due to the non-uniform electric field. Since the microelectrodes collected most of the capsules and very few microcapsules fall into other regions, the waste of drugs was minimized. The geometries of the assembled pattern can be designed by changing the electrode layout (*Figure 2b&d*). As the spray proceeded, the microcapsules stacked up and eventually formed the 3D microstructures with particulate morphology.

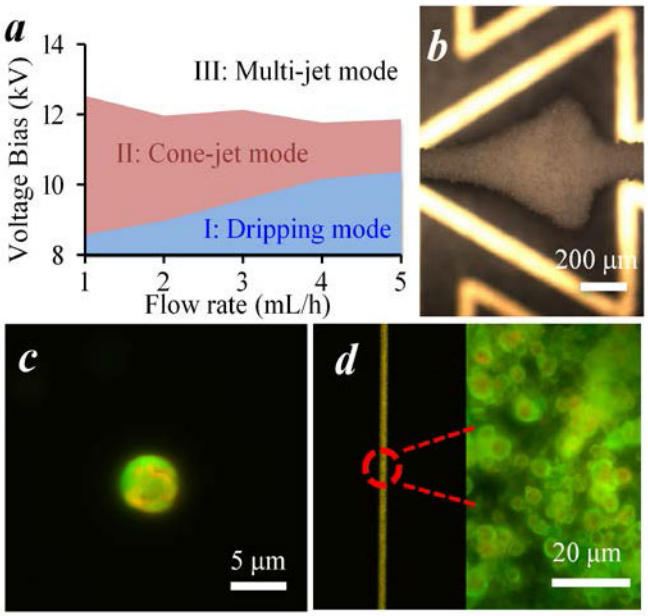

Figure 2: *Formation of the capsulated microstructure assemblies. (a) The effect of the total flow rate and the voltage bias on the CES instability. Region I: dripping mode; Region II: cone-jet mode; Region III: multi-jet mode. (b) A microstructure defined by a triangle ground/floating electrode layout. (c) An individual microcapsule. (d) An assembled capsulated microstructure. The cores of the microcapsules were stained by DiI (red) and shells were stained by coumarin 6 (green).*

The Effect of the Operating Parameters

The effects of the operating parameters on the characteristic dimensions of assembled microstructures were investigated. The results showed that the height-to-width ratio of these

microstructures varied with the electrode layout, the spraying time and the applied voltage bias. For example, when the voltage bias and the spraying time were constant (20 kV and 30 min), the electrode width of 50μm and the inter-electrode space of 400μm can lead to the highest height-to-width aspect ratio (about 3.02) (*Table 1*).

Table 1 *The effect of the width and the interelectrode spacing on the height-to-width aspect ratios of the assembled microstructures.*

Height-to-weight Aspect Ratios		**Electrode Width (μm)**		
		25	50	100
Inter-electrode spacing (μm)	200	1.1	2.13	1.64
	400	1.56	**3.02**	1.85
	1000	1.72	1.82	1.24

When the electrode layout and the voltage bias were kept unchanged, the height-to-width ratio of the assemblies increased with the spraying time at the beginning of the spraying. Almost all microcapsules were collected on the collecting electrodes with negative voltage bias (*Figure 2d*). The assembled microstructures thus had a good patterning contrast (*Figure 4a*). With continuous spraying, the height of the microstructure increased, whereas the width did not increase as much. Capsulated microstructures with higher aspect ratio were thus obtained (*Figure 4b*). As the spraying proceeded, the collecting electrodes were covered by a thick layer of the dielectric microcapsules. The non-uniformity of the electrostatic field reduced [10]. As a result, some microcapsules started to be deposited outside the collecting electrodes. This increased the lateral dimensions of the capsulated microstructures. The aspect ratio of the assembled structures decreased accordingly. In this study, the maximal height-to-width ratio was observed under the voltage bias of 20 kV (+10 kV at the needle and -10 kV at the collecting electrodes) and 40 min of spraying (*Figure 3*).

More complicated capsulated structures with varied lateral dimensions can be obtained by dynamically tuning the voltage bias at the needle. As shown in *Figure 4c&d,* a capsulated microstructure with two segments with distinct widths was obtained. This microstructure was created by setting the voltage biases at the needles at +8.5 kV for 20min, and then changing the voltage to +12.5 kV and holding the voltage for another 20 min.

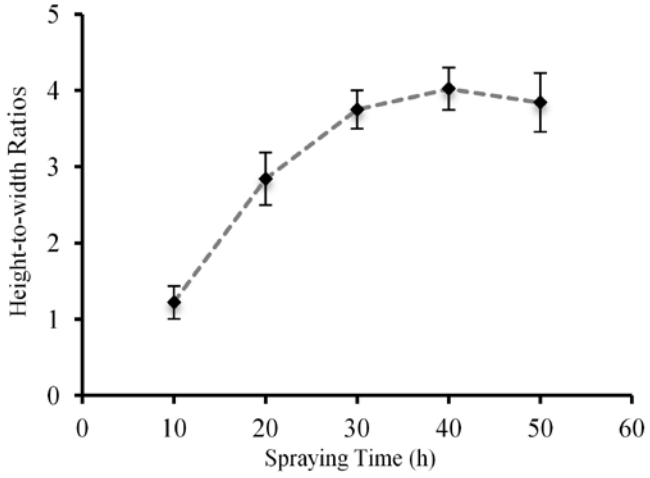

Figure 3: *The effect of microcapsule spraying time on the height-to-width ratio of the capsulated microstructures.*

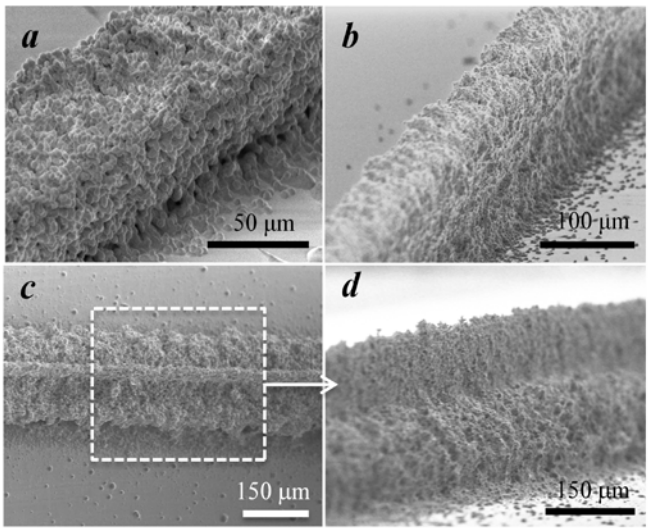

Figure 4: *The SEM of the capsulated microstructures. (a-b) The capsulated microstructure assemblies with different height-to-width ratios. (c-d) A capsulated microstructure assembly with two segments with distinct cross-sectional dimensions.*

Effect of Geometry of Individual Microcapsules on the Releasing Rate

Microcapsules with varied shell thicknesses were fabricated by using the different flow rates of the outer solution, and the same flow rate of the inner solution. The resulting capsules thus have the same core size but different shell thicknesses. Using CES, these microcapsules were assembled into capsulated microstructures with 200 μm×200 μm×20 mm (*Figure 5a*). The *in vitro* drug release experiment showed that the releases of all capsulated microstructures were sustainable up to one week (*Figure 5b*). The microstructure comprising of microcapsules with a thinner shell exhibited a faster-releasing rate the first 12 hours of the immersion. This suggested that the release of bioactive molecules or drugs from the microcapsulated scaffold can be modulated by changing the geometry of individual microcapsules.

Effect of the Shape of Capsulated Microstructures on the Releasing Rate

To investigate the effects of shape of the assembled capsulated microstructures on the releasing profile, microcapsules with the same geometries were assembled into microstructures. The cross-sectional dimensions of these microstructures were 50 μm×50μm and 200 μm×200 μm (*Figure 6a*). The longitudinal lengths of both microstructures were ~20 mm. The discrete microcapsules were also tested as the control. The *in vitro* drug release experiment showed that both capsulated microstructures exhibited extended releasing profiles than the discrete microcapsules (*Figure 6b*). The capsulated microstructures with the greater cross-sectional dimensions exhibited a significantly lower releasing rate within first 48 hours of the immersion.

In previous drug release studies using microcapsules, the drug release profile is often modulated only by the core-shell geometry of microcapsules. A thick shell with a small core was often used to extend the releasing period and to minimize the initial burst. This, however, limits the total dose of the drug that can be carried by the microcapsules. Our approach provides an additional route to control the drug releasing profile by changing the shape of the capsulated microstructures. Extended releasing profile can be obtained without reducing the total dose of the drug by stacking the microcapsules with appropriate core/shell geometries into the microstructure

assemblies with desired shape. The characteristic dimensions of the microstructures can be varied within a wide range from a few to hundreds of micrometers, which adds more flexibility for designing customized release profiles. Moreover, when the microcapsules carrying different drugs were used to construct the different segments of the capsulated structures that have different cross-sectional dimensions (as those shown in Figure 4c&d), the releasing of multiple drugs with distinct releasing profiles can be implemented.

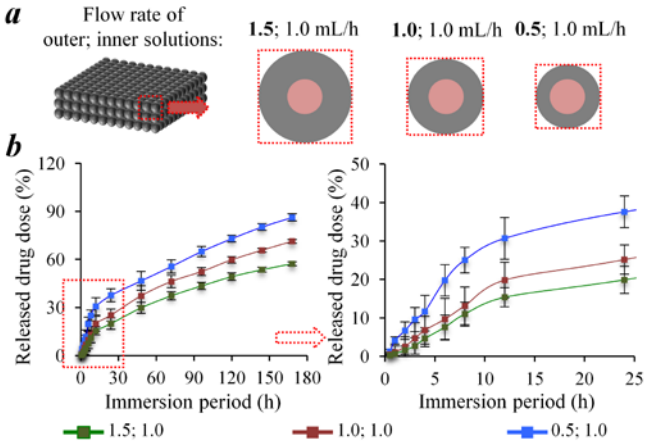

Figure 5: *The effect of the shell thickness of individual microcapsules on the release profile. (a) Microspheres with varied shell thickness were generated by modulating the flow rate of the outer fluid; and (b) The drug-releasing profile over 175 hours of immersion.*

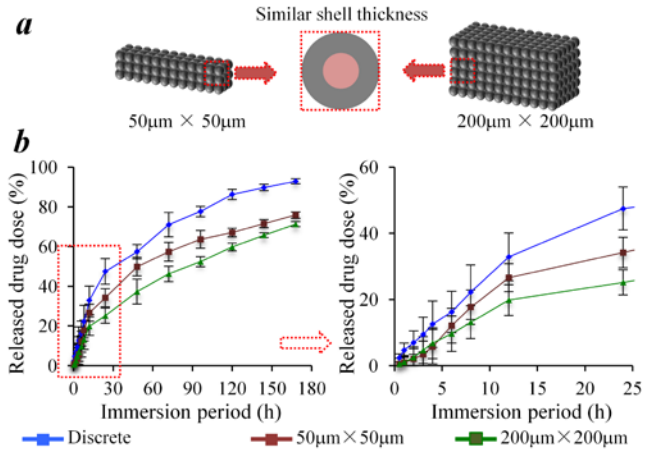

Figure 6: *The drug release profile changes with the shape of the microstructure assemblies. Two capsulated microstructure assemblies with the cross-sectional area of 50 μm ×50 μm and 200 μm ×200 μm (height × width) were tested. The lengths of the microstructure assemblies were 20 mm.*

CONCLUSION

In this paper, we report an approach to create 3D capsulated microstructure assemblies with desired geometries for controlled drug release. The floating electrode assisted coaxial electrospray was used to create microstructures comprising microcapsules that encapsulate bioactive molecules/drugs. The shell thickness of the microcapsules and the shape of the assembled microstructures are independently controllable, and both can modulate the drug releasing profile. This approach provides a powerful tool for obtaining the desired drug releasing profile in the local area that is otherwise difficult to obtain.

REFERENCES

[1] V. Gupta, Y. Khan, C. J. Berkland, C. T. Laurencin, and M. S. Detamore, "Microsphere-Based Scaffolds in Regenerative Engineering," *Annu Rev Biomed Eng,* vol. 19, pp. 135-161, Jun 21 2017.

[2] C. T. Laurencin, F. K. Ko, M. A. Attawia, and M. D. Borden, "Studies on the development of a tissue engineered matrix for bone regeneration," *Cells and materials,* vol. 8, pp. 175-181, 1998.

[3] J. J. Blaker, J. C. Knowles, and R. M. Day, "Novel fabrication techniques to produce microspheres by thermally induced phase separation for tissue engineering and drug delivery," *Acta Biomater,* vol. 4, pp. 264-72, Mar 2008.

[4] C. Berkland, K. Kim, and D. W. Pack, "Fabrication of PLG microspheres with precisely controlled and monodisperse size distributions," *J Control Release,* vol. 73, pp. 59-74, May 18 2001.

[5] Y. Yeo and K. Park, "Control of encapsulation efficiency and initial burst in polymeric microparticle systems," *Arch Pharm Res,* vol. 27, pp. 1-12, Jan 2004.

[6] L. de Juan and J. F. de la Mora, "Charge and Size Distributions of Electrospray Drops," *J Colloid Interface Sci,* vol. 186, pp. 280-93, Feb 15 1997.

[7] L. Zhang, J. Huang, T. Si, and R. X. Xu, "Coaxial electrospray of microparticles and nanoparticles for biomedical applications," *Expert Rev Med Devices,* vol. 9, pp. 595-612, Nov 2012.

[8] Y. H. Lee, F. Mei, M. Y. Bai, S. Zhao, and D. R. Chen, "Release profile characteristics of biodegradable-polymer-coated drug particles fabricated by dual-capillary electrospray," *J Control Release,* vol. 145, pp. 58-65, Jul 1 2010.

[9] S. Yuan, F. Lei, Z. Liu, Q. Tong, T. Si, and R. X. Xu, "Coaxial Electrospray of Curcumin-Loaded Microparticles for Sustained Drug Release," *PLoS One,* vol. 10, p. e0132609, 2015.

[10] X. Zhang and Y. Zhao, "Programmable patterning of polymeric microparticles by floating electrodes-assisted electrospray," *Journal of Micromechanics and Microengineering,* vol. 22, Apr 2012.

[11] M. Krampera, G. Pizzolo, G. Aprili, and M. Franchini, "Mesenchymal stem cells for bone, cartilage, tendon and skeletal muscle repair," *Bone,* vol. 39, pp. 678-83, Oct 2006.

[12] J. P. Vacanti and R. Langer, "Tissue engineering: the design and fabrication of living replacement devices for surgical reconstruction and transplantation," *Lancet,* vol. 354 Suppl 1, pp. SI32-4, Jul 1999.

[13] N. Mohan, V. Gupta, B. Sridharan, A. Sutherland, and M. S. Detamore, "The Potential of Encapsulating "Raw Materials" in 3D Osteochondral Gradient Scaffolds," *Biotechnology and Bioengineering,* vol. 111, pp. 829-841, Apr 2014.

[14] V. Gupta, N. Mohan, C. J. Berkland, and M. S. Detamore, "Microsphere-Based Scaffolds Carrying Opposing Gradients of Chondroitin Sulfate and Tricalcium Phosphate," *Front Bioeng Biotechnol,* vol. 3, p. 96, 2015.

CONTACT

*Yi Zhao, zhao.178@osu.edu; Tel: 614-247-7424

PRINTING BIOLOGICAL LIQUID ON HYDROPHOBIC 3D ELECTRODES

S. Chu[1], M.J. Lerman[3], J.N. Culver[4], J.P. Fisher[2], and R. Ghodssi[1,2,3]*
[1]Institute for Systems Research, Department of Electrical and Computer Engineering,
[2]Fischell Department of Bioengineering, [3]Department of Materials Science and Engineering,
[4]Institute for Bioscience and Biotechnology Research, Department of Plant Science and Landscape Architecture,
University of Maryland, College Park, Maryland, USA

ABSTRACT

This paper presents for the first time a programmable and scalable 3D electro-bioprinting (3D-EBP) process for patterning bionanoreceptors, cysteine-modified *Tobacco mosaic virus* (TMV1cys), on high-density micropillar array electrodes. The structural hydrophobicity in high aspect ratio geometries of micro/nano devices poses a critical challenge for assembling 3D biomaterial-device interfaces. Here, we have successfully integrated electrowetting principles with a modified state-of-the-art bioprinter for automated, high-throughput, and large-scale patterning of TMV1cys particles on hydrophobic 3D electrodes. The 3D-EBP processed bionanoreceptors maintained both structural and chemical functions as characterized via SEM and fluorescence microscopy. Overall, the innovative 3D biomanufacturing process creates excellent opportunities for advancing on-demand bio-integrated devices including multiplexed biosensors and bioenergy harvesting devices.

INTRODUCTION

The convergence between biochemistry and micro/nano manufacturing technologies has brought revolutionary advancements in the development of miniaturized devices and biomaterial integrated systems [1], [2]. Technology for bio-device integration has rapidly evolved over the past two decades based on biochemistry principles, processing methodologies learned from the micro/nano fabrication industry, and instrumental science/engineering. The diversity of biofabrication technologies have led to greater understanding of biomolecular activities through on-chip characterizations, and is enabling rapid advancement of high-density, multiplexed bioarrays necessary for biosensing and diagnostic applications.

Building upon the variety of methods, many researchers have demonstrated integration of biological materials with three-dimensional transducers in an effort to achieve enhanced bioelectronics performance at a miniaturized system scale [3], [4]. Three-dimensional structures at micro- and nano- scales offer a number of beneficial properties compared to their two-dimensional counterparts, allowing for an extensive range of applications including micro energy storage/harvesting device [5], micro/nano actuators [6], micro thermal management devices [7], water-repellent surfaces [8], optical modulators [9], 3D VLSIs [10], etc. The primary attractive feature of these approaches is the high density of physical interfaces between system components and materials within the restricted surface area budget, which can directly translate into large enhancements in performance. Moreover, precise control over the arrangement of the structures through microfabrication or emerging 3D printing technologies further highlights the utility of three-dimensional components with increased surface-to-volume ratio, functional uniformity and tunability.

One of the interesting characteristics present in small scale 3D structures is their limited wetting property known as structural hydrophobicity [11]–[13]. When micro- or nano- scale structural components are densely arranged, the wetting of 3D cavities with liquids is limited by surface tension at the solid-liquid, liquid-air, and solid-air interfaces. Considering most biological materials are stored in buffered aqueous solutions due to the narrow biological stability windows, the structural hydrophobicity can be a significant limiting factor when attempting to introduce biological materials into the 3D cavities for device functionalization. In our recent report, we have provided experimental evidence to highlight the potential limitation using cysteine-modified *Tobacco mosaic virus* (TMV1cys) and Au-coated Si micropillar array (µPA) electrodes. In addition, the electrowetting principle - which controls surface wettability with applied electric potential - has been introduced as an enabling technique for uniform and localized immobilization of the bionanoreceptors on densely-arranged µPA electrodes [14], [15].

Here, we have successfully integrated the electrowetting-assisted biofabrication technique with a customized bioprinter for automated, high-throughput, and large-scale printing of the bionanoreceptors on 3D electrodes. The simple system components, optimized printing process parameters including extrusion pressure/time and printing distance, combined with the electrowetting process determined from our previous work, allows a novel 3D bioprinting technique with excellent repeatability and consistency, ultimately offering a unique function to existing bioprinting systems to bring an on-demand programmable, scalable, and readily adaptable 3D biofabrication technology.

MATERIALS AND METHODS

Hydrophobic 3D Electrodes and Biological Ink

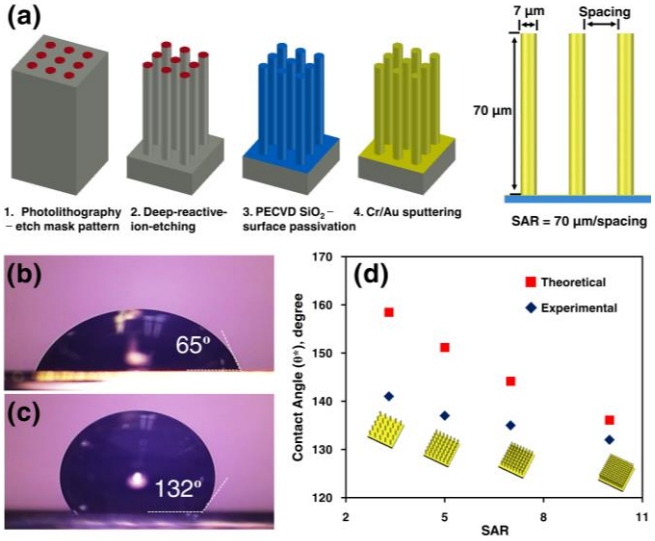

Figure 1: Au-coated µPA electrodes and their wettability. (a) Fabrication process and dimensions for the µPA electrodes. A comparison of TMV1cys solution droplet (10 µL) contact angles on (b) planar Au and (c) Au-coated µPA (SAR=10). (d) A plot of TMV 1cys solution droplet contact angles on Au-coated µPA at different SARs. The relationship between the contact angle/hydrophobicity and SARs follows the trend anticipated by Cassie-Baxter equation.

978-1-940470-03-0/HH2018/$25©2018TRF
DOI 10.31438/trf.hh2018.41

The Si micropillar array (μPA) electrodes have been fabricated through a standard microfabrication process as described in Figure 1a. A Si wafer is etched down via DRIE using a photolithographically patterned negative photoresist (NR9-1500PY, Futurrex) as the etch mask. The resulting Si μPAs are passivated by 500 nm PECVD SiO_2 followed by sputtering of Cr (30 nm)/Au (200 nm). The pillar aspect ratio was held constant at 10 (height: 70 μm, diameter: 7 μm) while the spacing aspect ratio (SAR) varied from 3.3 to 10 to investigate the effect of the structural hydrophobicity level on the final pattern size/resolution.

The biomaterial used in this work is genetically-modified TMV expressing cysteine residues on its outer surface (TMV1cys, the details of genetic modification and purification protocols can be found in previous report [16]). A TMV1cys solution of 0.2 mg/ml concentration in 0.1 M, pH 7 phosphate buffer (PB) solution is used as the bio-ink for all experiments. The enhanced metal binding properties of TMV1cys, such as self-assembly onto Au surfaces and surface metallization with Ni, provide effective means for characterization of functionalization morphology after the electrowetting assisted bioprinting process.

As an initial step, the structurally hydrophobic properties of the μPA electrodes were characterized via contact angle measurements of 10 μL sessile drops of the TMV1cys solution on Au-coated planar (Figure 1b) and μPA (Figure 1c) electrodes. While the planar Au surface exhibits a hydrophilic nature with a 65° contact angle, the μPA surface yields more hydrophobic characteristics as indicated by the 132° contact angle (SAR=10). This is close to the theoretically expected value (136º), calculated based on the *Cassie-Baxter* equation (Eq. 1), where θ^* is the apparent contact angle on the μPAs, ϕ_s is the fraction of the solid in contact with the TMV1cys solution, and θ_0 is the contact angle on the planar Au substrate [12].

$$\cos\theta^* = -1 + \phi_s(1 + \cos\theta_0) \quad (1)$$

Figure 1d plots both theoretically expected (derived from *Cassie-Baxter* equation (Eq. 1) with θ_0=65º, and ϕ_s calculated from the pillar geometry) and experimentally acquired contact angles (θ*) indicating that the hydrophobicity of the μPAs decreases with an increase in SAR. The disparity between the two can be attributed to the gentle pressure applied when loading the droplet onto the μPAs via syringe tips and hydrophilic surface (Au) inducing liquid pinning onto the pillar tips [14]. Such wetting state is only valid when there is no external disruption force due to the hydrophilicity of the Au surface. Once the *Cassie-Baxter* state is disrupted with an external force (e.g. mass loading), a faster transition of the wetting state - indicated by the droplet spreading into the cavities (transitioning to the *Wenzel* state) - is observed with the lower SAR μPAs (data not shown). It becomes a significant challenge to introduce the solution into narrower cavities (SAR >= 7) that do not easily transition to a *Wenzel* state, which can be attributed to less pressure loading per spacing segment. In other words, the wider spacing reduces ϕ_s which increases the fraction of the liquid droplet that is supported by the micropillars [11]. The TMV1cys droplets on such high SAR μPAs are readily movable with no traceable liquids remaining on the electrode surface.

Integration of 3D-EBP with a Bioprinter

The 3D electro-bioprinting (3D-EBP) technique has been integrated with a state-of-the-art commercial 3D bioprinter (3D Bioplotter, Envision TEC) by simply connecting a function generator (Agilent 33220A) to the printing nozzle and the substrate as described in Figure 2a. The built-in graphical user interface allowed a highly automated and programmable 3D-EBP with precise control over nozzle pressure, printing distance, array size/density, and solution temperature. As the 3D Bioplotter is mainly designed for printing materials carried in hydrogels (e.g. gelatin, alginate, corn starch, etc.), the controllable pressure and time ranges for ink extrusion at the nozzle are optimal for higher viscosity fluids compared to the buffer solution used in this work. Through multiple iterations at the lowest extrusion time and pressure ranges, the optimal process parameters have been determined as 0.3 second extrusion at 0.1 bar with a distance from the nozzle to the substrate set at 100 μm. It should be noted here that the optimization of the process parameters strongly depends on the nozzle size and the viscosity of the ink solution.

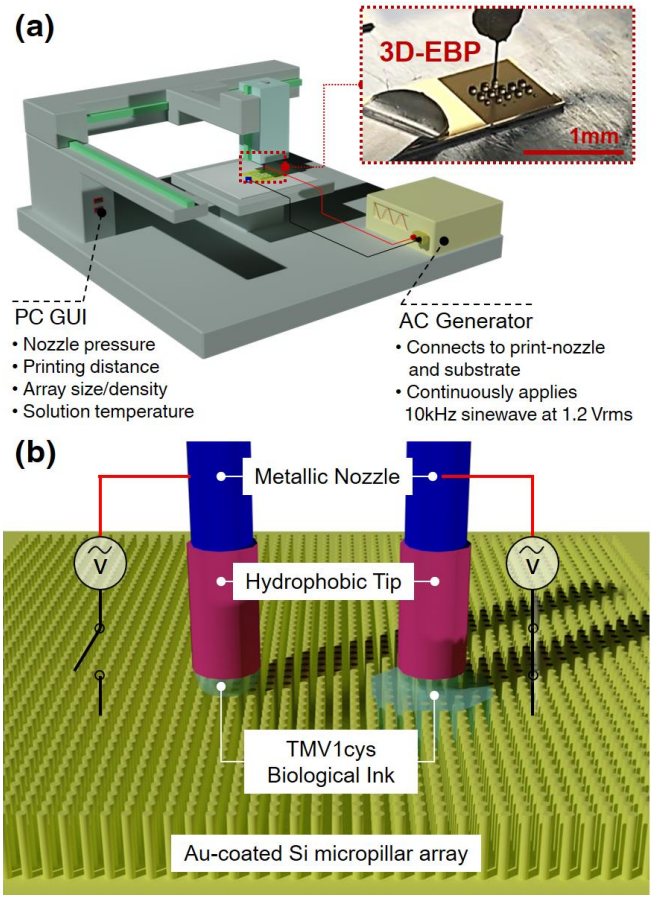

Figure 2: (a) Overview of the programmable 3D-bioprinting system integrating 3D-EBP with a commercial bioprinter. (b) Illustration of TMV solution impinging onto the μPA from teflon-modified needles. The solution impinging onto the μPA surface without electrowetting (left) keeps a spherical shape without further access/spreading into the microcavities (Cassie-Baxter state), while the droplet impinging with electrowetting (right) selectively wets the underlying cavities (Wenzel state).

In this initial demonstration, a 32-gauge stainless steel needle (inner diameter: 100 μm, outer diameter: 260 μm) was utilized with a hydrophobic modification at the tip via dip-coating with Teflon; the tip was dipped into Teflon solution (Teflon™ AF 400S1) and cured at 180°C for 3mins. A syringe was connected during the curing step to continuously flow air through the tip to prevent blockage during the curing process. The hydrophobic coating at the tip was critical to isolate the droplet forming towards the substrate during extrusion (Figure 2b); otherwise the extruded droplets would roll-up to the outer metallic surface causing inconsistency in droplet size and printing failures.

The electrowetting voltage was continuously applied during the printing process by seamlessly integrating the function generator to the metallic -nozzle and -printing bed without hindering the printing operation. Based on our previous work, a sinusoidal voltage signal of 1.2 V_{rms} at 10 kHz was applied to induce uniform and localized wetting of the TMV1cys ink into the µPAs [14]. All processes were conducted at room temperature with ambient humidity. Both the print-bed and the bio-ink cartridges were kept at 10°C for extended stability of TMV1cys particles throughout the multiple printing processes. The bio-printed electrodes were incubated overnight in a humid chamber for self-assembly of TMV1cys particles onto the electrode surface through thiol-Au binding [15].

RESULTS AND DISCUSSIONS

Bio-ink Printing on 3D µPA Electrodes

Figure 3 compares the printing processes on µPA electrodes (SAR: 10) under two different conditions emphasizing electrowetting as an enabling method. When the printing process is conducted without applying the electrowetting voltage (Figure 3a), the extruded droplets at the printing nozzle do not settle onto the µPA surface, and collectively accumulate at the nozzle until falling onto the surface due to gravity (the droplets loaded onto the µPA surface does not penetrate into the cavity). However, with the application of the electrowetting technique (Figure 3b), the 3D-EBP allowed consistent dispensing of ~1 uL of the bio-ink on the µPA electrodes throughout the programmed array patterns by successfully introducing the bio-ink into the designated micro-cavities. The spacing between the droplets has been set to 1 mm to prevent adjacent droplet from merging. Particularly for creating discrete patterns, the liquid merging between the neighboring droplets becomes problematic for lower SAR µPA electrodes as they are more susceptible to lateral spreading of liquid during the electrowetting process (further discussed in the next section). However, the merging event can be utilized for creating continuous patterns on the 3D substrate.

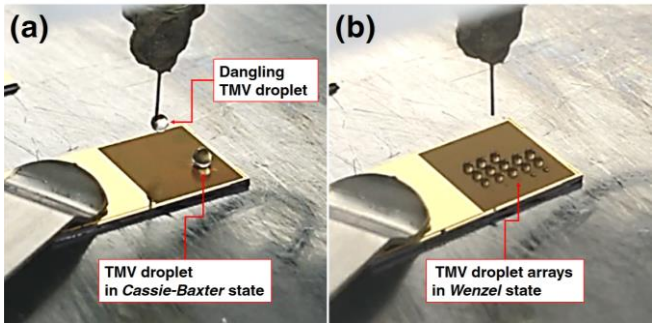

Figure 3: Optical images comparing the TMV1cys solution droplet printed µPA electrodes (SAR=10). (a) Hydrophobic nature of the µPA electrodes repels the droplets being loaded onto the surface resulting in failure in printing/patterning the droplets. (b) Continuous application of electrowetting voltage during the printing process allows successfully patterning of uniform droplet volumes on the µPA electrodes.

Functionalization Morphology and Pattern Sizes

In order to characterize the TMV1cys printed on the µPA electrodes using SEM, an electroless Ni coating was performed after the overnight incubation step. As shown in Figure 4a, all µPAs featuring different SARs/densities were successfully coated with the TMV1cys at the printed spots. The top-down SEM images taken at the droplet boundaries confirm the localized patterning of the TMV1cys within the 3D substrate with more surface functionalized particles identified on the printed side (left from the light-blue line) compared to the non-printed area (right from the light-blue line). However, it should be noted that the TMV1cys density on the µPA electrodes with higher SAR is noticeably less compared to that observed from the lower SAR electrodes. This can be attributed to limited TMV1cys diffusion from top to bottom of the electrodes for dense microstructures. Comparing with the µPAs without electrowetting (Figure 4b), the nanoparticles assembled on the lower bottom of the pillar surfaces in Figure 4a (SAR: 10) confirm that the ink solution has successfully reached the bottom surface with electrowetting, indicating that the use of higher concentration ink can help increase the biofunctionalization density on high SAR µPA electrodes.

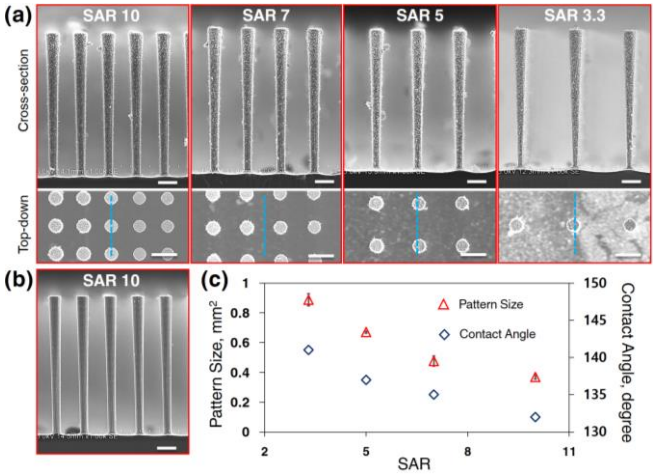

Figure 4: Process evaluation using SEM. (a, cross-section view) TMV1cys particle coating on all sidewalls of the µPAs has been achieved (observed as surface textures). (a, top-down view) Also, clear functionalization boundary has been observed at the wetting edges (blue-dotted line) of each of the µPAs highlighting the pattern fidelity enabled by structural hydrophobicity. (b) The clean surface of the µPAs processed without electrowetting further emphasizes the electrowetting as an enabling technique for bio-printing. (c) The pattern sizes ranged from 0.89mm² to 0.37mm² (N=5) following the hydrophobicity levels of the µPAs. (scale bars: 10µm).

The dependence of the pattern/spot sizes on the SARs/pillar densities have been characterized by estimating semi-circular pattern boundaries observed from top-down SEM images. Figure 4c compares the pattern sizes measured from the µPA electrodes with different SARs at the respective contact angles - representative of their hydrophobicity levels. The lower SAR µPA electrodes resulted in a larger pattern size due to the facile spreading of the bio-ink into the microcavities with the electrowetting (under the identical process settings, which is in a good agreement with our previous investigation. The statistical analysis using five different locationss of a printed array show a high consistency in pattern size per SARs, emphasizing the excellent uniformity and repeatability of the 3D-EBP process.

Scalable Biofunctionalization Density

Biochemical activity of the printed TMV-1cys particles is evaluated using a sulfhydryl (-SH on cysteine) specific fluorescent labeling reagent, Fluorescein-5-Maleimide (Thermo Fisher Scientific). As our previous report confirmed that the electrowetted TMV1cys on µPAs enhances bionanoreceptor density by surface area enhancement (SAE) factors anticipated from the 3D electrode geometries [14], this work has focused on achieving scalable nanoreceptor density per different SARs of the µPAs. Figure 5a

compares top-down fluorescent microscopy images taken from the printed spots on different electrode geometries. Under an identical exposure time, TMV1cys printed on µPA electrodes resulted in a significantly higher fluorescence compared to the planar electrodes with an excellent patterning fidelity (Figure 5a, bottom-right), due to the underlying microstructure. However, there is a noticeable discrepancy between the change in increment factor of the fluorescence intensity and the SAE factor calculated based on the µPA geometry (Figure 5b). This is attributed to the lower density of TMV1cys on the high SAR µPAs as supported by the SEM characterizations in Figure 4a, indicating that control over concentration of bio-ink may need to be optimized to obtain highly controllable functional scalability of the resulting nano/micro/bio-integrated components.

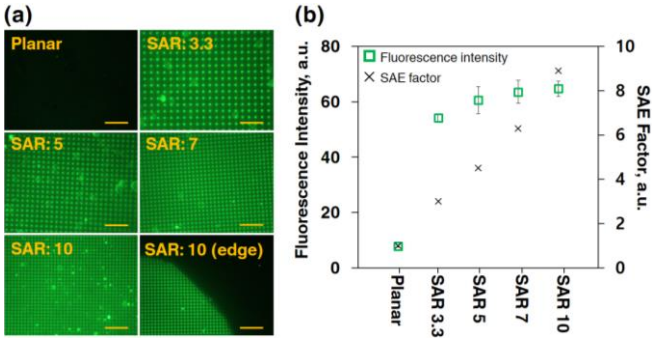

Figure 5: Characterization of fluorescence intensity from (a) TMV1cys functionalized on planar Au and µPA electrodes displaying SARs ranging from 3.3 to 10 (scale bars: 100µm). (b) A significant increase in functionalization density is achieve with the µPAs as reflected in the increase in fluorescence intensity (N=5).

CONCLUSIONS

This work offers a unique function to existing bioprinting systems bringing a simple, innovative, and technology enabling 3D biofabrication through integration of the core manufacturing technique based on the electrowetting principle. The presented system is fully automated, scalable, and readily adaptable for a wide range of applications. While the presented demonstration utilizes a particular biomaterial of interest to our work (TMV1cys), this manufacturing technology can be applicable for integrating other micro/nanomaterials (DNA, proteins, cells, carbon nanotubes, graphene, etc.), stored in aqueous media, onto conductive hydrophobic electrodes. Possible applications include areas developing energy storage/harvesting devices, biochemical sensors, optical metamaterials, heat management devices, superhydrophobic surfaces, and more. Overall, the innovative 3D biomanufacturing process generates excellent opportunities for advancing on-demand bio-integrated devices opening up unprecedented possibilities in micro/nano/bio integrated fabrication technologies and platforms.

ACKNOWLEDGEMENTS

This work was funded by the Biochemistry Program of the Army Research Office (W911NF-14-1-0286). The authors would like to acknowledge the support of the Maryland Nanocenter and its FabLab for support in fabrication and imaging processes.

REFERENCES

[1] Y. Liu, E. Kim, R. Ghodssi, G. W. Rubloff, J. N. Culver, W. E. Bentley, and G. F. Payne, "Biofabrication to build the biology-device interface.," *Biofabrication*, vol. 2, no. 2, p. 22002, Jun. 2010.

[2] K.-B. Lee, S.-J. Park, C. A. Mirkin, J. C. Smith, and M. Mrksich, "Protein Nanoarrays Generated By Dip-Pen Nanolithography," *Science (80-.).*, vol. 295, no. 5560, 2002.

[3] L. Shi, Z. Chu, Y. Liu, J. Peng, and W. Jin, "Three-dimensional porous microarray of gold modified electrode for ultrasensitive and simultaneous assay of various cancer biomarkers," *J. Mater. Chem. B*, vol. 2, no. 18, pp. 2658–2665, 2014.

[4] J. Liu, J. Wang, T. Wang, D. Li, F. Xi, J. Wang, and E. Wang, "Three-dimensional electrochemical immunosensor for sensitive detection of carcinoembryonic antigen based on monolithic and macroporous graphene foam," *Biosens. Bioelectron.*, vol. 65, pp. 281–286, 2015.

[5] K. Gerasopoulos, E. Pomerantseva, M. McCarthy, A. Brown, C. Wang, J. Culver, and R. Ghodssi, "Hierarchical three-dimensional microbattery electrodes combining bottom-up self-assembly and top-down micromachining," *ACS Nano*, vol. 6, no. 7, pp. 6422–6432, 2012.

[6] G. T. A. Kovacs, N. I. Maluf, and K. E. Petersen, "Bulk micromachining of silicon," *Proc. IEEE*, vol. 86, no. 8, pp. 1536–1551, 1998.

[7] S. Adera, D. Antao, R. Raj, and E. N. Wang, "Design of micropillar wicks for thin-film evaporation," *Int. J. Heat Mass Transf.*, vol. 101, pp. 280–294, 2016.

[8] N. Kumari and S. V. Garimella, "Electrowetting-induced dewetting transitions on superhydrophobic surfaces," *Langmuir*, vol. 27, no. 17, pp. 10342–10346, 2011.

[9] H. Inan, M. Poyraz, F. Inci, M. A. Lifson, M. Baday, B. T. Cunningham, and U. Demirci, "Photonic crystals: emerging biosensors and their promise for point-of-care applications," *Chem. Soc. Rev.*, p. , 2017.

[10] R. Reif, A. Fan, Kuan-Neng Chen, and S. Das, "Fabrication technologies for three-dimensional integrated circuits," in *Proceedings International Symposium on Quality Electronic Design*, pp. 33–37.

[11] A. Tuteja, W. Choi, M. Ma, J. M. Mabry, S. a Mazzella, G. C. Rutledge, G. H. McKinley, and R. E. Cohen, "Designing superoleophobic surfaces," *Science*, vol. 318, no. 5856, pp. 1618–22, 2007.

[12] V. Bahadur and S. V Garimella, "Electrowetting-based control of static droplet states on rough surfaces," *Langmuir*, vol. 23, no. 9, pp. 4918–4924, 2007.

[13] P. Liu, L. Cao, W. Zhao, Y. Xia, W. Huang, and Z. Li, "Insights into the superhydrophobicity of metallic surfaces prepared by electrodeposition involving spontaneous adsorption of airborne hydrocarbons," *Appl. Surf. Sci.*, vol. 324, pp. 576–583, 2015.

[14] S. Chu, T. E. Winkler, A. D. Brown, J. N. Culver, and R. Ghodssi, "Localized Three-Dimensional Functionalization of Bionanoreceptors on High-Density Micropillar Arrays via Electrowetting," *Langmuir*, vol. 34, no. 4, pp. 1725–1732, Jan. 2018.

[15] S. Chu, M.J. Lerman, J.N. Culver, J.P. Fisher, and R. Ghodssi, "Electrowetting for Bio-Printing on 3D Hydrophobic Electrodes," Presented at *The 9th International Conference on Microtechnologies in Medicine and Biology*, Monterey, CA, Mar-2018.

[16] E. Royston, A. Ghosh, P. Kofinas, M. T. Harris, and J. N. Culver, "Self-assembly of virus-structured high surface area nanomaterials and their application as battery electrodes," *Langmuir*, vol. 24, no. 3, pp. 906–912, 2008.

CONTACT

*R. Ghodssi, tel: +1-301-405-8158; ghodssi@umd.com

A BIODEGRADABLE SENSOR HOUSED IN 3D PRINTED POROUS TUBE FOR IN-SITU SOIL NITRATE DETECTION

Hongjie Jiang, Wuyang Yu, Rahim Rahimi, and Babak Ziaie
Purdue University, West Lafayette, IN, USA

ABSTRACT

In this work, we demonstrate a low-cost and biodegradable electrochemical sensor packaged in a 3D printed porous tube that can sample the nitrate ion from irrigated soil for detection while simultaneously protecting the sensor from any external interference when buried in soil; thus achieving a stable in-situ measurement of soil nitrate concentration with a controllable spatial resolution once deployed in an array format. The sensor array can also be coated/passivated by different biodegradable polymers (or thickness) having a controllable degradation rates, providing a time-delayed sensor exposure to the environment, hence allowing for a longer/tunable working period.

INTRODUCTION

Nitrate (NO_3^-) is a ubiquitous nitrogen compound existing in many different environments and used in various industries such as food [1, 2] and agriculture [3]. Nitrate presence is essential for crop growth since it is one of the key required nutrients in the soil. As one of the key targets in precision agriculture, accurate monitoring of nitrate is of extreme importance in optimizing fertilizer application rates and improving agricultural production. Nitrate also can be a source of contamination of surface and groundwater if its usage as the soil fertilizer is excessive and beyond the actual requirements. If these contaminated water is used to irrigate the plants, which are later consumed by animals and human, or directly used by animals and human, health problems can occur due to the toxicity of nitrate [3]. Therefore, for environmental and ecological sustainability, the nitrate utilities or sources need a strictly scientific regulation and management. To achieve these goals, deploying the in-field nitrate sensors is a critical step.

Based on different nitrate sensing requirements, several measurement methods capable of providing a quantitative result have been investigated [4], [5]. Optical non-contact methods, such as colorimetric or atomic absorption spectrometry, usually involve reducing nitrate to nitrite and measuring the nitrite absorbance at a specific wavelength of light. These methods need discrete soil sampling and sophisticated instruments, which are labor-intensive and costly. A more direct approach first exact the nitrate from the analyte sample and then measure its concentration through different techniques such as UV [6], fluorimetric [7], or mass spectroscopy [8]. These systems still are laboratory-based and will not allow for rapid in-situ measurement is agricultural settings. Diffuse reflectance spectroscopy has recently attracted considerable attention as a more direct method to detect the nitrate concentration in soil by measuring the level of light energy reflected by soil particles and nutrient ions. This has its unique advantages such as non-destructiveness and in-situ operation. However, this method is strongly soil dependent and require careful calibration [2], [4]. Electrochemical sensors [9] using ion selective electrode (ISE) is an attractive choice for in-field and cost-effective nitrate detection. For example, a prototype tractor-mounted field monitoring system comprised of a soil sampler and a fluidic module, to gather and transport the soil samples from 15 cm deep slot, was used to extract and analyze nitrate levels with an ISE with up to 95% accuracy [10]. In another example, an integrated agitated chamber module (IACM) was developed to contain ISEs and data acquisition system. This was attached to the commercial Veris® Mobile Sensor Platform in order to detect the nitrate concentration in a suspension of soil and water [11]. Although these on-the-go direct nitrate measurement systems have a high accuracy, their fabrication process is still complicated and their deployment face possible mechanical or electrical problems (e.g., clogging of the extractor). The planar electrochemical ISEs that use solid state electrodes to eliminate the requirement of the inner solution of conventional electrochemical sensor are suitable for scalable manufactory through mass-printing technologies (inkjet or screen printing).

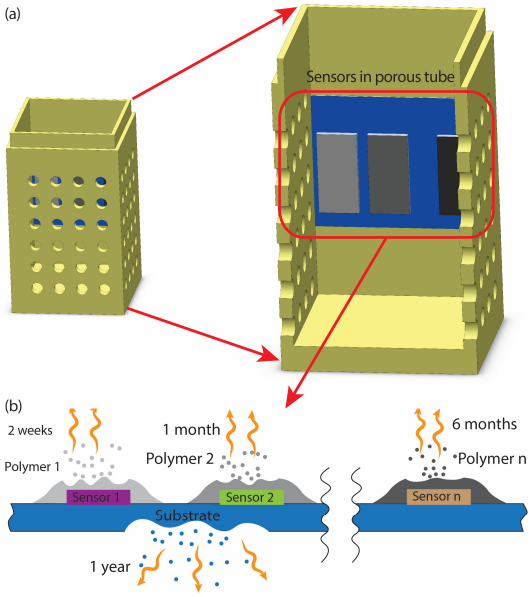

Figure 1: (a) Conceptual illustration of the printed biodegradable nitrate sensors array in 3D printed sampling tube for in-situ controllable temporal and spatial nitrate measurement; (b) Different biodegradable polymers erode at different times to expose the sensors.

In this work, we describe the development of screen printed potentiometric nitrate sensor with solid state working and reference electrodes housed in a 3D printed rectangular tube designed to have three porous and one non-porous side walls, Figure 1. The former with micro-pores is used to extract/filter the nitrate containing solution from the surrounding soil into the tube and thus create an aqueous environment for nitrate detection; the latter is used to hold the ISEs array inside the tube. Once equipped with nitrate sensors and inserted into the soil, the porous tube can be deployed at the predetermined regions or depths to achieve a desired spatial resolution of nitrate detection. In addition, a biodegradable polymer, PLGA in this context, is deposited into the sensors' sensing windows with different thicknesses. This results in different biodegradation periods, allowing the users to control the time-dependent activation of sensors. The 3D resin of tube and the substrates of sensor also can be selected to be biodegradable. Note that this conception can be extended to other electrochemical sensors for precision agricultural (e.g., pH, phosphate, and other micro and macronutrients) as a gateway to high resolution sensing platforms for precision agriculture.

978-1-940470-03-0/HH2018/$25©2018TRF
DOI 10.31438/trf.hh2018.42

FABRICATION

The ion-selective membrane (ISM) consists of tetra-n-octylammonium bromide (TOA-bromide), poly (vinyl chloride) (PVC), di-n-butyl phthalate (plasticizer), and tetrahydrofuran (THF) [12]. PVC was purchased from Aldrich, and the other three components were obtained from Alfa Aesar. Potassium nitrate (KNO_3) was purchased from Alfa Aesar and used as the primary ion in all the test procedures. Potassium chloride (KCl) were bought from Mallinckrodt Chemicals and used in the fabrication of reference electrodes and the selectivity coefficient experiments. Potassium phosphate monobasic (KH_2PO_4) and sodium sulfate (Na_2SO_4) were provided by Mallinckrodt Chemicals and used in the selectivity coefficient experiments. Poly Lactic-co-Glycolic Acid (PLGA) (719897, Mw 7,000 – 17,000 g/mol) was purchased from Sigma Aldrich.

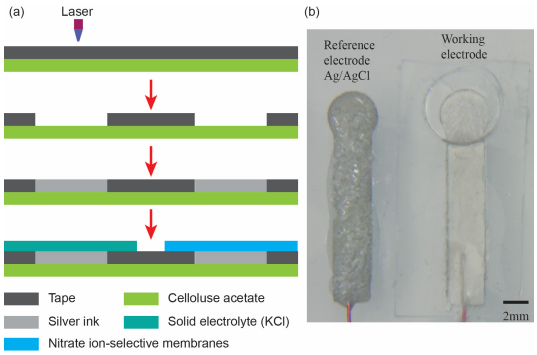

Figure 2: (a) Fabrication process of the sensor; (b) Photograph of the sensor.

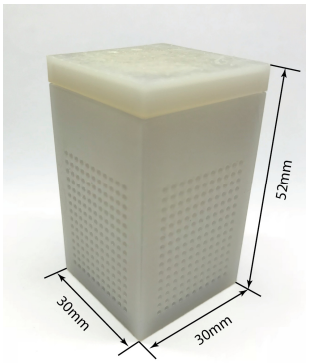

Figure 3: 3D printed porous tube.

The fabrication process of sensor is shown in Figure 2. First, a duct tape (0.22 mm thick) is attached to cellulose acetate substrate and laser-machined to create two electrode patterns. Then, silver ink (CreativeMaterials) are screen-printed onto the exposed regions and subsequently dried at 70 °C for 30 min. One silver electrode is immersed into 0.1M FeCl3 solution for 5 min to form the reference Ag/AgCl electrode, which is then covered with a mixture of UV curable epoxy and KCl powder in a 1:1 w/w ratio under 10 min UV light curing to form the solid electrolyte. Finally, a ~100 µm thick nitrate ion selective membrane (ISM) is solvent-casted on the second silver electrode to form the working electrode. Before measurement, the reference electrode is conditioned in 1M KCl solution for 30 min while the working electrode is conditioned in 0.1 M nitrate solution for 2 days.

The porous tube was 3D printed by a stereolithography (SLA) desktop 3D printer (Formlabs. Inc) using a photo-reactive resin (mixture of methacrylic acid esters and a photoinitiator), Figure 3, The pores were designed to be 1mm diameter, allowing a fast water sampling while keeping the soil outside.

The PLGA film is made by casting the PLGA powder in acetone with 10% w/v and leaving the polymer solutions in 70 ºC oven approximately 24 hours for complete drying.

EXPERIMENTS AND DISCUSSION

Potentiometric method was employed in the experiment in which the potential between the ISE and reference electrode was recorded by Agilent 34401A.

Sensor Characterization in Standard Solution

The sensitivity characterization was conducted with a set of 3 sensors tested at one time. The test solution was prepared by dissolving the KNO_3 powder in deionized water to reach four different nitrate concentrations, from 0.0001 M to 0.1 M. The sensors were then immersed into the solutions and their potentials were monitored for 5 minutes in each solution, sequentially from the lowest to the highest concentration. No ionic strength adjustment or buffer solution was used in the measurement to eliminate the effect of interference ions, especially in low nitrate concentration solution. The result showed a Nernstian sensitivity of averaged 57 mv/decade (SD=2.7 mv), Figure 4. The response time was short, between 5 and 10s.

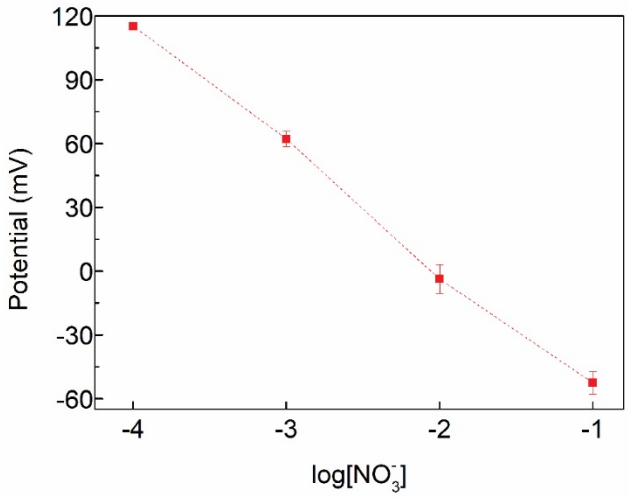

Figure 4: Sensitivity characterization of nitrate sensor in four standard solutions from .0001 M to .1 M.

Next, the potentiometric selectivity coefficients were measured and calculated using the definition of the Nicolsky-Eisenman equation as follows [13]:

$$E = E_0 + {RT}/{(Z_A F)} \ln[a_A + \sum_B K_{A,B}^{pot} (a_B)^{{Z_A}/{Z_B}}]$$

Where E is the measured potential; E_0 is the standard potential of the electrodes; Z_A and Z_B are charge numbers of the primary ion, A, and of the interfering ion, B; a_A and a_B are the activities of the primary ion, A, and of the interfering ion, B; and $K_{A,B}^{pot}$ is the potentiometric selectivity coefficient for the primary ion A against the interfering ion, B; R is the gas constant of 8.135 J/K/mol, T is the temperature in kelvin, and F is the Faraday's constant of 9.684 x

10^4 C/mol. In this work, the selectivity coefficients of nitrate sensors were measured in two separate solutions with the same ion activity ($a_A = a_B$), one contained only the primary ion, NO_3^- and the other contained only the interfering ion, Cl^-, or $H_2PO_4^-$, or SO_4^{2-}. The interfering ions were chosen as they are the most universal ions in the soil. The measurement protocol was the same as the sensitivity characterization, i.e., the sensor was continuously measured in each solution for 5 minutes. The result is shown in Table 1. The sensor has a high selectivity to the nitrate since all the measured selectivity coefficients were smaller than 1. The chloride ion has a little higher interference as compared to other interfering ions; however, as the normal nitrate concentration in soil is higher than 0.0001 M [2], this however will not compromise the nitrate sensor functionality, especially in nitrate pollution regulation since interfering of chloride ion decreases as nitrate concentration increases.

Table 1: Selectivity coefficients of the fabricated nitrate sensor

	Cl^-	$H_2PO_4^-$	SO_4^{2-}
0.0001M	5.02 E-01	1.82 E-01	3.10 E-04
0.001M	2.82 E-01	7.97 E-02	6.44 E-05
0.01M	1.39 E-01	1.63 E-02	6.41 E-06
0.1M	1.27 E-01	6.23 E-03	3.39 E-06

Finally, the long-term drift of the sensor was characterized by immersing the sensors in 0.1 M nitrate solution and continuously measuring the potential change at an interval of 50 s for one day. The results showed a ~0.8 mv/hour linear positive drift (19.2 mV in 24 hours, or 0.1 M drift) due to the change of inner potential induced by the formation of a thin aqueous layer [14], Figure 5. The long-term drift can be reduced or totally avoided by the biodegradation passivation on the sensing region as the sensor would only be activated and work at a programmed window.

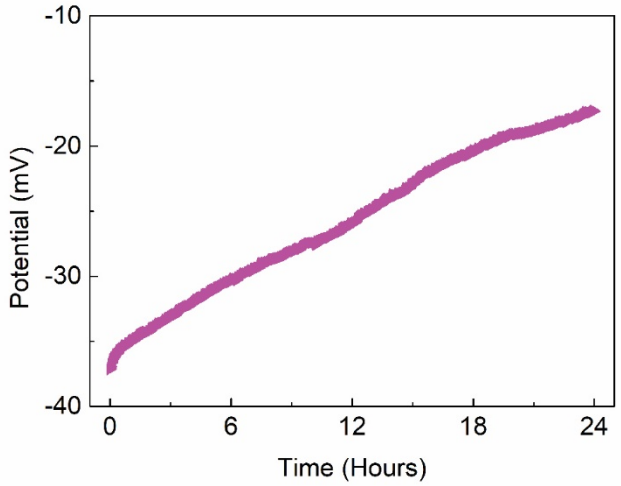

Figure 5: Drift of nitrate sensor immersed in 0.1M nitrate solution for one day.

Sensor Characterization in Soil Samples

The sensor capability to detect nitrate in real soil samples (silt loam) was also evaluated. First, the soil was mixed with DI water in a ratio of 3:5 w/w and nitrate levels were measured using the fabricated sensor and a commercial sensor (Cole-Parmer). High accuracy (~95%) was achieved, showing the nitrate concentration of soil as ~0.00017M, Figure 6(a). Later, the soil was mixed with standard nitrate solution in 3:5 w/w ratio and measured only by the fabricated sensor. The result was then compared to in nitrate solution without adding soil, where both the measurements were almost the same in the range of 0.001 to 0.1M while the 60% difference in the mixture of 0.0001M nitrate solution and soil was mostly ascribed to the intrinsic nitrate of soil (~0.00017M), thus further confirming the high accuracy, Figure 6(b).

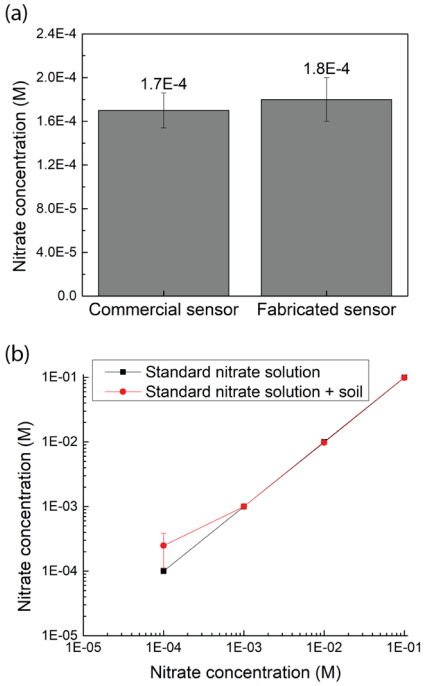

Figure 6: (a-b) Accuracy characterization of sensor with soil samples.

The PLGA degradation characteristics was measured by immersing a 100 µm thick PLGA film in the soil sampling solution and measuring its weight by gravimetric analysis. At the same time, a nitrate sensor with the sensing area coated with a layer of 100 µm thick PLGA was also immersed in the same solution with its potential monitored at a shorter interval. The results showed that the PLGA film lost an average of 15% weight within 10 days, enough to expose the sensor and initiate the measurement, Figure 7.

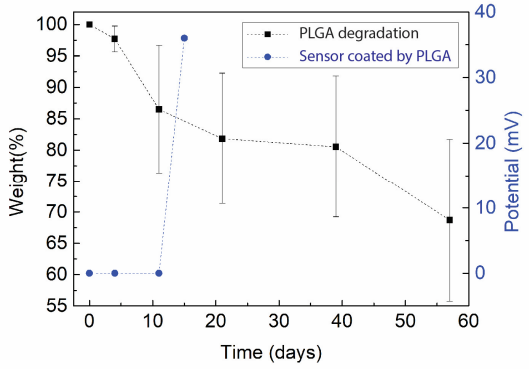

Figure 7: Biodegradation characterization of PLGA.

Finally, we tested in-situ performance of the sensor housed in the porous tube and inserted into soil. This was done by pouring DI water into the soil until the water reached the sensor through the tube pores, Figure 8(a). After an initial sharp increase from zero to a high value due to the surrounding medium changes from air to water, the measured potential dropped quickly to a stable value within few

minutes after the completion of nitrate ion sampling from soil to the water inside tube. Figure 8(b) shows the outputs, the sensor using tube sampling can detect a ~30 mv difference from two kinds of soils (compared to a ~20 mv difference measured by a commercial nitrate sensor directly inserted into the soil). This shows that the porous tube can be sued to house the ISE potentiometric sensor and provide for an accurate, stable, and fast in-situ detection of nitrate concentration in the soil.

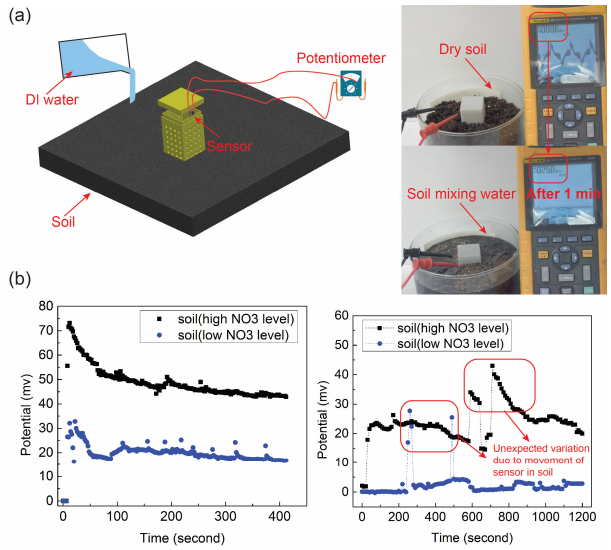

Figure 8: Nitrate measurement using in-situ sampling tube. (a) Experiment setup, (b) comparison of test results for between with (left) and without sampling tube (right).

CONCLUSIONS

In this work, we developed a screen-printed nitrate sensor using solid state working and reference electrodes. The fabricated sensor was able to achieve a 57 mv/dec linear sensitivity within the nitrate concentration range of 0.0001 M to 0.1 M, covering the normal range of nitrate in soil. The sensor had an average of 0.8 mv/hr drift, which could be mitigated by covering the sensing regions by a biodegradable polymer layer of varying thickness or chemical composition. A 3D printed porous tube was used to house the sensor and act as a sampling and protective enclosure. The sensor and its housing can be used for in-situ measurement of nitrate in farming soil at various spatio-temporal scale for precision agriculture.

ACKNOWLEDGEMENTS

The authors thank the staff at Purdue University Birck Nanotechnology Center and the Ziaie Biomedical Microdevices Laboratory members for their assistance in fabrication and experiments.

REFERENCES

[1] W. Clements, S.-R. Lee, and R. Bloomer, "Nitrate Ingestion: A Review of the Health and Physical Performance Effects", Nutrients, vol. 6, no. 11. 2014.

[2] H.-J. Kim, K. a Sudduth, and J. W. Hummel, "Soil Macronutrient Sensing for Precision Agriculture", J. Environ. Monit., vol. 11, no. 10, pp. 1810–24, 2009.

[3] N. S. Bryan, D. D. Alexander, J. R. Coughlin, A. L. Milkowski, and P. Boffetta, "Ingested Nitrate and Nitrite and Stomach Cancer Risk: an Updated Review", Food Chem. Toxicol., vol. 50, no. 10, pp. 3646–3665, 2012.

[4] M. Moorcroft, "Detection and Determination of Nitrate and Nitrite: A Review", Talanta, vol. 54, no. 5, pp. 785–803, 2001.

[5] A. Azmi, A. A. Azman, S. Ibrahim, and M. A. Yunus, "Techniques in Advancing the Capabilities of Various Nitrate Detection Methods : a Review", International Journal On Smart Sensing and Intelligent Systems, vol. 10, no. 2, pp. 223–261, 2017.

[6] D. C. Schroeder, "The Analysis of Nitrate in Environmental Samples by Reversed-Phase HPLC", J. Chromatogr. Sci., vol. 25, no. 9, pp. 405–408, 1987.

[7] S. H. Lee and L. R. Field, "Postcolumn Fluorescence Detection of Nitrite, Nitrate, Thiosulfate, and Iodide Anions in High-Performance Liquid Chromatography", Anal. Chem., vol. 56, no. 14, pp. 2647–2653, 1984.

[8] D. Tsikas, I. Fuchs, F. M. Gutzki, and J. C. Frölich, "Measurement of Nitrite and Nitrate in Plasma, Serum and Urine of Humans by High-Performance Liquid Chromatography, The Griess Assay, Chemiluminescence and Gas Chromatography-Mass Spectrometry: Interferences by Biogenic Amines And N(G) -Nitro-L-Arginine An", J. Chromatogr. B Biomed. Appl., vol. 715, no. 2, pp. 441–448, 1998.

[9] E. Cells, "Electrochemical Sensors", Anal. Chem., pp. 161–180, 2013.

[10] K. J. Sibley, J. F. Adsett, and P. C. Struik, "an on-the-go Soil Sampler for an Automated Soil Nitrate Mapping System", Transactions of the ASABE, vol. 51, no. 3, pp. 1895–1904, 2008.

[11] B. Sethuramasamyraja, V. I. Adamchuk, A. Dobermann, D. B. Marx, D. D. Jones, and G. E. Meyer, "Agitated Soil Measurement Method for Integrated on-the-go Mapping of Soil pH, Potassium and Nitrate Contents", Comput. Electron. Agric., vol. 60, no. 2, pp. 212–225, 2008.

[12] R. Pérez-Olmos, A. Rios, J. R. Fernández, R. A. S. Lapa, and J. L. F. C. Lima, "Construction and Evaluation of Ion Selective Electrodes for Nitrate with a Summing Operational Amplifier. Application to Tobacco Analysis", Talanta, vol. 53, pp. 741–748, 2001.

[13] Y. Umezawa, P. Bühlmann, K. Umezawa, K. Tohda, and S. Amemiya, "Potentiometric Selectivity Coefficients of Ion-Selective Electrodes. Part I. Inorganic Cations (Technical Report)", Pure Appl. Chem., vol. 72, no. 10, pp. 1851–2082, 2000.

[14] R. De Marco et al., "Evidence of a Water Layer in Solid-Contact Polymeric Ion Sensors", Phys. Chem. Chem. Phys., vol. 10, no. 1, pp. 73–76, 2008.

CONTACT

H. Jiang; jiang289@purdue.edu
*B. Ziaie; bziaie@purdue.edu

A SUB-PPB-LEVEL INTEGRATED ELECTROCHEMICAL HEAVY METAL ION MICROSENSOR

Huawei Jiang[1], Chen Yang[2], Ken Yang[2] and Liang Dong[2]*
[1]Iowa State University, Ames, Iowa, USA
[2]Analog Devices Inc., Wilmington, MA, USA

ABSTRACT

This paper reports a miniaturized on-chip electrochemical sensor with integrated microchannel and bismuth (Bi) planner electrode for detecting trace amount of Pb^{2+} ions by anodic stripping voltammetry (ASV). A low limit of detection (LOD) of 0.3 ppb and is achieved. The result is promising for trace heavy metal ion detections in industrial and residential water quality monitoring and treatment applications.

INTRODUCTION

Toxic heavy metal ions (Pb^{2+}, Cd^{2+}, Co^{2+} , Cr^{2+}, etc.) possesses severe threats to public health, due to the increasingly serious pollution worldwide. A rapid and accurate detection technology is thus in great demand. Lab tests use high-end instruments like inductively coupled plasma mass spectrometer and ion chromatography are bulky, expensive, time-consuming and limited usage for in situ environmental screening and monitoring, while less-expensive test papers and ion-selective electrodes suffer from severe ion cross-sensitivity, low sensitivity, or short operation lifetime. Therefore, it is of critical importance to develop a high-performance, cost-effective heavy metal ion detection platform for portable applications. Among the effective methods, electrochemical measurement of anodic stripping voltammetric analysis is recognized as the most sensitive electroanalytical technique [1-5].

Anodic stripping voltammetry (ASV) is considered one of the most sensitive methods for trace-amount determination of many metals and compounds in environmental and biological samples. Various materials have been used to form working electrodes of ASV sensors. Bismuth (Bi) is advantageous over mercury, Au [6], and carbon [7], due to the near-zero toxicity, wide potential window, and insensitivity to dissolved oxygen. It should be noted that several electrochemical heavy metal ion sensors have been reported using an assembled bulk electrochemical cell setup [8, 9]. In contrast, on-chip microsensors require using integrated circuit (IC) compatible materials and fabrications.

Here, we present a miniaturized ASV heavy metal ion sensor utilizing a Bi based thin-film working electrode (WE) formed via conventional evaporation and photolithography (Fig. 1a). Compared to Bi electrodes formed by *in situ* method, in which extra Bi^{3+} ions are added in the analyte solution and then co-electrodeposited with the target analyte metals to compensate for material consumptions [10] during ASV measurements (Fig. 1b), our *ex situ* Bi electrode will enable rapid test and mass production of sensors. Particularly, the microsensor consists of a Bi WE, a silver/silver chloride (Ag/AgCl) reference electrode (RE), and an Au counter electrode (CE) (Fig. 1c), embedded inside a microfluidic channel for the ASV detection of heavy metal ions in a miniaturized format (Fig. 1d).

EXPERIMENTAL

Following materials were used to prepare 0.1 M acetate buffer solution (pH = 4.6): 0.1 M Acetic acid (Fisher Scientific, Fair Lawn, NJ), 0.1 M sodium acetate (Sigma-Aldrich, St. Louis, MO), 0.1 M NaCl (Fisher Scientific, Fair Lawn, NJ), and deionized (DI) water. All electrochemical measurements were prepared from 1000 ppm Pb^{2+} (Sigma-Aldrich, St. Louis, MO) and Cd^{2+} (Fisher Scientific,

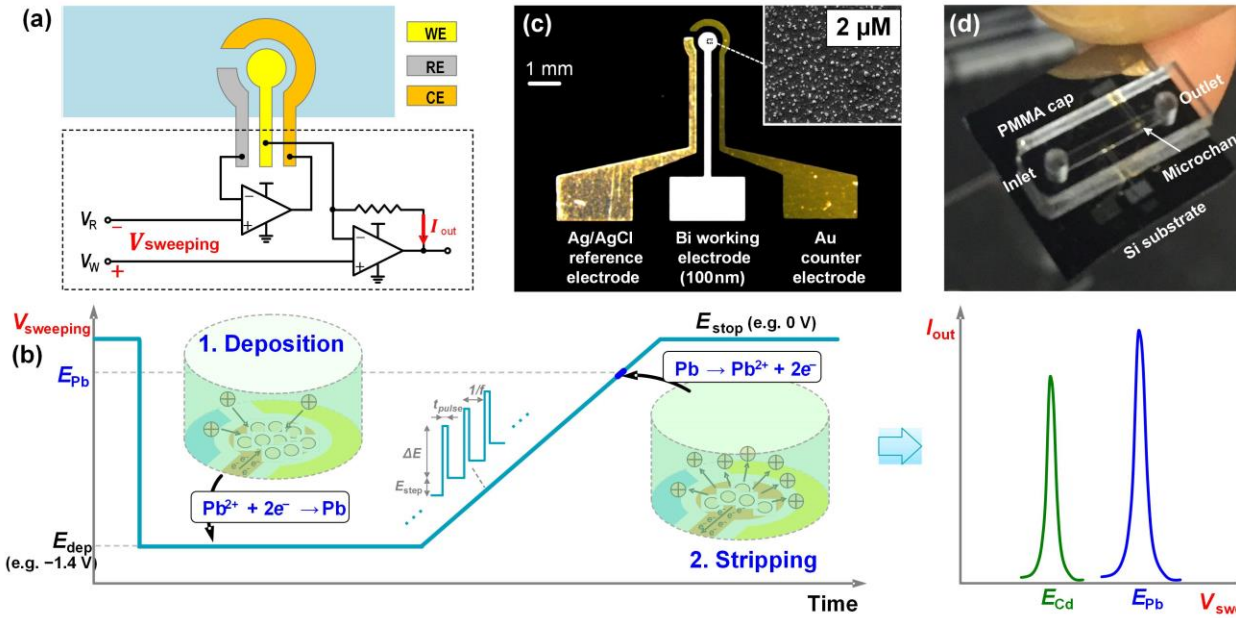

Figure 1: (a) Schematic of the electrochemical sensor and signal reading circuit. (b) Selective anodic stripping voltammetry (ASV) method. (c) Photos of the 3-electrodes prototype. (d) A sensing unit example with two sensors in the microchannel.

978-1-940470-03-0/HH2018/$25©2018TRF
DOI 10.31438/trf.hh2018.43

Fair Lawn, NJ) stock standard solution. Necessary dilutions were prepared with acetate buffer solution for various concentration study.

Standard fabrication processes were used to prepare the micro-sensor. A SiO_2 layer (300 nm thickness) was first grown on a silicon wafer via thermal oxidation. After a Ti/Au (5/80 nm thickness) layer was deposited on top of SiO_2 using e-beam evaporation, three Ti/Au electrodes were patterned via photolithography and wet chemical etching. Next, Ti/Bi (5/150 nm thickness) was deposited using e-beam evaporation and then patterned to form a WE on the surface of a Ti/Au electrode using a lift-off process. The same process was employed to form a Ti/Ag (5/500 nm thickness) electrode. Further, the device was immersed in a 0.1 M $FeCl_3$ solution containing 0.1 M HCl for 10 s to form a Ag/AgCl RE. Last, a poly(methyl methacrylate) or PMMA microfluidic channel (length: 8 mm; width: 1.5 mm; depth: 0.1 mm) was formed using hot embossing and then bonded with the substrate using an ultraviolet adhesive (PermiNex 2010, MicroChem, Westborough, MA). The sensing area of the WE is about 0.2 mm^2.

Square wave ASV was used to perform ion measurements. A deposition potential of -1.4 V was applied for 30 s, followed by applying a potential scan voltage from -1.4 to 0 V with an amplitude of 25 mV, a pulse width of 50 ms, a potential step of 4 mV, and a frequency of 5 Hz.

RESULTS AND DISCUSSION

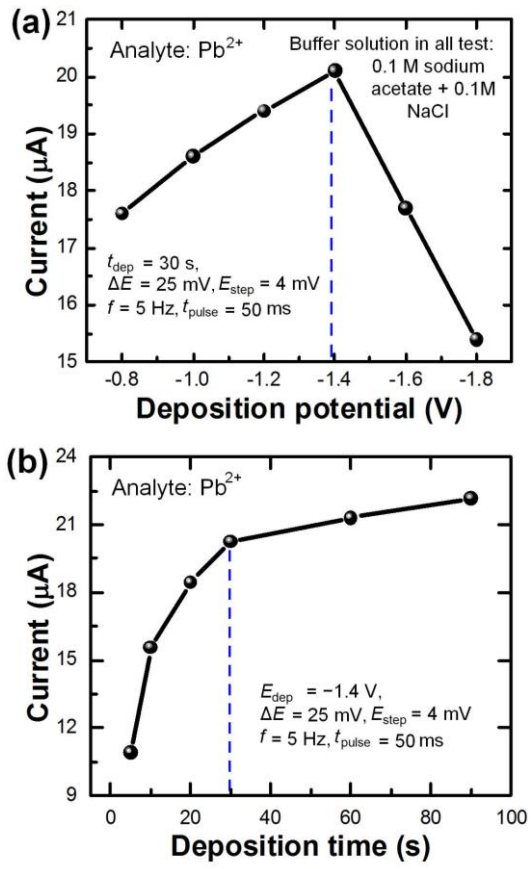

Figure 2: Effect of (a) the deposition potential and (b) deposition time on the stripping peak current of 100 ppb of Pb^{2+} in acetate buffer (pH 4.6).

Fig. 2a shows the effect of deposition potential in a range from -1.8 V to -0.8 V on the stripping peak current of 100 ppb Pb^{2+} at a deposition time of 30 s. As the deposition potential positively increased to -1.4 V, the highest peak current was observed. After that, the peak current declined significantly due to the enhancement of electrolytic hydrogen evolution. Thus, -1.4 V was used as the deposition potential in the following electrochemical measurement.

Fig. 2b demonstrates the influence of deposition time in a range from 5 s to 90 s on the stripping peak current at the -1.4 V deposition potential. The peak current increased sharply with increasing deposition time, because of the increased amount of Pb^{2+}. However, the stripping peak current started to increase slowly after the deposition time of 30 s, possibly due to the surface saturation of the WE. Therefore, 30 s was chosen as the optimal deposition time.

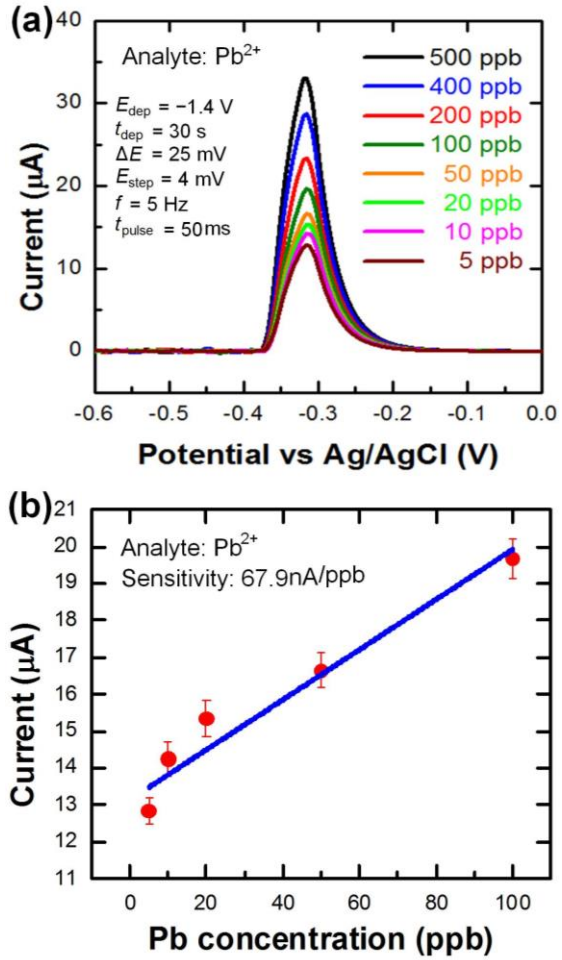

Figure 3:(a) Output current curves from varies concentrations of Pb^{2+}. (b) Calibration curve of (a).

Fig. 3a shows the stripping response of the sensor at different Pb^{2+} ion concentrations (5, 10, 20, 50, 100, 200, 400, and 500 ppb). The Pb^{2+} current peak appeared at -0.32 V with respect to the potential of the RE. The corresponding calibration curves exhibited a linear relationship over the concentration range of from 5 ppb to 100 ppb. The calculated sensitivity of the sensor is about 67.9 nA/ppb (Fig.3b). The LOD of the sensor (defined as the concentration which yield a measure peak with signal-to-noise ratio of 3) was calculated to be about 0.3 ppb of Pb^{2+}.

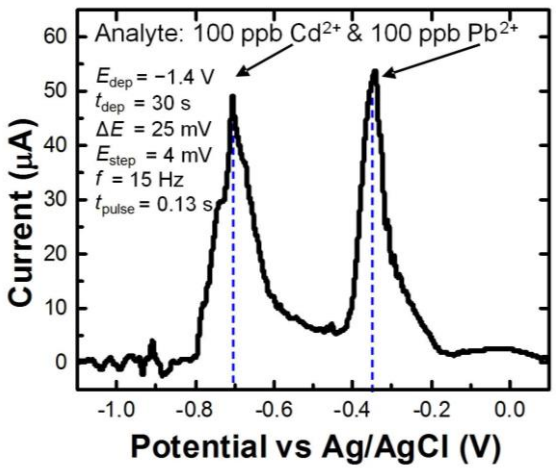

Figure 4: Output current peaks from the mixture of Cd^{2+} and Pb^{2+}.

Fig. 4 shows the output curve from the mixture of Cd^{2+} and Pb^{2+}, showing the high selectivity of the sensor. Compared to existing heavy metal ion sensors, the presented sensor offers not only a comparable or better LOD, but also higher compactness and IC compatibility.

CONCLUSION

We report a miniaturized heavy metal ion sensor able to detect sub-ppb-level Pb^{2+} in water. The sensor integrates a microfabricated planar Bi WE, an Au counter electrode and an Ag/AgCl RE into a microfluidic channel to perform ASV measurement of Pb^{2+}. The developed on-chip sensor exhibited a sharp stripping peak current and a low detect limit for Pb^{2+}. It could be used to monitor many other heavy metal ions in industrial and residential water.

ACKNOWLEDGEMENT

This work was supported by Analog Devices Inc., Norwood, MA. The authors thank Yingqi Jiang and Frank McNally at Analog Devices Inc., and Junhao Zhu, Azahar Ali, Ranjitha Narayanan, Yang Tian for discussions and technical supports.

REFERENCES

[1] M.B. Gumpu, S. Sethuraman, U.M. Krishnan, and J.B.B. Rayappan, "A review on detection of heavy metal ions in water–An electrochemical approach", Sensors and Actuators B: Chemical, 213, 515 (2015).

[2] S. Lee, S. Bong, J. Ha, M. Kwak, S.K. Park, and Y. Piao, "Electrochemical deposition of bismuth on activated graphene-nafion composite for anodic stripping voltammetric determination of trace heavy metals", Sensors and Actuators B: Chemical, 215, 62 (2015).

[3] J. Wang, J. Lu, S.B. Hocevar, P.A. Farias, and B. Ogorevc, "Bismuth-coated carbon electrodes for anodic stripping voltammetry", Analytical Chemistry, 72, 3218 (2000).

[4] E.P. Achterberg, and C. Braungardt, "Stripping voltammetry for the determination of trace metal speciation and in-situ measurements of trace metal distributions in marine waters", Analytica Chimica Acta, 400, 381 (1999).

[5] G.E. Batley, "Electroanalytical techniques for the determination of heavy metals in seawater", Marine Chemistry, 12, 107 (1983).

[6] A. Giacomino, A. R. Redda, S. Squadrone, M. Rizzi, M. C. Abete, C. La Gioia, T. Rosanna, A. Ornella, and M. Malandrino, "Anodic stripping voltammetry with gold electrodes as an alternative method for the routine determination of mercury in fish. Comparison with spectroscopic approaches", Food Chemistry, 221, 737 (2017).

[7] Z. Nie, C. A. Nijhuis, J. Gong, X. Chen, A. Kumachev, A. W. Martinez, M. Narovlyansky, and G. M. Whitesides, "Electrochemical sensing in paper-based microfluidic devices", Lab on a Chip, 10, 477 (2010).

[8] X. Dai, O. Nekrassova, M.E. Hyde, and R.G. Compton, "Anodic stripping voltammetry of arsenic (III) using gold nanoparticle-modified electrodes", Analytical Chemistry, 76, 5924 (2004).

[9] J. Wang, Ü.A. Kirgöz, J.W. Mo, J. Lu, A.N. Kawde, and A. Muck, "Glassy carbon paste electrodes", Electrochemistry Communications, 3, 203 (2001).

[10] N. Ruecha, N. Rodthongkum, D. M. Cate, J. Volckens, O. Chailapakul, and C. S. Henry, "Sensitive electrochemical sensor using a graphene–polyaniline nanocomposite for simultaneous detection of Zn (II), Cd (II), and Pb (II)", Analytica Chimica Acta, 874, 40 (2015).

CONTACT

* L. Dong, tel: +1-515-294-0388; ldong@iastate.edu

FLEXIBLE IMPEDANCE SENSOR FOR WIRELESS MONITORING OF CATHETER BIOFILMS

R.C. Huiszoon[1,3], J.M. Stine[1,2], L.A. Beardslee[1], P. Ramiah Rajasekaran[1], W.E. Bentley[3], and R. Ghodssi[1,2,3]*
[1]Institute for Systems Research, [2]Department of Electrical and Computer Engineering,
[3]Fischell Department of Bioengineering
University of Maryland, College Park, Maryland, USA

ABSTRACT

A microfabricated flexible impedance sensor (FlexIS) for wireless monitoring of bacterial biofilm formation on catheters is presented. The system consists of interdigitated electrodes on flexible polyimide film, interfaced with the cylindrical surface of a urinary catheter. An AD5933 impedance converter (AIC) measures sensor impedance and enables wireless readout by communicating with a smartphone via Bluetooth. A 5% decrease in impedance at 1 kHz corresponded to the growth of an Escherichia coli biofilm for 24 hours on the catheter surface, compared to an increase of 2% for an unseeded control. Measurement results from the AIC and a standard potentiostat were compared, showing a similar decrease in impedance with biofilm formation. Furthermore, the sensor response to biofilm formation was supported by measured changes in biofilm biomass. The FlexIS allows *in situ* biofilm characterization in complex and inaccessible environments in clinical and research settings.

INTRODUCTION

Biofilms are the primary mode of growth for many bacteria, where planktonic cells adhere to hydrated surfaces and encase themselves in a sticky, polysaccharide matrix [1]. The formation of biofilm is driven by intercellular communication via small molecules, in a process known as quorum sensing [2]. The biofilm phenotype affords the constituent bacteria increased tolerance to antibiotic therapy, requiring doses 50-500 times larger for complete killing compared to their planktonic counterparts [3]. Analogous to metastasis, biofilms can serve as a source of recurring infection, as cells slough off of mature biofilms, allowing the bacteria to spread and colonize other areas. Therefore, there is potential risk of chronic infection if the source biofilm is not eliminated. Biofilm colonization accounts for a significant portion of hospital-acquired infections, especially in patients with implanted or inserted medical devices. Notably, urinary catheters cause bacteriuria at a rate of 5-7% per day of implantation due to biofilm formation [4]. There is currently a lack of adequate tools for detecting biofilm formation on medical devices. Care providers typically rely on time-consuming and labor-intensive plate culture and colony counting methods to identify bacterial infections [5]. Furthermore, this quantifies only the viable cells, not the presence of biofilm. In research settings biofilms are often characterized by optical techniques which rely on end-point staining and bulky equipment [6-7]; this does not lend itself to *in situ* application on the complex surfaces where biofilms form.

A limited number of device-based approaches have been developed to address the challenges associated with characterizing and detecting biofilm formation. Mechanical, optical, and electrical microsensors have been investigated for real-time biofilm sensing. Optical approaches using charge coupled devices (CCDs) to sense biofilm via optical density changes have been explored. Mechanical microsensors have been investigated as well, including quartz tuning forks, quartz crystal microbalances, and surface acoustic wave sensors, which rely on the accumulation of mass at the sensor surface [9-11]. However, these rely on rigid crystalline materials which introduce packaging constraints when integrated with complex, 3D surfaces for *in situ* operation. Electrical sensors utilizing electrodes to detect biofilm via change in electrical or electrochemical properties have also shown promise. Several groups have been able to detect biofilm formation by monitoring the impedance of electrodes in a rigid, planar setting [12-14]. However, these microfabricated impedance sensors are not amenable to integration with the complex 3D surfaces that are vulnerable to biofilm. To overcome this challenge, our group has recently demonstrated a flexible electrode platform for detecting biofilm formation in real-time using impedance measured with a benchtop potentiostat [15-16]. This work enables wireless *in situ* biofilm monitoring using the AIC, which can be interfaced with a Bluetooth microcontroller. FlexIS allows the degree of biofilm formation to be identified quickly and non-invasively, enabling effective treatment (Figure 1).

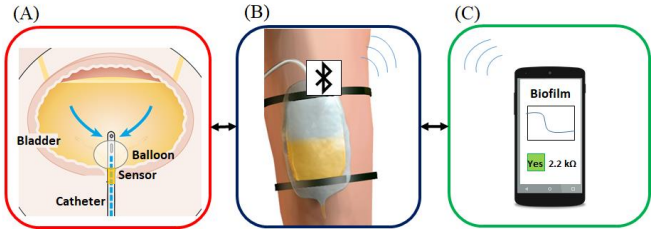

Figure 1: Schematic for a wireless FlexIS on catheter: (A) Flexible sensor embedded in urinary catheter; (B) Wireless electronics module attached to external catheter bag; (C) Smartphone app provides an alert in the presence of biofilm and allows prompt implementation of treatment.

MATERIALS AND METHODS

System Fabrication

The flexible impedance sensor is comprised of thin-film interdigitated electrodes (IDEs, Cr(20 nm)/Au(200 nm)) patterned on a 25.4 µm-thick polyimide substrate in a lift-off process. This process consists of affixing a piece of the polyimide (Kapton, DuPont) onto a four-inch Si wafer via heat-release tape (Semiconductor Equipment Corp.) followed by patterning of electrodes using a standard photolithography process with Shipley 1813 resist (Microchem). Each wafer was exposed to O_2 plasma for 1 minute at 200 W at 100 sccm to improve metal adhesion on the polyimide. The electrodes were deposited via e-beam evaporation (Angstrom Engineering). Electrode fabrication was completed by lift-off in acetone for 1 minute. The polyimide film with the devices was separated from the wafer by heating to 150 °C, prompting release by the tape. The devices, five per wafer, were cut into each die with scissors to complete fabrication. The final footprint of the IDEs was 10 mm x 40 mm, connected to contact pads by 30 mm leads. The IDE width and spacing was 300 µm. The sensor was integrated with the interior lumen of an 11 cm-long section of a 16 Fr silicone catheter (Allegro Medical) for testing. Uncured

978-1-940470-03-0/HH2018/$25©2018TRF
DOI 10.31438/trf.hh2018.44

polydimethylsiloxane (PDMS) (Dow-Corning) mixed at a ratio of 10:1 base to curing agent was coated on the interior of the catheter tube by introducing a large drop at the inlet, and spreading it over the entire surface with a wooden applicator rod. The flexible device was introduced while the surface was coated in uncured PDMS. Then, the PDMS was cured for 3 h at 60°C to fix the polyimide substrate in place. The device was connected to either a potentiostat or an electronic module including the AIC. The AIC can be programmed via a BGM121 Bluetooth microcontroller to run a frequency sweep and display the data on a computer terminal or smartphone app. The AIC and BGM121 can be combined in a wireless electronics module contained in a custom 3D-printed housing, with clasps to hold it in place at the base of the catheter near the connection to the catheter bag. Figure 2 shows the device adhered in a catheter, interfaced with the electronics for wireless communication in the custom 3D-printed housing.

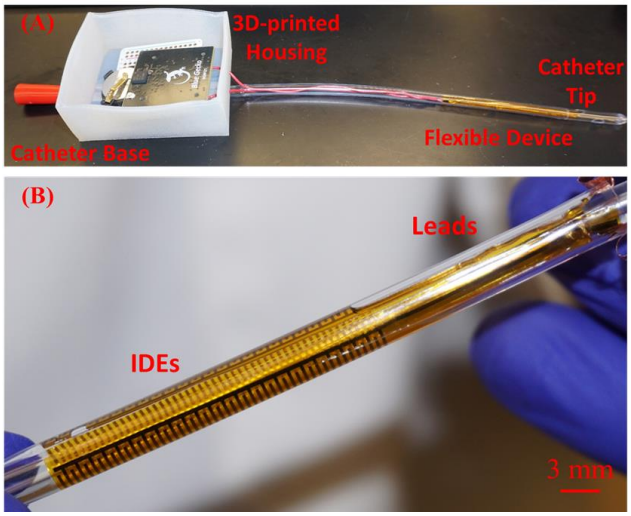

Figure 2: Optical images of the (A) urinary catheter with device integrated on the interior near the tip, connected to the AIC (under BGM 121) and BGM 121 Bluetooth microcontroller contained in a 3D-printed housing (printed with Agilus30) which is affixed to the base of the catheter and (B) close-up image of inserted device.

Device Testing

The flexible impedance sensor was characterized using a custom flow system consisting of a growth media reservoir, waste reservoir, and the device connected using tygon tubing and luer connectors (Cole-Parmer) in between the reservoirs. The entire system is sterilized for 45 minutes in an autoclave at 121 °C prior to the experiment, to prevent contamination by environmental microbes. The flow is driven by a peristaltic pump (Elemental Scientific). The sensor and tubing are placed in an incubator maintained at 37 °C, to mimic the temperature found in an inserted catheter. *Escherichia coli* K12 W3110 are cultured from frozen samples for 20 hours in 5 ml of Luria broth (LB) media (Sigma) in an Innova 4000 incubator shaker at 37 °C (New Brunswick Scientific) set to 250 rpm. The cultured bacteria are then diluted to an OD_{600} of 0.25, and 1 ml of the diluted *E. coli* solution is introduced into the catheter tube directly via syringe. The bacteria are allowed to attach to the interior surface under static (no flow) conditions for 2 hours. This is referred to as the 'Seeding' phase. Immediately following Seeding, pure LB media is flowed at a constant flow rate of 7 ml/h for 24 hours. This is referred to as the 'Growth' phase. Throughout the Growth phase, the system impedance is measured by the AIC every 2 minutes. The relative change is used to monitor biofilm formation. Devices without any bacterial cells introduced were also tested as a control. This procedure was also performed using a benchtop potentiostat (Electrochemical Workstation 660D, CHInstruments) for the impedance measurements, to serve as a comparison standard for evaluating the efficacy of the system. Crystal violet (CV) absorbance staining is used to quantify the end-point biomass. This serves to validate the impedance measurements by correlating them with the increase in strongly adhered biomass. This process involves flowing the CV stain into the tube and allowing it to bind to the adhered proteins and DNA associated with the biofilm; thus, bound stain is proportional to biofilm biomass. Then, the sample is rinsed with deionized water to remove unbound stain. Finally, decomplexation solution (80% ethanol: 20% acetone) is introduced into the system for 30 minutes. The stain is soluble in decomplexation solution and dissolves into the solution. Optical absorbance at λ=590 nm is measured, with increases corresponding to increased biomass. One-way analysis of variance (ANOVA) was used to determine statistical significance of the biomass quantification results.

RESULTS AND DISCUSSION

Potentiostat Impedance Sensing

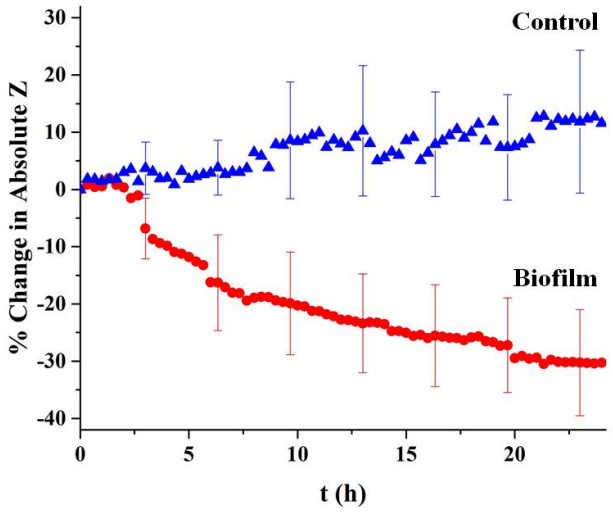

Figure 3: Average real-time impedance sensing results over the course of the 24-hour growth period, measured by the benchtop potentiostat. The blue triangles correspond to the control samples (without biofilm formation) and the red circles correspond to the samples with biofilm formation. The excitation signal used was AC 50 mV at 100 Hz, chosen to optimize sensitivity. The error bars correspond to standard error (N = 5); the large standard error is related to the inherent variability in biofilm formation.

Figure 3 shows the real-time change in impedance measured with the benchtop potentiostat. In the first 2 hours, the signals for both samples show relatively little change. However, from hours two to three, the impedance of the biofilm sample abruptly decreases by 7.2%. This is likely related to the rapid proliferation phase of biofilm growth. The impedance decrease slows after this initial drop; from hours three to 24 the impedance drops approximately 1% per hour. Over the course of the entire Growth phase the system impedance exhibits a dramatic 30% decrease. By comparison, the control sample exhibits a steady increase of about 10% over the entire growth phase. The impedance decrease is due to

the accumulation of charged proteins and ions on the sensor surface associated with the biofilm and biofilm metabolism causing a shift in the double layer capacitance [12],[17].

The resulting end-point biomass can be compared between samples with and without biofilm, and the trend can be compared with the impedance sensing results. The biomass quantification results for samples measured with the potentiostat are shown in Figure 4. The absorbance nearly doubled on average in samples with biofilm compared to the biofilm-free controls. The control signal represents the contribution from the LB media alone. The increased absorbance associated with biofilm was statistically significant according to one-way ANOVA ($p < 0.05$), confirming the increase in biomass. Furthermore, this increase in biomass is correlated with the decrease in impedance measured with the flexible sensor.

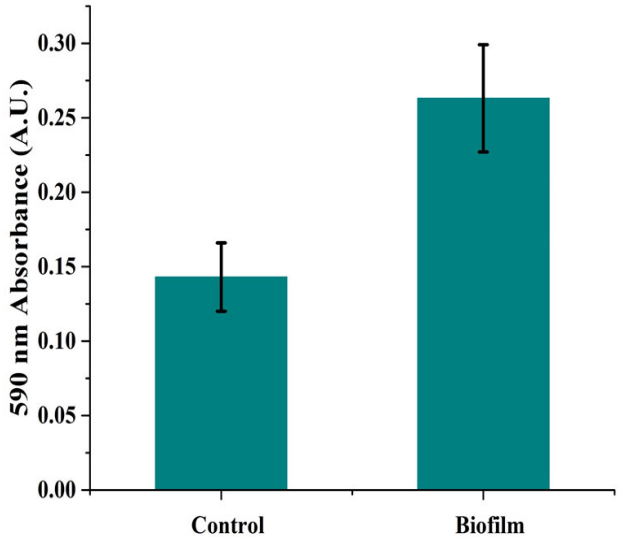

Figure 4: End-point biomass quantification for samples with and without biofilm. Error bars correspond to standard error (N = 3).

AIC Impedance Sensing

The real-time impedance sensing results from samples measured with the AIC are presented in Figure 5. The AIC measures a gradual decrease of approximately 5% after 24 hours of biofilm growth. The biofilm-free samples, by comparison, showed a slight increase of about 2% in impedance after 24 hours. This trend corresponds with the results obtained using the FlexIS with a standard benchtop potentiostat. Both measurement approaches indicate that a significant decrease in system impedance occurs with biofilm formation. In addition, they both show a slight increase in the control samples. While the trends were similar between the two approaches, the magnitudes of the changes were different; a significantly smaller impedance shift when measured by the AIC. This decreased sensitivity is attributed to the differences in how each system is calibrated. Additional electronic circuitry may be necessary to further improve the FlexIS sensitivity when using the AIC for wireless biofilm monitoring. The similar trends between each approach suggest that using the FlexIS with the AIC is a viable real-time wireless biofilm sensing tool.

A CV stain was also performed to quantify the end-point biomass for samples measured with the AIC, to correlate the change in impedance with an increase in biomass from biofilm. The biomass quantification results for samples measured with the AIC are shown in Figure 6.

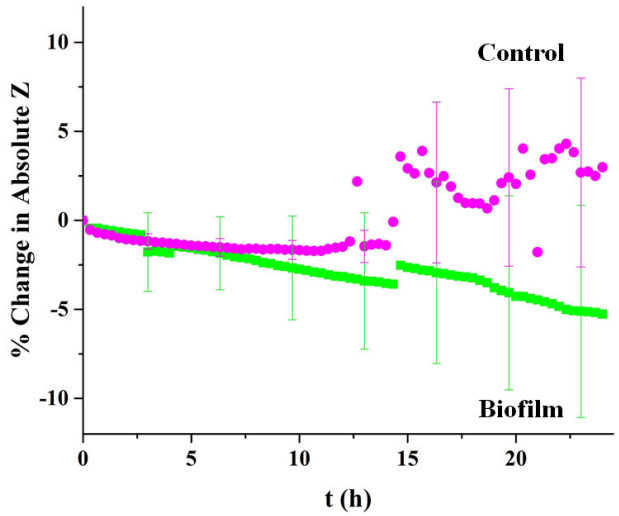

Figure 5: Average real-time impedance sensing results over the course of the 24-hour growth period, measured using the AIC. The pink circles correspond to control samples without biofilm and the green squares correspond to samples with biofilm formation. The excitation signal used was AC 200 mV at 1 kHz, chosen to optimize sensitivity. The error bars denote standard error (N = 3).

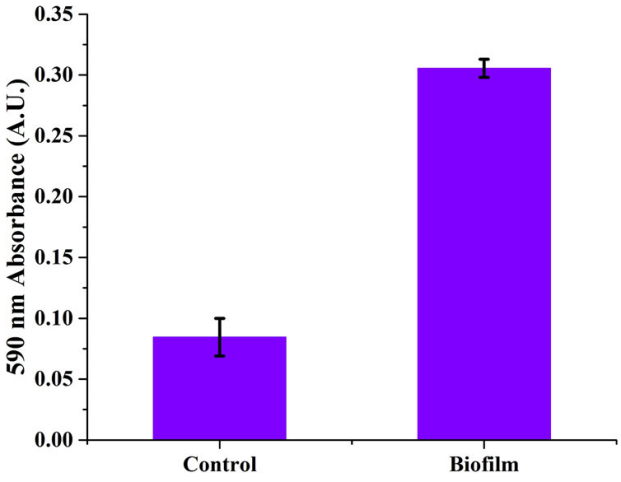

Figure 6: End-point biomass quantification for samples with and without biofilm measured with the AIC. Error bars correspond to standard error (N = 2).

These samples displayed a significant increase in biomass associated with the formation of biofilm compared to biofilm-free controls, similar to the potentiostat measured samples. The increased absorbance was statistically significant compared to LB media alone according to one-way ANOVA ($p < 0.05$). This indicates that the decrease in impedance is correlated with an increase in biomass. Essentially, the change that the AIC detects is related to increasing biofilm biomass on the FlexIS surface. This further confirms the viability of the FlexIS combined with the AIC for wireless biofilm monitoring.

Wireless monitoring was performed using the AIC interfaced with the BGM121 microcontroller. The impedance results for the FlexIS measured via wired UART and wireless Bluetooth are compared in Figure 7. The identical trend indicates that the FlexIS can be operated wirelessly without a decrease in performance.

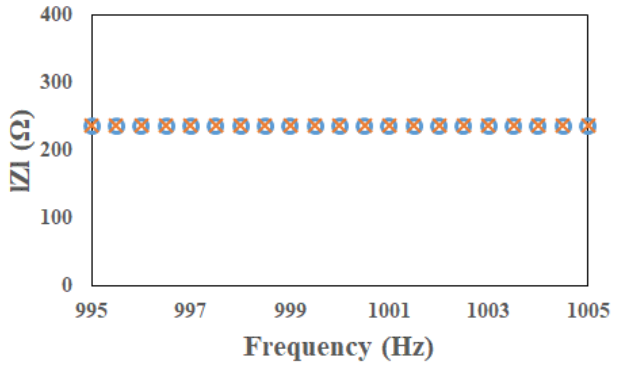

Figure 7: Frequency sweeps from 995-1005 Hz with wired (orange crosses) and wireless (blue circles) connections showing identical impedance responses from the FlexIS with growth media.

CONCLUSIONS

In this work, we have demonstrated the feasibility of the FlexIS as a platform for real-time, *in situ* monitoring of biofilm formation on catheters. The sharp decrease in impedance is correlated with a statistically significant increase in biofilm biomass. Successful implementation of this platform relies on its ability to operate *in situ* without impeding regular operation of the vulnerable device; in this case the flexible substrate allows the FlexIS to conform to the interior cylindrical lumen of a catheter and report on the level of biofilm colonization at the surface.

Initial characterization of this platform utilized a benchtop potentiostat for performing impedance measurements. However, bulky wired equipment is impractical for applications on inserted medical devices. Here, we demonstrate biofilm detection using the AIC to overcome this challenge. The AIC can be programmed with a BGM121 Bluetooth microcontroller to run impedance measurements and transmit the data wirelessly. The AIC was demonstrated as a viable approach for measuring biofilm formation with the FlexIS. The microcontroller measured a decrease in impedance with biofilm formation which correlated with an increase in biomass. Compared with the potentiostat standard, the AIC demonstrated reduced sensitivity. Nonetheless, the FlexIS was demonstrated as a viable tool for biofilm detection on catheter surfaces. This approach can be extended in the future to other vulnerable domains with complex, 3D geometry. Furthermore, the wireless control allows clinicians and researchers to read out data seamlessly without relying on bulky and wired equipment.

ACKNOWLEDGEMENTS

The authors would like to acknowledge the support of the Maryland Nanocenter and its FabLab for support in fabrication.

REFERENCES

[1] J.W. Costerton, P.S. Stewart, and E.P. Greenberg, "Bacterial biofilms: a common cause of persistent infections", Science, 284, 1318 (1999).

[2] A. Vendeville, K. Winzer, K. Huerlier, C.M. Tang, and K.R. Hardie, "Making "Sense" of Metabolism: Autoinducer-2, LUXS and Pathogenic Bacteria", Nat. Rev. Microbiol., 3, 383 (2005).

[3] H. Anwar, M.K. Dasgupta, and J.W. Costerton, "Testing the Susceptibility of Bacteria in Biofilms to Antibacterial Agents", Antimicrob. Agents Chemother., 34, 2043 (1990).

[4] J.W. Warren, "Catheter-Associated Urinary Tract Infections", Int. J. Antimicrob. Agents, 17, 299 (2001).

[5] D.G. Maki, C.E. Weise, and H.W. Sarafin, "A Semiquantitative Culture Method for Identifying Intravenous-Catheter-Related Infection", N. Engl. J. Med., 296, 1305 (1977).

[6] E. Peeters, H.J. Nelis, and T. Coenye, "Comparison of Multiple Methods for Quantification of Microbial Biofilms Grown in Microtiter Plates", J. Microbiol. Methods, 72, 157 (2008).

[7] R.J. Palmer and C. Sternberg, "Modern Microscopy in Biofilm Research: Confocal Microscopy and Other Approaches", Curr. Opin. Biotechnol., 10, 263 (1999).

[8] Y.W. Kim, M.P. Mosteller, M.T. Meyer, H. Ben-Yoav, W.E. Bentley, and R. Ghodssi, "Microfluidic biofilm observation, analysis and treatment (MICRO-BOAT) platform", Technical Digest of the 2012 Solid-State Sensor and Actuator Workshop, Hilton Head Isl., SC, 6/3-7/12, Transducer Research Foundation, Cleveland (2012), pp. 233 – 236.

[9] K. Waszczuk, G. Gula, M. Swiatkowski, J. Olszewski, W. Herwich, Z. Drulis-Kawa, J. Gutowicz, and T. Gotszalk, "Evaluation of Pseudomonas aeruginosa biofilm formation using piezoelectric tuning fork mass sensors", Sens. Actuators, B, 170, 7 (2012).

[10] V. Reipa, J. Almeida, and K.D. Cole, "Long-term monitoring of biofilm growth and disinfection using a quartz crystal microbalance and reflectance measurements", J. Microbiol. Methods, 66, 449 (2006).

[11] Y.W. Kim, S.E. Sardari, M.T. Meyer, A.A. Iliadis, H.C. Wu, W.E. Bentley, and R. Ghodssi, "An ALD aluminum oxide passivated Surface Acoustic Wave sensor for early biofilm detection", Sens. Actuators, B, 163, 136 (2012).

[12] J. Paredes, S. Becerro, F. Arizti, A. Aguinaga, J.L. Del Pozo, and S. Arana, "Real time monitoring of the impedance characteristics of Staphylococcal bacterial biofilm cultures with a modified CDC reactor system", Biosens. Bioelectron., 38, 226 (2012).

[13] X. Munoz-Berbel, F.J. Munoz, N. Vigues, and J. Mas, "On-chip impedance measurements to monitor biofilm formation in the water distribution network", Sens. Actuators, B, 118, 129 (2006).

[14] S. Subramanian, E.I. Tolstaya, T.E. Winkler, W.E. Bentley, and R. Ghodssi, "An Integrated Microsystem for Real-Time Detection and Threshold-Activated Treatment of Bacterial Biofilms", ACS Appl. Mater. Interfaces, 9, 31362 (2017).

[15] R.C. Huiszoon, P. Ramiah Rajasekaran, S. Subramanian, W.E. Bentley, and R. Ghodssi, "Flexible Impedance Sensor for In Situ Sensing of Catheter Biofilms", The 21st International Conference on Miniaturized Systems for Chemistry and Life Sciences (MicroTAS 2017), Savannah, GA, 10/22-26/17, The Chemical and Biological Microsystems Society, Washington (2017), pp. 130 – 131.

[16] R.C. Huiszoon, P. Ramiah Rajasekaran, W.E. Bentley, and R. Ghodssi, "Flexible Dual-Function Platform For In Situ Monitoring and Treatment of Bacterial Biofilms", The 9th International Conference on Microtechnologies in Medicine and Biology (MMB 2018), Monterey, CA, 3/26-28/18, Transducer Research Foundation, San Diego (2018).

[17] K. Ong, J. Wang, R.S. Singh, L.G. Bachas, and C.A. Grimes, "Monitoring of Bacteria Growth Using a Wireless, Remote Query Resonant-Circuit Sensor: Application to Environmental Sensing", Biosens. Bioelectron, 16, 305 (2001).

CONTACT

*R. Ghodssi, tel: +1-301-405-8158; ghodssi@umd.edu

FIRST LEAPS OF AN ELECTROSTATIC INCHWORM MOTOR-DRIVEN JUMPING MICROROBOT

Joseph Greenspun and Kristofer S.J. Pister
University of California, Berkeley, USA
Berkeley Sensor and Actuator Center

ABSTRACT

Here is presented the first MEMS microrobot capable of using onboard motors to store enough mechanical energy to jump. This 43 mg microrobot achieves this by utilizing an inchworm-of-inchworms motor topology, which allows the force from a standard electrostatic inchworm motor to be amplified by a factor of 10 while increasing its areal force density. An off-chip microcontroller has successfully run this motor through 14 steps, deflecting the main shuttle 560 μm and storing over 1 μJ of energy. The microrobot has jumped 1 mm using energy stored by its motors, and 6.5 mm when its springs were loaded externally.

INTRODUCTION

Researchers have been excited by the idea of creating, controlling, and manipulating objects at small scales since the mid-1900s [1]. From these early ideas evolved the dream of creating a fleet of tiny mobile robots that could operate autonomously, sense their surroundings, and communicate to accomplish group tasks. Today, these microrobots could be used in manufacturing, search and rescue, and medicine. However, as with many technological advances, their true niche may not be discovered until after their development. Even when microrobots were first proposed in the early 1980s, their development was likened to that of the computer and the hard-to-foresee creation of the video game market [2].

Although microrobots have been actively researched for decades, many challenges to their fundamental operation remain unsolved. Among these challenges is the basic ability to locomote. Researchers have had varying degrees of success creating walking, jumping, flying, and swimming microrobots. While all locomotion modalities have certain benefits and drawbacks, this work focuses on jumping microrobots. Jumping offers the ability to maneuver over obstacles many times the size of the microrobot which will be a crucial ability when navigating through most environments.

Although jumping microrobots have been built at many size scales, this work focuses on microrobots at the millimeter scale. At this scale it is common to store energy either chemically or mechanically and release that stored energy over a short period of time. Churaman et al. [3] designed a 4x4 mm^2 microrobot from silicon and an elastomer that could jump 32 cm into the air. The elastomer was chosen to mimic the protein that insects use to jump. This microrobot could jump many times, but had no motors on board, so it was primed and launched manually with tweezers. In the same paper, Churaman describes a jumping microrobot that is driven chemically. It used porous silicon infused with sodium perchlorate as its energy storage mechanism. When a light was shined on this microrobot, its onboard electronics would trigger the ignition of the sodium perchlorate and the microrobot jumped 8cm into the air. This microrobot, while not requiring any assistance to store energy, can only take a single jump.

The work described here is the first step towards creating an autonomous jumping microrobot capable of jumping 10s of centimeters at a rate of multiple times per minute. The microrobot uses large serpentine springs to store the mechanical energy used for the jump. These springs are loaded slowly over time using two electrostatic inchworm motors in tandem. In its current form, the microrobot is tethered with wires to provide power and control, however the long-term goal is to use a multi-chip solution. There will be a chip with high voltage relays and solar cells for power, as well as a custom CMOS chip with a microprocessor and radio [5] for the control and communication. Each chip will be connected through a MEMS zero insertion force socket [4].

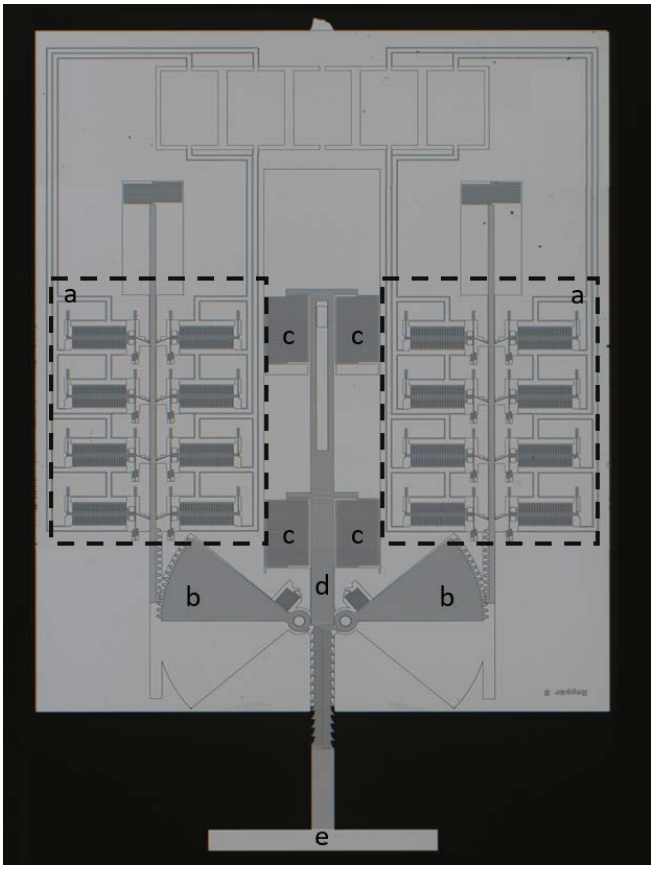

Figure 1: The 5.0 x 6.4 mm^2 jumping microrobot. (a) Electrostatic inchworm motors. (b) Pinions. (c) Energy storing serpentine springs. (d) Main shuttle. (e) Foot.

MICROROBOT OVERVIEW

The individual components required to create a fully autonomous jumping microrobot have been around for well over a decade, however no such microrobot has been developed. The integration of the motors, mechanisms, control, power, and energy storage has proven to be a challenging road block. This integration problem was a main driving force in many of the design choices for this jumping microrobot.

The entire microrobot is microfabricated using a two-mask silicon-on-insulator (SOI) process. This process is relatively simple to run in an academic cleanroom and exists as a standard process in industry, which would allow these microrobots to be made in large volumes. More importantly, this process allows for the creation of

978-1-940470-03-0/HH2018/$25©2018TRF
DOI 10.31438/trf.hh2018.45

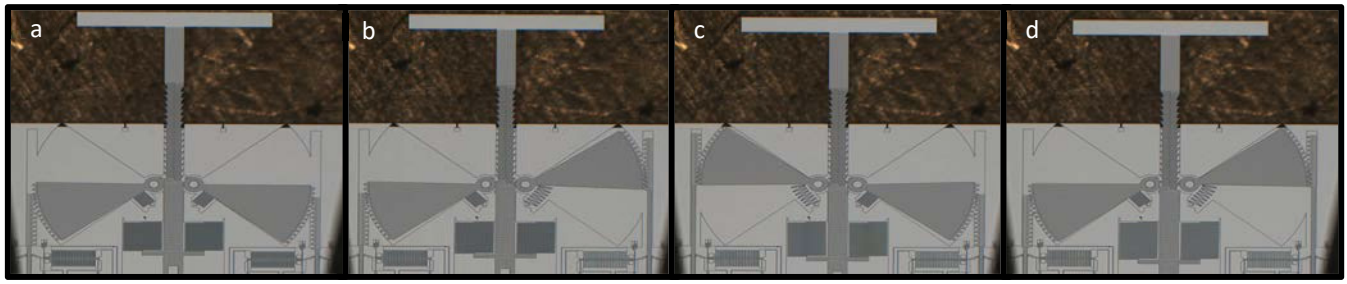

Figure 2: The inchworm of inchworms taking three macro steps. a) the jumping microrobot as fabricated, b) the right-side inchworm shuttle engages with the pinion and moves main shuttle 40 µm, c) the left-side inchworm shuttle engages with the pinion and moves the main shuttle 40 µm, allowing the right-side pinion to release, d) the process continues until the main shuttle is fully deflected. The foot is 2 mm long.

a wide variety of structures. Silicon is a versatile material that can be machined into a sensor, motor, and energy storage element all within the same process. So, where other jumping microrobots have required manual assembly of the energy storage materials [6], this process allows for the energy storage mechanisms to be fabricated next to the motors that will drive them. Figure 1 shows the jumping microrobot chip and its salient components.

ENERGY STORAGE

Mechanical energy storage is core to the operation of this microrobot. The more mechanical energy that can be stored, the higher the microrobot can jump and the more maneuverable it will be. When storing mechanical energy in a material, the maximum energy stored can be written as follows:

$$U_{max} = \frac{1}{2} AlE\epsilon_{max}^2 \quad (1)$$

Where A is the cross-sectional area, l is the length, E is the Young's Modulus, and ϵ_{max} is the maximum strain that the material can undergo before fracturing. The reported fracture strain of silicon ranges from 0.6% to 6.0% [7]. These microrobots were designed with a fracture strain of 0.8%.

As Churaman showed [3], the height that a jumping microrobot can achieve is related to the energy it stores by the following equation:

$$h = \frac{m_{robot}}{C_d A_{robot} \rho_{air}} ln\left(1 + \frac{C_d A_{robot} \rho_{air}}{m_{robot}^2 g} U_{stored}\right) \quad (2)$$

Here, h is the achieved height, m is the robot mass, A is the cross-sectional area of the robot, C_d is the drag coefficient, ρ is the density of air, g is the gravitational constant, and U is the initial stored energy. For the microrobot presented here, the mass is 43 mg, the cross-sectional area is 2.8 mm^2, and a value of 1.5 is used for C_d. To achieve a jump height of 10 mm, a microrobot of this size would theoretically need to store 4.3 µJ of mechanical energy and successfully convert all that mechanical energy into potential energy. This corresponds to only 0.004 % of the total volume of the microrobot needing to be strained to this limit of 0.8%. If even one tenth of a percent of the total microrobot volume is strained to this strain limit, it would be able to jump over 20 cm.

When designing this microrobot, a decision had to be made on the nature of the energy storage elements. A previously developed energy storage device, the MEMS Hammer, used beams in axial tension. This maximizes the stored energy in a given area by operating the beams in the cubic region of their force deflection curves [11]. Although this is an attractive option from an energy storage standpoint, the nonlinear nature of these beams requires much larger forces than those required for a linear serpentine spring to store the same amount of energy. Therefore, the energy storage

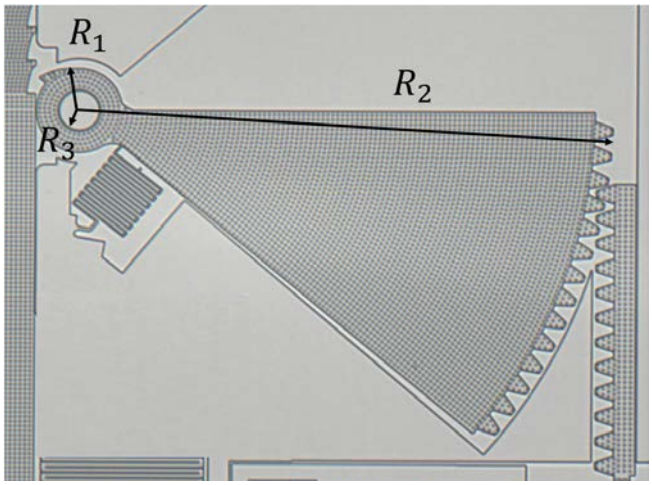

Figure 3: The pinion responsible for transferring and amplifying the force from the inchworm shuttle (rack) to the main shuttle. The latch on the pinion interfaces with the cutout holds on the main shuttle. The mechanical gain is roughly R2/R1. R2 is 1200 µm.

elements on this microrobot are four serpentine springs found in the center of the device, shown in Figure 1. These springs have a theoretical spring constant given by:

$$k = \frac{Ew^3t}{NL^3} \quad (3)$$

Here w, L, and t are the width, length, and thickness of the beams respectively, E is the Young's modulus of silicon, and N is the total number of beams in the serpentine structure. For this design, the beam width is 10 µm, length is 369 µm, thickness is 40 µm, and the number of beams per serpentine spring is 50. This gives a theoretical spring constant of 2.68 N/m per serpentine spring, and a total stiffness of 10.7 N/m for the whole structure. The spring constant is related to the energy stored in the spring by the following equation:

$$U_{stored} = \frac{1}{2} k\Delta x^2 \quad (3)$$

The deflection of these springs is variable, and will be discussed later, but the maximum possible deflection is 1120 µm. This gives a total theoretical stored energy of 6.5 µJ and a theoretical jump height of 15 mm. In order to store this energy, a force of 11.8 mN needs to be applied to the springs.

The spring constant of these serpentine springs was measured with a Dage 4000 Multipurpose Bondtester. The spring constant per serpentine spring was measured to be 1.62 ± 0.22 N/m. This leads to a total stored energy of 4.0 µJ, a maximum spring force of 7.1

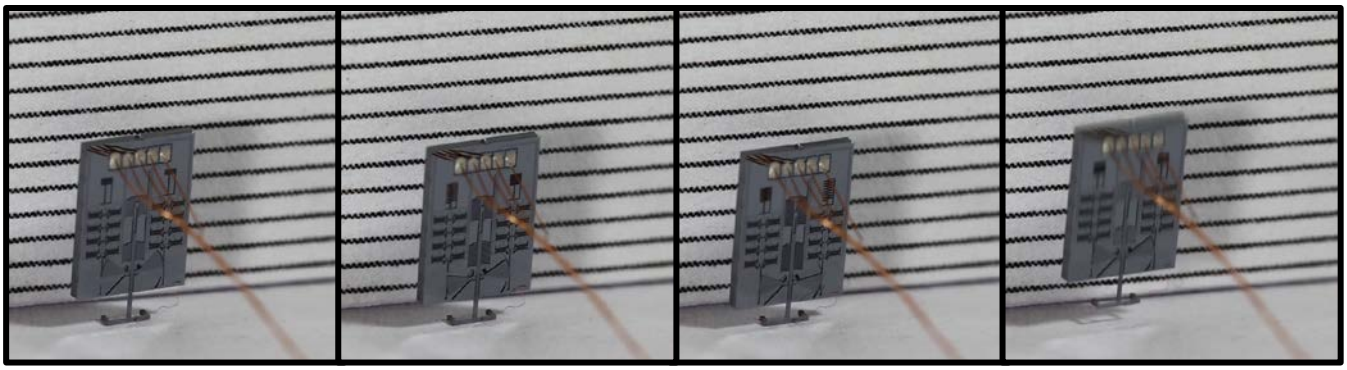

Figure 4: Stills from a 60-fps video of the jumping microrobot taking its first self-powered leap. It took 14 macro steps, storing 1.05 uJ of mechanical energy, before releasing that stored energy and jumping 1 mm. The line spacing is 1 mm.

mN, and a maximum jump height of 9.4 mm. The discrepancy between the measured and theoretical value is likely due to the rotational degree of freedom at the intersection between each beam and the perpendicular truss that connects it to the next beam. When the beams rotate like this, their strain is reduced which causes the spring constant of the entire structure to be lower than expected.

HIGH-FORCE INCHROWM MOTORS

For a jumping microrobot to be autonomous it must have a means of actively loading its energy storage elements. The electrostatic inchworm motor is an active area of research [8] and an ideal motor for an SOI process. These motors run at voltages ranging from 60–120 V and can apply forces on the order of a few millinewtons over a distance of 1 mm. A common figure of merit for an inchworm motor is the areal force density given in millinewtons per square millimeter. These values are, in the best case, between 1 and 2 mN/mm^2 for electrostatic inchworm motors running at 100 V. Additionally the maximum forces reported by electrostatic inchworm motors are typically under 2 mN [10]. The required forces to load this microrobot are well-above these values, so a new motor topology was designed and implemented.

The basic building block of an electrostatic inchworm motor is the gap closing actuator (GCA) array. This array can apply large electrostatic forces over distances of a few microns. By combining multiple correctly phased GCAs with a central shuttle, the electrostatic inchworm motor can apply this large force over a much longer distance. In this work, the entire inchworm motor is used as the basic building block for a motor, hereafter referred to as an inchworm-of-inchworms (IoI).

The IoI can be seen in operation in Figure 2. The images in this figure were taken at a probe station with the microrobot on its back. To begin loading the main shuttle, the inchworm motor on the right side of the microrobot takes 450 micro steps of 2 μm, which advances the rack by 900 μm. As the rack moves, it rotates the pinion by 80 degrees, moving the latch (shown on the top left side of the pinion in Figure 3) by 90 μm. During the end of this deflection, the latch engages with the main shuttle and deflects it 40 μm, defining a macro step. The latch holds on the main shuttle have a pitch of 80 μm and are offset by 40 μm on the left side versus the right side.

From here the right-side inchworm motor engages and holds its GCAs to keep the main shuttle in place while the left-side inchworm motor starts to actuate. After 180 micro steps of the left-side inchworm motor, the left-side pinion has just engaged with the main shuttle, the right-side inchworm motor GCAs release and the restoring spring snaps the right-side shuttle to its original location. The left-side inchworm motor continues to take an additional 270 micro steps, bringing the microrobot into the state shown in Figure 2c. The two pinions can take up to 28 macro steps of 40 μm each to generate a total main shuttle displacement of 1120 μm. The main shuttle spring energy is released when both inchworm motors disengage all their GCAs.

Electrostatic inchworm motors are attractive for their ease of integration and low power operation. The motors take micro steps at a rate of 80 hz and operate at 100 V. The total capacitance that must be driven during each micro step is 21 pF, which corresponds to an energy of 0.21 μJ per micro step. The energy required per macro step is then 94.5 μJ. If all 28 macro steps are taken, 2646 μJ of electrical input energy are required to store 4.0 μJ of mechanical energy. Currently it takes the microrobot 5.6 seconds for each macro step, meaning it can jump once every 2.5 minutes. These electrostatic inchworm motors have been shown to move at speeds up to 3.4 cm/s [9], which could theoretically lead to a jump rate of 1.3 jumps per second!

This IoI topology is advantageous because it allows the force from the inchworm motor to be amplified when it gets to the main shuttle. Figure 3 shows a detailed view of the pinion. When the inchworm motor shuttle applies a force at the right side of the pinion, it applies a moment, which in turn must be balanced by the moment applied by the R_1 lever and the main shuttle. This effectively amplifies the inchworm motor force by a factor of R_2/R_1. The serpentine spring that attaches the pinion to the field SOI decreases this amplification factor by less than 1%. R_2 and R_1 in this design are 1200 μm and 120 μm respectively so the mechanical gain we calculate for is 10. R_3 is bounded by the shear limit of the buried oxide that anchors the central pin to the substrate. Previous work has shown the fracture stress of this oxide is 54 MPa [11], so R_3 was chosen to be 47 μm to ensure this anchor remains fixed to the substrate.

The inchworm motors were measured to have a force density of 0.83 mN/mm^2 on their own, with no mechanical gain. Sizing this pinion correctly can greatly increase this areal force density. The theoretical force density with the mechanical gain stage is 6.1 mN/mm^2 but has yet to be experimentally verified.

TESTING AND RESULTS

It is complicated to test a mobile (non-autonomous) MEMS device because power and control are typically provided through probes under a microscope. Here, the power and control are provided through 60 μm copper wires that are bonded to the microrobot using a conductive epoxy. These wires, while allowing the microrobot to move, are exceedingly difficult to deal with due to their relatively large stiffness (~10 N/m). Braiding the wires together and removing any kinks before bonding proved critical to keeping the microrobot from being pulled around by the wires.

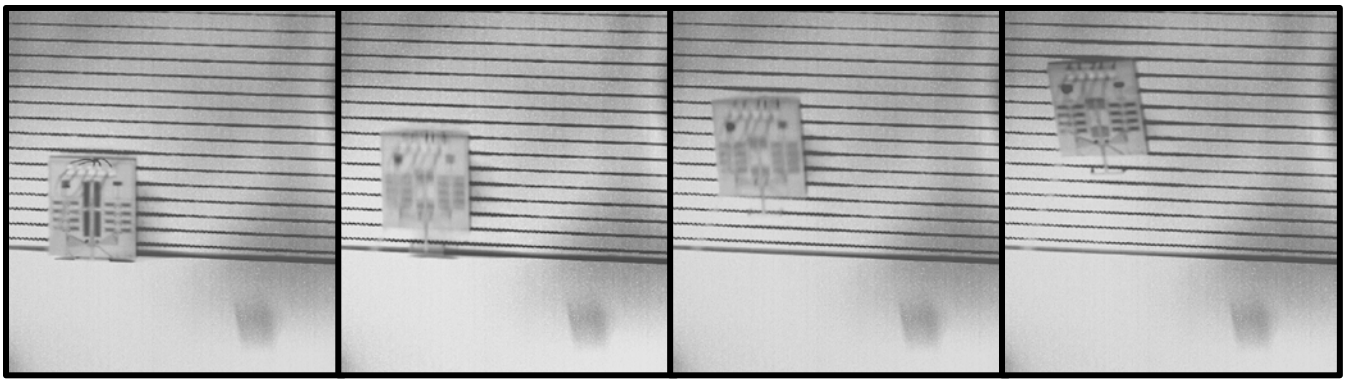

Figure 5: Stills from a 500-fps video of the jumping microrobot taking its largest leap to date, 6.5 mm. The robot leg was manually depressed but held in place by the GCAs. The microrobot jumped when the GCA voltage was released. The line spacing is 1 mm.

Once the microrobot was wired up, it was stood up on its foot with tweezers. The stills in Figure 4 show that there are small pieces of substrate silicon attached to the back of the foot. These protrusions allow the microrobot to stand up even when there are no wires bonded to it. The braided copper wires are taped down to the table to limit the torque applied to the microrobot during testing. Two different tests were performed. In the first test, the microrobot was only allowed to use its IoI to store mechanical energy. The result of this test is shown in Figure 4. The microrobot took 14 macro steps and eventually jumped 1 mm. The pinions sometimes had trouble resetting to their original positions, which limited the total number of macro steps to 14. It seems that something during the epoxy curing process led to an increase in stiction between the pinion and the substrate. In the second test, the serpentine springs were loaded manually with a probe tip. Once fully deflected, one side of the IoI was actuated to lock the main shuttle in place. When a button on the microcontroller was pressed, the IoI would release the main shuttle and the microrobot jumped. The results of this test are shown in Figure 5. The microrobot, while theoretically capable of jumping 9.4 mm only reaches a height of 6.5 mm. These loses can be due to several things including friction in the mechanisms, stiffness from the copper wires, and loses in the silicon springs themselves.

MATLAB MICROROBOT LIBRARY

The layout for this microrobot was generated entirely using a MATLAB library developed by the Pister group. This library contains high level functions that range in complexity from creating a circle, to a motor, to a full jumping microrobot. The repository can be found at the end of this paper under the contact information.

CONCLUSION AND FUTURE WORK

A jumping microrobot capable of storing and releasing mechanical energy was designed, fabricated, and tested. The IoI was the enabling advancement that made this microrobot possible by amplifying the force output of a standard inchworm motor. In the future, the stored energy and therefore the output force of the IoI will need to be increased to reach jump heights of 10s of cm. This can be accomplished in part by moving the energy storage components to the substrate layer. This would be beneficial because wider and thus more energy dense springs can be fabricated in the substrate. Additionally, this move makes more device side area available to be used as additional motor area. To create a truly autonomous microrobot, the copper wires that proved power and control must be eliminated. Using onboard solar cells and high voltage relays for power, and a bare die microcontroller and radio chip, the dream of an autonomous army of jumping microrobots could become a reality.

REFERENCES

[1] Feynman, Richard P. "There's plenty of room at the bottom [data storage]." Journal of microelectromechanical systems 1.1 (1992): 60-66

[2] Feynman, Richard. "Infinitesimal machinery." Journal of Microelectromechanical Systems 2.1 (1993): 4-14.

[3] Churaman, Wayne A., Aaron P. Gerratt, and Sarah Bergbreiter. ‘‘First leaps toward jumping microrobots.” Intelligent Robots and Systems (IROS), 2011 IEEE/RSJ International Conference on. IEEE, 2011.

[4] Gomez, H., et al. "Zero Insertion Force MEMS Socket for Microrobotics Assembly." Manipulation, Automation and Robotics at Small Scales (MARSS), 2017 International Conference on. IEEE, 2017.

[5] Wheeler, Brad, et al. "Crystal-free narrow-band radios for low-cost IoT." Radio Frequency Integrated Circuits Symposium (RFIC), 2017 IEEE. IEEE, 2017.

[6] Gerratt, Aaron P., and Sarah Bergbreiter. "Incorporating compliant elastomers for jumping locomotion in microrobots." Smart Materials and Structures 22.1 (2012): 014010.

[7] Johansson, Stefan, et al. “Fracture testing of silicon microelements insitu in a scanning electron microscope.” Journal of applied physics 63.10 (1988): 4799-4803.

[8] Greenspun et al. The MEMS Hammer, A tool to study microfracture Hilton Head 2016 Solid State Sensor and Actuator Workshop Technical Digest (Hilton Head Island, SC, 2016)

[9] Contreras, Daniel S., and Kristofer SJ Pister. "Dynamics of electrostatic inchworm motors for silicon microrobots." Manipulation, Automation and Robotics at Small Scales (MARSS), 2017 International Conference on. IEEE, 2017.

[10] Penskiy, I., and S. Bergbreiter. "Optimized electrostatic inchworm motors using a flexible driving arm." Journal of Micromechanics and Microengineering 23.1 (2012): 015018.

[11] Greenspun, J., T. Massey, and K. S. J. Pister. "The MEMS Hammer A tool to study microfracture." Hilton Head 2016 Solid State Sensor and Actuator Workshop Technical Digest.

CONTACT

Joey Greenspun, greenspun@eecs.berkeley.edu

https://github.com/pinxisimitu/MEMS_Microrobot_Library

SOFT ROBOTICS: FLUID-DRIVEN SELF-FOLDING PAPERS

Ha-Ill Chun, Maedeh Mohammadifar and Seokheun Choi,*
Bioelectronics & Microsystems Laboratory, Department of Electrical & Computer Engineering,
Center for Research in Advanced Sensing Technologies & Environmental Sustainability (CREATES),
State University of New York at Binghamton, New York, USA

ABSTRACT

We demonstrate a self-folding paper robot with capillary force driven fluid. When water is sprayed on fluidic channels patterned on paper, the 2-D sheet of paper can be controllably self-folded into various 3-D structures; half-oval, circle, round-edge square, triangle, half-circle, and table. The self-folding paper sheet can be readily fabricated via a double-sided wax printing method, forming a bilayer structure of the fluidic channel and the hydrophobic wax, in which these two layers have different swelling/shrinking properties. The patterned paper performs folding actuation with water and unfolding behavior with evaporation without being mechanically manipulated by external forces or moments. Finally, we create a paper gripper based on this self-folding actuation, conveying a low-weight object. This report demonstrates the possibility of paper microfluidics for self-folding actuation and soft robotics.

INTRODUCTION

Soft robotics has emerged as a promising field of research to revolutionize wearable, healthcare, and manufacturing applications [1-5]. Such robots offer considerable advantages over traditional hard robots in pursuing open-ended tasks in an unstructured environment and in physical interfaces with living organisms, including humans (NSF EFRI Solicitation 2018). In contrast to their rigid counterparts, soft materials may easily deform and adapt to a wide range of surroundings [6, 7]. Recently, active soft materials for self-folding robots have attracted significant attention because they inherently convert other forms of energy into mechanical force to create structures without the application of external manipulations [8]. Many self-folding techniques have been developed by using hydraulic, pneumatic, electrical, thermal or magnetic actuation [8-11]. Among those techniques, paper-based soft robotics is the most underdeveloped [12-14]. Even so, excitement is building, as paper possesses unique properties such as low cost, flexible, foldable, eco-friendly, and easily designable. Furthermore, the potential of paper for large-scale batch-fabrication has been demonstrated in recent publications [15]. Recently, the Hashimoto group created a novel method to print an actuator and a structure on a paper substrate [16, 17]. The ink printed on the paper induced the paper substrate to self-fold due to swelling and drying processes. However, this folding process occurred instantly with printing, limiting the on-demand operation and practical applications. Furthermore, this technique had little control of the degree of folding because of the uncontrollable penetration depth of ink in paper. Also, the drying process of the ink induced the paper to undesirably self-fold in the opposite direction.

Here, we introduced an innovative self-folding method with a microfluidic capillary force in paper, allowing on-demand activation with the simple spraying of water (Figure 1). This new technique enabled a flat paper sheet to self-fold with desired angles by controlling wax patterns/thicknesses. The thickness of the hydrophobic wax increased with heating time, reducing the thickness of the hydrophilic part of the paper and controlling the folding degree with water sprayed. This proposed technique will be advantageous for many applications inexpensively and autonomously in remote and dangerous environments.

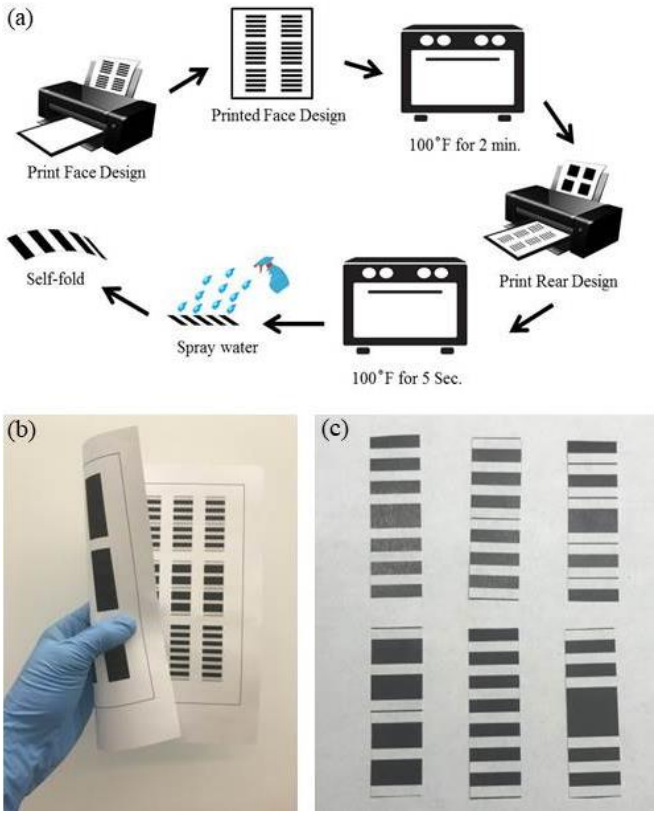

Figure 1: (a) Fabrication processes of the self-folding paper robot. (b) & (c) Photo-images of the 2-D sheet of papers with different wax patterns.

MATERIALS AND EXPERIMENTAL SET-UP

Device Fabrication

The hydrophilic channels were defined with hydrophobic wax boundaries on paper by double-sided printing and letting the wax penetrate asymmetrically (Figure 2) [18, 19]. The vertical penetration depth of the melted wax was controlled by adjusting the heating time. Specific wax/channel patterns were designed using AutoCAD software and printed out onto A4 printer papers using a Xerox Phaser printer (ColorQube 8570). The printed wax was heated for various times at 130 °C (E191047, VWR International, USA), controlling the wax/channel thickness.

Operating Principle

Figure 2 shows the operating principle of the fluidic actuation in paper, which consists of a swelling process with sprayed water and a drying process with evaporation. This actuation used a two-layer configuration with one passive wax layer and one active water layer. The passive layer developed a negligible mechanical

978-1-940470-03-0/HH2018/$25©2018TRF
DOI 10.31438/trf.hh2018.46

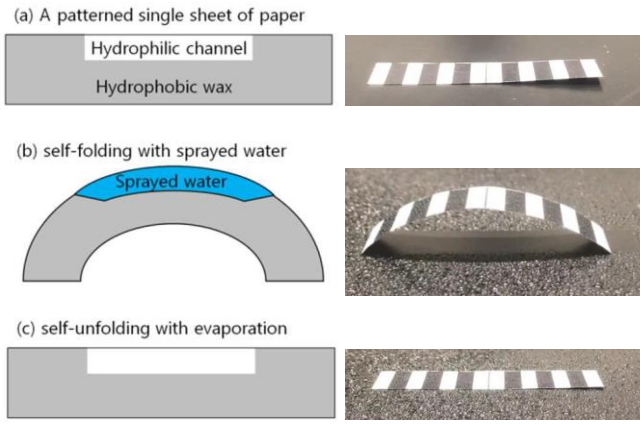

Figure 2: Schematic representations of the device operation principle with photo-images of the self-folding and self-unfolding paper.

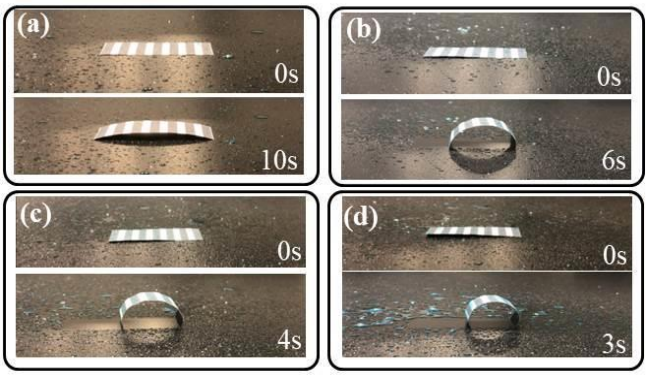

Figure 3: Time courses of our devices' self-folding with different amount of water; (a) 30% wetting (b) 60% wetting, (c) 80% wetting, and (d) 100% wetting.

move compared to the active layer with the water-based swelling process. This difference in expansion or contraction between the two layers generates localized bending of the paper sheet.

RESULT AND DISCUSSION

Self-folding papers

The bilayer of the wax and the hydrophilic channel had drastically different swelling behavior in response to water spraying, spontaneously folding-up and actuating from the 2-D pattern on the paper (Figure 2). The folding angle of the paper increased more rapidly as the more water was introduced (Figure 3). With the more water amount, the surface tension of the channel layer increased and thus the higher folding angle could be obtained. With 30% wetting of the paper channel, the paper did not fold even 10s after the water introduction while it rapidly self-folded within 3 seconds under 100% wetting condition. Furthermore, different 3-D paper structures were created with different wax/channel patterns in paper: (a) half oval, (b) circle, (c) round-edge square, (d) triangle, (e) half-circle, and (f) table (Figure 4). (a) The half oval structure was obtained using a relatively wide wax pattern in the middle and the periodic wax/channel patterns with the same width on the other sides.

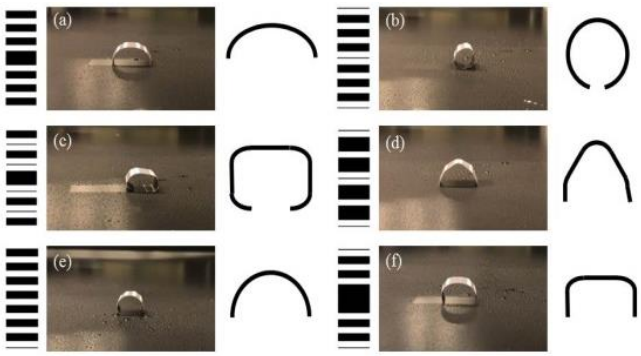

Figure 4: Different deformation based on different wax/channel designs. (a) Half-oval, (b) circle, (c) round-edge square box, (d) tip, (e) half-circle, and (f) table.

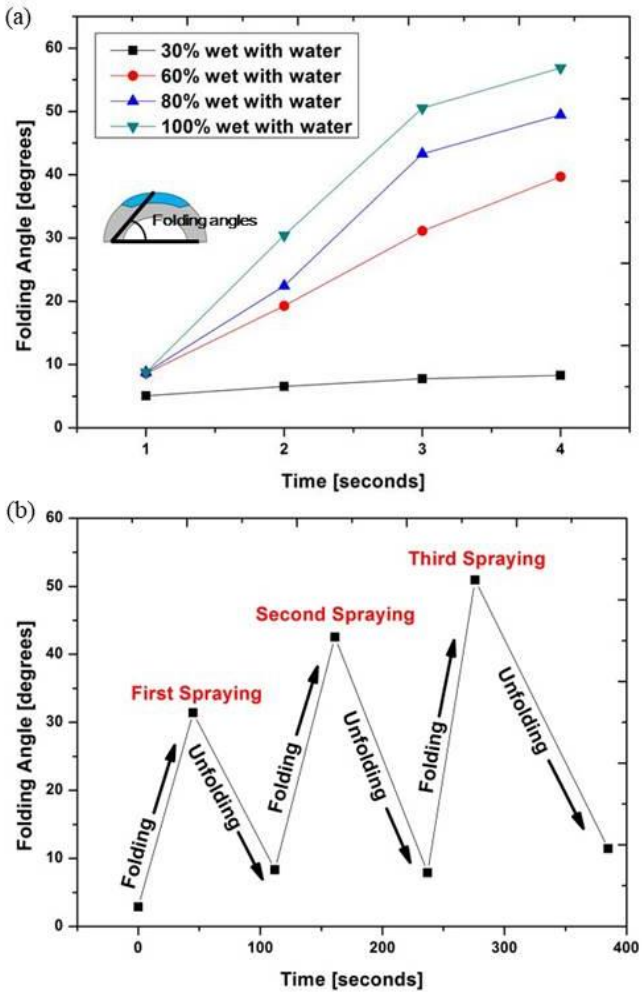

Figure 5: (a) Folding actuation with water. The folding angles increased with the higher wet percentage in paper. (b) Continuous folding/unfolding steps.

(b) The similar wax/channel patterns to the half oval one formed the circle structure except the edge and middle patterns having hydrophilic channels to provide the circular folding. (c) For the round-edge square box, the hydrophilic channel had to be enlarged while thin wax patterns were included within the channel. (d) The

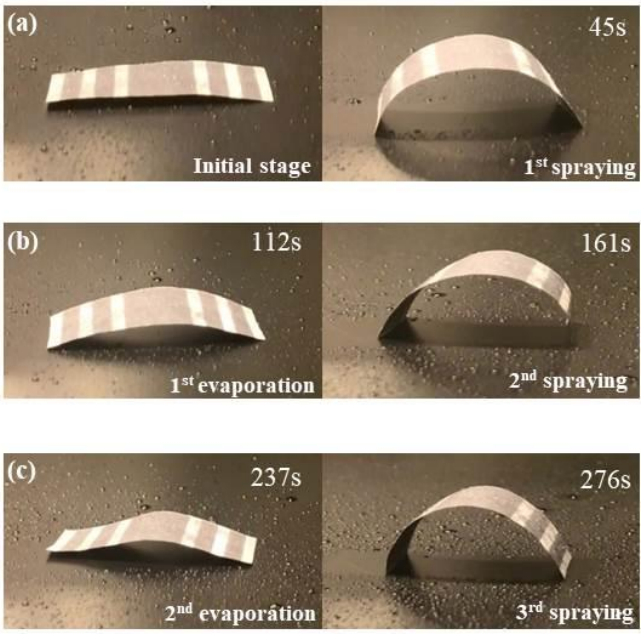

Figure 6: Time courses of continuous folding/unfolding steps. (a) Initial stage → 1st folding, (b) 1st unfolding → 2nd folding, and (c) 2nd unfolding → 3rd folding.

tip structure was formed with the increased widths of the wax patterns. (e) The half-circle structure was developed with the periodic wax/channel patterns with the same width. Finally, (f) the table was acquired with the increased wax width in the middle from the half circle pattern. Controlling shapes of the self-folding paper robots is very important not only to adapt to different environments but also to create different locomotion behaviors. The folding process relied on the water amount sprayed on the paper, demonstrating the folding angles more gradually increased with the higher wet percentage in paper (Figure 5a). At 4 seconds after water spraying, 100% wetting made a 57-degree bend while 50-degree, 38-degree, and 7-degree bends were made for 80%, 60%, and 30% wetting condition, respectively.

Repeated folding and unfolding

The folded structure can also unfold itself with evaporation (Figure 5b & Figure 6). Unlike the previous reports [16, 17], our paper with asymmetric wax/channel patterns did not reversely fold. Under repeated swelling and drying processes, the designed paper successfully folded and unfolded. However, it should be noted that the complete unfolding required more time, which did not return to its initial flat stage of the paper. During the repeated folding and unfolding, the folding angle gradually increased mainly because the paper rigidity decreased after multiple mechanical movements.

Paper grippers

In contrast to robots made from rigid materials, soft robots can gently grip and manipulate irregular/delicate objects [20-22]. These systems provide the unique advantage of inherently safe and adaptive contact with non-planar surroundings, which open a frontier for the next generation wearable and field robots [20]. In this task, we developed a six-legged paper gripper (Figure 7) in which each leg had the wax/channel patterns for the half-circle structure (Figure 4e). We selected the number of the legs and adjusted their lengths to effectively pick up and manipulate a soft

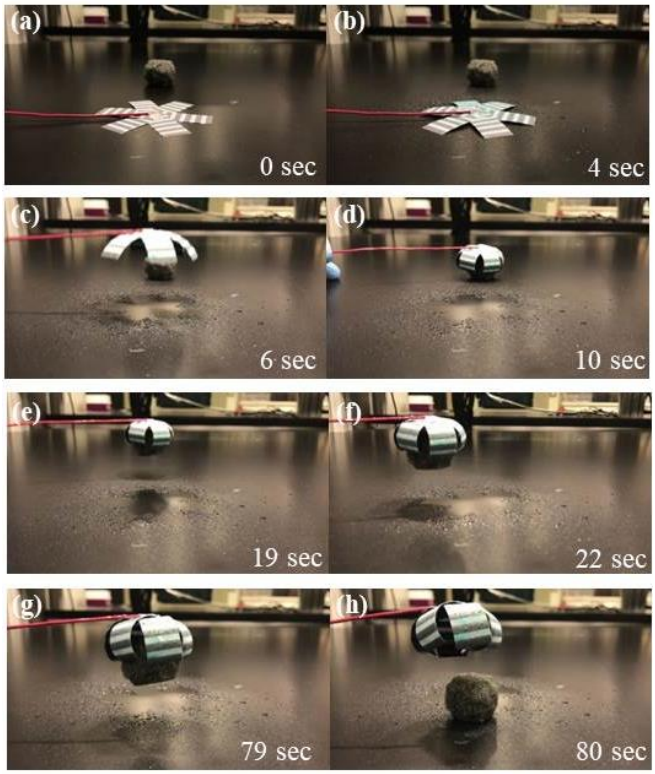

Figure 7: Still frames from a video of the paper gripper performing a manipulation task with an object. In this task, a sponge is grasped, manipulated, and released. Frames at: (a) 0s, (b)4s, (c)6s, (d) 10s, (e) 19s, (f) 22s, (g) 79s, and (h) 80s.

target object with specific size, weight and shape. Upon the water spraying, each leg self-folded to form a half circle structure. Our paper gripper successfully picked up the soft circular sponge with the same weight as the paper gripper and held it for more than a minute. When the water in the channel evaporated, the gripper released the object.

CONCLUSION

In this work, we demonstrated an innovative technique to fabricate fluid-driven self-folding papers, and their applications for robotics. The single 2D sheet of papers self-folded into various 3D structures when water was introduced. Folding times and shapes could be controlled by changing the designs of the hydrophilic and hydrophobic patterns and controlling the amount of water sprayed on paper. Furthermore, the paper could fold multiple times when water was re-introduced to the dried hydrophilic channels. The self-folding papers were leveraged to develop the paper gripper with six soft legs, which could pick up a small and low-weight object and hold it for about one minute. We believe that this microfluidic control with paper provides an important strategy to build more powerful and capable self-actuating robots.

ACKNOLOWDGMENT

This work is supported by NSF (ECCS #1503462) and the SUNY Binghamton Research Foundation (SE-TAE).

REFERENCES

[1] C. Majidi, "Soft Robotics: A Perspective - Current Trends and Prospects for the Future," Soft Robotics, 1, 154, 2014.

[2] S. Kim, C. Laschi, B. Trimmer, "Soft robotics: A bioinspired evolution in robotics," Trends in Biotech., 31, 287, 2013.

[3] G. Haghiashtiani, E. Habtour, S.H. Park, F. Gardea, M.C. McAlpine, "3D printed electrically-driven soft actuators," Extreme Mechanics Letters, 21, 1, 2018.

[4] H. Banerjee, Z.T.H. Tse, H. Ren, "Soft robotics with compliance and adaptation for biomedical applications and forthcoming challenges," International Journal of Robotics and Automation, 33, 69, 2018.

[5] A.W. Feinberg, "Biological Soft Robotics," Annual Review of Biomedical Engineering, 17, 243, 2015.

[6] N. Lu, D. Kim, "Flexible and Stretchable Electronics Paving the Way for Soft Robotics," Soft Robotics, 1, 53, 2014.

[7] T. Arnold, M. Scheutz, "The tactile ethics of soft robotics: Designing wisely for human-robot interaction," Soft Robotics, 4, 81, 2017.

[8] E.A. Peraza-Hernandez, et al., "Origami-inspired active structures: a synthesis and review," Smart Materials and Structures, 23, 094001, 2014.

[9] J.C. Breger, C. Yoon, R. Xiao, H.R. Kwag, M.O. Wang, J.P. Fisher, T.D. Nguyen, D.H. Gracias, "Self-folding thermos-magnetically responsive soft microgrippers," ACS Appl. Mater. Interfaces, 7, 3398, 2015.

[10] L. Hines, K. Petersen, G.Z. Lum, M. Sitti, "Soft actuators for small-scale robotics," Advanced Materials, 29, 1603483, 2017.

[11] S. Sundaram, D.S. Kim, M.A. Baldo, R.C. Hayward, W. Matusik, "3D-printed self-folding electronics," ACS. Appl. Mater. Interfaces, 9, 32290, 2017.

[12] M.M. Hamedi, V.E. Campbell, P. Rothemund, F. Guder, D.C. Christodouleas, J. Bloch, G.M. Whitesides,"Electrically activated paper actuators," Advanced Functional Materials, 26, 2446, 2016.

[13] A.S. Chen, H. Zhu, Y. Li, L. Hu, S. Bergbreiter, "A paper-based electrostatic zipper actuator for printable robots," 2014 IEEE International Conference on Robotics & Automation, May 31-June 7, 2014, Hong Kong, China, pp.5038-5043.

[14] X. Du, H. Wu, J. Qi, S.Y. Jeong, F. Ni, "Paper-based pneumatic locomotive robot with sticky actuator," MATEC Web of Conferences 42, 03014, 2016.

[15] P. Andersson, R. Forchheimer, P. Tehrani and M. Berggren, "Printable All-Organic electrochromic Active-Matrix displays," Advanced Functional Materials, 17, 3074, 2007.

[16] H. Shigemune, S. Maeda, Y. Hara, U. Koike, S. Hashimoto, "Kirigami robot: making paper robot using desktop cutting plotter and inkjet printer," 2015 IEEE/RSJ International Conference on Intelligent Robot and Systems, Sep. 28 – Oct. 2, 2015, pp.1091-1096.

[17] H. Shigemune, S. Maeda, Y. Hara, N. Hosoya, S. Hashimoto, "Origami robot: a self-folding paper robot with an electrothermal actuator created by printing," IEEE/ASME Transactions on Mechatronics, 21, 2746, 2016.

[18] S. Jeong, S. Lee, C. Choi, J. Kim, C. Lee, "Toward instrument-free digital measurements: a three-dimensional microfluidic device fabricated in a single sheet of paper by double-sided printing and lamination," Lab on a Chip, 15, 1188, 2015.

[19] Y. Gao, S. Choi, "Stepping toward self-powered papertronics: Integrating biobatteries into a single sheet of paper," Advanced Materials Technologies, 2, 1600194, 2017.

[20] X. Zhou, C. Majidi, O.M. O'Reilly, "Soft hands: an analysis of some gripping mechanisms in soft robot design," International Journal of Solids and Structures, 64065, 155, 2015.

[21] J. Zhou, S. Chen, Z. Wang, "A soft-robotic gripper with enhanced object adaptation and grasping reliability," IEEE Robotics and Automation Letters, 2, 2287, 2017.

[22] K. Tai, A. El-Sayed, M. Shahriari, M. Biglarbegian, S. Mahmud, "State of the art robotic grippers and applications," Robotics, 5, 11, 2016.

CONTACT

*Seokheun Choi, *Assistant Professor*, SUNY-Binghamton,
Email: sechoi@binghamton.edu
Website: http://ws.binghamton.edu/choi

THE μHAMMER: INVESTIGATING CELLULAR RESPONSE TO IMPACT WITH A HIGH THROUGHPUT MICROFLUIDIC MEMS DEVICE

Luke H.C. Patterson[1], Jennifer L. Walker[1], Evelyn Rodriguez-Mesa[2], Kevin Shields[2], John S. Foster[2], Megan T. Valentine[1,3,4], Adele M. Doyle[3,4], and Kimberly L. Foster[1,4]

[1]Department of Mechanical Engineering, [3]Neuroscience Research Institute, and [4]Center for Bioengineering, University of California, Santa Barbara, California, USA

[2]Owl Biomedical, Goleta, California, USA

ABSTRACT

We report the application of stress to biological cells at unprecedented strain (50%), strain rate (180,000 s^{-1}), and throughput (1,800 cells/min) using a high-speed, high actuation force magnetically-driven MEMS chip. This device is uniquely suited to study the effects of impact on large populations of inherently heterogeneous cells, enabling statistical analysis that can elucidate the cell-level ramifications of Traumatic Brain Injury (TBI). To demonstrate the capabilities of the μHammer, we applied TBI-relevant strains and strain rates to human leukemic K562 cells then monitored their proliferation for 9 days. We observed significantly repressed proliferation of the hit cells compared to both the negative and sham controls, indicating success in applying sublethal cellular damage.

INTRODUCTION

According to the CDC, approximately 2 million Traumatic Brain Injuries (TBIs) occur in the United States each year, resulting from either physical impacts such as those common in sports injuries or percussive waves such as those following explosive blasts [1]. The symptoms of these injuries can linger for years after the incident and have far-reaching medical, societal, and economic impact. Little is known about TBI's mechanisms of injury and loss of function, however, especially on the cellular level. This is due in part to the lack of instruments to replicate TBI-relevant loading conditions on individual cells. While several device platforms capable of applying compressive forces to individual cells exist (e.g. AFM, microplates), each is limited to some combination of low force (sub-μN), strain (<10%), and strain rate (<10 s^{-1}) [2-4]. Even more limiting is the low throughput of these devices (tens of cells per experiment), which makes gathering sufficient data for sensitive biological analysis of inherently heterogeneous cell populations difficult if not impossible [5]. These deficiencies have particularly hindered investigations of TBI, which typically involve peak tissue-level strains of 10-50% and strain rates of 10-1000 s^{-1}, parameters that may be even higher on the cellular level due to localized heterogeneities [6, 7].

To address these critical needs, we have developed a microfluidic MEMS device, the "μHammer," to subject individual cells to impact with an unprecedented combination of strain (10-75%), strain rate (10,000+ s^{-1}), and throughput (up to 3,000 cells/min). Cells are processed under sterile conditions and can be removed after the loading event for immediate analysis or cultured *in vitro* for long term tracking. Here, we demonstrate the capabilities of the μHammer by applying TBI-relevant strains and strain rates to a prototypical cell line, human leukemic K562 cells, and then monitoring their proliferation for 9 days.

MATERIALS AND METHODS

μHammer Components

The μHammer is composed of single-crystal silicon with an embedded NiFe armature in microchip format, magnetically driven by an external solenoid via an *in situ* NiFe pole (Figure 1). The device is fabricated by Owl Biomedical (USA) using a 14-layer process, with the silicon features etched via RIE/DRIE and the NiFe features deposited via electrochemical plating. The upper surface of the device is sealed with glass, while the bottom surface is bonded to a macroscale interposer that interrogates the three vias (one input, one output, one waste). This is finally bonded to a sterile cartridge, which holds up to 10 mL of input cells suspended in buffer and

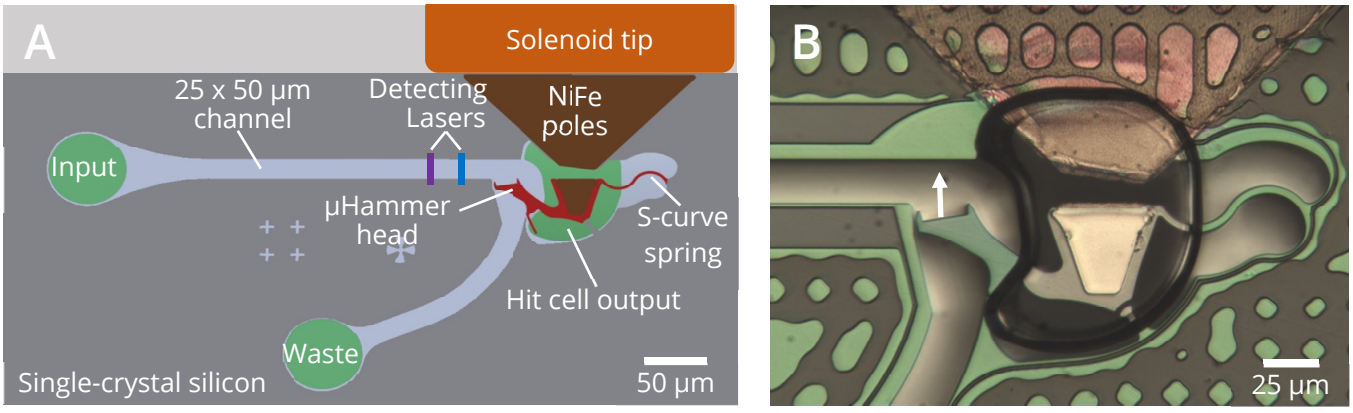

Figure 1A: μHammer device schematic. Chip (dark grey) is bonded to a sterilized macroscale cartridge (not shown) which interfaces with a flow-control pump and can be loaded with cells suspended in buffer. Cells enter chip through the input via, flow through channel, and are impacted by μHammer when external solenoid is activated, swinging lower magnet and μHammer head upward. Impacted cells exit through output via and are extracted for analysis. Figure 1B: μHammer micrograph. Arrow indicates direction of μHammer actuation.

978-1-940470-03-0/HH2018/$25©2018TRF
DOI 10.31438/trf.hh2018.47

Solid-State Sensors, Actuators and Microsystems Workshop
Hilton Head Island, South Carolina, June 3-7, 2018

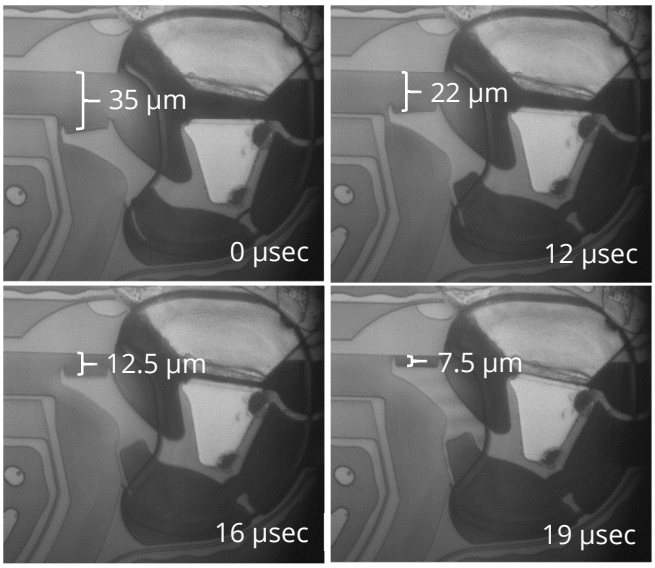

Figure 2: Strobed images of µHammer actuation without cells. Images taken at 1 µs intervals after solenoid trigger. Hundreds of images are averaged at each timestep to create the final image. Image tracking software is then used to track the gap distance (see white brackets) as a function of time.

collects the output for immediate extraction and analysis. The cartridge interfaces with the MACSQuant® Tyto® (Miltenyi Biotech, Germany) system with a flow-controlled pump. This pump applies positive pressure (120 ± 20 mbar) to flow fluorescently labeled cells through the input via to the device, where they pass through a 25 µm × 50 µm channel at a controlled velocity (1.25 ± 0.3 m/s). Two lasers aligned with the channel detect fluorescently labeled cells, both to monitor the speed for timing and to trigger the solenoid at a predetermined interval before the cell will reach the µHammer head (the 'pre-arrival time'). The released µHammer head extends from the NiFe armature and is anchored to the surrounding silicon substrate by a released S-curve spring. Once actuated, the µHammer head rotates about the anchor point at a tunable speed (that varies with current applied to the solenoid) across the channel to full actuation, where it can be held for a user-specified period before returning to rest to prepare for the next hit.

Device Characterization

To characterize the stiffness of the S-curve spring, we created a two-dimensional steady-state finite element model of the µHammer in COMSOL, solving for structural deformation under the influence of a point load on the edge of the released NiFe armature. The magnitude of this force was determined by a separate finite-element model of the solenoid and NiFe poles, solving for both the electric and magnetic fields as well as the resulting electromagnetic force.

To characterize the velocity of actuation and the subsequent strain rate the device applies, we used a high-speed camera to capture strobed images of the device at 1 µs intervals after triggering the solenoid. We then used feature-tracking software to determine the gap distance between the µHammer face and the top of the channel as a function of time (Figure 2). We did this first with buffer flowing through the channel and no cells present to determine the actuation profile of the valve and thus to select an appropriate pre-arrival time. We then used this information to successfully impact cells flowing through the channel, and captured strobed images of the µHammer under these conditions as well.

To validate this pre-arrival time for our system, we updated our COMSOL model of the µHammer to be time-dependent, solving for structural deformation, fluid velocity, and particle (cell) position. In this model, a fluid pressure was applied at the inlet of the device, which carried a 15 µm diameter model cell through the channel while the previously determined boundary magnetic force was applied to the NiFe armature for actuation.

K562 Impact Study

Human K562 cells (ATCC, USA) were fluorescently labeled with carboxyfluorescein succinimidyl ester (CFSE, Thermo Fisher Scientific, USA) which has excitation/emission of 492/517 nm. The cells were then suspended at 50,000 cells/mL in MACSQuant® Tyto® Running Buffer (Miltenyi Biotech, Germany), and flowed through the µHammer's sterilized microfluidic channel at 100,000 cells/hour. As each cell passed through the lasers, it was detected and timed for a µHammer impact which subjected each cell to 50% strain at a 180,000 s^{-1} strain rate (see Figure 3 for impact profile). A sham control population was fluorescently stained and flowed through the device without impact, while a negative control population was neither fluorescently stained nor introduced into the device.

After each treatment, four replicates of each group were seeded at 40,000 cells/mL and cultured in 12-well cell culture microplates (Thermo Fisher Scientific, USA). K562 cells were grown in RPMI-1640 media supplemented with 10% FBS, 25 mM HEPES, and 0.01% penicillin streptomycin (Lonza Biologics, UK) at 37°C and 5% CO2. Every 24 hours, cell density was measured in triplicate by flow cytometry (MACSQuant® Flow Cytometer, Miltenyi Biotech, Germany) to monitor each group's proliferation rate until the cell number reached 1,000,000 cells/well. After the density measurement on day 7, fresh media was added to the hit population wells to maintain sufficient volume for continued culturing. The doubling time, t_{double}, of each cell population's exponential growth phase was determined by plotting the number of cells, N, as a function of time

$$N = N_o e^{rt}$$

where

$$t_{double} = \frac{\ln(2)}{r}.$$

Significant difference between groups was determined via One-Way ANOVA with post-hoc Tukey's.

RESULTS

Device Characterization

As determined by observing the deflection of the NiFe armature in response to a point load, the stiffness of the S-curve spring is 85 ± 5 N/m, based on a Young's modulus for silicon of 170 ± 10 GPa. The magnitude of the magnetic force applied to the released NiFe armature by the solenoid at saturation increases from 0.29 to 1.2 mN as the armature travels toward the NiFe pole above. When this force is applied to the armature, it is pulled upward toward the top of the channel along with the µHammer head until it contacts the stationary NiFe pole above approximately 19 µs later, as shown in Figures 2 and 3. During transit, the µHammer head travels at an average speed of 2.7 ± 0.2 m/s during compression while closing to a 7.5 µm final gap (Figure 3). This translates to a strain rate of 180,000 ±13,000 s^{-1} and 50% maximum strain for a

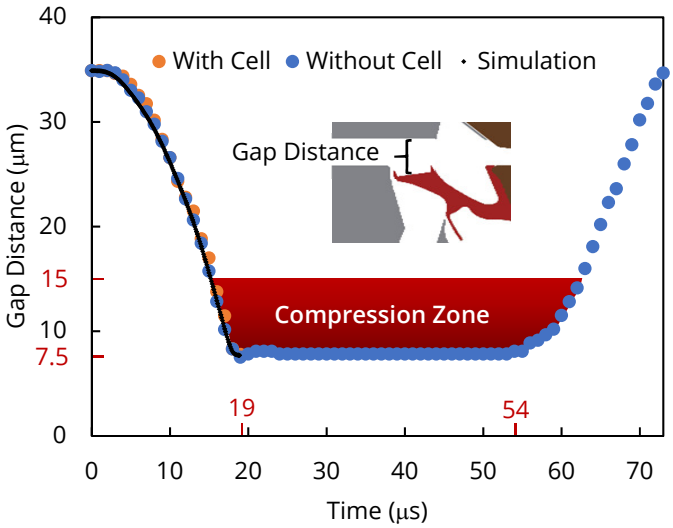

Figure 3: μHammer compression and recovery profile. Blue points from strobed images of devices actuated without cells. Images taken at 1 μs intervals after solenoid activation until full recovery after release (full actuation held for 35 μs before release). n = 4 devices, standard deviation less than marker size. Orange points from strobed images while impacting cells up to full actuation (n = 2 devices). Black line obtained using COMSOL simulations up to full actuation. Slope of the least squares best fit line in compression zone without cells is 2.7 ± 0.2 m/s, while slope with cells is 2.8 ± 0.2 m/s. Red marks on y-axis denote bounds of compression zone, while red marks on x-axis denote times of full actuation and release.

typical 15 μm diameter K562 cell. Once the μHammer is released, it returns to rest and is ready for the next actuation within 25 μs.

Due to the depth of the channel (50 μm), the majority of cells pass through the channel at a depth outside the focal plane of the camera. Combined with the large number of images averaged together to create each timestep, this currently limits our ability to resolve individual cells during impact. However, we were able to track the actuation profile of the μHammer head while impacting cells, which is almost identical to the actuation profile of the μHammer without cells in buffer (Figure 3). Furthermore, the hammer head velocity in the compression zone with cells (2.8 ± 0.2 m/s) is within the reported range of hammer head velocities without cells, indicating that the cell's presence does not alter the actuation of the μHammer. Since the Young's modulus of a cell (on the order of kPa) is orders of magnitude lower than the Young's modulus of silicon (170 GPa), this is not surprising and indicates that no detectable strain stiffening of the cell is occurring [8].

As shown in Figure 3, there is close agreement between the experimental actuation profiles and the simulated profile from our time-dependent COMSOL model of fluid-structure interaction. This model was run with the timing parameters calculated in the previous section, resulting in the plots shown in Figure 4. In this model, our simulated cell successfully flows through the channel with a smooth trajectory until impacting the middle of the μHammer face, demonstrating the correct parameters were used to time the solenoid actuation and subsequent cell impact.

K562 Impact Study

Hit, sham, and negative control cells were seeded for continued culture and measurement of cell proliferation. Although the three experimental groups were seeded at the same concentration of 40,000 cells/mL (for a total of 60,000 cells/well), the hit population's proliferation appears depressed compared to the sham and negative control populations (Figure 5). Both the sham and negative control populations grew exponentially from day 1 through day 6, at which point both groups surpassed 1,000,000 cells/well. During this exponential period, they both had a doubling time of approximately 27 hours. The hit cell population, however, did not enter exponential growth until day 2 (at least 24 hours later than the sham and negative controls), after which it had a doubling time of approximately 32 hours to reach 1,000,000 cells/well by day 9.

The lack of significant difference between the negative and sham controls demonstrates the extended lag phase and increased doubling time of the hit population is the result of the μHammer impact alone and not other variables arising from the device microfluidics. Further, the fact that the hit cells retained their ability to proliferate post-impact demonstrates that basic cellular functions (e.g. cell division and metabolism) of the population were not irreparably compromised following impact. This indicates the μHammer was not only successful in applying sublethal cellular damage, which is necessary for performing biological analyses of impacted cells on longer timescales, but also may recapitulate aspects of TBI-like damage.

CONCLUSIONS

Using K562 cells as proof-of-concept, we demonstrated the μHammer's ability to apply consistent high strain and strain rate impacts to large populations of cells. We further showed that these impacts repressed subsequent proliferation without compromising overall viability. Such controlled loading profiles can be applied to any suspended cell or microscale material (maximum diameter <20 μm), opening doors for microscale materials characterization at high

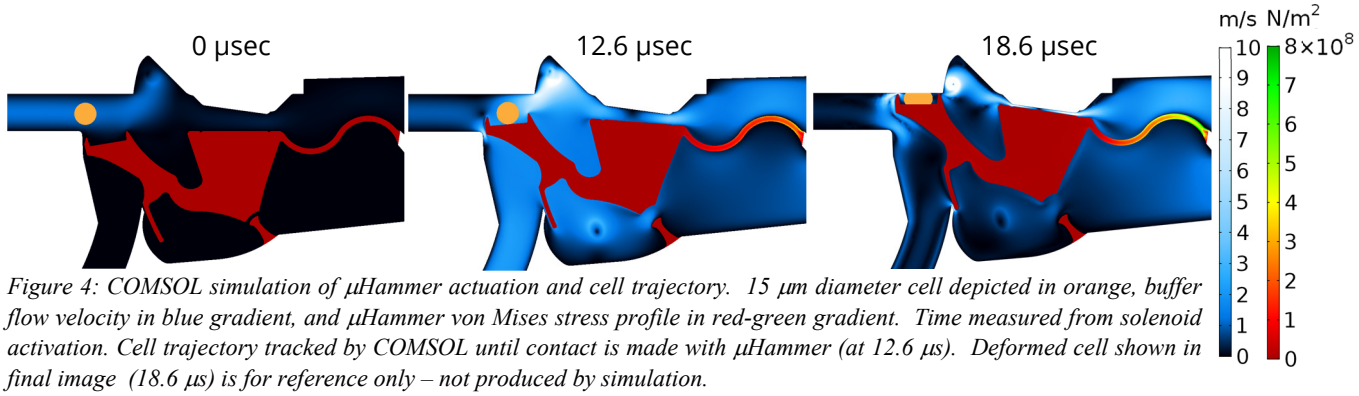

Figure 4: COMSOL simulation of μHammer actuation and cell trajectory. 15 μm diameter cell depicted in orange, buffer flow velocity in blue gradient, and μHammer von Mises stress profile in red-green gradient. Time measured from solenoid activation. Cell trajectory tracked by COMSOL until contact is made with μHammer (at 12.6 μs). Deformed cell shown in final image (18.6 μs) is for reference only – not produced by simulation.

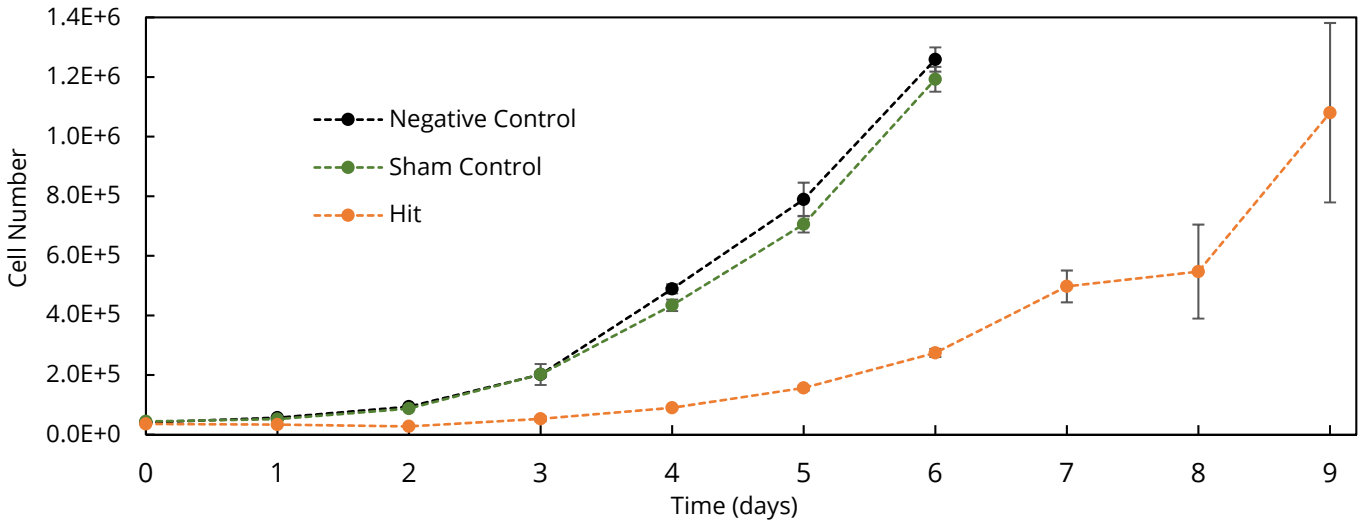

Figure 5: K562 cell growth over 9 days culturing post-μHammer experiment. Hit cell strain rate was 180,000 s^{-1}, total strain 50%, held for 35 μs (see Figure 3 for loading profile). All groups seeded at 60,000 total cells (at a density of 40,000 cells/mL) on day 0. n = 4 wells per group, all taken from same initial population of cells. Error bars depict standard deviation. At each time point there is no significant difference between the negative and sham controls.

strain rates or investigations of force-induced trauma in a number of biological systems.

Going forward, we are particularly interested in extending our analysis to neural and other brain injury-related cells. Though the forces and various extracellular cues applied by the μHammer to a single cell in suspension are likely different than those experienced by a cell embedded in brain tissue *in vivo*, the information provided by the μHammer provides a simplified model system to help fill the gap in our understanding of the relationship between force and injury in cells. Due to the μHammer's unprecedented combination of well-defined impact parameters and high throughput, we believe it is uniquely suited to study TBI on the cellular level. As such, our next step is to perform the same proliferation study with brain-derived cells to determine if they also exhibit repressed proliferation following impact, and if so, to determine the underlying reasons for this response. Future work can explore the broader range of functional, damage, and stress-related cellular assays at various strains and strain rates, investigating the link between these parameters and cellular injury. Through these and further studies, we hope to elucidate the mechanisms of cellular damage and recovery in the brain, ultimately leading to an improved understanding of impact-based cellular injuries and their treatment.

ACKNOWLEDGMENTS

Authors acknowledge support from the National Science Foundation through awards CBET-1631656 (to KLF, AMD and MTV) and CMMI-1254893 (to MTV). We also thank Carl Meinhart from the Department of Mechanical Engineering, UCSB, whose time-dependent COMSOL fluid-structure interaction model formed the basis of our own.

REFERENCES

[1] Centers for Disease Control and Prevention, "Rates of TBI-related Emergency Department Visits, Hospitalizations, and Deaths – United States, 2001 – 2010", https://www.cdc.gov/traumaticbraininjury/data/rates.html (2016).

[2] M. P. Stewart, Y. Toyoda, A. A. Hyman, D. J. Muller, "Tracking mechanics and volume of globular cells with atomic force microscopy using a constant-height clamp", Nature Protocols, 7, 143-154 (2012).

[3] B. P. Chan, C. H. Li, K. L. Au-Yeung, K. Y. Sze, A. H. Ngan, "A microplate compression method for elastic modulus measurement of soft and viscoelastic collagen microspheres", Annals of Biomedical Engineering, 36, 1254-1267 (2008).

[4] K. C. Neuman, A. Nagy, "Single-molecule force spectroscopy: optical tweezers, magnetic tweezers and atomic force microscopy", Nature Methods, 5, 491-505 (2008).

[5] D. Desmaele, M. Boukallel, S. Regnier, "Actuation means for the mechanical stimulation of living cells via microelectromechanical systems: A critical review", Journal of Biomechanics, 44, 1433-1446 (2011).

[6] D. F. Meaney, B. Morrison, C. D. Bass, "The mechanics of traumatic brain injury: a review of what we know and what we need to know for reducing its societal burden", Journal of Biomechanical Engineering, 136, 021008 (2014).

[7] F. Pervin, W. W. Chen, "Dynamic mechanical response of bovine gray matter and white matter brain tissues under compression", Journal of Biomechanics, 42, 731-735 (2009).

[8] N. Guz, M. Dokukin, V. Kalaparthi, I. Sokolov, "If Cell Mechanics Can Be Described by Elastic Modulus: Study of Different Models and Probes Used in Indentation Experiments", Biophysical Journal, 107.3, 564, (2014)

CONTACT

*L.H.C. Patterson, tel: +1-760-258-6341; lpatterson@ucsb.edu

TRANSIENT BIOBATTERIES: MICROFLUIDIC CONTROL FOR PROGRAMMABLE DISSOLUTION

Maedeh Mohammadifar and Seokheun Choi,*
Bioelectronics & Microsystems Laboratory, Department of Electrical & Computer Engineering,
Center for Research in Advanced Sensing Technologies & Environmental Sustainability (CREATES),
State University of New York at Binghamton, New York, USA

ABSTRACT

We report a simple approach to develop transient microbial fuel cells with the capability of dissolving in water after stable power generation within a programmed period. This novel water-soluble biobattery makes use of the integration of a dissolvable paper-based substrate, a simple pencil-drawn graphite anode, and a Prussian-blue (PB) cathode. The device features (i) a low cost transient paper-based platform, (ii) easily accessible electrode materials and simple fabrication steps and (iii) a time-controlled operation by using the number of serpentine microfluidic channels. The biobatteries reached to a maximum power of 0.5μW and a current 15.6μA and achieved full dissolution in less than 60 minutes.

INTRODUCTION

Transient electronics is an emerging technology with the interesting characteristics to physically disappear on demand [1]. Future research efforts in this realm will continue to revolutionize the fields of temporary biomedical implants, environmental friendly electronics, data-secure memory devices, and disposable consumer electronics [2-4]. However, there are significant challenges in developing transient electronics at a system level that contains an integrated, transient power source [5-9]. The transient power source is essential to creating an all transient system that can work independently and self-sustainably [5, 6]. Despite the vast promise and demand, however, research efforts on transient power sources or energy storage devices were quite limited. Several transient power sources such as lithium-ion batteries and nanogenerators were proposed to degrade into the surrounding environment by the external triggers such as light, temperature, pH, or special liquid [8, 9]. However, they do not sustain stable performance in a controllable manner and still contain a large amount of non-renewable and non-biodegradable heavy metals and polymers [10-14].

In this work, we report a bacteria-powered biobattery on a dissolvable paper that can be decomposed in a controlled manner after stable operation (Figure 1). Single sheet transient microbial fuel cells (MFCs) were directly created from a 2-D sheet of water-soluble paper consisting of four functional layers; ① an anode, ② a reservoir, ③ a proton exchange membrane (PEM), and ④ a cathode (Figure 2) [15, 16]. The hydrophilic microfluidic channels for microbial energy production were defined with hydrophobic wax boundaries which efficiently delayed the fast destruction of the substrate in water. A pencil-drawn graphite anode and a Prussian blue (PB) cathode were constructed on water-soluble paper [17], and electricity-producing bacterial cells were pre-inoculated and freeze-dried in the patterned channels. When the bottom of the device was dipped in water, the liquid was transported vertically via capillary force, rehydrating the freeze-dried cells and activating their respiration by transferring electrons to the anode (Figure 1) [18, 19]. Simultaneously, transiency was triggered while the water dissolved the paper substrate from the bottom. With the number of serpentine microfluidic channels, the transiency was controlled and programmed. This fabrication and material breakthrough allowed the creation of a novel on-demand transient microbial fuel cell (MFC) platform made only of simple and low-cost materials. A maximum power of 0.5μW and current 15.6μA were achieved.

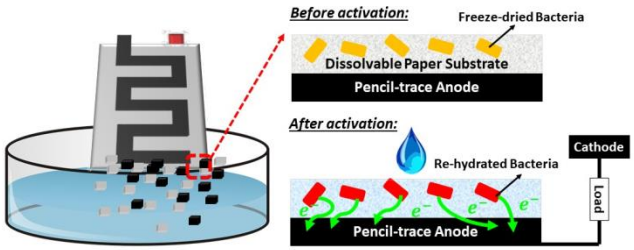

Figure 1: Schematic diagrams of our transient biobattery and its operating principle.

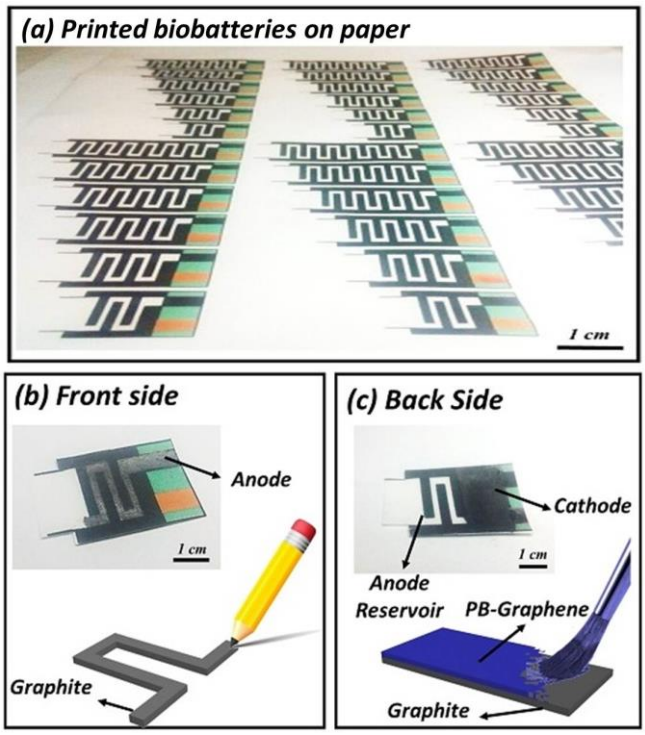

Figure 2: (a) Photo image of the devices with different number of serpentine microfluidic channels (n=1~6), (b) top and (c) bottom view of the device.

EXPERIMENTAL SET-UP

Materials

Poly(3,4-ethylened ioxythiophene):polystyrene sulfonate (PEDOT:PSS), dimethyl sulfoxide (DMSO) and Nafion solution

978-1-940470-03-0/HH2018/$25©2018TRF
DOI 10.31438/trf.hh2018.48

were purchased from Sigma Aldrich. Prussian Blue (PB) was obtained from Spectrum Chemical. Graphene was purchased from Angstron Materials, and dissolvable papers were obtained from Uline.

Device fabrication

Transient MFC devices were fabricated by using a wax printing technique. The hydrophobic wax patterns were designed using AutoCAD software and printed out onto the dissolvable paper using Xerox Phaser printer (ColorQube 8570). The printed paper was then placed in an oven set at 100°C for 50s, and the hydrophobic wax melted into the paper substrate, defining device boundaries and fluidic channels, forming PEMs, and mechanically strengthening the paper to delay rapid dissolving of the paper in water (Figure 2a).

Anodes on paper

To prepare pencil-graphite anode electrodes, an HB grade pencil was purchased from American Tombow Inc [20]. The electrodes were prepared by simple drawing on the pre-defined anodic microfluidic channels (Figure 2b). The pencil trace generated the coverage of graphitic layer on top of the reservoir/fluidic channel. The average surface resistance of 310 Ω was obtained throughout the anodic channel.

Cathodes on paper

The Prussian-Blue (PB)-based cathode was constructed by providing a conductive pencil trace layer on top of the wax-based proton exchange membrane (PEM). The drawn graphite provided the high conductivity of the cathode. The cathode material for each 1cm^2 area was prepared with 8mg of PB and 3mg of graphene in a conductive binder solution followed by ultrasonication for 10min. The conductive binder solution was prepared with (i) 30µL of PEDOT:PSS solution, (ii) 5 µL of 5 wt% Nafion, (iii) 100 µL of isopropanol. The mixture was brush coated on the pre-defined pencil-traced cathodic side of the paper (Figure 2c).

Inoculum

Shewanella oneidensis MR-1 were grown from -80ºC glycerol stock cultures by inoculating 20mL of L-broth medium with gentle shaking in air for 24h at 35ºC. The L-broth media consisted of 10.0g tryptone, 5.0g yeast extract and 5.0g NaCl per liter. Both cultures were then centrifuged at 5,000rpm for 5min to remove the supernatant. The bacterial cells were re-suspended in a new medium and used as an anolyte for the device.

Freeze-drying (lyophilization) procedure

After the MFC devices were inoculated with bacterial cells, they were placed in a low freeze drier (FreeZone Plus 2.5 Liter Cascade Benchtop Freeze Dry System, Labconco, MO, USA), the drying operation was performed at a pressure of 0.06atm for 12h with freezing and sublimation processes. During the freezing, the chamber temperature dropped to −50°C and then progressively increased back to room temperature. The device was not affected by the lyophilization processes.

Measurement setup

We measured the potentials between the anodes and the cathodes with a data acquisition system (National instrument, USB-6212), and recorded the readings every 1 min via a customized LabView interface. An external resistor was connected between the anode and the cathode to close the circuit. The current through this resistor was calculated using Ohm's law.

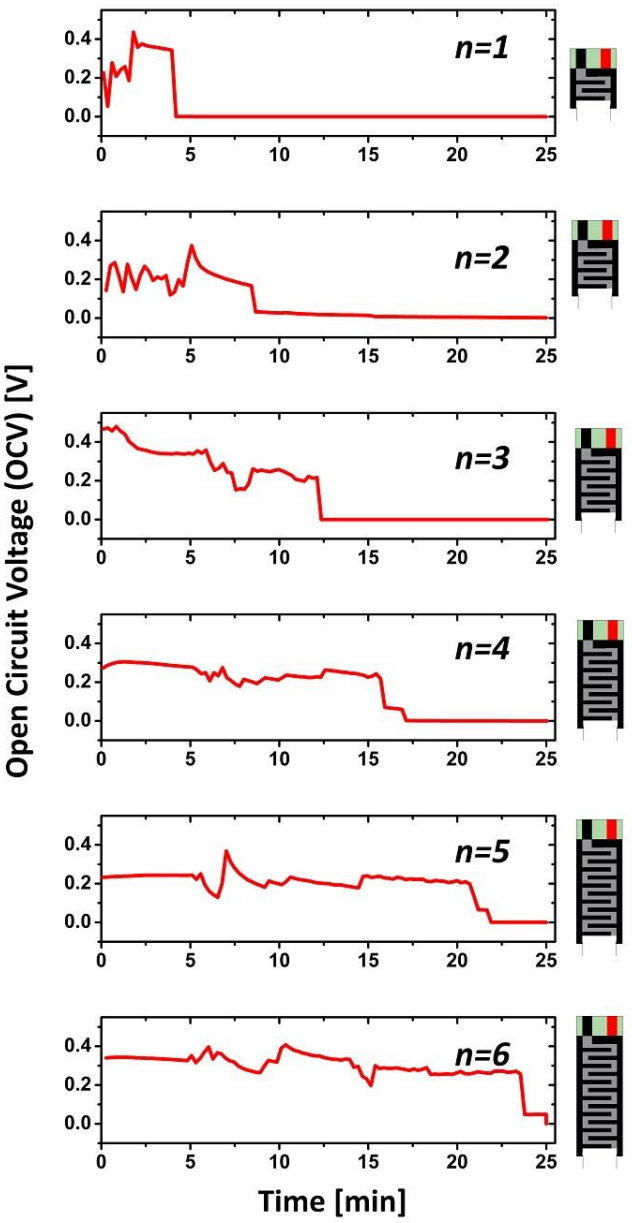

Figure 3: Operation period of the devices with different number of channels.

RESULT AND DISCUSSION

To effectively control and purposely prolong the device operation time, we defined the different lengths of microfluidic channels. The increase in the length of channels with the wax-printed boundaries as well as the pencil-drawn graphite channels prevented the biobattery from the instant dissolving of battery in the water. During operation, the devices were partially placed in a water container. The freeze-dried bacteria cells were activated through rehydration as the water flowed up the channel while the output voltage and current were monitored.

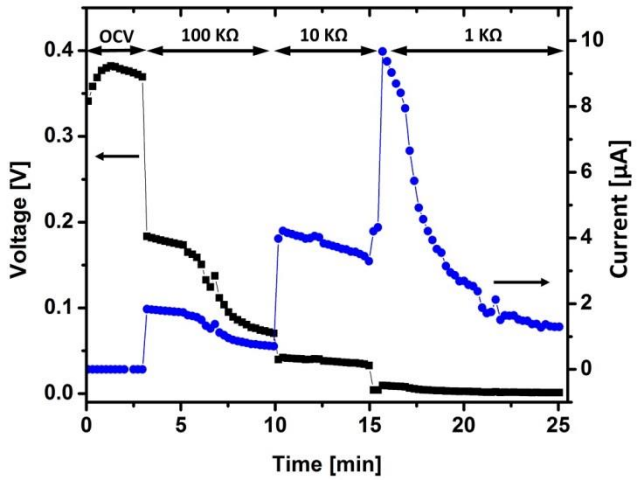

Figure 4: Voltage and current outputs of the transient biobattery (n=6)

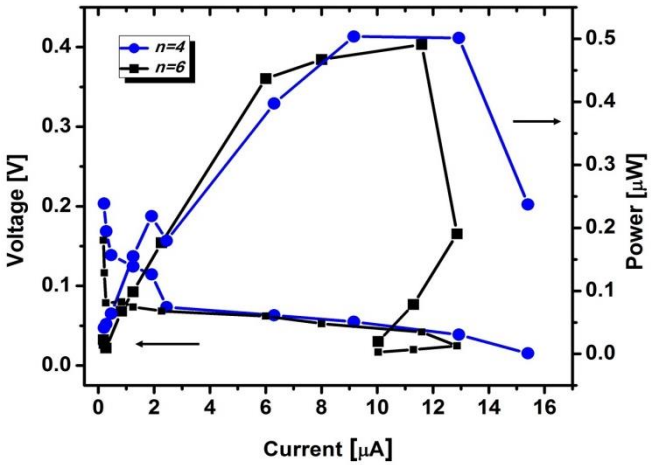

Figure 5: Polarization curve/output power for the transient biobatteries (n=4 & n=6) as a function of current.

Microfluidic channel numbers (n)

In this work, we tested six different designs with the different number of serpentine microfluidic channel curves (n=1~6). The open circuit voltage (OCV) for each device was continuously measured during the dissolving process. As shown in Figure 3, the increase in the channel length resulted in the prolonged device operation. The n=1 device operated only for 4min. while the voltage generation of the n=6 one was sustained for more than 22min. We further tested the n=6 device with three different resistors (100KΩ, 10 KΩ and 1 KΩ) to measure the current outputs (Figure 4). For 25min, the device successfully operated, generating current outputs in response to the resistors. Figure 5 shows the polarization curve and the power output of the devices with n=4 and n=6 channels. A maximum power of 0.5μW and current 15.6μA were produced from the biobattery (n=6).

Dissolvability

The dissolvability of the biobattery and its components (i.e. the substrate, printed wax boundaries and membrane, pencil-drawn electrodes and Prussian-Blue cathode) were evaluated in water. The substrate itself could completely dissolve within the less than 2 min while the wax-printed boundaries and the pencil-drawn traces required more time for the dissolution. Figure 6 demonstrates the dissolving courses of the entire battery with n=6 in water at the room temperature. For the complete dissolution of the device, it took about 60 min.

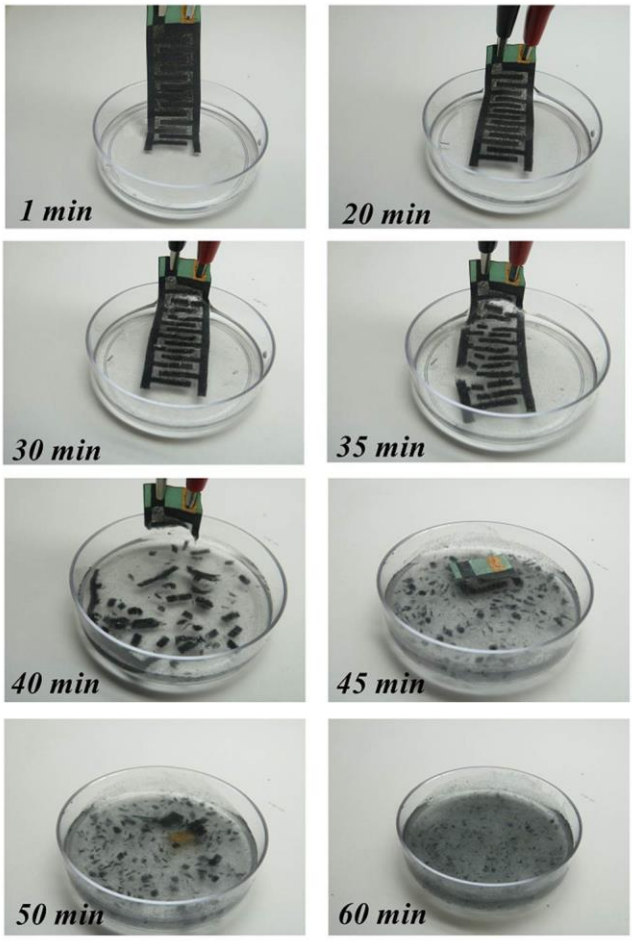

Figure 6: Transient test of the device (n=6) in water. After 60 min, the device completely dissolved in water.

CONCLUSION

This work provided a novel technique to develop a transient biobattery by using a microfluidic control for programmable dissolution. The transient paper-based MFC used the dissolvable paper as a substrate, the pencil-drawn graphite anode and the Prussian-blue (PB) cathode. The different lengths of the microfluidic channels controlled the operation time of the battery. The freeze-dried bacteria cells pre-loaded on paper can be very useful for on-demand battery operation in resource-limited environments. This work will provide an innovative strategy to develop a transient battery with an easy-to-use and inexpensive alternative fabrication method.

ACKNOWLEDGMENT

This work is supported by NSF (ECCS #1503462 & ECCS #1703394) and the SUNY Binghamton Research Foundation (SE-TAE).

REFERENCES

[1] K.K. Fu, Z. Wang, J. Dai, M. Carter, L. Hu, "Transient Electronics: Materials and Devices," Chem. Mater., 28, 3527, 2016.

[2] H. Cheng, V. Vepachedu, "Recent development of transient electronics," Theoretical and Applied Mechanics Letters, 6, 21, 2016.

[3] L. Yin, H. Cheng, S. Mao, R. Haasch, Y. Liu, X. Xie, S. Hwang, H. Jain, S. Kang, Y. Su, R. Li, Y. Huang, J.A. Rogers, "Dissolvable metals for transient electronics," Advanced Functional Materials, 24, 645, 2014.

[4] R. Li, H. Cheng, Y. Su, S. Hwang, L. Yin, H. Tao, M.A. Brenckle, D. Kim, F.G. Omenetto, J.A. Rogers," An analytical model of reactive diffusion for transient electronics," Advanced Functional Materials, 23, 3106, 2013.

[5] Y. Chen, R. Jameshidi, K. White, S. Cinar, E. Gallegos, N. Hashemi, R. Montazami, "Physical-chemical hybrid transiency: a fully transient Li-ion battery based on insoluble active materials," Journal of Polymer Science, Part B: Polymer Physics, 54, 2021, 2016.

[6] Y. Kim, S. Chun, J. Whitacre, C.J. Bettinger, "Self-deployable current sources fabricated from edible materials," Journal of Materials Chemistry B, 1, 3781, 2013.

[7] V. Edupuganti, R. Solanki, "Fabrication, characterization, and modeling of a biodegradable battery for transient electronics," Journal of Power Sources, 336, 447, 2016.

[8] K. Fu, et al., "All-component transient lithium-ion batteries," Advanced Energy Materials, 6, 1502496, 2016.

[9] Q. Zheng, Y. Zou, Y. Zhang, Z. Liu, B. Shi, X. Wang, Y. Jin, H. Ouyang, Z. Li, Z.L. Wang, "Biodegradable triboelectric nanogenerator as a life-time designed implantable power source," Science Advances, 2, e1501478, 2016.

[10] J. P. Esquivel, P. Alday, O. A. Ibrahim, B. Fernández, E. Kjeang, N. Sabaté, "A metal-free and biotically degradable battery for portable single-use applications," Advanced Energy Materials, 7, 1700275, 2017.

[11] M. Irimia-Vladu, "Green electronics: biodegradable and biocompatible materials and devices for sustainable future," 43, 588, 2014.

[12] G.A. Salvatore, J. Sulzle, F.D. Valle, G. Cantarella, F. Robotti, P. Jokic, S. Knobelspies, A. Daus, L. Buthe, L. Petti, N. Kirchgessner, R. Hopf, M. Magno, G. Troster, "Biodegradable and highly deformable temperature sensors for the internet of things,"Advanced Functional Materials, 27, 1702390, 2017.

[13] M. Irimia-Vladu, E.D. Glowacki, G. Voss, S. Bauer, N.S. Sariciftci, "Green and biodegradable electronics," Materials Today, 15, 340, 2012.

[14] X. Gao, L. Huang, B. Wang, D. Xu, J. Zhong, Z. Hu, L. Zhang, J. Zhou, "Natural materials assembled, biodegradable, and transparent paper-based electret nanogenerator," ACS Applied Materials & Interfaces, 8, 35587, 2016.

[15] M. Mohammadifar, J. Zhang, I. Yazgan, O. Sadik, S. Choi, "Power-on-paper: Origami-inspired Fabrication of 3-D Microbial Fuel Cells," Renewable Energy, 118, 695, 2018.

[16] Y. Gao, S. Choi, "Stepping Towards Self-powered Papertronics: Integrating Biobatteries into a Single Sheet of Paper," Advanced Materials Technologies, 2, 1600194, 2017.

[17] S.A.M. Shaegh, N. Nguyen, S.M.M. Ehteshami, and S.H. Chan, "A membraneless hydrogen peroxide fuel cell using Prussian Blue as cathode material," Energy & Environmental Science, 5, 8225, 2012.

[18] M. Mohammadifar, S. Choi, "A Papertronic, On-Demand and Disposable Biobattery: Saliva-Activated Electricity Generation from Lyophilized Exoelectrogens Pre-inoculated on Paper," Advanced Materials Technologies, 2, 1700127, 2017.

[19] M. Mohammadifar, S. Choi, "On-demand micro-power generation from an origami-inspired paper biobattery stack," Batteries, 4, 14, 2018.

[20] C. Lin, Z. Zhao, J. Kim, J. Huang, "Pencil drawn strain gauges and chemiresistors on paper," Scientific Reports, 4, 3812, 2014.

CONTACT

*Seokheun Choi, *Assistant Professor*, SUNY-Binghamton,
Email: sechoi@binghamton.edu
Website: http://ws.binghamton.edu/choi

VOLTAGE GATED NANOFLUIDIC CHIP FOR PROTEIN CAPTURE, AMPLIFICATION, AND RELEASE

Kaushik K. Rangharajan[1] and Shaurya Prakash[1]*
[1]Department of Mechanical and Aerospace Engineering, The Ohio State University, Columbus, Ohio, USA

ABSTRACT

We report on a nanofluidic 'field-effect' gated chip, with addressable gate electrodes to capture, amplify, and release a model protein, Bovine Serum Albumin (BSA). Fluidically isolated gates, embedded strategically along the length of the nanofluidic chip, when addressed facilitates generation of localized and spatially varying electric-field, driving protein amplification, *via* electro-migration, as opposed to diffusion driven amplification observed in existing state-of-art systems. A complementing numerical model was solved to capture the changes to the local space-charge density due to gating inside the nanofluidic chip, driving pre-concentration of BSA at various segments.

INTRODUCTION

Protein trafficking through nanometer scaled channels are ubiquitous in several biological processes. While microfluidic platforms have shown potential for protein pre-concentration *via* high-voltage concentration polarization methods [1], nanofluidic systems provide exclusive size and charge based selectivity to sense, trap, and amplify proteins for potential applications in proteomics, bioanalysis, clinical diagnosis, gene sequencing, and drug development. Nanofluidic platform can therefore serve as a central platform to trap proteins in their native environment. Voltage gated nanofluidic devices, geometrically analogous to solid state field effect transistors, are an attractive platform to re-configurably modulate the concentration of charged proteins *in vitro* [2].

Previously efforts to demonstrate field-effect control of proteins were achieved inside a nanofluidic channel consisting of an embedded gate electrode patterned over the entirety of the nanochannel [2, 3]. The net protein pre-concentration is therefore governed by the magnitude of electrostatic interaction between the charge protein and the entire charged nanofluidic wall. By modulating the polarity of the gate voltage, effective channel surface charge was altered, regulating protein transport inside the nanochannel in a diffusion limited pathway [2].

The purpose of this paper is to reduce the time-scale for protein pre-concentration by driving the amplification process *via* electro-migration as opposed to diffusion. To do so, individually addressable gate electrodes were patterned using lithography techniques on top of an SiO_2 dielectric, that fluidically isolated the metal gate from the nanochannel. The gate electrodes were located strategically along the length of the nanofluidic chip. When addressed with varying magnitudes of gate potential, localized and spatially varying electric fields (e-field) were generated inside the nanofluidic chip, driving protein amplification *via* electromigration.

THEORY

Ion concentration inside nanofluidic channels can be modified by altering the wall surface charge [2-9]. The potential drawback of modifying the surface chemistry of the wall *via* passive surface modification techniques is an irreversible, permanently altered wall surface charge state [4]. The wall surface charge can also be transiently controlled *via* application of transverse potential gradient through a metal gate which is typically separated from the nanofluidic channel walls *via* a thin strip (50 – 100 nm) of dielectric [5, 6]. With ψ and ϕ defined as potential distribution function inside the nanochannel and dielectric respectively, and ψ_0 defined as the surface potential of the wall, the boundary condition at the surface of the dielectric-electrolyte interface in the presence of a gate (along y, Fig. 1) is given by Equations 1 - 3 [7],

$$-\varepsilon_0\varepsilon_d\frac{d\phi}{dy}+\varepsilon_0\varepsilon_f\frac{d\psi}{dy}=-\sigma_s \quad (1)$$

$$\phi=\left(\psi_0-V_g\right)\frac{y}{\delta}+\psi_0 \quad (2)$$

$$\frac{d^2\psi}{dy^2}=-\frac{\sum_i Fc_iz_i}{\varepsilon_0\varepsilon_f} \quad (3)$$

Where δ, F, ε_0, ε_d, and ε_f are the dielectric thickness, Faraday constant, permittivity of free space, relative permittivity of the dielectric, and electrolyte respectively. Application of positive gate potential to a negatively charged surface (Fig. 1) increases the co-ion (negatively charged) concentration inside the nanochannel to satisfy Equation 1. Equation 2 indicates that the potential drops linearly across the dielectric from a magnitude of V_g at the gate to a constant surface potential of ψ_0 at the nanochannel wall. To produce a significant alteration to the potential distribution and ion concentration inside the nanochannel, $d\phi/dy$ must be non-trivial. This can be achieved by either increasing the applied gate potential or decreasing the dielectric thickness.

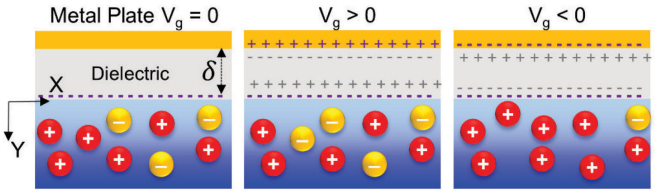

Figure 1: Schematic showing modulation of ion concentration inside nanochannel due to field-effect gating. Application of positive gate bias ($V_g > 0$) increases co-ion concentration and negative bias ($V_g < 0$) increases counter-ion concentration when compared to zero bias.

METHODS

Numerical Model

A coupled numerical model was solved in COMSOL Multiphysics (v5.2a) to calculate the electric-field and ion distribution inside the model gated nanofluidic device (Fig. 2). Poisson equation (electrostatics) was coupled with Nernst-Planck equation (Transport of diluted species) and Navier-Stokes equation (fluid flow) [8]. The surface charge density of the nanochannel and reservoir walls were assigned -5 mC/m^2 [9]. Specific gates were defined on top of the 40 nm thick dielectric. No-slip boundary conditions were defined for all walls. Reservoir protein concentration was fixed to 0.1 mM for the simulations, matching experimental condition. A custom meshing scheme was defined and refined, until mesh insensitive solutions were obtained.

Experimental Methodology

Our proof-of-concept nanofluidic field-effect chip dramatically advances our past work on fundamental investigation of ion transport with a "single gate" from Hilton Head 2014 and 2016 [10,

978-1-940470-03-0/HH2018/$25©2018TRF
DOI 10.31438/trf.hh2018.49

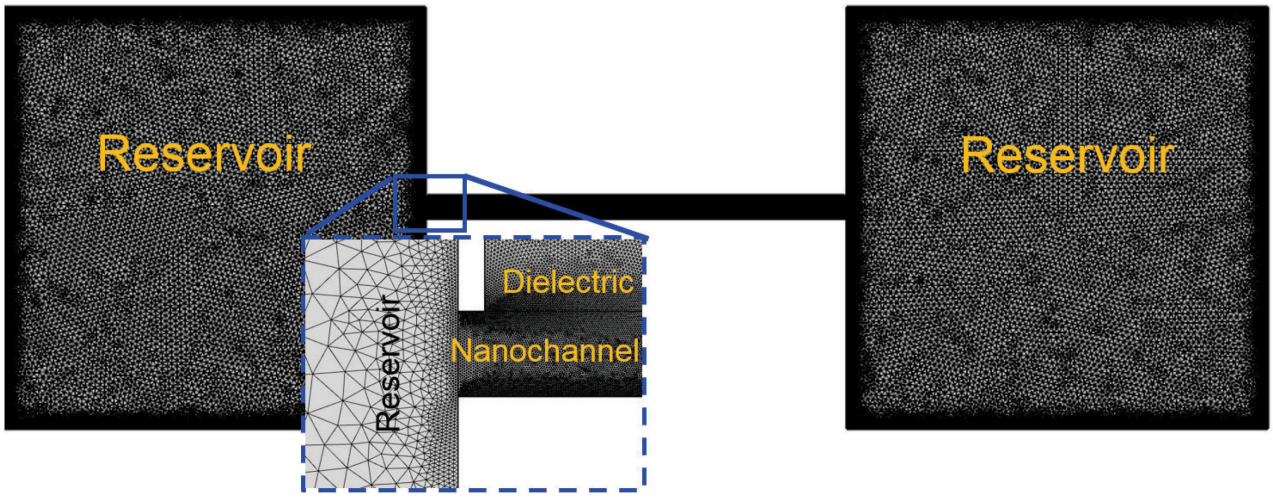

Nernst-Planck Equation

$$\nabla \cdot \mathbf{J}_i = 0$$

$$\mathbf{J}_i = -D_i \nabla c_i - \xi_i z_i F\, c_i \nabla \psi + c_i \mathbf{u}$$

Poisson Equation

$$\varepsilon_0\, \varepsilon_f\, \nabla^2 \psi = -\rho_s$$

$$\rho_s = F \sum z_i\, c_i$$

Navier-Stokes Equation

$$\nabla \cdot \mathbf{u} = 0$$

$$-\nabla p + \mu \nabla^2 \mathbf{u} - \rho_s \nabla \psi = 0$$

Figure 2: Geometry of the Reservoir-Nanochannel-Dielectric 'field-effect' gated system. Coupled Nernst-Planck, Poisson, and Navier-Stokes equation were solved in COMSOL Multiphysics (v5.2a) to estimate the spatially varying electric-field induced inside the nanochannel due to gating. Here, $\mathbf{J_i}$ is the specied flux constituting the diffusion, electro-migration and convection components. For a given species i, D_i is the diffusion coefficient, ξ_i is the ionic mobility, z_i is the ion valence, $\mathbf{u}$ is the convective velocity. In addition, ρ_s is the volumetric space charge density, μ is the electrolyte viscosity and p, the pressure distribution inside the reservoir-nanochannel system.

11]. The device uses two microfluidic channels (8 µm (H) x 50 µm (W) x 3 cm (L)) as fluidic reservoirs for a bank of three nanochannels 16 nm deep (30 µm (W) x 2.5 mm (L)) [10, 11]. An overview of top cover fabrication with embedded individually addressable electrodes is given in Fig. 3. Each electrode is made of Chromium and is 10 nm high and 30 µm wide.

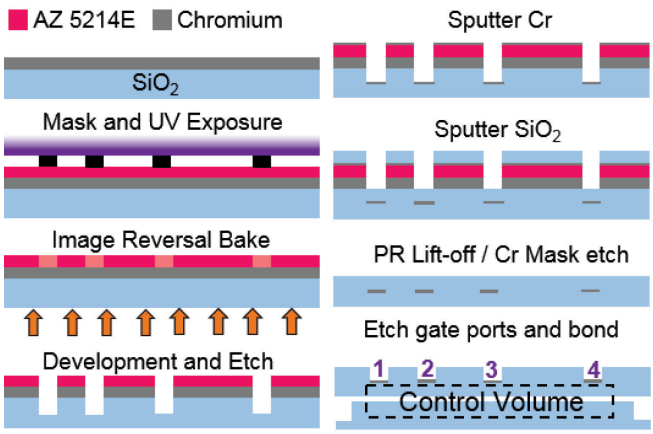

Figure 3: Fabrication sequence for embedding multiple gate electrodes on glass slide.

Several considerations were taken into account during the top cover fabrication. Chromium has a higher thermal conductivity compared to soda lime glass which helps to achieve adequate baking of photoresist AZ5214 during image reversal bake. Absence of Cr metal mask resulted in photoresist peeling during development. Second, a UV exposure of 3.5 secs and short development (35 sec) was chosen to have a straight side-wall profile of AZ5214. Having a negative side-wall profile (typical during a negative PR development) causes insufficient dielectric coverage during dielectric sputtering, shorting the channel when a potential is applied. Third, Cr and SiO_2 were sputtered at the same batch, to ensure proper insulation of Cr. Adequate SiO_2 coverage over the Cr electrode was verified by immersing the top cover in a Chromium etchant solution, followed by piranha cleaning for 15 minutes. Fourth, to remove inconsistencies in the deposition rate while sputtering Cr and SiO_2, deposition rate was calibrated before each batch. The fabricated top cover electrodes and the channel slide were then bonded using the Calcium bonding recipe [12]. The final schematic of the bonded nanofluidic channel, with the multi-electrode top cover is shown in Figure 4. The microfluidic and nanofluidic channels were initially filled with 0.1 mM Bovine Serum Albumin (66.5 kDa, stokes diameter = 6.96 nm) conjugated with Tetramethylrhodamine (TRITC, $\lambda_{ex}/\lambda_{em}$ = *541/572 nm)* in Phosphate-buffered saline (pH 7.4). Potential difference of 2 V (V_{gate}) was applied between gates 1–2 and gates 3–4 simultaneously (Fig. 4).

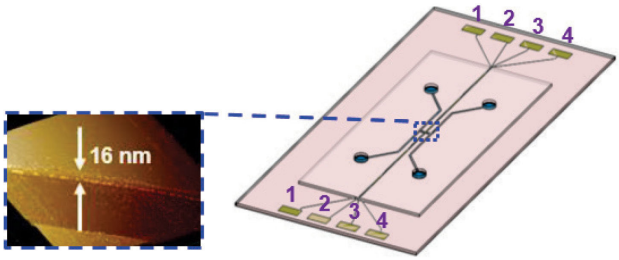

Figure 4: Schematic of bonded nanofluidic chip with inset showing AFM image of 16 nm dep nanochannel.

RESULTS

Universal gate Vs Local gate

Coupled multi-physics models using COMSOL Multiphysics showed that compared to a universal gate (Fig. 5a), application of gate potential in the present system (Fig. 5b) results in spatially varying non-uniform potential distribution in the gated and ungated region (Fig. 5c, d). In the case of a universal gate, no changes to the potential was observed inside the nanofluidic channel (Fig. 5 a, c). Application of gate potential in the present system causes a linear drop in potential across the 40 nm thick dielectric (Fig. 5d). To satisfy Equation 1, the local space charge density inside the nanofluidic channels is altered. Gating therefore, introduces a non-linear gradient in potential distribution inducing a non-uniform electric field inside the nanochannel (Fig. 5c, d).

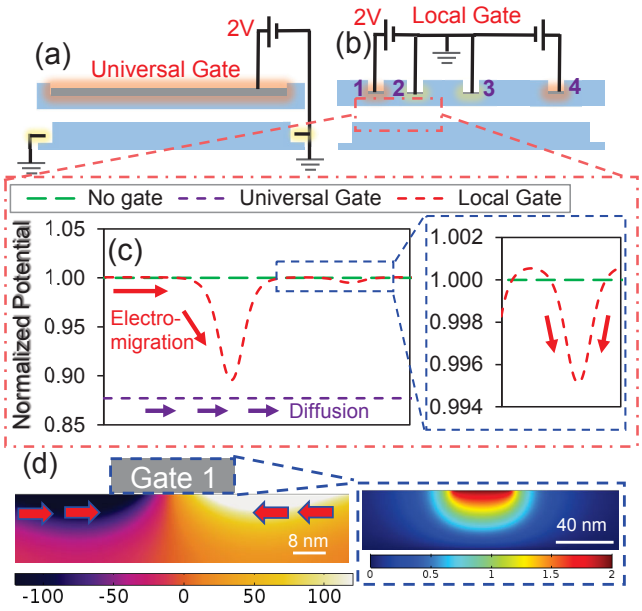

Figure 5: Design, potential distribution, and working principle of a (a) 'universally' gated nanofluidic channel and (b) individually addressable multi-electrode nanofluidic chip (present work). (c) Representative plots showing local potential changes inside the nanofluidic channels in the present device between gates 1 and 2 compared to uniform potential (similar to flow by diffusion) in the 'universally' gated nanochannel. Voltage inside the nanochannel under no gating is normalized to a value of 1. Application of gate potential modifies volumetric space charge density inside the nanochannel to satisfy electro-neutrality, resulting in modified potential distribution compared to ungated scenario [3, 5]. (d) A non-linear (and non-uniform) electric field inside the nanochannel drives the charged proteins via electromigration for faster amplification. Electric fields of opposing polarity at the either ends of gate 1, facilitate amplification of BSA transport (Red arrows) inside the nanochannel. Inset shows potential distribution (in V) inside the 40 nm deep SiO_2 dielectric layer.

BSA Capture, Amplification, and Release

The non-uniform electric field was used to tune the pre-concentration of BSA at various segments of the nanochannel in a time-dependent manner (Fig. 6) for amplification (pre-concentration) and subsequent release of BSA. The e-field facilitates BSA capture and amplification *via* electromigration up to ~6x (Fig. 6b, e) the initial concentration (Fig. 6a, e) in gates 2, 3 within 20 min. The depleted BSA at gates 1, 4 are subsequently replenished by a negative e-field on the far-side of the gates (Fig. 5c) that amplifies BSA concentration by ~6x, 9x at gates 1, 4 respectively. Upon removing V_{gate}, ~50% of trapped BSA is "released" driven by *diffusion* from all the gates within next 90 min (Fig. 6d, f). In the absence of applied gate potential, amplification or release was not observed during 120 min of imaging.

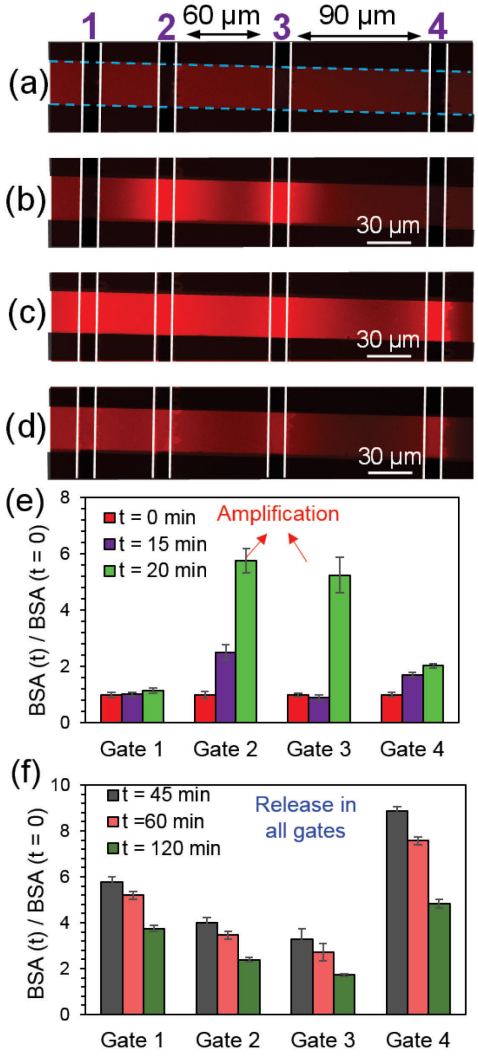

Figure 6: Fluorescence of BSA-TRITC inside the 16 nm deep channel was imaged when gates 1, 4 was set to a potential of +2 V while gates 2, 3 were grounded (exposure time ~ 30 s). Fluorescence images of BSA amplification at (a) t = 0 min, (b) t = 20 min and (c) t = 30 min. (d) Representative BSA "Release" phase fluorescence image at t = 120 min indicating reduction in BSA-TRITC concentration. Blue dashed line indicate nanochannel boundary in Fig. 6a and white-solid line indicates gated regions in Fig. 6a – d. (e) At t = 15 min, BSA concentration at gate 2 is ~2.5x higher than gate 3, as the shorter distance (30 µm) between gates 1 and 2, compared to 90 µm between gates 3 and 4 promote a higher local field to trap BSA at gate 2. At t = 20 min, BSA concentration saturates to 5.5x initial concentration at gates 2 and 3. (f) Switching off gate voltage at t = 30 min leads to gradual diffusion driven protein release over the next 90 min.

In summary, a novel system was demonstrated to trap and enrich protein concentrations using electrostatic field effect gating inside a nanofluidic chip with spatially inhomogeneous electric fields providing a new avenue for protein analysis.

ACKNOWLEDGMENTS

This work was supported by The Office of Energy and Environment at The Ohio State University, US Army Research Office (ARO) through grant W911NF09C0079 and the National Science Foundation (NSF) through grant CBET-1335946. The authors acknowledge computational support and research license from the Ohio Supercomputer Center (OSC), the OSU Nanotech West cleanroom staff for assistance in fabrication.

REFERENCES

[1] J. H. Lee, S. Chung, S. J. Kim, and J. Han, "Poly(dimethylsiloxane)-Based Protein Preconcentration Using a Nanogap Generated by Junction Gap Breakdown", Analytical Chemistry, 79, 1868 (2007).

[2] R. Karnik, K. Castelino, and A. Majumdar, "Field-effect Control of Protein Transport in a Nanofluidic Transistor Circuit", Applied Physics Letters, 88, 123114 (2006).

[3] T. James, *et al.*, "Voltage-Gated Ion Transport through Semiconducting Conical Nanopores Formed by Metal Nanoparticle-Assisted Plasma Etching", Nano Letters, 12, 3437 (2012).

[4] E. C. Yusko, *et al.*, "Controlling Protein Translocation through Nanopores with Bio-inspired Fluid Walls", Nature Nanotechnology, 6, 253 (2011).

[5] M. Fuest, C. Boone, K.K. Rangharajan, A.T. Conlisk, and S. Prakash, "A three-state nanofluidic field effect switch", Nano Letters, 15, 2365 (2015).

[6] R, Karnik, R. Fan, M. Yue, D. Li, P. Yang, and A. Majumdar, "Electrostatic control of ions and molecules in nanofluidic transistors" Nano Letters, 5, 943 (2005).

[7] X. Jin, and N. Aluru, "Gated transport in nanofluidic devices", Microfluidics and Nanofluidics, 11, 297 (2011).

[8] W. Guan, R. Fan, and M. Reed, "Field-effect reconfigurable nanofluidic ionic diodes", Nature Communications, 2, 506 (2011).

[9] M. Fuest, K.K. Rangharajan, C. Boone, A.T. Conlisk, and S. Prakash, "Cation dependent surface charge regulation in gated nanofluidic devices", Analytical Chemistry, 89, 1593 (2016).

[10] M. Pinti, H. A. Zambrano, K. K. Rangharajan, A.T. Conlisk, and S. Prakash, "Active Surface Potential Control for Artificial Ion Pumping", Technical Digest Solid-State Sensors, Actuators, and Microsystems Workshop, Hilton Head Island, South Carolina, June 8 – 12, (2014).

[11] C. Boone, V. Lochab, M. Fuest, and S. Prakash, "Time-dependent Gating in Nanofluidic Channels for Active Electric Double Layer Modulation for Ion Transport Control", Technical Digest Solid-State Sensors, Actuators, and Microsystems Workshop, Hilton Head Island, South Carolina, June 5 – 9, (2016).

[12] P. B. Allen, *et al.*, "Calcium-Assisted Glass-to-Glass Bonding for Fabrication of Glass Microfluidic Devices," Analytical Chemistry, 80, 7153 (2008).

CONTACT

*S. Prakash; Prakash.31@osu.edu

A FLEXIBLE, MICROFABRICATED IMPEDIMETRIC FLUID TEMPERATURE SENSOR

Alex Baldwin, Trevor Hudson, Eugene Yoon, and Ellis Meng
University of Southern California, Los Angeles, USA

ABSTRACT

A novel impedimetric temperature sensor which utilizes the electrochemical impedance between two electrodes exposed to an aqueous solution to transduce temperature is presented. The solution resistance between electrodes is highly temperature dependent since ionic mobility increases with temperature. High-frequency electrochemical impedance can be used to accurately measure solution resistance, and therefore transduce fluid temperature. A temperature sensor composed of two platinum electrodes on a thin film Parylene C substrate exposed to fluid was designed, fabricated, and tested. Fluid temperature was transduced with high sensitivity (-59.33 Ω/°C) by measuring the impedance magnitude between electrodes at an appropriate frequency where phase was minimized. Compared to conventional platinum resistance temperature detectors (RTDs), our sensor achieved over 4× higher sensitivity and resolution (±0.02°C). Furthermore, the sensor is specifically designed for use in liquids, and features flexible, biocompatible construction for biomedical or microfluidic applications.

INTRODUCTION

State-of-the-art methods for measuring fluid temperature include thermocouples and resistance temperature detectors (RTDs) [1, 2]. Thermocouples utilize the Seebeck effect, in which a temperature-dependent voltage occurs at the junction of two dissimilar conducting elements [3]. They are generally made using nickel alloys, though occasionally platinum and rhodium are used to enhance stability, and have temperature sensitivities up to 60 μV/°C. However, thermocouples have low accuracy and precision, and generally cannot distinguish temperature changes less than 2°C. Semiconductor junctions can also be used as thermocouples, with sensitivities up to 110 mV/°C and resolutions as good as ±0.8°C [1]. Thermocouples require packaging to protect conducting elements from water intrusion and to act as a barrier shielding the body from non-biocompatible sensor material.

RTDs are conductive or semiconductive elements whose resistance changes with temperature. The most common commercial RTD (PT100) is made of bulk platinum wire and defined by a resistance of 100 Ω at 0°C and a temperature coefficient of 0.385%/°C [2]. Platinum RTDs can also be microfabricated on thin-film substrates, though the temperature sensitivity of thin-film platinum is lower than bulk material. Most metal RTDs use platinum due to its high linearity, but other metals such copper and nickel can be used as well. Laboratory-grade RTDs operate between -200°C and 1000°C with precision approaching ±0.001°C, although commercial RTDs are closer to ±0.03°C. The main drawbacks of platinum RTDs are low sensitivity and the need for encapsulation when used in aqueous solutions.

Semiconductor materials, such as silicon, germanium, and metal oxides, exhibit lower electrical resistance when operating at higher temperatures [1, 4]. These semiconductor RTDs, also known as thermistors, possess temperature coefficients exceeding -2%/°C and have comparable precision to metal RTDs. However, semiconductors corrode and disintegrate under chronic soaking in physiological fluid [5, 6].

An alternate approach to measure temperature changes in physiological fluid via measurement of the fluid's resistivity is investigated. The resistivity of an aqueous solution is temperature dependent due to increased ionic mobility at higher temperatures. This sensitivity exceeds the temperature coefficient of semiconductor materials (Table 1), with a reported temperature coefficient of -1.98%/°C for human cerebrospinal fluid [7]. Measuring solution resistivity using high-frequency electrochemical impedance enables highly sensitive fluid temperature transduction. Impedance spectroscopy was used to transduce the internal temperature of lithium ion batteries [8, 9]. However, until now, no one has demonstrated the use of impedance measurement to transduce temperature in bulk solution.

Table 1. Temperature coefficient of resistance (TCR) of metals and semiconductors which have been used in resistive temperature sensors, as well as several ionic solutions including human cerebrospinal fluid (CSF).

Material	Temperature Sensitivity (%/°C)
Platinum	0.392
Copper	0.430
Polysilicon	-2.5 to 0.1
Germanium	-2.0
1.32M (5%) NaOH	-2.01
7.9M (30%) NaOH	-4.50
2.95M (20%) KCl	-1.68
Human CSF	-1.98

THEORY

The impedance between two electrodes exposed to solution can be approximated by a Randles circuit [10] (Figure 1). This circuit consists of a charge transfer resistance R_{ct} and a double layer capacitance C_{dl} at each electrode-electrolyte interface, as well as the solution resistance R_s between the electrodes.

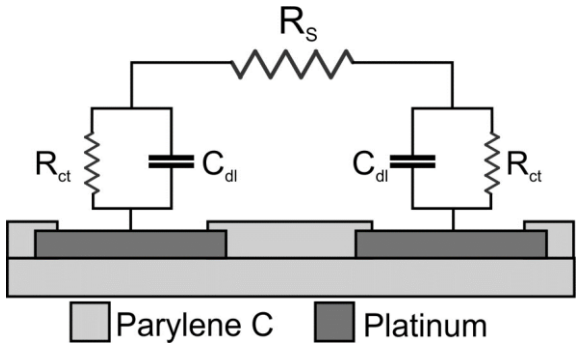

Figure 1: The electrochemical impedance between two electrodes consists of the solution resistance R_S, as well as a charge transfer resistance R_{ct} and double layer capacitance C_{dl} at each electrode interface. At high frequencies, the electrode-electrolyte interface is bypassed and impedance can be approximated as R_S.

978-1-940470-03-0/HH2018/$25©2018TRF
DOI 10.31438/trf.hh2018.50

R_{ct} describes the relationship between an electrode's overpotential v_0 and the resulting current due to faradaic reactions at the electrode surface. Assuming surface and bulk reactant concentrations are equal, the relationship between v_0 and the net current across the electrode-electrolyte interface i_{net} is given by the Butler-Volmer equation:

$$i_{net} = i_o\left\{e^{-\alpha_c nf v_0} - e^{(1-\alpha_c)nf v_0}\right\} \quad (1)$$

where α_c is a transfer coefficient which can range from zero to unity, n is number of electrons transferred, i_0 is the exchange current density, and f is equal to F/RT, where F is Faraday's constant, R is the gas constant, and T is temperature in Kelvin. At low overpotentials, the linear approximation of an exponential can be applied to equation 1, resulting in the following expression for charge transfer resistance:

$$i_{net} = \frac{-i_o nF}{RT} v_0 \qquad R_{ct} = \frac{dv_0}{di_{net}} = \frac{RT}{nFi_o} \quad (2)$$

This result implies a direct correlation between R_{ct} and temperature. Previously, charge transfer resistance was used to transduce the internal temperature of lithium ion batteries [8, 9]. However, the byproducts of faradaic reactions can be toxic [11], and many microelectrodes are too small for accurate measurement of charge transfer resistance. Therefore, electrochemical impedance measurement depends on C_{dl} and R_{ct}.

A double layer of electrostatically bound ions builds up at an electrode-electrolyte interface, leading to the formation of a capacitance C_{dl} [12]. Helmholtz, Gouy-Chapman, Stern, Graham, and others modeled this phenomenon, but the precise relationships between C_{dl} and temperature remains under active investigation and has not been fully characterized [13, 14].

Solution resistance R_S follows from a solution's conductivity, which is highly sensitive to changes in temperature. Electrolyte conductivity results from the movement of dissolved ions in response to an applied electric field. Bulk conductivity is proportional to ionic concentration, but a molar conductivity $\Lambda = G/c$ can be defined, where G is the bulk conductance and c is the molarity of ions [15]. As ionic concentration goes to zero, interionic forces disappear. This is known as a state of 'infinite dilution' and is useful for modeling conductivity in an aqueous solution. If an ion is modeled as a spherical charged particle within a continuous field of water and ionic mobility is defined as the limiting velocity per applied force, the conductivity at infinite dilution can be derived from Stoke's Law as

$$\lambda_0 = \frac{qF}{4\pi\eta r} \quad (3)$$

where λ_0 is conductivity at infinite dilution, q is ionic charge, η is water's viscosity, and r is ionic radius [16]. Only viscosity varies significantly with temperature; therefore, the temperature coefficient of a solution's conductivity at infinite dilution is inversely proportional to water's viscosity. Theoretical models for water's viscosity are generally inaccurate, but the following equation fits to empirical viscosity measurements within 1% accuracy for temperatures between 0 and 100°C and atmospheric pressure (0.1 MPa):

$$\frac{\eta}{10^{-6}\ Pa\ s} = \sum_{i=1}^{4} a_i \left(\frac{T}{300}\right)^{b_i} \quad (4)$$

i	a	b
1	280.68	-1.9
2	511.45	-7.7
3	61.131	-19.6
4	0.45903	-40.0

where η is in Pa·s and a and b are dimensionless, experimentally determined constants [17]. Using this formula, the infinite dilution temperature coefficient of conductivity can be shown to vary from -3%/°C to -1.5%/°C, with a value of -1.95%/°C at 37°C [18].

The Stoke's Law model of infinite dilution conductivity can be improved by including dielectric losses which occur due to the movement of charged particles. This results in the following:

$$\lambda_0 = \frac{qF}{4\pi\eta r + \frac{3}{8}q^2\frac{\varepsilon_0 - \varepsilon_\infty}{\varepsilon_0^2 r^3}\tau_0} \quad (5)$$

where ε_0 and ε_∞ are the high frequency and low frequency limits of the solution permittivity and τ_0 is the Debye relaxation time [19]. Both the Debye relaxation time and water's permittivity are temperature dependent [20, 21], but changes in viscosity still drive the temperature sensitivity of ionic solution conductivity.

Interionic forces must be considered at concentrations above infinite dilution. These can be modeled by the Debye-Huckel-Onsager equation, leading to the following relationship between concentration and conductivity:

$$\Lambda = \lambda^0 - \left(\frac{z^2 eF^2}{3\pi\eta\left(\frac{2}{\varepsilon RT}\right)^{\frac{3}{2}}} + \frac{xz^3 eF}{24\pi\varepsilon RT\sqrt{\frac{2}{\varepsilon RT}}}\lambda^0\right)\sqrt{c} \quad (6)$$

where Λ is conductivity, c is electrolyte concentration in moles per liter, z is the valency number of each ionic species, e is the electron charge, and x describes the symmetry of an ionic species [22]. The temperature sensitivity of a solution decreases as ionic concentration increases, but this decrease remains negligible in most cases. For example, cerebrospinal fluid (CSF) has an ionic concentration of 295 mM, but there is only a 0.19% difference in its temperature coefficient compared to a solution at infinite dilution.

The above equations are valid for ionic solution composed of strong electrolytes. Weak electrolytes are much more complex, but in general their temperature coefficients will be much higher at high concentrations and approach that of strong electrolytes at low concentrations. This is due to the temperature dependence of a weak electrolyte's disassociation constant, leading to large changes in ionic concentration when temperature is altered. Intuitively, one would assume that ultrapure water would be either non-conductive and thus insensitive to changes in temperature or would have a sensitivity similar to an ionic solution at infinite dilution. However, despite resistivities greater than 18 MΩ·cm at room temperature, pure water does indeed conduct electricity. This conduction is mediated by a small fraction of water molecules spontaneously disassociating into hydroxide and hydronium ions. Ultrapure water acts similar to a very weak acid or a very weak base and exhibits a much higher sensitivity to temperature changes than ionic solutions, with a temperature coefficient ranging from 7.4%/°C at 0°C to 2.3%/°C at 100°C [23]. However, the addition of ppb levels of impurities will cause baseline conductivity to change by a much higher factor than changes in temperature, and the solution will soon resemble a typical ionic solution.

The predictable and highly sensitive relationship between R_S and temperature suggests the possibility of temperature transduction. By measuring electrochemical impedance at high frequencies, the electrode-electrolyte interface is bypassed and impedance consists only of R_S. Therefore, fluid temperature can be transduced using high-frequency electrochemical impedance (Figure 2). Solution resistance measurement is at its most efficient when phase is minimized.

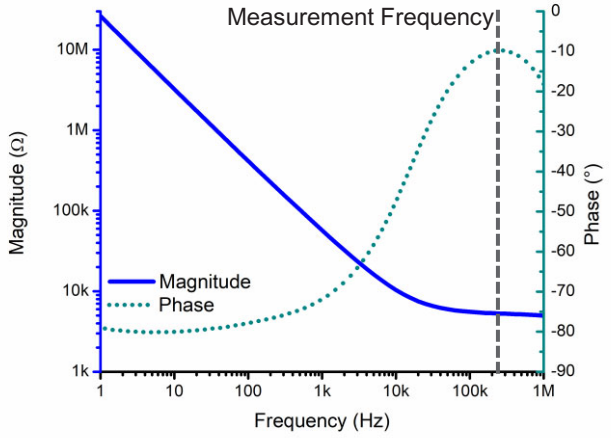

Figure 2. The magnitude and phase of temperature sensing electrodes, measured in 1×PBS. By measuring electrochemical impedance at the frequency where phase is minimized, solution resistance can be transduced.

EXPERIMENTAL DESIGN

We performed several experiments to demonstrate temperature transduction via high-frequency impedance. The temperature sensor used in these experiments consisted of a pair of platinum electrodes and a platinum resistor on a Parylene C substrate (Figure 3). The electrodes had exposed areas of 150 x 250 µm^2 with centers 750 µm apart. A platinum resistor, located 1 mm away from the electrodes on the same Parylene C substrate, was used as an RTD for benchmarking. The RTD consisted of a 25 µm wide serpentine trace and had a nominal DC resistance of ~450 Ω.

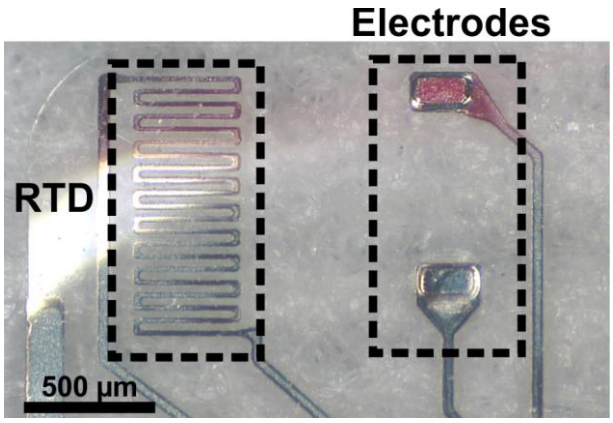

Figure 3: Impedimetric temperature sensing was tested using a pair of platinum electrodes on a Parylene C substrate. A microfabricated platinum RTD, fabricated on the same substrate, was used for benchmarking.

Sensors were primarily tested in phosphate-buffered saline (1× PBS), a common physiological fluid analog. 1× PBS is isotonic with cerebrospinal fluid and has a resistivity of 50 Ω·cm.

For electrochemical impedance spectroscopy (EIS) testing, sensors were sealed in glass vials filled with 1× PBS and placed in a water bath, which was heated to temperatures between 30 and 50°C. A Gamry Reference 600 potentiostat was used for EIS measurement (1 Hz – 1 MHz, 10mV$_{PP}$). For single-frequency impedance tests, solution was heated from room temperature (~20°C) to 50°C using a hot plate while a thermocouple/multimeter (Newport TrueRMS Supermeter, ±2°C accuracy) was used to monitor fluid temperature. Data was collected from impedance electrodes using an Agilent E4980A precision LCR meter at 0.1 V$_{PP}$ and from the RTD using a Keithley SourceMeter with 10 µA bias current. Impedance and resistance data was simultaneously collected and analyzed using a custom LabVIEW program.

RESULTS

EIS from 1 Hz to 1 MHz was measured from 30 to 50°C at 5°C temperature intervals (Figure 4). The results demonstrated a clear temperature dependency of impedance at frequencies from 1 to 100 kHz. The temperature coefficient was approximately -2%/°C, which matches reported temperature coefficient measurements in cerebrospinal fluid [7]. The discontinuities in the EIS graphs were likely a result of inadequate shielding by the chicken-wire Faraday cage. Although 10 kHz appeared to be the optimal measurement frequency due to its position in the center of the resistive range, single-frequency benchtop testing showed that measuring impedance at 100 kHz provided more consistent results.

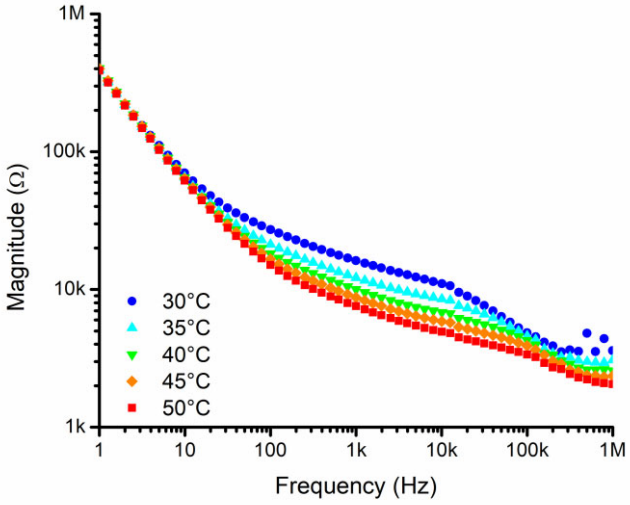

Figure 4: Electrochemical impedance spectroscopy of a pair of platinum electrodes at temperatures between 30°C and 50°C. As temperature increases, the impedance magnitude within the resistive range decreases.

The platinum RTD was calibrated by comparing its resistance to thermocouple measurements in 1× PBS, revealing a temperature coefficient of resistance of 1.21 Ω/°C. Temperature was then cycled between 20 and 50°C while simultaneously measuring impedance magnitude at 100 kHz and temperature using the RTD. The impedance magnitude correlated extremely well with temperature, with a temperature coefficient of -59.33 Ω/°C (Figure 5). Minimal hysteresis was observed over multiple cycles. Based on noise, 3σ resolution of impedance-based temperature sensing was measured to be ±0.02°C, compared to ±0.08°C for the platinum RTD.

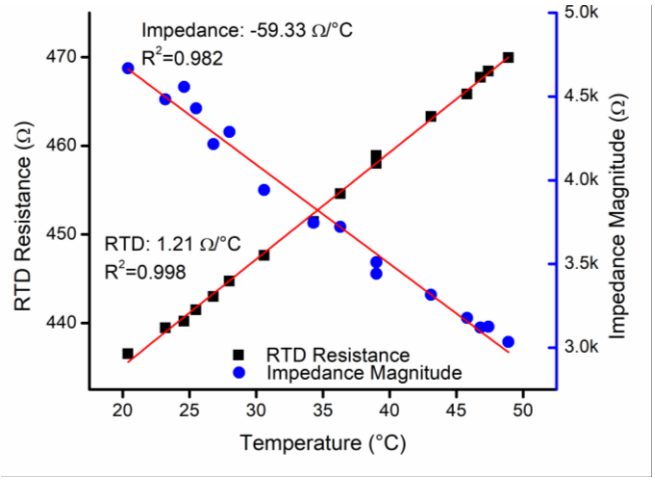

Figure 5: Impedance magnitude at 100 kHz was roughly linear with temperature, with a temperature coefficient of -59.33 Ω/°C and resolution of 0.02°C. This compared favorably to the RTD, which showed a temperature coefficient of 1.21 Ω/°C and a resolution of 0.08°C.

CONCLUSION

A novel method of measuring bulk fluidic temperature via electrochemical impedance was tested using a flexible, biocompatible temperature sensor. Results confirm theoretical predictions, and the impedimetric temperature sensor was able to measure sub-degree temperature fluctuations at a higher resolution than platinum RTDs, which are considered the gold standard for temperature transduction. Electrochemical impedance measurements are substrate-independent, and temperature measurement via electrochemical impedance can be implemented in any device with exposed electrodes in an aqueous solution. Future work will evaluate repeatable sensing in physiological fluids towards achieving chronic temperature monitoring in vivo, as well as exploring this technique's sensitivity to changes in ionic concentration and composition.

ACKNOWLEDGEMENTS

We would like to thank Dr. Brian Kim, Dr. Donghai Zhu of the Keck Photonics Lab, and all the members of the Biomedical Microsystems Lab for their help and support. This work was funded by the National Science Foundation under award EFRI-1332394.

REFERENCES

[1] P. Childs, J. Greenwood, and C. Long, "Review of temperature measurement," *Review of scientific instruments,* vol. 71, pp. 2959-2978, 2000.

[2] A. Tong, "Improving the accuracy of temperature measurements," *Sensor Review,* vol. 21, pp. 193-198, 2001.

[3] S. Kasap, "Thermoelectric effects in metals: thermocouples," *Canada: Department of Electrical Engineering University of Saskatchewan,* 2001.

[4] H.-M. Chuang, K.-B. Thei, S.-F. Tsai, and W.-C. Liu, "Temperature-dependent characteristics of polysilicon and diffused resistors," *Electron Devices, IEEE Transactions on,* vol. 50, pp. 1413-1415, 2003.

[5] A. Vanhoestenberghe and N. Donaldson, "Corrosion of silicon integrated circuits and lifetime predictions in implantable electronic devices," *Journal of Neural Engineering,* vol. 10, p. 031002, 2013.

[6] Y. Kanda, R. Aoshima, and A. Takada, "Blood compatibility of components and materials in silicon integrated circuits," *Electronics Letters,* vol. 17, pp. 558-559, 1981.

[7] S. B. Baumann, D. R. Wozny, S. K. Kelly, and F. M. Meno, "The Electrical Conductivity of Human Cerebrospinal Fluid at Body Temperature," *IEEE Transactions on Biomedical Engineering,* vol. 44, 1997.

[8] L. Raijmakers, D. Danilov, J. Van Lammeren, M. Lammers, and P. Notten, "Sensorless battery temperature measurements based on electrochemical impedance spectroscopy," *Journal of Power Sources,* vol. 247, pp. 539-544, 2014.

[9] R. R. Richardson, P. T. Ireland, and D. A. Howey, "Battery internal temperature estimation by combined impedance and surface temperature measurement," *Journal of Power Sources,* vol. 265, pp. 254-261, 2014.

[10] J. E. B. Randles, "Kinetics of rapid electrode reactions," *Discussions of the faraday society,* vol. 1, pp. 11-19, 1947.

[11] D. Merrill, E. Jeffrey, and L. Jay, "The Electrode—Materials and Configurations," *Essential Neuromodulation,* pp. 107-152, 2011.

[12] J. R. MacDonald, "Double layer capacitance and relaxation in electrolytes and solids," *Transactions of the Faraday Society,* vol. 66, pp. 943-958, 1970.

[13] A. A. Kornyshev, "Double-layer in ionic liquids: paradigm change?," ed: ACS Publications, 2007.

[14] M. Chen, Z. A. Goodwin, G. Feng, and A. A. Kornyshev, "On the temperature dependence of the double layer capacitance of ionic liquids," *Journal of Electroanalytical Chemistry,* 2017.

[15] R. A. Robinson and R. H. Stokes, *Electrolyte solutions*: Courier Corporation, 2002.

[16] M. Berkowitz and W. Wan, "The limiting ionic conductivity of Na+ and Cl− ions in aqueous solutions: Molecular dynamics simulation," *The Journal of chemical physics,* vol. 86, pp. 376-382, 1987.

[17] M. Huber, R. Perkins, A. Laesecke, D. Friend, J. Sengers, M. Assael, *et al.*, "New international formulation for the viscosity of H2O," *Journal of Physical and Chemical Reference Data,* vol. 38, pp. 101-125, 2009.

[18] A. Baldwin, L. Yu, and E. Meng, "An Electrochemical Impedance-Based Thermal Flow Sensor for Physiological Fluids," *Journal of Microelectromechanical Systems,* vol. 25, pp. 1015-1024, 2016.

[19] R. Zwanzig, "Dielectric friction on a moving ion. II. Revised theory," *The Journal of Chemical Physics,* vol. 52, pp. 3625-3628, 1970.

[20] H. J. Liebe, G. A. Hufford, and T. Manabe, "A model for the complex permittivity of water at frequencies below 1 THz," *International Journal of Infrared and Millimeter Waves,* vol. 12, pp. 659-675, 1991.

[21] W. Ellison, "Permittivity of pure water, at standard atmospheric pressure, over the frequency range 0–25 THz and the temperature range 0–100 C," *J. Phys. Chem. Ref. Data,* vol. 36, pp. 1-18, 2007.

[22] L. Onsager, "Theories of Concentrated Electrolytes," *Chemical Reviews,* vol. 13, pp. 73-89, 1933.

[23] T. S. Light, S. Licht, A. C. Bevilacqua, and K. R. Morash, "The Fundamental Conductivity and Resistivity of Water," *Electrochemical and Solid-State Letters,* vol. 8, p. E16, 2005.

CONTACT

Ellis Meng, ellis.meng@usc.edu

EFFECT OF DIELECTRIC LOSS ON THE QUALITY FACTORS OF PIEZOELECTRICALLY DRIVEN LENGTH EXTENSIONAL MODE RESONATORS

A. Qamar[1], S. Sherrit[2], X.-Q. Zheng[3], J. Lee[3], P. X.-L. Feng[3], and M. Rais-Zadeh[1,2]
[1]Electrical Engineering and Computer Science, University of Michigan, Ann Arbor, MI, USA
[2]Jet Propulsion Laboratory, California Institute of Technology, Pasadena, CA, USA
[3]Electrical Engineering, Case School of Engineering, Case Western Reserve University, Cleveland, OH, USA

ABSTRACT

In this paper, we present the effect of dielectric loss on quality factors of piezoelectrically actuated length extensional (LE) mode resonators. LE mode resonators having same lateral dimensions but different layer stacking structures, namely silicon (Si), aluminum/aluminum nitride (Al/AlN), AlN/Si and Al/AlN/Si, are designed and fabricated. The corresponding resonance and quality factors (Qs) are measured using optical and electrical readout techniques. The effect of different loss mechanisms in each layer on the Qs is investigated by methodically removing each layer in simulation and fabrication. Thermoelastic damping (TED) in an assumed homogenous AlN film and anchor loss have been investigated by COMSOL, and the dielectric loss or loss tangent in the piezoelectric layer has been modelled by using the Mason's network model. The effect of AlN dielectric loss tangent on measured Q values is analyzed using Mason's model, and its dependence on piezoelectric loss is discussed.

INTRODUCTION

Piezoelectric thin films have been investigated since the early developments of MEMS resonator technology. Zinc oxide (ZnO), lead zirconate titanate (PZT), lithium niobate ($LiNbO_3$), and AlN are the main piezoelectric thin film materials in MEMS industry today. AlN is much suitable choice for many RF applications due to its fabrication simplicity and reproducibility as well as its low dielectric loss [1], minimal electronic contamination issue, and high thermal conductivity [2]. Piezoelectrically actuated resonators may utilize high-quality single-crystal Si as the structural layer and a thin film piezoelectric only as the transduction layer [3]. However, the presence of the piezoelectric layer degrades the Q considerably, a phenomenon, which is not completely understood up to now. Different loss mechanisms including anchor loss [4], TED in the metal electrodes [5], and charge redistribution loss [6,7], have been investigated as possible dominant loss mechanisms in different types of piezoelectric resonators. Among a broad spectrum of losses including mechanical, dielectric and piezoelectric [8], dielectric losses have not been comprehensively considered in piezoelectrically actuated resonators. This loss mechanism does not affect the thickness-mode resonators (due to the presence of a negative capacitance in its effective model). In length extensional (LE) mode resonators that have lower $f \times Q$ values, dielectric loss is a factor we explore here in detail.

In this study, we analyzed the loss tangent using the Mason's network model for lateral length extensional resonators, along with the network model of an elastic layer vibrating along its length. The composite resonator consists of different heterostructures of thin film materials coalesced at their interfaces. Using the extended model, the effect of dielectric loss in piezoelectric layer (AlN) has been analyzed for the first time, with measured value for loss tangent of AlN at the frequency of resonance. In addition to studying the effect of dielectric losses on mechanical Qs of the resonators, we study the effect of all other losses that were proposed as the main Q limiting mechanisms and explain their contributions, which are measured and analyzed to be small and not dominant.

DESIGN AND FABRICATION

LE mode resonators having a resonance frequency of ~10 MHz are designed for studying their Q values and loss mechanisms. The LE mode was chosen due to the insensitivity of its resonance frequency to the number of layers in the resonance stack, as well as due to its substantially lower measured Q compared to what is expected due to known Q limiting loss mechanisms. COMSOL finite element modeling (FEM) tool was used to assess the exact resonance frequency of each type of resonator with its specific structural stack of constituting layers. Anchor loss using perfectly matched layers (PML) model was used to design the tethers and calculate the anchor loss using COMSOL. TED for each type of stack with and without metal electrodes was analyzed using standard thermoelasticity modelling of COMSOL. Akheizer loss values for Si and AlN layers are taken from [9] and accounted for in total estimated Q values. The simulated Q value for each layer is given in Fig. 1 along with the fundamental resonance mode of LE resonator.

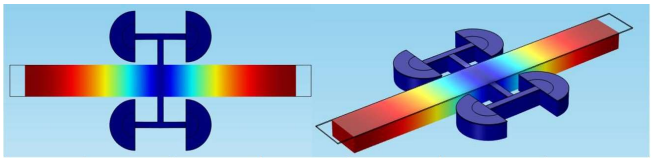

Stack	Si	AlN	Al	AlN/Si	Al/AlN/Si	Al/AlN
Q_{ANC}	1.627E7	1.241E7	1.165E7	1.044E7	1.432E7	1.205E7
Q_{TED}	1.351E7	1.365E7	4.481E5	1.510E5	1.399E5	2.648E6
Q_{Akh}	2.700E6	1.000E6	-	2.378E6	2.378E6	1.00E6
Q_{Total}	1.975E6	8.886E5	4.313E5	1.400E5	1.308E5	6.812E5

Figure 1: Simulation of the LE resonance mode, with corresponding simulated Q for each type of stacking.

LE mode resonators having different heterostructures stacking were fabricated using standard MEMS processes of photolithography, dry etching and XeF_2 releasing as shown in Fig. 2, to study the Q limiting mechanism in this type of resonators. A vector network analyzer (VNA) was used to measure the electrical transmission response of Al/AlN/Si heterostructure resonators, and to calculate the Q values as shown in Fig. 3(a). A custom-built optical in-plane (lateral) displacement measurement system based on knife-edge effect, as shown in Fig. 3 (b), was used to measure the Q of each layer, especially for the stacks without Al electrodes. Figure 3(c) shows the optically measured resonance response and Q of the Al/AlN/Si resonator using the optical measurement system, which agrees well with the electrical measurements.

EXPERIMENTAL RESULTS AND DISCUSSION

The results for all the remaining resonator stacks without Al electrodes, measured using optical technique, are shown in Fig. 4. A complete summary of measured and simulated Qs is given in Table 1. It can be observed from Table 1 that TED, which is proposed as the dominant loss mechanism in piezoelectric resonators and is believed to be originating from metal electrode [5], is in fact not the

978-1-940470-03-0/HH2018/$25©2018TRF
DOI 10.31438/trf.hh2018.51

dominant loss mechanisms for LE mode resonators. This can be observed by comparing the Q drop from Si only to AlN/Si resonators in Table 1; also comparing simulated Qs of Al/AlN/Si and Al/AlN suggest the TED Q should be even higher for Al/AlN resonators but that is not the case in experiment. The reason the simulated Q for AlN only and Al/AlN resonators is high is due to the very good thermal property of an assumed homogenous AlN film. But in experiment, comparing the Qs of all stacks shows the main lossy layer is the AlN itself and not the metal layer on top of it. Analysis of measured and simulated Qs for each type of resonator also reveals that the anchor loss is not the dominant mechanism in these resonators either (Table 1). Charge redistribution loss cannot explain the very low Q seen in these resonators with thin AlN film acting as the main structural layer. If this mechanism was the main mechanism, the Q of Al/AlN/Si should have been about half of AlN/Si resonators but the drop of measured Q when adding Al is insignificant compared to the drop seen when adding AlN to the starting Si layer.

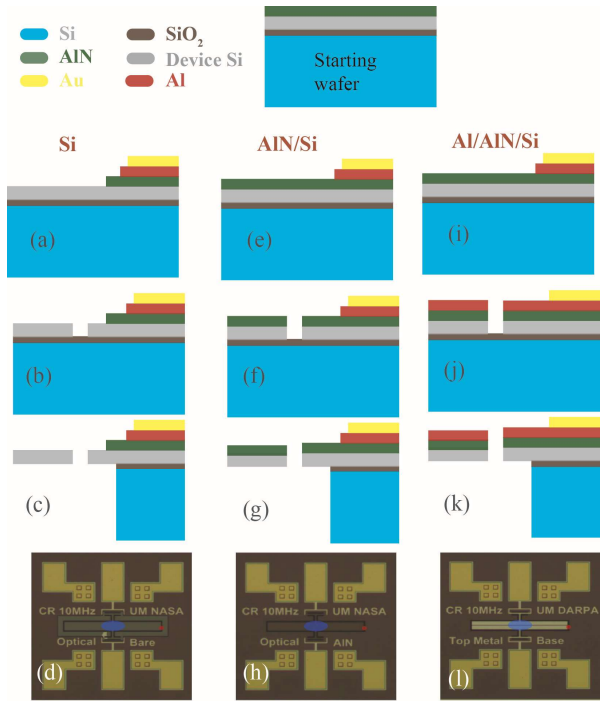

Figure 2: Device structure and fabrication process with starting SOI wafer, (a)-(c) Si resonator, (e)-(g) Al/Si resonator, (i)-(k) Al/AlN/Si resonator, (d),(h),(l) fabricated device images. DRIE was used for backside etching and XeF_2 release was used for front side release of Si device layer. Al/AlN resonators were fabricated by releasing the Si device layer of Al/AlN/Si resonator in XeF_2.

Let us summarize the effect of each of the known charge mechanisms: 1) TED loss in the metal layer, as proposed in [5] to be the dominant mechanism, is found experimentally here to be not significant. Comparing the measured Q of Si only, AlN/Si, and Al/AlN/Si resonators shows that the main drop in Q is observed when AlN is added to the Si only stack (Q of Si only resonator is >300,000, whereas Q of the AlN/Si device is only 27,800 and Q of the Al/AlN/Si resonator (~22,000) is very similar in value to that of the AlN/Si resonator). Anchor loss is simulated to be at least an order of magnitude larger than the measured Q for all resonator stacks. Charge redistribution loss should reduce the Q of Al/AlN/Si resonator to half the value of AlN/Si resonator but that is not the case (in fact the Qs of these two resonators is found to be quite close and only 20% different).

As TED, anchor loss, and charge redistribution loss are unable to explain the observed drop of Q in LE mode resonator, the loss tangent was next investigated by using the Mason's network model. We have used Mason's network model to investigate the effect of loss tangent, because COMSOL default simulation does not account for such losses in the dielectrics. Additionally, Mason's network model provides analysis of piezoelectric loss and any intrinsic loss separately; and their interdependence on each other as discussed in the next section.

Table 1: Simulated and measured Q in million for resonators with different stack materials. Simulated Q only accounts for TED, anchor loss, and Akheizer loss in Si and AlN layers (Fig. 1).

	Si	AlN	Al	AlN/Si	Al/AlN/Si	Al/AlN
Q Simulated	1.97	0.88	0.43	0.14	0.13	0.68
Q Measured	0.30	-	-	0.0278	0.022	***0.0024***

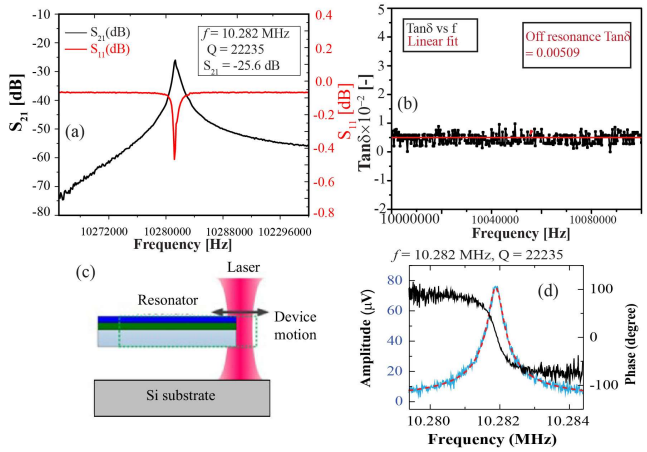

Figure 3: (a) Al/AlN/Si electrical transmission measurements along with the measured Q value. (b) Measurement of tanδ in AlN using impedance data. (c) Optical measurement illustration. (d) Optically measured resonance of Al/AlN/Si resonator.

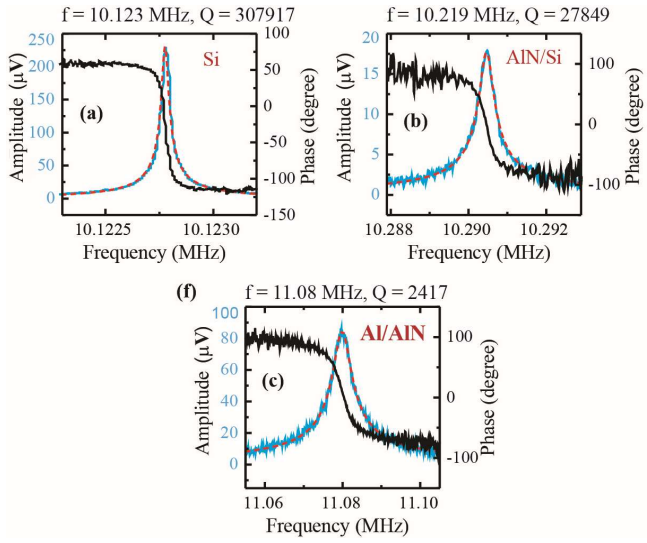

Figure 4: Optical measurement results for each type of resonator labelled on the plot.

LOSS TANGENT BY MASON'S MODELLING

In order to model piezoelectric transducers, different 1D modelling techniques were used before the development of FEM commercial software packages, such as COMSOL. It is quite difficult to find analytical solutions to the wave equation in piezoelectric materials using first principles. Mason [10] showed that network theory can be used for one-dimensional analysis to overcome most of the difficulties in deriving the solutions. He presented an exact equivalent circuit that separated the piezoelectric material into an electrical port and two acoustic ports with an ideal electromechanical transformer for a length thickness resonator geometry. Berlincourt et al. investigated a variety of modes [11] and Sherrit et al. [12] extended the models to include losses in all the material constants to account for various damping mechanisms. In an effort to remove circuit elements between the top of the transformer and the node of the acoustic transmission line, Krimholtz, Leedom and Matthae [13] published an alternative equivalent circuit which was found to produce identical results [12].

The model we used to fit the optical experimental data is based on Mason's network equivalent for a piezoelectric resonator and is shown in Fig. 5. In the mechanical network, forces act like voltages and currents, represent the velocity of a face of the resonator. The model below represents three layers (Si, AlN and Al of 20 μm, 1 μm, 0.1 μm, respectively). The force is applied via laser excitation, which causes the resonator bar to vibrate with a velocity v. The velocity of the free face v can be integrated to get the displacement amplitude ($d = v/i\omega$), where ω is the frequency of the excitation. During the resonance the strain, displacement and velocity are considered the same. This data can then be fit to the optical measurements and material constants in the model can be adjusted to look at the effect of the elastic, dielectric and piezoelectric loss. The elastic, dielectric, and piezoelectric constants of the model are treated as complex quantities with the imaginary component representing the loss. The functions Z_T and Z_S are based on the tan and secant functions with the frequency, density, length, area, and acoustic velocity of the layers. N is the turn's ratio for the piezoelectric transformer and the Z_o term represents the static capacitance of the piezoelectric layer. The elastic constants can then be written as

$$Y = Y_r + iY_i = Y_o(1 - i\,1/Q)\cdot \quad (1)$$

While the piezoelectric and dielectric constant can be written as:

$$d_{31} = d_{31_r} + id_{31_i}, \quad (2)$$

$$\varepsilon_{31} = \varepsilon_{31_r} + i\varepsilon_{31_i}. \quad (3)$$

An example of the fit to the Si/AlN/Al and Al/AlN optical data is shown in Fig. 6 using measured value for loss tangent of AlN (as shown in Fig. 3). The baseline material properties used for each layer of the resonator are shown in Table 2. In each of the resonator models, we had to adjust the Young's modulus of the AlN layer to account for changes in the layer boundary conditions and its effect on the acoustic velocity in the layer, to match the resonance peak. In addition, a slight modification in the real part of the elastic constant was required to adjust for the different piezoelectric coefficients. The mechanical Q of the Si layer was fixed at 307,91 as determined experimentally from the bare Si resonator. The Q of the Al was fixed at 60,000 (a large enough value not to be the dominant effect to allow studying the effect of dielectric loss in AlN only). The imaginary part of the permittivity ($tan\delta$) was adjusted according to measured value from impedance data (Fig. 3d) to reproduce the experimental data of optically measured 2 and 3 layer stacked devices, using 3 different values of the piezoelectric coefficient (d_{31} =-2.1 *pC/N*, -1.1 *pC/N* and complex d_{31} =(-1.1 - 0.0223i) *pC/N*). The results for the analysis are shown in Figure 6.

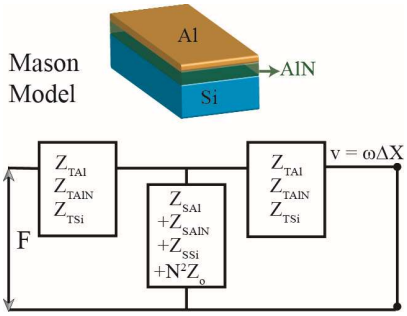

Figure 5: The electromechanical network equivalent of three-layer resonator vibrating in the LE mode based on Mason's network equivalent [8,9]. The electrical impedance of the piezoelectric Z_o has been transformed to the acoustic elements and represents a dissipation that can reduce the effective Q of the resonator.

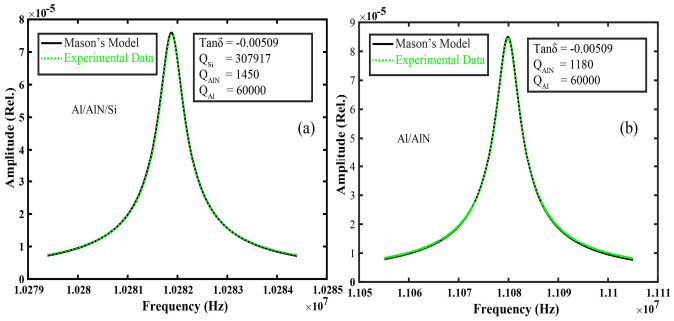

Figure 6: The optical resonance data and a fit using the model shown in Figure 5 for (a) The Al/AlN/Si stack and (b) Al/AlN layers.

Table 2: The real component of the material properties of each material in the resonator stack.

Material	Si	Al	AlN in AlN/Si	AlN in Al/AlN/Si
Density (kg/m^3)	2328	2700	3260	3260
Y Elastic Constant (N/m^2)	1.69 ×10^{11}	0.69 ×10^{11}	3.3199 × 10^{11}	2.7549 × 10^{11}
ε Permittivity (F/m)	-	-	1.434 × 10^{-10}	1.434 × 10^{-10}
d_{31} Piezoelectric Constant (pC/N)	-	-	-1.1 to -2.1	-1.1 to -2.1

The data in Fig. 7 show the required effective Q of the AlN layer applied to the model to match the optical data with varying the electrical tanδ. The data in Figure 7 and the data in Table 3 are modeled to produce optical resonance curves that match the optical data in Table 3. For example, for a given d_{31} = -1.1 *pC/N* and no piezoelectric loss on the Al/AlN/Si resonator, the measured $tan\delta$ of 0.00509 suggests that the mechanical Q of the AlN needs to be of the order of 1450 to model the curve in Figure 6a. However, if the

piezoelectric coefficient was 2.1 *pC/N*, a *tanδ* of 0.07 would require a mechanical *Q* in the AlN film to be 10,000. The measured dielectric loss (*tanδ*) of these films, measured slightly off resonance suggests that mechanical *Q* of the films is the limiting factor in the overall *Q* of the resonator. One thing which is evident is that the larger the piezoelectric coefficient, the smaller the required dielectric loss to account for the *Q* of the experimental data as shown in Fig. 7. The sign of the piezoelectric loss is also seen to be a factor to have influence on the measured *Q* values. The more negative the piezoelectric loss, the smaller the electrical *tanδ* required to account for the *Q* of the resonator.

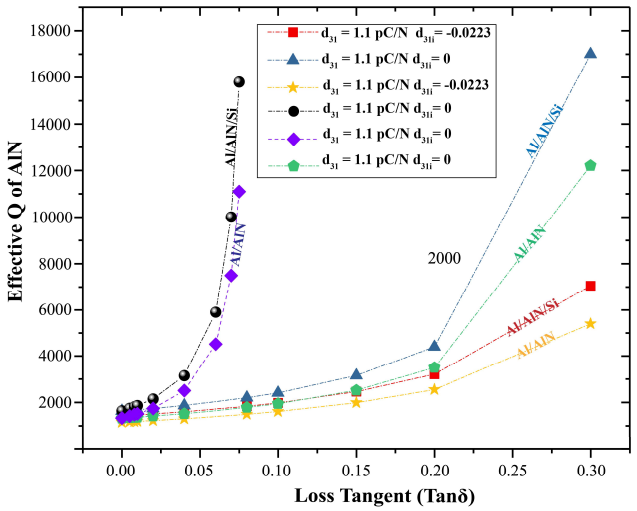

Figure 7: The required Q of the AlN resonator as a function of the tanδ of the piezoelectric AlN to match the optical data for the 3 layers of Al/AlN/Si and 2 layers of Al/AlN. Here, Tanδ$_d$ = d_{31i}/d_{31} is the piezoelectric loss tangent.

Different possible scenarios for the *Q* of each layer and the composite resonators are given in Table 3. It can be observed from Table 3 that the experimentally observed value of *Q* for Al/AlN and Al/AlN/Si resonators can be explained if the dielectric loss values were high (the low value of 0.005 shows the dielectric loss is the not dominant *Q* limiting mechanism either). In addition, the low *Q* can only be explained only if AlN layer has a high mechanical loss that is not considered in conventional TED, anchor loss, and surface loss models [14]. Si layer is known to have a high *Q* as extracted from the measured *Q* using optical technique.

Table 3: Mason Model estimation of tanδ and other internal losses within each material to match the measured Q for AlN/Al (last column) and Al/AlN/Si resonators. Measured value of loss tangent is 0.005 which means the contribution of dielectric loss in AlN in not significant and some other loss in AlN needs to be high to match the measured Q.

tanδ	***Q* mechanical: Al**	***Q* mechanical: AlN**	***Q* total**
0.0003	2474	2474	2474
0.022	6000	3000	2474
0.034	60000	3000	2474
0.042	60000	60000	2474
0.0050	60000	2474	2474

CONCLUSION

Effect of dielectric loss on the quality factors of piezoelectrically driven LE mode resonators is investigated. The effect of different heterostructure stacking on the *Q*s is analyzed by COMSOL simulations and then by experimentally measuring the *Q*s using electrical and optical readout techniques. Mason's model together with the experimental data is used to investigate the effect of dielectric loss in AlN thin film. It has been found that the AlN has low dielectric loss and the mechanical *Q* of AlN is responsible for low *Q*s in the LE mode resonators.

ACKNOWLEDGEMENT

This work is supported by Army Research Office (ARO), the Defense Advanced Research Project Agency (DARPA), and by NASA.

CONTACT

*A. Qamar, tel: +1-(734) 730-8083; afzaal@umich.edu
*M. Rais-Zadeh, tel: +1-(734) 764-4249; minar@umich.edu

REFERENCES

[1]. E. Savrun et al., "High thermal conductivity aluminum nitride ceramics for high power microwave windows," Fifth IEEE International Vacuum Electronics Conference, (IEEE Cat. No.04EX786) 2004, pp. 45-46.
[2]. J. C. Doll et al., "Aluminum nitride on titanium for CMOS compatible piezoelectric transducers," Journal of micromechanics and microengineering : structures, devices, and systems, 20, 25008 (2010).
[3]. A. Jaakkola, et al., "Piezoelectrically transduced single-crystal-silicon plate resonators," IEEE Ultrason Symp, Beijing (2008), pp. 717–720
[4]. J. Segovia-Fernandez et al., "Anchor losses in AlN contour mode resonators," JMEMS, 24, 265 (2015).
[5]. J. Segovia-Fernandez et al., "Thermoelastic damping in the electrodes determines Q of AlN contour mode resonators," JMEMS, 26, 550 (2017).
[6]. A. Peczalski, et al., "Effects of heterostructure stacking on acoustic dissipation in coupled-ring resonators," IEEE MEMS, Las Vegas (2017), pp. 954-957.
[7]. R. Tabrizian et al., "The effect of charge redistribution on limiting the kt2.Q product of piezoelectrically transduced resonators, "Transducers-18th International Conference on Solid-State Sensors, Actuators and Microsystems, Anchorage (2015), pp. 981-984.
[8]. A. V. Mezheritsky, "Elastic, dielectric, and piezoelectric losses in piezoceramics: how it works all together," in IEEE Transactions on Ultrasonics, Ferroelectrics, and Frequency Control, 51, 695 (2004).
[9]. R. Tabrizian et al., "Effect of phonon interactions on limiting the f.Q product of micromechanical resonators," Transducers-International Solid-State Sensors, Actuators and Microsystems Conference, Denver (2009), pp. 2131-2134.
[10]. W.P. Mason, Electromechanical Transducers and Wave Filters, Princeton, NJ, Van Nostrand, 1948.
[11]. D.A. Berlincourt et al., Academic Press, W.P. Mason- editor pp. 169-270.
[12]. S. Sherrit et al., "Comparison of the Mason and KLM equivalent circuits for piezoelectric resonators in the thickness mode," Proceedings of the IEEE Ultrasonics Symposium, Lake Tahoe (1999), pp. 921-926.
[13]. R. Krimholtz et al., "New equivalent circuits for elementary piezoelectric transducers," Electronics Letters, 6, (398) 1970.
[14]. Explaining the anomalous low quality factors in piezoelectrically driven length extensional mode thin Film resonators (under review).

BROADBAND LONG-WAVELENGTH INFRARED MICROMECHANICAL PHOTOSWITCH FOR ZERO-POWER HUMAN DETECTION

Sungho Kang, Sila Deniz Calisgan, Zhenyun Qian, Vageeswar Rajaram, Nicol E. McGruer, and Matteo Rinaldi*
Northeastern University, Boston, Massachusetts, USA

ABSTRACT

This paper reports on the first demonstration of a long-wavelength infrared (LWIR) micromechanical photoswitch (MP) suitable for human detection with zero-power consumption in standby. The proposed MP employs a highly-efficient broadband IR absorber (η~80%, λ=8-12μm), spectrally matching with the IR radiance of a human body. An ultra-low detection threshold of ~140 nW is experimentally demonstrated for the first time thanks to the high thermal sensitivity (~1.44 nm/nW) and stiffness (~0.033 nN/nm) of the optimized bimaterial actuating beams and the aggressively scaled nanoscale contact gap (<200 nm) maintained by the built-in temperature and stress compensation mechanisms. Such low threshold potentially enables human detection with a lens at a projected distance of 5.7 m.

INTRODUCTION

IR-based human detection technologies have been extensively used in motion-triggered automation, indoor/outdoor security, search-and-rescue and many other applications [1]. However, the relatively high-power consumption of state-of-the-art motion detectors limits their battery life and increases the maintenance cost of sensor networks deployed in remote or hazardous locations. For instance, commercial off-the-shelf motion detectors based on a pyroelectric IR sensor consume about 200 μW continuously in standby [2]. Their lifetime is limited to less than one year (powered by a coin battery) when deployed in regions where energy harvesting is not available. The constant power consumption is attributed to the use of active electronics for signal conditioning and processing which accounts for the great majority of total consumed power. The high maintenance cost associated with limited sensor lifetime has been a major limiting factor for the implementation of high capacity sensor networks for security monitoring in regions such as tunnels, underground facilities and national borders. Driven by the growing need for persistent monitoring with long sensor lifetime, significant efforts have been devoted into developing completely-passive switch-based sensors capable of digitizing the signal of interests without using active electronics [3-4].

Recently, our group has demonstrated zero-power IR sensors based on plasmonically-enhanced micromechanical photoswitches (MPs) [4-7]. MPs exploit IR signature emissions from targets of interests to form an electrical channel between the device terminals via thermomechanical coupling. An MP can be placed in between a battery and active electronics, such as shown in Figure 1(a), to eliminate power consumption when there is no event of interests. In other words, it is only when the absorbed IR power exceeds the designed threshold level (~500 nW) that the mechanical switch is closed to supply power to the active electronics. A large ON/OFF conduction ratio (>10^{12}) and near-infinite subthreshold slope are measured to demonstrate the zero-standby-power consumption [4]. One of the crucial components in the previously demonstrated MPs is the narrowband plasmonic absorbers tailored for near-unity absorption in mid-wavelength IR (MWIR) spectral range specifically for detection of hot exhaust plumes [8]. Nevertheless, the reported narrowband absorption of the plasmonic absorbers in MWIR and the relatively high detection threshold of ~ 500 nW prevents the use of such previously-demonstrated MPs for the detection of objects with a temperature significantly lower than that of exhaust plumes, such as the one of a human body.

In this work, a long-wavelength infrared (LWIR) MP with a reduced IR threshold (~140 nW) is demonstrated for the first time, suitable for human detection with zero-power consumption in standby. Differently from state-of-the-art human detectors that rely on pyroelectric IR sensors and active digitizing electronics, the device proposed here exploits the energy contained in the LWIR radiation emitted from a warm object to trigger a micromechanical switch. The first-of-its-kind prototype presented here is selectively activated by a broadband LWIR radiation (λ = 8-14 μm) closely matching the spectral content of IR radiation emitted by a human body (Figure 1a). The proposed technology therefore demonstrates the great potential for the realization of persistent zero-power human detection to be deployed in remote regions where high maintenance cost is to be avoided.

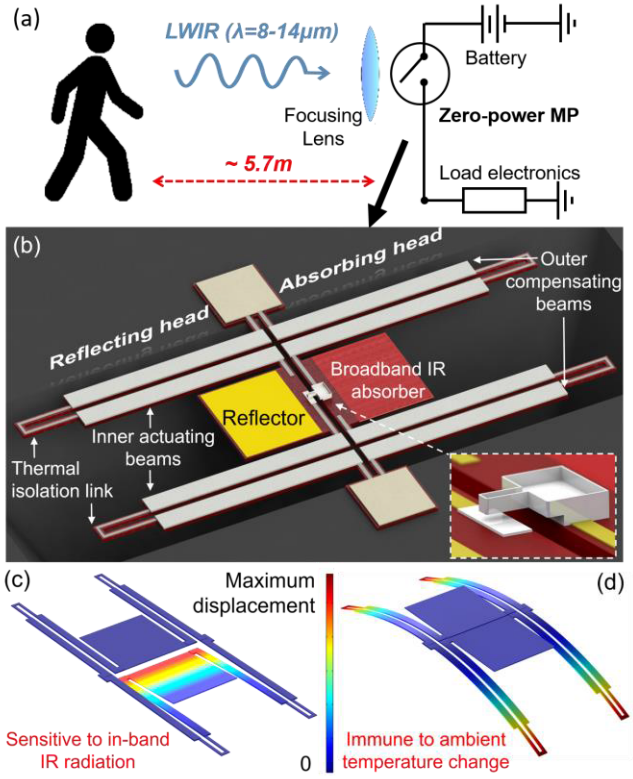

Figure 1: (a) The near-zero power broadband MP used for human detection. (b) The 3-dimensional schematic of the broadband MP. The inset shows a zoomed-in schematic highlighting the bowl-shaped platinum (Pt) contact tip. (c) Finite Element Method (FEM) simulation result showing the downward bending of MP in response to in-band (LWIR) IR absorption. (d) FEM simulation result showing the complete immunity to the ambient temperature change.

978-1-940470-03-0/HH2018/$25©2018TRF
DOI 10.31438/trf.hh2018.52

DEVICE DESIGN

The MP proposed here consists of a pair of symmetric released cantilevers, each composed of an absorbing (or reflecting) head and an inner and outer pair of thermally sensitive bimaterial legs separated by a thermal isolation link as shown in Figure 1b. The broadband absorbing head can selectively convert impinging optical power in LWIR regime. Upon the absorption of broadband LWIR radiation in the absorbing head, a large and fast increase of temperature in the corresponding inner pair of legs results in a downward displacement of the cantilever, bringing a high-stiffness platinum (Pt) tip into contact with the opposite terminal (Figure 1c). It is worth noting that the switch remains open until it absorbs LWIR radiance (e.g. from a human nearby) regardless of the change in ambient temperature, thanks to the symmetric design of the two cantilevers (Figure 1(d)). The sub-micron air-gap maintained in standby translates directly into essentially zero leakage current and zero-standby power IR sensing.

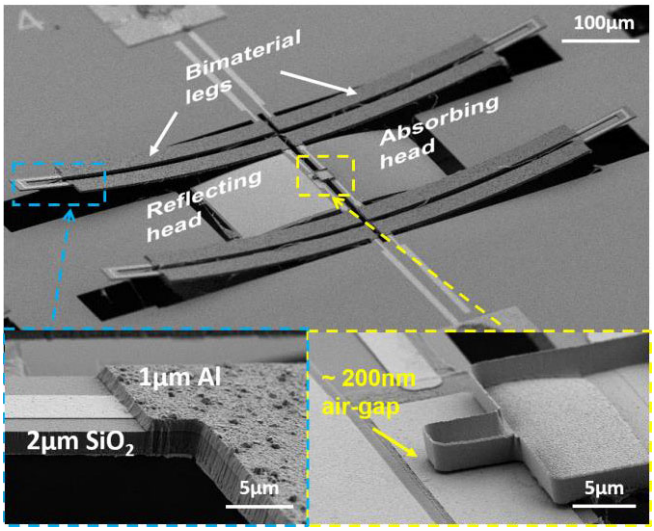

Figure 2: Scanning electron microscope (SEM) image of the fabricated device. The insets show close-up images of the bi-material leg and the Pt contact-tip, highlighting the increased Al thickness and the aggressively scaled contact gap of ~200nm.

Low Detection Threshold MP for LWIR Sensing

In this work, a 2-µm silicon dioxide (SiO_2) slab backed by a metal reflector is employed as the IR absorbing element in an optimized micromechanical photoswitch for ultra-low threshold IR detection in the LWIR range (Figure 2). Replacing the plasmonic absorber used in previous demonstration for narrowband mid-IR absorption, this broadband dielectric absorber exploits the intrinsic absorption of the SiO_2 layer. The intrinsically high loss of SiO_2 slab due to vibrational modes of longitudinal-optical (LO) phonons leads to a consistently high broadband absorption in LWIR specifically suitable for human detection applications [9].

To improve the detection threshold, two approaches were adopted. First, the thermal sensitivity of the bimaterial actuating beams is increased by optimizing thickness ratio of aluminum (Al) and SiO_2. Differently from the previous demonstrations, the device in this paper employs 1-µm Al on a 2-µm SiO_2 as shown in the bottom left inset of Figure 2. This ratio in fact corresponds to the maximum thermal sensitivity (1.44 nm/nW, corresponding to more than 15% increase compared to previous demonstrations) for a fixed 2-µm SiO_2 layer (Figure 3).

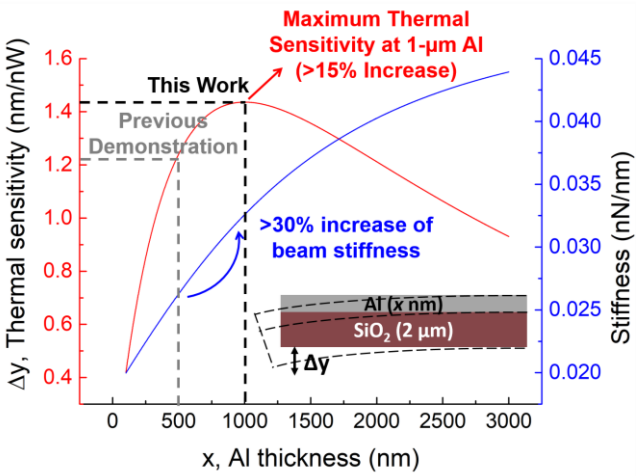

Figure 3: Thermal sensitivity (left y-axis) and beam stiffness (right y-axis) of the bimaterial legs as a function of the Al thickness for a fixed SiO2 thickness of 2-µm. The vertical displacement, Δy, per unit absorbed IR power is maximum for an Al thickness of 1-um.

Second, the contact-gap is scaled down to reduce the actuation threshold. The smaller contact-gap was defined by the thickness of amorphous silicon layer, which serves as a sacrificial layer between the Pt contact and the electrical terminal on the opposite head [4]. It is worth noting that, although the contact gap can be in principle arbitrarily scaled within fabrication limits, a small gap inevitably yields an insufficient restoring force causing stiction of the contacts. In the device presented here, however, stiction-free contacts are achieved, despite the aggressive gap scaling, thanks to the optimization of the bimaterial beams, which not only increased the thermal sensitivity but also the overall stiffness of the folded beam structure (~ 0.033 nN/nm). Compared to the previous demonstration of narrowband MPs in [4], the optimized bimaterial design led to more than 15% increase in maximum thermal sensitivity and at the same time, the beam stiffness increased by more than 30% (Figure 4).

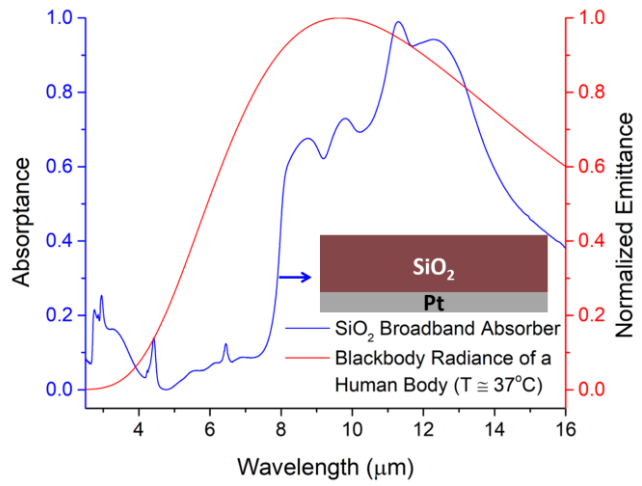

Figure 4: The spectral response of the broadband SiO_2 absorber in LWIR (blue curve, left y-axis) and the normalized blackbody emission at 37°C (red curve, right y-axis). The inset shows the cross-section schematic of the broadband SiO_2 absorber.

EXPERIMENTAL RESULTS

The spectral response of the fabricated device was characterized using a Fourier Transform Infrared Spectroscopy (FTIR) microscope. The reference was first measured on the gold reflecting head, then the reflection (R) of the SiO_2 dielectric absorber on the absorbing head was measured. Since the optically-thick (~100 nm) continuous Pt plate underneath efficiently suppress the transmitted power (transmittance, T), the absorptance (A) can be calculated as follows assuming negligible transmittance: $A = 1\text{-}R\text{-}T \approx 1\text{-}R$. The fabricated dielectric absorber exhibits the absorption as high as $\eta \sim 98.8\%$ at $\lambda = 11.3$ μm and consistently high absorption ($\eta > 80\%$) in the wide LWIR regime ($\lambda = 8\text{-}14$ μm) (Figure 4). The measured absorption shows a good spectral overlap with the emission spectrum of a blackbody at 37°C (closely representing a human body), which guarantees an effective sampling of the emitted IR power from a human body.

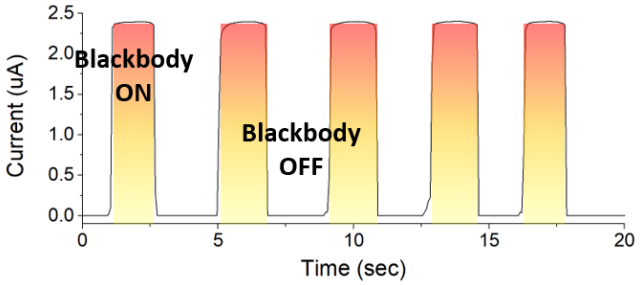

Figure 5: Measured current (using sourcemeter with a 10mV bias) through the MP in response to chopped IR radiation emitted by the calibrated blackbody source.

The function of the device was tested in a vacuum chamber using a calibrated blackbody IR source. The current through the device was monitored using a sourcemeter with a constant bias of 10 mV, while the blackbody radiation is manually chopped. Several consecutive ON/OFF cycles were recorded when the device was exposed to chopped broadband IR radiation (Figure 5). The minimum absorbed power to trigger the device ON was estimated based on the measured absorption spectrum and the calibrated power density, and found to be ~140 nW. The achieved detection threshold corresponds to a minimum detectable IR power density of ~6.2W/m^2, which is equivalent to the IR radiation collected from a human body at 5.7m distance, with a 25mm focal length lens. The same high-stiffness bowl-shaped Pt contact demonstrated in [4] is employed in the LWIR MPs, which guarantees the outstanding reliability with numerous consecutive ON/OFF cycles (up to 8000 cycles measured). It is worth noting that a blackbody temperature of 300°C had to be used to deliver to the sensor a power density equivalent to the one that would be received from a 37°C human body without the attenuation of the vacuum chamber window. That is, the inherent absorption in CaF_2 optics limits the transmission and allows only a fraction of the available power from the blackbody in LWIR regime.

CONCLUSION

An ultra-low detection threshold of ~140 nW is experimentally demonstrated for the first time thanks to the high absorption (η~80%) of the SiO_2 broadband absorber, the high thermal sensitivity (~1.44 nm/nW) of the optimized bimaterial actuating beams, and the aggressively scaled nanoscale contact-gap (<200 nm) maintained by the built-in temperature and stress compensation mechanisms. These results demonstrate the great potential of the proposed technology for the realization of persistent zero-power human detection. The drastically increased sensor lifetime with the MPs will enable the unprecedented zero-power IR sensor network that can be deployed virtually anywhere.

ACKNOWLEDGEMENTS

The authors would like to thank the staff of the George G. Kostas Nanoscale Technology and Manufacturing Research Center at Northeastern University, Boston. This work was funded by the DARPA N-ZERO program contract no. HR0011-15-2-0048.

REFERENCES

[1] M. Shankar, "Human-tracking systems using pyroelectric infrared detectors," *Opt. Eng.*, vol. 45, no. 10, p. 106401, Oct. 2006.

[2] "Low-Power PIR Motion Detector With Sub-1GHz Wireless Connectivity Enabling 10-Year Coin Cell Battery Life," *Texas Instruments*, 2016. [Online]. Available: http://www.ti.com/lit/ug/tiduau1b/tiduau1b.pdf.

[3] R. H. Olsson, R. B. Bogoslovov, and C. Gordon, "Event driven persistent sensing: Overcoming the energy and lifetime limitations in unattended wireless sensors," in *2016 IEEE SENSORS*, 2016, pp. 1–3.

[4] Z. Qian, S. Kang, V. Rajaram, C. Cassella, N. E. McGruer, and M. Rinaldi, "Zero-power infrared digitizers based on plasmonically enhanced micromechanical photoswitches," *Nat. Nanotechnol.*, vol. 12, no. 10, pp. 969–973, Sep. 2017.

[5] Z. Qian, S. Kang, V. Rajaram, C. Cassella, N. E. McGruer, and M. Rinaldi, "Zero-power light-actuated micromechanical relay," in *IEEE MEMS*, 2017, pp. 940–941.

[6] V. Rajaram, Z. Qian, S. Kang, and M. Rinaldi, "MEMS-Based Near-Zero Power Infrared Wireless Sensor Node," in *IEEE MEMS*, 2018, pp. 17–20.

[7] V. Rajaram, Z. Qian, S. Kang, C. Cassella, N. E. McGruer, and M. Rinaldi, "Microelectromechanical detector of infrared spectral signatures with near-zero standby power consumption," in *19th International Conference on Solid-State Sensors, Actuators and Microsystems (TRANSDUCERS)*, 2017, pp. 846–849.

[8] S. Kang, Z. Qian, V. Rajaram, A. Alu, and M. Rinaldi, "Ultra narrowband infrared absorbers for omni-directional and polarization insensitive multi-spectral sensing microsystems," in *19th International Conference on Solid-State Sensors, Actuators and Microsystems (TRANSDUCERS)*, 2017, pp. 886–889.

[9] A. Lehmann, L. Schumann, and K. Hübner, "Optical Phonons in Amorphous Silicon Oxides. I. Calculation of the Density of States and Interpretation of Lo-To Splittings of Amorphous Sio2," *Phys. status solidi*, vol. 117, no. 2, pp. 689–698, Jun. 1983.

CONTACT

*S. Kang, tel: +1-626-290-6741; kang.su@husky.neu.edu

FBAR-BASED SENSOR FOR WIRELESS RFID AUTHENTICATION OF INTEGRATED CIRCUITS

Anton A. Shkel, Matin Barekatain, and Eun Sok Kim
Department of Electrical Engineering-Electrophysics
University of Southern California, Los Angeles, California, USA

ABSTRACT

This paper describes an integrated circuit (IC) authentication and tamper detection system, based on a Film Bulk Acoustic Resonator (FBAR) and passive Radio-Frequency Identification (RFID), which allows for wireless detection of tampering or counterfeiting in packaged ICs. We demonstrate the concept through the use of a 2.6 GHz FBAR based on a Zinc Oxide (ZnO) thin film. The FBAR is series connected to a piezoelectric energy harvester, which can generate voltage pulses with a peak amplitude of 56 V when tampering activity is detected. Our measurements validate this concept and demonstrate that we can permanently alter the high frequency resonance characteristics of the FBAR through dielectric breakdown caused by tampering.

INTRODUCTION

Counterfeiting of ICs is a growing global problem, costing an estimated annual loss of $7.5 billion for US-based semiconductor companies alone [1]. Existing methods of assessing whether an IC is a counterfeit involve time-consuming imaging tests, electrical verification, or destructive testing. Additionally, existing authenticity verification methods cannot be applied on a bulk-scale.

IC-level tamper detection sensors have been proposed, for example with integrated photo-detectors [2], to destroy critical program information through detection of tampering activity, but these rely on power from the IC to function. The use of random number generators for generating cryptographic keys, such as those based on tamper-sensitive MEMS arrays [3], is another common counterfeit-prevention technique, however these are only helpful in preventing reverse-engineering and not sensitive to repackaging attempts by the counterfeiter.

In this paper we propose a system containing an embedded tamper sensor to allow for rapid wireless scanning of ICs to detect signs of tampering activity that has produced a permanent change to RFID tag. We demonstrate the wireless tamper detection concept through device fabrication, simulation and measurement.

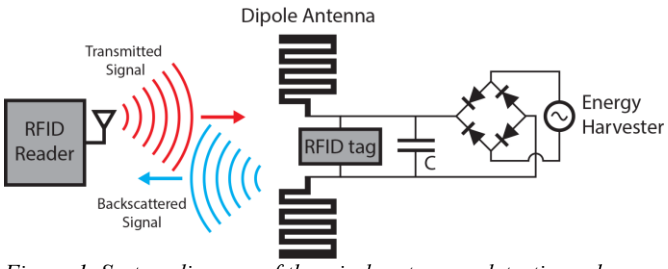

Figure 1. System diagram of the wireless tamper detection scheme. An external RFID reader transmits a sinusoidal signal and measures the backscattered signal strength from the tamper detection chip. The strength of the backscattered signal depends on the relationship of impedances between the RFID dipole antenna and series-connected FBAR. A piezoelectric energy harvester, connected to the FBAR via a rectifier and capacitor, generates a large voltage spike when a sufficient mechanical impulse is applied during the detaching process of the chip. This voltage spike will irreversibly break down the FBAR and permanently alter the characteristic of the backscattered signal.

DEVICE

A common technique employed by counterfeiters to remove an IC from a printed circuit board (PCB) involves raising the IC to an elevated temperature to melt the solder, and then striking the PCB with forceful impacts to remove the IC chip. The proposed system, illustrated in Figure 1, converts these impulses to large voltage pulses using a piezoelectric energy harvester, and irreversibly alters the spectral characteristic of an RFID tag. Such a system can be embedded within an IC package to passively detect tampering activity, and can be designed to be extremely difficult for counterfeiters to reverse the detection mechanism.

The main components of the RFID tag system are the RFID antenna, series-connected FBAR and energy harvester. The resonant frequency of the FBAR (that depends on the thicknesses of the layers) serves as the encoded ID of the tag. The RFID tag is designed to function passively, allowing the integrity of the chip to be assessed without any electrical connection, special configuration, precise alignment, or other measurement complexities that existing tamper detection mechanisms rely on.

Film Bulk Acoustic Resonator (FBAR)

The FBAR is designed such that it is permanently destroyed through dielectric breakdown when exposed to a large voltage. This breakdown will permanently alter the spectral characteristics of the FBAR, which results in an identifiable change in spectral shape of the interrogated signal.

The FBAR is fabricated on a silicon wafer coated with LPCVD Silicon Nitride (SiNx) (Figure 2a). The silicon nitride serves as an etch mask for KOH wet etching, which is used to open a window on the bottom of the wafer and to form a silicon nitride supporting diaphragm. After forming the diaphragm, a bottom electrode is deposited with 0.2 µm thick evaporated aluminum, and patterned. A piezoelectric ZnO layer is then deposited with RF sputtering such

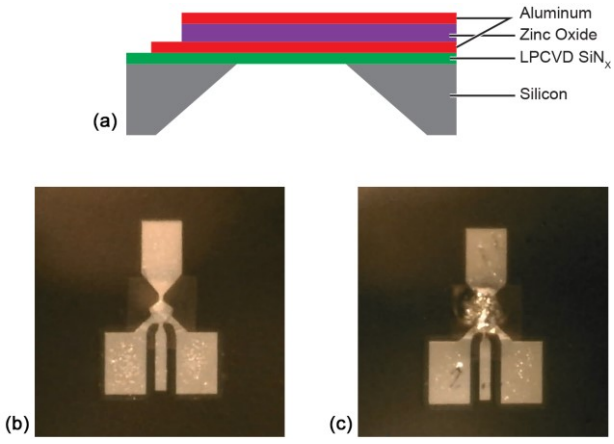

Figure 2. (a) Cross-section diagram of the FBAR device, which is composed of silicon nitride (SiNx), zinc oxide, and aluminum layers on a silicon wafer. (b) Photograph of the FBAR prior to tampering and (c) photograph of the same FBAR after permanent dielectric breakdown induced by tampering.

978-1-940470-03-0/HH2018/$25©2018TRF
DOI 10.31438/trf.hh2018.53

that the thickness is half of the wavelength of the target resonant frequency, for longitudinal waves travelling in bulk ZnO. In this study we target a resonant frequency of 2.6 GHz, which requires a ZnO layer with a thickness of about 0.54 µm. Finally, an aluminum top electrode is deposited and is patterned along with ZnO. The active portion of the resonator, which sits on the supporting diaphragm, has a pentagonal shape in the lateral plane to minimize the lateral resonances and spurious modes. A top view photograph of a completed FBAR is shown in Figure 2b.

The breakdown voltage of the FBAR is determined by the thickness of the FBAR's ZnO layer. For a more sensitive FBAR device that is easier to force into breakdown, it is necessary to increase the interrogation frequency, which limits the interrogation distance and may increase hardware complexity of the interrogator. The top-down photograph of the device after the dielectric breakdown of ZnO is shown in Figure 2c.

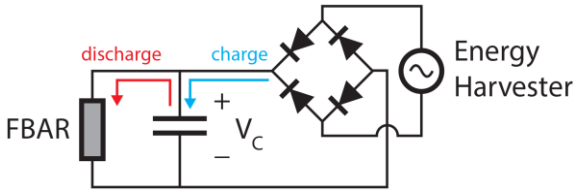

Figure 3. Diagram showing the charging and discharging paths of the energy harvester. An additional capacitor is required to ensure that a sufficient current is developed to permanently breakdown the FBAR and to leverage multiple impacts.

The FBAR is connected with the energy harvester through a full-wave rectifier to ensure a fixed polarity of the potential developed across the FBAR (Figure 3). A capacitor is necessary to accumulate sufficient charge to induce permanent breakdown in the FBAR. This threshold charge was experimentally determined to be a minimum of about 12 µC for a 2.6 GHz FBAR with a minimum threshold voltage applied (5 V). During tampering activity, multiple impacts may be used to remove the IC, so such a capacitor can leverage the multiple voltage peaks generated by the energy harvester to meet the current threshold. The capacitor cannot be too large, however, since the time for charging to the threshold voltage would be too long and also because a large capacitance would complicate impedance matching with the antenna.

We characterized the breakdown of an FBAR with a ZnO thin-film thickness of 0.54 µm with an experimental setup consisting of a Rigol DM3058 for current measurement and a Rigol DP831A for voltage sweeping with a current limit of 2 mA. The breakdown measurements are performed by ramping the applied voltage from zero to 20 V, with sufficient time given at each measurement for the current to stabilize. The results of sweeping the applied voltage and observing the current through a single FBAR are plotted in Figure 4, with error bars indicating the range of leakage currents observed over a period of about 30 seconds.

We can see that dielectric breakdown occurs when about 5 V is applied to the FBAR. Prior to reaching this point, the voltage sweep can be repeated with identical results. Once the breakdown condition of 5 V is reached, the current drawn through the FBAR is consistently elevated above previous low voltage measurements, and the DC resistance drops permanently by about 30 times. But with the current limit from the source, the breakdown does not cause a thermal run away, and the DC resistance increases as the applied voltage is increased until 13 V, at which point we observe a permanent delamination of the electrodes from the FBAR, and the FBAR behaves like an open circuit. This characteristic is repeatably observed in FBARs on a single wafer, but varies with ZnO thickness and quality from batch to batch.

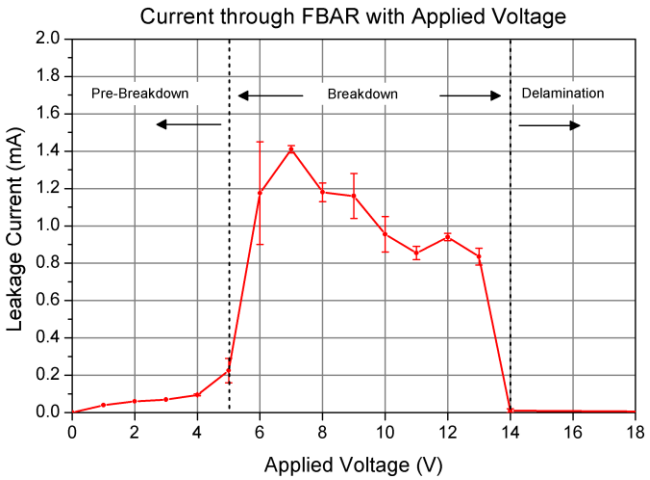

Figure 4. Measured characterization of FBAR breakdown as a function of applied voltage for a Zinc Oxide thickness of 0.54 µm. Breakdown occurs in two phases, with dielectric breakdown occurring at 5 V, and delamination of the metal layer occurring at 13 V. Time-dependent dielectric breakdown occurs in the region between 5 V and 13 V, with delamination occurring given sufficient exposure time.

The breakdown characteristic of the FBAR is time-dependent, consistent with other time-dependent dielectric breakdown mechanisms, such as those in the gate oxide of MOSFETs [4]. This time-dependency can create a breakdown and even delamination at low voltages when exposed over long periods of time, which was observed in 2.6 GHz FBARs when 2 V was applied over a 1 to 2 minute period. In the context of tamper detection, this is not a dependable breakdown mechanism, since pulses supplied by a piezoelectric energy harvester will be short in duration.

The output of piezoelectric energy harvesters is primarily characterized by high voltage and low current. For this reason, we also characterize the breakdown curve as a function of time after applying a voltage step from zero to 20 V (Figure 5). The peak current of 0.141 mA flows through the FBAR, and the current lasts for about 25 ms before the electrodes are delaminated. Integrating this pulse indicates that a total charge of about 1.76 µC is necessary for the FBAR breakdown with a 20 V potential. The total charge necessary for breakdown increases with a reduced voltage peak, and design of a high-voltage output piezoelectric energy harvester is more practical than optimizing current output at low peak voltages.

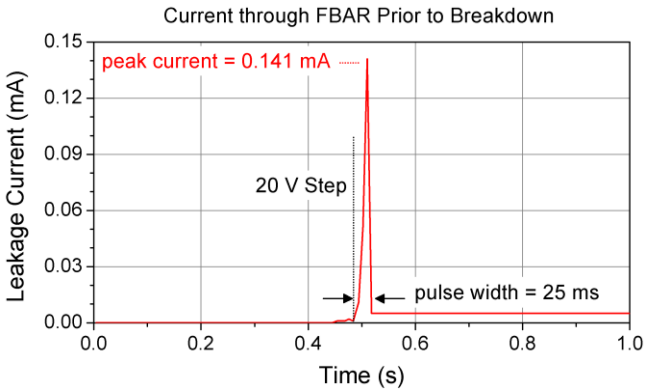

Figure 5. Measured current through FBAR under a step function with a 20 V DC voltage applied. The FBAR draws a current with a peak of 0.141 mA for a duration of 25 ms before permanent breakdown (delamination).

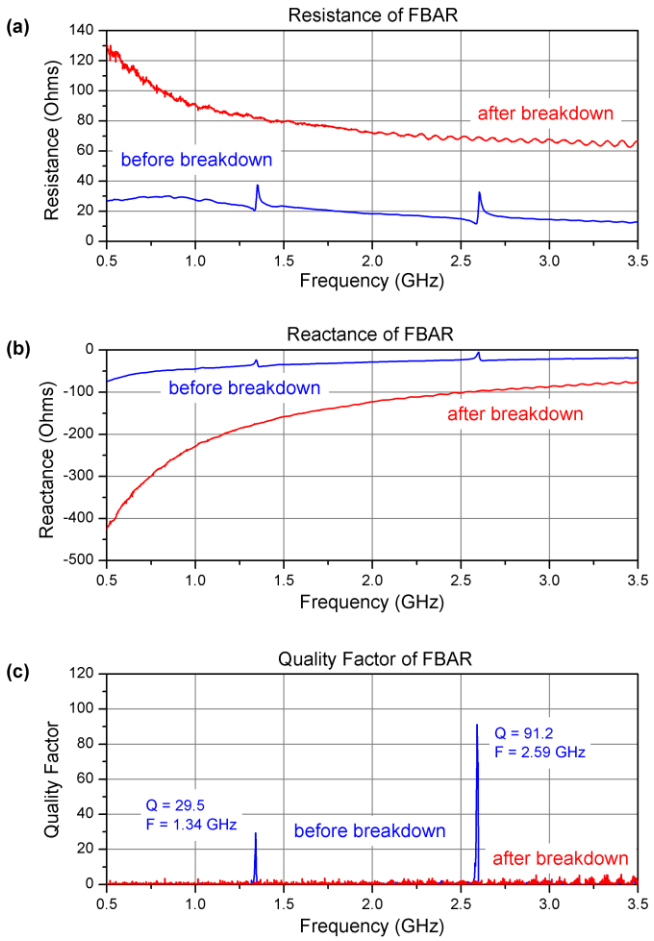

Figure 6. Measured (a) FBAR resistance, (b) FBAR reactance, and (c) estimated quality factor before and after the breakdown of the FBAR, showing a destruction of resonance effects due to tampering.

The high frequency electrical properties of the FBAR are characterized (Figure 6), and the FBAR is measured to have a resonant frequency of 1.34 GHz with a quality factor of 29.5 at the first peak, and a resonant frequency of 2.59 GHz with a quality factor of 91.2 at the secondary peak. After breakdown, the resistance of the FBAR is increased at high frequencies, and the capacitance is reduced.

RFID Antenna

We designed a meandering dipole RFID antenna (Figure 7a) and simulated its electromagnetic characteristics with the SONNET software suite (Figure 7b), to ensure a complementary impedance

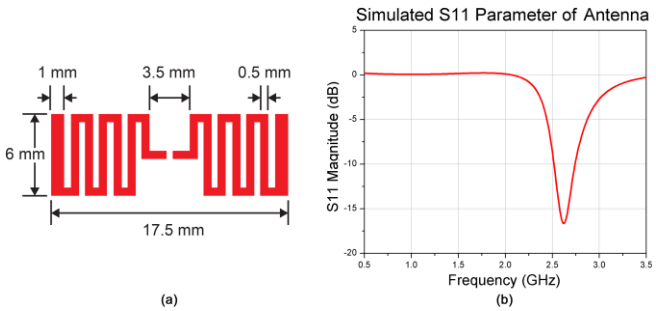

Figure 7. (a) Diagram illustrating the meandering dipole design of the RFID antenna with key dimensions. (b) Simulated S11 parameter of the RFID antenna.

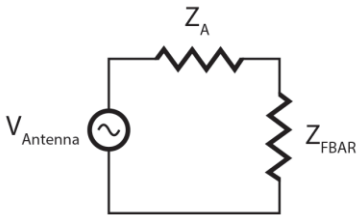

$$P_{re-radiated}=KP_AG$$

$$K=\frac{4R_A^2}{|Z_A+Z_{FBAR}|^2}$$

Figure 8. Circuit diagram showing the method of estimating the backscattered signal power. The re-radiated power is a function of the backscatter coefficient K and the antenna gain G. K is the relative strength of the backscattered power as a function of the antenna impedance and FBAR impedance.

and a matched antenna resonant frequency of 2.6 GHz. To further reduce the dimensions of such a dipole antenna to fit within an IC package, additional meandering can be introduced into the design, for example with spiral loop geometries or fractal geometries [5]. The antenna impedance with this design is primarily capacitive, but can be made more inductive by using T-matching. An alternative antenna design is an inductive loop-based tag, which will provide better impedance matching to the FBAR, but reduce the overall range of the RFID antenna to near-contact.

We estimate the backscattered signal strength using the circuit model shown in Figure 8. From the given expression, we see that the power of the re-radiated signal is dependent on the gain of the antenna, and the backscatter coefficient K. The backscatter coefficient is a function of the antenna impedance and FBAR impedance, with a maximum value achieved when the two are complex conjugates. The estimated impedance of the antenna is obtained from a software simulation, and is applied to the expression along with the measured FBAR parameters to estimate the backscatter coefficient before and after breakdown of the FBAR, shown in Figure 9.

The tag ID in this system is encoded in the spectral signature of the re-radiated signal. Figure 9 shows that the original backscattered signal will have two closely-spaced peaks at 2.59 GHz and 2.70 GHz when the FBAR and antenna are designed to have overlapping frequencies. After the breakdown, the FBAR no longer exhibits high-Q resonance, and the overall capacitance increases. This increases the impedance mismatch between the FBAR and RFID antenna, creating a low-Q peak with a center frequency shifted to 3.04 GHz, and an 11 times weaker maximum backscattered power.

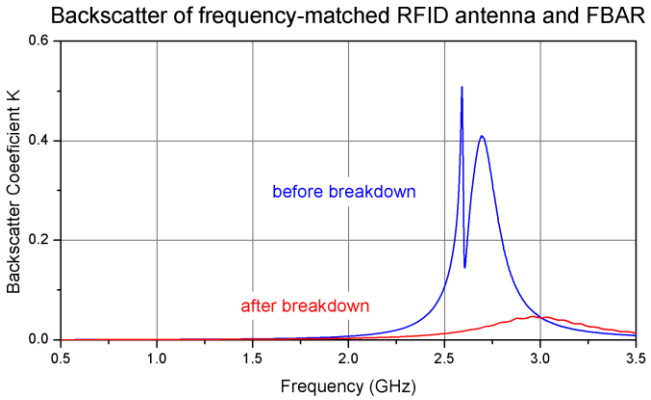

Figure 9. Estimated backscatter coefficient K based on the simulated RFID antenna impedance and measured FBAR impedances before and after the breakdown of the FBAR.

This change in spectral signature can be identified with three receiver measurements of backscattered signal intensity at 2.59 GHz, 2.70 GHz, and the local minimum between them at 2.61 GHz. Common passive RFID interrogators function with tag IDs embedded within time-varying backscattered signals, which are typically implemented with surface acoustic wave (SAW) reflectors or active circuits. However for this application, since the spectral characteristics of the backscattered signal are the coded information that is detected, the RFID interrogator must be implemented to read frequency-encoded tags. Such an encoding scheme has been demonstrated to be effectively interrogated with ultra-wideband pulses [6] and frequency-tunable RFID readers [7].

Energy Harvester

The tamper detection system can be built with an energy harvester based on a piezoelectric PZT bimorph cantilever, fabricated with two bulk PZT layers separated with a spun-on adhesive layer (Figure 10). The energy harvester has dimensions of 11 mm x 1 mm x 0.6 mm, which can be further reduced to fit within a given IC package. With this device, an open circuit voltage of about 2.97 V is measured when 2.6 g acceleration is applied. Since impact pulses of about 50 g are applied during tampering activity, we estimate that the energy harvester will generate about 56 V during the tampering. Since only 5 V is necessary to cause irreversible breakdown of the 2.6 GHz FBAR, there is a sufficient margin for the energy harvester with a similar bimorph geometry to be miniaturized to a such level to be incorporated into IC package. If the generated voltage and current is sufficiently large, the circuit shown in Figure 3 may not be necessary.

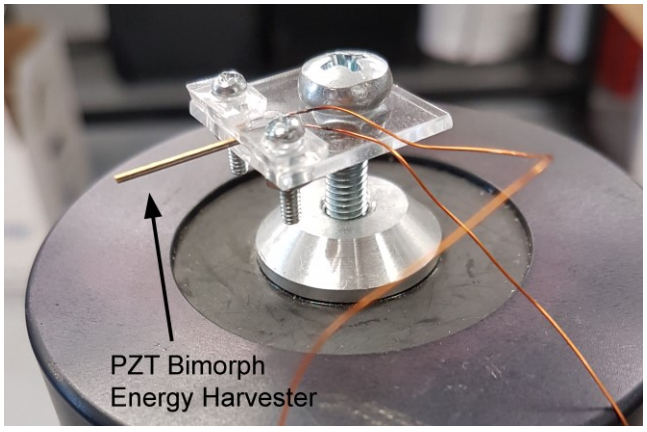

Figure 10. Photograph a bimorph cantilever, clamping system, and shaker. The cantilever has total dimensions of 11 mm x 1 mm x 0.6 mm. Such a cantilever can generate an open circuit voltage of approximately 56 V due to tampering activity.

DISCUSSION

As future work, we aim to integrate this system with a microfabricated energy harvester, such that the entire system can be embedded within a typical IC package. This can be supported by increasing the FBAR resonant frequency to 5 GHz, which would reduce the ZnO thickness of the FBAR and lower the necessary breakdown voltage to about 3 V. This would allow us to relax the constraints on the energy harvester design and further miniaturize the energy harvester. Operating at a higher frequency would also allow miniaturization of the antenna, with the disadvantage of reducing the range for wireless interrogation.

This tamper detection scheme has an advantage over other anti-counterfeiting measures, in that FBAR's exact resonant frequency (which depends on the ZnO thickness) must be known (down to parts-per-thousand level for Q of 1,000) for a counterfeiter to roll-back or duplicate that tamper detection system after the permanent breakdown. Once a tamper detection system is destroyed, the exact resonant frequency cannot be recovered, since ZnO thickness variation over a wafer is typically more than 1%.

A similar tamper detection system could also be implemented with a SAW-based device. Since the resonance frequency of a SAW filter is determined by the spacing of interdigitated electrodes, dielectric breakdown will permanently destroy all surface patterns. Use of SAW filters will also allow integration of reflectors to enable temporally-encoded tag IDs [8].

CONCLUSION

These simulations and measurements are a promising preliminary demonstration of the approach of using dielectric breakdown of FBAR structures for tamper detection in the IC supply chain. Such a detection scheme can be similarly applied for wireless detection of damage during package handling and shipping, and other impact detection applications. The use of this tamper-detection mechanism can also be easily integrated with existing anti-counterfeit measures, such as obfuscation, for more complete protection against many types of attackers.

ACKNOWLEDGEMENT

This work is supported by National Science Foundation under grant CNS-1716953 and Semiconductor Research Consortium under contract 2017-TS-2771.

REFERENCES

[1] F. Koushanfar, et al., "Can EDA Combat the Rise of Electronic Counterfeiting?", Design Automation Conference (DAC) 2012, San Francisco, CA, (2012), pp. 133-138.

[2] D. Shahrjerdi, et al., "Shielding and securing integrated circuits with sensors", Proceedings of the 2014 IEEE/ACM International Conference on Computer-Aided Design, 2014.

[3] J. English, et al., "MEMS-assisted cryptography for CPI protection", IEEE Security & Privacy, (2007).

[4] C.H. Ho, S.Y. Kim, and K. Roy. "Ultra-thin dielectric breakdown in devices and circuits: A brief review.", Microelectronics Reliability 55.2, (2015), pp. 308-317.

[5] G. Marrocco, "The art of UHF RFID antenna design: Impedance-matching and size-reduction techniques", IEEE antennas and propagation magazine, 50.1, 2008.

[6] P. Kalansuriya, N.C. Karmakar, and E. Viterbo, "On the detection of frequency-spectra-based chipless RFID using UWB impulsed interrogation", IEEE Transactions on Microwave Theory and Techniques, (2012).

[7] S. Preradovic, and N.C. Karmakar, "Multiresonator based chipless RFID tag and dedicated RFID reader." Microwave Symposium Digest, 2010.

[8] V. P. Plessky, and L. M. Reindl, "Review on SAW RFID tags", IEEE transactions on ultrasonics, ferroelectrics, and frequency control 57.3, 2010.

CONTACT

*A.A. Shkel, tel: +1-949-394-9040; shkel@usc.edu

THE EFFECT OF BIAS CONDITIONS ON ALGAN/GAN 2DEG HALL PLATES

Karen M. Dowling[*1], *Hannah S. Alpert*[1], *Pengxiang Zhang*[2], *Andrea N. Ramirez*[1], *Ananth Saran Yalamathy*[1], *Helmut Köck*[3], *Udo Ausserlechner*[3], *and Debbie G. Senesky*[1]

[1]Stanford University, Stanford, California, USA, [2]Tsinghua University, China, and [3]Infineon Technologies AG, Villach, Austria

ABSTRACT

This paper describes the operation of AlGaN/GaN two-dimensional electron gas (2DEG) Hall plates under various supply conditions (0.026 V to 1.27 V). The 100-µm-diameter octagon-shaped devices were microfabricated using metal-organic chemical vapor deposition of AlGaN/GaN on <111> silicon wafers and traditional photolithography techniques. Upon device characterization at various Hall supply voltages, we observed an increase in the residual offset from 0.1 mT to 1.4 mT (from 9% of measured signal to over 60% in a 1 mT magnetic field). In addition, the sensitivity (scaled with bias voltage) was constant at 76 ± 2.5 mV/V/T (stable within 3%) with high linearity ($R^2 > 0.99$) across the tested operating conditions. This work demonstrates improved understanding of AlGaN/GaN sensor elements that may be monolithically integrated with power electronics, as well function within extreme environments.

INTRODUCTION

Hall-effect devices are used in diverse sensing applications such as position and velocity sensors in automobiles and current sensing in power electronics [1]. However, silicon-based Hall-effect sensors have limitations in extreme environments because of the influence of temperature on intrinsic carrier concentration – low-doped materials (< 10^{16} cm^{-3}) become saturated with carriers around 300°C. Recently, two-dimensional electron gas (2DEG) material systems, including AlGaN/GaN, have gained high interest for power electronics monitoring and extreme environment sensing due to their durable nature, wide bandgap, and potential for monolithic integration with electronics [2]. Additionally, piezoelectric and spontaneous polarization create a stable 2DEG carrier concentration across a wide temperature range [3], which enables robust Hall-effect sensing [4], [5]. However, sensing low magnetic field signatures (< 10 mT) under high bias conditions has not been investigated with AlGaN/GaN 2DEG Hall plates.

The Hall-effect can be leveraged for sensing magnetic field signatures through a 4-probe scheme. Constant current is applied across two contacts, and the induced electric potential from the external magnetic field is measured by a Hall voltage reading on the other two contacts. AlGaN/GaN 2DEG plates are promising candidates for Hall-effect sensing because of their high mobility (~2200 $cm^2/V{\cdot}s$) [4] and high temperature stability.

In applications with low magnetic field levels, sensors are required to have high signal accuracy to overcome issues with background fields such as Earth's field or from electromagnetic interference. Hall devices generally have high raw offset values (larger than Earth's magnetic field of 50 µT) when no external magnetic field is applied due to inherent material defects or from various steps in microfabrication [6], [7]. This limits the minimum detectable signal to inconvenient ranges and reduces sensor accuracy. To overcome this issue, current spinning [7] and orthogonal layouts [8] have been adopted in practice to remove these "raw" offsets for silicon devices. These techniques can reduce the raw offset to a "residual" offset below 10 µT under various conditions [6], [7], [9], [10], corresponding to an improvement by a factor of up to 4,000.

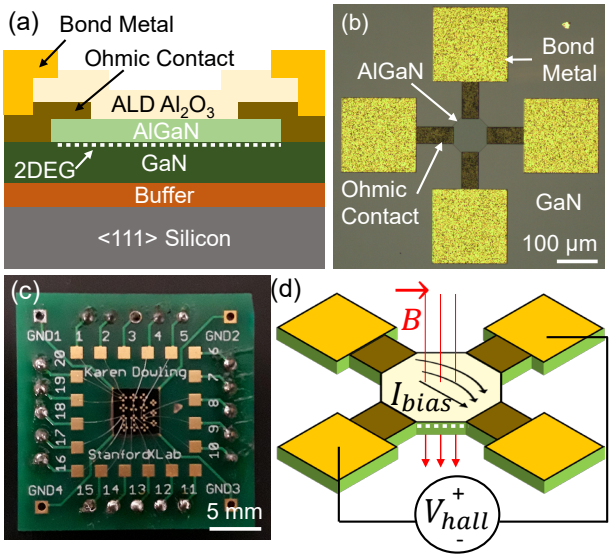

Figure 1: (a) Cross sectional schematic of the AlGaN/GaN 2DEG Hall plate. (b) Optical image of the 2DEG Hall plate with 4 contacts (no top plate). (c) Packaged Sensor #1 for testing with floating substrate. (d) Device operation. Constant current is applied across a 4-contact van der Pauw structure and the Hall voltage is measured across the other two contacts.

In addition to low residual offset values, sensors are also required to have high sensitivity in many applications. Sensitivity is defined as a ratio of the change in Hall voltage (V_{Hall}) due to an external magnetic field (B). It is well known that the Hall voltage scales with supply voltage (or current), so most reports show either sensitivity scaled with supply current (S_I) or sensitivity scaled with supply voltage (S_V). However, in most applications, Hall plates are operated with a constant supply voltage to enable ease of integration with interface circuitry.

In this paper, we present the methodology for Hall-effect sensor microfabrication and characterization with a current spinning technique to study offset values in low magnetic fields (<5 mT). We also examine the sensitivity and residual offset in AlGaN/GaN 2DEG Hall plates as influenced by supply voltage. We observed that the sensor exhibited large residual offset values (60% of the signal in a 1 mT field) under high supply voltage conditions, as well as a constant sensitivity of 76 ± 2.5 mV/V/T. A discussion on the leading contributions to residual offset in these high bias schemes is provided. It should be noted that the AlGaN/GaN Hall-effect sensors have higher sensitivity values compared to silicon-based Hall plates and with proper offset calibration can be used over a large temperature range for extreme environments.

METHODOLOGY

Fabrication

To study the effect of bias conditions on AlGaN/GaN 2DEG Hall plate performance, we examined two devices (4-contact van der

978-1-940470-03-0/HH2018/$25©2018TRF
DOI 10.31438/trf.hh2018.54

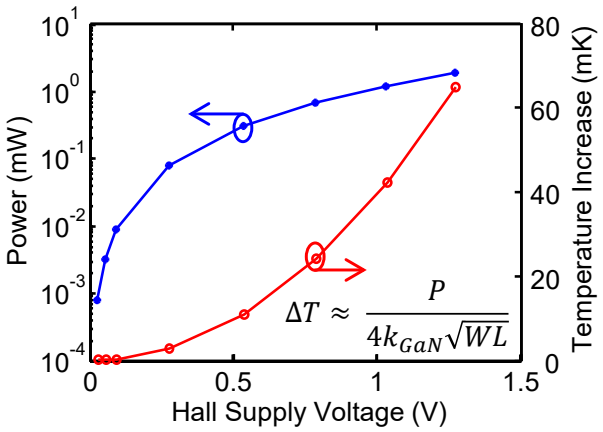

Figure 2. Average operating power of 2DEG Hall plates under various supply voltages, and expected average temperature increase along current path from thermal resistance approximation.

Pauw structures) from different chips. Fig. 1 shows a cross-sectional schematic of the 2DEG Hall plate (Fig. 1a). To microfabricate the device, AlGaN/GaN films were grown on <111> silicon using metal-organic chemical vapor deposition (MOCVD). Then, a 100-µm-diameter octagon mesa with Ti/Al/Pt/Au Ohmic contacts and a 50-nm-thick alumina passivation layer was microfabricated (Fig. 1b) [11]. The Hall plate device was then bonded to a printed circuit board (PCB) with epoxy and electrically connected with aluminum wirebonds. The packaged device is shown in Fig. 1c. The two tested devices have lateral resistances (R) of 867 ± 22 Ω and 896 ± 30 Ω (variation among bias conditions) and the operating power rose from 0.83 µW to as high as 1.91 mW (Fig. 2).

Experimental Set Up

The sensor's principle of operation is shown in Fig. 1d. To characterize the sensitivity of the device, current was applied with a Keithley 2400 current source from 30 µA to 1.5 mA, which correspond to average supply voltages of 0.026 V to 1.2 V. The Hall voltage was then measured with a multimeter (Agilent 34401A). Current spinning was used to suppress offset errors [6] with an Agilent U2715A switching matrix (1 s/measurement).

A magnetic field was applied using a home-built and calibrated Helmholtz coil (up to ±5 mT) inside a zero-field Mu-metal® chamber. Finite element modeling (FEM) with COMSOL® was leveraged to design a compact Helmholtz coil system to apply magnetic fields from -5 to 5 mT within 1 A of supply current (Fig. 3a). Once the design was selected, a 3D-printed scaffold was made to support the hand-wound coils. Each coil pictured in Fig. 3b is 250 turns of copper wire in a 1x1 cm cross-section. The Hall sensor is placed in the center of the coils through the top of the scaffold with a custom sample holder (not pictured). Since the fields being measured are relatively small, the entire setup was placed within three concentric magnetic shielding canisters made of MuMetal®. This shielding reduced the background field to ~6 µT, checked with a gaussmeter (1 nT resolution) from AlphaLab, Inc. The vertical coil pair, which was used in this study, was calibrated with another gaussmeter (1 µT resolution, ±80 mT range) from AlphaLab, Inc. Once assembled, the entire set up was controlled using LabView (National Instruments) to control the current spinning, measurements, and magnetic field (Fig. 3c).

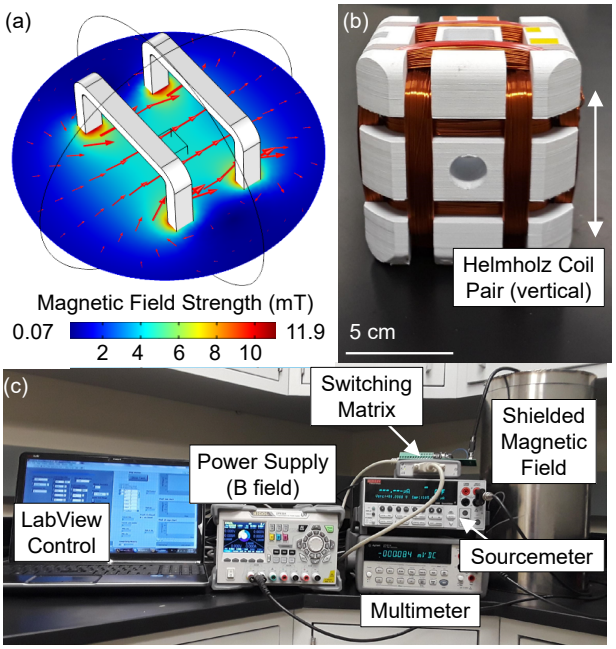

Figure 3. (a) Finite element model of the magnetic field profile from a Helmholtz coil with 250 turns of 9 x 9 cm of copper wire powered at 1 A. (b) Home-made Helmholtz coil pair using a 3D printed scaffold. (c) Complete test setup, the Helmholtz coil scaffold sits inside the shielding canisters.

RESULTS

Hall Voltage

The net Hall voltage after current spinning is plotted with respect to magnetic field in Fig. 4a and the residual offset was calculated from the x-intercept of the linear fit of these curves. Ideally, the x-intercept should be near zero, which would indicate a high accuracy sensor. However, the increased supply power seems to cause an additional offset that cannot be canceled with current spinning. Visualizing the data from another perspective (Fig. 4b), the Hall voltage is compared to the supply voltage directly. It can be clearly seen that the data is skewed with a positive Hall voltage, especially at higher supply voltages as indicated in Fig. 4b. When this offset voltage is removed from the measured data, the resulting calibrated data show Hall voltages linear with supply voltage. This further confirms the need for Hall calibration at high supply bias on the devices.

Sensitivity

Voltage-scaled sensitivity (S_V) for the two devices is shown in Fig. 5. S_V was constant at 76 ± 2.5 mV/V/T, which is within 3% and has high linearity with respect to magnetic field. The small variations are subject to the power supply variation and slightly non-Ohmic nature of some sensor contacts, which would affect the average supply voltage. Current-scaled sensitivity (S_I), similarly measured, is around 68 V/A/T ± 1.3 V/A/T. From these values, the sheet density was calculated to be 9.3 x10^{12} cm^{-2} and the mobility was calculated to be around 1635 $cm^2/V{\cdot}s$. These values agree with similar 2DEG characteristics from previously reported values for AlGaN/GaN Hall plates [4], [5], [12]. Since the sensor shows relatively stable sensitivity, the residual offset must be addressed to enable AlGaN/GaN 2DEG Hall plates for extreme environment sensing.

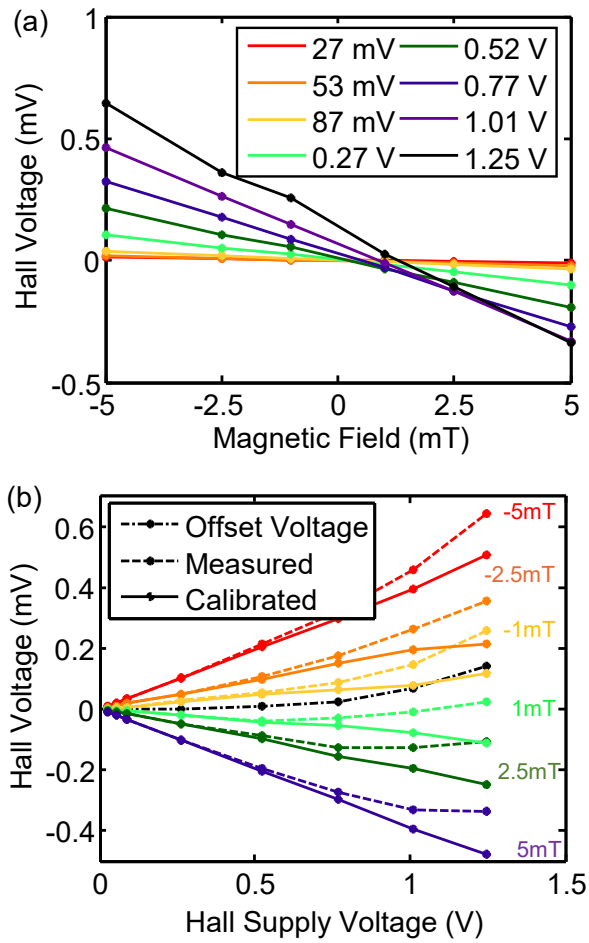

Figure 4. (a) Hall output voltages under varied magnetic fields and Hall supply current of sensor #1. (b) Hall output voltages before and after calibration by removal of residual offset voltage at each magnetic field condition.

Residual Offset

The residual offset is defined as the magnitude of magnetic field that is read in a zero-field. The x-intercepts from Fig. 4a are shown in Fig. 5. Here, the 2DEG Hall plates have residual magnetic offset values that are quadratically proportional to the supply voltage. Fig. 5 shows that a residual offset as high as 1.4 mT is present at 1.25 V, which is over 60% of the measured signal at $B = 1$ mT. These results will be further examined in the discussion section below.

DISCUSSION

The residual offset increases with supply voltage as a function of V^2. There are many possible physical mechanisms that contribute to the increase in residual offset with supply voltage. The potential contributions to the nonlinear offset are summarized in Table 1 [6], [7], [11], [13]–[15] and are discussed in this section in detail.

The first contribution is due to thermoelectric effects from self-heating. The increase in supply voltage (and supply current) corresponding to an increase in operating power of the Hall plate. Power (P) increases with V^2/R (and I^2R), which causes the device to increase in temperature (ΔT). The device is an octagonal Hall plate, but the highest current concentration is across the supply contacts, so the majority of heating occurs across the octagon length (L) and

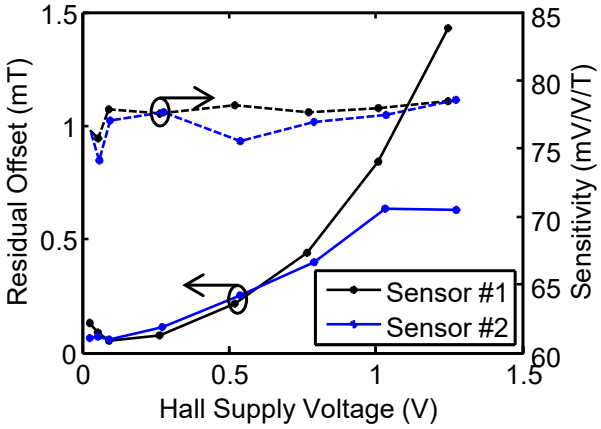

Figure 5. Residual magnetic offset of two AlGaN/GaN 2DEG Hall plates under varied bias voltages. Sensitivity (scaled with Hall supply voltage) under various supply voltages on the secondary axis.

Table 1. Possible contributions to increase in residual offset with high bias conditions.

Offset Source	Explanation
Seebeck Voltage	Increase in residual offset directly proportional to input power, combined with inhomogenous current density around defects and contacts causes localized heating [11], [13], [14]
Buffer effect	Underlying GaN substrate induces Hall voltage prominent at higher bias conditions. [6]
Packaging	Thermal and mechanical stress in substrate and packaging from high bias operation[7]Also induced magnetic fields from bond wires [15]
Asymmetry	Linear imbalance due to geometrical asymmetries is removed with current spinning, Nonlinear effects remain [7]

contact width (W). Using Eq. (1),

$$\Delta T = \frac{P}{4k_{GaN}\sqrt{WL}}, \qquad (1)$$

an estimated average temperature rise of at least 65 mK in the current path is expected, assuming an in-plane thermal conductivity (k_{GaN}) of 115 W/m·K [11]. AlGaN/GaN 2DEG devices have been recently reported to have a lateral Seebeck coefficient of 120 μV/K [11] at room temperature. Thus, the thermal gradients generated in the Hall plate from high supply voltages could be generating an additional voltage measured on the Hall contacts, regardless of measurement orientation or external magnetic field direction.

The second potential contribution to residual offset could be due to underlying material buffers. Larger supply voltages (and currents) could start to cause a portion of the current to flow through underlying buffer structures (Fig. 1a). When the current values get large enough, this buffer could be causing an additional contribution of Hall voltage to the sensor. However, the Hall plate still has constant S_V at high supply voltage, and a buffer component would alter the sensitivity, which is not seen here.

A third potential source of the residual offset could be from packaging. Strain has been reported to cause an increase in residual offset in silicon devices, due to the directional change in resistance from its asymmetric piezo-resistive components. Analogously, the

AlGaN/GaN 2DEG forms from a combination of spontaneous and piezoelectric polarization, so any strain from packaging could cause local changes in the 2DEG concentration, and thus would contribute to resistance asymmetry. In addition to packaging stress, these sensors were electrically connected using wirebonding with different wire layouts. At higher supply power, the induced magnetic field of the wirebonds could interfere with the device measurement. However, simple finite element modeling predicts this additional external field to be around 12 μT when supplied with 1 V, much smaller than the measured conditions.

The final contribution mechanism considered here is the linear imbalance from fabrication. Current spinning successfully removes linear offsets in contact resistance from lithography misalignment. However, nonlinear differences in contact resistance from misalignment remain (ΔR is not constant between measurement phases). Our sensors had up to 60 Ω difference between the orthogonal current paths in the sensor, which is around 7% change between lateral and longitudinal directions of current spinning. This could contribute to a nonlinear offset in V_{Hall} that scales with increased current. This could be improved with tighter fabrication tolerances in future work.

CONCLUSION

Here, we presented work on AlGaN/GaN 2DEG Hall plates with high, stable sensitivity values, which match results of Si-based Hall plates found in the literature and even slightly better sensitivity due to higher electron mobility. Current spinning was used to reduce the offset voltages, but there were large residual offsets when biased with a large supply voltage. This is particularly problematic when operating to sense small magnetic fields (<5 mT). While AlGaN/GaN sensors are of interest for extreme environment applications, these electrical operation conditions need to be further understood for proper calibration and use. We discussed some key factors that cause residual offsets, including self-heating and nonlinear contact resistance asymmetry. Future work should focus on reducing the causes of large signal offset to enable improved sensing capability. Regardless, this work confirms that AlGaN/GaN 2DEG Hall plates could be used as magnetic field sensors and offers a monolithically integrated sensing solution for GaN power electronics, as well as harsh environment operation.

ACKNOWLEDGEMENTS

This work was supported in part by the National Science Foundation (NSF) Engineering Research Center for Power Optimization of Electro Thermal Systems under Grant EEC-1449548, National Science Foundation Graduate Research Fellowship under Grant DGE-114747, and Stanford SystemX Alliance. The microfabrication process used in this paper was conducted in the Stanford Nanofabrication Facility (SNF) at Stanford University. The authors would like to thank the staff of the SNF, Ricardo Peterson, and Maximillian Holliday for their support.

REFERENCES

[1] H. P. Baltes and R. S. Popovic, “Integrated Semiconductor Magnetic Field Sensors,” Proc. IEEE, 74, 8, (1986), pp. 1107–1132.

[2] D. G. Senesky, H. So, A. J. Suria, A. S. Yalamarthy, S. R. Jain, C. A. Chapin, H. C. Chiamori, and M. Hou, “Gallium Nitride Microelectronics for High-Temperature Environments,” in Semiconductor-Based Sensors, World Scientific, (2016), pp. 395–433.

[3] N. Maeda, K. Tsubaki, T. Saitoh, and N. Kobayashi, “High-temperature electron transport properties in AlGaN/GaN heterostructures,” Appl. Phys. Lett., 79, 11, (2001), pp. 1634–1636.

[4] H. Lu, P. Sandvik, A. Vertiatchikh, J. Tucker, and A. Elasser, “High temperature Hall effect sensors based on AlGaN/GaN heterojunctions,” J. Appl. Phys., 99, (2006), pp. 114510:1-4.

[5] S. Koide, H. Takahashi, A. Abderrahmane, I. Shibasaki, and A. Sandhu, “High temperature hall sensors using AlGaN/GaN HEMT structures,” J. Phys. Conf. Ser., 352, 1, (2012), pp. 012009:1-4.

[6] U. Ausserlechner, “Limits of offset cancellation by the principle of spinning current hall probe,” Proc. IEEE Sensors, (2004), pp. 1117–1120.

[7] P. J. A. Munter, “A low-offset spinning-current hall plate,” Sensors Actuators A. Phys., 22, 1–3, (1989), pp. 743–746.

[8] J. C. van der Meer, F. R. Riedijk, E. van Kampen, K. A. A. Makinwa, and J. H. Huijsing, “A fully integrated CMOS Hall sensor with a 3.65μT 3σ offset for compass applications,” IEEE Int. Solid-State Circuits Conf. ISSCC, (2005), pp. 246–247.

[9] G. S. Randhawa, “Monolithic integrated Hall devices in silicon circuits,” Microelectronics J.,12, 6, (1981), pp. 24–29.

[10] S. Bellekom and L. Sarro, “Offset reduction of Hall plates in three different crystal planes,” Proc. Int. Conf. Solid-State Sens., Actuators Microsys. TRANSDUCERS, 1, (1997), pp. 233–236.

[11] A. S. Yalamarthy, H. So, M. M. Rojo, A. J. Suria, X. Xu, E. Pop, and D. G. Senesky, “Tuning Electrical and Thermal Transport in AlGaN/GaN Heterostructures via Buffer Layer Engineering,” Adv. Funct. Mater., In Press (2018).

[12] T. P. White, S. Shetty, M. E. Ware, H. A. Mantooth, and G. J. Salamo, “AlGaN / GaN Micro-Hall Effect Devices for Simultaneous Current and Temperature Measurements from Line Currents,” IEEE Sens. J., PP, (2018), pp. 1–8.

[13] R. Aubry, J. C. Jacquet, J. Weaver, O. Durand, P. Dobson, G. Mills, M. A. di Forte-Poisson, S. Cassette, and S. L. Delage, “SThM temperature mapping and nonlinear thermal resistance evolution with bias on AlGaN/GaN HEMT devices,” IEEE Trans. Electron Devices, 54, 3, (2007), pp. 385–390.

[14] K. L. Grosse, M. H. Bae, F. Lian, E. Pop, and W. P. King, “Nanoscale Joule heating, Peltier cooling and current crowding at graphene-metal contacts,” Nat. Nanotechnol., 6, 5, (2011), pp. 287–290.

[15] P. Ruther, U. Schiller, R. Janke, and O. Paul, “Thermomagnetic residual offset in integrated Hall plates,” IEEE Sens. J., 3, 6, (2003) pp. 693–699.

CONTACT

*K.M.Dowling, tel: +1-734-883-5131; kdow13@stanford.edu

TRENCH-ISOLATED BULK-TYPE PRESSURE SENSOR ON SILICON-ON-INSULATOR FOR HIGH-TEMPERATURE AND HIGH-PRESSURE DOWNHOLE APPLICATIONS

Elena Chan[1], Dequan Lin[1, 2, 3], Lei Lu[1, 4], Kevin Chau[1, 2], and Man Wong[1]
[1] The Hong Kong University of Science and Technology, Hong Kong, China
[2] The Institute of Geology and Geophysics, Chinese Academy of Sciences, Beijing, China
[3] The University of Chinese Academy of Sciences, Beijing, China
[4] The HKUST Jockey Club Institute for Advanced Study, Hong Kong, China

ABSTRACT

Presently reported is a dielectric-isolated bulk-type pressure sensor fabricated on silicon-on-insulator (SOI) that offers higher pressure capability than conventional diaphragm-type pressure sensors and wider temperature operating range than a recently reported junction-isolated bulk-type pressure sensor. The isolated piezoresistors are realized on the SOI device layer via trench etching and oxidation. Two types of trenches are formed: narrow ones that are completely filled with silicon dioxide and wide ones that are thermally oxidized on the sidewalls but partially filled. The pressure sensitivity is enhanced by relieving the transverse stress acting on selected piezoresistors isolated with the wide trenches.

INTRODUCTION

Resonant quartz pressure sensor (Fig. 1a) currently sets the benchmark for downhole pressure measurements. While MEMS pressure sensor with its relatively low cost and small size has the potential to replace the resonant quartz pressure sensor, it is still hindered by a number of limitations. A recent attempt [1] has been made to address some of the issues by replacing the conventional diaphragm-type with a bulk-type pressure sensor to handle the targeted high-pressure load (≥ 200 MPa), but the junction-isolation of the piezoresistors must be replaced by the presently demonstrated dielectric-isolation to handle the anticipated high operating temperature (≥ 200 °C).

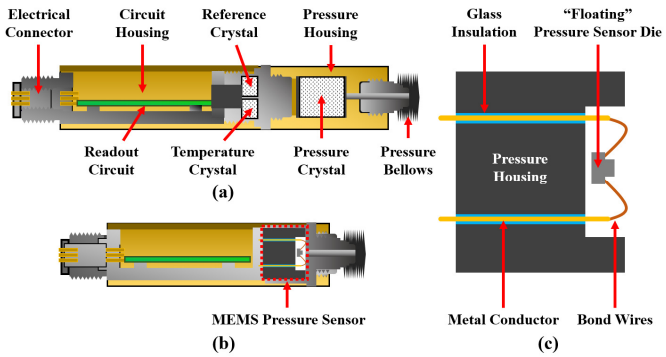

Figure 1: (a) Schematic diagram of a resonant quartz pressure sensor package. (b) Schematic diagram showing the quartz crystals replaced by a MEMS pressure sensor. (c) Magnified schematic of the MEMS pressure sensor die suspended by bond wires.

A higher pressure sensitivity is desirable for reducing the electrical offset and its associated temperature coefficient. To achieve this, selective trenching of the piezoresistors to release specific stress components is explored. In addition, the package-induced stress that ultimately determines sensor repeatability, hence compensability, must also be minimized. Presently proposed is a MEMS pressure sensor designed as a direct drop-in replacement of the quartz resonator capsule in an inconel package that is proven for downhole applications (Fig. 1b). The MEMS sensor die is suspended only by its bond wires, hence largely relieved of the package-induced stress (Fig. 1c). This potentially allows accurate temperature compensation, despite the temperature coefficient of a piezoresistive silicon sensor being intrinsically two orders of magnitude higher than that of a resonant quartz sensor.

PRINCIPLE OF OPERATION

The bulk-type pressure sensor is formed by eutectically bonding a [110]-oriented SOI sensor wafer and a cap wafer under vacuum (Fig. 2). Two orthogonal pairs of piezoresistors respectively aligned to the [001] and [1$\bar{1}$0] orientations are realized in the center region on the sensor-side of the vacuum cavity and electrically configured to form a Wheatstone bridge.

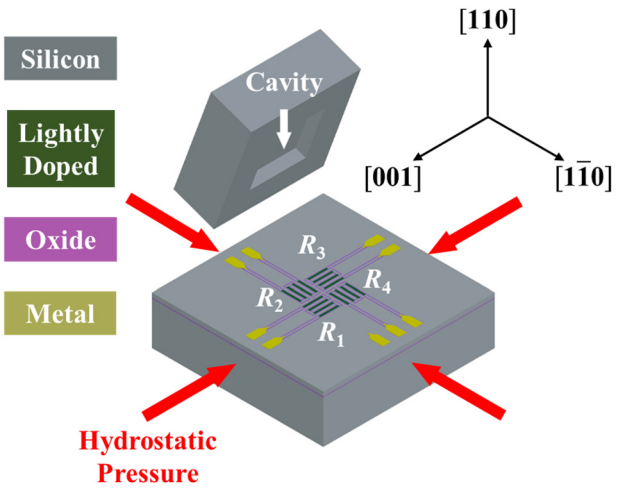

Figure 2: Bulk-type pressure sensor schematically shown with the cap die separated from the SOI sensor die.

The relative change of the resistivity $\Delta\rho'_{11}/\rho$ along the longitudinal direction of a piezoresistor is given by [2]

$$\frac{\Delta\rho'_{11}}{\rho} = \pi'_{11}\sigma'_{11} + \pi'_{12}\sigma'_{22} + \pi'_{16}\sigma'_{12} \approx \pi'_{11}\sigma'_{11} + \pi'_{12}\sigma'_{22}, \quad (1)$$

where π'_{11}, π'_{12} and π'_{16} are the respective longitudinal, transverse and shear piezoresistive coefficients and σ'_{11}, σ'_{22} and σ'_{12} are the respective longitudinal, transverse, and shear stress components. Furthermore, σ'_{12} is small enough to be neglected under hydrostatic pressure loading conditions [2].

978-1-940470-03-0/HH2018/$25©2018TRF
DOI 10.31438/trf.hh2018.55

For the piezoresistors isolated and bound by the completely-filled narrow trenches, the relative change in the longitudinal resistivity is given by (1). For those isolated by the partially-filled wide trenches, σ'_{22} can be largely relieved by a proper design of the trench dimensions, thus reducing the biaxial stress field to a uniaxial stress field. In this case, the relative change in the longitudinal resistivity is given by

$$\frac{\Delta\rho'_{11}}{\rho} \approx \pi'_{11}\sigma'_{11}. \qquad (2)$$

A 2-dimensional finite-element analysis was carried out to investigate the dependence of σ'_{22} on the dimensions of the trench and the piezoresistor (Fig. 3). It is concluded that the width w of the piezoresistor should be ≤ 3 times the depth h of the trench in order to effectively relieve the transverse stress σ'_{22} on the piezoresistor.

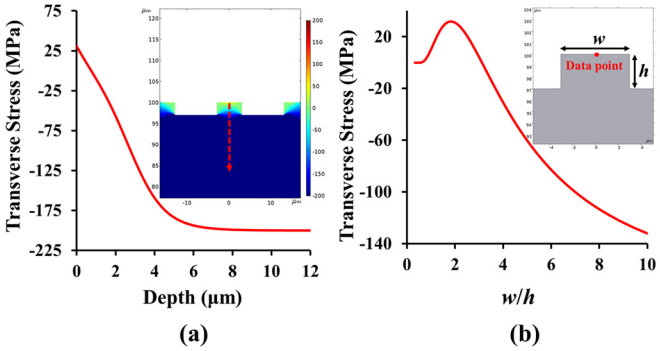

Figure 3: 2-dimensional finite-element analysis of a trenched piezoresistor under 200-MPa lateral compression. (a) The transverse compressive stress is plotted along the dotted path from the top and (b) the dependence of the transverse stress on w/h at the top of a piezoresistor defined by two wide trenches.

Under an applied hydrostatic pressure P of 200 MPa, the simulated values of $\sigma_{[1\bar{1}0]}$ and $\sigma_{[001]}$ are respectively −126 and −100 MPa around the center of the die where the piezoresistors are located [2]. The relative sensitivity of the pressure sensor, estimated and summarized in Table I, is proportional to the magnitude of the difference $\left|\Delta\left(\frac{\Delta\rho}{\rho}\right)\right|$ between the $\frac{\Delta\rho}{\rho}$ of the two orthogonal pairs of piezoresistors: R_1 and R_3 aligned to the [001] orientation, and R_2 and R_4 aligned to the $[1\bar{1}0]$ orientation.

Table I: Relative pressure sensitivity $\left|\Delta\left(\frac{\Delta\rho}{\rho}\right)\right|$ for all combinations of wide and narrow trenches in both p- and n-type piezoresistors.

R_1, R_3	R_2, R_4	$\left\|\Delta\left(\frac{\Delta\rho}{\rho}\right)\right\|$ (%) (p-Type)	$\left\|\Delta\left(\frac{\Delta\rho}{\rho}\right)\right\|$ (%) (n-Type)
Wide	Wide	8.4	6.3
Narrow	Narrow	8.4	4.9
Narrow	Wide	8.5	0.4
Wide	Narrow	8.3	11.6

It can be seen that wide and narrow trenches have little impact on the pressure sensitivity for an implementation with p-type piezoresistors. The impact is, however, significant for an implementation with n-type piezoresistors for which the highest sensitivity is obtained by having wide trenches on R_1 and R_3, and narrow trenches on R_2 and R_4. With this configuration the sensitivity of an implementation using n-type piezoresistors can be ~1.4 times higher than that of an implementation using p-type piezoresistors.

A schematic layout of the sensor and trench designs for the best n-type piezoresistor configuration is shown in Fig. 4. Implemented are R_1 and R_3 defined by 10-μm wide trenches, and R_2 and R_4 by 1-μm narrow trenches.

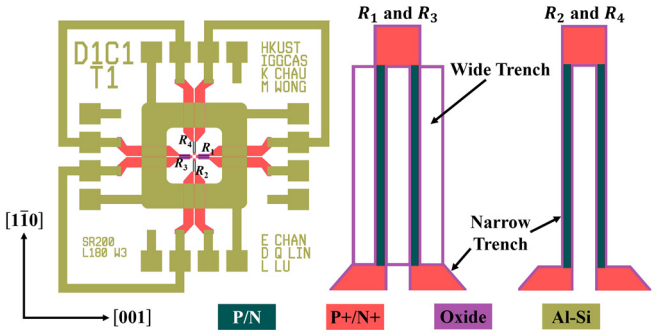

Figure 4: Sensor layout showing piezoresistors R_2 and R_4 defined by completely-filled narrow trenches and piezoresistors R_1 and R_3 defined by partially-filled wide trenches for the relief of the transverse stress.

FABRICATION

Sensor fabrication started with an SOI wafer with a 3-μm thick [110]-oriented device layer. 1-μm and 10-μm wide trenches were etched on the device layer reaching the buried oxide layer (Fig. 5a). These were subsequently oxidized to define the piezoresistor active areas. Incidentally, a small notch (Fig. 6) was formed on the top of the oxide-filled narrow trenches resulting from the oxidation process. A blanket boron implantation at an energy of 27 keV and dose of 2.6×10^{15} cm^{-2}, and a second selective boron implantation at the same energy but a higher dose of 2×10^{16} cm^{-2} were performed, respectively to adjust the doping level of the p-type piezoresistors and to form the P+ electrical leads (Fig. 5b). A 200-nm thick cover silicon dioxide was then deposited by low-pressure chemical vapor deposition, prior to the activation of the implanted dopants at 1000 °C for 30 min. Contact holes were opened through the cover oxide layer and a 1.5-μm aluminum-silicon (Al-Si) alloy was deposited and patterned to form the contact pads and the bond ring for the subsequent aluminum-germanium (Al-Ge) eutectic bonding.

A separate silicon cap wafer was prepared, on which 200-μm deep cavities were formed using deep reactive-ion etching and subsequently covered with a 500-nm thick evaporated Ge (Fig. 5c). Eutectic bonding of the device and cap wafers (Fig. 5d) was carried out under a force load of 40 kN at 430 °C for 5 min in vacuum. The eutectic melt was able to overcome the topography of the small notch, thus resulting in hermetic sealing of the cavity. The 2.5×2.5 mm^2 sensor die (Fig. 7) was packaged after dicing and tested in a custom setup [2].

The same process could be applied to fabricate sensors with n-type piezoresistors by changing the implanted species from boron to phosphorus, energy to 50 keV, and implant doses to 10^{15} and 10^{16} cm^{-2}, respectively, for the piezoresistors and the N+ electrical leads.

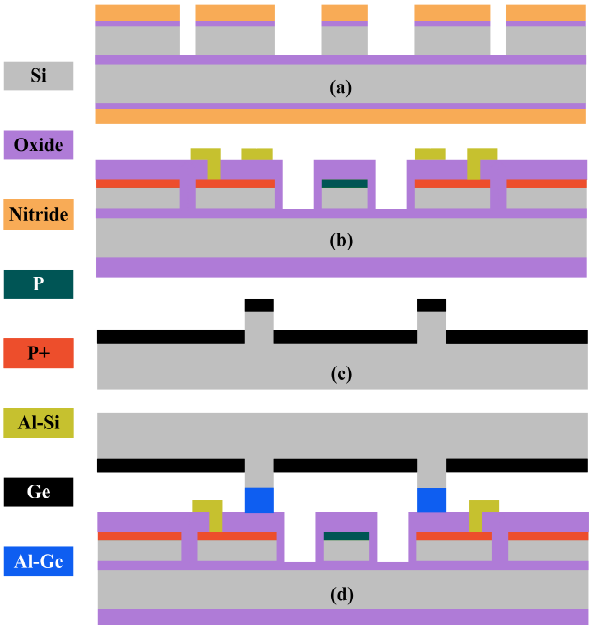

Figure 5: Schematic cross-sections illustrating the fabrication of the SOI pressure sensor having piezoresistors with narrow and wide trenches. (a), (b) SOI wafer, (c) cap wafer, and (d) Al-Ge bonding.

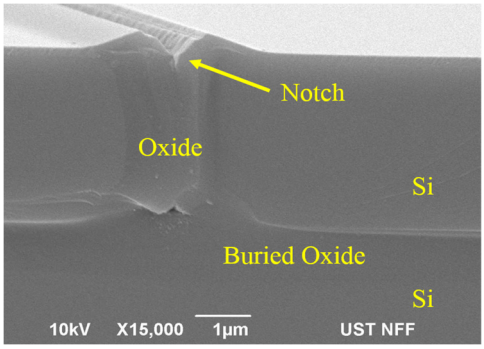

Figure 6: SEM micrograph of the oxide-filled narrow trench.

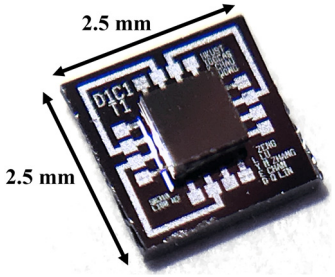

Figure 7: Photomicrograph of the fabricated SOI pressure sensor die.

TEST RESULTS

SOI pressure sensor with p-type piezoresistors was first realized. The pressure sensor was subjected to an applied hydrostatic pressure P and the dependence of the resistance of individual piezoresistors on P was characterized at room temperature. The test results shown in Fig. 8 are from a pressure sensor in which all four p-type piezoresistors are defined by wide trenches. Consistent with the theory [2], R_1 and R_3 aligned with the [001] orientation are almost independent of P, whereas R_2 and R_4 aligned with the [1$\bar{1}$0] orientation are sensitive to P. The resistance of R_2 and R_4 decreases by ~2.8% over the 200 MPa range of applied P.

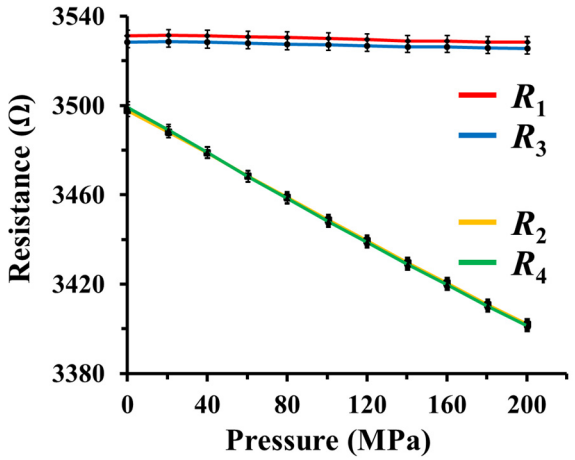

Figure 8: Dependence of the resistance of individual piezoresistors on the applied pressure at room temperature for the SOI pressure sensor with p-type piezoresistors all defined by wide trenches.

The measured Wheatstone bridge output voltage V_{OUT} of the SOI pressure sensor versus P and temperature is shown in Fig. 9. The discontinued plot at 225 °C was due to a pressure seal failure of the test-package beyond 100 MPa at which point the pressure sensor die was still functional. A room-temperature sensitivity of 66 μV/V/MPa over 200 MPa and a temperature coefficient of sensitivity of −1000 ppm/°C over 200 °C were obtained. On the other hand, the leakage current of the present dielectric-isolated pressure sensor remained low, reaching only 0.1 nA at 175 °C (Fig. 10a). This is less than one thousandth of the leakage current of a junction-isolated pressure sensor (Fig. 10b). A comparison of the sensor characteristics of this work and others is shown in Table II.

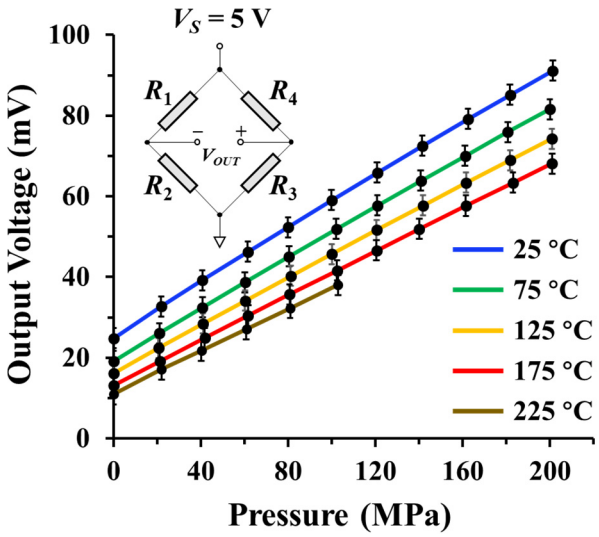

Figure 9: Wheatstone bridge output voltage of the SOI pressure sensor with p-type piezoresistors all defined by wide trenches.

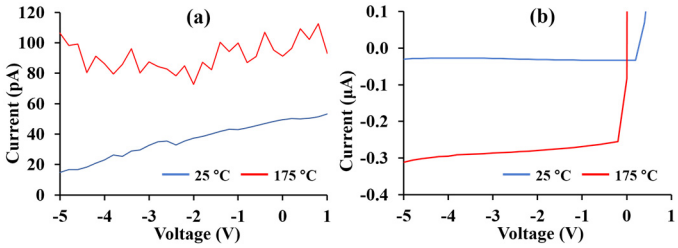

Figure 10: Leakage current of (a) dielectric- and (b) junction-isolated pressure sensors.

Table II: MEMS piezoresistive high-pressure sensor comparison.

Ref.	Type	P_{max} (MPa)	ΔV_{out} (mV)	Power Supply	Temp. (°C)
[1]	All-Si Bulk	120	58	5 V	25~125
[2]	All-Si Bulk	200	79	5 V	25~175
[3]	Si-Glass Diaphragm	150	50	5 V	20~150
[4]	Si-Glass Diaphragm	150	167	1.5 mA	≤ 200
[5]	Si-Glass Bulk	200	22	5 V	N/A
[6]	Si-Glass Bulk	60	62	5V	–40~125
This Work	SOI Bulk	200	66	5 V	25~225

DISCUSSION AND CONCLUSION

A dielectric-isolated bulk-type pressure sensor on SOI with the piezoresistors defined by isolation trenches was designed and fabricated. Theoretical analysis shows that selective trenching on p- or n-type piezoresistors should result in appreciable difference in the pressure sensitivity, with n-type piezoresistors having better performance. Finite-element analysis shows that the applied stress acting on the piezoresistors could be biaxial or uniaxial, depending on the design of the trenches.

The fabricated sensor with p-type piezoresistors was characterized with pressure loading up to 200 MPa and temperature up to 225 °C. The respective sensitivity and temperature coefficient of sensitivity are ~66 μV/V/MPa and −1000 ppm/°C. The high temperature performance of the SOI pressure sensor was experimentally demonstrated. The leakage current of the present dielectric-isolated pressure sensor was 0.1 nA at 175 °C, which is less than one thousandth of the leakage current of a junction-isolated pressure sensor.

ACKNOWLEDGMENT

This work was supported by the Key Research Program of Chinese Academy of Sciences, Grant No. ZDRW-ZS-2016-1-3, and the Strategic Priority Research Program of Chinese Academy of Sciences, Grant No. XDA14040202.

Device fabrication was carried out at the Nanosystem Fabrication Facility (NFF) of the Hong Kong University of Science and Technology.

REFERENCES

[1] D. Lin, E. Chan, L. Lu, S. Guo, F. Zeng, Y. Zhang, M. Wong, and K. Chau, "A 1200-atmosphere bulk-type all-silicon pressure sensor," in Proc. Transducers, Kaohsiung, Taiwan, Jun. 2017, pp. 2119–2122.

[2] E. Chan, D. Lin, L. Lu, D. Zhang, S. Guo, Y. Zhang, K. Chau, and M. Wong, "Realization and characterization of a bulk-type all-silicon high pressure sensor," J. Microelectromech. Syst., vol. 27, no. 2, pp. 231–238, 2018.

[3] T. Toriyama, K. Sawa, Y. Tanimoto, and S. Sugiyama, "A new piezoresistive high pressure sensor utilizing combination of three-axis normal stress components," in Proc. Int. Symp. Micromechatronics Human Sci., Nagoya, Japan, Nov. 1999, pp. 215–220.

[4] Z. Niu, Y. Zhao, and B. Tian, "Design optimization of high pressure and high temperature piezoresistive pressure sensor for high sensitivity," Rev. Sci. Instrum., vol. 85, no. 1, p. 015001, 2014.

[5] P. Heinickel and R. Werthschützky, "Functionality of a novel overload resistant silicon high pressure sensing element," in Proc. Transducers, Denver, CO, USA, Jun. 2009, pp. 252–255.

[6] M. Baumann, P. Ruther, and O. Paul, "Modeling and characterization of a CMOS sensor with surface trenches for high-pressure applications," in Proc. MEMS, Cancun, Mexico, Jan. 2011, pp. 601–604.

A YARN-BASED BACTERIA-POWERED BATTERY FOR SMART TEXTILES

Yang Gao, Lin Liu, and Seokheun Choi,*
Bioelectronics & Microsystems Laboratory, Department of Electrical & Computer Engineering,
Center for Research in Advanced Sensing Technologies & Environmental Sustainability (CREATES),
State University of New York at Binghamton, New York, USA

ABSTRACT

We report a flexible and wearable bacteria-powered battery in which four functional yarns are placed in parallel for biological energy harvesting. A current collecting yarn is sandwiched between two conductive/hydrophilic active yarns including electricity-generating bacteria while a polymer-passivated cathodic yarn is located next to one of the active yarns to form a biological fuel cell configuration. The device uses *Shewanella oneidensis* MR-1 as a biocatalyst to produce a maximum power of 17μW/cm^3 and current density 327μA/cm^3, which are enough to power small-power applications. This yarn-structured biobattery can be potentially woven or knitted into an energy storage fabric to provide a higher power for smart textiles. Furthermore, sweat generated from the human body can be a potential fuel to support bacterial viability, providing the long-term operation of the battery.

INTRODUCTION

Textile-based wearable electronics have recently emerged as a technology that promises next generation, ubiquitous health monitoring [1, 2]. Even under extreme mechanical deformation, their flexible and stretchable characteristics allow conformal and reliable contact with asymmetrical and non-uniform human skin with minimum discomfort. However, there has been a significant challenge in creating a truly self-reliant and stand-alone wearable sensing system that does not rely on an external power source [3]. Recently, our group, for the first time, demonstrated a textile-based bacteria-powered biobattery and ensured its practical efficacy as a flexible and stretchable power supply [4, 5]. Bacteria-powered biobatteries are arguably the most underdeveloped for wearable electronic applications because microbial cytotoxicity may pose health concerns. However, if we consider that humans possess many bacterial cells more than human cells in their bodies, the direct use of bacterial cells as a power resource interdependently with the human body is conceivable for wearable electronics. Our previous research efforts in flexible bacteria-powered batteries focused on integrating electronic components into a single sheet of 2-D fabric through a top-down approach [4, 5].

In this work, we presented a yarn-based biobattery for flexible and wearable textile integration (Figure 1). The realization of biobattery on flexible substrates, such as paper or textile, has been mentioned in literature [4-6]. Unlike the prior arts where functional regions and parts are constructed directly on the substrate, direct functionalization of basic yarns can enable more flexible and controllable device fabrication in a smaller device footprint, enhance the versatility of the device design and improve performance per unit volume. This bacteria-powered energy harvester was built on 1-D yarns through a bottom-up approach from which various electronic components of a large textile can be weaved or knitted.

MATERIALS AND EXPERIMENTAL SET-UP

Device Fabrication

The anodic compartment consisted of three yarns; a conductive thread as a current collector and two PEDOT:PSS (poly(3,4-ethylenedioxythiophene) polystyrene sulfonate) functionalized cotton yarns (or active yarns) were placed in parallel shown in (Figure 1 & Figure 2). The cathodic yarn was based on the same conductive thread as the anode. The silver-based cathodic paste was first applied the cathodic yarn and a microporous polytetrafluoroethylene (PTFE) membrane as a proton exchange membrane was coated over the cathode yarn.

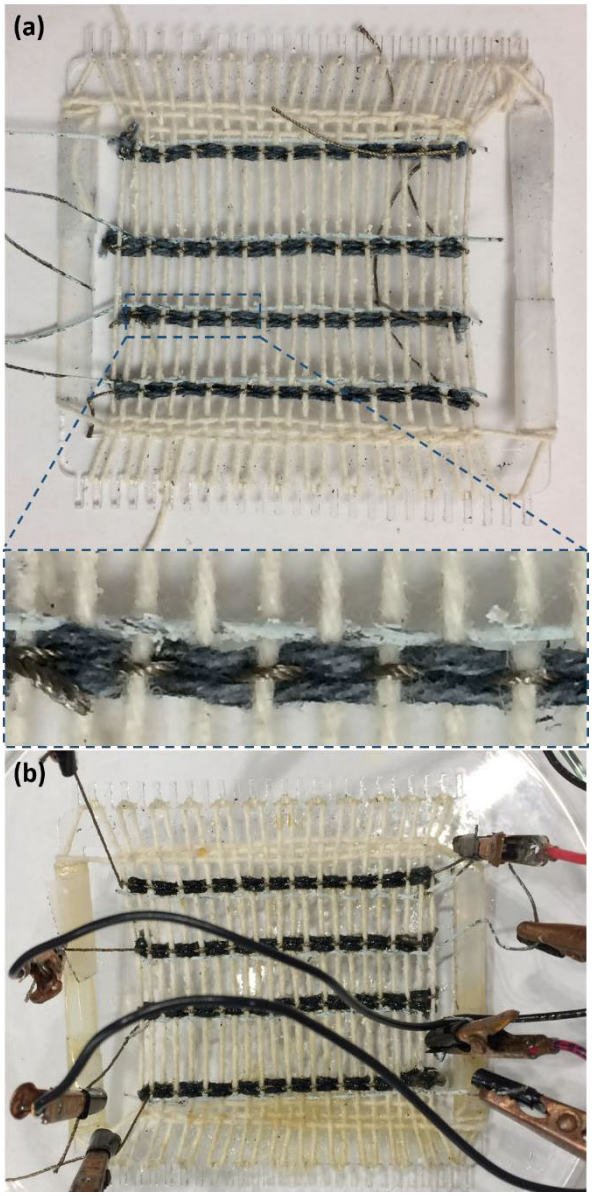

Figure 1. (a) Photo-images showing the textile weaving process of four yarn-based biobatteries and the enlarged view of the interlaced structure of one biobattery with four functional yarns. (b) Operating biobatteries.

978-1-940470-03-0/HH2018/$25©2018TRF
DOI 10.31438/trf.hh2018.56

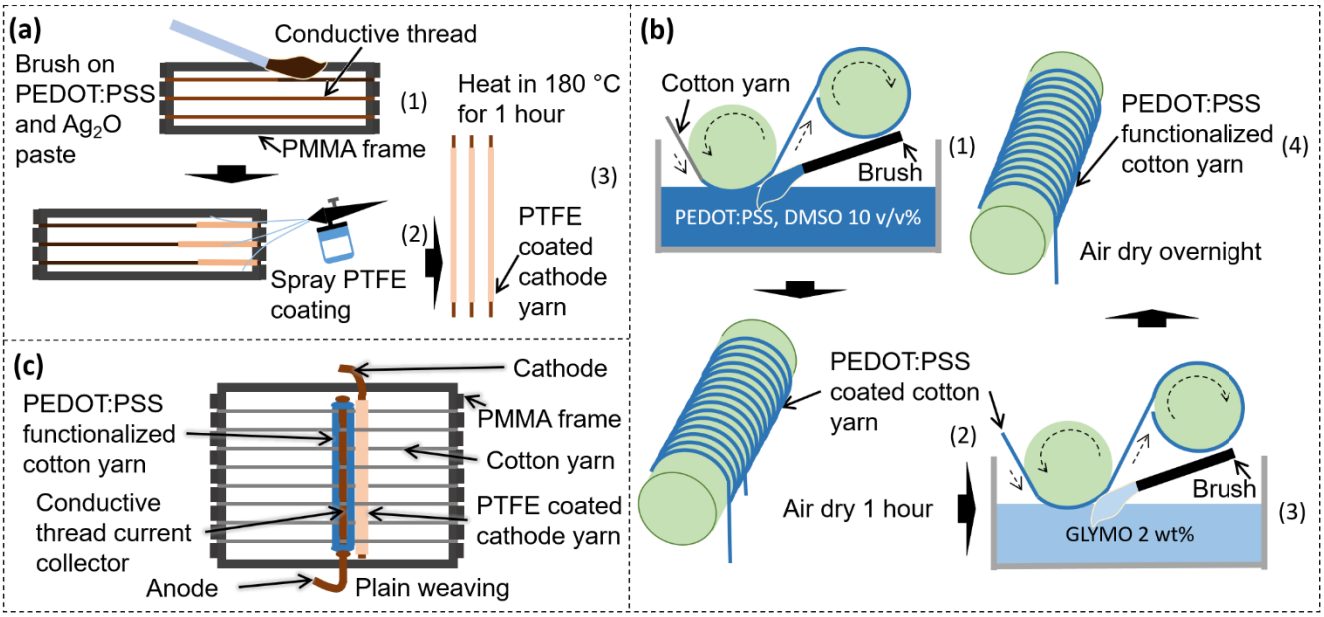

Figure 2: Schematic illustration of the processes employed to fabricate yarn-based biobattery, (a) cathodic yarns, (b) anodic yarns and (c) woven textile with anode and cathode in weft direction.

Four functional yarns were weaved into a plain weaving pattern (Figure 2) as the prototype yarn-based biobattery (Figure 3).

Cathodic yarn fabrication

Commercial cotton yarns were first sterilized by immersing in 70 v/v % ethanol with sonication for 30min, followed by drying in a ventilated oven at 50℃. The silver-based cathodic paste was prepared by mixing silver (I) oxide (Sigma-Aldrich) with 1wt% PEDOT:PSS. The PEDOT:PSS weight percentage increased from 1 wt% to 2 wt% by further heating and stirring processes on a hot plate stirrer (60℃ with 110 rpm). After the pre-cleaned conductive threads were stretched on the poly(methyl methacrylate) (PMMA) frame, the cathodic paste was brushed onto the thread and air-dried (Figure 2a). To passivate the treated cathodic yarn, 60 wt% PTFE water emulsion was mixed with isopropyl alcohol and sonicated for 30 min, yielding a uniform 40 wt% PTFE emulsion. The emulsion was sprayed onto the conductive cathodic thread and dried at 180℃ for 1 h.

Anodic yarn fabrication

Conductive ink was prepared by mixing 1 wt% PEDOT:PSS (Clevios™ PH1000, Heraeus) with dimethyl sulfoxide (DMSO, Sigma-Aldrich) at a volume ratio of 9:1. The cleaned cotton yarns were pulled through PEDOT:PSS conductive ink via a customized reeling setup (Figure 2b). A brush was pressed on the cotton yarns to facilitate the conductive ink penetration. The conductive cotton yarns were air-dried for 1 h to allow the solvent to evaporate. Then, the yarns were treated with 2 wt% 3-glycidoxypropyl-trimethoxysilane (GLYMO, Sigma-Aldrich) to improve its hydrophilic property. The functionalized yarns were further air-dried overnight.

Weaving of biobatteries

The cleaned non-conductive threads were used as warp yarns and held stationary in the PMMA frame (Figure 2c). The anodic and cathodic yarns were weaved through the warps in a plain pattern (Figure 3).

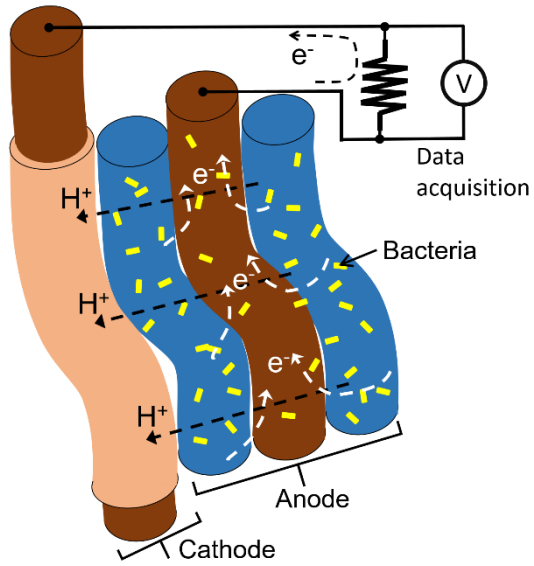

Figure 3: Schematic diagram of the yarn-based biobattery.

Inoculum

Cryostock *Shewanella oneidensis* MR-1 was cultured in 3 wt% soy broth media for 24 h, and diluted with fresh media. Growth was monitored by measuring the optical density at 600nm (OD_{600}), and the culture reached an OD_{600} of 1.6.

Operating principle and measurement setup

The yarn-based biobatteries were connected to a National Instrument (NI) data acquisition module (USB-6212) with a customized user interface for voltage measurements. To activate the biobattery, 260µL of bacterial inoculum was pipetted to each

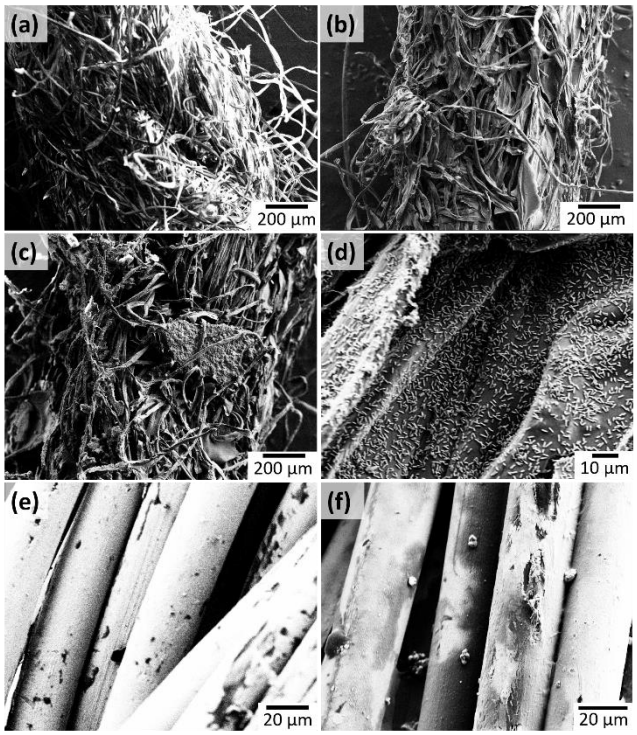

Figure 4: SEM images of (a) the cotton yarn without treatment, (b) the PEDOT:PSS functionalized anodic cotton yarn, (c & d) the anodic yarns after inoculation, (e) the conductive cathodic yarn and (f) the cathodic yarn with PTFE coating.

device. Resistive loads were connected to the biobatteries, and the output current and power were calculated via Ohm's law.

RESULTS AND DISCUSSION

The cotton yarn (Figure 4a) was chosen because of its good hydrophilicity, resistance to organic solvents, fabric integrity at elevated temperatures and low cost [7]. Adding the conductive polymer PEDOT:PSS to the cotton yarn created a conductive matrix with the high specific surface, improving bacterial attachment and their respiration (Figure 4b, 4c & 4d) [5, 8]. Therefore, the treatment for the conductive yarn engineering can reduce the anodic and cathodic resistance and minimize the ohmic loss of the device, increasing the performance (Figure 4e) [4]. Our prior arts demonstrated great potential of the silver (I) oxide with PEDOT:PSS as a stable- and high-preforming cathodic material for flexible biobatteries [5]. To encapsulate the silver-based cathode and promote ion-exchange between the anode and the cathode, a PTFE was selected to form a microporous proton exchange membrane [9]. The cathodic yarn was passivated with the homogenous PTFE membrane at 180℃ (Figure 4f).

When *S. oneidensis* MR-1 inoculum were introduced to the anodic yarns (Figure 3), the capillary force of the hydrophilic yarns rapidly wicked the anolyte to fill the anodic yarn of the biobattery. While the conductive PEDOT:PSS functionalized anodic yarns harvested electrons from bacterial respiration, the anodic conductive thread provided an efficient electrical pathway through which electrons flowed to the external circuit and reached the cathode. The protons produced by bacterial metabolism

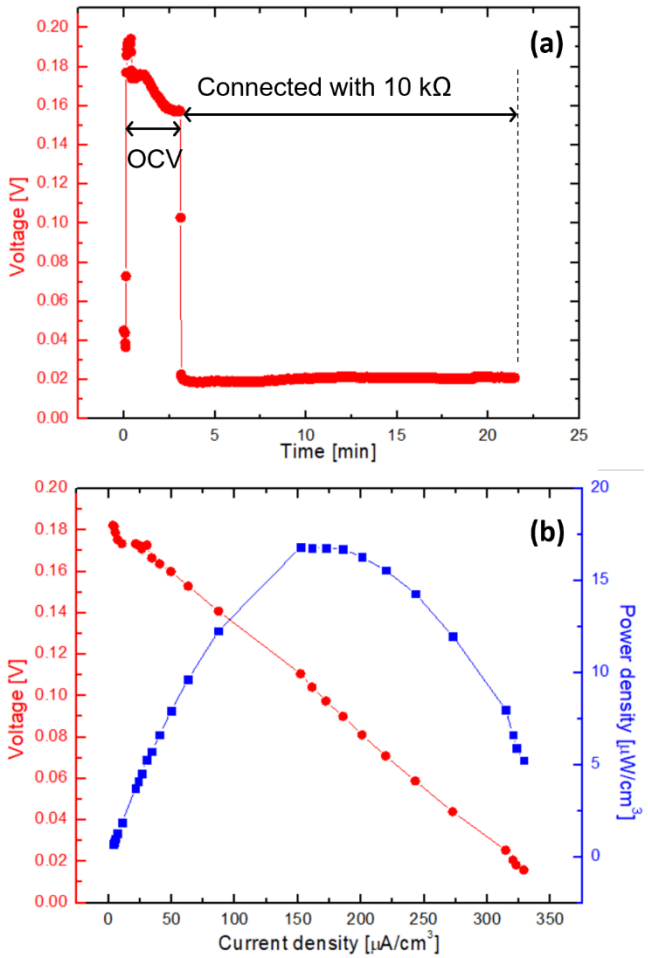

Figure 5: (a) Output voltage measured from a single yarn-based biobattery with or without the external resistor and (b) polarization curve/output power as a function of current.

traveled to the cathodic yarns through the passivated PTFE membrane. The electrons and protons moved from the anodic yarns finally reduced Ag_2O to Ag at the cathodic yarn.

The open circuit voltage (OCV) of 168mV on average was obtained from the yarn-based biobatteries. A stable current of 2.2µA was produced with a 10kΩ resistor between the anode and cathode, providing a proof-of-concept demonstration of the bacterial battery (Figure 5a). The low OCV could be addressed by serially connecting the individual cells with various easy-to-configure threading or weaving patterns. A cell polarization curve and power output of the battery were measured and obtained based on the saturated current value at a given external resistance (Figure 5b). Slight bending of the textile did not affect the device performance. However, further detailed stretching and bending tests are needed to optimize the device fabrication and configuration. After the device operation, some parts of the PTFE membrane were slightly peeled off from the cathodic yarn (Figure 4f). This exposure of cathode would cause potential releasing of hazardous antibacterial silver ions, cathode biofouling, or short-circuit between anode and cathode, all of which would negatively affect the biobattery performance. Fabrication improvement of the PTFE membrane would be necessary, and further studies regarding mechanical strength, flexibility, and porosity of the

membrane are required. Our yarn-based biobattery will be suitable for wearable sensors, such as wrist health monitors [10], textile integrated electrochemical sensors [11], flexible and economical point-of-care diagnostic devices [12].

CONCLUSION

This work demonstrated the first integration of the bacterial-powered biobattery into yarns with a simple, scalable and fabrication-friendly fashion. The biobattery was built on 1-D yarns through a bottom-up approach, which can be potentially woven into a large energy storage fabric to ultimately deliver high power for practical, flexible applications.

ACKNOWLEDGMENT

This work is supported by NSF (ECCS #1503462, IOS #1543944, & ECCS #1703394) and the SUNY Binghamton Research Foundation (SE-TAE).

REFERENCES

[1] M. Stoppa and A. Chiolerio, "Wearable electronics and smart textiles: A critical review," Sensors, vol. 14, pp. 11957-11992, 2014.

[2] S. Choi, H. Lee, R. Ghaffari, T. Hyeon and D. Kim, "Recent advances in flexible and stretchable Bio-Electronic devices integrated with nanomaterials," Advanced Materials, vol. 28, pp. 4203-4218, 2016.

[3] Q. Huang, D. Wang and Z. Zheng, "Textile-Based electrochemical energy storage devices," Advanced Energy Materials, vol. 6, pp.1600783, 2016.

[4] S. Pang, Y. Gao and S. Choi, "Flexible and stretchable microbial fuel cells with modified conductive and hydrophilic textile," Biosensors and Bioelectronics, vol. 100, pp. 504-511, 2017.

[5] S. Pang, Y. Gao and S. Choi, "Flexible and stretchable biobatteries: Monolithic integration of Membrane-Free microbial fuel cells in a single textile layer," Advanced Energy Materials, vol. 8, pp.1702261, 2017.

[6] Y. Gao and S. Choi, "Stepping toward Self-Powered papertronics: Integrating biobatteries into a single sheet of paper," Advanced Materials Technologies, vol. 2, pp.1600194, 2017.

[7] H. Bi, Z. Yin, X. Cao, X. Xie, C. Tan, X. Huang, B. Chen, F. Chen, Q. Yang and X. Bu, "Carbon fiber aerogel made from raw cotton: A novel, efficient and recyclable sorbent for oils and organic solvents," Advanced Materials, vol. 25, pp. 5916-5921 2013.

[8] C. Kaewprasit, E. Hequet, N. Abidi and J.P. Gourlot, "Quality measurements," J. Cotton Sci, vol. 2, pp. 164-173 1998.

[9] S. Park, J. Lee and B.N. Popov, "Effect of PTFE content in microporous layer on water management in PEM fuel cells," J. Power Sources, vol. 177, pp. 457-463, 2008.

[10] J.M. Nassar, K. Mishra, K. Lau, A.A. Aguirre-Pablo and M.M. Hussain, "Recyclable nonfunctionalized Paper-Based Ultralow-Cost wearable health monitoring system," Advanced Materials Technologies, vol. 2, pp.1600228, 2017.

[11] J. Kim, R. Kumar, A.J. Bandodkar and J. Wang, "Advanced materials for printed wearable electrochemical devices: A review," Advanced Electronic Materials, vol. 3, pp.1600260, 2016.

[12] S. Wang, T. Chinnasamy, M.A. Lifson, F. Inci and U. Demirci, "Flexible substrate-based devices for point-of-care diagnostics," Trends Biotechnol., vol. 34, pp. 909-921, 2016.

CONTACT

*Seokheun Choi, *Assistant Professor*, SUNY-Binghamton,
Email: sechoi@binghamton.edu
Website: http://ws.binghamton.edu/choi

A NANOMECHANICAL IDENTIFICATION TAG TECHNOLOGY FOR TRACEABILITY AND AUTHENTICATION APPLICATIONS

Mehrdad Ramezani, Angela R. Newsome, Mayur Ghatge,
Fengchao Zhang, Swarup Bhunia, and Roozbeh Tabrizian
University of Florida, USA

ABSTRACT

This paper reports on a novel ultra-miniaturized identification technology that enables non-clonable tags for a wide span of applications, ranging from consumer electronic systems to commercial goods and products. The new labeling technology is based on nanomechanical resonators with spectral signatures composed from multiple high quality-factor resonance peaks. The spectral signature of the resonant nanomechanical label is used to generate a unique digital tag. Benefitting from highly randomized variations in spectral signature induced by the nanofabrication processing, an array of resonant labels can realize a set of highly randomized tags to serve as watermarks with a large entropy. Proof-of-concept resonant nanomechanical labels, implemented in an ultra-thin stack of aluminum nitride on silicon, demonstrate 28 randomly distributed resonance peaks over 25-100MHz span. A unique digital translation procedure, based on the frequency of resonance peaks, is developed yielding rigid digital tags with 63-bit length. The nanomechanical resonant labels are measured over wide temperature variations and excitation powers to verify the consistency of their major performance metrics including digital tag randomness, uniqueness and repeatability.

INTRODUCTION

As the explosive increase in product counterfeiting becomes a major treat to the global economy in recent years [1, 2], the development of effective identification and authentication approaches stands as an imminent challenge that calls for immediate action. Counterfeiting attacks affect the supply chain through targeting a wide range of goods, including consumer electronic systems, currency, medicine and food products. Growing complexity of globally distributed supply chain for majority of products increases their vulnerability for counterfeiting. In addition to the large-scale economic effect of counterfeiting, global trades in specific counterfeit goods, such as food, medicine and pesticides, carry serious health and safety issues [2]. Hence, there is a critical need to protect today's supply chain from the destructive effects of counterfeiting attacks. To this end, various identification and authentication techniques have been used to enable traceability of genuine products and identify the fake counterparts. These techniques include Universal Product Code (UPC) barcodes [3], quick response (QR) codes [4], radio-frequency identification tags (RFID) [5], and surface acoustic wave (SAW) labels [6]. Such techniques rely on designation of a digital tag, through a specific operation physics, to a physical label that is attached or imprinted on the product; hence enabling traceability and authentication of the host.

Although relatively successful to control and combat the growth of counterfeiting, the available approaches suffer from fundamental limitations that make a label susceptible to cloning, tampering, damage/distortion, and abolishment. While UPC barcodes rely on optical readouts and are required to be in the line of sight of the reader, they can be easily identified, removed and replicated. Furthermore, UPC generators and decoders are widely available to counterfeiters for reproduction and cloning of tags. RFID tags use an integrated circuit (IC), that generally contain 96-512 bits of identification information, and an antenna to function.

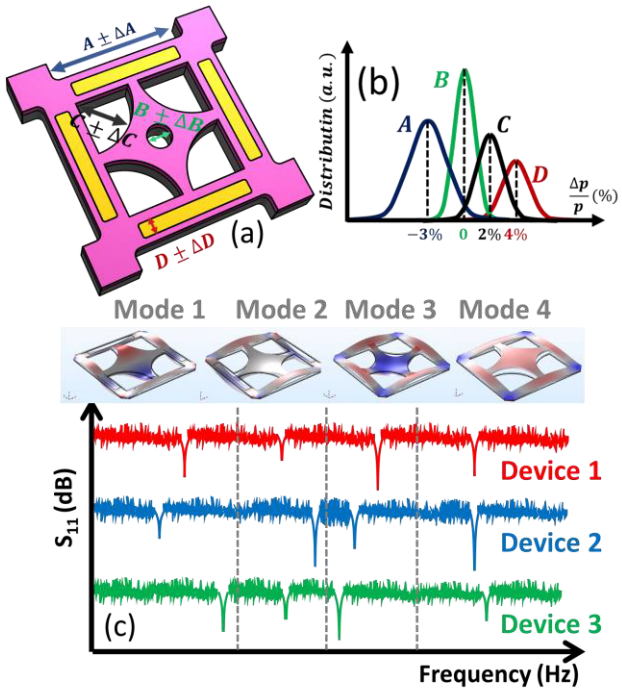

Fig. 1: (a) Resonant NEMS label implemented in AlN-on-Si, highlighting fabrication process uncertainties; (b) Gaussian distribution of various geometrical parameters resulted from fabrication uncertainties; (c) Distinct spectral signature of devices with identical designs, implemented in a single batch. The signature contains several high-Q acoustic resonance modes.

The bits contained within the IC are used to identify the host object. Unlike UPC barcodes, RFID tags and their corresponding code cannot be visually identified, hence a counterfeiter would require complex reverse engineering techniques. However, since RFIDs rely on electromagnetic read-out techniques at low to moderate frequencies, they require large label area and are prone to destructive / malicious interference. Furthermore, RFIDs are not applicable to metallic products such as vehicle parts, due to the reflection and destructive interference of the electromagnetic waves in conductive media, as well as the detuning of spectral characteristics of its constituent components. SAW labels rely on interaction of surface waves with patterned metal lines on the chip and use a similar read-out technology as RFID tags. Therefore, although SAW labels provide superior performance in extreme conditions, they suffer from similar limitations of RFID tags, including large form-factors and limited resolution in cluttered environment [6].

In this paper, we present a novel product labeling approach based on resonant nano-electro-mechanical systems (NEMS) for realization of ultra-miniaturized labels that substantially surpass fundamental limitations of the current labeling technologies for product identification and authentication. Resonant NEMS labels are implemented in ultra-thin piezoelectric-on-silicon stack and engineered to have multiple high quality-factor (Q) resonance

978-1-940470-03-0/HH2018/$25©2018TRF
DOI 10.31438/trf.hh2018.57

modes in their spectral signature (i.e. frequency response). The frequency and amplitude of the resonance modes in the spectral signature of the micromechanical resonant labels are randomly defined through the fabrication variations and are used to generate digital labels with extra-large entropy (Fig. 1). Benefiting from ultra-miniaturized form-factors and high-Q of constituent modes, non-clonable and tamper-resistant NEMS labels operating at high frequencies can be realized with extreme robustness and resolution over wide temperature ranges, to surpass fundamental limitations of the current state-of-art identification label technologies.

RESONANT NEMS LABEL CONCEPT

A resonant NEMS label is a perforated plate that is implemented in an ultra-thin aluminum nitride on silicon (AlN-on-Si) stack and geometrically engineered to have multiple resonance modes in a relatively small frequency span. Opting for proper thicknesses of AlN and Si as well as optimization of lateral dimensions of the label enable high-Q energy trapping of various flexural and extensional mechanical resonance modes in a single device (Fig. 1). Benefiting from the large electromechanical coupling of the piezoelectric AlN film and large mechanical Qs enabled by low loss Si layer the resonance modes of the device can be excited with relatively small input powers, which enable robust contact-less read-out of the resonant NEMS label with superior signal-to-noise ratios.

The performance of resonant NEMS labels, i.e. the frequency of high-Q peaks and their relative amplitudes in the spectral signature, is closely correlated with nanofabrication uncertainties, including lithographical alignment imperfections and exposure dose nonuniformities, and variation of piezoelectric film thickness and texture over the substrate. Such inherent uncertainties demonstrate a Gaussian randomness, which propagates to the performance of the implemented resonant NEMS label; hence naturally realizing digital tags with a large entropy and without a need for an external random generator. The intrinsic nature of random tag generation results in substantial immunity of NEMS labels to reproduction or cloning.

LABEL FABRICATION AND CHARACTRIZATION

An array of resonant NEMS labels is implemented in a stack composed from 50nm/120nm/50nm Mo/AlN/Mo transduction stack

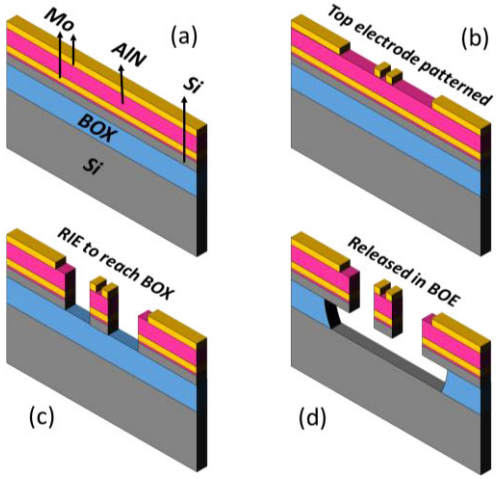

Fig. 2: Fabrication process for implementation of resonant MEMS label. (a) Starting with a stack of Mo/AlN/Mo/AlN(seed)/Si/BOX with thicknesses of 50nm, 120nm, 50nm, 20nm. 70nm, and 2μm, respectively. (b) Patterning top Mo to make the top electrodes. (c) Etching up to BOX layer to define the device geometry. (d) Releasing the device in HF.

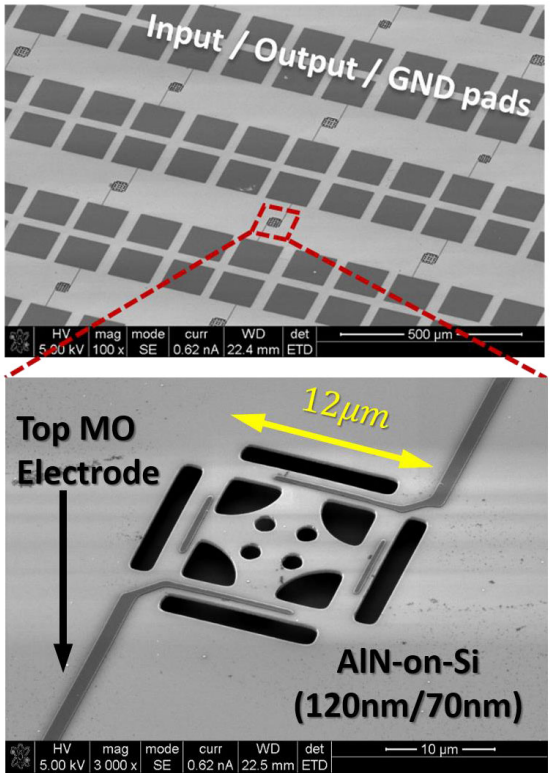

Fig. 3: (top) An array of resonant NEMS labels implemented in a single batch. (bottom) An individual NEMS label with an overall thickness of ~300nm and lateral dimensions of 12μm.

on top of a 70nm single crystal silicon layer. Fig. 2 demonstrates the fabrication process flow for the implementation of the resonant NEMS labels. Mo/AlN/Mo transduction stack is sputtered on the SOI substrate. The top Mo layer is patterned to form input / output electrodes. This is followed by the RIE of the entire stack to pattern the lateral geometry of the label. Finally, the device is released through etching the buried silicon dioxide (BOX) layer in HF. Fig. 3 (a) demonstrate the SEM image of an array of resonant NEMS labels along with corresponding pads to enable their electrical characterization. Fig. 3 (b) shows an individual resonant NEMS label, highlighting the excitation / read-out electrodes on the AlN film as well as the lateral dimensions of the label. Fig. 4 shows the transmission response (i.e. $|S_{21}|$) of a resonant NEMS label over the frequency span of 25-100 MHz. As evident in Fig. 4, the spectral signature of the label contains 28 distinctive high-Q resonant peaks with different insertion losses. Qs over 300-1000 are measured for the resonance modes, which are 1-2 orders of magnitude higher compared to electronic resonator counterparts. Such high Q directly

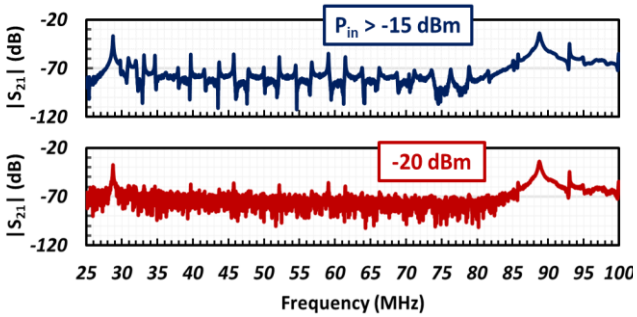

Fig. 4: Measured spectral signature of the resonant NEMS label for different excitation power levels.

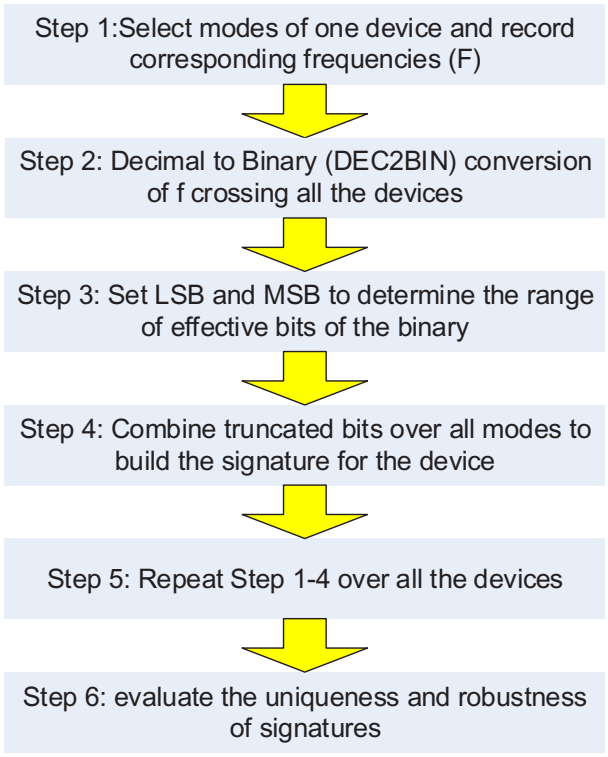

Fig. 5: The systematic procedure used for extraction and translation of the digital tags and examination of their robustness for each resonant NEMS label.

translates to the signal-to-noise ratio of the read-out system; enabling robust codes that are immune to environmental variations or destructive noise / interference. The 28 peaks of the spectral signature are used to generate a digital tag for the corresponding NEMS label, as described in the next section.

DIGITAL TAG TRANSLATION

A systematic procedure is used for generation of digital tags for each resonant NEMS label (Fig. 5). The digital tags are generated based on utilization of the frequency of resonance peaks in the corresponding spectral signature. For each device, strong peaks are identified and corresponding frequencies (*f*) are recorded. Then decimal to binary (dec2bin) conversion is conducted to covert the decimal value to binary. After that, the resulting binary is truncated to ideal length for high entropy and stability against noise, following by combination of the result of all modes together to generate the final signature corresponding to each device. Such a procedure is repeated for several labels implemented in the same batch and the extracted signatures are evaluated in terms of randomness, uniqueness and robustness. Table 1 shows the corresponding digital tag of the device with spectral signature in Fig. 4, along with six other devices with identical design, measured on the same die. A 63-bit tag is extracted for each device, highlighting the large entropy of the resonant NEMS label technology.

The uniqueness of signatures is evaluated by the inter device Hamming Distance (inter HD) and the histogram of inter HD ($interHDavg$) is shown in Fig. 6. The averaged inter HD is calculated as:

$$interHD_{avg} = \frac{2}{n(n-1)} \sum_{i=1}^{m-1} \sum_{j=i+1}^{m} HD_{i,j} \qquad (1),$$

where $HD_{i,j}$ stands for the inter HD between devices i and j.

Table 1: The extracted digital tags for seven resonant NEMS label implemented on the same die, having identical designs, measured in 30℃ using an excitation / read-out power of -5dBm.

	Digital Tag (Frequency) - 63bits
Device1	0011000001001100011001100110001110011010111001011010101100000000
Device2	1000100101001001100011011000100011000101100010101110100110011100
Device3	0110111010111100001000000111000101100100000110101001110101100000
Device4	0110000010110100100111000110111101111000001001100011101001111111
Device5	0101000100101100100110000100110011010110111100110011100000010011
Device6	1000101110011000000011110100100111010101001100101101100110101111
Device7	0111010101001000111001011100111010100111110101001011001010100110

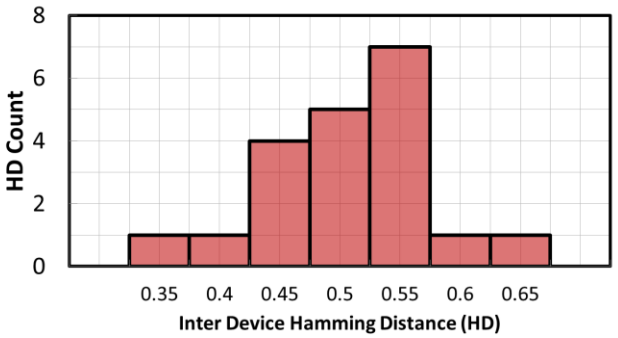

Fig. 6: The histogram of inter HD of the seven devices with digital tags detailed in Table 1; all devices are fabricated on the same die.

TAG ROBUSTNESS EVALUATIONS

To evaluate the robustness and consistency of the resonant NEMS labels two experiments are performed. In the first experiment, the consistency of extracted digital label is examined under various read-out / excitation power levels ranging over -80dBm to 15dBm. A minimum excitation power of -15dBm is required for reliable and repeatable read-out of the spectral signature. Lower excitation powers, below -15dBm, results in low signal to noise ration of read-out, which prevents from reliable identification of resonance peaks and extraction of digital tags. Fig. 4 compares the spectral signature for two excitation powers below (i.e. -20dBm) and above (i.e. > -15dBm) the required threshold. Table 2 summarizes the frequency of the first 9 resonance peaks of the signature, measured with three different excitation powers of -5dBm, 5dBm and 15dBm. Besides the excitation power evaluation, the resonant NEMS label is characterized over temperature range of 30°C - 70°C. Table 3 summarizes the frequency of the first 9 resonance peaks of the resonant NEMS label of Fig. 4, at three different temperature points of 30°C, 50°C, and 70°C. Fig. 7 demonstrates the extracted robustness of the resonant NEMS labels under different excitation power levels and operation temperatures, through the bit error rate (BER).

Table 2: The extracted decimal tags of the resonance peaks for different excitation powers.

Device1 Freq. at 30°C -5dbm (Hz)	Device1 Freq. at 30°C 5dbm (Hz)	Device1 Freq. at 30°C 15dbm (Hz)
28,750,000.0	28,750,000.0	28,750,000.0
30,929,687.5	30,648,437.5	30,929,687.5
31,984,375.0	32,335,937.5	31,984,375.0
33,109,375.0	32,734,375.0	33,109,375.0
34,656,250.0	34,820,312.5	34,656,250.0
39,695,312.5	39,343,750.0	39,695,312.5
43,703,125.0	43,539,062.5	43,679,687.5
45,765,625.0	46,164,062.5	45,742,187.5
52,164,062.5	52,164,062.5	52,164,062.5

Table 3: The decimal tags extracted for a NEMS label at three different operation temperatures, with an excitation power of 5dBm.

Device1 Freq. at 30°C 5dbm (Hz)	Device1 Freq. at 50°C 5dbm (Hz)	Device1 Freq. at 70°C 5dbm (Hz)
28,750,000.0	28,726,562.5	28,703,125.0
30,648,437.5	30,906,250.0	30,953,125.0
32,335,937.5	31,960,937.5	31,937,500.0
32,734,375.0	33,085,937.5	33,062,500.0
34,820,312.5	34,632,812.5	34,609,375.0
39,343,750.0	39,671,875.0	39,648,437.5
43,539,062.5	43,656,250.0	43,632,812.5
46,164,062.5	45,718,750.0	45,695,312.5
52,164,062.5	52,140,625.0	52,093,750.0

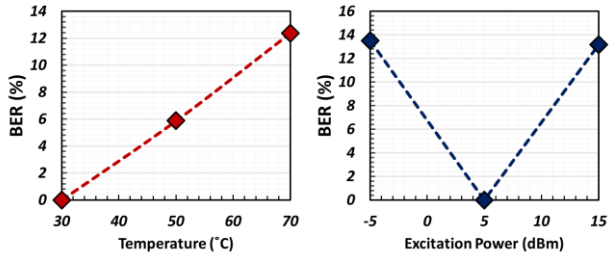

Fig. 7: Measured bit error rate (BER) versus (a) temperature variations and (b) excitation power variations.

Table 4: The qualitative comparison amongst common barcode technologies, with the presented resonant NEMS label.

	QR Code	RFID	Resonant M/NEMS Label
Size	***Minimum size:*** • 21 modules by 21 modules (dots) ***Maximum size:*** • 177 modules x 177 modules (dots)	***IC Minimum size:*** • 0.15mm x 0.15mm (smallest recorded size by Hitachi)	***Minimum Size:*** • Nano-meter scaling (sub 100-nm)
Invisibility	• Cannot be invisible due to sizing requirements for QR code dots for functionality.	• Visible due to the RF antenna and actual "tag" the microchip sits on.	• Not visible to the human eye without mechanical assistance.
Entropy	• 40 possible QR Code versions ranging from a minimum of 7 binary bits and a maximum of 2,953 binary bits	• Typically stores 96-512 bits of memory	***MEMS prototypes:*** • Entropy can be set based on frequency range set for device.
Cost	• Price based on the QR Code generator used. • Estimated $5/QR Code • QR code scanner prices range from $40-$300	• Ranges from $0.05 to $50, depending on the application. • RFID Tag scanner prices range from $500- $2,000	***Envisioned*** • $0.01-$0.05 benefiting from wafer-level batch fabrication / miniaturized size.
Robustness	• Can be used for different applications. • Error code correction allows functionality with some damage and distortion to QR Code. • Readable from all directions.	• Cannot be used on all materials such as: liquid and metal products. • Environmental variations (such as sensor signal clutters, temperature, etc.) can cause dysfunctionality.	• Physical and variations (i.e., electrode positioning and number of nanodots, temperature, power) will not distort digital signature • Ability to use on most material platforms
Vulnerability to Tampering	• Can be decoded using QR decoder techniques found via internet. • No true security • Easy malicious manipulation by hackers.	• Can be duplicated using reverse engineering techniques • Easily damaged or destroyed • Easily removed	• Clandestine (visually untraceable) • If detected, intrusive tampering will damage device / not allow for reverse engineering. • Vulnerability VERY limited due to size.
Application Space	• Consumer goods • Retail • Entertainment (i.e., concert and sports tickets) • Electronics • Social Applications	• Retail • Access management (i.e., hotel rooms, ID badges) • Military • Transportation • Toll collection • Government documents (i.e., passports) • Human Implantation	***Envisioned:*** • Consumer goods • Retail • Entertainment • Electronics • Currency • Government documents • Access management • Military Applications

The relatively small BER measured for excitation power and temperature variations demonstrates the robustness of the tags and highlights the potential of the resonant NEMS technology for realization of non-clonable ultra-miniaturized labels for anti-counterfeit authentication and identification. Table 4 presents a qualitative comparison for the tree most common barcode technologies from [4] [7-10], with the presented NEMS label technology.

CONCLUSION

This paper presents a novel resonant NEMS labeling technology, which can be applied to diverse class of products to reliably identify and authenticate them. Such technology enables realization of ultra-miniaturized labels for traceability and authentication applications, towards securing the supply chain against counterfeiting and piracy. Resonant NEMS labels are implemented in an ultra-thin AlN-on-Si stack piezoelectric and are engineered to have multiple high-Q resonance peaks in a small frequency span. The spectral characteristics of the resonant NEMS labels are used, along with a systematic translation procedure, to extract corresponding digital tags. Benefiting from 28 high-Q resonance modes that are randomly distributed in correlation with fabrication process uncertainties, 63-bit digital tags with large entropy are extracted for the NEMS labels. Robustness characterization, under various excitation powers and operation temperatures confirms the consistency of the digital tag of the corresponding resonant NEMS label.

REFERENCE

[1] Corben, R. *Economic Report Predicts Rise in Global Counterfeiting, Piracy*, https://www.voanews.com/a/global-trend-in-counterfeiting-and-piracy/3783360.html

[2] Hargreaves, S. *Counterfeit goods becoming more dangerous* http://money.cnn.com/2012/09/27/news/economy/counterfeit-goods/index.html

[3] Nachtrieb, J. and Profile, J. (n.d.). *The Seven Most Common Reasons That Barcodes Fail*. [Online] Barcode Test. Available at: http://barcode-test.com/the-seven-most-common-reasons-that-barcodes-fail-2/ [Accessed 9 Dec. 2017].

[4] Wikipedia. (n.d.). *QR code*. [online] Available at: https://en.wikipedia.org/wiki/QR_code [Accessed 10 Dec. 2017].

[5] Burke, P. and Rutherglen, C. (2009). *Towards a single-chip, implantable RFID system: is a single-cell radio possible?*. [online] National Center for Biotechnology Information. Available at: https://www.ncbi.nlm.nih.gov/pmc/articles/PMC2896640/ [Accessed 9 Dec. 2017].

[6] Barton, R. (n.d.). [online] NTRS NASA. Available at: https://ntrs.nasa.gov/archive/nasa/casi.ntrs.nasa.gov/20140000415.pdf [Accessed 9 Dec. 2017].

[7] Dion Label Printing. (n.d.). *UPC A Barcode Size Standard*. [online] Available at: http://www.dionlabel.com/tl_files/dion/Downloads/Dion%20Label%20Printing%20Barcode%20Information.pdf [Accessed 10 Dec. 2017].

[8] ADC Barcode. (2017). *RFID and Inventory Control - ADC Barcode*. [online] Available at: http://adcbarcode.com/news/rfid-and-inventory-control/ [Accessed 10 Dec. 2017].

[9] QR Code.com. (2017). *Information capacity and versions of QR Code*. [online] Available at: http://www.qrcode.com/en/about/version.html [Accessed 10 Dec. 2017].

[10] Journal, R. (n.d.). *RFID Frequently Asked Question - RFID Journal*. [online] RFID Jourdan. Available at: https://www.rfidjournal.com/faq/show?86 [Accessed 10 Dec. 2017].

CONTACT

*Mehrdad Ramezani; tel: +1-352-328-7462; mehram@ufl.

CIRCULARLY POLARIZED MECHANICAL RESONANCES

Pen-Li Yu and Sunil A. Bhave
OxideMEMS Lab, Purdue University, West Lafayette, Indiana, USA

ABSTRACT

We demonstrate a new type of rotational resonance, circularly-polarized mechanical resonance (CPMR), where a normal mode of a circular membrane revolves around its center. Clockwise or counter-clockwise full-angle rotation of normal mode is observed in circular membranes with a diameter of 710 µm or 960 µm and a thickness of 15 µm. We measure the (1,1) and higher order CPMR resonances with rates up to 5.3 million revolutions/second.

INTRODUCTION

Generating large and stable angular momentum at microscale has applications in spinning-mass MEMS gyroscopes, precision rotation stages, and micro-motors. Ultrasonic motors rely on nonlinear bifurcation of the stator's mode to cause rotation [1], while electrowetting requires complicated assembly [2], and levitation demands large, perfectly symmetric voltages [3,4]. Circular movement of nano-cantilever requires large vibration amplitude beyond "classical" Duffing regime [5,6].

Our discovery of CPMR provides a novel and simple way to generate large angular velocity. The excitation of CPMR only requires an axial piezo actuator and a sinusoidal tone. It is operated in the linear regime with no threshold. A rotation rate of 33.5 million radians per second for a higher order mode is observed. The range of mode frequencies is only limited by the bandwidth of our piezoelectric transducer.

RESONATORS AND EXPERIMENTAL SETUP

Fig. 1 (a) and (b) illustrate the fabrication process of the membranes. We carry out deep reactive ion etch (DRIE) on the backside of 4H SiC wafers [7,8]. By timing the etching, suspended circular membrane resonators are fabricated. The process is like backside release process except there is no stop layer. The membrane has a diameter of 710 µm or 960 µm and thickness of 15 µm. The thickness of the membrane is determined by measuring the depth of the trench [Fig. 1 (c)]. A photograph of the diaphragm chip is shown in Fig. 1 (d).

We employ a scanning Laser Doppler Vibrometer (LDV, Polytec MSA-400) to characterize mechanical motion [9,10]. The apparatus is located on a vibration isolation slab that meets NIST-A1 vibration standards. The membrane is bonded to the edge of an axial piezo actuator [Fig. 2 (a)]. The laser beam of the interferometer is focused through a 5× microscope objective and incident normal to the membrane plane. The laser wavelength is 633 nm, and the laser power is less than 1 mW. We raster scan the laser spot over ~ 1000 points on the membrane and measure frequency and time-domain responses at each point. We drive the piezo actuator with a broadband, pseudo-random excitation and perform Fast-Fourier Transform (FFT) to construct frequency spectrum. Alternatively, we can drive the piezo actuator with a single-tone, sinusoidal excitation, and measure the membrane displacement as a function of time. The velocity resolution is less than 1 um/s which corresponds to a displacement resolution of < 1 pm at 1 MHz.

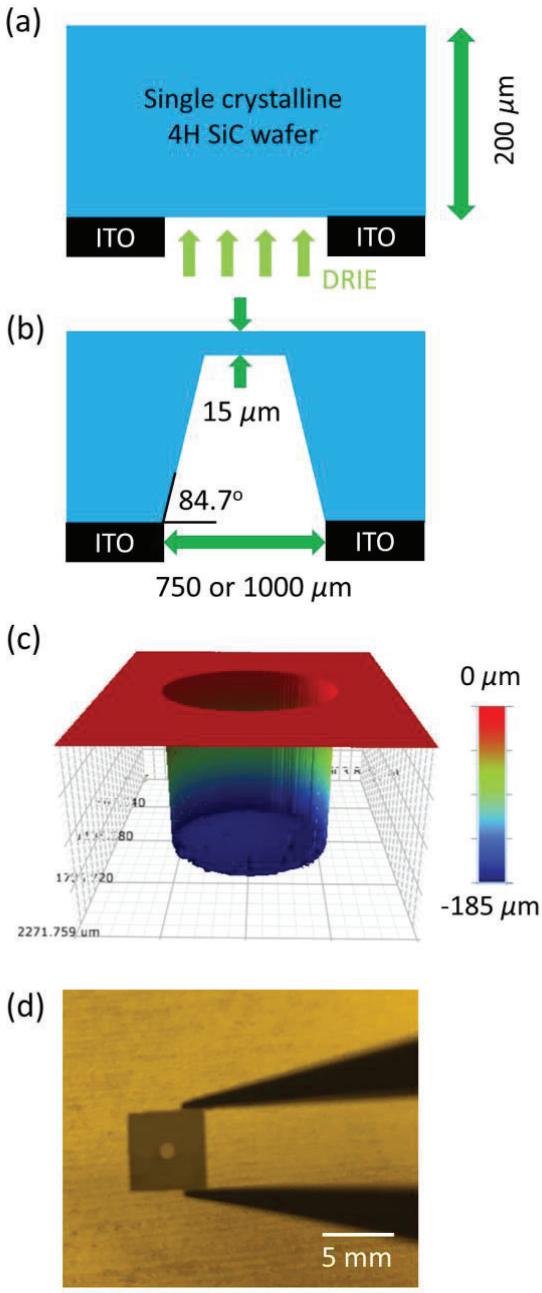

Figure 1: (a)-(b) Timed DRIE of 4H SiC to fabricate suspended membrane resonators [7,8]. Indium Tin Oxide (ITO) is used as a hard mask. 84.7° sidewall is achieved. (c) A DRIE trench profile measured by a 3-dimensional optical profiler (GT-K). The thickness of the membrane is obtained by subtracting the depth of the trench from the chip thickness. (d) Photograph of the diaphragm chip. The 5-mm square chip has a 15 µm thin membrane which looks like a pinhole because it is transparent to visible light. The membrane diameter is 960 µm.

978-1-940470-03-0/HH2018/$25©2018TRF
DOI 10.31438/trf.hh2018.58

RESULTS

Fig. 2 shows the measured displacement spectra of a 960 μm diameter membrane. We first measure the broadband displacement spectrum over 0-5 MHz. Many membrane modes are observed [7]. Their mode shapes and resonant frequencies are consistent with COMSOL simulation to within 4%. Next, we do a fine scan of the displacement spectra near the (1,1) mode. We observe the normal modes and two CPMR (1,1) modes at 746 kHz and 790 kHz with clockwise and counterclockwise revolutions. Table 1 shows the measured timestamps of the CPMRs observed in Fig. 2 (c) and many higher order CPMRs of a 710 μm diameter membrane. The CPMR modes complete one revolution in a period $T = 1/f$, where f is the excitation frequency. In 1 second, the (1,1) CPMR mode completes 746000 revolutions, while the (2,2) CPMR mode of the 710 μm membrane completes 5.3 million revolutions.

We also plot the time-average mode shape in the last column of Table 1. In contrast to the normal modes, the time-average mode shape of CPMRs show circular symmetry, as expected from the revolutions. A distinct feature of CPMR is that the location of maximum displacement travels around the membrane. Each point reaches its maximum displacement at a time corresponding to its angular position on the membrane plane. We perform time-domain measurements at 6 locations equidistant from the center [Fig. 3. (a)]. At 763 kHz, all points reach their maximum and minimum points concurrently, as is expected for a normal mode [Fig. 3 (b)]. Fig. 3 (c) shows the displacements as function of time for the (1,1) clockwise CPMR mode. In contrast to Fig. 3 (b), points at smaller angular position reach maximum displacement later, leading to clockwise rotation.

Up to the resolution of the LDV, we do not observe any "onset" or threshold point for the revolution. We measure a linear relationship between drive amplitude and piezo stimulus up to the maximum voltage allowed by the LDV system [Fig. 4(a)]. The CPMR does not arise from nonlinear model coupling [1,5,6].

Operating at the resonant peak [blue line in Fig. 4(b)] gives us almost perfect traveling wave revolution. However, the amplitudes are not exactly uniform throughout the rotation, as shown by the time-averaged mode shape and Fig.3 (c). By operating at 10 kHz off the resonance [purple line in Fig. 4(b)], we observe a perfectly smooth revolution [see legends of Fig. 4 (b)]. The difference between on and off-peak response indicates that the CPMR is not an eigenmode of the membrane, but a superposition of eigenmodes that is perfectly balanced in amplitude and phase.

DISCUSSION

Here we provide a mathematical framework to describe the CPMR. We model CPMRs as the excitation of two spatially orthogonal normal modes with out-of-phase oscillations (See Fig. 5 for a visual illustration). To be more precise, we start with the general solutions $u_{mn}(r,\theta,t)$ of the vibrating drum head:

$$(A\cos c\lambda_{mn}t + B\sin c\lambda_{mn}t)J_m(\lambda_{mn}r)(C\cos m\theta + D\sin m\theta),$$

where $J_m(\lambda_{mn}r)$ is the Bessel function, $\lambda_{mn} = \alpha_{mn}/a$, α_{mn} is the n-th positive root of J_m, a is the radius of the membrane, *and* c is the wave speed. The Bessel function and index m define the number of nodal circles. The index m defines the number of nodal diameters. Constants C and D define the mode orientation, while constants A and B define the phase relation between the driving voltage and displacement. The two spatially orthogonal normal modes are described by two solutions with same indices m and n, but with $(C,D) = (0,1)$ and $(1,0)$, respectively (See Fig. 5). When these two modes oscillate out of phase, that is, the first mode oscillates as $\cos c\lambda_{mn}t$ $[(A,B) = (1,0)]$ while the second mode oscillates as $\sin c\lambda_{mn}t$ $[(A,B) = (0,1)]$, the superposition of these two modes generates full-angle counterclockwise rotation in one period of oscillation. On the other hand, if the first mode oscillates as $\sin c\lambda_{mn}t$ and the second mode oscillates as $\cos c\lambda_{mn}t$, the superposition of these two modes lead to clockwise rotation. Exact source of out-of-phase signaling is currently under investigation.

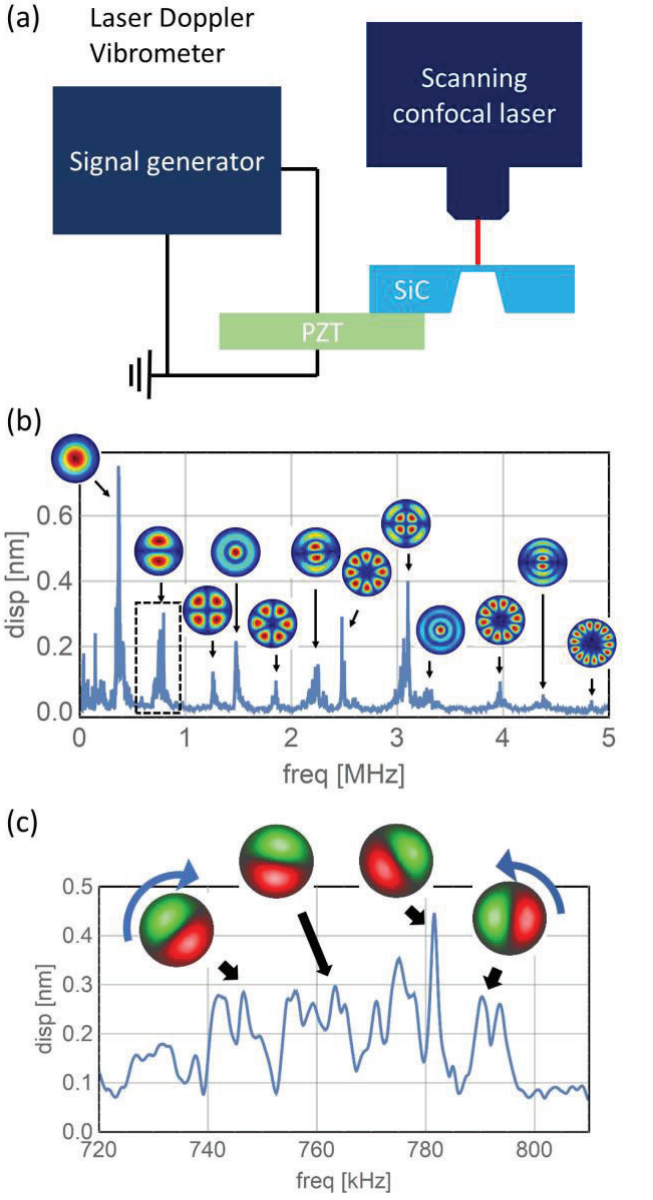

Figure 2: (a) LDV measurement setup with one key caveat — the sample is glued to the PZT at the edge of the actuator. The laser is raster scan over ~1000 points on the membranes. (b) Displacement spectrum of a 960 μm *membrane in 0-5 MHz range measured by the LDV in FFT mode. [Picture and plot are reproduced from [7] to provide context to] (c) Fine scan of the displacement spectrum around the (1,1) normal mode at 780 kHz. The CPMR modes are on either side of the normal modes.*

Table 1: Measured timestamps of the normal (1,1) mode (second row) compared to the (1,1) and higher order CPMR resonances. Two membranes with diameters of 960 μm and 710 μm are measured. *CPMR with rate up to* 5.3 million revolutions/second is observed. The period T is given by $T = 1/f$. *The time-average mode shapes (last column) for the CPMR modes have circular symmetry because of revolution.*

Dia. [mm]	Mode	f [MHz]	Direction	$t = 0$	$T/6$	$2T/6$	$3T/6$	$4T/6$	$5T/6$	Time Avg.
0.96	(1,1)	0.763	---							
0.96	(1,1)	0.746	↺							
0.96	(1,1)	0.789	↻							
0.71	(1,1)	1.397	↺							
0.71	(2,1)	2.263	↻							
0.71	(3,1)	3.260	↺							
0.71	(1,2)	3.875	↻							
0.71	(2,2)	5.326	↺							

Fig. 3 (b)

Fig. 3 (c)

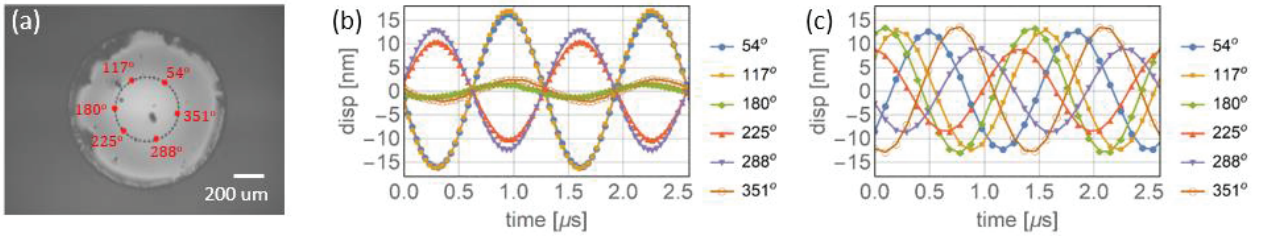

Figure 3: The vibration phase is the most distinctive feature of the CPMR modes. (a) We positioned laser spots on six points to measure their displacement as a function of time with respect to the drive (3 Volt). (b) For the normal mode, all points vibrate coherently. They reach their amplitude maximum and minimum at the same time. (c) For the CPMR mode, consecutive points reach maximum displacement with 60º phase delay. There is no instant in time where all points have zero displacement, as seen in Fig. 3(b) at 0.6 μs.

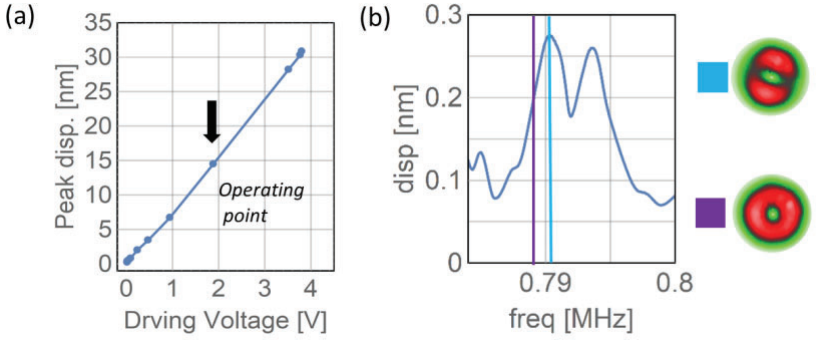

Figure 4: (a) *The membrane vibrates in the linear regime. The peak displacement of the (1,1) CPMR mode at 1.397 MHz as a function of driving voltage. (b) Time-average deflection shapes at the excitation frequencies. A perfectly smooth revolution (with circular symmetry) is achieved by driving 10 kHz off resonance (purple line).*

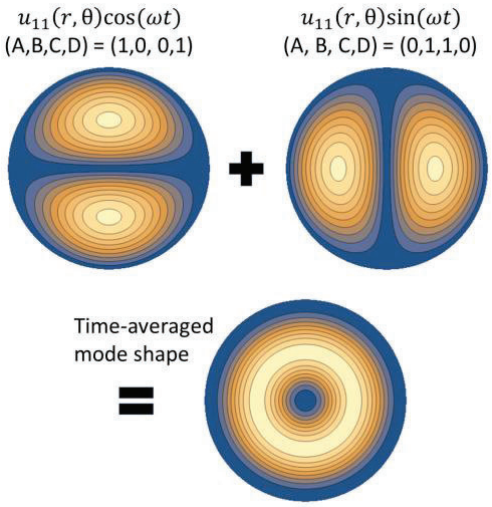

Figure 5: *Illustration of a mathematical model for CPMR. Two spatially-orthogonal normal modes (upper left and upper right) oscillating out of phase leads to CPMR. The rotation direction depends on the A, B, C, D coefficients.*

In conclusion, we present the observation of CPMRs in microfabricated membranes. We measure normal modes revolving under single tone excitation from an axial piezo actuator. CPMRs undergo full-angle, ultra-fast rotation (the mode rotates, not the resonator) and can be selectively biased to revolve clockwise or counter-clockwise rotational direction. We measure the (1,1) and higher order CPMR resonances with rates up to 33.5 million radians per second. The CPMR modes complete one revolution in one period of oscillation. We model the CPMR as a superpositions of two normal modes with out-of-phase vibrations. The direction of vibration is determined by the relative phase of the two modes.

ACKNOWLEDGEMENTS

We thank Devin Kalafut, Conor Pyles, and Sen Dai for technical assistance in LDV setup. This work was supported by AFOSR MURI grant. We thank M. M. Torunbalci, A. Bhat, and Y. He, and T.-H. Chang for discussions.

REFERENCES

[1] S. Tin, M. Pandey, and A. Lal, "Experimental Verification and Characterization of Sub-Harmonic Traveling Wave on an Ultrasonic Micromotor", Ultrasonics Symposium 2010, San Diego, California, USA, October 11-14, 2010, pp. 1841-1844.

[2] G. Sun, T. Liu, P. Sen, W. Shen, C. Gudeman, and C.-J. Kim, "Electrostatic Side-Drive Rotary Stage on Liquid-Ring Bearing", J. MEMS, 23 (2013), pp. 147-156.

[3] S. Nakamura, "MEMS inertial sensor toward higher accuracy & multi-axis sensing", IEEE Sensors 2005, Irvine, CA, USA, Oct. 30-Nov. 3, 2005, pp. 939-942.

[4] B. Damrongsak and M. Kraft, "A micromachined Electrostatically Suspended Gyroscope with Digital Force Feedback", IEEE Sensors 2005, Irvine, CA, USA, Oct. 30-Nov. 3, 2005, pp. 401-404.

[5] S. Perisanu., T. Barois, A. Ayari, P. Poncharal, M. Choueib, S. T. Purcell, and P. Vincent, "Beyond the linear and Duffing regimes in nanomechanics: Circularly polarized mechanical resonances of nanocantilevers", Phy. Rev. B 81, 165440 (2010).

[6] W. G. Conley, A. Raman, C. M. Krousgrill, and S. Mohammadi, "Nonlinear and Nonplanar dynamics of Suspended Nanotube and Nanowire Resonators", Nano Lett., 2008, 8 (6), pp. 1590-1595.

[7] P. -L. Yu, N. Opondo, S. Dai, B. Jiang, D. T. Morisette, and S. A. Bhave, "Single Crystalline 4H SiC Membrane Resonators", IEEE International Frequency Control Symposium 2018, Olympic Valley, CA, USA, May 21-24, 2018.

[8] S. -D. Ko, B. Hamelin, J. Yang, and F. Ayazi, "High-Q Monocrystalline Silicon Carbide Disk Resonators Fabricated Using DRIE of Thick SiC-on-Insulator Substrates", MEMS 2018, Belfast, UK, Jan. 21-25, 2018, pp. 996-999.

[9] J. F. Portoles, P. J. Cumpson, J. Hedley, S. Allen, P. M. Williams, and S. J. B. Tendler, "Accurate velocity measurements of AFM-cantilever vibrations by Doppler interferometry", J. Exp. Nanosci., 2006, 1:1, 51-52.

[10] L. B. Biedermann, R. C. Tung, A. Raman, R. G. Reifenberger, "Flexural vibration spectra of carbon nanotubes measured using laser Doppler vibrometry", Nanotechnology 20 (2009) 035702.

CONTACT

*Pen-Li (Ben) Yu, tel: +1-765-430-6400; yu586@purdue.edu

ENHANCING MICRO-OVEN POWER AND STIFFNESS IN ENCAPSULATED DEVICES FOR TIMING REFERENCE APPLICATIONS

Lizmarie Comenencia Ortiz[1], Dustin D. Gerrard[1], Ian B. Flader[1], Gabrielle D. Vukasin[1], David B. Heinz[1], Janna Rodriguez[1], Saisneha Koppaka[1], Dongsuk D. Shin[1], Hyun-Keun Kwon[1], Saurabh Chandorkar[2], and Thomas W. Kenny[1]*

[1]Stanford University, Stanford, California, USA

[2]IISc Bangalore, Bangalore, India

ABSTRACT

In this paper, we investigate the tradeoff between power-usage and stiffness to find an in-chip device layer micro-oven design with optimal yield. A variety of micro-ovenized double-ended tuning forks (DETFs) anchored via a serpentine heater or micro-oven are fabricated in an ultra-clean vacuum seal encapsulation process. The micro-ovens contain beams of varying lengths, widths, and thicknesses. We compare the power required to raise the micro-ovens to a fixed temperature and the yield of the devices. These results are the first report of yield statistics for in-chip device-layer ovenized devices. We show that a serpentine micro-oven located in the device layer of an encapsulated device with a thermal conductance of 0.17 mW/°C and a 25% yield, has 4X improvement over the power required for earlier, stiffer micro-oven designs.

INTRODUCTION

MEMS timing references are replacing quartz clocks in industrial applications due to their improved stability, small size, and low cost [1]. To achieve the high frequency stability required for MEMS sensors in industrial applications, temperature compensation methods are essential. Previous work has shown that a combination of passive and active temperature compensation methods can achieve the frequency stability required in timing reference applications [1-11]. Active temperature compensation can be achieved using a resistor or micro-oven embedded within the device layer, which heats only the suspended resonating element that is thermally isolated within the die [1,3-5]. This "in-chip ovenization" enables a significant size and power reduction that can heat the resonating element to a specific temperature and allow its frequency to remain constant with drastic changes in the temperature of its surroundings. Although power is significantly reduced in the device layer micro-ovenization in comparison to a cap layer micro-oven (3mW/°C) [2], the stiffness of the mechanical support may be sacrificed.

Thermal conductance depends on the length, width, and thickness of the micro-oven beams. Generally, operating power can be reduced by increasing the length of the beams and decreasing the width and thickness of the beams. As these parameters are changed to increase thermal resistance, the micro-oven becomes more flexible and therefore more prone to fatal in-process stiction, which occurs during the fabrication process [12].

It is necessary to investigate the relationship between the micro-oven stiffness and thermal conductance to determine the limits of the thermal properties that can be achieved with a micro-oven embedded in the device layer in our encapsulation process. In this paper, we study a series of devices with different micro-oven designs to find this relationship and find the tradeoff between micro-oven power and yield.

DESIGN AND FABRICATION

We study the properties of a set of micro-ovens attached at the anchor of a double-ended tuning fork (DETF), as shown in Figure 1. We model the eigenfrequency mode for the DETF inplane bending mode using the COMSOL Structural Mechanics module. The frequency of the bending mode is 1MHz at room temperature, as shown in Figure 1.

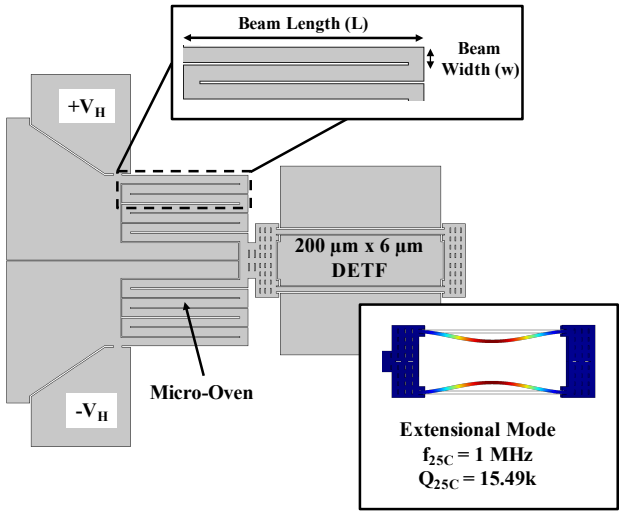

Figure 1: Diagram of micro-ovenized DETF with parameters studied.

We model the thermal conductance of the micro-oven with the COMSOL Joule Heating and Thermal Expansion module. We apply a split heater voltage of 1V at the micro-oven terminals ($+V_H$ and $-V_H$) and set the temperature at the terminals to 25°C, as shown in Figure 3. The voltage applied to the micro-oven induces an electric potential across the micro-oven beams, which elevates their temperature to approximately 100°C. The DETF structure is heated via conduction from the micro-oven. The parameters used in the simulations are defined in Table 1.

We designed and fabricated a range of micro-ovens with varying beam widths, lengths, and thicknesses to compare the thermal conductance of micro-ovens with varying stiffness. Additionally, we designed and fabricated micro-ovens with geometric variations to compare the effect of differences in the beam geometry. The variations include serpentine heaters with beam holes, round edges, and variable beam widths, as shown in Figure 2. These structures contain two suspension structures, aligned with the X and Y axis to isolate the thermal gradients in these axes, such as the ones described in [3].

We model the effective stiffness of each device using the COMSOL Solid Mechanics module. We apply a 100mN force at the tip of the DETF along the Y-axis and measured the inplane deformation of the device along the Y-axis, we similarly model the out-of-plane stiffness (Z-axis) of each device. The parameters for beam variations and simulation results are summarized in Table 2.

The devices were fabricated on p-type SOI wafers with a 40µm and a 60µm device layer using an epitaxial vacuum encapsulation

978-1-940470-03-0/HH2018/$25©2018TRF
DOI 10.31438/trf.hh2018.59

process. Each device has the same DETF resonating structure and variations in the micro-oven structure attached at the anchor. The structures had an overetch of approximately 300nm, which was accounted for in our simulations.

Table 1: Key parameters used in Joule heating and solid mechanics models.

Parameter	*Value*	*Source*
Thermal Conductivity	110.5 W/m-K	Calculated using [18]
Heat Capacity	711 J/kg-K	Estimated [10]
Electrical Conductivity	1.18E4 S/m	Wafer doping
Young's Modulus	169 GPa	[17]
Poisson's Ratio	0.064	[17]

Table 2: Summary of properties and simulation results for range of micro-ovens fabricated and tested with different dimensions.

µOven	*L (µm)*	*w (µm)*	*t (µm)*	*Effective Stiffness (N/m)*		*Thermal Resistance (mW/°C)*
				k_Y	k_Z	
1	30	5	60	21.6	96.4	0.54
2	60	5	60	4.32	86.6	0.22
3	60	10	60	50.6	199	0.62
4	90	10	60	105.9	143.2	0.41
5	150	10	60	6.58	36.8	0.19
6	120	10	40	9.36	14.4	0.20
7	150	10	40	4.38	7.84	0.13 (No yield)

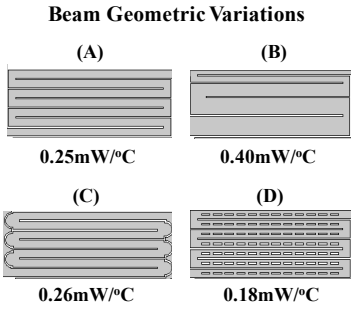

Figure 2: Summary of micro-ovens fabricated with varying geometries: (A) normal, (B) variable beam width, (C) round edges, (D) beam with holes.

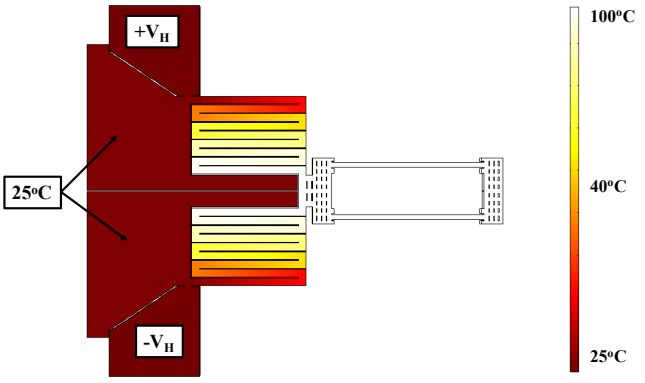

Figure 3: Temperature profile of micro-ovenized DETF with 1V applied at the micro-oven terminals and initial temperature at 25°C.

METHODS

The temperature dependence of the resonant frequency and quality factor for the bending mode of the DETF were measured from -10°C to 70°C, as shown in Figure 4. The quality factor was determined using the 3dB method of the frequency sweeps at stabilized temperatures. The frequency vs. temperature slope was -21.3ppm/°C. This ratio was used to estimate the temperature of the resonator at different heating voltages during operation of the micro-oven.

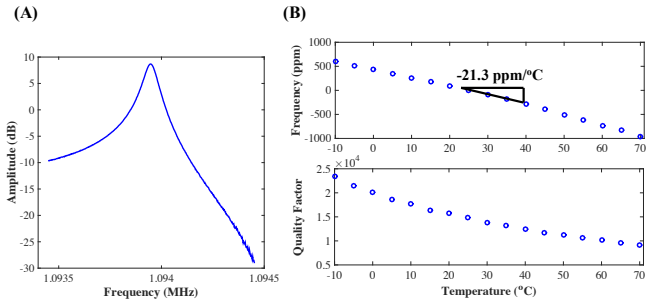

Figure 4: Characterization of DETF TCf and TCQ: (A) resonant frequency at 25°C, (B) frequency and quality factor dependence over temperature.

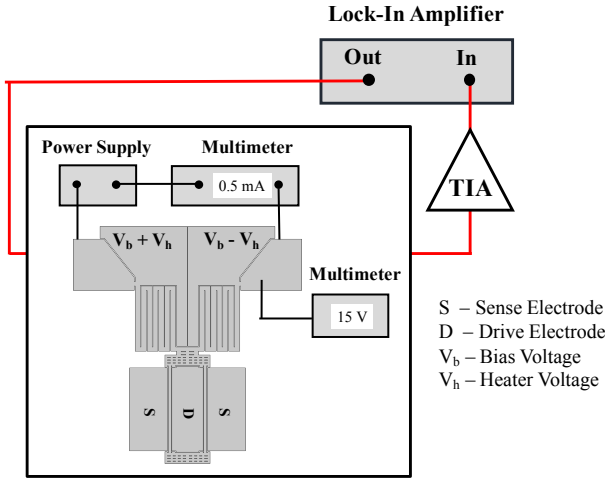

Figure 5: Experimental set up: a lock-in amplifier was used to collect open loop sweeps of the frequency over temperature.

A Zurich Instruments lock-in amplifier and transimpedance amplifiers were used in the configuration shown in Figure 5 to collect open loop frequency sweeps and measure the resonant frequency of each DETF as a function of applied micro-oven power to characterize the performance of each type of micro-oven. Split-heater voltages of 0V to 1V were applied at the terminals of each micro-oven stepwise to induce Joule heating through the beams and increase the temperature of the DETF structure. A benchtop multimeter (HP 34401A) was used to record the current and voltage through the micro-oven at each step. The ambient temperature surrounding the encapsulated die was maintained at 25°C using a benchtop temperature chamber, while the DETF temperature was elevated from 25°C to 100°C. The 75°C increase in temperature caused a change in the DETF resonant frequency of approximately 1600 ppm.

To further understand the relationship between the thermal conductance and the stiffness, we measured the survival rate of dozens of devices fabricated in the same process. We probed the devices for electrical conductivity after fabrication to determine if any two surfaces were fused into contact, or stiction occurred. We used a benchtop multimeter (HP 34401A) to measure the resistance between the surfaces.

RESULTS

Micro-Oven Power

We first characterize the performance of each micro-oven with the current and voltage relationship, shown in Figure 6. The darker lines show the low power micro-ovens, that have a steep slope versus other designs that require more power. The results in Figure 7 show that the power required to reach a device temperature of 100°C varies with the stiffness and topology of the micro-oven. The change in frequency of each DETF varies linearly with the micro-oven power. Each device had a different slope, depending on the properties of the micro-oven attached at the anchor. From these results, we find that a micro-oven with a stiffness of 15.6N/m can achieve a temperature rise of 75°C with a micro-oven power as low as 12.5mW, which is an 18X improvement over the cap layer heater architecture [2].

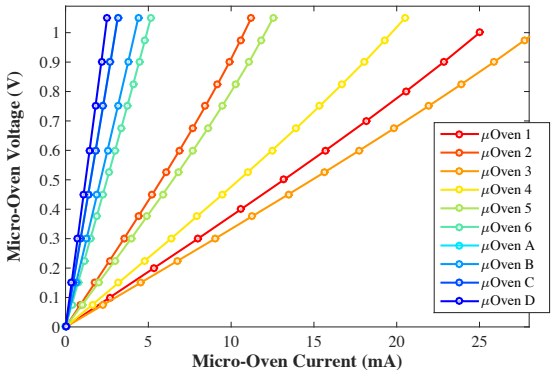

Figure 6: Current and voltage relationship for heaters tested.

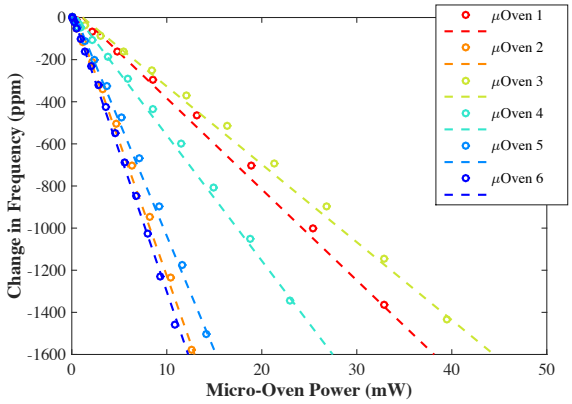

Figure 7: Change in frequency with the application of 1V at the terminals of a range of micro-ovens with varying stiffness.

Micro-Oven Geometric Variations

We compared the heating properties of micro-ovens with geometric variations on the beams, described in Figure 2. We find that modifying the geometry with round edges does not affect significantly the thermal resistance, as shown in Figure 8, since any sharp edges in the structure become smooth due to the thermal annealing step in our fabrication process; whereas adding holes to the beams increases the electrical and thermal resistance of the heater and reduces the required micro-oven power by 30%. Adding a variable beam width increases the stiffness of the beams and decreases the thermal resistance of the heater and therefore increases the power required to elevate the device temperature to 100°C.

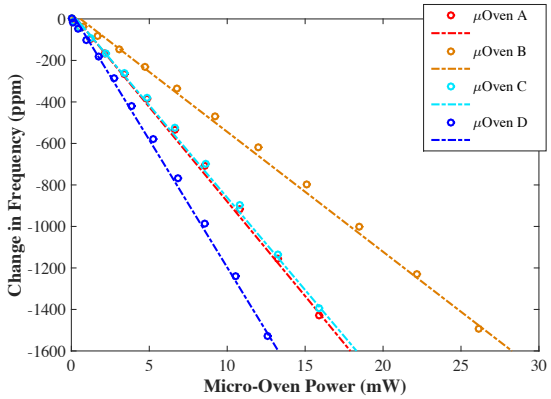

Figure 8: Change in frequency with the application of 1V at the terminals of a range of micro-ovens with varying geometry.

Micro-Oven Stiffness and Power Relation

We have explored the relationship between the micro-oven stiffness and the power required to elevate the device temperature from 25°C to 100°C. The results shown in Figure 9, demonstrate that as the effective out-of-plane stiffness of the micro-oven increases, the power increases linearly. The parameters necessary to reduce the effective stiffness of the micro-oven allow for the micro-oven to be thinner and longer, which is also necessary to reduce the power requirements. The results show that an optimal out-of-plane stiffness of 86.6N/m and a low power of 15mW can be achieved with shorter and thinner beams (L = 60μm, w = 5μm, t = 60μm).

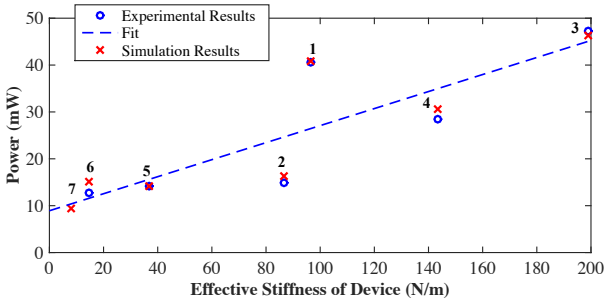

Figure 9: Power required to elevate the DETF temperature to 100°C with varying device out-of-plane stiffness (micro-ovens 1-7).

Micro-Oven Survival Rate

We demonstrate that more power-efficient ovenized devices can be designed by increasing the resistance of serpentine beams. This comes at the cost of making the device less stiff, resulting in lower yield. Our results show that an increase in the effective inplane and out-of-plane stiffness of the device increases the chances of survival by reducing the potential for fatal stiction. Stiffness and survival rate are exponentially related, as shown in Figure 10. These results show a trend of stiffer designs that require more power have less stiction. Devices with an inplane stiffness of 20-40N/m and an out-of-plane stiffness of 50-80N/m require low power and have a chance of survival of 60-80%, which makes this range suitable for our studies of timing references. Additionally, the results in Figure 10 suggest that the inplane stiffness is related to the yield of the micro-ovens with beam geometric variations (designs A-D). The double suspension structure in the X and Y axes lowers the inplane stiffness for these devices making them more prone to inplane stiction than to out-of-plane stiction.

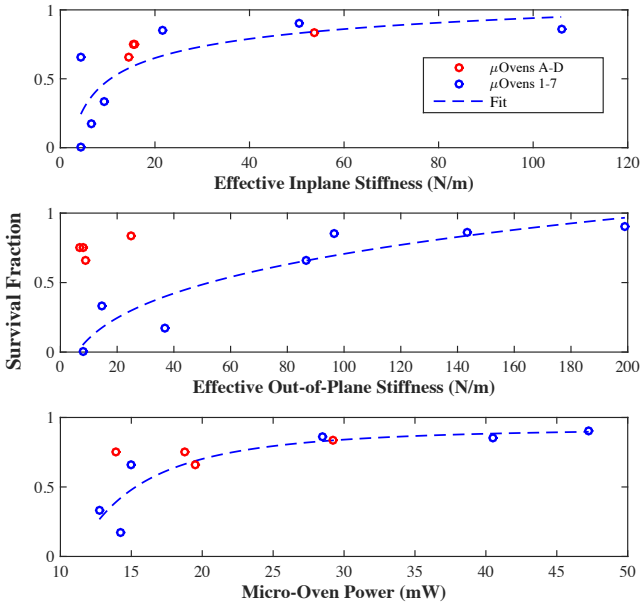

Figure 10: Survival rate of micro-ovens after fabrication with varying stiffness and power; Dozens of samples were tested.

CONCLUSION

In this paper, we investigate the relationship between micro-oven power and the yield of the device. We find that the effective stiffness of the device and the power of the micro-oven are related linearly, and that the yield of the device is related exponentially to its stiffness. Thus, there is a trade-off between in-process survival and performance of the micro-oven. We find that to minimize power and maximize the yield, we must design a micro-oven with an inplane stiffness of 20-50N/m and an out-of-plane stiffness of 50-80N/m. These results provide useful insight into micro-oven shape and variations that require low power to be used in future designs.

ACKNOWLEDGEMENTS

This work was supported by the Defense Advanced Research Projects Agency (DARPA) Precision Navigation and Timing program (PNT) managed by Drs. Robert Lutwak and Ron Polcawich under contract # N66001-12-1-4260. The fabrication work was performed at the Stanford Nanofabrication Facility (SNF), which was supported by National Science Foundation through the National Nanotechnology Infrastructure Network under Grant ECS-9731293. The author would also like to thank the National Science Foundation and the Graduate Research Program (NSF-GRFP) program.

REFERENCES

[1] C. T.-C. Nguyen, and R. T. Howe, "Microresonator frequency control and stabilization using an integrated micro oven", in Technical Digest of the 1993 Transducers Conference, Yokohama, Japan, 6/7-10/93, IEEE, (1993), pp. 1040-1043.

[2] Y. Chen, E. J. Ng, D. D. Shin, C. H. Ahn, Y. Yang, I.B. Flader, V. A. Hong, and T. W. Kenny, "Ovenized Dual-Mode Clock (ODMC) Based on Highly Doped Single Crystal Silicon Resonators", Technical Digest of the 2016 MEMS Shanghai, China, 6/24-28/16, IEEE and IEEE Robotics and Automation Soc. (2016), pp. 91-94.

[3] J. Salvia, R. Melamud, S. A. Chandorkar, S. F. Lord, and T.W. Kenny, "Real-Time Temperature Compensation of MEMS Oscillators Using an Integrated Micro-Oven and a Phase-Locked Loop," Microelectromechanical Systems,19, 1, (2010).

[4] C. Jha, M. A. Hopcroft, S. A. Chandorkar, J. C. Salvia, M. Agarwal, R. N. Candler, R. Melamud, B. Kim, and T. W. Kenny, "Thermal Isolation of Encapsulated MEMS Resonators," Microelectromechanical Systems, 17, 1, (2008).

[5] W. You, B. Pei, K. Sun, L. Zhang, H. Yang, and X. Li, "Oven controlled N++ [1 0 0] length-extensional mode silicon resonator with frequency stability of 1 ppm over industrial temperature range". Micromech. and Microeng., 27, 9, (2017).

[6] C. Y. Liu, M. H. Li, H. G. Ranjith and S. S. Li, "A 1 MHz 4 ppm CMOS-MEMS oscillator with built-in self-test and sub-mW ovenization power," Technical Digest of 2016 Int. Electron Devices Meeting, San Francisco, CA, 12/3-7/16, IEEE, (2016), pp. 26.7.1-26.7.4.

[7] L. Comenencia Ortiz, et. al, "Thermal Effects of Ovenized Clocks on Episeal Encapsulated Inertial Measurement Units", Technical Digest 2018 MEMS, Belfast, Ireland, 6/21-25/18, IEEE and IEEE Robotics and Automation, (2018).

[8] Z. Wu and M. Rais-Zadeh, "A Temperature-Stable Piezoelectric MEMS Oscillator Using a CMOS PLL Circuit for Temperature Sensing and Oven Control," Microelectromechanical Systems, 24, 6, (2015).

[9] S. Zaliasl *et al*., "A 3 ppm 1.5 × 0.8 mm 2 1.0 μA 32.768 kHz MEMS-Based Oscillator," Solid-State Circuits, 50, 1, (2015).

[10] E. Ng, V. A. Hong, Y. Yang, C. H. Ahn, C. L. M. Everhart, and T. W. Kenny, "Temperature Dependence of the Elastic Constants of Doped Silicon", Microelectromechanical Systems, 24, 3, (2015).

[11] R. Melamud, S. A. Chandorkar, B. Kim, H. K. Lee, J. C. Salvia, G. Bahl, M. A. Hopcroft, and T. W. Kenny, "Temperature-Insensitive Composite Micromechanical Resonators", Microelectromechanical Systems, 18, 6, (2009).

[12] D. B. Heinz, V. A. Hong, C. H. Ahn, E. J. Ng, Y. Yang, and T. W. Kenny, "Experimental Investigation Into Stiction Forces and Dynamic Mechanical Anti- Stiction Solutions in Ultra-Clean Encapsulated MEMS Devices," Microelectromechanical Systems, 25, 3, (2016).

[13] M. H. Li, C.-Y- Chen, C.-S. Li, C.-H. Chin, S.-S Li, "A Monolithic CMOS-MEMS Oscillator Based on an Ultra-Low -Power Ovenized Micromechanical Resonator", Microelectromechanical Systems, 24, 2, (2015).

[14] D. Yang, J.-K. Woo, S. Lee, J. Mitchell, A. D. Challoner, and K. Najafi, "A Micro Oven-Control System for Inertial Sensors", Microelectromechanical Systems, 26, 3, (2017).

[15] K. E. Wojciechowski, M. S. Baker, P. J. Clews, and R. H. Olsson, "A Fully Integrated Oven Controlled Microelectromechanical Oscillator Part I: Design and Fabrication," Microelectromechanical Systems, 24, 6, (2015).

[16] K. E. Wojciechowski, and R. H. Olsson, "A Fully Integrated Oven Controlled Microelectromechanical Oscillator Part II: Characterization and Measurement," Microelectromechanical Systems, 24, 6, (2015).

[17] M. A. Hopcroft, W. D. Nix, and T. W. Kenny, "What is the Young's modulus of silicon?", Microelectromechanical Systems, 19, 2, (2010).

[18] M. Asheghi, K. Kurabayashi, R. Kasnavi, and K. E. Goodson, "Thermal conduction in doped single-crystal silicon films." Applied Physics, 91, 8, (2002).

CONTACT

*L. Comenencia Ortiz, tel: +1-787-608-9044;
lcomenen@stanford.edu

HIGH $k_t^2 \cdot Q$ LAMB-WAVE SCALN-ON-SILICON UHF AND SHF RESONATORS

Mayur Ghatge[*1], *Valeriy Felmetsger*[2], *and Roozbeh Tabrizian*[1]
[1]University of Florida, FL, USA
[2]OEM Group LLC., AZ, USA

ABSTRACT

This paper reports, for the first time, on waveguide-based resonators implemented in scandium-doped aluminum nitride-on-silicon (ScAlN-on-Si) stack to simultaneously benefit from large piezoelectric constants of ScAlN and low acoustic dissipation in single crystal silicon. 1µm-thick ScAlN film with Sc content of 7% is reactively sputtered on silicon substrates using ac-powered dual-target S-gun magnetron with Al targets containing embedded pure Sc pellets. A Cl_2/H_2 based low-power plasma etching recipe is developed to pattern resonators with smooth vertical sidewalls. In- and out-of-plane waveguide-based resonator prototypes with large electromechanical coupling coefficient (k_t^2) and high quality-factor (Q) are implemented over 80 MHz – 3.5 GHz demonstrating k_t^2 of 0.7%-2.9% and Q of 2000-6400. Specifically, a high $f_0 \times Q$ of 4.3×10^{12} is measured for a resonator at 3.5 GHz, and a high $k_t^2 \times Q$ of 51 is measured at 108 MHz. The large $k_t^2 \times Q$ of ScAlN-on-Si waveguide-based resonators along with lithographical frequency tailorability demonstrate their potential for realization of highly integrated front-end filters for multi-band 5G systems.

INTRODUCTION

With the exponential growth of wireless users resulted from the emerging internet of things era and the ever-increasing quest for higher data rates, the new generation of wireless systems (i.e. 5G) target integration of multi-band RF transceivers to enhance communication capacity. To enable multi-band transceivers, there is an urgent need for an acoustic resonator technology that simultaneously provides extensive on-chip frequency tailorability while sustaining large k_t^2 and Q. Benefiting from lithographical frequency scalability AlN Lamb-wave resonators are potential candidates for realization of integrated multi-band RF filters [1-3]. However, to materialize such potential Lamb-wave resonators must overcome their shortcomings in major resonator performance metrics, i.e. the coupling coefficient (k_t^2) and quality factor (Q), that are significantly lower compared to thickness-extensional bulk acoustic counterparts (i.e. FBAR and SMR). Various approaches are exploited to improve the k_t^2 of Lamb-wave resonators, including the use of two-dimensional vibration modes that simultaneously benefit from two or three piezoelectric constants for enhanced transduction, or opting for alternative materials, such as lithium niobate ($LiNbO_3$) with enhanced piezoelectric properties. While two-dimensional vibration modes provide a higher $k_t^2 \times Q$ compared to lateral-extensional counterparts, reaching the performance of FBAR / SMR has remained a formidable challenge. Besides, opting for $LiNbO_3$ to replace AlN imposes fabrication and integration complexities and results in resonators with significantly larger temperature sensitivity due to the large temperature coefficient of elastic constants. To address the challenge of low k_t^2 in Lamb-wave resonators, a recent wave of research efforts focuses on enhancing the piezoelectric properties of AlN films through introduction of scandium (Sc) doping [4-6]. Experimental studies on the piezoelectric characteristics of Sc-doped AlN (i.e. ScAlN) thin films has shown a 400-500% improvement in the piezoelectric coefficients for a doping concentration of 40% [7]. Such an improvement translates to a k_t^2 of ~30% [6], a value that is 4-5 times larger compared to state-of-art thickness-mode AlN FBARs.

Although successful in improving the k_t^2, ScAlN Lamb-wave resonators suffer from low Qs that are nearly an order of magnitude lower compared to FBARs at the same frequency. The degradation in Q with Sc doping can be attributed to (a) formation of (100)-crystalline inclusions in (002) oriented ScAlN films [6] and (b) non-ideal etching profile of the films that results in rough and tapered sidewalls [8].

To surpass the limitations with the low Q of ScAlN resonators, this paper presents a new technology that fuses the high k_t^2 of ScAlN films with ultra-low acoustic dissipation of single crystal silicon to realize Lamb-wave resonators with large $k_t^2 \times Q$. ScAlN film with reduced density of inclusions is sputtered on silicon substrate and etched through a low-power RIE process that yields smooth sidewalls. Dispersion engineering of ScAlN-on-Si waveguides are used to implement resonators with large $k_t^2 \times Q$ and lithographical frequency scalability over UHF and SHF.

RESONATOR DESIGN

Resonators with high k_t^2 are designed using acoustic engineering of ScAlN-on-Si waveguides. The dispersion characteristic of Lamb waves is used to realize energy localization of extensional waves thorough cascading ScAlN-on-Si waveguides with different lateral dimensions. In this approach the dimensions of constituent waveguides are chosen to enable acoustic coupling of extensional bulk acoustic waves in the central electroded region with evanescent waves in the flanks. Figure 1 demonstrates the SEM image of a waveguide-based resonator and the dispersion characteristic of the constituent waveguides that are used for energy trapping of the 5th width-extensional (WE_5) mode with a high k_t^2.

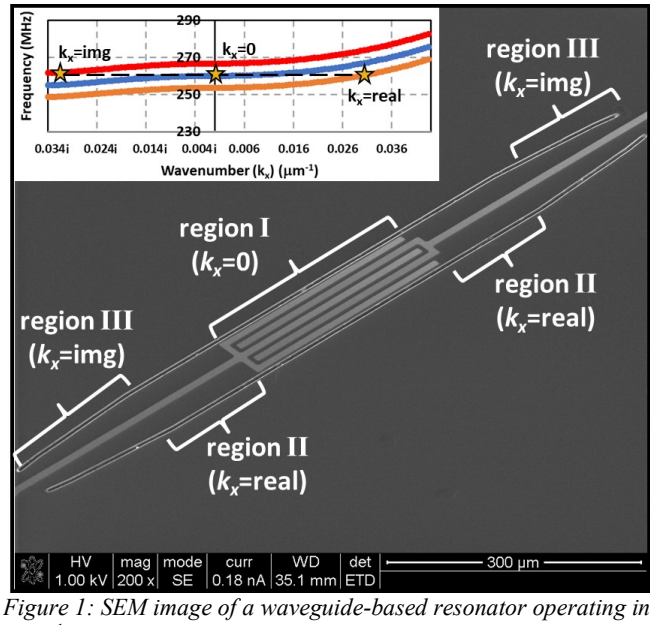

Figure 1: SEM image of a waveguide-based resonator operating in the 5th width-extensional mode. The inset shows dispersion curves of the corresponding Lamb waves that forms the mode, for constituent waveguides (i.e. regions I-III). The corresponding solutions at the resonance frequency are highlighted by stars.

978-1-940470-03-0/HH2018/$25©2018TRF
DOI 10.31438/trf.hh2018.60

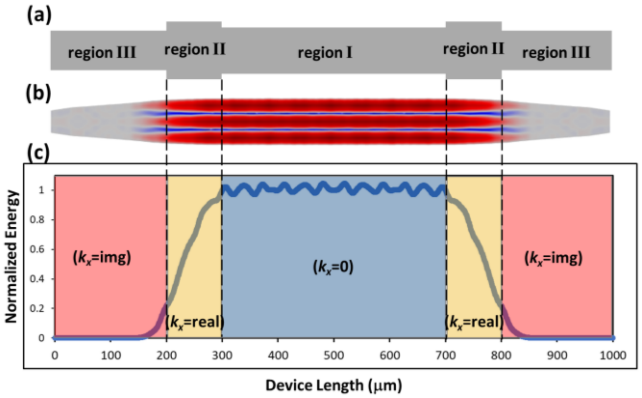

Figure 2: (a) Waveguide-based resonator concept: cascaded waveguides with varying widths. (b) COMSOL mode-shape of the device. (c) Normalized energy across the central axis of the device showing "piston"-shaped mode of vibration.

The corresponding solutions in constituent waveguides that contribute to form the resonance mode are highlighted through stars. Figure 2 demonstrates the COMSOL-simulated mode shape for the resulting WE_5 mode. Opting for proper length of the waveguides to satisfy displacement and strain continuity at transitions, the bulk acoustic wave ($k_x = 0$) in the central region (i.e. region I) can be coupled to evanescent waves in the flanks (i.e. region III), through Lamb waves with finite wavelength ($k_x \neq 0$) in region II. Figure 2(c) demonstrates the normalized acoustic energy across the central axis of the waveguide-based resonator in Figure 1. The proper acoustic engineering has resulted in a uniform energy distribution over the central / electrode region, which translates to a large k_t^2. Furthermore, the exponentially decaying acoustic energy in flanks is evident, which results in efficient energy trapping of the WE_5 mode with a high Q. In this paper the dispersion-based acoustic engineering is used for realization of high k_t^2 waveguide-based resonators operating in width-extensional harmonics as well as fundamental thickness-extensional modes over UHF and SHF regimes.

FABRICATION PROCESS

A stack of 1μm ScAlN film with Sc content of 7%, sandwiched between 50-100nm molybdenum (Mo) layers, is reactively sputtered on single crystal silicon substrate using ac-powered dual-target S-gun magnetron with Al targets containing embedded pure Sc pellets [9]. This technique enables the growth of ScAlN film with strong (002) preferred orientation (FWHM = 1.89°) and low stress of -189MPa. Proper optimization of processing condition enables reduction of the density of (100) conical intrusions in the film. Top Mo layer is patterned to form input and output transducers in the active region of the waveguide-based resonator. This is followed by dry-etching of ScAlN film. Unlike AlN, ScAlN films are highly resistant to BCl_3-based RIE recipes, resulting in very low etch rates and poor selectivity to photoresist or silicon dioxide mask layers. Furthermore, the Sc-based non-volatile byproducts of the etching process remains / accumulates during the etching process [8], which results in undesirable nano-masking of subsequent etching of bottom Mo in trenches as well as DRIE of silicon and yields waveguides with rough sidewalls and consequently low Q. To address the etching challenges of ScAlN while sustaining a reasonably low RIE/ICP power and high etching selectivity, a Cl_2/H_2 based RIE recipe is developed to realize comparable etch rates to AlN thin films. Besides improving the etch rate, the developed recipe physically removes the Sc-based byproducts

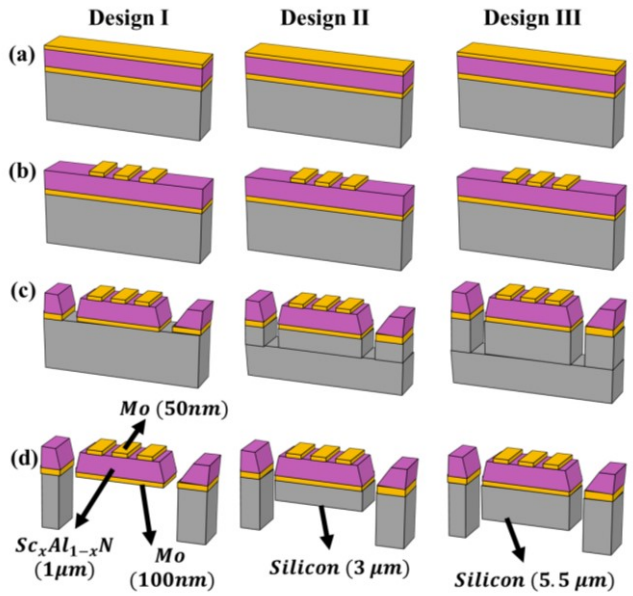

Figure 3: Fabrication process flow for the resonators with different Si thickness: (a) MO/ScAlN/Mo/Si stack. (b) Top Mo Patterning (c) Timed etching of ScAlN/Mo/Si selectively to get the desired silicon-substrate thicknesses. (d) Backside DRIE of silicon to release the devices. Backside etch timed to release the device with desired

Table 1: ScAlN RIE process parameters.

Parameter	*Values*
Cl_2 flow rate (sccm)	60
H_2 flow rate (sccm)	40
He flow rate (sccm)	10
RF Bias (W)	100
ICP Bias (W)	300

resulting in smooth surface after etching ScAlN film. In the next step, silicon layer is etched through Bosch DRIE of silicon substrate from top and bottom to form the released acoustic cavity with proper lateral geometry. Figure 3 summarizes the fabrication process flow. Samples with different silicon trench depths are prepared and released through proper timing of the backside DRIE to facilitate implementation of waveguides with different silicon thicknesses

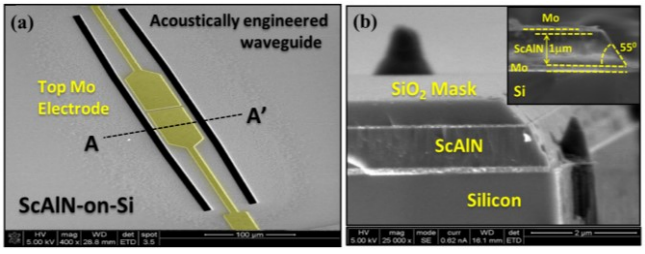

Figure 4: (left) SEM images of ScAlN-on-Si waveguide-based resonator operating in the fundamental width-extensional mode. (right) the cross-sectional SEM of the resonator detailing the ScAlN sidewall, after RIE in Cl_2 / H_2, and Si, after Bosch DRIE. A hard mask of SiO_2 is used for etching the resonator stack.

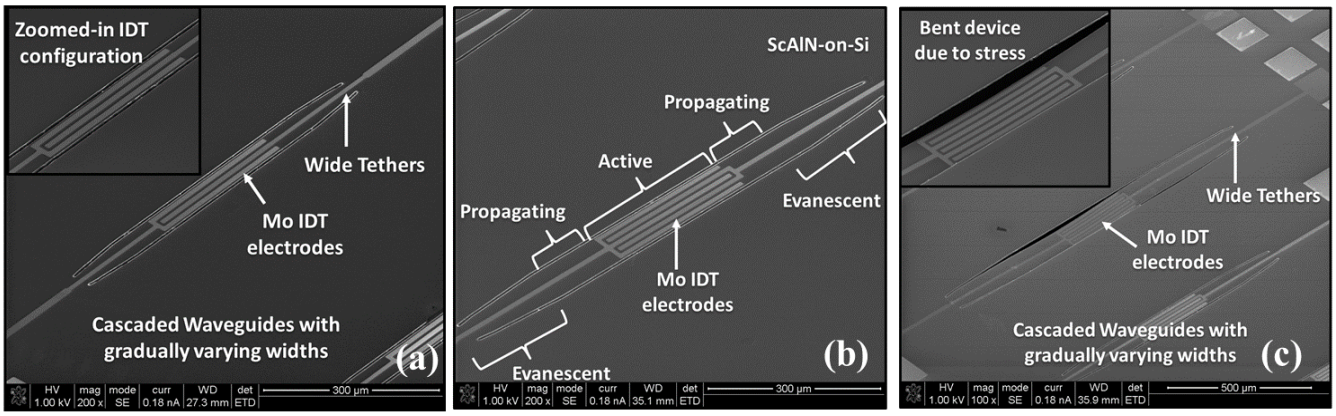

Figure 5: SEM images of (a) 3rd, (b) 5th, and (c) 7th width-extensional ScAlN-on-Si resonators. Waveguides are acoustically engineered through coupling evanescent and propagating waves to enable efficient energy trapping of the targeted Lamb-wave.

(Design I-III). This enables experimental evaluation of the effect of silicon on resonator Q and k_t^2. Table 1 summarizes the ScAlN RIE process details, highlighting the gas composition and low bias power. Figure 4 (a) demonstrate the SEM image of the ScAlN-on-Si waveguide-based resonator operating in fundamental width-extensional mode. Figure 4 (b) demonstrate the cross-sectional SEM of an unreleased waveguide after trench etching. The smooth and tapered sidewall profile of the ScAlN as well as an etch-resistant (100) conical intrusion are evident. The tapered profile of ScAlN sidewall is due to the high pressure of constituent gasses that is used to facilitate removal of Sc-based non-volatile compounds. Figure 5 shows the SEM images of 3rd, 5th and 7th width-extensional resonators implemented in ScAlN-on-Si (0-6μm silicon thickness). Interdigitated electrodes are patterned lithographically within the active region (i.e. central waveguide) of the resonators to facilitate excitation of width/thickness-extensional modes with high k_t^2.

CHARACTERIZATION

Two-port ScAlN-on-Si Lamb-wave resonators with various silicon thicknesses are implemented and characterized to facilitate

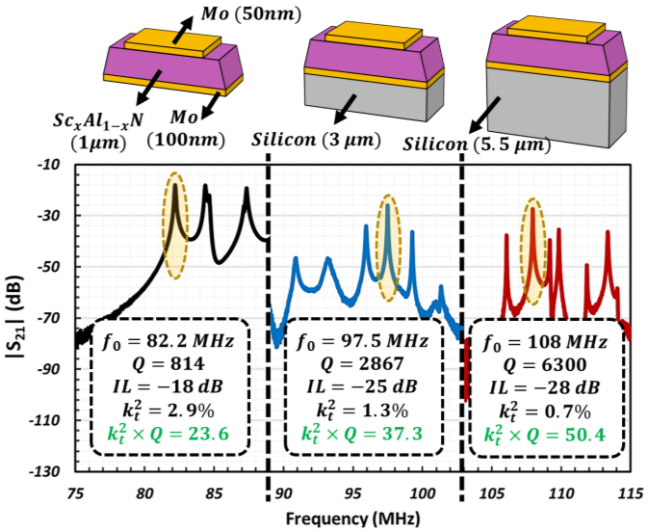

Figure 6: Measured frequency response of ScAlN-on-Si waveguide-based resonators with different silicon thicknesses. Increasing the silicon thickness from 0 to ~6μm improves the Q with ~1-order of magnitude, resulting in a high $k_t^2 \times Q$ of 51.

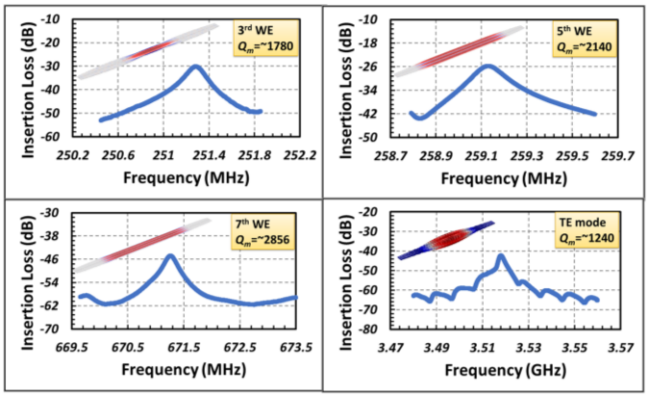

Figure 7: Measured frequency response of the high-order ScAlN-on-Si resonators shown in Figure 5, with frequencies over 250 MHz to 3.5 GHz. The inset shows the COMSOL-simulated mode shapes.

comparison of the k_t^2 and Q and experimental quantification of the enhancing effect of silicon substrate on $k_t^2 \times Q$. Figure 6 demonstrate the measured frequency response of resonators with different silicon thicknesses (i.e. 0-6μm). While the increase in silicon thickness reduces the k_t^2, the Q of the resonator is significantly enhanced thanks to the ultra-low acoustic dissipation of single crystal silicon, resulting in a high $k_t^2 \times Q$ of 51 measured at 108 MHz. The presence of multiple closely placed peaks with comparable Q can be attributed to (100) conical intrusions as well as tapered sidewalls of the ScAlN film resulted from RIE process. Figure 7 shows the short-span frequency responses for higher-order extensional and thickness-mode resonators shown in Figure 5. High

Table 2: The summary of measured performance metrics of fundamental-mode and high-order Lamb-wave ScAlN-on-Si resonators shown in Figure 1 and Figure 3. A record high $f_0 \times Q$ of 4.3×10^{12} is measured at 3.5 GHz, which is the highest ever-reported value for any ScAlN-based resonator.

Mode Shape	Q	f	fxQ
3rd WE Mode	1780	251.3MHz	4.4×10^{11}
5th WE Mode	2140	259.1MHz	5.5×10^{11}
7th WE Mode	2856	671.2MHz	1.9×10^{12}
Thickness Extensional	1240	3.51GHz	4.3×10^{12}
Fundamental Mode	6386	106MHz	6.7×10^{11}

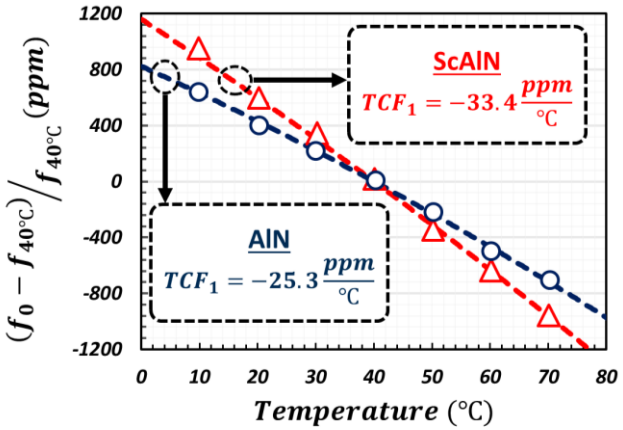

Figure 8: Temperature characteristic of frequency for pure ScAlN Lamb-wave resonator, compared to AlN counterpart.

*Q*s over 1300-2900 are measured for waveguide-based ScAlN-on-Si resonators operating over 250MHz-3.5GHz in width/thickness-extensional modes. Such high *Q*s is a result of ultra-low acoustic dissipation of single crystal silicon as well as efficient acoustic energy localization that suppresses energy leakage out of the resonator active region.

Table 2 summarizes the performance metrics of the resonators in Figure 4 and 5. A record high $f_0 \times Q$ of 4.3×10^{12} is measured for an ScAlN-on-Si resonator at 3.5 GHz, which is the highest ever-reported value for any ScAlN-based resonator. Moreover, similar high $f_0 \times Q$ values are measured for resonators operating at 100-700MHz and summarized in Table 2.

Finally, Figure 8 demonstrates the temperature characteristic of the frequency for ScAlN waveguide-based resonator operating in fundamental width-extensional mode. A similar design is used to implement an AlN resonator; hence, facilitating the evaluation of the effect of Sc doping on linear temperature coefficient of frequency (TCF_1). TCF_1 of $-33.4 \frac{ppm}{°C}$ and $-25.3 \frac{ppm}{°C}$ are measured for AlN and ScAlN resonators, respectively. The close TCF_1 values for AlN and ScAlN facilitates integration of ScAlN-based resonators into frequency control applications through exploiting similar compensation techniques that are well developed for AlN counterparts.

CONSLUSION

This paper presents high-*Q* ScAlN-on-Si waveguide-based resonators with lithographically defined frequencies over UHF and SHF regimes. The combination of high-k_t^2 of Sc-doped AlN film with ultra-low acoustic dissipation in single crystal silicon results in the enhancement of resonator $k_t^2 \times Q$. Acoustic engineering of the waveguides based on dispersion characteristics of Lamb-waves is used to efficiently trap the acoustic energy with a uniform energy distribution in active region. New recipes for deposition and etching of ScAlN are developed to yield films with low distribution of (100) intrusions and smooth sidewall etching profile. Waveguide-based resonator prototypes operating in fundamental and harmonics of width- and thickness-extensional modes are implemented over 80 MHz – 3.5 GHz demonstrating k_t^2 of 0.7%-2.9% and *Q* of 2000-6400. Specifically, a high $f_0 \times Q$ of 4.3×10^{12} is measured for a resonator at 3.5 GHz, and a high $k_t^2 \times Q$ of 51 is measured at 108 MHz. The large $k_t^2 \times Q$ of ScAlN-on-Si waveguide-based resonators along with lithographical frequency tailorability demonstrate their potential for realization of highly integrated front-end filters for multi-band 5G systems.

ACKNOWLEDGEMENT

The authors thank Dr. David Hays at the Nanoscale Research Facility in University of Florida for the helpful discussions on fabrication process of the devices.

REFERENCES

[1] Jo, B., Ghatge, M., & Tabrizian, R. (2017, June). d 15-Enhanced shear-extensional aluminum nitride resonators with k_t^2> 4.4% for wide-band filters. In *Solid-State Sensors, Actuators and Microsystems (TRANSDUCERS), 2017 19th International Conference on* (pp. 94-97). IEEE.

[2] Cassella, C., Chen, G., Qian, Z., Hummel, G., & Rinaldi, M. (2016, June). Unprecedented figure of merit in excess of 108 in 920 MHz aluminum nitride cross-sectional Lamé mode resonators showing k_t^2 in excess of 6.2%. In *Proc. Solid-State Sens., Actuators Microsyst. Workshop (Hilton Head)* (pp. 94-96).

[3] Cassella, C., Oliva, N., Soon, J., Srinivas, M., Singh, N., & Piazza, G. (2017). Super High Frequency Aluminum Nitride Two-Dimensional-Mode Resonators With k_t^2 Exceeding 4.9%. *IEEE Microwave and Wireless Components Letters*, *27*(2), 105-107.

[4] Moreira, M., Bjurström, J., Katardjev, I., & Yantchev, V. (2011). Aluminum scandium nitride thin-film bulk acoustic resonators for wide band applications. *Vacuum*, *86*(1), 23-26.

[5] Zhu, Y., Wang, N., Chua, G., Sun, C., Singh, N., & Gu, Y. (2017). ScAlN-Based LCAT Mode Resonators Above 2 GHz With High FOM and Reduced Fabrication Complexity. *IEEE Electron Device Letters*, *38*(10), 1481-1484.

[6] Henry, M. D., Timon, R., Young, T. R., Nordquist, C., & Griffin, B. (2017). AlN and ScAlN Contour Mode Resonators for RF Filters. *ECS Transactions*, *77*(6), 23-32.

[7] Akiyama, M., Kano, K., & Teshigahara, A. (2009). Influence of growth temperature and scandium concentration on piezoelectric response of scandium aluminum nitride alloy thin films. *Applied Physics Letters*, *95*(16), 162107.

[8] Colombo, L., Kochhar, A., Xu, C., Piazza, G., Mishin, S., & Oshmyansky, Y. (2017, September). Investigation of 20% scandium-doped aluminum nitride films for MEMS laterally vibrating resonators. In *Ultrasonics Symposium (IUS), 2017 IEEE International* (pp. 1-4). IEEE.

[9] Felmetsger, V., Mikhov, M., DeMiguel-Ramos, M., Clement, M., Olivares, J., Mirea, T., & Iborra, E. (2015, April). Sputtered Al (1− x) Sc x N thin films with high areal uniformity for mass production. In *Frequency Control Symposium & the European Frequency and Time Forum (FCS), 2015 Joint Conference of the IEEE International* (pp. 117-120). IEEE.

CONTACT

*M Ghatge, tel: +1-614-377-7228; ruyam@ufl.edu

3D PRINTED MICROFLUIDIC SELECTABLE RATIO MIXER PUMP IN 2 MM^3

G.P. Nordin, H. Gong, and A.T. Woolley*
Brigham Young University, Provo, Utah, USA

ABSTRACT

We report the use of 3D printing to fabricate a selectable ratio mixer pump in a volume of only 2 mm^2. Our custom 3D printer and material is used to make very compact individual elements such as fluid channels, valves, and pumps that are laid out in 3D to achieve small overall device volume. The device includes two pumps, each connected to its own fluid source, and a two-chamber mixing unit that both mixes the fluid pumped into it from each fluid source, and acts itself as a pump to expel the mixed fluid.

INTRODUCTION

Our group has focused on developing 3D printing tools and materials for fabrication of microfluidic devices. To date, the key inhibiting factor for 3D printing has been the inability of commercial 3D printers and materials to fabricate truly *micro*fluidic (≤100 μm) structures rather than millifluidic structures [1]. The critical characteristic of microfluidic devices is that they consist primarily of a series of small, interconnected voids inside a bulk material. Such voids form a variety of necessary structures that include passive components (e.g., flow channels, splitters, mixers, reaction chambers, and droplet generators) and active components such as valves and pumps. Since the requirement for small, interlinked voids is in direct contrast to standard (non-microfluidic) 3D printing applications in which external features or sparse structures tend to be important, the vast majority of 3D printing technology development has been directed toward different goals than those required for successful printing of microfluidic devices.

We recently developed a custom stereolithographic 3D printer and a new photopolymerizable resin that enables the fabrication of flow channels with cross section as small as 18 x 20 μm^2, which is a factor of ~200 smaller than the best that has been achieved with commercial tools and materials [2]. In this presentation, we demonstrate how the new printer and resin enable the realization of extremely small membrane valves and pumps, and focus particularly on the integration of such components in a dense 3D layout to realize a combination selectable ratio mixer and pump in a volume of only 2 mm^3 (i.e., the size of a sesame seed). This device is an example of what can be achieved with purpose-built tools and associated custom materials for 3D printing of microfluidics.

3D PRINTED VALVES AND PUMPS

In Ref. 3 we demonstrated and characterized 3D printed microfluidic valves and pumps using a commercial 3D printer and custom resin formulation, resulting in membrane valves (Figs. 1(a) and 1(b)) 1.08 mm in diameter. With our new custom 3D printer and material, we can substantially reduce valve and pump size. For example, a single fabricated valve is shown in Fig. 1(c) and a test array of 45 valves in Fig. 1(d) [4]. The valve diameters are 300 μm. Each row of valves in the array has been tested to 10,000 actuations, except for the bottom row, which was tested to 1,000,000 actuations. In all cases, there was no observable degradation in performance of the valves. Control and fluid channels are routed to the valves through compact chip-to-chip interconnects that are directly 3D printed as part of the device. We have demonstrated 400 interconnects at a density of 53/mm^2 [4].

We have recently reduced the size of 3D printed valves even further (150 μm diameter), which results in valves that occupy a factor of 130x smaller volume compared to our work in Ref. 3.

Pumps consist of two valves and a valve-like structure, and are operated with a 5-phase cycle. Using the smaller valves fabricated with our custom 3D printer and resin, pump size is commensurately reduced.

SELECTABLE RATIO MIXER PUMP

The decrease in component size can be used to create extremely compact devices. As an example, consider the combination mixer and pump in Fig. 2, which features the ability to mix selectable ratios of two fluids. A block diagram is shown in Fig. 2(a), with a corresponding 3D CAD layout in Fig. 2(b). A microscope photo of a finished device is shown in Fig. 2(c), where the square shapes around the periphery are controlled compression integrated microgaskets (CCIMs), as described in Ref. [4], to make chip-to-chip interconnects to an interface chip.

To test operation of the device, a dye solution is mixed with water and video of the mixing process is analyzed. An example video analysis for 4 units of dye combined with 2 units of water is shown in Fig. 3. Based on a new mathematical model we have developed to guide our video analysis, the blue curve is the relative dye concentration in the output channel. After approximately 9 mixer-pump cycles, the relative dye concentration asymptotes to 0.71, compared to an ideal value of 0.67.

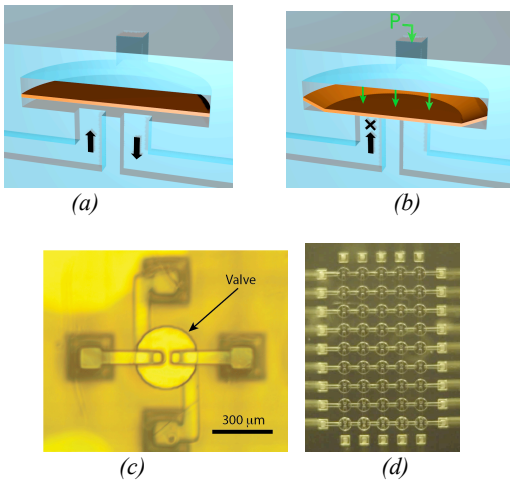

Figure 1: Schematic illustration of a pneumatic membrane valve open (a) and closed (b). (c) Microscope photo of a 3D printed membrane valve and (d) an array of 45 300 μm diameter valves in a test configuration.

The measured relative dye concentration as a function of designed dye concentration is shown in Fig. 4(a). Using our new image analysis method, we can estimate the uniformity of the concentration across the outlet channel for each video frame. The smaller the standard deviation of the concentration within a frame, the better the fluid is mixed. The frame-to-frame standard deviation of the in-frame standard deviation is a measure of the degree of mixing over time, which is shown in Fig. 4(b). The

978-1-940470-03-0/HH2018/$25©2018TRF
DOI 10.31438/trf.hh2018.61

results indicate that 4 to 5 mixing periods in the active mixer is sufficient to reach the noise floor of the measurement method.

CONCLUSIONS

We have demonstrated that 3D printing with our custom 3D printer and material can realize compact functional elements in a 3D (as opposed to planar) geometry that would be very difficult or impossible to fabricate with traditional methods.

REFERENCES

[1] MJ Beauchamp, GP Nordin, and AT Woolley, "Moving from millifluidic to truly microfluidic sub-100-mum cross-section 3D printed devices", Anal Bioanal Chem. 409, 4311 (2017).

[2] H Gong, BP Bickham, AT Woolley, and GP Nordin, "Custom 3D printer and resin for 18 um x 20 um microfluidic flow channels", Lab Chip. 17, 2899 (2017).

[3] H Gong, AT Woolley, and GP Nordin, "High density 3D printed microfluidic valves, pumps, and multiplexers", Lab Chip. 16, 2450 (2016).

[4] H Gong, AT. Woolley, and GP. Nordin, "3D printed high density, reversible, chip-to-chip microfluidic interconnects," Lab on a Chip, 18, 639-647 (2018).

CONTACT

*G.P. Nordin, tel: +1-801-422-1863; nordin@byu.edu

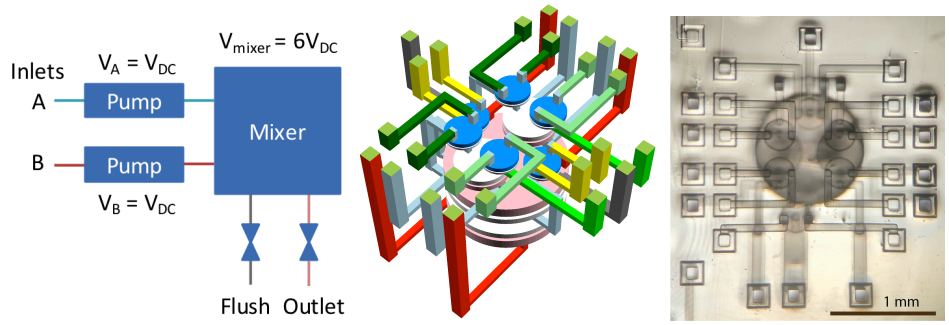

(a) *(b)* *(c)*

Figure 2: (a) Functional illustration of mixer-pump. (Vxx are volumes.) (b) 3D CAD layout with chip-to-chip interconnects. (c) Microscope photograph of 3D printed mixer-pump and chip-to-chip interconnects. The volume occupied by only the mixer-pump itself is 1.2 mm x 1.5 mm x 1.1 mm = 2 mm^3.

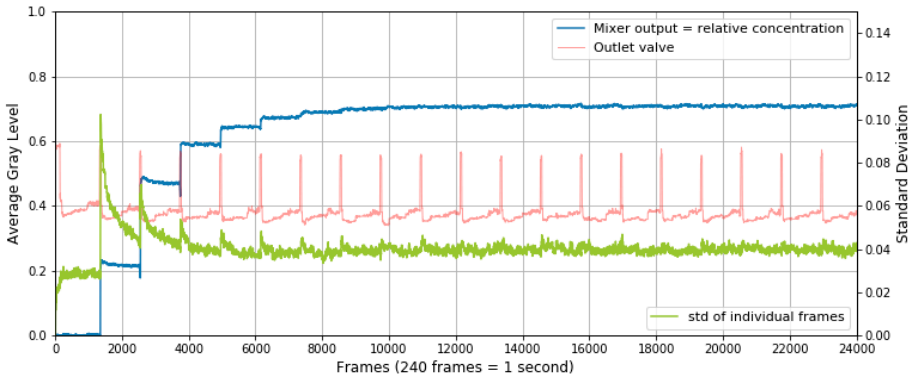

Figure 3: Result of processing video of mixer pump during operation. Blue—relative concentration, Green—standard deviation of relative concentration within each video frame, Red—outlet valve opens during short peaks.

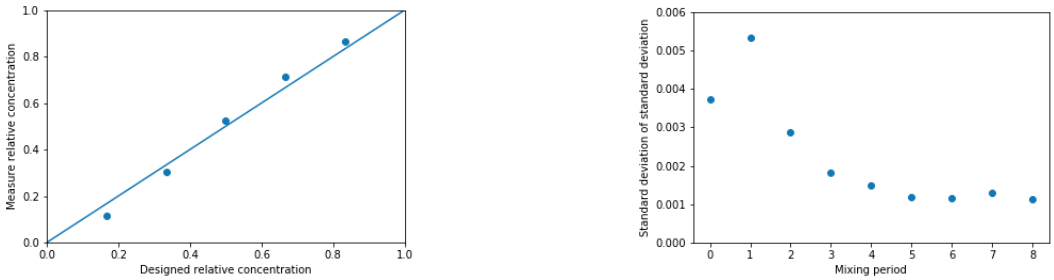

(a) *(b)*

Figure 4: (a) Measured relative concentration as a function of designed relative concentration. Circles are measurements, line is ideal relationship. (b) Frame-to-frame variation of the in-frame concentration variation as a function of how many periods of back-and-forth fluid flow is performed in the mixer structure.

A FULLY-INTEGRATED WEARABLE MICROFLUIDIC ACTUATION AND SENSING PLATFORM FOR BIOMARKER ANALYSIS

H. Lin[1], S. Lin[1], Y. Zhao[2], H. Hojaiji[1], S. Pilehvar[1], S. Thakur[3], M. Karapetian[1], K. King[1], R. Frias[1], and S. Emaminejad[1]

[1] Department of Electrical Engineering and Computer Sciences, University of California, Los Angeles, CA, USA
[2] Department of Materials Science and Engineering, University of California, Los Angeles, CA, USA
[3] Department of Bioengineering, University of California, Berkeley, CA, USA

ABSTRACT

Here, we devise a suite of electro-fluidic and electrothermal interfaces, integrated within a wearable microfluidic platform, to implement an illustrative set of critical biofluid actuation (including pumping and valving) and sensing operations, thus enabling autonomous wearable sample processing and analysis.

INTRODUCTION

Recent advances in electrochemical sensor development, flexible device fabrication, and low power electronics have created an unprecedented opportunity to realize wearable biomarker monitoring platforms that provide frequent and objective measurements of the health condition of individuals. Previously reported wearable biomarker monitoring platforms demonstrated suitable sensing schemes for the detection of target analytes in biofluid samples (*e.g.* sweat and interstitial fluid) that are passively collected in absorbent pads or microfluidic channels. However, due to the lack of controlled biofluidic handling strategies, their operations cannot be scaled to perform autonomous sample processing and analysis.

RESULTS AND DISCUSSION

Figure 1 illustrates the system level diagram of our platform's operation. The wearable microfluidic module is integrated into a miniaturized and custom-developed wireless printed circuit board to realize seamless biofluid control and analysis.

To implement pumping, we exploit AC electrothermal flow (ACEF) which is amenable for high conductivity fluid handling (*e.g.*, biofluids). ACEF arises in the presence of a non-uniform electric field which results in temperature gradient and fluid motion. Here, we used a pair of asymmetric ACEF electrodes, which creates imbalanced temperature and electric field profiles to break the symmetric competitive vortices, resulting in directionally-induced fluid motion (*i.e.* pumping) [1], as verified by our COMSOL simulation (Fig. 2a). Our design consists of a narrow electrode (width: 40 μm) and a wide electrode (width: 90 μm), which are separated by 30 μm and patterned onto the bottom of the channel to establish the intended non-uniform electric field profile. To validate the pumping functionality, we applied 1.4 V_{RMS} (> 1MHz) across the asymmetric electrode pair, and tracked the motion of the fluid, through time-sequential imaging of a group of microbeads suspended in artificial sweat (Fig. 2b). By increasing the applied voltage levels across the pumping electrode pair, we validated that the induced velocity profile is correlated with the fourth power of the applied voltage ($R^2 = 0.97$, Fig. 2c), which is in agreement with previous studies [1].

To realize on-chip valving, we exploit a stimuli-responsive hydrogel, specifically, poly(N-isopropylacrylamide) (PNIPAM), which significantly shrinks in response to local temperature increments. The PNIPAM-valve can be opened when desired by heating the hydrogel above its transition temperature. Accordingly, in our approach, we embedded the hydrogel structure into the microfluidic channel, with a programmable microheater, patterned at its bottom. As shown in Fig. 3a, by applying voltage (~3 V) across the terminals of the heater, we maintained the local temperature above 48 °C, to subsequently shrink the hydrogel and open the microfluidic channel. We validated the functionality of the controlled valving methodology on body by performing human subject testing (Fig. 3b).

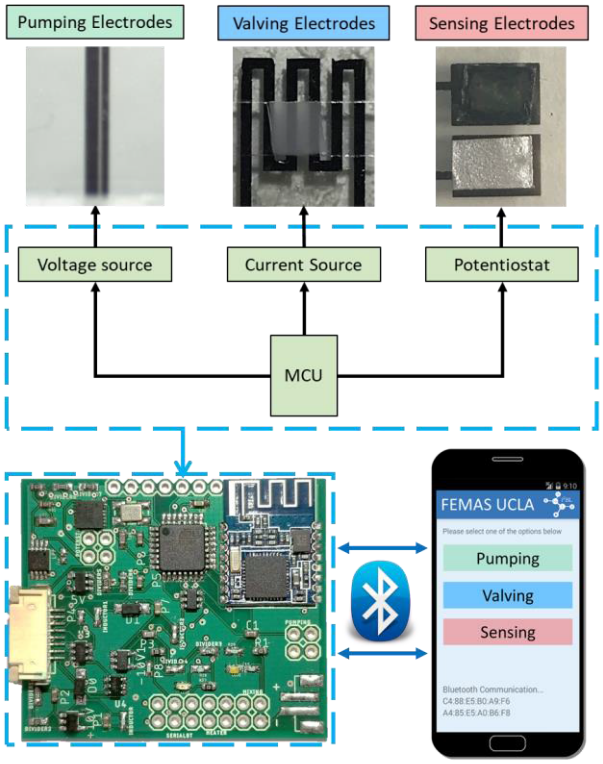

Figure 1: The schematic diagram of our fully-integrated wearable microfluidic platform. The microfluidic module contains: i) an asymmetric electrode pair to induce pumping, ii) an embedded hydrogel/heater configuration to implement valving, and iii) an enzymatic sensing interface for biomarker quantification (e.g. glucose). The system-level operation is achieved through integration of the microfluidic module with a wireless and miniaturized circuit board. The data communication/control commands are communicated via Bluetooth to/from a custom-developed mobile application.

To demonstrate our platform's biomarker sensing capability, we developed (following our previous protocol [2]) and embedded enzymatic sensing electrodes in our microfluidic module to measure the glucose content of sweat samples. As shown in Fig. 4a, the corresponding glucose sensor calibration curve demonstrates high degree of linearity within physiologically relevant range of glucose concentration.

978-1-940470-03-0/HH2018/$25©2018TRF
DOI 10.31438/trf.hh2018.62

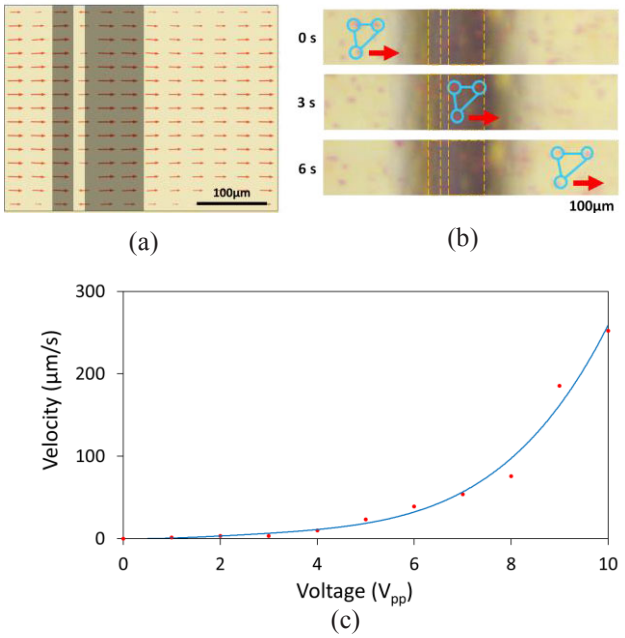

*Figure 2: **(a)** COMSOL-simulated flow velocity profile induced by a pair of asymmetric electrodes. **(b)** Time-sequential imaging of artificial sweat pumping. A representative group of beads are tracked as they move unidirectionally from left to right in the time span of 6 s. **(c)** Measured pumping velocity profile with respect to applied voltage levels.*

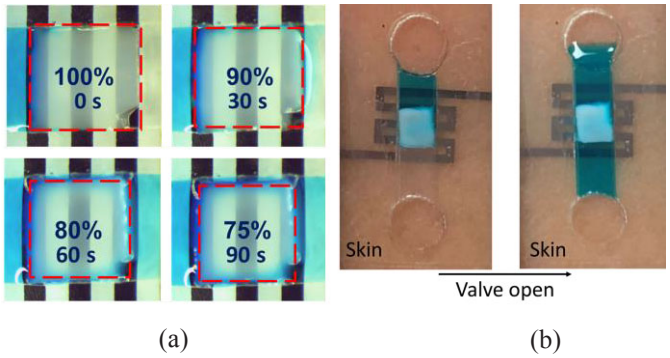

*Figure 3: **(a)** Timeline of Hydrogel shrinkage upon activating the heater (temperature maintained above 48 ºC). Blue-dyed artificial sweat passes through the valve from left to right as valve shrinks. **(b)** Demonstration of on-body valving as controlled by our circuit board.*

We validated our glucose sensor functionality by analyzing the iontophoretically-stimulated sweat samples, collected from a subject during 12-h fasting and 0.5 h after 30 g glucose intake (Fig.4b). Our results indicate that oral glucose consumption in the fasting state is followed by increased sweat glucose levels (here, from 254 μM to 345 μM).

In conclusion, we developed and validated the functionalities of a fully-integrated wearable actuation and sensing microfluidic platform for autonomous biofluid processing and analysis.

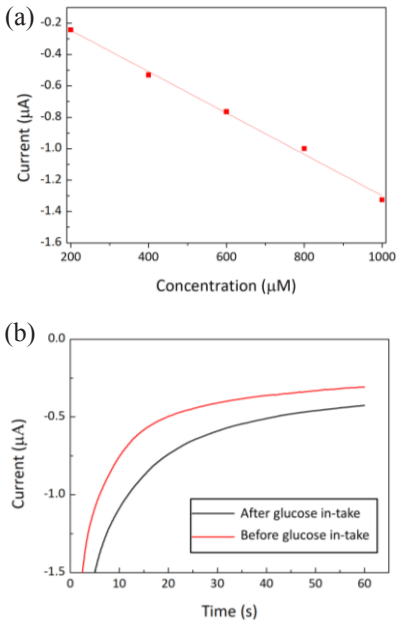

*Figure 4: **(a)** Calibration curve of our developed glucose sensor response (performed in spiked artificial sweat samples). **(b)** Our sensor response to the sweat samples of a subject during 12-h fasting state and 30 minutes after 30 g of glucose intake, demonstrating the elevation in sweat glucose level after glucose intake.*

REFERENCES

[1] J. Wu, M. Lian, and K. Yang, "Micropumping of biofluids by alternating current electrothermal effects", Applied Physics Letters 90, 234103 (2007).

[2] S. Emaminejad, W. Gao, H. Y. Y. Nyein, S. Challa, R. W. Davis, A. Javey, "Flexible Systems for Wearable Physiological Monitoring Applications", Solid State Sensors, Actuators, and Microsystems Conference, (Hilton Head), pp. 108-109, June 2016.

ACKNOWLEDGEMENTS

The authors appreciate the members of UCLA nanoelectronics research facility and Lux Lab from UCLA Library for their help in device fabrication.

A HIGHLY SENSITIVE IMPEDIMETRIC APTASENSOR FOR WEARABLE DETECTION OF HORMONES

Sanaz Pilehvar[1], Shuyu Lin[1*], Hannaneh Hojaiji[1], Yichao Zhao[1,2], and Sam Emaminejad[1]*
[1] Department of Electrical and Computer Engineering, University of California, Los Angeles, CA, USA
[2] Department of Materials Science and Engineering, University of California, Los Angeles, CA, USA
* Equal Contribution

ABSTRACT

A highly sensitive impedimetric aptamer-based sensing method is developed for the wearable detection of hormones, that are present in biofluids at nanomolar concentrations. The methodology is applied to monitor the cortisol diurnal profile in iontophoretically-induced sweat.

INTRODUCTION

Wearable sweat analysis offers a promising pathway toward non-invasive and continuous monitoring of hormones for a diverse set of clinical and personalized health monitoring applications. While previously reported sweat sensors successfully demonstrated on-body measurement of a panel of target analytes, because of the lack of suitable *in-situ* signal enhancement strategies, their detection limit remained in µM to mM range. To overcome this barrier, here, we devise and combine two synergistic sensor development strategies: 1) direct electrochemical detection of probe-target analyte based on DNA-aptamer-target biomarker interactions using electrochemical impedance spectroscopy (EIS) technique and 2) incorporation of a redox-probe treated protective layer which enhances the sensitivity of the EIS measurements, while preventing the sensor surface degradation caused by the inherent etching effect of redox probes. As a proof of concept, we applied this approach for sensitive and on-body detection of cortisol, which is present in nanomolar levels in biofluids (including sweat) and has promising clinical utility (as a key metabolic regulator and a stress marker).

RESULTS AND DISCUSSION

In our approach, the underlying EIS based sensing mechanism relies on monitoring the interfacial resistance change of the working electrode, which is measured in the presence of the reversible redox probe $[Fe(CN)_6]^{3-}/[Fe(CN)_6]^{4-}$.

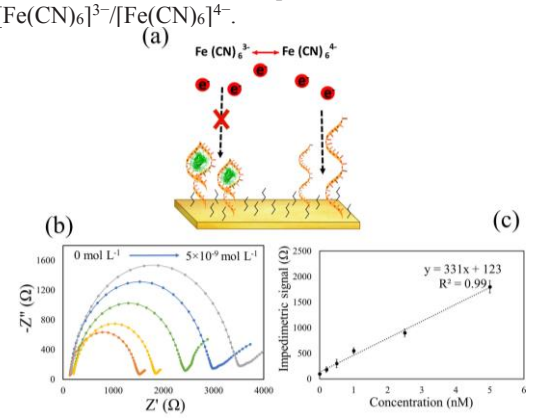

Figure 1: (a) Schematic diagram of the aptasensor operation, illustrating the partial blockage of electron transfer due to the formation of aptamer-target analyte complex, (b) EIS responses to different concentration of cortisol. (c) The sensor's corresponding calibration curve.

The sensing interface consists of DNA-aptamer-based cortisol recognition elements, which are covalently immobilized on the surface of a working electrode. The formation of aptamer-cortisol complex at the surface results in the partial blockage of electron-transfer (as shown in Fig. 1a). This leads to an increase in the interfacial resistance which is correlated to the concentration of cortisol (our corresponding measurement results are shown in Fig. 1b, c). Additionally, to overcome the etching effect of the redox probes, we incorporate them into a protective layer mounted on the sensor surface. Here, the etching effect is induced by CN^- released from the $[Fe(CN)_6]^{3-}/[Fe(CN)_6]^{4-}$ couple, which leads to gradual removal of the self-assembled monolayer of DNA probes [1].

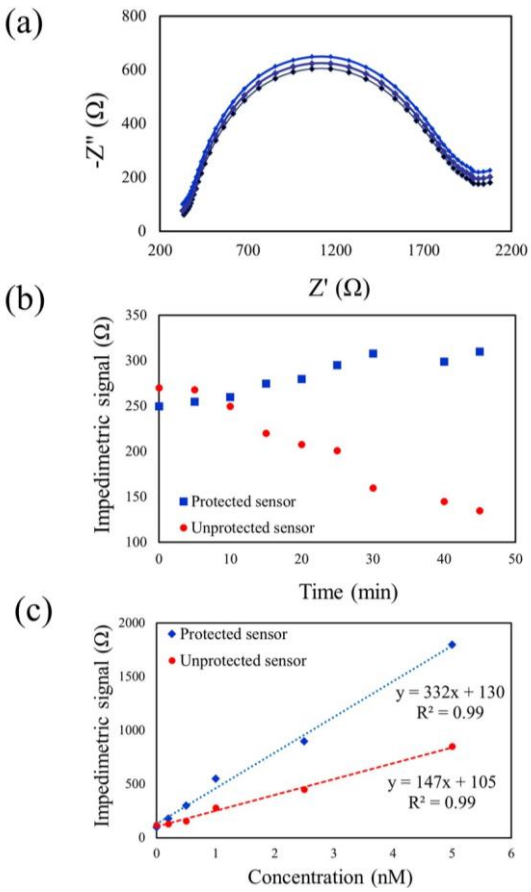

Figure 2: (a) Intermittent impedance measurements (Nyquist plots) with 10 min intervals, illustrating preserved stability of the sensing layer with the use of the protective layer. (b) Comparison of the protected vs. unprotected sensor response to a 5 nM cortisol solution: the response of the unprotected sensing interface degrades over time. (c) Comparison of the protected vs. unprotected sensor calibration curve, illustrating the enhanced sensitivity of the protected sensor.

The incorporated protective layer preserves the sensing surface from direct exposure to CN^- containing medium, while facilitating the originally intended signal transduction mechanism (Fig 2 a-c).

978-1-940470-03-0/HH2018/$25©2018TRF
DOI 10.31438/trf.hh2018.63

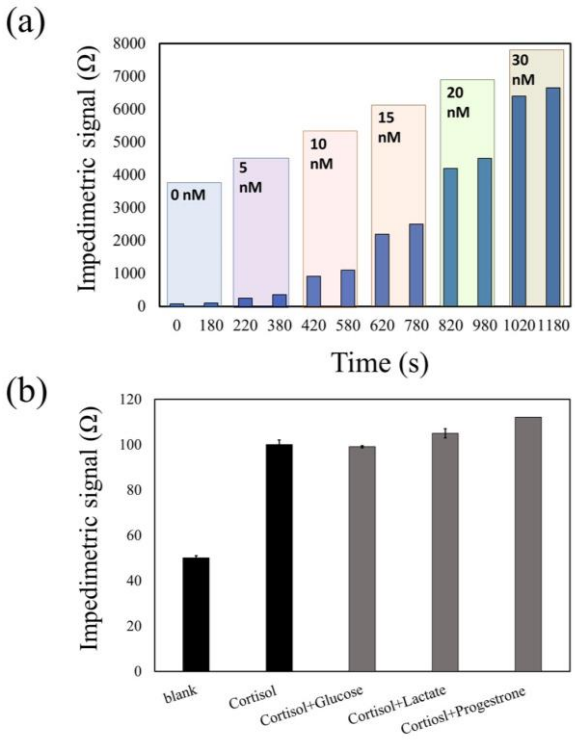

Figure 3: (a) Continuous sensor response characterization for progressively increasing cortisol concentration. (b) Aptasensor interference study: comparison of the sensor response to 5 nM cortisol solution, to that with added interfering non-target analytes, including glucose (100 μM), lactate (100 μM) and progesterone (5 nM) (all spiked in Tris buffer).

To characterize our sensor, first, the continuous response of the sensor for different cortisol concentration regimes (5, 10, 15, and 20 nM) is evaluated over time. As shown in Fig. 3a, our results indicate the preserved stability of the sensor's progressive response. Additionally, we performed interference studies to characterize the selectivity of the sensor to ensure that the non-target compounds in sweat (some with several orders of magnitude of higher concentration) do not interfere with the sensor response. To this end, we evaluated the sensor response against an illustrative panel of non-target analytes including glucose, lactate, and progesterone (within their physiologically relevant range of concentrations). The obtained data shows that non-specific bindings have minimal influence on the sensor response (as evident from small changes in the transduced signal, Fig 3b).

To inform the potential future clinical applications, the devised methodology was applied to analyze the cortisol content of iontophoretically-induced sweat samples, collected from a healthy subject during a day (Fig. 4a). We validated our sensor accuracy by comparing the concentration values, as estimated by our sensor response, with those obtained from High Performance Liquid Chromatography (HPLC, as a gold standard technique, Fig. 4b). The high degree of agreement for obtained measurements (R^2 = 1) demonstrates our sensor's remarkable level of accuracy. The versatility of our methodologies allows for their use, with minimal effort and reconfiguration, to target various other hormones and metabolites in other non/minimally-invasive biofluids such as saliva, interstitial fluid, and urine. Therefore, we envision that the presented methodologies would open new directions for personalized health monitoring.

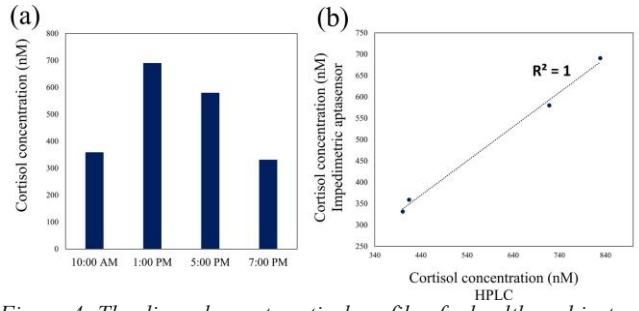

Figure 4: The diurnal sweat cortisol profile of a healthy subject, as measured by our developed aptasensor (a), The correlation of gold standard HPLC and our aptasensor, demonstrating our sensor's high level of accuracy (b).

The high degree of agreement for obtained measurements demonstrates our sensor's remarkable level of accuracy (R^2 = 1). The versatility of our methodologies allows for their use, with minimal effort and reconfiguration, to target various other hormones and metabolites in other non/minimally-invasive biofluids such as saliva, interstitial fluid, and urine. Therefore, we envision that the presented methodologies would open new directions for personalized health monitoring.

REFERENCES

[1] S. Vogt, Q. Su, C. Gutiérrez-Sánchez, and G. Nöll, "Critical View on Electrochemical Impedance Spectroscopy Using the Ferri/Ferrocyanide Redox Couple at Gold Electrodes", Analytical chemistry, 88, 4384 (2016).

CONTACT

S. Emaminejad, emaminejad@ucla.edu

AN ULTRASONICALLY POWERED ACTIVE STENT FOR ENDOVASCULAR DISEASES

Sayemul Islam[1] and Albert Kim[1]*
[1]Department of Electrical Engineering, Temple University, Philadelphia, Pennsylvania, USA

ABSTRACT

Endovascular aneurysm repair (EVAR) is a preferred treatment for patients with abdominal aortic aneurysm, especially for people who are not a good candidate for open surgery. However, the failure of endograft device can lead to post-EVAR sequela. It is imperative to develop an active stent that monitors the endovascular flow. This paper presents an ultrasonically powered active stent platform with a wireless sensing system. The active stent, which is an ultrasonic receiver is made of 110µm-thick polyvinylidene fluoride (PVDF). The stent incorporates surface machined patterns that induce negative Poisson's ratio and power (i.e., vibration) enhancement. A cantilever-type flow sensor (cut from the PVDF) modulates the frequency of a surface integrated RF transmitter for wireless monitoring of blood flow. The flow sensor showed an average sensitivity of 0.11mV/mL/min when the RF transmitter could send the flow information 1 meter away to the receiver wirelessly with the frequency range of 81-88MHz.

INTRODUCTION

Endovascular aneurysm repair (EVAR) is a minimally invasive treatment for abdominal aortic aneurysm patients by implanting a graft. It has been an exceedingly common technique, practiced since the first graft implantation in 1991 [1]. A bare-metal stent is inserted through a small incision and is positioned at the aneurysm site with an aid of image-guided system. The stent is then expanded within the artery to restore blood flow. This approach offers reduced post-surgical trauma, time under general anesthesia, length of hospital stays, and lowering mortality rates [2]. However, there are EVAR complications (e.g., arterial thrombosis, clot embolization into aortic side-branches, and pseudoaneurysm formation) due to device failure, procedural issues, and endoleaks which requires immediate surgical intervention [3]. Periodic monitoring of abdominal aortic blood flow after EVAR could predict such ischemic complications. In this paper, we report an ultrasonically powered active stent platform that incorporates a blood flow sensor and an RF transmitter to potentially minimize EVAR complications. Figure 1(a) shows a schematic view, and Figure 1(b) shows a block diagram of the active stent. The active stent consists of a surface machined and rolled PVDF sheet, a cantilever-type flow sensor, and surface integrated electronics (a rectifier, an amplifier, and LC tank modulated RF transmitter).

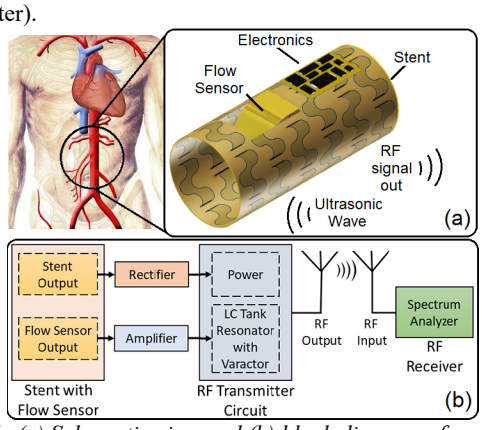

Figure 1: (a) Schematic view and (b) block diagram of an ultrasonically powered active stent with wireless flow sensor.

MATERIALS AND METHODS

As ultrasound is applied from outside the body, the stent with piezoelectric characteristics converts the mechanical energy to electrical power to energize the embedded sensor and electronics. The stent was designed with a surface pattern which has three important roles: 1) allowing shrinkage and expansion like traditional stents (negative Poisson's ratio), 2) providing anchoring, and 3) increasing power output by enabling vibration amplification [4].

For the flow sensor, a cantilever is cut from the main stent surface and bent towards the direction of blood flow. The flow induces deflection of the cantilever, which generates an electrical potential proportional to blood flow rate [5]. The electrical potential is then amplified (Gain = 37dB) and fed to a voltage-controlled varactor which is a part of the LC tank of the RF transmitter. The 7.5mm×4mm cantilever generated 53mV to 131mV for the flow rate range of 30mL/min to 980mL/min, which is within the normal range of blood flow rate [6]. Both power and amplified sensor output are fed to a Colpitts oscillator-based RF transmitter (i.e., FM transmitter) for wireless blood flow monitoring. The FM transmitter was designed to carry a base frequency of 81MHz.

Such ultrasonic power-in, RF data-out interrogation scheme can be demonstrated in the stent design and the fabrication process is shown in Figure 2. The custom pattern and the cantilever-type sensor are machined out of PVDF using a cutter/plotter, Figure 2(a)-(b). After completing the electrical connections, a thin layer of polydimethylsiloxane (PDMS) is deposited for passivation, Figure 2(c). During curing (after 30 min), the sample is removed and placed in a vacuum oven for full curing, Figure 2(d). This process introduces a very thin layer of passivation (~10µm). Then it is rolled into a cylindrical shape and sutured using FDA-approved nylon thread. The active stent is completed by assembling electronic components on the surface, Figure 2(e). Figure 2(f)-(g) shows pictures of a prototype. The overall stent dimension was 30mm×10mm (thickness=110µm), and the flow sensor was 7.5mm×4mm.

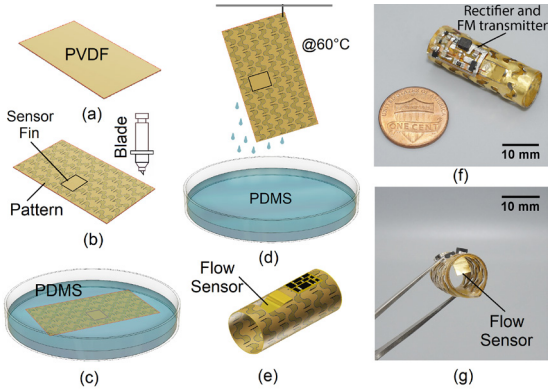

Figure 2: Fabrication process: (a) planar PVDF; (b) patterning with cutter/plotter; (c) submerging into PDMS for passivation; (d) half-cured PDMS dripping to form a thin layer; (e) rolled and sutured; (f) prototype; (g) top view shows the flow sensor fin.

The prototype of the active stent was characterized *in vitro* using the experimental setup illustrated in Figure 3. A sinusoidal

978-1-940470-03-0/HH2018/$25©2018TRF
DOI 10.31438/trf.hh2018.64

signal from a function generator is fed into an RF amplifier to drive an ultrasonic transducer (Lead zirconate titanate, PZT5H, Piezo Inc.) to operate at 6.7MHz frequency while its acoustic intensity was below FDA limit (720mW/cm^2). A mass flow pump modulated the water flow to mimic a blood flow through closed-loop tubing while its flow rate was monitored by an inline digital flow meter and an active stent flow sensor. The sensor readout was monitored by a spectrum analyzer which was placed approximately 1m away to monitor frequency changes corresponding to the change in flow rate.

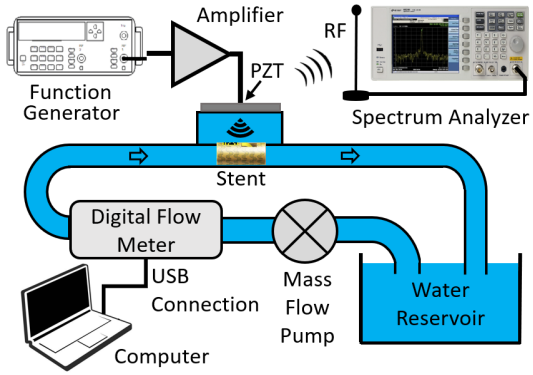

Figure 3: Experiment setup: Amplified sine wave is fed to a PZT transducer to induce ultrasonic wave; mass flow pump mimics blood flow inside tubing; spectrum analyzer is receiving RF output signal from active stent; digital flow meter is used to verify output data.

RESULTS

The mechanical characterization of the stent designs was performed at first, shown in Figure 4. Figures show the change in stent diameter, Figure 4(a), and change in the angle of the fins (patterns stood up), Figure 4(b), while changing the length of the stent for different samples with various pattern placements varied in arrowed direction, Figure 4(c). As shown in Figure 4, the optimized mechanical performance was 2.4mm expansion in diameter and 34.8º rising in fin angle when the length expansion was 2.91mm.

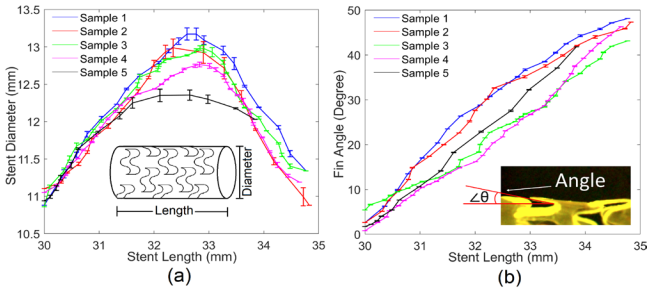

Figure 4: Mechanical relationship of expansion: (a) diameter changes and, (b) fin angle changes with stent length expansion; (c) Pattern placements varied towards arrowed direction for different samples.

After the stent platform characterization, the flow sensor and the RF transmitter were characterized. Figure 5 shows the output characteristics of the cantilever-type flow rate sensor. The sensor could measure flow rate ranging from 30 to 980mL/min with a linear sensitivity of 0.16mV/mL/min in 30-200mL/min range and 0.06mV/mL/min in 201-980mL/min range. Wireless sensing readout is shown in Figure 6. The range of the received frequency peak was in 81-88MHz range on the spectrum analyzer while the flow sensor's flow rate varied between 30 to 980mL/min range.

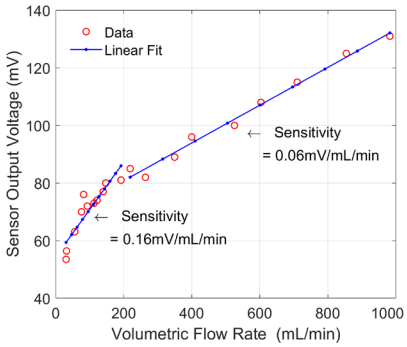

Figure 5: Flow sensor output voltage varying with flow rates.

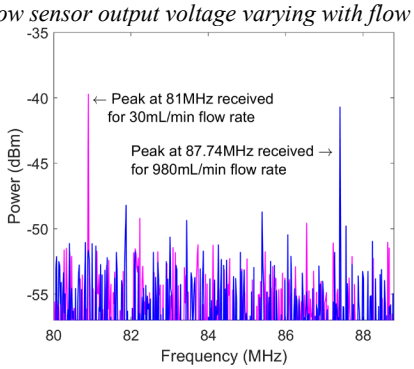

Figure 6: Received frequency on spectrum analyzer for minimum (30mL/min) and maximum (980mL/min) flow rates.

CONCLUSION

Ultrasonically powered wireless interrogation scheme was developed and implemented in an active stent with a flow rate sensor and an RF transmitter. It is expected to reduce the post-EVAR complication and provide convenient access to diagnostic information of the patients.

ACKNOWLEDGEMENTS

The authors would like to thank Dr. Dennis Silage for his valuable advice and help with the experimental setup.

REFERENCES

[1] J. C. Parodi, J. C. Palmaz, and H. D. Barone, "Transfemoral Intraluminal Graft Implantation for Abdominal Aortic Aneurysms," *Ann. Vasc. Surg.*, vol.5, no.6, pp.491–499, 1991.

[2] Greenhalgh, R. (2004). Comparison of endovascular aneurysm repair with open repair in patients with abdominal aortic aneurysm (EVAR trial 1), 30-day operative mortality results: randomized controlled trial. *The Lancet, 364*(9437), 843-848.

[3] G. Maleux, M. Koolen, and S. Heye, "Complications after Endovascular Aneurysm Repair," *Semin. Intervent. Radiol.*, vol. 26, no. 1, pp. 3–9, 2009.

[4] A. Putra, Y. M. Cheah, N. Muhammad, A. Rivai, and C. M. Wai, "The Effect of Perforation on the Dynamics of a Flexible Panel," *Advances in Acoustics and Vibration*, vol. 2014, pp. 1–17, 2014.

[5] Y. Xin *et al.*, "The use of polyvinylidene fluoride (PVDF) films as sensors for vibration measurement: A brief review," *Ferroelectrics*, vol. 502, no. 1, pp. 28–42, 2016.

[6] B. A. J. Angelsen and A. O. Brubakk, "Transcutaneous measurement of blood flow velocity in the human aorta," *Cardiovasc. Res.*, vol. 10, no. 3, pp. 368–379, 1976.

CONTACT

*Prof. Albert Kim, albertkim@temple.edu

ELECTROCHEMICALLY-FUNCTIONALIZED AND VERTICALLY CONDUCTIVE ADHESIVE TAPES FOR WEARABLE SWEAT BIOMARKER MONITORING

Yichao Zhao[1], Hannaneh Hojaiji[2], and Sam Emaminejad[2]
[1]Department of Materials Science and Engineering, University of California, Los Angeles, California, USA
[2] Department of Electrical Engineering, University of California, Los Angeles, California, USA

ABSTRACT

A vertically conductive and electrochemically functionalized adhesive sensor is developed, which can be simply taped onto/detached from a wearable circuit board's sensor-designated contact pads. These sensors are used in human subject testing experiments to monitor the sweat metabolites' concentrations.

INTRODUCTION

The exponential growth in the Internet of Things (IoT) devices and wearable sensing technologies have created an unprecedented opportunity to enable personalized medicine, through real-time biomonitoring of individuals and enabling actionable feedback. Currently, commercialized IoT devices and wearable sensors are only capable of tracking physical activities and vital signs and fail to access molecular-level biomarker information to provide insight into the body's dynamic chemistry. Sweat-based wearable biomonitoring has emerged as one of the most promising candidates to merge this gap. Sweat is a rich source of biomarkers that can be retrieved unobtrusively [1]. Previously reported sweat analysis platforms have successfully demonstrated the *in-situ* measurement of sweat analytes in wearable formats. However, the lack of suitable sensor fabrication/integration schemes continue to prevent us from incorporating these sensors into commercialized wearable technologies to scale them for population-level adoption. Specifically, the presented platforms comprise of physically-decoupled sensor arrays and readout circuit board modules and rely on 2D electrical connections (on the same plane as the sensing interface) and cables to relay the transduced signal. Therefore, inherently, they are spatially inefficient and their integration into existing wearable technologies is non-trivial. To overcome these bottlenecks, here, we devise a novel sensor fabrication/integration methodology, which allows for seamless and compact integration of disposable electrochemical sensors with permanent readout electronics.

RESULTS AND DISCUSSION

As conceptualized in Fig. 1, in our approach, we construct our electrochemical sensing layer on a vertically-conductive adhesive substrate that can be simply taped onto/detached from the electrical contact pads of a wearable electronic reader. As a proof of concept, we applied our methodology to create enzymatic glucose and lactate sensors and validated their functionalities by performing human sweat sample analysis. To construct our sensing layer, we first evaporate gold on a z-axis electrically-conductive adhesive tape (which exploits gold particles, embedded in its structure, for electron transfer in vertical direction). Then, the gold-coated surface is functionalized with glucose/lactate oxidase enzymes entrapped in chitosan films. These sensing interfaces effectively output electrical current correlating to the concentration of the target analytes. Because of the sensor structure's unique z-direction electron transfer property, and stable adhesion to metal contacts or common printed circuit board substrates (including gold and copper), the electrochemically-functionalized tape can be vertically integrated into electronic platforms (*e.g.* smartwatch).

Figure 2 illustrates the calibration curves for the glucose and lactate sensors, demonstrating the corresponding sensors' highly linear responses (R^2 = 0.99) within the physiologically relevant ranges of concentrations.

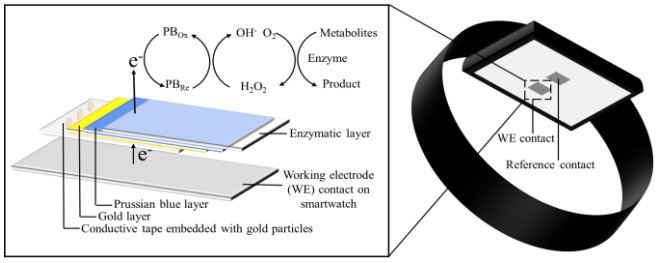

Figure 1: Schematic diagram for a representative enzymatic sensor, where the disposable working electrode (WE) can be simply taped onto the corresponding metal contact of the backside of a smartwatch (as an electronic reader). The placement of the reference electrode follows the same procedure.

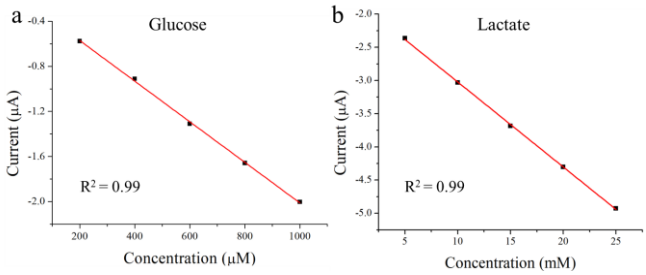

Figure 2: The calibration curves of glucose (a) and lactate (b) sensors (characterized in phosphate-buffered saline) demonstrating the high degree of linearity of the sensors' responses.

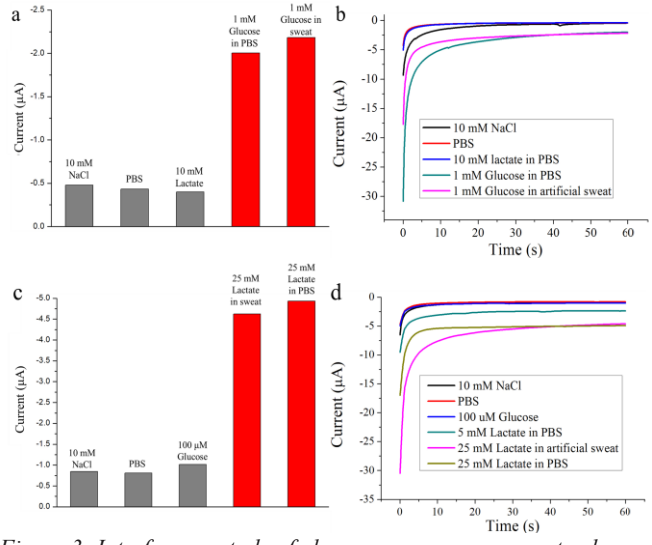

Figure 3: Interference study of glucose sensor response: steady state (a) and corresponding amperometric response (b). The equivalent interference study figures for lactate sensor are shown in (c) and (d).

978-1-940470-03-0/HH2018/$25©2018TRF
DOI 10.31438/trf.hh2018.65

We validated our sensors' selectivity, by studying the effect of non-target compounds (present in sweat) on our sensors' responses. As can be seen in Fig. 3, the sensors' output current levels due to interfering molecules are negligible as compared to those generated in response to target analytes.

To validate our glucose sensor functionality, we collected iontophoretically-stimulated sweat samples from three subjects during 12-h fasting and 0.5 h after glucose intake (30 g glucose). As shown in Fig. 4, the sweat glucose level is clearly increased in all three subjects. Therefore, it is a promising method to achieve non-invasive blood glucose monitoring.

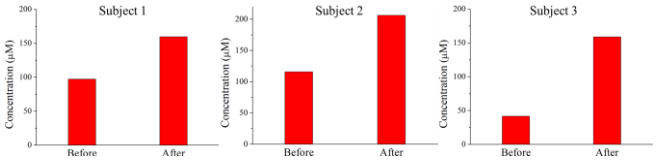

Figure 4: Sweat glucose levels of three subjects during 12-h fasting state and 30 minutes after 30 g of glucose intake.

Additionally, we integrated our lactate sensor into a smartwatch to perform real-time sweat analysis during a graded-load cycling exercise (Fig. 5). In this study, the exercise intensity was increased at two steps (700 and 900 s after beginning the exercise). The sweat secretion initiated at about 800 s after beginning the exercise. The wirelessly transmitted sweat lactate information demonstrated that the readily stabilized sweat lactate concentration elevated in response to the second increase in the exercise intensity level (as expected).

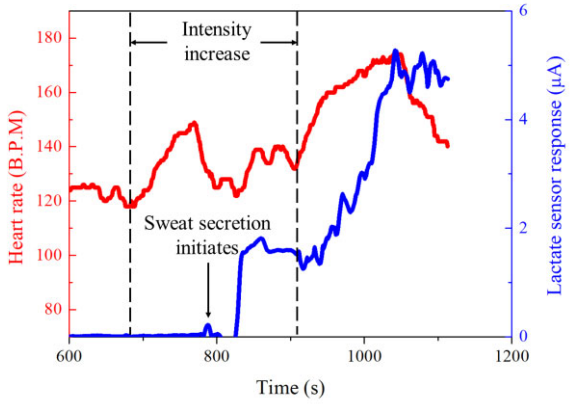

Figure 5: On-body sweat lactate measurement during physical exercise (stationary cycling with three different intensities). The measured readings are low-pass filtered at 0.1 Hz in digital domain. The upper curve indicates the heart rate profile, measured by a commercial heart rate sensor (left axis) and the lower curve shows the sweat lactate concentration profile (right axis). The exercise intensity was increased at two steps (700 s and 900 s after beginning the exercise), which immediately followed by increase in the measured heart rate. The sweat secretion initiated at about 800 s after beginning the exercise and the sweat lactate level was elevated in response to the second increase in power intensity.

Our scalable sensor fabrication and seamless integration methodology paves the way for incorporation of sweat sensors in commercialized wearable technologies for general population health monitoring.

REFERENCES

[1] S. Emaminejad, W. Gao, H. Y. Y. Nyein, S. Challa, R. W. Davis, A. Javey, "Flexible Systems for Wearable Physiological Monitoring Applications", Solid State Sensors, Actuators, and Microsystems Conference, Hilton Head Isl., 06 (2016) pp. 108-109.

CONTACT

*S. Emaminejad, emaminejad@ucla.edu

HOLLOW FLEXURAL RESONATORS WITH NANOSCALE THICKNESS

Wujoon Cha[1], Samuel M. Nicaise[1], Drew E. Lilley[1], Chen Lin[1] and Igor Bargatin[1]
[1]University of Pennsylvania, Philadelphia, PA, USA

ABSTRACT

Hollow resonators with nanoscale thickness have similar resonance frequencies but much lower spring constants and quality factors than solid resonators of the same dimensions, offering unique advantages in sensor applications. We report hollow beam cantilevers fabricated by performing atomic layer deposition of Al_2O_3 on solid silicon molds and then etching the internal mold. Compared to their solid counterparts, these hollow cantilevers demonstrate reduction of spring constant by up to 100x, quality factor by 10x, and resonance frequency by 1.5x. The reduced spring constant offers enhanced sensitivity in biological or chemical sensing applications while the reduced quality factor increases the bandwidth by approximately 5x.

INTRODUCTION

Resonators with nanoscale thickness (<100 nm) can offer high effective surface area and, therefore, high sensitivity in biological or chemical sensing applications. However, solid resonators with nanoscale thickness typically exhibit low flexural resonance frequency because the frequency is proportional to the thickness of the solid resonator: $f_0 \sim ct/l^2$, where c is the speed of sound of the resonator material, t is the thickness, and l is a characteristic lateral dimension (e.g., the length of a cantilevered beam). Reducing the lateral dimensions can be used to push the frequency back up but the resulting cantilevers have high spring constants and small total areas, which is disadvantageous in some sensing applications [1].

These tradeoffs can be avoided by using hollow beam geometries, in which the resonance frequency is approximately independent of the wall thickness and instead scales with the height of the hollow beam. Although hollow beam cantilevers have been previously used for chemical [2] and biological [3] applications, the thickness of the walls was typically comparable to the height of the resonators, making their resonant properties similar to those of their solid counterparts. Here, we report hollow cantilever resonators with nanoscale thickness and micron-scale heights, resulting in greatly reduced mass, spring constants, and quality factors but nearly unchanged resonance frequency relative to solid counterparts of the same dimensions.

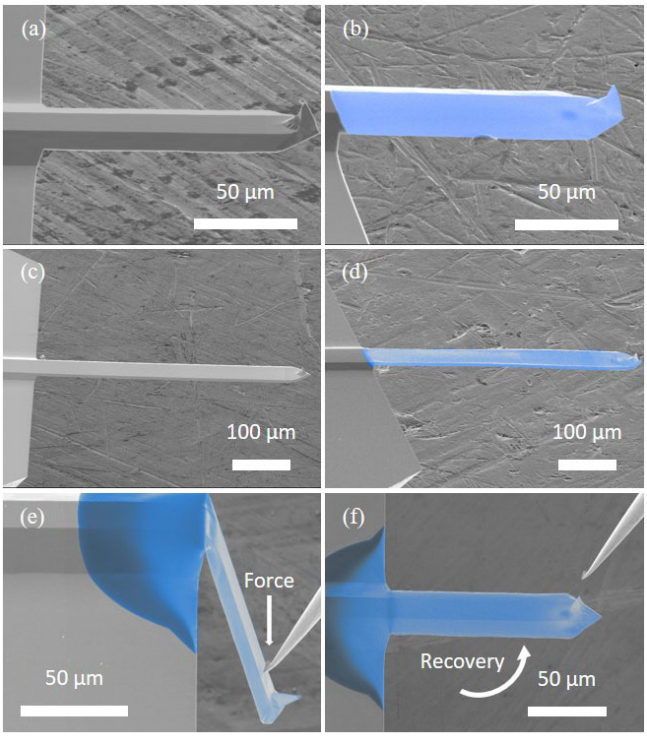

Figure 1: Scanning-electron micrographs of (a) solid and (b) hollow tapping mode cantilevers, as well as (c) solid and (d) hollow contact mode cantilevers. The released hollow shells are artificially colored for clarity. The etch-hole is visible near the tip of the cantilever in panel (b). The hollow cantilevers are mechanically robust, recovering from sharp bending by a micromanipulator probe without damage (e and f).

FABRICATION

We fabricated cantilevered hollow resonators by depositing various thicknesses (20-110 nm) of aluminum oxide (Al_2O_3) on silicon molds using atomic layer deposition (ALD). We used a variety of commercial AFM cantilevers as convenient silicon molds but also fabricated custom silicon molds for larger resonators. After deposition, an etch hole was opened on the top or the sides of the cantilevers using pulsed laser micromachining. Finally, isotropic etching with XeF_2 removed the internal silicon mold, leaving only hollow shell cantilevers. Figures 1a and 1c show original solid cantilever molds while Figures 1b and 1d show hollow cantilevers after fabrication.

RESULT AND DISCUSSION

We determined the resonance frequency, quality factor, and spring constant from both the thermal noise spectra and driven resonance curves (Figure 2). The measurement was first done for solid cantilever molds and then repeated for the final hollow cantilevers. Figure 3 shows the ratio of the resonance frequency (f), quality factor (Q), and the spring constant (k) of solid cantilever to

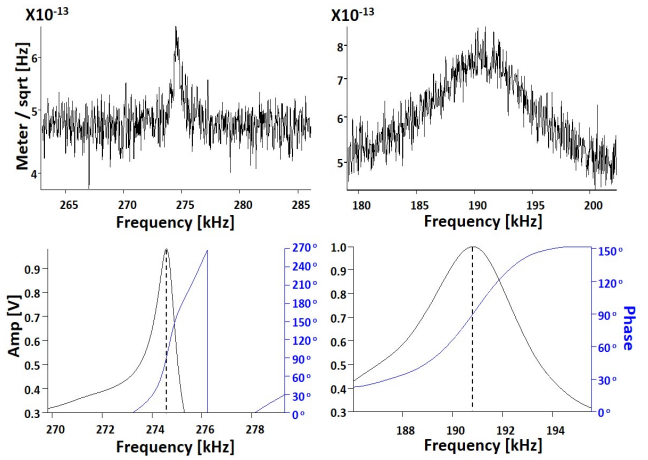

Figure 2: Thermal noise spectra (top) and driven resonance response (bottom) of a solid (left) and hollow (right) cantilever with a length of 140 µm, width of 37.5 µm, height of 4 µm, and thickness of 70 nm. The thermomechanical noise peak is more prominent in hollow cantilevers because the reduction in the quality factor is more than compensated by the reduction in the spring constant.

978-1-940470-03-0/HH2018/$25©2018TRF
DOI 10.31438/trf.hh2018.66

those of hollow cantilever as a function of the ALD Al_2O_3 thickness.

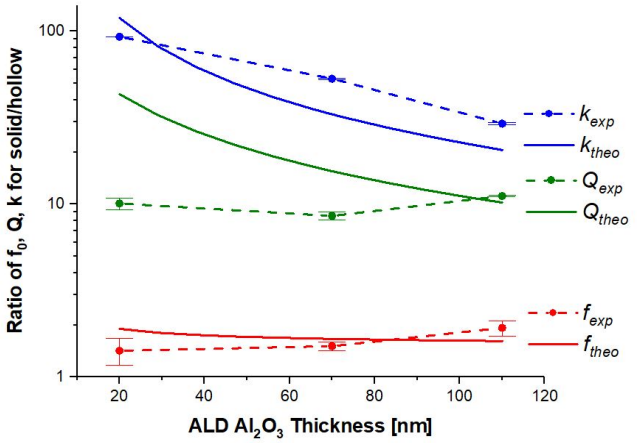

Figure 3: Ratios of the resonance frequency, quality factor, and spring constant of a solid cantilever to those of a hollow cantilever of the same dimensions. The circles with error bars and dashed lines show the experimental data while the solid curves show theoretical predictions.

Ratio with a value larger than 1 indicates that the parameter is reduced in a hollow cantilever relative to that of its solid counterpart. The reduced spring constant and frequency values agreed with the theoretical predictions obtained by approximating the cantilevers as a hollow beam with a rectangular cross-section. The frequency reduction was by a factor of ~1.5x and, as expected, largely independent of Al_2O_3 thickness.

Experimentally, the quality factor in the air was typically reduced by a factor of 10, although theoretical models [4,5] predicted even higher reduction, up to 50x for an Al_2O_3 thickness of 20 nm. The spring constant of the hollow cantilevers ranged from 0.3 to 1.4 N/m, a reduction by a factor of up to 100x. The greatly reduced spring constant offers enhanced sensitivity in biological and chemical sensing applications. In addition, the cantilevers demonstrate extreme mechanical robustness under bending deformations (Figures 1e and 1f), similar to our previously reported hollow mechanical metamaterials [6,7].

Finally, as a result of the greatly reduced quality factor in air and only a small change in the resonance ferquency (Fig. 3), the ringdown time, $\tau_r = Q/2\pi f$, was approximately five times smaller in hollow cantilevers. Figure 4 shows how the smaller ringdown time enhances the spatial resolution of the tapping mode AFM. At the scan rate of 4.88 lines/per second (left panels), the tip spends ~400 microseconds acquiring data for each pixel, which is sufficiently long to reach a steady state for both hollow and solid cantilevers. However, at a scan rate of 9.77 Hz (right panels), the pixel dwell time is reduced to ~200 microseconds, which becomes comparable to the ringdown time of the solid cantilever measured experimentally: $\tau_{r,solid} = 372/(2\pi(287\ kHz)) = 206$ microseconds. As a result, the image obtained with a solid cantilever becomes distorted, especially in the areas of abrupt topography changes. In contrast, the hollow cantilever has a ringdown time that is more than five times smaller $\tau_{r,hollow} = 43/(2\pi(190\ kHz)) = 36$ microseconds and can still resolve the topography. Since the ringdown time is the inverse of the resonator bandwidth, the hollow cantilevers offer greatly increased bandwidths and, therefore, increased data acquisition rates. Similar bandwidth enhancements can be achieved for other resonator geometries and for other resonant sensor applications (e.g., chemical gas sensing, ultrasound transduction, etc.).

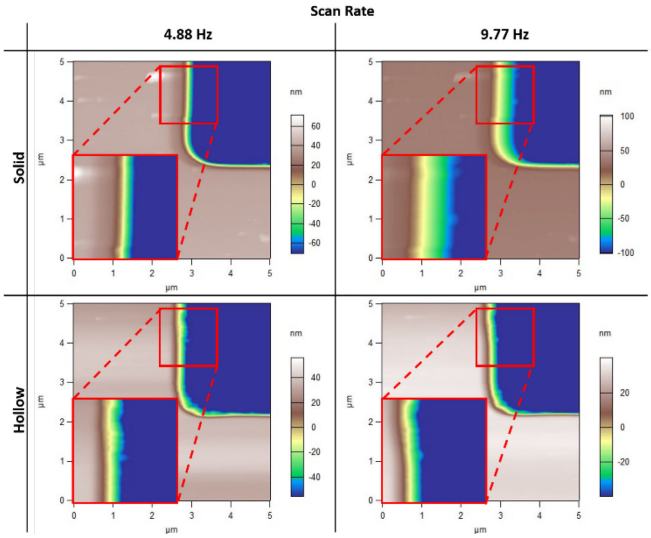

Figure 4: AFM scan images with scan size of 5 µm of a corner of a rectangular calibration grid hole with 200 nm depth using solid and hollow cantilevers at scan rates of 4.88 Hz and 9.77 Hz. The inset images show the zoomed-in view of the edges. At higher scan rate, the solid cantilever does not respond to the probe velocity as quickly as the hollow cantilever, resulting in a distorted edge profile (top right panel).

REFERENCES

[1] I. Bargatin, E.B. Myers, J.S. Aldridge, C. Marcoux, P. Brianceau, L. Duraffourg, et al., "Large-Scale Integration of Nanoelectromechanical Systems for Gas Sensing Applications", Nano Letters, 12, 1269-1274 (2012).

[2] T.P. Burg, M. Godin, S.M. Knudsen, W. Shen, G. Carlson, J. S. Foster, et al., "Weighing of biomolecules, single cells and single nanoparticles in fluid", Nature, 446, 1066 (2007).

[3] M.K. Ghatkesar, H.H.P. Garza, and U. Staufer, "Hollow AFM cantilever pipette", Microelectronic Engineering, 124, 22-25 (2014).

[4] J.E. Sader, "Frequency response of cantilever beams immersed in viscous fluids with applications to the atomic force microscope", Journal of Applied Physics, 84, 64-76 (1998).

[5] K. Naeli and O. Brand, "Dimensional considerations in achieving large quality factors for resonant silicon cantilevers in air", Journal of Applied Physics, 105, 014908 (2009).

[6] K. Davami, L. Zhao, E. Lu, J. Cortes, C. Lin, D.E. Lilley, P.K. Purohit, I. Bargatin, "Ultralight shape-recovering plate mechanical metamaterials," Nat. Comm., 6, 10019 (2016).

[7] J. Bryan, E. Lu, K. Davami, J. Cortes, C. Lin, D.E. Lilley, I. Bargatin, "Two-layer plate mechanical metamaterials", Technical Digest of Hilton Head 2016: A Solid-State Sensors, Actuators, and Microsystems Workshop, Hilton Head Isl., SC, 6/5-6/9 (2016).

IMPLANTABLE, MICROFIBER NEUROELECTRODES FABRICATED OUT OF POLYCRYSTALLINE DIAMOND AND BORON-DOPED DIAMOND

*Yue Guo, **Cory A. Rusinek, **Robert Rechenberg, *Bin Fan, **Michael F. Becker, and *Wen Li
*Michigan State University, East Lansing, Michigan, USA
**Fraunhofer USA, Inc - Center for Coatings and Diamond Technologies, East Lansing, Michigan, USA

ABSTRACT

This abstract presents micromachined, implantable, all diamond microfibers to facilitate reliable, precision recording of extracellular biopotentials and neurotransmitter concentrations in neural networks (**Fig. 1**). Each of such microfibers consists of a conductive boron-doped polycrystalline diamond (BDD) core encapsulated in a thin insulating polycrystalline diamond (PCD) cladding. The BDD core enables single-unit recording and neurotransmitter sensing from target neurons with high spatiotemporal resolution and fidelity, while the PCD encapsulation serves as a biocompatible and hermetic package as well as a dielectric barrier to prevent signal cross-talking. The fully developed fibers had been successfully tested *ex vivo* in different chemicals under different concentrations.

Keywords: Boron Doped Diamond (BDD), Polycrystalline Diamond (PCD), Neurotransmitter, Neural Recording.

INTRODUCTION

The central nervous system (CNS) consists of large networks of neurons that communicate with each other both electrically and chemically for information processing, analysis, and generation of outputs to achieve complex brain functions and behaviors. Rapid, transient, long-distance communication in neural circuits primarily occurs via electrical impulses (action potentials) along the axon, while neuron-to-neuron communication occurs chemically at the synapses [1]. Dysregulated level of neurotransmitters (NTs) in the brain is believed to be the main cause of several neurological disorders, such as Parkinson's and Alzheimer's diseases, schizophrenia, and epilepsy [2-4]. In particular, dopamine (DA) is one of the most important NTs that modulates motor activity, motivation, reinforcement learning, among many other functions. Abnormal DA activity in the basal ganglia has been demonstrated as an important indicator for monitoring Parkinson's disease and schizophrenia [5-8]. Hence, a complete understanding of these brain diseases will require real-time monitoring of dynamic changes in both extracellular electrical and DA signaling.

Such comprehensive research demands advanced brain mapping tools with minimal invasiveness and high spatiotemporal resolution. Of many different mapping approaches, implantable microelectrodes capable of recording extracellular biopotentials and neurochemical signals from small, targeted groups of neurons have shown great promises for neuroscience research and emerging clinical applications. While extremely popular in their use, metal microwires and silicon-based microelectrodes suffer from signal instability and degradation after chronic implantation for several months to a few years, resulting primarily from inflammatory responses and fibrous encapsulation evoked by electrode insertion and subsequent relative motion [9, 10]. Increasing evidence suggests that the dimension and stiffness of implanted electrodes contribute greatly to tissue damage and fibrosis in chronic implantation [11]. To overcome the problem of traditional hard material-based electrodes, soft electrode technology has been explored aggressively to reduce their mechanical mismatch with the surrounding tissues [12]. However, fabrication of soft electrodes with small dimensions and good durability is still challenging due to the physical limitations and tradeoffs between size and mechanical strength. Recently reported carbon fiber (CF) ultramicroelectrodes have a small cross-sectional footprint (8-9 μm diameter) and low stiffness that promise to reduce chronic tissue damage and neuron death upon implantation [13, 14]. Despite their many advantages, currently, fabrication of these carbon fiber electrodes requires laborious and time-consuming alignment and assembly of individual fibers onto pre-patterned printed circuit board (PCB) substrates, which is impractical for building high-channel-count carbon fiber electrode arrays. In addition, thin polymer encapsulation does not provide an impermeable barrier for carbon fiber electrodes [15], and its long-term efficacy for chronic implants remain undefined.

In this paper, we present a micromachined, implantable, all diamond fiber ultramicroelectrodes to facilitate reliable, precision recording of extracellular biopotentials and chemical signals from brain networks for potential applications in both neuroscience and clinical research. Our device takes advantages of the unique properties of polycrystalline diamond (PCD) thin films, such as high biocompatibility, long-term stability, and biochemical inertness [16]. Compared to commonly used electrode materials (e.g. platinum and glassy carbon), diamond also exhibits excellent chemical non-reactivity, low double-layer capacitance, and a wide aqueous potential window, which make it an ideal material for neurotransmitter sensing [17, 18]. Our diamond microfibers are completely made of thin films of doped and undoped microcrystalline diamond and differ from conventional diamond electrodes, in which only the tips of sharpened and insulated metal wires were covered by a thin layer of boron-doped polycrystalline diamond (BDD) [18].

DEVICE DESIGN

As shown in Fig. 1, the unassembled fiber contains three main parts: a fiber shank, a contact pad, and an anchor. The fiber shank consists of a conductive BDD core encapsulated in a thin insulating PCD cladding. The BDD core is exposed at the tip with a small cross-sectional area to enable single-unit recording and neurotransmitter sensing from target neurons with high spatiotemporal resolution and fidelity. The PCD encapsulation serves as a hermetic package and a dielectric barrier to prevent signal cross-talking during neural recording. The anchor is designed to fix the fibers onto the silicon wafers during fabrication, and eventually will be removed by cleavage, in order to expose the fiber end as the recording site. The contact pad, as illustrated in Fig. 1, has the exposed BDD layer to form interconnect to a custom-designed, printed circuit board (PCB) using conductive epoxy. The PCB is connected to testing instruments via a surface-mount connector and ribbon wire. The devices designed for rat's model have different widths of 10-20 μm, lengths of 1-3 mm, and an overall thickness of 6.9 μm. The contact pads are designed in two different ways, one with holes that go through the pads in order to

978-1-940470-03-0/HH2018/$25©2018TRF
DOI 10.31438/trf.hh2018.67

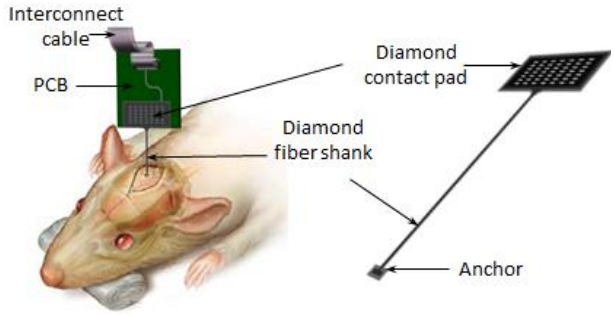

***Fig. 1**: Conceptual diagram of the all diamond fiber microelectrode*

fix the pads with the silver epoxy, and one without the holes. Besides single-shank microfibers, two-dimensional (2D) fiber arrays are also designed, combining multiple shanks with the same or various lengths and widths on a single platform.

FABRICATION METHOD

Fig. 2 shows details of the fabrication process. As illustrated, in the step a), a 1.9-µm-thick polycrystalline diamond layer (PCD) was deposited on top of a 3-inch silicon wafer as the bottom insulator, and a 3.7-µm-thick boron-doped-diamond (BDD) layer was deposited on top of the PCD insulating layer. Both diamond layers were synthesized using a custom-designed 2.45 GHz microwave plasma assisted chemical vapor deposition reactor (MWPACVD) with a gas mixture of hydrogen-diborane and methane (1%) in a hydrogen atmosphere, under a 700 °C temperature. The B-to-C ratio was 20,000 ppm and the B-to-H ratio was 200 ppm. The deposited BDD layer was initially terminated by hydrogen, and after being exposed to air for a long time, the surface was converted gradually to a partially oxygen-terminated surface.

In step b), a 1.3-µm-thick copper layer was deposited using thermal evaporation (Edward Auto306 thermal evaporator, Edward, Inc.), and patterned via ultraviolet (UV) photolithography (ABM, Inc.) and chemical etching of copper to be used as a hard mask for the following diamond etching step. In the diamond etching step, BDD and PCD layers were patterned by being etched in an electron cyclotron resonance reactive ion etcher (RIE, Lambda Technologies, Inc.) using $SF_6/Ar/O_2$ with a microwave power of 400 W and a radio-frequency (RF) bias of 100 W (150 V). After the diamond layers were patterned, the copper mask was removed by the copper etchant.

In steps c) and d), another layer of PCD with a thickness of 1.3 µm was grown on top of the patterned diamond layers and exposed regions of the silicon wafer, using the above equipment and approach. Afterward, another copper layer was deposited and selectively patterned on top of the new PCD layer to be used as the hard mask for etching the top PCD layer. In order to be sure that the needle part of BDD layer underneath would be fully covered, the copper mask is slightly larger (from 2-10 µm) than the BDD layer. This mask also exposes the contact pad at the backbone of the fiber, so after the top PCB layer was removed from the contact areas, the BDD layer underneath would be exposed for good connectivity. The top PCD layer would be patterned using the RIE method with the new copper mask. After that, the device was released from the wafer using chemical etching of silicon in a hydrofluoric acid/nitric/acetic acid (HNA) solution (step (d)). Then the anchor on the tip end of the fiber was cleaved using a pair of tweezers in order to expose the recording site at the tip of the fiber (step (e)). Finally, the released

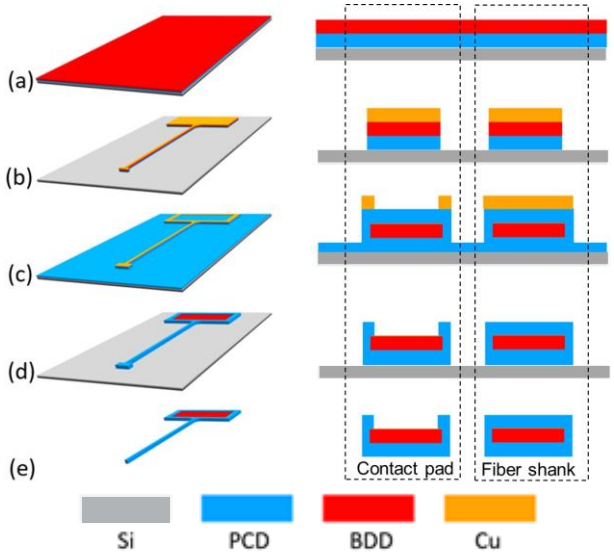

***Fig. 2**: Process flow for making the all diamond microfibers. a) Deposit BDD /PCD thin films on top of the Si substrate; b) Pattern BDD/PCD with a copper mask; c) Deposit the top PCD layer and pattern the Cu mask; d) Etch the top PCD layer and remove the Cu mask; e) Release the device and open the tip of the microfiber.*

device was bonded onto the PCB stick using the conductive silver epoxy.

DEVICE CHARACTERIZATION AND RESULTS

A. Fabricated Diamond Microfiber

Fig. 3 (a) shows prototypes of the fabricated diamond microfibers. The cross-sectional view in Fig. 3 (b) gives clear indication that the BDD microfiber core was completely insulated by the dense PCD cladding. The tip had a trapezoidal cross section due to isotropic nature of plasma etching of diamond films. Our fabrication method allows batch production of diamond electrodes with different geometries on the same wafer and is compatible with conventional microfabrication techniques. Each 3-inch silicon wafer contains 440 devices, including 248 single microfibers and 32 2D arrays each of which includes 6 fibers.

B. Mechanical Flexibility

Analytical approaches were used to study the mechanical properties of the diamond microfibers since the previous studies show that mechanical property mismatch between the hard implant and soft tissue may increase risks of negative neural response, glial scar formation, inflammation, and mechanically induced trauma [11, 19, 20]. Although diamond has a relatively high Young's modulus (1050 GPa), the bending stiffness of the microfiber is a more relevant indicator of device-tissue interactions than Young's modulus [21]. Given the rectangular cross-section of the fiber, its bending stiffness can be calculated by: $F/d=(4Ewt^3)/L^3$, where F is the force, d is the deflection, E is Young's modulus, w is the width of the cross-section area, t is the thickness of the cross-section area, and L is the length of the device. As such, our diamond fibers are relatively compliant with the F/d value ranging from 511 mN/m to 27.59 N/m depending on different dimensions of the fibers.

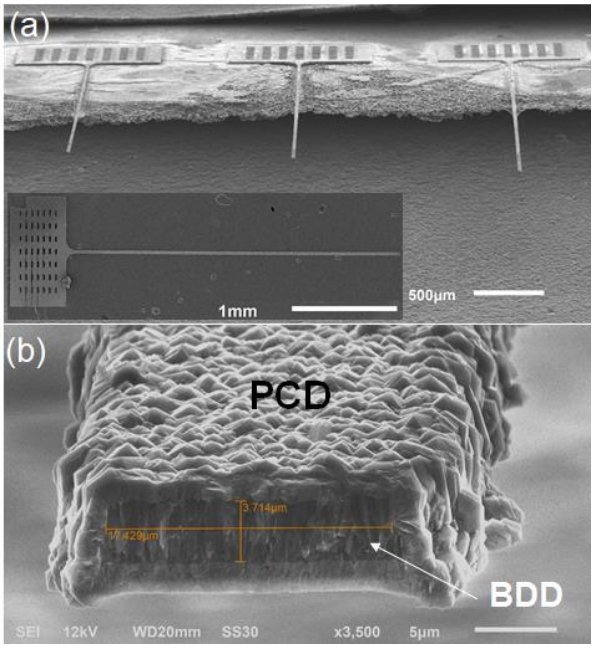

Fig. 3*: (a) SEM images of a microfabricated, all diamond microfiber array. Inset shows a released single fiber. (b) SEM image shows the cross-section of a diamond microfiber with dimensions of ~17.4 µm in width and ~3.7 µm in thickness.*

However, the flexibility of the fiber imposes a challenge for device insertion into the brain tissue. It is well known that fibers with large lengths and small cross section diameters may mechanically buckle under minor loads, which can be studied using the critical buckling force: $F_{buckling} = (\pi^2 E w t^3)/(5.88 L^2)$. As a result, the critical buckling load for different fiber designs varies from 643.3 µN to 11.6 mN, which is mostly larger than the insertion force required to penetrate brain tissue (~1 mN) [22].

C. Electrochemical Properties

Experiments were performed to evaluate the general electrochemical characteristics of the all diamond microfibers using electrochemical impedance spectroscopy (EIS) and cyclic voltammetry (CV). All measurements were done with a three-electrode cell comprised of the diamond microelectrode as a working electrode (WE), a platinum wire as a counter electrode (CE), and a standard Ag/AgCl electrode as a reference electrode (RE). The electrochemical impedance of the electrode at 1 kHz was 1.3 MΩ, in an acceptable range of the extracellular recording. Cyclic voltammograms (CVs) of the devices were measured in different chemicals, including phosphate-buffered saline (PBS), ferri/ferrocyanide ($Fe(CN)_6^{3-/4-}$), ruthenium hexamine ($Ru(NH_3)_6^{2+/3+}$), and DA. Fig. 4 (a) shows the CVs of the diamond microfibers in pH=7.4 PBS under various scan rates. The double-layer capacitance (C_{dl} in $F \cdot cm^{-2}$) of 18 µF/cm^2 was calculated based on $C_{dl} = i_{av}/\nu A$, where i_{av} (in $C \cdot s^{-1}$) is the average current of the forward and reverse sweeps of the CV, and ν (in $V \cdot s^{-1}$) is the scan rate of the CV, and A (in cm^2) is the electrode area [23]. CVs of two one-electron transfer redox couples, $Fe(CN)_6^{3-/4-}$ and $Ru(NH_3)_6^{2+/3+}$, are shown in Fig. 4 (b). In both cases, the diamond microfibers exhibit the trademark sigmoidal response characteristic of microelectrodes, occurring when the radius of the electrode is smaller than that of the diffusion profile of the analyte. The magnitude of the steady-state current responses for the anodic and cathodic scans are nearly identical, indicating a reversible electron transfer process. The BDD electrode exhibits featureless background current and a much wider potential window in PBS (~3.8 V) than standard gold, platinum, and glassy carbon electrodes Fig. 4 (c), permitting detection of analytes across a wide range of voltages without the interference of faradaic background current.

Square-wave voltammetry (SWV) was used to demonstrate the feasibility of *ex vivo* DA sensing using the fabricated microfibers. In this case, DA was serially diluted in 0.1 M, pH=7.4 PBS. Fig. 5 shows the response at lower DA concentrations of 0-25 µM; sharp

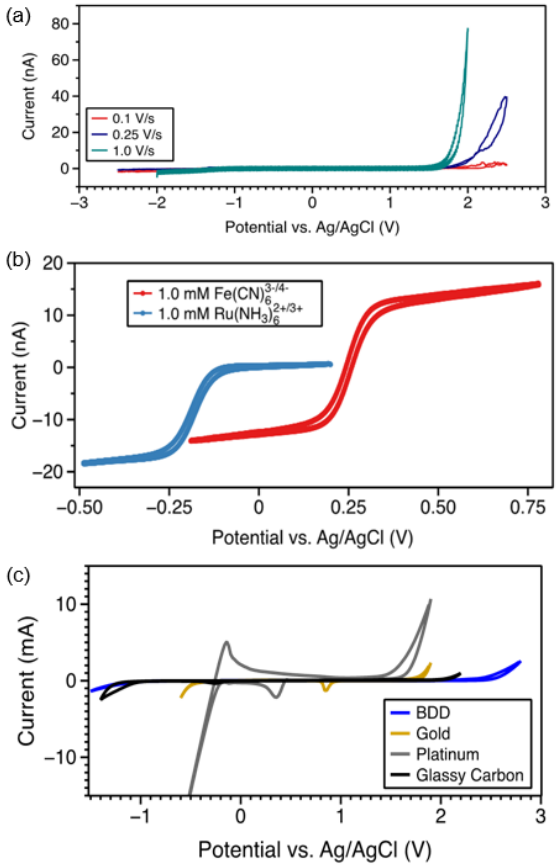

Fig. 4*: Cyclic voltammograms (CVs) of the diamond microfiber measured (a) in the pH=7.4 PBS buffer under various scan rates and (b) in two redox couples. (c) Comparison of the potential window of various electrode materials.*

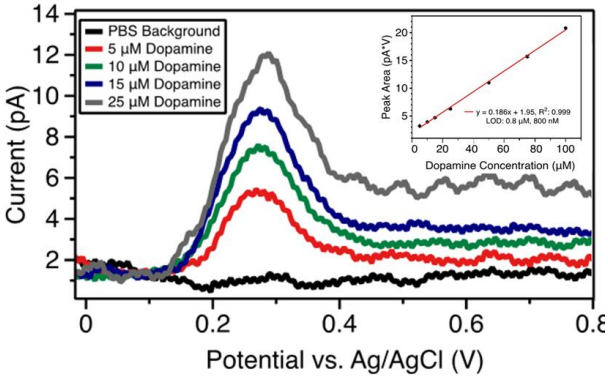

Fig. 5*: SWVs of the diamond microfiber measured under different dopamine concentrations of 0-25 µM. The inset shows the linear fitting of dopamine concentration vs. peak area.*

and well-resolved oxidation peaks in response to different dopamine concentrations were observed. A direct correlation between the dopamine concentration and the current amplitude was observed with excellent linearity ($R^2 = 0.999$) over the tested concentration range.

CONCLUSIONS

This paper reports the design, fabrication, and characterization of all diamond microfibers for potential applications in neurophysiological recording and neurotransmitter sensing. A wafer-level approach was developed to monolithically fabricate the microfibers with high yield and productivity. The fabricated microfiber has a small cross-section area that matches the size of neurons, suitable for single unit recording. Results of electrochemical measurements demonstrate that the diamond fiber is able to detect low concentrations of DA with excellent linearity. Ongoing work includes *in-vitro* and *in-vivo* characterization of the devices using cell cultures and rat's models.

ACKNOWLEDGMENTS

This work was supported by the National Institutes of Health (NIH R21NS096637-02). The authors would like to thank Dr. Baokang Bi for the help in microfabrication

REFERENCES

[1] E. R. Kandel, J. H. Schwartz, and T. M. Jessell, *Principles of Neural Science* vol. 4: McGraw-Hill New York, 2000.

[2] S. J. Lewis and R. A. Barker, "Understanding the dopaminergic deficits in Parkinson's disease: insights into disease heterogeneity," *Journal of Clinical Neuroscience,* vol. 16, pp. 620-625, 2009.

[3] H. Gunduz-Bruce, "The acute effects of NMDA antagonism: from the rodent to the human brain," *Brain Research Reviews,* vol. 60, pp. 279-286, 2009.

[4] M. Glass and M. Dragunow, "Neurochemical and morphological changes associated with human epilepsy," *Brain Research Reviews,* vol. 21, pp. 29-41, 1995.

[5] P. Brown, "Oscillatory nature of human basal ganglia activity: relationship to the pathophysiology of Parkinson's disease," *Movement Disorders,* vol. 18, pp. 357-363, 2003.

[6] J. Obeso, M. Rodriguez-Oroz, C. Marin, F. Alonso, I. Zamarbide, J. Lanciego, and M. Rodriguez-Diaz, "The origin of motor fluctuations in Parkinson's disease Importance of dopaminergic innervation and basal ganglia circuits," *Neurology,* vol. 62, pp. S17-S30, 2004.

[7] C. Hammond, H. Bergman, and P. Brown, "Pathological synchronization in Parkinson's disease: networks, models and treatments," *Trends in Neurosciences,* vol. 30, pp. 357-364, 2007.

[8] C. Mehler-Wex, P. Riederer, and M. Gerlach, "Dopaminergic dysbalance in distinct basal ganglia neurocircuits: implications for the pathophysiology of Parkinson's disease, schizophrenia and attention deficit hyperactivity disorder," *Neurotoxicity Research,* vol. 10, pp. 167-179, 2006.

[9] M. Jorfi, J. L. Skousen, C. Weder, and J. R. Capadona, "Progress towards biocompatible intracortical microelectrodes for neural interfacing applications," *Journal of Neural Engineering,* vol. 12, p. 011001, 2014.

[10] A. Weltman, J. Yoo, and E. Meng, "Flexible, penetrating brain probes enabled by advances in polymer microfabrication," *Micromachines,* vol. 7, p. 180, 2016.

[11] J. Subbaroyan, D. C. Martin, and D. R. Kipke, "A finite-element model of the mechanical effects of implantable microelectrodes in the cerebral cortex," *Journal of Neural Engineering,* vol. 2, p. 103, 2005.

[12] J. H. Lee, H. Kim, J. H. Kim, and S.-H. Lee, "Soft implantable microelectrodes for future medicine: prosthetics, neural signal recording and neuromodulation," *Lab on a Chip,* vol. 16, pp. 959-976, 2016.

[13] P. R. Patel, K. Na, H. Zhang, T. D. Kozai, N. A. Kotov, E. Yoon, and C. A. Chestek, "Insertion of linear 8.4 μm diameter 16 channel carbon fiber electrode arrays for single unit recordings," *Journal of neural engineering,* vol. 12, p. 046009, 2015.

[14] T. D. Y. Kozai, N. B. Langhals, P. R. Patel, X. Deng, H. Zhang, K. L. Smith, J. Lahann, N. A. Kotov, and D. R. Kipke, "Ultrasmall implantable composite microelectrodes with bioactive surfaces for chronic neural interfaces," *Nature materials,* vol. 11, pp. 1065-1073, 2012.

[15] P. E. Donaldson, "The encapsulation of microelectronic devices for long-term surgical implantation," *IEEE Transactions on Biomedical Engineering,* pp. 281-285, 1976.

[16] A. Kraft, "Doped diamond: a compact review on a new, versatile electrode material," *Int. J. Electrochem. Sci,* vol. 2, pp. 355-385, 2007.

[17] M. Hupert, A. Muck, J. Wang, J. Stotter, Z. Cvackova, S. Haymond, Y. Show, and G. M. Swain, "Conductive diamond thin-films in electrochemistry," *Diamond and Related Materials,* vol. 12, pp. 1940-1949, 2003.

[18] Y. Einaga, J. S. Foord, and G. M. Swain, "Diamond electrodes: diversity and maturity," *Mrs Bulletin,* vol. 39, pp. 525-532, 2014.

[19] V. S. Polikov, P. A. Tresco, and W. M. Reichert, "Response of brain tissue to chronically implanted neural electrodes," *Journal of neuroscience methods,* vol. 148, pp. 1-18, 2005.

[20] J. Harris, J. Capadona, R. Miller, B. Healy, K. Shanmuganathan, S. Rowan, C. Weder, and D. Tyler, "Mechanically adaptive intracortical implants improve the proximity of neuronal cell bodies," *Journal of neural engineering,* vol. 8, p. 066011, 2011.

[21] R. Chen, A. Canales, and P. Anikeeva, "Neural recording and modulation technologies," *Nature Reviews Materials,* vol. 2, p. 16093, 2017.

[22] B. Wester, R. Lee, and M. LaPlaca, "Development and characterization of in vivo flexible electrodes compatible with large tissue displacements," *Journal of Neural Engineering,* vol. 6, p. 024002, 2009.

[23] B. Fan, Y. Zhu, R. Rechenberg, C. A. Rusinek, M. F. Becker, and W. Li, "Large-scale, all polycrystalline diamond structures transferred onto flexible Parylene-C films for neurotransmitter sensing," *Lab on a Chip,* vol. 17, pp. 3159-3167, 2017.

TEMPERATURE-DEPENDENT TRANSIENT BEHAVIOR OF AlGaN/GaN HIGH ELECTRON MOBILITY PRESSURE SENSORS

Caitlin A. Chapin[1], Karen M. Dowling[1], Hoang-Phuong Phan[1,2], Ruiqi Chen[1], and Debbie G. Senesky[1]
[1]Aeronautics and Astronautics Department, Stanford University, Stanford, CA, USA
[2]The Queensland Micro-Nanotechnology Centre, Griffith University, Queensland, Australia

ABSTRACT

For the first time, the time-dependent response of an AlGaN/GaN high electron mobility transistor (HEMT) pressure sensor is characterized at elevated temperatures. We show that temperature affects the sensitivity and the transient behavior of the sensor's response to pressure. At a temperature above 125°C, the drain current response after the application of pressure transitions from exponentially decaying to exponentially growing. Using an Arrhenius model of trap activation energy, we demonstrate that two traps in the AlGaN/GaN heterostructure at 0.62 eV and 0.87 eV cause the temperature-dependent transient behavior. This work paves the way for creating reliable GaN-based sensing devices.

INTRODUCTION

Electronics and sensors have been developed using the gallium nitride (GaN) heterostructure platform. These devices leverage a conductive sheet of electrons that forms at the interface of GaN and III-nitride alloys (e.g., AlGaN), known as a 2-dimensional electron gas (2DEG). The 2DEG is partially formed based on the piezoelectric nature of the materials and has thus been leveraged to develop strain [1] and pressure sensors [2]. There is a growing interest in engineering these GaN-based sensors to operate at high temperatures. This vision is supported by a recent demonstration of GaN HEMTs up to 1000°C [3]. However, transient effects of GaN-based strain/pressure sensors, which have plagued both transistor and optical device architectures [4], have been overlooked by researchers to date.

EXPERIMENT

To study the time-, pressure- and temperature-dependent response of the GaN 2DEG, a GaN-based micro-pressure sensor was microfabricated leveraging an AlGaN/GaN high electron mobility transistor (HEMT) positioned at the center of a fully-suspended diaphragm. To microfabricate the device, an AlGaN/GaN-on-silicon wafer grown via metal organic chemical vapor deposition (MOCVD) from DOWA Electronic Materials Co., Ltd. was used. The fabrication of the HEMT included a mesa-isolation etch (Figure 1b), Ohmic and Schottky metal depositions (Figure 1c), passivation with plasma-enhanced atomic layer deposition of Al_2O_3, etching vias, and bond metal deposition (Figure 1d). The pressure sensor is released by patterning a SiO_2 hard mask on the back side (Figure 1b) and etching the silicon to create a diaphragm with a deep reactive ion etch (DRIE) (Figure 1e).

The device was tested on a high-temperature probe station from 25°C to 200°C. Pressure was applied by placing the diaphragm over a vacuum port and pulling a vacuum of 6.9 ± 0.1 psi. At the center of diaphragm, the HEMT is in biaxial compressive strain in basal plane when the pressure is applied. The transient response (I_D-t) at V_{DS} = 2.5 V and V_{GS} = −3 V was measured using a semiconductor parameter analyzer (Agilent B1500A).

RESULTS AND DISCUSSION

The transient drain current (normalized by the current immediately before the first pressure application) response, I_D-t, is shown in Figure 2 at room temperature, 75°C, 150°C, and 200°C.

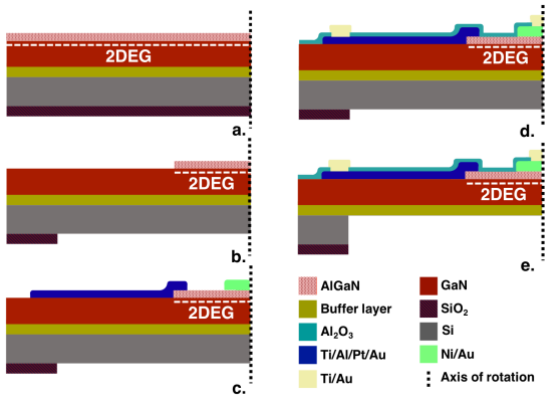

Figure 1: Microfabrication of AlGaN/GaN-on-silicon micro-pressure sensor grown via MOCVD (a). Fabrication includes: mesa etch isolation, hard mask pattering (b) deposition of Ohmic and Schottky contact (c), passivation and deposition of metal for wire bonding. The device is released by etching the silicon with DRIE process.

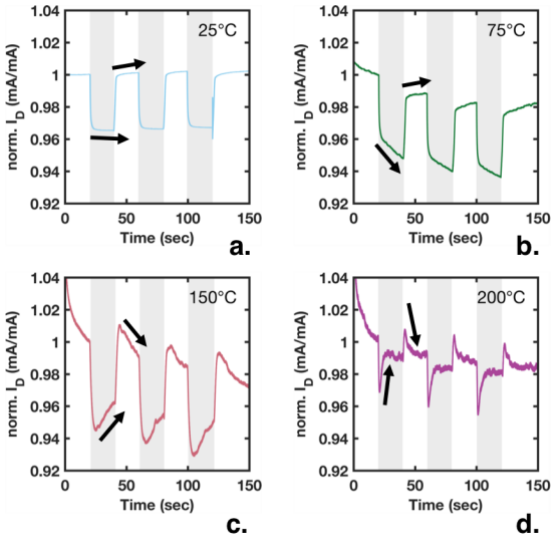

Figure 2. Transient drain current (normalized) response of an AlGaN/GaN pressure sensor at various temperatures under 6.9 psi of applied pressure (gray regions). The arrows highlight the increasing or decreasing behavior of the drain current during and after the pressure stimulus

The sensitivity is calculated based on measurements immediately before and after the application of pressure and the magnitude is plotted as a function of temperature in Figure 3. We observe that the magnitude of the sensitivity increases from room temperature to 150°C, 0.34 %/psi to 0.49 %/psi, and then shifts to a sharply decreasing trend reaching 0.34 %/psi at 200°C.

Additionally, at temperatures between 75°C and 125°C, when pressure is applied, there is an initial drop in current due to a

978-1-940470-03-0/HH2018/$25©2018TRF
DOI 10.31438/trf.hh2018.68

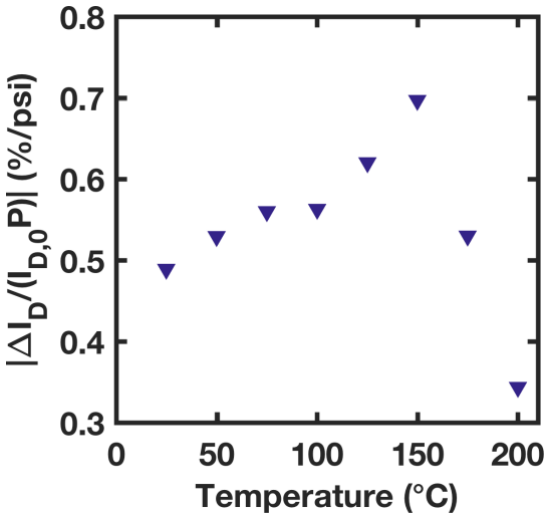

Figure 3: Magnitude of sensitivity of AlGaN/GaN pressure sensor as function of temperature.

reduction in the piezoelectric effect, followed by a decay in the current. At temperatures above 125°C, the current increases after the initial drop in the current. The temperature-dependent transient behavior can be explained by the existence of two traps (caused by material defects) in different locations in the AlGaN/GaN heterostructure (Figure 4). If the trap is at the top surface of the AlGaN and above the Fermi level, the trap will be pulled below the Fermi level upon application of compressive strain due to a reduction in Schottky barrier height [5]. This causes a reduction in the 2DEG concentration and the current. Likewise, if the trap is near the AlGaN/GaN interface, the trap will be pulled above the Fermi level and cause the 2DEG density and current to increase.

The time constant of the transient response, τ, is found by fitting the data to

$$I_D(t) = I_1 + I_2 \exp\left(-\frac{t}{\tau}\right)^{\beta} \quad (1)$$

where the sum of I_1 and I_2 are the steady state current and β is a stretching factor. The time constant is expected to be exponentially dependent on the energy level of the trap, E_T and the inverse of temperature, T, such that

$$\tau = \frac{1}{\sigma_T v_{th}(T) N_C(T)} \exp\frac{E_T - E_C}{kT} \quad (2)$$

where σ_T, v_{th}, N_C, E_C, k are the trap cross sectional area, the thermal velocity of the electron, the density of states in the conduction band, the conduction band energy, and the Boltzmann constant, respectively. By plotting the time constant on an Arrhenius plot, two trap energy levels are extracted at 0.62 eV and 0.87 eV, and their associated trap cross sectional areas are 8.9×10^{-18} cm^2 and 1.9×10^{-19} cm^2, respectively. These values match previously reported trap levels [6], [7]. The study of traps and their effect on the sensitivity and transient behavior is important for the development of reliable and sensitive high-temperature GaN-based pressure sensors. This work sets the foundation for further examination.

CONCLUSION

In this work, the transient response of a micro-pressure sensor was studied from room temperature to 200°C. The magnitude of the sensitivity of the device is seen to increase until 150°C from 0.49 %/psi to 0.70 %/psi, at which point is starts sharply dropping to 0.34 %/psi at 200°C. At 125°C, the transient response switches from decaying after the initial decrease in current due to the pressure application to exponentially growing. This change in the transient behavior is attributed to two traps at 0.62 eV and 0.87 eV.

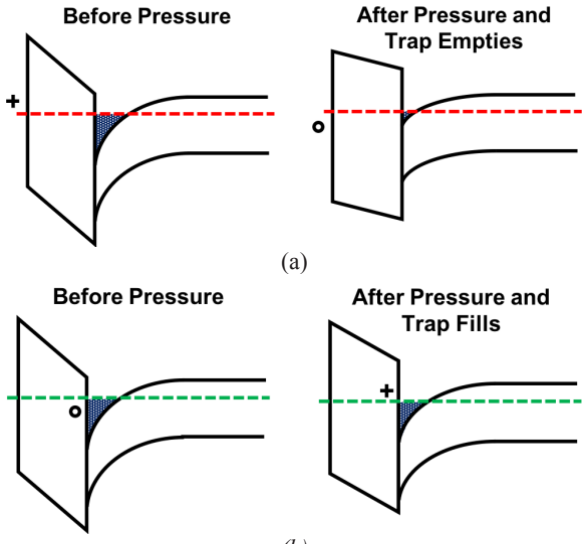

Figure 4: Schematic illustration of the conduction band of GaN heterostructure at lower temperatures showing a decay in current. A trap at the AlGaN surface is pulled below the Fermi level, fills, and reduces the charge available to the 2DEG. (a) Schematic illustration of the conduction band of GaN heterostructure at high temperatures showing an increase in current. A trap at the AlGaN/GaN interface is pulled above the Fermi level, empties, and increases the charge available to the 2DEG. (b)

REFERENCES

[1] B. S. Kang *et al.*, "Effect of external strain on the conductivity of AlGaN/GaN high-electron-mobility transistors," *Appl. Phys. Lett.*, vol. 83, no. 23, pp. 4845-4847, 2003.

[2] E. D. Le Boulbar *et al.*, "Effect of bias conditions on pressure sensors based on AlGaN/GaN High Electron Mobility Transistor," *Sensors Actuators A Phys.*, vol. 194, pp. 247–251, 2013.

[3] D. Maier *et al.*, "InAlN/GaN HEMTs for operation in the 1000 °C regime: A first experiment," *IEEE Electron Device Lett.*, vol. 33, no. 7, pp. 985–987, 2012.

[4] S. C. Binari, P. B. Klein, and T. E. Kazior, "Trapping effects in GaN and SiC microwave FETs," *Proc. IEEE*, vol. 90, no. 6, pp. 1048–1058, 2002.

[5] K. Yao, S. Khandelwal, F. Sammoura, A. Kazama, C. Hu, and L. Lin, "Piezoelectricity-Induced Schottky Barrier Height Variations in AlGaN/GaN High Electron Mobility Transistors," *IEEE Electron Device Lett.*, vol. 36, no. 9, pp. 902–904, 2015.

[6] S. Dasgupta *et al.*, "Slow detrapping transients due to gate and drain bias stress in high breakdown voltage AlGaN/GaN HEMTs," *IEEE Trans. Electron Devices*, vol. 59, no. 8, pp. 2115–2122, 2012.

[7] M. Florovic, J. Skriniarova, J. Kovac, and P. Kordos, "Trapping Analysis of AlGaN/GaN Schottky Diodes via Current Transient Spectroscopy," *Electronics*, vol. 5, no. 20, pp. 1-7, 2016.

CONTACT

*C.A. Chapin, cchapin3@stanford.edu

WHAT IS EFFECTIVE QUALITY FACTOR?

James M. Lehto Miller[1], Azadeh Ansari[2], David B. Heinz[1], Yunhan Chen[1], Ian B. Flader[1], Dongsuk D. Shin[1], L. Guillermo Villanueva[3], and Thomas W. Kenny[1]

[1]Department of Mechanical Engineering, Stanford University, Stanford, CA 94305

[2]Department of Electrical and Computer Engineering, Georgia Institute of Technology, Atlanta, GA 30309, USA

[3]Advanced NEMS Lab, École Polytechnique Fédérale de Lausanne (EPFL), Switzerland

INTRODUCTION

Many mechanisms have emerged for tuning the effective quality factor (Q_{eff}) of micro- and nano-electromechanical (MEM/NEM) resonators, including parametric amplification [1], thermal-piezoresistive pumping (TPP) [2], external velocity-proportional feedback [3], piezoelectric amplification [4], and optomechanical back-action [5]. These techniques have far-reaching applications for improving the signal-to-noise ratio (SNR) and bandwidth of MEM/NEM sensors. But these methods raise questions about the relationship between the mechanical quality factor, the effective quality factor, and the noise within a resonator.

The quality factor, Q, is an inverse measure of the dissipation of a resonator [6], and determines the mechanical transfer function and the mean squared thermal noise force via the fluctuation-dissipation theorem [7]. The larger the dissipation, the larger the variance in the thermal noise force. The effective quality factor, Q_{eff}, results from a third terminal source or sink of energy, which modifies the resonator transfer function but not the thermomechanical noise force. The ultimate limit to resolution of a resonant sensor is imposed by the thermal noise floor of the underlying MEM/NEM resonator, which can be reduced by increasing Q, but not Q_{eff} [8]. It is therefore important to distinguish between changes in Q and Q_{eff} in a MEM/NEM resonator.

The most common technique for measuring Q of a MEM/NEM resonator is the bandwidth (or 3-dB) method, given by:

$$Q = \frac{\omega_n}{\Delta\omega}, \tag{1}$$

where ω_n is the resonant frequency and $\Delta\omega$ is the linewidth of the resonance. The bandwidth method uses the resonant frequency and the width of the driven response peak at half-max to estimate Q. The second technique is the Lorentzian fit, given by:

$$A(\omega) = \sqrt{G\frac{4k_BT\left(\frac{\omega_n}{mQ}\right)}{({\omega_n}^2-\omega^2)^2+\left(\frac{\omega\omega_n}{Q}\right)^2}+N_a^2}, \tag{2}$$

where $A(\omega)$ is the amplitude spectral density (ASD) of the voltage at the amplifier output for a resonator driven only by its intrinsic thermal noise, G is the squared scale factor between resonator displacement and amplifier output, m is the lumped mass of the mode, k_B is Boltzmann's constant, T is the resonator bulk temperature, and N_a is the amplifier noise floor. In Eq. 2, the denominator of the first term corresponds to the mechanical transfer function while the numerator corresponds to the thermomechanical noise force. To extract Q, the Lorentzian fit method fits Eq. 2 to the displacement noise of the resonator at resonance, which requires a very sensitive displacement readout. Often the displacement transduction noise greatly exceeds the resonator thermal noise, so an external driving force must be used, which invalidates Eq. 2.

Q_{eff} tuning modifies the denominator of the first term in Eq. 2, but not the numerator, which results in an ASD given by:

$$A_{eff}(\omega) = \sqrt{G\frac{4k_BT\left(\frac{\omega_n}{mQ}\right)}{({\omega_n}^2-\omega^2)^2+\left(\frac{\omega\omega_n}{Q_{eff}}\right)^2}+N_a^2}\,. \tag{3}$$

Fig. 1 compares the resonator thermomechanical displacement noise at resonance by plotting Eqs. 2 and 3. Modifying Q or Q_{eff} modifies the linewidth of the mechanical transfer function in the same manner, while only a change in Q changes the thermal noise floor.

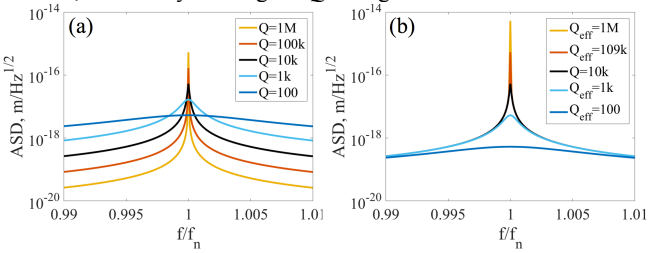

Figure 1: Displacement noise amplitude spectral density (ASD) near resonance for changing (a) Q, and (b) Q_{eff}. This is obtained by plotting Eqs. 2 and 3, respectively, for zero amplifier noise ($N_a = 0$) and unity amplifier gain ($G = 1$).

EXPERIMENTS

We experimentally illustrate the difference between Q and Q_{eff} using a silicon resonator subjected to parametric amplification and TPP. We fabricated the device shown in Fig. 2 within a wafer-scale encapsulation process [9]. Our setup allows us to simultaneously bias the device for capacitive actuation and sensing while flowing a direct current to induce TPP. We can alternately parametrically amplify the resonator motion by applying a voltage at $2\omega_n$ to the drive electrode to modulate the electrostatic spring constant.

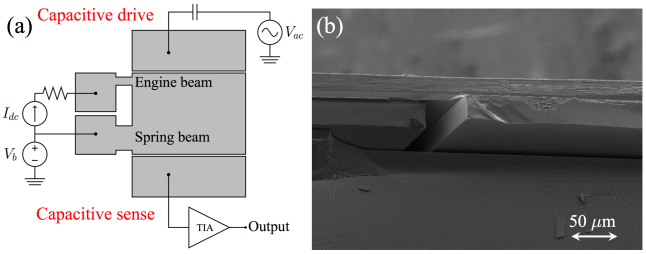

Figure 2: (a) Measurement setup. We bias one anchor of the resonator at V_b and flow a current I_{dc} through the device. (b) Cross-section of our device after encapsulation.

Fig. 3 demonstrates parametric amplification and TPP using an open-loop sweep. For increasing parametric pump or increasing direct current, the resonator amplitude increases and the linewidth decreases, which corresponds to an increase in Q_{eff} using the bandwidth method. Because we use an external driving force, we can only measure the resonator mechanical transfer function, so changes to Q or Q_{eff} are indistinguishable.

To show that TPP and parametric amplification tunes Q_{eff}, not Q, we must study the thermomechanical motion of the resonator directly. We remove the external drive and use a custom low-noise transimpedance amplifier (TIA) and a large bias voltage to capacitively detect the displacement fluctuations driven by the thermal noise force. Fig. 4 shows the ASD of the amplifier output at resonance, measured using a scalar spectrum analyzer, as we apply a progressively larger parametric pump and zero direct current. As the pump is increased, the thermal noise at resonance is increased while the noise away from resonance does not change: the ASD in

978-1-940470-03-0/HH2018/$25©2018TRF
DOI 10.31438/trf.hh2018.69

Fig. 4 qualitatively matches the ASD in Fig. 1 (b), not Fig. 1 (a). This clearly shows that parametric amplification only modifies the mechanical transfer function, not the thermal noise force, so parametric amplification tunes Q_{eff}, not Q. In Fig. 5, we repeat this measurement by switching off the parametric pump and increasing the direct current through the resonator. We again see that Fig. 5 matches Fig. 1 (b), not Fig. 1 (a), so TPP tunes Q_{eff}, not Q. Eq. 3 fits the resonator noise excellently in both Fig. 4 and Fig. 5 with a constant Q and more than a ten-fold increase in Q_{eff}.

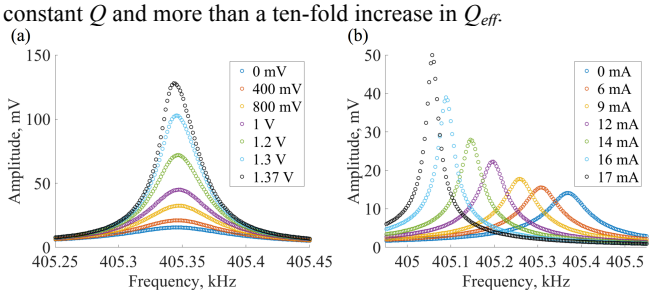

Figure 3: Open-loop amplitude sweep of our device subjected to (a) degenerate parametric amplification, and (b) thermal-piezoresistive pumping (TPP). The frequency downshifts for TPP because of the heating that accompanies a direct current through the device.

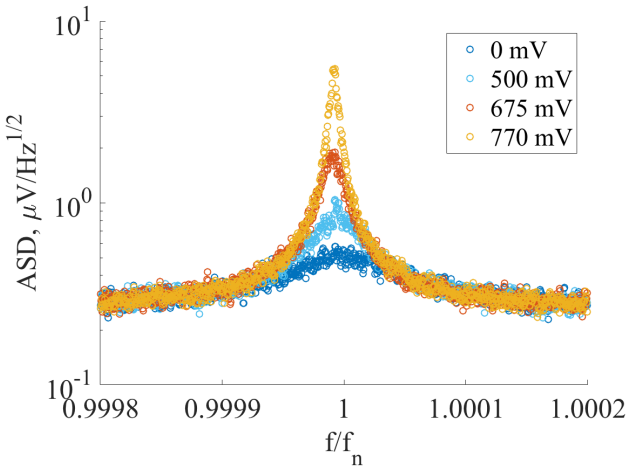

Figure 4: Amplitude spectral density (ASD) of thermomechanical displacement fluctuations of our resonator for increasing parametric pumping voltage, which induces degenerate parametric amplification.

Parametric amplification differs from other Q_{eff} tuning mechanisms because it is quadrature-specific; the thermal motion in-phase with the parametric pump is amplified while the motion anti-phase to the pump is suppressed [1]. For TPP and other linear feedback mechanisms, the noise motion is amplified equally for all phases [10]. Because we measure the displacement noise magnitude in Figs. 4 and 5 with averaging, Fig. 4 corresponds to an ensemble average of parametric Q_{eff} enhancement in-quadrature and parametric Q_{eff} suppression in the anti-quadrature, which still only modifies the resonator transfer function, not the thermal noise force.

CONCLUSION

Parametric amplification and TPP modifies Q_{eff}, not Q. Readers should be skeptical of claims of mechanical Q tuning in a MEM/NEM resonator with a third terminal. Credible claims should be accompanied by a measurement of the thermal displacement noise that matches Fig. 1 (a), not Fig. 1 (b).

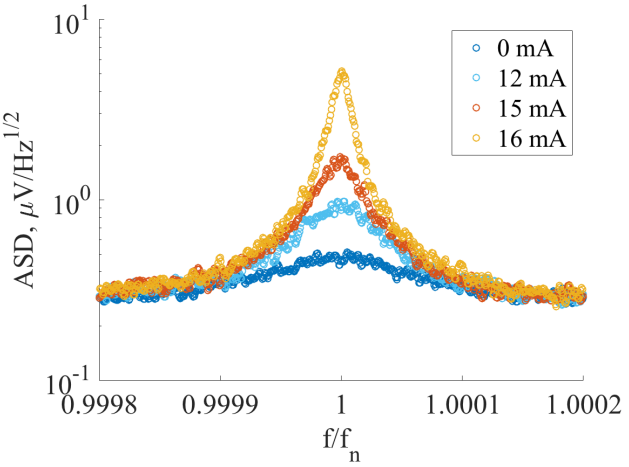

Figure 5: Amplitude spectral density (ASD) of thermomechanical displacement fluctuations of our resonator for increasing direct current, which induces thermal-piezoresistive pumping.

ACKNOWLEDGMENTS

J.M.L.M. is supported by the NDSEG Fellowship and the E.K. Potter Stanford Graduate Fellowship. Work was supported by NSF CMMI-1662464 and ECCS-1542152, and the DARPA Guidance for Munitions (PRIGM) Program, managed by Dr. Robert Lutwak.

REFERENCES

[1] D. Rugar and P. Grutter, "Mechanical Parametric Amplification and Thermomechanical Noise Squeezing," *Physical Review Letters,* vol. 67, no. 6, pp. 699-702, Aug 5 1991.

[2] P. Steeneken *et al.*, "Piezoresistive heat engine and refrigerator," *Nature Physics,* vol. 7, pp. 354-359, 2011.

[3] C.-H. Liu and T. W. Kenny, "A high-precision, wide-bandwidth micromachined tunneling accelerometer," *Journal of microelectromechanical systems,* vol. 10, no. 3, pp. 425-433, 2001.

[4] V. J. Gokhale and M. Rais-Zadeh, "Phonon-Electron Interactions in Piezoelectric Semiconductor Bulk Acoustic Wave Resonators," *Scientific Reports,* vol. 4, Jul 8 2014.

[5] T. J. Kippenberg and K. J. Vahala, "Cavity optomechanics: back-action at the mesoscale," *science,* vol. 321, no. 5893, pp. 1172-1176, 2008.

[6] F. Ayazi, L. Sorenson, and R. Tabrizian, "Energy dissipation in micromechanical resonators," in *SPIE Defense, Security, and Sensing*, 2011, pp. 803119-803119-13: International Society for Optics and Photonics.

[7] P. R. Saulson, "Thermal Noise in Mechanical Experiments," (in English), *Physical Review D,* vol. 42, no. 8, pp. 2437-2445, Oct 15 1990.

[8] J. M. Lehto Miller, A. Ansari, *et al.*, "Effective quality factor tuning mechanisms in micromechanical resonators," under review, 2018.

[9] J. M. Lehto Miller, D. B. Heinz, I. B. Flader, Y. Chen, D. D. Shin, and T. W. Kenny, "Effective quality factor and temperature dependence of self-oscillations in a thermal-piezoresistively pumped resonator," in *Solid-State Sensors, Actuators and Microsystems (TRANSDUCERS), 2017 19th International Conference on*, 2017, pp. 1907-1910: IEEE.

[10] Z. Mohammadi, J. M. Lehto Miller, K. L. Foster, T. W. Kenny, and L. G. Villanueva, "On resonator sensing improvement using linear feedback and parametric pumping," in preparation, 2018.

REALIZING RADIO FREQUENCY ACOUSTIC DELAYS AND TRANSVERSAL FILTERING WITH SUB-2 DB INSERTION LOSS AND 10% FRACTIONAL BANDWIDTH

Tomás Manzaneque, Ruochen Lu, Yansong Yang and Songbin Gong*
University of Illinois of Urbana-Champaign, USA

ABSTRACT

This work demonstrates a lithium niobate thin film-based radio frequency (RF) acoustic delay structure with a low insertion loss (IL) of 2 dB and a fractional bandwidth (FBW) of 10%. In both aspects, this work surpasses the state of the art (SOA) delay lines.

INTRODUCTION

Acoustic delay structures are instrumental for a wide range of passive signal processing functions, including transversal filters [1], matched filters [2], and true time delays. These devices consist of a pair of electromechanical transducers as the input and output to access the acoustic domain. A transversal or matched filter convolutes the frequency domain transfer functions of the input and output transducers to produce either a passband or correlated pulse response, while a delay line uses the separation between input and output to impose a wave propagation-induced time delay. All of abovementioned devices harness the small wavelengths and low phase velocities of acoustic waves at RF to achieve form factors and delay lengths that are unattainable with their electromagnetic counterparts. Despite these advantages, their applications in recent years are quite limited due to their unfavorable tradeoff between insertion loss (IL) and factional bandwidth (FBW). Fundamentally, the limit in such a tradeoff arises from the insufficient electromechanical coupling (k^2) of existing electromechanical systems built on various electrostatic and piezoelectric platforms.

DEVICE DESCRIPTION AND MODELLING

In this work, we resort to the fundamental shear horizontal mode (SH0) in suspended lithium niobate (LiNbO3) thin films, which has recently been demonstrated with high k^2 and low loss simultaneously, to overcome the limits of SOA [3]. As seen in Fig. 1, the device consists of two 100 nm gold interdigital transducers (IDT) on a 700 nm LiNbO3 thin film. To eliminate the bidirectionality and subsequently minimize the IL, a type of single phase unidirectional transducers (SPUDT), known as electrode width controlled (EWC), is employed [4]. The transducer, as seen in Fig. 1, has a periodicity of λ_0, which is also the acoustic wavelength at the design frequency and the width of the unit cell. In each unit cell, two types of electrodes are adopted. A pair of transduction electrodes in the middle are configured with a width of $\lambda_0/8$ to be non-reflective. Electrodes of width $\lambda_0/4$ introduce distributed reflection along the IDT. The asymmetric arrangement of the reflectors causes constructive interference for the waves radiated towards acoustic port 2 (FWD), and destructive interference towards acoustic port 1 (BWD), giving rise to the desired directionality towards port 2. Taking advantage of our suspended structure, a higher directionality is obtained compared to traditional delay lines based on SAW, due to the greater reflections introduced by the larger mass loading of reflection electrodes on the thin film. Note this work focuses on low loss constant group delays with large FBW, thus differing from our prior effort in chirp compressors where dispersion engineering and

Table 1: Comparison of the obtained results with previously reported filters based on acoustic delay lines.

Reference	IL	FBW
[6]	3.5 dB	4%
[7]	2.6 dB	5%
This work	2 dB	10%

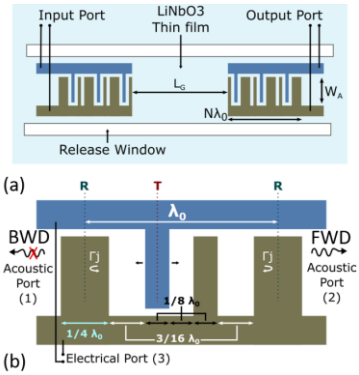

Parameter	Symbol	Value
Center wavelength	λ_0	20 µm
# of unit cells/port	N	10
Acoustic aperture	W_A	200 µm
Delay Gap	L_G	120 µm
Film thickness	t_{LN}	700 nm
Au thickness	t_{Au}	100 nm

(c)

Figure 1: (a) Schematic of an acoustic delay line formed by two Au IDTs in a thin film of $LiNbO_3$. (b) Unit cell of an EWC-based SPUDT. The unit cell is depicted as a three-port device, with one electrical and two acoustic ports. The wide electrodes behave as reflectors for the acoustic waves of wavelength λ0, with an equivalent reflector center in the middle of the electrode, and a complex reflection coefficient. The distance from a transducer center (T) to its closest reflection center (R) on the left is different from the distance to the closest reflection center on the right. (c) Design parameters of the fabricated delay line.

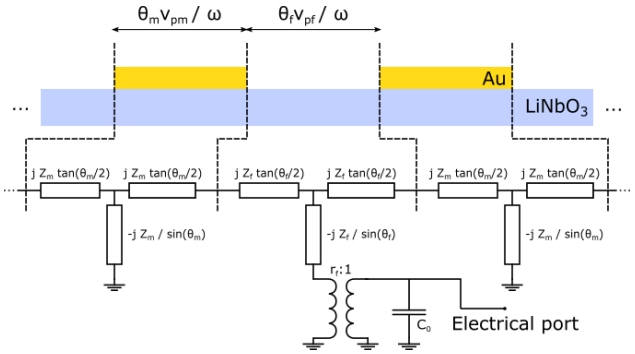

Figure 2: Sectional equivalent circuit of the transducer based on Mason model. Different acoustic characteristics are prescribed to the metallized and non-metallized sections to account for acoustic reflections.

978-1-940470-03-0/HH2018/$25©2018TRF
DOI 10.31438/trf.hh2018.70

compression is the focus [5].

The performance of the device is carefully modeled using

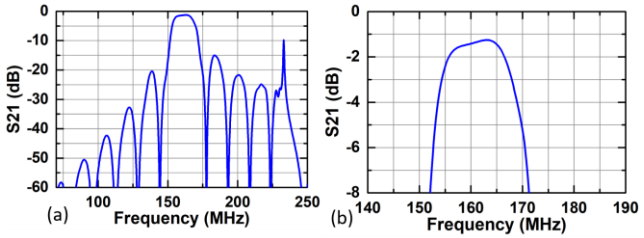

Figure 3: (a) S21 predicted by Mason model for the SPUDT-embeded delay line shown in Fig. 1(a). The model assumes no propagation loss in the delay line. (b) Zoom-in showing the passband with an IL below 1.5 dB.

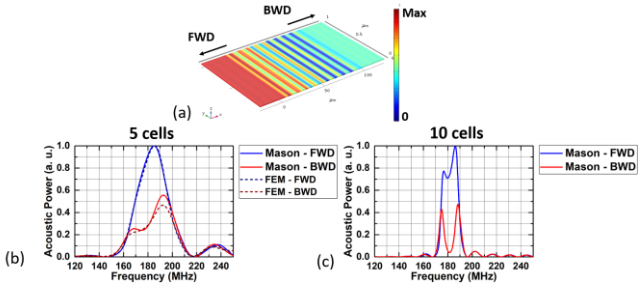

Figure 4: (a) FEA model of a SPUDT to test directionality. Power radiated to the FWD and BWD acoustic ports, calculated with Mason model and FEA for SPUDT with (b) 5 and (c) 10 unit cells.

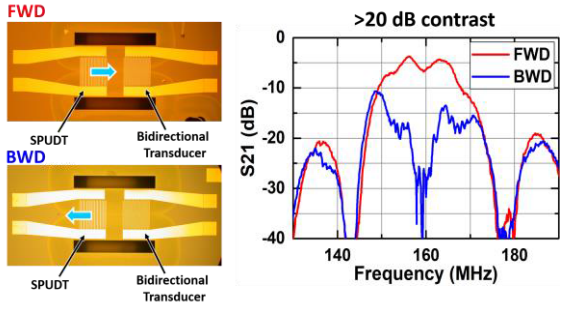

Figure 5: Fabricated devices for testing directionality. The devices have SPUDT on one side and conventional bidirectional IDT on the other side. The directionality of SPUDT is configured toward the bidirectional IDT in FWD, and toward the opposite direction in BWD. The contrast between measured transmissions of these two configurations indicts the measured directionality, which exceeds 20 dB at the center frequency, and agrees with modeled results.

Mason's model (Fig. 2). For the designed device without considering propagation loss, an IL below 2 dB is predicted as seen in Fig. 3. Fig. 4 shows the predicted directionality using Mason's model and FEM simulation.

EXPERIMENTAL RESULTS

The device was fabricated with the process detailed in [5]. Two test devices for measuring the directionality were included. The results, as shown in Fig. 4, show a directionality above 20 dB at the center of the transmission band. The measured S-parameters of the SPUDT-embedded delay line are shown in Fig. 5. The measured performance shows a delay around 60 ns with a minimum insertion loss of 2 dB. The bandwidth obtained is above 15 MHz at a center frequency of 160 MHz. These results show that

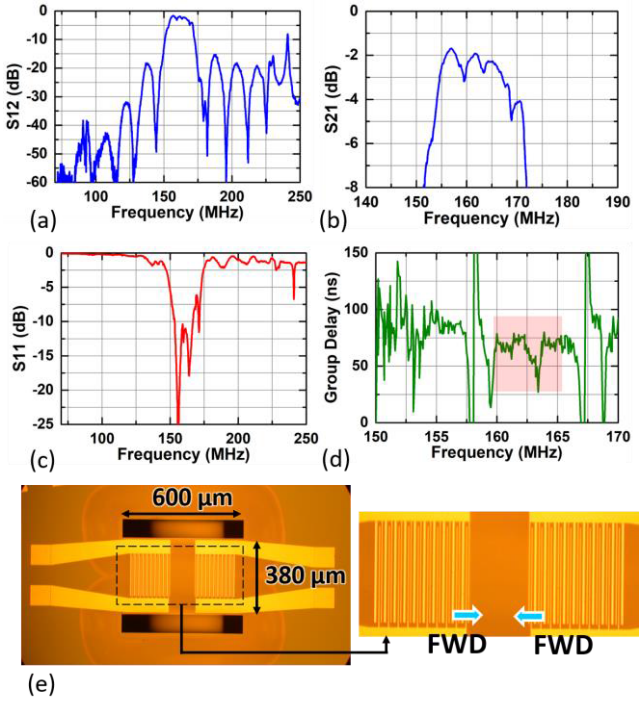

Figure 6: Measured S-parameter results of the fabricated delay line with SPUDTs. (a) S21. (b) zoomed-in view of the passband. (c) S11. (d) Group delay. (e) Top-view optical picture of the device and zoomed-in showing the SPUDTs each with 10 unit cells.

SH0 mode on thin-film LiNbO3 can enable low IL and high bandwidth delay lines and transversal filters, thanks to the high coupling and high reflectivity of the electrodes.

CONCLUSION

A new type of acoustic delay line has been demonstrated based on shear-horizontal waves on lithium niobate. The high electromechanical coupling and low loss of this platform allows for delays in the range of tens of nanoseconds with a sub 2 dB insertion loss and a fractional bandwidth in excess of 10%.

REFERENCES

[1] R. H. Tancrell and M. G. Holland, "Acoustic surface wave filters," *Proc. IEEE*, vol. 59, no. 3, pp. 393–409, Jan. 1971.

[2] T. Manzaneque, R. Lu, Y. Yang and S. Gong, "An SH0 lithium niobate correlator for orthogonal frequency coded spread spectrum communications," *2017 Joint Conference of the European Frequency and Time Forum and IEEE International Frequency Control Symposium (EFTF/IFCS)*, Besancon, 2017, pp. 143-147.

[3] Y. H. Song and S. Gong, "Wideband Spurious-Free Lithium Niobate RF-MEMS Filters," in *Journal of Microelectromechanical Systems*, vol. 26, no. 4, pp. 820-828, Aug. 2017.

[4] C. S. Hartmann and B. P. Abbott, "Overview of design challenges for single phase unidirectional SAW filters," in *Proceedings., IEEE Ultrasonics Symposium*, 1989, pp. 79–89.

[5] T. Manzaneque, R. Lu, Y. Yang and S. Gong, "Lithium Niobate MEMS Chirp Compressors for Near Zero Power

Wake-Up Radios," in *Journal of Microelectromechanical Systems*, vol. 26, no. 6, pp. 1204-1215, Dec. 2017.
[6] Hikita, M., Y. Kinoshita, H. Kojima, T. Tabuchi, and A. Sumioka, "800 MHz low loss SAW filter using new phase weighting," in Microwave Symposium Digest, 1982 IEEE MTT-S International, pp. 46-48. IEEE, 1982.
[7] Kodama, Toshikazu, Hirokazu Kawabata, Hiroaki Sato, and Yoshihiko Yasuhara, "Design of low–loss saw filters employing distributed acoustic reflection transducers," Electronics and Communications in Japan (Part II: Electronics) 70, no. 9 (1987): 32-44.

CONTACT

*T. Manzaneque; tmanzane@illinois.edu

LOW THERMAL BUDGET SURFACE MICROMACHINING PROCESS FOR PIEZOELECTRIC MICROMACHINED ULTRASONIC TRANSDUCER ARRAYS WITH IN-SITU VACUUM SEALED CAVITIES

Qi Wang, Guo Lun Luo, Yuri Kusano, and David A. Horsley
University of California, Davis, USA

ABSTRACT

This paper presents a low thermal budget surface micromachining process for piezoelectric micromachined ultrasonic transducer (PMUT) arrays with *in-situ* vacuum sealed cavities and high fill-factor. Low-temperature PECVD amorphous silicon (a-Si) and CMOS compatible aluminum nitride (AlN) are used in this process, making it possible to fabricate PMUT arrays on top of CMOS wafers directly at a low cost. The presented square PMUT array has a high fill-factor of 79% with a resonant frequency at 5.5 MHz in Fluorinert (FC-70, 3M), suitable for medical imaging applications. The transmitting surface pressure of this array is 2.93 kPa/V, 1.25x higher than previously reported PMUT arrays for fingerprint sensors and the receiving sensitivity is 0.5 V/kPa with a 10 V/pC charge amplifier. The presented fabrication process also showed tunability of PMUT 3-dimension (3D) profile by controlling the AlN residual stress in the deposition process and the possibility to increase the dynamic responses. Meanwhile, the reliability of the PMUTs was tested for 21 hours continuous driving and was tested for seal quality when immersed in Fluorinert.

INTRODUCTION

Ultrasonic sensing for medical and biometric identification applications have been developed based on the recent research efforts with micromachined ultrasonic transducers (MUT) [1]–[3]. Both capacitive (CMUT) and piezoelectric micromachined ultrasonic transducers (PMUT) have been demonstrated as an alternative to current bulk piezoelectric ultrasonic transducers due to its small size, low cost for array fabrication, and CMOS integration compatibility. Cavities are essential for all MUT structures. Ideally, vacuum sealed cavities can eliminate the squeeze film damping during MUT operation and improve efficiency [4]. For CMUT, a small gap cavity is required to achieve high sensitivity [5]. Meanwhile, the small gap impedes a large displacement amplitude. For PMUT, the cavity gap can be made large. Currently available process to achieve this gap includes backside etching [6], utilizing cavity SOI wafers [7], wafer bonding [8] and epitaxial encapsulation [9]. Backside etching requires substrate thinning process and deep reactive etching (DRIE) from the backside of the wafer. The finished structure can be fragile due to the most released areas of the cavities. The cavities are exposed to the atmosphere and generate additional acoustic damping during the PMUT operation. Cavity SOI wafers can provide vacuum sealed cavities but are limited by a minimum spacing of 20 µm which is large for high-frequency PMUT applications. Wafer bonding process was utilized in prior art fingerprint sensors. The process is expensive, unreliable and needs even larger bonding areas (>400m^2) limiting the fill-factor of high-frequency PMUT arrays [10]. Here we present a surface micromachining process to fabricate PMUT arrays with high fill-factor, high yield, vacuum sealed cavities, and reliable structures with high performance.

FABRICATION PROCESS

Figure 1 illustrates the four-mask PMUT surface micromachining process to achieve high fill-factor. The process

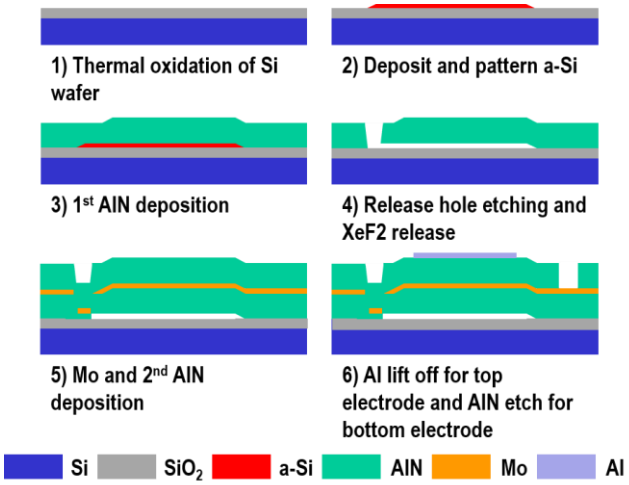

Figure 1: the surface micromachining process for high fill-factor PMUT arrays.

starts by depositing a 500 nm thick silicon dioxide (SiO_2) as an insulation layer. Then a 500 nm thick PECVD a-Si was deposited and patterned with the 1st mask to form the cavity sacrificial layer. The surface roughness of the SiO_2 and a-Si is important for the subsequent aluminum nitride layer depositions. The minimum spacing between a-Si patterns defines the fill-factor and can be made as small as 5 µm here, 4x smaller than the limits in commercially available cavity SOI wafers. The thickness of the a-Si layer defines the cavity depth. 500 nm thick is large enough for PMUT immersed applications like medical imaging or fingerprint sensors. A 500 nm AlN was firstly sputtered with an optimized recipe for achieving a lowest possible residual stress. The AlN layer was then patterned with the 2nd mask to open the release holes. The diameter of the releasing holes can vary from 2 µm to 10 µm depends on cavity sizes. Then the a-Si sacrificial layer was removed in xenon difluoride (XeF_2) gas within 50 cycles. Each cycle lasts for 30 seconds and the XeF_2 pressure is around 3.5 Torr. The minimum cavity spacing distance can be further reduced from 5 µm if the anchors can sustain the released membranes. After the a-Si were completely removed, another 500 nm AlN, 150 nm molybdenum (Mo) and a 1 µm AlN were sputtered in the same tool without breaking the vacuum. This deposition provided the *in-situ* vacuum sealed cavities due to the high vacuum in the chamber in the deposition process. The purpose of sputtering the bottom AlN layer in two steps is to provide a robust seal. The top 1 µm AlN deposition recipe is optimized to achieve a highly c-axis oriented crystalline structure for good piezoelectric responses. Then the 3rd mask is used to etch the top AlN layer and open the vias to bottom Mo electrode. In the last step, the top aluminum (Al) electrode with 300 nm thickness was evaporated and patterned with the 4th mask in a lift-off process.

FABRICATION RESULTS

The crystalline structure of the top AlN thin film is the key to

978-1-940470-03-0/HH2018/$25©2018TRF
DOI 10.31438/trf.hh2018.71

Solid-State Sensors, Actuators and Microsystems Workshop
Hilton Head Island, South Carolina, June 3-7, 2018

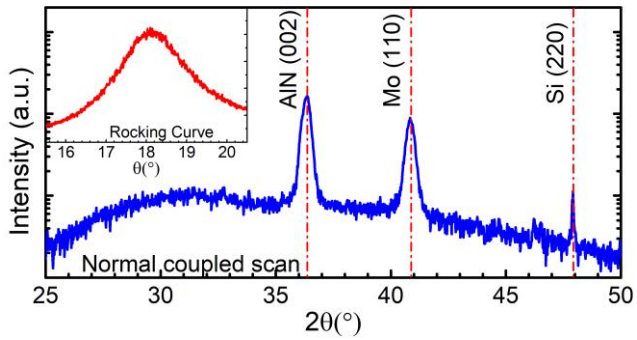

Figure 2: the X-ray diffraction normal coupled measurement results of the top AlN thin films; inset figure is the rocking curve measurement of the AlN (002) peak.

achieve good transmitting and receiving performance, and it was tested using X-ray diffraction (XRD, Siemens D5000 X-ray Diffractometer). Figure 2 shows the normal coupled θ-2θ scan results. Single AlN (002) peak is shown without other orientations, indicating that the film is c-axis oriented. Inset figure is the rocking curve measurement results at AlN (002) peak. The full-width-half-maximum (FWHM) angle is 1.9°, indicating the AlN thin film is well oriented and predicting a good piezoelectric property.

This fabrication process allows us to create a 3D PMUT profile with AlN residual stress engineering. The same AlN sputtering recipe was used to deposit the bottom 1 µm AlN thin film with a target of lowest residual stress on two wafers. Then different AlN sputtering recipes were used to deposit the top 1 µm AlN thin films with different residual stresses. Therefore, different stress gradients were created on the top AlN in two wafers. The static deformation of the PMUTs was measured using a confocal microscope (Olympus LEXT OLS400) and the results are shown in Figure 3. Figure 3(a) indicates a convex PMUT profile with top AlN thin film to have more compressive stress than the bottom AlN thin film. Figure 3(b) shows the opposite results. A 2D symmetric finite element model (FEM) was created in COMSOL to study the effect of top AlN residual stresses. We assume that the bottom AlN thin film was stress-free and the top AlN thin films had residual stresses varying from -100 MPa to +100 MPa. Figure 4(a) is showing the static

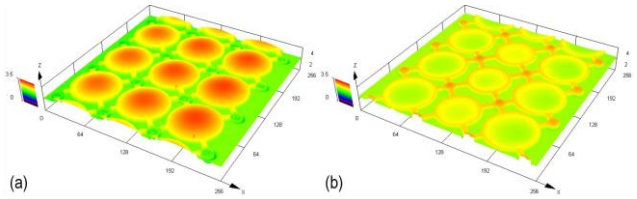

Figure 3: the confocal microscopic image of (a) convex and (b) concave PMUT array under different AlN deposition recipes.

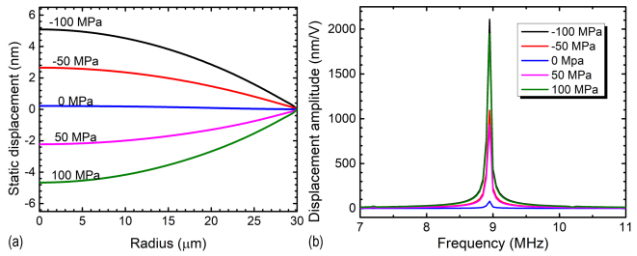

Figure 4: FEM simulation results of (a) symmetric static deformation profile and (b) dynamic displacement amplitude of PMUTs with a top AlN layer with a residual stress varying from -100 MPa to 100 MPa and a bottom AlN layer with no residual stress.

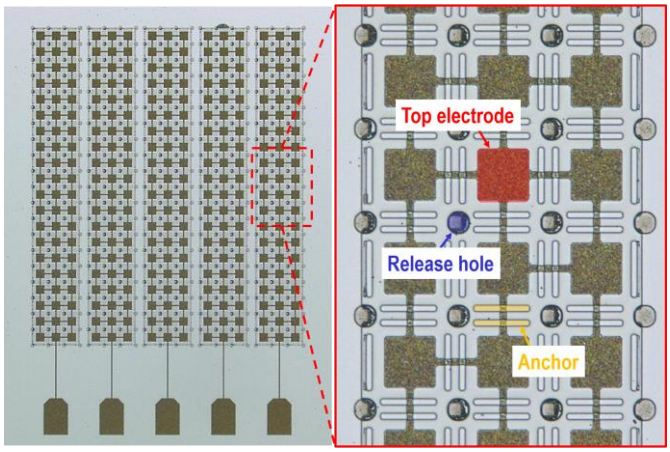

Figure 5: the optical microscopic image of the fabricated high fill-factor PMUT array.

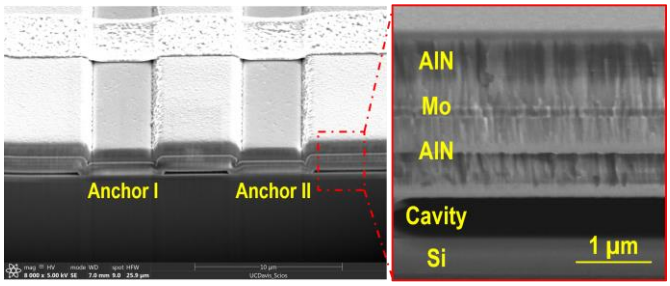

Figure 6: (left) the SEM image of the anchors and the well-sealed cavities; (right) the SEM image of the AlN/Mo/AlN layers with dense columnar AlN structures.

deformation caused by the stress variation. The results indicated that a tensile residual stress generated concave PMUT profile and a compressive residual stress generated convex PMUT profile as expected. The PMUT bending amplitude is proportional to the absolute value of the top AlN residual stress. The simulation results are consistent with the results shown in Figure 3. Figure 4(b) is showing the dynamic responses of the PMUT with top AlN thin films of varying residual stresses. The displacement amplitude increases with the increase of the absolute value of the residual stress. The signs of the residual stress does not influence the dynamic performance.

An optical microscopic image of the fabricated square PMUT array is shown in figure 5. The PMUT cavity is 50 µm wide and the electrode is 35 µm wide, targeting a ~ 5 MHz resonance in Fluorinert. The anchors are marked in the figure with the yellow color. The releasing hole of a diameter of 10 µm is marked in the figure with blue color. The fill factor of this PMUT array is 79%, the highest value for PMUT arrays to our best knowledge. In each element, there are 3 x 20 PMUT cells inside and are connected in parallel to increase the output charge/current. The number of the cells can be adjusted for electrical matchings with the transmitting or receiving circuitry. Five elements are fabricated here and the pitch between each element is ~ 230 µm.

A focused ion beam (FIB, Scios Dual Beam SEM/FIB system) was used to open a trench of the approximate dimension of 50 µm wide, 20 µm long and 5 µm deep. The scanning electron microscopic (SEM) image of the cross-section is shown in figure 6. The two anchors and the cavities in between are shown in the figure. The AlN/Mo/AlN thin films stack is dense and continuous without any cracking. This shows that the cavity is properly sealed with the current fabrication process. A zoom-in figure of the SEM shows the

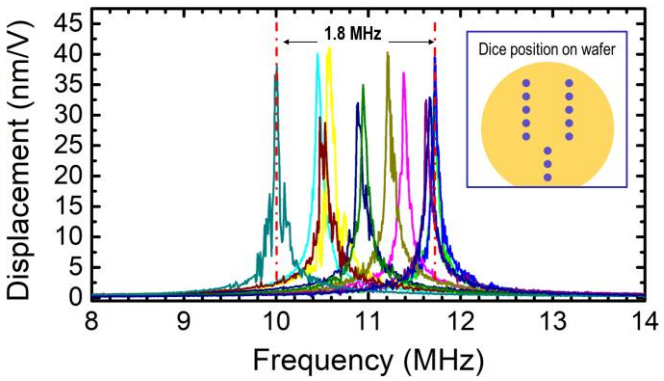

Figure 7: LDV measurement results of 13 50 µm wide square PMUTs across a wafer indicating a high displacement amplitude, and high yield. Inset figure shows the dice locations on the wafer.

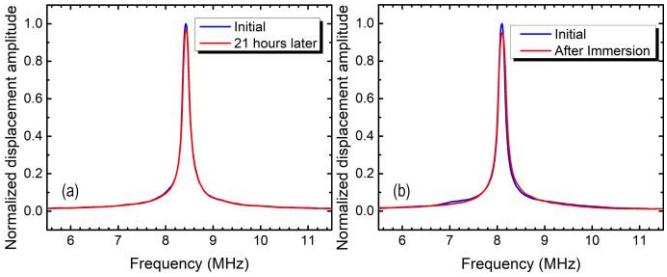

Figure 8: the displacement amplitude of a PMUT (a) before and after 21 hours continuous driving with 2.5 V_{pp} at 8.5 MHz (b) before and after it is immersed in the fluid. No changes are observed indicating a good reliability and a good seal of the structure.

dense columnar structure of the AlN thin films with Mo electrode and the cavity. An interface of the bottom AlN can be seen in the figure and this is due to the different sputtering steps as mentioned earlier in the fabrication process.

CHARACTERIZATIONS

Dynamic responses

13 PMUT dices are selected across the wafer and the frequency responses are tested in the air with a laser Doppler vibrometer (LDV, OFV 512 and OFV 2700, Polytech) in conjunction with a network analyzer (E5601B, Agilent Technology). The results are plotted in figure 7. Inset figure is showing the positions of the 13 tested dices. The average displacement amplitude is ~36 nm/V, the average resonant frequency is ~ 11 MHz and the average quality factor is ~142. The displacement amplitude is 1.6x higher than circular $Sc_{0.15}Al_{0.15}N$ PMUT as reported in [7]. The variation of the resonant frequency is ~ 1.8 MHz and the probable reason for this change is the AlN residual stress variation across the wafer. Further efforts on better controlling the AlN stress across the wafer is needed to reduce the resonant frequency variation. The tested 13 dices all indicated high displacement amplitude is showing a high yield from this surface micromachining process. The differences in the resonant frequency in the air will not be influential when the devices are immersed in liquid and the small quality factor due to the large acoustic loading in liquid.

Reliability

A circular PMUT with 35 µm radius was selected from the wafer and continuously driven in air at the resonant frequency, 8.5 MHz, with 2.5 V_{pp} sinusoid voltages for 21 hours. The displacement amplitude of the PMUT was continuously monitored via LDV. Figure 8(a) shows the frequency response of the PMUT before (blue) and after (red) this long time running tests. No obvious performance decay was observed from the figure. The testing results showed that the fabricated PMUTs are robust and can endure long working times without performance degradation. The negligible change in the frequency response also indicated that no structural damaged during this testing process.

Another circular PMUT with the same geometry was also tested for the cavity seal quality. The frequency response of this PMUT was first measured and the results are indicated in Figure 8(b) in blue. The PMUT dice was then immersed in Fluorinert for one hour. After the immersion, the dice was picked out and air dried to remove the surface attached Fluorinert liquid. In the end, the PMUT frequency response was measured again and the results are shown in the red line in figure 7(b). The frequency response before and after immersion overlapped and no obvious resonant frequency change or amplitude degradation was observed from this test. If there were leakage happened during this testing, the resonant frequency would be lower, and the quality factor would be smaller due to the added liquid damping induced by the liquid leakage. The results showed that the cavity is well sealed, and no leakage was found in this case.

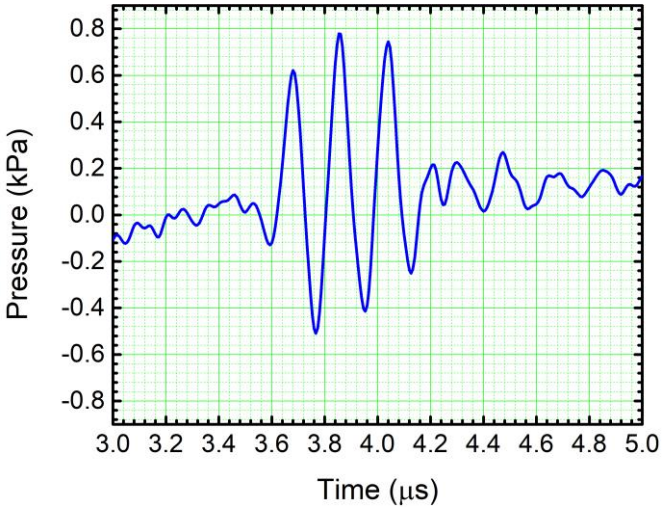

Figure 9: measured acoustic pressure in Fluorinert at 3 mm away from the PMUT surface.

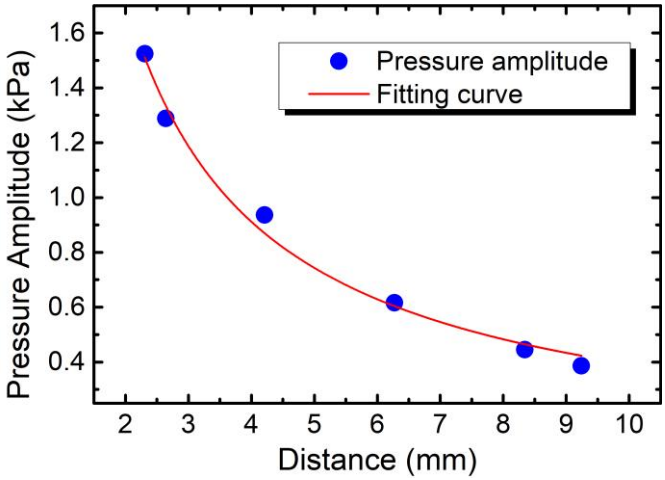

Figure 10: the measured pressure versus the measurement distance from the hydrophone to PMUTs surface and its fitting curve.

Pressure measurement

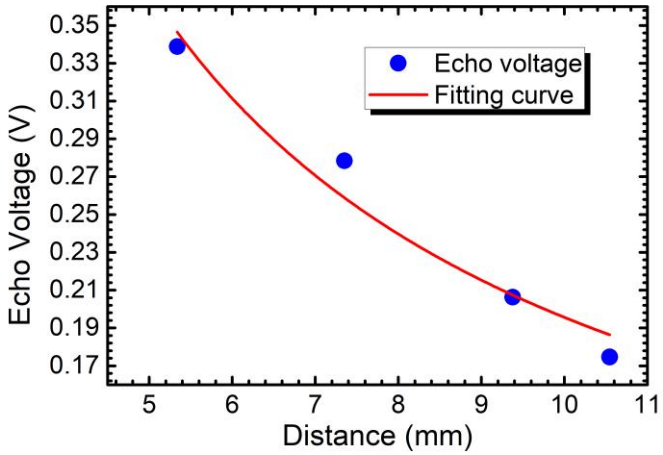

Figure 11: the measured echo output voltages versus the acoustic path and its fitting

One element of the square PMUT array was used to test its transmitting sensitivity. The PMUT element was immersed in Fluorinert and driven by a high voltage pulser (Microchip, HV7355DB1) with 3 unipolar pulses at 5.5 MHz with 30 V_{pp}. A hydrophone (Precision acoustics) with 75 µm diameter was used to measure the transmitted acoustic pressure on top of the PMUT surface. Figure 9 shows the measured acoustic pressure amplitude was ~ 1.3 kPa and it was measured 3.6 µs after the pulses were generated. The measured time corresponding to the relative distance between the hydrophone and the PMUT surface. The hydrophone was lifted gradually so that the output pressure at different heights were measured and results are shown in figure 10. The measured pressure amplitudes were fitted with the following equation, $p(x) = 0.0058x^{-0.92}$, where x is the acoustic path distance. The Rayleigh distance of this element is ~ 67.6 µm and the output surface pressure is ~ 2.93 kPa/V, 1.25x higher than reported in [11].

Pulse-echo measurement

The pulse-echo measurement was conducted with one element used as a transmitter and a neighbor element is used as a receiver. The same pulser was utilized in this measurement with the same condition as mentioned in pressure measurement. The receiving element was connected to a charge amplifier (FEMTO, HQA-15M-10T) with a gain of 10 V/pC. The output pressure propagated to the interface of the Fluroinert and air and then reflected. The PMUT receiving voltage from the echo pressure was amplified and shown on an oscilloscope. The Fluroinert height was adjusted so that the relationship between PMUT receiving voltage and acoustic path distance can be obtained. The results are plotted in figure 11 and are fitting results are $V(x) = 0.0029x^{-0.91}$. The receiving sensitivity can be obtained using *V(x)/p(x)*, which leads to 0.51 V/kPa. The imaging depth of this element is around 1 cm under 30 V_{pp} pulses and it can be increased with large element sizes, higher transmitting voltages, and driving more elements with beam forming for real medical imaging applications.

CONCLUSION

Here, we presented a low cost, low thermal budget, CMOS compatible surface micromachining process with four-mask and *in-situ* vacuum sealed cavities for fabricating high fill-factor PMUT arrays. The proposed fabrication process demonstrated PMUTs with high transmitting and receiving sensitivities, high yield, and high reliability. This fabrication process also enables us to tune the 3D geometry of the fabricated PMUT with either convex or concave structures without complicated etching steps as mentioned in [12] and improved the AlN piezoelectric properties. This fabrication process can be further improved with the potentials of using different sacrificial layer and elastic layer selections to create more robust, higher sensitivity PMUT structures and arrays.

ACKNOWLEDGMENT

The devices were fabricated in Berkeley Marvell Nanofabrication Laboratory. The authors thank Berkeley Sensor and Actuator Center (BSAC) industrial members for financial support.

REFERENCES

[1] Y. Lu *et al.*, "Ultrasonic fingerprint sensor using a piezoelectric micromachined ultrasonic transducer array integrated with complementary metal oxide semiconductor electronics," *Appl. Phys. Lett.*, vol. 106, no. 26, p. 263503, Jun. 2015.

[2] A. Caronti *et al.*, "Capacitive micromachined ultrasonic transducer (CMUT) arrays for medical imaging," *Microelectron. J.*, vol. 37, no. 8, pp. 770–777, Aug. 2006.

[3] F. L. Degertekin, "Microscale systems based on ultrasonic MEMS-CMOS integration," in *2017 19th International Conference on Solid-State Sensors, Actuators and Microsystems (TRANSDUCERS)*, 2017, pp. 397–401.

[4] Y. Lu and D. A. Horsley, "Modeling, Fabrication, and Characterization of Piezoelectric Micromachined Ultrasonic Transducer Arrays Based on Cavity SOI Wafers," *J. Microelectromechanical Syst.*, vol. 24, no. 4, pp. 1142–1149, Aug. 2015.

[5] I. O. Wygant, *et al.*, "Analytically calculating membrane displacement and the equivalent circuit model of a circular CMUT cell," in *2008 IEEE Ultrasonics Symposium*, 2008, pp. 2111–2114.

[6] Benjamin Eovino, *et al.*, "Broadband ring-shaped PMUTs based on acoustically induced resonance." in *2017 IEEE 30th International Conference on Micro Electro Mechanical Systems (MEMS)*, 2017, pp. 1184-1187.

[7] Q. Wang, *et al.*, "Design, Fabrication, and Characterization of Scandium Aluminum Nitride-Based Piezoelectric Micromachined Ultrasonic Transducers," *J. Microelectromechanical Syst.*, vol. 26, no. 5, pp. 1132–1139, Oct. 2017.

[8] J. M. Tsai, *et al.*, "Versatile CMOS-MEMS integrated piezoelectric platform," in *2015 Transducers - 2015 18th International Conference on Solid-State Sensors, Actuators and Microsystems (TRANSDUCERS)*, 2015, pp. 2248–2251.

[9] Y. Chen, *et al.*, "Robust Method of Fabricating Epitaxially Encapsulated MEMS Devices with Large Gaps," *J. Microelectromechanical Syst.*, vol. 26, no. 6, pp. 1235–1243, Dec. 2017.

[10] Y. Lu *et al.*, "Waveguide piezoelectric micromachined ultrasonic transducer array for short-range pulse-echo imaging," *Appl. Phys. Lett.*, vol. 106, no. 19, p. 193506, May 2015.

[11] X. Jiang *et al.*, "Monolithic 591x438 DPI ultrasonic fingerprint sensor," in *2016 IEEE 29th International Conference on Micro Electro Mechanical Systems (MEMS)*, 2016, pp. 107–110.

[12] S. Akhbari, *et al.*, "Highly responsive curved aluminum nitride pMUT," in *2014 IEEE 27th International Conference on Micro Electro Mechanical Systems (MEMS)*, 2014, pp. 124–127.

CONTACT

*Q. Wang, tel: +1-530-746-1632; qixwang@ucdavis.edu

A TWO-MINUTE ASSAY FOR ELECTRONIC QUANTIFICATION OF ANTIBODIES IN SALIVA ENABLED THROUGH MULTI-FREQUENCY IMPEDANCE CYTOMETRY AND MACHINE LEARNING ANALYSIS

Zhongtian Lin[1], Jianye Sui[1], Pengfei Xie[1], Karan Ahuja[1] and Mehdi Javanmard[1]
[1]Department of Electrical and Computer Engineering, Rutgers University, USA

ABSTRACT

At present, the use of saliva as a diagnostic fluid is more and more common due to its ability to monitor health status, onset and progression of disease and treatment progress in a noninvasive way. Rapid detection of antibodies in saliva can enable point-of-care diagnosis for auto-immune diseases like sepsis. For the first time, to the best of our knowledge, we have developed an electronic assay using impedance cytometry in conjunction with supervised machine learning, capable of quantifying immunoglobulins in saliva within two minutes.

INTRODUCTION

At present, the use of saliva as a diagnostic fluid is more and more common due to its ability to monitor health status, onset and progression of disease and treatment progress in a noninvasive way. [1] The state of various diseases can be diagnosed by monitoring the level of certain protein biomarkers in saliva. For example, in the case of chronic diseases like hepatitis B virus (HBV) and hepatitis C virus (HCV), HBV and HCV DNAs, antibodies exist in the saliva having a correlation with their levels in blood samples. [2-5] Auto-immune diseases like sepsis also have related biomarkers in saliva. [6] However, current technologies for performing biomarker assays usually involve bulky instrumentation with optical technologies like sandwich ELISA or protein microarrays. Light weight, highly sensitive and inexpensive ultra-compact platforms for point of care diagnosis are needed for those diseases.

Electrical impedance based technology are one of the most promising solutions to build portable platforms. Previously, we demonstrated detection of protein biomarkers in bioactivated microchannel [7] and used protein capture beads and impedance cytometry for detection of proteins with low abundance. [8] We also demonstrated another method for detection of protein based on bead aggregate sizing. [9] Besides, Carbonaro et. al. demonstrated a method for label free biomarker detection based on size changes of beads due to biomarker binding. [10] Tien-Li et. al. described a detection method for protein based on nanogap electrodes. [11] Tami et. al. demonstrated a frequency dependent electrochemical impedance spectroscopy to detect protein biomarkers. [12] And Gengfeng et. al. demonstrated a label-free multiplexed electrical detection of cancer makers using silicon-nanowire field-effect sensor arrays. [13] Jay et. al. demonstrated a label-free electrical detection of cardiac biomarker in real time using silicon nanowire sensor arrays. [14] For the first time, to the best of our knowledge, we have developed an electronic assay using impedance cytometry in conjunction with supervised machine learning, capable of quantifying immnunoglobulins in saliva within two minutes.

Figure 1 illustrates the assay steps and device operation. The assay works by using magnetic anti-IgG (primary antibody) coated beads to capture soluble IgG (target antigen) molecules in saliva. Anti-IgG (detector antibody) is then added to the magnetic beads to further increase the effective radius of the bead-protein complex. The beads flow through an impedance cytometer that probes the impedance of the beads at eight frequencies. The use of multi-frequency electrical impedance cytometry and machine learning technique allows for electronically determining the level to which beads have captured target IgG molecules in saliva. We independently confirmed that binding properly occurred by fluorescently tagging (FITC) the detector anti-IgG molecules and imaged optically.

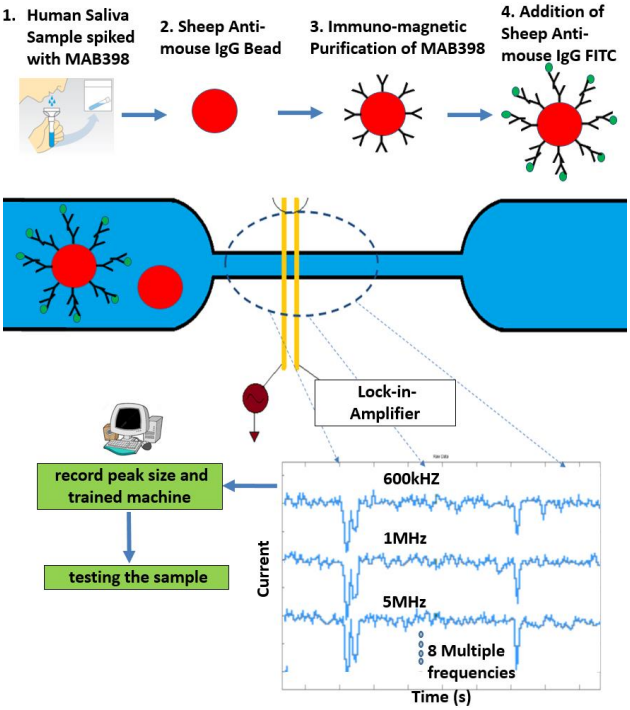

Figure 1. Schematic of biochip. Presence of IgG in saliva sample results in beads binding to IgG which enables the labeling of FITC markers to the beads. Multi-Frequency Impedance based sizing and machine learning technique were used for differentiating between FITC coated beads and unbound beads.

THEORY

The particle inside the channel with the electrode/electrolyte interface can be modelled using the circuit shown in Figure 2. We assumed an ideal polarizable electrode model without charge transfer resistance at the interface as we used gold as our electrode material, which is inert. The model involves two Debye layer capacitances (Cdl) at each electrode in series with the solution resistance in series with an impedance network representing beads. We consider beads consists of a capacitance (Cb) at its surface in series with resistance (Rb).

$$Z = \frac{2}{j\omega C_{dl}} + R_{solution} + \frac{1}{j\omega C_{bead}} + R_{baed} \quad \text{(Eq. 1)}$$

The impedance of the beads depends on the bead size and conductivity and dielectric permittivity at the bead surface. The binding of IgG modulates these properties at small levels, which makes it difficult to be detected by normal impedance cytometry at one or two frequencies Thus multi-frequency impedance cytometry and machine learning analysis are used in order to detect the

978-1-940470-03-0/HH2018/$25©2018TRF
DOI 10.31438/trf.hh2018.72

differences.

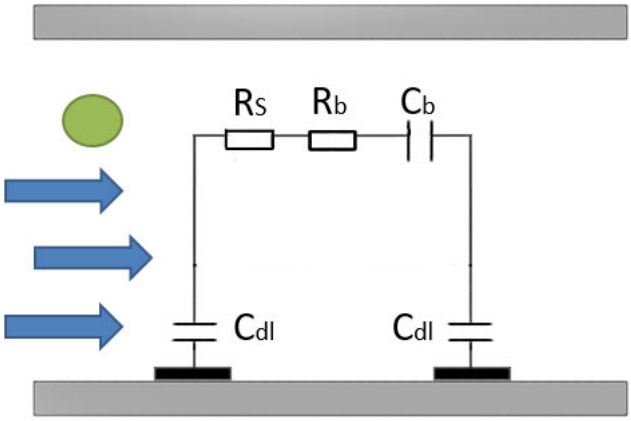

Figure 2. The equivalent circuit model for a two electrode pair system with a bead suspended in buffer.

EXPERIMENTAL

Electrodes Fabrication

The microfabricated biochip (Fig 3a and Fig 3b) consists of two gold microelectrodes on a glass substrate with the PDMS (Polydimethyl Siloxane) channel above it. To fabricate the gold electrodes, standard photolithography was applied on a 3inch fused silica wafer. The whole process includes photo-pattering resist on a fused silica wafer, performing electron beam metal evaporation and lift off process. The photo-pattering process consists of cleaning the wafer, spin coating photoresist, photoresist soft bake, ultra-violet light exposure through a four inch chromium mask, resist development, followed by a hard bake. 5 nm of chromium was deposited on the wafer via electron beam evaporation for enhancing the adhesion of the 100 nm gold layer to the wafer which was deposited after using the same methodology. Lift off was performed last using ultrasonic cleaner in acetone.

Microfluidic Channel Fabrication

The micro-channel starts from a 300 µm wide and 20 µm high channel part and tapers down to a 30 µm wide and 20 µm high sensing pore. The smaller cross sectional area of the sensing pore improves the focusing of particles above sensor and also increase electrical sensitivity to the extent where 2.8 µm anti-IgG beads and IgG bind 2.8 µm anti- IgG beads can be differentiated. The spacing between the two electrodes is 30 µm and the width of each electrode is 20 µm. The micro-channel was made in PDMS from a master mold fabricated using soft lithography. The fabrication process consists of cleaning the wafer, spin coating, soft bake, photo-pattering an inverse feature onto a three inch silica wafer, UV light exposure, development and hard bake. To make PDMS channels, pre-polymer and curing agent were mixed at the ratio of 10 to 1 and poured onto the master mold. After curing the PDMS for about 1 hour, we peeled it off, cut the channels out and punched holes to make inlets and outlets. At last, the microfluidic channel was aligned to the electrode substrate and bonded onto the glass wafer covalently by treating both substrates with oxygen plasma.

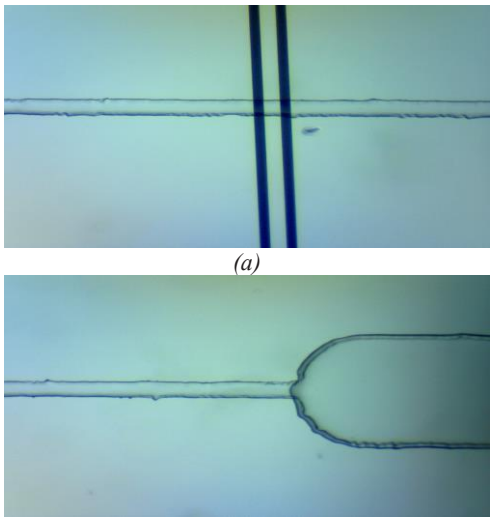

(a)

(b)

Figure 3. (a) Microfabricated electrodes (b) Entrance of micropore

Measurements

In order to make the beads flow without the help of a pump to minimize the influences from external interference, we first performed plasma treatment on the channel to make it hydrophilic and filled it with PBS to keep its hydrophilicity. Due to the pressure differences between the inlet and outlet, which was generated by the differences in fluid volume in the well, the beads were then injected into the inlet of the biosensor and directed to the multi-frequency impedance sensor which was connected to a lock-in amplifier (Zurich Instrument HF2 series). The input AC voltage was 400 mV peak-to-peak and the gain was 1 kV/Amp. As particles passed over the electrodes, impedance responses at 8 discrete frequencies from 600 kHz to 24 MHz were captured simultaneously. A metal box was used to electrically insulate the sensor from external interference during testing. The recorded data was then processed using a custom-written Matlab code which performed detrending, denoising, peak finding, and differentiating the beads bound to IgG from the normal beads with the help of machine learning. At the same time, in order to confirm the binding both electrically and optically, we tagged the beads with fluorescent markers and observed the beads under a fluorescent microscope immediately after the assay.

Sample Preparation

To demonstrate proof-of-concept, saliva samples were spiked with mouse IgG at concentrations of 1667 nM, 167 nM and 17 nM. We used 2.8 µm paramagnetic Dynal beads (Life Technologies, Carlsbad, CA) coated with anti-mouse IgG antibodies to capture the mouse IgG in the saliva sample. The protocol for performing the 2 min assay went as follows: Sheep anti-mouse IgG beads were washed three times in PBS 0.1 % BSA. The beads were then mixed with mouse IgG spiked saliva sample off chip in the epindorph tube and rotate for 2 min. In order to confirm that the binding properly occurred, we then washed the beads three times with PBS 0.1 % BSA and mixed with FITC tagged sheep anti-mouse IgG. Beads were washed with PBS to ensure all the unbound antibodies were washed away before the electrical testing.

Machine learning algorithm

To improve classification accuracy and be able to detect the differences between beads that captured no analyte and beads that captured IgG, a support vector machine (SVM) machine learning

algorithm is employed, where peak amplitudes at 8 frequencies are used as features in the feature vector. Classification of different particles improves effectively in high-dimensional space. The SVM model gets trained using part of the data, and the rest of the data are used for testing. Comparing the prediction with the true category, the accuracy was calculated.

RESULTS AND DISCUSSION

Experiments were performed both optically and electrically at multiple IgG concentrations to verify the viability and repeatability of the 2 minute assay. Figure 4a shows the fluorescent image of the positive assay where beads were incubated for two minutes in an IgG positive saliva sample and Fig. 2d for the control assay where beads incubated for the same time in an IgG negative saliva sample. The positive assay shows strong florescent signal compared to the black background negative control assay as a result of specific anti-IgG fluorescently tagging. The image confirmed that the IgG bind to the beads.

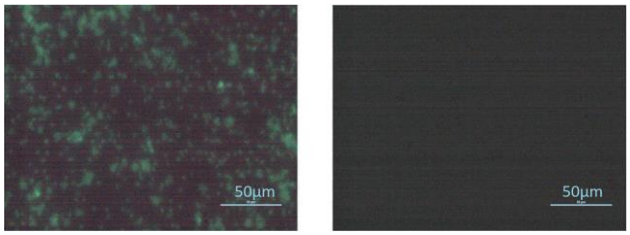

Figure 4. (a) IgG positive beads (anti-IgG detector antibody FITC tagged) (b) IgG negative beads.

As for the electrical testing, when the sample was injected onto the biosensor using pressure driven flow, particles passed over the electrodes, which were connected to an AC voltage source and a multi-frequency lock-in amplifier, a frequency dependent change in current is exhibited as showed in raw data (Fig 5).

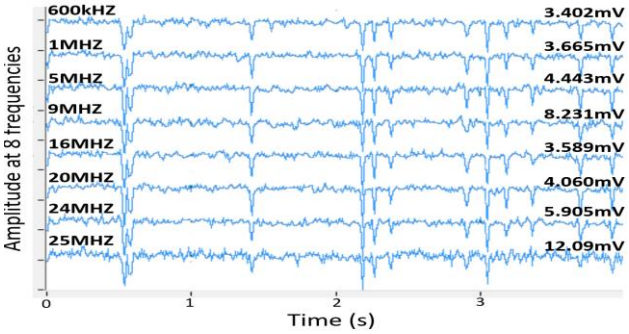

Figure 5. Raw data of beads passing through impedance cytometer at multiple frequencies. The frequencies were 600K, 1M, 5M, 9M, 16M, 20M, 24M, 25MHz. The amplitudes of the Input AC voltage were 400mV.

The amplitude of the current peak at different frequencies depends on bead size and conductivity and dielectric permittivity at the bead surface. Single and even dual frequency analysis alone makes it difficult to distinguish different bead types from each other as shown in the scatter plot for voltage peak intensity at 600 kHz and 24 MHz (Fig 6) or at 1Mhz and 20Mhz (Fig 7).

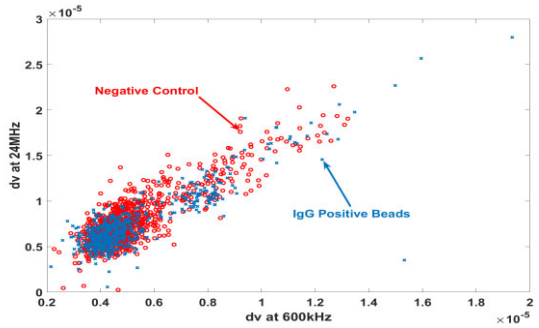

Figure 6. Scatter plot for voltage peak intensities at 600 kHz and dv at 24 MHz.

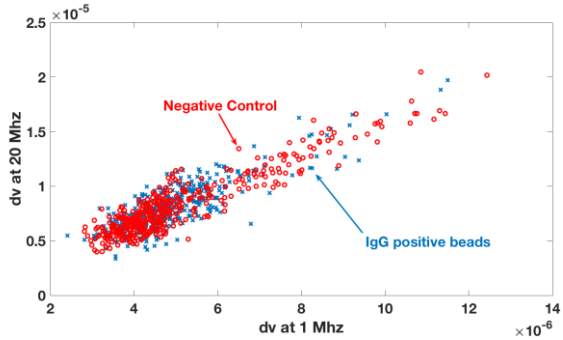

Figure 7. Scatter plot for voltage peak intensities at 1 MHz and dv at 20 MHz.

The use of eight frequencies, however, in conjunction with machine learning makes bead differentiation and thus target IgG quantification feasible. We trained the SVM (Support Vector Machine) model with peak intensities from IgG positive and IgG negative data at eight frequencies, and then verified this model on test data from different samples and determined algorithm classification accuracy for IgG positive and IgG negative beads. As the concentration of target IgG in saliva decreases, SVM classification accuracy decreases. We used this classification accuracy as a metric to quantify IgG levels (Fig. 8). We formulated a biomarker quantification score (Eq. 2) to provide a self-calibrated method of quantifying biomarker levels. Figure 5 shows a biomarker quantification score dynamic range of 3 orders of magnitude.

$$Biomarker\ Quantification\ Score = \frac{SVM\ Accuracy - 50}{50} \quad \text{(Eq. 2)}$$

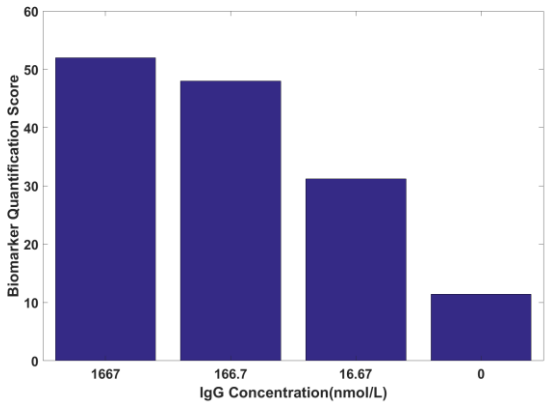

Figure 8. Bar graph of Biomarker Quantification Score to IgG concentrations at 0 to 1667 nM;

CONCLUSIONS

In conclusion, our experimental results show that through the combination of multi-frequency microfluidic impedance cytometry and supervised machine learning, that we are able to qualify immunoglobulins in saliva within two minutes. Though in this work, IgG was used as the biomarker for testing in saliva samples, the method can be performed in a wide variety of proteins as long as a comparable high affinity antibody pair is available. The work shown here has potential to be developed into an integrated biochip to rapidly quantify certain biomarker levels in complex samples like saliva and urine. Our future work will be focused on increasing the sensitivity for this assay from nanoMolar to picoMolar to make it comparable to the gold standard ELISA method and validate this method in a variety of proteins.

ACKNOWLEDGEMENTS

This project was funded by PhRMA Foundation Starter Grant for Early Faculty. This research was sponsored by an anonymous corporation. The devices were fabricated in the Microelectronics Research Laboratory (MERL) in Rutgers University.

REFERENCES

[1] Streckfus, C. F., and L. R. Bigler. "Saliva as a diagnostic fluid." Oral diseases 8, no. 2 (2002): 69-76.

[2] Yoshizawa, Janice M., Christopher A. Schafer, Jason J. Schafer, James J. Farrell, Bruce J. Paster, and David TW Wong. "Salivary biomarkers: toward future clinical and diagnostic utilities." Clinical microbiology reviews 26, no. 4 (2013): 781-791.

[3] Chen, Lizhang, Fuqiang Liu, Xuegong Fan, Jianming Gao, Nengzhi Chen, Tom Wong, Jun Wu, and Shi Wu Wen. "Detection of hepatitis B surface antigen, hepatitis B core antigen, and hepatitis B virus DNA in parotid tissues." International Journal of Infectious Diseases 13, no. 1 (2009): 20-23.

[4] Gonçalves, Patrícia L., Carla B. Cunha, Solange CU Busek, Guilherme C. Oliveira, Rodrigo Ribeiro-Rodrigues, and Fausto EL Pereira. "Detection of hepatitis C virus RNA in saliva samples from patients with seric anti-HCV antibodies." Brazilian Journal of Infectious Diseases 9, no. 1 (2005): 28-34.

[5] González, V., E. Martró, C. Folch, A. Esteve, L. Matas, A. Montoliu, J. R. Grifols et al. "Detection of hepatitis C virus antibodies in oral fluid specimens for prevalence studies." European Journal of Clinical Microbiology & Infectious Diseases 27, no. 2 (2008): 121-126.

[6] Cho, Sung-Yeon, and Jung-Hyun Choi. "Biomarkers of sepsis." Infection & chemotherapy 46, no. 1 (2014): 1-12.

[7] Javanmard, Mehdi, Amirali H. Talasaz, Mohsen Nemat-Gorgani, Fabian Pease, Mostafa Ronaghi, and Ronald W. Davis. "Electrical detection of protein biomarkers using bioactivated microfluidic channels." Lab on a Chip 9, no. 10 (2009): 1429-1434.

[8] Mok, Janine, Michael N. Mindrinos, Ronald W. Davis, and Mehdi Javanmard. "Digital microfluidic assay for protein detection." Proceedings of the National Academy of Sciences 111, no. 6 (2014): 2110-2115.

[9] Lin, Z., X. Cao, P. Xie, M. Liu, and Mehdi Javanmard. "PicoMolar level detection of protein biomarkers based on electronic sizing of bead aggregates: theoretical and experimental considerations." Biomedical microdevices 17, no. 6 (2015): 119.

[10] Carbonaro, A., and L. L. Sohn. "A resistive-pulse sensor chip for multianalyte immunoassays." Lab on a Chip 5, no. 10 (2005): 1155-1160.

[11] Chang, Tien-Li, Chien-Ying Tsai, Chih-Chen Sun, Chun-Chi Chen, Long-Sheng Kuo, and Ping-Hei Chen. "Ultrasensitive electrical detection of protein using nanogap electrodes and nanoparticle-based DNA amplification." Biosensors and Bioelectronics 22, no. 12 (2007): 3139-3145.

[12] Lasseter, Tami L., Wei Cai, and Robert J. Hamers. "Frequency-dependent electrical detection of protein binding events." Analyst 129, no. 1 (2004): 3-8.

[13] Zheng, Gengfeng, Fernando Patolsky, Yi Cui, Wayne U. Wang, and Charles M. Lieber. "Multiplexed electrical detection of cancer markers with nanowire sensor arrays." Nature biotechnology 23, no. 10 (2005): 1294.

[14] Chua, Jay Huiyi, Ru-Ern Chee, Ajay Agarwal, She Mein Wong, and Guo-Jun Zhang. "Label-free electrical detection of cardiac biomarker with complementary metal-oxide semiconductor-compatible silicon nanowire sensor arrays." Analytical chemistry 81, no. 15 (2009): 6266-6271.

CONTACT

*Mehdi Javanmard; mehdi.javanmard@rutgers.edu

MULTI-MODAL MICROELECTRODE ARRAYS FOR THE INVESTIGATION OF PROTEIN ACTIN'S ELECTRO-MECHANOSENSING MECHANISMS TOWARD NEURODEGENERATIVE DISEASE MODELS ON A CHIP

*Nilab Azim, Nicholas Castaneda, Angie Diaz, Hyeran Kang and Swaminathan Rajaraman**
NanoScience Technology Center, University of Central Florida, Orlando, Florida, USA

ABSTRACT

We have developed multi-modal Microelectrode Arrays (MEAs) with electrodes and microfluidics, with successful manipulation of actin filaments and bundles onto the devices for electro-mechanosensing studies. The application of our MEAs to the characterization of actin filaments/bundles will allow fundamental understanding of actin cytoskeleton's mechanical and electrodynamic properties in neurodegenerative disease signatures on a chip.

INTRODUCTION

The essential protein actin provides cells with structural integrity and mechanical support for motility. Actin filaments are charged polyelectrolytes [1] which may function as biological "electrical wires" [2]. The organization of actin filaments into higher ordered bundles or networks provide cells with structural support. Filopodia at the leading edge of a nerve cell are highly dynamic bundled structures in which actin filament assembly and mechanics are key players for neuronal growth cone motility and synapse activity. Dysfunctions in actin have been tied to serious and often debilitating neurodegenerative diseases [3, 4].

The actin cytoskeleton actively responds to mechanical stimuli such as tension and bending deformation. These stimuli potentially affect how filaments interact with actin binding proteins that tightly regulate filament assembly dynamics. Considering that actin filaments potentially can serve as electric transmitters by conducting ionic currents [2], actin assembly dynamics and mechanics may play a central role in synaptic plasticity and neuronal activities. However, it is not well established how electric stimuli modulate the mechanical properties of actin filaments and/or bundles or vice-versa.

The electrical and mechanical activity of actin can potentially be monitored by multi-modal microelectrode array (MEA) devices. MEA devices are well established platforms that are non-invasive, label-free, applicable for long-term studies and can provide quantitative electrical activity [5]. These devices have traditionally been applied to monitoring the activity of electrogenic cells, which generate momentary changes in potential across their cell membrane. MEAs additionally are capable of actively stimulating cells and recording the effects of the stimulation. Therefore, MEAs can passively record the electrical activity of actin upon assembly and different macro-mechanical factors (e.g. flow rates). Stimulation of actin via the MEAs can provide insight into understanding the effect of electrical stimuli in modulating the properties of actin.

The advantage of MEAs over other electrical recording platforms is the high spatial and temporal resolution to improve the sensor sensitivity and signal-to-noise ratio, which are important with regards to the small size of actin [5]. On top of the electrical detection modality, MEA devices also provide the ability for optical detection due to their transparency if fabricated on glass substrates. Optical detection techniques are prevalently used in biological sciences and can be based on fluorescence or chemiluminescence [6].

The integration of microfluidics with MEA devices introduces novel micro-mechanical functionalities such as the integration of sample handling and preparation, mixing, and detection [6] that enable the ability to flow analytes and record the changes electrically or the other way around. A previous study has been performed on the application of microfluidics to study the mechanical tension of an elongating actin filament [7]. In the study, microfluidic flow produced piconewton pulling forces on the anchored filaments during filament elongation and concluded that formin is mechanosensitive and elongation rates were increased by the application of pulling forces [7]. This study heavily relied on optical detection. However, by introducing electrical stimulation and recording in addition to optical and micro-mechanical stimulation through microfluidics, a complete understanding in structure, assembly, and mechanical properties of actin can be obtained.

Our goal is to determine the biophysical, biomechanical, and electrophysical properties of actin filaments and bundles, utilizing novel multi-modal MEAs and coupling these devices with analysis tools such as total internal reflection fluorescence (TIRF) microscopy, impedance spectroscopy, cyclic voltammetry (CV) and electrophysiological characterization (Figure 1). The implementation of microfluidics with MEA technology allows for the manipulation of actin to investigate its electro-mechanosensing mechanisms, thereby ultimately leading to novel neurodegenerative disease models on a chip, which has yet been well established.

MATERIALS AND METHODS

Multi-modal MEA Fabrication and Packaging

The MEA chips were fabricated as per our previous study [5]. MEA chips of 12 mm by 12 mm size with insulation and metal layers were designed to contain an 8 by 8 array of 64 electrodes with diameters of 25μm and pitch of 200μm. The chips were designed to have four internal reference ground electrodes with the dimensions of 740μm by 120μm for reduced infection rates, better grounding and improved Signal to Noise Ratios (SNRs).

The fabrication of the MEA chips involved using traditional surface micromachining techniques. A 4 inch, 500μm thick glass wafer was processed with traditional lift-off technology to define metal traces, electrode landing pads and recording sites. Subsequently, the insulation layer was defined using a layer of SU-8 and exposed to UV through the recording sites mask. The photoresist was developed and hard-baked to achieve the full properties of the insulation layer. Lastly, an Nd:YAG laser operating at a wavelength of 532 nm, energy of 2.7 mJ, and set at 50 Hz pulses using the 50X objective lens with scan rate of 200μm/s was used to scribe the wafer, followed by accurate cleaving to dice it.

Printed Circuit Boards (PCBs) were designed separately with 72 contact pads and routing traces defined in a two-layer PCB. The minimum feature size between the traces, which had widths of 250μm, was 75μm. Through metal vias interconnecting the top and bottom pads for bottomside electronics access were 500μm in diameter with a pitch of 650μm. The PCBs were designed to have a central port to allow for the viewing of actin by TIRF microscopy.

978-1-940470-03-0/HH2018/$25©2018TRF
DOI 10.31438/trf.hh2018.73

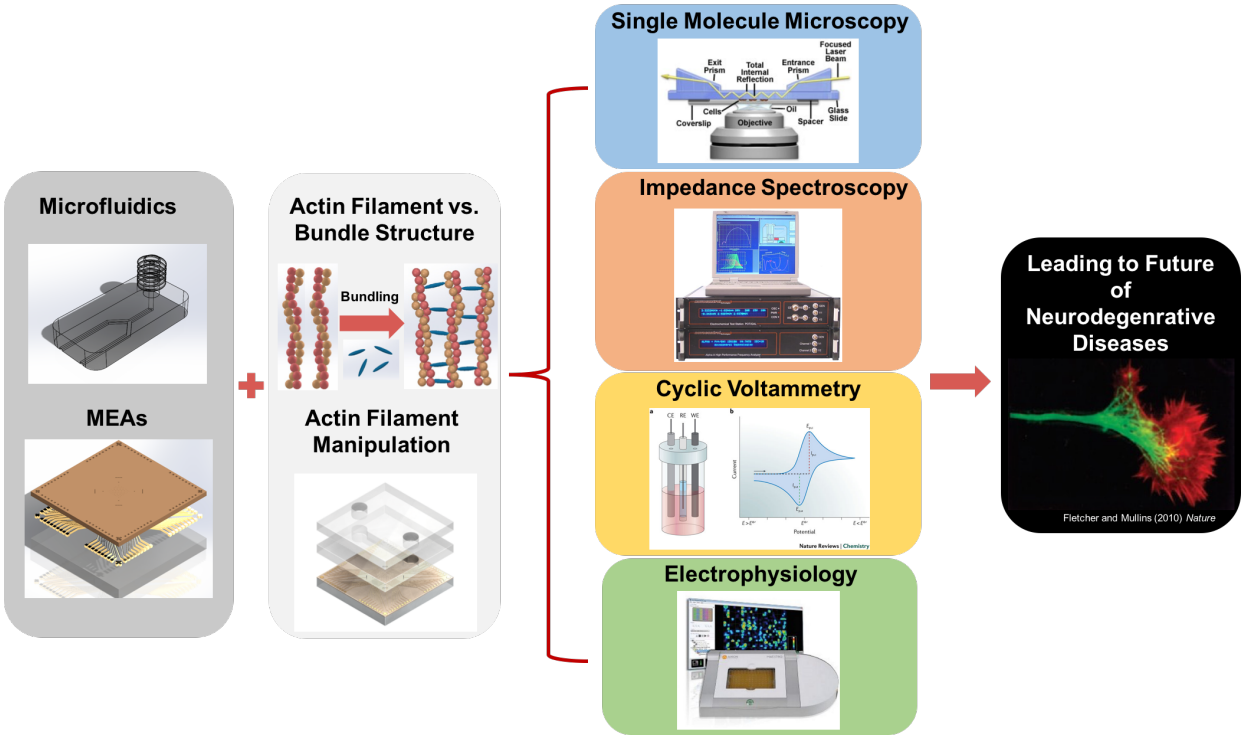

Figure 1: ***Schematic representation of our experimental setup*** *– Multi-modal MEAs with microfluidic channels with actin addition and immobilization in order to visualize actin filament and bundle interactions on the device. Experimental tools such as microscopy and quantitative electrochemical analysis of protein electrophysiology will allow for future work in neurodegenerative diseases.*

Microfluidic channels were integrated atop the device by micromilling a channel (375µm wide) with inlet and outlet ports on a two-layer polyethylene terephthalate (PET) substrate and an adhesive sandwiched between the layers. Each PET layer was 50µm thick and adhesive was 25.4µm, with a total of ~125µm. One layer of the PET was peeled off and the remaining PET layer with the adhesive was aligned and bonded to the MEA chip. The channel had a length of 1 mm and width of 375µm with port openings 500µm in diameter. Another layer of PET with adhesive and 500µm diameter micromilled ports was attached on top of channel to bond and seal the microchannel resulting in the multi-modal MEA device. Figure 2 provides the schematic demonstrating the process flow. Although the schematic depicts a straight channel, the simplicity of the technique allows for the fabrication of more complicated channel structures for various functionalities.

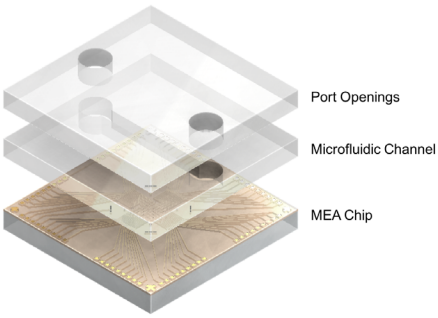

Figure 2: ***Schematic representation of multi-modal MEA device*** *- Exploded view to demonstrate the MEA chip, microfluidic channel and port openings milled on PET adhesive sheets.*

The MEA chips were aligned and attached to PCBs using an epoxy. To electrically connect the MEA chip to the PCB, a gold ball bonding process was utilized [5]. Cell culture wells were designed to contain the solution on top of the device. The wells were 3D printed and attached to the devices using an epoxy and ready to be used in experimentation. In order to integrate the microchannel, it will have to be attached to the MEA chips before wire bonding and packaging. This will be achieved by trimming the PET sheets with milled microchannels and port openings to expose the contact pads to allow for wirebonding.

Actin Preparation and TIRF Microscopy Imaging

Actin was purified from rabbit skeletal muscle and gel filtered over Sephacryl S-300 in buffer A (0.2mM $CaCl_2$, 1mM NaN_3, 2mM Tris-HCl pH 8.0, 0.2mM ATP, 0.5mM DTT) as described [8]. Rhodamine labeled G-actin (0.4mg/ml) (Cytoskeleton, Inc.) was mixed with calcium bound unlabeled actin monomers, and exchange of cation Ca^{2+} to Mg^{2+} was done by addition of 20mM EGTA and 1mM $MgCl_2$, equal to the actin concentration plus 10µM [8]. Actin polymerization was achieved by addition of 0.1 volume of 10X polymerization KMI buffer (500mM KCl, 20mM $MgCl_2$, 100mM Imidazole pH 7.0, 10mM ATP, and 10mM DTT). Final concentration of actin filaments prior to imaging was 8 µM. Bundle formation was achieved by addition of 1X buffer containing high concentration of divalent cations (30mM Mg^{2+}, 10mM Imidazole pH 7.0, 1mM ATP, and 1mM DTT).

TIRF imaging was performed at room temperature (~22°C) using a Nikon Eclipse Ti TIRF microscope equipped with a Hamamatsu Image EM X2 CCD camera, 100X oil immersion objective (numerical aperture 1.49). Filaments equilibrated at room temperature for 1 hour and diluted with 1X imaging buffer (KMI or bundle polymerization buffer with addition of 0.15M glucose, 1mg/ml catalase, 0.2mg/ml glucose oxidase). Placement of

filaments onto the multi-modal MEA device was achieved by placing a 1µL droplet of diluted sample on the device and gentle placement of a coverslip prior to imaging.

Electrochemical Measurements

Electrochemical impedance spectroscopy (EIS) was performed in respective electrolyte solutions using a Bode 100 system. The reference electrode was a titanium wire coated platinum (Pt/Ti) and impedance measurements were recorded with a frequency sweep from 10 Hz to 100 kHz. For cyclic voltammetry measurements, a three-electrode system [4] was used to obtain CV plots sweeping the voltage from -1 V to 1 V using an eDAQ potentiostat. The fabricated microelectrodes were used as the working electrodes, Pt/Ti wire was used as the counter electrode, and a Ag/AgCl was used as the reference electrode. Electrophysiological measurements were performed but will be reported in a future study after careful analysis.

RESULTS AND DISCUSSION

Figure 3A-B depicts optical images of the milled PET microchannel integrated on the glass MEA. The channel with no flow (Figure 3A) measures ~375µm in width as designed. Fluid flow demonstration with no leaks is depicted in Figure 3B. In addition to the PET microchannel enabled multi-modal MEAs, SU-8 insulation openings were modeled as test channels and characterized. The use of SU-8 openings as microchannels provided preliminary imaging results for photolithographically fabricated microchannels. Figure 3C-D depicts circular and rectangular microelectrodes that were used in the characterization of actin along with SU-8 microfluidic channels running through the electrodes in Figure 3D. The SU-8 microchannel as demonstrated in Figure 3D allows for unobstructed passage of filaments within the device.

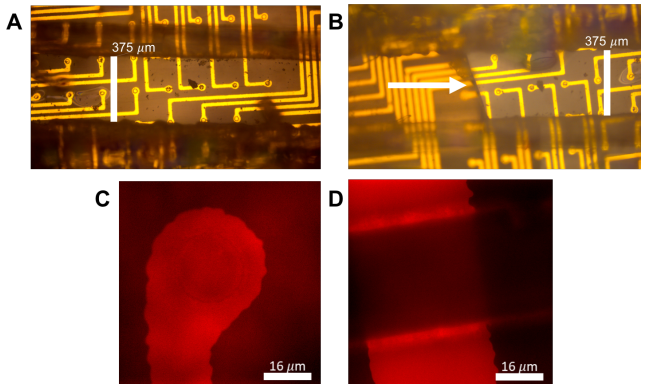

Figure 3: ***Representative images of fabricated MEA devices using optical and fluorescence microscopy -*** *(A) Optical image of MEA chip with empty PET micromilled channel. (B) Optical image demonstrating fluid flow of Congo Red dye within the micromilled microchannel. (C-D) Representative fluorescence images of MEA electrode and microchannel. Scale bar for optical images is 375µm and 16µm for the fluorescence images.*

Representative images of the electrode device with immobilized filaments can be seen under fluorescence microscopy (Figure 4 A-C). The immobilization of actin filaments onto the multi-modal MEA is depicted. TIRF microscopic images of filaments on the microelectrodes are shown to be in insulation areas of the device. Immobilization of filaments inside the electrode allows for electrophysical and electrochemical characterization. The adherence of actin filaments on the SU-8 insulation layer and on top electrodes indicates no potential adverse interactions are occurring on the filaments by either the electrode or insulation layers. As shown in Figure 4B, filaments are clearly visible allowing for proper electrophysical measurements, while in Figure 4B-C various focal planes detailing the layers within the electrode device are visible with filaments. Thus, adherence of biopolymers to the device is possible without the use of adherence coating agents.

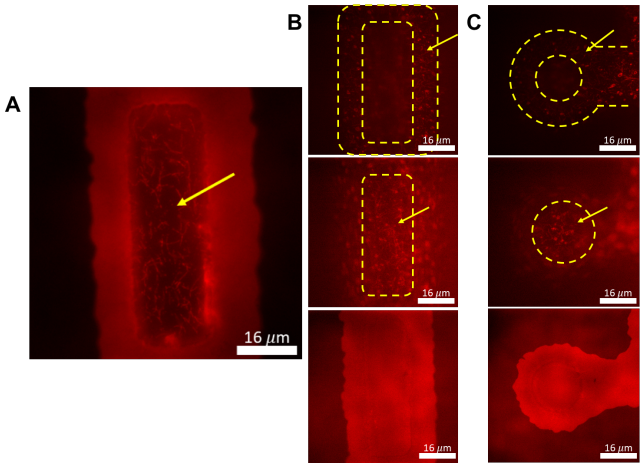

Figure 4: ***Images of actin filaments in and around rectangular and circular electrodes indicated by arrow -*** *(A) TIRF microscopy image of actin filaments on top of electrode. (B-C) actin filaments on SU-8 insulation layer, on metal layer, and metal layer focal plane images, respectively. [actin] = 1µM. Scale bar is 16µm.*

Time-lapse images with flow indicate actin filament movement around the electrode into the well (Figure 5), demonstrating an ability to precisely manipulate filaments with fluid flow into the recording site of the multi-modal MEA for stimulation/recording. The filament is shown to fluctuate freely while gradually flowing into the electrode for further characterization. Our experiments were able to determine the visualization of filament fluctuations prior to entry into the device.

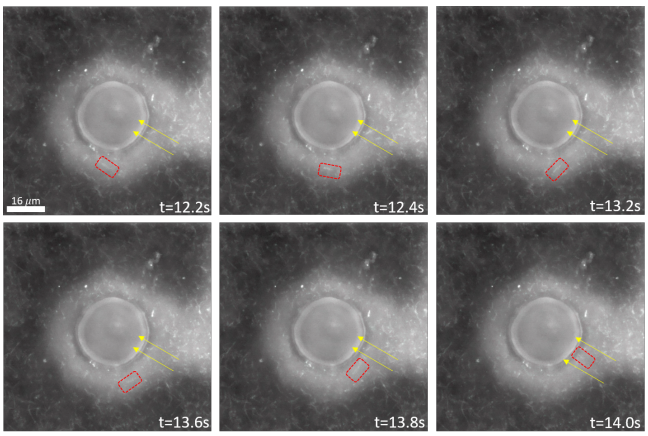

Figure 5: ***Time lapse images of an actin filament flow into an electrode via the microchannel*** *– A filament moves along the electrode in response to flow. Indication of potential filament fluctuation and mechanical response to flow before entering the channel can be visualized. Time (t) = seconds and [actin] = 1µM. Scale bar is 16µm.*

MEA microelectrodes form a double layer of charge with the electrolyte, behaving like a parallel plate capacitor, called the double

layer capacitance (C_{dl}). Since electrochemical reactions take place at the interface of the microelectrodes, charge leaks across the double layer, can experience a charge transfer resistance (R_{ct}). Ions diffusing from the solution to the interface of the microelectrode, gives rise to an impedance and to a current flow [9]. The solution resistance (R_s) as the name implies is the resistance ions experience as they travel through the solution. Therefore, the microelectrode interface impedance can be expressed as a circuit model with the C_{dl} and R_{ct} in parallel and R_s in series.

Once the impedance of a microelectrode in an electrolyte is measured, a Nyquist plot can be generated in order determine the circuit elements from the shape of the profile [10]. It is important to note that actin proteins carry a charge, hence the electrical interaction on the interface of microelectrodes was measured to study the structural properties. This was performed on two actin structures: filaments and bundles. The Nyquist plot provided in Figure 6A indicates a shift to the right for the bundles, an electrical indication of the structural differences in the actin. Cyclic Voltammetry (CV) measurements indicate irreversible coupling and demonstrate the potential for the determination of actin concentration using these devices (Figure 6B). Furthermore, the CV analysis of actin can be used to determine the capacitance of the double layer. Future experimentation will be aimed to build upon the characterization of these proteins using CV, especially to extricate the differences between *in vitro*, genetically modified proteins representing disease signatures and normal actin. Electrophysiological measurements will additionally be performed and reported in a future study.

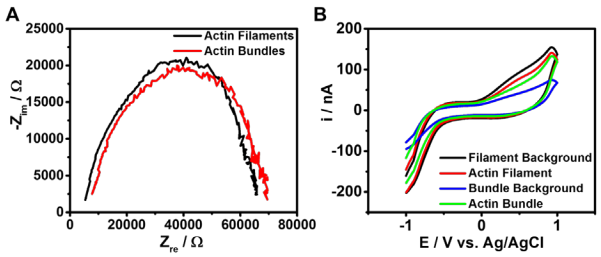

Figure 6: ***Electrical and electrochemical spectroscopy*** *- (A) Nyquist plot comparing actin filaments and actin bundles. (B) Cyclic voltammogram vs. Ag/AgCl resulting in irreversible coupling for all actin samples and a distinguishable bundle background anodic peak.*

Table 1 summarizes a Randles' equivalent circuit [9] model components mathematically extracted from the Nyquist plot. The C_{dl} of the bundles was less than half that of the C_{dl} of the filaments, due to a smaller surface area of the bundles interacting with the microelectrode surface.

Table 1: ***Circuit Model Extraction*** **-** Values of components mathematically extracted from respective Nyquist plots utilizing a Randles' equivalent circuit.

Circuit Component	Actin Filaments	Actin Bundles
R_s (kΩ)	3.67	5.19
R_{ct} (kΩ)	148.3	59.3
C_{dl} (nF)	5.63	2.34

The difference in R_{ct} between the bundles and the filaments indicates electrical cable-type behavior of the bundles. The R_s indicates the differences in electrolyte composition of the two structures, which was as expected since the bundle solution contained components such as glucose, glucose oxidase, and catalase in addition to the KMI solution. The presence of these additional biomolecules slowed the rate of ion flow, therefore increasing the resistance.

CONCLUSIONS

In conclusion, we built multi-modal MEA devices with surface micromacined MEA die and subtractive benchtop micromilling/ photolithographic modeled microfluidics. Preliminary CV and impedance data of actin immobilized on multi-modal MEAs was recorded to suggest that further data analysis and experiments are possible for specific actin chemical redox and electrophysiological characterization. Finally, both structure and solution composition was verified using the MEA as a transducer, signifying it as a powerful tool. The microelectromechanical manipulation of actin filaments/bundles utilizing multi-modal MEAs and extraction of various characteristics is the first step toward the development of vital *in vitro* neurodegenerative disease models on a chip.

REFERENCES

[1] J. X. Tang and P. A. Janmey, "The polyelectrolyte nature of F-actin and the mechanism of actin bundle formation.," *J. Biol. Chem.*, vol. 271, no. 15, pp. 8556–63, Apr. 1996.

[2] E. C. Lin and H. F. Cantiello, "A novel method to study the electrodynamic behavior of actin filaments. Evidence for cable-like properties of actin," *Biophys. J.*, vol. 65, no. 4, pp. 1371–1378, Oct. 1993.

[3] J. R. Bamburg and G. S. Bloom, "Cytoskeletal pathologies of Alzheimer disease.," *Cell Motil. Cytoskeleton*, vol. 66, no. 8, pp. 635–49, Aug. 2009.

[4] C. T. McMurray, "Neurodegeneration: diseases of the cytoskeleton?," *Cell Death Differ.*, vol. 7, no. 10, pp. 861–865, Oct. 2000.

[5] N. Azim, F. Sommerhage, M. Aubin, J. Hickman, and S. Rajaraman, "Precision Plating of Electrogenic Cells on Microelectrodes Enhanced with Nano-Porous Platinum for Cell-Based Biosensing Applications," *Meet. Abstr.*, vol. MA2017-01, no. 42, pp. 1954–1954, Apr. 2017.

[6] R. Bashir, "BioMEMS: State-of-the-art in detection, opportunities and prospects," *Adv. Drug Deliv. Rev.*, vol. 56, no. 11, pp. 1565–1586, 2004.

[7] A. Jégou, M.-F. Carlier, and G. Romet-Lemonne, "Formin mDia1 senses and generates mechanical forces on actin filaments," *Nat. Commun.*, vol. 4, p. 1883, May 2013.

[8] H. Kang *et al.*, "Identification of cation-binding sites on actin that drive polymerization and modulate bending stiffness," *Proc. Natl. Acad. Sci.*, vol. 109, no. 42, pp. 16923–16927, 2012.

[9] E. T. McAdams, A. Lackermeier, J. A. McLaughlin, D. Macken, and J. Jossinet, "The linear and non-linear electrical properties of the electrode-electrolyte interface," *Biosens. Bioelectron.*, vol. 10, no. 1–2, pp. 67–74, Jan. 1995.

[10] Y. Barsukov and J. R. Macdonald, "Electrochemical Impedance Spectroscopy," in *Characterization of Materials*, Hoboken, NJ, USA: John Wiley & Sons, Inc., 2012, pp. 1–17.

CONTACT

*Swaminathan Rajaraman; Tel: +1-407-823-4339 Email: swaminathan.rajaraman@ucf.edu

A SIMPLE FABRICATION METHOD FOR DOUBLY REENTRANT OMNIPHOBIC SURFACES VIA STRESS INDUCED BENDING

Kyle L. Wilke[1], Manuel Garcia[1], Daniel J. Preston[1], and Evelyn N. Wang[1]*
[1]Massachusetts Institute of Technology, Cambridge, Massachusetts, USA

ABSTRACT

We developed omniphobic, doubly reentrant surfaces fabricated with a simple method suitable for use with traditional microfabrication processes. Intrinsic stresses in deposited layers of silicon nitride induced bending of a singly reentrant microstructure, creating the doubly reentrant geometry. Due to the use of standard microfabrication processes, this approach may be extended to a variety of materials and feature sizes, increasing the viability of applying omniphobic doubly reentrant structures for use in areas such as superomniphobicity, anti-corrosion, heat transfer enhancement, and drag reduction.

INTRODUCTION

Doubly reentrant microstructures enable omniphobic surfaces that repel even completely wetting (i.e., low surface tension) fluids without the use of low-surface-energy coatings [1-3]. Such surfaces have use in a range of applications such as anti-fouling[4], chemical shielding [5], heat transfer enhancement [6], drag reduction [7], self-cleaning [8], and water purification [9]. In order to achieve omniphobicity, reentrant microstructures with characteristic length smaller than the liquids capillary length are required [1]. The level of reentrance necessary depends on the fluid's intrinsic contact angle, θ, with the surface material (Figure 1a). The black arrow in the figure represents the contact line force. In order for liquid to be repelled, a component of the contact line force must act in the vertical direction. Therefore, a regular microstructure without reentrance only repels liquids with $\theta > 90$ °. This large intrinsic contact angle is not possible for many liquids on solid surfaces or requires chemical modification for many others. Adding reentrant geometry can reduce the necessary contact angle to below 90 °. However, for a small θ, the vertical component of the contact line force is also small, making it difficult to repel highly wetting liquids. Therefore, to repel all liquids, including those with a small contact angle, a large degree of reentrance is required (i.e., doubly reentrant), which has been difficult to fabricate at the necessary characteristic length scales (100s of microns or smaller). Due to these difficulties, the fabrication of doubly reentrant surfaces has been limited in materials used, i.e., specialized polymers [2], or required complex fabrication techniques, i.e., high temperature oxidation of silicon (not suitable for other materials) and multiple etch steps [1].

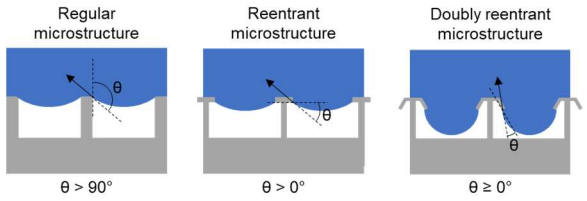

Figure 1: Types of microstructures along with corresponding intrinsic contact angle, θ, for which the structure can practically repel liquid. The black arrow represents the contact line force that prevents liquid from entering the structure, which must act in the vertical direction in order to repel the liquid. To successfully repel liquids with low contact angle, doubly reentrant structures are necessary.

In this work, we developed a simple fabrication method using traditional microfabrication processes and demonstrated omniphobicity of the surface. The method relies on intrinsic stresses of deposited materials to induce bending of singly reentrant structures to create doubly reentrant geometry. Because this fabrication technique is based on singly reentrant surfaces, for which robust, scalable processes are already well-developed [10-12], it enables simple fabrication of doubly reentrant structures for a wide variety of materials.

RESULTS

The level of double reentrance, α, influences the component of contact line force that acts in the vertical direction, F_y, which prevents liquid from entering the structures and maintains omniphobicity. Figure 2 shows the vertical component of F, for different θ and α, normalized by the theoretical maximum that occurs when the force is completely vertical, $F_{y,max}$, and is defined as:

$$F_{norm} = \frac{F_y}{F_{y,max}} = \frac{P\gamma \sin(\theta + \alpha)}{P\gamma} \qquad (1)$$

where P is the length of the contact line (determined by microstructure geometry), and γ is the surface tension of the liquid. If the sum of θ and α is greater than 90 °, then $F_{norm} = 1$ due to the fact that a maximum occurs in F_y for a contact angle below the intrinsic value, which is still a stable state. This is why the curves for different θ reach a stable value of 1 with increasing α. This figure highlights a number of key points. First, in order to produce adequate repellency of fluids with $\theta = 0$ °, α must be larger than 0. Second, the repellency force increases with α, which creates a more

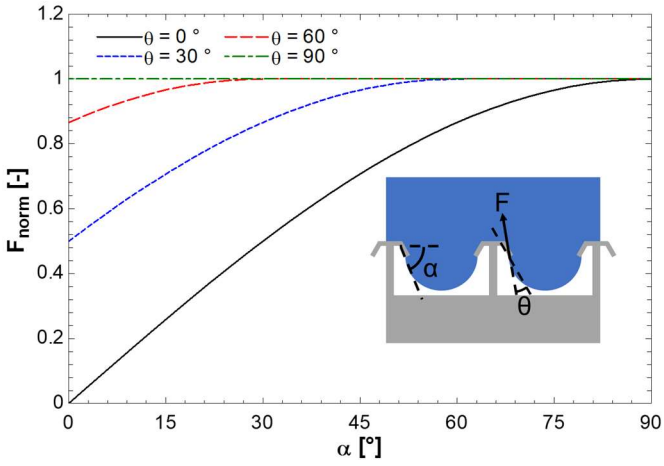

Figure 2: The normalized vertical component of the contact line force for different contact angle, θ, and level of reentrance, α. For a perfectly wetting liquid, α must be greater than 0 ° for the surface to have repellency. The maximum is reached when θ + α = 90 °.

978-1-940470-03-0/HH2018/$25©2018TRF
DOI 10.31438/trf.hh2018.74

Solid-State Sensors, Actuators and Microsystems Workshop
Hilton Head Island, South Carolina, June 3-7, 2018

robust omniphobicity, but reaches its maximum value when $\theta + \alpha = 90$ °. We note that though the maximum repellency is reached at $\theta + \alpha = 90$ °, a lesser value of α may still produce adequate repellency.

Figure 3 shows our fabrication process. Thin films of silicon nitride with intrinsic stresses were deposited on the polished silicon wafer with an STS PECVD system, which allowed stresses in the deposited material to be controlled (i). Next, features were defined with photolithography (ii). A 2.5 µm thick layer of Microposit S1823 was spin coated on the wafer and exposed using an MLA150 Maskless Aligner. The resist was developed in CD-26 for 90 seconds. Structures were then etched with DRIE (iii). An STS ICP RIE was used to etch the silicon nitride layers. Subsequently, an SPTS Rapier DRIE was used to etch the underlying silicon. Finally, an isotropic silicon etch was used to undercut the thin films of silicon nitride (iv). Both XeF_2 and SF_6 were successfully used for the isotropic etch due to the etch selectivity between silicon nitride and silicon. Due to the intrinsic stresses in the nitride films, tunable bending (based on film thickness, stress, and undercut distance) occurred and formed the doubly reentrant surface.

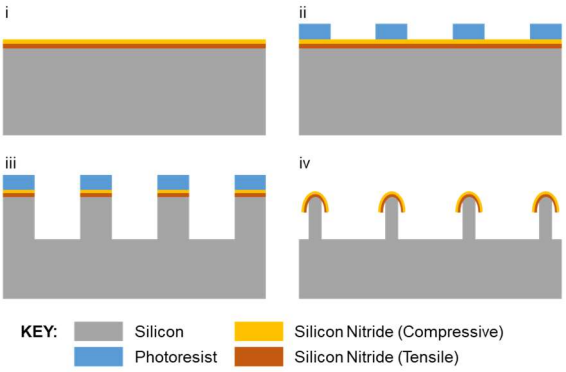

Figure 3: Fabrication method of doubly reentrant structures. i: Deposition of films with tensile and compressive stress. Silicon nitride was deposited with PECVD in this study. The film stresses induce bending in the final fabrication step to create the doubly reentrant geometry. Stresses and film thicknesses were chosen based on modeling of the bending ii: Etch mask defined using standard photolithography. iii: Deep reactive ion etch (DRIE) of structures. iv: Isotropic silicon etch with SF6 in the DRIE to create doubly reentrant feature due to stress induced bending.

Figure 4a shows a cross-section SEM of a fabricated doubly reentrant stripe-textured hoodoo (type of reentrant surface with parallel lines as features) surface with $\alpha = 62$ °. The bottom film of silicon nitride was 100 nm thick and low stress (less than 50 MPa), while the upper layer was 100 nm and had compressive stress (763 MPa measured using an FLX-2320 S), which induced the bending. Finite element analysis was used to choose the necessary film thicknesses, stresses, and geometry (Figure 4b) to achieve a high level of double reentrance, and showed reasonable agreement with fabricated surfaces. For stresses achievable in PECVD silicon nitride, this required the length, L, of the undercut to be between 10 and 100 times larger than the combined thickness of the deposited films. This ratio between film thicknesses and undercut length is a key parameter and will vary depending on material choice.

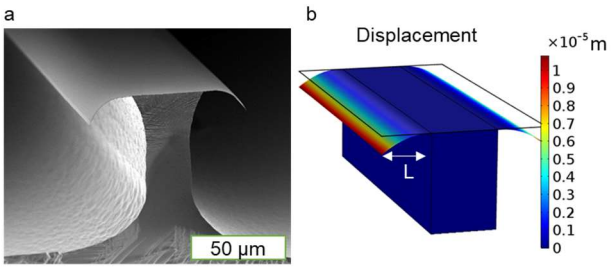

Figure 4: a: Cross-section SEM of the fabricated doubly reentrant (α = 62 °) stripe-textured hoodoo surface. b: COMSOL model used to predict surface bending based on stresses and film thicknesses. This model determined the necessary stresses and thicknesses to realize a doubly reentrant surface with significant bending. For silicon nitride, this required the ratio of the length of the feature undercut, L, to the combined film thicknesses to be between 10 and 100, where 100 is shown in this figure.

We characterized the apparent advancing and receding contact angle of the fabricated surface for a variety of liquids using the experimental setup depicted in Figure 5. A syringe was used to add and remove liquid from a droplet on the surface. A collimated light source behind the droplet illuminated it while a DSLR camera recorded video as the droplet grew and shrunk. The video was then used to extract the advancing and receding contact angles in ImageJ.

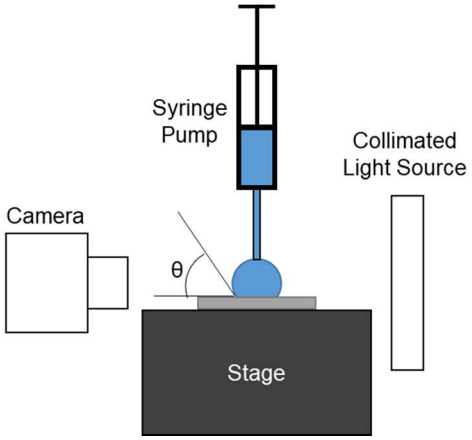

Figure 5: Schematic of experimental setup for characterizing contact angle. A syringe is used to add and remove liquid from a droplet on the surface, creating an advancing and receding contact line, respectively.

Images of the apparent advancing contact angle of both water, with a surface tension of 72.8 mN/m and FC 40, a common refrigerant with a very low surface tension of 16 mN/m, are shown in Figure 6. Due to the double reentrant structures and surface omniphobicity, both fluids were repelled regardless of the liquid surface tension.

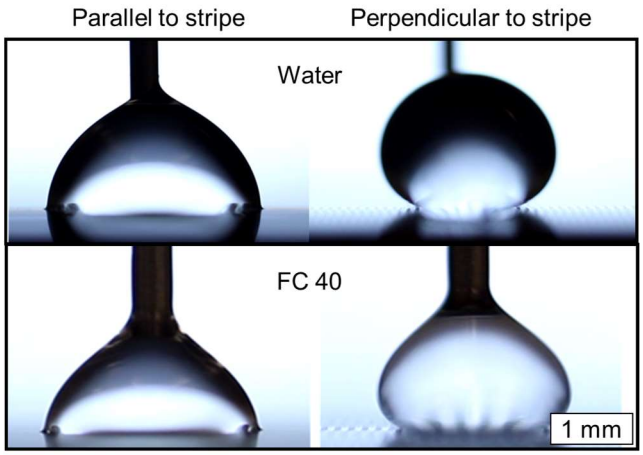

Figure 6: Images of advancing contact angle on the stripe-textured hoodoo surface, both parallel and perpendicular to the stripe for both water and FC 40. Both fluids were repelled due to the surface omniphobicity.

Advancing and receding contact angle measurements were conducted for liquids with a wide range of surface tensions (FC-40, ethanol, isopropanol, ethylene glycol, and water) in Figure 7. The observed contact angles agree well with theoretical values [11]. For the stripe-textured hoodoo surfaces the advancing contact angle perpendicular to the stripes, $\theta_{adv,perpendicular}$, is given by:

$$\cos\theta_{adv,perpendicular} = -1 \qquad (2)$$

which gives an expected value of 180 °. The observed values are slightly lower due to vibrations in the laboratory causing the droplets to partially relax. The advancing contact angle parallel to the stripes, $\theta_{adv,parallel}$, is given by:

$$\cos\theta_{adv,parallel} = r\phi\cos\theta - (1-\phi) \qquad (3)$$

where r is the roughness of the wetted solid (taken as 1 in this work due to the thin nitride films), and ϕ is the local areal solid fraction of the advancing droplet, 0.5 for the surface demonstrated here. This gives a predicted value of 90 °, similar to the experimentally observed values. Finally, the receding contact angle in both the parallel and perpendicular directions, θ_{rec}, is given by:

$$\cos\theta_{rec} = r\phi\cos\theta - (1-\phi) \qquad (4)$$

For the stripe-textured surface used here the predicted receding angle is the same as the advancing angle parallel to the stripes, leading to a low contact angle hysteresis, which is necessary for liquid shedding. Furthermore, due to the doubly reentrant geometry the fluid properties do not appear in equations 2 through 4. Therefore, measured contact angles in Figure 7 are independent of the liquid contacting the surface, which agrees well with observed values. The advancing contact angles on a flat silicon nitride surface are also shown. Despite the nearly perfectly wetting liquids used, they were still successfully repelled.

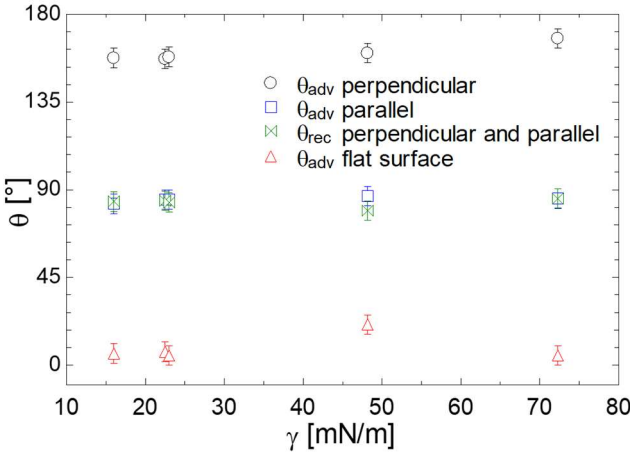

Figure 7: Apparent advancing and receding contact angle of liquids with different surface tension, γ, both parallel and perpendicular to the stripe. Receding angle was the same in both directions. Advancing contact angle on a flat silicon nitride surface is also shown. All fluids were repelled, highlighting the omniphobicity, which can only be achieved with doubly reentrant geometry.

We are currently working to demonstrate different material sets and types of reentrant geometry (other than stripe-textured). Though silicon nitride was used in this work, other materials also have controllable stresses (including metals, oxides, nitrides, and polymers) and are potential material choices. Table 1 lists a variety of materials and residual stresses observed in literature after growth/deposition with different techniques such as chemical vapor deposition (CVD), plasma-enhanced chemical vapor deposition (PECVD), magnetron sputtering, spin coating, and atomic layer deposition (ALD). Although this incomplete list represents candidate materials, further research should be done to determine necessary deposition parameters, how stresses in the films may evolve with time, as well as what α may be achieved. Furthermore, in order to fabricate the reentrant geometry, etch selectivity between the deposited material and the underlying substrate is necessary, which may limit material choices.

Table 1: Possible materials, deposition techniques, and residual stresses reported in the literature. A negative stress is compressive.

Material	Deposition Technique	Residual Stress [MPa]	Reference
Silicon nitride	PECVD	300 to -600	[13]
Metals	Sputtering	1000 to -2000	[14]
Parylene	CVD	50 to 20	[15]
Polyimide	Spin coat	30	[16]
Aluminum Oxide	ALD	500 to 200	[17]

CONCLUSIONS

This fabrication procedure simplifies the ability to create doubly reentrant surfaces. Stress induced bending of singly reentrant geometry into doubly reentrant geometry was achieved by relying on intrinsic stresses of deposited silicon nitride films. Finite element analysis (FEA) was used to predict the necessary stresses, film thicknesses, and undercut length, L, to achieve a high level of reentrance. A stripe-textured hoodoo surface was fabricated and

good agreement was observed with the FEA model. Due to the high level of reentrance achieved (α = 62 °), the fabricated surface was able to repel all tested liquids with surface tension ranging from 16 to 72.8 mN/m, including liquids with very small intrinsic contact angle on silicon nitride. Furthermore, the observed contact angles matched well with predicted values based on previously developed models. Due to the use of standard microfabrication processes, the process developed here expands the potential materials sets, and widens the potential application of doubly reentrant omniphobic surfaces.

ACKNOWLEDGEMENTS

This work was supported by the Cooperative Agreement between the Masdar Institute of Science and Technology (Masdar Institute), Abu Dhabi, UAE and the Massachusetts Institute of Technology (MIT), Cambridge, MA, USA - Reference 02/MI/MIT/CP/11/07633/GEN/G/00. This work was performed in part at the Center for Nanoscale Systems (CNS), a member of the National Nanotechnology Infrastructure Network (NNIN), which is supported by the National Science Foundation under NSF award no. ECS-0335765. CNS is part of Harvard University.

REFERENCES

[1] T. Liu and C.-J. Kim, "Turning a surface superrepellent even to completely wetting liquids". Science, 346(6213), (2014).

[2] J. Choi, W. Jo, S.Y. Lee, Y.S. Jung, S.-H. Kim, and H.-T. Kim, "Flexible and Robust Superomniphobic Surfaces Created by Localized Photofluidization of Azopolymer Pillars". ACS nano, 11(8): p. 7821-7828, (2017).

[3] R. Hensel, R. Helbig, S. Aland, A. Voigt, C. Neinhuis, and C. Werner, "Tunable nano-replication to explore the omniphobic characteristics of springtail skin". NPG Asia Materials, 5(2): p. e37, (2013).

[4] D.C. Leslie, et al., "A bioinspired omniphobic surface coating on medical devices prevents thrombosis and biofouling". Nature biotechnology, 32(11): p. 1134-1140, (2014).

[5] S. Pan, A.K. Kota, J.M. Mabry, and A. Tuteja, "Superomniphobic surfaces for effective chemical shielding". Journal of the American Chemical Society, 135(2): p. 578-581, (2012).

[6] T. Liu and C.-J. Kim. *Doubly re-entrant cavities to sustain boiling nucleation in FC-72*. in *Micro Electro Mechanical Systems (MEMS), 2015 28th IEEE International Conference on*. 2015: IEEE.

[7] C.-H. Choi and C.-J. Kim, "Large slip of aqueous liquid flow over a nanoengineered superhydrophobic surface". Physical review letters, 96(6): p. 066001, (2006).

[8] Y. Lu, S. Sathasivam, J. Song, C.R. Crick, C.J. Carmalt, and I.P. Parkin, "Robust self-cleaning surfaces that function when exposed to either air or oil". Science, 347(6226): p. 1132-1135, (2015).

[9] J. Lee, C. Boo, W.-H. Ryu, A.D. Taylor, and M. Elimelech, "Development of omniphobic desalination membranes using a charged electrospun nanofiber scaffold". ACS Applied Materials & Interfaces, 8(17): p. 11154-11161, (2016).

[10] A. Tuteja, W. Choi, J.M. Mabry, G.H. McKinley, and R.E. Cohen, "Robust omniphobic surfaces". Proceedings of the National Academy of Sciences, 105(47): p. 18200-18205, (2008).

[11] W. Choi, A. Tuteja, J.M. Mabry, R.E. Cohen, and G.H. McKinley, "A modified Cassie–Baxter relationship to explain contact angle hysteresis and anisotropy on non-wetting textured surfaces". Journal of colloid and interface science, 339(1): p. 208-216, (2009).

[12] A. Tuteja, W. Choi, M. Ma, J.M. Mabry, S.A. Mazzella, G.C. Rutledge, G.H. McKinley, and R.E. Cohen, "Designing superoleophobic surfaces". Science, 318(5856): p. 1618-1622, (2007).

[13] M.P. Martyniuk, J. Antoszewski, C.A. Musca, J.M. Dell, and L. Faraone. *Determination of residual stress in low-temperature PECVD silicon nitride thin films*. in *Device and Process Technologies for MEMS, Microelectronics, and Photonics III*. 2004: International Society for Optics and Photonics.

[14] D. Hoffman and J.A. Thornton, "Effects of substrate orientation and rotation on internal stresses in sputtered metal films". Journal of Vacuum Science and Technology, 16(2): p. 134-137, (1979).

[15] T.A. Harder, T.-J. Yao, Q. He, C.-Y. Shih, and Y.-C. Tai. *Residual stress in thin-film parylene-C*. in *Micro Electro Mechanical Systems, 2002. The Fifteenth IEEE International Conference on*. 2002: IEEE.

[16] M.G. Allen, M. Mehregany, R.T. Howe, and S.D. Senturia, "Microfabricated structures for the insitu measurement of residual stress, young's modulus, and ultimate strain of thin films". Applied physics letters, 51(4): p. 241-243, (1987).

[17] O.M. Ylivaara, et al., "Aluminum oxide from trimethylaluminum and water by atomic layer deposition: The temperature dependence of residual stress, elastic modulus, hardness and adhesion". Thin Solid Films, 552: p. 124-135, (2014).

CONTACT
*K.L. Wilke, tel: +1-608-620-4977; klwilke@mit.edu

ACTIVE SELF-CLEANING SURFACES ON SOLAR MODULES

D. Sun[1] and K. F. Böhringer[1]*
[1]University of Washington, Seattle, Washington, USA

ABSTRACT

This paper describes an active self-cleaning surface using an anisotropic ratchet conveyor (ARC) to move a water droplet under orthogonal vibrations. The ARC system was fabricated by creating hydrophilic micro-sized patterns on hydrophobic Cytop thin films, successfully developed by utilizing parylene as a stencil mask. Droplet transport speed is 20.5 mm/s at frequency 52 Hz and acceleration 3.3 g (g = 9.8 m/s^2). Optical transmission measurements show Cytop can improve optical transmittance by 2.5~3.5% over the entire visible wavelength range. Solar cell module power output is measured to verify the output power efficiency gain. The efficiency can be improved from 69% to 92% after cleaning contaminants on top of the solar module with surface dimensions of 30 mm by 24 mm.

INTRODUCTION

The power generation efficiency of photovoltaic (PV) modules can be affected by the accumulation of dust and environmental contaminants over time [1]. This problem, which is often called soiling, has become a growing concern in the effort to improve PV module efficiency and reliability. The composition of dust particles majorly consists of quartz and silicate minerals, with a distribution size in the 10~100 μm range [2]. Researchers have been exploring self-cleaning surfaces to clear the surface contaminants away and improve efficiency. The ideal properties of self-cleaning coatings and their system design include low adhesion of dust, optical transparency without degradation of light transmission, and the capability to remove dust particles from the top of the solar cell.

Water droplets can be directed along a surface using chemical gradients [3], thermal gradients [4], electrowetting [5], and micro textures [6-7]. Earlier, we developed an active self-cleaning surface system using anisotropic ratchet conveyors (ARC) with trimethylsilanol (TMS, contact angle 53°) and perfluorooctyltrichlorosilane (FOTS, contact angle 108°) self-assembled monolayers (reported in Transducers'17 [8]). Unlike that system, where the substrate was first treated with a hydrophilic TMS layer and patterned with lithography, we developed a new process to pattern directly on hydrophobic Cytop thin films. Cytop is an amorphous fluoropolymer with good transparency over the visible and UV wavelength range, good chemical resistance, excellent water repellence and low surface tension. Micro-patterning on hydrophobic surfaces (like Teflon, Cytop) is difficult using standard photolithography due to poor adhesion between the photoresist and substrate. Methods have been proposed using a metal buffer layer [9-10] or plasma pretreatment of the surface, but the original surface properties will suffer after treatment and exhibit decreased water droplet contact angle. Parylene can be etched with oxygen plasma, making it compatible with standard lithography processes. It has been used to create biomolecular stencil arrays [11] and patterns on soft substrates [12]. By adopting parylene-C as a stencil mask, we create hydrophilic patterns on top of the Cytop surface without degrading the original surface properties.

In this paper, we demonstrate an active self-cleaning surface system using water droplets to clean surface contaminants on solar module cover glass. A hydrophobic thin film is successfully patterned using parylene-C as a stencil mask. Droplet transportation performance and solar module level cleaning effects is characterized and discussed.

SYSTEM DESIGN

Theory Background

To initiate transport of a sessile droplet sitting on a horizontal surface, force anisotropy needs to be created at the boundary of the solid-liquid-gas interface, which is termed the three-phase line (TPL). As the droplet is agitated by external forces (*e.g.* vibration, alternating electric field, *etc.*), the contact angle at the TPL will be different from the equilibrium status according to Young's equation during the droplet expansion and recession phase. The difference of the droplet TPL contact angle during expansion and recession phase is termed as contact angle hysteresis (CAH). Shown in Fig. 1, at equilibrium state, at the infinitesimal length of TPL (noted as ε), the net forces can be expressed as:

$$(\gamma_{SG} - \gamma_{SL} - \gamma_{LG}\cos\theta_e)\varepsilon = 0 \quad (1)$$

where γ is surface tension between solid, liquid and gas phase.

In the advancing and receding state, the contact angle will change because of external forces. The net forces can be expressed repectively as:

$$(\gamma_{SG} - \gamma_{SL} - \gamma_{LG}\cos\theta_a)\varepsilon = F_{ex,a} \quad (2)$$

$$(\gamma_{SG} - \gamma_{SL} - \gamma_{LG}\cos\theta_r)\varepsilon = F_{ex,r} \quad (3)$$

where $F_{ex,a}$ and $F_{ex,r}$ are the portion of the external driving forces that are opposed by pinning on the substrate during advancement and recession, respectively, and θ_a and θ_r are the contact angles during advancement or recession. By combining eqation (2) and (3), as for a complete cycle of TPL advancement and recession processes, it is useful for us to define a contact line hysteresis force (F_{hys}) to express the average force on the TPL during each expansion and recession cycle:

$$F_{hys} = F_{ex,a} - F_{ex,r} = (\cos\theta_r - \cos\theta_a)\,\gamma_{LG}\,\varepsilon \quad (4)$$

The contact line hysteresis force serves as the pinning force to prevent the droplet boundary from moving. In order to transport the water droplet, we have designed anisotropic ratchet conveyors, which are abbreviated as ARCs. As shown in Fig. 1 (b), hydrophilic semicircular rungs are patterned on a hydrophobic background and a sessile droplet is dispensed on the ARC tracks. Because of the surface ratchet pattern design, the TPL of the droplet leading and trailing edge has different line fraction overlaps at the hydrophobic and hydrophilic region boundaries. We denote the line fraction lying on the hydrophobic-hydrophilic boudary as χ_b, which provides the anisotropy at the leading and trailing edges of the water droplet. We define the anisotropy force of the water droplet on the ARC surface as $F_{anisotropy}$, which can be expressed as:

$$F_{anisotropy} = F_{hys,leading} - F_{hys,trailing} \quad (5)$$

We assume that recession occurs when $\theta_r = \theta_1$ and advancement occurs when $\theta_a = \theta_2$, where θ_1 and θ_2 are contact angles for hydrophilic and hydrophobic regions, respectively. We integrate the hysteresis force over the contact line at the surface hydrophobic and hydrophilic boundaries. The anisotropy force can then be expressed as [7]:

$$F_{anisotropy} = (\chi_{b,leading} - \chi_{b,trailing})w(\cos\theta_1 - \cos\theta_2)\,\gamma_{LG} \quad (6)$$

where w is the contact line width of the droplet and χ_b is the line fraction. $\chi_{b,leading}$ is larger than $\chi_{b,\,trailing}$. The contact angle hysteresis is larger for the leading edge than the trailing edge by measurement. The water droplet will be driven forward and moved along the surface.

978-1-940470-03-0/HH2018/$25©2018TRF
DOI 10.31438/trf.hh2018.75

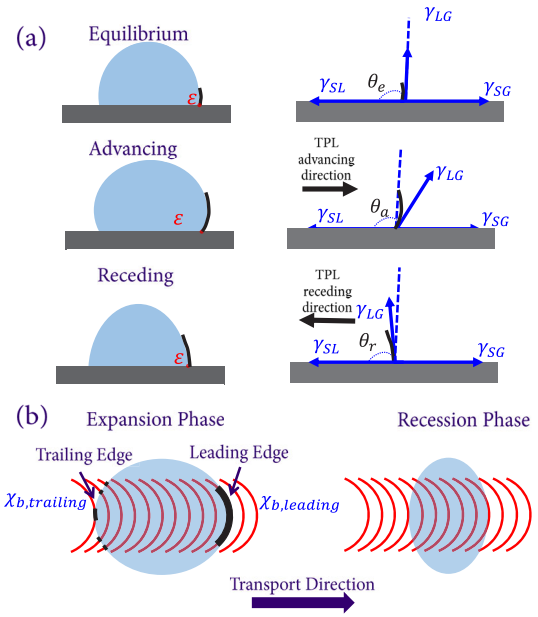

Figure 1: (a) Force analysis of the droplet at advancing, equilibrium, and receding phases. At advancing and receding phases, the external forces to change the contact angle at the TPL boundary can come from vibration or electrical agitation. (b) Top view of TPL movement during one vibration cycle of expansion phase and recession phase. The black highlighted regions are contacts between the water droplet TPL and the substrate. The red semi-circular curves are hydrophilic regions.

Fabrication Process

To fabricate the ARC surfaces, a silicon wafer was first cleaned with piranha solution at 110°C for 10 min, rinsed with deionized (DI) water and dried with nitrogen gas using a spin rinse dryer (ClassOne Technology). After Si/glass wafer cleaning, diluted Cytop (Cytop CTL-809M: CTL-Solv.180= 3:1) was spin coated on a silicon wafer and baked under 180°C for 1 hour. Then 2.5 µm parylene was evaporated on the Cytop using a commercial parylene coater (PDS 2010, Specialty Coating Systems) under vacuum. 6 µm photoresist (AZ9620) was coated and patterned. The parylene stencil mask and Cytop were etched through with O_2 plasma using reactive ion etching (Vision RIE). Then the parylene stencil mask was peeled off with tweezers. The surface was treated with spin-on TMS (MicroPrime MP-P20) and baked at 110°C for 2 min.

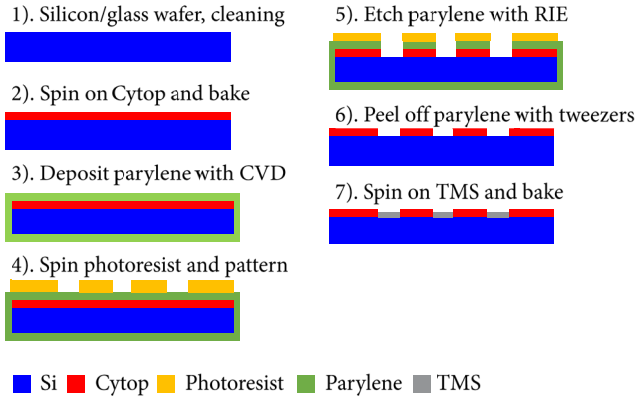

Figure 2: Cytop-TMS system using parylene as a stencil mask. Cytop will keep its hydrophobicity after peeling off parylene coating.

Experimental Setup

We use a vibration stage setup to characterize droplet transport on the ARC surface. The test wafer was mounted on an aluminum platform, which was attached to the vibration exciter (Brüel and Kjær type 4809) with double adhesive tape. A sinusoidal wave signal was generated by the function generator and amplified by the power amplifier to drive the vibration exciter (Brüel and Kjær type 2718). The vibration amplitude was monitored with the vibrometer (Polytec OFV) on the oscilloscope (Agilent Infiniium). The water droplet movement was captured by high speed camera (FASTCAM Mini UX100) at 2000 fps. The video was processed with MATLAB custom code. We also measured light transmission data of the two ARC surface coatings on soda lime glass substrate with a Cary 5000 UV-Vis-NIR spectrophotometer (Agilent Technologies). A custom source meter was used for the I-V curve output of the solar modules. We used flood light as the light source and the distance between the solar cell modules and the light source was kept the same for each measurement.

CHARACTERIZATION RESULTS

Droplet transport on ARC

The patterned Cytop is shown in Fig. 3 with ~70 nm thickness. Cytop hydrophobicity was not degraded after peeling off parylene. Each hydrophilic semicircular rung has 10 µm rung width and 100 µm center to center gap width between the adjacent rungs. The radius of curvature is 1000 µm and the curve angle is 120°.

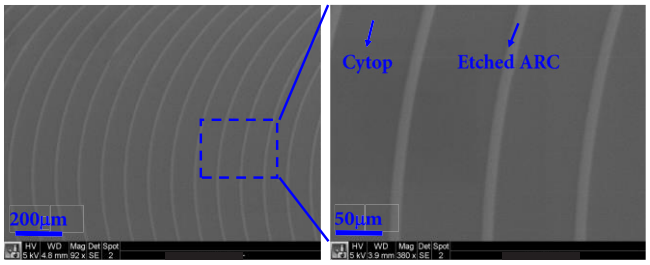

Figure 3: SEM images of ARC patterns on Cytop. For each semi-circular rung, the radius of curvature is 1000 µm, the etched linewidth is 10 µm, and the period between adjacent rung centers is 100 µm.

The wafer was mounted on a vibration platform. A range of 5~15 µL water droplet was pipetted on the surface. The vibration amplitude was monitored by vibrometer. We tested the minimum required vibration acceleration to drive a water droplet over the frequency bandwidth of 35~100 Hz. As a comparison to FOTS-TMS surfaces, Cytop-TMS surfaces directed the droplet movement with lower stage vibration amplitude as shown in Fig. 4. The minimum acceleration to drive the water droplet on Cytop-TMS surfaces was as low as ~0.7 g at a frequency of 55 Hz, 5 times lower than on the FOTS-TMS surface (~3.6 g).

Optical transmission measurements within the visible wavelength range are shown in Fig. 5 (a). As for the FOTS-TMS system, the light transmission was degraded due to the added coating of monolayers, but within a range of less than 1%. The glass after FOTS-TMS treatment was transparent and optically flat. Meanwhile, the Cytop-TMS system improved the transmission with an enhancement of 2.5% ~3.5% over the visible wavelength range even with an added coating on top of the glass. The reason was that the refractive index of Cytop is ~1.34, which is between air (n_{air} = 1.0) and the glass substrate (n_{glass} = 1.5), providing a refractive index match. Like Rayleigh's film, a portion of the incoming light reflects

both at the interface of air/Cytop and Cytop/glass but has less reflection as compared to the single reflection at the air/glass interface with a larger refractive index mismatch. Fig. 5 (b) shows the I-V curve measurements for assembled photovoltaic (PV) modules. The ARC structure was patterned in a zig-zag way covering a 2" by 2" area in the upper right of the solar cell. The Cytop-TMS coating generated larger optical output power compared with bare glass and FOTS-TMS surface treatment, in accordance with the light transmission measurements.

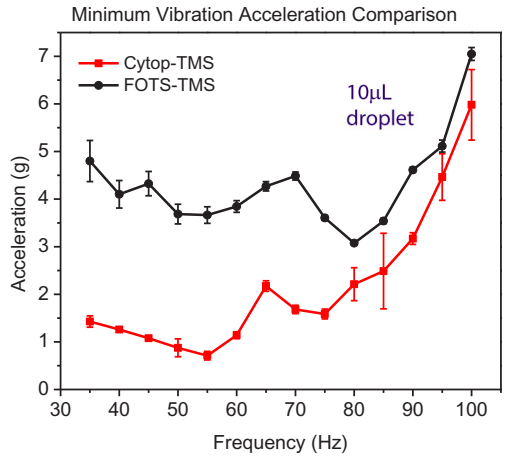

Figure 4: Minimum vibration acceleration required to move the water droplets along the ARC surface for both systems.

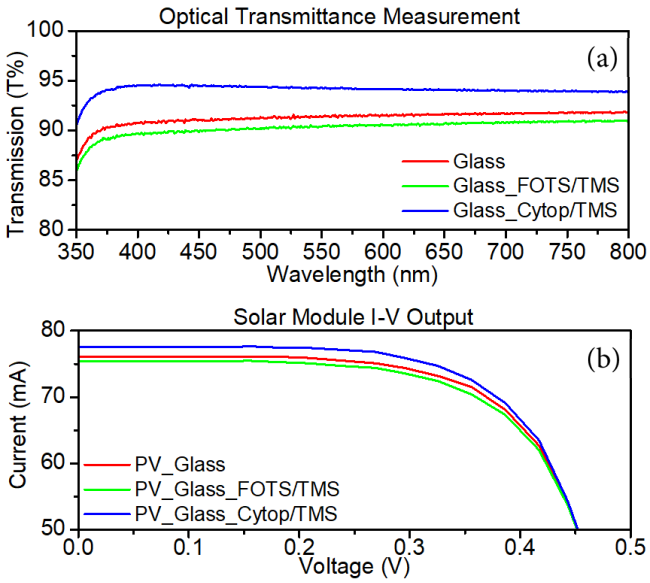

Figure 5. (a) Optical transmittance measurement results with a wavelength range of 350~800 nm. 4" soda lime glass wafers were used as the substrate baseline. (b) I-V output of solar module assembly with coated cover glass.

Self-cleaning Surface Design

We assembled solar modules with the patterned cover glass on top. As shown in Fig. 6, a piece of solar cell cut to the size of 30 mm by 24 mm was assembled with a Cytop-TMS ARC patterned glass. Silicon nitride particles (with a total mass of 10 mg) were evenly applied on the surface through polyester mesh. A 13.5 μl droplet was pipetted atop and followed the zig-zag ARC track while cleaning the surface contaminants. The solar module output efficiency response was monitored in real-time. It increased by more than 23 percentage points, rising from 69.1% after contamination to 92.1% after 15 s of cleaning.

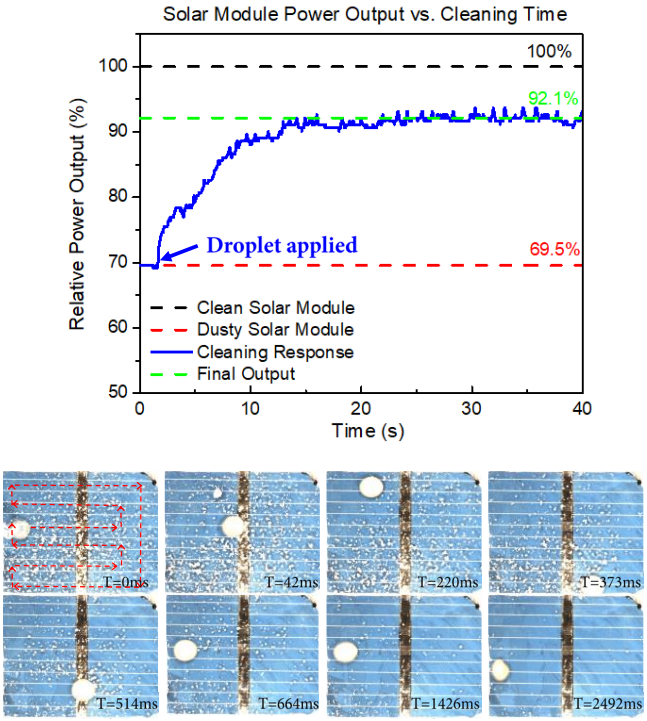

Figure 6. [top] Real-time power output response of solar module during the cleaning process. The solar module was connected with a resistive load for power monitoring. [bottom] Top view of cleaning process with continuous 3 cleaning cycles. The droplet is 13.5 μL in volume at a vibration frequency of 50 Hz. The droplet zig-zag path is shown at T=0 ms with the red dotted line.

We tested the surface cleaning function with different categories of typical contamination, including dust and dirt particles, soluble and insoluble contaminations, summarized in Table I. From the table, most water-soluble materials (like salt and sweetener) plus low surface adhesion insoluble particles (like sand, SiO_x, SiN_x, carbon powers) can be effectively cleaned with the droplet from the self-cleaning surface. Hydrophobic surface contaminants like polytetrafluoroethylene (PTFE) cannot be cleaned with the droplets. The hydrophobic particles tended to stay at the boundary of the water droplet instead of being trapped inside the droplet. The droplet surface was gradually covered with solid powder so that the surface tension at the TPL was reduced. Eventually a "droplet marble" was formed jumping on the surface as agitated by vibration. We also tested pepper and dry soil. However, these contaminants contained contents with a tendency of adhering to the surface and preventing the droplet from moving.

Table 1: Materials tested on the self-cleaning surface.

Material	*Sand (< 600 μm)*	*Salt*	*Sweetener*	*SiO_x and SiN_x*	*Carbon powder*	*PTFE*
Can be cleaned or not	Y	Y	Y	Y	Y	N

To understand the cleaning mechanism, silicon nitride powder was deposited on top of the Cytop-TMS surface. The droplet silhouette was monitored by high-speed camera. When an air-water interface is in contact with dust particles, the interfacial force can be decomposed into vertical and horizontal components. The vertical component detaches the dust particles from the surface and the horizontal component pushes the accumulated particles to another location (Fig. 7). The droplet was able to carry the SiN_x particles along. Similar phenomena could also be seen with the carbon powder.

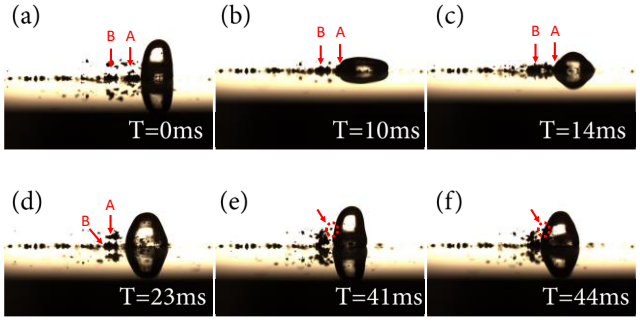

Figure 7: (a)-(d) demonstrates how the bulk hydrophilic SiN_x powder is detached from the surface and relocated by the interfacial surface tension. When the droplet expands, the water-air interfacial force removes powder particles from point A to point B location. (e)-(f) show the particles (highlighted in the dotted line circle) captured by the droplet at the interface. Eventually, they will be trapped inside the droplet and carried away with the droplet movement.

CONCLUSIONS AND FUTURE PLAN

In this paper, we demonstrate a proof of concept self-cleaning surface system with ARC tracks using Cytop-TMS coatings. Cytop was successfully patterned using parylene as the stencil mask. Solar module level optical transmission and solar cell power I-V measurements were performed, demonstrating Cytop coating can provide antireflection properties on the soda lime cover glass and improve solar output efficiency. Different surface contaminants including water soluble, insoluble, hydrophobic and hydrophilic dust particles were characterized. Our system relies on the surface tension anisotropy at the TPL of the droplet boundary to move the droplet along while dislodging and removing surface contaminants during droplet expansion and recession phases under vibrations. Compared with hydrophobic surfaces utilizing the lotus effect, our system has the advantage of systematically transporting the droplet to designated locations compared with uncontrolled droplet rolling by gravity on hydrophobic surfaces. The cleaning process only utilizes a sessile droplet with minimized water usage.

As for the future plan, we will explore the large scale patterning process. Printing is a promising option. By combining flexographic and gravure printing techniques, a high resolution (10 μm) Cytop patterning was achieved [13]. Meanwhile, the power consumption is another concern for the fielding application. A high quality factor vibration motor optimized at the droplet resonance frequency is required to minimize the system power consumption. The cleaning time of the system can be limited to a short period of time depending on the local dust accumulation rate so that the solar module power gain from the cleaning processes can compensate for the cleaning power consumption.

ACKNOWLEDGEMENT

Fabrication was performed at the Washington Nanofabrication Facility (WNF), a member site of the NSF National Nanotechnology Coordinated Infrastructure (NNCI), with support from NSF award ECCS-1308025. We would like to thank the funding and fellowship support from CoMotion, the Clean Energy Institute at the University of Washington and the Amazon Catalyst Fund.

REFERENCES

[1] M. Gostein, B. Littmann, J. R. Caron, and L. Dunn, "Comparing PV power plant soiling measurements extracted from PV module irradiance and power measurements," Conference Record of the IEEE Photovoltaic Specialists Conference, pp. 3004–3009, 2013.

[2] L. L. Kazmerski, A. S. A. C. Diniz, C. B. Maia, M. M. Viana, S. C. Costa, P. P. Brito, C. D. Campos, L. V. M. Neto, S. De Morais Hanriot, and L. R. De Oliveira Cruz, "Fundamental studies of adhesion of dust to PV module surfaces: Chemical and physical relationships at the microscale," IEEE Journal of Photovoltaics, vol. 6, no. 3, pp. 719–729, 2016.

[3] M. K. Chaudhury and G. M. Whitesides, "How to Make Water Run Uphill," Science, vol. 256, no. 5063, pp. 1539–1541, 1992.

[4] D. E. Kataoka and S. M. Troian, "Patterning liquid flow on the microscopic scale," Nature, vol. 402, no. 6763, pp. 794–797, 1999.

[5] M. G. Pollack, A. D. Shenderov, and R. B. Fair, "Electrowetting-based actuation of droplets for integrated microfluidicsElectronic supplementary information," Lab on a Chip, vol. 2, no. 2, p. 96, 2002.

[6] T. A. Duncombe, J. F. Parsons, and K. F. Böhringer, "Directed drop transport rectified from orthogonal vibrations via a flat wetting barrier ratchet.," Langmuir : the ACS journal of surfaces and colloids, vol. 28, no. 38, pp. 13765–70, 2012.

[7] A. Shastry, M. J. Case, and K. F. Böhringer, "Directing droplets using microstructured surfaces," Langmuir, vol. 22, no. 14, pp. 6161–6167, 2006.

[8] D. Sun and K. F. Böhringer, "Self-cleaning surfaces using anisotropic ratchet conveyors," in TRANSDUCERS 2017 - 19th International Conference on Solid-State Sensors, Actuators and Microsystems, 2017, vol. 1, pp. 1773–1776.

[9] C. C.Cho, R. M. Wallace, and and L.A. Files-sesler, "Patterning and Etching of Amorphous Teflon Films," Journal of Electronic Materials, vol. 23, no. 8, 1994.

[10] S. A. Makohliso, L. Giovangrandi, D. Leonard, H. J. Mathieu, M. Ilegems, and P. Aebischer, "Application of Teflon-AF(R) thin films for bio-patterning of neural cell adhesion," Biosensors & Bioelectronics, vol. 13, no. 11, pp. 1227–1235, 1998.

[11] C. P. Tan, B. R. Cipriany, D. M. Lin, and H. G. Craighead, "Nanoscale resolution, multicomponent biomolecular arrays generated by aligned printing with parylene peel-off," Nano Letters, vol. 10, no. 2, pp. 719–725, 2010.

[12] I. Sanzari, M. Callisti, A. De Grazia, D. J. Evans, T. Polcar, and T. Prodromakis, "Parylene C topographic micropattern as a template for patterning PDMS and Polyacrylamide hydrogel," Scientific Reports, vol. 7, no. 1, pp. 1–11, 2017.

[13] G. C. Schmidt, M. Bellmann, B. Meier, M. Hambsch, K. Reuter, H. Kempa, and A. C. Hübler, "Modified mass printing technique for the realization of source/drain electrodes with high resolution," Organic Electronics: physics, materials, applications, vol. 11, no. 10, pp. 1683–1687, 2010.

CONTACT

*K. F. Böhringer, tel: +1-206-221-5177; karl@ee.washington.edu

DIRECTED SELF ASSEMBLY OF COLLOIDAL PARTICLES FOR HIGH ASPECT RATIO BANDS

Varun Lochab[1], Andrew Yee[2], Yanrong Li[3], Minami Yoda[2], A. Terrence Conlisk[1], and Shaurya Prakash[1]*
[1]Department of Mechanical and Aerospace Engineering, The Ohio State University, Columbus, OH, USA
[2]The George W. Woodruff School of Mechanical Engineering, Georgia Institute of Technology, Atlanta, GA, USA
[3]Department of Mechanical Engineering, Ibaraki University, Hitachi, Japan

ABSTRACT

Current state-of-art nano- (< 100 nm diameter) and colloidal particle (> 100 nm, < 1μm) assembly methods require particle aggregation followed by assembly to fabricate usable structures. A single-step method that aggregates and assembles particles dynamically in a continuous-flow system has the potential to provide new avenues for nanomaterial fabrication. Here, we present observations with initial analyses of the mechanics of directed self-assembly of colloidal particles into stable, high aspect-ratio bands within microchannels in combined steady Poiseuille and electroosmotic flow with opposed applied pressure and potential gradients.

INTRODUCTION

Recent advances in nano-/colloidal particle synthesis enable a broad range of tunable functions using different size and surface charge. With a wide variety of designed and engineered properties possible for both nano- and colloidal particles, these material systems present a major building block for generating new assembled materials with remarkable functionality [1]. At present, the fundamental understanding of particle migration/aggregation required to predict and eventually engineer such materials is lacking, and there are few, if any, practical and systematic approaches for particle aggregation and subsequent assembly into usable structures. In this paper, we present observations of a new type of particle assembly along with initial efforts to analyze the mechanics of the assembly of colloidal particles in stream-wise bands within continuous flow in a microchannel.

In 1961, Segré & Silberberg [2] reported that particles migrate slowly to a thin concentric region at a radial location about 0.6 times the pipe radius in the Poiseuille flow of a dilute suspension of neutrally-buoyant rigid spherical particles in a Newtonian fluid. Later, Jeffrey and Pearson [3] observed that particles denser than the fluid migrated rather rapidly to a location near the pipe walls for downwards Poiseuille flow in a vertical pipe, and towards the centerline for upwards flow (Figure 1a).

Bretherton [4] showed that when inertia was neglected with respect to viscous forces, no force along the lateral (*i.e.*, cross-stream) direction can exist for a body of revolution, for example, a spherical particle in a unidirectional flow. The lateral migration of the particle is therefore due to the inertia of the fluid and the particle. Particularly, the migration of non-neutrally buoyant particles, as observed by Jeffrey and Pearson, was explained by inertial forces called 'slip-shear' induced lift forces, which dictate that a particle travelling faster than the undisturbed fluid flow migrates towards the boundaries while a particle lagging the fluid velocity migrates towards the center of the channel [5-7].

Hogg [6] provided another model and described that fluid inertia affects the particle motion either by inertial interaction with the wall or, if the particle is moving in a sufficiently large domain relative to particle size, the inertial effects of the far field, arising from Oseen-like inertial corrections. In Hogg's work [6], the ratio of magnitude of the wall effect to the inertial effects of the far field scaled with channel Reynolds number, $R_c^{-1/2}$. Where, R_c ($= \rho U_c H/\mu$) is the channel Reynolds number based on the channel height, H as the critical length scale and centerline velocity U_c. For $R_c << 1$, inertial interactions with the walls dominate the lateral motion of the particle, while for $R_c >> 1$, Oseen-like inertial migration effects dominate, and thus, the fluid may be treated as unbounded. For $R_c \sim 1$, however, both types of effects are important. Saffman [8, 9] studied inertial effects in Oseen-like regions, and obtained the slip-shear induced lift force on a particle moving relative to the fluid in an unbounded linear shear flow. Later, Drew [10] and McLaughlin [11] considered the particle migration in the shear flow bounded by a single planar wall. Ho and Leal [12] also studied the inertial lift forces in the Poiseuille flows for $R_c <<1$, where inertial interactions with the walls dominate.

Given the various scaling parameters (discussed in more details in the results and discussion section), in this work, initial analysis on mechanics of directed self-assembly of colloidal particles is developed using the methods described by Hogg [6].

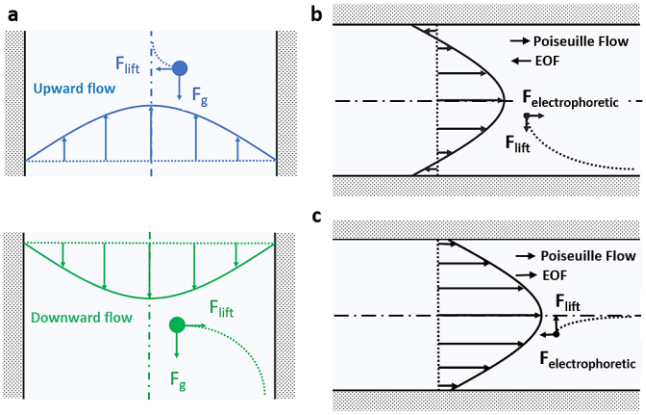

Figure 1: (a) Particles with a slightly greater density lag the fluid in an upwards Poiseuille flow due to negative buoyancy and migrate towards the pipe axis, while they lead the fluid in a downwards flow and migrate towards the walls. (b) A negatively charged neutrally buoyant particle leads the flow due to electrophoresis in combined Poiseuille and counter EOF; the particle experiences a lift force towards the channel walls. (c) A negatively charged neutrally buoyant particle lags the combined flow due to electrophoresis in combined Poiseuille and electroosmotic "co-flow"; the particle then experiences a lift force towards the center of the channel. Dotted lines show particle motion in response to the lift forces.

Hogg reported that for the flow of non-neutrally buoyant article in vertical channels that the denser non-neutrally buoyant particles

978-1-940470-03-0/HH2018/$25©2018TRF
DOI 10.31438/trf.hh2018.76

in downward Poiseuille flow will migrate to the wall when they lead the flow, and move towards the center of the channel (Figure 1a) in upwards flow when they lag the flow, in agreement with the observations by Jeffrey and Pearson.

We *hypothesize* here that similar 'slip-shear' effects can be induced by the electrophoretic motion of charged colloidal particles in combined Poiseuille and electroosmotic (EO) flow, where particles can either lead or lag the undisturbed fluid velocity based upon the direction of the applied electric field (*cf.* Figure 1b, 1c). An extensive literature search yielded only two recent papers [7, 13] that report observations of electrophoretic-induced migration in combined Poiseuille and EO flow.

In a recent report by the Yoda group, colloidal particles not only aggregate near the wall in combined Poiseuille and opposing EOF, but also form stream-wise bands in the channel under a range of parameters [14]. We also conjecture that this phenomenon could be due to fluid flow instabilities, the exact nature of these flow instabilities remains yet unknown.

METHODS

Model polydimethylsiloxane (PDMS) microchannel (4 cm [L; x]) × 34 µm [H; y] × 340 µm [W; z]) were fabricated using well-accepted soft lithography methods. Briefly, we spin-coated (2150 RPM, 60 s) photoresist (SU-8 2025, MicroChem Corp., Newton, MA) on silicon wafer after it was cleaned in Piranha solution (4:1, H_2SO_4:H_2O_2) and blow dried with Nitrogen. Wafer was subjected to a two-step pre-exposure bake at 65° C (5 min) and 90° C (10 min), respectively to evaporate the remaining solvent and to densify the photoresist film. We employed a thin, transparent film, and printed (10,000 dpi) negative photomask for the near-UV (320-450 nm) flood exposure (240 mJ/cm^2) of the wafer. Later, two-step post-exposure bake at 65° C (3 min) and 90° C (10 minutes) was executed, and the photoresist was developed for 7 minutes in SU-8 developer and hard-baked at 200° C for 15 minutes to yield a positive mold of the model microchannel.

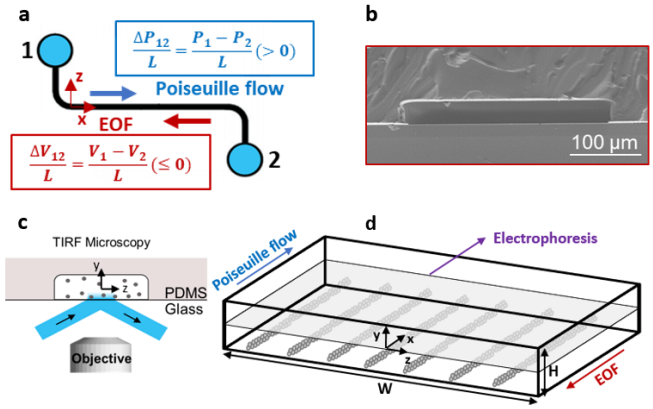

Figure 2: (a) Schematic of the microchannel (4 cm [L; x]) × 34 µm [H; y] × 340 µm [W; z]) (b) Scanning Electron Microscopy (SEM) micrograph of channel cross-section. (c) Experimental setup showing TIRF for imaging near-wall (~500 nm) particles. (d) Stream-wise bands assemble near the glass wall spanning the width of the channel, as shown in the schematic.

Liquid PDMS was degassed and poured on the silanized ((Tridecafluoro-1,1,2,2-Tetrahydrooctyl) – Trichlorosilane) mold and was cured for 4 h at 70° C. PDMS microchannels were then bonded to the fused quartz glass slides (Figure 2) by exposing both to O_2 plasma at 45 W RF power and 280 mTorr pressure for 40 seconds.

The flow experiments used a dilute colloidal solution (particle fraction = 0.17, 0.33 % v/v) of negatively charged neutrally buoyant polystyrene particles (radius a = 245 nm, zeta potential ~ -50 mV) in sodium tetraborate solution (1 mM), driven by opposed Poiseuille and EO flow (Figure 2) as reported earlier [14]. Total internal reflection fluorescence (TIRF) microscopy (Figure 2) was used for visualizing polystyrene nanoparticles within the first ~1 µm of the channel walls [14].

High aspect ratio bands with cross-section of a few µm and length comparable to the channel length of O(cm)were observed (Figure 2d). In all cases, band formation was preceded by particle aggregation near the channel walls. Two-dimensional flow analysis was done where the effect of side walls (H/W = 0.1) was neglected. The top and bottom walls are subjected to no-slip boundary conditions and symmetric wall zeta potential (ζ_w~ -100 mV) was used for modeling and analysis. For evaluation of particle migration to the walls, we use analytical force expressions for inertial forces reported previously [8, 9, 12].

RESULTS AND DISCUSSION

After the potential difference was applied (T = 0 s), the particles migrated to the wall (Figure 3), and subsequently formed high-aspect ratio stream-wise bands in combined Poiseuille and opposing EOF, for certain combinations of pressure and potential gradients as reported previously [14].

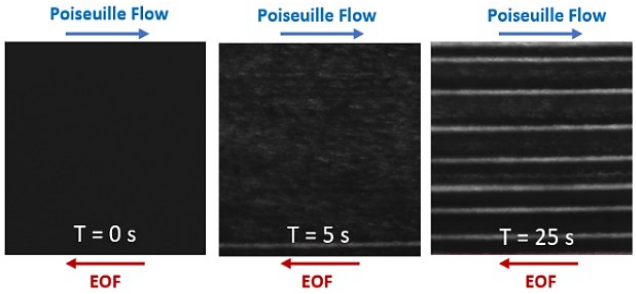

Figure 3: Near-wall bands at $\Delta P_{12}/L$ = 0.56 bar/m and $\Delta V_{12}/L$ = -117 V/cm switched on at T = 0 s. Image area: 203 µm × 203 µm.

Flow Analysis

Fluid velocity profiles were obtained by solving the coupled Navier-Stokes and Poisson-Boltzmann equations for 2D flow. As with previous reports, we assume fully developed, steady flow with no-slip boundary condition at the physical microchannel walls, whereas reservoir conditions were as shown in Figure 2a. The stream-wise (x) momentum equation is given by:

$$\frac{\partial P}{\partial x} = \mu \frac{d^2 U}{dy^2} - \varepsilon E_x \frac{d^2 \varphi}{dy^2} \qquad (1)$$

The potential distribution, $\varphi(y)$, is obtained analytically from the solution of Poisson-Boltzmann equation [16], where, for boundary conditions, wall zeta potential (ζ_w) is assumed to be symmetric for the top and bottom walls; P is pressure, and U is fluid velocity; μ and ε are dynamic viscosity and permittivity of water, respectively, at 1 atm and 25° C. Equation 1 is linear, thus, the solution for the flow velocity can be decomposed into two parts.

$$U = U_{Poiseuille} + U_{EOF} \qquad (2)$$

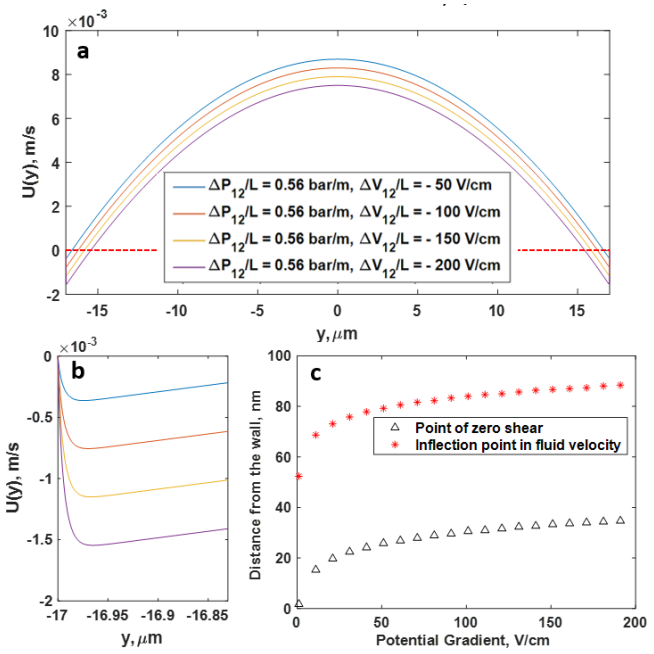

Figure 4: (a) Fluid velocity profiles across the channel, where direction of flow is in x-direction (cf. Figure 2d). (b) Negative fluid velocity ($U<0$), i.e., flow reversal, near the wall due to opposing EO flow. (c) Point of zero shear represent the position where the forces due to pressure-gradient ($\Delta P_{12}/L$ = 0.56 bar/m) and opposing potential gradient balance; this results in an inflection point ($d^2U/dy^2 = 0$) in the velocity indicating that flow instabilities might exist.

We observe two specific characteristics of the resultant velocity profile (Figure 4a, 4b) for the conditions in our experiments: 1) an inflection point ($d^2U/dy^2 = 0$); 2) flow reversal near the walls ($U<0$).

The inflection point is at ~80 nm from the wall for the conditions ($\Delta P_{12}/L$ = 0.56 bar/m) used in the experimental data reported here and there is zero shear, where the forces due to applied pressure and adverse potential gradient balance at ~30 nm from the wall. The presence of inflection point indicates the possibility of flow instability arising near the wall. Previous reports [15] have suggested that, at the inflection point ($d^2U/dy^2 = 0$), where the viscous force term ($\mu\, d^2U/dy^2$) vanishes to zero and the lateral energy gradient ($d\,(P + \rho U^2/2)/dy$) exists, any small disturbance to the flow could be amplified by the energy gradient without being dampened by viscous losses, making the flow unstable.

Particle Dynamics

The lateral migration of the particles in unidirectional fluid flow has been previously attributed to fluid and particle inertia [4, 6]. Ho and Leal [12] solved for inertial lift forces, F_I, on neutrally buoyant spheres in 2D unidirectional flows, where the Oseen inertial correction [6] is negligible compared with the interactions with the walls.

$$F_I \propto U_c^2 a^4/H^2 \qquad (3)$$

These inertial lift forces yield an equilibrium position away from the wall where net force on the particle is zero, similar to that also observed by Segré & Silberberg [2].

As described in the introduction section, for the experimental conditions reported here and use of dilute colloidal suspensions leading to band-formation, no complete model have been reported. The first step is to confirm whether the particles will travel to the near-wall region as opposed to the channel centerline. Since, we use negatively charged particles that lead the fluid flow by the electrophoretic velocity (relative particle velocity), $\varepsilon\zeta_p E_x/\mu$.

For instance, at $\Delta P_{12}/L$ = 0.56 bar/m & $\Delta V_{12}/L$ = -100 V/cm, the particle velocity, U_p = 0.0091 m/s at the channel center, while U_c = 0.0083 m/s. Thus, the particles lead the fluid velocity, where the ratio of magnitude of particle relative velocity to the channel center line velocity is 0.10, rounded to the second decimal place. Moreover, R_c = 0.16 based on channel center line velocity of combined Poiseuille flow and EOF; the ratio of magnitude of the wall effects and inertial effects from Oseen like inertial regions is 2.50 ($R_c^{-1/2}$), thus, both effects are comparable [6].

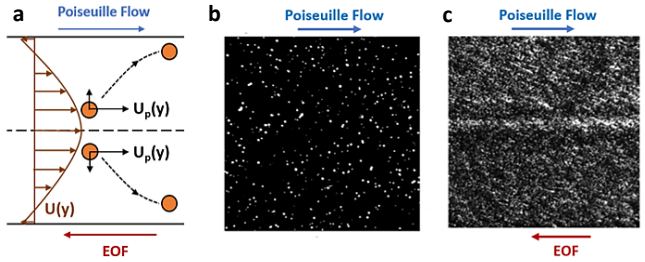

Figure 5: (a) The particle movement towards the wall in response to slip-shear lift forces. (b) Poiseuille flow, $\Delta P_{12}/L$ = 0.34 bar/m, and (c) particle crowding in combined Poiseuille flow and EOF as $\Delta V_{12}/L$ = -28 V/cm is applied [5].

Hogg's analysis solved for lateral migration of particles in Poiseuille flow for R_c of order unity, where both wall effects and far field effects were important. For denser non-neutrally buoyant particles in downward Poiseuille flow in vertical channels, he also observed that the particle migration velocity (and, hence the lateral force) reaches a maximum at ~0.15 the depth of the channel due to wall effects. For combined Poiseuille and opposing EOF, negatively charged neutrally buoyant particles lead the flow due to electrophoresis and migrate to the wall (Figure 5) as observed experimentally here.

Hogg introduced the effect of buoyancy using the normalized parameter B, ratio of Stokes' settling velocity ($V_b = \frac{2}{9} a^2 \Delta\rho g/\mu$) to the channel center line velocity (U_c). The equation for particle motion with no acceleration is given by equation 4; while for the normalized equation 5, σ, hydrodynamic stress on the particle, is normalized by $\mu U_c/a$ and area is normalized by a^2, and $\hat{b}$ is the unit vector in direction of body force:

$$\int \sigma.\hat{n} dS = -6\pi\mu a V_b \hat{b} \qquad (4)$$

$$\int \sigma^*.\hat{n} dS^* = -6\pi B \hat{b} \qquad (5)$$

Using particle Reynolds number $R_p = \rho U_c a^2/\mu H$ and channel Reynolds number as $R_c = \rho U_c H/\mu$, he found that the lift forces in a vertical channel scale as O ($BR_p^{1/2}$) given $1 \gg R_c B^2$ and $1 \gg \alpha^2/B$, where $\alpha = a/H$.

If Hogg's analysis can be extended to the effects of slip-shear due to electrophoretic motion, the parameter B_e would be the ratio of particle electrophoretic velocity (V_e) to the channel center line

velocity. Under the thin EDL assumption (here, $\lambda/a \sim 10^{-2}$) for electrophoretic force on the particle [17], the equation for particle motion is given by:

$$\int \sigma.\hat{n}dS = -6\pi\mu a V_e \hat{b} \quad (6)$$

$$\int \sigma^*.\hat{n}dS^* = -6\pi B_e \hat{b} \quad (7)$$

Here, equation 6 was normalized as equation 5. For $\Delta P_{12}/L$ = 0.56 bar/m and $\Delta V_{12}/L$ = -100 V/cm, channel Reynolds number is 0.16, while the parameters $R_c B_e^2$ = 0.0015, and α^2/B_e= 0.0006 satisfy the regime conditions solved by Hogg: $1 \gg R_c B^2$ and $1 \gg \alpha^2/B$.

Hogg's analysis in this regime considered the gravitational body force. If the analysis can be used for the electromagnetic body forces, the lateral lift force scales as O ($B_e R_p^{1/2}$), thus, the lift forces induced by electrophoretic motion of the particles scales linearly with B_e (the ratio of particle electrophoretic velocity, $V_e \propto \Delta V_{12}/L$, to the channel center line velocity), whose magnitude increases as potential gradient is increased.

The higher lift forces at higher potential gradient should result in a higher particle fraction at a given x-location. This increase in particle fraction is supported by the observation that the location of banding moves upstream as the applied potential difference was increased (Fig. 6a, 6b), suggesting that banding likely depends on particle fraction as well, and consequently particle aggregation near the wall may be a precursor, if not a prerequisite, to particle assembly into stream-wise bands.

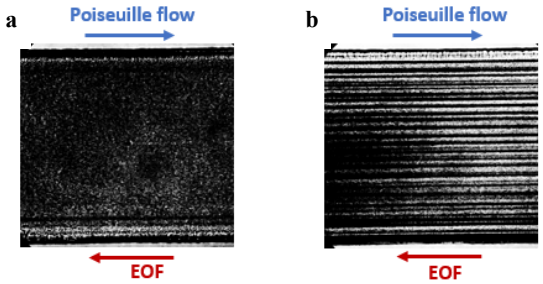

Figure 6: (a) Bands move upstream at higher $|\Delta V_{12}/L|$. At $x \approx 0$ cm, $\Delta P_{12}/L$ = 0.73 bar/m, no bands were observed at $\Delta V_{12}/L$ = -47.3 V/cm compared to (b) $\Delta V_{12}/L$ = -94.6 V/cm. However, bands were observed downstream for $\Delta V_{12}/L$ = -47.3 V/cm. Image area: 203 µm × 203 µm.

SUMMARY AND CONCLUSION

Previous experimental studies report that particles from a dilute colloidal solution self-assemble into stream-wise bands in a continuous flow system with opposed Poiseuille and EO flow. Here, we show that the fluid velocity has an inflection point near the wall, which likely indicates the presence of flow instabilities. For particle aggregation, our analysis suggest that the particles could migrate towards the walls due to inertial-type lift forces due to an electrophoretic "slip" velocity. When the EO flow opposes the Poiseuille flow, the negatively charged particles leads the fluid flow due to electrophoresis, and a particle leading the fluid flow migrates towards the wall, by using previously reported analysis methods. However, for an accurate description of particle motion, the analysis of Hogg, who considered particle-fluid slip due to buoyancy mismatch, will need to be extended to particle-fluid slip due to electromagnetic forces.

ACKNOWLEDGEMENTS

We acknowledge the support from the US Army Research Office through grant number W911NF-16-0278. We also thank the staff of Nanotech West, The Ohio State University, for helping with device fabrication and characterization.

REFERENCES

[1] O. Gang, "Nanoparticle assembly: from fundamentals to applications: concluding remarks," Faraday Discussions, 186 (2016), pp. 529-537.

[2] G. Segré and A. Silberberg, "Radial Particle Displacements in Poiseuille Flow of Suspensions," Nature, 189 (1961), pp. 209-210.

[3] R. C. Jeffrey and J. R. A. Pearson, "Particle motion in laminar vertical tube flow," Journal of Fluid Mechanics, 22 (1965), p. 721.

[4] F. P. Bretherton, "The motion of rigid particles in a shear flow at low Reynolds number," Journal of Fluid Mechanics, 14 (1962), p. 284.

[5] J. Zhang, S. Yan, D. Yuan, G. Alici, N. T. Nguyen, M. Ebrahimi Warkiani, *et al.*, "Fundamentals and applications of inertial microfluidics: a review," Lab on a chip, 16 (2016), pp. 10-34.

[6] A. J. Hogg, "The inertial migration of non-neutrally buoyant spherical particles in two-dimensional shear flows," Journal of Fluid Mechanics, 272 (1994), p. 285.

[7] Y. W. Kim and J. Y. Yoo, "Axisymmetric flow focusing of particles in a single microchannel," Lab on a chip, 9 (2009), pp. 1043-5.

[8] P. G. Saffman, "The lift on a small sphere in a slow shear flow," Journal of Fluid Mechanics, 22 (1965), p. 385.

[9] R. Mei, "An approximate expression for the shear lift force on a spherical particle at finite reynolds number," International Journal of Multiphase Flow, 18 (1992), pp. 145-147.

[10] D. A. Drew, "The lift force on a small sphere in the presence of a wall," Chemical Engineering Science, 43 (1988), pp. 769-773.

[11] J. B. McLaughlin, "The lift on a small sphere in wall-bounded linear shear flows," Journal of Fluid Mechanics, 246 (1993), p. 249.

[12] B. P. Ho and L. G. Leal, "Inertial migration of rigid spheres in two-dimensional unidirectional flows," Journal of Fluid Mechanics, 65 (1974), p. 365.

[13] D. Yuan, C. Pan, J. Zhang, S. Yan, Q. Zhao, G. Alici, *et al.*, "Tunable Particle Focusing in a Straight Channel with Symmetric Semicircle Obstacle Arrays Using Electrophoresis-Modified Inertial Effects," Micromachines, 7 (2016), p. 195.

[14] N. Cevheri and M. Yoda, "Electrokinetically driven reversible banding of colloidal particles near the wall," Lab on a chip, 14 (2014), pp. 1391-4.

[15] Hua-Shu Dou, "Viscous flow instability of inflectional velocity profile", Presented in Fourth International Conference on Fluid Mechanics, (2004).

[16] P. Dutta and A. Beskok, "Analytical solution of combined electroosmotic/pressure driven flows in two-dimensional straight channels: finite Debye layer effects," Analytical chemistry, 73 (2001), pp. 1979-86.

[17] R. F. Probstein, *Physicochemical hydrodynamics : an introduction*. New York: Wiley, 1994.

CONTACT

*Shaurya Prakash, Email ID: prakash.31@osu.edu

MECHANICAL CHARACTERIZATION OF ADDITIVELY MANUFACTURED MICROSTRUCTURES USING A PROCESS INTEGRATED MEMS TENSILE TESTER

Ian S. Ladner[1,2†], Joon H. Cho[2], David R. Cayll[2], Vu H. Nguyen[1], Michael A. Cullinan[2], and Sourabh K. Saha[1*]*
[1]Lawrence Livermore National Laboratory, USA
[2]University of Texas at Austin, USA

ABSTRACT

With the rapid growth of additive manufacturing technologies, mechanical characterization of printed structures is becoming increasingly important to ensure their suitability as functional components. However, characterization of microstructures is traditionally compression testing due to handling challenges of at-scale parts. To overcome that limitation, we have designed, fabricated, and tested custom microelectromechanical system (MEMS) tensile tester that enables direct integration with additively manufactured (AM) parts with nm displacement resolution and mN force range. This work characterizes the mechanical behavior of two AM parts stitched together. At yield, the failure strain is 3.1%, which is 3x lower than under compression.

INTRODUCTION

Miniaturization of mechanical testing instruments through use of microelectromechanical systems (MEMS) has been successfully performed in the past to characterize small-scale structures [1]. Unfortunately, indirect integration through pick-and-place techniques is not appropriate for characterization of additively manufactured (AM) polymeric parts, which are easily-deformed. Additionally, existing MEMS tensile testers fail to maintain their functionality after direct integration of AM parts onto the sensors. To overcome these limitations, we have designed, built, and tested custom MEMS tensile testers that enable direct integration of AM parts (Fig. 1). Suitability for AM process integration was ensured through geometric design that minimizes stiction effects. Preliminary design of the tensile testers was presented at the ASPE 2017 annual meeting [2]. Here, we present the device fabrication, sensor calibration, and mechanical testing data (stress-strain curve) generated from the MEMS testers with integrated AM parts.

We have used two-photon lithography (TPL) to fabricate test structures in this work. TPL is a laser-based polymerization technique that enables fabrication of sub-diffraction features that are 100 – 500 nm wide and smaller than the focused light spot (Fig. 2). Sub-diffraction resolution is ensured by the underlying non-linear two-photon absorption process that occurs at the high light intensities (~TW/cm^2) achieved through focusing of femtosecond lasers. Microstructures are generated by scanning the focused light spot in 3D space. Due to the limited range of scanners, larger structures are generated by "stitching" multiple sections. These stitch lines often act as regions of reduced strength due to alignment errors and need to be characterized to enable deterministic design of millimeter-scale parts.

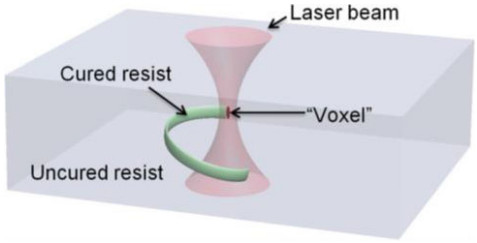

Figure 2: Schematic of two-photon lithography illustrating sub-diffraction printing [3].

DESIGN

The tensile tester is comprised of a chevron style thermal actuator and two differential capacitive sensors for load and displacement sensing (Fig. 1.a). A thermal actuator was chosen to achieve the high force and relatively large displacement required to achieve > 2% strain on the AM microstructures. Single-sided differential capacitors were selected to generate a high selectivity for a given footprint to achieve nm displacement resolution (Fig. 1.c). A two-sensor design was selected to simultaneously measure stress and strain without requiring an additional vision-based metrology system. The actuator and displacement sensor share the same moving shuttle that is guided by a flexure bearing whereas the load sensor is guided by a separate flexure bearing. The tip of the displacement sensor and the load sensor is the print location for the AM part with the gap. For dimensions and details on design method see [2].

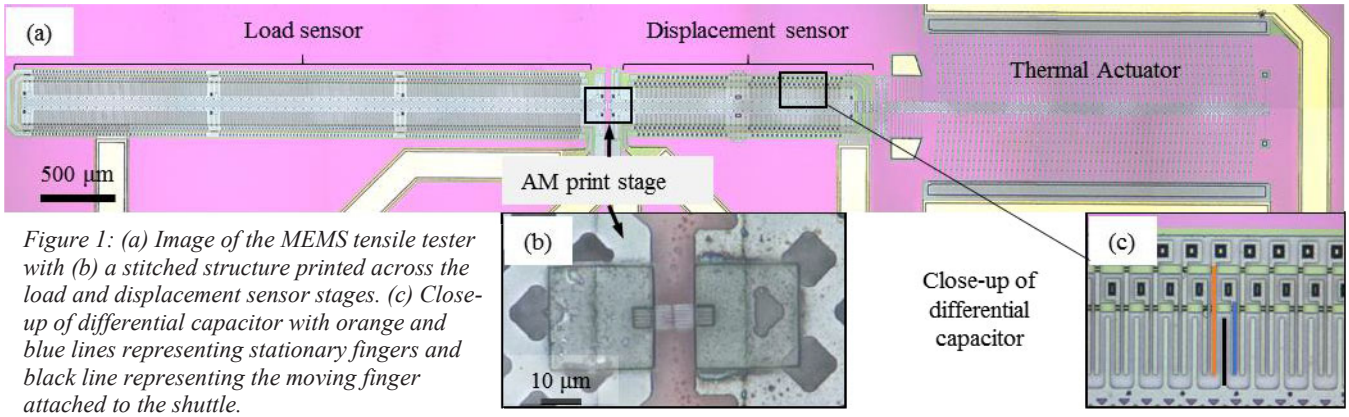

Figure 1: (a) Image of the MEMS tensile tester with (b) a stitched structure printed across the load and displacement sensor stages. (c) Close-up of differential capacitor with orange and blue lines representing stationary fingers and black line representing the moving finger attached to the shuttle.

978-1-940470-03-0/HH2018/$25©2018TRF
DOI 10.31438/trf.hh2018.77

FABRICATION

A two-layer PolyMUMPs process was used for this work, which is required for the single-sided differential capacitors. A simplified process flow is shown in Fig. 3. A 600 nm silicon nitride layer was deposited as an electrical insulator between the tester and a heavily doped silicon substrate. One micron of amorphous silicon was deposited and doped with a spin-on phosphosilicate glass (PSG) dopant. An anneal was run at 1050°C to dope and crystallize the layer into polysilicon. The Polysilicon 1 layer was patterned to form the electrical network between components. A 1 µm layer of thermal oxide, Oxide 1, was deposited to planarize the area under the thermal actuator. The second thermal oxide layer, Oxide 2, was deposited to create the 2.5 µm air gap under the device layer and patterned with holes to connect the device layer to Polysilicon 1. Next, the 8 µm device layer, Polysilicon 2, was deposited and doped with PSG. Prior to patterning the device layer, 300 nm of gold was deposited with a bi-layer lift-off to form electrical traces and bond pads. Polysilicon 2 was pattern with deep reactive ion etching (DRIE) to define the thermal actuator and capacitive sensor features. After dicing, a buffered oxide etch (BOE) and deionized water (DI) solution was used to remove the two thermal oxide layers and release the suspended portions of the Polysilicon 2 layer. Chips were transferred into DI followed by isopropyl alcohol (IPA) and drying in air to complete the release process. The chips were wire bonded to a custom PCB package, which was designed for integration into the Nanoscribe Photonic Professional (GT) 3D printing system.

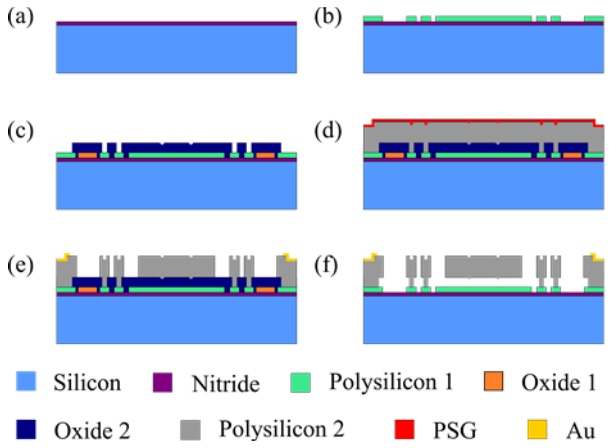

Figure 3: Fabrication process flow

CALIBRATION

Thermal actuator was calibrated to generate a displacement versus input voltage curve. Digital image correlation (DIC) was used to measure the displacement of moving finger on the shuttle (black finger in Fig. 1.c) with respect to the pair of stationary fingers (orange and blue fingers in Fig. 1.c) at each thermal actuator voltage. Fig. 4.a shows the calibration curve, whose non-linear response at higher voltage is as predicted [2].

With the displacement sensor connected to the shuttle of the thermal actuator, the change in capacitance for a given displacement was measured at the same time. The change in the capacitance, ΔC, of the sensor was calculated from the voltage response of the Irvine Sensors MS3110IC capacitive readout. Fig. 4.b shows the ΔC versus displacement calibration curves for the displacement sensor. The load sensor calibration was generated during the initial portion of the tensile test. The

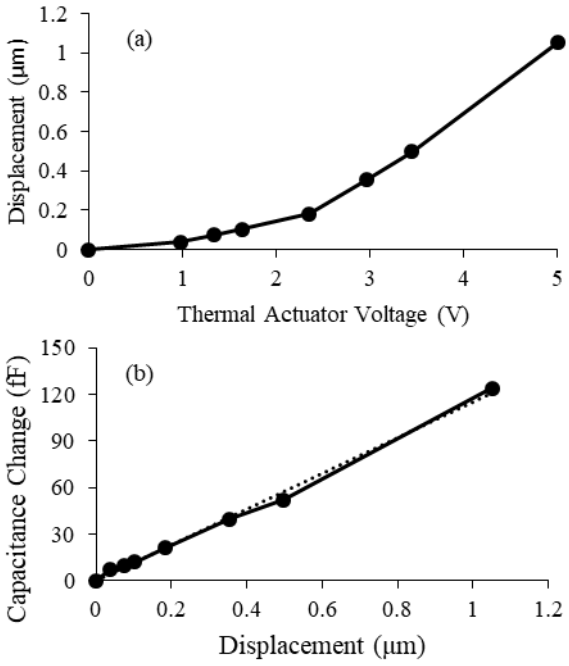

Figure 4: (a) Displacement vs. thermal actuator voltage, and (b) ΔC vs. displacement calibration curve for the displacement sensor

fabricated displacement sensor has a calibrated resolution of 3 nm and an operating range of 1.05 µm.

RESULTS AND DISCUSSION

A stitched part was printed directly on top of the MEMS tester with writing power of 20 mW and speed at 10 mm/s (Fig. 1.b) using the AM integration summarized in Fig. 5. A droplet of photoresist was placed on the tester and loaded into the Nanoscribe Photonic Professional (GT). The galvanometer

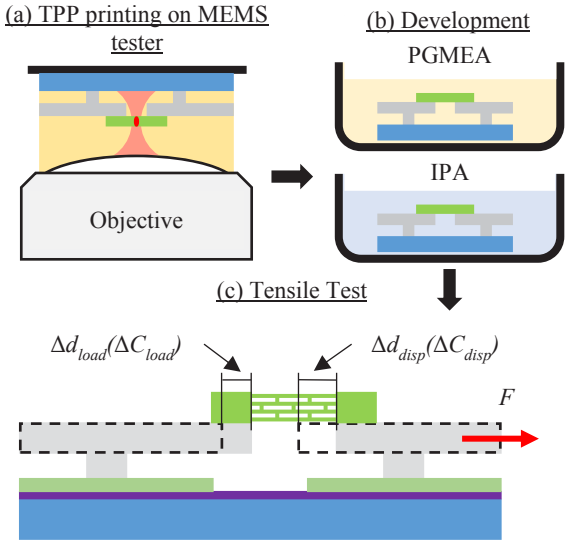

Figure 5: Schematic of AM + MEMS process flow: (a) TPL printing directly on MEMS tester, (b) PGMEA and IPA to develop and clean, and (c) tensile testing after drying.

scanner wrote the microstructure between the shuttle ends of each sensor. The un-patterned resist was removed by propylene glycol monomethyl ether acetate (PGMEA), and the device was cleaned in IPA. After air drying, the device was connected to the electronics and ready for tensile testing.

A schematic of the stitched region of the structure is shown in Fig. 6. The voxel lines were printed 10 µm long in X and 6 µm in Y with a cross section of approximately 350 nm in diameter, *d*, and 1.25 µm in height. The pitch, *P*, in the top view was 500 nm in both direction. At the stitch, the offsets were δ_X = 375 nm and δ_Y = 250 nm between the red and blue structures. In the cross section view, the vertical offset was 500 nm for each of the 5 layers. The gauge length for the printed structure was 10.02 µm with a final thickness of 2.75 µm.

For testing the stitched structure, a dc voltage was applied to the thermal actuator while output signal from the MS3110IC for displacement and load sensors were captured. Deformation of the stitch part was recorded optically. The voltage was increased through the full range of the thermal actuator. Displacement measured from the load sensor was converted into force using the known stiffness of 12.9 kN/m for the flexure bearings [2] with a resolution of 38.7 µN and range of 0.3 mN.

The engineering stress-strain curve is shown in Fig. 7. The measured Young's modulus of the stitched part was 1.45 GPa. At yield, necking was observed at the stitched region shown in Fig. 7.b. The failure strain was 3.1% which is significantly lower than the failure strain in compression (>10%).

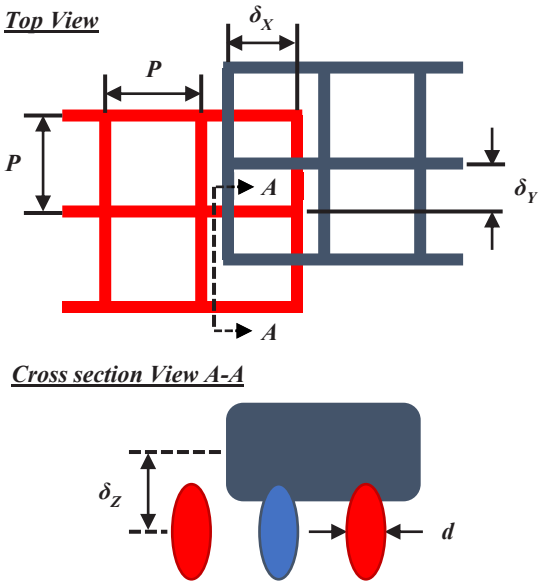

Figure 6: Top view of the stitched structure with pitch, P, and in-plane offsets, δ_X and δ_Y, and cross section view with the voxel width, d, and z spacing, δ_Z, between the lateral and longitudinal layers.

CONCLUSION

The mechanical properties of a TPL stitched AM part were quantified by printing directly onto a custom MEMS tensile tester. The measured properties show a lower yield threshold when compared to the traditional compression testing methods demonstrating the value of direct tensile testing. The process integration demonstrated in this work will lead to mechanical characterization of scale-dependent phenomena, well-characterized custom resists, and more accurate quantification of the effect of process parameters on material properties. These are critical to ensure growth of TPL into a robust manufacturing technique. Additionally, these sensors open the door to study other liquid transferable nano- to microscale materials which require scale-dependent testing with minimal impact due to sample handling.

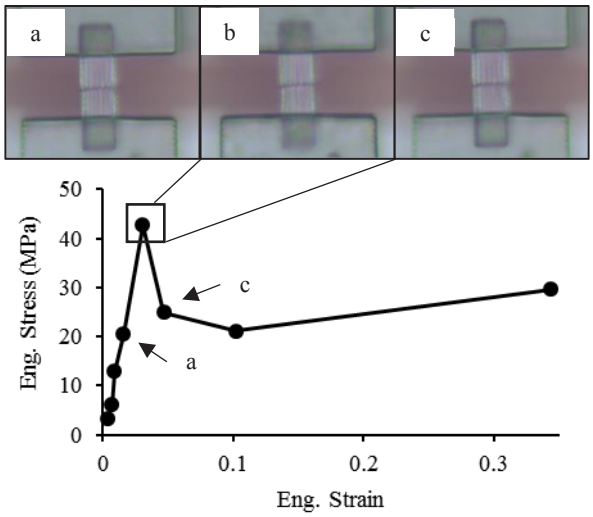

Figure 7: Eng. stress vs. Eng. strain curve with images before (a), during (b), and after yielding (c). Young's modulus measured at 1.45 GPa.

ACKNOWLEDGEMENTS

This work was performed under the auspices of the U.S. Department of Energy by Lawrence Livermore National Laboratory under Contract DE-AC52-07NA27344 and by the University of Texas at Austin under subcontracts B617787, B621043, B626195. Funding available from LDRD-16-ERD-047. LLNL-PROC-748753. The authors thank the staff at the Microelectronics Research Center of University of Texas at Austin for assistance during fabrication, Marianne Ammendolia (LLNL) for packaging of chips, and Steve Hunter (LLNL) for assistance in the design of the sensing electronics.

REFERENCES:

[1] Y. Zhu and T.H. Chang, *"A review of microelectromechanical systems for nanoscale mechanical characterization," J. Micomech. Microeng.*, vol. 25, no. 9, 2015.

[2] I.S. Ladner et. al., "*Design of high resolution and high force MEMS tensile tester for direct metrology of additive manufactured submicron features," in 32nd Annual American Society of Precision Engineering,* Charlotte, NC, 2017.

[3] S.K. Saha et. al., *"Effect of Proximity of Features on the Damage Threshold during Submicron Additive Manufacturing Via Two-Photon Polymerization," J. Micro Nano-Manufacturing,* vol. 5, no. 3, 2017.

Contact:

†I. S. Ladner, tel: 1-925-424-4260; ladner2@llnl.gov
*Corresponding authors: michael.cullinan@austin.utexas.edu, saha5@llnl.gov

MULTILAYER ALD CERAMIC FILMS FOR ENHANCEMENT OF PARYLENE BARRIER PROPERTIES IN COMPLIANT NEURAL PROBES WITH BONDED CHIPS

*Mats Forssell, Xiao Chuan Ong, and Gary K. Fedder**
Carnegie Mellon University, Pittsburgh, Pennsylvania, USA

ABSTRACT

The insulation capabilities of parylene-C thin films in phosphate buffered saline (PBS) are improved through their combination with ALD nanolaminate Al_2O_3 and TiO_2 films. Insulation structures sealed with this ceramic exhibit a 5X lower failure rate compared to those sealed with parylene alone. The insulation of parylene-C probes including 50 µm-thick Si chips bonded using anisotropic conductive film (ACF) is also investigated. The insulation is less effective with the bonded chip present, but samples maintain an impedance above 1 GΩ at 0.1 Hz for over 5 weeks. Addition of nanolaminate results in a lower, but more stable impedance.

INTRODUCTION

Despite its excellent mechanical properties, parylene-C has not been conclusively demonstrated as a viable electrical insulating material for long-term biological implantation, as would be desirable for its use in compliant neural sensors. This is in part because its insulating characteristics degrade over a period of hours to days when inserted in body fluid[1]–[7]. Because ceramic materials have a lower water vapor transmission rate (WVTR), they are a promising alternative for long-term *in vivo* insulation. Atomic layer deposition (ALD) allows deposition of sub-nanometer thick layers of ceramic oxides. Therefore compliant probes can be made in spite of the higher stiffness of the materials, using thin (<100 nm) layers.

Multilayer insulations combining parylene and ceramic have ultimately proven ineffective using Al_2O_3 [8]. However, nanolaminates formed by alternating monolayers of Al_2O_3 and TiO_2 have shown superior water corrosion resistance[9], [10]. Silicon carbide thin films have also been used to insulated neural probes[11], and have shown good compatibility with polyimide[12]. However, combinations of Al_2O_3 and TiO_2 provide greater corrosion resistance than thin films of SiC in hot saline[13] Combining parylene and Al_2O_3/TiO_2 nanolaminate is a promising avenue for extending the lifetime of parylene neural probes.

Highly reliable insulation is especially critical for the development of active compliant parylene probes. Active chips can be used to increase the electrode count on neural probes, and increase the recorded signal quality. However, the DC voltage required to power the probe accelerates the degradation of the insulation. Moreover, failure of the insulation can result in not only the expected probe failure, but also cause high leakage currents in the tissue, which can be hazardous. 1.8 V is a commonly used supply voltage for analog CMOS designs due to an excellent combination of performance and cost. Even operated on a dual rail ±0.9 V, the voltage required exceeds the electrochemical water window of [-0.6 V; 0.8 V] (against Ag/AgCl)[14].

The addition of chips in parylene thin films [15] was previously shown to degrade the insulation capabilities due to cracking of the insulation when tested at 77 °C in saline. A more reliable integration method that maintains a high insulation quality is therefore required.

FABRICATION

Insulation structures

Test structures are fabricated to characterize the insulation properties of parylene with additional nanolaminate films. First, a 4"-diameter glass wafer (Soda Lime, University Wafer, Boston, MA) is dipped in a solution of A-174 adhesion promoter (A174:H2O:IPA = 1:100:100 by volume) and air dried. A 2 µm-thick layer of parylene-C is deposited on the wafer (SCS Labcoter 2, Specialty Coating Systems, Inc., Indianapolis, IN) (Fig. 1(a)). Atomic layer deposition (ALD) is used to deposit 6 nm of TiO_2 as an adhesion layer, followed by 80 nm of Al_2O_3/TiO_2 nanolaminate (Fiji Cambridge Nanotech system, Veeco Instruments, Inc., Plainview, NY) formed by alternating the deposition of Al_2O_3 and TiO_2 layers (Fig. 1(b)). A 125 nm Pt layer is sputter deposited (6J, Perkin-Elmer) with 10 nm Ti adhesion layer on both sides and patterned via liftoff (Fig. 1(c)). A second 80 nm layer of nanolaminate is deposited, followed by a 6 nm layer of TiO_2 adhesion layer (Fig. 1(d)). The nanolaminate is etched in Cl_2 inductively coupled plasma reactive ion etch (Versaline ICP-RIE system, Plasma-Therm, St. Petersburg, FL) (Fig. 1(e)). A wet etch using buffered hydrofluoric acid (BHF) was also investigated, but residue led to a poor insulation quality (Fig. 2). A final 2 µm parylene layer is deposited, following which the parylene-C is etched using O_2 RIE (Trion Technology, Inc., Tempe, AZ) using a Cr hard mask. Individual dies are heated for 3 h at 300 °C in a vacuum chamber at 10 mTorr using N_2 backfill to anneal the parylene layers, which improves the insulation [6].

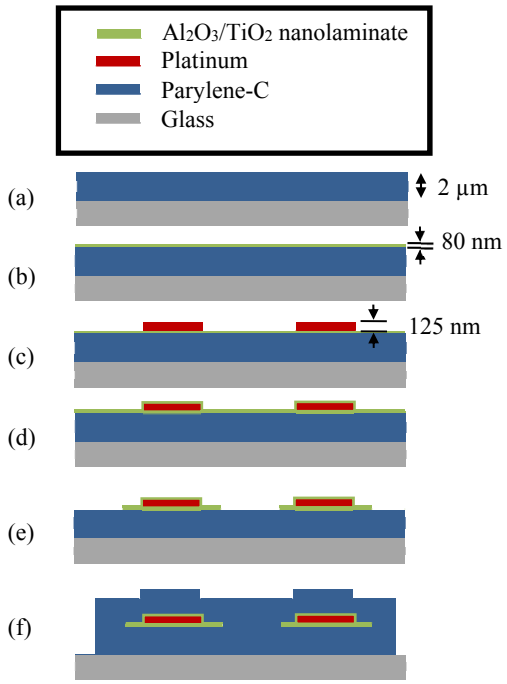

Figure 1: Insulation test structure fabrication simplified process flow

978-1-940470-03-0/HH2018/$25©2018TRF
DOI 10.31438/trf.hh2018.78

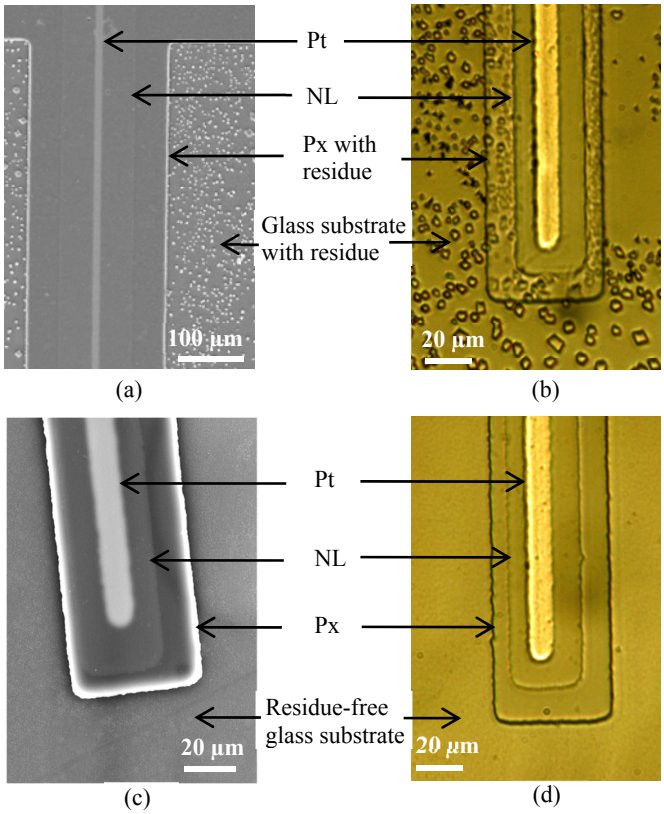

Figure 2: SEM (a),(c) and optical (b),(d) images of insulated Pt wires in which the NL layer was etched using BHF (a),(b) and RIE (c),(d)

Each fabricated sample contains 16 metal traces that are 10 µm wide and 2 cm long. The ceramic insulation surrounding these wires varies from 10 µm to 100 µm in width, while a continuous parylene layer covers all the wires. Samples without ceramic encapsulation were also fabricated. The samples are inserted in phosphate buffered saline (PBS), with around 1 cm of the insulated traces immersed, and placed in a sandbath at either 37°C or 60°C. Periodically, the samples are removed from the sandbath and the impedance between the insulated traces and a counter electrode is measured at room temperature using a potentiostat (PGSTAT301N, Metrohm, AG, Herisau, Switzerland).

ACF chip bonding

In the chip bonding experiments, 1 mm by 1.2 mm by 50 µm-thick silicon chips are integrated in parylene thin films using anisotropic conductive film (CP34531-18AB, Dexerials Corporation, Tokyo, Japan). The chips are bonded before the final parylene deposition (Fig. 1(f)) using a flip-chip die bonder (M9A, BE Semiconductor Industries N.V. (Besi), Duiven, The Netherlands). For bonding tests, the dimensions of the die is 1.2 cm by 0.9 cm, and the parylene thickness is 4.5 µm for each layer. Si is used as a substrate for parylene/ceramic for simpler processing.

Bonding conditions are optimized to ensure that electrical connection between the chip and the substrate is made, without damage to the underlying films. Excessive bonding pressure causes breakage of the platinum wiring, resulting in loss of electrical connection (Fig. 3). Cracks in the platinum could also propagate through the insulation stack and result in leakage.

The presence of protruding pads on the chips facilitates bonding by reducing the requirement on planarity: without protruding pads, a slight tilt between the chip and probe results in a high force applied at the edge of the chip, as seen in Fig. 3. A 2.2 µm protrusion is sufficient to ensure that the electrical connection is made with high yield.

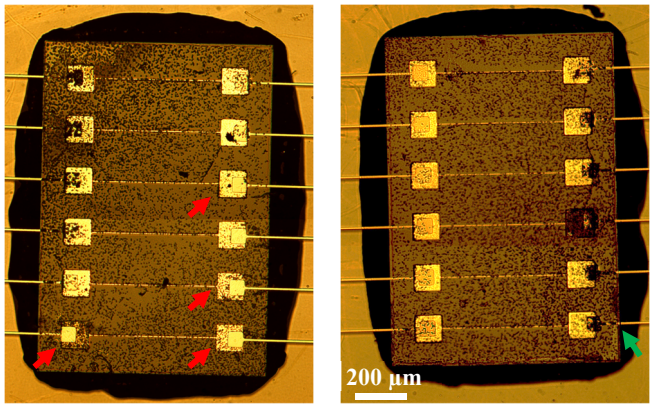

Figure 3: Bottom view of chips without protruding pads connected to probes via ACF. The black dots are the ACF conductive microparticles. The lack of balls on pads indicated by red arrows indicate that the electrical contact is not made. A break in the wire at the edge of the chip is indicated by a green arrow. The left chip was bonded with 4 kg of force, the right chip with 8 kg.

RESULTS AND DISCUSSION

Insulation testing

The impedance at 0.1 Hz in PBS provides a metric for the quality of the insulation. For non-defective insulated samples, the 0.1 Hz impedance theoretically follows an exponential decay

$$|Z| = Z_0 \exp(-t/\tau). \quad (1)$$

However, defects in the insulation result in some channels having a more rapid impedance drop. Empirically, a minimum limit criterion of $Z_L = (10^{10}\ \Omega) \exp(-t/2000\ \text{h})$ allows to distinguish between non-defective and defective channels. Figure 4 shows the impedance at 37°C averaged over 16 channels for non-defective samples, as well as the proportion of non-defective channels over time.

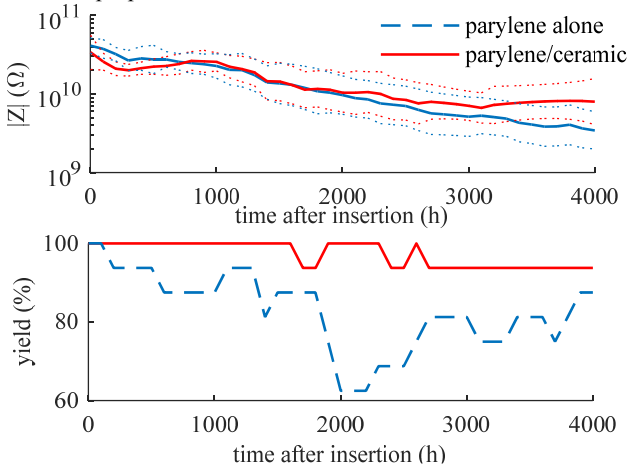

Figure 4: Comparison of (top) 0.1 Hz impedance variation at 37°C and (bottom) proportion of functional channels (n=16 channels). The dotted lines in the impedance plot denote one standard deviation from the mean (solid line).

The time constant for the impedance decay is extracted by fitting the impedance to (1) and the failure rate is extracted by fitting the yield

to a linear decrease (Table 1). Because the impedance decay is initially faster, the fitting is limited to $t > 1000$ h. The parylene/ceramic insulation has a lower impedance decrease for non-defective channels, consistent with the improvement in insulation expected from using the additional ceramic layer. In addition, the samples with ceramic have a lower number of defective channels. This indicates that the additional ALD insulation is less susceptible to defects during fabrication.

Table 1: Performance comparison at 37 °C

	parylene-C alone	parylene-C/ ceramic
Time constant (h)	1639	3253
Failure rate (%/h)	0.76	0.16

Using a higher temperature of 60 °C accelerates the degradation of the insulation. The samples insulated using parylene alone experience a rapid decrease in impedance of over 10 times in a short period of time (< 24 h). This rapid decrease associated with a total insulation failure only occurs after 500 h with the ceramic.

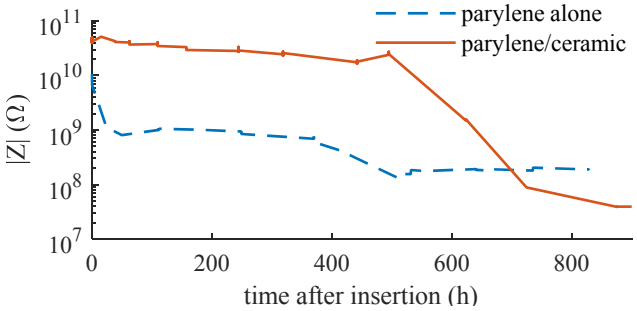

Figure 5: Typical impedance at 0.1 Hz in PBS at 60°C.

Bonded chip insulation

Bonding test structures consist of insulated partial loops as shown in Fig. 6. When the chip is electrically connected, the loop resistance is between 1-2 kΩ; most of the resistance originates from the platinum film resistance. If the bond fails due to a poor ACF connection, or because of cracking of the platinum film, the loop becomes an open circuit.

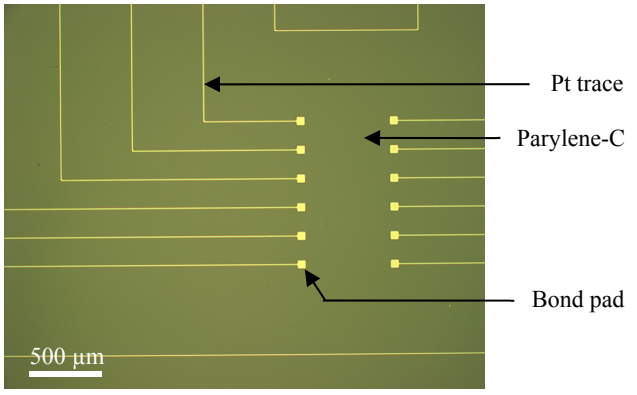

Figure 6: Photograph of a test structure prior to bonding. The bonded chip forms a connection between the right and left pads

Fig. 7 shows the impedance at 0.1 Hz of surviving loops over 900 h of insertion in PBS at room temperature. After 300 h, a 3 V_{pp} sinusoidal voltage with frequency 33 mHz was applied continuously to the loops. After 500 h, the voltage stimulation was changed to a 3 V_{pp} square wave with a frequency of 10 mHz. The additional voltage stimulation does not appear to change the insulation characteristics over short time scales.

After chip bonding under a 1 kg load, 4/6 loops survived for the parylene alone case, while only 1/6 loops survived for parylene/ceramic insulation. Most of the loop failures occurred during fabrication, with only one failure occurring after PBS insertion, in a sample without ceramic. Because the nanolaminate is more brittle than parylene, its presence increases the likelihood of cracks during the chip bonding and the subsequent processing steps. Improvements in that assembly step are ongoing to improve the fabrication yield.

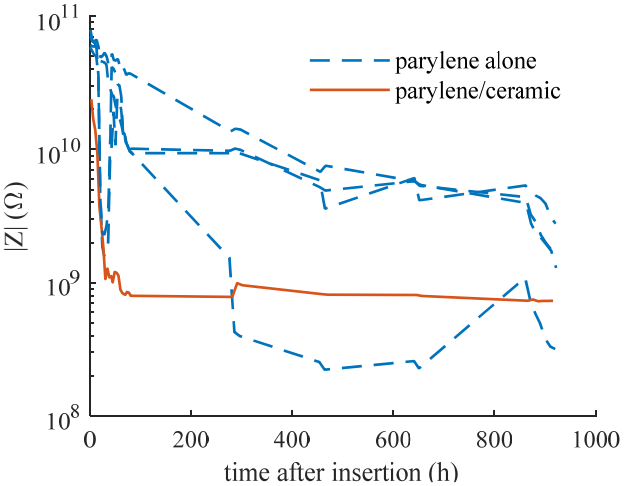

Figure 7: 0.1 Hz impedance at room temperature of insulated traces including a bonded chip.

The time constants obtained from fitting to (1) are 356 h, 570 h, 626 h, and 837 h for the four parylene-alone samples. The time constant measured without the bonded chip (Table 1) is between 2 and 4 times larger. This is partly because the impedance decreases faster shortly after insertion in PBS, but the presence of the chip also results in a poorer insulation.

In the case of parylene with nanolaminate, the impedance decreases quickly, but stabilizes around 1 GΩ. Even though the parylene insulation fails, the nanolaminate layer provides a barrier to prevent additional leakage. Compared to samples with parylene alone, the 1 GΩ impedance at 0.1 Hz mainly results from the thin nanolaminate dielectric layer, which displays a more capacitive characteristic. The phase is around −15° for parylene alone and around −45° for parylene/ceramic

Because active chips must be powered with voltages outside the electrochemical water window, the current will increase exponentially with voltage. Therefore relying on the small-signal impedance spectroscopy measurement does not guarantee that high currents might not happen at higher voltages. Cyclic voltammetry (CV) performed between −1.5 V and +1.5 V at a rate of 0.1 V/s verifies that nonlinear increases in current do not occur in the normal range of operation of CMOS chips. Fig. 8 shows that leakage currents for both parylene and parylene/ceramic are limited to 1.5 nA within the −0.9 V to +0.9 V supply range. The capacitive nature of the parylene/ceramic sample is apparent in the gap between the current measured when the applied potential is increasing compared to when the potential is decreasing.

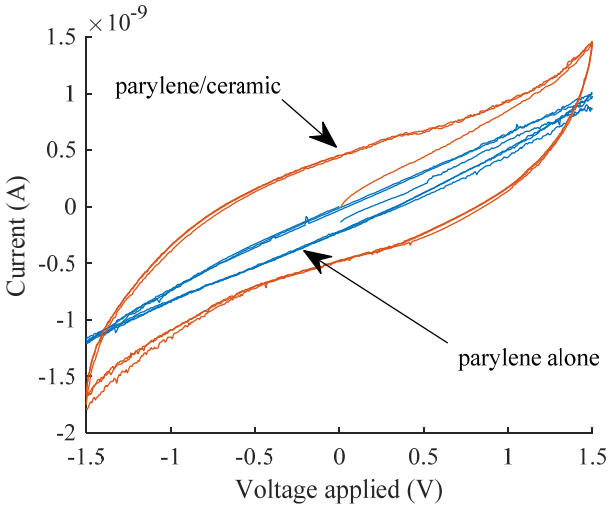

Figure 8: Cyclic voltammetry performed after 900 h in PBS on insulated traces including a bonded chip.

CONCLUSION

The insulation of parylene thin film structures on glass is improved by the addition of an ALD ceramic Al_2O_3/TiO_2 nanolaminate. The nanolaminate reduces the susceptibility of the samples to defects, enabling a five-fold reduction in failure rate. Additionally, it provides an additional barrier to leakage, resulting in a two-fold improvement in impedance decrease.

The high-performing insulation allows the development of probes containing active circuits. A simple process for integrating chips in parylene structures using ACF is demonstrated. The insulation performance is degraded when the chip is added, but leakage currents stay below 1.5 nA with ±0.9 V operation for over 900 h. The nanolaminate layer results in an impedance that is initially lower, but is more stable over long time periods. The results demonstrate that active chips embedded into parylene thin films can reliably operate for over a month.

Improvements in the fabrication process to increase the yield are underway: cracking in the insulation layers is thought to be caused by compliance mismatch between the rigid chip and the flexible layers; a gradual change in transition between the two regions can lower the stress at the interface. These measurements were performed on glass substrates; since compliant probes is a main application of parylene, measurement of insulation of released parylene structures is a logical next step.

ACKNOWLEDGEMENT

We thank Dr. Matt Moneck and his staff at the Carnegie Mellon Nanofabrication Facility for equipment and process support. Part of this work was sponsored by the Defense Advanced Research Projects Agency (DARPA) ElectRx Program under the auspices of Dr. Doug Weber through the Space and Naval Warfare Systems Center Contract No. HR0011-15-2-0009.

REFERENCES

[1] H. Yasuda, Q. . Yu, and M. Chen, "Interfacial factors in corrosion protection: an EIS study of model systems," *Prog. Org. Coatings*, vol. 41, no. 4, pp. 273–279, May 2001.

[2] W. Li, D. Rodger, P. Menon, and Y. Tai, "Corrosion behavior of parylene-metal-parylene thin films in saline," *ECS Trans.*, vol. 11, no. 18, pp. 1–6, 2008.

[3] J. Seymour, "Advanced polymer-based microfabricated neural probes using biologically driven designs," University of Michigan, 2009.

[4] J.-M. Hsu, L. Rieth, R. A. Normann, P. Tathireddy, and F. Solzbacher, "Encapsulation of an Integrated Neural Interface Device With Parylene C," *IEEE Trans. Biomed. Eng.*, vol. 56, no. 1, pp. 23–29, Jan. 2009.

[5] C. Hassler, R. P. von Metzen, P. Ruther, and T. Stieglitz, "Characterization of parylene C as an encapsulation material for implanted neural prostheses.," *J. Biomed. Mater. Res. B. Appl. Biomater.*, vol. 93, no. 1, pp. 266–74, Apr. 2010.

[6] R. P. von Metzen and T. Stieglitz, "The effects of annealing on mechanical, chemical, and physical properties and structural stability of Parylene C.," *Biomed. Microdevices*, vol. 15, no. 5, pp. 727–35, Oct. 2013.

[7] W. Chun, N. Chou, S. Cho, S. Yang, and S. Kim, "Evaluation of sub-micrometer parylene C films as an insulation layer using electrochemical impedance spectroscopy," *Prog. Org. Coatings*, vol. 77, no. 2, pp. 537–547, Feb. 2014.

[8] R. Caldwell, H. Mandal, R. Sharma, F. Solzbacher, P. Tathireddy, and L. Rieth, "Analysis of Al 2 O 3 - parylene C bilayer coatings and impact of microelectrode topography on long term stability of implantable neural arrays," *J. Neural Eng.*, vol. 14, no. 4, p. 46011, Aug. 2017.

[9] A. I. Abdulagatov, Y. Yan, J. R. Cooper, Y. Zhang, Z. M. Gibbs, A. S. Cavanagh, R. G. Yang, Y. C. Lee, and S. M. George, "Al2O3 and TiO2 atomic layer deposition on copper for water corrosion resistance.," *ACS Appl. Mater. Interfaces*, vol. 3, no. 12, pp. 4593–601, Dec. 2011.

[10] L. H. Kim, K. Kim, S. Park, Y. J. Jeong, H. Kim, D. S. Chung, S. H. Kim, and C. E. Park, "Al 2 O 3 /TiO 2 Nanolaminate Thin Film Encapsulation for Organic Thin Film Transistors via Plasma-Enhanced Atomic Layer Deposition," *ACS Appl. Mater. Interfaces*, vol. 6, no. 9, pp. 6731–6738, May 2014.

[11] X. Lei, S. Kane, S. Cogan, H. Lorach, L. Galambos, P. Huie, K. Mathieson, T. Kamins, J. Harris, and D. Palanker, "SiC protective coating for photovoltaic retinal prosthesis," *J. Neural Eng.*, vol. 13, no. 4, p. 46016, 2016.

[12] J. S. Ordonez, C. Boehler, M. Schuettler, and T. Stieglitz, "Improved polyimide thin-film electrodes for neural implants," *Proc. Annu. Int. Conf. IEEE Eng. Med. Biol. Soc. EMBS*, pp. 5134–5137, 2012.

[13] J. M. Herrera Morales, J.-C. Souriau, and G. Simon, "Corrosion Protection of Silicon Micro Systems with Ultra-Thin Barrier Films for Miniaturized Medical Devices," *ECS Trans.*, vol. 69, no. 26, pp. 9–26, Dec. 2015.

[14] S. F. Cogan, "Neural stimulation and recording electrodes.," *Annu. Rev. Biomed. Eng.*, vol. 10, pp. 275–309, Jan. 2008.

[15] W. Li, D. C. Rodger, E. Meng, J. D. Weiland, M. S. Humayun, and Y.-C. Tai, "Wafer-Level Parylene Packaging With Integrated RF Electronics for Wireless Retinal Prostheses," *J. Microelectromechanical Syst.*, vol. 19, no. 4, pp. 735–742, Aug. 2010.

CONTACT

*G. K. Fedder; tel: +1-412-268-8443; fedder@cmu.edu

NANOPRINTING OF MINIATURE COMPOUND REFRACTIVE LENSES FOR DESKTOP HARD X-RAY IMAGING

Mona Mirzaeimoghri [1,2], Alejandro Morales[1], Caroline McCue[2], Don L. DeVoe[2], Han Wen [1]
[1] Imaging Physics Laboratory, Biochemistry and Biophysics Center,
National Heart, Lung and Blood Institute, National Institute of Health, Bethesda, MD
[2] Dept. of Mechanical Engineering, University of Maryland, College Park, MD

ABSTRACT

Focusing hard x-rays for microscopy has been a long standing challenge. Compound refractive lens (CRL) technology represents one approach to addressing this challenge using series of lenses than can accumulate the small refraction of each lens. A novel fabrication approach using a two-photon laser photopolymerization system to pattern epoxy-based CRLs by direct 3D nanoprinting is utilized here to report the first instance of a nano-printed lens for hard x-ray microscopy, with evaluation of its imaging performance. The resulting lens technology was found to enable benchtop microscopy to image and assess the size and stability of the focal spots of tungsten-target micro-focus x-ray sources.

INTRODUCTION

Miniature X-ray optics can create new opportunities for compact imaging systems for use in science, medicine, and technology. Compared to visible light, x-rays have shorter wavelengths which give it the ability to penetrate deeper into matter, making them highly useful for applications in microanalysis and imaging where it is desirable to probe beyond the surface of the material under analysis. Focusing hard x-rays for microscopy has been a challenging task for decades, particularly for small-scale imaging systems. Focusing elements for x-ray microscopy for soft x-ray (<10 keV photon energy) include curved mirrors (Kirkpatrick-Baez) in benchtop microscopy [1], zone plates at 8 keV [2] and compound refractive lenses (CRL) which consist of linear arrays of individual refractive lenses [3]. However, complexity of fabrication and limitation of hard x-ray performance make it difficult to achieve an ideal form of focusing optics element.

Compound refractive lens (CRL) technology represents one approach to addressing this challenge that offers good efficiency and robustness by employing a series of focusing elements than can accumulate small refraction changes provided by each lens. Different kinds of linear CRL fabrication processes have been investigated, such as drilling an array of holes in an aluminum block [3] and using electron lithography or deep x-ray lithography to produce CRLs in silicon and polymer. However, two cylindrically-focused CRLs arranged perpendicular to each other are required to form a proper lens for microscopy, leading to directional aberration and doubling of length. A more elegant solution is a truly two-dimensional CRL. The idea has been demonstrated in the form micro-bubbles in epoxy [4], patterned planar lens structures [5],[6], and polymer based CRLs[7]. However, current limitations in the fabrication of 3D structures limit their use for soft 9 keV x-rays and long focal lengths of >10 cm.

Methods and Material

Design

In order to focus a beam to a spot, the exit wavefront should have a spherical profile (Figure 1). To obtain that profile, the beam passing through the polymer and air should have accumulated different phases. Due to fact that the refractive index of the x-ray is less than one, the wavefront is phase shifted forward inside the polymer. The profile of the lens should produce a spherically shaped wavefront. Referring to Fig. 1 the forward shift of the wave front at spherical radius R, for R << focal length f, should be

$$\Delta = \sqrt{R^2 + f^2} - f \approx f\left(1 + \frac{1}{2}\frac{R^2}{f^2}\right) - f = \frac{R^2}{2f} \quad (1)$$

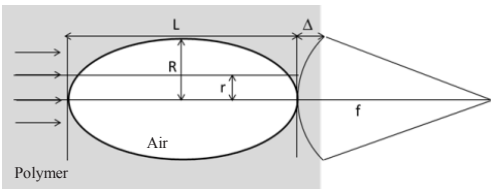

Figure 1. Refraction of a beam passing through a parabolic surface

The refractive index of the lens is n=1- δ, hence the maximum length (L) necessary for Δ is given by:

$$\delta L = \frac{R^2}{2f} \quad (2)$$

Similarly, for the rest of the structure, the beam equation can be written as:

$$L(r) = \frac{r^2}{2f\,\delta} \quad (3)$$

Which is a parabolic equation. For that reason, in order to produce the spherical wave, a parabolic lens is needed. Therefore, For a CRL made of a series of N concave lenses each having a parabolic surface of length l, the focal length is:

$$f = \frac{R^2}{2Nl\delta} \quad (4)$$

Fabrication

We present a fabrication process using a two-photon laser photopolymerization system to pattern epoxy-based CRLs by direct 3D nanoprinting. To fabricate the lenses, a droplet of photoresist (IP-DIP) was drop-casted on the edge of the 700 µm thick fused silica substrate. Micrometer-scale lenses were patterned in the resist by two-photon polymerization using a Nanoscribe instrument operated in immersion (DILL) mode with 30 mW power laser and 400 nm hatching distance and layer height, followed by 15 min immersion in PGMEA developer and 15 min post bake at 70°C.

Two different designs for one and two dimensional CRLs are explored in this paper. First is a new horizontal design in which a 16 blocks of cylindrical lens are placed end to end with a 5 µm gap between adjacent lens elements. The 5 µm gap served to eliminate the shadowing effect of the laser beam that occurred when writing separate blocks next to each other. Each block is 100 µm tall, 100 µm wide and 100 µm long, and consists of three columns of cylindrical ducts, with each column containing five cylindrical

978-1-940470-03-0/HH2018/$25©2018TRF
DOI 10.31438/trf.hh2018.79

ducts stacked horizontally. The cross-section of each duct is 6 μm wide and 9 μm deep (Figure 2). The x-rays pass through the lenses in parallel with the substrate and will be focused in one direction. This design eliminates the limitation of the height and stitching error Nanoscribe and no absorption will occur due to the substrate thickness (Figure 2).

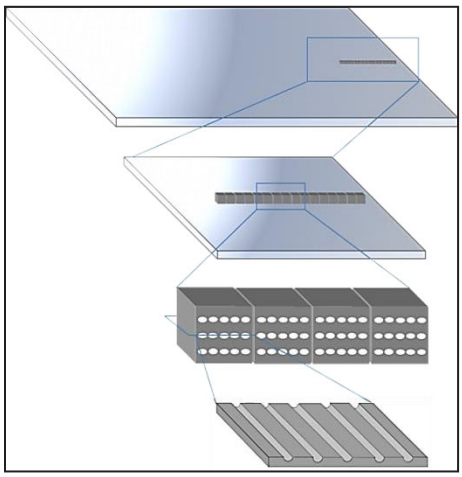

Figure 2. *Schematic of the horizontal one dimensional cylindrical CRL*

The second structure is a linear area of 32 concave lens blocks with 7 μm gap (Figure 3). Each block in this design is 100 μm tall, 100 μm wide, and 50 μm long, and contains an array of 3x3 parabolic indents at both the front and back. Each parabolic surface indent has a depth $\boldsymbol{l}$ of 24 μm and a radius $\boldsymbol{r}$ of 6 μm. This design provides 3x3 replicate CRL columns, giving 3x3 replicate images in the microscopy set up to allow measurements of variability among them. The x-rays pass through the lenses in parallel with the substrate and are focused in two dimensions. Based on the refractive index of the photosensitive polymer material, the focal length at 22 keV according to Eq. (4) is 21.5 mm.

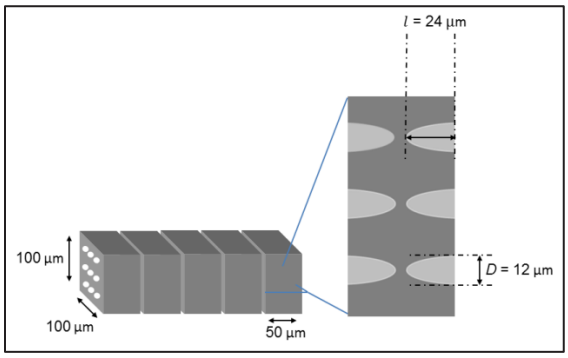

Figure 3. *Schematic of the horizontal two dimensional cylindrical CRL*

Scanning electron microscopy was used to inspect the CRL structures to verify the size of each blocks and the gap between adjacent them. SEM images of one and two dimensional CRLs are shown in Figure 4.

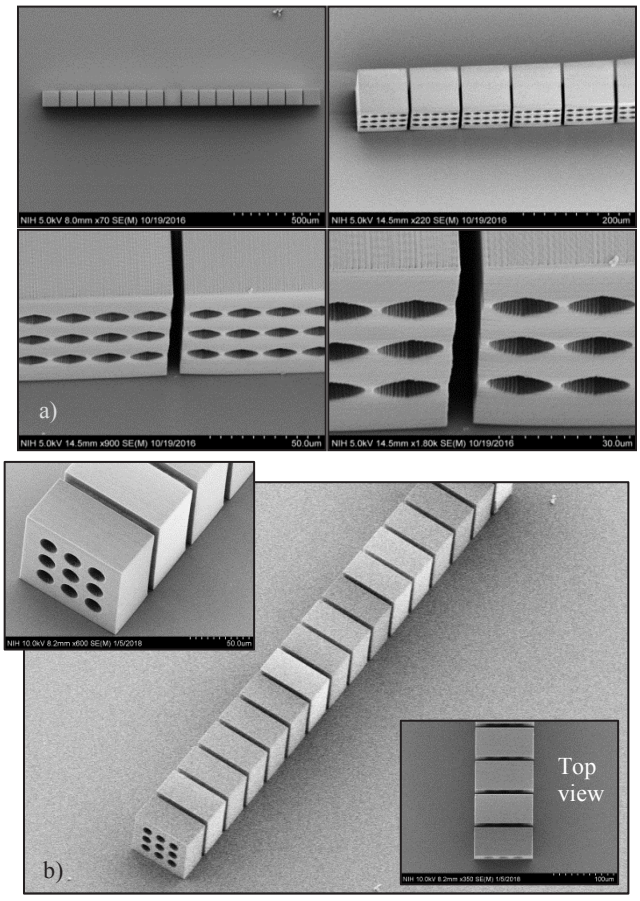

Figure 4. *Scanning electron microscopy images of the horizontal (a) one dimensional (b) two dimensional CRL.*

Results

Focusing the x-ray beam of a microCT scanner with cylindrical lenses

A micro-computed tomography (microCT) scanner was used to analyze the energy of the incident radiation and focusing performance of the lens. The Skyscan microCT provides an 11 Mp X-ray camera (12-bit cooled CCD fiber-optically coupled to scintillator) with a micropositioning stage, an array size of 4000x2000 pixels at the lowest binning, and a 5 μm source spot size with 20-100 kV source voltage and 10 W source power.

Figure 5 shows the focusing effect of the horizontal CRLs in the Skyscan system. The source is operated at 60 keV and 167 μA (10 W). The intensity of the x-ray beam is clearly enhanced while passing through the lenses. The maximum intensity is 250 (A.U.) and lens shows 67 % improvement in x-ray beam focusing effect.

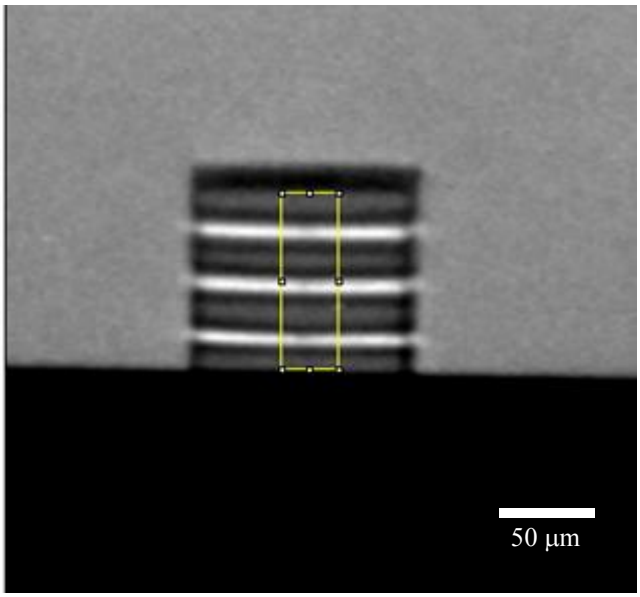

Figure 5. *Focusing effect in the cylindrical refractive lens.*

Microscopy Test

We used an experimental x-ray microscopy set up as illustrated in Figure 6, using the nano printed x-ray polymer lens as the magnifying lens. The imaged sample was a 4.8 µm period gold grating (Microworks, GmbH, Karlsruhe, Germany). The x-ray source is a fixed-anode, tungsten-target micro focus tube operating at 30 kVp/10 W (Oxford UltraBright 96004, Oxford Instruments, Oxfordshire, United Kingdom), with an average focal spot size of 13.37 ± 0.35 µm. An indirect flat panel radiography detector with a pixel size of 83 µm (PaxScan 3024M, Varian, CA, USA) was used to image the grating. The geometric distances were L_1 = 10 mm from the source to the sample, $L_2 - L_1$= 20 mm from the sample to the lens, and $L_3 - L_2$ = 1640 mm from the lens to the detector.

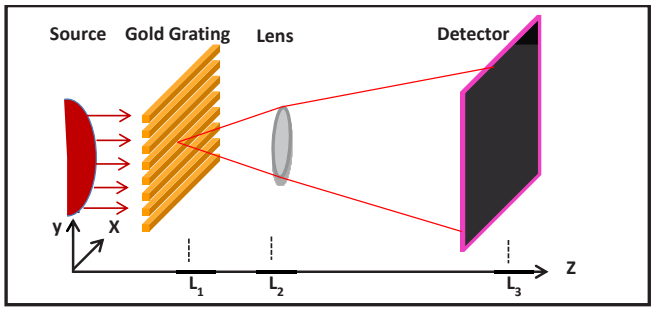

Figure 6. *The cone beam from an X-ray tube is exposed to the grating and the diffracted beams are detected at the detector after focusing on the object and passing through the lens.*

The gratings were magnified by a factor of $(L_3-L_2)/(L_2-L_1)$ = 82 (Figure 7). The vertical field of view of each CRL approached the 25 µm spacing between them. As a result the three groups of grating lines appear to connect with each other. Outside the lens area, direct geometric projection was not able to resolve the grating lines due to the fact that the size of the x-ray tube focal spot is nearly three times the grating period.

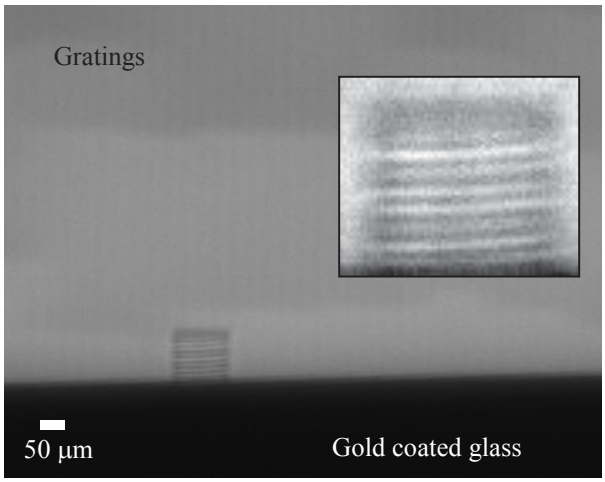

Figure 7. *Magnified image of the 4.8* ***µ****m grating using the micron-scale CRL arrays with 19 mm focal length, 82x magnification.*

Imaging and evaluation of x-ray focal spots with the concave CRL

Benchtop imaging of the x-ray focal spot was achieved, and direct study of the lens using the Gaussian fit was provided (Figure 8). The micro-focus x-ray source (Thermo Scientific Kevex) was studied at a range of tube kV settings and a range of sample-to-lens distances (SLDs) in the imaging setup.

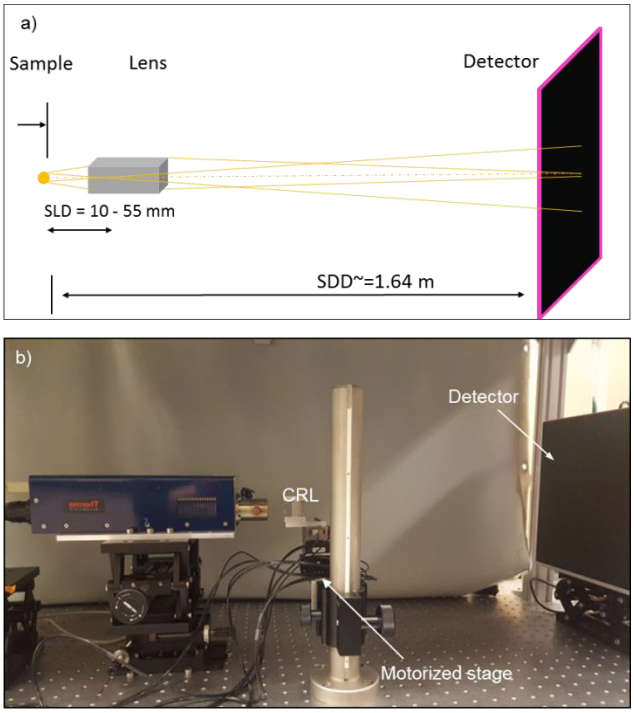

Figure 8. *(a) A schematic of the x-ray microscopy setup for imaging the focal spots of x-ray sources.* ***(b)*** *In this photograph of an imaging experiment, the focal spot of a tungsten-target micro-focus source was being imaged.*

The nanofabricated CRL was able to focus the x-ray beam (Figure 9) to exceptionally small length scales as small as 19 mm,

and maintained focusing at x-ray tube voltages from 25 kV up to 85 kV (Figure 10). Images of the x-ray tube focal spot at 80x magnification were acquired in seconds. An imaging spot size of 5 μm was measured.

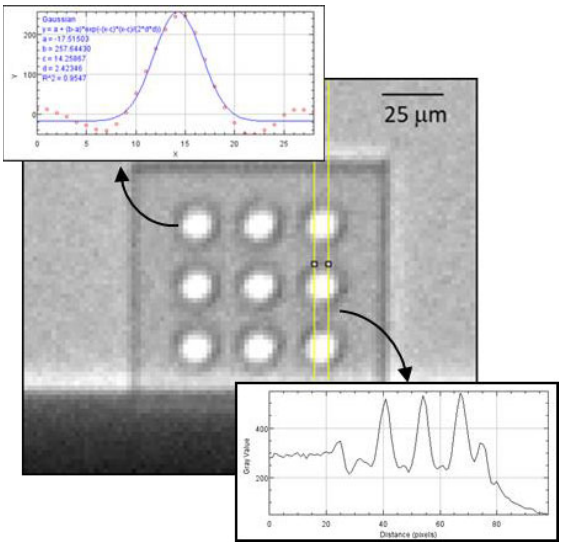

Figure 9. *Microscopy image of the 5 μm focal spot size of the x-ray source.*

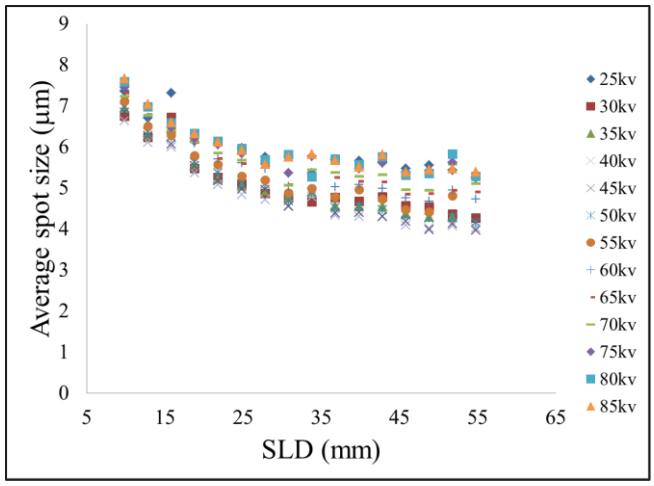

Figure 10. *A plot of the average measured focal spot size and standard deviation over the scanned range of SLDs. The standard deviations were < 0.14 μm for all measurements.*

Discussion

The results demonstrate that sub-micrometer resolution 3D printing based on two-photon photopolymerization is suitable for producing miniature compound refractive lenses for hard x-rays. The fabricated CRL devices offer the smallest size and shortest focal length that has been reported in the literature for operation with photons in the range of 10s of keVs. The devices were able to successfully achieve 19 mm focal length and 1.1 μm pixel resolution. The polymer lens arrays were also shown to be capable of maintaining focus over a range of x-ray tube voltages from 25 kV to 85 kV, and enabling rapid imaging and assessment of the focal spots of tungsten-anode x-ray tubes at up to 159x magnification.

The measured focal spot size of the x-ray source decreased gradually with increasing SLD, even beyond the designed focal distance (Figure 11). We speculate two possible reasons for the trend. One is that at large SLDs/low magnification, each detector pixel covers a larger area of the focal spot, leading to increasing under-sampling of the spot profile and possible systematic under-estimation of the width of the underlying profile. Another possible reason was that the higher parts of the x-ray spectrum (> 22keV) continually come into focus with increasing SLD.

The fabrication time is significantly shorter than the previously reported techniques so that a structure as tall as 1.5 mm can be written in 2 hours. The nanoprinted lens technology is expected to enable novel benchtop x-ray imaging systems for industrial, material science and medical applications.

References

[1] Jach T, Durbin SM, Bakulin A, et al. Wide-field x-ray microscopy with Kirkpatrick-Baez optics. In: McNulty I (ed). International Society for Optics and Photonics, pp. 38–44.

[2] Gary CK, Park H, Lombardo LW, et al. High resolution x-ray microscope. *Appl Phys Lett*; 90. Epub ahead of print 2007. DOI: 10.1063/1.2734895.

[3] Snigirev A, Kohn V, Snigireva I, et al. A compound refractive lens for focusing high-energy X-rays. *Nature* 1996; 384: 49–51.

[4] Dudchik YI, Komarov FF, Piestrup MA, et al. Using of a microcapillary refractive X-ray lens for focusing and imaging. *Spectrochim Acta - Part B At Spectrosc* 2007; 62: 598–602.

[5] Terentyev S, Polikarpov M, Snigireva I, et al. Linear parabolic single-crystal diamond refractive lenses for synchrotron X-ray sources. In: *Journal of Synchrotron Radiation*. 2017, pp. 103–109.

[6] Aristov V V., Grigoriev M V., Kuznetsov SM, et al. X-ray focusing by planar parabolic refractive lenses made of silicon. *Opt Commun* 2000; 177: 33–38.

[7] Etrov AKP, Essonov VOB, Brashitova KAA, et al. Polymer X-ray refractive nano-lenses fabricated by additive technology. 2017; 25: 3256–3259.

NANOSTENCIL FABRICATION WITH DOUBLE EXPOSURE OPTICAL LITHOGRAPHY FOR SCALABLE RESIST-FREE PATTERNING OF METAL ON POLYMERS

Joseph S. Katz[1], Woosung Park[2], Michael T. Barako[3], Aditya Sood[4], Mehdi Asheghi[2], and Kenneth E. Goodson[2]*
[1]Department of Electrical Engineering, Stanford University, Stanford, California, USA
[2]Department of Mechanical Engineering, Stanford University, Stanford, California, USA
[3]NG Next Basic Research laboratory, Northrop Grumman Corporation, Redondo Beach, CA
[4]Department of Materials Science and Engineering, Stanford University, Stanford, California, USA

ABSTRACT

Engineers require scalable processes for patterning nanoscale features on sensitive substrates to enable widespread manufacturability of advanced nanoelectronics. Nanostencils have shown promise, but prior work has relied on electron-beam (e-beam) and focused ion beam (FIB) processes. Nanostencils also frequently exhibit significant edge roughness. Here, we present a fabrication process for nanostencils using double exposure optical lithography and a novel capillary-driven lamination technique to reduce edge blurring, demonstrating sub-diffraction limit features of ~200nm on poly(methyl methacrylate) films. We demonstrate the utility of these stencils by generating metal patterns for use with the 3ω thermal conductivity measurement technique. We find a thermal conductivity of 0.24 $Wm^{-1}K^{-1}$ and an anisotropy ratio of 9.7. This work demonstrates that nanostencils can be used for scalable, resist-free patterning of nanoscale features on sensitive substrates.

INTRODUCTION

Traditional photolithography and patterning often requires exposure to caustic chemicals, high temperatures, and/or plasmas, which can damage non-traditional materials for heterogeneous integration applications, such as gate dielectrics [1], organic materials [2] (e.g. BEOL processes [3]), and 2D materials [4]. In particular, organic materials are commonly used in electronics packaging but are often thermally limiting, leading the research community to seek polymers with increased thermal conductivity. The 3ω method, a common thermal characterization technique, is well suited for studying polymers because it can be used on thin films and can distinguish between thermal conduction in multiple directions [5-6]. Although useful, the 3ω method has been difficult to implement with polymers due to the requirement of metal patterning and the incompatibility of many polymers with standard microfabrication techniques.

Nanostencils have shown promise as a method of decoupling damaging fabrication processes from sensitive materials by evaporating metals and other materials through nanoscale apertures in contact with the surface [7-8]. Stencils with sub-micron features are generally fabricated using FIB or e-beam lithography, which are slow and costly, so it is valuable to improve manufacturability.

Another key issue for nanostencils is that the gap between the substrate and membrane causes edge blurring. Ingle used a magnetic shadow mask and a magnet to pull the mask closer to the substrate to reduce the size of the penumbra [9]. Sidler *et al.* reported that compliant membranes showed reduced penumbra due to the ability of the membrane to follow the surface topography, including non-ideal roughness [10].

Here, we describe a scalable fabrication platform for nanostencil devices using double exposure optical lithography. We employ a novel capillary-driven lamination technique to bring the membranes into intimate contact with the substrates.

We have used these stencils to fabricate platinum features as small as 200 nm on poly(methyl methacrylate) (PMMA) films without e-beam or FIB patterning, offering the first demonstration of manufacturing sub-diffraction limit stencils with double exposure optical lithography. We have also used the stencils to fabricate test structures for 3ω thermal conductivity measurements. Our measurements of a 170nm thin spin-cast PMMA sample show a through-plane thermal conductivity of 0.24 $Wm^{-1}K^{-1}$, and nearly an order of magnitude anisotropy. The strong anisotropy, favoring in-plane thermal conduction, is due to the alignment of polymer chains during viscous shearing while spin coating. Kurabayashi *et al.* observed this phenomenon in spin-cast polyimide films [11]. This work extends prior work by Kurabayashi *et al.* by reporting a higher anisotropy ratio in a thinner film. Due to the high anisotropy ratio, heaters nearly an order of magnitude wider than the film thickness demonstrate significant sensitivity to anisotropy.

FABRICATION

Stencil Fabrication

The process for fabricating the nanostencils is shown in fig. 1, from top to bottom. First, silicon wafers are coated with 500 nm low stress LPCVD silicon nitride and annealed at 1100°C for three hours to further reduce film stress. Next, the back side is coated with 0.7 μm SPR-955 photoresist, exposed in an ASML PAS5500 stepper, and developed with MF-26A developer. The nitride is partially etched in CF_4 plasma using a PlasmaTherm Versaline LL ICP etcher. The resist is then stripped, and the lithography process repeated with a shift in the exposed features depending on the desired final aperture size. The exposed nitride is etched such that only the part of the film that was etched both times is completely removed. Fig. 2a shows a cross sectional SEM of a trench patterned with this double exposure technique. The top-side nitride is similarly patterned with contact lithography and no double exposure due to the coarse features.

The silicon is etched from the top side using KOH, and the membranes are left suspended with patterned apertures. In some cases, a thin nitride layer remains at the bottom of the features if the etch did not penetrate deep enough into the narrow gaps. In these cases, another CF_4 etching step is done after the KOH etch, with the membranes facing a carrier wafer, to fully open the apertures.

Stencil-Based Device Fabrication

The process for fabricating 3ω thermal conductivity measurement devices is shown in fig. 1, from left to right along the bottom. PMMA is spin coated from an anisole solution onto an oxidized silicon substrate and baked to remove the solvent.

The first stencil layer is used to pattern the polymer film such that there are areas for contact pads to be placed directly on the oxidized silicon substrate; this is done because metal pads for electrical contact are damaged by probes scratching through them when the pads are on a soft polymer film. To protect the desired sample area, an aluminum hard mask layer is deposited through the

978-1-940470-03-0/HH2018/$25©2018TRF
DOI 10.31438/trf.hh2018.80

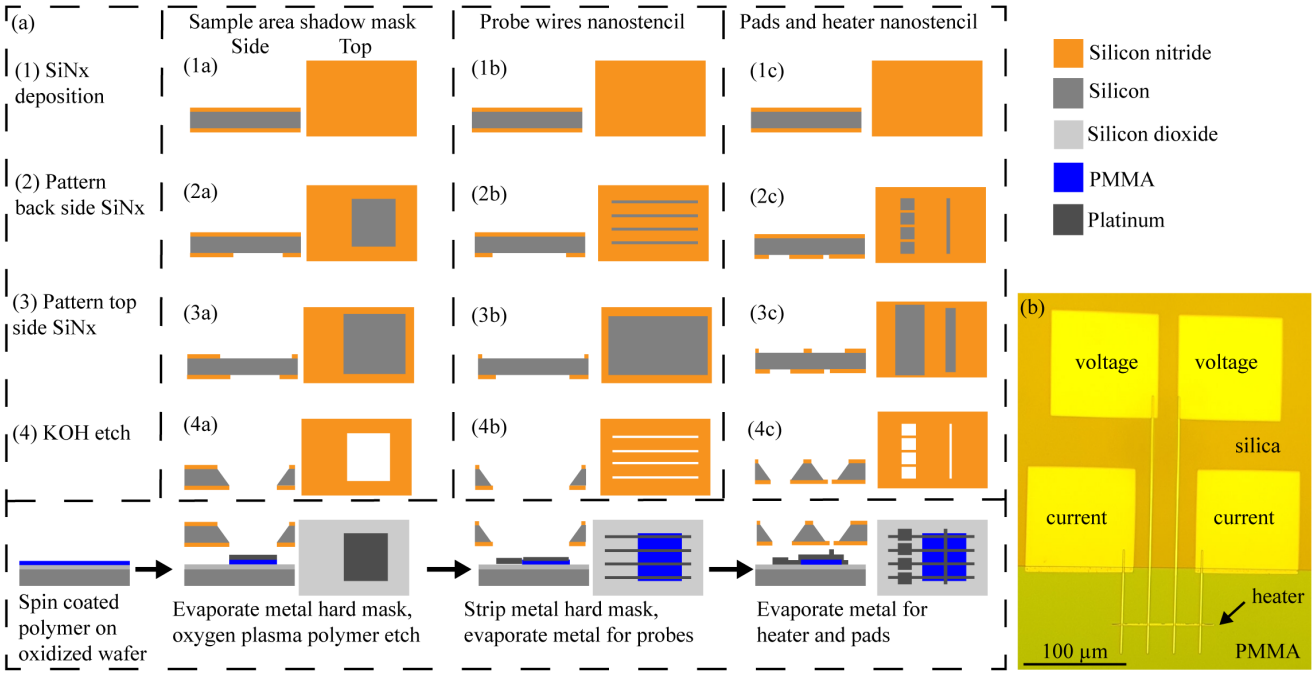

Figure 1: (a) process flow to produce stencils (top to bottom, three separate columns for three different stencil patterns) and corresponding 3ω devices (bottom left to bottom right), (b) completed 3ω device.

first stencil. Next, the polymer not protected by aluminum is etched using oxygen plasma. The aluminum is then stripped, leaving a patterned PMMA film.

The second stencil, which consists of lines going from the sample polymer area to the bare oxidized silicon area for pads, is attached to the substrate. The wafer is held over a beaker of boiling water for a few seconds so that a thin layer of condensate forms on the substrate and membranes. The wafer is then blow dried with compressed air, and the capillary forces from the drying process draws the membrane into intimate contact with the substrate. Next, platinum, with a titanium adhesion layer, is evaporated through the second stencil to form probe lines bridging from the bare, oxidized silicon substrate up to the top of the PMMA film.

The third stencil layer follows an identical process to the second with different feature patterns. The third stencil is used to form the platinum line, to act as heater and thermometer for the 3ω measurement, and pads for electrical contact.

Examples of stencils and corresponding platinum features on PMMA are shown in fig. 2. The difference in edge blurring between fig. 2e and fig. 2f highlights the effectiveness of the capillary-driven lamination in reducing the significance of this phenomenon.

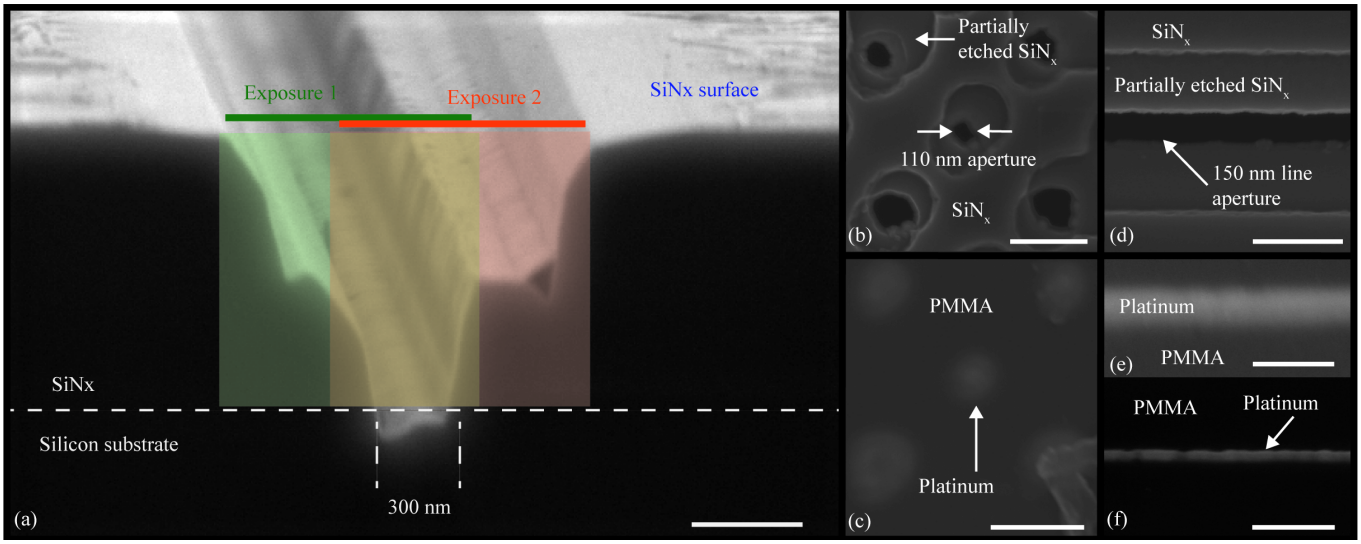

Figure 2: (a) cross section of etched SiNx film before being suspended, showing double exposure, (b) etched membrane with dot apertures and (c) corresponding platinum dots on PMMA, (d) etched membrane with line aperture and (e) corresponding platinum line on PMMA, (f) minimal edge blurring in platinum line on PMMA when using capillary-driven membrane lamination. All scale bars are 500nm.

Fabrication Repeatability

Processes involving multiple exposures and/or etching steps per layer directly on the primary substrate, have long been used in industry for devices with feature sizes well below the diffraction limit [12], and are very repeatable. In contrast, edge blurring is often severe in nanostencil lithography and detrimental in many applications, including in 3ω devices because the heater width affects the sensitivity to anisotropy and the heat source is typically assumed to be uniform with a precise boundary. Capillary-driven lamination, described above, substantially reduced the significance of edge blurring; however, there is still edge roughness and variation along the length of the line, as shown in fig. 3a. Edge roughness in the metal features may be due to edge roughness in the corresponding stencils, which is visible in fig. 2b & d. It is also possible that the evaporating water left residue at the edges of the features. Signs of residue are observed in fig. 3a.

In some cases, a combination of stencil defects, edge residue, and mechanical abrasion from lifting the stencils after deposition causes discontinuities in deposited lines, as highlighted by the differences between fig. 3b and fig. 3c. In the narrowest lines used for process debugging, ~200nm, there were often lines with many discontinuities, e.g. fig. 3d. The narrowest device used for a 3ω measurement in this paper was 1.4 μm, so the edge roughness of ~50nm is substantially smaller than the heater widths used for measurements reported here.

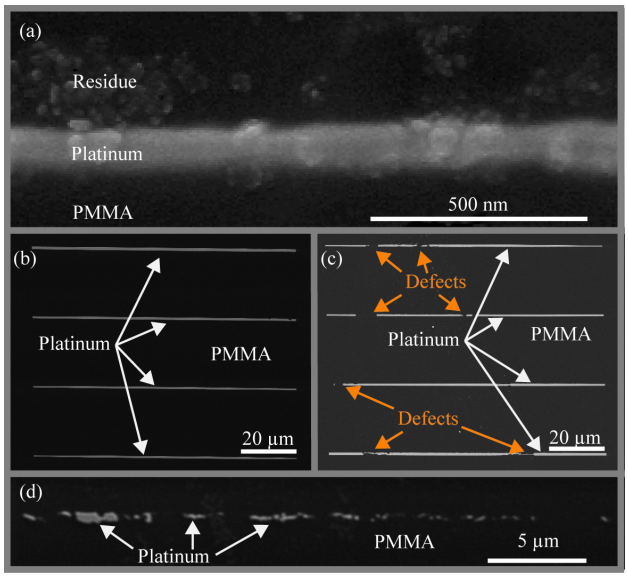

Figure 3: (a) SEM of platinum line with residue, (b) SEM of platinum lines on PMMA, (c) SEM of platinum lines with discontinuities on PMMA, (d) SEM of narrow platinum line with many discontinuities on PMMA.

3ω THERMAL CONDUCTIVITY MEASUREMENT

Experimental method

The 3ω method is a Joule heating technique that relies on the linear relationship between temperature and resistance of a single metal line acting as both a heater and a thermometer. A sinusoidal current is applied at a frequency, 1ω, which causes a power dissipation at frequency 2ω. Power dissipation causes temperature oscillations at the same frequency, which in turn causes resistance oscillations. The product of the 1ω current and 2ω resistance is a voltage at 3ω, which is a function of the temperature rise, and thus the thermal properties of the sample material. The details of the 3ω method have been described extensively in literature [9-10].

Sensitivity Analysis

Sensitivity is defined as a fractional change in a measured parameter divided by the fractional perturbation in the sensed variable that caused the change. The through-plane and in-plane thermal conductivity sensitivities are, respectively,

$$S_{k_z} = \frac{\partial \Delta T}{\Delta T} \Big/ \frac{\partial k_z}{k_z} \qquad (1a)$$

$$S_{k_x} = \frac{\partial \Delta T}{\Delta T} \Big/ \frac{\partial k_x}{k_x} \qquad (1b)$$

$$S_w = \frac{\partial \Delta T}{\Delta T} \Big/ \frac{\partial w}{w} \qquad (1c)$$

$$S_{TCR} = \frac{\partial \Delta T}{\Delta T} \Big/ \frac{\partial TCR}{TCR} \qquad (1d)$$

where ΔT is the measured temperature rise over ambient, k is the thermal conductivity in the direction indicated by the subscript, w is the heater width, and TCR is the temperature coefficient of resistance (S_{TCR} is unity).

Wide heaters cause predominantly through-plane thermal conduction and are thus mainly sensitive to through-plane thermal conductivity. Narrower heaters cause substantial conduction both through and within the film, so they can be sensitive to in-plane conductivity. This phenomenon is illustrated in the inset of fig. 4.

To determine the sensitivities numerically, we use a model based on the harmonic line heater solution by Feldman [13]. A fractional perturbation, ∂k/k, of 0.01 is used for both k_x and k_z sensitivity calculations. Fig. 4 shows the sensitivity to through-plane and in-plane thermal conductivity versus heater width for the sample considered in this study, and nominal conductivity values of k_z = 0.24 $Wm^{-1}K^{-1}$ and k_x = 2.33 $Wm^{-1}K^{-1}$, as measured. While narrower heaters would be more sensitive, the 1.4 μm heater width used in this study shows appreciable anisotropy sensitivity.

Thermal Measurement Results

The spin cast PMMA demonstrates high thermal conductivity anisotropy, which is consistent with the expectation for a high degree of backbone alignment. The measured results are presented in fig. 5, alongside polyimide data from ref. [11].

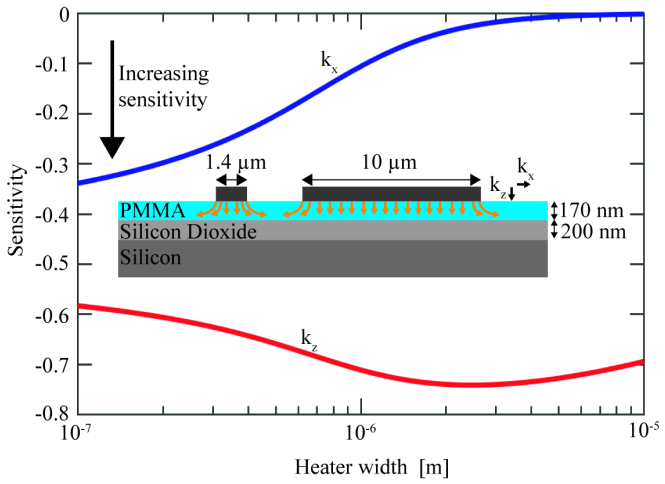

Figure 4: Sensitivity versus heater width for both k_x (blue) and k_z (red). Inset: heater cross section schematic showing both in-plane and through-plane heat conduction for a narrow heater but primarily through-plane conduction for a wide heater.

The measured through-plane thermal conductivity is 0.24 ± 0.005 $Wm^{-1}K^{-1}$, which is within the commonly accepted range of values for bulk PMMA thermal conductivity. The in-plane conductivity is 2.33 ± 1.55 $Wm^{-1}K^{-1}$, corresponding to an anisotropy ratio of 9.7 from polymer backbone alignment. The heaters are oriented orthogonally to the radius of the wafer, so the measured thermal conductivities are the vertical and radial conductivities.

Uncertainty is calculated using a sum of squares approach:

$$\sigma_{k_z} = \frac{k_z}{S_{k_z}} \sqrt{(S_{TCR} \frac{\sigma_{TCR}}{TCR})^2 + (S_w \frac{\sigma_w}{w})^2} \quad (2)$$

Through-plane conductivity is an input for in-plane conductivity calculation, so in-plane uncertainty is

$$\sigma_{k_x} = \frac{k_x}{S_{k_x}} \sqrt{(S_{TCR} \frac{\sigma_{TCR}}{TCR})^2 + (S_w \frac{\sigma_w}{w})^2 + (S_{kz} \frac{\sigma_{k_z}}{k_z})^2} \quad (3)$$

We assume a 1% uncertainty in TCR and 50nm uncertainty in heater width. Anisotropy uncertainty can be lowered with narrower heaters, and with more heaters and multi-parameter fitting [14].

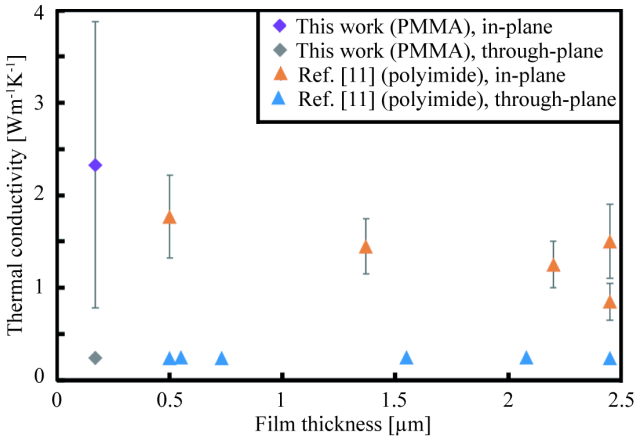

Figure 5: Measured in- and through-plane thermal conductivity.

CONCLUSIONS

We have demonstrated that nanostencils can be fabricated using double exposure optical lithography as a scalable platform for resist-free patterning of nanoscale features on polymers and other sensitive substrates. We have deposited platinum features of ~200 nm on PMMA films. We have used the stencils to fabricate measurement structures for a 3ω thermal conductivity measurement of a 170nm spin-cast PMMA film, and report a thermal conductivity anisotropy ratio of 9.7, favoring in-plane conduction.

ACKNOWLEDGEMENTS

J.S.K. thanks the Semiconductor Research Corporation (SRC) and the Intel Education Alliance for a Graduate Research Fellowship. This work was supported by the SRC through GRC task 2666. Work was performed in part in the nano@Stanford labs, which are supported by the National Science Foundation as part of the National Nanotechnology Coordinated Infrastructure under award ECCS-1542152. The authors are grateful to the process staff at the SNF and Prof. Yan Xia in the Department of Chemistry at Stanford for helpful discussions.

REFERENCES

[1] C.J. Brennan, C.M. Neumann, and S.A. Vitale, "Comparison of Gate Dielectric Plasma Damage from Plasma-Enhanced Atomic Layer Deposited and Magnetron Sputtered TiN Metal Gates", Journal of Applied Physics, 118, 045307 (2015).

[2] H.-K. Kim, D.-G. Kim, K.-S. Lee, M.-S. Huh, S. H. Jeong, K. I. Kim, and T.-Y. Seong, "Plasma Damage-Free Sputtering of Indium Tin Oxide Cathode Layers for Top-Emitting Organic Light-Emitting Diodes", Applied Physics Letters, 86, 183503 (2005).

[3] R. Mahajan, R. Sankman, N. Patel, D.-W. Kim, K. Aygun, Z. Qian, Y. Mekonnen, I. Salama, S. Sharan, D. Iyengar, and D. Mallik, "Embedded Multi-Die Interconnect Bridge (EMIB) – A High Density, High Bandwidth Packaging Interconnect", Proceedings of the 2016 IEEE 66th Electronic Components and Technology Conference (ECTC), Las Vegas, NV, 5/31-6/3/16, Institute of Electrical and Electronics Engineers, Piscataway (2016), pp. 557-565.

[4] H.S. Song, S.L. Li, H. Miyazaki, S. Sato, K. Hayashi, A. Yamada, N. Yokoyama, and K. Tsukagoshi, "Origin of the Relatively Low Transport Mobility of Graphene Grown through Chemical Vapor Deposition", Scientific Reports, 2, 337 (2012).

[5] D.G. Cahill, "Thermal Conductivity Measurement from 30 to 750K: the 3ω Method", Review of Scientific Instruments, 61, 802 (1990).

[6] C. Dames, and G. Chen, "1ω, 2ω, and 3ω Methods for Measurement of Thermal Properties", Review of Scientific Instruments, 76, 124902 (2005).

[7] J. Brugger, J.W. Berenschot, S. Kuiper, W. Nijdam, B. Otter, and M. Elwenspoek, "Resistless Patterning of Sub-Micron Structures by Evaporation through Nanostencils", Microelectronic Engineering, 53, 403, (2000).

[8] O. Vazquez-Mena, L. Gross, S. Xie, L.G. Villanueva, and J. Brugger, "Resistless Nanofabrication by Stencil Lithography: A Review", Microelectronic Engineering, 132, 236 (2015).

[9] F. W. Ingle, "A Shadow Mask for Sputtered Films", Review of Scientific Instruments, 45, 1460 (1974).

[10] K. Sidler, L.G. Villanueva, O. Vazquez-Mena, V. Savu, and J. Brugger, "Compliant Membranes Improve Resolution in Full-Wafer Micro/Nanostencil Lithography", Nanoscale, 4, 773 (2012).

[11] K. Kurabayashi, M. Asheghi, M. Touzelbaev, and K.E. Goodson, "Measurement of the Thermal Conductivity Anisotropy in Polyimide Films", IEEE Journal of Microelectromechanical Systems, 8, 2 (1999).

[12] M. Maenhoudt, J. Versluijs, H. Struyf, J. Van Olmen, and M. Van Hove, "Double Patterning Scheme for Sub-0.25 k1 Single Damascene Structures and NA=0.75, λ=193nm", Proceedings of SPIE 5754 Optical Microlithography XVII, San Jose, CA, 5/12/04, Society of Photo-Optical Instrumentation Engineers, Bellingham (2004), pp. 1508-1518.

[13] A. Feldman, "Algorithm for Solutions of the Thermal Diffusion Equation in a Stratified Medium with a Modulated Heating Source", High Temperatures High Pressures, 31, 293 (1999).

[14] J.S. Katz, M.T. Barako, W. Park, A. Sood, M. Ashaeghi, K.E. Goodson, "Highly Anisotropic Thermal Conductivity in Spin-Cast Polystyrene Nano-Films", Proceedings of the 2018 17th IEEE Intersociety Conference on Thermal and Thermomechanical Phenomena in Electronic Systems (ITherm), San Diego, CA, 5/29-6/1/18, Institute of Electrical and Electronics Engineers, Piscataway (2018).

CONTACT

*K. E. Goodson, tel: +1-650-725-2086; goodson@stanford.edu

NOVEL ROOM TEMPERATURE MICROFLUIDIC DEVICE FABRICATION: A HIGH-RESOLUTION, 3D PRINTING APPROACH USING ELECTROHYDRODYNAMIC JET PRINTING

Christopher Pannier[1], Zhi Wang[2], David Hoelzle[3], and Kira Barton[1]*
[1]University of Michigan, Ann Arbor, Michigan, USA
[2]University of Notre Dame, Notre Dame, Indiana, USA
[3]The Ohio State University, Columbus, Ohio, USA

ABSTRACT

For the first time, electrohydrodynamic-jet printing is used to fully fabricate a microfluidic device, achieving higher resolution (<20 µm channel width) and increased build material diversity compared to fully fabricating microfluidic devices by inkjet printing. This process is conducted at room temperature, making possible the inclusion of temperature-sensitive build materials during fabrication. A prototypical resistive pulse sensor (Coulter counter) is designed and printed to demonstrate the process. In the sensor, printed electronics are leveraged in the form of chemically sintered silver ink. Microfluidic channels are defined by a printed water-soluble polymer channel mold that is later washed away. Channel profiles are measured during fabrication, and channel profile shaping is demonstrated using an alternative, UV curable, channel mold material.

INTRODUCTION

Microfluidic devices have emerged as critical chemical, biological, and clinical instruments. The conventional microfluidic device fabrication processes, photolithography and soft lithography, have limited prototyping and customization capabilities due to the requirement of generating a photomask or mold for each device geometry change. Additionally, conventional processes use high-temperatures that preclude the incorporation of temperature-sensitive biomaterials and chemistries in device construction. Additive manufacturing (AM) of microfluidic devices offers rapid design iteration for prototyping and customization, with reduced fixed costs [1, 2]. The AM-fabricated microfluidic device resolution and build material diversity depend on the particular AM process. Recently, fully inkjet printed microfluidic devices have been demonstrated with 60 µm minimum channel width [3]. The devices were built from SU-8 epoxy build material, and had a maximum process temperature of 150ºC. Fully 3D printing a microfluidic device at room temperature with higher viscosity materials at a higher resolution than inkjet printing would be a key enabler for advancing the potential of bioprinting microfluidic devices.

One candidate AM process for improved 3D printing of microfluidic devices is electrohydrodynamic-jet (abbreviated here as e-jet, although some authors use EHD-jet) printing [4], which has demonstrated sub-100 nm resolution capability [5], and 3 orders of magnitude larger build material viscosities than inkjet printing [6]. E-jet printed applications include electronic sensors, bioassays, and bio-sensors [5, 6]. In contrast to other jet-based printing techniques, e-jet uses an *electric field* to initiate drop ejection. A high voltage, typically between 200 V and 2000 V, is applied to a conductive microcapillary nozzle of tip diameter between 100 nm and 30 µm held at a small standoff height, typically 10 µm to 200 µm above the substrate, as shown in the inset of Fig. 1. The resulting electric field focuses the liquid meniscus into a conical shape, termed a Taylor cone, from which build material is ejected.

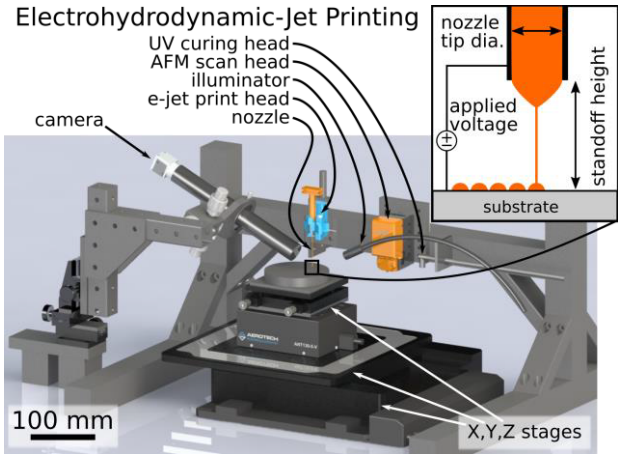

Figure 1: Rendering of the integrated e-jet/AFM system used for fully fabricating microfluidic devices. Inset is a schematic showing e-jet printing with key printing parameters.

Coordinated motion and jetting enable the printing of drops, lines, and layers onto a substrate. Build material is solidified by physical processes such as solvent evaporation, sintering, or UV curing. Successive deposition and solidification enable the fabrication of 3D microscale topographies [7, 8].

This work demonstrates the first use of e-jet printing to fully fabricate a microfluidic device entirely at room temperature. Full fabrication means that there are no spin coating or molding steps. The substrate is removed from the printer for a washing step at the end of the process. Printing, UV curing, and atomic force microscope (AFM) scanning is performed on the integrated e-jet/AFM system housed at the University of Michigan [9], shown in Fig. 1. The use of e-jet printing greatly expands the available material diversity and resolution capability (<20 µm) of jet printed microfluidic sensors.

The paper is organized as follows: The processes required to fully e-jet print a microfluidic device incorporating sensor electrodes and channels are selected and described in Process Design. The selection of a resistive pulse sensor (Coulter counter) as a demonstrative microfluidic device is described in Device Design. Printing steps and materials are reported in Experimental Methods. Achieved microfluidic channel geometry, improved channel resolution, and channel profile shaping are demonstrated in Results and Discussion. Finally conclusions and directions for future work are presented in Conclusion.

PROCESS DESIGN

Room Temperature Processing

Two challenging features for jet printing a microfluidic device are the covered microfluidic channel, which is a void supporting a

978-1-940470-03-0/HH2018/$25©2018TRF
DOI 10.31438/trf.hh2018.81

channel wall, and the electrode, which must contact the microfluidic channel for sensing. The process design for forming channels and electrodes is key to fully realizing e-jet printing of a device at room temperature. Channels are produced by printing support material as a positive mold that is later dissolved. Electrodes are printed by leveraging a chemical sintering system from inkjet printed electronics.

A popular AM technique for producing voids is printing overhanging material with a printed dissolvable support material. A dissolvable support approach to printing microfluidic channels is taken in [3] by printing a build material solution of poly(methyl methacrylate) (PMMA) in anisole and dimethyl sulfoxide (DMSO). After printing, the solvent evaporates from the 40ºC heated substrate and a subsequent 120ºC hotplate solvent evaporation step. However, to achieve the room-temperature processing constraint proposed in this work, a dissolvable positive mold is printed using polyvinylpyrrolidone (PVP) in water and glycerol. In this approach, the bottom of the channel takes the shape of the already-printed layer. Next, the dissolvable material is printed to act as a positive mold for the channel. Subsequently, a non-dissolvable top layer is printed to cover the channel mold. The channel mold is dissolved in a solvent bath at the completion of the printed layers.

A common route to printed electronics, metal nanoparticle inks sintered after deposition, is used in this work. Thermally driven sintering at process temperatures of 80ºC or higher is a standard sintering technique. Recently, room temperature chemical sintering has become commercially available for inkjet printable silver nanoparticle inks with instantly sintered sheet resistance within a factor of 4 of equivalent dimension copper trace sheet resistance [10]. Chemical sintering of these inks require a porous, chemical coating that is commercially available on polyethylene terephthalate (PET) film and glossy inkjet photo paper substrates. To meet the room temperature processing requirement, chemical sintering is used instead of thermal sintering in this work.

It is undesirable to locate a channel on a porous coating as leakage may result. Hence, an isolation layer is printed beneath the channel, except in the locations where electrode contact with a channel is desired. From bottom to top, the coated substrate, printed electrodes, isolation layer, channel mold, and top layer are shown for a channel that touches two electrodes in Fig. 2.

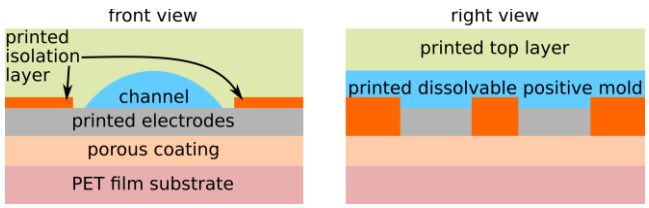

Figure 2: Front and right cross-section schematics of a resistive pulse sensor with e-jet printed electrodes, isolation layer, dissolvable channel mold, and top layer.

Device Fabrication Steps

Step a: E-jet print electrodes. First the substrate is loaded onto a vacuum chuck. The substrate will remain on the chuck throughout the fabrication until the final wash step. A nozzle containing the silver nanoparticle solution is loaded into the print head. The substrate *z-axis* position is adjusted to bring the nozzle to the appropriate standoff height relative to the substrate. The camera lens focal point is used for *x-* and *y-axis* nozzle-to-substrate registration; nozzle and camera positions are adjusted to center the nozzle tip at the focal point of the camera lens. Coordinated motion and nozzle voltage is actuated from a script based on a sliced STL model.

Step b: E-jet print the isolation layer. After loading a nozzle containing UV curable build material for the isolation layer, the nozzle position is adjusted to center the nozzle tip in the camera field of view for registration with a standoff height set by the substrate *z-axis* stage motion. Printing is performed from a script. UV curing is performed after translating the substrate to the UV curing head.

Step c: E-jet print the channel mold. Replacing the nozzle with a nozzle containing dissolvable build material for the channel mold, the nozzle position is adjusted to bring the nozzle tip to the focal point of the camera for registration before setting the standoff height. Printing is performed from a script. UV curing is applied in the case of a UV curable channel mold build material. Optionally, AFM scanning of the channel mold is performed for channel metrology.

Step d: Print and then UV cure the top layer. The process in Step b is then repeated using a different printing script.

Step e: Wash the device. The substrate is unchucked from its mount and immersed in a solvent bath to clear the channel. The five printing steps are labeled a-e in Fig. 3.

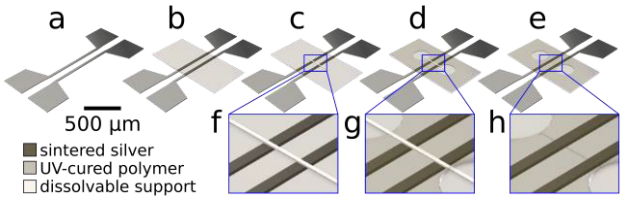

Figure 3: Steps to e-jet print a microfluidic resistive pulse sensor: (a) print electrodes onto substrate, (b) print isolation layer, (c) print dissolvable channel mold, (d) print top layer, and (e) wash support material in the channel. Detailed views of (c-e) are shown in (f-h).

DEVICE DESIGN

To demonstrate the e-jet printing of a microfluidic device, a single-channel resistive pulse sensor, a type of Coulter counter for particle counting and sizing, is designed and fabricated [11]. This sensor has a single 200 µm long microfluidic channel with parallel electrodes beneath it to sense resistive pulses as a particle in an electrolyte solution flows past the electrodes. The electrodes are printed with contact pads on both sides of the device to verify printed trace conductivity. An isolation layer forms the base of the microfluidic channel. The channel is defined by a printed dissolvable positive mold. The top layer has ports for loading and unloading analyte liquid drops. To conserve build material and build time, the ports are designed for capillary driven flow into the device. Each port is a depression formed by printing a rim of build material in the top layer. A printed sensor is shown in Fig. 4.

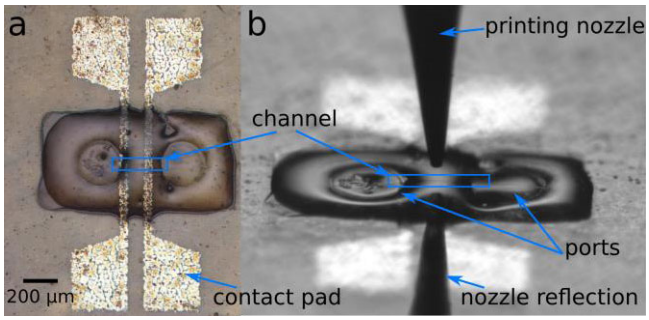

Figure 4. Top view (a) and side view (b) of an e-jet printed resistive pulse sensor just after fabrication step d. The 30 µm tip diameter nozzle used to print the top layer is visible in (b).

EXPERIMENTAL METHODS

The electrode build material is a chemically sinterable silver nanoparticle ink (NBSIJ-MU01, Mitsubishi Imaging). Glycerol is added to the silver nanoparticle ink to avoid nozzle clogging from solvent evaporation. A 10 µm nozzle tip diameter is used with the silver ink. The substrate is a flexible PET film substrate with porous chemical coating for instant chemical sintering of the ink (NB-TP-3GU100, Mitsubishi Imaging). The isolation and top layer build material is a viscous (0.3 Pa-s), UV curable, thiol-ene based resin, Norland Optical Adhesive 81 (NOA81, Norland Products). A 30 µm nozzle tip diameter is used for increased NOA 81 deposition rate. NOA 81 is a commonly used build material for e-jet printing and other AM processes due to its fast (<10 s) UV curing, transparency, and solvent resistance [12]. The Young's modulus of NOA 81 (O(1) GPa), is comparable to that of SU-8 used in [3], and is intermediate between that of photolithographically-produced glass or silicon devices (O(100) GPa) and soft-lithographically-produced polydimethylsiloxane (PDMS) devices (O(0.001) GPa), making it a suitable material for microfluidic device construction.

For the channel mold build material, two dissolvable support materials are investigated. The first is an aqueous solution of the water-soluble polymer poly vinylpyrrolidone (PVP K15, average molecular weight 10,000 Da, Sigma-Aldrich) with added glycerol. A 10 µm nozzle tip diameter is used for the PVP solution. The second is viscous (0.35 Pa-s), UV curable, acetone-debondable Norland Blocking Adhesive 107 (NBA107, Norland Products). A 10 µm nozzle tip diameter is used for NBA107.

RESULTS AND DISCUSSION

A test device with 2.5 mm long channel is shown in Fig. 5c (with no electrodes). The PVP channel mold of the test device is scanned by the AFM during fabrication step c for channel metrology. An optical top view image is shown with the height profile inset in Fig. 5a. The channel width is 100 µm, and the channel height is 4.5 µm. The PVP channel mold forms an elliptical segment profile, similar to the results in [3]. To demonstrate flow in the channel, a solution of green food dye in water is loaded at the port and flows into the device by capillary action. The green dye with an air bubble in the channel is shown in Fig. 5b.

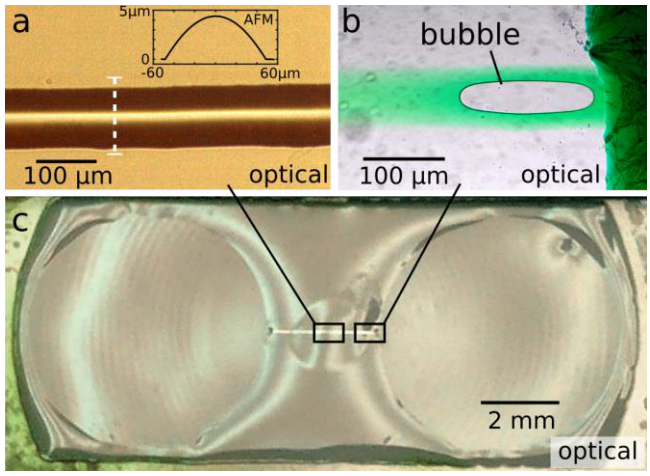

Figure 5. E-jet printed microfluidic channel test device without electrodes: (a) Top view of PVP channel mold after fabrication step c. Inset is a height profile of the channel collected by AFM scan along dashed line. (b) Top view of capillary filling of green dye into the finished device channel. (c) Top view of the completed device.

The influence of printing parameters on channel profile shape is studied for PVP channel molds. The number of printing passes is varied from 1 to 5. The standoff height is varied between two values: a large standoff height of 70 µm, which gives a reduced deposition rate, and a reduced standoff high of 55 µm, which gives an increased deposition rate. The resulting channel images and profiles are shown in Fig. 6. The channel profiles are ellipsoidal caps with a variable contact angle. Channel widths below 30 µm are achieved using the PVP channel mold.

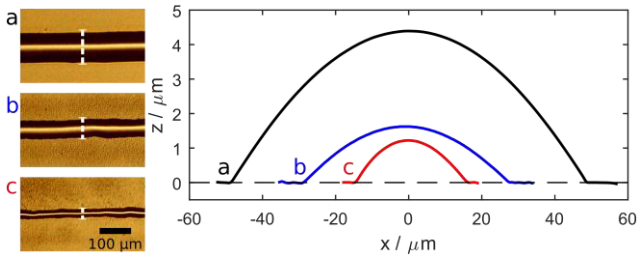

Figure 6. Top view microscope images and height profiles collected by AFM scans of three e-jet printed PVP channel molds. Varying printing parameters: (a) 5 passes at 45 µm standoff height, (b) 3 passes at 70 µm standoff height, and (c) 1 pass at 70 µm standoff height, gave varying channel width, height, and contact angle.

Channel profile shaping is demonstrated using the UV curable NBA107 as the channel mold build material. Two variations of the printing procedure for multiple pass printing of NBA107 are investigated: one in which the deposited material is UV cured between each pass, and the alternative of UV curing only after the final pass has been deposited. The uncured NBA107 channel mold material cannot be AFM scanned because it is a liquid, so channel profiles are only available after UV curing to solidify the NBA107. When UV curing is applied at the end (a and d), an elliptical segment profile results, similar to the PVP results. UV curing applied

between passes (b and c) results in a peaked profile with a pedestal, shown in Fig. 7.

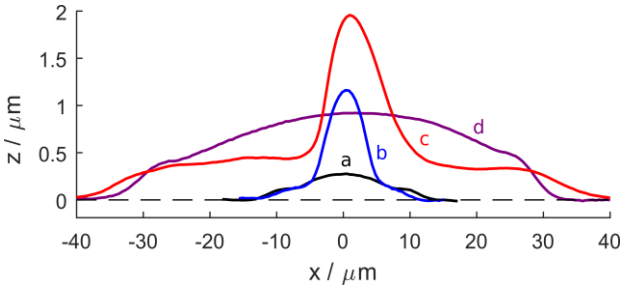

Figure 7. Height profiles collected by AFM scans of e-jet printed NBA107 channel molds printed as: (a) 1 pass (b) 4 passes, curing between passes, (c) 10 passes, curing between passes, (d) 10 passes, curing only after pass 10.

Channel widths below the 60 µm inkjet minimum reported in [3] are readily achieved by e-jet printing the channel mold with either PVP (<30 µm) or NBA107 (<20 µm). Further reduction in e-jet printed channel width is expected for smaller nozzles and printing parameter optimization.

CONCLUSION

This work demonstrates the first microfluidic device fully fabricated by the microscale additive manufacturing technique e-jet printing. Importantly, the fabrication process is conducted entirely at room temperature, with no spin coating or molding processes. Microfluidic channels are formed by printing water-soluble positive molds. Electrodes are printed using chemically sintered silver nanoparticle ink onto a chemically coated substrate. Whereas [3] uses thermally sintered silver nanoparticle ink for its electrodes and thermally crosslinked photoresist SU-8 for its isolation and top layers, the use of chemically sintered silver nanoparticle ink and UV adhesives in this work allows the device to be fabricated entirely at room temperature. Channel profiles are measured before printing the top layer onto the channel mold. The polymer channel mold formed by solvent evaporation assumes an ellipsoidal segment shape; however, channel profile shaping is demonstrated for a UV curable channel mold. This channel profile metrology technique offers the possibility of building up desired channel geometry in a controlled fashion through iterative printing and scanning steps. This demonstration of a fully e-jet printed microfluidic sensor at room temperature introduces e-jet printing as a powerful tool for high-resolution microfluidic device fabrication that enables the inclusion of temperature-sensitive materials.

Future areas to explore with this technique include methods to print chemically sintered electrodes in offset planes that are non-parallel to the substrate plane, as well as further demonstrations of build material diversity. In particular, future work aims to investigate e-jet printing of a microfluidic device constructed of thermally and chemically sensitive biomaterials that cannot be patterned conventionally, but are made possible using the presented room temperature e-jet printing technique.

ACKNOWLEDGEMENTS

This work was supported in part by NSF Awards CMMI-1434660, CMMI-1434693, and GRFP-1256260. Travel support has been generously provided by the Transducer Research Foundation.

REFERENCES

[1] C.M.B. Ho, S.H. Ng, K.H.H. Li, Y.-J. Yoon, "3D Printed Microfluidics for Biological Applications", Lab Chip, 15, 3627 (2015). doi.org/10.1039/c5lc00685f

[2] R.D. Sochol, E. Sweet, C.C. Glick, S. Venkatesh, et al., "3D Printed Microfluidic Circuitry via Multijet-Based Additive Manufacturing", Lab Chip, 16, 668 (2016). doi.org/10.1039/c5lc01389e

[3] W. Su, B.S. Cook, Y. Fang, and M.M. Tentzeris, "Fully Inkjet-Printed Microfluidics: A Solution to Low-Cost Rapid Three-Dimensional Microfluidics Fabrication with Numerous Electrical and Sensing Applications", Scientific Reports, 6, 35111 (2016). doi.org/10.1038/srep35111

[4] J.-U. Park, M. Hardy, S.J. Kang, K. Barton, et al., "High-Resolution Electrodynamic Jet Printing", Nature Materials, 6, 782 (2007). doi.org/10.1038/nmat1974

[5] M.S. Onses, E. Sutanto, P.M. Ferreira, A.G. Alleyne, and J.A. Rogers, "Mechanisms, Capabilities, and Applications of High-Resolution Electrohydrodynamic Jet Printing", Small, 11, 4237 (2015). doi.org/10.1002/smll.201500593

[6] C.P. Pannier, Z. Wang, D.J. Hoelzle, and K.L. Barton, "Electrohydrodynamic Jet Printing: A 3D Printing Technique for Sensor Fabrication," Technical Digest of the 2016 Solid-State Sensor and Actuator Workshop, Hilton Head Isl., SC, 6/5-9/16, Transducer Research Foundation, Cleveland (2016), pp. 149 - 152.

[7] Z. Wang, C. Pannier, K. Barton, D.J. Hoelzle, "Application of Robust Monotonically Convergent Spatial Iterative Learning Control to Microscale Additive Manufacturing", Mechatronics (2018). Submitted.

[8] Z. Wang, P.M. Sammons, C.P. Pannier, K. Barton, and D.J. Hoelzle, "System Identification of a Discrete Repetitive Process Model for Electrohydrodynamic Jet Printing," Proc. of the 2018 American Control Conference, Milwaukee, WI, 6/27-29/18, Institute of Electrical and Electronics Engineers, New York (2018). Accepted.

[9] C.P. Pannier, L. Ojeda, Z. Wang, D. Hoelzle, K. Barton, "An Electrohydrodynamic Jet Printer with Integrated Metrology", Mechatronics (2018). Accepted.

[10] Y. Kawahara, S. Hodges, B. S. Cook, C. Zhang, and G. D. Abowd, "Instant Inkjet Circuits: Lab-Based Inkjet Printing to Support Rapid Prototyping of UbiComp Devices", Proc. of the 2013 ACM International Joint Conference on Pervasive and Ubiquitous Computing, Zurich, Switzerland, 9/8-12/13, Association for Computing Machinery, New York (2013), pp. 363-372. doi.org/10.1145/2493432.2493486

[11] J. Zhe, A. Jagtiani, P. Dutta, J. Hu, and J. Carletta, "A Micromachined High Throughput Coulter Counter for Bioparticle Detection and Counting", J. Micromech. Microeng., 17, 304 (2007). doi.org/10.1088/0960-1317/17/2/017

[12] K.W. Bong, J. Xu, J.-H. Kim, S.C. Chapin, M.S. Strano, K.K. Gleason, P.S. Doyle, "Non-Polydimethylsiloxane Devices for Oxygen-Free Flow Lithography", Nature Comm., 3, 805 (2012). doi.org/10.1038/ncomms1800

CONTACT

*C.P. Pannier, PANNIER @ UMICH . edu

PRECISE MICROSCALE PATTERNING OF BEADLESS AND UNIFORM NANOFIBER VIA EXTREME NEAR-FIELD ELECTROSPINNING

Dongwoon Shin[1], Jonghyun Kim[1], and Jiyoung Chang[1]*
[1]Department of Mechanical Engineering, University of Utah, Salt Lake City, Utah, USA

ABSTRACT

Complicated microscale patterns of a beadless and uniform nanofiber were precisely fabricated via extreme Near-Field electrospinning (NFES). Although the bending instability effect could be prevented by shortening Tip-To-Collector Distance (TTCD) less than the critical length in typical NFES, complex patterns in microscale have not been reported up to the date due to the ignorance of the importance of jet speed. To understand the effect of the parameters on jet speed for precise microscale patterning, an experimental study on the process parameters such as applied voltage, TTCD, and an electric field was performed. It has been realized that reducing the applied voltage and the TTCD simultaneously could minimize the jet speed, which results in significant improvement of the accuracy of the deposition. Fabrication of microscale patterns of nanofiber will broaden applications of NFES such as fiber-based electronics, customized cell culture matrix fabrication to name a few.

INTRODUCTION

Nanofiber has gotten many attentions due to its excellent characteristics such as superior mechanical properties [1], the high surface area to volume ratio [2], cost-effective, and its utilization. More applications based on electrospinning are expected to be unlocked if the fiber can be deposited at the desired location. However, creating certain patterns of nanofiber seemed to be challenging because of long tip-to-collector distance in conventional electrospinning. Long tip-to-collector distance, typically more than tens of centimeter, causes the jet to experience severe electrical stretching and bending in which the jet starts traveling along whipping path. To overcome this issue, Near-Field electrospinning (NFES) was developed in 2006 by shortening the tip-to-collector distance below few millimeters [3]. After the introduction of NFES, the fabrication of patterns of nanofibers has been developed via Near-Field electrospinning, but the patterns were limited to either the arrays of simple straight lines or relatively big scale [4–6]. To improve the accuracy of deposition and reduce the jet speed, NFES with TTCD less than 1mm were utilized as shown in Figure 1 (a). In spite of that, precise patterning requires the condition where the absolute value of the jet speed normal to the collector is equivalent to the absolute value of the collector speed (Figure 1 (c)). On the other hand, the drawn pattern could be distorted because of slower jet speed than the collector speed (Figure 1 (b)). Also, the pattern could be drawn with the coiled or wavy shape of the fiber formation rather than the straight line (Figure 1 (d)). Therefore, it is essential to secure the jet speed that agrees with the collector speed for precise patterning. We here report not only NFES system using established Graphic User Interface (GUI), but also precise microscale patterns of bead-less and uniform nanofibers that consists of both curves and straight lines.

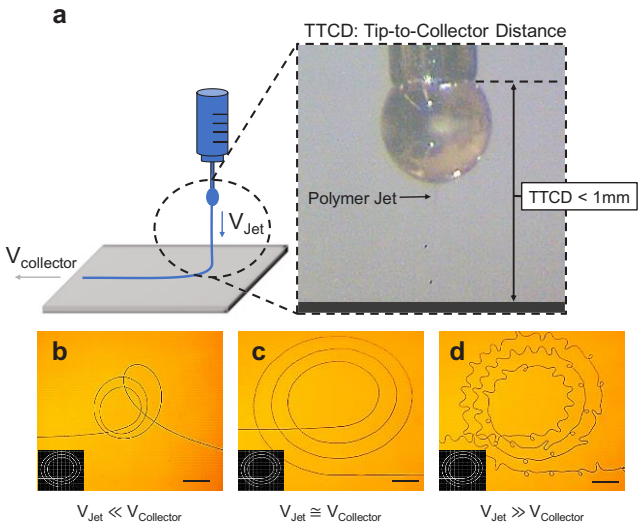

Figure 1: (a) Schematic illustration of extreme near-field electrospinning where tip-to-collector distance is less than 1mm (b) Optical image showing an example of failed fiber pattern because of faster collector speed than the jet speed (c) Optical image of an example of successful fiber pattern owing to the equivalence between the jet and the collector speed (d) Optical image showing an example of failed fiber pattern because of faster jet speed than the collector speed

EXPERIMENTS & METHODS

NFES system consists of XY-Stage, Z-stage, Microfluidic pump, long-distance microscope, High-Voltage supply, and Real-time control system via LabVIEW to control all of these devices as shown in Figure 2. A 1 ml syringe with a 32 gauge (Nordson®) metal needle was chosen, and a silicon wafer was selected as a conductive collector, where the needle tip was connected to the positive side of the DC supply, and the collector was grounded. 10% wt of Polyethylene oxide (PEO, MW=400,000, Sigma Aldrich) was prepared in Deionized water. 10% wt of PEO solution was selected because high concentration solution could generate uniform and beadless fiber, and higher viscosity results in the slower jet speed compared to the ones from lower concentration solutions.

978-1-940470-03-0/HH2018/$25©2018TRF
DOI 10.31438/trf.hh2018.82

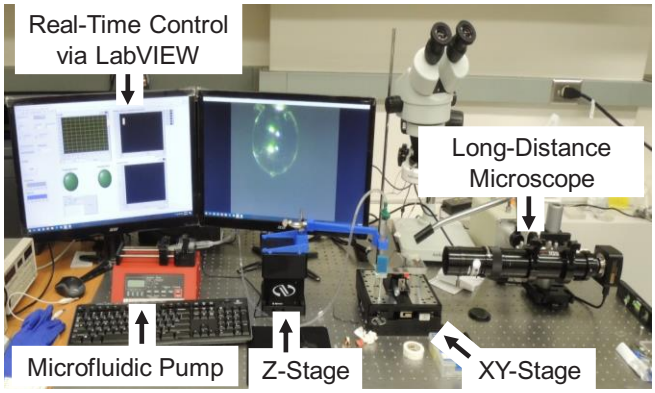

Figure 2: Image of the actual setup of extreme near-field electrospinning system with the established GUI

UNIFORM AND BEADLESS NANOFIBER

In order to secure uniform and beadless nanofiber, it is important to keep the voltage lower than the critical point where the excessive electrostatic force occurs. Figure 3 (a) shows the uniform and beadless nanofiber while the Figure 3 (b) exhibits the irregular and damaged nanofiber. This issue was caused by too strong impact to the jet when the jet impinged on the collector since the jet still contains most of the solvent in NFES. However, the electrostatic force generated by the applied voltage less than 2500V with the TTCD of 1.0 mm could not overcome the surface tension, resulting in no initiation of the jet according to Taylor's equation [7]

$$V_c^2 = 4\ln(2h/R)(1.3\pi R\gamma)(0.09) \quad (1)$$

Where V_c is the critical voltage, h is the distance from the needle tip to collector surface, R is the outer radius of the needle, γ is the surface tension of the solution. Therefore, we added mechanical force to the existing electrical force by poking the meniscus so that the jet initiation could be accomplished by much less applied voltage than 2500 V as shown in Figure 3 (c).

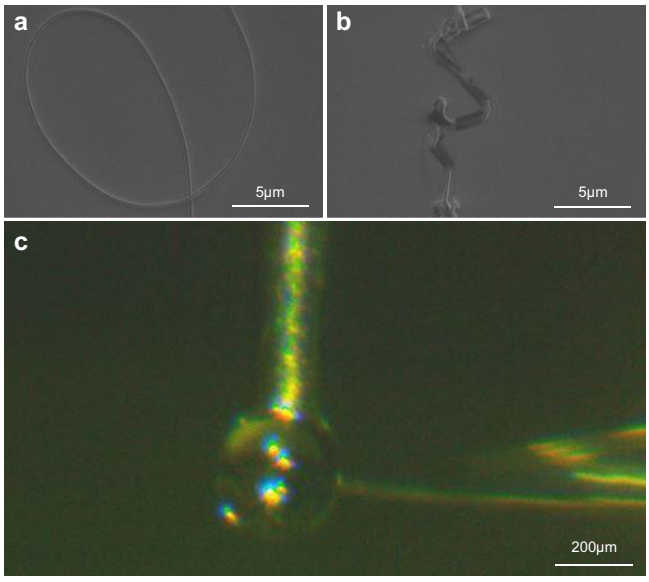

Figure 3: (a) Uniform and beadless electrospun nanofiber using extreme near-field electrospinning (b) irregular electrospun nanofiber by applying an excessive voltage (c) Optical image of onset of initiation

EFFECT OF PARAMETERS ON JET SPEED

In NFES, three different shapes of the electrospun fiber such as straight, wavy and coiled can be presented depending on the relationship between the jet and the collector speed as shown in Figure 4 (a-c). To understand the effect of the parameters on the jet speed, controlling the parameters such as the applied voltage and the TTCD was executed. When the applied voltage was controlled during a continuous NFES process, the jet speed variation displayed significant variation as shown in Figure 4 (a). This is because the more electric field was formed and more charges were induced by increasing the applied voltage, resulting in a much bigger electrostatic force that leads to much faster jet speed. On the other hand, the jet speed while changing the TTCD does not exhibit big changes as shown in Figure 4 (b). While TTCD is lowered, the corresponding electric field was increased, but the actual jet travel distance was reduced. Hence, these two factors trigger opposite effects on jet speed. As a result, the jet speed did not vary in the operation range.

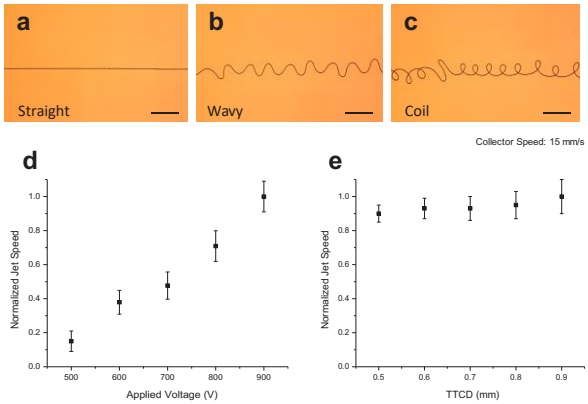

Figure 4: (a) Straight line electrospun fiber (b) Wavy shape electrospun fiber (c) coiled-shape electrospun fiber (d) Plot of normalized jet speed under varying the applied voltage (e) Plot of normalized jet speed under varying the tip-to-collector distance

IMPORTANCE OF DROPLET SIZE CONTROL

When it comes to NFES, droplet size was noticed to affect the process. In conventional electrospinning with TTCD of tens of centimeters, the droplet size was not treated as one of the process parameters since it is not influential owing to its small portion of the length out of the TTCD. On the other hand, the droplet size shows its effect as TTCD is shortened less than 1mm, where the droplet size takes more than 30 % of the length out of the TTCD. As shown in Figure 5, the droplet size happens to vary if the feed rate and the deposition rate does not agree to each other. With the varying droplet size, the corresponding electric field and the jet travel distance (JTD) changes. Therefore, it denotes the importance of controlling the droplet size in NFES to secure identical electrospun fiber regarding its shape and diameter. The droplet size control in this experiment was performed by established vision control using LabVIEW. The established vision system can trace the droplet size in real-time so that it calculates the difference between the feed rate and the deposition rate, and it communicates with the microfluidic pump to either increase or decrease the feed rate.

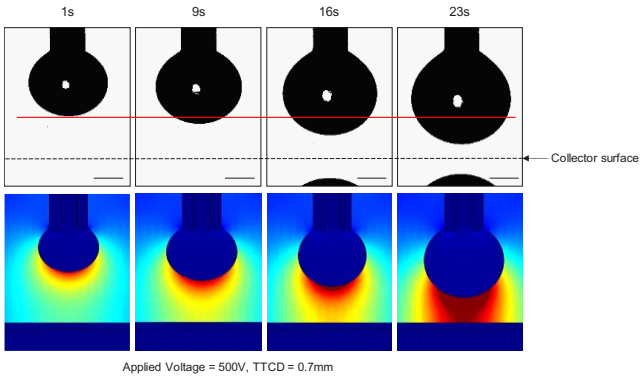

Figure 5: The changes in the corresponding electric field and the jet travel distance by the variation of the droplet size in NFES

RELIABILITY & CONTROLLABILITY

Controlling applied voltage has shown the most variation regarding jet speed and diameter in the previous section. Therefore, another experiment with varying the applied voltage was executed to secure the reliability and controllability of jet behavior. While the applied voltage changed in the range between 500 and 900 V, the measured jet speed showed the reasonable agreement at each applied voltage as shown in Figure 6 (a). Likewise, the measured diameter of the electrospun fiber at each applied voltage was placed in the similar range as shown in Figure 6 (b).

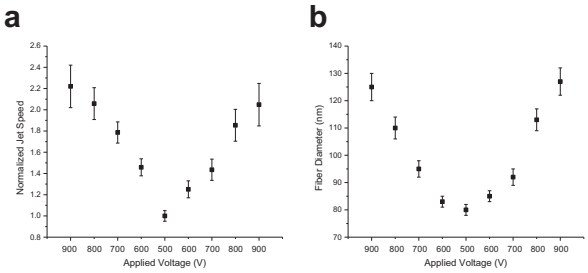

Figure 6: (a) Normalized jet speed under varying the applied voltage up and down between 500 and 900 V (b) Fiber diameter under varying the applied voltage up and down between 500 and 900 V

CONCLUSION

To sum up, we introduced the extreme near-field electrospinning with tip-to-collector distance less than 1mm as well as the uniform and beadless nanofiber patterning. In order to fabricate precise fiber pattern, it is important to have the speed of the jet and the collector to be equivalent to each other. Therefore, the effect of the parameters on jet speed during a continuous electrospinning process was investigated, and it turns out that the applied voltage appears the most dominant effect on jet speed than the tip-to-collector distance and the average electric field. In addition, the importance of controlling droplet size in NFES was detected since it affects the properties of the electrospun fiber regarding the shape and the diameter. Also, the reliability and controllability of the jet behavior were tested by adjusting applied voltage. Finally, we here present the microscale serpentine patterns of the beadless and uniform nanofiber.

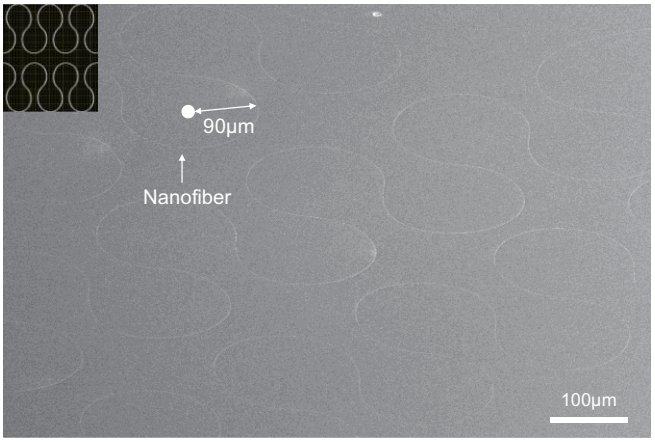

Figure 7: SEM image of a microscale serpentine pattern of beadless and uniform nanofiber

REFERENCES

[1] Kim J, Reneker DH. Mechanical properties of composites using ultrafine electrospun fibers. Polym Compos 1999;20:124–31. doi:10.1002/pc.10340.

[2] Demir M., Yilgor I, Yilgor E, Erman B. Electrospinning of polyurethane fibers. Polymer (Guildf) 2002;43:3303–9. doi:10.1016/S0032-3861(02)00136-2.

[3] Sun D, Chang C, Li S, Lin L. Near-Field Electrospinning 2006. doi:10.1021/nl0602701.

[4] Chang C, Limkrailassiri K, Lin L. Continuous near-field electrospinning for large area deposition of orderly nanofiber patterns. Cit Appl Phys Lett Appl Phys Lett J Vac Sci Technol B Microelectron Nanom Struct Process Meas Phenom 2008;93:123111–1829. doi:10.1116/1.3154516.

[5] Bisht GS, Canton G, Mirsepassi A, Kulinsky L, Oh S, Dunn-Rankin D, et al. Controlled Continuous Patterning of Polymeric Nanofibers on Three-Dimensional Substrates Using Low-Voltage Near-Field Electrospinning. Nano Lett 2011;11:1831–7. doi:10.1021/nl2006164.

[6] Li X, Li Z, Wang L, Ma G, Meng F, Pritchard RH, et al. Low-Voltage Continuous Electrospinning Patterning. ACS Appl Mater Interfaces 2016;8:32120–31. doi:10.1021/acsami.6b07797.

[7] Taylor G. Electrically Driven Jets. Proc R Soc Lond A Math Phys Sci 1969;313:453–75. doi:10.2307/2416488.

CONTACT

*Jiyoung Chang, tel: +1-801-581-7400; jy.chang@utah.edu

A MICRO COLLECTOR INJECTOR (μCOIN) FOR μGC SYSTEMS

Muhammad Akbar,[1] Nicolás Nuñovero,[1] Robert Hower,[1] Changhua Zhan,[1] Joseph Potkay,[2] and Edward Zellers[1,3]
[1]Department of Environmental Health Sciences, [2]Department of Surgery, [3]Department of Chemistry,
Center for Wireless Integrated MicroSensing & Systems (WIMS[2]), University of Michigan, Ann Arbor, USA

ABSTRACT

We report a microscale collector-injector (μCOIN) suitable for gas chromatographic microsystems (μGC) comprising two series-coupled devices: a micro passive preconcentrator (μPP) and a micro progressively heated injector (μPHI). The μPP collects volatile organic compounds (VOC) via passive diffusion. Discrete μPPs demonstrated sampling rates close to theory, a high adsorption capacity, and efficient thermal desorption. The μPHI accepts vapors transferred from the μPP (by thermal desorption with pumping) and thermally generates a sharp injection. Discrete μPHIs demonstrated capacities that varied with VOC polarity and volatility, and 190 ms injections via progressive heating.

INTRODUCTION

The direct determination of VOCs in field or clinical settings is of interest for personal exposure monitoring, point-of-care medical diagnostics, and the detection of explosives or other chemical threats. μGC has several inherent potential advantages for such applications, and efforts to produce such microsystems have been reported [1-5]. The key analytical components of a typical μGC comprise a preconcentrator/injector for sample capture (via pump) and introduction, a column for separation of mixture components, and a detector or array of detectors.

Typical microscale adsorbent-packed/lined preconcentrators also serve as injectors [1-7]. The dual function of such devices requires performance tradeoffs between capacity on the one hand and desorption efficiency and power dissipation on the other. Among reported micro-preconcentrators, injection band widths of VOCs are typically > 1 s, preconcentration factors are relatively low, and power consumption can be high due, in part, to the use of a mini-pump to draw air samples into the device.

The μCOIN device described here (Fig. 1) consists of a μPP coupled to a μPHI. The μPP collects vapors by passive diffusion. It redesigns a predecessor technology [8] to reduce (>10×) the required desorption flow rate, increase flow uniformity, and minimize energy consumption. However, the μPP is incapable of producing sharp injections upon thermal desorption and transfer (under flow). The μPHI, a new design that combines concepts from previously reported micro focuser-injectors [7,9], accepts the broad vapor bolus transferred from the μPP and then is rapidly and progressively heated (under flow) to yield the sharp injection pulse needed for efficient μGC separations with short columns. Carbon adsorbents permit trapping of vapors with a wide range of structure/volatility. This paper describes the design and preliminary characterization of discrete μPP and μPHI devices as well as first results from the hybrid-integrated μCOIN.

EXPERIMENTAL

Design and Fabrication

The μPP and μPHI devices are formed from a top silicon-on-insulator (SOI) substrate and a bottom glass substrate (Fig. 2). The top layer of the μPP SOI substrate has a grid of 171 parallel 50×50×180 μm (L×W×H) apertures through which vapors diffuse at a known rate according to Fick's laws. The bottom layer of the μPP SOI substrate contains two concentric adsorbent cavities

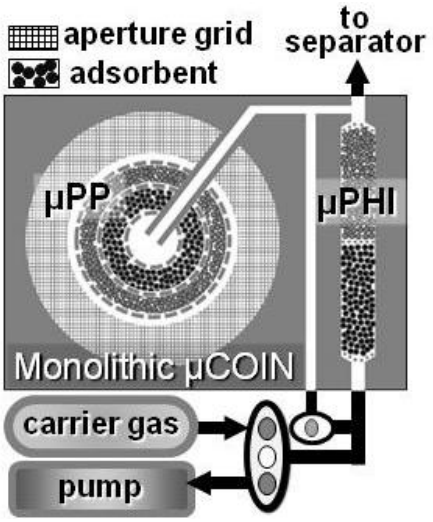

Figure 1: Conceptual diagram of monolithic 8x8 mm μCOIN.

separated by pillars and filled with ~800 μg of Carbopack B (C-B, surface area: 100 m^2/g, outer) and 700 μg Carbopack X (C-X, surface area: 100 m^2/g, inner). Heaters and temperature sensors (Ti/Pt) located on the top surface of the glass substrate are used for heating the adsorbents to 250 °C during thermal desorption.

The μPHI has linear topology with adjacent adsorbent beds containing ~500/400 μg of C-B/C-X also separated by pillars (Fig. 2b). In the μPHI, the adsorbent region is split into an array of 10 thermally isolated and in individually addressed heaters that enable advanced (progressive) heating for compressing injection peaks.

The diffusion path through the μPP (Fig. 2a) can be formally parsed into three segments with specific lengths and areas, L_i and A_i, through which the mass transfer of vapors is constant at steady state. The effective sampling rate, S (volume/time), can be estimated as $S=D/(L_1/A_1+L_2/A_2+L_3/A_3)$, where D is the vapor diffusion coefficient [7]. By design, S is primarily a function of the total area of the aperture grid (A_1). The capacity of the device is a function of its design as well as the nature and number of VOCs and the time of exposure. After collection is complete, the sample is transferred from the μPP to the μPHI under suction flow via thermal desorption.

After the sample is transferred to the μPHI, external valves are used to introduce He carrier gas from a canister in the reverse direction (back flushing) and the μPHI heaters are sequentially activated, progressively desorbing VOCs from inlet to outlet and "rolling up" (i.e., focusing) the mixture into a sharp injection pulse.

Discrete μPP and μPHI devices were created using the same microfabrication process flow. The sampling aperture grid (μPP), adsorbent cavities and fill ports, and flow channels were fabricated using DRIE. Ti/Pt heaters/RTDs and an oxynitride overlayer were deposited on the bottom glass substrate using PVD and PECVD tools, respectively. Au-Si eutectic bonding joined the substrates (Fig. 3) [9]. Adsorbents were loaded, interconnecting capillaries were epoxy sealed, and then devices were mounted & wire-bonded onto printed circuit boards (PCB; Fig.4).

978-1-940470-03-0/HH2018/$25©2018TRF
DOI 10.31438/trf.hh2018.83

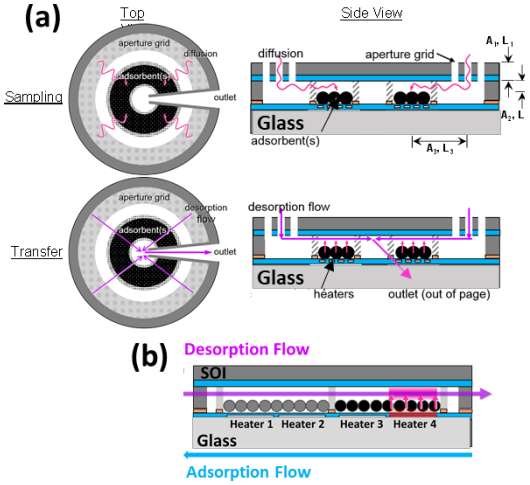

Figure 2: Design and operation of (a) µPP (b) µPHI.

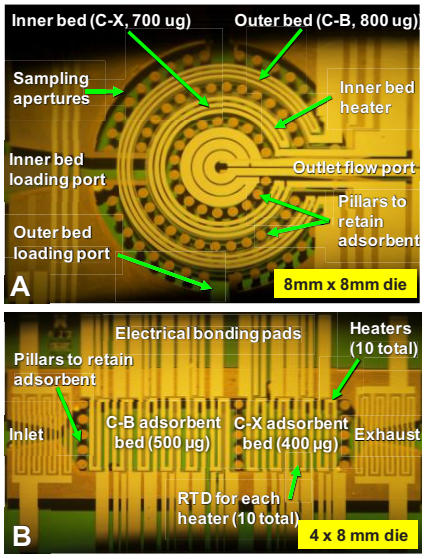

Figure 3: Optical image of fabricated (a) µPP (b) µPHI devices.

Discrete Device Tests

Test chemicals were obtained at high purity from standard sources and used without purification. Test atmospheres containing vapors of the test chemicals were generated from fritted-glass bubblers diluted with clean, dry air, and were verified by loop injection into a pre-calibrated GC-FID. Certain tests were performed using a thermogravimetric analyzer (TGA, Perkin Elmer). For other tests, a PCB-mounted µPP device was mounted in a custom stainless steel chamber with electrical feedthroughs in the chamber floor. The capillary used for sample transfer was wrapped with heater coils and raised to 70 °C during transfer. Following exposure for a given time period, the chamber was purged with clean, dry air. Then, both substrate heaters were activated to heat the adsorbent beds to 250 °C while drawing air through it with a small pump at 10 mL/min. The sample was passed through a surrogate focuser [7] where the vapors were temporarily trapped and then injected into the GC-FID equipped with either a short capillary separation column or a section of (uncoated) deactivated silica guard column.

For the µPHI, samples of the test chemicals were passed to the device as low-volume vapor boluses either from a sample loop connected to a 6-port valve or from a bench-scale GC. For the latter the test chemical was either pure or dissolved in a volatile solvent and injected through the heated GC injection port using an autosampler syringe. The mass of test chemical was verified by pre-calibrated FID.

Device heaters were controlled and RTDs monitored by custom programs written in LabVIEW and run from laptop computers. The µPP had feedback controlled heating (via pulse width modulation). The µPHI had open loop heater control with independent voltages applied during the ramp up and hold periods.

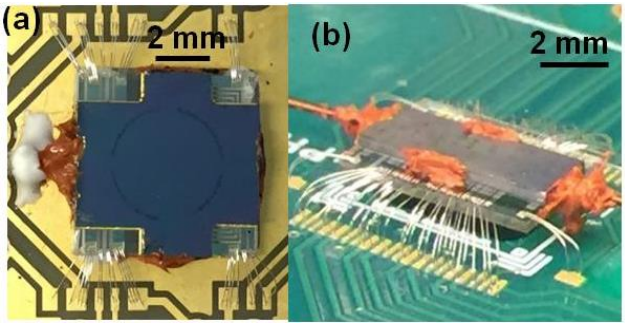

Figure 4: (a) Optical image of the wire-bonded (a) µPP (b) µPHI device.

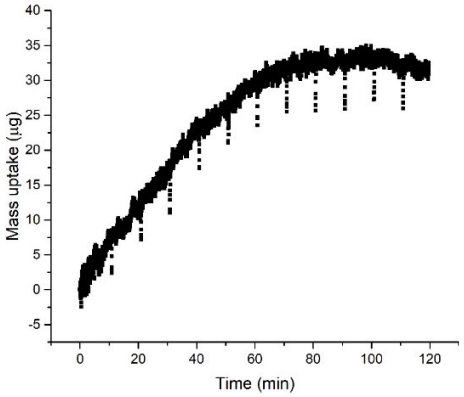

Figure 5: TGA output of suspended µPP device showing constant sampling rate (linear mass uptake) for ~40 min and saturation at ~80 min (33 µg of xylene at the challenge concentration of 2,000 mg/m^3).

RESULTS AND DISCUSSION

In initial tests, separate 3-mg samples of C-X and C-B adsorbents were loaded into a sample pan, suspended from the TGA balance, and exposed to m-xylene vapor (one of the highest-vapor pressure targets studied). After allowing uptake of relatively large masses of 5-8 µg of m-xylene per mg of adsorbent there was no loss (bleed) of the captured vapor after two hours of purging with clean air at ambient temperature. This confirms that test vapors should be retained by the µPP even during periods of non-exposure.

A µPP was then device suspended in the TGA and exposed to 2000 mg/m^3 of m-xylene vapor, and mass uptake via passive sampling was measured in real time. Results are shown in Fig. 5. The sampling rate was constant for ~40 min, dropped by 30% from 40-60 min, and then dropped to zero (saturation). The total mass uptake was 32 µg and the sampling rate was constant up to 23 µg, which is a very high capacity. Other tests showed that capacity was inversely proportional to vapor pressure for homologous aromatic hydrocarbons, meaning that the capacity should be

sufficient for most/many VOCs of interest. TGA tests with the polar dimethylmethylphosphonate (DMMP) were not successful.

Chamber tests with the µPP showed that the sampling rate for m-xylene was constant over 3 orders of magnitude in concentration (i.e., from 8 to 5,600 mg/m^3; 15-min samples). Furthermore, tests with both m-xylene and DMMP showed that the sample rates were within 15% of those predicted by theory/modeling (see Table 1). Figure 6 shows a chromatogram from passively sampling a simple mixture of vapors with the µPP (in chamber), transferring to the surrogate focuser, and injecting to a bench-scale GC-FID. Desorption efficiencies were 88-98%.

Table 1: µPP sampling rate for m-xylene and DMMP.

VOC	Modeled S (mL/min)	Exper. S (mL/min)	Ratio
m-xylene	0.60	0.69	1.15
DMMP	0.44	0.48	1.09

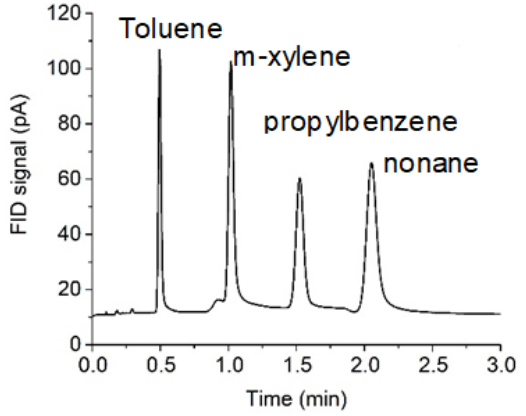

Figure 6: GC-FID chromatogram for a 4-vapor mixture passively sampled with the µPP, transferred to a surrogate focuser and injected.

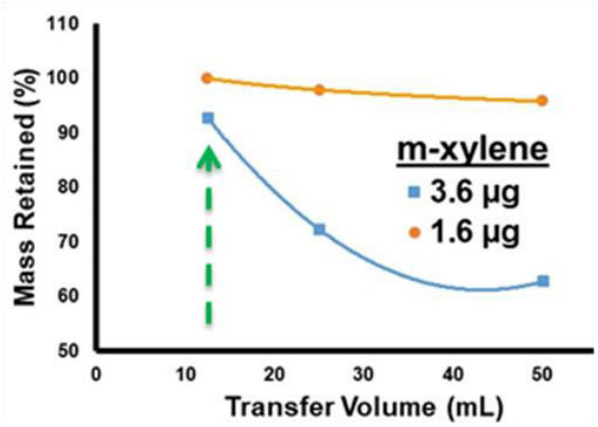

Figure 7: Plots of fractional retention (capacity) of m-xylene versus the transfer volume for the µPHI for bolus challenges of 1.6 and 3.6 ug at 5 mL/min. Retention is >90% for transfer volumes < 12 mL.

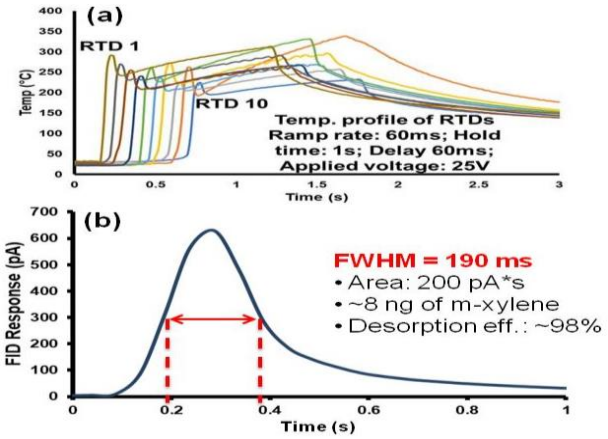

Figure 8: (a) Rapid (4000 °C/s) heating (60 ms delay time) of µPHI bed with low thermal crosstalk (b) Sharp ((full width at half maximum = 190 ms) desorption peak-width at 50 µL/min flow during heater ramp period (~1 s) and 3 mL/min afterwards

To test of the capacity of the discrete µPHI, breakthrough was monitored by FID using boluses of known test atmospheres passed directly through the device in a certain volume of carrier gas to mimic desorption from the µPP. The µPHI was subsequently heated to 250 ºC using global or progressive heating to desorb the retained vapors. The percentage of mass retained was evaluated by the ratio of challenged vapor concentration/mass to the desorbed peak area.

Initial tests were performed with boluses containing 1.6 µg and 3.6 µg of m-xylene. These masses can be related to possible µCOIN exposure scenarios. For example, the µPP would collect 1.6 µg within 30 min (S = 0.6 mL/min) when exposed to 90 mg/m^3 and it would collect 3.6 µg in 30 min at 200 mg/m^3. We anticipate that the volume of air required to transfer samples from the µPP to the µPHI will be < 3 mL. Figure 7 shows that the µPHI can retain > 95% of 3.6 µg sample of m-xylene if the transfer volume is < 12 mL. For a 1.6 µg sample the capture efficiency is > 95% for transfer volumes as large as 50 mL! These results demonstrate excellent capacity for m-xylene with the µPHI.

The capacity for DMMP was significantly lower than that for m-xylene, despite its vapor pressure being ~9x lower. In fact, above ~200 ng it was not possible to achieve >90% retention, regardless of the sample volume. At 75 ng of DMMP, corresponding to a 30 minute sample at 5 mg/m^3 (S = 0.44 mL/min), the retention was 90% for a 1 mL transfer volume. Clearly, the polarity of DMMP plays a significant role in its adsorption on C-B and C-X adsorbents. We have explored the use of ionic liquid coatings as a means to enhance retention of polar VOCs on these adsorbents with modest success (data not shown). Desorption efficiencies ~98 % were observed for m-xylene and DMMP.

For desorption tests the µPHI heaters were operated globally or sequentially. The control software allowed adjustment of the individual ramp rate, heater ON time (hold-time) and delay between adjacent heaters (Fig. 8a). Experiments were performed to assess the combination of heating and flow parameters that would provide the sharpest injection band. The best results were obtained when the residence time of vapor above each heater was held close to the firing delay between individual heaters (~100 ms). For this purpose, the flow rate was reduced to ~50 µL/min (residence time ~300 ms) during the desorption process until all heaters reached 250 °C and the sample was completely injected, at which point

flow was increased to 3 mL/min to complete the transfer to the FID (no column was used). The full width at half maximum for the m-xylene peak was ~190 ms (Fig. 8b).

CONCLUSIONS

The concept introduced here of combining devices for passive sampling and progressively heated injection appears to be sound. Preliminary test results are promising. The capability of the µPP to passively sampling vapors at rates close to modeled values, to retain captured vapors at high mass loading levels, and to efficiently desorb vapors thermally for transfer to the µPHI all support its continued development. The capability of the µPHI to retain transferred samples of volatile non-polar vapors such as m-xylene is encouraging but polar vapors are less effectively retained. The use of ionic liquid modifiers shows promise for improving the retention of polar vapors and results of such testing will be described in a future report. Regardless, the progressive heating feature of the µPHI appears to be effective, with injection bands < 200 ms already having been achieved at low flow rates compatible with µGC separation columns. A hybrid-integrated µCOIN prototype has been assembled but data could not be generated in time for this publication. Nonetheless, results reported here augur well for the ultimate implementation of a monolithically integrated µCOIN to serve as a collector module for future µGC systems.

ACKNOWLEDGMENT

This research has been supported by the Office of the Director of National Intelligence (ODNI), Intelligence Advanced Research Projects Activity (IARPA). The views and conclusions contained herein are those of the authors and should not be interpreted as necessarily representing the official policies, either expressed or implied, of ODNI, IARPA, or the U.S. Government. The U.S. Government is authorized to reproduce and distribute reprints for governmental purposes notwithstanding any copyright annotation therein. Preliminary studies were supported by a pilot grant from the NIOSH-sponsored, University of Michigan Center for Occupational Health and Safety Engineering.

REFERENCES

1. J. Wang, et al., "Compact prototype microfabricated gas chromatographic analyzer for autonomous determinations of VOC mixtures at typical workplace concentrations," *Microsystems & Nanoengineering*, 4, 17101 (2018).
2. A. Garg, et al., "Zebra GC: A mini gas chromatography system for trace-level determination of hazardous air pollutants," *Sensors and Actuators B: Chemical*, 212, 145 (2015)
3. Y. Qin and Y. B. Gianchandani, "A fully electronic microfabricated gas chromatograph with complementary capacitive detectors for indoor pollutants," *Microsystems & Nanoengineering*, 2, 15049 (2016).
4. J. Wang, et al., "Microscale Gas Chromatography with Microsensor Array Detection: Challenges and Prospects," *Proceedings Eurosensors 2017,* September 3-6, 2017, Paris, France, 1, 633 (2017).
5. T. Sukaew, and E.T. Zellers, "Evaluating the dynamic retention capacities of microfabricated vapor preconcentrators as a function of flow rate," *Sensors and Actuators B: Chemical*, 183, 163 (2013).
6. J. Bryant-Genevier, and E.T. Zellers, "Toward a microfabricated preconcentrator-focuser for a wearable micro-scale gas chromatograph," *Journal of Chromatography A*, 1422, 299 (2015).
7. J. H. Seo, S. K. Kim, E. T. Zellers, K. Kurabayashi, "Microfabricated passive vapor preconcentrator/injector designed for micro gas chromatography," *Lab Chip*, 12, 717 (2012).
8. A. D. McBrady, F. Nusseibeh, "PHASED micro gas analyzer", *Final Report (Honeywell)*, BAA 03-40: Micro Gas Analyzers (MGA), DARPA Contract No.: FA8650-04-C-2502, June 27, 2008.
9. J. Mitchell, G. Lahiji, K. Najafi, "Encapsulation of vacuum sensors in a wafer level package using a gold-silicon eutectic", *Technical Digest, 13th Conf. on Solid-State Sensors, Actuators and Microsystems, Transducers '05,* pp. 928-931 (2005).

CONTACT

E. T. Zellers, tel: +1-734-936-0766; ezellers@umich.edu

ENHANCING SELECTIVITY OF CANTILEVER-BASED RESONANT CHEMICAL SENSORS THROUGH TRANSIENT MEASUREMENTS AT ELEVATED TEMPERATURES

P. Getz[1], C. Carron[1, 2], and O. Brand[1]
[1]School of Electrical and Computer Engineering, Georgia Institute of Technology, Atlanta, GA, USA
[1]Institute for Electronics and Nanotechnology, Georgia Institute of Technology, Atlanta, GA, USA
[2]Harris Corporation, Melbourne, FL, USA

ABSTRACT

This paper introduces a method to increase the selectivity of mass-sensitive chemical sensors towards volatile organic compounds (VOCs) by analyzing transient data as a function of device temperature. Heating pulses applied to a resonant, mass-sensitive cantilever cause a 3 °C to 30 °C rise in the sensing film temperature and, thus, a reduction in the partition coefficient, resulting in analyte desorption at the elevated temperature. Extracted temperature-dependent diffusion rates can be fit to an Arrhenius-type relationship whose coefficients can be used for analyte discrimination.

INTRODUCTION

In recent years, microelectromechanical systems (MEMS) based sensing devices have been incorporated into a variety of products, often as an inexpensive alternative to benchtop devices. While MEMS-based chemical sensors typically cannot offer superior performance (measured by selectivity, sensitivity and stability) compared to traditional desktop or laboratory units, MEMS solutions can be designed for applications where system requirements exclude traditional instrumentation, such as gas chromatography and mass spectroscopy units, due to their high cost, limited portability and high-power requirements [1, 2].

Many MEMS-based chemical sensors rely on analyte sorption into a polymeric sensing film [3]. Because these polymer sensing films are only partially selective to any analyte, sensors relying on analyte absorption into the polymer sensing film as a single data point face inherent uncertainty [4, 5]. As such, often arrays of sensors coated with different partially-selective films are used to decrease the uncertainty and improve the selectivity of the sensing system [6-8].

Various methods have been previously explored to increase the selectivity of a chemisorbing sensor via analyzing acquired transient data. Kummer et al. and Su et al. demonstrated the effectiveness of using a valve-generated signal transient to discriminate between similar analytes in a chemicapacitor [9] and resonant cantilever [3], respectively. Traditional valves that generate analyte absorption transients can be replaced with integrated heating resistors, which enable analyte desorption from the sensing film via the temperature-dependence of the partition coefficient [10]. Moreover, it is well known that diffusion rates of gaseous chemicals into a sensing film exhibit an Arrhenius relationship with temperature [9, 11]. Building on these efforts, this work explores analyte sorption transients recorded at different elevated temperatures to extract the analyte-specific (for a particular sensing film) coefficients of the Arrhenius relationship and improve the sensor selectivity.

THEORY

Analyte absorption and desorption into a sensing film generally follows Fick's law of diffusion and can be simplified, for most chemical sensors, by considering one-dimensional diffusion into a film terminated at one end. The normalized mass gained by this film is given by [3]

$$\frac{M(t)}{M_\infty} = 1 - 8 \cdot \sum_{n=0}^{\infty} \frac{1}{[(2n+1)\pi]^2} e^{-(t/4\tau)[(2n+1)\pi]^2} \quad (1)$$

where $M(t)$ is the mass gained or lost at time, t, and M_∞ is the equilibrium mass gained or lost. The characteristic diffusion time, τ, is defined as

$$\tau = h^2/D(T) \quad (2)$$

where h is the film thickness and the diffusion coefficient, D, is a function of temperature in Kelvin, T. For the initial mass gain or loss, this infinite sum can be approximated as

$$\frac{M(t)}{M_\infty} = \frac{2}{h}\sqrt{\frac{D(T)\cdot t}{\pi}} \quad (3)$$

for $M(t)/M_\infty \leq 0.5$. Thus, the temperature-dependent diffusivity coefficients can be estimated from measured sensor transients.

The temperature dependence of the analyte diffusivity into a polymer sensing film can be approximated by the linearized form of the Arrhenius relationship [9]

$$\ln D(T) = -\frac{E}{R}\left(\frac{1}{T}\right) + \ln D_0 \quad (4)$$

where the measured diffusivity from Eq. (3) is a function of the film temperature, the activation energy for diffusion of analyte molecules into the sensing film, E, the gas constant, R, and the Arrhenius pre-exponential factor, D_0, relating to the diffusivity as temperature approaches infinity.

SENSING SYSTEM

Figure 1 shows the heated mass-sensitive chemical sensor used for this work, comprising a semi-circular hammerhead-like suspended resonator fabricated in the device layer of an SOI wafer. The fabrication procedure follows the process developed for

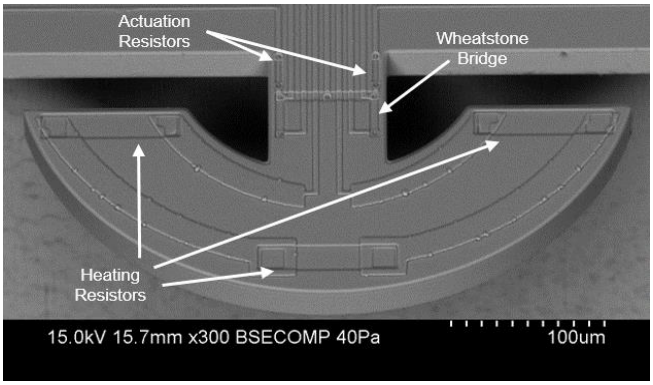

Figure 1: SEM micrograph of a resonant cantilever with a near-semicircular head supported by a 75 µm wide, 100 µm long beam. Resistors for thermal excitation and piezoresistive detection of in-plane vibrations are located at the cantilever base. Three heating resistors, for thermal modulation, are visible on the head region.

978-1-940470-03-0/HH2018/$25©2018TRF
DOI 10.31438/trf.hh2018.84

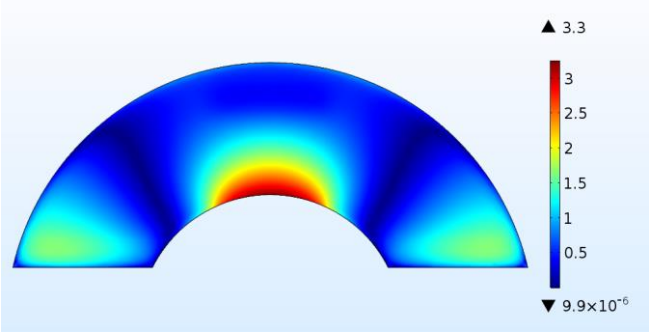

Figure 2: COMSOL finite element model analysis of temperature uniformity within a 5 µm PIB sensing film: displayed is the absolute deviation in percent from the mean film temperature due to thermal modulation from the integrated heating resistors on the heated cantilever's hammerhead region.

resonant chemical sensors in our group [10, 12]. The hammerhead region is spray-coated via shadow masking with an appropriate sensing film, polyisobutylene (PIB) in the present work, for the analytes of interest. The hammerhead region is anchored via a 100 µm long, 75 µm wide beam and the sensor's resonance frequency prior to coating is 740-760 kHz. Three diffused resistors in the hammerhead region enable rapid, localized heating to modulate the sorption kinetics and generate temperature-modulated sorption transients.

The device's geometry seeks to maintain thermal uniformity within the coated hammerhead region, maximize heating power efficiency while minimizing thermal rise times. Additionally, the heating resistors' location at the distal end of the cantilever minimizes temperature rise near the beam's anchor point and limits the effects of self-heating on the resonant frequency shift due to the temperature dependency of silicon's Young's modulus.

A COMSOL finite element analysis of the steady-state temperature elevation of the device with coated film in Figure 2 shows the deviation in percent from the average film temperature. The analysis highlights a fairly uniform film temperature with a <1% deviation from the mean temperature rise for 66% of the film and a <3% deviation for 99.8% of the film. This ensures a consistent partition coefficient and diffusivity coefficient throughout the absorbing film.

Figure 3 shows the normalized simulated thermal transient of the heated hammerhead structure and coated sensing film from a COMSOL simulation for a 6 µm PIB coated device. The 90% thermal rise time of the coated film is approximately 3 ms. Since typical absorption transients for this polymer thickness are expected

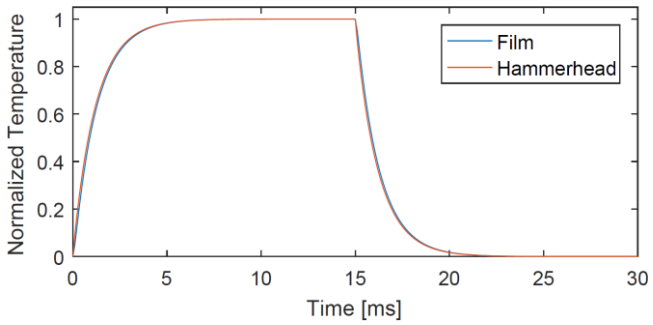

Figure 3: COMSOL finite element simulation of the normalized temperature transient of the silicon hammerhead region (red line) and the 5 µm PIB sensing film (blue line) for a 15 ms heating pulse applied to the heating resistors.

to be on the order of tens to hundreds of seconds, such short thermal transients of the device ensure that they will not influence the measured sorption transients or extracted Arrhenius coefficients.

EXPERIMENTAL

The gas mixing setup used has been described in detail by Su [3]. It features multiple mass flow controllers and glass bubblers with liquid analyte for a carrier gas (nitrogen) to flow through to control analyte and reference gas streams. A high-speed pneumatic four-way valve switches between an ultra-high purity nitrogen reference gas stream and an analyte-loaded gas stream from the liquid bubbler (set in a temperature-controlled bath) that has been diluted from its Antoine equation partial pressure by nitrogen. The setup enables analyte concentrations from hundreds to thousands of ppm, depending on the analyte's partial pressure.

The hammerhead resonators are embedded in an amplifying feedback loop on a dedicated printed circuit board that ensures continuous operation at their fundamental in-plane resonance frequency. The resonance frequencies of a coated and an uncoated cantilever are measured simultaneously with a frequency counter. The uncoated cantilever compensates for environmental fluctuations within the sensing chamber not relating to analyte sorption. The LabVIEW-controlled setup measures the devices' resonant frequencies at 2-5 samples per second.

On experiment start, the system flows pure carrier gas over the resonator until equilibrium is reached. A chemical measurement begins as the four-way valve switches from carrier gas to analyte loaded gas. After the room-temperature analyte-loaded equilibrium is reached, a voltage is applied to the integrated resistors for a set time via a function generator or source-meter, thus modulating the sensing film's temperature with the applied power. The elevated temperature reduces the film's partition coefficient, causing analyte to desorb out of the sensing film. After a set heating period (10 minutes for the experiments in this work), the heating voltage is turned off and the film returns to its original temperature and partition coefficient. This causes the analyte to re-absorb into the sensing film. This sequence is repeated multiple times with various heating powers (5 mW, 10 mW, 20 mW, and 40 mW) to generate data points for the Arrhenius relationship fit.

Upon conclusion of the heating pulse chain, the valve system changes back to the pure carrier gas flow and the system is brought back to equilibrium as a reset prior to subsequent measurements. Figure 4 shows the response of the sensor to heating pulses under

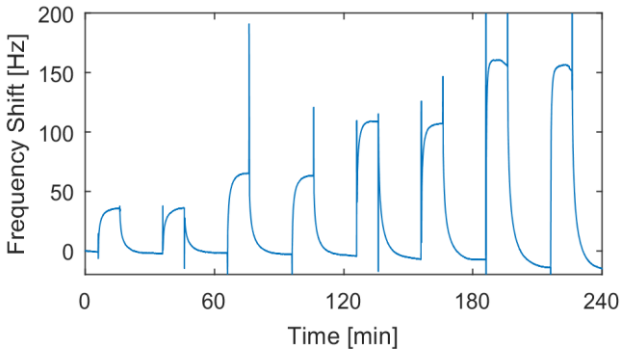

Figure 4: Frequency shift due to heating-induced analyte desorption for two 10-minute long heating pulses each at a heating power of 5, 10, 20 and 40 mW. The resonator is coated with a PIB sensing film and exposed to a constant 630 ppm concentration of ethyl-benzene during the 4-hour measurement period. Signal spikes at the beginning/end of the heating pulses are artifacts stemming from signal analysis and limited sampling rate.

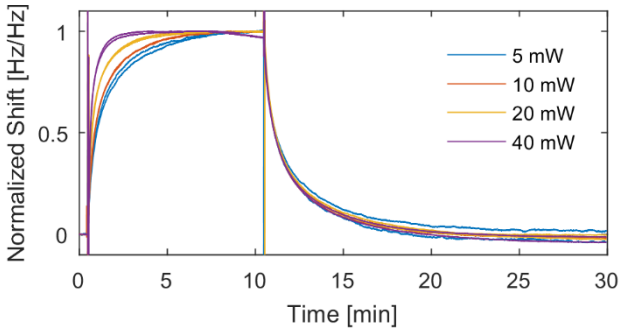

Figure 5: Measured normalized sensor frequency shift due to analyte sorption during 10-minute heating pulses (5, 10, 20 and 40 mW pairs). A positive shift indicates desorption due to the increased temperature, while a negative shift after a heating pulse indicates re-absorption into the sensing film. Desorption transients show different time constants at different temperatures because of the temperature dependence of the analyte diffusivity in the sensing film. The re-absorption is happening at room temperature and thus exhibits the same time constant for all heating pulses.

approximately 630 ppm ethyl-benzene exposure after the effect of device heating on the sensor response is removed in post-processing. This procedure is repeated for the five other analytes in this work: pentane, chloroform, benzene, toluene and o-xylene. The tests with different analyte were performed sequentially using the same 6.1 µm thick PIB sensing film.

Figure 5 overlays the responses of the sensor with a 6.1 µm thick PIB sensing film for different heating pulse powers. The data is normalized based on the steady-state frequency shift for each heating power (which can also be used as an independent metric to increase selectivity). The differing diffusion time coefficients are easily distinguishable during the initial 10-minute heating phase and can be fit to the Arrhenius curve via a first order polynomial fit (y=mx+b) according to (4).

RESULTS

Figures 6 and 7 show the extracted diffusivity data as a function of temperature and the logarithm of the diffusivity as a function of the inverse temperature (according to Eq. (4)), respectively. Table I summarizes the extracted numerical values for E and D_0 for the tested six volatile organic compounds. Thereby, the temperature

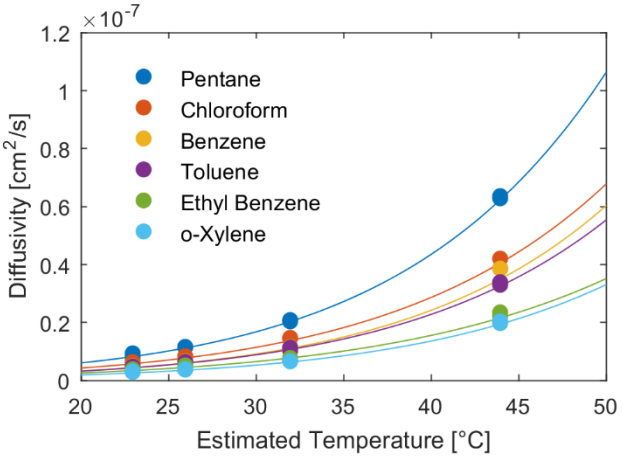

Figure 6: Extracted diffusivity for six different analytes in a PIB sensing film as a function of temperature. The measured data points are fitted to the Arrhenius equation (solid lines).

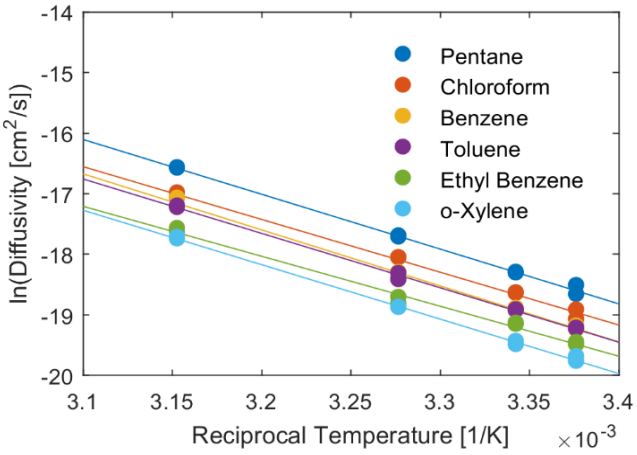

Figure 7: Logarithm of extracted diffusivity as a function of the inverse sensing film temperature for six different analytes in a PIB sensing film. According to the linearized form of the Arrhenius equation (see Eq. (4)), different D_0 *are seen as different y-intercepts, while different activation energies* E *result in different slopes.*

rise per applied heating power is estimated from COMSOL simulations and calibration measurements in an environmental chamber to be 0.6 °C/mW. Clear numerical differentiation, particular in case of D_0, shows the ability of this method to distinguish between analytes. In case of similar D_0, the activation energy, E, assists to discriminate between analytes, enhancing the ability of sensors to distinguish between different analytes with similar diffusivity constants at room temperature.

The extracted data suggests that even chemically similar analytes, such as benzene, toluene, o-xylene and ethyl-benzene, can be distinguished using the presented method. These analytes have a common benzene ring and differ with the addition of carbon groups added to the ring. Optimization of polymer thickness and type can further target specific analytes and lead to an improved sensor performance with improved selectivity based solely on the temperature dependence of the analyte diffusivity.

Table I: Summary of extracted Arrhenius diffusivity coefficients D_0 and E for six analytes in a PIB sensing film. Differentiation in both D_0 and E lead to an increased ability to distinguish analytes from one another and increases sensor selectivity.

Analyte	D_0 [m²/sec]	E [kJ/mol]
Benzene	8.159	75.16
Chloroform	1.897	70.93
Ethyl Benzene	0.304	67.71
Pentane	16.91	75.47
Toluene	6.368	74.61
o-Xylene	2.801	73.85

CONCLUSION

This paper demonstrates the design of a chemisorbing mass-sensitive heated cantilever and method to increase system selectivity via analyzing recorded analyte transients as a function of sorbing film temperature. Diffusivity coefficients extracted from analyte desorption transients, induced by a temperature increase of the sensing film, for different volatile organic compounds were fitted to an Arrhenius relationship. This relationship yielded parameters that can help distinguish between analytes and, thus, improve sensor selectivity. In future work, the sensor response to analyte mixture will be investigated.

ACKNOWLEDGEMENTS

This work was performed at Georgia Tech's Institute for Electronics and Nanotechnology (IEN), a member of the National Nanotechnology Coordinated Infrastructure (NNCI), which is supported by the National Science Foundation (Grant ECCS-1542174). The authors would like to thank the IEN staff for their assistance during device fabrication and testing.

REFERENCES

[1] C. K. Ho, A. Robinson, D. R. Miller, and M. J. Davis, "Overview of sensors and needs for environmental monitoring," *Sensors,* vol. 5, no. 1, pp. 4-37, 2005.

[2] C. K. Ho, M. T. Itamura, M. Kelley, and R. C. Hughes, "Review of chemical sensors for in-situ monitoring of volatile contaminants," *Sandia Report,* 2001.

[3] J.-J. Su, C. Carron, S. Truax, K. Demirci, L. Beardslee, and O. Brand, "Assessing polymer sorption kinetics using micromachined resonators," in *Solid-State Sensors, Actuators and Microsystems Conference (TRANSDUCERS), 2011 16th International*, 2011, pp. 1420-1423: IEEE.

[4] A. Hierlemann, A. J. Ricco, K. Bodenhöfer, A. Dominik, and W. Göpel, "Conferring selectivity to chemical sensors via polymer side-chain selection: thermodynamics of vapor sorption by a set of polysiloxanes on thickness-shear mode resonators," *Analytical chemistry,* vol. 72, no. 16, pp. 3696-3708, 2000.

[5] A. Hierlemann, E. T. Zellers, and A. J. Ricco, "Use of linear solvation energy relationships for modeling responses from polymer-coated acoustic-wave vapor sensors," *Analytical chemistry,* vol. 73, no. 14, pp. 3458-3466, 2001.

[6] F. Battiston *et al.*, "A chemical sensor based on a microfabricated cantilever array with simultaneous resonance-frequency and bending readout," *Sensors and Actuators B: Chemical,* vol. 77, no. 1-2, pp. 122-131, 2001.

[7] G. Yoshikawa *et al.*, "Sub-ppm detection of vapors using piezoresistive microcantilever array sensors," *Nanotechnology,* vol. 20, no. 1, p. 015501, 2008.

[8] A. S. Pavluchenko, A. V. Mamykin, A. L. Kukla, N. V. Konoshchuk, O. Y. Posudievsky, and V. G. Koshechko, "Estimation of multicomponent organic solvent vapor mixture composition with electroconducting polymer chemiresistors," *Sensors and Actuators B: Chemical,* vol. 232, pp. 203-218, 2016.

[9] A. M. Kummer, T. P. Burg, and A. Hierlemann, "Transient signal analysis using complementary metal oxide semiconductor capacitive chemical microsensors," *Analytical chemistry,* vol. 78, no. 1, pp. 279-290, 2006.

[10] C. Carron, P. Getz, S. M. Heinrich, F. Josse, and O. Brand, "Cantilever-based resonant microsensors with integrated temperature modulation for transient chemical analysis," in *Transducers 2015, 18th International Conference on Solid-State Sensors, Actuators and Microsystems*, 2015, pp. 1511-1514.

[11] J. L. Duda, J. S. Vrentas, S. T. Ju, and H. T. Liu, "Prediction of diffusion coefficients for polymer-solvent systems," *AIChE Journal,* vol. 28, no. 2, pp. 279-285, 1982.

[12] L. A. Beardslee, A. M. Addous, S. Heinrich, F. Josse, I. Dufour, and O. Brand, "Thermal Excitation and Piezoresistive Detection of Cantilever In-Plane Resonance Modes for Sensing Applications," *Microelectromechanical Systems, Journal of,* vol. 19, no. 4, pp. 1015-1017, 2010.

CONTACT

P. Getz, tel: +1-916-850-5585; patrick.getz@gatech.edu
O. Brand, tel: +1-404-894-9425; oliver.brand@ece.gatech.edu

MATTRESS-BASED SWEAT MONITORING FOR HUMAN HEALTH MONITORING AND SMART HOMES

Spyridon Pavlidis[1,2], Meng-Yen Tsai[2], Billyde Brown[2], Decarle Jin[2], John-David Velilla[3], Michael DeFranks[3], and Eric Vogel[2†]*
[1]North Carolina State University, Raleigh, North Carolina, USA
[2]Georgia Institute of Technology, Atlanta, Georgia, USA
[3]Serta Simmons Bedding, Norcross, Georgia, USA

ABSTRACT

Mattress-based sweat sensing systems can provide non-intrusive, continuous health monitoring. Commercialization of physical sensors in beds has already been achieved, while chemical sensing within the same platform is still in its infancy. We describe our approach towards the development of flexible potentiometric sensors and demonstrate low-temperature fabrication of these devices. Three commonly used mattress fabrics have been contrasted as sweat capture layers, leading to pH sensing with a sensor embedded within the hydrophilic fabric. It is found that noise, sensitivity and linearity can be affected by the rate of liquid flow, temperature of the Al_2O_3 deposition and stability of the thin film Ag/AgCl reference electrode realized on-chip.

INTRODUCTION

As electronics continue to become smaller, the sensors market has penetrated deeper into our daily lives, ranging from personal use to industrial use, among other applications. Mainstream commercial sensors in the market today largely rely on physical sensors, such as accelerometers and gyroscopes within smartphones, to track movement. Wearable sensors of this type have also emerged, allowing for more continuous and less intrusive capture of data. Wearable chemical sensors, however, remain a very active subject of research, with recent work focused on sweat analysis to assess one's health [2-4]. Compared to blood, sweat is a particularly attractive analyte since it can be acquired non-invasively and contains chemical markers with significant physiological correlation [5]. Despite the many uses of wearable sensors, in particular when the user is in transit and activity tracking is of interest, there exist applications where wearing a device is not practical or even possible.

One such scenario is health monitoring while lying on a mattress, which can be used both for everyday sleep analysis, as well as in-patient monitoring for bed-bound patients. Since humans spend an average of one third of their lives lying on mattresses, they represent a unique yet heretofore untapped opportunity to monitor one's health and enable smart home systems that tailor our environments to optimize our wellbeing. Unlike wearable sensors, in-built mattress sensors would not require user installation or training and would therefore facilitate use. They also do not interfere with one's comfort, or force a change of habit in terms of what is worn during sleep.

In this work, we investigate the development of flexible chemical sensors embedded in mattresses for sweat-based health monitoring. To our knowledge, this is the first time that flexible chemical sensors have been integrated into mattress materials to detect pH, which is tied to electrolyte [6] and lactic acid [7] concentrations, among other constituents. This paper introduces our mattress-integrated sweat sensing approach, describes the implementation challenges and associated design choices that have been made to make progress towards this system. A low-temperature and scalable microfabrication process is also described, with prototypes demonstrated on both silicon and flexible polyimide substrates. We compare three commonly used mattress fabrics for their suitability as liquid-absorbing interfaces to the sensor's surface. By leveraging an extended gate sensor configuration, we also present results on the performance of these sensors when integrated into the mattress material, the effect of decreasing deposition temperature for the pH-sensitive dielectric thin film, and the stability of the on-chip reference electrode.

MATTRESS SENSOR CONCEPT AND DESIGN

A first generation of mattress sensors has already been commercialized by Serta Simmons Bedding as accessories to their Beautyrest® line of mattresses (Figure 1) [1]. The Sleeptracker® sensing system consists of physical sensors and a processing unit that can be installed between the mattress and the bed frame/base. The sensors are responsible for tracking the heart and breathing rates as well as the motion/movement of the bed's occupants, while the processor, which is located underneath the base/frame operates the sensors, collects the data and transfers them to the cloud for storage. The data can then be retrieved by users on their smartphone or computer. Access to this information allows the user to monitor the quality of their sleep by quantifying the time spent in different sleep cycles, without having to wear a bracelet or other device. Serta Simmons's aim is to enable users to improve the quality of sleep – for example, they can optimize the timing of a pre-programmed alarm to wake a user during the most comfortable sleep cycle.

This infrastructure forms a strong foundation for the development of a new generation of chemical sensors, which is the focus of this work. However, the design of sweat-sensitive sensors must address new challenges compared to the already existing physical sensors. Design requirements include: close proximity to the sleeper in order to collect the sweat prior to sample spoiling or evaporation; operation with low sample volume; high sensitivity;

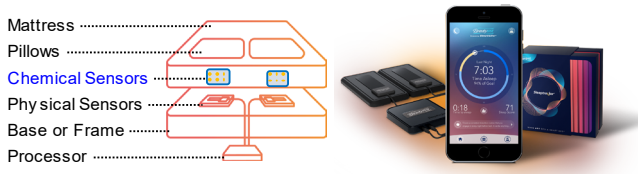

Figure 1: Serta-Simmons Bedding has commercialized a Beautyrest® line of mattresses with Sleeptracker® technology that does not necessitate the use of wearable devices. (a) These physical sensors are placed in between the mattress and bed base/frame to monitor one's heart and breathing rates, as well as their movement to report the time spent sleeping. The focus of this work is the development of novel chemical sensors, located in the upper layers of the mattress, to detect sweat content. (b) The sensor data is collected by a processor unit, which uploads information to the cloud and can be accessed remotely. [1]

978-1-940470-03-0/HH2018/$25©2018TRF
DOI 10.31438/trf.hh2018.85

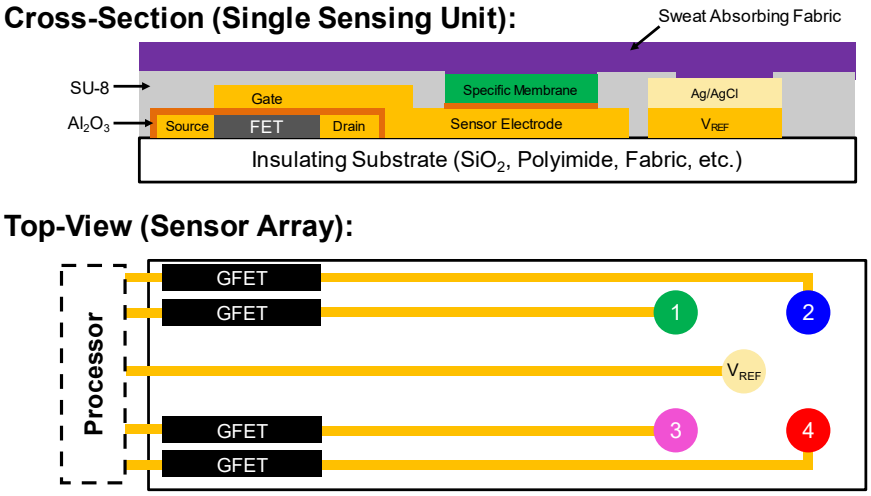

Figure 2: System overview for mattress-integrated sensor array for sweat analysis to provide health monitoring and smart home capabilities. The cross-sectional view shows the critical components of a single module in the system, including the functionalized sensor electrodes, while the top-view demonstrates how each module can be cascaded to realize the multi-component sensing array. The FETs are depicted conceptually as potentiometers.

high selectivity to detect different components of the sweat; and a thin, flexible form factor so as to not interfere with sleep quality. Additional system-level challenges include data transfer, power supply and long-term stability or ease of replacement. The latter two are of particular importance since the average lifetime of a mattress is ten years.

An illustration of the conceived sweat-sensing system for in-mattress integration is depicted in Figure 2. The cross-section outlines the three major components of each sensor: (1) sensor electrode, (2) reference electrode and (3) FET transducer. The entire platform is fabricated on an insulating substrate. The sensor electrode consists of an alumina (Al_2O_3) thin film deposited on gold. Al_2O_3 has been chosen since it can be deposited with high quality at a wide range of temperatures and has been demonstrated to be pH sensitive [8]. To enhance specificity, an analyte-specific layer can be added on top of the Al_2O_3, which will dictate that any change in potential observed at the Al_2O_3's surface is due to the change in concentration of the specific ion in question. In close proximity to the sensor electrode, a Ag/AgCl reference electrode is formed. This electrode is critical to this work, and it is important to characterize and consequently improve its operational stability.

The sensor electrode is connected to the gate electrode of a charge-sensitive field-effect transistor (FET). This separation of the FET and sensor surface is known as the extended gate configuration, and serves two advantages compared to the traditional ion-sensitive field-effect transistor (ISFET) layout: (1) it enhances operational reliability of the FET by isolating it from direct contact with the liquid-phase analyte, and (2) permits independent development of the sensor electrode from the FET device itself. Graphene has been identified as a suitable channel material for the FET since it can be deposited over large areas and has already been demonstrated for use in potentiometric biosensors [9]. The FET and metal traces on-chip are protected by an SU-8 microfluidic isolation layer. This thin film is patterned with openings located only at the sensor and reference electrode surfaces. Given the aim of this work to integrate the sensors into a mattress, the top of the chip is fitted with a mattress fabric. This material must be carefully chosen to absorb sweat and consequently bring it into contact with the sensor's surface.

The bottom half of Figure 2 presents a top-side view of a sensor array that can be implemented using the architecture described above. To minimize size requirements, a common reference electrode is leveraged for multiple, individually-functionalized sensor electrodes to detect different components of sweat. Each of these is connected to a potentiometer (i.e., the high impedance gate of a FET) whose respective signals are fed to a computer or microcontroller that processes the information and makes it available to the user for analysis.

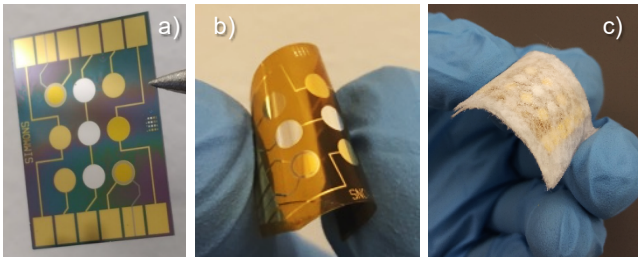

Figure 3: (a) Extended gate sensors fabricated on silicon substrate, (b) flexible sensors fabricated on polyimide substrates and (c) packaged in fabric used in commercial mattress.

SENSOR FABRICATION

The sensors were fabricated on both silicon (Figure 3a) and polyimide (Figure 3b) substrates. In this paper, we focus on the development and characterization of the sensor and reference electrodes, paying particular attention to the effects of low-temperature fabrication on their performance and methods to improve them. We therefore employ a FET-less fabrication flow, made possible by the extended gate configuration described above. By using flexible substrates, direct embedding of the sensors within a mattress fabric can be achieved, as shown in Figure 3c. In the case where silicon (Si) wafers were used, a thermal silicon oxide (SiO_2) was created prior to metal deposition. To improve metal adhesion as well as robustness to wet processing when working with the polyimide substrates [10], they were first annealed in vacuum at 200 ˚C for 8 hours, treated with O_2 plasma for 60 sec and then both sides were coated with 150 nm of plasma-enhanced chemical vapor deposited PECVD silicon nitride (SiN_x) at 100 ˚C. A first metal layer consisting of chrome/gold/aluminum (Cr/Au/Al) with thickness 25/300/2 nm was deposited using electron-beam evaporation and patterned using lift-off. The top Al surface was descummed using an O_2 plasma that also facilitates the adhesion of the consequent atomic layer deposition (ALD) of Al_2O_3. The Al_2O_3 layer was deposited at 250 ˚C and 150 ˚C with a thickness of 15 nm, the effects of which are discussed below. In order to gain access to the metal layers, vias are etched into the Al_2O_3. This is executed using Al Etchant (based on phosphoric acid) that is heated to 50 ˚C for 2.5 minutes. The samples are once again descummed with O_2 plasma, prior to the electron-beam evaporation of the reference

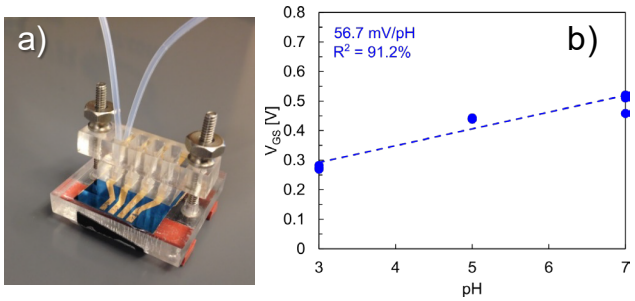

Figure 4: (a) Initial extended-gate samples were fabricated on silicon wafers using shadow masking techniques to produce high-quality interfaces. For testing, they were packaged in PDMS microfluidics and off-chip FET was used as a transducer. (b) For a reference current of 100 nA, a sensitivity of 56.7 mV/pH was observed, which is near-Nernstian.

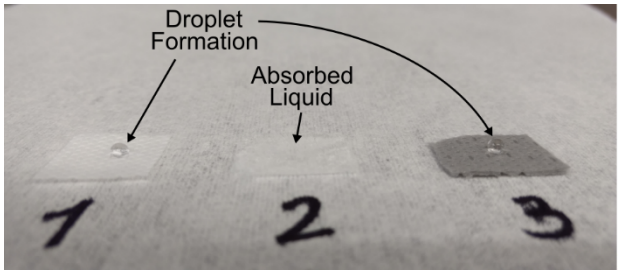

Figure 5: In order for analyte to reach the sensor's surface, the mattress fabric must be hydrophilic. Three materials commonly used by the mattress industry were tested: 1) spun bonded, nonwoven polypropylene, 2) long staple fiber, needle punched, nonwoven polypropylene, 3) spun bonded and needle punched, nonwoven polypropylene. With Samples 1 and 3 exhibiting hydrophobic behavior, Sample 2 was chosen.

electrodes consisting of titanium/silver (Ti/Ag) thin films with 30/150 nm thickness, which are also patterned using lift-off. SU8-3005 is then spin-coated and patterned, resulting in a 5 µm thick microfluidic isolation layer. Finally, the exposed Ag thin film is chloridized to Ag/AgCl by drop coating ferric chloride ($FeCl_3$)-based copper etchant for 1 minute, before rinsing thoroughly with DI water.

RESULTS

To establish a baseline of performance against which to compare the microfabricated sensors, a set of chips was fabricated using shadow masks and tested using PDMS-based microfluidics, as shown in Figure 4a. Since initial process development was performed on Si substrates without temperature constraints, the Al_2O_3 layer was deposited at 250 ˚C. The sensor electrodes were connected to the gate of an FET, while the on-chip Ag/AgCl reference electrodes were biased in order to capture V_{GS}-I_D for each pH solution. It is known that a change in the pH on the dielectric surface results in an effective change in the threshold voltage (V_{TH}), which can be extracted from the FET's transfer curve. The maximum sensitivity is known as the Nernstian Limit, which corresponds to 59 mV/pH. To establish some stastical significance, each measurement was completed four times. Figure4b shows the change in V_{GS} for a reference current of 100 nA. From this, it is gleaned that the sensitivity is 56.7 mV/pH (very close to Nernstian) and the linearity is 91.2%.

Three samples of mattress material were evaluated for their suitability of integration with the sensor. This test was conducted by dropping water droplets onto the surface and consequently

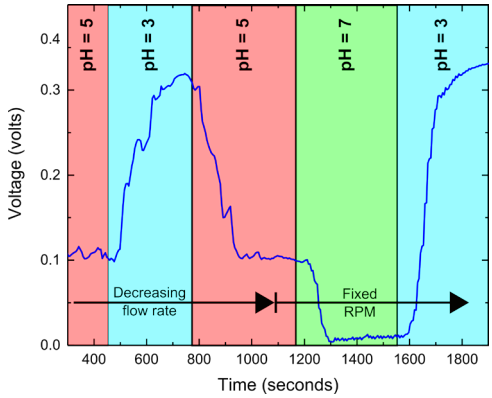

Figure 6: The potentiometric transient response of the sensors to various pH solutions was measured. The backside of the chip was attached to flexible PDMS and embedded within the liquid absorbing mattress fabric, the latter now replacing the conventional microfluidic structure.

determining if they were absorbed by the fabric, or retained as a droplet. The three materials that were compared were: 1) spun bonded, nonwoven polypropylene fabric, 2) long staple fiber, needle punched, nonwoven polypropylene fabric, 3) spun bonded and needle punched, nonwoven polypropylene fabric. As shown in Figure 5, Sample 2 is the only one that absorbed the droplet and will therefore serve as a good top interface for the sweat sensor

To address mattress integration, low-temperature sensor chips were fabricated with a maximum thin film deposition temperature of 150 ˚C in order to be compatible with the thermal budget of polyimide and other flexible substrates. These were first characterized on a silicon-based chip whose backside was attached to soft and flexible PDMS for support while the top was covered with the hydrophilic fabric identified above. Using a peristaltic pump, it was possible to control the flow rate of pH solutions that were dropped onto the fabric to study the effect of flow rate, as well as switch between different pH values to assess sensitivity. Transient data is depicted in Figure 6. From t = 0 to t = 1100 sec, the flow rate was decreased from 40 RPM to 3 RPM. During this window, there is observable noise in the voltage response. After t = 1100, where the flow rate remains 3 RPM, the noise decreases significantly. The relationship between signal noise and flow rate necessitates further study, and the consideration of design techniques to reduce its effect. Control of the flow rate could be achieved through localized mattress heating and/or iontophoresis. The sensitivity of the response is also non-linear. For the transition between pH = 5 and pH = 7, the sensitivity is 48.2 mV/pH. This is slightly less than what was observed when high temperature Al_2O_3 was used in Figure 4b, but still sufficient. Moreover, the sensitivity for the transition between pH = 7 and pH = 3 increased. The source of this non-linearity was investigated by examining two variables: (1) the effect of the ALD Al_2O_3 temperature, (2) the on-chip Ag/AgCl reference electrode's stability in liquid.

To isolate the impact of ALD temperature on pH sensing performance, sensors with Al_2O_3 deposited at 100 ˚C were tested in PDMS-based microfluidic structures, with I-V curves extracted from a gate-connected FET and an off-chip flow-through Ag/AgCl reference electrode. As shown in Figure 7, the sensitivity of these films was found to be 23.8 mV/pH with a significantly decreased linearity of 66.6%. It has been noted in the literature that oxidation of Al_2O_3 films can improve pH sensing performance [11]. Thus, the sensors were subjected to 30 sec O_2 plasma at 50 W before another round of testing. This treatment resulted in an improvement in both the sensitivity (34 mV/pH) and the linearity (74.5%). Further

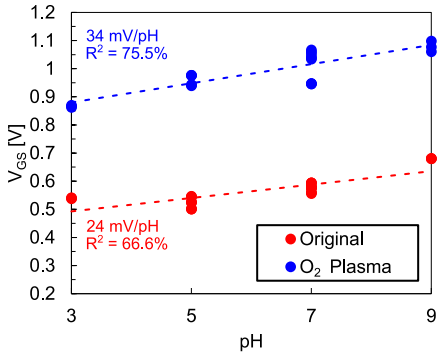

Figure 7: It was found that reduction of the ALD Al_2O_3 deposition temperature to 100˚C lowered both the sensitivity and linearity of the pH response compared to the original 250˚C case. This can be counteracted through the use of O_2 plasma treatment on the film.

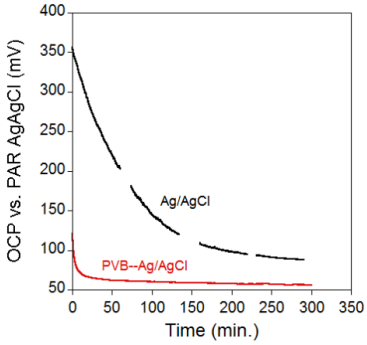

Figure 8: The stability of the e-beam evaporated Ag/AgCl reference electrode can also contribute to the response, but can be improved through the use of a PVB coating.

investigation is required to understand this effect, though it is hypothesized at this stage that it could be related to the impact of film stoichiometry, with decreased oxygen incorporation in Al_2O_3 when deposited at low temperature requiring compensation via O_2 plasma versus direct high temperature deposition.

Most pH sensors in the literature rely on off-the-shelf macro-scale Ag/AgCl reference electrodes for demonstration. In benchtop testing scenarios, this is an acceptable approach, however it cannot be adopted in our application, which requires full on-chip integration. It is therefore important to characterize the effect of the thin film-based reference electrode we have constructed. Figure 8 demonstrates that over a period of 5 hours, a bare Ag/AgCl reference electrode subjected to constant bias in a KCl solution can exhibit over 200 mV of drift. To combat this, previous studies [4, 12] have proposed the use of a polyvinyl butyral (PVB) coating. We have tested this approach and found that it indeed reduces the "burn-in" time required for the electrode to reach a stable state. While other studies have examined these reference electrode preparation techniques for short- to medium-term use (e.g., disposable wearables), further study is required to understand their long-term stability, for example over one year. Care must also be taken to characterize the reference electrode's potential versus pH and ionic strength to ensure stability against these variations.

CONCLUSION

Wearable sensors offer much potential in terms of continuous health monitoring, but there exist scenarios where sensors fully integrated into the objects of our environment can help improve quality of life. In this work, we have presented an approach to embedding potentiometric sensors into mattress fabrics for sweat analysis during sleep. We have described an architecture for such a system, and demonstrated microfabrication of these sensors. Our results reveal several factors impacting the performance of these sensors as we move away from conventional microfluidic approaches, such as the rate of analyte capture, the low temperature deposition of the pH sensing Al_2O_3 film and the stability of the on-chip Ag/AgCl reference electrode. Methods to successfully combat these effects have been presented, thus motivating further study and development of these sensors.

ACKNOWLEDGMENTS

This work was supported by Serta Simmons Bedding, LLC. Fabrication was performed at the Georgia Tech Institute for Electronics and Nanotechnology (IEN), a member of the National Nanotechnology Coordinated Infrastructure, which is supported by the National Science Foundation (Grant ECCS-1542174).

REFERENCES

[1] Simmons Bedding Company LLC. (2018). *Beautyrest Sleeptracker*. Available: https://www.beautyrest.com/Sleeptracker

[2] W. Jia *et al.*, "Electrochemical Tattoo Biosensors for Real-Time Noninvasive Lactate Monitoring in Human Perspiration," *Analytical Chemistry,* vol. 85, no. 14, pp. 6553-6560, 2013.

[3] D. P. Rose *et al.*, "Adhesive RFID Sensor Patch for Monitoring of Sweat Electrolytes," *IEEE Transactions on Biomedical Engineering,* vol. 62, no. 6, pp. 1457-1465, 2015.

[4] W. Gao *et al.*, "Fully integrated wearable sensor arrays for multiplexed in situ perspiration analysis," *Nature,* Letter vol. 529, no. 7587, pp. 509-514, 2016.

[5] J. Moyer, D. Wilson, I. Finkelshtein, B. Wong, and R. Potts, "Correlation Between Sweat Glucose and Blood Glucose in Subjects with Diabetes," *Diabetes Technology & Therapeutics,* vol. 14, no. 5, pp. 398-402, 2012.

[6] D. Kaiser, R. Songo-Williams, and E. Drack, "Hydrogen ion and electrolyte excretion of the single human sweat gland," *Pflügers Archiv,* vol. 349, no. 1, pp. 63-72, 1974.

[7] F. M. Thurmon and B. Ottenstein, "Studies on the Chemistry of Human Perspiration with Especial Reference to its Lactic Acid Content," *Journal of Investigative Dermatology,* vol. 18, no. 4, pp. 333-339, 1952.

[8] S. Chen, J. G. Bomer, E. T. Carlen, and A. van den Berg, "Al2O3/Silicon NanoISFET with Near Ideal Nernstian Response," *Nano Letters,* vol. 11, no. 6, pp. 2334-2341, 2011/06/08 2011.

[9] A. Tarasov, M.-Y. Tsai, E. M. Flynn, C. A. Joiner, R. C. Taylor, and E. M. Vogel, "Gold-coated graphene field-effect transistors for quantitative analysis of protein–antibody interactions," *2D Materials,* vol. 2, no. 4, p. 044008, 2015.

[10] K. H. Cherenack, N. S. Munzenrieder, and G. Troster, "Impact of Mechanical Bending on ZnO and IGZO Thin-Film Transistors," *IEEE Electron Device Letters,* vol. 31, no. 11, pp. 1254-1256, 2010.

[11] H. Y. Liu, W. C. Hsu, C. S. Lee, B. Y. Chou, and W. F. Chen, "Enhanced Performances of AlGaN/GaN Ion-Sensitive Field-Effect Transistors Using H2O2-Grown Al2O3 for Sensing Membrane and Surface Passivation Applications," *IEEE Sensors Journal,* vol. 15, no. 6, pp. 3359-3366, 2015.

[12] T. Guinovart, G. A. Crespo, F. X. Rius, and F. J. Andrade, "A reference electrode based on polyvinyl butyral (PVB) polymer for decentralized chemical measurements," *Analytica Chimica Acta,* vol. 821, pp. 72-80, 2014.

CONTACT

*S. Pavlidis, tel: +1-919-513-3018; spavlidis@ncsu.edu
†E.M. Vogel, tel: +1-385-7235; eric.vogel@mse.gatech.edu

RAPID DIFFERENTIATION OF HOST AND PARASITE EXOSOME VESICLES USING PHOTONIC CRYSTAL BIOSENSOR

Yifei Wang[1], *Wang Yuan*[2], *Michael Kimber*[*2], *Meng Lu*[*1,3,4], *and Liang Dong*[*1,3]
[1]Department of Electrical and Computer Engineering, [2]Department of Biomedical Sciences
[3]Microelectronics Research Centre, [4]Department of Mechanical Engineering
Iowa State University, Ames, Iowa 50011, USA

ABSTRACT

The analysis of membranous extracellular vesicles, such as exosomes vesicles (EV) opens a new direction for the rapid disease diagnosis because EVs can carry molecular constituents of their originating cells [1]. Secreted by mammalian cells, the size of most membrane-bound phospholipid EVs ranges from 50 to 150 nm in diameter. Recent studies have demonstrated the potential of using EVs for cancer diagnosis and treatment monitoring [2-3]. To diagnose infectious diseases using EVs, the ability to discriminate EVs from host cells and parasites is key. Here, we report a rapid EV analysis assay that can discriminate EVs based on a host-specific transmembrane protein (CD63 antigen) using a label-free optical biosensor.

INTRODUCTION

Cancer cells secrete cytokines, chemokines and nucleic acids that have traditionally served as biomarkers for disease diagnosis and prognosis [4]. Profoundly, membranous extracellular vesicles, including nanoscale exosomes and other vesicles actively secreted from cancer cells, have also been found in the blood of cancer patients [5]. Exosome like vesicles (ELV) secreted from the helminth containing effector molecules including functional proteins and small RNAs. These membrane-bound phospholipid nanovesicles ranging from 50 to 150 nm in diameter actively secreted by mammalian cells [6].

Recently, label-free biosensors have been demonstrated for the analysis of exosomes. More recently, detection and molecular profiling of exosome based on surface plasmonic resonance demonstrate by Im *et al* [1]. Lee and Weissleder group at Massachusetts General Hospital have developed a miniaturized nuclear magnetic resonance-based platform (μNMR) to sensitively measure exosomes [7]. Wang *et al.* develop a nanotetrahedrom assisted aptasensor using electrochemical method for exosome detection [8]. In the paper, we detected the exosome vesicles from host and parasite captured on photonic crystal (PC) biosensor. Based on this method, we invent a method can rapid differential exosome vesicles from host and parasite using the host-specific antibody CD-63 based on the label-free optical biosensor. The PC-based biosensor offers the ability to tailor biological purification of exosomes using unique or atypical protein markers that would allow parasite exosomes to be differentiated from host exosomes based on parasite-specific proteins.

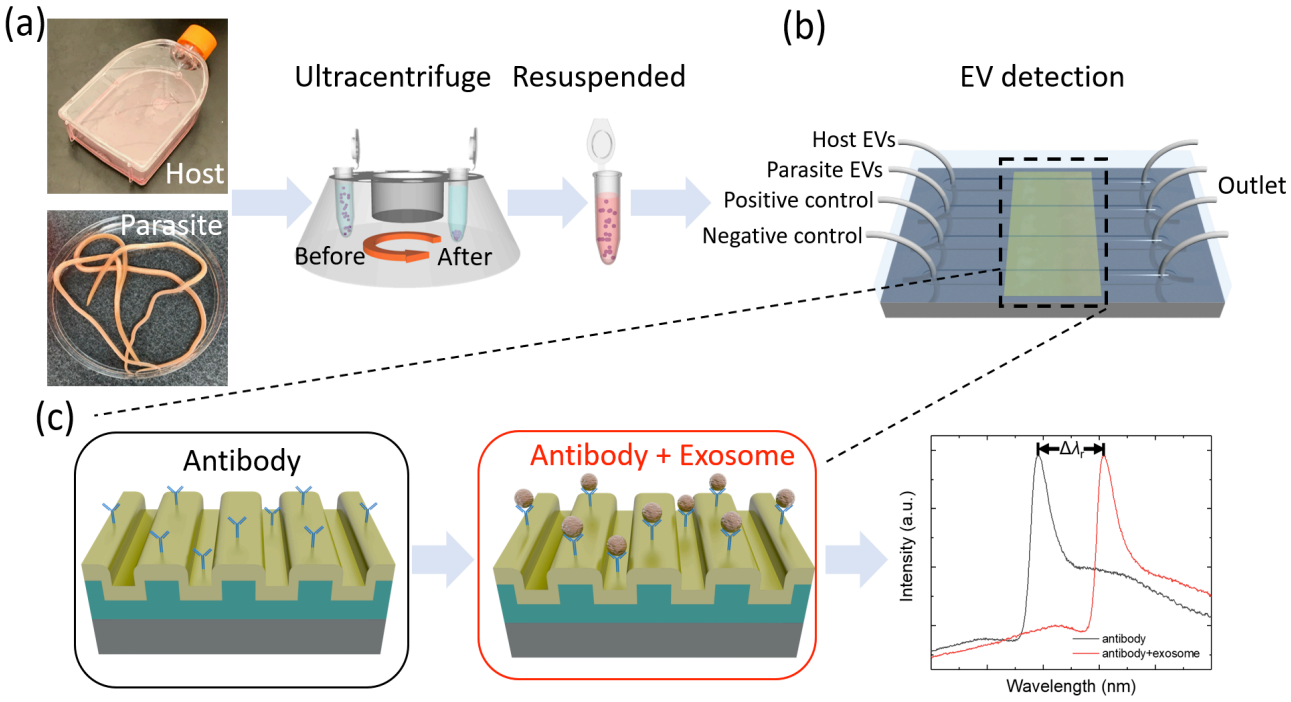

Figure 1: *(a) The process diagram of EV extraction for host and parasite cells. (b) PC biosensor schematic integrated with microfluidic channels. (c) Schematic of the PC biosensor functionalized with the antibody (black box), the exosome vesicles captured on the antibody (red box) illustrated by detecting the resonance wavelength shift Δλr.*

978-1-940470-03-0/HH2018/$25©2018TRF
DOI 10.31438/trf.hh2018.86

RESULTS

Preparation of host and parasite EV samples

Female adult *Ascaris suum* was cultured in Ascaris ringer's solution. Murine macrophage cell line (J774) was cultured in DMEM containing 10% FBS, 10000 Units of penicillin, 10000 units of streptomycin, and L-glutamine. Culture media were filtered using 0.22-µm filters to remove the debris and then loaded on ultracentrifuge tube. After centrifuge at 120,000 g/min for 90 min, the EVs were washed by PBS and followed with a 90-min centrifuge at 120,000 g/min. Then the pellet was re-suspended in PBS and transferred into 1.5 ml Beckman ultracentrifuge tube. Then they were spun at 55,000 rpm/min for 2 hours and the pellet was re-suspended in PBS stored in -80 °C. All the centrifuge was processed at 4 °C. The contractions of EVs were measured by a dynamic light scattering method. The EVs extracted from J774 were diluted 100 times with PBS and loaded into the Nanoparticle Tracking Analysis System (NanoSight LM10, Malvern Instruments Inc.). Fig.1(a) shows the process diagram of EV extraction for host and parasite cells.

PC biosensor and readout instrument

The photonic crystal (PC) biosensor, as shown in fig. 1(b), was chosen to detect EVs by monitoring the change of PC reflectance. To facilitate the analysis of EV sample, the PC sensor was incorporated into microfluidics channels (fig. 1(b)). A broadband light (700–900 nm) was used as the excitation and the narrowband reflectance from the PC was recorded using a spectrometer. The spectral shift of the narrowband reflectance was defined as the sensor output. The schematics of the biosensor detection mechanisms is shown in Fig. 1(c), biomolecules (exosome vesicles) interaction on the biosensor surface (red box), was illustrated by detecting the resonance wavelength shift $\Delta\lambda_r$.

Surface functionalization for the PC biosensor

To capture the EVs, the PC sensor surface was functionalized using a four-step protocol. As shown in fig. 2(a), the PC biosensor surface was treated using polyvinyl amine (PVA) and glutaraldehyde (GA). Then, the anti-CD63 capture antibody was deposited on the GA-treated PC sensor at the concentration of at 0.1 mg mL^{-1}. Before performing the detection of EVs, we used bovine serum albumin (BSA) to block the GA-treated surface that was not conjugated with CD63 antibodies. During the label-free experiment, the sensor outputs were measured in real time. Each step of the assay protocol of the resonance wavelength shift was shown in Fig. 2 (b). The resonance wavelength measured and recorded every 2 seconds. Fig. 2(c) shows the resonance wavelength shift $\Delta\lambda_r$ for each step base on assay protocol.

Detection of EVs secreted by Murine macrophage

As a label-free detection method, the biosensor can monitor the analyte-ligand binding process by recording the sensor output in real time. The PC sensor outputs measured for the EV from the host, corresponding positive control, and negative control samples are shown in fig. 3(a). The detection of EVs secreted from the host cells generated an output of ~0.7 nm (black line). The host EVs concentration was 2×10^{11} particles/mL. For the positive control experiment, most host EVs were captured on the GA-treated PC surface and resulted in an output of 2 nm (red line). For the negative control experiment, the surface was coated using the BSA, rather than the anti-CD63 antibody. The sensor output is nearly zero for the negative control experiment (blue line).

Fig. 3(b) shows the time-dependent change of the sensor output when the host EVs flowed through the microfluidic channel. The association rate (k_a) and dissociation rate (k_d) can be calculated by fitting the sensor gram in fig. 3(b) using the Langmuir model. Based on fitting results, the association and dissociation rates are

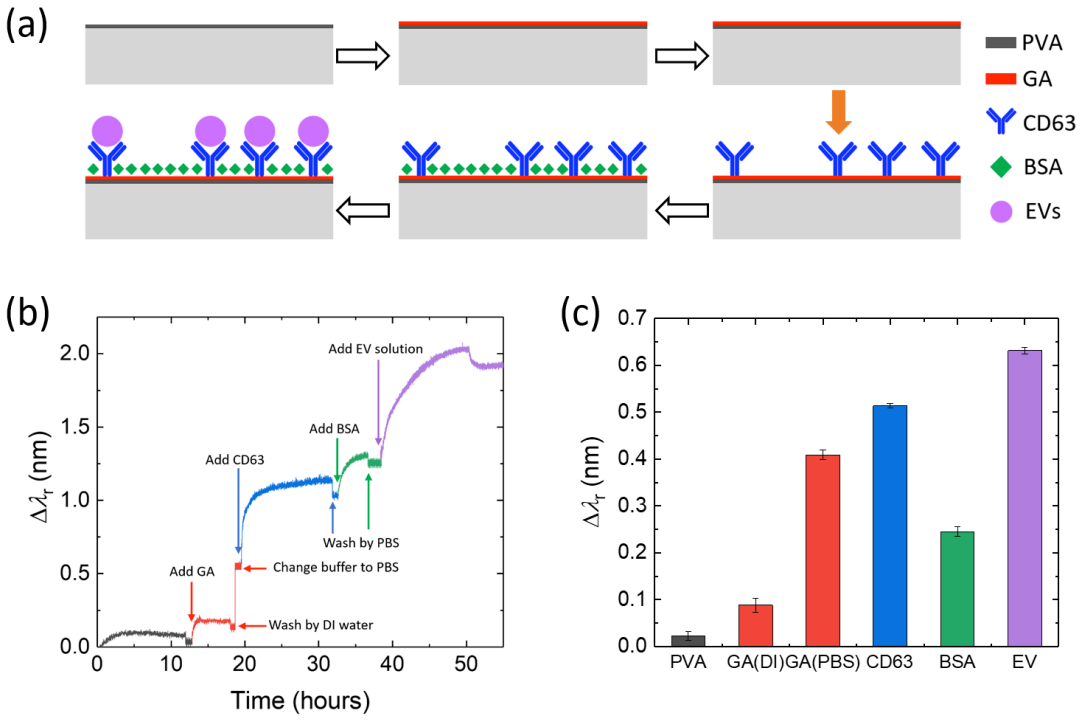

Figure 2: *(a) Schematics of the assay protocol for each step. (b) Measured kinetics binding for each step of the the functionalization assay protocol on PC biosensor surface. (c) Column plot of measured resonance wavelength shift of the assay protocol (PVA, GA with DI water, GA with PBS, antibody CD63, BSA, and EV).*

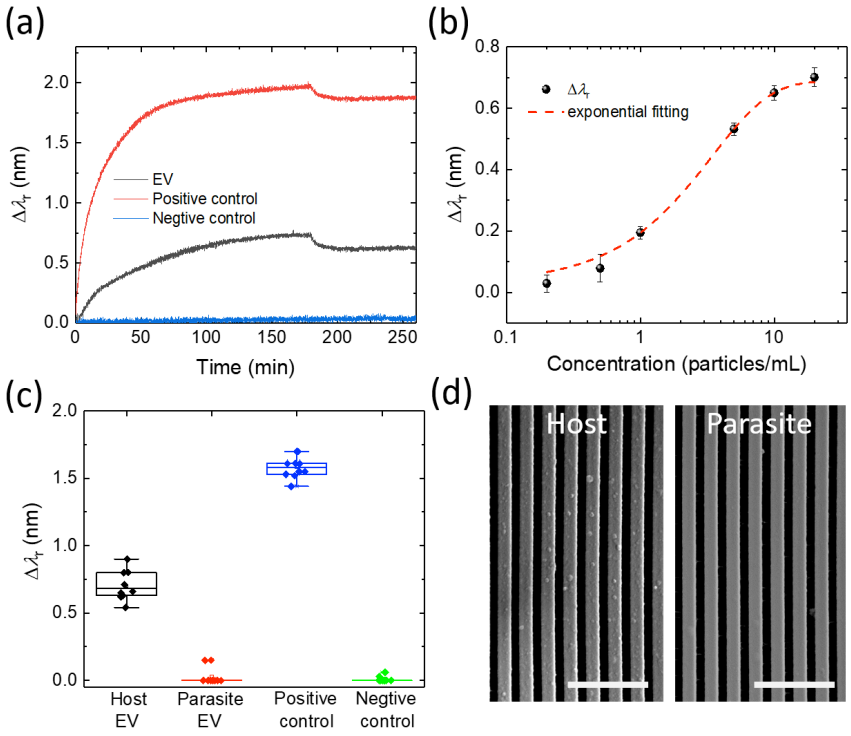

Figure 3: *(a) Kinetic binding of anti-CD63 and host EVs at the concentration of c =2×10^{11} particles/mL. (b) Measured resonance wavelength shifts as a function of 6 different concentrations of exosome vesicles from 2×10^{9} particles/mL to 2×10^{11} particles/mL. The experiment data is fitted (red dash line). (c) Box plot of the resonance wavelength shift for host and parasite exosome (c = 2×10^{11} EVs/mL) detection with the positive control and negative control. (d) SEM image of the host and parasite EVs immobilized on the PC surface at the concentrations of 2×10^{11} particles/mL. Scale bar: 2000 nm.*

k_a=1.6×10^9 particles mL^{-1} s^{-1}, and k_d=0.203 s^{-1}, respectively. The does-response curve was fitted as shown in fig. 4(b).

Differentiation of host and parasite EVs

The box plot in fig. 3(c) shows the resonance wavelength shift for host and parasite exosome detection with the positive control and negative control. Compared to the host EVs, the parasite EVs do not carry CD63 antigens. The detection of the parasite EVs using the anti-CD63 antibody coated PC sensor generated a nearly zero output. For the positive control experiment, the EVs were captured regardless of the type of transmembrane proteins. The positive control experiment shows a signal of 1.3 nm shift. The results in fig. 3(c) demonstrate the capability of discriminating EVs from host cells and parasites. The label-free assay can be utilized to diagnose infectious disease using EVs. Fig. 3(d) shows the scanning electron microscope (SEM) image of the host EVs and parasite EVs immobilized on the PC surface at the concentrations of 2×10^{11} particles/mL. The average size of the EVs is approximately 100 nm. Based on the label-free biosensor, we can rapid differentiation of exosome vesicles from host and parasite in 1 hours without any label.

REFERENCES

[1] H. Im, H. L. Shao, Y. I. Park, V. M. Peterson, C. M. Castro, R. Weissleder, *et al.*, "Label-free detection and molecular profiling of exosomes with a nano-plasmonic sensor," *Nature Biotechnology,* vol. 32, pp. 490-U219, May 2014.

[2] H. L. Shao, J. Chung, K. Lee, L. Balaj, C. Min, B. S. Carter, *et al.*, "Chip-based analysis of exosomal mRNA mediating drug resistance in glioblastoma," *Nature Communications,* vol. 6, May 2015.

[3] S. D. Ibsen, J. Wright, J. M. Lewis, S. Kim, S. Y. Ko, J. Ong, *et al.*, "Rapid Isolation and Detection of Exosomes and Associated Biomarkers from Plasma," *Acs Nano,* vol. 11, pp. 6641-6651, Jul 2017.

[4] R. Etzioni, N. Urban, S. Ramsey, M. McIntosh, S. Schwartz, B. Reid, *et al.*, "The case for early detection," *Nature Reviews Cancer,* vol. 3, pp. 243-252, Apr 2003.

[5] S. Pant, H. Hilton, and M. E. Burczynski, "The multifaceted exosome: Biogenesis, role in normal and aberrant cellular function, and frontiers for pharmacological and biomarker opportunities," *Biochemical Pharmacology,* vol. 83, pp. 1484-1494, Jun 1 2012.

[6] R. M. Maizels and H. J. McSorley, "Regulation of the host immune system by helminth parasites," *Journal of Allergy and Clinical Immunology,* vol. 138, pp. 666-675, Sep 2016.

[7] K. Lee, H. L. Shao, R. Weissleder, and H. Lee, "Acoustic Purification of Extracellular Microvesicles," *Acs Nano,* vol. 9, pp. 2321-2327, Mar 2015.

[8] S. Wang, L. Q. Zhang, S. Wan, S. Cansiz, C. Cui, Y. Liu, *et al.*, "Aptasensor with Expanded Nucleotide Using DNA Nanotetrahedra for Electrochemical Detection of Cancerous Exosomes," *ACS Nano,* vol. 11, pp. 3943-3949, Apr 2017.

CONTACT

*M. Kimber, tel: +1-515-294-4415; michaelk@iastate.edu
*M. Lu, tel: +1-515-294-9951; menglu@iastate.edu
*L. Dong, tel: +1-515-294-0388; ldong@iastate.edu

MEMS AIRFOIL WITH INTEGRATED INCHWORM MOTOR AND FORCE SENSOR

Brian Kilberg[*]*, Daniel Contreras, Joseph Greenspun, Hani Gomez, Eric Liu, and Kristofer S. J. Pister*
University of California-Berkeley, Berkeley, California, USA

ABSTRACT

We demonstrate a MEMS-actuated aerodynamic control surface integrated with a piezoresistive force-sensing platform and fabricated in a simple 3-mask silicon-on-insulator (SOI) process. This 47-mg actuator/sensor system generates 0.25 mN of aerodynamic lift force in 23 m/s airflow while operating at 40V, with a rotational displacement of 11 degrees, and a slew rate of 100 degrees/s. This is the first use of an electrostatic inchworm motor to actuate an aerodynamic control surface and generate lift.

INTRODUCTION

Small unmanned aerial systems (sUAS) and micro-air-vehicles (MAVs) have demonstrated useful applications such as search and rescue, aerial photography, crop inspection and biopsy, and industrial chimney inspection [1]–[3]**.** Scaling these systems down to the pico-air-vehicle (PAV) realm, where dimensions and masses less are than 5 cm and 500 mg, will improve energy consumption, decrease cost, increase ensemble density, and increase data granularity of unmanned aerial systems [3].

Recent advances in mesh networking, MEMS technology, and novel propulsion methods are increasing the feasibility of PAVs [3]. Some of these PAVs include flapping wings, hovering ionocrafts, and potentially ion jet planes [3]–[5]. These vehicles will require millimeter-scale control surfaces in order to control their flight.

Some MEMS control surfaces used arrays of MEMS actuators to manipulate airflow over a centimeter-scale to meter-scale delta wing [6]–[8]. These MEMS arrays aren't suitable for PAVs in their current form because their array size is too large. In [9], Wood et al. developed miniature piezoelectric actuators that were eventually used to actuate the ailerons on a 2 gram microglider [10]. Millimeter-scale control surfaces that are suitable for PAVs will resemble control surfaces like these.

In addition to piezoelectric actuators, electrostatic inchworm motors are also suitable for millimeter-scale control surfaces. Inchworm motors are easy to integrate with transmissions and mechanisms by using simple silicon-on-insulator (SOI) fabrication processes [11]. In MARSS 2017, we reported the design and fabrication of a millimeter-scale MEMS control surface using electrostatic inchworm motors, but did not demonstrate its ability to generate aerodynamic forces [12].

This control surface could be improved by an integrated force measurement system. Integrated force sensing eliminates the need for complicated and cumbersome external force measurement systems, and it enables force feedback applications. Integrated force measurements can be used to improve microbotic control systems. For example, B. Yang et al. used simulated motor force outputs along with machine learning and dynamic simulations of a microrobotic hexapod to design an optimized hexapod gait [13]. Integrated motor force sensors will be necessary in order to evaluate and tune control schemes like these when they are implemented on a physical microrobot.

Several piezoresistive and capacitive force sensors for microrobotic applications have been developed [14]–[16]. The systems in [15] and [16] both were fabricated in an SOI process compatible with an SOI inchworm motor system. Xu et al. integrated a capacitive force sensor with an electrostatically-actuated microgripper, which demonstrated the integration of force sensors with actuator systems in SOI processes [17].

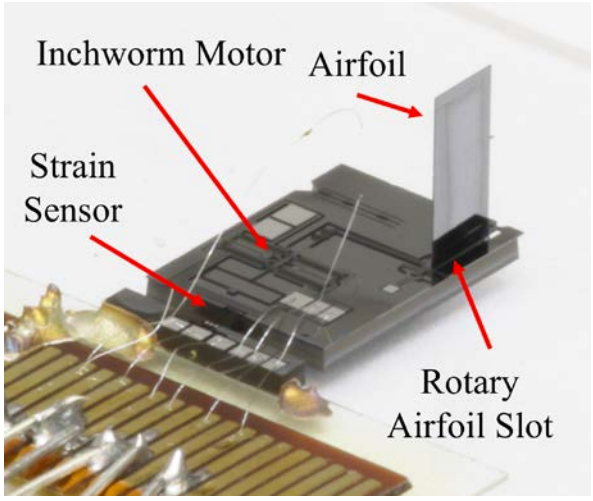

Figure 1: The MEMS control surface consists of an inchworm motor, a 2x4 mm² SOI device layer silicon airfoil, a rotary airfoil slot, and a piezoresistive half-bridge strain sensor. Six wire bonds are used to electrically connect the strain sensor and the motor. The silicon airfoil is inserted into the rotary airfoil slot and stands vertically out of plane from the rest of the device. The strain sensor measures generated lift force.

This paper describes the design of a MEMS control surface actuation system integrated into a piezoresistive force sensor using a simple SOI process. The SOI process included a 550 µm single-crystal silicon (SCS) substrate, a 2 µm oxide layer, a 40 µm SCS device layer, and a metallization layer. The process steps were a substrate deep reactive ion etch (DRIE), a device-layer DRIE, a metal deposition, and a sacrificial oxide etch.

THEORY AND DESIGN

Aerodynamics and Airfoil Design

Most aircraft use control surfaces such as ailerons, elevons, and rudders to control their trajectories. For thin airfoil theory, where F_l is lift force, ρ is the density of air, V is airflow velocity, C_l is the lift coefficient of the airfoil, A is airfoil area, and α is the angle attack of the airfoil, with $\alpha < 15$ degrees [18]:

$$F_l = \frac{1}{2}\rho V^2 2\pi\alpha A$$

The control surface uses inchworm motors and rotational linkages to rotate a 2x4 mm² device-layer silicon airfoil to change its angle of attack [12]. The airfoil is fabricated in 40-micron thick device layer silicon using the SOI process. As a result of the airfoil's aspect ratio, thin airfoil theory should be an appropriate model. The estimated lift force generated at 23 m/s is 2.8 mN.

Previous simulations showed that control surfaces generating ~10 mN of lift force are sufficient for controlling a millimeter-scale rocket [3].

MEMS Mechanism

The MEMS control surface consists of electrostatic inchworm motors and rotary joints to actuate a rotary airfoil slot (Figure 2), which are fabricated in the 40-um device layer.

978-1-940470-03-0/HH2018/$25©2018TRF
DOI 10.31438/trf.hh2018.87

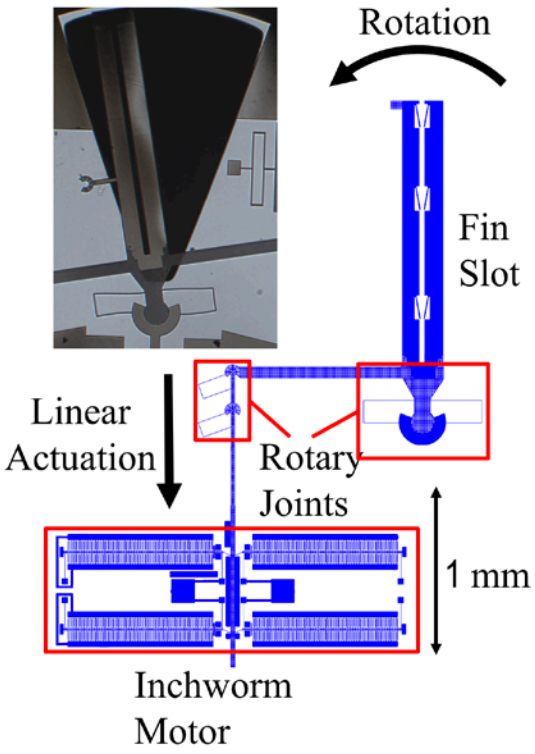

Figure 2: The inchworm motor linearly actuates the rotary joint mechanism which rotates the airfoil slot. The inset shows a microscopic photograph of the airfoil slot after rotation.

In the previous design iteration of this device, airfoil assembly was a significant challenge and decreased the yield of the device assembly process. A self-aligning airfoil slot was designed to avoid this problem. Instead of inserting the fin into the slot from above, the fin is inserted form the side, while spring-loaded mechanisms align and secure the airfoil (Figure 3). A small amount of epoxy was used to permanently fasten the airfoil into the slot. This improvement decreased the failure rate of this assembly step to zero.

Integrated Force-Sensing Platform

The motor, mechanism, and airfoil are fabricated into a platform that has integrated SOI half-bridge strain gauges (Figure 4). When aerodynamic forces are applied to the airfoil, the strain sensor beam deflects and the strain gauge registers a change in voltage. The integrated force sensing platform allowed us to easily measure the aerodynamic forces generated by the airfoil and could enable force feedback control schemes in future PAVs.

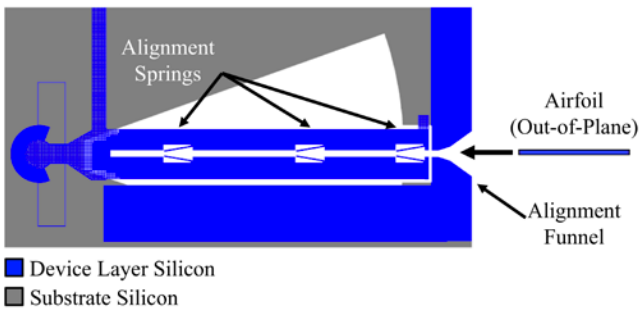

Figure 3: A patterned backside trench underneath the airfoil slot and a device-layer alignment funnel comprise the airfoil alignment mechanism. This mechanism guides the vertically-oriented airfoil into this slot as it is inserted. During airfoil insertion, cantilever springs align and secure the airfoil.

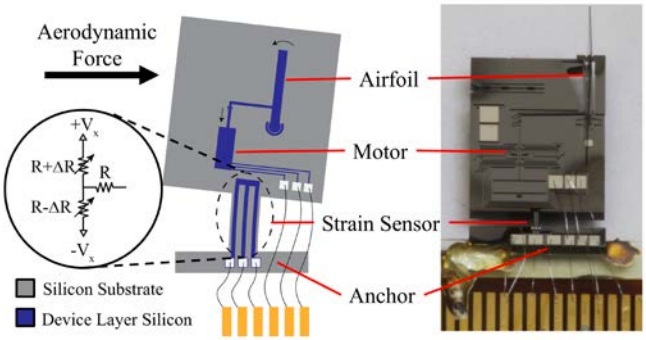

Figure 4: The strain sensor consists of a substrate layer cantilever with device layer piezoresistors patterned on top of the cantilever. When the cantilever deflects, it induces a differential strain in the piezoresistors on the edges of the cantilever. The anchor of the strain sensor is glued to a mount, so the rest of the device is suspended. When the airfoil rotates in airflow, it generates an aerodynamic lift force that deflects the strain sensor.

Theoretically, the output voltage of the half-bridge strain gauge is $V_o = G\epsilon_{avg}V_x$ where G is the gauge factor, V_x is the differential bridge voltage, and ϵ_{avg} is the average strain throughout the length each of the gauge's piezoresistors. The following equation shows the relationship between force applied to the airfoil and the average strain in the piezoresistors of the strain gauge, where F_l is the load force, d is the distance between the neutral axis of the substrate beam and the piezoresistor, L_g is the length of the L_f is the distance between the point where the load force is applied by the airfoil and calibration weights and the end of the beam, E is the Young's modulus of silicon, and I is the moment of inertia of the beam:

$$\epsilon_{avg} = \frac{F_l d(L_f + \frac{L_g}{2})}{EI}$$

With V_x=1.63 V this calculation predicts that the strain sensor will have a scale factor of 1.5 mV/mN.

The strain sensor was calibrated by using known weights to apply force to the sensor and its output was measured through an 1000x amplifier. V_x was 1.64 V. Linear regression was performed on the calibration data, which yielded a linear fit with a slope of 1.96 V/mN and an R^2 value of 0.986. This scale factor of 1.96 V/mN is 31% greater than the predicted 1.5 V/mN (adjusting for amplification) scale factor, and the average standard deviation of each measurement was 0.0175 mN.

AERODYNAMIC PERFORMANCE

Aerodynamic Performance of Static Fin

The theoretical performance of the airfoil was compared to actual performance by an experiment where the strain sensor was manually rotated with an attached airfoil. The results of this experiment are in figure 5. Airfoil lift force depended linearly on angle of attack for small angles. Lift force was not quadratically related to airflow speed.

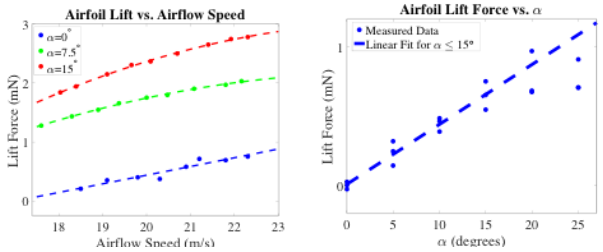

Figure 5: Left and center: Measured relationship between lift force, angle of attack, and airspeed for a 2x4 mm² silicon airfoil. In left graph, experiments were run at 15 m/s flow speed. Right: a device with an immobilized airfoil in a wind tunnel was rotated while measuring the lift force.

Active Actuator Aerodynamic Performance

The next experiment measured the amount of aerodynamic force the MEMS control surface could generate while running in airflow. Once placed in 23 m/s airflow, the airfoil was periodically actuated while the strain sensor measured lift force. Figure 6 shows the device setup in this experiment.

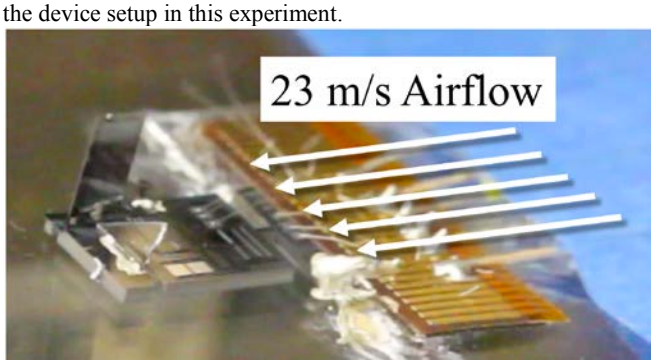

Figure 6: Image of the MEMS control surface system mounted for aerodynamic force experiments.

Low frequency drift was present in the measurement signal, which required signal processing to remove. Force measurements were extracted by comparing force measurements at times when the fin was actuated to times when the fin was at rest (Figure 7). The measured periodic force signature correlated with fin deflection only occurs when both the fin is moving and the control surface is in 23 m/s of airflow, showing that the force measurement is due to aerodynamic force generated by the fin. The average measured lift force was 0.25 mN, which was less than the predicted amount.

SYSTEMS INTEGRATION

Integrated Rocket System

These MEMS control surfaces will be used to create a pencil-sized autonomous rockets. In order to do that, we developed a process to assemble four control surfaces using standard wirebonding techniques and flexible printed circuit boards (PCBs) (Figure 8). Once the control surfaces are mounted on the PCB, it is wrapped around a custom fuselage fabricated by an inkjet 3D printer (Stratasys Objet260 Connex3).

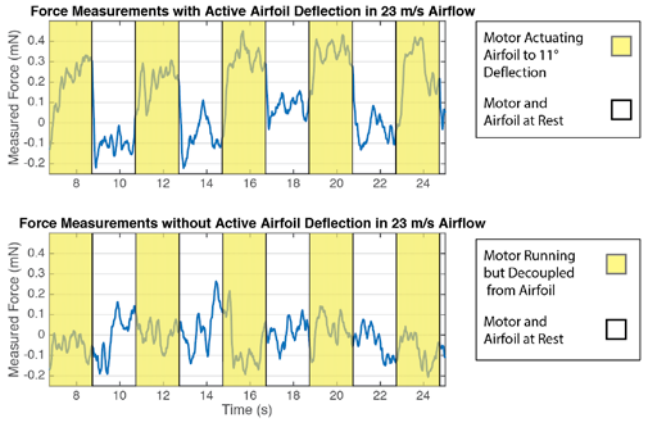

Figure 7: Aerodynamic performance graph. Top: Lift force generated by a periodically actuated airfoil. Noticeable force spikes occur when the fin is rotated by 11 degrees. Bottom: Control experiment showing force exerted on strain sensor when no actuation is occurring in 23 m/s airflow. In this control, the motor is running but is decoupled from the airfoil, so the airfoil doesn't deflect. In both plots, the 4 second moving average was subtracted from the signal

The inchworm motors require 45V – 110V to operate, which poses a power supply challenge at small scales. We designed a portable 90V power supply system using a commercially-available boost-converting integrated circuit (Linear Technologies LT4382), which has a 3mm x 3mm footprint. This system has demonstrated the ability to run a control surface for an hour on a single-cell lithium ion battery. This board was 3.8 cm x 1.5 cm and weighed 2 g. Figure 10 shows an assembled pencil sized rocket including one control surface, battery, and control electronics (Figure 9).

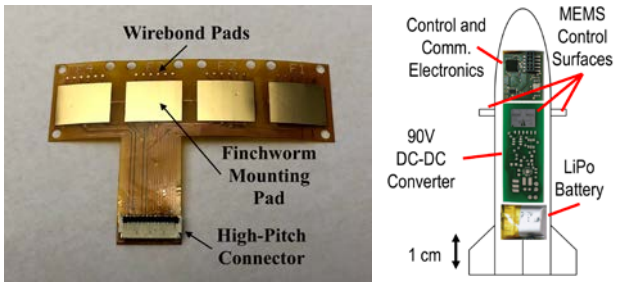

Figure 8: Integrated rocket system components. Left: Flexible PCB designed for assembling and routing control and power signals for the control surface system. The PCB is wrapped around a 3D-printed MEMS control surface fuselage module. Right: All of the electronics necessary to utilize the MEMS control surfaces has been demonstrated in a 1.5 cm diameter body tube.

Island Buckle Joint for Out-of-Plane Stability

Preventing out-of-plane forces from dislocating the silicon mechanisms requires manually glueing a grid of device-layer silicon on top of the rotary pin joint and the securing it with epoxy. This process is laborious and can potentially damage the device beyond repair. In order to avoid this assembly step, we designed a integrated SOI mechanism that prevents out-of-plane dislocation. This mechanism replaces rotary joint in the control surface. Figure 10 illustrates the operation of this island buckle joint. Inchworm motors were able to rotate the joint to half of the rotation range of the original rotary joint.

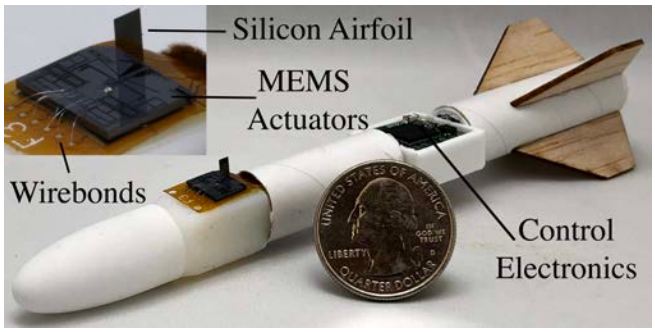

Figure 9: Pencil-sized rocket with one assembled MEMS control surface, LiPo battery, and control electronics attached.

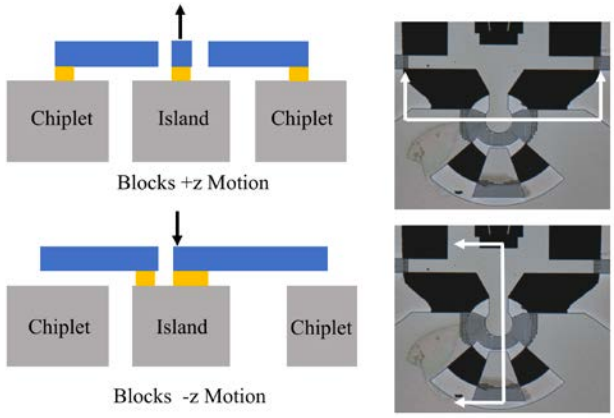

Figure 10: Cross-sections of an island buckle joint illustrate how it prevents out-of-plane dislocations of the device-layer mechanisms. Movement in the positive z direction is constrained by chiplet-anchored cantilevers, while movement in the negative z direction is contained by island-anchored cantilevers.

CONCLUSION

We demonstrated the ability of a MEMS-actuated aerodynamic control surface integrated with a piezoresistive force-sensing platform to generate aerodynamic force up to 0.25 mN. Compared to similar scale piezoelectric control surfaces, this device required 5x lower operating voltage and produced 5x more rotational displacement [10]. The assembly-friendly features added to the control surfaces permit mounting the control surface onto a pencil-sized rocket and will allow for control of the rocket.

REFERENCES

[1] M. Nieuwenhuisen, J. Quenzel, M. Beul, D. Droeschel, S. Houben, and S. Behnke, "ChimneySpector: Autonomous MAV-based indoor chimney inspection employing 3D laser localization and textured surface reconstruction," *2017 Int. Conf. Unmanned Aircr. Syst. ICUAS 2017*, pp. 278–285, 2017.

[2] D. Orol, J. Das, L. Vacek, I. Orr, M. Paret, C. J. Taylor, and V. Kumar, "An aerial phytobiopsy system: Design, evaluation, and lessons learned," *2017 Int. Conf. Unmanned Aircr. Syst. ICUAS 2017*, pp. 188–195, 2017.

[3] D. S. Drew, B. Kilberg, and K. S. J. Pister, "Future mesh-networked pico air vehicles," *2017 Int. Conf. Unmanned Aircr. Syst. ICUAS 2017*, pp. 1075–1082, 2017.

[4] D. S. Drew and K. S. J. Pister, "First takeoff of a flying microrobot with no moving parts," *Int. Conf. Manip. Autom. Robot. Small Scales, MARSS 2017 - Proc.*, 2017.

[5] K. Y. Ma, P. Chirarattananon, S. B. Fuller, and R. J. Wood, "Controlled flight of a biologically inspired, insect-scale robot," *Science (80-.).*, vol. 340, no. 6132, pp. 603–607, 2013.

[6] A. Huang, C. Folk, C.-M. Ho, Z. Liu, W. W. Chu, Y. Xu, and Y.-C. Tai, "Gryphon M3 system: integration of MEMS for flight control," no. October 2001, pp. 85–94, 2001.

[7] C. Folk and C.-M. Ho, "Micro-actuators for control of delta wing with sharp leading edge," *39th Aerosp. Sci. Meet. Exhib.*, no. January, 2001.

[8] A. Huang, C. Folk, C. Silva, B. Christensen, Y.-F. Chen, G.-B. Lee, M. Chen, S. Newbern, F. Jiang, C. Grosjean, C.-M. Ho, and Y.-C. Tai, "Applications of MEMS devices to delta wing aircraft: From concept development to transonic flight test," *39th Aerosp. Sci. Meet. Exhib.*, no. January, 2001.

[9] R. J. Wood, E. Steltz, and R. S. Fearing, "Optimal energy density piezoelectric bending actuators," *Sensors Actuators A Phys.*, vol. 119, no. 2, pp. 476–488, 2005.

[10] R. J. Wood, S. Avadhanula, E. Steltz, M. Seeman, J. Entwistle, A. Bachrach, G. Barrows, S. Sanders, and R. S. Fear, "An autonomous palm-sized gliding micro air vehicle," *IEEE Robot. Autom. Mag.*, vol. 14, no. 2, pp. 82–91, 2007.

[11] I. Penskiy and S. Bergbreiter, "Optimized electrostatic inchworm motors," *J. Micromech. Microeng.*, vol. 23, 2013.

[12] B. G. Kilberg, D. S. Contreras, J. Greenspun, and K. S. J. Pister, "MEMS aerodynamic control surfaces for millimeter-scale rockets," *Int. Conf. Manip. Autom. Robot. Small Scales, MARSS 2017 - Proc.*, 2017.

[13] B. Yang, G. Wang, R. Calandra, D. Contreras, S. Levine, and K. Pister, "Learning Flexible and Reusable Locomotion Primitives for a Microrobot," pp. 1–8, 2018.

[14] P. Estevez, J. M. Bank, M. Porta, J. Wei, P. M. Sarro, M. Tichem, and U. Staufer, "6 DOF force and torque sensor for micro-manipulation applications," *Sensors Actuators, A Phys.*, vol. 186, pp. 86–93, 2012.

[15] F. Beyeler, S. Muntwyler, and B. J. Nelson, "Design and calibration of a microfabricated 6-axis force-torque sensor for microrobotic applications," *Proc. - IEEE Int. Conf. Robot. Autom.*, pp. 520–525, 2009.

[16] W. Zhang, V. T. Truong, K. B. Lua, A. S. Kumar, T. T. Lim, and K. S. Yeo, "Design and characterization of a silicon piezoresistive three-axial force sensor for micro-flapping wing MAV applications," vol. 9302, no. 65, pp. 1–10, 2015.

[17] Q. Xu, "Design, Fabrication, and Testing of an MEMS Microgripper With Dual-Axis Force Sensor," *IEEE Sens. J.*, vol. 15, no. 10, pp. 6017–6026, 2015.

[18] G. N. Ward, *Linearized Theory of High-Speed Flow*. Cambridge University Press, 1955.

[19] Y. Kanda, "Piezoresistance effect of silicon," *Sensors Actuators A. Phys.*, vol. 28, no. 2, pp. 83–91, 1991.

CONTACT

*Brian Kilberg, bkilberg@berkeley.edu

CMOS COMPATIBLE GHZ ULTRASONIC FRESNEL MICROFLUIDIC ACTUATOR

Adarsh Ravi[1*], *Justin Kuo*[1], *and Amit Lal*[1]
[1]*Sonic*MEMS Laboratory, School of Electrical and Computer Engineering, Cornell University, New York, USA

ABSTRACT

We report on an aluminum nitride based gigahertz frequency ultrasonic transducer to realize a microfluidic actuator using acoustic radiation force and acoustic streaming. The transducer uses focusing transducers placed in a Fresnel lens configuration, which generates bulk acoustic waves through the silicon substrate adding in phase at the focus. The transducer is planar and is fabricated with a CMOS compatible process, with no thin-film release steps. Peak displacement of 250pm was achieved at the focus with 1.06GHz and 5V amplitude input. Acoustic vortices were formed with microfluidic streaming velocity >2.6mm/s in water droplets placed on top of the transducer.

INTRODUCTION

Micro-particle manipulation in liquid is useful in many chemical, bio-medical, and biological applications [1]. Among the contactless manipulation mechanisms, optical and acoustic techniques are the most common. The laser based optical technique can produce a few pico-Newtons of trapping forces but cannot control larger biological objects and operate in a medium of high optical opacity [2]. On the other hand, acoustic devices can be more easily integrated with the microfluidic channel and have been shown to handle biological particles better because of longer wavelengths and higher radiation forces [1-3].

An acoustic wave propagating through a medium carries energy and momentum. Wave energy is dissipated into the liquid due to absorption and diffraction, and leads to momentum transfer to the liquid. When the wave encounters an object, scattering and net radiation forces can move the object [3, 4, 7]. These forces can result in particle trapping, streaming, and atomization [3, 4, 6]. As the acoustic radiation and streaming forces increase inversely with the acoustic wavelength in the medium, recent works have increasingly utilized higher frequencies for microparticle actuation [4]. The gradient force, resulting from the radiation force can further be enhanced by having a larger intensity difference between the center of the beam and the peripheral region [3].

Acoustic beam based manipulators such as acoustic tweezers that use high frequency focused ultrasonic beams have recently been explored [3, 5, 10]. Most of the high frequency ultrasonic beam manipulators reported so far use surface acoustic wave (SAW) transducers on non-CMOS compatible substrates such as lithium niobate, lithium tantalate or lead zirconate titanate (PZT) [3, 8, 9]. Further, their actuation requires >10V drive voltage.

Micro-particle actuators based on bulk acoustic wave (BAW) have also been reported for driving circulatory motion in microfluidic chambers and micro droplet ejection [3, 4, 6]. These millimeter scale devices have used PZT transducers, operate below 200 MHz frequencies [4, 6], and typically require a drive voltage of a few 10s-100s of volts.

Despite the advantages of using high frequency focused ultrasonic beams for manipulation of fluid-laden particles, several challenges in the implementation prevents easy adoption. The expense of fabrication, and generation and amplification of high voltages at these frequencies are two reasons often mentioned [3]. Another technological impediment is that considerable chip area is required to isolate the electrical interconnects of the transducers from the fluidic sample; as the fluid is placed on the same surface as the transducer.

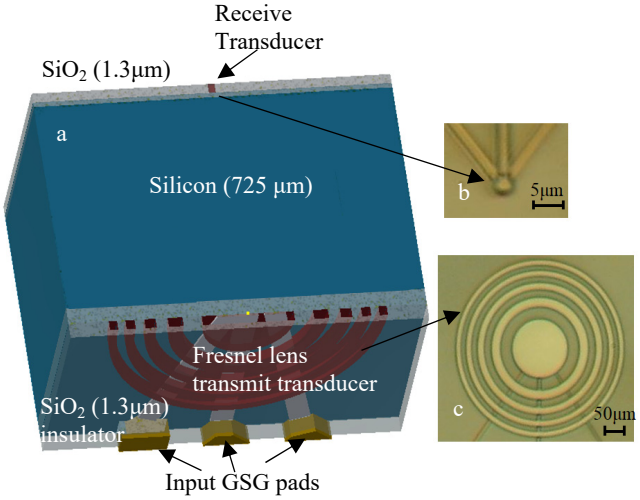

Figure 1: a. Cross sectional schematic of the structure of the AlN-Si stack; b. image of the circular transducer on the receive side after fabrication; c. image of the Fresnel lens transmit transducer after fabrication.

In this paper, we present a microscale GHz focused-beam bulk acoustic wave microparticle manipulator which decouples the fluidic side from the actuator side. The device is fabricated without any thin-film release steps, using CMOS compatible materials such as aluminum nitride (AlN) solidly mounted to silicon substrate. Microfluidic streaming action was observed near the vicinity of the focus and the streaming velocity in water with 2µm diameter polystyrene microspheres was measured to be about 2.6mm/s for a 5V amplitude, 1.06GHz frequency continuous wave (CW) input.

FRESNEL MICROFLUIDIC ACTUATOR DESIGN

Planar AlN based transducer stack for GHz ultrasonics, similar to the one previously reported by our group [11], was used here. The AlN transducers were fabricated at the Institute of Microelectronics (IME) in Singapore under the IARPA - Trusted Integrated Chips (TIC) program. Resonant frequency of the transducer was 1.06GHz. The transducer consisted of 200nm molybdenum as electrode layers, 2µm thin film piezoelectric AlN, and 1.3µm thick insulating silicon dioxide layer, on a 725µm thick silicon wafer.

The electrodes on one (transmit) side of the silicon substrate were patterned in Fresnel zone plate (FZP) configuration in order to focus the emanating acoustic field through the substrate onto the opposing receive side. The receive electrodes were patterned to form a circular transducer of 2µm radius. Figure 1 shows the cross-sectional sketch of the simplified GHz transducer stack with planar FZP shaped AlN transducer on the transmit side and a small circular AlN transducer on the receive side. AlN in the regions without transduction are not shown here for simplicity.

In a Fresnel lens design, the distance from each annular zone to the point of focus is an integral multiple of the wavelength. As a result, the acoustic waves reach the focal point in phase, interfering constructively. If the wavelength of the wave in the medium is λ_{Si}, the focal length is F, then the radius of each annular zone is given

978-1-940470-03-0/HH2018/$25©2018TRF
DOI 10.31438/trf.hh2018.88

by [12]

$$r_n = \sqrt{\frac{n\lambda_{Si}}{2}\left(F + \frac{n\lambda_{Si}}{8}\right)} \quad (1)$$

The longitudinal speed of sound in silicon being c_{Si} = 7963m/s, the AlN Fresnel lens radii were optimized to achieve a focal length of ~725µm in silicon for 1.06GHz using PZFlex simulation software. Five Fresnel rings were used, and the radius of the outermost ring was 165µm. The 2D PZFlex simulation result for normalized acoustic pressure in silicon showed a maximum pressure around 725µm (Figure 2).

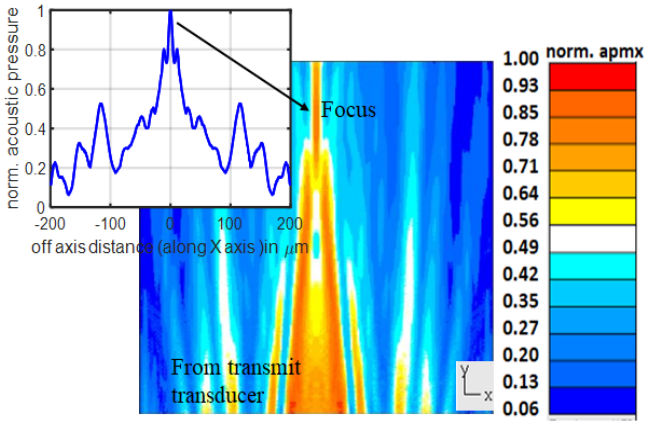

Figure 2: PZFlex simulation results showing the focal length to be around 725µm in silicon.

ACOUSTIC STREAMING IN FLUIDS

Propagation of an acoustic wave results in acoustic radiation forces on particles and acoustic streaming of fluids. These are second order effects that are caused by nonlinearities in governing physics [3]. When the particle size is very small compared to the acoustic wavelength of the incident wave, i.e., $ka << 1$ where, k is the propagation constant in the fluid and 'a' is the radius of the particle, the acoustic force on the particle is determined by the spatial gradient of the force potential field U, with the particle movement from the region of high force potential to low force potential. The acoustic radiation force is given by [3, 4]

$$F_R = -\nabla U \quad (2)$$

and the force potential field is

$$U = \frac{4\pi}{3}a^3\left[f_1\frac{1}{2}\kappa_0\langle|p_l|^2\rangle - f_2\frac{3}{4}\rho_0\langle|v_l|^2\rangle\right] \quad (3)$$

$$f_1 = 1 - \frac{\kappa_p}{\kappa_l} \text{ and } f_2 = \frac{2\left(\frac{\rho_p}{\rho_l}-1\right)}{\frac{2\rho_p}{\rho_l}+1} \quad (4)$$

$$\kappa = \frac{1}{\rho c^2} \quad (5)$$

In the above equations, $f_{1,2}$ parameters represent the monopole and dipole scattering coefficients, $\langle|p_l|^2\rangle$ is the mean squared pressure, $\langle|v_l|^2\rangle$ is the mean squared particle velocity in the fluid, ρ is the density and κ is the compressibility. The subscripts l denote the fluid and p denote the particle in the fluid medium.

In the Rayleigh regime, where $ka << 1$, scattering force due to the reflection of propagating waves from the particle is small and is often neglected [3]. Whereas, in Mie scattering regime, where the particle size is comparable or larger than the acoustic wavelength, i.e. $ka > 1$, scattering becomes important. The force acting on the particle is now [4]

$$-F = \langle\int_S p_2 n\, dS\rangle + \langle\int_S \rho_l\,(n.v_l)\,v_l\, dS\rangle \quad (6)$$

The integration is over an arbitrary surface, S that encloses the particle, and $\vec{n}$ is the vector normal to the surface. The second order pressure p_{2l} for an inviscid fluid can be obtained from first order terms

$$p_{2l} = \frac{1}{2}\kappa_0\langle|p_l|^2\rangle - \frac{1}{2}\rho_0\langle|v_l|^2\rangle \quad (7)$$

As the force potential is proportional to the cube of the particle radius, i.e., $F \propto a^3$, larger particles are displaced further away from the center of the ultrasonic beam compared to smaller particles [3]. Further, as the force gradient scales inversely with the acoustic wavelength, high frequency ultrasonic waves increase both radiation and streaming forces. It is observed that with increasing frequency, the radiation force increases much faster than the force due to streaming [5].

At higher frequencies, attenuation in fluids also play a key role as the attenuation coefficient, $\alpha(f) = \alpha_0 f^2$, is a strong function of frequency. In pure water, the characteristic attenuation length, α^{-1}, is below 100µm for frequencies above 500MHz at room temperature (Figure 3). This indicates that the force fields can be highly localized at GHz frequencies. This can be used in applications such as particle and cell separation, concentration, droplet production, encapsulation, active sorting, controlled heating, nanotube alignment, viscosity measurement, and aerosol production [4].

In harmonic systems, the particle velocity in fluid, v_l, is given by $v_l = \omega u_l$, where ω is the angular frequency of the acoustic wave and u_l is the displacement of the fluid due to the propagation of the ultrasonic wave. For fluids with low Mach numbers, $M = \frac{v_l}{c} \ll 1$, where c is the acoustic velocity in the fluid, the second order streaming velocity is related to the first order velocity in fluid by $v_{2s} \propto v_l^2$[4]. As the displacement u_l, is proportional to the applied voltage, it can be inferred that the second order streaming velocity increases as the square of the applied voltage, i.e., $v_{2s} \propto V_{in}^2$.

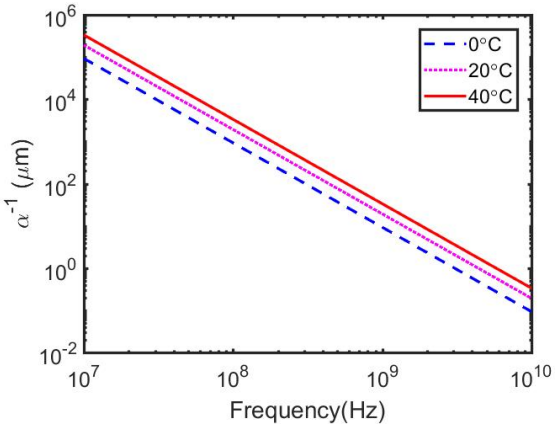

Figure 3: Characteristic attenuation length in water [13].

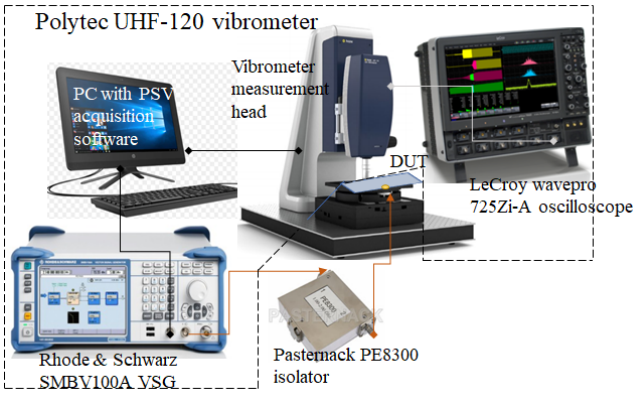

Figure 4: Experimental setup with Polytec UHF-120 vibrometer

EXPERIMENTS AND RESULTS

The GHz FZP actuator displacement profile was characterized using a Polytec UHF-120 vibrometer (Figure 4). Continuous wave (CW) signal from the vector signal generator (VSG) was applied to the Fresnel lens type transducer. Keeping the amplitude at 5V, frequency of the VSG was varied from 1.01GHz to 1.1GHz to determine the resonant frequency of the device. Figure 5a shows the plot of surface displacement on the receive side of the device under test (DUT) for various frequencies. Peak displacement profile was observed at 1.06GHz, which closely matches with the PZFlex simulation. Figure 5b shows the surface displacement profile of the DUT with peak displacement occurring at the location of the circular receive transducer. These two results confirm focusing of the acoustic wave emanating from the planar Fresnel lens transmit transducer.

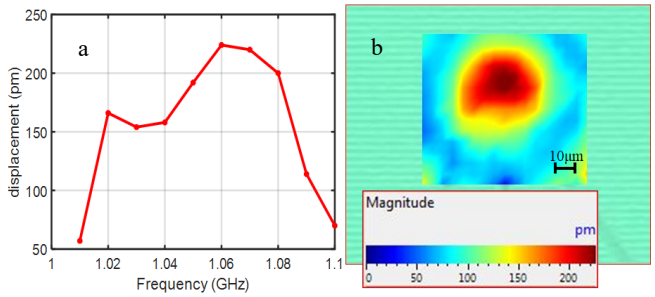

Figure 5: a. Plot of surface displacement at point of focus vs. input frequency; b. scan profile showing surface displacement on the receive side.

The peak surface displacements at the center of the receive transducer as a function of applied voltages for a CW signal of 1.06GHz is shown in figure 6. The expected linear behavior of the displacement with applied voltage is observed.

From the displacement data for 5V amplitude input, the average acoustic intensity I_{avg},

$$I_{avg} = \frac{1}{2} pv_l, \qquad (8)$$

with ultrasonic pressure $p = \rho cv$, was calculated to be 1.7KW/cm^2 on the silicon dioxide surface located on the receive side. Thus, a very high intensity ultrasonic beam was realized from the GHz FZP microfluidic actuator.

A metal washer/cylinder was adhesively attached on the receive transducer side such that the receive transducer was centered within the washer. The inner diameter of the cylinder was 3.25mm and the height was 0.8mm. This formed a fluid capacity of 6.6μl. The well formed by the cylinder was filled with a mixture of deionized water, polystyrene (PS) microspheres of 2μm diameter, and soap solution for reducing surface tension between spheres and water. Figure 7a shows the 3D model of the microfluidic actuator with the well and liquid mixture.

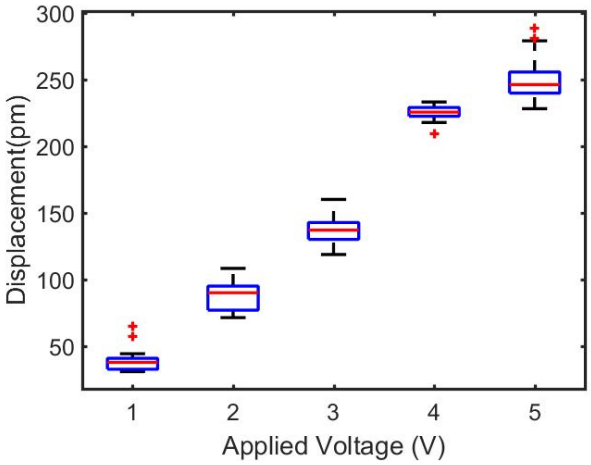

Figure 6: Box plot of surface displacement at the point of focus with different applied voltages. Twenty data points are plotted for each voltage.

The test setup was slightly modified for the microfluidic experiments; the input to the DUT came from the same VSG, but the DUT was now placed under a Keyence VW-9000 high speed microscope. Upon application of an input signal from the VSG to the transmit transducer, streaming vortices around the receive transducer, or the region of focus was observed. Figure 7c shows an image of the streaming patterns observed around the region of focus.

The amplitude of the input signal was varied from 1 – 5V, and the videos of the micro particle streaming movements were recorded. From these videos, the streaming velocity of the particles were estimated. The quadratic behavior of streaming velocity with applied voltage is shown in Figure 8. Average streaming velocity of about 2636μm/s was observed for an applied voltage of 5V. Such high streaming velocities were observed because of the enhanced radiation and streaming forces arising due to GHz frequency acoustic waves, and highly localized microbeam from the Fresnel lens configuration.

CONCLUSION

In this paper, a GHz ultrasonic microfluidic actuator is presented. The device employs a thickness mode AlN piezoelectric transducer stack, which is in principle CMOS compatible. The thickness mode resonance of the FZP transducer generates bulk waves into the silicon substrate that focus constructively at the intended focal point, which is on the opposite side of the wafer. Although a smaller receive transducer was used here to measure the received signals electrically, the receive transducer is not required for microfluidic actuation. The focused ultrasonic wave displaces the silicon dioxide surface on the receive side which then propagates through the fluid.

Owing to high dissipation of the GHz ultrasonic field in water,

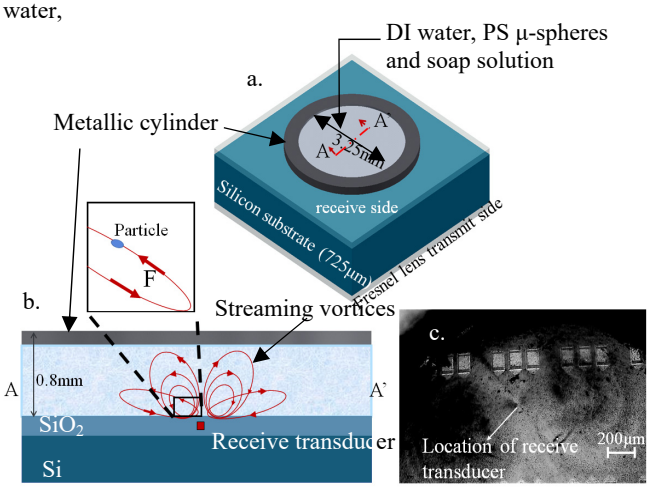

Figure 7: a. 3D sketch of the microparticle actuator assembly; b. cross sectional sketch showing the streaming vortices in liquid around the receive transducer; c. streaming patterns observed around the circular transducer in the receive side.

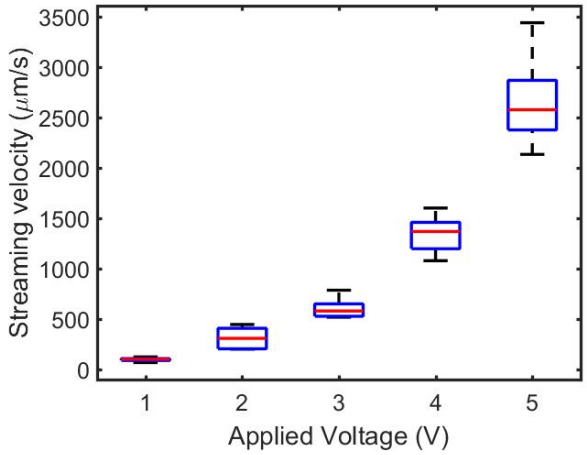

Figure 8: Box plot of streaming velocity versus applied voltage. Ten data points are plotted for each voltage.

a strong acoustic streaming force is generated; which pushes the fluid out and recirculates forming spherical vortex shell around the focal point. The highly defined focal point is an opportunity to create microfluidic systems with distributed fluidic sources controlled from the transmit transducer side.

The ability to change the frequency of the ultrasound and amplitude can also be used to spread the spatial extent of the force and its amplitude. Since the voltages required are CMOS compatible, and the fabrication process is also CMOS compatible, microfluidic samples placed on the receive side of the silicon die can be enabled easily with the ultrasonic actuator presented here. Further work is required to investigate the effect of microfluidic channel boundary conditions to contain the field and generate flow in channels.

In summary, a GHz actuator was designed, fabricated and tested for microparticle actuation. This can find applications in microparticle capturing, and biological assays requiring localized mixing and pumping. The device when integrated with CMOS can not only reduce the size and cost of the test setting drastically, but also enable digital control and automation of particle manipulation in a closed lab-on-chip environment.

ACKNOWLEDGMENT

The authors would like to acknowledge the IARPA - Trusted Integrated Chips (TIC) program for funding; under which the Institute of Microelectronics (IME), Singapore fabricated the devices.

REFERENCES

[1] Y. Tu, S. Chen, and Y. Hwang, “Design of fresnel lens- type multi-trapping acoustic tweezers,” Sensors, 16, 1973 (2016).

[2] C. Lee, J. Lee, S. T. Lau, Q. Zhou, and K. K. Shung, “Single microparticle manipulation by an ultrasound beam,” IEEE International Ultrasonics Symposium, pp. 849-852 (2010).

[3] B. W. Drinkwater, “Dynamic-field devices for the ultrasonic manipulation of microparticles,” Lab Chip, 16, 2360 (2016).

[4] D. J. Collins, Z. Ma, and Y. Ai, “Highly localized acoustic streaming and size-selective submicrometer particle concentration using high frequency microscale Focused Acoustic Fields,” Analytical Chemistry, 88, 10, pp. 5513-5522 (2016).

[5] J. Wu, and G. Du, “Acoustic radiation force on a small compressible sphere in a focused beam,” The Journal of the Acoustic Society of America, 87, 997 (1990).

[6] C. Lee, W. Pang, S. C. Hill, H. Yu, and E. S. Kim, “Airborne particle generation through acoustic ejection of particles-in-droplets,” 42:10, pp. 832-841 (2008).

[7] M. K. Araz, C. Lee, and A. Lal, "Ultrasonic separation in microfluidic capillaries," IEEE Symposium on Ultrasonics, 2, pp. 1111-1114 (2003).

[8] H. Yu, J. W. Kwon, and E. S. Kim, "Microfluidic mixer and transporter based on PZT self-focusing acoustic transducers," Journal of Microelectromechanical Systems, vol. 15, no. 4, pp. 1015-1024 (2006).

[9] C. Lee, and A. Lal, "Single microdroplet ejection using an ultrasonic longitudinal mode with a PZT/tapered glass capillary," IEEE Transactions on Ultrasonics, Ferroelectrics, and Frequency Control, vol. 51, no. 11, pp. 1514-1522 (2004).

[10] B. Zhu, J. Xu, Y. Li, T. Wang, K. Xiong, C. Lee, X. Yang, M. Shiiba, S. Takeuchi, Q. Zhou, and K. K. Shung, “Micro particle manipulation by single beam acoustic tweezers based on hydrothermal PZT thick film,” AIP Advances, 6, 3, 035102 (2016).

[11] J. Hoople, J. Kuo, J. Soon Bo Woon, N. Singh, and A. Lal, “Optimized response of AlN stack for chipscale GHz ultrasonics,” IEEE International Ultrasonics Symposium, pp. 1-4 (2015).

[12] K. Yamada, and H. Shimizu, “Planar-Structure Focusing Lens for Acoustic Microscope,” IEEE International Ultrasonics Symposium, pp. 755-758 (1985)

[13] A. Briggs, and O. Kolosov, “Acoustic Microscopy”, Oxford, 2009.

[14] R. M. Moroney, R. M. White, and R. T. Howe, “Microtransport induced by ultrasonic Lamb waves”, Appl. Phys. Lett. 59, 774 (1991).

[15] S. Liu, Y. Yang, Z. Ni, X. Guo, L. Tuo, J. Tu, D. Zhang, and J. Zhang, “Investigation into effect of acoustic radiation force and acoustic streaming on particle patterning in acoustic standing wave fields,” Sensors, 17, 1664 (2017).

CONTACT

*A. Ravi, tel: +1-408-832-7408; ar2256@cornell.edu

A 5-BIT DIGITALLY OPERATED MEMS ACCELEROMETER

Amin Abbasalipour[1], Varun Kumar[1], Roozbeh Jafari[2] and Siavsh Pourkamali[1]
[1]University of Texas at Dallas, USA
[2]Texas A&M University, USA

ABSTRACT

This work presents an electrostatically tunable MEMS acceleration switch and its operation as a 5-bit digital accelerometer. The concept of operating tunable acceleration switches as digital MEMS accelerometers and a 2-bit prototype have been previously demonstrated [1]. Such devices only require bias voltages for operation (zero static power consumption) enabling significant power reduction by eliminating the need for an analog-front-end. This work demonstrates increased resolution (higher number of output bits) for such devices by successful fabrication and operation of digital accelerometers with up to 5-bits of resolution. The sensor consists of an acceleration switch (proof mass with an output contact electrode) surrounded by sets of electrostatic actuators each corresponding to one bit of the digital binary output (Fig. 1). Performing a binary search and activating different actuators in proper order (e.g. by a digital controller), the applied acceleration can be determined [1]. The tested 5-bit prototype shows good agreement between the applied acceleration and sensor output with resolution limited by the number of bits, i.e. 1/32 of the full-scale acceleration (159 mg and 62.5 mg for full-scale acceleration of 5.1g and 2g, respectively).

INTRODUCTION

Compact, low cost, and low power accelerometers are required for numerous industrial, biomedical, geological and automotive applications that include smartphones [2], early detection of Alzheimer disease [3], Detection of Driving Events [4]. MEMS based accelerometers offering much of what is desirable for high volume applications, while providing adequate sensitivity, have become very successful commercial products and are widely used in modern integrated systems. Over the past few decades, different types of accelerometers based on various operation principles have been demonstrated. Some of the most popular detection mechanisms used in MEMS accelerometers includes piezoresistive [5], piezoelectric [6], capacitive [7], and electron tunneling readout [8]. Most commercially successful MEMS accelerometers work based on capacitive detection, which involves measuring the change in the capacitance between stationary electrodes fixed to the substrate and movable electrodes on a suspended mass. The suspended mass, also called the proof mass, has to be relatively large (typically in the millimeter range) so as to have a highly sensitive accelerometer. In today's modern wireless world, power consumption is one of the most essential limiting factors which directly affects the life or suitability of a sensor system. In most cases, frequent charging or replacement of the battery due to power loss is simply not feasible. With aggressive power reduction in digital electronics in recent years, MEMS sensors remain one of the most power-hungry components in integrated systems. For example, Lee et al have demonstrated a wireless sensor network (WSN) for monitoring the health and performance of motors which includes MEMS sensors, two signal processors, and the communication modules. The total nominal power consumption of the WSN is as high as 35mW, out of which close to 62% (21.6mW) is the power required for operation of the MEMS sensors, with the wireless link and signal processing unit being responsible for only close to a third of the total power consumption [9]. In most cases the large power consumption of MEMS sensors is attributed to the analog front end needed for reading, processing, and analog to digital conversion of the sensor output, which is typically responsible for most to all the power consumption of the whole sensor [10]. Therefore, significant power savings (in some cases close to zero static power consumption) can be achieved by elimination of the analog front-end. This calls for a paradigm shift in MEMS sensor design moving from analog sensors towards sensors with direct digital operation/output. For example, Kobayashi et al have demonstrated a piezoelectric accelerometer connected to an array of CMOS converters with satellite capacitors. The on-state and off-state of CMOS inverters correspond to logic '0' and '1'. The number of on-state CMOS inverters responses to increasing the acceleration applied to the piezoelectric accelerometer [11]. In an effort to dramatically reduce the power consumption of MEMS inertial sensors, we have demonstrated a fully digital 5-bit MEMS accelerometer by digitally operating a tunable MEMS acceleration switch.

OPERATING PRINCIPLE

Background

Acceleration switches are simple devices with an output that can be high (ON) or low (OFF) depending on the predetermined acceleration threshold of the device and the acceleration the device is subjected to [12]. Most acceleration switches are comprised of a suspended mass anchored to a substrate with flexible tethers. If the device is subjected to an acceleration higher than its threshold value, the suspended mass will come in contact with an electrode closing a circuit and signaling that the acceleration threshold has been reached. Hence, such devices require close to no power for operation and their output can be directly fed to a digital processor without any further processing. However, an acceleration switch can only indicate whether the applied acceleration is higher or lower than the set threshold and cannot provide quantitative information about how much acceleration is applied to the device at each moment. In other words, an acceleration switch can be referred to as a single bit digital accelerometer. The approach demonstrated in this work is to add digital control ability via electrostatic tuning to acceleration switches and turn them into multi-bit digital accelerometers. Therefore, devices shown in this work are acceleration switches that can perform quantitative acceleration measurements with the help of a digital controller.

Device Structure

Figure 1 shows the schematic view of the 5-bit accelerometer prototype operating based on the principle of an acceleration switch with digitally tunable threshold. The structure consists of sets of electrostatic actuators mounted around a large proof mass. Each bit of resolution in the sensor response is associated with an electrostatic actuator acting on the proof mass. Once activated, each actuator applies an electrostatic force to the proof mass lowering its switching threshold (by pulling the proof mass towards the output contact electrode). Each actuator applies twice as much force to the proof mass compared to the actuator associated with the next less significant bit. For each combination of activated actuators, depending on whether the proof mass contacts the output electrode or not, it can be determined whether the applied acceleration is

978-1-940470-03-0/HH2018/$25©2018TRF
DOI 10.31438/trf.hh2018.89

Solid-State Sensors, Actuators and Microsystems Workshop
Hilton Head Island, South Carolina, June 3-7, 2018

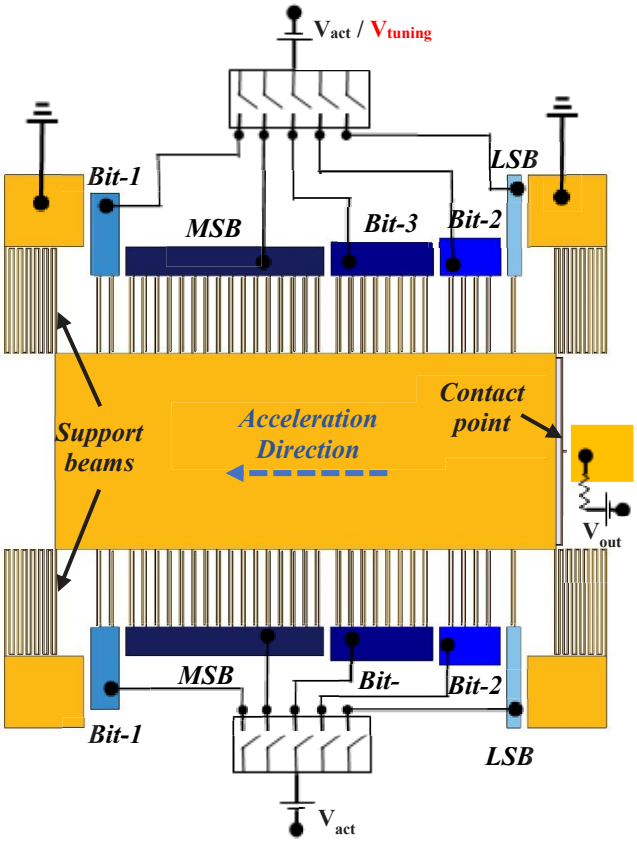

Figure 1: Simplified schematic of the 5-bit digitally operated accelerometer

larger or smaller than the acceleration threshold for that combination. The proof mass moves back and forth in the horizontal direction as a result of the applied acceleration. The proof mass connected to ground (GND) has a metallic tip that comes in contact with a stationary contact electrode when the applied acceleration exceeds the threshold. The stationary output contact electrode is biased with a bias voltage (V_{out}) through a large resistor, hence setting the output electrode voltage to zero. Application of an assistive force which pulls the metallic tip of proof mass towards the output contact electrode will lower the acceleration threshold and vice versa. In this manner, having an arrangement of multiple electrostatic actuators with appropriate strengths (electrode finger size and number) around the proof mass and selectively turning them ON or OFF, a binary search can be performed to find the value of the applied acceleration [1]. The mass of the proof mass and the stiffness of the tethers is to be chosen in a way that when the device is subjected to full scale acceleration and all electrode voltages are set to zero, the displacement is equal to the gap size between the metallic tip and the proof mass, i.e.:

$$K*g=m*a_{max} \qquad (1)$$

where K is the stiffness of the tethers, g is the gap size between the metallic tip of proof mass and the contact output electrode, m is the mass of the proof mass and a_{max} is the full-scale acceleration.

To perform an acceleration measurement, the tuning electrodes are to be turned ON or OFF in a sequential manner via an interfaced digital controller. Turning an electrode ON means application of a pre-determined fixed voltage to the electrode by the digital controller. The actuator associated with the most significant bit (MSB), which is Bit 4 in this case (Figure 1), has twice the number of identical parallel plate actuator fingers compared to the next most significant bit (Bit 3). In other words, Bit 4 provides an actuation force which is exactly twice that of Bit 3 when turned on. Similarly, the number of actuator fingers goes down by a factor of two from the most significant bit to the next less significant bit and the least significant bit (Bit 0) has the minimum number of actuator fingers. The number of electrodes, electrostatic actuator gap size, and electrode areas are to be chosen so that upon application of the ON voltage to the MSB actuator a force equal to 50% of the full-scale acceleration force is applied to the proof mass.

Also, the device is tunable for different full-scale accelerations by decreasing the contact gap between the contact tip of proof mass and the output contact electrode. To reduce the contact gap, a pre-determined tuning voltage could be applied to the electrostatic actuators on one side of the device. Electrostatic actuators on the opposite end were then given a separate actuating voltage (ON voltage) to define the different thresholds of acceleration for each specific bit of resolution.

FABRICATION

Monocrystalline silicon with a relatively thick coating of gold was used as the structural material for the accelerometers. Figure 2 shows the fabrication process used to fabricate the devices on an SOI substrate (50 µm thick device layer, 2µm thick buried oxide layer) using a two-mask micromachining process. First, a very thin layer (100 nm) of chromium has been patterned on the SOI device layer as a hard mask (Figure 3(a)). Backside was then patterned and etched to avoid any potential stiction issues for the large proof masses. Then the buried oxide layer has been removed in hydrofluoric acid (HF) (Figure 3(b)). The accelerometer silicon skeleton was then defined in the SOI device layer via deep reactive ion etching (DRIE) all the way down to release the device (Figure

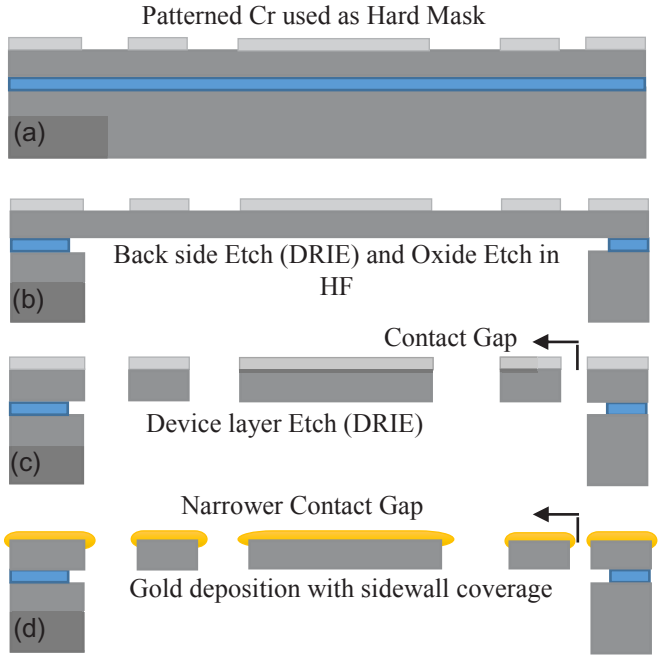

Figure 2: Schematic side view showing the microfabrication process flow: (a) Patterned Cr used as hard mask, (b) Backside etch (DRIE) and oxide etch in HF. (c) Device layer etch (DRIE) (d) Gold deposition with sidewall coverage.

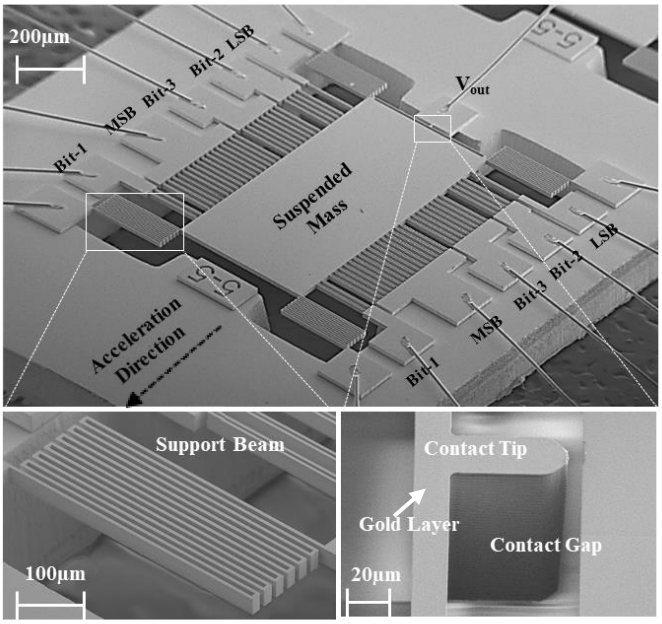

Figure 3: SEM views of the fabricated five-bit digital accelerometer along with the zoomed-in views of the output contact tip and support beam

3(c)). To further narrow down the gap between the tip of proof mass and the output electrode, a thick layer of gold with slight sidewall coverage was sputtered on the fabricated fully silicon devices. The sputtered gold on the sidewalls also provides a high-quality metal-metal electrical contact between the tip of proof mass and the output electrode (Figure 3(d)). Thickness of the deposited gold on the sidewalls was thoroughly monitored to adjust the gap size between the contact tip and the proof mass. Figure 3(a) and (b) show SEM views of the digital accelerometer structure fabricated using the described fabrication sequence. Regular lithography and plasma etch constraints restrict the gap size between the proof mass and the metallic tip ~3 µm. By depositing a layer of gold with side wall coverage, gap sizes as small as 2.5µm were achieved (Figure 3(c)).

Ten identical electrostatic actuator finger sets are included in the device shown in Figure 3(a) allowing operation of the device as a 5-bit accelerometer with 32 of the electrodes associated with the Most Significant Bit, 16 electrodes for the Bit 3, 8 electrodes for Bit 2, 4 electrodes for Bit 1 and 2 electrodes for the Least Significant Bit.

MEASUREMENT SETUP AND RESULTS

The tested 5-bit prototype (Figure 3) has a 1mm×1.9mm proof mass (225µg), four support beams with overall stiffness of 5N/m, and contact gap of 2.5µm leading to full-scale acceleration of 5.1g (binary output of 11111). This relatively big full-scale acceleration would require sophisticated high-g test and characterization equipment that were not available.

The MEMS chip was placed on a printed circuit board and thus tested for acceleration only less than 1g which could be easily applied by tilting the board at various angles with respect the horizon. It was determined that actuation voltage of 12.4V is to be applied to the actuators associated with MSB, Bit-3, Bit-2, Bit-1 and Bit-0 (LSB) actuators to lower the threshold acceleration by 1/2, 1/4, 1/8, 1/16 and 1/32 of full-scale acceleration, respectively.

Device performance was validated by applying different accelerations and monitoring the output while manually turning different actuators ON/OFF. To test the device with accelerations in the zero to 1g range, actuation voltage was applied to Bit-4 (MSB) and Bit-3 to keep these bits turned ON and hence, reduce the contact gap in a way that all the digital outputs would correspond to an acceleration less than 1g. By manually switching ON and OFF the actuation voltages to different combinations of the actuators of Bit-2, Bit-1 and Bit-0 all the possible binary outputs between 11010 to 11111 were selectively tested. Table 1 shows resulting sensor binary outputs for different applied accelerations showing the closest possible binary output in each case.

Furthermore, full-scale acceleration of the devices was tuned by utilizing one set of electrostatic electrodes (located on one side of the proof mass) as tuning electrodes. By applying a voltage of 12.5V to the tuning electrodes, the contact gap was effectively reduced from 2.5um to 1um. This eventually tuned he full scale acceleration from 5.1g to 2g. The device could now be tested for a as a 5-bit accelerometer in the zero to 2g range. To the other set of electrostatic actuators, an actuating voltage of 10.5V was applied

Table 1: Measurement results of the five-bit 5.1g full-scale accelerometer for six selected applied accelerations (Bit values in the Table indicate the ON/OFF (1/0) status of the actuator of the respective bit when contact occurs). Input accelerations are produced from the earth gravity (g) by mounting the sensor chip with a certain tilt angle also shown in the table.

Actuators status					Sensor Mounting Angle (θ)	Input Acceleration $a = g\sin(\theta)$	Measured Acceleration (g)	Sensor Binary Output
MSB	Bit-3	Bit-2	Bit-1	LSB				
1	1	0	1	0	62	0.882	.796≤g<.956	(00101)
1	1	0	1	1	45	0.708	.637≤g<.796	(00100)
1	1	1	0	0	32	0.530	.478≤g<.637	(00011)
1	1	1	0	1	20	0.355	.318≤g<.478	(00010)
1	1	1	1	0	15	0.265	.159≤g<.318	(00001)
1	1	1	1	1	0	0	g<.159	(00000)

Table 2: Measurement results of the five-bit accelerometer tuned for 2.0g full-scale acceleration for eight selected applied acceleration (Bit values in the Table indicate the ON/OFF (1/0) status of the actuator of the respective bit when contact occurs). Input accelerations are produced from the earth gravity (g) by mounting the sensor chip with a certain tilt angle also shown in the table.

Actuators status					Sensor Mounting Angle (θ)	Input Acceleration $a = g\ sin(\theta)$	Measured Acceleration (g)	Sensor Binary Output
MSB	Bit-3	Bit-2	Bit-1	LSB				
1	0	0	0	0	70	0.94	.9375≤g<1	(01111)
1	0	0	0	1	62	0.882	.875≤g<.9375	(01110)
1	0	0	1	0	56	0.829	.8125≤g<.875	(01101)
1	0	0	1	1	31	0.515	.5≤g<.5625	(01100)
1	1	0	0	0	16	0.275	.25≤g<.3125	(00111)
1	1	1	0	0	8	0.139	.125≤g<.1875	(00011)
1	1	1	1	0	4	0.069	.0625≤g<.125	(00001)
1	1	1	1	1	0	0	g<.0625	(00000)

and the binary search was followed to obtain digital outputs for various accelerations as shown in Table 2.

CONCLUSION

It was demonstrated that the concept of contact-based acceleration switches can be enhanced to perform higher resolution quantitative acceleration measurements. A digitally operated MEMS accelerometer with a 5-bit of resolution was successfully demonstrated. A simple 2-mask fabrication process was used to fabricate the devices and the contact gap size was reduced by a simple mask less fabrication technique. Also, it has been demonstrated that the device can be tunable for different full-scale acceleration. The same device principle can be utilized to implement 7-bit, 8-bit or even higher resolution digital accelerometers. Elimination of the need for the analog front-end and analog signal conditioning can lead to significant power savings and a leap forward towards ultra-low power MEMS inertial sensors.

REFERENCES

[1] V. Kumar, R. Jafari, S. Pourkamali, "Ultra-Low Power Digitally Operated Tunable MEMS Accelerometer," IEEE Sensors Journal, VOL. 16, NO. 24, DECEMBER 15, 2016

[2] Y Lu, Y Wei, L Liu, J Zhang, L Sun, Y Liu, "Towards unsupervised physical activity recognition using smartphone accelerometers," Multimedia Tools and Applications, April 2017,

[3] R. Varatharajan, G. Manogaran, M.k. Priyan, R. Sundarasekar, "Wearable sensor devices for early detection of Alzheimer disease using dynamic time warping algorithm," The Journal of Networks, Software Tools and Applications, 2017

[4] C. Saiprasert, T. Pholprasit, S. Thajchayapong, "Detection of Driving Events using Sensory Data on Smartphone" International Journal of Intelligent Transportation Systems Research, 2017, Volume 15

[5] k. Hari, S. Kumar, I.R. Praveen, V. Seena, "Out-of-plane dual flexure MEMS piezoresistive accelerometer with low cross axis sensitivity" Microsystem Technologies, 2017

[6] Y. Wang, H. Ding, X. Le, W. Wang, J. Xie, "A MEMS piezoelectric in-plane resonant accelerometer based on aluminum nitride with two-stage microleverage mechanism, Sensors and Actuators, Volume 254, 1 February 2017

[7] X. Zhou, L. Che, S. Liang, Y. Lin, X. Li, Y. Wang, "Design and fabrication of a MEMS capacitive accelerometer with fully symmetrical double-sided H-shaped beam structure", Nicroelectronic Engineering, pp51-57, 2015.

[8] V. Kumar, X. Guo, S. Pourkamali, "Single-Mask Field Emission based tunable MEMS Tunneling Accelerometer,", in Press, IEEE Nano, 2015.

[9] Lee D, "Wireless and powerless sensing node system developed for monitoring motors,'' Sensors pp5005-5022, 2008.

[10] B.V. Amini and F. Ayazi, "A 2.5V 14-bit Sigma-Delta CMOS-SOI Capacitive Accelerometer," J. SSC, Dec. 2004, pp. 2467-2476.

[11] T. Kobayashi, H. Okada, T. Masuda, R. Maeda, and T. Itoh, " A digital output accelerometer using MEMS-based piezoelectric accelerometers and arrayed CMOS inverters with satellite capacitors," Smart Materials and Structures, Volume 20, Number 6, 2011.

[12] R. Abdolvand, B.V. Amini, and F. Ayazi, "Sub-micro-gravity in-plane accelerometers with reduced capacitive gaps and extra seismic mass," IEEE Journal of Microelectromechanical Systems, Vol. 16, pp. 10361043, Oct. 2007.

CONTACT

*A. Abbasalipour, tel: +1-2144038822;
amin.abbasalipour@utdallas.edu

ON DECOUPLED QUANTIFICATION OF ENERGY DISSIPATION MECHANISMS IN TOROIDAL RING GYROSCOPES

Yusheng Wang[1], Yu-Wei Lin[1], Janna Rodriguez[2], Gabrielle D. Vukasin[2], Dongsuk D. Shin[2], Hyun-Keun Kwon[2], David B. Heinz[2], Yunhan Chen[2], Dustin D. Gerrard[2], Thomas W. Kenny[2], and Andrei M. Shkel[1]*

[1]MicroSystems Laboratory, University of California, Irvine, CA, USA

[2]Micro Structures & Sensors Lab, Stanford University, CA, USA

ABSTRACT

We present a study on the quantification of the energy dissipation mechanisms in Toroidal Ring Gyroscopes (TRG). Our approach is based on suppression of the viscous air damping and controlling thermoelastic dissipation (TED), thus exposing the anchor loss of the device. During testing, energy dissipative factors, such as viscous air damping, TED, and surface loss, were minimized by venting the encapsulation, pumping down to ultrahigh vacuum (UHV), and sweeping the temperature down to 123K, so that anchor loss became the dominant factor that influenced the overall quality factor of the device. The anchor loss limit of the tested TRG was measured to be 1.35 million, and this value was on the same level as predicted by PML method. This study demonstrates the use of a methodology for analysis of energy dissipation mechanisms in MEMS devices and the possibility of quantifying the contribution of each mechanism independently.

INTRODUCTION

Quality factor is a parameter describing the energy loss of vibratory MEMS devices [1]. It is used as a metric to optimize device design in order to enhance its performance. In Coriolis Vibratory Gyroscopes (CVG), for example, lower energy consumption and better in-run noise performance, such as bias stability and Angle Random Walk (ARW), can be achieved with a higher quality factor. The quality factor of a resonator is limited by many energy dissipation mechanisms, such as viscous air damping, TED, anchor loss, surface loss, and intrinsic material loss. The total quality factor of a vibratory structure can be expressed as

$$Q_{total}^{-1} = Q_{viscous}^{-1} + Q_{TED}^{-1} + Q_{anchor}^{-1} + Q_{surface}^{-1} + Q_{others}^{-1}. \quad (1)$$

Viscous air damping increases rapidly as the resonator's surface-to-volume ratio increases [2]. Therefore, its effect is more dominant in micro-fabricated resonators than in devices of larger scales. Viscous air damping is proportional to air pressure in the molecular region, which for a device sealed with an ideal gas scales as the inverse square root of temperature. Viscous air damping can be suppressed by packaging and vacuum sealing. TED is related to the coupling of thermal and elastic deformation fields of the resonator through the Coefficient of Thermal Expansion (CTE) of the material [3, 4]. TED can be reduced by optimizing the design [5], or building devices with materials with lower CTE, such as Fused Quartz [6]. Anchor loss is due to vibratory wave propagation from the resonator into the substrate through the anchor and it is related to the mode shape, mechanical properties of the substrate, and anchor geometry. A numerical technique called Perfectly Matched Layer (PML) is available in the COMSOL MultiPhysics Package, and has become popular for modeling anchor loss in resonating MEMS [1]. Dynamic balancing of the resonator [7] and careful anchor designs [8] have been demonstrated to reduce the anchor loss in resonators. The surface loss is related to the dissipation of energy by defects, impurities, and roughness of the surface of the resonator [9]. High temperature annealing and etching of the device [10], as well as surface reflow [11] have been experimentally proven to reduce the surface loss of the resonators.

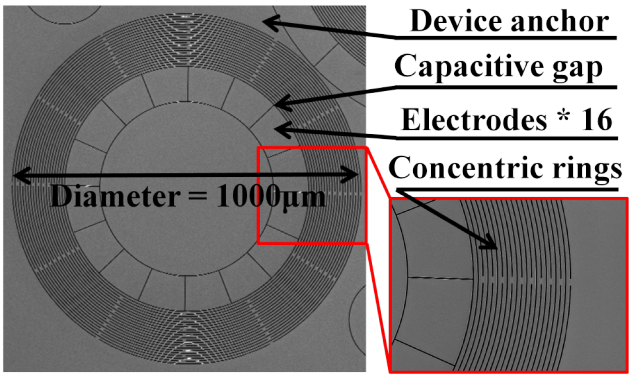

Figure 1: SEM image of the TRG.

All the factors mentioned above contribute to the overall energy dissipation of resonators. In practice, it is difficult to experimentally identify the dominant dissipation mechanism [2]. As a result, although many techniques have been developed to reduce dissipative sources of resonators, they cannot be effectively applied without first identifying the dominant energy dissipation mechanism [12].

In this paper, we present a study on the energy dissipation mechanisms of the TRG. We utilize a previously demonstrated method which relies on measurements of quality factor as a function of temperature from the room temperature down to cryogenic temperatures, for encapsulated and vented devices, and separate measurements of the quality factor as a function of pressure near the room temperature [13].

TOROIDAL RING GYROSCOPE

The TRG was selected for its structural simplicity and a demonstrated potential for high performance [14]. It consists of a concentric ring structure, an outer anchor that encircles the rings, and an inner electrode assembly. The outer anchor structure leads to a more robust support of the structure compared to devices with a central anchor. The device was fabricated using the Epi-Seal process [15], which utilizes epitaxially grown silicon to seal the device layer at extremely high temperatures, resulting in an ultra-clean wafer-level sealing. The device was fabricated on single-crystal <111> silicon wafers to achieve a better structural symmetry, enabling the operation in the n=2 mode. The SEM image of the device is shown in Fig 1. The diameter of the ring structure is 1000μm and it includes 20 concentric rings with a width of 6μm. The rings are connected to each other with 6 spokes in between two consecutive rings. The thickness of the device is 60μm and the gaps in between the rings are 1.5μm. The designed resonant frequency of the n=2 mode of the TRG was 68.7kHz and the experimentally measured frequency was 54.5kHz. The difference in frequency is possibly due to the over-etching of the device.

978-1-940470-03-0/HH2018/$25©2018TRF
DOI 10.31438/trf.hh2018.90

One of the benefits of this specific design is that the n=2 mode is the mode with the lowest natural frequency. It comes before all the out-of-plane modes because of the large thickness-to-width ratio of the rings. It also comes before the n=1 rocking mode due to the phenomenon of mode ordering [16]. This order of the modes helps to improve the common mode rejection of external accelerations.

ENERGY DISSIPATION ANALYSIS

Viscous Air Damping

Viscous air damping of a resonator is related to the pressure surrounding the resonator and its geometry. Although devices fabricated in the Epi-Seal process are sealed with pressure near 0.1Pa [15], the narrow gap and a low frequency motion of the beams of the resonator will induce some viscous damping, especially if other dissipation mechanisms are suppressed.

It is impossible to directly measure the pressure inside the cavity of the Epi-Seal devices. Therefore, we utilized the overall quality factor of the resonator as an indicator of the pressure. The quality factor of the sealed device was first measured over a wide temperature range. The quality factor at room temperature was found to be 128,000. Then, we used the Focused Ion Beam (FIB) to form a small hole through the cap, exposing the interior of the resonator to the surrounding atmosphere, as shown in Fig. 2.

The device was placed into a vacuum chamber with adjustable air pressure and the quality factor of the device was measured as a function of pressure at room temperature. The relation between the air pressure and the quality factor of the device is shown in Fig. 3. The figure shows that the quality factor of the device reached 170,000 with air pressure below 0.001Pa, indicating that viscous air damping was overwhelmed by other dissipation mechanisms at pressures below 0.001Pa. The original quality factor of 128,000 for the sealed device corresponded to a pressure level of 0.04Pa, providing a good estimate for the pressure in the cavity of the device before venting. To suppress the effects of viscous air damping on the overall quality factor, we tested the vented device at pressures below 0.0001Pa in the following sections.

Thermoelastic Damping

Thermoelastic damping is related to the exchange of energy between temperature and elastic deformation fields in resonating structures. The coupling term between the two fields is the CTE of the material. It has been shown that the TED of a cantilever beam is proportional to the square of CTE of the material, as shown in Equation (2), where ρ is the density, C_p is the heat capacity, α is CTE, T is the temperature, and E is Young's modulus. For the TRG devices that we studied, the general principle of TED through CTE-coupling between the temperature and elastic deformation fields still applies although they have a more complicated geometry. Silicon is a material whose CTE is strongly dependent on the temperature and it crosses zero at temperature of near 123K [17]. Because of these effects, the TED contribution to the overall quality factor as a function of temperature should have a strong and recognizable signature, making it possible to quantify TED in this resonator.

$$Q_{TED} \propto \frac{\rho C_p}{\alpha^2 T E} \qquad (2)$$

The encapsulated resonator was first placed in a vacuum chamber and the chamber was cooled down by conductive contact with a liquid Nitrogen reservoir. The device was characterized at different ambient temperatures ranging from 80K to 300K. The quality factor of the device was measured by the ring-down method for better accuracy while the temperature slowly rose due to the ambient temperature of the room. The device was tested before and after the FIB-venting of the device. The relations between the temperature and the quality factor of the device, before and after venting, are shown in Fig. 4.

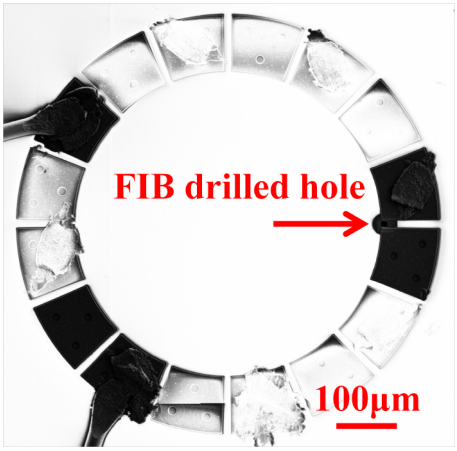

Figure 2: SEM image of the device (cap layer) with the hole drilled by FIB.

The device showed a higher quality factor after venting and operating below 0.0001Pa, as expected from the earlier pressure-sweep results in Fig. 3. Overall, the difference between the Q-T curves for the sealed and vented device was consistent with the expected temperature dependence of the viscous air damping, which should be inversely proportional to the square root of temperature. The magnitude of viscous air damping could be estimated by the difference of the two curves.

The maximum quality factor for the vented device rose to 1.35M at temperature of around 123K, and then decreased again at lower temperatures. This was the expected signature of a strong contribution from TED. The same signature was present in the data from the sealed device, but the additional contribution from viscous air damping suppressed the signature.

A model for TED in the TRG device was developed with Finite Element Analysis (FEA) in COMSOL MultiPhysics Package. The thermo-mechanical module was utilized to model the coupling of thermal and elastic deformation fields. At room temperature, the model predicted a Q of 200,000, which was in reasonable agreement with the experimental result of 170,000. Using the full set of temperature-dependent material parameters [17], prediction of the

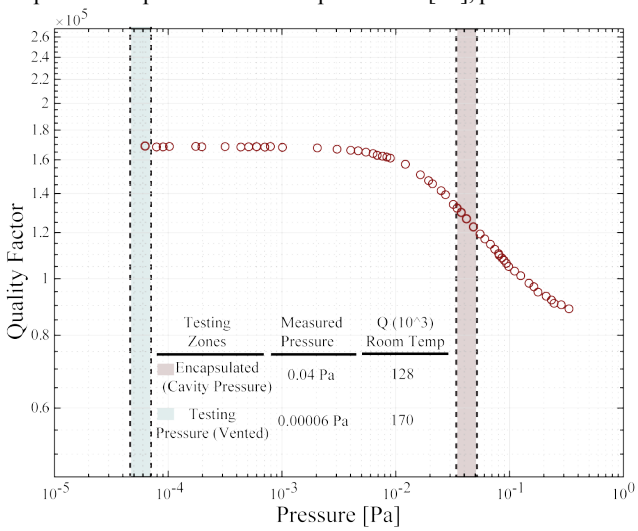

Figure 3: The relation between the air pressure and the quality factor of the device at room temperature.

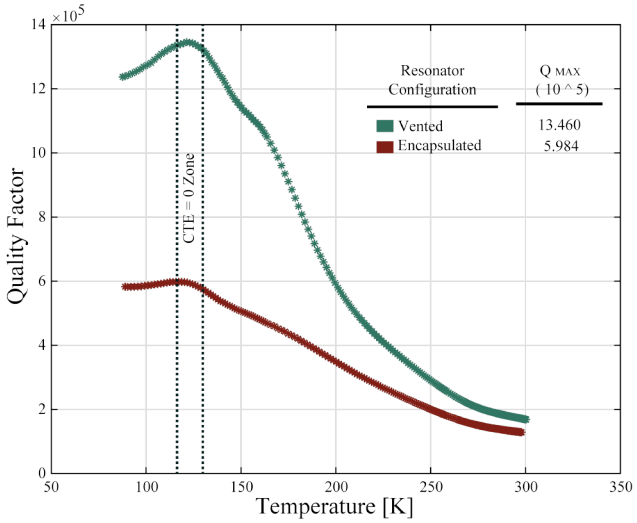

Figure 4: The relation between the temperature and the quality factor of the device before and after the device was vented by FIB.

temperature dependence of the TED contribution to the quality factor was built, and is plotted along with other models in Fig. 7.

At the peak of the Q-T curve for the vented device, we effectively suppressed contributions from viscous damping and TED, which left the anchor loss as the most likely remaining source of dissipation. This data alone was not sufficient to positively identify the anchor loss as the limiting mechanism at Q=1.35M.

Anchor loss

All of the most commonly-discussed models for anchor loss depend only on material's mechanical properties, such as Young's modulus, and geometry. In this study, the relevant material properties and geometries were almost invariant over a large temperature range, so we hypothesized that the anchor loss was temperature-invariant.

To confirm this hypothesis, the resonant frequency of the device was measured over a large temperature range from 80K to 300K. An overall frequency shift of only 64Hz was demonstrated over a 220K temperature range. The results are shown in Fig. 5. The very small shift in frequency (<1300ppm) indicated a weak temperature dependence of the mechanical properties of silicon, such as Young's modulus and Poisson's ratio.

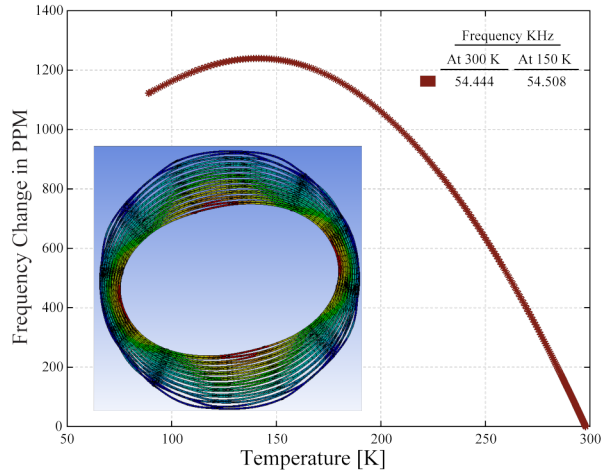

Figure 5: The relation between the temperature and the resonant frequency of the encapsulated device. Inserted is the mode shape of n=2 mode of TRG.

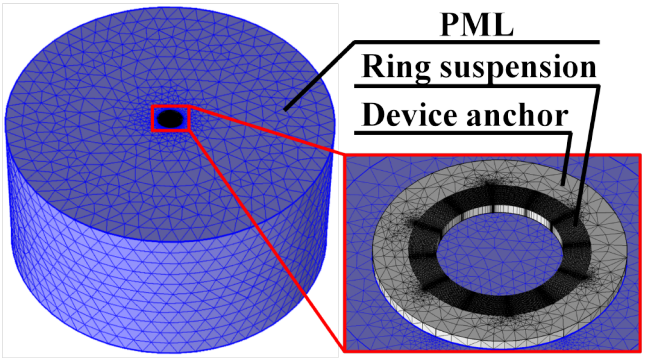

Figure 6: Anchor loss model in COMSOL MultiPhysics. The blue part is PML.

In order to help to confirm that the dissipation mechanism limiting the quality factor to 1.35M is the anchor loss, we turned to the FEA model for anchor loss analysis in COMSOL MultiPhysics Package with the Perfectly Matched Layer (PML) model. In this model, the PML was built in a cylinder shape with the height of 15cm and diameter of 30cm. Even though these dimensions far exceed the dimensions of the physical die, they were selected to be 20% greater than the wavelength in silicon at 68kHz (0.12m). The PML model is presented in Fig. 6.

In one set of simulations, the anchor loss model showed a quality factor limit of 1.32M with meshing errors of less than 5%, which agreed with the highest quality factor of the device after venting and cooling down to 123K (Fig. 4). Although the model matched the experimental results, there are still many free parameters in the model, such as the size of the substrate, the scaling factor and the shape of PML, that have not been explored. Based on this, we believe that the PML model in COMSOL Multiphysics does not refute our conclusion, but is not predictive enough to provide a strong confirmation.

OVERALL QUALITY FACTOR ANALYSIS

The overall quality factor of a resonator is related to many energy dissipation mechanisms. For the TRG device that we tested, the effects of Akhiezer damping and Landau-Runer damping were not considered since the f*Q product is far too small. Surface loss could also be eliminated due to the ultra-clean cavity fabricated in the Epi-Seal process. Ohmic dissipation was also unlikely since the quality factor measurement was independent of the bias voltages used during testing. Therefore, our model for analysis of the quality factor only considered the effects of viscous air damping, TED, and the anchor loss.

The strongest test of the validity of the decision to neglect other dissipation mechanisms and to focus just on the viscous air damping, TED, and the anchor loss is a comparison between the Q(T) predicted by the model and the experimental results. We utilized the TED model described above with no adjustable parameters; to this we added a temperature-independent term representing the anchor loss, where the magnitude was taken from the peak of the experimental Q(T) curve, and was shown to be consistent with the PML model result. In Fig. 7, we compared the reciprocal sum of the TED and the constant anchor loss term with the experimentally measured Q(T) for the vented device (blue points, red curve), and close match with errors less than 5% was demonstrated over the entire temperature range. This is a very strong confirmation that our experiment is well-represented by the reciprocal sum of TED and a temperature-independent anchor loss term, and that there are no other residual dissipation mechanisms playing a significant role.

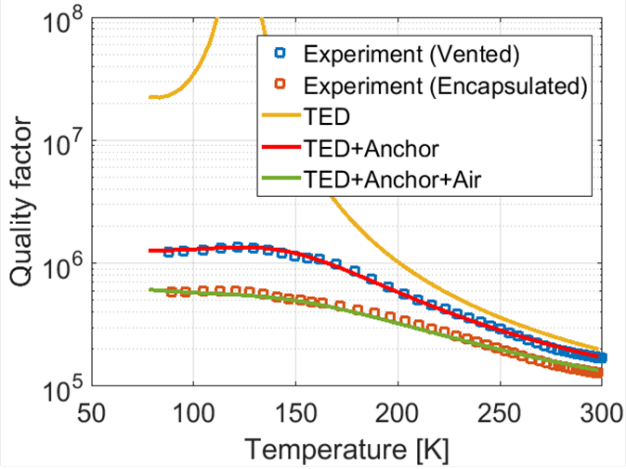

Figure 7: Comparison between the estimated Q-T relation and the measured Q-T relation.

Finally, we added a viscous air damping term to the reciprocal sum. The magnitude of the air damping was determined by the Q(P) measurement at room temperature, and we asserted a $1/(T^{1/2})$ scaling. Again, the experimental result for the encapsulated device was an extremely good fit to this model with errors less than 10%.

The agreement between model and experiment, including the qualitative shape and the quantitative match, is the strongest possible confirmation that the explanation for the results is valid.

CONCLUSION

This study follows a recently-established methodology for analysis of the energy dissipation mechanism in resonant MEMS devices [13], which includes measurements of the Q(T) over a wide temperature range for sealed and vented devices, and measurements of Q(P) for the vented device. In this study, we analyzed the energy dissipation mechanisms of a TRG device. The viscous air damping, TED, and the anchor loss were identified as the major loss mechanisms that affected the overall quality factor of the device. The value of each damping mechanism was estimated and a complete model representing the relation between the quality factor and temperature was constructed. Close match between the model and the experimental results confirmed the validity of the model.

ACKNOWLEDGEMENT

This work was supported by the Defense Advanced Research Projects Agency (DARPA) and U.S. Navy under Contract No. N66001-16-1-4021 at UC Irvine and Contract No. N66001-16-1-4023 at Stanford University. The fabrication work was performed in part at the Stanford Nanofabrication Facility (SNF), supported by the National Science Foundation under Grand ECS- 9731293. Special thanks to all the staff at SNF for their help during the fabrication process.

REFERENCES

[1] M. Weinberg, R. Candler, S. Chandorkar, J. Varsanik, T. Kenny, and A. Duwel. “Energy Loss in MEMS Resonators and the Impact on Inertial and RF Devices”. *Solid-State Sensors, Actuators and Microsystems Conference (TRANSDUCER)*, Denver, CO, 6/21-25/09, IEEE, (2009), pp. 688-695.

[2] J. Yang, T. Ono, and M. Esashi, "Energy dissipation in submicrometer thick single-crystal silicon cantilevers," *IEEE Journal of Microelectromechanical systems*, 11, 6, (2002).

[3] C. Zener, "Internal friction in solids. I. Theory of internal friction in reeds," *Physical review*, 52, 3, (1937).

[4] C. Zener, "Internal friction in solids II. General theory of thermoelastic internal friction," *Physical Review*, 53, 1, (1938).

[5] D. D. Gerrard, Y. Chen, S. A. Chandorkar, G. Yu, J. Rodriguez, I. B. Flader, D. D. Shin, C. D. Meinhart, O. Sigmund, and T. W. Kenn,. "Topology optimization for reduction of thermo-elastic dissipation in MEMS resonators," *Solid-State Sensors, Actuators and Microsystems (*TRANSDUCERS), Kaohsiung, Taiwan, 6/18-22/17, IEEE, (2017), pp. 794-797.

[6] D. Senkal, M. J. Ahamed, M. H. Asadian, S. Askari, and A. M. Shkel, "Demonstration of 1 Million Q-Factor on Microglassblown Wineglass Resonators With Out-of-Plane Electrostatic Transduction," *IEEE Journal of Microelectromechanical Systems*, 24, 1, (2015).

[7] S. A. Zotov, B. R. Simon, I. P. Prikhodko, A. A. Trusov, and A M. Shkel, "Quality Factor Maximization through Dynamic Balancing of Tuning Fork Resonator," *IEEE Sensors Journal*, 14, 8, (2014).

[8] A. Darvishian, B. Shiari, J. Y. Cho, T. Nagourney, and K. Najafi, "Anchor loss in hemispherical shell resonators". *IEEE Journal of Microelectromechanical Systems*, 26, 1, (2017).

[9] G. Palasantzas, "Quality factor due to roughness scattering of shear horizontal surface acoustic waves in nanoresonators," *Journal of Applied Physics*, 104, 5, (2008).

[10] J. J. Bernstein, M. G. Bancu, J. M. Bauer, E. H. Cook, P. Kumar, E. Newton, T. Nyinje, G. E. Perlin, J. A. Ricker, W.A. Teynor, and M. S. Weinberg, "High Q diamond hemispherical resonators: fabrication and energy loss mechanisms." *Journal of Micromechanics and Microengineering*, 25, 8, (2015).

[11] Y. Wang, M. H. Asadian, and A. M. Shkel, "Modeling the Effect of Imperfections in Glassblown Micro-Wineglass Fused Quartz Resonators," *Journal of Vibration and Acoustics*, 139, 4, (2017).

[12] Y. Wang, A. M. Shkel, "Study on Surface Roughness Improvement of Fused Quartz After Thermal and Chemical Post-Processing," *IEEE Inertial Sensors*, Laguna Beach, CA, 2/23-25/16, IEEE, (2016), pp. 101-104.

[13] J. Rodriguez, D. D. Gerrard, S. Chandorkar, Y. Chen, G. M. Glaze, I. B. Flader, C. H. Ahn, E. J. Ng, and T. W. Kenny, "Wide-range temperature dependence studies for devices limited by thermoelastic dissipation and anchor damping," *Solid-State Sensors, Actuators and Microsystems (TRANSDUCERS)*, Kaosiung, Taiwan, 6/18-22/17, IEEE, (2017), pp. 1100-1103.

[14] D. Senkal, S. Askari, M. J. Ahamed, E. Ng, V. Hong, Y. Yang, C. H. Ahn, T. W. Kenny, and A. M. Shkel, "100k Q-Factor Toroidal Ring Gyroscope Implemented in Wafer-level Epitaxial Silicon Encapsulation Process, " *IEEE MEMS Conference*, San Francisco, CA, 1/26-30/14, IEEE, (2014), pp. 24-27.

[15] Y. Yang, E. J. Ng, Y. Chen, I. B. Flader, and T. W. Kenny "A Unified Epi-seal Process for Fabrication of High-stability Microelectromechanical Devices," *IEEE Journal of Microelectromechanical Systems*, 25, 3, (2016).

[16] A. Efimovskaya, D. Wang, Y. Lin, and A. M. Shkel, "On Ordering of Fundamental Wineglass Modes in Toroidal Ring Gyroscope," *IEEE Sensors Conference*, Orlando, FL, 10/30-11/2/16, IEEE, (2016), pp. 1-3.

[17] T. Middelmann, A. Walkov, G. Bartl, and R. Schödel, "Thermal expansion coefficient of single-crystal silicon from 7 K to 293 K," *Physical Review B*, 92, 17, (2015).

CONTACT

*Yusheng Wang, tel: +1-949-562-9560; yushengw@uci.edu

CAPACITIVE TRANSDUCER ENHANCEMENT ON QUADRATURE COMPENSATION ELECTRODE OF YAW RATE GYROSCOPE

Peng Shao, Eduardo Canales, and Peiqing Zhu
NXP Semiconductors, Chandler, Arizona, USA

ABSTRACT

Being the major error source of Coriolis vibratory gyroscope, quadrature error is always well-compensated for high performance MEMS gyroscopes. This paper presents a novel design of quadrature compensation unit (QCU) electrodes for yaw rate gyroscope, with enhanced compensation efficiency. The design decreases the effective capacitance gap during half cycle of the drive oscillation. Theoretical analysis indicates that, these QCU electrodes will create a sinusoidal force that is inherently modulated by drive mode displacement, with about 3X increase in compensation efficiency. Both QCU designs are implemented on the same gyroscope test structure. Wafer level probe data is showing the predicted increase of QCU efficiency and assembled parts data is showing a reduced voltage needed for quadrature compensation.

INTRODUCTION

With the boost of automotive industry, there is a need of high performance MEMS gyroscopes with small offset drift and noise density, for the applications of Electronic Stability Control (ESC), Advanced Driver Assistance Systems (ADAS), and Autonomous Driving.

Quadrature error is a major error source of Coriolis vibratory gyroscope. It is mainly caused by variations of MEMS process technology, such as etching uniformity, side wall slope and is difficult to predict. Large quadrature error forces the analog front-end to have wide operating range which decreases the noise and power performance [1]. It also tends to shift with temperature and causes large temperature coefficient of offset (TCO) and temperature coefficient of sensitivity (TCS). For high performance gyroscopes, quadrature error needs to be compensated by dedicated electrodes with a closed loop control system. The controller reads out the demodulated quadrature signal from sense electrode as an error signal and tries to null it with compensation voltages.

The most commonly used method of nulling quadrature error is to apply a DC voltage on Quadrature Compensation Unit (QCU), which is placed on the portion of mass that has both drive mode and sense mode motion at the same time [2]–[4]. The QCU consists of interdigitated fingers, whose gaps are defined by the minimum trench width of the process technology. In this paper, a novel QCU structure design with capacitive transducer enhancement is introduced. The design reduces the effective capacitance gap during half period of the drive oscillation. By placing QCU in pairs, compensation force will be magnified by 3 times [5].

This paper first describes the working principle of quadrature compensation and its conventional design, then propose a method of improving its compensation efficiency. Two types of design are built into the same gyroscope test structure. Wafer probe data and assembled parts data are shown to prove the theory.

THEORY

Conventional Design (Type A)

Quadrature error originates from structural non-ideality of drive oscillator. Drive suspensions are design as such that they are flexible in drive direction and rigid in sense direction. However, the stiffness of drive suspension in sense direction is finite, and will create coupling between drive and sense mode. Moreover, manufacturing imperfection will couple drive mode into sense mode as well. Consider a lumped parameter model of a vibratory gyroscope:

Figure 1: Conventional Quadrature Compensation Unit (Type A) Structure Design with biased electrostatic gap

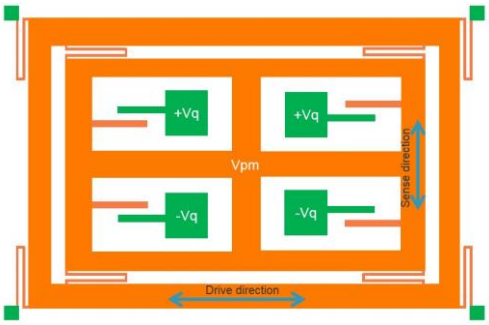

Figure 2: Configuration of Four Groups of QCU fingers

$$\begin{bmatrix} m_d & 0 \\ 0 & m_s \end{bmatrix}\begin{bmatrix} \ddot{x} \\ \ddot{y} \end{bmatrix}+\begin{bmatrix} c_x & 0 \\ 0 & c_y \end{bmatrix}\begin{bmatrix} \dot{x} \\ \dot{y} \end{bmatrix}+\begin{bmatrix} k_x & k_{xy} \\ k_{yx} & k_y \end{bmatrix}\begin{bmatrix} x \\ y \end{bmatrix}=\begin{bmatrix} F_d \\ -2m_C\Omega_z\dot{x} \end{bmatrix} \quad (1)$$

Where m_d and m_s are drive mass and sense mass, respectively, F_d is driving force, the term $-2m_c\Omega_z\dot{x}$ represents Coriolis force from yaw rate, k_{xy} and k_{yx} are two stiffness cross-coupling term, in which k_{yx} stands for the coupling from drive axis (x) to sense axis (y). The term $k_{yx}x$ can be defined as quadrature force, which is a time varying force in phase with drive displacement. To cancel this quadrature force, a compensation force in phase with drive displacement is required.

In order to generate a compensation force in phase with drive displacement, interdigitated fingers with bias gaps are used as figure 1 shows. The overlapping of movable and stationary fingers is larger than the travel range of movable mass. Figure 2 shows the configuration of four groups of QCU fingers placed inside Coriolis mass of a single mass gyroscope. The top two groups have the same electric potential of $+V_q$, while the bottom two groups have the electric potential of $-V_q$. Movable mass is biased at V_{pm}. The quadrature compensation force of the upper left group is,

$$F_{qc\_ul}=-\frac{\partial E}{\partial y}=\frac{1}{2}N\varepsilon h\frac{x_0+x\sin\omega_d t}{{y_0}^2}\left(V_{pm}-V_q\right)^2 \quad (2)$$

Where x_0 is the stationary overlapping length, N is the number of fingers, x is the drive direction, y is the sense direction, h is the structure layer thickness, ω_d is drive resonator frequency.

Considering the 180 degree phase difference and opposite in direction of right finger, and the -Vq bias for the bottom groups of

978-1-940470-03-0/HH2018/$25©2018TRF
DOI 10.31438/trf.hh2018.91

fingers, the quadrature compensation force of the upper right group is,

$$F_{qc\_ur} = -\frac{1}{2} N\varepsilon h \frac{x_0 - x\sin\omega_d t}{{y_0}^2}\left(V_{pm} - V_q\right)^2 \quad (3)$$

The total force from upper two groups that biased at $+V_q$ is,

$$F_{qc\_ua} = N\varepsilon h \frac{x\sin\omega_d t}{{y_0}^2}\left(V_{pm} - V_q\right)^2 \quad (4)$$

Similarly, the total force from lower two groups is,

$$F_{qc\_la} = -N\varepsilon h \frac{x\sin\omega_d t}{{y_0}^2}\left(V_{pm} + V_q\right)^2 \quad (5)$$

By adding the forces from upper group and lower group together, the total quadrature compensation force will be,

$$F_{qc} = 4N\varepsilon h \frac{V_{pm}V_q}{{y_0}^2} x\sin\omega_d t \quad (6)$$

The total compensation force is proportional to number of fingers, layer thickness, proof mass voltage, quadrature voltage and drive amplitude, inversely proportional to the square of gap size, which is a limiting factor defined by the design rule of the process technology.

Novel Design (Type B)

The novel design proposed in this paper introduces a way of enhancing the capacitance as illustrated in Figure 3. The enhanced structure modifies both movable and fixed fingers, reducing the effective capacitive gap during the positive half cycle, while the fingers on the other side reduces the gap during the negative half cycle. The combination of two groups of fingers create a sinusoidal force with larger amplitude and is in phase with drive amplitude.

Figure 3: Proposed Quadrature Compensation Unit (Type B) Structure Design with enhancement structure

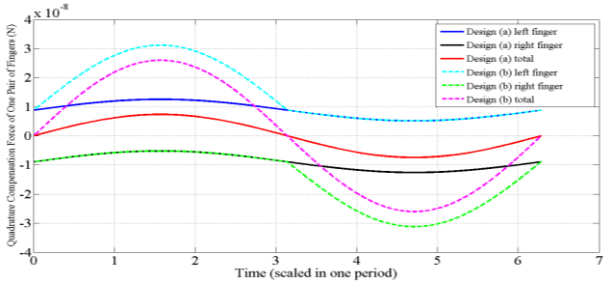

Figure 4: Comparison of both QCU finger design. The blue and black solid line is the force of left finger and right finger of QCU design type A. They added together (red solid line) to be the total force of design type A. The dotted blue line and dotted green line is the force of left finger and right finer of QCU design type B, who added together (dotted pink line) to be the total force of new finger design. (dimensions: initial overlap = 12um, drive amplitude = 5um, structure thickness = 23.5um, nominal gap = 1.5um, reduced gap during travel = 0.7um

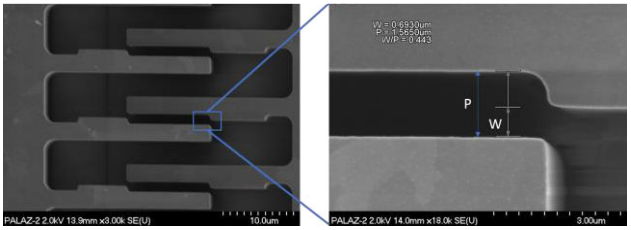

(a) (b)

Figure 5: SEM image of (a) one group of QCU fingers; (b) Zoomed-in view and detailed dimension measurement

Even though at the edge of the added block, the gap is smaller than the minimum gap, it will not affect manufacturability since the overlapping area is negligible. DRIE can define narrower capacitive gap with small overlapping area, compared with long trenches for springs and interdigitated fingers.

Figure 4 shows the compensation force of both designs in one cycle. The blue and black solid line is the force of left finger and right finger of QCU design type A (conventional finger design). They added together (red solid line) to be the total force of design type A. The dotted blue line and dotted green line is the force of left finger and right finger of QCU design type B (novel finger design), who added together (dotted pink line) to be the total force of design type B. It can be seen from figure 4, design type B is providing 3 times force design type A can provide, while keeping a sinusoidal compensation force. The dimensions in this calculation are numbers from process technology and MEMS design, and listed in Figure 4.

EXPERIMENT

Wafer Level Probe

To verify the increase of efficiency of QCU design, both designs were implemented on the same MEMS gyroscope design respectively, and were fabricated using the same process technology reported in [6]. The process technology is capable of defining parallel plate capacitor with minimum gap of 1.5um. For short trenches whose length is smaller than 2um, trenches with 0.7um in width can be etched. These trenches are usually used to define lateral shock stops. Figure 5 shows the SEM image of the improved design, (a) is a set of QCU fingers and (b) is zoomed-in view of detailed structure. The measurement of the SEM image shows a nominal gap of 1.565um, and enhanced gap of 0.673um.

The MEMS wafer was probed using lock-in amplifier as illustrated in figure 6. Lock-in amplifier actuate drive resonator from Drive Actuation Unit (DAU), and acquire drive motion signal from Drive Measurement Unit (DMU), and quadrature signal from Sense Measurement Unit (SMU) at the same time. Both magnitude and phase value need to be read for correct polarity of quadrature signal.

The current drawn from DMU is calculated as:

$$i_{drv} = N_{DMU}\frac{\varepsilon_0 HV}{d}\frac{\partial x}{\partial t} = N_{DMU}\frac{\varepsilon_0 HV x_d \omega_d \cos\omega_d t}{d} \quad (7)$$

Where, N_{DMU} is the number of capacitors of DMU fingers, H is the silicon layer thickness, V is the biased voltage on proof mass, d is the capacitance gap size of DMU and SMU, x_d is the drive resonator amplitude, ω_d is the drive resonator angular frequency.

The current drawn from SMU is calculated as:

$$i_{quad} = -N_{SMU}\frac{\varepsilon_0 LHV}{d^2}\frac{\partial y}{\partial t} = -N_{SMU}\frac{\varepsilon_0 LHV y_q \omega_d \cos(\omega_d t)}{d^2} \quad (8)$$

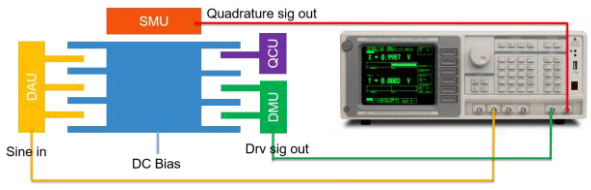

Figure 6: Schematic of wafer level quadrature probing. DAU: Drive Actuation Unit. DMU: Drive Measurement Unit. SMU: Sense Measurement Unit. QCU: Quadrature Compensation Unit.

Where, N_{SMU} is the number of capacitors of SMU, y_q is the displacement on sense axis as a result of quadrature, L is the SMU length.

By taking the ratio between drive signal and quadrature signal, the ratio between drive displacement amplitude and quadrature displacement amplitude can be calculated as:

$$\frac{y_q}{x_d} = \frac{|i_{quad}|}{|i_{drv}|} \cdot \frac{N_{DMU} \cdot d}{N_{SMU} \cdot L} \quad (9)$$

The quadrature displacement amplitude then can be scaled with rate sensitivity for the quadrature level in degree per second (dps). Consider a Coriolis induced displacement,

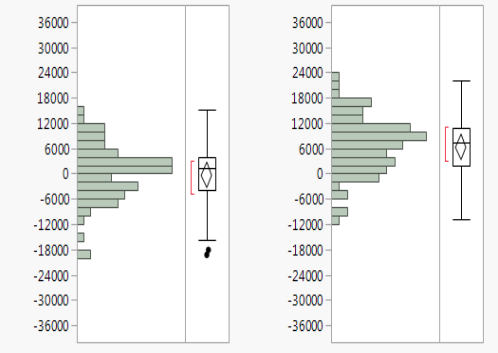

(a) (b)

Figure 7: Quadrature level (in dps) measured from QCU design type A, (a) without no QCU differential voltage; (b) with 1VDC differential voltage

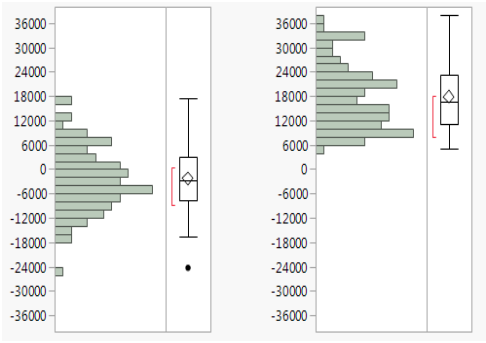

(a) (b)

Figure 8: Quadrature level (in dps) measured from QCU design type B, (a) without no QCU differential voltage; (b) with 1VDC differential voltage

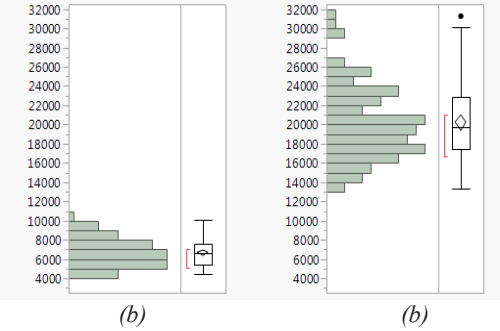

(b) (b)

Figure 9: Quadrature compensation efficiency (dps/V) of (a) QCU design type A ; (b) QCU design type B, demonstrating higher efficiency type B QCU design

$$y_{cor} = \frac{F_{cor} Q_{eff}}{k_y} = \frac{2 m_s \Omega x_d \omega_d Q_{eff}}{m_s {\omega_s}^2} = \frac{2 \Omega x_d \omega_d Q_{eff}}{{\omega_s}^2} \quad (10)$$

Where, m_s is the mass of sense resonator, Ω is the angular rate, Q_{eff} is the effective quality factor considering the frequency spacing between drive and sense mode, ω_s is the angular frequency of sense resonator.

Quadrature signal can be scaled as:

$$\Omega = \frac{|i_{quad}|}{|i_{drv}|} \cdot \frac{N_{DMU} \cdot d}{N_{SMU} \cdot L} \cdot \frac{{\omega_s}^2}{2 \omega_d Q_{eff}} \quad (11)$$

To compare the QCU compensation efficiency, the above procedure was repeated with 1V QCU differential voltage (+1VDC on QCU+, -1VDC on QCU-). The difference of the quadrature level between the two measurement is the QCU efficiency in terms of dps/V. Designs with both types of QCU are evaluated as described above.

Figure 7(a) and figure 8(a) demonstrate the distribution of quadrature level without QCU differential voltage for design type A and design type B, respectively. Their average values are both close to 0dps as expected, and go from -18000dps to +18000dps. Figure 7(b) and figure 8(b) shows the quadrature level with 1V QCU voltage for design type A and design type B. As the figures are showing, design type B is shifting the quadrature level much more than design type A. Figure 9 plots the QCU compensation efficiency of both designs. Type A design has the mean value of 6700 dps/V, with variation from 4000 dps/V to 11000 dps/V. Type B design has the mean value of 20200 dps/V, and varies from 13000 dps/V to 37000 dps/V, due to the process variation of MEMS technology. This demonstrates 3X higher efficiency of type B compared with type A.

Quadrature efficiency is mapped and plotted on wafer scale to see the trend within single wafer. Two type of designs are on two different wafers. In general, QCU efficiency goes from high to low from northeast to southwest of the wafer. Some minor deviation is due to wafer-to-wafer variation.

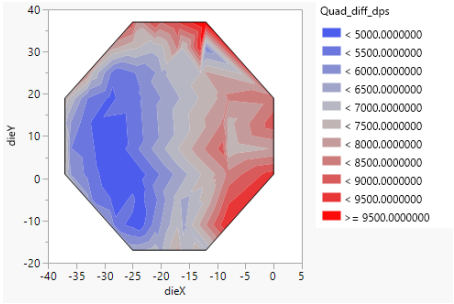

(a)

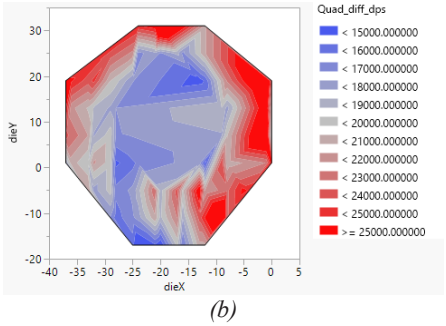

(b)

Figure 10: Wafer map of QCU efficiency. (a) Wafer of type A design; (b) Wafer of type B design

Figure 11:Board-mounted in-frame package for evaluation of QCU differential voltages of engineering samples.

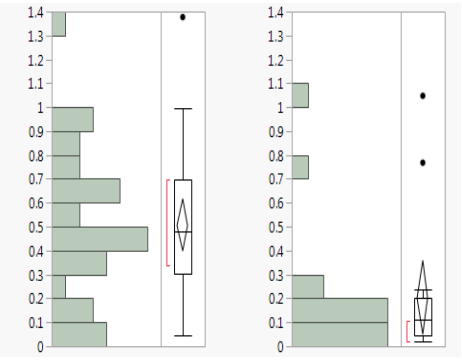

(a) *(b)*

Figure 12: QCU differential voltage to cancel quadrature error (a) QCU design type A; (b) QCU design type B.

Assembled Part Characterization

MEMS dies are built with ASIC dies that can provide QCU voltage with a closed loop control system. The board-mounted in-frame premolded package is shown in figure 11. Quadrature loop is trimmed to extract QCU voltages used to null quadrature error, shown in figure 12(a) and (b) for type A and type B design, respectively. The QCU driver has certain limit on the voltage that can be provided, leaving some type A parts not trimmable (not included in figure 12(a)).

SUMMARY

This paper proposed a novel quadrature compensation electrode design to improve its efficiency, thus power and/or die area can be saved. Analytical calculation predicts 3X increase in efficiency. Both QCU designs are implemented on the same gyroscope test structure. Both wafer level probe and assembled part evaluation demonstrate the increase in efficiency that agrees with the analysis. Table 1 is summarizing the mean value for all the measurement done on both designs.

Table 1. Summary of measured mean value

QCU Design	Quad. @ 0V (dps)	Quad. @ 1V (dps)	QCU Efficiency (dps/V)	QCU voltage (V)
A	-397	6273	6671	0.5
B	-2307	17902	20209	0.2

REFERENCES

[1] C. Acar and A. Shkel, MEMS Vibratory Gyroscopes. 2009.
[2] M. A. Lemkin, W. A. Clark, T. N. Juneau, and A. W. Roessig, "Structure for attenuation or cancellation of quadrature error," US7051590 B1, 30-May-2006.
[3] E. Tatar, S. E. Alper, and T. Akin, "Quadrature-Error Compensation and Corresponding Effects on the Performance of Fully Decoupled MEMS Gyroscopes," J. Microelectromechanical Syst., vol. 21, no. 3, pp. 656–667, Jun. 2012.
[4] M. F. Zaman, A. Sharma, Z. Hao, and F. Ayazi, "A Mode-Matched Silicon-Yaw Tuning-Fork Gyroscope With Subdegree-Per-Hour Allan Deviation Bias Instability," J. Microelectromechanical Syst., vol. 17, no. 6, pp. 1526–1536, Dec. 2008.
[5] P. Shao, "Mems device with capacitance enhancement on quadrature compensation electrode," US20170138734 A1, 18-May-2017.
[6] A. D. Oliver, Y. L. Teo, A. Geisberger, R. F. Steimle, T. Cassagnes, K. Adhikari, D. Sadler, and A. McNeil, "A new three axis low power MEMS gyroscope for consumer and industrial applications," in 2015 Transducers - 2015 18th International Conference on Solid-State Sensors, Actuators and Microsystems (TRANSDUCERS), 2015, pp. 31–34.

CONTACT

*P. Shao, tel: +1-480-814-2958; P.Shao@nxp.com

FACILE FABRICATION OF LOW-COST PASSIVE WIRELESS HUMIDITY SENSOR FOR SMART PACKAGING VIA ALL-LASER PROCESSING OF METALIZED PAPER

Rahim Rahimi[1,2], Jiawei Zhou[1,2], Hongjie Jiang[1,2], Tahereh Soleimani[3], and Babak Ziaie[1,2]*
[1]Purdue University, West Lafayette, Indiana, USA
[2]Birck Nanotechnology Center, West Lafayette, Indiana, USA
[3]Michigan State University, East Lansing, Michigan, USA

ABSTRACT

We have developed a scalable and rapid process for creating a low-cost humidity sensing transponder for wireless monitoring of moisture level within packaged goods. The sensor is composed of a moisture sensitive interdigitated capacitor connected to a planar spiral coil, forming a parallel LC circuit whose resonant frequency is a function of environment humidity. The fabrication process is composed of a series of laser processing steps performed on a commercially available metallized paper which included selective metal etching and welding using a Nd-YAG (1.06µm) laser and cutting the paper substrate by a CO_2 (10.6µm) laser. Selective laser ablation of the 10µm laminated Al film on the paper substrate was found to provide a unique one-step patterning of the conductive film on the paper substrate into the desired electrical patterns while simultaneously creating high surface area Al_2O_3 nanoparticles within the ablated regions. The intrinsic humidity-responsive characteristics of the laser induced metal oxide nanostructures provided a unique humidity sensitivity to the wireless sensor with a 10 folds higher performance than a similar LC resonant sensor that was prepared by conventional photolithography-based processes on a PCB substrate. The frequency change of the sensor was observed to be a linear function of RH (within the range of 0−85%RH), with an average sensitivity of -87 kH/RH and good reversibility and repeatability.

INTRODUCTION

Nearly one third of all food produced in the world for human consumption (~1.3 billion tons), worth US$990 billion, is thrown away each year, due to improper packaging, random food deterioration, and spoilage[1], [2]. Smart packaging technologies with integrated sensors that can monitor the quality of the product and its package play a vital role in reducing food waste by maximizing the shelf life of products and informing consumers with accurate information about the packaged product[3][4]. One of the major causes of food spoilage is the presence of excess moisture in the package of both fresh (i.e. fruits and vegetables) and dried products. Moisture absorbent pads, sheets, and blankets are often used to soak up excess liquid from the fresh foods such as fish, meat, fruits, and vegetables. Dried products (i.e. cereal, oats and wheats) are often packed with protective atmosphere gases such as carbon dioxide (CO_2) and nitrogen (N_2) with the aim of extending the shelf life by minimizing chemical deterioration and possible growth of aerobic spoilage microbes inside the packaged food[5], [6]. While simple standardized expiration dates have been made based on the materials used in the packaging of food products, most of these "expiration dates" are based on cautious estimates and in most cases the food product can be consumed well after these dates[7]. Furthermore, the possibility of food spoilage due to damages in the package, usually is not taken into account [8]. Therefore, an ideal way to ensure the quality and safety of the product is to monitor the moisture content within the sealed package using wireless and remote sensing systems. Due to this importance, different remote humidity sensing concepts with potential usage in food packaging have been explored and reported over the past few years that have explored the use of different active and passive RF wireless humidity sensing [9]–[12]. However, the high cost of manufacturing and assembly has made them uneconomical for widespread commercial use in food industry. To address this need, we have developed a novel method of manufacturing low-cost, wireless, passive humidity sensor based on an inductive-capacitive resonant circuit made by all laser processing of a commercially available wrap pan lining paper (WPLP) used for food cooking purposes that is composed of laminated films of aluminum (Al) foil (~10µm) and hydrophobic parchment paper (~60µm). The presented laser processing technology allows the wireless sensors to be fabricated at an extremely low cost and is appropriate for disposable packaging application where production cost is crucial for the viability of the technology.

SENSOR DESIGN AND WORKING PRINCIPLE

Fig. 1 shows an illustration of the wireless humidity sensing device for in situ monitoring of packaged goods. The sensor, referred to as the LC sensor, consists of an interdigital capacitor (IDC) and a spiral inductor laser ablated onto the 10µm Al film on a commercially available WPLP. The final assembled sensor is modeled as an LC tank resonant circuit. The resonant frequency for this circuit is expressed as

$$f_s = (1/2\pi) \times (L_s C_s)^{-0.5} \quad (1)$$

where L_s is the inductance of the spiral coil, C_s is the total equivalent capacitance of the IDC and built-in stray capacitances induced by the spiral coil. The key humidity sensing element within this circuit is Cs which is strongly dependent on the dimension of its electrodes and the relative permittivity (dielectric constant) of the substrate. The change in RH, alters the effective dielectric constant of the substrate which in turn shifts the sensor's resonant frequency. This change in resonant frequency can wirelessly be interrogated with an external reader.

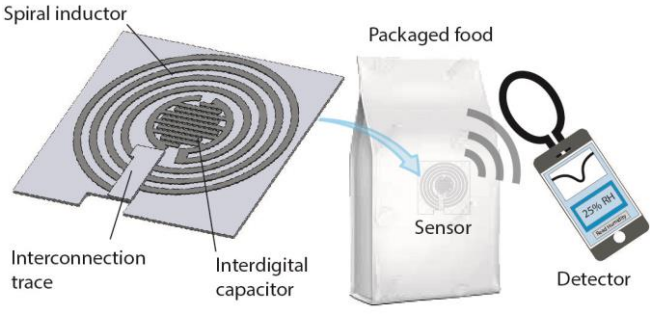

Figure 1: Design concept of a battery-less LC sensor that measures the humidity level inside a sealed package. The sensors resonant frequency can be remotely measured using an external coil connected to an RF reader.

978-1-940470-03-0/HH2018/$25©2018TRF
DOI 10.31438/trf.hh2018.92

DEVICE FABRICATION

Fig. 2a-d illustrate the sequential processes used in the fabrication of the wireless humidity sensor. The fabrication process of the sensor was all performed by a computer-controlled laser engraver system (PLS6MW, Universal Lasers, Inc., Scottsdale, AZ) equipped with two lasers, a CO_2 laser (10.6 µm) and a Nd:YAG fiber laser (1.06 µm). Before the start of fabrication process, the aluminum coating of the paper was wiped with an IPA solution and rinsed with DI water, followed by a nitrogen drying step. The WPLP was attached to a 1mm glass substrate using scotch tape (3M) to provide easy handing while also ensuring that the paper substrate was always within the focal point of the laser throughout the fabrication steps. Next, the IDC and spiral coil were laser ablated onto the surface of the aluminum film using the Nd:YAG pulsed laser with pulse duration and repetition frequency set at 10ns and 30kHz, respectively. The operating power of 18W and scanning speed 1.6m/s were optimized to completely remove the aluminum layer while causing minimum damage to the paper substrate. After completing the selective laser removal, the CO_2 laser with power and speed settings of 10.5W and 1.6m/s was used to cut through the paper substrate to release the sensor and its interconnection trace from the bulk WPLP film. At this point, the indented part of the paper with the dashed laser cut was folded onto the interconnection trace of the sensor. The folded paper prevented the electrical shorting of the coil by providing an insulating barrier between the interconnection trace and underlying traces of the spiral coil. This simple folding mechanism eliminated the need for printing any passivation layers on the sensor. The interconnection part was then laid over the sensor with aligning the connection pads. Next, a temporary 1mm glass slide was placed onto the device to secure the interconnection trace. The electrical connection between the IDC and inductor was completed by laser welding the two connection pads using the Nd:YAG laser set at the power and speed of 18W and 1.6m/s. The low optical absorption of the glass and paper substrate at 1.06µm allows the laser beam to pass through the top glass and paper and only be absorbed by the thin aluminum foils at the center. The laser beam provides a concentrated heat at the interface of the two conductive aluminum films and fuses them together. After the laser welding process, the top glass layer is removed and fabrication process is complete. Fig. 2 e and f show the commercial WPLP film used in this process and also some examples of coils with different number of turns, as well as the final assembled wireless humidity sensor.

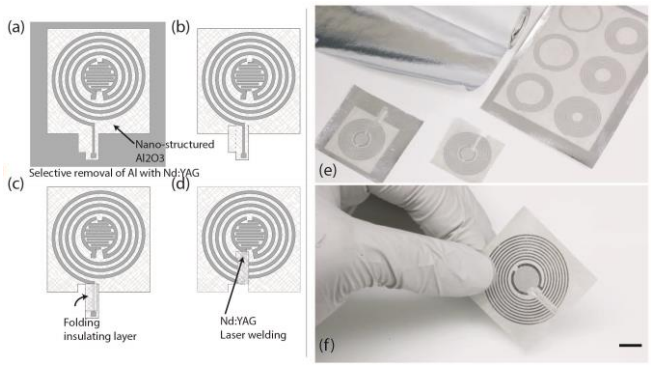

Figure 2: (a-d) Selective removal of Al and generation of nano-structured Al_2O_3 using Nd:YAG laser, cut through the paper substrate using CO_2 laser, folding insulating layer, laser welding to complete the resonant circuit (e, f) photograph of pristine and final wireless humidity sensor. Scale bar: 1cm

RESULT AND DISCUSSION

Optical and SEM images were used to evaluate the surface morphology and the effective removal of the Al layer from the WPLP substrate. Cross-section SEM images of before and after laser ablation show a clear removal of the conductive 10µm Al layer with minimal damage to the 60µm underlying parchment paper substrate, Fig3 a, b. Fig. 3 c shows the SEM image of the laser ablated IDC sensor, composed of an array of 190µm wide Al electrodes with 25µm spacing. Close up SEM images of the laser ablated regions between the Al electrodes, reveal a clear change in the surface morphology with the generation of nanostructured Al_2O_3 particles on the fibrous surface of the paper, Fig. 3d. Static water contact angles on the pristine WPLP and Nd:YAG laser abated surface shows a significant decrease from 89.17° to less than 11° indicating the hydrophilic nature of the laser ablated region of the paper, Fig. 4a, b. High-resolution XPS spectra of the pristine Al surface shows the typical asymmetric Al2p peaks only observed for Al metal with the thin naive oxide layer. However, the Nd:YAG laser ablated samples showed a distinct signature of pure Al_2O_3 with a single symmetric peak within the Al2p region with binding energy of 74.2eV and a full width at half maximum

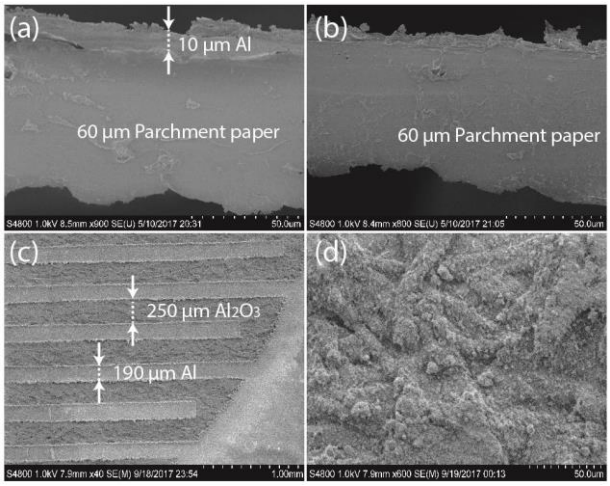

Figure 3: Cross-section SEM image of (a) before and (b) after selective laser removal of Al layer from WPLP (c) SEM image of laser ablated IDC, (d) high magnification of laser induced nano-structured Al_2O_3 on the surface of the paper substrate.

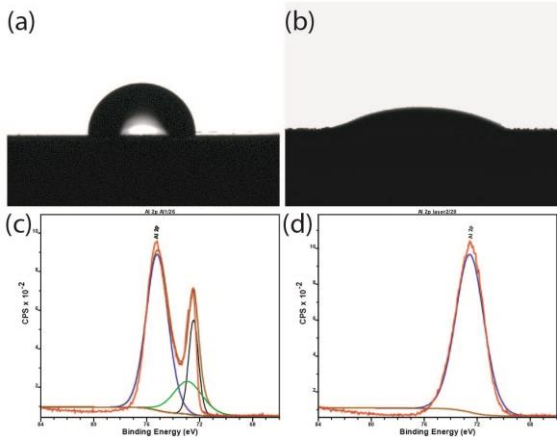

Figure 4: Static water contact angles on (a) pristine Al surface and (b) laser ablated Al surface, high resolution XPS spectra of Al2p of the Al layer (c) before and (d) after laser ablation with Nd:YAG laser

of 1.3eV[13].

Fig. 5a shows a schematic of the setup used for characterizing the wireless humidity sensing performance of the LC sensor. An HP 4195A network/spectrum analyzer (HP/Agilent Technologies Inc., Santa Clara, CA) under standard settings was utilized in connection with an 8 cm-diameter single turn coil made of standard 18 AWG insulated copper wire to serve as the external reader for wireless measurement of resonant frequencies using the phase dip technique. A computer was connected to the impedance analyzer via a GPIB interface and continuous data acquisition was implemented using custom designed Matlab-based program for visualization and data analysis. The sensor response to RH was characterized in a humidity chamber at a constant temperature (21°C) while the relative humidity was changed from 0% to 85%. The humidity level in the chamber was accurately measured with a commercial humidity sensor (Fluke 971). Humidity level within the chamber was controlled by the mixing ratio of dry and humidified N_2 streams. The electrical parameters of the sensors including the inductance of the spiral coil and capacitance of the IDC components were first obtained through direct on-chip probing at 40% RH. The measured capacitance of the IDC sensor was 5.6pF and inductance of the spiral coil was 1.98μH which results is a calculated resonant frequency of 47.9MHz. Fig. 5c shows the measured phase plot taken at a distance of approximately 3mm between the sensor and readout coil before and after completing the circuit at 40% RH. As illustrated, the impedance phase dip decreased from 124MHz to 50.1MHz after connecting the IDC to the inductor. The 4% difference between calculated and experimental results through phase dip measurements can be explained by the errors that was introduced by parasitic capacitance of the electrical connections used in the on-chip probing measurements.

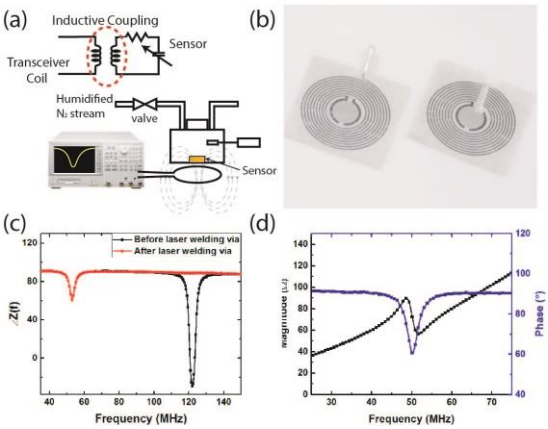

Figure 5: (a) Experimental setup, (b) optical image of LC sensor and (c) impedance phase versus frequency before and after laser welding interconnection, (d) impedance phase and magnitude readings at the terminals of the readout coil coupled with the LC sensor at 40% RH

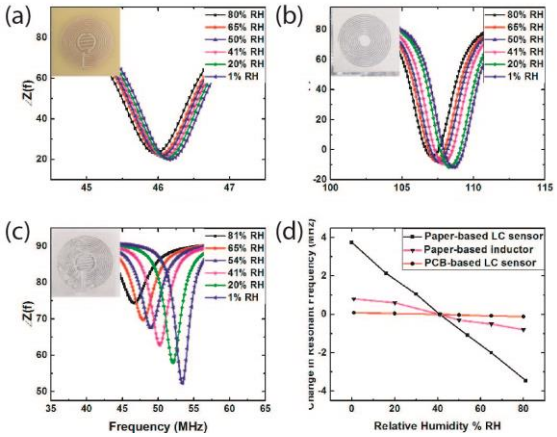

Figure 6: (a-d) Impedance phase vs freq. at different RH for PCB LC resonant sensor, laser etched single inductor and LC resonant.

Fig. 6 shows the frequency sweeps of impedance phase of three different wireless humidity sensors in response to different humidity levels. The three sensors included a PCB-etched LC resonant sensor using standard photolithography-and wet etching processes, and a paper-based LC resonant sensor, and an inductor with 12-turns that were prepared by laser processing. The results show that the increases in RH will shift the phase dip towards lower frequencies in all three sensors. This indicated that the absorption of water vapor to all of the sensors substrates resulted in a decrease in resonant frequency. However, among all three sensors, the paper-based LC resonant sensors showed a greater shift in the location and size of the minimum phase with changes in RH. The decrease in the dip size indicated a decrease in quality factor Q of the sensor due to the capacitive loss within the IDC at higher RH levels.

Fig. 6d plots the changes in resonant frequency of all three sensors as a function of RH. As the plot shows, the PCB etched LC resonant sensor had the lowest sensitivity (-2.6kH/RH) which can be explained by low water vapor absorption sites on the active sensing area on the plastic substrate. However, the laser etched single inductor and LC resonant sensor on the WPLP showed a higher sensitivity to change in RH with the average sensitivity of 19.1 and -87kH/RH, respectively. As expected, the high surface area of the laser induced Al_2O_3 nanoparticles provide considerably higher water vaper adsorption sites which evidently result in greater humidity sensing performance.

Fig. 7 shows the reversible changes in the resonant frequency of the paper-based LC sensor as the relative humidity was varied cyclically between 40%-0% and 40%-85% RH. The sensor showed a high degree of reversible performance at both high and low humidity levels. The response and recovery times under testing cycle from 40% to 0% RH were 51 min and 44 min, respectively. Although, during higher RH cycles from 40% to 85%, the average response and recovery time were shorter, 9.6 min and 14.3 min, respectively. The longer recovery phase from higher to lower RH can be explained by the fact that it takes a longer time for the water vapor to evaporate than to absorb on the Al_2O_3 nanostructure surface.

This phenomenon is prominent and slower in cases were moister is adsorbed in the form of water molecules within the inner walls and inside the Al_2O_3 nanostructure (cycles between 40 to 0% RH). However, at higher humidity level swings (40 to 85% RH), the

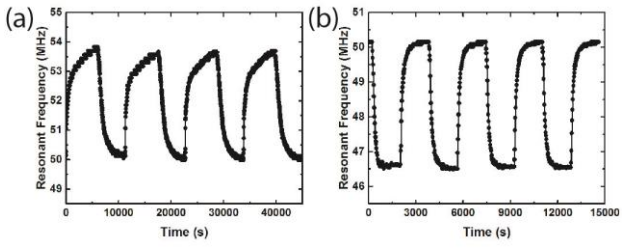

Figure 7: Cyclically varied RH between (e) 0%-40% and (f) 40%-85%.

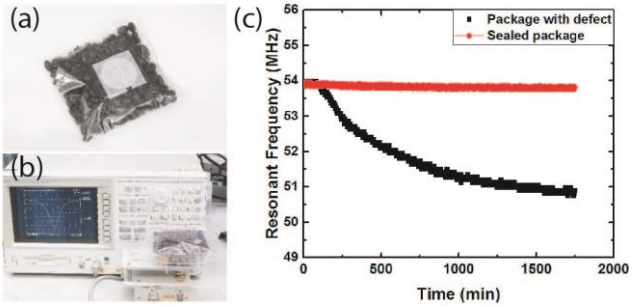

Figure 8: (a) LC sensor placed in coffee bean package (b) readout setup, (c) resonant frequency reading from well-sealed and defected package.

change in dielectric properties of the sensor is influenced by physical absorption of water molecules known as capillary condensation that take places within nanostructure pores of the sensor. Capillary condensation has a much faster attachment and removal from the surface. Therefore, the overall response and recovery time of the sensor is shorter at higher moister levels. Finally, as a proof of concept, the sensor was placed inside packaged roasted coffee beans that was filled with nitrogen gas, Fig. 8. As shown in Fig. 8c, the resonant frequency of the sensor in the well-sealed packaging remained stable at 53.8 MHz. After perforating the package with a sharp needle, the resonant frequency slowly decreased to 50.1MHz due to water vapor adsorption into the package.

CONCLUSIONS

We have developed an inexpensive and scalable fabrication technique for manufacturing a wireless paper-based humidity sensor for monitoring food packaging quality. The sensor was made of a planar inductor-capacitor resonant circuit with a resonant frequency that is dependent on the environment moisture. The sensor's resonant frequency was wirelessly interrogated through an inductive coupling link with an external reader. The sensor was made by an all laser processing of a commercial WPLP with a 10μm laminated Al foil. In this study, we established the ability to selectively remove the conductive Al layer while concurrently generate high-surface area Al_2O_3 nanostructures within the ablated regions using Nd:YAG laser radiation under ambient conditions. The intrinsic humidity-responsive properties of laser induced Al_2O_3 nanostructures provided a unique and relatively high sensitivity to the laser etched LC sensors as compared to wet etched PCB-based LC sensor with similar design and dimensions. This work might inspire both industrial and scientific communities to reexamine the potential use of the presented laser processing approach in scalable production of future low-cost energy storage and bio-sensing devices.

REFERENCES

[1] M. F. Bellemare, M. Çakir, H. H. Peterson, L. Novak, and J. Rudi, "On the Measurement of Food Waste," *Am. J. Agric. Econ.*, vol. 99, no. 5, pp. 1148–1158, Oct. 2017.

[2] K. L. Thyberg and D. J. Tonjes, "Drivers of food waste and their implications for sustainable policy development," *Resour. Conserv. Recycl.*, vol. 106, pp. 110–123, Jan. 2016.

[3] K. B. Biji, C. N. Ravishankar, C. O. Mohan, and T. K. Srinivasa Gopal, "Smart packaging systems for food applications: a review," *J. Food Sci. Technol.*, vol. 52, no. 10, pp. 6125–6135, Oct. 2015.

[4] J. P. Kerry, M. N. O'Grady, and S. A. Hogan, "Past, current and potential utilisation of active and intelligent packaging systems for meat and muscle-based products: A review," *Meat Sci.*, vol. 74, no. 1, pp. 113–130, Sep. 2006.

[5] A. R. Davies, "Advances in modified-atmosphere packaging," in *New Methods of Food Preservation*, Boston, MA: Springer US, 1995, pp. 304–320.

[6] I. S. Arvanitoyannis and A. C. Stratakos, "Application of Modified Atmosphere Packaging and Active/Smart Technologies to Red Meat and Poultry: A Review," *Food Bioprocess Technol.*, vol. 5, no. 5, pp. 1423–1446, Jul. 2012.

[7] A. Giménez, F. Ares, and G. Ares, "Sensory shelf-life estimation: A review of current methodological approaches," *Food Res. Int.*, vol. 49, no. 1, pp. 311–325, Nov. 2012.

[8] M. G. Corradini, "Shelf Life of Food Products: From Open Labeling to Real-Time Measurements," *Annu. Rev. Food Sci. Technol.*, vol. 9, no. 1, pp. 251–269, Mar. 2018.

[9] R. A. Potyrailo, N. Nagraj, Z. Tang, F. J. Mondello, C. Surman, and W. Morris, "Battery-free Radio Frequency Identification (RFID) Sensors for Food Quality and Safety," *J. Agric. Food Chem.*, vol. 60, no. 35, pp. 8535–8543, Sep. 2012.

[10] T. J. Harpster, S. Hauvespre, M. R. Dokmeci, and K. Najafi, "A passive humidity monitoring system for in situ remote wireless testing of micropackages," *J. Microelectromechanical Syst.*, vol. 11, no. 1, pp. 61–67, 2002.

[11] a. D. DeHennis and K. D. Wise, "A wireless microsystem for the remote sensing of pressure, temperature, and relative humidity," *J. Microelectromechanical Syst.*, vol. 14, no. 1, pp. 12–22, 2005.

[12] A. V. Quintero, F. Molina-Lopez, E. C. P. Smits, E. Danesh, J. van den Brand, K. Persaud, A. Oprea, N. Barsan, U. Weimar, N. F. de Rooij, and D. Briand, "Smart RFID label with a printed multisensor platform for environmental monitoring," *Flex. Print. Electron.*, vol. 1, no. 2, p. 025003, 2016.

[13] T. Song, Q. Liu, J. Liu, W. Yang, R. Chen, X. Jing, K. Takahashi, and J. Wang, "Fabrication of super slippery sheet-layered and porous anodic aluminium oxide surfaces and its anticorrosion property," *Appl. Surf. Sci.*, vol. 355, pp. 495–501, Nov. 2015.

CONTACT

*B. Ziaie, bziaie@purdue.edu

NANOSCALE TUNING FORK CAVITY OPTOMECHANICAL TRANSDUCERS WITH DESIGN-ENABLED FREQUENCY TUNING AND TEMPERATURE COMPENSATION

Rui Zhang[1], Robert Ilic[2], Yuxiang Liu[1], and Vladimir Aksyuk[2]
[1]Department of Mechanical Engineering, Worcester Polytechnic Institute, USA
[2]Center for Nanoscale Science and Technology, National Institute of Standards and Technology, USA

ABSTRACT

In this work, we design, fabricate and characterize monolithic, nanoscale Si_3N_4 tuning fork cavity optomechanical transducers with design enabled tuning of mechanical resonant frequencies and passive temperature compensation. Both frequency tuning and temperature compensation are achieved by the design of a nonlinear mechanical clamp. The compensation reduces the temperature sensitivity of frequency by ≈ 60 times, achieving fractional frequency sensitivity of $(3.2 \pm 0.4)\cdot 10^{-6}$ K^{-1}. The design simultaneously increases the stress in the tuning fork by more than a factor of two relative to the residual stress, and makes the resulting high resonator frequency insensitive to the residual stress and temperature variations. These stable resonators may find uses for stable transduction of force and motion in MEMS devices via frequency readout.

INTRODUCTION

Many mechanical sensors, such as high performance inertial sensors, demand integrated mechanical motion detection with low noise, high bias stability, large dynamic ranges, and high bandwidths. Monitoring the resonant frequency change of a high-quality mechanical resonator is a widely accepted approach for motion detection. This approach is immune to low-frequency electronic noise and bias drift, and both a high mechanical frequency (f_m) and a high mechanical quality factor (Q_m) are preferred since high f_m can provide high transduction bandwidth/temporal resolution and the force sensitivity scales as $1/(f_m^{0.5}Q_m^{0.5})$ [1]. Nanomechanical resonators made of high intrinsic tensile stress silicon nitride (Si_3N_4) have shown great potential for such sensing applications [2] because of their high mechanical quality factors, high frequencies, and facile fabrication. Recently developed nanoscale Si_3N_4 tuning fork resonators [3] achieve very large frequency-quality factor (f_mQ_m) products ($Q_m \approx 2.2\times10^5$ at $f_m \approx$ 29 MHz) through a design-enabled stress tuning approach, and open unprecedented opportunities for on-chip motion metrology and sensing. However, the frequency of such tuning forks is determined by both designed geometry and the intrinsic stress (σ_0), and σ_0 varies with different fabrication processes [4]. In addition, the performance of the tuning fork mechanical resonator can be influenced by ambient environmental factors, especially the temperature [5]. For example, temperature fluctuations can influence the tensile stress in a doubly-clamped Si_3N_4 tuning fork, due to the difference of coefficient of thermal expansion (CTE) between the Si_3N_4 device layer and the Si substrate. Thermal stress fluctuations in tum influence the thermal stability of the resonant frequency [6]. The majority of approaches made to compensate temperature-induced frequency variation rely on matching different materials [7] or active temperature control [8].

Here we design, fabricate, and characterize a monolithic nonlinear mechanical clamp for single-layer Si_3N_4 tuning fork nanomechanical resonators that renders the natural frequencies insensitive to temperature fluctuations by a passive, design-enabled compensation method. In addition, by introducing a reference length

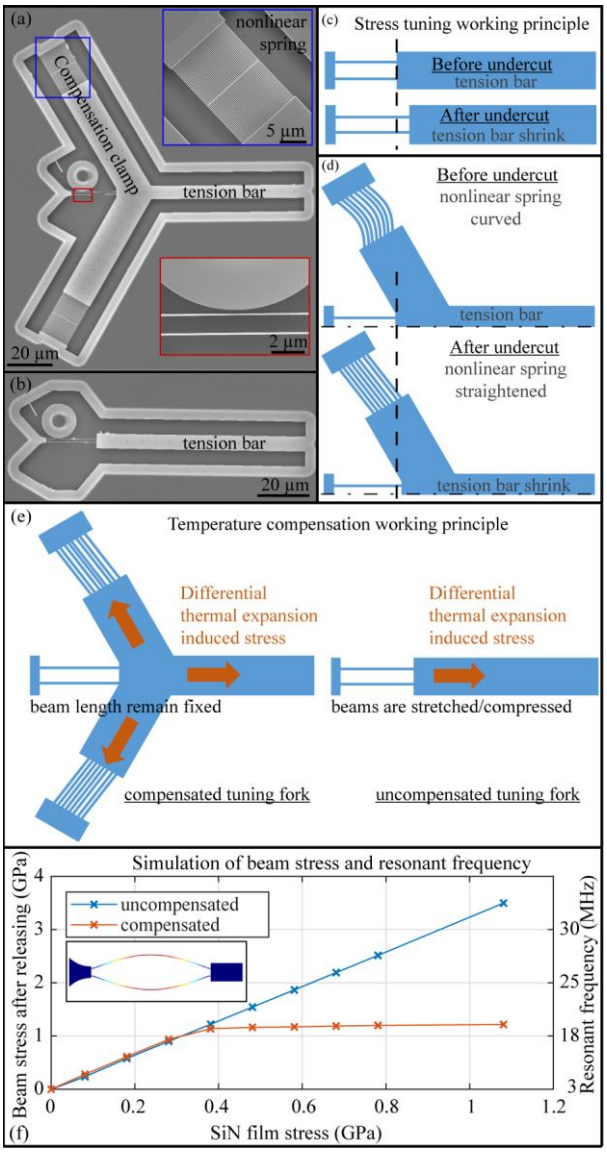

Figure 1: (a) SEM of a tuning fork with temperature compensation and integrated photonic readout. (Top inset) Zoom-in of straightened nonlinear springs. (Bottom inset) Coupling region between tuning fork beam and microdisk optical resonator. (b) SEM of tuning fork without temperature compensation. (c) Working principle of stress tuning in uncompensated tuning fork. (d) Working principle of stress tuning in compensated tuning fork. (e) Working principle of temperature compensation. (f) Simulation of beam stress and device frequency with different Si_3N_4 film stress. The inset shows the simulated tuning fork in-plane squeezing mode shape with exaggerated deformation.

978-1-940470-03-0/HH2018/$25©2018TRF
DOI 10.31438/trf.hh2018.93

scale via the device layout, this clamp design can achieve the same designed resonator strain and resonant frequency over a wide range of intrinsic stress values and enables geometry-determined on-chip stress tuning capability. Different temperature compensation strengths including under-compensation, proper compensation, and over-compensation can be achieved by varying the design and are demonstrated in the experiments. The device with the best temperature compensation has a temperature sensitivity of -54 Hz/K ± 6 Hz/K with $f_m \approx 16.5$ MHz. The tuning fork without temperature compensation has a temperature sensitivity of 5360 Hz/K ± 170 Hz/K with $f_m \approx 27.76$ MHz. All reported statistical uncertainties are 95 % confidence ranges unless noted otherwise. The nonlinear mechanical clamp can be adapted for a wide range of doubly-clamped nanomechanical resonators to reduce temperature sensitivity.

Scanning electron microscopy (SEM) images of temperature compensated and uncompensated tuning forks are shown in Figures 1(a) and (b), respectively. The uncompensated tuning fork consists of two parallel cantilever beams, and is doubly clamped with a long tension bar on the right. By comparison, the compensated tuning fork has two additional inclined clamps, resulting in a Y-shaped clamp at the right end of the tuning fork. Each of the inclined clamps is attached to the supporting structure by an array of nonlinear springs. All the devices are fabricated in a 250 nm thick stoichiometric Si_3N_4 layer, which is grown by low-pressure chemical vapor deposition (LPCVD) on a 3 μm thick silicon dioxide (SiO_2) layer on a silicon substrate. We first used electron-beam (E-beam) lithography to define the geometry in a layer of positive tone E-beam resist. The pattern was then transferred to the Si_3N_4 film by a $CHF_3/Ar/O_2$ inductively-coupled plasma reactive ion etch (ICP RIE). Device fabrication is finished by a buffered oxide etch (BOE) undercut, which selectively removes the SiO_2 to release the device with minimal etching of Si_3N_4.

The nominal length and width of the tuning fork beams are 20 μm and 150 nm, respectively, in all the fabricated devices. The tension bar on the right-hand side of the tuning fork is 80 μm long. In the uncompensated device, the tension bar shrinks after device release due to the redistribution of the initially uniform Si_3N_4 stress, such that the stress in the tuning fork beam increases, as shown in Figure 1(c). Because the length of the tension bar determines the final stress in the tuning fork after undercut, one can tune the fork mechanical frequency simply by the design of the tension bar. This design-enabled tuning has been demonstrated in our previous work to achieve an up-to-three-fold stress increase, compared with the intrinsic Si_3N_4 film stress, and 1.5 times increase in the fork fundamental frequency compared with the fork without the tension bar [3].

In the temperature-compensated device (shown in Figure 1(a)), the Y-shaped clamp includes two symmetric inclined clamps and a tension bar. Each of the two symmetric, inclined compensation clamps has an array of nonlinear springs close to one end. The springs are curved before undercut with the shape defined by one period of a cosine function (0.48 μm) × cos(x/(20 μm) × 2π), where 0.48 μm is the modulation of the cosine geometry and x is the position in micrometers along the longitudinal direction. The symmetric inclined clamps and the curved springs allow the tuning fork beam stress to be insensitive to the intrinsic Si_3N_4 stress, while retaining the stress tuning capability, as described below. During the release process (Figure 1(d)), the tension bar first shrinks, as in the uncompensated device, stretching the tuning forks and straightening the curved springs in the inclined clamps. As a result, the tuning fork beam stress and frequency are tuned by the tension bar design, until the curved springs are fully straightened. If the intrinsic Si_3N_4 film stress is large enough to fully straighten the nonlinear springs, the stiffness of the straight nonlinear springs increases significantly compared with that of curved springs. This is because the spring deformations change from curved beam bending to straight beam stretching. The inclined clamps then provide an effective balancing force in the opposite direction of the stretching force produced by the tension bar. As a result, the right-hand end-point of the tuning fork beams is fixed and hence the tuning fork beam stress as well as mechanical frequency become insensitive to the intrinsic Si_3N_4 film stress.

The stress insensitivity of the frequency enabled by the clamp design is verified by a proof-of-concept Finite-Element-Method (FEM) simulation. The simulated final beam stress and mechanical frequency at different Si_3N_4 intrinsic stress are shown in Figure 1(f). In the uncompensated device, the beam stress is linearly proportional to the intrinsic stress. In the compensated device, the beam stress in the tuning fork increases similarly for small intrinsic stress, before the nonlinear springs are fully straightened. However, the beam stress is almost constant for the intrinsic stress above a threshold value at which the nonlinear springs become straight and stiff. The final beam stress in the compensated device is determined by the clamp geometry (the threshold displacement required to straighten the nonlinear spring) and is insensitive to the exact value of the Si_3N_4 intrinsic film stress.

The inclined clamps also enable the tuning fork frequency to be insensitive to temperature changes. The working principle of temperature compensation is shown in Figure 1(e). When the temperature changes, the differential thermal expansion due to CTE mismatch between the Si_3N_4 device layer and the silicon substrate results in thermal stress in the uncompensated devices. Specifically, the Si substrate expands more than the Si_3N_4 device layer when the temperature increases, increasing the beam stress and in turn the resonant frequency of the tuning fork. However, in the compensated devices, the temperature-induced stress from the tension bar is balanced by that from the inclined clamps. Thus, the tuning fork beam anchor remains fixed regardless of temperature variation, providing a temperature independent mechanical frequency. The compensation strength can also be tuned by the clamp geometry. For example, the temperature induced force from the compensation clamps can be tuned by the width of the nonlinear springs. The temperature induced force from the tension bar can be tuned by the width of the tension bar. As a result, small, proper, and large ratios of nonlinear-spring to tension-bar width can produce under-compensated, properly compensated, and over-compensated tuning forks, respectively. FEM simulation shows that a device with a 3.2 μm wide tension bar and 200 nm wide nonlinear springs can have almost zero temperature sensitivity. Thus, to investigate the influence of the width ratio between the nonlinear spring and the tension bar on the compensation strength, we fabricated devices with the nominal tension bar width varying from 2.8 μm to 3.7 μm and nonlinear spring widths varied from 194 nm to 211 nm.

The mechanical frequencies of the tuning forks are measured through a near-field cavity-optomechanical readout [9]. Each tuning fork is near-field coupled across an ≈ 150 nm gap to a Si_3N_4 microdisk optical cavity. The disk has a nominal diameter of 14 μm and supports whispering-gallery (WGM) optical modes. When the light wavelength is tuned to the shoulder of a microdisk optical resonance, the tuning fork beam motion can modulate the optical resonance and hence change the transmitted light intensity. Then the output light signal can be transduced into electric signal by a photodetector for post processing. The optomechanical coupling parameter $g_{om}/2\pi$ between the tuning fork in-plane squeezing mechanical mode and the microdisk WGM optical mode is calculated to be ≈ 140 MHz/nm, which indicates the optical resonance frequency shift per unit modal displacement of the

mechanical resonator. This near-field optical readout yields ≈ 1 fm/Hz$^{0.5}$ displacement resolution [9] and enables a monolithic, robust, and fiber-pigtailed sensor technology [10].

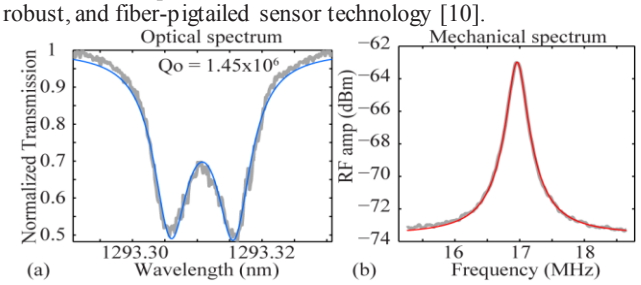

Figure 2. Experimentally measured (a) optical spectrum (b) mechanical spectrum. Colored lines are theory fits.

To measure the mechanical frequencies, light was emitted from a 1300 nm wavelength band tunable laser and evanescently coupled to the optical microdisk resonator through a fiber taper helix probe [11]. The transmitted light intensity was measured by a photo detector (PD), with the output split into two channels. One channel connected to a data acquisition (DAQ) board for swept-wavelength spectroscopy of the optical cavity modes (Figure 2(a)). The other channel connected to an Electrical Spectrum Analyzer (ESA) to measure the mechanical frequency (Figure 2(b)). Since the optomechanical transduction noise is well below the random motion of the tuning fork driven by thermomechanical noise [12], the mechanical frequencies were measured from the thermal motion spectra of the tuning forks without external excitation. The temperature was stably controlled within ± 0.1 K by a ceramic heater with a proportional–integral–derivative (PID) controller. The device was enclosed inside an acrylic chamber, with desiccant boxes placed in the chamber and constant desiccated air flowing through the chamber, to minimize the influence from moisture on the devices. At room temperature the frequencies of the first-order squeezing mode were ≈ 27.7 MHz and ≈ 16.5 MHz for the uncompensated and compensated tuning forks, respectively.

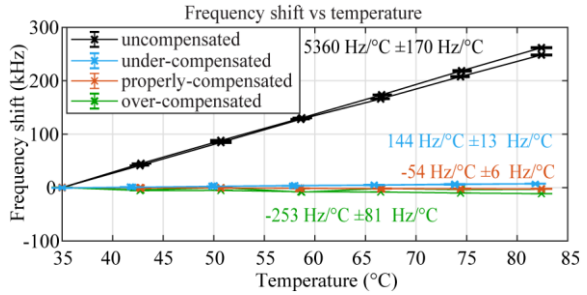

Figure 3. Experimentally measured temperature induced frequency shift. The frequency uncertainties are determined by nonlinear least squares fits to the data. The uncertainties for the temperature sensitivity are determined by the linear least squares fits.

To verify the temperature compensation effect, the mechanical frequency shifts of different devices over the temperature range from 35 °C to 82 °C were measured and shown in Figure 3. The resonant frequency of uncompensated device increased linearly with temperature at the rate of ≈ 5360 Hz/K ±170 Hz/K. For a beam vibration dominated by the tensile stress, the fundamental mode resonant frequency f_m as a function of temperature T can be described as [6]

$$f_m(T) = \frac{1}{2L}\sqrt{\frac{\sigma - AE(\alpha_{beam}-\alpha_{sub})(T-T_0)}{\rho}} \quad (1)$$

where L is the beam length, σ is the tensile stress along the beam at reference temperature, ρ is the density of the beam, E is the Young's modulus of the beam material, α_{beam} and α_{sub} are the CTE of the beam and substrate, respectively, and T_0 is the reference temperature. For the tuning fork with a tension bar, the stress is amplified by an amplification ratio $A = \sigma/\sigma_0$, and the stress variation due to temperature is similarly amplified. As a result, for the tuning fork with stress tuning, equation (1) is modified,

$$f_m(T) = \frac{1}{2L}\sqrt{\frac{\sigma - AE(\alpha_{beam}-\alpha_{sub})(T-T_0)}{\rho}} \quad (2)$$

in which σ is the amplified beam stress. Since the CTE of the Si substrate (≈ 2.6·10^{-6} K^{-1}) is larger than that of Si_3N_4 device layer (≈ 1.6·10^{-6} K^{-1}), the f_m increases as temperature increases. In addition, because $\sigma \approx 1.81$ GPa (calculated by FEM) is much larger than $E(\alpha_{beam}-\alpha_{sub})T_0$, the higher order terms of $f_m(T)$ can be neglected. Thus, f_m is approximately linearly-proportional to T which agrees with the experiment result. The temperature sensitivity can be then calculated as

$$S = \left.\frac{\partial f_m}{\partial T}\right|_{T=T_0} = -\frac{AE(\alpha_{beam}-\alpha_{sub})}{4L\sqrt{\rho\sigma}} \quad (3)$$

By using FEM-calculated values of $A \approx 3.12$, $E \approx 310$ GPa and $\rho \approx 3000$ kg/m^3 for the Si_3N_4 film, the temperature sensitivity is calculated to be ≈ 5200 Hz/K, which also matches the experiment.

For compensated devices, the resonant frequencies are also linearly-proportional to the temperature change but with much lower temperature sensitivity. This indicates that the nonlinear springs are fully deployed and the differential thermal strain is compensated by the nonlinear clamp design. The two inclined compensation clamps pull the center of the Y shaped structure in the direction opposite to that of the tension bar, balancing out the thermal stress induced motion. In addition, the strength of the compensation achieved by the Y-shaped clamp can be engineered by changing the width ratio between nonlinear springs and tension bar. With a proper width ratio, the temperature-induced movement of the center of Y-shaped clamp is such that the tuning fork does not experience a change in stress, which results in a perfect temperature compensation in the tuning fork. The thermal stress in the tension bar is dominant if the width ratio is too small, resulting in under-compensation, while a too large width ratio results in over-compensation.

As shown in Figure 3, three temperature compensation strengths are experimentally demonstrated using different nonlinear spring to tension-bar width ratios. Specifically, a device with nominally 177 nm wide nonlinear springs and a 3.14 µm wide tension bar (width ratio 0.056) has a temperature sensitivity of 144 Hz/K ± 13 Hz/K, indicating this device is under-compensated. A device with -253 Hz/K ± 81 Hz/K temperature sensitivity (over-compensated) has 230 nm wide nonlinear springs and a 3 µm wide tension bar (width ratio 0.077). The minimum temperature sensitivity -54 Hz/K ± 6 Hz/K (fractional frequency sensitivity of (3.2 ± 0.4)·10^{-6} K^{-1}) is measured from device with a 183 nm wide spring and a 2.96 µm wide tension bar (width ratio 0.062). Comparing to the uncompensated tuning fork which has 5360 Hz/K ± 170 Hz/K (fractional sensitivity (193 ± 6)·10^{-6} K^{-1}), the temperature sensitivity is reduced by a factor of ≈ 60 using the temperature compensation design. Temperature sensitivity uncertainties are determined from the linear fits.

Although our devices have not yet been tested directly as mechanical motion sensors, the displacement sensitivity of the resonance frequency is numerically and analytically estimated to be ≈ 51 kHz/nm for the uncompensated fork and ≈ 74 kHz/nm for the compensated fork based on the device dimension and resonant frequency measured in the experiments. These results confirm that the additional inclined clamps help to reduce the temperature induced frequency variability and the tuning fork transducer can be potentially used for force and displacement sensing with better stability.

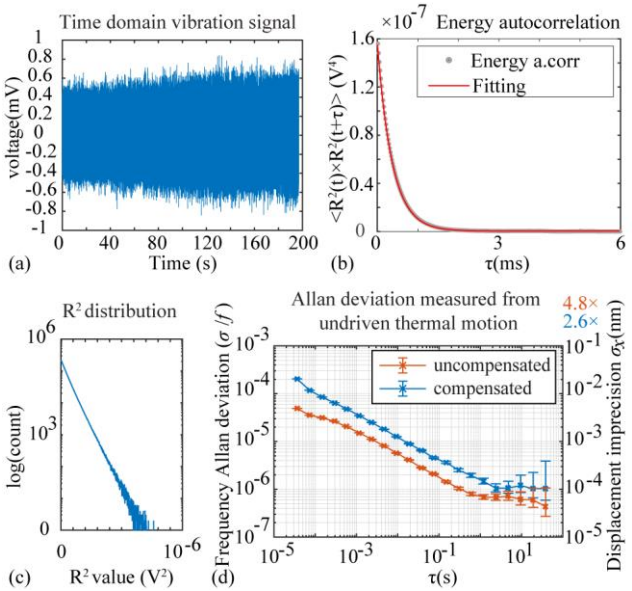

Figure 4. (a). Tuning fork time domain vibration signal. (b). Energy autocorrelation calculated from time domain signal. (c). R^2 distribution in log scale. (d). Experimentally measured frequency Allan deviation for compensated and uncompensated tuning forks, without excitation. Right-hand-side axis shows the corresponding calculated Allan deviation for a displacement sensing application with scale multipliers 4.8× (uncompensated) and 2.6× (compensated) due to different displacement sensitivity. The uncertainties for Allan deviation are determined by Chi distribution.

To further investigate the frequency stability of the tuning fork resonators, the time-domain vibration signal (quadrature, IQ, components at resonance) of the tuning fork thermal motion was also measured in vacuum using a lock-in amplifier. The I component of the uncompensated tuning fork time domain vibration signal is shown in Figure 4(a). Figure 4(b) shows the auto-correlation of its potential energy $Sa(\tau)=\langle R^2(t) \times R^2(t+\tau)\rangle$ where R is the signal amplitude. The calculated energy relaxation time $T_1 \approx 10^{-4}$ s indicates a sensor bandwidth exceeding 1 kHz. Figure 4(c) shows the distribution of R^2, which is a straight line in log scale indicating that, as expected, the energy obeys the Maxwell–Boltzmann distribution ($\propto \exp(-\alpha R^2/(2k_BT))$), where k_B is the Boltzmann constant and α is a constant. This indicates the linearity of the readout and of the system itself being mechanically linear and in thermodynamic equilibrium. From the time domain data, the frequency was measured as a function of time and the Allan deviation calculated, shown in Figure 4(d). The Allan deviation slope measured for the uncompensated tuning fork with 28 MHz mechanical frequency is $\approx 10^{-6}\,\mathrm{Hz}^{-0.5}$ below 1 s averaging, which is thermodynamically limited [12]. The relative bias stability is $\approx 10^{-6}$ above 1 s averaging. The Allan deviation measured from the compensated device is similar to that for the uncompensated one, indicating that the temperature compensation is achieved without increasing noise from other noise sources [12].

In conclusion, we have developed Si_3N_4 tuning fork cavity optomechanical transducers with nonlinear temperature compensation clamps. The clamp design allows the tuning fork mechanical frequency to be determined only by the geometry, regardless of the Si_3N_4 intrinsic film stress. Control and reduction of temperature sensitivity was experimentally demonstrated by tuning the design geometry. Temperature sensitivity ranges from -253 Hz/K ± 81 Hz/K (over-compensation) to 144 Hz/K ± 13 Hz/K (under-compensation) are achieved. The minimum temperature sensitivity is -54 Hz/K ± 6 Hz/K while that of an uncompensated tuning fork is 5360 Hz/K ± 170 Hz/K. The slope of measured thermodynamically-limited Allan deviation is $\approx 10^{-6}\,\mathrm{Hz}^{-0.5}$ below 1 s averaging and the relative bias stability is $\approx 10^{-6}$ above 1 s averaging. The temperature-compensated resonant transducer presented here demonstrates a promising new high-precision, low-drift displacement measurement approach that can enable a variety of precision MEMS sensor applications.

REFERENCES

[1] K. Y. Yasumura, T. D. Stowe, E. M. Chow, T. Pfafman, T. W. Kenny, B. C. Stipe, et al., "Quality factors in micron-and submicron-thick cantilevers," Microelectromechanical Systems, Journal of, vol. 9, pp. 117-125, 2000.

[2] A. Suhel, B. D. Hauer, T. S. Biswas, K. S. D. Beach, and J. P. Davis, "Dissipation mechanisms in thermomechanically driven silicon nitride nanostrings," Applied Physics Letters, vol. 100, p. 173111, 2012.

[3] R. Zhang, C. Ti, M. I. Davanço, Y. Ren, V. Aksyuk, Y. Liu, et al., "Integrated tuning fork nanocavity optomechanical transducers with high f_MQ_M product and stress-engineered frequency tuning," Applied Physics Letters, vol. 107, p. 131110, 2015.

[4] P. Temple-Boyer, C. Rossi, E. Saint-Etienne, and E. Scheid, "Residual stress in low pressure chemical vapor deposition SiNx films deposited from silane and ammonia," Journal of Vacuum Science & Technology A: Vacuum, Surfaces, and Films, vol. 16, pp. 2003-2007, 1998.

[5] T. Kose, K. Azgin, and T. Akin, "Design and fabrication of a high performance resonant MEMS temperature sensor," Journal of Micromechanics and Microengineering, vol. 26, p. 045012, 2016.

[6] T. Larsen, S. Schmid, L. Grönberg, A. Niskanen, J. Hassel, S. Dohn, et al., "Ultrasensitive string-based temperature sensors," Applied Physics Letters, vol. 98, p. 121901, 2011.

[7] D. R. Myers, R. G. Azevedo, L. Chen, M. Mehregany, and A. P. Pisano, "Passive Substrate Temperature Compensation of Doubly Anchored Double-Ended Tuning Forks," Journal of Microelectromechanical Systems, vol. 21, pp. 1321-1328, 2012.

[8] J. C. Salvia, R. Melamud, S. A. Chandorkar, S. F. Lord, and T. W. Kenny, "Real-Time Temperature Compensation of MEMS Oscillators Using an Integrated Micro-Oven and a Phase-Locked Loop," Journal of Microelectromechanical Systems, vol. 19, pp. 192-201, 2010.

[9] Y. Liu, H. Miao, V. Aksyuk, and K. Srinivasan, "Wide cantilever stiffness range cavity optomechanical sensors for atomic force microscopy," Optics express, vol. 20, pp. 18268-18280, 2012.

[10] J. Chae, S. An, G. Ramer, V. Stavila, G. Holland, Y. Yoon, et al., "Nanophotonic Atomic Force Microscope Transducers Enable Chemical Composition and Thermal Conductivity Measurements at the Nanoscale," Nano Letters, vol. 17, pp. 5587-5594, 2017/09/13 2017.

[11] Y. Ren, R. Zhang, C. Ti, and Y. Liu, "Tapered optical fiber loops and helices for integrated photonic device characterization and microfluidic roller coasters," Optica, vol. 3, pp. 1205-1208, 2016.

[12] M. Sansa, E. Sage, E. C. Bullard, M. Gély, T. Alava, E. Colinet, et al., "Frequency fluctuations in silicon nanoresonators," Nature Nanotechnology, vol. 11, p. 552, 02/29/online 2016.

CONTACT

*V. Aksyuk, tel: +1-301-975-2867; vladimir.aksyuk@nist.gov

SMARTPHONE BASED FOCUS-FREE MACROSCOPY USING AN ADAPTIVE DROPLET LENS

Hanyang Huang, and Yi Zhao[*]
The Ohio State University, Columbus, Ohio, USA

ABSTRACT

Smartphones have been extensively used for macroscopic imaging by both professional and amateur photographers. Current macroscopic lenses for smartphones often have a fixed focusing power and a narrow depth of field. One has to move the smartphone to keep the image in focus. This is challenging for imaging small and moving objects. This paper reports a smartphone based macroscope that allows for focusing-free image acquisition. A tunable droplet lens is placed in front of the smartphone camera and driven dynamically by a dielectric elastomer actuator to scan the entire field. The desired object planes can be extracted by after-the-fact "focusing". The adaptive focusing capability of the device thus enables macroscopic imaging in an easier and faster way.

INTRODUCTION

Optical macroscopy has been widely used for various applications including healthcare, agriculture, education, and biomedical fields [1-4]. Current macroscopes are often laboratory-based and have high cost and bulky volume, which considerably limit their applications in low-resource settings. During the last few years, smartphone technology has been rapidly growing. The built-in illumination, high-resolution cameras and display, advanced smartphone apps and high-speed networks of modern smartphones strongly promotes the next generation of miniature, portable, and cost-effective macroscopy. The smartphone-based macroscopy thus expects extensive applications in photography, machine vision, and other imaging applications in the field.

The methodologies that are used in the pioneer studies of smartphone-based macroscopic/microscopic imaging can be divided into two categories [5-8]: lens-free technologies and add-on lens(es). The lens-free imaging devices utilize the holographic imaging principle and reconstruct images from the captured fringe patterns. This approach often requires the removal of the camera lens [9, 10]. The add-on lenses approach is implemented by attaching one or multiple solid refractive optical components to the camera [1, 11, 12]. These solid optical components often have a fixed optical power and a small depth of field. The operator has to change the distance between the smartphone and the object to keep the image in focus. Such operation is challenging for imaging small and moving objects. Although it is possible to adjust the focus by displacing one or more lens components along the optical axis, the operation associates with increased system/operation complexity and requires larger overall device size. The miniaturization advantage of smartphone devices is largely compromised.

Tunable lenses with adjustable focusing capability make it possible to achieve miniature varifocal imaging without any moving any optical components [13-19]. Among various actuation mechanisms, dielectric elastomer actuator (DEA) is attracting considerable interests due to its simple configuration, fast response and low cost [20-22].

In this study, we report a smartphone based macroscope using a tunable droplet lens. The droplet lens is driven by a DEA and has a large focusing power range and fast response. This allows the device to scan a large depth of field within a short time. The driven voltage is reduced using a high voltage converter. By working in conjunction with the video mode of the smartphone camera, the fast scanning of an extended depth of field was implemented. The desired object planes of the objects of interest can be extracted from the video using after-the-fact "focusing".

MATERIAL AND METHOD

Principle and Design

The device consists of a dielectric elastomer membrane, carbon black nanoparticles, a super-hydrophobic coating, a droplet lens, a high voltage converter, and an acrylic frame (**Figure 1a**). The dielectric membrane was made of VHB 4910 (3M) and stretched equibiaxially by 350%. The thickness of the stretched membrane was 80 μm. The dielectric membrane was self-bonded to an annular acrylic frame which has the inner diameter of 10 mm. Carbon black nanoparticles were coated into an annular area of both sides of the membrane using patterned pad printing. The annular area has the inner diameter of 6 mm and the outer diameter of 10 mm. Copper tapes were applied to the two sides of the membrane and were connected to the carbon black. The copper tape on the top surface of the actuation membrane was connected to a high voltage converter, and that on the bottom surface was grounded. The high-voltage converter was used to amplify the DC voltage by 1000 times. The super-hydrophobic coating was applied to the top surface of the dielectric membrane except for a circular area of 3 mm in inner diameter at the center. The droplet fluid was 40% wt/wt glycerol-DI water mixture. The droplet was positioned at the center of the dielectric membrane and was confined within the area not covered by the super-hydrophobic coating. The overall dimensions of the device were Φ14mm × 1mm. Once a DC voltage was applied, the pre-stretched dielectric membrane exhibited an in-plane expansion, which compresses the center areas that are not covered by the carbon black coating. This changes the contact radius of the droplet, and in turn changes the curvature and the focal length of the droplet lens (**Figure 1b**). The optical path for smartphone-based macroscopic imaging is illustrated in **Figure 1c**. The object is located at the focal plane of the droplet lens. Collimated light forms once the light from the object passes through droplet lens, which is subsequently focused on the image sensor by the camera lens. By changing the focal length of the droplet lens, the objects from different working distances can be focused.

The focal length of the droplet lens (f) is determined by the refractive index (n), the droplet volume (V), and the radius of its contact area with the dielectric membrane (r). By assuming the droplet as a spherical cap, the radius of curvature R of the droplet can be derived from the equation:

$$V = \frac{1}{3}\pi(2R + \sqrt{R^2 - r^2})(2R^2 - r^2 - 2R\sqrt{R^2 - r^2}) \quad (1).$$

The focal length f of the droplet lens can be calculated using the Gaussian thin lens equation:

$$f = \frac{R}{n-1} \quad (2).$$

The change of the focal length of the droplet lens (f) with the droplet volume (V) and the contact radius (r) is plotted in **Figure 2**. In this study, the refractive index of the liquid (n) is a constant, *i.e.*, 1.38. When the contact radius r is constant, the focal length decreases with the increasing droplet volume. This indicates that in order to examine an object with a very short distance from the lens, a relatively large droplet volume should be used. On the contrary, a

978-1-940470-03-0/HH2018/$25©2018TRF
DOI 10.31438/trf.hh2018.94

Solid-State Sensors, Actuators and Microsystems Workshop
Hilton Head Island, South Carolina, June 3-7, 2018

small droplet volume should be used for viewing the objects placed distant from the lens. **Figure 2** also shows that with a given droplet volume *V*, the focal length increases with the increasing contact radius *r*. The changing range of the focal length can thus be estimated from the droplet volume and the contact radius. When the contact radius changes from 1.5 mm to 1.2 mm, the focal length of a 2.9 µl droplet changes from 4.51 mm to 2.12 mm. For a 0.5 µl droplet, the focal length changes from 24.18 mm to 9.98 mm. This shows that a smaller droplet volume can lead to a wider range of the focal length under the same change of the contact radius.

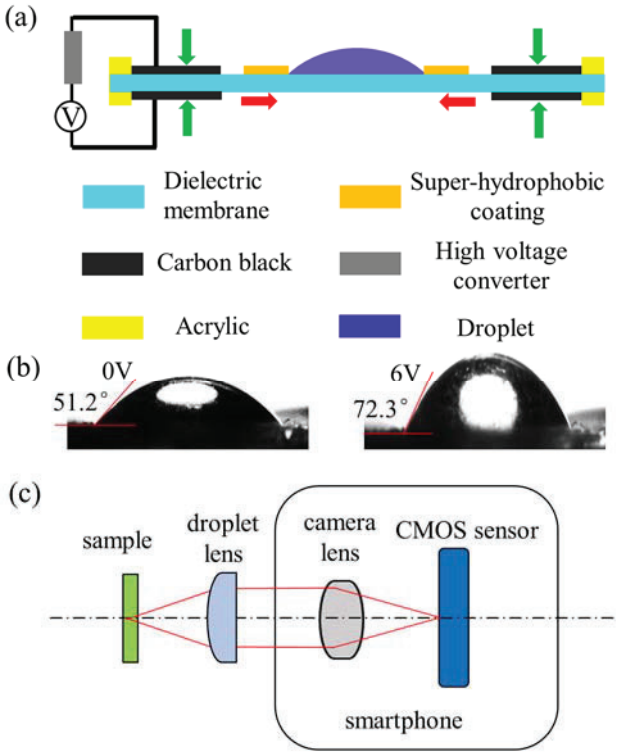

Figure 1. Schematic of the droplet lens. *(a) The cross-section view of the droplet lens; (b) The curvature of droplet lens changes upon a voltage bias of 6V; and (c) The optical path for smartphone-based macroscopic imaging.*

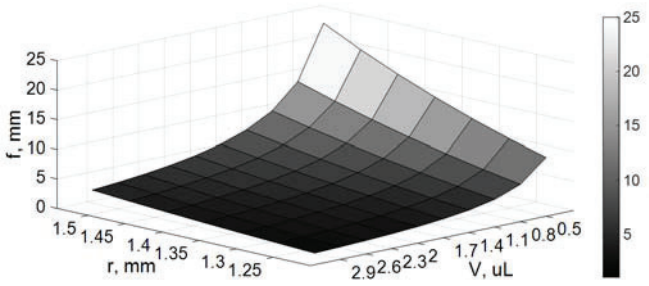

Figure 2. The change of focal length with the contact radius and the droplet volume.

RESULT AND DISCUSSION

Droplet Lens Characterization

The focal lengths of the droplet lenses were experimentally measured with systematically varied droplet volumes and applied voltages. The results showed that when the applied voltage increased from 0 to 6V, the contact radius that was defined by the area not covered by the superhydrophobic coating exhibited about 17% change (from 1509 µm to 1259 µm) (**Figure 3a**). The focal length change of the droplet lenses with 0.5 µl and 3 µl volumes is shown in **Figure 3b**. The focal length of the 0.5 µl droplet changed from 23.58 mm at 0V to 10.76 mm at 6V. The focal length of the 3.0 µl droplet changed from 4.38 mm at 0V to 2.05 mm at 6V. These results agree with the previous estimation, indicating that Equations 1&2 can be used to predict the initial focal length of the droplet lens and the changing range of the droplet lens upon actuation.

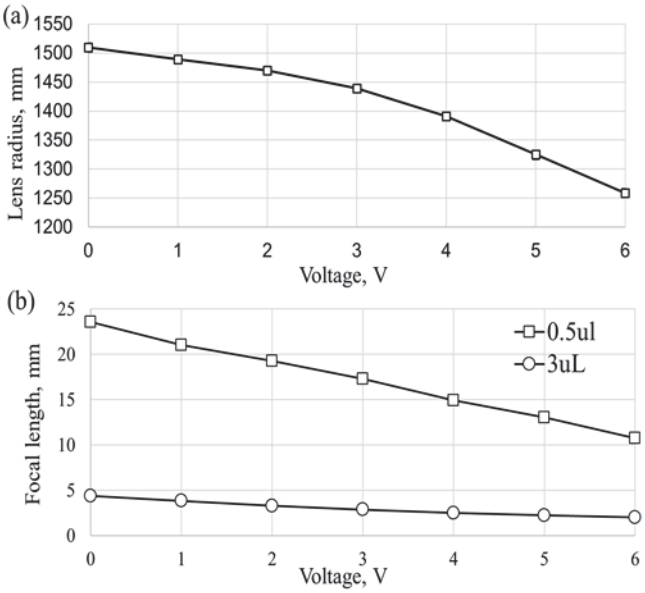

Figure 3. The experimentally measured contact radius change and the focal length change upon actuation. *(a) The change of contact radius, and (b) The change of focal length.*

Response and Recovery Time

Fast response is needed for acquiring the images at different object planes for the "after-the-fact" focusing. Here, the response and recovery time of the droplet lens were measured by passing a collimated laser beam through the droplet lens and examining the size change of the laser beam on a screen placed on the other side of the droplet lens. In this measurement, the collimated laser beam was 3 mm in diameter. The volume of the droplet lens was 0.5 *µl*. The screen was placed 25 mm away from the lens. The actuation voltage was increased from 0V to a positive bias, held for an extended period, and returned to 0V. The size of the laser beam on the screen during

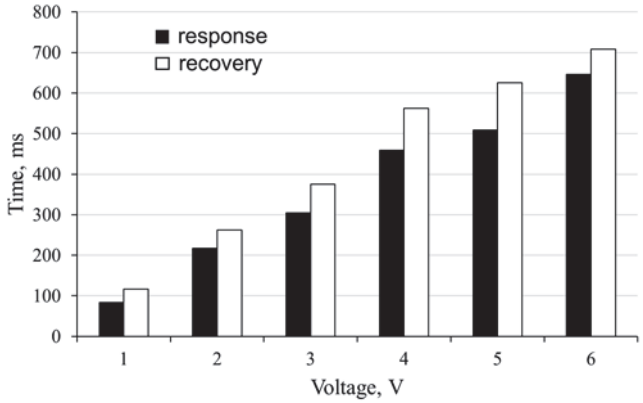

Figure 4. Response and recovery time under different voltage changes during the actuation and recovery processes.

the entire procedure was monitored and recorded at the frame rate of 300 *fps* using the high-speed camera. The response time refers to the response of the droplet shape change upon a voltage increase, while the recovery time refers to the response of the droplet shape change upon a voltage decrease. The response and recovery time were approximated as the moment when the change of the spot size reached 90% of the design value. **Figure 4** shows the measured response and recovery time of the droplet lens upon different voltage changes. As expected, the response and recovery time both increased with the increasing voltage change. The response time for the voltage change from 0V to 1V (corresponding to the working distance from 23.58 mm to 21.03 mm) was 83 ms. The value became 646 ms for the voltage change from 0V to 6V (corresponding to the working distance from 23.58mm to 10.76 mm). The recovery time was slightly longer than the response time for the same voltage change, *e.g.* the recovery time was 117 ms for the voltage change from 1V to 0V and 708 ms for the voltage change from 6V to 0V.

Gravity Effect

When the dielectric membrane where the droplet sits is placed vertically, the droplet becomes asymmetric due to the gravity and the imaging performance may be impaired. The imaging resolutions of the droplet lens under the horizontal and the vertical arrangements were quantified by imaging a USAF 1951 resolution target with iPhone SE (**Figure 5a**). The droplet lens was attached to the smartphone and aligned with the camera. The droplet volume was 3 μl. The applied voltage was 6V. Under the horizontal arrangement (when the droplet was placed on a horizontal surface), the minimal resolvable line bar was group 6 element 6, which corresponds to the spatial frequency of 114 line pairs per mm. Under the vertical arrangement, however, the minimal resolvable line bar was group 5 element 5 which corresponds to the spatial frequency of 50.8 line pairs per mm. It shows that the gravity deteriorates the imaging performance. The horizontal arrangement of the lens is thus preferable for high resolution imaging.

The deteriorated optical resolution under the vertical arrangement is caused by the asymmetric droplet shape. The contact angle difference between the top and bottom edges of the droplet lens at different applied voltages was measured (**Figure 5b**). A 3 μl droplet was placed on the dielectric membrane and the membrane was positioned vertically. The result showed that the contact angle difference increased with the increasing voltage. The initial contact angle difference between the top and the bottom edges of the droplet was 13.8°. The contact angle difference increased to 18.3° when the applied voltage increased to 6V. This indicated that the droplet shape asymmetry increased with the applied voltage, which may further impair the image performance. Future study is deserved to reduce the contact angle difference between the top and bottom edge of the droplet for enhancing the optical resolution.

Focus-free Macroscopic Imaging

A proof-of-concept experiment was performed to demonstrate the efficacy of the tunable droplet lens for focus-free macroscopic imaging. In this study, the distance of the objects from the lens was estimated. Appropriate droplet volume and applied voltage were determined based on the object distance range. The high-speed video was recorded while increasing the voltage across the dielectric membrane from 0V to a positive value. The individual image frames that represent different object planes were extracted from the video, where the objects at different distances were brought in focus. **Figure 6a** shows the "after-the-fact" focusing of three objects that were placed at different distances from the lens. The picture of a castle was 100 mm away, the rule was 40 mm away, and the tweezer was 20 mm away from the lens, respectively. A droplet lens with the

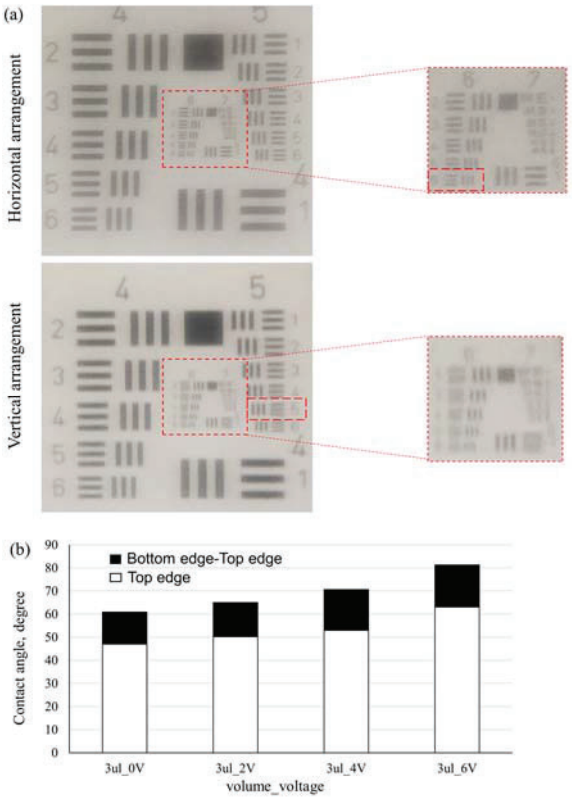

Figure 5. Gravity effect examination. *(a) The optical resolution measurement using a USAF 1951 resolution target when the droplet was placed horizontally and vertically. (b) The contact angle difference between the top and bottom edges of the droplet at different voltages.*

volume of 0.3 μl was used. It took about 800 ms to change the voltage from 0V to 6V. After the scanning, the in-focus images of the castle picture, the ruler, and the tweezer were extracted from the video. Similarly, "after-the-fact" imaging was demonstrated by placing a piece of paper at an angle with the dielectric membrane, where the four letters on the paper have different distances from the lens (**Figure 6b)**. The first letter 'E' was 10 mm away, and the last letter 'E' was 20 mm away from the lens. A droplet lens with the volume of 0.5 μl was used. The "in-focus" images of the four letters can be extracted from the video. **Figure 6c** shows the imaging of a multi-layered microfluidic device that was placed 2mm away from the lens. The microfluidic device had three channels of the same width (200 μm) that were placed into three layers. Each layer was 500 μm thick. The lateral dipalcement between the neighboring channels was 300 μm. To differentiate the channels at different distances, the top channel (that was closest to the lens) was filled with blue ink, the middle channel was filled with red ink, and the bottom channel was filled with green ink. Since the microfluidic channel was very close to the lens, a small droplet volume was needed. According to the experimental measurement shown in **Figure 3**, the droplet lens with the volume of 3 μl was used. By increasing the voltage to 6V, the minimum working distance of 2 mm can be reached. The three microfluidic channels can be brought into focus sequentially. In all above measurements, it took less than one second to scan through the field. Manual focusing is not needed.

CONCLUSION

In this paper, a smartphone based macroscope that allows for

fast and focus-free image acquisition is proposed. The macroscope utilizes a tunable droplet lens to scan the entire depth of field. The droplet lens is actuated by a miniature DEA, with a 120% focal length variance with the response and the recovery time less than 800 ms. The focusing range can be adjusted by changing the droplet volume, providing flexibility for extensive imaging applications.

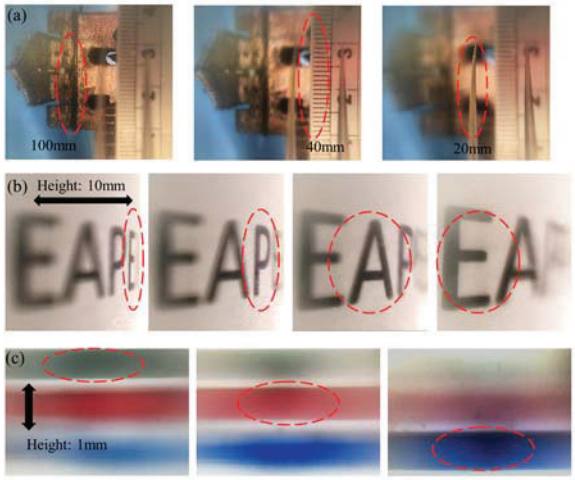

Figure 6: Demonstration of focus-free macroscopic imaging. *The extracted "after-the-fact" focused images of (a) three objects, (b) four letters on a piece of paper and (c) multi-layered microfluidic channels placed at different working distances from the high-speed videos. The focused areas are indicated by the red dashed lines.*

ACKNOWLEDGEMENT

The authors thank the support from National Science Foundation under the grant number 1509727. The authors also thank graduate fellowship support from Pelotonia program.

REFERENCES

[1] D. N. Breslauer, R. N. Maamari, N. A. Switz, W. A. Lam, and D. A. Fletcher, "Mobile Phone Based Clinical Microscopy for Global Health Applications," *Plos One,* vol. 4, Jul 22 2009.

[2] S. C. Gopinath, T.-H. Tang, Y. Chen, M. Citartan, and T. Lakshmipriya, "Bacterial detection: From microscope to smartphone," *Biosensors and Bioelectronics,* vol. 60, pp. 332-342, 2014.

[3] S. Sumriddetchkajorn, A. Somboonkaew, and S. Chanhorm, "Mobile device-based digital microscopy for education, healthcare, and agriculture," *Electrical Engineering/Electronics, Computer, Telecommunications and Information Technology (ECTI-CON), 2012 9th International Conference,* pp. 1-4, 2012.

[4] S. B. Kim, K.-i. Koo, H. Bae, M. R. Dokmeci, G. A. Hamilton, A. Bahinski, *et al.*, "A mini-microscope for in situ monitoring of cells," *Lab on a Chip,* vol. 12, pp. 3976-3982, 2012.

[5] S. Dong, K. Guo, P. Nanda, R. Shiradkar, and G. Zheng, "FPscope: a field-portable high-resolution microscope using a cellphone lens," *Biomedical optics express,* vol. 5, pp. 3305-3310, 2014.

[6] O. Mudanyali, D. Tseng, C. Oh, S. O. Isikman, I. Sencan, W. Bishara, *et al.*, "Compact, light-weight and cost-effective microscope based on lensless incoherent holography for telemedicine applications," *Lab on a Chip,* vol. 10, pp. 1417-1428, 2010.

[7] N. A. Switz, M. V. D'Ambrosio, and D. A. Fletcher, "Low-cost mobile phone microscopy with a reversed mobile phone camera lens," *PloS one,* vol. 9, p. e95330, 2014.

[8] A. Arpa, G. Wetzstein, D. Lanman, and R. Raskar, "Single lens off-chip cellphone microscopy," *Computer Vision and Pattern Recognition Workshops (CVPRW), 2012 IEEE Computer Society Conference,* pp. 23-28, 2012.

[9] W. Bishara, T.-W. Su, A. F. Coskun, and A. Ozcan, "Lensfree on-chip microscopy over a wide field-of-view using pixel super-resolution," *Optics express,* vol. 18, pp. 11181-11191, 2010.

[10] D. Tseng, O. Mudanyali, C. Oztoprak, S. O. Isikman, I. Sencan, O. Yaglidere, *et al.*, "Lensfree microscopy on a cellphone," *Lab on a Chip,* vol. 10, pp. 1787-1792, 2010.

[11] J. S. Cybulski, J. Clements, and M. Prakash, "Foldscope: origami-based paper microscope," *PloS one,* vol. 9, p. e98781, 2014.

[12] H. Zhu, O. Yaglidere, T.-W. Su, D. Tseng, and A. Ozcan, "Cost-effective and compact wide-field fluorescent imaging on a cell-phone," *Lab on a Chip,* vol. 11, pp. 315-322, 2011.

[13] H. Huang, K. Wei, and Y. Zhao, "Adaptive optofluidic lens (es) for switchable 2D and 3D imaging," in *Proceeding of SPIE. Microfluidics, BioMEMS, and Medical Microsystems XIV*, 2016, p. 97050P.

[14] S. Kuiper and B. Hendriks, "Variable-focus liquid lens for miniature cameras," *Applied physics letters,* vol. 85, pp. 1128-1130, 2004.

[15] K. Wei, H. Huang, Q. Wang, and Y. Zhao, "Focus-tunable liquid lens with an aspherical membrane for improved central and peripheral resolutions at high diopters," *Optics Express,* vol. 24, pp. 3929-3939, 2016.

[16] H. Y. Huang, K. Wei, and Y. Zhao, "Variable Focus Smartphone Based Microscope Using an Elastomer Liquid Lens," *2016 IEEE 29th International Conference on Micro Electro Mechanical Systems (MEMS),* pp. 808-811, 2016.

[17] Y. K. Fuh, Z. H. Lai, L. H. Kau, and H. J. Huang, "A lab-on-phone instrument with varifocal microscope via a liquid-actuated aspheric lens (LAL)," *Plos One,* vol. 12, Jun 26 2017.

[18] K. Wei, H. Y. Huang, Q. Wang, and Y. Zhao, "Focus-tunable liquid lens with an aspherical membrane for improved central and peripheral resolutions at high diopters," *Optics Express,* vol. 24, pp. 3929-3939, Feb 22 2016.

[19] K. Wei, H. S. Zeng, and Y. Zhao, "Insect-Human Hybrid Eye (IHHE): an adaptive optofluidic lens combining the structural characteristics of insect and human eyes," *Lab on a Chip,* vol. 14, pp. 3594-3602, 2014.

[20] K. Wei, N. W. Domicone, and Y. Zhao, "Electroactive liquid lens driven by an annular membrane," *Optics Letters,* vol. 39, pp. 1318-1321, Mar 1 2014.

[21] P. Brochu and Q. B. Pei, "Advances in Dielectric Elastomers for Actuators and Artificial Muscles," *Macromolecular Rapid Communications,* vol. 31, pp. 10-36, Jan 4 2010.

[22] S. Shian, R. M. Diebold, and D. R. Clarke, "Tunable lenses using transparent dielectric elastomer actuators," *Optics Express,* vol. 21, pp. 8669-8676, Apr 8 2013.

CONTACT

*Y. Zhao, tel: +1-614-247-7424; zhao.178@osu.edu

TWO-CHANNEL WAKEUP SYSTEM EMPLOYING ALUMINUM NITRIDE BASED MEMS RESONANT ACCELEROMETERS FOR NEAR-ZERO POWER APPLICATIONS

Robert W. Reger, Sean Yen, Bryson Barney, Michael Satches, Andrew I. Young, Tammy Pluym, Michael Wiwi, Matthew A. Delaney, and Benjamin A. Griffin
Sandia National Laboratories, Albuquerque, New Mexico, USA

ABSTRACT

The Defense Advanced Research Project Agency has identified a need for low-standby-power systems which react to physical environmental signals in the form of an electrical wakeup signal. To address this need, we design piezoelectric aluminum nitride based microelectromechanical resonant accelerometers that couple with a near-zero power, complementary metal-oxide-semiconductor application specific integrated circuit. The piezoelectric accelerometer operates near resonance to form a passive mechanical filter of the vibration spectrum that targets a specific frequency signature. Resonant vibration sensitivities as large as 490 V/g (in air) are obtained at frequencies as low as 43 Hz. The integrated circuit operates in the subthreshold regime employing current starvation to minimize power consumption. Two accelerometers are coupled with the circuit to form the wakeup system which requires only 5.25 nW before wakeup and 6.75 nW after wakeup. The system is shown to wake up to a generator signal and reject confusers in the form of other vehicles and background noise.

INTRODUCTION

Through the Near-Zero Power RF and Sensor Operations (N-ZERO) program, the Defense Advance Research Project Agency (DARPA) is addressing needs for near-zero-power wakeup systems that monitor activity in remote locations [1]. The power budget of deployed systems is presently dominated by their standby power consumption because events of interest are typically infrequent. Commercial-off-the-shelf (COTS) solutions to infrequent wakeup events have costly battery maintenance or replacement cycles on the order of weeks to months, making them infeasible for use in wide ranging, distributed system architectures.

Piezoelectric based microelectromechanical systems (MEMS) offer solutions for sensing infrequent events as they require zero input power to produce an electrical output. Therefore, the only power requirement comes from the external decision-making circuit. The complementary metal-oxide semiconductor (CMOS) application specific integrated circuit (ASIC) employs current-starvation and sub-threshold biasing to ensure that the decision-making circuit also operates at near-zero power, roughly defined as 10 nW or less.

In this work we employ aluminum nitride (AlN) as the piezoelectric material. AlN is commonly used in radio-frequency filter applications for cellular phones. Piezoelectric AlN is chosen over other piezoelectric thin films, such lead zirconate titanate (PZT), due to is superior open circuit sensitivity coefficient, larger signal-to-noise ratio, and established, large volume manufacturing base [2]. Unlike PZT or zinc oxide, AlN is also fully CMOS compatible allowing for future CMOS integration leading to increased performance gains [3].

Here, we develop a near-zero-power sensor system employing AlN based MEMS resonant accelerometers (Figure 1) coupled with an ASIC operating at sub-threshold, designed for infrequent wakeup applications. Two accelerometers are employed simultaneously to increase system robustness to false positives. We start with the design, fabrication, and characterization of the resonant accelerometer. Then we discuss the CMOS ASIC in a piecewise manner, beginning with the bias cell, moving to the comparator and concluding with the self-latching comparator circuit. We then discuss the integrated system level performance and conclude with future work.

ACCELEROMETER

Design

While conventional accelerometers are designed to operate over a large bandwidth below resonance, resonant accelerometers operate with a narrow bandwidth near resonance [4]. A high quality factor resonant response increases sensitivity over that of a flat-band accelerometer and attenuates undesirable out-of-band signals. Thus, the sensors act as passive filters in the mechanical domain.

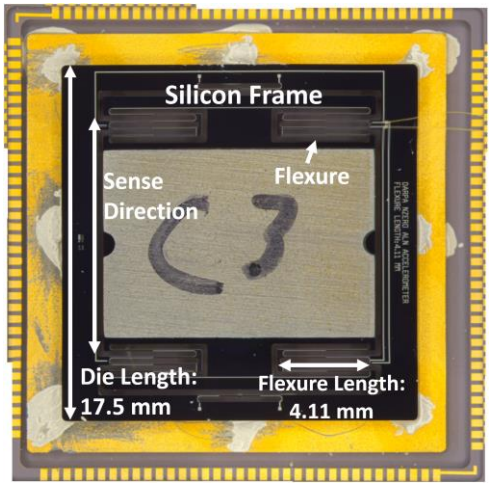

Figure 1 - Packaged resonant MEMS accelerometer with tungsten proof mass.

The resonant accelerometers discussed herein are full-wafer thickness and consist of an outer silicon frame connected to a large proof mass by four single-crystal silicon compliant tethers. Each tether is a double-folded flexure with AlN incorporated for zero-power transduction of physical strain into an electrical output. The resonant frequency of the devices is set by the stiffness of their flexures (k) and the proof mass (m),

$$f_r = \frac{1}{2\pi}\sqrt{\frac{k}{m}}.$$

Instead of using a silicon proof mass defined exclusively by microfabrication processes, we incorporate *macro*-machined tungsten plugs (with 10× the density of silicon) during packaging. These tungsten plugs provide two advantages: 1.) They enable higher quality factors due to increased mass ($Q \propto \sqrt{km}$) and 2.) They allow tuning of the resonant frequency post-fabrication due to the modularity.

978-1-940470-03-0/HH2018/$25©2018TRF
DOI 10.31438/trf.hh2018.95

Solid-State Sensors, Actuators and Microsystems Workshop
Hilton Head Island, South Carolina, June 3-7, 2018

Fabrication

The fabrication process for the resonant accelerometers is provided in Figure 2. (a) Start with a 675 µm high-resistivity silicon wafer with 1 µm oxide. Etch 200 nm into the oxide, deposit tungsten, and performed a chemical mechanical polish to form tungsten plugs for via formation. (b) Pattern 20/50/100 nm titanium/titanium nitride/aluminum bottom metal for electrodes. (c) Deposit 750 nm AlN. (d) Etch through the AlN to form vias to the tungsten, then deposit and pattern the top electrode (100/25 nm aluminum/titanium nitride). (e) Pattern to form the frame and flexures and etch films down to silicon then (f) DRIE through the full silicon wafer.

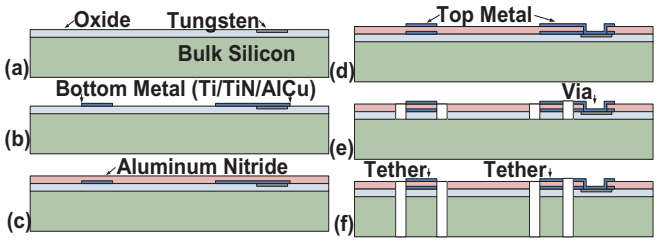

Figure 2 - Accelerometer fabrication process.

Characterization

The MEMS accelerometers are characterized without the CMOS present on a Data Physics Corporation S-011 shaker. A broadband reference accelerometer is included on the shaker for calibration. Figure 3 shows the time series response of the MEMS and reference accelerometers provided a Honda 6500 personal generator as the input signal. The MEMS accelerometer filters the frequency content contained in the reference signal to such a degree that the MEMS output appears to be purely sinusoidal.

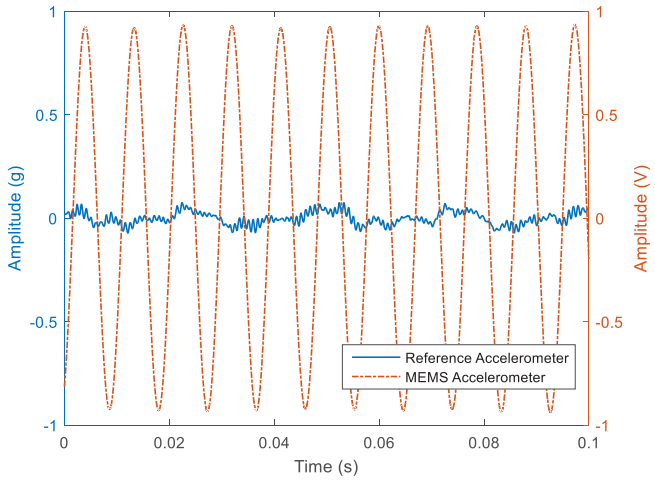

Figure 3 - Comparison of the time series output from a reference accelerometer and the MEMS accelerometer given the generator input. The MEMS accelerometer mechanically filters the generator input to the frequency of interest.

Shown in Figure 4 is a sample transfer function (V/g) utilizing the MEMS and reference accelerometers. The resonant MEMS accelerometers have been demonstrated with resonant frequencies as low as 43 Hz, resonant sensitivities as high as 490 V/g, and quality factors over 12,500.

CMOS ASIC

A near-zero-power ASIC fabricated in Sandia's CMOS7 process interrogates the electrical output of the piezoelectric accelerometer. Sandia's CMOS7 is a 0.35 µm trench-isolated silicon-on-insulator process. The power consumption is minimized using low-current, long-channel transistors (W/L = 2 µm/20 µm) in sub-threshold biasing, and current starvation in the circuits (bias current 0.75 nA). In addition, the power supply is reduced to V_{DD} = 1 V. The ASIC contains a pair of comparator/latch circuits (Figure 5) connected to a pair of accelerometers. The two comparator/latch outputs are connected to an AND gate. Each circuit compares the output from the accelerometer to a pre-defined threshold voltage and has self-latching positive feedback. When both comparators latch, the ASIC outputs a 1 V wakeup signal. The comparator thresholds are set by mirroring the bias current across resistors. In measurement, the two-channel ASIC requires only 5.25 nW while alert and 6.75 nW after wakeup.

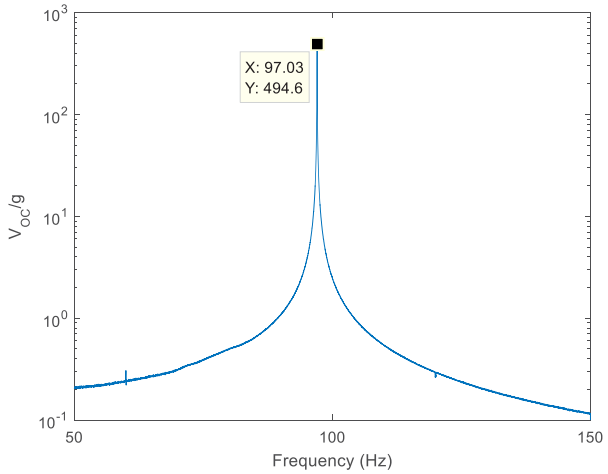

Figure 4 - Sample transfer function illustrating resonant MEMS accelerometer sensitivity.

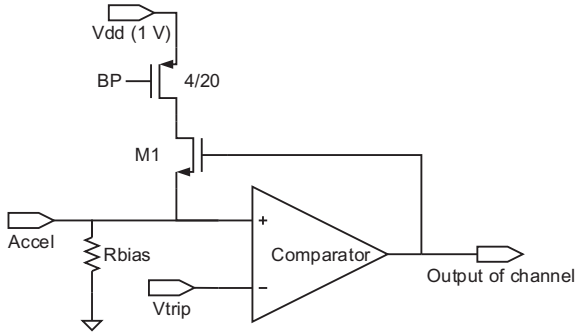

Figure 5 - CMOS comparator/latch unit.

Bias Cell

The bias cell, shown in Figure 6, generates a supply-independent 0.75 nA bias current, which is key to the lower power consumption in the ASIC. The bias cell consists of PMOS and NMOS current mirrors in a bootstrap configuration, with the current inversely proportional to the external bias resistor R_{BIAS}. The transistors are sized with very long channels (L = 20 µm) and biased in the subthreshold regime ($|V_{GS}| < |V_{TH}|$), which allows the supply voltage to be lowered to 1 V while retaining high drain resistance of the mirrors. R_{BIAS} is typically in the 100 MΩ range in order to set

nA-level currents. The "BP" and "BN" nodes are the gate voltages for P- and N-type current mirrors used throughout the ASIC. Additional mirrors (not shown) are provided in the bias cell to produce the trip voltages for the comparators by running 0.75 nA across an external resistor.

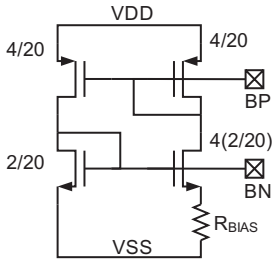

Figure 6 - Schematic of the bias cell with W/L noted. Startup circuit not shown.

Comparator

The comparator consists of a differential pair followed by a common-source stage. The two tail PMOS connect to "BP" from the bias cell such that about 0.75 nA flows through each branch, for a total of about 1.5 nW. The input is designed such that the comparator achieves gain while the inputs are biased near *VSS*. Figure 8 shows the input and output of a standalone comparator, showing successful operation at 200 Hz at a 100 mV trip point. The circuit experiences a slight offset at the input (it trips at about 10-25 mV higher than V_{trip}) due to both manufacturing mismatch and circuit bandwidth.

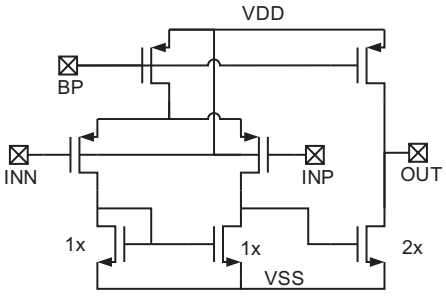

Figure 7 - Schematic of the comparator. The PMOS connected to BP have W/L = 4/20

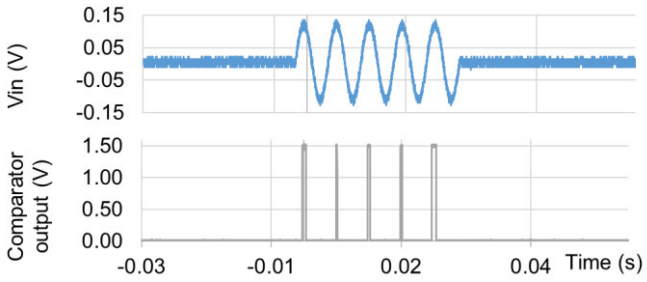

Figure 8 - Measured comparator input (top) and output (bottom) in for a 200 Hz 130 mV sinusoid compared to a 100 mV threshold.

Self-latching circuit

A positive feedback loop, wrapped around the comparator (Figure 5), performs latching. When the comparator output rises, transistor M1 turns on, allowing the 0.75 nA (current-starved by BP) to flow into the positive input node. Therefore, the power consumption of the self-latching comparator post-wakeup is 0.75 nW greater than pre-wakeup. To provide a bias to *VSS* for the input prior to latching but generate a latching voltage under positive feedback, R_{bias} is sized such that R_{bias}×0.75 nA > V_{trip} for values of V_{trip} we expect to use in the system. Figure 9 shows the measured input and output of the self-latched comparator as the input is dialed from about 124 mV to 125 mV at the time of the vertical cursor. The input rises as the feedback pumps current into the input (the input is a benchtop current source so it does not enforce the DC voltage level). The feedback takes several cycles to latch because the feedback current needs to charge parasitic capacitance at the positive input node.

INTEGRATED SYSTEM PERFORMANCE

The wakeup system (Figure 10) is realized by combining two MEMS resonant accelerometers with the ASIC on a custom printed circuit board (PCB), which we mounted on a shaker table to test performance. The power consumption is tabulated in Table 1.

A generator's vibration signature was targeted with characteristic frequencies of 80 and 160 Hz. Confusers from urban environment background noise and a truck signal were used to assess false positives. Figure 11 shows the results of the wakeup tests using the generator signal with (a) the 160 Hz filtered, (b) the 80 Hz signal filtered, and (c) the entire generator vibration profile present, as shown by the provided spectrum. We observe that when filtering either of the two targets below threshold, no wakeups occur. When the entire target signature is present a wakeup event occurs in each of the 30-second time blocks, returning to zero once a reset signal is provided.

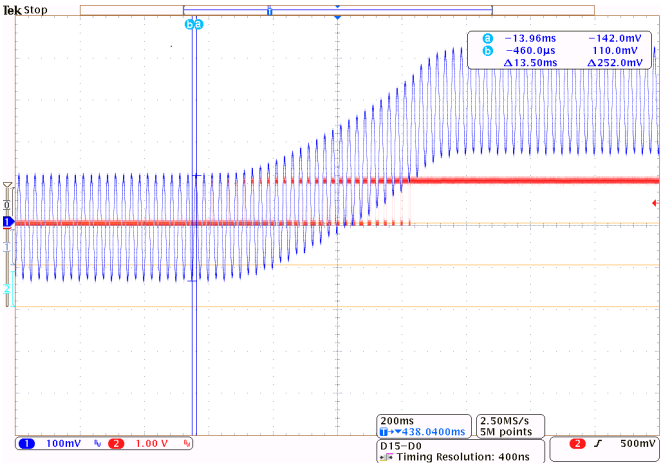

Figure 9 – Measured input (blue) and output (red) of the self-latched comparator for a 40 Hz 125 mV input compared to a 100 mV threshold. The vertical scale is 100 mV/div for the input and 1 V/div for the output; the horizontal scale is 200 ms/div. The input was dialed from about 124 mV to 125 mV around the time of the vertical cursors.

Table 1 - Power consumption of system components before and after wakeup. The total power consumption for a two-channel system therefore would be 5.25 nW before and 6.75 nW after wakeup.

Component	Before wakeup	After wakeup
Bias cell	1.5 nW	
Self-latched comparator	1.5 nW/channel	2.25 nW/channel
V_{trip} generation	0.75 nW shared by 2 channels	
AND logic	Below measurement floor	

To characterize the margin between false alarms and probability of detection, we set a threshold value and record when

the wakeup occurs under diminishing generator signal levels and increasing background levels, then we repeat this process for a higher threshold. Results are shown in Figure 12 (a) and (b). We observe margins between the generator and background noise of over 2000× with margins comparing the generator and truck of ~100×.

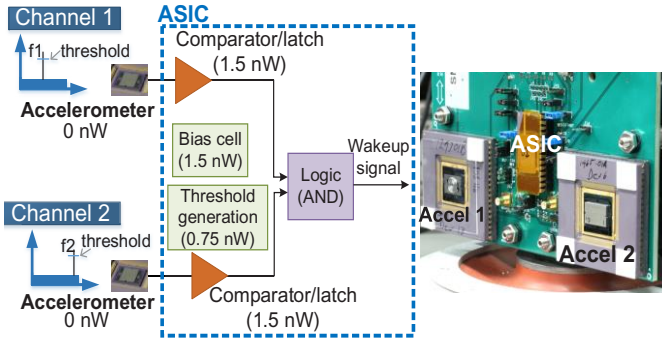

Figure 10 - Notional diagram and image of dual-channel wakeup system.

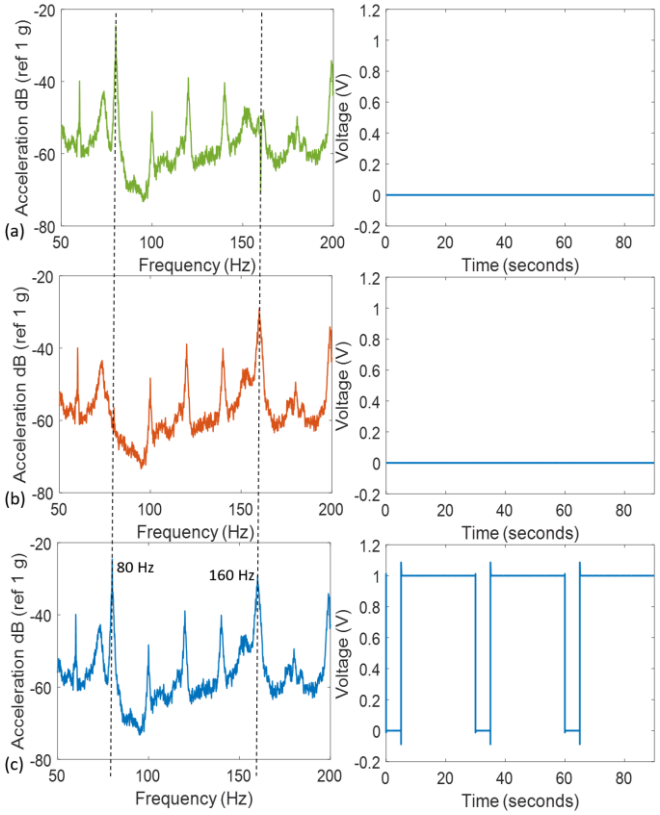

Figure 11 - Measured 2-channel wakeup results, (a) 160 Hz filtered, (b) 80 Hz filtered, (c) entire generator vibration profile. 5-second reset provided every 30 seconds.

SUMMARY AND CONCLUSIONS

We designed a near-zero power system to wake up to physical inputs from the environment employing two MEMS resonant accelerometers coupled to a CMOS ASIC. The MEMS accelerometers require zero power by utilizing piezoelectric AlN to transduce physical strain in the flexures to an electrical output signal. Accelerometers have demonstrated resonant frequencies as low as 43 Hz, sensitivities as large as 490 V/g, and quality factors upwards of 12,500.

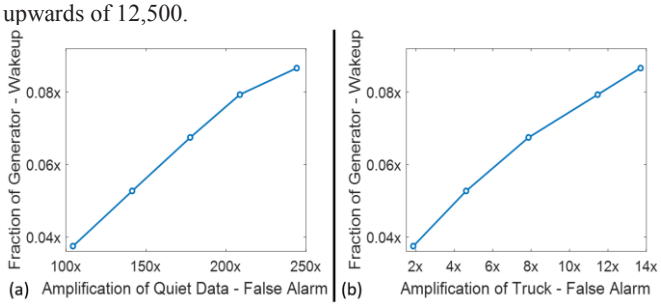

Figure 12 – Measured fraction of generator signal to trigger wakeup at various thresholds versus (a) amplification of background noise and (b) amplification of truck data (at the same comparator trip point) to trigger a false alarm.

The CMOS ASIC receives the electrical output from the accelerometers and compares them to the threshold with self-latching comparators. When the signal from both accelerometers exceeds the programmable threshold, the ASIC produces a 1 V wakeup. The CMOS ASIC requires only 5.25 nW of power before wakeup and 6.75 nW of power post-wakeup. The full system is able to selectively wakeup to a generator signal and successfully reject confusers in the form of urban background noise or a truck.

In future work, we intend to investigate shock and temperature hardness of this system needed for deployment.

ACKNOWLEDGEMENTS

Sandia National Laboratories is a multimission laboratory managed and operated by National Technology & Engineering Solutions of Sandia, LLC, a wholly owned subsidiary of Honeywell International Inc., for the U.S. Department of Energy's National Nuclear Security Administration under contract DE-NA0003525. The views expressed in the article do not necessarily represent the views of the U.S. Department of Energy or the United States Government. This work was supported by the DARPA N-ZERO project, managed by Dr. Roy H. Olsson. The views, opinions, and/or findings expressed are those of the authors and should not be interpreted as representing the official views or policies of the Department of Defense or the U.S. Government. We acknowledge fabrication support by the Sandia MESAFab operations team.

REFERENCES

[1] R. H. Olsson III, R. B. Bogoslovov, and C. Gordon, "Event Driven Persistent Sensing: Overcoming the Energy and Lifetime Limitations in Unattended Wireless Sensors," *Sensors 2016*, Orlando, FL, Nov. 2016.

[2] S. Trolier-McKinstry, and P. Muralt, "Thin film piezoelectrics for MEMS," *Journal of Electroceramics*, Vol. 12, No. 1-2, pp. 7-17, Jan. 2004.

[3] K. E. Wojciechowski, R. H. Olsson, M. R. Tuck, E. Roherty-Osmun, and T. A. Hill, "Single-chip precision oscillators based on multi-frequency, high-Q aluminum nitride MEMS resonators," *TRANSDUCERS 2009*, Denver, CO, 2009.

[4] S. B. Horowitz, et al., "A low frequency MEMS vibration sensor for low power missile health monitoring," In *IEEE Aerospace Conference*, Big Sky, MT, May 2013.

CONTACT

*B. Griffin, tel: +1-505-844-7370; bagriff@sandia.gov

MICRO BUCKLED BEAM BASED ULTRA-LOW FREQUENCY VIBRATION ENERGY HARVESTER

Ruize Xu, Haluk Akay, and Sang-Gook Kim
Massachusetts Institute of Technology, Cambridge, MA, USA

ABSTRACT

We present a bi-stable buckled beam MEMS energy harvester which achieved low operating frequency, low operating amplitude and wide bandwidth, all packaged in the size of a coin. Bi-stable buckling was induced by controlling the built-in compression from the residual stress in the multi-layer beam structure, a way that is compatible to the micro-fabrication process. A fully functional piezoelectric device has been designed, monolithically fabricated, and tested to induce bi-stable buckling of ~200μm. The first batch device generated peak power of 85nW with 50% half-power bandwidth under 70Hz at 0.5g. Considering the figure of merit (power over device swing volume and input acceleration^2), this device shows at least one order of magnitude improvement to piezoelectric MEMS harvesters ever reported.

INTRODUCTION

Vibration energy harvesting at MEMS scale will promisingly enable exciting applications such as large wireless sensor networks and Internet of Things (IoT) due to its high power-generation efficiency and small form factor. Nonetheless, the high operating frequencies of current MEMS energy harvesters have long hindered wide applications of this technology. For instance, our previous MEMS device based on nonlinear resonance has achieved high output power of 45μW and wide bandwidth of >20%, while the operation frequency and input vibration amplitude were impractically high (>1000Hz at 4g) [1]. We now report that our new design addresses this major challenge to realize the MEMS-scale energy harvesting technology to a real product: energy harvesting at low frequencies (<100Hz) and low amplitudes (<1g).

Past approaches to lower the operating frequency include designing new geometries [2-7], using soft materials [7–9], and up-conversion mechanisms [10-13]. For examples, buckling has been employed as an up-conversion mechanism [10]; a rotary mass with magnetic catch-and-release has been designed [11]; and a multi-mode buckled beam has been implemented [12]. Soft materials may not be effective to absorb the input energy; most of the devices for low frequency operation are in macro scale, which inherently have low-frequency resonance; the up-conversion approaches typically need auxiliary structures such as magnets which inevitably increase the device size. The concept of bi-stable nonlinear oscillator-based energy harvesting has been previously proposed with either magneto-elastic structures [14] or axial compression-based configurations [15], which would require costly assembly and were never implemented at the MEMS-scale.

Our new design adopts the bi-stable oscillation but has been implemented at MEMS scale, demonstrating the low-frequency energy harvesting. Bi-stable oscillation, with its large-amplitude snapping motion at low frequencies was found to be suitable for low-frequency energy harvesting. To enable the bi-stable oscillation, intentional but controllable buckling was generated through mono-lithic fabrication processes. Through the extensive in-process characterization and model-based analytical composite beam design, the compression stress in the micro-beam structures could be controlled to induce the desirable buckling of the structure. The testing results validates the feasibility of this approach as described below.

DESIGN AND MODELLING

To capture the features of the newly designed energy harvester, including the low operating frequency, MEMS-fabricated multi-layer structure, and the embedded piezoelectric layer that converts the mechanical energy into electricity, we developed a theoretical framework with an electromechanically coupled lumped model, which incorporates the multi-layer structure and residual stress. The model is solved analytically with harmonic balance to obtain the frequency response of the energy harvesters, which is of our primary interest.

The energy harvester we model has a clamped-clamped beam structure of a stack of thin films including structural layer, piezoelectric layer and passivation layer (Fig.1). A heavy proof mass is concentrated at the middle of the beam to capture the external vibration and excites the whole beam to oscillate out-of-plane. Piezoelectric elements work in d_{33} mode with top interdigitated electrodes, coupling the electrical response with mechanical strain. The multi-layer beam is designed to buckle by incorporating compressive residual stress in the micro-fabricated thin films. Statically, the beam either buckles up or down (two equilibria), and the dynamics becomes complex when the system is continuously excited in post-buckling regime. To simplify the analysis of the complex problem but still capture the essence of the snapping, the beam's vibration mode is assumed, and a one degree-of-freedom model has been constructed. The non-homogeneous cross section beam structure has been taken into account by considering different thicknesses and material properties of the layers. Furthermore, residual stress of each layer is built in as part of the stiffness of the beam and induces buckling. The electrical and mechanical domains are coupled with the piezoelectric coupling, so that the generated electrical signal can be obtained.

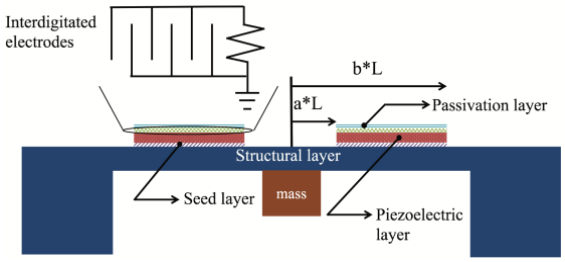

Figure 1: Schematics of the doubly clamped beam based energy harvester. The piezoelectric element is in 33 mode with top interdigitated electrodes. The piezoelectric element and electrode span symmetrically from $-b \bullet L$ to $-a \bullet L$ and $a \bullet L$ to $b \bullet L$ on the substrate.

The governing equation of the mechanical domain can be obtained and written in a compact form [16],

$$m\ddot{w} + k_L w + k_N w^3 + b\dot{w} + c_N w V_N + c_L V_L = F \quad (1)$$

978-1-940470-03-0/HH2018/$25©2018TRF
DOI 10.31438/trf.hh2018.96

$$C_0\left(\dot{V}_L+\dot{V}_N\right)+\frac{V_L+V_N}{R}=I_L+I_N \tag{2}$$

where k_L, k_N, b, c_L, c_N and F are the linear stiffness and nonlinear stiffness of the beam, the mechanical damping coefficient, the linear and nonlinear electromechanical coupling, and the external excitation force respectively, C_0 and R are the internal capacitance of the piezoelectric element and the load resistance respectively. These lumped parameters are functions of the device dimensions and material properties, which are useful for device design:

$$k_L=\left[\frac{2\pi^4 W}{3l^3}\sum_{i=1}^{n}c_{33,i}^{E}\left(H_{U,i}^3-H_{L,i}^3\right)\right]+\left[\frac{\pi^2 W}{2l}\sum_{i=1}^{n}T_{0,i}H_i\right] \tag{3}$$

$$k_N=\frac{\pi^4 W}{8l^3}\sum_{i=1}^{n}c_{33,i}^{E}H_i \tag{4}$$

$$c_L=\frac{\pi e_{33}W\left(H_{U,P}^2-H_{L,P}^2\right)\left(\sin(2\pi b)-\sin(2\pi a)\right)}{lg} \tag{5}$$

$$c_N=\frac{\pi^2 e_{33}WH_p(b-a)}{lg} \tag{6}$$

where W, H, l are the width, thickness and length of the beam, T_0 is the residual stress, c and e are the elastic constant and piezoelectric constant respectively, subscript i denotes the i-th layer, a and b denote the span of the electrodes on the beam (Fig.1), and g is the gap between two electrode fingers; the subscript p denotes the variable is associated to the piezoelectric layer. It should be noted that the linear stiffness has two parts: the first part is from bending of the beam and the second comes from the residual stress. More particularly, when the residual stress is negative (compressive) and large enough, the linear stiffness k_L will be negative, so that equation (1) becomes a characteristic bi-stable *Duffing* equation.

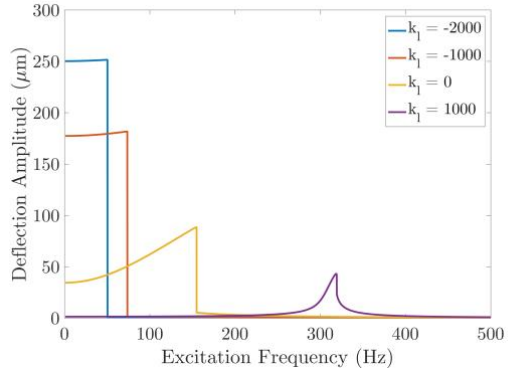

Figure 2. Simulated dynamic responses of the MEMS energy harvester with varying linear stiffness (stress) and other parameters the same. The deflection's amplitude at low frequencies increases with the linear stiffness k_l varying from positive to negative.

The nonlinear governing equations (1) and (2) are solved analytically using the harmonic balance method, so that the frequency responses are obtained. Both softening (intra-well) and stiffening (inter-well) responses are derived, but the inter-well oscillations have larger amplitude and generate more power. The enhancement of the bi-stable oscillator on the low-frequency operation is illustrated in Fig. 2. The frequency response of the MEMS energy harvester changes with varying the linear stiffness but fixing the nonlinear stiffness, which is the case when varying only the residual stress in the beam structure. The frequency response shifts to lower frequency with higher amplitude when the linear stiffness switching from positive to negative as shown in Fig. 2. When the negative stiffness's amplitude becomes larger, the response is in ultra-low frequency range with significantly larger deflection amplitude, which characterizes the large-amplitude snap through of bi-stable nonlinear oscillators. The shift of the frequency response to desirable direction, lower frequency and larger amplitude, by tuning the stiffness provides the critical design knob for the new generation energy harvester.

To implement the residual stress induced buckling in the multi-layer beam, the linear and nonlinear stiffness are designed by matching the simulation of the model to the target operating condition. Both the residual stress and thickness as the critical parameters in the linear stiffness term (the second term in equation (3)), can then be designed to achieve the desired linear stiffness by parametric sweeping using the analytical form of the linear stiffness. However, the compressive residual stress is bi-axial and could induce the buckling in lateral direction as well. A small-width beam array (like a louver) is then devised to minimize the critical buckling load in the lateral direction to eliminate the buckling in that direction.

The newly designed bi-stable nonlinear oscillator-based MEMS energy harvester has a clamped-clamped beam structure with a stack of thin-films having 28 pairs of beams 0.4mm wide in a silicon frame of 15mm×12mm. Each beam has approximately 500 interdigitated Au fingers over 0.2 μm thick PZT. A proof mass is located at the middle, connecting the beam array to synchronize their out-of-plane motion and minimize the rotation during oscillation. The schematic of the new design is illustrated in Fig. 3.

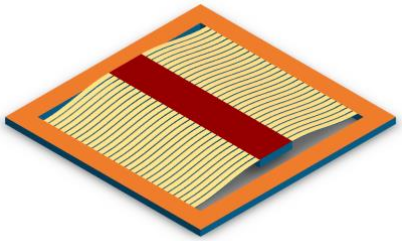

(a)

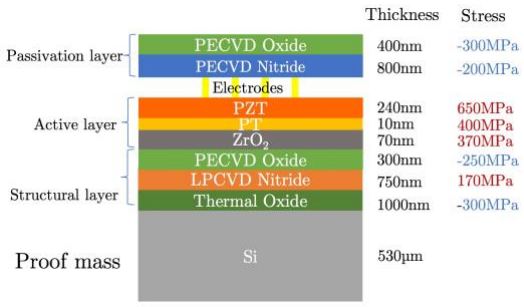

(b)

Figure 3. (a) 3D rendition of the buckled beam based energy harvester (The buckling of the beam is exaggerated). (b) Beam composition of the MEMS energy harvester.

FABRICATION

The fabrication process is based on 4" <100> silicon wafers. 300nm thermal dioxide is grown with wet oxidation, as the bottom layer of the multi-layer beam and serves as the etch stop of the final DRIE release. One LPCVD silicon nitride layer (tensile) and one PECVD silicon dioxide layer (compressive) are then deposited as the structural layer to support the proof mass. The dual-frequency plasma deposition of the ST Systems CVD enables flexible stress control in a wide range from tensile to compressive by tuning parameter is the ratio of the duration of the applied high (13.56MHz) and low (380kHz) frequency plasma. The growth rate and residual stress of the PECVD thin films have been characterized by measuring the thickness, and the wafer bow before and after the deposition. The data guides the control of the injected compression in the structure and the balance of the stress in the stack. ZrO_2, PbTi are the diffusion barrier and the seed layer which were sol-gel spin coated. The PZT solution has a composition of Pb/(Zr+Ti) of 118/100 along with a Zr/Ti ratio of 52/48, is spun on the substrate at 500 rpm for 5s and 3000 rpm for 30 s. The precursor gel film is pyrolyzed at 390 ◦C for 5 min on a hot plate. This deposition process cycle is repeated twice to make a PZT layer of 150nm thickness. The PZT film is then annealed at 700 ◦C for 1 min. PECVD silicon nitride and dioxide as the passivation layers are deposited on top to balance the stress in the stack. Reactive ion etching (RIE) is used to etch through the whole silicon dioxide and nitride stack from the top to define the beam structure and leave openings to the contact pads, and from the backside to pattern the frame and proof mass, leaving opening for the deep reactive ion etching (DRIE). Finally, etching through the whole wafer thickness from the back (DRIE) releases the device. An extra step of XeF_2 etching is used to gently remove the residual silicon. A photo of the released device is displayed in Fig. 4.

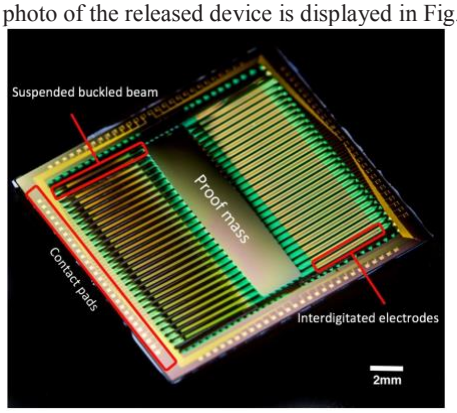

Figure 4. Photo of the released device.

EXPERIMENTAL RESULTS

The released beam show buckling that are visible to naked eyes. To accurately characterize the buckling and verify the bi-stability of the buckled structure, optical profiling of the surface was performed. Wyko NT9800 optical profilometer was used to scan the surface profile, and the stitching assembled multiple scans to cover the whole beams' surface profile. The surface profile of the whole device is shown in Fig. 5(a). The 28 beams on the same device show good consistency in buckling, and the measured surface profile matches well with the design (Figure 3). The device's surface was scanned first with top surface facing up, and then flipped so the beams buckle to the other direction and the bottom surface of the beams are scanned. Since the weight of the proof mass applies 1g loading to the beam structure, which is higher than the threshold of the snap, we could observe the bi-stable buckling (Fig.5(b)). The buckling in both directions shows similar mid-point deflection within 5% from designed value of 200µm, which demonstrates no significant asymmetrical stress distribution that leads to only one direction buckling. The surface profile and the large buckling in longitudinal direction also proves the narrow beam width effectively eliminates the buckling in the transverse direction and preserves the buckling in the desired direction.

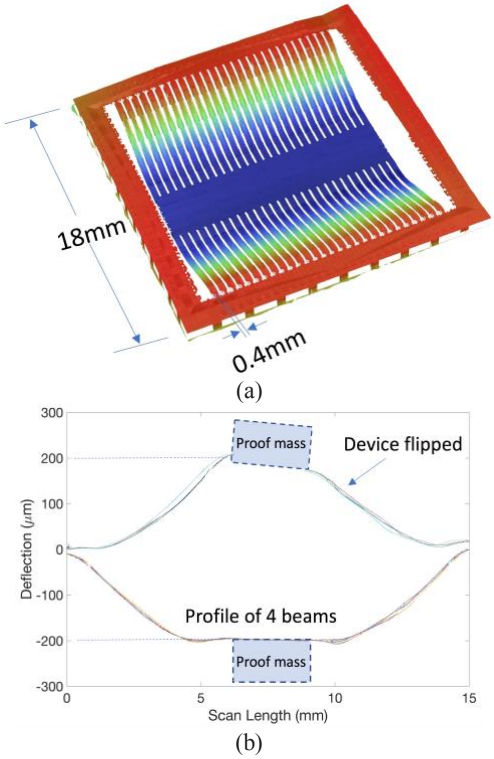

Figure 5. Surface profile scan: (a) Three-dimensional representation of the whole surface of the released device. (b) Surface profile of four beams showing the buckling on both sides (bi-stable) at around 200 µm.

The dynamic testing of the device further validated the design concepts that the buckled beam device could have large-amplitude oscillations with low-frequency and low-amplitude inputs (<100Hz and 0.5g). The frequency response was obtained by measuring the deformation of the beam with controlled input vibrations. The device was mounted on an electromagnetic shaker, whose vibration was monitored by an accelerometer (Analog Device ADXL335), and the input harmonic signal's frequency and amplitude are controlled by the signal generator (Prema ARB1000) and the power amplifier (Labworks PA138). A laser vibrometer (Polytec Scanning Vibrometer PSV300) was employed to measure the velocity of different spots on the device to calculate the relative movement of the beam to the frame.

The input harmonic vibrations were set at fixed frequencies below 100Hz and at different input amplitude level below 0.5g. The device was tested with an initial static state, and the input vibration's amplitude increase to reach the target value at a constant frequency. In this way, we could make the device start with lowest energy state and observe if the input energy was enough to trigger the snap. The relative displacement of the mass

to the frame was calculated by subtract the displacement amplitude of the mass by the displacement amplitude of the frame. Since the vibrometer cannot scan the two spots simultaneously but only sequentially, the phase difference cannot be obtained, especially with the abrupt bi-stable snapping that may not be perfectly the same in each cycle. The estimation is an underestimation as a result, since the phase difference between the two is not always 180°. But the trend shows large amplitude snap in a wide frequency range below 100Hz. With the proof mass of the wafer-thick central silicon proof mass ($13.9mm \times 3mm \times 525\mu m$), the frequency response is shown in Fig. 6.

The harvester with an added tungsten mass was also connected to a load resistor ($1M\Omega$) to measure the power consumed as an indication of the generated power. The voltage across the resistor is measured at a sample rate of 5.2 kHz. The power consumed by the resistor is calculated as $P = V^2/R$. During a period of 3.2s, the peak voltage is identified for each fixed frequency and amplitude and is used to calculate the peak power. At 0.5g, the peak power spectrum shows 50% of the jump-down frequency half-power bandwidth from 30Hz to 70Hz (Fig. 11).

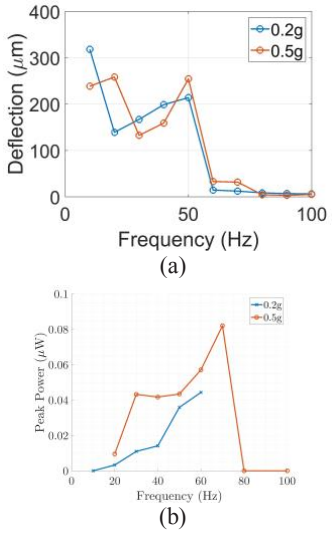

Figure 6. (a) Dynamic testing: displacement of the mass relative to the frame at ultra-low frequencies (silicone mass). (b) The peak power on a 1MΩ load resistor (with added 0.22g tungsten mass).

CONCLUSION

Bi-stable nonlinear oscillator-based energy harvester is realized and demonstrated at MEMS scale for the first time. The MEMS buckled beam oscillator utilizes the large-displacement snapping motion in a wide bandwidth at low frequencies to generate power. Residual stress is intentionally introduced and controlled along the MEMS monolithic fabrication processes of 10 thin film layers. Compression induced buckling of the release device was about $200\mu m$, which is within 5% of the designed amount. Static testing demonstrated the bi-stability of the buckled beam. Dynamic testing of the first-batch fully functional energy harvester with PZT thin film demonstrates the state-of-the-art operating conditions of MEMS energy harvesters of 50% bandwidth below 70Hz at 0.5g input with a peak power of 85nW.

ACKNOWLEDGEMENT

This work is supported by the funding from the MIT-SUTD International Design Center.

REFERENCES

[1] A. Hajati and S.-G. Kim, "Ultra-wide bandwidth piezoelectric energy harvesting," Appl. Phys. Lett., vol. 99, no. 8, p. 83105, 2011.

[2] Kim, In-Ho, et al. "A performance-enhanced energy harvester for low frequency vibration utilizing a corrugated cantilevered beam." Smart Materials and Structures 23.3 (2014): 037002.

[3] Xu, Chundong, et al. "Cantilever driving low frequency piezoelectric energy harvester using single crystal material 0.71 Pb (Mg1/3Nb2/3) O3-0.29 PbTiO3." Applied Physics Letters 101.3 (2012): 033502.

[4] Massaro, Alessandro, et al. "Freestanding piezoelectric rings for high efficiency energy harvesting at low frequency." Applied physics letters 98.5 (2011): 053502.

[5] Deng, Jiadong, et al. "Topology optimization and fabrication of low frequency vibration energy harvesting microdevices." Smart Materials and Structures 24.2 (2014): 025005.

[6] Liu, Huicong, et al. "A new S-shaped MEMS PZT cantilever for energy harvesting from low frequency vibrations below 30 Hz." Microsystem technologies 18.4 (2012): 497-506.

[7] Liu, Wen, et al. "Low frequency wide bandwidth MEMS energy harvester based on spiral-shaped PVDF cantilever." Science China Technological Sciences 57.6 (2014): 1068-1072.

[8] Edamoto, M., et al. "Low-resonant-frequency micro electret generator for energy harvesting application." Micro Electro Mechanical Systems, 2009. MEMS 2009. IEEE 22nd International Conference on. IEEE, 2009.

[9] Xie, Mengying, Kean C. Aw, and Wei Gao. "A multi-layered polydimethylsiloxane structure for application in low-excitation, broadband and low frequency energy harvesting." Sensors and Actuators A: Physical 222 (2015): 140-148.

[10] Jung, Seok-Min, and Kwang-Seok Yun. "Energy-harvesting device with mechanical frequency-up conversion mechanism for increased power efficiency and wideband operation." Applied Physics Letters 96.11 (2010): 111906.

[11] Pillatsch, Pit, Eric M. Yeatman, and Andrew S. Holmes. "A piezoelectric frequency up-converting energy harvester with rotating proof mass for human body applications." Sensors and Actuators A: Physical 206 (2014): 178-185.

[12] Burgueno R, Lajnef N 2013 *United States patent application* US 13/960,356

[13] Halim, Miah A., and Jae Y. Park. "Theoretical modeling and analysis of mechanical impact driven and frequency up-converted piezoelectric energy harvester for low-frequency and wide-bandwidth operation." Sensors and Actuators A: Physical 208 (2014): 56-65.

[14] A. Erturk, J. Ho mann, and D. J. Inman, "A Piezomagnetoelastic Structure for Broadband Vibration Energy Harvesting," Applied Physics Letters, 94(25):254102, 2009.

[15] F. Cottone, et al., "Piezoelectric Buckled Beams for Random Vibration Energy Harvesting," Smart Materials and Structures, 21(3):035021, 2012.

[16] R. Xu, and S.-G. Kim, "Modeling and Experimental Validation of Bi-Stable Beam Based Piezoelectric Energy Harvester." Energy Harvesting and Systems 3.4 (2016): 313-321.

CONTACT

*Sang-Gook Kim, tel: +1-617-452-2472; sangkim@mit.edu

A SINGLE-CRYSTAL SILICON RESONATOR FOR AM DEMODULATION WITH ADDED SECOND-HARMONIC MODULATION

Mary E. Galanko[1], Yi-Chung Lin[1], Tamal Mukherjee[1], and Gary K. Fedder[1,2]*
[1]Department of Electrical and Computer Engineering and [2]The Robotics Institute
Carnegie Mellon University, Pittsburgh, PA

ABSTRACT

We report a single-crystal silicon MEMS resonator that functions as a demodulator in a near-zero-power wake-up receiver. The receiver detects an AM signal at a certain carrier frequency f_c and primary modulation frequency f_m; the demodulator resonates and filters at f_m and leverages the quadratic dependence of electrostatic force upon input voltage to convert from high-frequency to baseband. Two key advantages are passive operation and very high out-of-band rejection. In order to increase the sensitivity of the demodulator, we propose the use of additional second-harmonic modulation to increase the response amplitude for a given AM input power. This work considers both the resulting parametric force, which is negligible, and additional direct force, a significant component. This device is the first to our knowledge to demonstrate multi-harmonic mixing and investigate parametric amplification in response to an amplitude-modulated (AM) signal with added modulation at a second-harmonic pumping frequency.

INTRODUCTION

A "wake-up" receiver (WuR) is designed to detect the presence of a particular signal while consuming very little power. When a signal is present, the WuR produce a voltage change that triggers higher-power circuitry to process the signal, so that the radio is continuously alert to the signal yet does not consume this high processing power when no signal is present. The bulk Si MEMS resonator in this work serves as a near-zero-power demodulator for use in a WuR. This device builds upon past work and designs [1] in a different technology while exploring the nonlinear response of these devices to multi-frequency modulation. This modulation scheme has not been considered in this application but carries advantages in demodulator sensitivity.

Motivation

To maximize battery life and hence maximize the advantage of a WuR, it should operate at as little power as possible. The active blocks of an AM receiver generally include a front-end filter, a demodulator, and baseband signal processing circuitry. One approach [2] to minimizing power is to implement the front-end and demodulator at near-zero power using passive MEMS devices, so that the only significant power consumption is in the final baseband stages, which may consume only tens of nW.

The front-end is a lithium niobate (LN) piezoelectric resonator [3], which operates around 40-400 MHz, filtering and increasing the voltage of AM signals with a particular carrier frequency in that range. The demodulator is a capacitive MEMS resonator, operating around 50-200 kHz. As recently demonstrated in a CMOS-MEMS implementation [1], the demodulator leverages the quadratic dependence of capacitive electrostatic force upon drive voltage to generate forces at various frequencies, including the resonance f_r. The system will only respond significantly and produce a "wake-up" signal when the demodulator is forced at f_r via to the modulation frequency f_m of the input signal. This property affords the MEMS demodulator a major advantage in false alarm rate compared with a CMOS envelope detector, where sharply filtering around f_m would consume too much additional power.

In this complex, multi-technology system, system-level optimization is critical to achieve performance goals. Given design limits of each device, impedance matching between all three stages is the primary factor in performance [2]. This system context impacts the MEMS demodulator technology and design choices.

Background

Several past works [4-6] have proposed the use of MEMS devices as passive mixers. Koskenvuori et al. [7] implemented a capacitive MEMS resonant mixer that used the same quadratic mechanism to convert an AM signal to baseband, but noted the problem of low sensitivity and conversion efficiency. This problem is always a concern in designs that spread the input signal power in frequency, but is addressed in [1] by system-level optimization that identifies a matched design for sufficient sensitivity.

Few works have explored multi-frequency forcing and mixing. Koskenvuori and Tittonen proposed a modified resonant mixer design that improves sensitivity via parametric amplification [8]. Thompson and Horsley [9] have shown that parametric amplification can increase the sensitivity of a magnetometer. However, both of these works required a local oscillator. We investigate the possible advantages of multi-frequency mixing in a demodulator specifically for a near-zero-power RF WuR. Because the power budget precludes the use of a local oscillator, this work uniquely considers force variations created by changing the modulation of a low-power AM input signal. This condition greatly limits the use of parametric amplification, but brings advantages in direct force.

The "Epi-Seal" process [10], in 60 μm bulk Si, is used partly because it offers larger capacitances and better impedance matching according to the findings in [2] relative to CMOS-MEMS. A CMOS-MEMS demodulator offers direct integration with the baseband circuit, but less capacitance per unit area is possible than in a very thick bulk Si process. For a given gap size, higher capacitance per unit area also maximizes parametric force, providing a better platform to test feasibility of parametric forcing.

MULTI-SIDEBAND FORCING

Figure 1 shows an equivalent circuit for the demodulator. The electrostatic force acts upon a basic mechanical resonator to produce an AC output current i_{mot} proportional to velocity and polarization V_P. Assuming no loading by the readout circuit, and neglecting

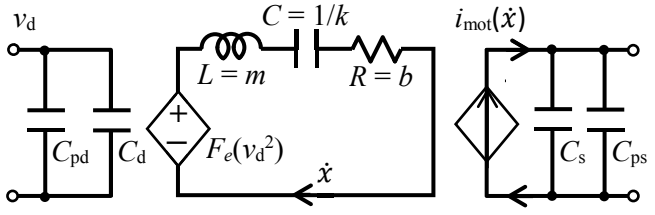

Figure 1: Equivalent circuit of the demodulator, a mass-spring-damper with force $F_e \propto v_d^2$. Input and output loads include device capacitances C_d, C_s and parasitic capacitances C_{pd}, C_{ps}.

978-1-940470-03-0/HH2018/$25©2018TRF
DOI 10.31438/trf.hh2018.97

mechanical and electrostatic nonlinearities due to small displacement, the demodulator is governed by the canonical equation of motion (EoM) in displacement x:

$$m\ddot{x} + b\dot{x} + k_{eff}x = F_e \tag{1}$$

where m is the effective mass of the device; b is the damping coefficient; and $k_{eff} = k_0 + k_e$ is the effective spring constant after electrostatic softening $k_e < 0$ of the mechanical spring k_0.

The demodulator is sensitive to arbitrary input waveform shapes and carrier frequencies. It mixes the voltage V_d across its drive capacitance C_d according to

$$F_e = \frac{1}{2}{V_d}^2\frac{\partial C_d}{\partial x} \tag{2}$$

Plugging an AM waveform with amplitude V_{in} into (2) yields

$$\begin{aligned} F_e &= \frac{1}{2}\frac{\partial C_d}{\partial x}[V_{in}\cos(\omega_c t)\cdot 0.5\,(1+\cos(\omega_m t))]^2 \\ &= \frac{{V_{in}}^2}{8}\left(\frac{1+\cos(2\omega_c t)}{2}\right)\left(\frac{1+\cos(2\omega_m t)}{2}+2\cos(\omega_m t)+1\right) \end{aligned} \tag{3}$$

The largest low-frequency force component is at ω_m. If $\omega_m = \omega_r$, this force drives the demodulator into resonance. There is also a smaller force component at $2\omega_m$.

From this force equation, we aim to quantify the direct and parametric forces possible during AM demodulation and measure their effects. Neglecting out-of-band force terms, the EoM may be rewritten successively from (1), (3) to reach the final form

$$m\ddot{x} + b\dot{x} + k_{eff}x = F_1\cos(\omega_m t) + F_2\cos(2\omega_m t) \tag{4}$$

$$m\ddot{x} + b\dot{x} + \left(k_{eff} + \Delta k\sin(2\omega_m t)\right)x = F_1\cos(\omega_m t + \varphi) \tag{5}$$

where

$$F_1 = \frac{{V_{in}}^2}{8}\frac{\partial C_d}{\partial x}, F_2 = \frac{{V_{in}}^2}{16}\frac{\partial C_d}{\partial x}, \Delta k = -\frac{\partial^2 C_d}{\partial x^2}\frac{{V_{in}}^2}{16} \tag{6-8}$$

and $\varphi = \pi/2$ using the input waveform in (5) where the direct and parametric forces are in phase. Past work [9,11] has shown that in systems of this EoM form, the parametric forcing term results in an output current amplification factor

$$G = \left[\left(\frac{\cos\varphi'}{1+{Q\Delta k}/{2k_0}}\right)^2 + \left(\frac{\sin\varphi'}{1-{Q\Delta k}/{2k_0}}\right)^2\right]^{1/2} \tag{9}$$

$$G|_{\varphi={\pi}/{2}} = \left(1-{Q\Delta k}/{2k_0}\right)^{-1/2} \tag{10}$$

For values achievable in the Epi-Seal demodulator ($Q = 10000$, $\Delta k = 10^{-4}$ N/m, $k = 130$ N/m, $V_{in} = 30$ mV), this amplification is not significant (< 1%).

Adding AM sidebands at $2\omega_m$ with generic amplitude B and phase φ relative to the modulation at ω_m, the input force (3) becomes

$$\begin{aligned} F_e = \frac{1}{2}\frac{\partial C_d}{\partial x}&[V_{in}\cos(\omega_c t) \\ &\cdot 0.5(1+\cos(\omega_m t) + B\cos(2\omega_m t+\varphi))]^2 \end{aligned} \tag{11}$$

Expanding and isolating force terms at ω_m and $2\omega_m$ yields

$$\begin{aligned} F_e = \frac{{V_{in}}^2}{8}&\left(\frac{1+\cos(2\omega_c t)}{2}\right)\left[\frac{1}{2}\cos(2\omega_m t)\right. \\ &\left.+2B\cos(2\omega_m t+\varphi) + 2\cos(\omega_m t) + B\cos(\omega_m t+\varphi)\right] \end{aligned} \tag{12}$$

These additional terms change Δk only incrementally, resulting in only minimal change in the parametric amplification gain G (10). Conversely, the direct force increases significantly with B:

$$\Delta k = -\frac{\partial^2 C_d}{\partial x^2}\frac{{V_{in}}^2}{16}\left[2B\cos(\varphi) + \frac{1}{4} + 4B^2\right]^{1/2} \tag{13}$$

$$F_e|_{\omega=\omega_m} = \frac{{V_{in}}^2}{16}\frac{\partial C_d}{\partial x}[B^2 + 4B\cos\varphi + 4]^{1/2} \tag{14}$$

The addition of $2\omega_m$ sidebands also changes the ratio of force at ω_m to total normalized input signal power P_0:

$$\begin{aligned} P_0 = P_{in}\cdot Z_{in} = {V_d}^2(t) &= \frac{1}{2}\left(\left(\frac{V_{in}}{2}\right)^2 + 2\left(\frac{V_{in}}{2}\right)^2 + 2\left(\frac{B\cdot V_{in}}{2}\right)^2\right) \\ &= \frac{{V_{in}}^2}{16}(B^2+3) \end{aligned} \tag{15}$$

$$\frac{F_e|_{\omega=\omega_m}}{P_{in,0}\cdot Z_{in}} = \frac{\partial C_d}{\partial x}\frac{[B^2 + 4B\cos\varphi + 4]^{1/2}}{B^2+3} \tag{16}$$

This relationship is not monotonic but results in greater F_e for fixed P_0 for certain sideband amplitudes B. The device and tests in this work validate these models.

DEMODULATOR DESIGN

The Epi-Seal process fabricates devices in a 60 µm silicon-on-insulator (SOI) device layer using a Bosch silicon etch process with on-chip epitaxial vacuum encapsulation [10,12]. The process is well-understood and reliable for certain applications, but for low-frequency capacitive resonators, it presents yield risks and imposes important design constraints. The maximum silicon etch aspect ratio restricts the minimum layout gap size to 0.7 µm, and the cap deposition process limits the maximum width of a continuous released area to about 450 µm [12]. Furthermore, past work in this process has shown that low-spring constant, high-capacitance Epi-Seal resonators at around 100 kHz are prone to post-release stiction.

Figure 2 shows a layout view of the resulting demodulator design. It consists of a proof mass with capacitive rotor comb fingers, anchored through in-plane springs. The rotor fingers

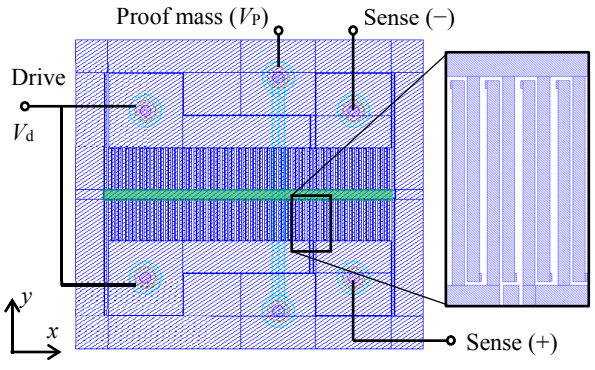

Figure 2: Epi-Seal demodulator layout diagram. Green denotes the proof mass, with fixed-fixed spring beams on either end. The inset shows the capacitive comb finger geometry. The device moves in x.

interface with fixed stator comb fingers for drive and sense transduction. The device moves perpendicular to the fingers so that resonant motion varies the parallel-plate gap size. V_P is applied across the sense comb fingers to produce an output motional current i_{mot} proportional to this displacement:

$$i_{mot}(t) = V_P \frac{\partial C_x}{\partial x}\frac{\partial x}{\partial t} \approx V_P \frac{\partial C_x}{\partial x}\frac{F_e Q}{k_{eff}} \quad (17)$$

To prevent substrate stiction, the proof mass area is minimized, and the springs are fixed-fixed beams designed to maximize out-of-plane stiffness. The risk of stiction between the rotor and stator comb fingers depends mostly on the device capacitance (i.e., comb finger area and geometry) and frequency. For this application, the demodulator resonant frequency was fixed at around 50 kHz, and among designs with various total capacitance, we use the highest-capacitance device that is found to be fabricated without in-plane stiction. The device contains a total of $N_d = 58$ drive and $N_s = 22$ sense comb fingers. These and other design values are summarized in Table 1.

Table 1: Quantitative details of the demodulator design used.

Variable	Description	Value	Unit
m_{eff}	Effective mass	$1.77 \cdot 10^{-9}$	kg
k_{eff}	Effective spring	132	N/m
Δk	Parametric k variation	$8.29 \cdot 10^{-5}$	N/m
C_1	Comb pair capacitance	16.7	fF
N_d	# drive comb fingers	58	-
N_s	# sense comb fingers	22	-

The comb finger capacitance C_1 is adjusted to measurements by modifying the gap size in calculations to correct for bloat. A bloat of about 400 nm per side from the layout gap dimension of 0.7 µm gives a comb finger width of about 2.2 µm, as validated in Figure 3, and total device capacitance of about 2.1 pF, which agrees reasonably with measurements, as detailed in the following section.

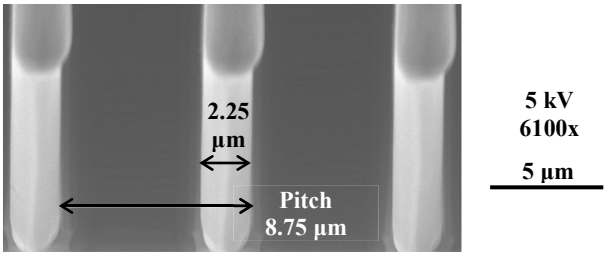

Figure 3: SEM image of an axial view of demodulator comb fingers (stators only), showing the finger width and pitch, which validate the effective parallel plate gap size used in analysis.

RESULTS

Basic frequency response measurements are performed first to characterize the resonator, followed by tests to validate models (14)-(16) for $2\omega_m$ demodulation. Figure 4 shows a frequency response for direct harmonic forcing, where a polarization V_P is applied across both drive and sense comb fingers, so that the output current is a response to a low-frequency AC voltage and force at f_m. Drive voltages < 1 mV are still in the linear regime. In the nonlinear regime, there is a hardening nonlinearity contributed by the fixed-fixed beam springs and an electrostatic softening nonlinearity from the parallel-plate comb fingers, but the mechanical hardening

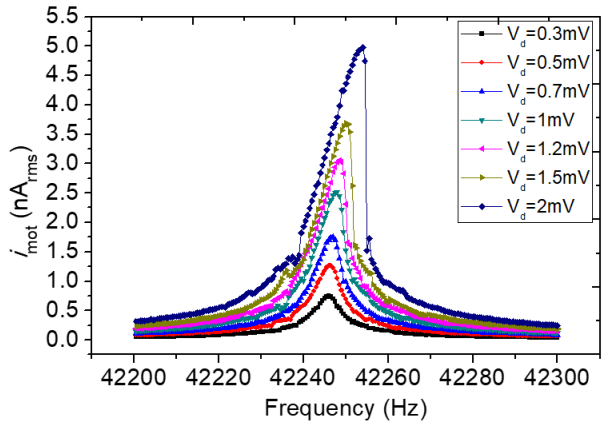

Figure 4: Frequency response of the resonant demodulator to direct harmonic drive for V_P = 2.5 V and various AC drive amplitudes V_d.

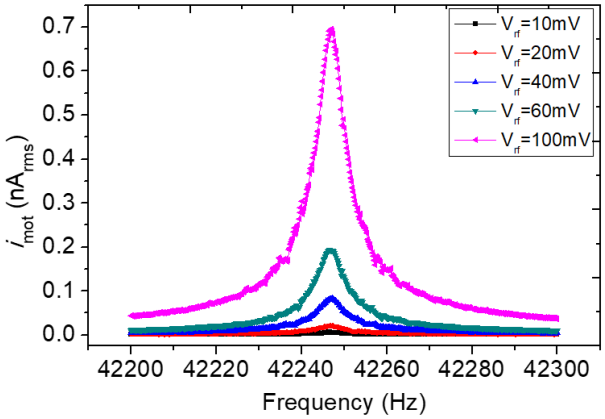

Figure 5: Demodulation of AM input signal with amplitude $V_{in} = V_{rf}$, in response to a sweep of the modulation frequency around resonance. The sense polarization is V_P = 2.5 V; the drive comb fingers have no DC bias. The response scales quadratically with V_{in}.

nonlinearity is greater. Focusing on linear k_{eff} to simplify analysis and focus on the small signals relevant to the WuR, these linear responses agree with models within about 15%. Figure 5 shows pure AM forcing results, with no second-harmonic modulation. These measurements also reasonably agree with calculations, within about 15% for low amplitudes in the linear regime.

Next, sidebands at $2\omega_m$ were added to the original AM input signal, as depicted in Figure 6. As the relative amplitude B and phase φ vary, the response scales in agreement with the expected amplification relation in (16). For fixed $B = 1$, Figure 7(a) shows response scaling for various φ; these values agree with expected scaling (16) within about 17%. Phase $\varphi = 0$ yields a maximal

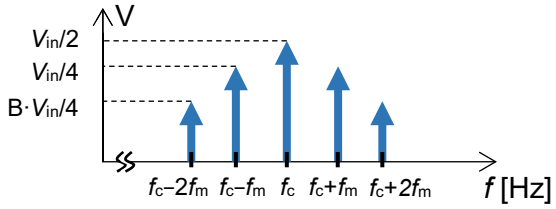

Figure 6: Frequency domain representation of the AM signal with second-harmonic modulation of relative amplitude B.

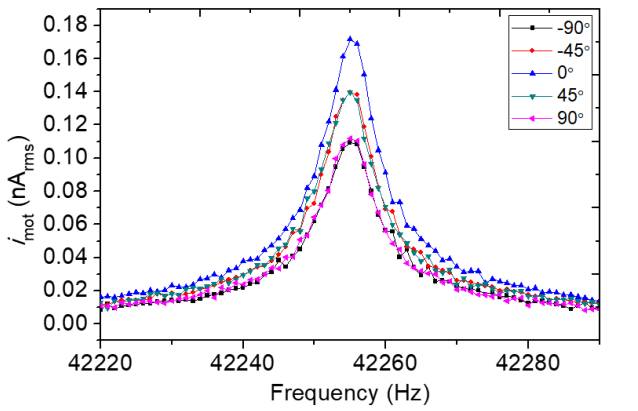

(a)

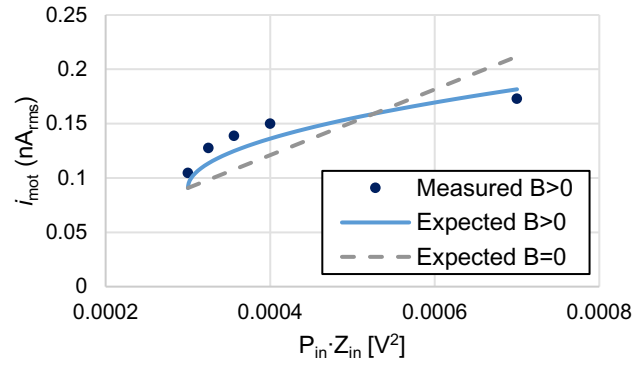

(b)

Figure 7: (a) Response with V_{in} = 40 mV, B = 2, and various phases φ of the 2ω_m modulation relative to the ω_m modulation. (b) Response to similar signals with V_{in} = 40 mV, φ = 0, and various relative 2ω_m modulation amplitudes B. For B > 0, power varies only by varying B; B = 0 data represent pure AM signals at the same power.

response increase as expected. Figure 7(b) shows scaling for various B and P_0, also in agreement with (14-16), with an average error of about 11%. For $B \approx 0.5$, there is an increase in response normalized to input power. Intuitively, this result and (16) show that adding sidebands at $2\omega_m$ marginally increases the convolution product at baseband and hence may increase the efficiency of input signal power to resonant force, but for large B, too much input signal power goes into other force components, diminishing efficiency.

CONCLUSIONS

This work presents a single-crystal vacuum-encapsulated bulk silicon resonant demodulator for a wake-up receiver. The device resonates in response to AM signals with any carrier frequency and any modulation envelope shape such that the quadratic force vs. V_{in} relationship yields a force at the resonance ω_m. For certain device designs and input signals, modulation at both ω_m and $2\omega_m$ may increase the power of the post-mixing force component at ω_m, for a given input signal power, and hence increase device performance. A $2\omega_m$ modulation also increases the force at frequency $2\omega_m$, but significant parametric amplification is difficult to achieve solely from this low input force rather than a local oscillator.

In summary, using an input waveform of this form incrementally increases demodulator sensitivity for certain B, but additional design techniques are needed to achieve orders-of-magnitude improvement in sensitivity. However, the demonstration of multi-harmonic direct forcing in this work shows that a MEMS resonant WuR may be tuned to complex multi-frequency signals, while offering the same power and out-of-band rejection advantages that this architecture offers for simple AM input signals.

ACKNOWLEDGMENTS

This work was supported by the Defense Advanced Research Projects Agency (DARPA) under contract No. HR0011-15-C-0137. Any opinions, findings, and conclusions or recommendations expressed in this publication are those of the authors and do not necessarily reflect the views of DARPA.

Demodulator fabrication was performed by the Micro Structures & Sensors Lab at Stanford University. The authors thank the principal investigator, Prof. T.W. Kenny, and thank L.C. Ortiz and D. Shin for valuable fabrication and layout support.

REFERENCES

[1] M.E. Galanko, A. Kochhar, G. Piazza, T. Mukherjee, and G.K. Fedder, "CMOS-MEMS resonant demodulator for near-zero-power RF wake-up receiver," in *TRANSDUCERS 2017*, Kaohsiung, Taiwan, 2017, pp. 86-89.

[2] L. Colombo, M. Galanko, H. Abdelsalam, G. Vidal-Álvarez, T. Mukherjee, J. Paramesh, J. Weldon, G.K. Fedder, and G. Piazza, "Ultra-Low-Power and High Sensitivity Resonant Micromechanical Receiver," in *IEEE Sensors*, Glasgow, UK, 2017.

[3] F. Pop, A. Kochhar, G. Vidal-Álvarez, and G. Piazza, "Laterally vibrating lithium niobate MEMS resonators with 30% electromechanical coupling coefficient," in *IEEE Int. Conf. on Microelectromechanical Systems*, Las Vegas, NV, 2017, pp. 966-969.

[4] C.T.-C. Nguyen, "Transceiver front-end architectures using vibrating micromechanical signal processors," in *IEEE Topical Meeting on Silicon Monolithic Integrated Circuits in RF Systems*, Ann Arbor, MI, 2001.

[5] G.K. Fedder, "CMOS-MEMS resonant mixer-filters," in *IEEE Int. Electron Devices Meeting,* Washington, DC, 2005.

[6] F. Chen et al., "CMOS-MEMS resonant RF mixer-filters," in *IEEE Int. Conf. on Microelectromechanical Systems*, Miami, FL, 2005, pp. 24-27.

[7] M. Koskenvuori, I. Tittonen, and A. Alastalo, "GHz-range FSK-reception with microelectromechanical resonators," *Sensors and Actuators A*, vol. 147, no. 1, Sept. 2007, pp. 346-351.

[8] M. Koskenvuori and I. Tittonen, "Improvement of the conversion performance of a resonating multimode microelectromechanical mixer-filter through parametric amplification," *Electron Device Lett.*, vol. 28, no. 11, Nov. 2007, pp. 970-972.

[9] M. J. Thompson and D. A. Horsley, "Parametrically amplified Z-axis Lorentz forced magnetometer," *J. Microelectromech. Sys.*, vol. 20, no. 3, June 2011, pp. 702-710.

[10] R.N. Candler, M.A. Hopcroft, B. Kim, W.-T. Park, R. Melamud, M. Agarwal, G. Yama, A. Partridge, M. Lutz, and T.W. Kenny, "Long-term and accelerated life testing of a novel single-wafer vacuum encapsulation for MEMS resonators," *J. Microelectromech. Sys.*, vol. 15, no. 6, 2006, pp. 1446-1456.

[11] D. Rugar and P. Grutter, "Mechanical parametric amplification and thermomechanical noise squeezing," *Phys. Rev. Lett.*, vol. 67, no. 6, pp. 699–702, Aug. 1991.

[12] D. Shin, "Invitation to Design in the Next Epi-Seal Run: Hot Dog XV and Dorayaki V," Stanford University, 2016.

CONTACT

*M.E. Galanko, tel: +1-412-216-5759; galanko@cmu.edu

CROSS-SECTIONAL QUASI- LAMÉ MODES IN THIN-FILM PIEZOELECTRIC-ON-SILICON RESONATORS

Sarah Shahraini[1], Hedy Fatemi[2] and Reza Abdolvand[1]
[1] University of Central Florida, Orlando, Florida, USA
[2] Qorvo, Apopka, Florida, USA

ABSTRACT

In this work, it is demonstrated for the first time that cross-sectional quasi-Lamé modes (CQLM) could be efficiently excited in silicon with reasonably high quality factor (*Q*). Third-harmonic Lamé modes of a silicon block are piezoelectrically exited in thin-film-piezoelectric on silicon (TPoS) resonators in which the thickness is chosen to be in proximity of half acoustic wavelength. Finite element analysis is used to show that the support loss in these resonators could be reduced by an order of magnitude through usage of acoustic isolation techniques. A quality factor of 14,500 is measured in partial vacuum for a third-harmonic 67 MHz CQLM-TPoS resonator designed within a circular acoustic isolation frame and fabricated on a 40μm thick silicon-on-insulator (SOI) substrate.

INTRODUCTION

Planar Lamé modes are commonly excited in capacitive silicon resonators at low-frequencies (MHz regime) and offer unique properties such as turn-over temperatures higher than any other conventional modes in degenerately doped silicon [1]. Such resonators are great candidates for extremely stable reference oscillators (e.g. oven controlled MEMS oscillators).

Planar Lamé modes, however, can't be efficiently excited in silicon through piezoelectric transduction. This is because the sputtered piezoelectric thin-films such as AlN are isotropic in the plane of the substrate. Therefore, the opposing in-plane stress components of a planar Lamé mode, result in near-zero charge accumulation on metal electrodes placed across the thin piezoelectric film (Fig.1).

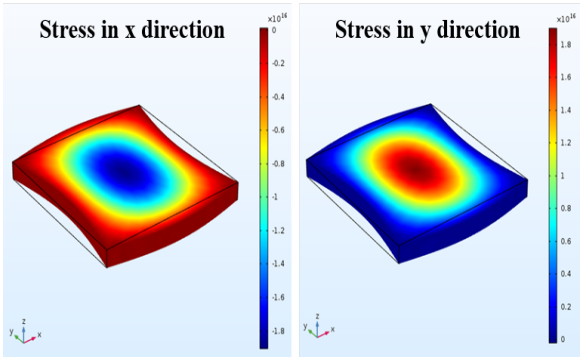

Figure 1: The simulated stress field in x and y direction for a planar Lamé mode. In each half vibration cycle, stress field is tensile in one direction and compressive in the other direction and because of that, such planar Lamé mode cannot be excited piezoelectrically.

On the other hand, Cross-sectional Lamé mode resonators (CLMR) have been recently demonstrated in thin-film AlN resonators [2,3] by targeting Lamé modes in the thickness of the AlN slab. These resonators offer coupling factors larger than what is achievable in lateral-extensional mode (contour-mode) resonators due to the fact that in CLMRs both d_{31} and d_{33} piezoelectric coefficients constructively contribute in the excitation of a two-dimensional mechanical vibration (excitation of the Lamé mode in the cross section of AlN film). Contrary to the case of FBAR resonators in which the center frequency could mainly be tuned by varying the thickness of the resonator, in CLMRs the center frequency could be defined lithographically (to some degree) due to the dependency of center frequency on both the thickness of the film and also to the lateral (in-plane) dimension. However, the achievable center frequency is limited to relatively high frequencies since the thickness of the sputtered AlN layer can't be practically more than a few micrometers. Also to guarantee the maximum coupling factor, the wave displacement in lateral and thickness directions should be almost equal.

In this work we first demonstrate that cross-sectional *quasi*-Lamé modes (CQLMs) could be efficiently excited in silicon with reasonably high *Q* using a thin-film piezoelectric transducer sputtered on top of the substrate. Next, we will propose an acoustic isolation technique to effectively reduce support loss for the CQLM resonators implemented in the thin-film piezoelectric-on-silicon (TPoS) platform. Finally, the frequency responses measured for CQLM-TPoS resonators fabricated on a relatively thick silicon-on-insulator (SOI) substrate (40μm) are presented in partial vacuum.

CQLM-TPOS RESONATORS

Overtone lateral-extensional (contour) resonance modes of a silicon block have been utilized in TPoS resonators to achieve a wide range of frequencies in the past [4,5]. In such resonators the d_{31} piezoelectric coefficient is mainly responsible for energy coupling between the mechanical and electrical domains as the z-axis electric field between the metal electrodes is transduced to in-plane xy stress and vice versa. The higher harmonics in such resonators are excited by forming an interdigitated electrode pattern on the rectangular resonator body (Fig. 2.a). The distance between two adjacent fingers is called the finger pitch (*FP*) and is equal to the half wavelength. *FP* is typically chosen larger than the thickness of the silicon block as a clean lateral-extensional mode shape is only achieved if the thickness to wavelength ratio is small. The simulated mode-shape of a 126μm × 50μm × 8μm (6μm silicon+2μm AlN) thin-film piezoelectric-on-silicon (TPoS) slab is presented in Fig. 2.b.

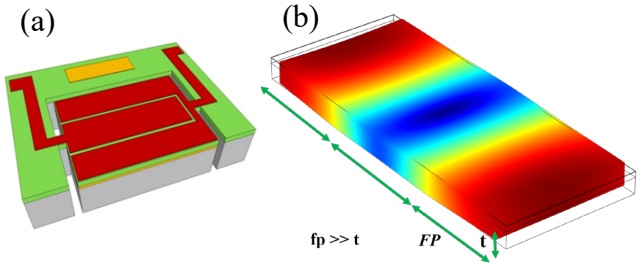

Figure 2: A schematic viewgraph of a two-port third-order TPoS resonator (a) and the Stress field for lateral-extensional mode TPoS resonator(b).

978-1-940470-03-0/HH2018/$25©2018TRF
DOI 10.31438/trf.hh2018.98

In the same rectangular block resonator, the in-plane extensional mode will deform and finally cease to exist as the thickness of the slab approaches the finger pitch. Instead, in such structures a different resonance mode evolves in which a mode-shape similar to that presented in Fig. 1 develops on the cross section of the slab; hence the name cross-sectional Lamé modes [2]. This mode can be exited using the thin piezoelectric film deposited on the slab, as the electrical charge corresponding to the opposite in-plane and out-of-plane stress components will constructively combine through opposite signs of d_{31} and d_{33} piezoelectric coefficients in AlN (Fig. 3.a). It should be noted that this mode deviates from pure Lamé-mode properties as the presence of the AlN and the metal layers disrupts the symmetry of the acoustic medium in the cross section of the resonator. Therefore, we will refer to such modes as Cross-Sectional Quasi Lamé modes (CQLM).

The electrode design for these resonators is the same as those used in lateral-extensional mode resonators (i.e. interdigitated pattern). The third-order harmonic CQLM in a 126 µm (3×42 µm) × 50 µm × 42 µm (40µm silicon+2µm AlN) thin-film piezoelectric-on-silicon (TPoS) slab is presented in (Fig. 3.b). The total displacement is shown in 3D to emphasize the close resemblance of this mode to a pure Lamé mode; hence the name *quasi*-Lamé.

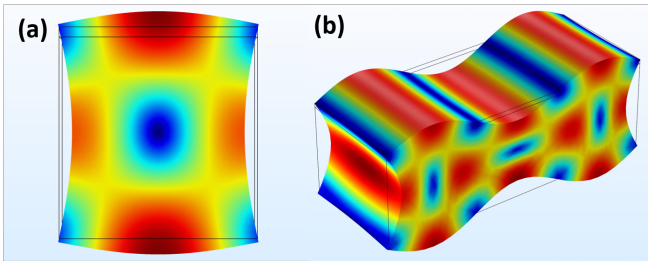

Figure 3:The simulated total displacement in a fundamental- (a) and third-harmonic (b) CQLM-TPoS resonator.

In this work, CQLM-TPoS resonators are fabricated with a finger pitch (35 µm or 51 µm) that differs from the thickness (42 µm). Nevertheless, the quasi-Lamé mode is detectable. The simulated mode shape for a third-harmonic CQLM in a 153 µm x 226 µm x 42 µm rectangular block is shown in Fig.4 highlighting the similarity of the mode to a pure Lamé.

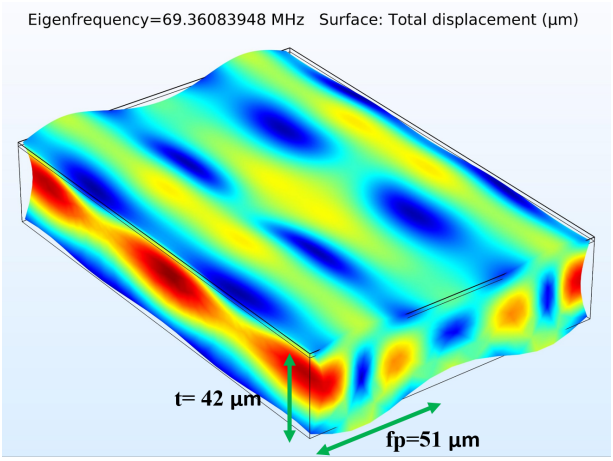

Figure 4: The simulated mode shape for a 153 µm×226 µm × 42 (40 µm of silicon + 2 µm AlN) block. The ~69 MHz simulated center frequency matches the 67 MHz measured center frequency fairly well.

SUPPORT LOSS IN CQLM-TPOS RESONATORS

Achieving reasonably high Q is crucial in most applications such as oscillators and sensors since resonator Q is directly impacting the system noise floor. For piezoelectric resonators, support loss, interface loss and electrical losses are the main sources of energy dissipation.

Common methods to avoid excessive support loss include: placing the tethers at pseudo-nodal points, optimizing tether geometry and dimensions, using planar acoustic reflector's, etc. For CQLM-TPoS resonators, there are no nodal points at the side of the resonator body. This is because, the Lamé mode is formed in the cross section of the resonator and therefore a large portion of the acoustic energy would be transferred to the substrate through tethers. Consequently, implementation of a planar acoustic reflector by etching trenches around the device [6,7] is an attractive solution. By placing these trenches at a proper distance, the reflected acoustic wave would constructively interfere with the standing waves inside the resonant body. In order to optimize the design of CQLM-TPoS resonator, a perfectly matched layer (PML)-based model is developed in COMSOL to predict the support Q. The PML region should be large enough to attenuate all the acoustic wave propagating through this medium.

In this work a novel circular frame around the resonator body is proposed to efficiently isolate the acoustic cavity from the substrate and to reduce the support loss. The COMSOL model used for simulating the support Q of a third-order CQLM-TPoS resonator enclosed within the acoustic isolation frame is shown in Fig. 5. A One-way symmetry is used in the model to reduce computational load.

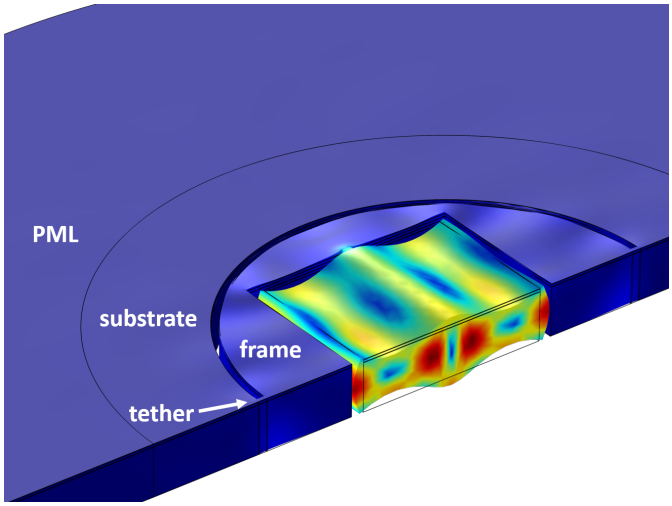

Figure 5: The PML-based finite element model developed for support loss prediction of a 153µm × 226µm × 42µm (silicon + AlN) device with isolation frame. There are no nodal points at the side of the resonator. For the resonators within an acoustic frame, the support loss is effectively reduced.

The dimension of the described acoustic isolation frame (i.e. the diameter) is varied to characterize the support Q. The simulated Q for the resonators with and without reflector frame confirm the substantial improvement that could be achieved with an isolation frame provided that the isolation frame is designed properly (Table.1). For the reflected wave to be constructively interfering with the resonator's standing wave, the acoustic isolation frame should have a diameter of $(2n\times\lambda/4) + 2 \times$ (tether-length). The support quality factor is improved by an order of magnitude when the frame diameter is an even factor of the quarter acoustic

wavelength. The optimum reflector distances are studied thoroughly in a recent work of our group [7].

Table 1: Modeled support quality factor for CQLM resonators with and without acoustic isolation frame

	Resonator without isolation frame	**Resonator with isolation frame**			
Isolation frame diameter	–	**$2\times tl + 3\lambda$**	**$2\times tl + 3\lambda + \lambda/4$**	**$2\times tl + 3\lambda + 2\lambda/4$**	**$2\times tl + 3\lambda + 3\lambda/4$**
***Q* (*k*)**	**4.5**	**40.1**	**3.4**	**61.2**	**7.6**

** In this table tl is the tether-length and λ is the acoustic wavelength.*

CQLM-TPOS RESONATORS FABRICATION

CQLM-TPoS resonators are fabricated on a relatively thick (40µm) degenerately n-type doped <100> SOI substrate in a five mask process. The sputtered AlN film is 2µm thick and is sandwiched between two 100nm thick layers of Molybdenum. First, the Mo/AlN/Mo stack would be sputtered and the top metal is dry-etched in an SF_6/O_2 plasma to shape the top electrodes (Fig. 6.a). Then, the AlN is wet etched in a heated TMAH solution to create access to the bottom electrode (Fig. 6.b). The resonator body is then shaped by plasma etching the full stack of material down to the SOI buried oxide (BOX) layer (Fig. 6.c). Handle layer silicon is then etched from the backside in a deep-reactive-ion-etching chamber using Bosch process and the resonator is finally released by wet etching the BOX layer in a buffered oxide etchant (BOE) (Fig. 6.d).

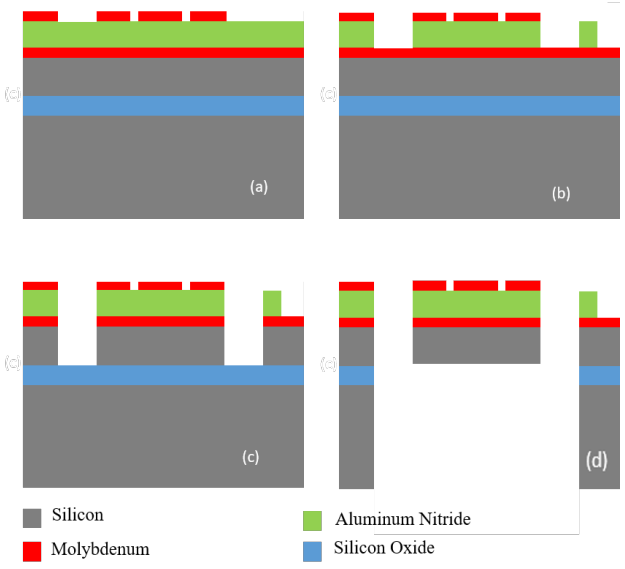

Figure 6: The simplified process flow for fabrication of the CQLM-TPoS resonators.

The scanning electron micrographs (SEMs) of two similar fabricated devices one directly connected to the substrate and the other surrounded with a circular acoustic isolation frame are shown in Fig.7 and Fig.8.

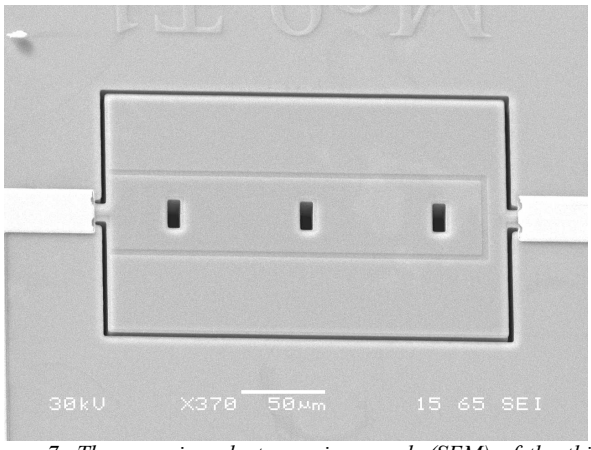

Figure 7: The scanning electron micrograph (SEM) of the third-order CQLM-TPoS resonators without acoustic isolation frame.

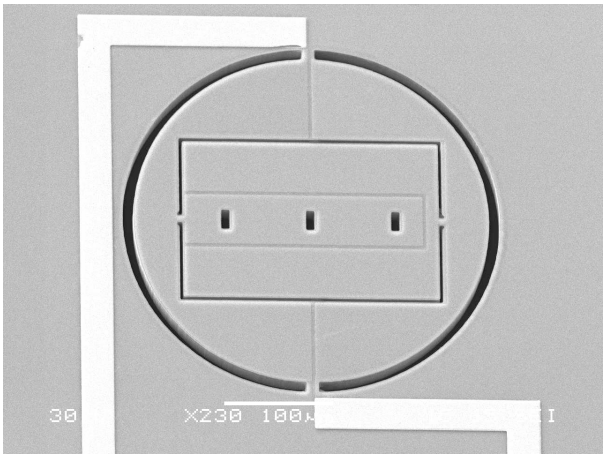

Figure 8: The scanning electron micrograph (SEM) of the third-order CQLM-TPoS resonators with acoustic isolation frame.

EXPERIMENTAL RESULTS

The frequency response of fabricated CQLM-TPoS resonators are measured both in atmospheric pressure and in partial vacuum. Third-order CQLM-TPoS resonators with a finger pitch (FP) of 51 µm and a seventh-order resonator with a finger pitch of 35µm are characterized using a Rohde & Schwarz *ZNB 8* network analyzer and a pair of GSG probes (Cascade Microtech Inc) at ambient temperature. The loaded quality factors (Q_{loaded}) are measured and the unloaded quality factors are extracted based on the results.

For the third harmonic CQLM, the quality factor is measured both with and without isolation frame in partial vacuum (Fig.9). The first order lateral-extensional mode of these resonators is also measured for comparison purposes. As seen, for the resonator with an acoustic isolation frame a significantly improved *Q* is measured (from 4.6k to 14.5k). By comparing the data in Table.1 and the measured quality factor for the resonator without isolation frame it could be concluded that the support loss is the dominant source of loss in the CQLM-TPoS resonators. This loss could be significantly improved by designing the CQLM-TPoS resonator within a properly designed acoustic isolation frame.

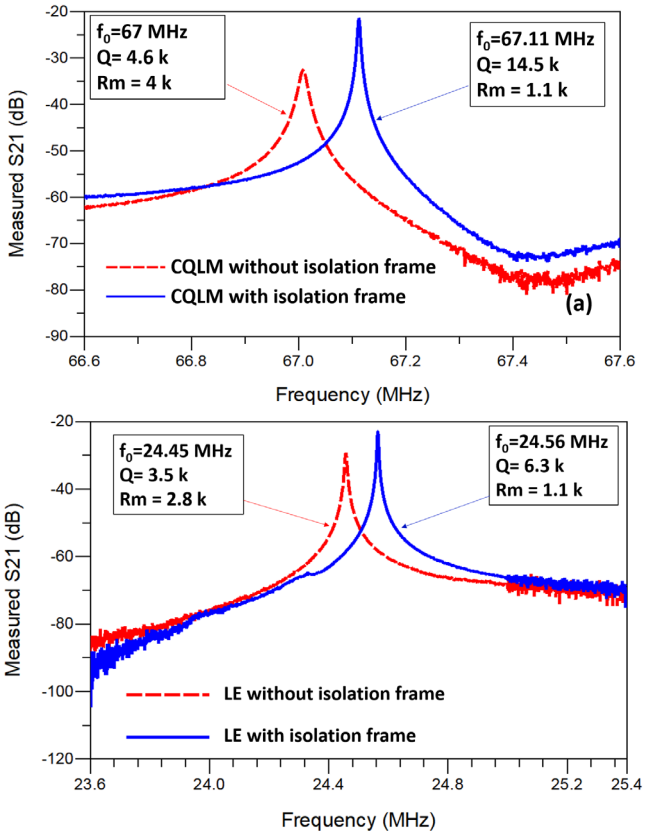

Figure 9: The measured S21 plots for a third-order CQLM (a) and first order lateral-extensional mode (b) in vacuum for resonator with and without reflector frame. Results support that the isolation frame efficiently reduces the support loss.

A seventh order CQLM is also measured for a TPoS resonator with a finger pitch of 35µm without an acoustic isolation frame and the frequency response is shown in Fig.10. A seen, the motional resistance has improved from ~4 kΩ for the third-harmonic without the frame to ~1 kΩ when the higher-order harmonic CQLM (seventh order) was excited.

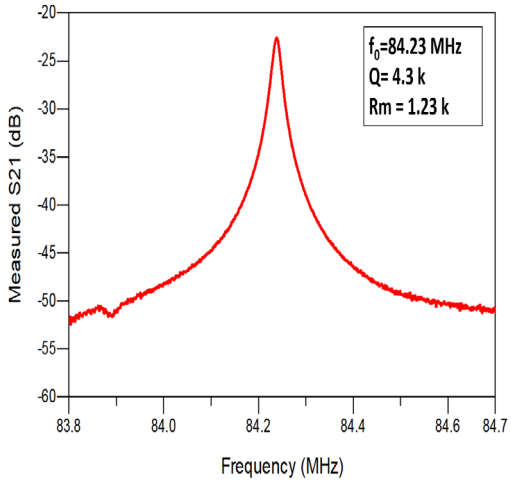

Figure 10: The measured frequency response for seventh order CQLM-TPoS resonator without an acoustic isolation frame.

CONCLUSION

In this paper, a new class of resonators coined as cross-sectional quasi Lamé mode (CQLM) thin-film piezoelectric-on-silicon (TPoS) is introduced for the first time. These resonators were fabricated on an SOI wafer and an acoustic isolation frame was used to effectively improve the support quality factor. Frequency response of these resonators are measured for the resonators with and without acoustic isolation frame. A 14500 quality factor was measured for a CQLM resonator with an isolation frame at ~67MHz. The presented CQLM-TPoS resonators are believed to be one of the best candidates for extremely stable time keeping applications.

REFERENCES

[1] E. J. Ng, V. A. Hong, Y. Yang, C. H. Ahn, C. L. M. Everhart and T. W. Kenny, "Temperature Dependence of the Elastic Constants of Doped Silicon," in *Journal of Microelectromechanical Systems*, vol. 24, no. 3, pp. 730-741, June 2015.

[2] C. Cassella, Y. Hui, Z. Qian, G. Hummel, and M. Rinaldi, "Aluminum Nitride Cross-Sectional Lamé Mode Resonators," J. Microelectromechanical Syst., pp. 1–11, 2016.

[3] C. Cassella, G. Chen, Z. Qian, G. Hummel and M. Rinaldi, "Cross-Sectional Lamé Mode Ladder Filters for UHF Wideband Applications," in *IEEE Electron Device Letters*, vol. 37, no. 5, pp. 681-683, May 2016.

[4] G. K. Ho, R. Abdolvand, A. Sivapurapu, S. Humad and F. Ayazi, "Piezoelectric-on-Silicon Lateral Bulk Acoustic Wave Micromechanical Resonators," in Journal of Microelectromechanical Systems, vol. 17, no. 2, pp. 512-520, April 2008.

[5] R. Abdolvand, H. M. Lavasani, G. K. Ho and F. Ayazi, "Thin-film piezoelectric-on-silicon resonators for high-frequency reference oscillator applications," in *IEEE Transactions on Ultrasonics, Ferroelectrics, and Frequency Control*, vol. 55, no. 12, pp. 2596-2606, December 2008.

[6] B.P. Harrington, R. Abdolvand "In-plane acoustic reflectors for reducing effective anchor loss in lateral–extensional MEMS resonators,". J Micromech Microeng 21(8):085021, 2011.

[7] H. Mansoorzare, S. Moradian, S. Shahraini, J. Gonzales, and R. Abdolvand, "Achieving the Intrinsic Limit of Quality Factor in VHF Extensional-Mode Block Resonators," accepted to IFCS 2018.

CONTACT

*Sarah Shahraini, email: sarah.shahraini@knights.ucf.edu, tel: +1-321-263-9109.

EIGENMODE OPTIMIZATION AND TOPOLOGICALLY PROTECTED STATES IN MAGNETO-MECHANICAL ULF TRANSMITTER ARRAYS

Inbar (Hotzen) Grinberg[*], *JunHwan Kim, and Gaurav Bahl*
University of Illinois at Urbana-Champaign, USA

ABSTRACT

Electromagnetic signals in the Ultra-Low Frequency (ULF) range 0.3-3 kHz are important for underground and underwater wireless communication systems, due to relatively low absorption through water, rock, and soil. However, the extremely large wavelength (~10^6 m) causes man-portable ULF antennas to be inefficient to the point of impracticality. In this work, we present a new ULF transmitter approach through direct production of oscillating magnetic fields by an array of magneto-mechanical torsional resonators. We demonstrate transmitter power optimization through eigenmode engineering, and discuss the formation of topologically protected states. Our work illuminates a path to MEMS-based ULF transmitters capable of communicating through water and earth over km distances.

INTRODUCTION

Underground and underwater wireless communication is required for communication with divers, submarines, miners or trapped population in case of natural disaster, and also for employing sensor networks for monitoring the underground or underwater conditions [1]–[8]. Unlike wireless communication through air, underground and underwater communication presents a much greater challenge, due to high attenuation of the signals in rock, soil and water [2]–[4]. Ultra low Frequencies (ULF) which have very long wavelengths and thus larger penetration depth, are suitable for this type of communication [1], [5]. Traditional antennas structures are desired to be comparable in size to the operating wavelength for efficiency, in the ULF range this size is in the order of tens of kilometers, rendering them impractical [9], [10].

A different way for producing a low frequency signal is using a time varying magnetic field produced by an oscillating dipole, e.g. with a coil [1], [8], [11]. However, still large coils and large powers are required for transmission range more than a few meters [11]. Using a rotating permanent magnet to produce the time varying magnetic field, can reduce significantly the power requirements and thus the size of the transmitter. For example, to produce the same dipole, a coil occupying a volume of 0.1ft^3 will require power in the order of 100 kW, while rotating a permanent magnet of that volume will be in the range of only 10 W. High field permanent magnets are readily available and can also be implemented in MEMS arrays [12].

Thus, here we focus on the later approach where the carrier signal is produced by mechanical oscillating motion of a permanent magnet. The magnetic field frequency is the resonance frequency of a dynamical system comprised of a mechanical spring, on which a permanent magnet is mounted, therefor it can be easily designed to be in the desired ULF range. We show that in order to decrease power consumption an array of many small magnets is desired, and therefore eigenmodes analysis is important for understanding the system behavior. Moreover, through eigenmode optimization the power consumption can be decreased.

DESIGN AND ANALYSIS

A permanent magnet rotating around its axis (Fig. 1a) produces a time varying magnetic field, proportional to the magnetic moment m, and the angular deflection θ, that can be sensed at some arbitrary receiver location $\vec{r}$. We mount a magnet on a mechanical torsional spring, and produce a system oscillating at a frequency ω. The magnetic field generated by a point dipole at a location $\vec{r}$ at is given by:

$$\vec{B} = \frac{\mu_0|\vec{m}|}{4\pi r^3}(3\hat{r}(\hat{m}\cdot\hat{r}) - \hat{m}) \qquad (1)$$

where $\mu_0 = 4\pi\cdot 10^{-7}\ [N/A^2]$ is the magnetic permeability, $\vec{m}$ is the magnetic dipole, given by $\vec{m} = m(-sin(\theta)\hat{x} + cos(\theta)\hat{z})$ for a dipole pointing in $\hat{z}$ direction and oscillating about the $\hat{y}$ axis (as shown in Fig.1a), and the deflection angle for an oscillating case is $\theta = \theta_{max}cos(\omega t)$. $\hat{m},\hat{r}$ are unit vectors in the direction of $\vec{m},\vec{r}$ respectivly. We start our analysis with determining the best point in space to position our receiver, assuming we wish to sense the ω component of the oscillating magnetic field $\tilde{\vec{B}}$ with the highest amplitude. To this end, we fit each component of $\tilde{\vec{B}}$ (i.e. $\tilde{B}_x, \tilde{B}_y, \tilde{B}_z$) to a polynomial in θ and by taking only the ω components from this fit we form a new vector $\tilde{\vec{B}}_\omega = \tilde{B}_{x,\omega}\hat{x} + \tilde{B}_{y,\omega}\hat{y} + \tilde{B}_{z,\omega}\hat{z}$, which is the best vector orientation for a sensor (receiver) at each receiver location $\vec{r}$. The simulated $\tilde{\vec{B}}_\omega$ at various receiver locations are presented in Fig. 1c, where vectors represent the greatest magnetic field for sensing, the best position for a receiver will be where the amplitude of $\tilde{\vec{B}}_\omega$ is maximum (red dot in Fig. 1c). From these simulations we can determine that this optimal sensing point for the ω component is along the $\hat{x}$ axis. Using the same analysis we can also obtain the best location for sensing the 2ω component which is found to be along the $\hat{z}$ axis, however this component has a much smaller amplitude.

For the spring-magnet resonator system, the dissipated mechanical power is given by:

$$P_{res} = \frac{\omega^3 I\,\theta^2}{2Q} \qquad (2)$$

where I is the cross-sectional moment of inertia and Q is the mechanical quality factor for the torsional mode. A target value of the received oscillating magnetic field (for given $\vec{m},\theta$) can be obtained either by a single large magnet, or by N smaller magnets with the same overall volume (Fig. 1b) undergoing synchronized motion. Assuming the cross section dimensions of a single large rectangular magnet are reduced by $1/\sqrt{N}$ to produce N smaller magnets. The moment of inertia I_{small} of a small magnet scales as $1/N^2$ relative to I_{large} of the single large magnet, and thus the power dissipated by N smaller magnets is reduced by a factor of N (see eq. 3), relative to the power dissipated by a single large magnet (P_{large}), promoting a MEMS approach.

$$I_{small} = \frac{M}{12N}\left(\frac{w^2}{N} + \frac{h^2}{N}\right) = \frac{I_{large}}{N^2}$$
$$P_{total} = NP_{small} = N\frac{\omega^3\,\theta^2}{2Q}\frac{I_{large}}{N^2} = \frac{P_{large}}{N} \qquad (3)$$

Our mechanical torsional spring is fabricated from a 0.4mm thick aluminum, we mount a neodymium N52 magnet $1/4$ inch in diameter and $1/16$ inch thick on the spring (Fig. 2a). We drive the torsional resonance mode (Fig. 2b) using a coil and sense local motion via magnetic field using a Hall sensor (Fig. 2a).

978-1-940470-03-0/HH2018/$25©2018TRF
DOI 10.31438/trf.hh2018.99

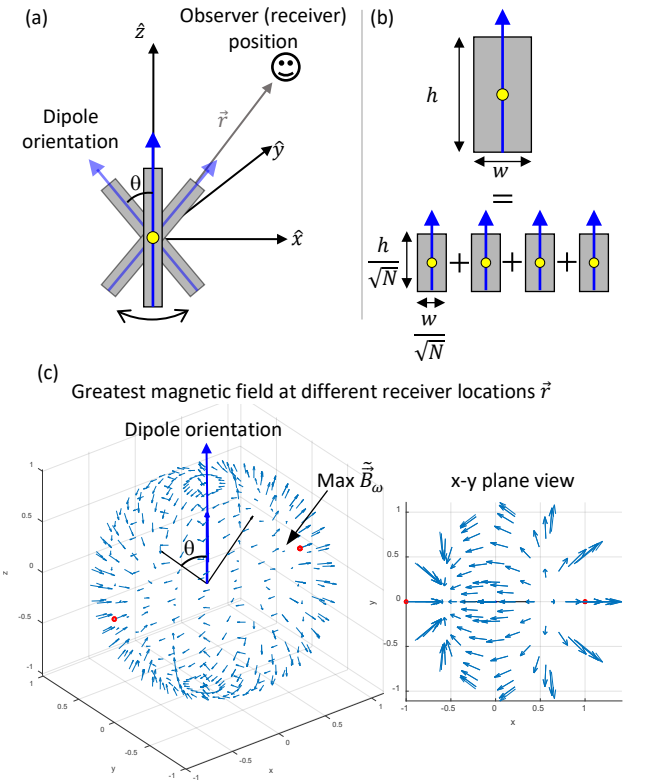

Figure 1: (a) Illustration of a magnetic dipole pointing in $\hat{z}$ and rotating around $\hat{y}$ with angular deflection θ. (b) Illustration of a single magnet divided to N=4 smaller magnets with the same overall volume. The use of smaller magnets may lead to lower dissipative power while maintaining the same amplitude of the sensed magnetic field. (c) Simulated magnetic field at different locations in space, the arrows represent the direction and magnitude of the greatest magnetic field for sensing. The middle blue arrow is the dipole orientation, and the two black arrows represent the angular deflection θ. The red dots mark the position of the maximal field.

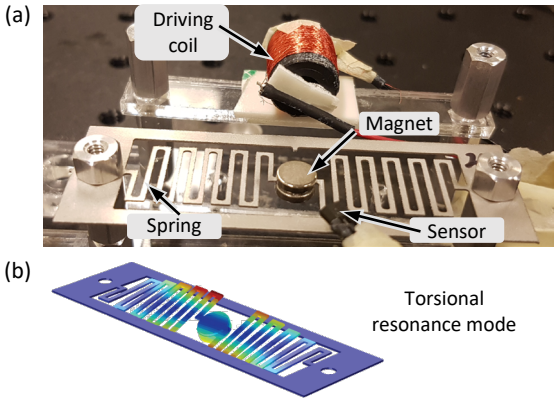

Figure 2: (a) Photograph of the magneto-mechanical resonator fabricated from 0.4mm thick Aluminum. A small magnet is mounted in the center, and the system is mounted on an acrylic holder with plastic or aluminum screws (to prevent any interference from surrounding metals). (b) The resonator torsion resonance mode.

EXPERIMENTAL RESULTS

We produced a test array of eight coupled magneto-mechanical resonators. Figure 3 shows a picture of the array and the lumped model used to characterize the dynamics of the system. The dynamics of the array are modeled using the coupled equations of motion, which for the i[th] resonator in an array with symmetric coupling is given by

$$I\ddot{\theta}_i + c\dot{\theta}_i + (\kappa - \gamma)\theta_i + 2\gamma(\theta_{i-1}+\theta_{i+1}) = \tau. \quad (4)$$

Here c is a damping coefficient, κ is the torsional spring constant, τ a driving torque, and the parameter γ indicates the magnetic interaction that produces both coupling and a magnetic spring effect. For a linearized magnetic torque using small angles approximation, and for the array configuration in Fig. 3 (where all dipoles are the same and oriented in $\hat{z}$, rotating around $\hat{y}$, and are spaced only in $\hat{x}$) this magnetic parameter is given by

$$\gamma = \frac{3\mu_0 m^2}{4\pi d^3}. \quad (5)$$

Since γ is proportional to $1/d^3$, where d is the distance between magnets, the inter-magnet coupling can be tuned as needed.

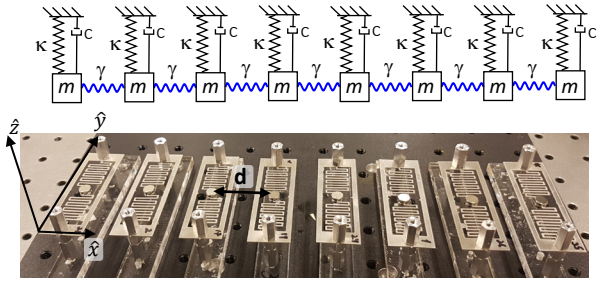

Figure 3: Lumped model describing the resonator array, and a picture of an array with 8 resonators. In this array all the dipoles point in the $\hat{z}$ axis direction, and are equally spaced by distance d in the $\hat{x}$ direction. When driven in a torsional resonance mode the dipoles (magnets) rotate around the $\hat{y}$ axis.

To maximize the oscillating magnetic field produced by the array, a synchronized mode of vibrations is necessary. To that end, eigenmode analysis was used to characterize the system. We use $\tilde{\theta}_i$ to indicate the angular displacement for the i[th] resonator (normalized such that $\sum \tilde{\theta}_i = 1$, corresponding to a fixed transmitted $\left|\tilde{\vec{B}}\right|$) in a specific eigenmode. For an equidistant array of resonators, the synchronized eigenmode (Fig. 4b) is similar to a string mode where the end points have no deflection. However, since the dissipated power is $P \propto \sum \tilde{\theta}_i^2$ we find that this simplistic mode, while synchronized, is not power optimized. To better explain this, consider a target transmitted magnetic field $\tilde{B}^*$ which is obtained by an array of N magnets oscillating with a uniform angular deflection amplitude $\tilde{\theta}^*$. The magnetic field is proportional to $\sum \tilde{\theta}_i^* = N\tilde{\theta}_i^*$ and the dissipated power proportional to $\sum \tilde{\theta}_i^{*2} = N\tilde{\theta}_i^{*2}$. If however, the deflections are not uniform across the array but we wish to maintain the same amplitude of the magnetic field, it will result in some angular deflections being larger than $\tilde{\theta}^*$ and some smaller. This will maintain the same value of $\sum \tilde{\theta}_i^*$, however in terms of power the squared values results in a much larger dissipation. Meaning the more uniform the deflections across the array, the more power efficient the system is.

With this in mind, a more optimal configuration can be achieved by using a non-equal resonator spacing, in turn producing non-uniform inter resonator couplings, so that the eigenmode acquires a more evenly distributed amplitude. We analytically modeled and experimentally tested the optimized mode for improving power efficiency. We use an iterative approach in

Matlab, starting from equal distances between the resonators and changing them gradually until reaching the minimal power for a given array. We start the process with normalized equal distances of r=1 (Fig. 4c), than, each distance is assigned an index number symmetrically around the middle. For example for an eight resonator array the middle distance is the nominal r=1, and going outwards the following distances are r_1-r_3 (Fig. 5d). We first change the most outer distance (r_3 for the eight resonator example) until reaching a convergence criteria on the power, than we move to changing the next distance, and so on until the last distance (r_1). This process is than repeated until there is no more change to the power value, and we obtain the required ratio of distances for optimal power (Fig. 5b).

For our eight resonator array the simulations of this approach showed an improvement (reduction) in power dissipation of 14% (Fig. 4a). In our experiment setup however, there are discrete increments of spacing where we can position the resonators, and we are not able to meet the exact ratios of the distances needed. For the set of distances (closest to the optimal) possible to obtain in the experiment the reduction in power is about 10.5%. The simulated and experimental mode shapes for the initial equal distances and for the final modified distances are shown in Fig. 4c,d respectively, where circles represent deflection amplitude. In the experiment $\sum \theta_i^{*2}$ was reduced by 11%, which is very close to the simulation predicted value.

While adjusting the distances (topology) between resonators for power optimization, the system may form potentially undesired modal structures. Thus, we also experimentally tested how topological changes affect the eigenmodes and the overall frequency response of the array. Arrangements with different symmetries can results in very different frequency response characteristics, including having a bandgap or strong spatial localizations. Here we present the frequency response of three different configurations and demonstrate the formation of conductive, insulating, and topologically insulator phase having localized protected states (Fig. 5) [13]. A trivial insulator is formed by alternating the coupling between resonators from weak and strong, starting with a strong coupling (Fig. 5a), and as expected from an insulator we obtain a bandgap in the frequency response. A conductor is formed by an array with equally spaced resonators, having a conducting band and no bandgap (Fig. 5b). A topological insulator is a unique insulator having a band gap in the bulk, but strongly localized modes on the edges with frequencies in the middle of this band gap. This type of response is achieved simply by having an arrangement with alternating coupling while starting with a weak coupling (Fig. 5c).

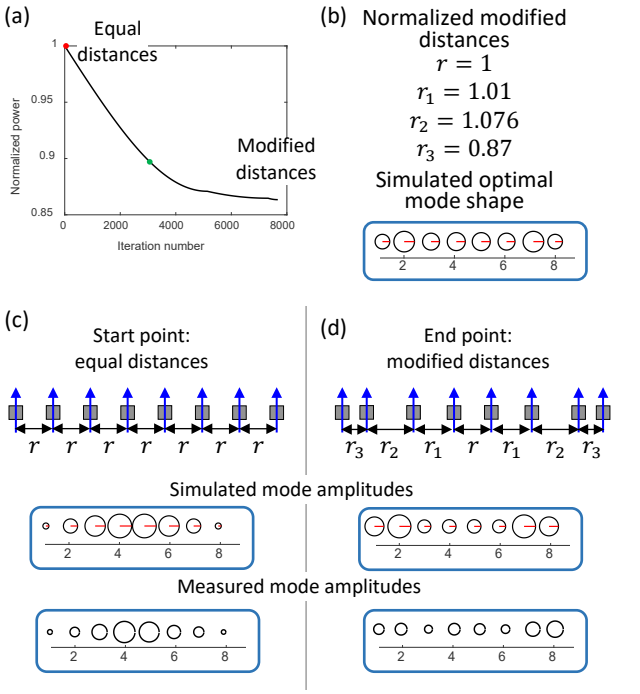

Figure 4: Power optimization process shown for an 8 resonator ULF transmitter array. (a) Simulated normalize power consumption per iteration, in each iteration the distances between resonators are modified. (b) The normalized distances received from the optimization process (for the initial case all distances are r=1), and the eigenmode shape for the most optimal case. Circles represent resonator amplitude, the red lines the direction of the phase, and the numbers indicate resonator spatial index. (c),(d) Simulated, and experimentally measured mode amplitudes, and a schematic illustration of the distances between resonators, for the starting point with equal distances (red dot in a) and the best modified case that we could obtain in experiments (green dot in a) respectively. We could not reach the final configuration because we are limited to discrete distances between resonators.

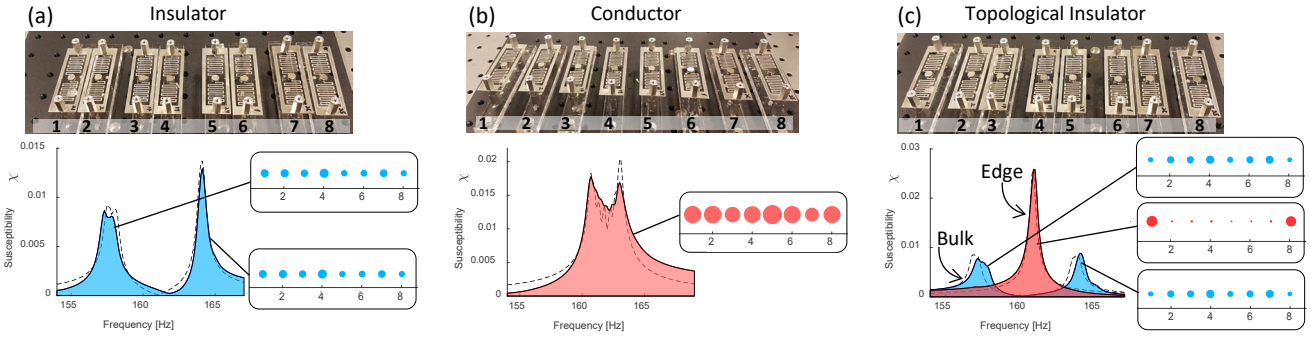

Figure 5: Experimentally measured band structure of different array arrangements. (a) A trivial insulator (b) A conductor (c) A topological protected state. In each experiment we individually drive and sense each resonator and obtain the system frequency response. For each case the plot shows the average susceptibility (amplitude/driving power) per frequency. For the topological case we separate the response of edge (pink) and bulk (blue) resonators. The insets shows each resonator average susceptibility across a range of frequencies, where circle sizes correspond to amplitude, and demonstrate the spatial distribution of the mode for each case.

SUMMARY

In this work we presented the equations of motions describing an array of magneto-mechanical resonators, where mechanical resonators are coupled through magnetic interaction that also produces a spring effect. We showed that through eigenmode optimization we can decrease the power dissipation of the system. This is achieved by changing the distances between resonators which in turn change the coupling strengths (effective spring stiffness), and deform the eigenmode shape. When deforming the eigenmodes, different and possibly undesired topologies can be formed in the system. We demonstrate three different arrangements of the coupling between resonators that result in very different frequency responses (trivial insulator, conductor and topological insulator). We also illustrate that a MEMS approach is recommended for further reduction of power. This work is a preliminary study opening a path towards MEMS based ULF transmitters.

ACKNOLEDMENTS

The authors would like to acknowledge the support of the US National Science Foundation (NSF) Emerging Frontiers in Research and Innovation (EFRI) grant EFMA-1627184, and the Defense Advanced Research Project Agency (DARPA) A Mechanically Based Antenna (AMEBA) grant HR0011-17-20057. We additionally wish to acknowledge support from the US Office of Naval Research (ONR) Director for Research Early Career Grant.

REFERENCES

[1] S.-C. Lin, I. F. Akyildiz, P. Wang, and Z. Sun, "Distributed Cross-Layer Protocol Design for Magnetic Induction Communication in Wireless Underground Sensor Networks," IEEE Trans. Wirel. Commun., vol. 14, no. 7, pp. 4006–4019, Jul. 2015.

[2] I. F. Akyildiz, D. Pompili, and T. Melodia, "Underwater acoustic sensor networks: research challenges," Ad Hoc Networks, vol. 3, no. 3, pp. 257–279, May 2005.

[3] I. F. Akyildiz, Z. Sun, and M. C. Vuran, "Signal propagation techniques for wireless underground communication networks," Phys. Commun., vol. 2, no. 3, pp. 167–183, Sep. 2009.

[4] N. Srivastava, "Challenges of Next-Generation Wireless Sensor Networks and its impact on Society," J. Telecommun., vol. 1, no. 1, 2010.

[5] I. F. Akyildiz and E. P. Stuntebeck, "Wireless underground sensor networks: Research challenges," Ad Hoc Networks, vol. 4, no. 6, pp. 669–686, Nov. 2006.

[6] L. Lanbo, Z. Shengli, and C. Jun-Hong, "Prospects and problems of wireless communication for underwater sensor networks," Wirel. Commun. Mob. Comput., vol. 8, no. 8, pp. 977–994, Oct. 2008.

[7] M. C. Domingo, "Overview of channel models for underwater wireless communication networks," Phys. Commun., vol. 1, no. 3, pp. 163–182, Sep. 2008.

[8] Zhi Sun and I. F. Akyildiz, "Magnetic Induction Communications for Wireless Underground Sensor Networks," IEEE Trans. Antennas Propag., vol. 58, no. 7, pp. 2426–2435, Jul. 2010.

[9] H. A. Wheeler, "Fundamental Limitations of Small Antennas," Proc. IRE, vol. 35, no. 12, pp. 1479–1484, Dec. 1947.

[10] J. S. McLean, "A re-examination of the fundamental limits on the radiation Q of electrically small antennas," IEEE Trans. Antennas Propag., vol. 44, no. 5, p. 672, May 1996.

[11] I. F. Akyildiz, P. Wang, and Z. Sun, "Realizing underwater communication through magnetic induction," IEEE Commun. Mag., vol. 53, no. 11, pp. 42–48, Nov. 2015.

[12] J. A. Little, M. J. Mazzoleni, B. P. Mann, R. Carroll, N. Garraud, and D. P. Arnold, "Investigation of wave propagation behavior in magnetically coupled mems oscillators," Proc. ASME Des. Eng. Tech. Conf., vol. 4, 2015.

[13] S. D. Huber, "Topological mechanics," Nat. Phys., vol. 12, no. 81, pp. 215–216, 2016.

CONTACT

*Inbar Grinberg ; inbar28@Illinois.edu

PRECISE LOCAL TEMPERATURE MEASUREMENT OF FULLY ENCAPSULATED OVENIZED MEMS DEVICES

Hyun-Keun Kwon[1], David B. Heinz[1], Dongsuk D. Shin[1], Yunhan Chen[2], Lizmarie C. Ortiz[1], Gabrielle D. Vukasin[1], and Thomas W. Kenny[1]*
[1]Stanford University, California, USA
[2]Apple, Cupertino, California, USA

ABSTRACT

In this paper, a simple and precise method is proposed to non-invasively monitor localized temperatures of fully encapsulated, suspended and ovenized MEMS devices. By placing clamped-clamped (CC) beams at multiple locations within the device layer and measuring the resonant frequencies, an accurate temperature profile of the entire suspended device can be measured. This method has a small foot print that can be incorporated in any ovenized devices and the measured temperatures can be used to improve temperature control schemes. Compared with an IR-optical or direct 4-point resistance measurement, the frequency measurement offers better resolution with minimal impact on the actual device temperature.

INTRODUCTION

Due to small size and compatibility with conventional silicon integrated circuit (IC) design, MEMS oscillators exhibit great potential for use as time references [1, 2]. Fully-encapsulated silicon-based oscillators are now available and have begun to displace quartz crystal oscillators [3]. However, MEMS oscillators suffer from an inherit temperature dependence of frequency (TCf) of about 30 ppm / °C [4]. This results in a large frequency variation compared to quartz crystals. In order to overcome this issue, numerous passive compensation schemes have been introduced such as doping [5] and composite materials [6] that can effectively reduce the TCf without applying additional external power.

Besides the aforementioned methods, state-of-the-art frequency stability has been achieved with an active-ovenization scheme, where the device is controlled at a set temperature above the operating temperature to suppress any remaining temperature dependence [7]. In order to achieve extreme stability, an accurate measurement of the resonator body temperature is crucial as it provides the control signal to maintain operation at the target temperature. Previous instruments utilize a dual-mode operation, where one resonator body is driven with two independent vibrational modes. These two modes exhibit a very different temperature dependence and so the frequency difference between the two modes can be utilized as a high-resolution temperature sensor. This approach has been used to achieve a frequency stability of about ± 250 ppb from -20 to 80°C range [8].

In order to further improve the frequency stability, a more local understanding of the temperature profile of an encapsulated ovenized resonator is required. Any thermal gradient within the resonator body will introduce an error in the temperature measurement and this problem has to be addressed by an improved, locally-precise measurement scheme. Although a resistive temperature detector (RTD) can be fabricated within this MEMS process, RTD based systems suffer from separation from the resonator and self-heating and are not ideal candidates to monitor localized temperatures [9]. In this paper, we present a frequency-based small foot print temperature measurement method for ovenized MEMS device applications.

DESIGN AND FABRICATION

A bulk-type resonator with device layer heater is designed and fabricated for this study. Figure 1 (a) shows the overall diagram of the fabricated device. The entire device is suspended by two anchor points where the bias and heating voltages are applied. The main device is a 400 µm X 400 µm X 40 µm Lamé-mode resonator suspended from a frame, which is suspended from the anchors. The suspension frame not only serves as a mechanical support for the resonator body but also provides separation from a temperature gradient present at the heaters. Within the suspension frame, 8 CC beams are included with sense/drive electrodes for capacitive measurement as shown in Figure 1 (b) with dimensions of 190 µm X 3.23 µm X 40 µm. To ovenize the device, a DC current flows between through the suspension structures, acting to raise the temperature of the frame via Joule heating. The folded-beam design of the heater provides a large thermal resistance between the device and the ambient to allow a large temperature increase.

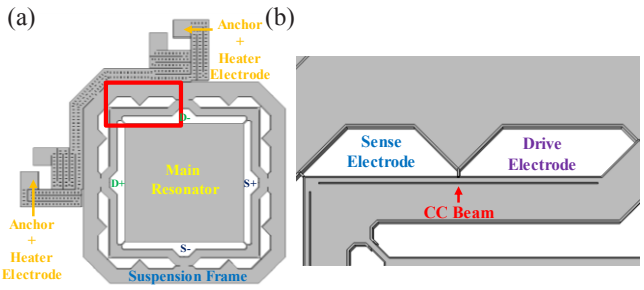

Figure 1. (a) Diagram of bulk-type resonator device layer with an in-plane heater suspending the entire frame. (b) Detailed look into the CC beams within the suspension frame.

The device was fabricated using a wafer-level encapsulation process (*epi-seal*) co-developed by Robert Bosch Research and Technology Center and Stanford University. The device is fabricated on a (100) N-Type (Phosphorous) SOI wafer with a 40 µm single-crystal silicon device layer, aligned with <110> crystal orientation and doping level of ~2.3e19 cm^{-3}. The doping level plays a critical role in determining the TCf characteristics of silicon resonators [5] and this will be examined more closely in the following section. A variation of this process allows fabrication of etch-hole free bulk-type resonators with high quality factors and seals the device inside a low-pressure cavity (< ~1Pa) without any moisture, oxygen and other contaminations [9]. By placing the heater within the device layer, a low-power operation is enabled by minimizing heat loss via conduction or convention from the resonator to the rest of the die [7]. Figure 2 shows the top-view SEM image of fabricated device.

978-1-940470-03-0/HH2018/$25©2018TRF
DOI 10.31438/trf.hh2018.100

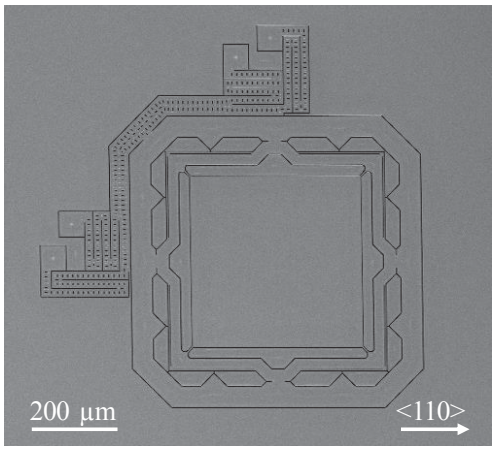

Figure 2. Top-view SEM image of the fabricated device. Scale bar of 200 µm. The arrow indicates <110> direction of the single-crystal silicon orientation.

EXPERIMENT CHARACTERIZATION

All the experiments were carried out in a temperature-controlled oven. Operation of the device was done by applying a DC bias to the resonator structure via the heater electrodes and AC drive voltages were applied to the drive electrodes. The motional current was amplified via a PCB mounted trans-impedance amplifier and measured with a Zurich HF2LI-PLL. As for the Lamé-mode, the device is driven differentially through a 180-Degree phase splitter and sensed through an instrumentation amplifier. Only the MEMS device was placed in the oven; the rest of the system operated in the lab environment. Figure 3 shows the block diagram of the experimental setup.

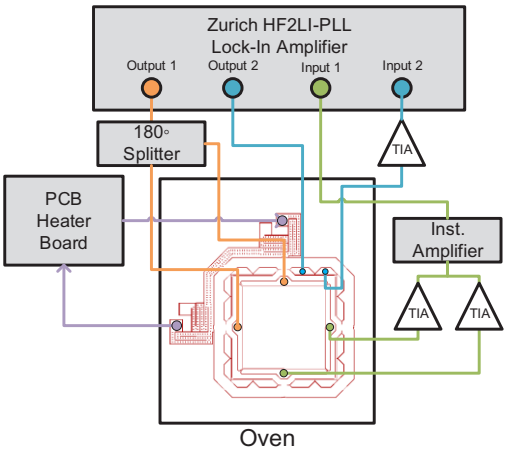

Figure 3. Block diagram of the experimental setup. Both the Lamé mode and CC beam flexural mode can be driven/sensed for frequency measurement.

Open-loop Electrostatic Frequency Measurement

The open-loop frequency sweeps at 25 °C show resonant frequencies of 10.34Mhz for the Lamé-mode and 630.3kHz for the CC beam flexural mode. Respective mode-shapes and frequency response are shown in Figure 4. The CC beams exhibited mechanical coupling with other CC beams within the suspension frame and therefore required application of a small bias voltage at each sense or drive electrodes of other CC beams in order to isolate the single CC beam of interest. Application of the isolation voltage did not impact the operation of the Lamé-mode.

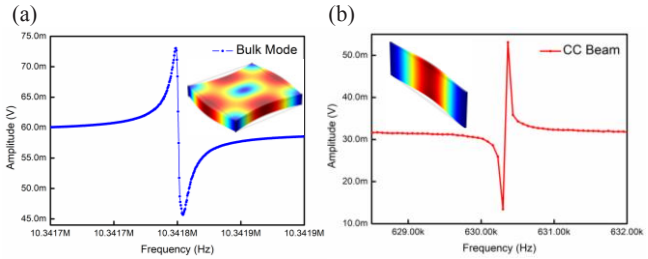

Figure 4. (a) The resonant frequency of the Lamé-mode at 25°C temperature. Insert shows the COMSOL simulation of the mode shape. (b) the resonant frequency of the CC beam flexural mode.

For the temperature measurement, we first ran a temperature-sweep of the Lamé-mode and 4 CC beams. 4 beams were chosen such that 2 are closer to the heater and 2 are further apart to investigate the temperature gradient within the device layer (shown in Figure 5 (a)). The resonant peaks were tracked from -20 to 80 °C with 5 °C steps and the frequencies were recorded as shown in Figure 5 (b) and (c). As for the Lame-mode, the temperature sweep resulted in a TCf of -317 Hz/°C and the 4 beams were about -16 Hz/°C. Despite the identical design, 4 CC beams exhibited slightly different resonant frequency and temperature dependence due to fabrication variations.

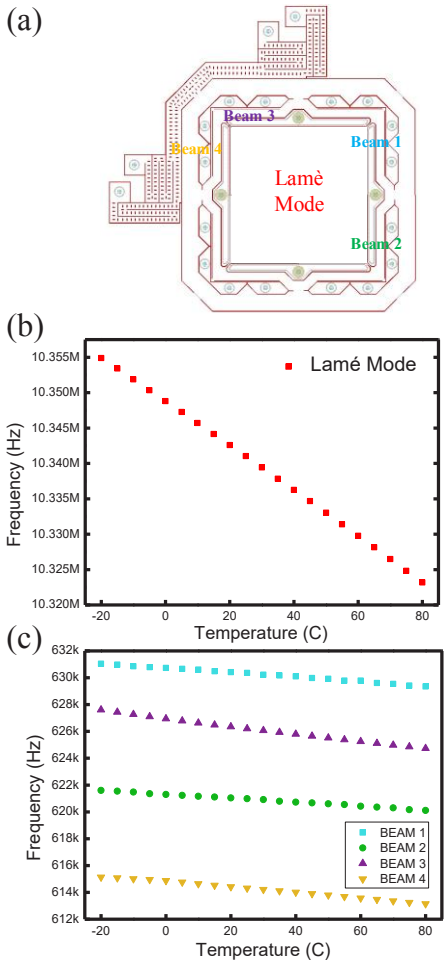

Figure 5. (a) Diagram of the tested device with measured beams labeled. (b) Temperature sweep of the Lamé-mode and (c) 4 beams measured from -20 °C to 80 °C in a temperature-controlled oven. Nonidentical characteristics are shown from the fabricated beams.

These unique TCf curves are fitted with a 2nd-order polynomial and were used in the subsequent test to back-track the temperature of the ovenized device. The main advantage of this method is that the TCf characteristics of these resonators are very repeatable and fairly insensitive to external environmental factors. The incorporated CC beams are very compact and can be tailored to fit in almost any bulk-type devices. For places where in-plane electrodes are not applicable, out-of-plane electrodes can be utilized to sense/drive the CC beams. Moreover, the same setup for measuring frequency can be applied without any additional circuitry thus making this approach very simple to implement.

Ovenization Temperature Results

To study the temperature profile during ovenized operation, varying heating voltages were applied to the heater electrodes and observed the open-loop frequency sweep. All of the testing was conducted with the oven set at -20 °C ± 1 °C. As anticipated, the resonator increased in temperature as the heater voltage increased as shown in Figure 6.

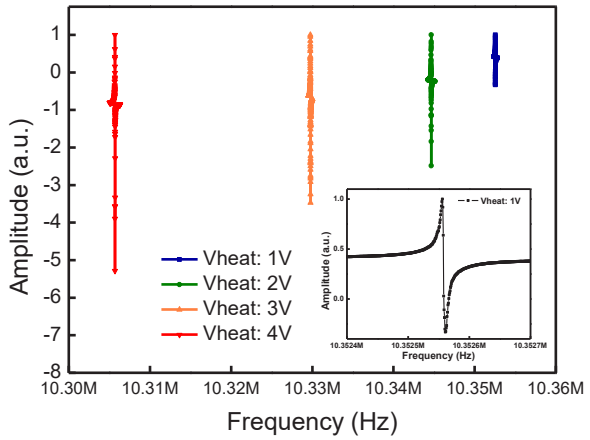

Figure 6. Open-loop sweep of the Lamé-mode with varying heater voltage. From this data and comparing with the fitted TCf curves, temperature of the structure as well as the localized areas of the CC beams can be measured. Peak amplitude normalized to 1. Inset shows a magnified look into the resonant peak at 1V heater voltage.

Table 1. Local temperature measurement results within an encapsulated, suspended and ovenized MEMS resonator.

Applied Heater Voltage	Temperature (°C) (ΔT between the Lamé and the beams)				
	Lamé-Mode	*Beam 1*	*Beam 2*	*Beam 3*	*Beam 4*
1.0 V	-11.8108	-12.7447 (-0.9339)	-12.1221 (-0.3113)	-11.9215 (-0.1107)	-11.8895 (-0.0787)
2.0 V	13.1074	12.9239 (-0.1838)	12.8261 (-0.2813)	13.4393 (+0.3319)	13.6460 (+0.5386)
3.0 V	59.7742	58.9421 (-0.8321)	58.9121 (-0.8621)	60.5002 (+0.7260)	60.7070 (+0.9328)
4.0 V	135.8975	135.2130 (-0.6845)	135.3251 (-0.5724)	136.3546 (+0.4571)	136.5121 (+0.6326)

DISCUSSION

Table 1 shows the result of the frequency-based temperature measurement. For each applied heater voltage, frequencies were measured and the temperatures were back-calculated from the previously mentioned 2nd-order polynomial fitted TCf curves. Also, the difference (ΔT) between the Lamé-mode and each beam is shown.

From these results, it is evident that the temperature profile of the entire device is not uniform and shows that the beams positioned closer to the heater are indeed somewhat warmer than the beams positioned on the opposite side of the frame. Moreover, the Lamé-mode sits at about the middle point between the two ends of the frame. Up to 1.76 °C temperature difference between the beams were measured at 3.0V heater voltage. This non-uniformity can be caused by radiation heat lass throughout the device as well as convective heat loss. These results provide an improvement in understanding of the device temperature profile when incorporated with an in-plane heater design with bulk-mode operation.

To further investigate, a COMSOL simulation with 4.0V heater voltage across the micro-oven was conducted with the results shown in Figure 7. The simulation reveals the hot spots located at the folded-beam heaters that are beside the suspension frame. It can be inferred that although the suspension frame assists in uniform heating, the hot spots near the frame and thermal radiation leads to a slight temperature gradient as observed from the experimental results. These results were also observed in previous ovenization devices [11].

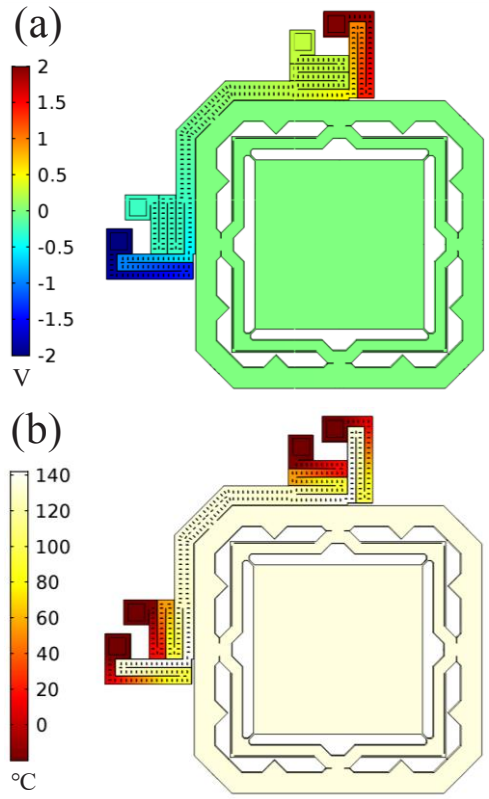

Figure 7. (a) Electric potential profile of the in-plane ovenized device. (b) Temperature profile of the device with 4.0V heater voltage applied. This reveals the hotspots near the folded-beam micro-ovens. Electrical conductivity was derived from the doping of the device wafer.

This method, however, is not without any fault. Since the TCf curve was fitted with a 2nd-order polynomial, it cannot guarantee an absolute measurement. Moreover, the accuracy drops for temperatures beyond the temperature sweep points. In addition, any small fluctuations within the oven during the calibration can lead to errors in controlling the frame temperature. In this particular test, the oven was set to each temperature for about 30 minutes to allow settling to the new temperature and smoothing out of any initial temperature gradients.

Despite these non-idealities, these results provide a good understanding of how the in-plane suspended devices can perform under ovenization. For example, this data can be used to provide an additional correction/compensation signal to the heater control feedback loop. Also, for this particular device, a dual-heater with heaters on both sides of the suspension frame should provide a more uniform temperature profile.

CONCLUSION

In this paper, we have investigated a compact frequency-based temperature measurement scheme that can accurately monitor the temperature profile of an ovenized MEMS device. Compared to optical or RTD based measurements, the frequency-based temperature sensing offers a non-invasive method with no additional circuitry. From the in-plane ovenized device, we observed a temperature gradient of up to 1.76 ℃ Additionally, this data has the potential to improve future ovenized device designs. In our future work, we will focus on different heater designs, frame designs and how these design parameters impact the formation of the temperature profile within the device layer to improve the temperature stability of ovenized MEMS resonators.

REFERENCES

[1] C. Nguyen, "MEMS Technology for Timing and Frequency Control", IEEE Trans. Ultrasonics, Ferroelectrics and Frequency Control, 54, 2, (2007) pp. 251-270.

[2] J.T.M van Beek and R. Puers, "A review of MEMS oscillators for frequency reference and timing applications", J. Micromech. Microeng, 22, 1 (2011)

[3] M. Lutz, A. Partridge, P. Gupta, N. Buchan, E. Klaassen, J. McDonald, and K. Petersen, "MEMS oscillators for high volume commercial applications", in Proc. TRANSDUCERS, Lyon, France, 6/10-14 (2007) pp. 49-52.

[4] R. Melamud, S. A. Chandorkar, B. Kim, H. K. Lee, J. C. Salvia, G. Bahl, M. A. Hopcroft and T. W. Kenny, "Temperature-Insensitive composite micromechanicalresonators", J. Microelectromech. Syst., 18, 6, (2009).

[5] A. Jaakkola, M. Prunnila, T. Pensala, J. Dekker, and P. Pekko, "Determination of doping and temperature-dependent elastic constants of degenerately doped silicon from MEMS resonators", IEEE UFFC, 61, 7, (2014).

[6] V. A. Thakar, Z. Wu, A. Peczalski, M. Rais-Zadeh, "Piezoelectrically Transduced Temperature-Compensated Flexural-Mode Silicon Resonators", J. Microelectromech. Syst., 22, 3, (2013).

[7] J. C. Salvia, R. Melamud, S. A. Chandorkar, S. F. Lord, and T. W. Kenny, "Real-Time Temperature Compensation of MEMS Oscillators Using an Integrated Micro-Oven and a Phase-Locked Loop", J. Microelectromech. Syst., 19, 1, (2010).

[8] Y. Chen, E. J. Ng, D. D. Shin, C. H. Ahn, Y. Yang, I. B. Flader, V. A. Hong, and T. W. Kenny, "Ovenized dual-mode clock (ODMC) based on highly doped single crystal silicon resonators," in Proc. IEEE MEMS, Shanghai, China, 1/24-28 (2016) pp. 91-94

[9] Z. Wu, A. Peczalski, and M. Rais-Zadeh, "Low-power ovenization of fused silica resonators for temperature-stable oscillators," in Proc. IEEE IFCS, Taipei, Taiwan 5/19-22 (2014) pp. 1-5

[10] E. J. Ng, Y. Yang, Y. Chen, and T. W. Kenny, "An etch hole-free process for temperature-compensated, high Q, encapsulated resonators," Solid-State Sensors, Actuators, and Microsystems Workshop, Hilton Head Isl., SC, 6/8-12, Transducer Research Foundation, Cleveland (2014), pp. 99-2014, 99-100

[11] Y. Chen, E. J. Ng, Y. Yang, C. H. Ahn, I. Flader, and T. W. Kenny, "In-Situ ovenization of Lamé-Mode silicon resonators for temperature compensation", in Proc. IEEE MEMS, Estoril, Portugal 1/18-22 (2015) pp. 809-812

ACHKNOWLEDGEMENTS

This work was supported by the Defense Advanced Research Projects Agency (DARPA) grant "Precise Robust Inertial Guidance for Munitions (PRIGM)", managed by Dr. Ron Polcawich, Contract Number # N66001-16-1-4023. This work was performed in part at the Stanford Nanofabrication Facility (SNF), supported by the National Science Foundation under Grand ECS- 9731293. Special thanks to all the staffs at SNF for their help during the fabrication process.

CONTACT

*H.-K. Kwon, tel: +1-650-575-7216; ryankwon@stanford.edu

750 MHZ ZERO-POWER MEMS-BASED WAKE-UP RECEIVER WITH -60 DBM SENSITIVITY

C. Cassella[*], *M. Assylbekova, W. Z. Zhu, G. Chen, P. Kulik, G. Michetti, N. McGruer and M. Rinaldi*
Northeastern University, Boston, Massachusetts, USA

ABSTRACT

In this work, we present the first fully-passive RF wake-up receiver (WUR). The WUR relies on a solid-state envelope detector (*ED*) and a MEMS-based cantilever switch (*RS)* acting as a resonant comparator vibrating at 75.3 kHz. The device exhibits a quality factor (*Q)* of 4700 when operating in its linear regime (*i.e.* far from pull-in voltage). The demonstrated WUR enables the achievement of high sensitivity (P_{min}=-60 dBm) while not consuming any stand-by power. For this reason, the presented WUR opens up exciting scenarios in the development of next-generation smart wireless sensors nodes operating within the *Internet-Of-Things* (IoT).

INTRODUCTION

The recent development of the internet of things (*IoT*) has led to an urgent need for low-power wireless sensing nodes (WSNs) communicating within complex miniaturized networks. WSNs are formed by a group of sensors whose captured information is only transmitted when requested by other interrogating nodes. Depending on their operational state (*on* or *idle*), WSNs may drain different amounts of energy from their batteries. In particular, for most practical cases, the battery life of WSNs is significantly reduced by the amount of power they dissipate when operating in their idle state (P_{idle}). For this reason, WSNs relying on RF wake-up receivers (WURs) have been recently proposed to minimize P_{idle}. Such radios use the received RF-power to control both the state of WSNs and the amount of energy released by their batteries. The performance of WURs can be characterized in terms of two key parameters: the stand-by power (P_{sb}) and the sensitivity (P_{min}). P_{sb} is defined as the power consumed when not driven by any input RF-signal. In contrast, P_{min} is defined as the minimum input RF-power (P_{in}) required to trigger them.

In this work, we report on the first fully-passive WUR demonstrated to date (Fig. 1). This relies on a solid-state envelope detector (*ED*) and a MEMS-based resonant cantilever switch [3-4] (*RS*) to achieve high sensitivity (P_{min}=-60 dBm), zero stand-by power (P_{sb} = 0) with low system complexity. The theory, fabrication and the experimental performance of WUR will be reported.

THEORY AND OPERATION

The schematic representation of the WUR demonstrated in this work is shown in Fig. 1. The *ED* includes a diode (D1), an inductor (L1=82 nH) and two capacitors (C1=10 pF and C2=100 nF). L1 is used to resonate the static capacitance of the diode (C_s~0.1 pF) at the desired operational frequency (750 MHz). In contrast, C1 and C2 are used to limit the power released at undesired frequency components and prevent power leakage into the diode. As evident, this signal is generated through an ON/OFF amplitude modulation applied to a RF Continuous-Wave (CW) signal. The modulation is characterized by an optimal duty-cycle value which allows to maximize the mechanical force (F_m) acting on the *RS*. $v_{gs}(t)$ is applied between the gate and source contacts of the RS. This is attained after combining the envelope signal achieved from $v_{in}(t)$ through the ED ($v_{dem}(t)$) with a DC-voltage (V_{gg}) applied between the same RS-terminals through a large biasing resistor (1 MΩ). The large resistor is needed to apply V_{gg} without generating power leakage from the output of the ED into the input of the adopted DC-supply. The use of V_{gg} allows to increase both F_m and its sensitivity with respect to $v_{in}(t)$. It is also important to point out that the use of V_{gg} and V_{dd} also determines a reduction of both the actuation and contact gaps of the RS, thus further lowering P_{min}. The flow of current from V_{dd} determines the activation of the WUR and, consequently, allows to trigger future WSNs relying on their use to minimize P_{idle}.

The built WUR is driven by an amplitude modulated RF-signature ($v_{in}(t)$ (Fig. 2-a)) characterized by a carrier frequency of 750 MHz and a modulation frequency, f_m, matching f_{res}. In particular, when $v_{in}(t)$ drives the *ED*, it is first demodulated ($v_{dem}(t)$) and then applied, together with V_{gg}, between the gate and source of the *RS* (see $v_{gs}(t)$ in Fig. 2-b). Consequently, F_m is generated inducing a resonant displacement of the *RS* that is amplified by its high quality factor. The magnitude of F_m is proportional to the magnitude of $v_{gs}(t)$. So, when the received RF-power exceeds a certain threshold (P_{min} =-60 dBm), the drain and source of the RS come in contact (Fig. 1-c), enabling the flow of current ($I_{ds}(t)$) from a DC-voltage supply (V_{dd}) and, consequently, the activation of the WUR.

It is important to emphasize that, differently from any WUR architecture relying on voltage rectifiers to operate, the presented system has a sensitivity that is only limited by the white-noise of the employed *ED*. This special feature is enabled by the use of the MEMS-component as a high-frequency resonant comparator. In fact, thanks to this system characteristic, the WUR demonstrated in this work can operate with modulation-frequencies that are larger than the corner-frequency relative to the *1/f* flicker noise affecting the operation of the *ED*. So, the noise power affecting the *SNR*, between the gate and source contacts of the RS, is only determined by the white-noise, at the *ED* output (point B in Figure 1), integrated in the narrow frequency band (<20 Hz) of the RS. This explains why the presented architecture has potential to achieve sensitivity as low as -90 dBm through a more optimized and controlled RS-design and fabrication.

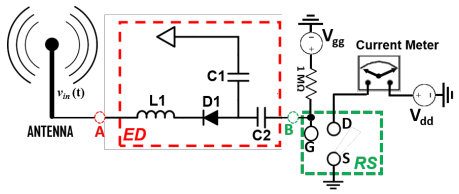

Figure 1: Schematic representation of the WUR demonstrated in this work.

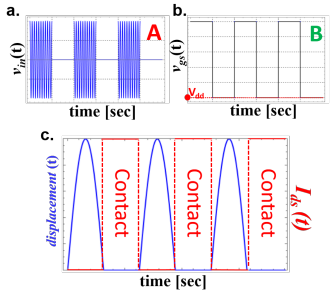

Figure 2: a-b) Representation of the time mode-shapes relative to

978-1-940470-03-0/HH2018/$25©2018TRF
DOI 10.31438/trf.hh2018.101

Solid-State Sensors, Actuators and Microsystems Workshop
Hilton Head Island, South Carolina, June 3-7, 2018

the signals at the input (A) and output (B) terminals of the WUR (in A in Fig. 1)); c) time mode-shape of the displacement and current waveforms, upon contact, relative to the fabricated RS.

FABRICATION AND EXPERIMENTAL RESULTS

The RF WUR is realized by a commercial solid-state envelope detector (AVAGO-HSMS2852) (Fig. 3-a) built on a printed circuit board (*PCB*) and an in-house fabricated MEMS-based resonant cantilever switch (*RS,* Fig. 3-b).

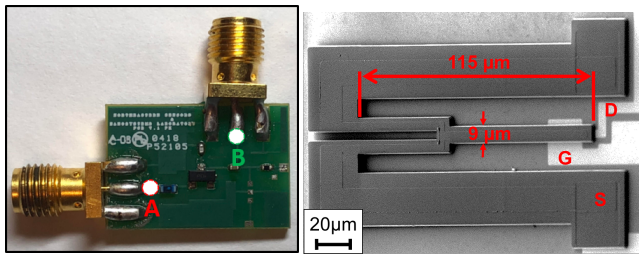

a) b)

Figure 3: a) Top-view of the PCB of the ED; b) Scanning Electron Microscopy (SEM) picture of the RS in this work.

The device relies on a 600 nm actuation gap (between gate and source) and on a 300 nm contact gap (between drain and source). The gate and source area results into a rest capacitance (C_{act}) that is ~30 fF. The position of the three *RS*-terminals is highlighted. It is also important to point out that the *RS*-design relies on an etched slot to attain second-order stress-gradient compensation. The fabricated *RS* was connected to the *ED* through probing and loaded in a vacuum probe station (5×10^{-5} Pa) for testing. A Polytec vibrometer was used to measure the out-of-plane velocity relative to the tip of the beam and, consequently, its displacement. Both the resonance frequency (f_{res}~75.3 kHz) and the quality factor (Q=4700) of the built *RS* were extracted through the direct vibrometer measurements after biasing the *RS* with the same DC voltages applied in the WUR (*i.e.* V_{gg}=15.8 V and V_{dd}=6 V), as shown in Fig. 4. The performance of the built WUR was extracted after driving it through a commercial RF-arbitrary waveform generator, which allowed for a more reliable characterization of its performance. We report, in Fig 5, the measured DC-component of $I_{ds}(t)$ for two received P_{in}-values around the measured P_{min}-value (-60 dBm).

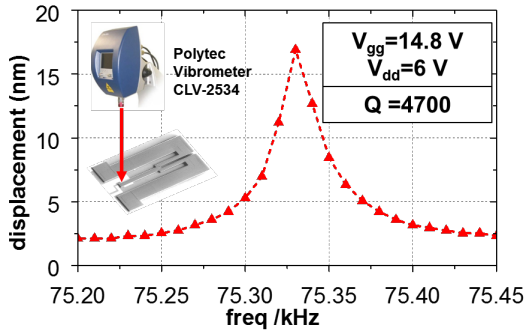

Figure 4: Measured magnitude of the AC-displacement component relative to the tip of the built RS and extracted after applying slightly lower DC-biases than used in the built WUR (Fig. 1) for P_{in}=-55 dBm.

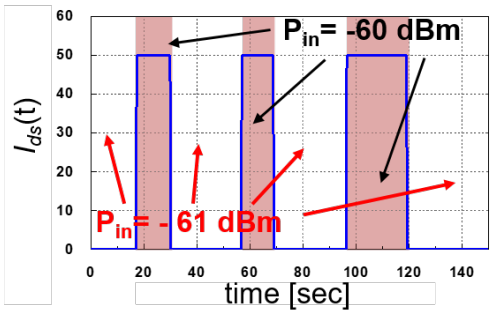

Figure 5: Measured DC-component of $I_{ds}(t)$ and relative to two P_{in}-values randomly swept over few testing cycles. The current value was mostly limited by the high input impedance (>1 MΩ) of the adopted current meter.

The described WUR were also analyzed through a novel *ad-hoc* circuit simulation platform capturing both the electrical behavior of the *ED* and the electromechanical nonlinear behavior of the built *RS*. We report in Fig. 6 the simulated trend of the displacement magnitude relative to the *RS*-tip vs. P_{in}. As evident, the simulated and measured P_{min}-values match closely, further demonstrating the effectiveness of our simulation approach in predicting the complex nonlinear electromechanical behavior of the built WUR.

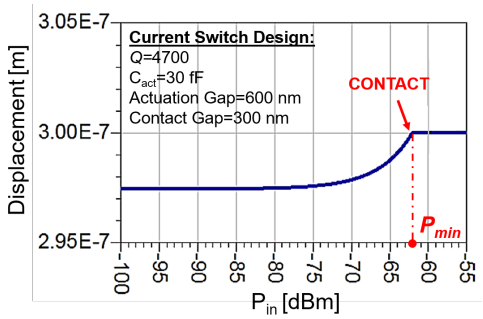

Figure 6: Simulated displacement relative to the tip of the built RS for P_{in}-values ranging from -100 dBm to -55 dBm.

CONCLUSIONS

In this paper, the first fully-passive RF wake-up receiver with zero standby power, high sensitivity and low system complexity was demonstrated. The reported results show its potential as the enabling technology for "Asleep-yet-Aware" ultra-low-power RF systems.

REFERENCES

[1] C. Cassella, G. Chen, T. Wu, Z. Qian, and M. Rinaldi, "Low impedance arrays of coupled Cross-Sectional Lamé mode resonators with high figure of merit in excess of 100," in *Solid-State Sensors, Actuators and Microsystems (TRANSDUCERS), 2017 19th International Conference on*, 2017, pp. 1935–1838.

[2] T. Wu *et al.*, "Design and fabrication of AlN RF MEMS switch for near-zero power RF wake-up receivers," 2017, pp. 1–3.

[3] T. Wu, G. Chen, Z. Qian, W. Zhu, M. Rinaldi, and N. McGruer, "A microelectromechanical AlN resoswitch for RF receiver application," 2017, pp. 2123–2126.

[4] R. Liu, J. N. Nilchi, W.-C. Li, and C. T.-C. Nguyen, "Soft-impacting micromechanical resoswitch zero-quiescent power AM receiver," 2016, pp. 51–54.

CONTACT

* C. Cassella, tel: +1-267-992-5507; c.cassella@northeastern.edu

A HIGH-MASS, EIGHT-FOLD SYMMETRIC SILICON CARBIDE MEMS GYROSCOPE

Eugene Cook[1], Michael Tomaino-Iannucci[1], Jonathan Bernstein[1], Marc Weinberg[1], Jennifer Choy[1], Karl Hobart[2], Lunet Luna[2], Marko Tadjer[2], Rachael Myers-Ward[2], Fritz Kub[2], Yushi Yang[3], Eldwin Ng[3], Ian Flader[3], Yunhan Chen[3], and Thomas Kenny[3]*

[1]Draper, Cambridge, Massachusetts, USA

[2]U.S. Naval Research Laboratory, Washington DC, USA

[3]Stanford University, Stanford, California, USA

ABSTRACT

A novel MEMS gyroscope is presented, which blends the best aspects of traditional tuning fork gyroscopes with modern whole-angle capable designs such as rings and disks. The gyroscopes were fabricated in both silicon and silicon carbide. The resonators were measured to have quality factors of 120,000 (SiC) and 260,000 (Si), and frequency splits of 0.08% (SiC) and 0.24% (Si). Open loop rate mode gyroscope operation was demonstrated on both gyroscopes.

GYRO DESIGN

The gyro incorporates large masses and displacements for high sensitivity and reduced Brownian motion (like a traditional tuning-fork gyro), while also exhibiting a symmetric in-plane modal pattern commonly called "n=2" and illustrated in Figure 4. Eight wedges are arranged on flexures and coupled together. The symmetric, Coriolis-coupled modes enable mode-reversal and parameter-identification-based in-situ calibration techniques, as well as whole-angle mode operation [1]. Electrostatic drive, sense, and tuning electrodes are incorporated for matched frequencies.

FABRICATION

Gyroscopes were built in silicon (Figure 3), using the epi-seal process [2]. Additionally, a new Silicon Carbide-based process (Figure 1) was developed to explore the performance benefits available from this novel material [3]. Silicon carbide offers superior material properties (Table 1) and superior material isoelasticity [4], leading to reduced material-driven asymmetry, important for whole-angle gyro operation. The process begins with wafer bonding and thinning to form a 40-µm thick single crystal 4H Silicon Carbide-on-insulator (SiCOI) wafer. A nickel mask is used to deep reactive ion etch features with aspect ratio up to 10:1 into the device layer. Metal contact pads are formed and the devices are released in HF vapor. The finished devices (Figure 2) are the first bulk SiC resonators with traditional MEMS flexures and masses.

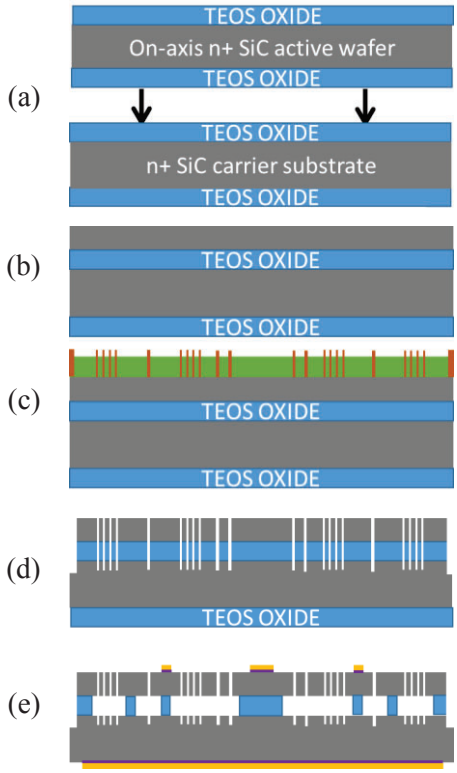

Figure 1: The silicon carbide on insulator (SiCOI) fabrication process for the gyro is illustrated, including wafer bond (a), thinning of the top layer (b), electroplated nickel mask (c), deep reactive ion etch (d), and vapor HF release and metallization (e).

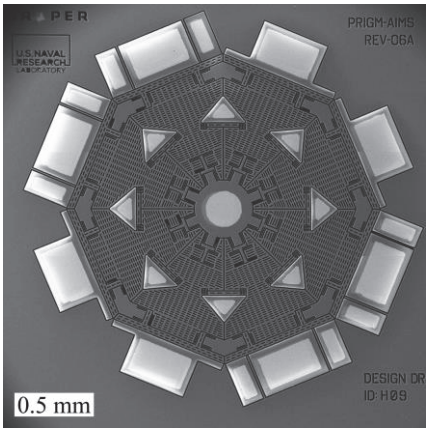

Figure 2: SEM showing a complete silicon carbide gyro with metal wirebond pads.

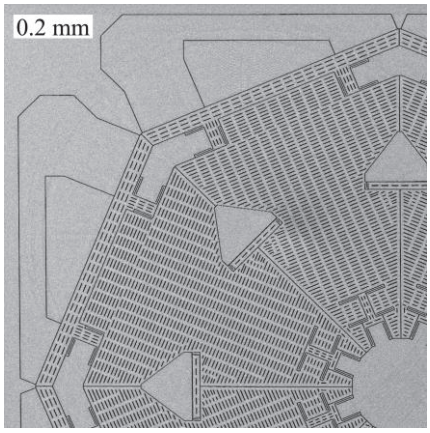

Figure 3: SEM showing details of a silicon gyro, including flexures and release slots.

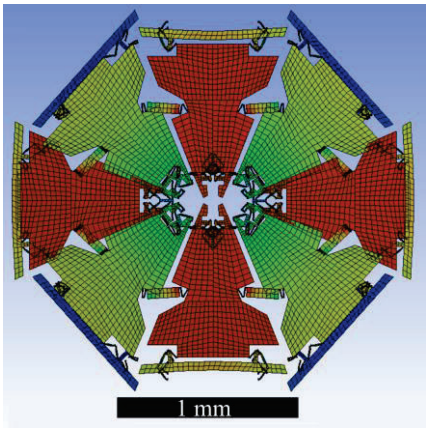

Figure 4: The gyro n=2 mode shape is simulated by the finite element method.

978-1-940470-03-0/HH2018/$25©2018TRF
DOI 10.31438/trf.hh2018.102

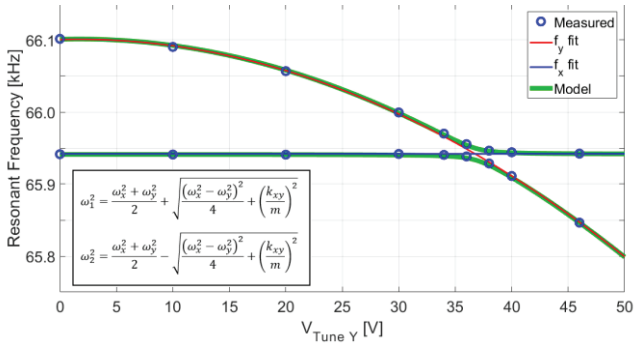

Figure 5: Electrostatic tuning of the silicon device to achieve matched vibratory modes is measured and modeled. The two modes are brought together with one of the on-axis tuning electrodes. Blue circles represent measured resonant frequencies at different voltages applied to one of the tuning electrodes. Green curves are the modeled results according to the formulae. Between 30 and 40 volts, the nonzero cross-axis term (k_{xy}/m, estimated at 4.2×10^7 s^{-2}) prevents perfect tuning. The cross-axis tuning electrode would be used to tune out k_{xy} and remove the residual split.

RESULTS

Resonators with n=2 frequencies from 20 to 150 kHz were built. Quality factors (Q) of 120,000 and 260,000 were measured in vacuum for the 88 kHz SiC and 65.9 kHz Si resonators, respectively. Q is limited by thermoelastic damping (TED):

$$Q_{TED} = K_{TE}\frac{(1+\omega_0^2/\omega_{TE}^2)}{\omega_0/\omega_{TE}},$$

where thermoelastic frequency is

$$\omega_{TE} = \kappa \,/\, \left(C_p\rho(w/\pi)^2\right),$$

and the scaling constant is

$$K_{TE} = C_p\rho/ET\alpha^2.$$

Given the properties of SiC (Table 1) and the beam widths here (5 µm), $\omega_{TE}/2\pi = 6$ MHz. The relative distance between ω_{TE} and the resonance ω_0 yields large TED; minimum Q_{TED} would occur at $\omega_{TE} = \omega_0$. Moving ω_{TE} up (and Q_{TED} up) requires thinner beams, a capability yet to be developed in SiC fabrication technology. Conversely, ω_{TE} for Si, where thinner beams of 2 µm are used, is 22 MHz, farther from the point of maximum TED. Improved SiC fab tolerances will permit higher Q. Frequency splits of 70.8 Hz (out of 88 kHz) and 161 Hz (out of 65.9 kHz) were measured on SiC and Si resonators, respectively. Electrostatic tuning of k_x, k_y, and k_{xy} was also demonstrated (Figure 5), and tuned the frequency split below 12 Hz. Damping mismatches $\Delta(\omega_0\,/\,2Q)$ were measured at 0.07 Hz for both devices.

Both Si and SiC gyros were also operated in open-loop rate mode. On a rate table, one of the n=2 vibratory modes was located and a function generator applied an input at half the resonant frequency. The amplitude of the drive and sense axis pickoffs were measured and demodulated, enabling separation of the quadrature signal. Rates up to +/- 200 deg/sec were applied, and the gyro response (demodulated sense amplitude divided by drive amplitude) is plotted in Figure 6 (SiC), and Figure 7 (Si). Scale factor depends on the frequency split (as described in the model equation in Figure 7) and the Bryan angular gain factor AG, which is typically between 0.6 and 0.8 for n=2 devices. The difference in slope between model and measurement in Figure 7 is therefore partially from AG, yielding an estimate of $AG = 0.75$ for the Si gyros. The model also differs from the measurement because of demodulation phase error, and offset between function generator and resonance frequencies, errors that would largely be remedied by closed-loop electronics. These discrepancies did not permit a reliable estimate of AG for SiC gyros. Scale factor varied inversely with frequency split as the electrostatic tuning was refined, agreeing with the rate-mode model. Whole angle mode was not yet demonstrated, but is planned once electronics are completed.

REFERENCES

[1] D. D. Lynch, "Vibratory Gyro Analysis by Method of Averaging," in Second St. Petersburg Conference on Gyroscope Technology and Navigation, St. Petersburg, Russia (1995)

[2] R. Candler, et al. "Single wafer encapsulation of MEMS devices," IEEE Transactions on Advanced Packaging (2003)

[3] L. E. Luna, et al. "SiC MEMS technology based on wafer bonding and deep etching," in International Conference on Silicon Carbide and Related Materials, Washington, DC (2017)

[4] F. J. Kub, et al. "Whole Angle MEMS Gyroscope on Hexagonal Crystal Substrate." US Patent Application A1/20160341552, 24 November 2016.

CONTACT

*E. Cook, tel: +1-617-258-4123; ecook@draper.com

Table 1: Silicon carbide and silicon material properties

Material	C_p	ρ	E	κ	α
	J/(kg K)	kg/m^3	GPa	W/(m K)	ppm/K
SiC	750	3210	444	370	4.5
Si	670	2330	165	140	2.5

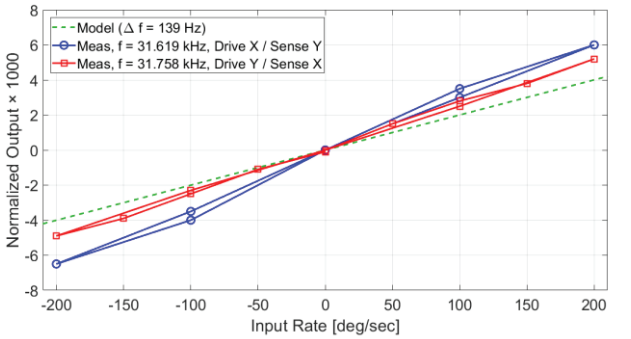

Figure 6: Rate mode gyroscope operation of the SiC device, driven on the x mode (blue) and the y mode (red), with bias removed. Normalized output is the demodulated sense amplitude divided by drive amplitude. Scale factor was low because of the large frequency split.

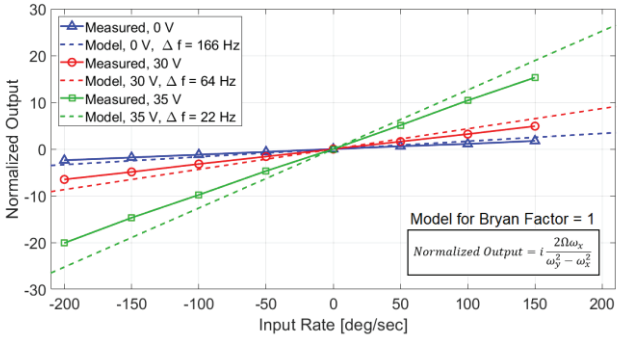

Figure 7: Rate mode gyroscope operation of the Si device, with bias removed. Gyro scale factor is increased (blue to green curve) by tuning the frequency split by applying the listed electrostatic tuning voltages to the sense axis.

A SILICON OPTOMECHANICAL ACCELEROMETER WITH HIGH BANDWIDTH AND SENSITIVITY

Y. Bao[1,2], F. Zhou[1], T.W. LeBrun[1], and J.J. Gorman[1*]*
[1]National Institute of Standards and Technology, Gaithersburg, MD, USA
[2]Theiss Research, La Jolla, CA, USA

ABSTRACT

Accelerometers with high sensitivity and bandwidth are required for numerous critical applications, including structural testing of buildings and bridges, seismic testing for oil and gas exploration, and aerospace systems. This paper presents a new optomechanical accelerometer design for precision vibration measurements that uses a hemispherical optical microcavity to transduce the motion of a proof mass. Experimental testing of the accelerometer shows that this design is capable of resolution below 147 μm/s²/√Hz (15 μg/√Hz) between 725 Hz and nearly 10 kHz.

INTRODUCTION

Fabry-Pérot interferometry is known to be one of the most sensitive approaches for measuring displacement, making it an attractive transduction solution for accelerometers. It has been used in accelerometers previously with several different optical cavity geometries, including an out-of-plane cavity design [1], and in-plane cavity designs with waveguides [2] and optical fibers [3,4]. This paper reports on the design, operation, and first demonstration of an optomechanical accelerometer that uses a silicon hemispherical Fabry-Pérot microcavity to transduce the motion of the accelerometer's proof mass. Our focus here is on achieving both high bandwidth and sensitivity for vibration applications rather than sensors for inertial navigation.

ACCELEROMETER DESIGN AND OPERATION

The optomechanical accelerometer design is shown in Fig. 1. Two silicon chips are assembled together with a spacer between them to form an optical microcavity. One chip has a concave silicon micromirror [5] and the other has a 10 mg proof mass (3 mm x 3 mm x 0.5 mm) that is suspended with microscale silicon nitride beams. This design combines a highly stable hemispherical cavity, unlike the plane-parallel cavities used in [1,2], with a wafer-scale microfabrication process, unlike the accelerometers described in [3,4]. The assembled chips are packaged with an optical fiber and mode matching lens that couple light in and out of the microcavity. The reflected optical signal is measured using a circulator, photodetector, data acquisition system, and signal analyzer.

The optical spectrum of the microcavity is shown in Fig. 2, which is found by scanning the laser wavelength while measuring the reflected intensity. In this case, a low-finesse optical cavity (i.e., a cavity with high optical loss) is used to generate a broad optical resonance for measuring displacement. The proof mass displacement is measured by positioning a stable laser at the point of highest slope on one of the optical resonances. When the proof mass moves, the optical resonances will shift in wavelength, generating a change in the reflected intensity. The displacement can then be determined from the equation in Fig. 2. A low-finesse cavity is used here because laser locking to the cavity resonance is not required, resulting in a simpler readout approach. However, we are also pursuing accelerometers with high-finesse cavities to maximize the sensitivity.

EXPERIMENTAL RESULTS

The accelerometer was first tested on a commercial shaker using a swept-sine excitation (Fig. 3). The fundamental resonance

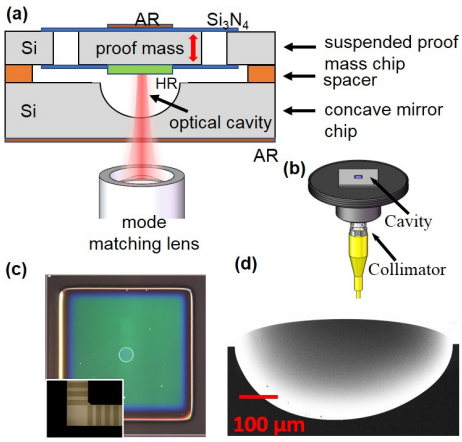

Figure 1: The optomechanical accelerometer design. (a) Cross-sectional schematic, AR: Anti-reflection coating, HR: mirror coating. (b) Packaging for the fiber coupled accelerometer. (c) and (d) Images of a fabricated suspended proof mass (3 mm square) and a silicon concave mirror, respectively.

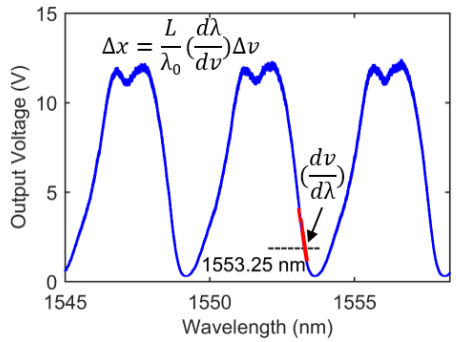

Figure 2. Optical spectrum of the Fabry-Pérot microcavity when measured in reflection with a tunable wavelength laser. Displacement sensing is performed with a fixed laser wavelength that is selected to provide the highest sensitivity (i.e., where the slope is greatest, ≈ 1553.25 nm). The measured voltage is converted to displacement using the included equation, where λ_0 is the operating wavelength and L is the length of the microcavity, as determined from the microcavity's free spectral range.

of the suspended proof mass is at 9.6 kHz, and a second resonance in the accelerometer package is also seen at lower frequency. We are currently redesigning the accelerometer package to achieve a purer frequency response. The linearity of the accelerometer was also investigated on the shaker, as shown for a 2 kHz excitation in Fig. 4. The accelerometer is clearly linear within the test range, which ran from the noise floor up to about 180 mm/s². The relationship between the input acceleration and the displacement of the proof mass at 2 kHz was found to be 0.143 nm/m/s² (1.4 nm/g).

The displacement noise spectrum was measured without excitation and with vibration and acoustic isolation to determine the acceleration resolution. The measured displacement noise is shown

978-1-940470-03-0/HH2018/$25©2018TRF
DOI 10.31438/trf.hh2018.103

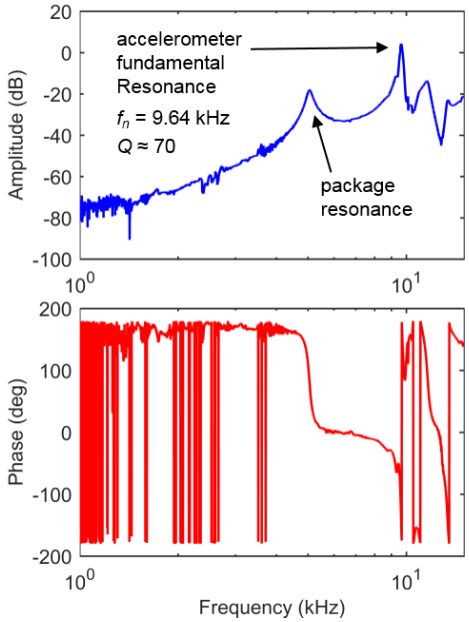

Figure 3. Frequency response of the accelerometer when measured on a commercial shaker with a swept-sine excitation.

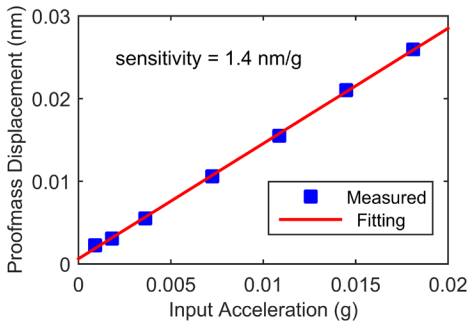

Figure 4. Accelerometer linearity test at 2 kHz. The acceleration provided by the shaker was varied and the proof mass displacement was measured with the microcavity. The accelerometer is highly linear from the noise floor to at least 180 mm/s² (≈ 18 mg). 1 g = 9.81 m/s²

in Fig. 5, where the noise floor is 35 fm/√Hz. This is only about a factor of two higher than the thermomechanical noise of the proof mass on resonance. The suspended proof mass was designed to behave like a simple harmonic oscillator, with all other vibration modes located at significantly higher frequencies by design [6]. In this case, the acceleration noise can be estimated by multiplying the displacement noise by the inverted harmonic oscillator model [3], resulting in Fig. 6. The acceleration noise is below 147 μm/s²/√Hz (15 μg/√Hz) beyond 725 Hz. This sensitivity and bandwidth performance is better than reported in [1,2] and equivalent to that found in [4], while also providing a more scalable micromechanical design and fabrication process. Since the first resonance is 9.6 kHz, the accelerometer has considerable bandwidth while also achieving near micro-*g* resolution, making it well suited for precision vibration measurements at high frequency.

ACKNOWLEDGMENTS

Research performed in part in the NIST Center for Nanoscale Science and Technology Nanofab.

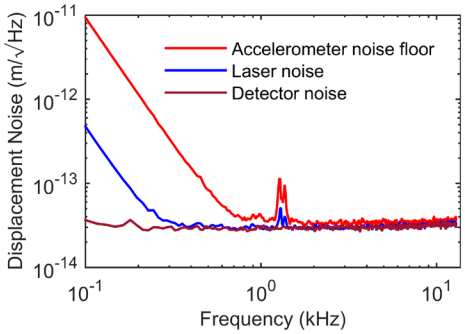

Figure 5. Proof mass displacement noise measured with the microcavity readout when the external acceleration is zero and the accelerometer is isolated from vibration and acoustic noise.

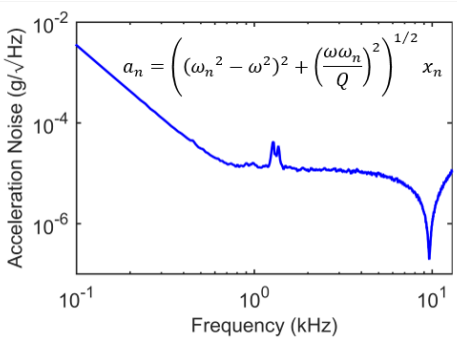

Figure 6. Estimated acceleration noise, a_n, based on the displacement noise and frequency response of the suspended proof mass. The accelerometer is assumed to behave as a simple harmonic oscillator. Using the equation in the figure, the displacement noise, x_n, is converted to a_n [3], where ω_n is the natural frequency, Q is the quality factor, and ω is the input frequency. For frequencies above 725 Hz, the noise floor is typically better than 147 μm/s²/√Hz (15 μg/√Hz) . The low-frequency response is dominated by 1/f noise in the laser, which can be improved through better laser stabilization. 1 g = 9.81 m/s²

REFERENCES

[1] M.A. Perez and A.M. Shkel, "Design and Demonstration of a Bulk Micromachined Fabry-Pérot μg-Resolution Accelerometer", IEEE Sensors Journal, 7, 1653 (2007).

[2] K. Zandi, J.A. Bélanger, and Y.-A. Peter, "Design and Demonstration of an In-Plane Silicon-on-Insulator Optical MEMS Fabry–Pérot-Based Accelerometer Integrated with Channel Waveguides", Journal of Microelectromechanical Systems, 21, 1464 (2012).

[3] F. Guzmán Cervantes et al., "High Sensitivity Optomechanical Reference Accelerometer Over 10 kHz", Applied Physics Letters, 104, 221111 (2014).

[4] O. Gerberding et al., "Optomechanical reference accelerometer", Metrologia, 52, 654 (2015).

[5] Y. Bao, F. Zhou, T.W. LeBrun, and J.J. Gorman, "Concave Silicon Micromirrors for Stable Hemispherical Optical Microcavities", Optics Express, 25, 15493 (2017).

[6] Y. Bao, F. Zhou, T.W. LeBrun, and J.J. Gorman, "A Photonic MEMS Accelerometer with a Low-Finesse Hemispherical Microcavity Readout", Int. Conf. Optical MEMS and Nanophotonics, Santa Fe, NM, 111 (2017).

CONTACT

*J. Gorman, gorman@nist.gov, T. LeBrun, thomas.lebrun@nist.gov

DEMONSTRATION OF A MICROFABRICATED SELF-OSCILLATING FLUIDIC HEAT ENGINE (SOFHE)

T. Monin[1,2,3] A. Tessier-Poirier[1], A. Amnache[1], T. Skotnicki[3], S. Monfray[3], F. Formosa[2] and L.G. Fréchette[1]*
[1] Laboratoire Nanotechnologies et Nanosystèmes (LN2), Interdisciplinary Institute for Techn. Innovation (3IT), Université de Sherbrooke, Canada
[2]SYMME, Université Savoie Mont Blanc, Annecy-le-vieux, France
[3]STMicroelectronics, Crolles, France

We present the first microfabricated heat engine based on the self-induced oscillations of a liquid piston exposed to a constant heat source. The unique operating principle of this self-oscillating fluidic heat engine, or *SOFHE*, was previously introduced at the macroscale [1] as an approach to convert waste heat into electricity to power wireless sensors. Here, we have implemented the core principle in a glass microchip for the first time and demonstrated the self-oscillating behavior at microscale.

NEED FOR THERMAL ENERGY HARVESTING

By integrating sensors everywhere around us, the Internet of Things (IoT) promises to truly connect the physical and cyber worlds, without the need for human intervention. Distributed sensors will however require long lasting power sources, which would ideally be recharged perpetually from ambient energy. Heat is often available to power sensors, therefore low-cost and compact thermal energy harvesters could play a key role in realizing the IoT's potential. Other than thermoelectrics, various MEMS-based heat engines have been studied [2-4]. They typically require an actuated or bi-stable thermal switching mechanism to induce the cyclic behavior required to implement a thermodynamic cycle.

OPERATING PRINCIPLE

In our previous work [1], we proposed a new principle to create the cyclic motion from a steady heat source. It consists of creating a vapor bubble in a tube filled with liquid, by locally heating the tube (Fig 1). As the evaporation occurs, the bubble pressure increases, pushing on the surrounding liquid column acting as a liquid piston (LP). Once the bubble grows beyond the hot zone, the vapor condenses, reducing the bubble pressure and pulling the LP back into the hot zone. Given the inertia of the LP, it tends to overshoot the equilibrium position and enters further into the hot zone. This promotes evaporation, repeating the cycle. The system can be viewed as a spring-mass system, where the compressible vapor in the bubble acts as the spring and the LP as the mass (Fig 1). Phase change acts as a negative damping (or feedback) and leads to the start-up of the engine by making the equivalent mechanical oscillator unstable. From the start-up, the oscillating amplitude increases until the system reaches a steady-state limit cycle. Although we have studied this unique behavior experimentally and analytically [1,5], this work is the first to implement it on a chip, as a building block for thermal energy harvesters.

SOFHE MICROFABRICATION AND RESULTS

The microfabricated SOFHE consists of a liquid-filled microchannel with internal grooves, heated at one end and cooled at the other. The chip is made of glass to minimize heat conduction along the chip, which is detrimental for thermal efficiency and achievable temperature gradient. Based on our experience at macroscale, wicking structures in the channel were beneficial to facilitate the self-oscillating behavior, so the microchannel was formed by wet etching two half-channels of slightly different widths on separate chips that are then bonded to form the channel (Fig. 2). The overhang creates a sharp corner in the channel, acting as the desired wicking structure. Borosilicate glass is etched by HF (49%) with a Cr-Au-Kapton mask, allowing depths over 250 microns (Fig. 3). The wafers where then bonded by forming a eutectic mixture between Au on one wafer and PECVD amorphous silicon on the other wafer (Fig. 4).

The test apparatus is presented in Fig. 5, with the meniscus oscillations extracted from high-speed video (Fig. 6). The engine's self-induced oscillation frequency was 542 Hz, with an amplitude of >10 microns. This is the first demonstration of the self-oscillating behavior on a chip, providing an initial building block for a new class of thermal energy harvesting MEMS.

WORD COUNT: 598

REFERENCES

[1] T. Monin, A. Tessier-Poirier, É. Léveillé, A. Juneau-Fecteau, T. Skotnicki, F. Formosa, S. Monfray, L.G. Fréchette, "First experimental demonstration of a self-oscillating fluidic heat engine (SOFHE) with piezoelectric power generation," J. of Phys.: Conf. Ser., vol. 773, no 012039, from 16th Int'l Workshop on Micro and Nanotech. for Power Generat. and Energy Convers. Apps (PowerMEMS 2016), Paris, France, 6-9 Dec., (2016).

[2] S. Whalen, M. Thompson, D. Bahr, C. Richards, R. Richards, "Design, fabrication and testing of the P3 micro heat engine", Sensors and Actuators, Vol. 104, pp. 290-298, (2003).

[3] O. Puscasu, S. Monfray, C. Maitre, J.P. Permeant, F. Boeuf, G. Savelli, F. Gaillard, D. Guyomar, T. Skotnicki, "A disruptive technology for thermal to electrical energy conversion", Microelectronics Journal, Vol. 45, No. 5, pp. 554-558, (2014).

[4] T. Huesgen, J. Ruhhammer, G. Biancuzzi and P. Woias, "Detailed study of a micro heat engine for thermal energy harvesting", J. Micromech. Microeng. Vol. 20, (2010).

[5] A. Tessier-Poirier, T. Monin, É. Léveillé, F. Formosa, S. Monfray, L.G. Fréchette, "Influence of nonlinearities on the power output of the Self-Oscillating Fluidic Heat Engine (SOFHE), " J. of Phys.: Conf. Ser., vol. 773, no 012113, from 16th Int'l Workshop on Micro and Nanotech. for Power Generat. and Energy Convers. Apps (PowerMEMS 2016), Paris, France, 6-9 Dec., (2016).

[*] Currently at X-Fab, Corbeil-Essonnes, France

978-1-940470-03-0/HH2018/$25©2018TRF
DOI 10.31438/trf.hh2018.104

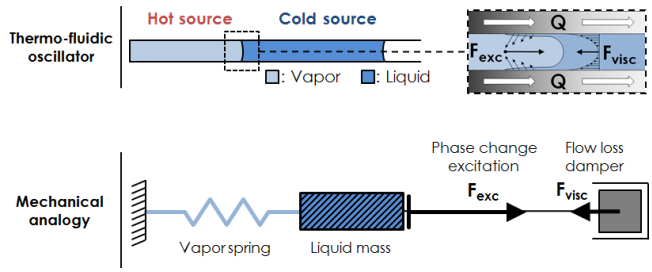

Figure 1: Schematic of the self-oscillating fluidic heat engine (SOFHE), with the spring-mass analogy.

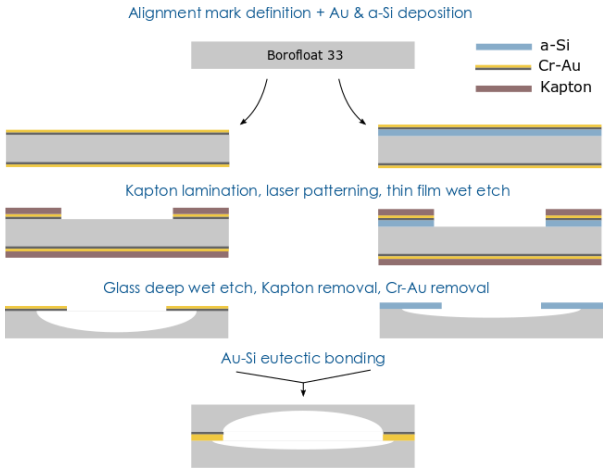

Figure 2: Process flow.

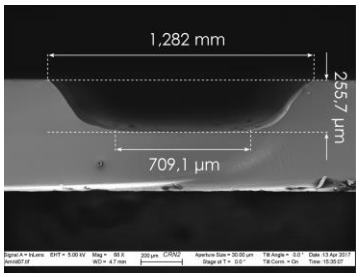

Figure 3: Wet etched half-microchannel in Borosilicate glass.

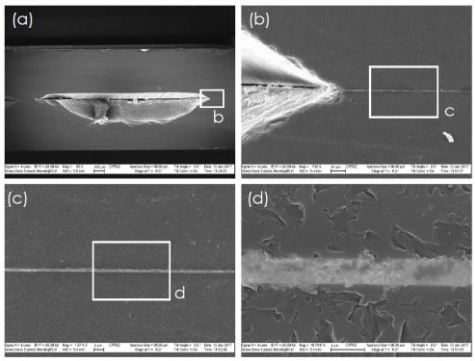

Figure 4: Device cross section after bonding, showing sharp corner formed for wicking purpose and the eutectic bonded interface using a thin PECVD a-Si layer and an Au layer to join the Borosilicate glass wafers.

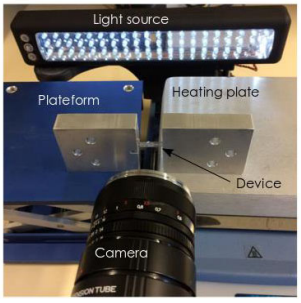

a) Test apparatus

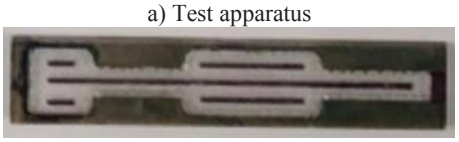

b) SOFHE microfluidic chip (6 x 25 mm)

Figure 5: Test apparatus (a), consisting of hot and cold plates supporting the chip at opposite ends, and a high-speed camera to visualize the meniscus position over time. Test chip close-up(b).

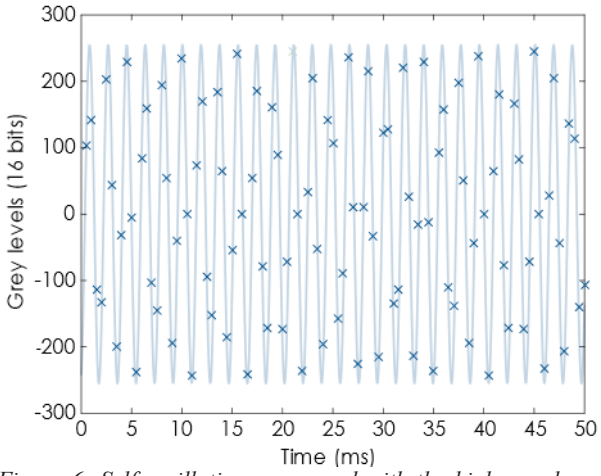

Figure 6: Self-oscillations measured with the high-speed camera, achieved using water in the above SOFHE chip at a hot plate temperature of 175°C.

Table 1: Measured operating conditions for the microfabricated SOFHE.

Self-oscillating operation	
Frequency	542 Hz
Amplitude	> 10 µm

DIRECT MEASUREMENTS OF ANCHOR DAMPING IN PRESSURE-LIMITED RING RESONATORS

G.D. Vukasin[1], J. Rodriguez[1], L. Comenencia Ortiz[1], G.M. Glaze[1], D.D. Gerrard[1], C.H. Ahn[1], Y. Yang[2], J. Lake[3], R.N. Candler[4], and T.W. Kenny[1]

[1]Stanford University, Stanford, CA, USA, [2]Integrated Device Technology Incorporated, San Jose, CA, USA, [3]uBeam, Los Angeles, CA, USA, [4]University of California, Los Angeles, CA, USA

ABSTRACT

We measure the quality factor (Q) due to gas damping, thermoelastic dissipation (TED), and anchor damping of a ring resonator operating in the wineglass mode. We analyze the Q over a range of temperatures and pressures and compare anchor damping of two different anchor designs. This method provides a path towards better understanding of anchor damping in MEMS.

INTRODUCTION

MEMS resonators lose energy due to gas damping, thermoelastic damping, anchor damping, and the Akhiezer effect. The effect of these damping mechanisms on the performance of MEMS resonators is expressed by the quality factor (Q), which determines fundamental noise in MEMS devices [1, 2]. The total Q can be calculated as the reciprocal sum of each damping mechanism:

$$\frac{1}{Q} = \sum \frac{1}{Q_{factors}} = \frac{1}{Q_{Gas}} + \frac{1}{Q_{TED}} + \frac{1}{Q_{Anchor}} + \frac{1}{Q_{Akhiezer}} + \frac{1}{Q_{Others}} \quad (1)$$

Previously, we have studied resonators whose primary damping mechanisms were thermoelastic dissipation (TED) and anchor damping [3]. In this paper, we have found a device that is dominated by gas damping and includes contributions from TED and anchor damping, and we quantitatively identify the contributions from each of these mechanisms.

METHODS

The device is a ring resonator operated in the *n=2 wineglass* mode at 145 kHz, as illustrated in Figure 1. There are two anchor designs for this device. The first is a pure silicon anchor fixed to the center (10 µm in diameter) of the device, which is attached to the epitaxial polysilicon cap. The polysilicon cap is attached to the substrate via the device layer and a layer of silicon oxide. The other design includes anchors at two points on the perimeter (3 µm wide) of the ring resonator in the device layer, which are connected to the substrate via silicon oxide. Examples of the two anchor designs are shown in Figures 1a and 1b. The die was fabricated with the established epi-seal encapsulation process [4].

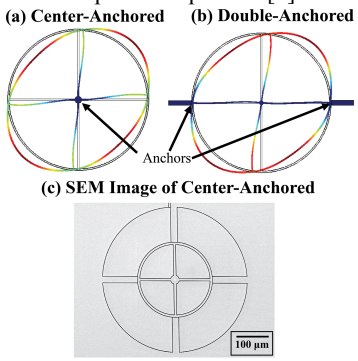

Figure 1: (a) COMSOL simulation of displacement in the wineglass mode (n=2) of center-anchored ring, (b) COMSOL simulation of wineglass mode (n=2) of double-anchored ring. These mode shapes are similar, but not exactly identical. (c) SEM image of center-anchored ring prior to completion of encapsulation process.

For each device, we used a liquid nitrogen cooled ultra-high vacuum (UHV) pressure chamber to study Q as a function of temperature (85 K to 300 K) and pressure (10^{-4} Pa to 10^{-1} Pa). We begin with measurements of Q(T) for sealed devices, followed by using a focused ion beam (FIB) to vent these sealed devices enabling Q(P) measurements at room temperature to identify the contribution of pressure damping in the sealed devices. Finally, we measure Q(T) for vented devices at UHV pressures over temperature.

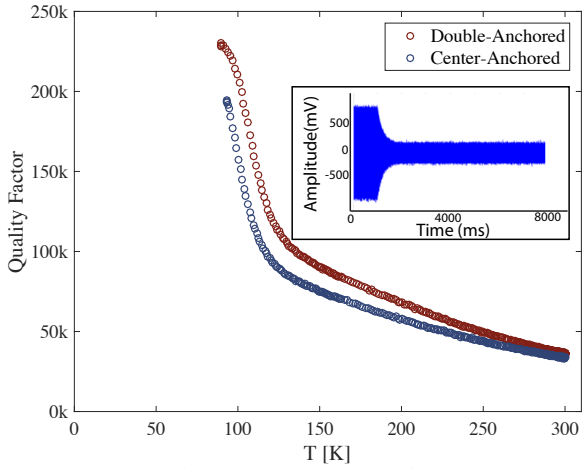

Figure 2: Quality factor vs. temperature of encapsulated double and center-anchored rings. The inset shows a representative ringdown measurement, which is used to calculate Q.

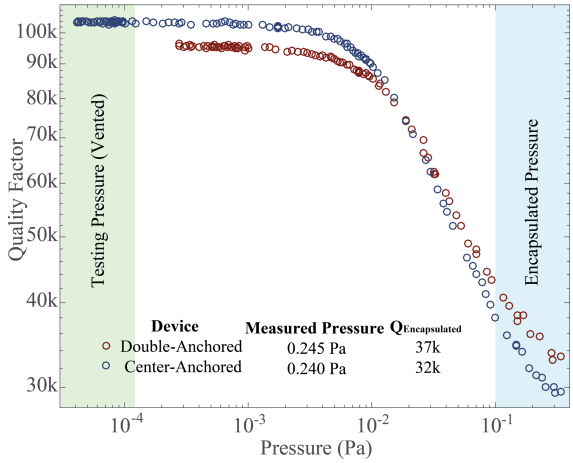

Figure 3: Pressure sweep of double and center-anchored devices at room temperature. The areas indicate the typical pressure range for our encapsulated device (blue) and the pressure where the vented devices were tested (green).

978-1-940470-03-0/HH2018/$25©2018TRF
DOI 10.31438/trf.hh2018.105

As described in previous work [3, 5] our measurements of Q(T) at low temperature on vented devices reveal Q in the absence of pressure damping (UHV conditions) and TED (the thermal expansion coefficient in Si crosses zero at 120 K, which disables coupling between mechanical and thermal effects, and therefore disables TED) [6]. Therefore, we directly detect anchor damping at the peak of the Q(T) curve.

RESULTS

As seen in Figure 2, Q increases at low temperature for both devices without a Q(T) peak at 120 K, which would be the unique signature of a strong TED contribution [5]. For both devices, we see a dramatic change in the slope around 140 K, possibly indicating presence of a two-component gas mixture inside this encapsulation.

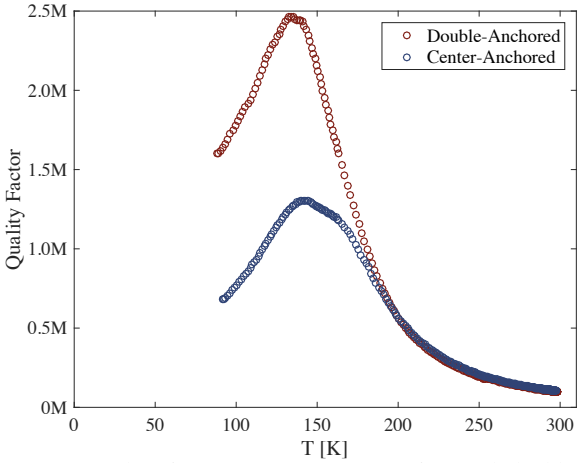

Figure 4: Quality factor vs. temperature of vented double and center-anchored rings. The peak Q of the double-anchored ring is 2.5M and peak Q of the center-anchored ring is 1.3M. These peaks are a consequence of the zero-crossing in the temperature dependence of the thermal expansion coefficient of Si, which disables TED, leaving only a contribution from anchor damping.

After FIB-venting, Q(P) measurements (Figure 3) indicate that the sealed devices were dominated by pressure damping, and that vented devices operated in vacuum reach a limit from other damping mechanisms. Q(T) experiments on vented devices of both designs under UHV conditions are shown in Figure 4. These Q(T) *measurements* for both devices have a profile that is characteristic of TED limited devices [5], with the Q at the peak in Q(T) indicating the contribution of anchor damping.

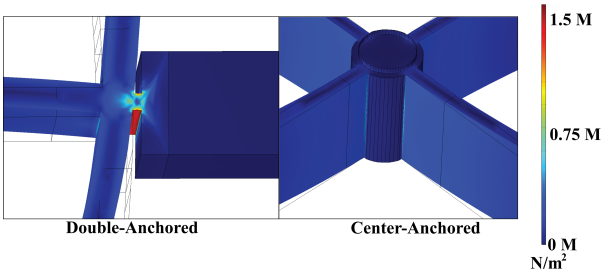

Figure 5: Plots of von Mises stress in the double-anchored device (left) and center-anchored device (right).

These experiments lead to the initially surprising conclusion that the anchor damping of a center-anchored ring resonator is stronger than for a ring resonator with a pair of side anchors. Figure 5 shows simulations of the von Mises stress for both types of anchors. Looking closely at these stress distributions, it is clear that there is significantly more stress trapped in the flexures that connect the rings to the side anchors of the double-anchored device than in the center anchor. The stresses that are not trapped in the anchors must propagate further into the substrate, and would be expected to cause stronger energy loss from the vibrational mode.

Another interesting result is that at UHV, the room-temperature Q of the center-anchored device is larger (Figure 3). We believe this means that the center-anchored device has more pressure damping than the double-anchored device due to the difference in mode shape of the two devices.

An important result of this study is the recognition that this comprehensive experimental investigation (Q(T) for sealed devices, Q(P) for vented devices, Q(T) for vented devices) was necessary to construct an accurate understanding of the damping mechanisms in these devices. If we had relied only on room temperature measurements, we could not have accurately accounted for TED, and therefore it would have been impossible to make convincing arguments about the anchor damping contribution.

We recommend that a process like this be carried out in any study in which researchers are interested in achieving a complete and accurate understanding of damping mechanisms in their devices.

CONCLUSION

Measuring Q(T) over a wide temperature range is the best path to reliable identification and quantification of damping mechanisms in MEMS resonators. For the ring resonators studied here, we demonstrate this method and provide the first direct measurement of anchor damping in these devices. At the conclusion of this work, we were surprised to find that the single, center-anchored resonator had stronger anchor damping than the dual-side anchored design. Looking ahead, we will use experiments like this on many more resonators to build capability for quantitative prediction of anchor damping in MEMS.

REFERENCES

[1] J. T. M. van Beek and R. Puers, "A review of MEMS oscillators for frequency reference and timing applications", Journal of Micromechanics and Microengineering, 22, 1 (2012).

[2] T. B. Gabrielson, "Mechanical-thermal noise in micromachined acoustic and vibration sensors", IEEE Transactions on Electron Devices, 40, 5 (1993).

[3] J. Rodriguez, D.D. Gerrard, G.M. Glaze, S. Chandorkar, L. Comenencia, Y. Chen, I. B. Flader, T.W. Kenny, "Direct measurements of anchor damping in MEMS resonators", Technical Digest of the 2017 IEEE Sensors, Glasgow, Scotland, UK, 10/30 – 11/1/17, IEEE (2017), pp. 1-3.

[4] E A. Partridge and M. Lutz, "Epi-seal pressure sensor and method for making an episeal pressure sensor", U.S. Patent 6928879, 2005., U.S. Patent 6928879, 2005.

[5] J. Rodriguez, D. D. Gerrard, S. Chandorkar, Y. Chen, G. M. Glaze, I. B. Flader, C. H. Ahn, E. J. Ng, and T. W. Kenny, "Wide-range temperature dependence studies for devices limited by thermoelastic dissipation and anchor damping", Technical Digest of the 2017 19th International Conference on Solid-State Sensors, Actuators and Microsystems, Kaohsiung, Taiwan, 6/18-22/17, IEEE and Electron Devices Society (2017), pp. 1100-1103.

[6] T. Middelmann, A. Walkov, G. Bartl, and R. Schödel, "Thermal expansion coefficient of single-crystal silicon from 7 K to 293 K", Phys. Rev. B, 92, 17 (2015).

IMAGING GIGAHERTZ DYNAMICS IN MICROMECHANICAL RESONATORS USING ULTRAFAST PULSED LASER INTERFEROMETRY

L. Shao[1,2], V.J. Gokhale[1,3], J.C. Kuo[4], A. Lal[4], and J.J. Gorman[1]*
[1]National Institute of Standards and Technology, Gaithersburg, Maryland, USA
[2]Department of Mechanical Engineering, University of Michigan, Ann Arbor, Michigan, USA
[3]Electrical Engineering and Computer Science Department, University of Michigan, Ann Arbor, Michigan, USA
[4]School of Electrical and Computer Engineering, Cornell University, Ithaca, New York, USA

ABSTRACT

Optical measurements of resonant MEMS can provide direct insight into their dynamics and guide improvements in device performance. This paper presents an optical method based on pulsed laser interferometry that can measure vibrations of MEMS resonators under coherent RF excitation with sub-picometer resolution and at arbitrary frequencies potentially well beyond 10 GHz. Vibration amplitude and phase can be measured across the entire resonator, thereby enabling experimental modal analysis and the imaging of complex dynamics, including mode mixing.

INTRODUCTION

Resonant MEMS operating at frequencies above 1 GHz [1,2] are of great interest for efficient filtering and signal processing in wireless communications and advanced computing. However, the performance of these resonators is still not well understood, including their nonlinear dynamics, dissipation mechanisms, and vibrational modes. This is largely due to limitations in the measurement tools that are available. For example, electrical RF test equipment, although widely used, cannot provide information on mode shapes or the causes of acoustic loss. This paper presents a new interferometric approach that can measure vibrations beyond 10 GHz with sub-picometer resolution, which provides direct insight into the dynamics of resonators operating above 1 GHz.

Conventional optical methods, including interferometric [3], photoelastic [4], and knife-edge techniques [4], use a continuous-wave (CW) laser whose frequency, phase, or intensity is modulated by resonator vibrations. For these methods, a photodetector with bandwidth greater than the vibration frequencies of interest must be used to measure the optical signal. However, resonator vibrations typically become progressively smaller with increasing frequency. Furthermore, the noise in photodetectors and amplifiers, parasitic capacitance and coupling in cables, and electromagnetic interference all increase with increasing frequency. The combination of these issues makes the use of conventional CW optical methods above 1 GHz extremely challenging.

INTERFEROMETRIC METHOD

Due to the above limitations, we have developed a new approach using ultrafast pulsed laser interferometry (PLI) (Fig. 1(a)) that addresses these issues. The laser pulse train forms an electrical frequency comb with individual teeth equally spaced by the repetition rate (f_p), as measured using a fast photodetector (Fig. 1(b)). By tuning f_p, one of the comb frequencies ($n*f_p$) can be placed close to the resonator excitation frequency (f_{ex}), with a measurable offset ($f_b = |f_{ex}-n*f_p|$). Thus, the laser pulse acts like a strobe that mixes down high-frequency vibrations to a beat signal, f_b. A low-bandwidth photodetector is used to measure f_b, which is processed with a lock-in amplifier. While stroboscopic interferometric techniques have been previously reported, they have been limited to operation either below 1 GHz [5] or at discrete, widely separated frequencies [6]. Our approach works at any frequency above 0.95 GHz and has a noise floor comparable to a CW interferometer operating below 1 MHz (≈ 30 fm/√Hz, which is shot noise limited).

RESULTS AND DISCUSSION

Vibration results for two MEMS resonators are presented here. The first is a silicon width-extensional bulk acoustic resonator (BAR) [4] with a third-order in-plane mode around 0.983 GHz (Fig. 2(a)). The out-of-plane displacement is measured, which results due to the Poisson effect. The excitation was swept by 1 MHz around resonance, beating with the 19th tooth (981.35 MHz) of the comb (f_p = 51.65 MHz). The frequency response found with PLI is compared to that obtained by conventional CW laser interferometry in Fig. 3. The signal-to-noise ratio (SNR) is already 4 dB better for PLI while only just approaching 1 GHz. Figure 4 shows surface maps of the vibration amplitude (≈ 3 pm) and phase for the third-order mode.

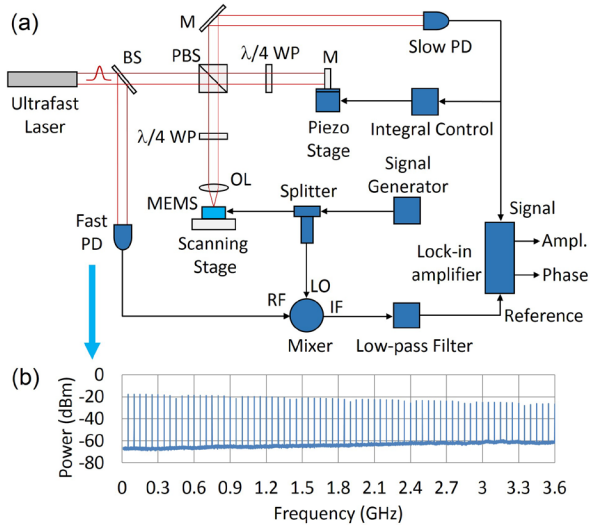

Figure 1: (a) Schematic of the ultrafast pulsed laser interferometer (PLI) (BS: beam splitter, PBS: polarizing beam splitter, PD: photodetector, M: mirror, λ/4 WP: quarter wave plate, OL: objective lens). (b) Power spectrum of the laser pulse train measured with a 12.5 GHz fast photodetector, showing a frequency comb with individual teeth spaced by the pulse repetition rate (50.00 MHz). The maximum operational frequency of the PLI is set by the bandwidth of the fast PD, the splitter, and the mixer.

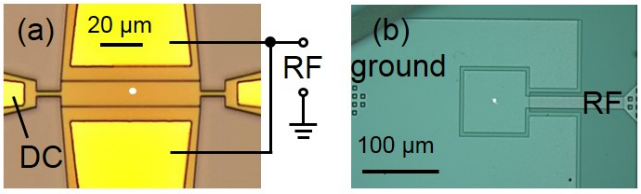

Figure 2: (a) Optical micrograph of a silicon width-extensional bulk acoustic resonator (BAR) with a width of 11.5 μm. Its measured third width-extensional mode is approximately 0.983 GHz. (b) Optical micrograph of an AlN bulk acoustic wave (BAW) transducer with a measured resonance frequency of approximately 2.35 GHz. The transducer size is 75 μm × 75 μm.

978-1-940470-03-0/HH2018/$25©2018TRF
DOI 10.31438/trf.hh2018.106

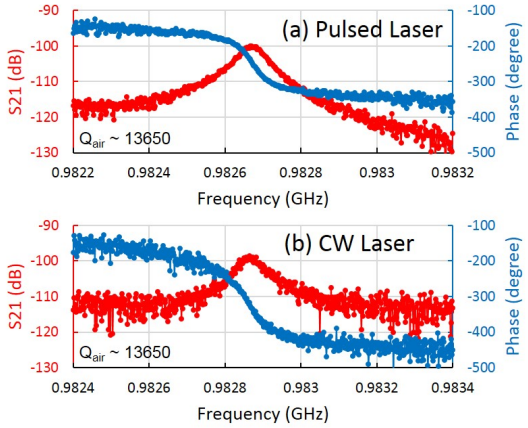

Figure 3: Frequency response of the BAR obtained by (a) pulsed laser interferometry and (b) CW laser interferometry. The resonator was operated in air with +10 dBm RF power and 21 V DC bias. The center frequencies differ slightly due to thermal drift and internal frequency inaccuracies in the different RF instruments used.

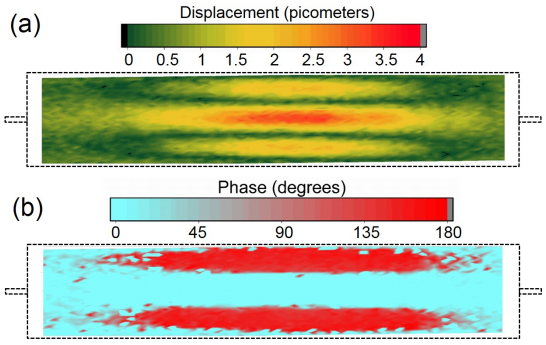

Figure 4: Mapping the BAR vibrations at 0.9827 GHz using pulsed laser interferometry: (a) vertical vibration amplitude and (b) phase. Drive conditions: 21 V DC bias and +10 dBm RF power. The dashed lines represent the outer dimensions of the BAR, 11.5 µm × 65 µm. The amplitude map clearly shows the expected third-order width-extensional mode. The phase transition along the width of the resonant body is nearly 180°, as expected.

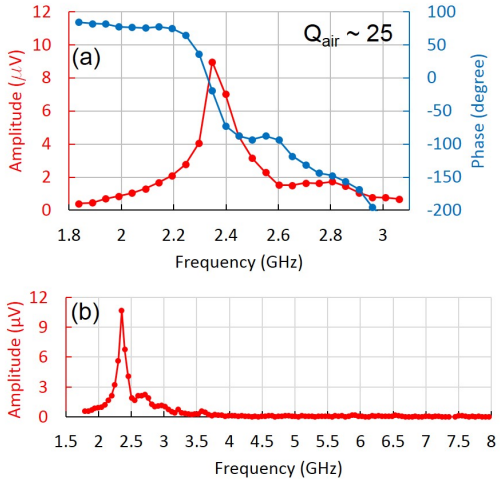

Figure 5: Frequency response of the AlN BAW obtained by pulsed laser interferometry, while operated in air with +10 dBm RF power: (a) mechanical resonance at 2.35 GHz and (b) up to 8.0 GHz.

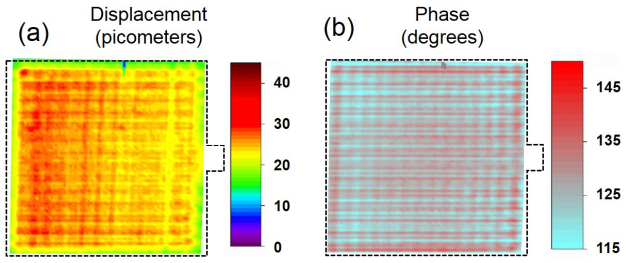

Figure 6: Mapping the BAW vibrations at 2.351 GHz: (a) vibration amplitude and (b) phase. The dashed lines represent the perimeter of the BAW. The mode shape shows the superposition of the main thickness mode with other lateral resonance modes.

The second device is an AlN bulk acoustic wave transducer (Fig. 2(b)) [7]. Its fundamental mode at 2.35 GHz is extremely difficult to measure using CW laser techniques. Since the resonance linewidth spans multiple comb teeth, the measurement is performed here by using a series of teeth (f_p = 50.0 MHz) while f_b is kept constant. The frequency response of the first thickness mode is shown to have an SNR of nearly 30 dB (Fig. 5(a)) and the BAW can be measured out to 8 GHz (Fig. 5(b)). The vibration amplitude and phase maps (Fig. 6) show the superposition of multiple modes, demonstrating that PLI can reveal complex dynamics. Since both displacement and phase are obtained, animations of modes can be generated, making PLI an invaluable tool for investigating the dynamics of gigahertz resonators.

ACKNOWLEDGMENTS

Research performed in part in the NIST Center for Nanoscale Science and Technology Nanofab. BAW fabricated by A*STAR.

REFERENCES

[1] D. Weinstein, and S.A. Bhave, "The Resonant Body Transistor", Nano Letters, 10, 1234 (2010).

[2] M. Rinaldi, C. Zuniga, C. Zuo, and G. Piazza, "Super-high-frequency Two-port AlN Contour-mode Resonators for RF Applications", IEEE transactions on ultrasonics, ferroelectrics, and frequency control, 57, 38 (2010).

[3] K. Kokkonen, and M. Kaivola, "Scanning Heterodyne Laser Interferometer for Phase-sensitive Absolute-amplitude Measurements of Surface Vibrations", Applied Physics Letters, 92, 063502 (2008).

[4] V.J. Gokhale, and J.J. Gorman, "Approaching the Intrinsic Quality Factor Limit for Micromechanical Bulk Acoustic Resonators Using Phononic Crystal Tethers", Applied Physics Letters, 111, 013501 (2017).

[5] K.L. Telschow, V.A. Deason, D.L. Cottle, and J.D. Larson, "Full-field Imaging of Gigahertz Film Bulk Scoustic Resonator Motion", IEEE Transactions on Ultrasonics, Ferroelectrics, and Frequency Control, 50, 1279 (2003).

[6] T. Fujikura, O. Matsuda, D.M. Profunser, O.B. Wright, J. Masson, and S. Ballandras, "Real-time Imaging of Acoustic Waves on A Bulk Acoustic Resonator", Applied Physics Letters, 93, 261101 (2008).

[7] J.C. Kuo, J.T. Hoople, M. Abdelmejeed, M. Abdel-moneum, and A. Lal, "64-pixel Solid State CMOS Compatible Ultrasonic Fingerprint Reader", 2017 IEEE 30th International Conference on Micro Electro Mechanical Systems (MEMS), Las Vegas, NV (2017), pp. 9-12.

CONTACT

*J.J. Gorman, tel: +1-301-975-3446; gorman@nist.gov

KNUDSEN-PUMP-BASED MICRO-HOVERCRAFTS

J. Cortes, C. Stanczak, and I. Bargatin
The University of Pennsylvania, Philadelphia, Pennsylvania, USA

ABSTRACT

We introduce polymer-membrane micro-hovercrafts which utilize incident light to generate the lift force. The light is absorbed by a carbon nanotube layer on one side of the membrane resulting in a temperature gradient along the thickness of the membrane, which in turn pumps air under the membrane via the mechanism of thermal transpiration. The hovercrafts float over a substrate at heights of ~50 µm, which agrees with the predictions of our theoretical model.

INTRODUCTION

The term "micro-flyer" is often used as a misnomer to describe centimeter-scale robotic systems that achieve sustained flight [1, 2]. However, the scaling of traditional propeller-based aircraft to dimensions of less than 1 cm, let alone the true micro scale, is extremely challenging [1], possibly requiring new flight mechanisms at the millimeter or micron scales. As a recent possible approach, the Knudsen force was used to make microscopic polycrystalline silicon plates hover and jump above microfabricated resistive heaters [3, 4]. Here, we show that that commercially available nano-porous membranes can hover above flat surfaces using thermal transpiration, which is also known as the Knudsen pump effect. When illuminated by light, the membranes can hover a few tens of microns above any flat surface, rather than only above a microheater.

PRINCIPLE OF OPERATION

Thermal transpiration, also known as thermal creep, is the flow of gas along channel walls that feature a temperature gradient along the length of the channel [5, 6]. The gas typically flows from the cold reservoir towards the hot reservoir (Fig. 1), which can be used to create a Knudsen pump [7]. If the bottom side of a porous membrane absorbs light more effectively than the top, thermal transpiration through the pores (channels) can be controlled by simply heating the membrane with a controlled light input. The resulting Knudsen pumping will push the gas under the membrane, floating the membrane above the surface on an air bearing, similar to toy pucks on air hockey tables.

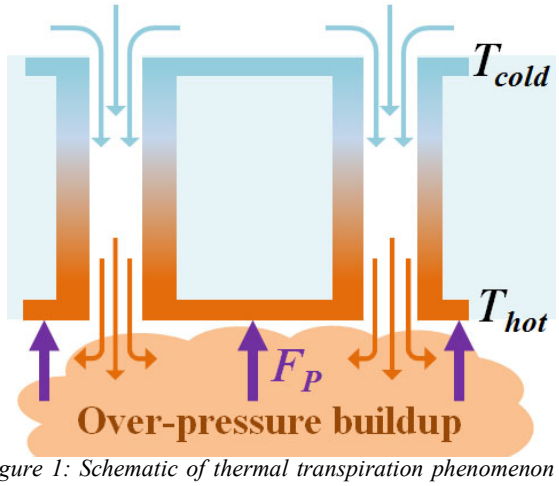

Figure 1: Schematic of thermal transpiration phenomenon at atmospheric pressure.

ASSEMBLY AND CHARACTERIZATION

10-µm-thick Sterlitech polycarbonate membranes are used as the basis for our micro-hovercrafts. These membranes feature hole diameters in the 80-100 nm range with a spacing of ~0.5 – 1 µm. Crucially, the membranes are poor thermal conductors, with a manufacturer-reported thermal conductivity of 0.20 W/(m·K). Similar thermally insulating porous membranes have shown the ability to pump gas using the Knudsen pump effect [7] at atmospheric pressure.

We coated one side of the membranes with carbon nanotubes to act as an absorbing layer which created the temperature difference required for thermal transpiration. To minimize thermal stress-induced deflection, some of the membranes were glued to a microfabricated silicon ring. This ring was 200 µm tall with a wall thickness of 50 µm. Figure 2 shows a photograph of the microfabricated silicon ring and a scanning electron micrograph of the membrane.

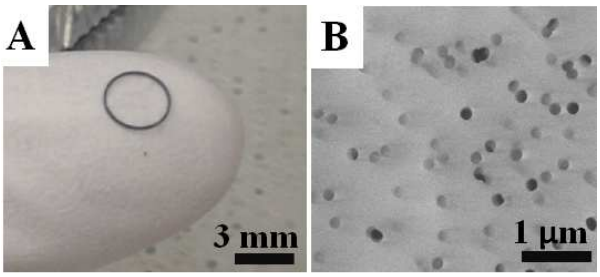

Figure 2: A) Picture of microfabricated Si ring which can be added for rigidity and flatness B) SEM pictograph of a membrane's surface with pores showing as dark circles.

THEORETICAL MODEL

The mass flow rate through a long tube due to a temperature gradient between two large reservoirs can be expressed as [5, 8]:

$$\dot{M}^{tb} = -\alpha P + \gamma \Delta T, \qquad (1)$$

where P is the over-pressure under the membrane, ΔT is the temperature differential between the top and bottom surfaces and α and γ are functions derived using numerical data presented by Sharipov [8] for varying levels of rarefaction. The generated over-pressure distribution can be modeled by equating the downward flow through the membrane to the radial outward flow underneath the membrane. Assuming Poiseuille flow underneath the patterned membrane, the over-pressure profile can be obtained by solving the differential equation:

$$-\frac{d^2P}{dr^2} - \frac{dP}{dr}\left(\frac{1}{r}\right) + \frac{8FF\alpha\mu P}{\sqrt{3}\rho h^3 b^2} = \frac{8FF\gamma\mu\Delta T}{\sqrt{3}\rho h^3 b^2}, \; P(R) = 0, \; P'(0) = 0, \qquad (2)$$

where h is the gap height, FF is the geometric fill factor, ρ is the air density, μ is the air viscosity, R is the radius of the hovercraft membrane, and b is the pitch between the tubes. The imposed boundary conditions assure that at the edge of the patterned disk, the over-pressure goes to zero, so that it equals the surrounding environmental pressure. Additionally, it is assumed that over-pressure profile flattens at the center of the disk due to the radial symmetry. Assuming that the membrane and the air in the pores

978-1-940470-03-0/HH2018/$25©2018TRF
DOI 10.31438/trf.hh2018.107

conduct heat in parallel, the temperature difference between the top and bottom surfaces of the disk can be expressed as:

$$\Delta T = \frac{L\epsilon I(6b^2-\sqrt{3}a^2\pi)}{6b^2\kappa_{pc}+\sqrt{3}a^2\pi(\kappa_{air}-\kappa_{pc})}, \quad (3)$$

where a is the tube radius, L is the membrane thickness, ϵ is the carbon nanotube film absorbance (assumed to be approximately 90%), I is the incident optical flux and κ_{pc} and κ_{air} are the thermal conductivities of the polycarbonate membrane and air, respectively.

The lift force can be calculated by integrating the resulting over-pressure distribution over the surface of the disk. Figure 3 shows the generated lift force as a function of the height. The gap heights that can be achieved by micro-hovercrafts can be found by equating the lift force to the weight of the membrane, and are on the order of 50 µm above a substrate.

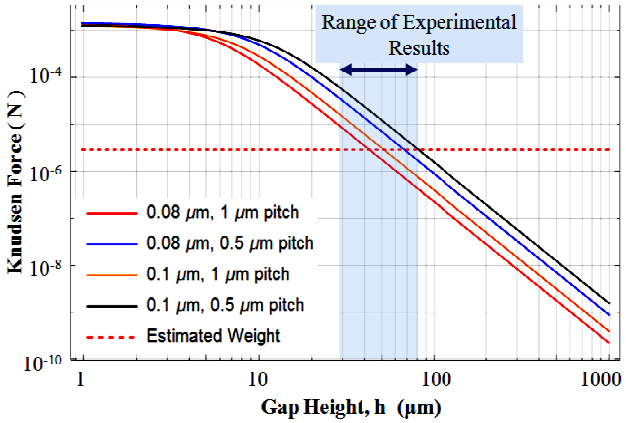

Figure 3: Estimated lift force generated by membranes with various pore diameters and pitch (solid curves). The dashed line shows the estimated device weight. The maximum height that can be achieved is represented by the intersection of the force line with the dotted estimated weight of the micro-flyer.

TESTING RESULTS

Testing of the micro-hovercrafts was performed at atmospheric temperature and pressure conditions and inside of a glass enclosure to minimize the effects of the ventilation currents in the room. A 100-watt LED array was used as the light source. Figure 4 shows the testing setup.

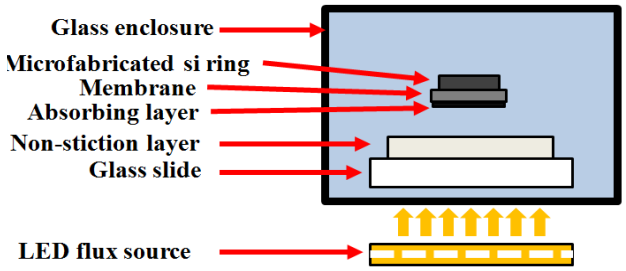

Figure 4: Schematic of the testing setup from the microscope camera point of view.

Figure 5 shows a progression of screenshots from a test flight. Numerous test flights have shown heights in the range of ~30-80 µm, consistent with the predictions of our theoretical model. The lift force and the hovering heights can be optimized further by using membranes with other pore diameters and spacing.

Our results demonstrate that low-thermal-conductivity porous membranes/films can float under illumination, opening new possibilities for levitating MEMS sensors and microflyers at the millimeter and micron scales.

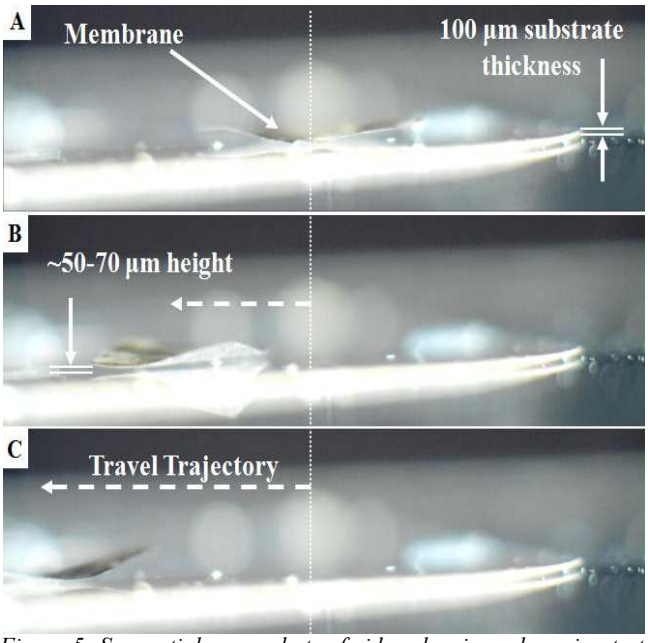

Figure 5: Sequential screenshots of video showing a hovering test flight (A→B→C). The 100-µm thick underlying substrate serves as a reference for in-flight gap height measurements using a microscope camera setup.

REFERENCES

[1] M. Piccoli, et al. "Piccolissimo: The Smallest Micro Aerial Vehicle." 2017 IEEE International Conference on Robotics and Automation (ICRA), 2017.

[2] K.Y. Ma, et al. "Controlled Flight of a Biologically Inspired, Insect-Scale Robot." Science, vol. 340, no. 6132, 2013, pp. 603–607.

[3] V. Foroutan, et al. "Levitation of untethered stress-engineered microflyers using thermophoretic (Knudsen) force," in Tech. Dig. Hilton Head Workshop 2014: A Solid-State Sensors, Actuators and Microsystems Workshop, Jun. 2014, pp. 105–106.

[4] S. Ward, et al. Towards Microscale Flight: Fabrication, Stability Analysis, and Initial Flight Experiments for 300 µm x 300 µm x 1.5 µm Sized Untethered MEMS Microflyers. IEEE Transactions on Nanobioscience. Volume 14, No. 3. 2015.

[5] A. Passian, et al. "Thermal Transpiration at the Microscale: A Crookes Cantilever." Physical Review Letters, vol. 90, no. 12, 2003.

[6] G.E. Karniadakis, et al. Microflows and Nanoflows: Fundamentals and Simulation. Springer New York, 2005.

[7] N. Gupta, et al. "A High-Flow Knudsen Pump Using a Polymer Membrane: Performance at and below Atmospheric Pressures." 2010 IEEE 23rd International Conference on Micro Electro Mechanical Systems (MEMS), 2010.

[8] F. Sharipov, et al. "Data on Internal Rarefied Gas Flows." Journal of Physical and Chemical Reference Data, vol. 27, no. 3, 1998, pp. 657–706.

ORIGAMI-ENABLED MICROFLUIDICS

X. Xie[1], C. Kelly[1], T. Liu[1], R.J. Lang[2], S. Gandolfo[1], Y. Boukataya[3], and C. Livermore[1]
[1]Northeastern University, Boston, Massachusetts, USA
[2]Lang Origami, Alamo, California, USA
[3]University of Pennsylvania, Philadelphia, Pennsylvania, USA

ABSTRACT

Conventional polymer microfluidics manipulate flows for cell culture and analysis of biological specimens at low cost, but they do not accurately replicate the 3D microstructure and complex transport of living tissues. We present a new paradigm for rapidly creating microfluidics that embody the 3D microstructure and complex transport of natural tissues. In this origami-based approach, polyimide tape patterned to define flow pathways and crease locations is co-folded with nanoporous membranes in an interlocked architecture. The folding produces a multi-material, 3D microfluidic architecture with pressure-driven flow in continuous channels mimicking vasculature and diffusion across nanoporous membranes mimicking perfusion from the bloodstream into adjacent tissues. The simulated perfusion is experimentally characterized using a chemical marker. The results are consistent with Fick's Law, indicating that the origami-enabled, multi-material architecture replicates biomimetic flow and diffusive transport.

INTRODUCTION

Creating biomimetic, chip-based tissue models with 3D microstructure remains a challenge. Traditional microfluidic architectures excel at creating in-plane complexity [1-3], but increasing 3D complexity requires a corresponding increase in the number of fabrication steps. In addition, the traditional materials of polymer microfluidics can accurately mimic flow through blood vessels, but they do not accurately replicate more complex in vivo transport. For example, fluids perfuse from capillary beds into neighboring tissues, and nutrients in the liver diffuse from the bloodstream to the hepatocytes to prevent shear stress from pressure-driven flow. The present work demonstrates the design and simple, straightforward manufacture of self-aligned, origami-enabled, multi-material microfluidic devices that enable both flow and diffusive transport in a scalable 3D platform.

EXPERIMENTAL

Figure 1 shows schematic diagrams of the basic origami-folded architecture. One inlet and outlet serve one set of unstructured microchannels; a second inlet and outlet serve a second set of microchannels that are interleaved between the first. Adjacent microchannels are separated by the folded nanoporous membrane. Figure 2 illustrates the fabrication process, in which a strip of laser-cut polyimide tape is cross-folded with a strip of nanoporous membrane. The final structure (Figure 3) includes a set of two "source" microchannels above and below a third "target" microchannel. Figure 4 shows an alternate device in which the out-of-plane microstructure is complemented by in-plane microstructure, in this case a hexagonal flow architecture that reflects the hexagonal symmetry of a liver lobule.

To characterize the device's flow/diffusion performance, the channels are first filled with water. A syringe pump drives a solution of 1000:1 water:acetic acid through the source channels and water through the target channel at various flow rates. The flow exiting the target channel is captured, and its pH is recorded vs. flow rate.

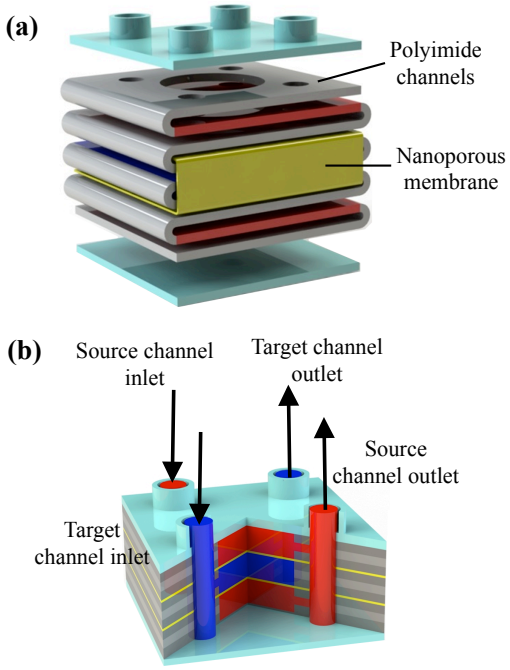

Figure 1: (a) Schematic diagram of the architecture of the flow/diffusion microfluidic device, showing the interlocked folding of polyimide channels and nanoporous membrane perpendicular to each other. Gray indicates the polyimide tape in which the functional chambers (large circles) and the inlet and outlet ports (four smaller circles) are defined; red indicates the portions of the polyimide tape in which the functional chambers are connected to the inlet and outlet ports; and yellow indicates the nanoporous membrane. (b) Schematic diagram of the resulting flow architecture, gray and yellow indicating polyimide channels and nanoporous membranes, respectively. Red indicates the interior of the source channels (analogous to blood vessels), and blue indicates the interior of the target channels (analogous to adjacent tissues). Source channels are connected to a common inlet and outlet, while target channels have their own inlet and outlet. The source and target channels are connected to each other via diffusion across the nanoporous membrane that separates them.

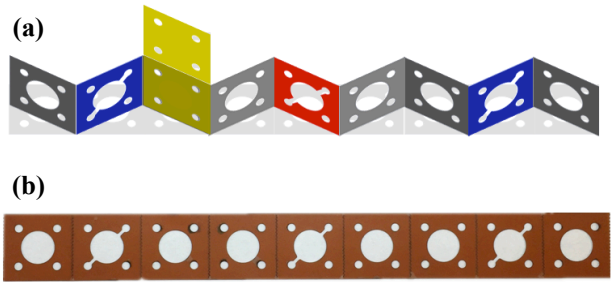

Figure 2: (a) Diagram of the interlocked cross-folding process; photograph of channels and creases laser-cut in polyimide tape.

978-1-940470-03-0/HH2018/$25©2018TRF
DOI 10.31438/trf.hh2018.108

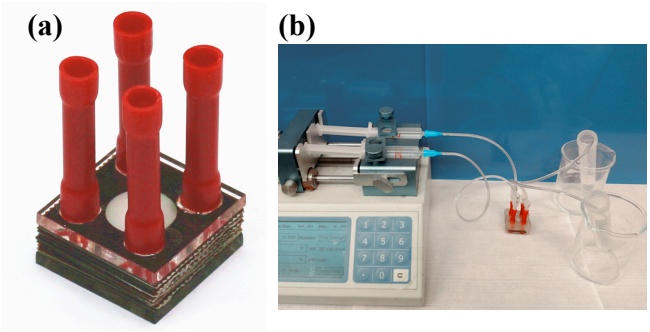

Figure 3: (a) Photograph of a 2 cm square, origami-folded microfluidic flow/diffusion device with attached tube connectors. The polyimide layers are 240 μm thick; each functional chamber comprises three polyimide layers as shown in Figure 1b, for a total chamber thickness of 720 μm. The nanoporous membranes are 10 μm thick polycarbonate Whatman Nuclepore Track-Etched Membranes with a pore size of 0.2 μm. (b) Photograph of the device under test.

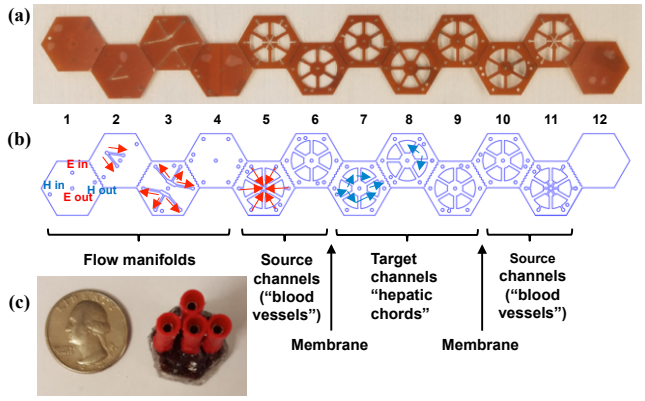

Figure 4: (a) Photograph and (b) layout of polyimide tape patterned such that, upon co-folding with a nanoporous membrane, it mimics the in-plane hexagonal and out-of-plane layered architecture of a liver lobule, with miniature blood vessels interspersed with sheets of hepatocytes. (c) Photograph of the completed hexagonal microfluidic device (20 mm in its widest dimension).

RESULTS

Flow through a laminar, pressure-driven network reflects the network's flow resistances, and flow distribution is largely independent of flow rate. In contrast, diffusive transport should increase concentration in the target channel in inverse proportion to the flow rate. The increase in concentration of H_3O^+ in the target channel (neglecting the effects of buffering) is plotted vs. the inverse flow rate in Figure 5, showing an increasing trend that is consistent with Fick's Law. The results indicate that the simple origami-folded devices are functionally free of pressure-driven leakage between the interacting fluid networks while also exhibiting the intended diffusive behavior.

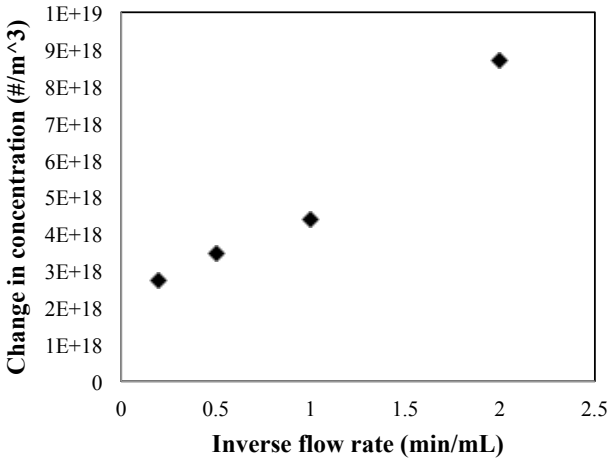

Figure 5: Change in concentration of H_3O^+ as deduced from pH values measured in the flow exiting the target channel and plotted vs. the inverse flow rate. Effects of buffering are neglected. The change in concentration increases as flow rate decreases, consistent with the predictions of Fick's Law in which flux is determined by the difference in concentration, the geometry, and the diffusivity. With the reduced residence time of higher flow rates, the same flux produces a smaller change in concentration, in contrast to the expected behavior for pressure-driven flow.

The devices created in this way exceed the capabilities of conventional microfluidics. Their fabrication is simple and straightforward, and their creased origami structure automatically ensures correct interlayer alignment. This technique offers an accessible pathway to 3D microstructured, engineered tissues that manifest the complex flow/diffusion functionality of native tissues.

REFERENCES

[1] G.M. Whitesides, "The origins and the future of microfluidics", *Nature* 442, 368 (2006).

[2] M.A. Unger, H-P. Chou, T. Thorsen, A. Scherer, and S.R. Quake, "Monolithic microfabricated valves and pumps by multilayer soft lithography", *Science* 288, 113-116 (2000).

[3] D.M. Hoganson, H.I. Pryor, I.D. Spool, O.H. Burns, J.R. Gilmore, and J.P. Vacanti, "Principles of biomimetic vascular network design applied to a tissue-engineered liver scaffold", *Tissue Engineering Part A* 16, 1469-1477 (2010).

ACKNOWLEDGMENTS

This research was funded by NSF and AFOSR through the EFRI-ODISSEI Program under award number 1332249.

CONTACT

C. Livermore, tel. +1-617-373-4922; livermore@neu.edu

Author Index

Scroll to the author and select a **Blue** link to open a paper. After viewing the paper, use the bookmarks to the left to return to the beginning of the Author Index.

C

D

E

F

G

H

I

J

K

L

M

S

T

V

W

X

Y

Z

Keyword Index

Scroll to the keyword and select a **Blue** link to open a paper. After viewing the paper, use the bookmarks to the left to return to the beginning of the Keyword Index.

D

E

F

G

H

I

J

K

L

M

N

O

P

Q

R

S

T

U

V

W

X

Y

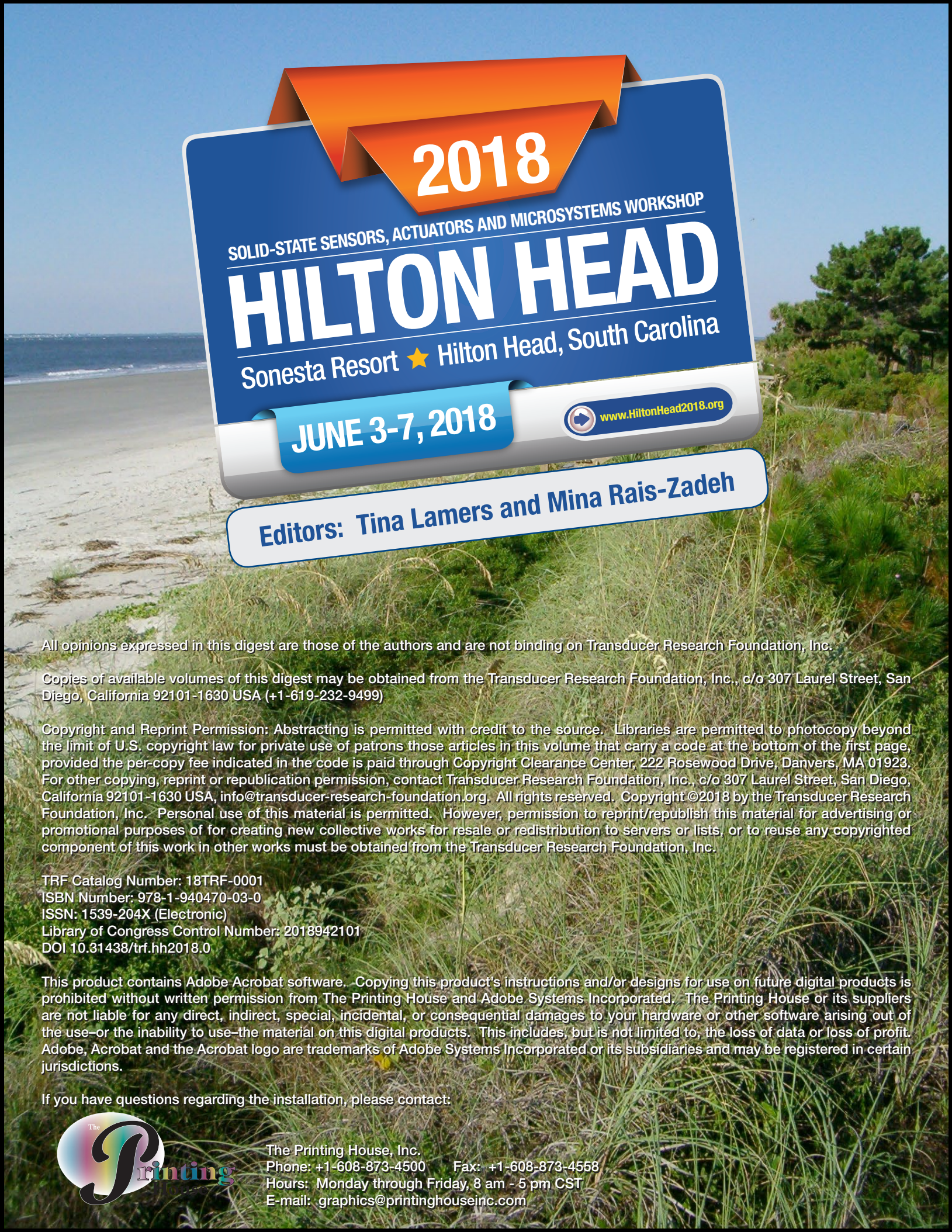

TRF Catalog Number: 18TRF-0001
ISBN Number: 978-1-940470-03-0
ISSN: 1539-204X (Electronic)
Library of Congress Control Number: 2018942101
DOI 10.31438/trf.hh2018.0